JOURNAL OF THE ELECTROCHEMICAL SOCIETY

ECTROCHEMICAL
ENCE AND TECHNOLOGY

LID-STATE
ENCE AND TECHNOLOGY

EWS AND NEWS
Spring Meeting Program
Call for Papers—
Washington, D.C., Meeting
all for Recent News Papers—
San Francisco, California, Meeting

VOL. 130, NO. 3 MARCH 1983

JESOAN 130 (3) 533-736, 45C-160C

FUTURE MEETINGS

SAN FRANCISCO, CALIFORNIA—MAY 8-13, 1983— HEADQUARTERS AT THE ST. FRANCIS HOTEL

Final program published in the March 1983 issue of **This Journal.**

WASHINGTON, DC—OCTOBER 9-14, 1983— HEADQUARTERS AT THE SHERATON-WASHINGTON HOTEL

The detailed Call for Papers published in the December 1982-May 1983 issues of **This Journal.** Final program published in the August 1983 issue of **This Journal.**

Planned symposia for the Washington Meeting include the following Divisions, Groups, Subcommittee, and subjects: **Battery**—Secondary Alkaline Batteries, Flow Batteries, Lithium Batteries, General Session; **Battery/Energy Technology**—Advances in Battery Materials and Processes; **Battery/Physical Electrochemistry**—Alkaline and SPE Fuel Cells, Electrolyzers and Regenerative Systems; **Corrosion**—General Session; **Corrosion/European Federation of Corrosion**—Fundamental Aspects of Corrosion Protection by Surface Modification; **Corrosion/Physical Electrochemistry**—Hydrodynamic Effects of Corrosion; **Dielectrics and Insulation/Corrosion/Electronics**—Materials Problems in Device Packaging; **Dielectrics and Insulation/Electronics**—Patterning Science and Technology 1983, Thin Film Interfaces and Interactions; **Electrodeposition**—Nonaqueous Electrodeposition Processes, General Session; **Electrodeposition/Corrosion**—Electric Contacts, Connectors, and Interconnections; **Electronics**—Business and Government Aspects of the Semiconductor Industry; **Electronics/Dielectrics and Insulation**—High Pressure Oxidation for Semiconductor Devices, Semiconductor Interconnects and Contacts, Joint General Session, Joint Recent News Papers Session; **Electronics/Physical Electrochemistry**—Electrochemistry in Semiconductor Technology; **Energy Technology**—General Session; **Energy Technology/Battery**—Operational Experience with Emerging Energy Conversion and Storage Technologies; **Energy Technology/Battery/Industrial Electrolytic/Physical Electrochemistry**—Oxygen Electrodes for Energy Applications; **High Temperature Materials/Corrosion**—High Temperature Erosion and Corrosion; **High Temperature Materials/Electrodeposition/Industrial Electrolytic**—Electrodeposition of Refractory Metals; **Industrial Electrolytic**—General Session; **Luminescence and Display Materials/Electronics**—Materials and Fabrication Techniques for Display Devices; **Physical Electrochemistry**—The Use of Computers in Experimental Electrochemistry, General Session; **New Technology Subcommittee**—Reindustrialization of the United States.

CINCINNATI, OHIO—MAY 6-11, 1984—HEADQUARTERS AT STOUFFERS CINCINNATI TOWERS

The detailed Call for Papers published in the July-November 1983 issues of **This Journal.** Final program published in the March 1984 issue of **This Journal.**

Planned symposia for the Cincinnati Meeting include the following Divisions, Groups, Subcommittee, and subjects: **Corrosion**—General Session; **Corrosion/High Temperature Materials/Energy Technology**—Mechanisms of High Temperature Corrosion in Advanced Energy Systems; **Dielectrics and Insulation/Electrodeposition/Electronics**—Electrophoretic Deposition; **Dielectrics and Insulation/Electronics**—Thin Films of Tunneling Dimensions; **Electronics/Dielectrics and Insulation**—VLSI Science and Technology: Materials for High Speed/High Density Applications, Joint General Session, Joint Recent News Papers Session; **Energy Technology**—Electrode Materials and Processes for Energy Conversion and Storage, Photobiological Energy Conversion, General Session; **High Temperature Materials/Dielectrics and Insulation/Electronics**—Ninth International Conference on Chemical Vapor Deposition; **Industrial Electrolytic**—Chlorine and Chlorate Cell Technology, General Session; **Industrial Electrolytic/Energy Technology**—Electrochemistry in Mineral and Metal Processing; **Luminescence and Display Materials**—Electroluminescent Materials and Devices for Display Applications, Luminescence in Amorphous Materials, General Session; **Organic and Biological Electrochemistry**—Biomass Electrochemistry, Electro-Organic Synthesis, Redox Mechanisms and Interfacial Properties of Molecules of Biological Importance. 2; General Session; **Physical Electrochemistry**—Electrode Processes IV, General Session; **Physical Electrochemistry/Battery**—Separators and Membranes; **Physical Electrochemistry/Corrosion/Battery/Energy Technology/High Temperature Materials**—In Situ Nonelectrochemical Techniques for the Study of Electrode Reactions; **New Technology Subcommittee/Electrodeposition/Industrial Electrolytic**—Advances in Pollution Monitoring, Pollution Control, and Metal Abatement in Waste Streams.

NEW ORLEANS, LOUISIANA—OCTOBER 7-12, 1984—HEADQUARTERS AT SHERATON HOTEL

The detailed Call for Papers published in the December 1983-May 1984 issues of **This Journal.** Final program published in the August 1984 issue of **This Journal.**

Planned symposia for the New Orleans Meeting include the following Divisions, Groups, Subcommittee, and subjects: **Battery**—Molten Carbonate Fuel Cells, New Developments in Lead-Acid Batteries, Manganese Dioxide Electrode, High Temperature Batteries and Fuel Cells; **Battery/Physical Electrochemistry**—Lithium Batteries, Solid-State Electrolytes and Batteries; **Corrosion**—Transient Techniques in Corrosion Research, Advances in Anodic and Cathodic Protection, General Session; **Corrosion/New Technology Subcommittee**—Corrosion of Nuclear Waste Containers; **Dielectrics and Insulation/Electronics**—Plasma Processing, Multilevel Metal and Insulators, Glass Applications in Electronics; **Dielectrics and Insulation/Corrosion/Electronics/Energy Technology**—Energy Conversion and Storage Devices; **Electrodeposition**—Alloy Deposition, Electrochemical Coatings for Solar Cells, Analytical Techniques for Investing Electrodeposition Procedures, Surfaces, and Resulting Materials; **Electrodeposition/New Technology Subcommittee**—Electrochemical Metals Deposition on Nonmetallic Materials; **Electronics**—III-V Semiconductors for High Speed Applications; **Electronics/Dielectrics and Insulation**—Process and Device Modeling, Defect/Contamination Control for VLSI, Measurement and Control of Micrometer and Smaller Dimension Structures, Joint General Session, Joint Recent News Papers Session; **Energy Technology**—Materials and New Process Technology for Photovoltaics, General Session; **Energy Technology/Corrosion/Dielectrics and Insulation**—Reliability and Failure Analysis of Energy Conversion and Storage Devices; **High Temperature Materials**—High Temperature Battery Materials, Electronic and Ionic Grain Boundary Transport; **High Temperature Materials/Dielectrics and Insulation/Electronics**—Electromigration of Metals; **Industrial Electrolytic**—Inorganic Synthesis Other than Chlor-Alkali; **Industrial Electrolytic/Electrodeposition/New Technology Subcommittee**—Metal Conservation/Recovery and Waste Disposal Abatement; **Physical Electrochemistry**—Nonaqueous Electrochemistry, Polymeric and Modified Electrodes, Physical Chemistry of Electrolyte Solutions Especially Concentrated Electrolytes, General Session; **New Technology Subcommittee/Corrosion**—Materials Considerations in Prosthetics and Other Implantable Devices; **New Technology Subcommittee/Energy Technology**—High Performance Propulsion Systems.

THE ELECTROCHEMICAL SOCIETY BOOKS IN PRINT

Society Proceedings Series

The following softbound proceedings volumes are sponsored and published by The Electrochemical Society, Inc., 10 South Main Street, Pennington, N.J. 08534-2896. Orders filled at the list price given, subject to availability. Enclose payment with order.

Fundamentals of Electrochemical Machining. C. L. Faust, Editor. A 1970 symposium. 365 pages, **$4.50.**

Electron and Ion Beam Science and Technology, Fifth International Conference. R. Bakish, Editor. A 1972 symposium. 420 pages, **$5.50.**

Electrochemical Contributions to Environmental Protection. T. R. Beck, O. B. Cecil, C. G. Enke, J. McCallum, and S. T. Wlodek, Editors. A 1972 symposium. 173 pages, **$4.00.**

Electrochemical Bioscience and Bioengineering. H. T. Silverman, I. F. Miller, and A. J. Salkind, Editors. A 1973 symposium. 268 pages, **$8.00.**

Chlorine Bicentennial Symposium. T. C. Jeffery, P. A. Danna, and H. S. Holden, Editors. A 1974 symposium. 404 pages, **$11.00.**

Metal-Slag-Gas Reactions and Processes. Z. A. Foroulis and W. W. Smeltzer, Editors. A 1975 symposium. 1032 pages, **$20.00.**

Chemistry and Physics of Aqueous Gas Solutions. W. A. Adams, G. Greer, J. E. Desnoyers, G. Atkinson, G. S. Kell, K. B. Oldham, and J. Walkley, Editors. A 1975 symposium. 522 pages, **$11.00.**

Thermal and Photostimulated Currents in Insulators. D. M. Smyth, Editor. A 1975 symposium. 215 pages, **$7.00.**

Electron and Ion Beam Science and Technology, Seventh International Conference. R. Bakish, Editor. A 1976 symposium. 632 pages, **$18.00.**

International Symposium on Molten Salts. J. P. Pemsler, J. Braunstein, K. Nobe, D. R. Morris, and N. E. Richards, Editors. A 1976 symposium. 632 pages, **$16.00.**

Properties of High Temperature Alloys. Z. A. Foroulis and F. S. Pettit, Editors. A 1976 symposium. 851 pages, **$12.00.**

Semiconductor Silicon 1977. H. R. Huff and E. Sirtl, Editors. A 1977 symposium. 1100 pages, **$15.00.**

A History of The Electrochemical Society. The first 75 years. R. M. Burns with E. G. Enck. 160 pages, **$5.00.**

Semiconductor-Liquid Junction Solar Cells. A. Heller, Editor. A 1977 symposium. 340 pages, **$10.00.**

Load-Leveling. N. P. Yao and J. R. Selman, Editors. A 1977 symposium. 412 pages, **$13.00.**

High Temperature Metal Halide Chemistry. D. L. Hildenbrand and D. D. Cubicciotti, Editors. A 1977 symposium. 678 pages, **$17.00.**

Thin Film Phenomena—Interfaces and Interactions. J. E. E. Baglin and J. M. Poate, Editors. A 1977 symposium. 525 pages, **$14.00.**

Semiconductor Characterization Techniques. P. A. Barnes and G. A. Rozgonyi, Editors. A 1978 symposium. 532 pages. **$16.00.**

Selected Topics in the History of Electrochemistry. George Dubpernell and J. H. Westbrook, Editors. A 1977 symposium. 523 pages, **$11.00.**

Chemical Vapor Deposition, Seventh International Conference. T. O. Sedgwick and H. Lydtin, Editors. A 1979 symposium. 658 pages, **$16.00.**

Laser and Electron Beam Processing of Electronic Materials. C. L. Anderson, G. K. Celler, and G. A. Rozgonyi, Editors. A 1979 symposium. 560 pages, **$13.00.**

Thin Film Interfaces and Interactions, J. E. E. Baglin and J. M. Poate, Editors. A 1979 symposium. 536 pages, **$16.00.**

Electrode Processes, S. Bruckenstein, J. D. E. McIntyre, B. Miller, and E. Yeager, Editors. A 1979 symposium. 500 pages, **$21.00.**

Power Sources for Biomedical Implantable Applications and Ambient Temperature Lithium Batteries. B. B. Owens and N. Margalit, Editors. A 1979 symposium. 652 pages, **$18.00.**

Electronic and Optical Properties of Polycrystalline or Impure Semiconductors and Novel Silicon Growth Methods. K. V. Ravi and B. O'Mara, Editors. A 1980 symposium. 280 pages, **$15.00.**

Electron and Ion Beam Science and Technology, Ninth International Conference, R. Bakish, Editor. A 1980 symposium. 672 pages, **$28.00.**

Lithium Nonaqueous Battery Electrochemistry. E. B. Yeager, B. Schumm, Jr., G. Blomgren, D. R. Blankenship, V. Leger, and J. Akridge, Editors. A 1980 workshop. 328 pages, **$18.00.**

Ion Exchange: Transport and Interfacial Properties. R. S. Yeo and R. P. Buck, Editors. A 1980 symposium. 396 pages, **$15.00.**

Materials and New Processing Technologies for Photovoltaics. J. A. Amick, E. Sirtl, P. Rai-Choudhury, and J. P. Dismukes, Editors. A 1980 symposium. 368 pages, **$14.00.**

Lithium Batteries. H. V. Venkatasetty, Editor. A 1980 symposium, 516 pages, **$26.00.**

Semiconductor Silicon 1981. H. R. Huff, R. J. Kriegler, and Y. Takeishi, Editors. A 1981 symposium. 1064 pages, **$25.00.**

Electrocrystallization. R. Weil and R. G. Barradas, Editors. A 1981 symposium. 352 pages, **$13.00.**

Chemical Vapor Deposition, Eighth International Conference. J. M. Blocher, Jr., G. E. Vuillard, and G. Wahl, Editors. A 1981 symposium. 836 pages, **$30.00.**

Corrosion and Corrosion Protection. R. P. Frankenthal and F. Mansfeld, Editors. A 1981 symposium. 304 pages, **$10.00.**

Corrosion in Batteries and Fuel Cells, Corrosion in Solar Energy Systems. C. J. Johnson and S. L. Pohlman, Editors. A 1981 symposium. 554 pages, **$22.00.**

Third International Symposium on Molten Salts. G. Mamantov, M. Blander, and G. P. Smith, Editors. A 1981 symposium. 600 pages, **$23.00.**

Second International Symposium on Molten Salts. J. Braunstein and J. R. Selman, Editors. A 1978 symposium. 420 pages, **$16.00.**

High Temperature Materials Chemistry. D. D. Cubicciotti and D. L. Hildenbrand, Editors. A 1981 symposium. 498 pages, **$21.00.**

Electrocatalysis. W. E. O'Grady, P. N. Ross, Jr, and F. G. Will, Editors, A 1981 symposium. 428 pages, **$18.00.**

Photoelectrochemistry: Fundamental Processes and Measurement Techniques. W. L. Wallace, A. J. Nozik, S. K. Deb, and R. H. Wilson, Editors. A 1981 symposium. 736 pages, **$35.00.**

The Nickel Electrode. R. G. Gunther and S. Gross, Editors. A 1981 symposium. 324 pages, **$15.00.**

Semiconductor Technology. D. A. Doane, D. B. Fraser, and D. W. Hess, Editors. A 1982 symposium. 264 pages, **$18.00.**

Plasma Processing. J. Dieleman, R. G. Frieser, and G. S. Mathad, Editors. A 1981 symposium. 528 pages, **$25.00.**

VLSI Science and Technology. C. J. Dell'Oca and W. M. Bullis, Editors. A 1982 symposium. 392 pages, **$20.00.**

Materials and New Processing Technologies for Photovoltaics. J. P. Dismukes, E. Sirtl, P. Choudhury, and L. P. Hunt, Editors. A 1982 symposium. 544 pages, **$25.00.**

Inorganic Resist Systems. D. A. Doane and A. Heller, Editors. A 1982 symposium. 302 pages, **$15.00.**

Transport Processes in Electrochemical Systems. R. S. Yeo, T. Katan, and D-T. Chin, Editors. A 1982 symposium. 288 pages, **$18.00.**

EDITOR
Norman Hackerman
Jackie Bourne, **Assistant to the Editor**

DIVISIONAL AND GROUP EDITORS

BATTERY
R. J. Brodd — G. F. Nordblom
Elton J. Cairns — Darrel Untereker
Eugene G. Gagnon

CORROSION
J. R. Ambrose — Florian Mansfeld
J. W. Faust, Jr. — E. McCafferty
R. P. Frankenthal — Ken Nobe
Jerome Kruger — W. H. Smyrl
D. D. MacDonald

DIELECTRICS AND INSULATION
Robert S. Alwitt — T. W. Hickmott
Edmund B. Davidson — S. P. Murarka
Rudolf G. Frieser — George L. Schnable
Dennis Hess — Alan W. Swanson

ELECTRODEPOSITION
Ugo Bertocci — Y. Okinaka
Huk Y. Cheh — Mordechay Schlesinger

ELECTRONICS
Ephraim Banks — Ernest Paskell
D. M. Brown — Bertram Schwartz
Ted F. Ciszek — Frederic N. Schwettmann
George R. Cronin — Thomas O. Sedgwick
John A. DeLuca — Don W. Shaw
Murray Gershenzon — Melvin Tecotzky
James S. Harris — C. C. Wang
Simon Larach — P. Wang
Subhash Mahajan — J. M. Woodall
David L. Nelson

ENERGY TECHNOLOGY GROUP
Lee F. Donaghey — S. Srinivasan
A. R. Landgrebe — M. Tomkiewicz

HIGH TEMPERATURE MATERIALS
William A. Adams — Peter J. Meschter
Joan B. Berkowitz — R. A. Rapp
Leo Brewer — David A. Shores
E. D. Cater — Donald R. Vissers
Daniel Cubicciotti — Gene F. Wakefield
Lee P. Hunt — Jack H. Westbrook
V. K. Kapur

INDUSTRIAL ELECTROLYTIC
Richard C. Alkire — Scott Lynn

ORGANIC AND BIOLOGICAL ELECTROCHEMISTRY
Martin Blank — Stanley Wawzonek
M. Dale Hawley

PHYSICAL ELECTROCHEMISTRY
Gregory C. Farrington — Robert A. Osteryoung
David S. Ginley — C. W. Tobias
Adam Heller — F. G. Will
Gleb Mamantov — Ronald H. Wilson
Barry Miller — M. S. Wrighton
William E. O'Grady

News Editor—Jack H. Westbrook

JOURNAL OF THE
ELECTROCHEMICAL SOCIETY
(USPS 284-140)
ISSN 0013-4651

The JOURNAL OF THE ELECTROCHEMICAL SOCIETY (USPS 284-140) is published monthly by The Electrochemical Society, Inc. at 215 Canal St., Manchester, N.H. 03108. The address for the Executive Offices, Editorial and Advertising Office, and Circulation Department of The Electrochemical Society, Inc., is 10 South Main St., Pennington, N.J. 08534-2896. Subscription to members as part of membership service; subscription to nonmembers $135.00 plus $15.00 for postage outside U.S. and Canada. Single copies $7.00 to members, $12.00 to nonmembers.
© Copyright 1983 by The Electrochemical Society, Inc.
Second Class Postage paid at Pennington, New Jersey and at additional mailing offices.

POSTMASTER: Send address changes to THE ELECTROCHEMICAL SOCIETY, INC., 10 South Main St., Pennington, N.J. 08534-2896.

March 1983

ELECTROCHEMICAL SCIENCE AND TECHNOLOGY

TECHNICAL PAPERS

Ion Clustering and Proton Transport in Nafion Membranes and its Applications as Solid Polymer Electrolyte
R. S. Yeo 533

A Zinc Paste Primary Battery
R. Jasinski, R. McCarron, G. Brilmyer 539

Incorporation of Chloride Ion in Passive Oxide Films on Nickel
B. MacDougall, D. F. Mitchell, G. I. Sproule, M. J. Graham 543

Experimental Determination of the Passive-Active Transition for Iron in 1 M Sulfuric Acid
P. P. Russell, J. Newman 547

Laser-Enhanced Electroplating on Good Heat-Conducting Bulk Materials
H. K. Kuiken, F. E. P. Mikkers, P. E. Wierenga 554

Current Distribution During Electroplating within a Tubular Electrode of High Ohmic Resistance
M. Ben-Porat, J. Yahalom, E. Rubin 559

A Preparation of Perpendicular Magnetic Recording Media by an Electroless Plating Method
T. Osaka, N. Kasai, I. Koiwa, F. Goto, Y. Suganuma 568

Electric Field Enhanced Diffusion in Trans-(CH)$_x$
J. H. Kaufman, E. J. Mele, A. J. Heeger, R. Kaner, A. G. MacDiarmid 571

Studies of the Reduction of Oxygen on Gold in Molten Li_2CO_3-K_2CO_3 at 650°C
W. M. Vogel, S. W. Smith, L. J. Bregoli 574

Structural and Compositional Characterization of Mixed CdS-CdSe Films Grown by Cathodic Electrodeposition
A. S. Baranski, W. R. Fawcett, K. Gatner, A. C. McDonald, J. R. MacDonald, M. Selen 579

Filtration Coefficient and Hydraulic Permeability of Nafion 125 Membranes in Metal Alkali Solutions
C. Fabiani, S. Scappa, L. Bimoi, M. De Francesco 583

Cyclic Voltammetry in Solutions of Aluminum Bromide and KBr in Aromatic Hydrocarbons. II: The Behavior of Pb and Sn
M. Elam, E. Peled, E. Gileadi 585

Application of the "Swiss-Roll" Electrolysis Cell in Vitamin-C Production
P. M. Robertson, P. Berg, H. Reimann, K. Schleich, P. Seiler 591

Electrochemical Determination of Cation Radical Stabilities of Monomethylbenzo[a]pyrenes
D. A. Tryk, S.-M. Park, G. H. Daub 597

Crystallographic Anisotropies in Electrochemical Etching of Pt
R. Caracciolo, L. D. Schmidt 603

ELECTROCHEMICAL SOCIETY

Vol. 130 • No. 3

The Electroreduction of Carbon Dioxide and Formic Acid on Tin and Indium Electrodes
.....S. Kapusta, N. Hackerman 607

Polymer Films on Electrodes. XI. Electrochemical Behavior of Polymer Electrodes Produced by Incorporation of Tetrathiafulvalenium in a Polyelectrolyte (Nafion) Matrix
.....T. P. Henning, A. J. Bard 613

Different Aging Effects of Electrosorbed Oxygen Monolayers. The Polycrystalline Platinum/Molten Potassium Acid Sulfate Interface
.....M. E. Folquer, N. R. de Tacconi, A. J. Arvía 622

TECHNICAL NOTES

A Lithium Electrode with a Zinc Substrate for Secondary Batteries
.....Y. Matsuda, M. Morita, H. Katsuma 627

Lithium Cycling in Polymethoxymethane Solvents
.....J. S. Foos, J. McVeigh 628

Electrodeposition of Calcium and Strontium Ions on Carbon Electrode
.....H. J. Huang 630

Mechanism of Hole Injection on Ferric Oxide Photoelectrodes
.....T. Pajkossy 632

Reliable Glass-Polyethylene Dropping Mercury Electrode for Electrocapillary Measurements
.....M. Carlá, G. Aloisi 636

SOLID-STATE SCIENCE AND TECHNOLOGY

TECHNICAL PAPERS

Low Temperature Deposition of Silicon Nitride by Reactive Ion-Beam Sputtering
D. Bouchier, G. Gautherin, C. Schwebel, A. Bosseboeuf, B. Agius, S. Rigo 638

Sputter-Etching Planarization for Multilevel Metallization
.....H. Kotani, H. Yakushiji, H. Harada, K. Tsukamoto, T. Nishioka 645

Langmuir Probe Measurements on CHF_3 and CF_4 Plasmas: The Role of Ions in the Reactive Sputter Etching of SiO_2 and Si
.....Ch. Steinbrüchel 648

A Laser Interferometer System to Monitor Dry Etching of Patterned Silicon
.....M. Sternheim, W. van Gelder, A. W. Hartman 655

Control of Silicon Dioxide Properties by RF Sputtering
.....M. K. Lee, C. Y. Chang, J. S. Tzeng, Y. K. Su 658

The A-C Conductivity of Polycrystalline LISICON, $Li_{2+2x}Zn_{1-x}GeO_4$, and a Model for Intergranular Constriction Resistances
.....P. G. Bruce, A. R. West 662

Lattice Parameter Changes in $Al_{0.39}Ga_{0.61}As$ Due to O, Ge, Si, and S Doping
.....W. R. Wagner, N. E. Schumaker, J. L. Zilko, P. J. Anthony, V. Swaminathan 670

DIVISION AND GROUP OFFICERS

Battery Division
Theodore Katan, Chairman
Sidney Gross, Vice-Chairman
Eugene Gagnon, Secretary-Treasurer
General Motors Corp.
Research Laboratories, Dept. 37
12 Mile and Mounds Rds.
Warren, Mich. 48090-9055

Corrosion Division
Florian Mansfeld, Chairman
Robert A. Rapp, Vice-Chairman
Edward McCafferty, Secretary-Treasurer
Naval Research Laboratory
Code 6314
Washington, DC 20375

Dielectrics and Insulation Division
Werner Kern, Chairman
John L. Mauer IV, Vice-Chairman
Laura Rothman, Treasurer
Norman Goldsmith, Secretary
RCA Laboratories
Princeton, NJ 08540

Electrodeposition Division
Lubomyr Romankiw, Chairman
Thomas Franklin, Vice-Chairman
Mordechay Schlesinger, Secretary-Treasurer
Dept. of Physics
University of Windsor
Windsor, Ont., Canada N9B 3P4

Electronics Division
Ronald E. Enstrom, Chairman
Edward H. Nicollian, Vice-Chairman (Semiconductors)
F. N. Schwettmann, Vice-Chairman (New Electronic Technologies)
Patricia L. Castro, Treasurer
Carlton M. Osburn, Secretary
IBM T. J. Watson Research Center
P.O. Box 218
Yorktown Heights, N.Y. 10598

High Temperature Materials Division
William A. Adams, Jr., Chairman
Lee P. Hunt, Senior Vice-Chairman
Wayne Worrell, Junior Vice-Chairman
Frederick S. Pettit, Secretary-treasurer
University of Pittsburgh
848 Benedum Hall
Pittsburgh, Pa. 15261

Energy Technology Group
James McBreen, Chairman
Arthur J. Nozik, Vice-Chairman
Vijay K. Kapur, Treasurer
A. J. Appleby, Secretary
Electric Power Research Institute
P.O. Box 10412
Palo Alto, Calif. 94303

Industrial Electrolytic Division
Morris Grotheer, Chairman
Robert S. Karpiuk, Vice-Chairman
W. Bruce Darlington, Secretary-Treasurer
PPG Industries, Inc.
P. O. Box 31
Barberton, OH 44213

Luminescence and Display Materials Group
Martin Royce, Chairman
Charles Struck, Vice-Chairman
William McAllister, Secretary-Treasurer
Westinghouse Electric Corp.
Bloomfield, NJ 07003

Organic and Biological Electrochemistry Division
John H. Wagenknecht, Chairman
Martin Blank, Vice-Chairman
Petr Zuman, Secretary-Treasurer
Dept. of Chemistry
Clarkson College of Technology
Potsdam, N.Y. 13676

Physical Electrochemistry Division
Elton J. Cairns, Chairman
Robert A. Osteryoung, Vice-Chairman
Larry R. Faulkner, Secretary-Treasurer
Dept. of Chemistry
University of Illinois
Urbana, Ill. 61801

SOCIETY OFFICERS AND STAFF

Frederick J. Strieter, President
Honeywell Inc.
7814 Fallmeadow Lane
Dallas, Texas 75240

J. Bruce Wagner, Vice-President
Center for Solid State Science
Arizona State University
Tempe, Ariz. 85281

Paul C. Milner, Vice-President
Bell Laboratories
Room 1D-259
Murray Hill, N.J. 07974

Richard C. Alkire, Vice-President
Dept. of Chemical Engineering
University of Illinois
Urbana, Ill. 61801

Forrest A. Trumbore, Secretary
Bell Laboratories
Room 1E-208
Murray Hill, N.J. 07974

Jerome Kruger, Treasurer
National Bureau of Standards
B254 Materials Building
Washington, D.C. 20234

V. H. Branneky, Executive Secretary
The Electrochemical Society, Inc.
10 South Main Street
Pennington, N.J. 08534-2896

Roque J. Calvo, Assistant Executive Secretary
The Electrochemical Society, Inc.
10 South Main Street
Pennington, New Jersey 08534-2896

PUBLICATION STAFF

Sarah A. Kilfoyle, **Publication Editor**

PUBLICATION COMMITTEE

Robert P. Frankenthal, **Chairman**
Forrest A. Trumbore
Norman Hackerman
Newton Schwartz
Glenn W. Cullen
Rudolf Keller
Rudolf T. Frieser
Isaac Trachtenberg
Gary McGuire

Manuscripts submitted to the JOURNAL should be sent in triplicate to the Editorial Office at 10 South Main Street, Pennington, N.J. 08534-2896. They should conform to the revised "Instructions to Authors" available from Society Headquarters. Manuscripts so submitted, as well as papers presented before a Society technical meeting, become the property of the Society and may not be published elsewhere in whole or in part without written permission of the Society. Address such requests to the Editor.

The Electrochemical Society does not maintain a supply of reprints of papers appearing in its JOURNAL. A photoprint copy of any particular paper may be obtained from University Microfilms, Inc., 300 N. Zeeb St., Ann Arbor. Mich. 48106.

Inquiries regarding positive microfilm copies of issues should be addressed to University Microfilms, Inc., 300 N. Zeeb St., Ann Arbor, Mich. 48106.

Walter J. Johnson, Inc., 355 Chestnut St., Norwood, N.J. 07648, have reprint rights to out-of-print volumes of the JOURNAL, and also have available for sale back volumes and single issues with the exception of the last two calendar years.

The JOURNAL OF THE ELECTROCHEMICAL SOCIETY combines the JOURNAL and TRANSACTIONS OF THE ELECTROCHEMICAL SOCIETY. Statements and opinions given in articles and papers in the JOURNAL OF THE ELECTROCHEMICAL SOCIETY are those of the contributors, and The Electrochemical Society, Inc. assumes no responsibility for them.

Claims for a missing issue should be reported within 60 days of normal delivery date to the Circulation Dept., The Electrochemical Society, Inc., 10 South Main Street, Pennington, N.J. 08534-2896.

Notice of a change in address should be sent to the Circulation Dept., The Electrochemical Society, Inc., 10 South Main Street, Pennington, N.J. 08534-2896. Include the mailing label or the number from the mailing label from your previous issue of the JOURNAL to ensure proper identification.

SOLID-STATE SCIENCE (Cont.)

Deposition of GaAs Epitaxial Layers by Organometallic CVD. Temperature and Orientation Dependence
D. H. Reep, S. K. Ghandhi 675

The Uranyl Ion, Fluorescent and Fluorine-like A Review
C. K. Jørgensen, R. Reisfeld 681

Contact Angles Between III-V Melts and Several Substrates
U. König, W. Keck 685

Effects of Ion Implantation on the Thermal Growth of Pt and NiPt Silicides
T. W. Orent, C. I. Knudson, J. A. Sartell, S. Lee, T. L. Brewer 687

Compositional Depth Profile of a Native Oxide LPCVD MNOS Structure Using X-Ray Photoelectron Spectroscopy and Chemical Etching
J. A. Wurzbach, F. J. Grunthaner 691

A Study of Impurities and Traps in Liquid Phase Epitaxial InP in Relation to Melt Prebaking
J. K. Rhee, P. K. Bhattacharya 700

Evaluation and Control of Resistivity in N/N Epitaxial Depositions
J. L. Sachitano, V. C. Kannan 704

Some Illumination on the Mechanism of SiO_2 Etching in HF Solutions
H. Nielsen, D. Hackleman 708

Amorphous Silicon Photovoltaic Modules
Y. Uchida, H. Sakai, N. Furusho, M. Nishiura, H. Haruki 712

TECHNICAL NOTE

Incidence Angle Dependence of Planar Channeling in Boron Ion Implantation into Silicon
M. Miyake, M. Yoshizawa, H. Harada 716

ACCELERATED BRIEF COMMUNICATIONS

Phenomenological Model for Silicon Oxidation in Dry Oxygen in the Presence of HCl
A. I. Ellis, K. M. Gardiner, T. E. Cyr 721

The Growth of Zn_3P_2 by Metallorganic Chemical Vapor Deposition
J. Long 725

Metal Oxidation as a Heat Pump
D. Cubicciotti 729

Activated Ir: An Electrode Suitable for Reversible Charge Injection in Saline Solution
L. S. Robblee, J. L. Lefko, S. B. Brummer 731

Dinitrogen Electrochemical Reduction to Ammonia over Iron Cathode in Aqueous Medium
A. Sclafani, V. Augugliaro, M. Schiavello 734

REVIEWS AND NEWS

PROGRAM 49C

NEWS 142C

JOURNAL OF THE ELECTROCHEMICAL SOCIETY

ELECTROCHEMICAL SCIENCE AND TECHNOLOGY

MARCH 1983

Ion Clustering and Proton Transport in Nafion Membranes and Its Applications as Solid Polymer Electrolyte

Richard S. Yeo*

Pinnacle Research Institute, Cupertino, California 95014

ABSTRACT

The concentrations of fixed ion in Nafion® membranes have been calculated based on both the homogeneous model and the ion cluster model while the concentrations of co-ion were calculated from the Donnan expression. The experimental results on the concentrations of co-ion reveal that the ions in this material do form clusters and the membrane also exhibits a strong Donnan exclusion effect. The ionic mobilities obtained from the conductivity and diffusivity studies are in fairly good agreement. Strong acidity coupled with high proton mobility in this membrane provide an important solid polymer electrolyte for a variety of electrochemical applications. The impact of polymer morphology on cell performance is also discussed.

Interest in perfluorosulfonic acid (Nafion®) has increased considerably in recent years (1-23) and it has been an important subject in many recent scientific meetings (24-30) because of its industrial importance, especially in electrolytic processes. Because of their excellent chemical stability and high conductivity, Nafion membranes find applications in chlor-alkali cells (10), water electrolyzers (4, 12, 13), hydrogen-air fuel cells (12), hydrogen-halogen cells (2, 3), zinc-bromine cells (11), and Donnan dialyzers (19).

Nafion belongs to a class of materials known as ion-containing polymers (31). Although a significant number of studies have been undertaken on the ion-containing polymers to date, the state and structure of the ion aggregation, and the modifications which occur on hydration are generally not known quantitatively, even though they may have major importance. The reasons for the lack of understanding of the microstructure of ion-containing polymers lie in their complexity. One series of studies (1, 15, 32-36) postulates the existence of sizable regions, of dimensions of *ca.* 50Å, in which the ions are clustered (37), the most direct evidence coming from small angle x-ray scattering. Another group (38-40) suggests that the ions are dispersed throughout the sample in a very low state of aggregation, *i.e.*, either as ion pairs or ion quartets. The evidence in support of these small ionic groups was derived from dynamic mechanical data (38), nuclear magnetic resonance data (39), and viscosity measurements (40).

Ion cluster phenomena in Nafion were first indicated by Yeo and Eisenberg based on small angle x-ray scattering and thermo-rheological data (1). Many recent studies (5, 7, 9, 14-17) have also arrived at the same conclusion that the ions are clustered. This ion cluster morphology of Nafion accounts for its many unusual properties, such as thermo-rheological complexity (1), dual cohesive energy densities (5), and percolative ion transport (14).

Extensive studies have been made on the transport of the alkali ions (9, 10, 14), especially the sodium ion, in Nafion membranes because of their wide application in the chlor-alkali industry. In contrast, there have been few studies on transport properties of Nafion in acidic electrolytes (2, 3, 7, 11).

In this study an attempt is made to bridge the gap between the basic polymer science concerning the microstructure of this perfluorinated ionomer and the electrochemical criteria determining the performance characteristics of this polymer for various electrochemical applications. This research is aimed at investigating the role the ion clustering of the polymer plays in cell performance. The results of this study may provide some direction for the future development of high performance membrane cells in industrial electrolytic or separation processes. Finally, this paper serves the purpose of demonstrating the use of a "simple" electrolyte sorption technique in investigating the mysterious ion clustering phenomena in ionomers.

Experimental

Membrane materials.—Measurements were made on Nafion membranes, obtained from du Pont, that had an equivalent weight of 1200 and a thickness of 0.025 cm. Equivalent weight (*EW*) is defined as the weight of acid polymer that will neutralize one equivalent of base. *EW* is equal to the reciprocal of ion exchange capacity (IEC). The received material absorbs *ca.* 17 weight percent (w/o) water when immersed in water. These samples are assigned as normal (N) form. The water uptake of the material increases to *ca.* 30 w/o when boiled in water for more than 30 min and these samples are denoted as expanded (E) form. The membrane will continue to hold that same amount of water at room temperature, unless the effect is destroyed by drying at elevated temperatures (22).

Electrolyte concentration in membranes.—The equilibrium electrolyte content of the membrane was determined by a method previously described (3). Also, the membrane, on reaching equilibrium in the electrolyte, was removed, surface dried, and then thoroughly leached with water. The extract was titrated for acid content. The concentration of co-ion in the membrane was calculated from the electrolyte content and the amount of acid leached out of the membrane.

Electrolyte diffusion in membranes.—A dry film sample was immersed in the electrolyte in a constant-

* Electrochemical Society Active Member.
Key words: electrolyte, polymers, separators, transport.

temperature bath. After a certain time period, the sample was removed from the electrolyte, surface dried, and the weight gain (M_t) was determined. The same sample was then replaced in the bath at the same temperature for a second time period, and the weight was redetermined. The procedure was repeated until there was no further weight gain; the total weight gain is referred to as the equilibrium sorption M_∞. All the weighing procedures were done in less than 10 sec.

Membrane conductivity.—The membrane conductivities were measured in a Teflon cell described elsewhere (7). The electrodes were bonded onto the membrane surface by a hot pressing method. The electrodes were connected to an a-c bridge (Gen Rad 1658 RLC Digibridge). Measurements were made at 1 kHz.

Results and Discussion

The sulfonic acid groups of Nafion membranes are highly ionized in water. The proton of these groups is a mobile, replaceable ion (so-called counterion) while the sulfonate group is fixed into or retained by the polymeric matrix (so-called fixed ion). The anions, with charge similar to the fixed ions, are called co-ions.

Concentration of fixed ion.—Homogeneous model.—If one assumes low, or no, ion aggregation in the membrane, then the membrane is regarded as a microscopically homogeneous medium. The amount of ionic groups is given by IEC whereas the volume that the ionic groups represent is equal to the whole volume of the wet membrane, V_0. V_0 can be estimated from the weight and the density of the wet membrane. The concentration of fixed ion (in term of mol/liter) can be given by

$$\bar{C}_f = 1000 \times \frac{\text{IEC}}{V_0} = \frac{1000}{EW} \times d_0 \qquad [1]$$

where d_0 is the density of the wet membrane, which can either be estimated from the expression given elsewhere (23) or by direct measurements.

Ion cluster model.—In this model, two basic types of ionic aggregates are postulated (37): small aggregates consisting of a few ion pairs termed multiplets and larger aggregates termed ion clusters. The structure of Nafion membrane can be broadly described as that of a microphase-separated system in which a matrix of low ion content (due to multiplets) is interspersed with ion-rich domains (ion clusters). Part of the water contained within the membrane is associated with the sulfonic acid groups; part interacts with the organic matrix (17, 18, 20); while still another part forms water clusters (16). Roche *et al.* (16) has proposed a two-phase model in which the ion clusters are considered as a hydrophilic phase whereas the organic matrix is the hydrophobic phase.

The amount of ionic groups within the hydrophilic phase (ion clusters) is equal to IEC $\times$ f_i where f_i is the fraction of ionic groups in the ion clusters. The volume of the ion cluster is given by $V_w \times f_w$ where V_w is the volume of electrolyte absorbed by the membrane and f_w is the fraction of electrolyte in the ion clusters. V_w can be calculated from the electrolyte uptake of the membrane.

If one assumes that the concentration of fixed ion in the hydrophilic phase can represent that of the whole membrane, that concentration can be given by

$$\bar{C}_f = 1000 \times \frac{\text{IEC}\, f_i}{V_w f_w} = \frac{1000 d_e}{EW\, f_e} \times \left(\frac{f_i}{f_w}\right) \qquad [2]$$

where f_e and d_e are the weight fraction and density of the electrolyte absorbed by the membrane, respectively.

Although the structure of Nafion membrane has been characterized, the evaluation of f_i and f_w values seems quite difficult because of the limitation of available research tools. In addition, these values change with the prehistory of the membrane and the environment the membrane encounters. Roche *et al.* (16) have made a rough estimation of f_i and f_w for Nafion-Na by using a small angle neutron scattering technique. They found that f_i and f_w are >40% and >76%, respectively, for N-form samples whereas the values are >60% and >84%, respectively, for E-form samples. Falk also estimates that about three quarters of the water is in the ion cluster based on infrared data (18). Therefore, the value of f_i probably varies between 0.4 and 1.0 whereas the value of f_w varies in the range of 0.76-1.0. Accordingly, the ratio of f_i/f_w varies between 0.4 and 1.32. It is very likely that $f_i/f_w \approx 1$ because of the hydrophilic nature of the ionic groups. Since no perfectly satisfactory values of f_i and f_w can be used, it is assumed that $f_i/f_w = 1$ for the sake of simplicity in calculation. The error in this assumption, to a reasonable approximation, may be mitigated by the experimental error in determining the value of f_e. Moreover, Gierke (15) has assumed that both f_i and f_w are equal to 1 in the estimation of the size of ion clusters.

The water uptake of Nafion for various *EW* has been reported previously (22). Figure 1 shows the calculated concentration of fixed ions for Nafion of various *EW* in equilibrium with water. For the case of no ion aggregation, the concentration of fixed ion decreases with increasing *EW* due to less ionic groups present in the sample while V_0 varies very little with *EW*. In contrast to the homogeneous model, the concentration of fixed ion increases with *EW* if the ion clustering concept is adopted, because V_w is far smaller than V_0. Thus, the decrease of ionic groups with increasing *EW* is less significant in comparison with the decrease of V_w, which in turn is related to the water uptake. Another important feature is that membrane pretreatment has a strong effect on the concentration of fixed ion, especially in the case of ion clustering. The concentration of fixed ions is higher for N-form samples than for E-form samples since water uptake increases by boiling the sample in water. It is expected that the concentration of fixed ion could further increase by drying the membrane at elevated temperatures prior to the soaking in water (3).

It is important to note that the material should exhibit a very strong acidic behavior in water when ion clustering occurs. As can be seen from Fig. 1, the concentration of fixed ion for Nafion of 1200 *EW* in E-form is equivalent to 13 w/o sulfuric acid and it is in good agreement with the value of 10 w/o sulfuric acid reported by LaConti *et al.* (41). Recently, an apparent $pK_a < 1$ for Nafion of 1150 *EW* has been observed, suggesting a strong acidic behavior in this material (10).

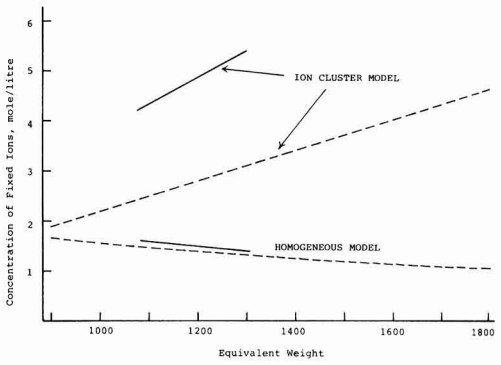

Fig. 1. Calculated concentration of fixed ion for Nafion of various *EW* in equilibrium with water at 25°C. —— N-form, --- E-form.

The electrolyte uptake of Nafion in various electrolytes has been reported previously (3, 22, 42). Figure 2 shows the dependence of concentration of fixed ion on HCl concentration for Nafion of 1200 *EW*. As ion clustering occurs the concentration of fixed ion increases drastically with electrolyte concentration.

Concentration of co-ions.—The equilibrium of this ion exchange membrane with a uni-univalent salt in a solution of concentration C is given by the Donnan expression

$$C^2 = \bar{C}_n(\bar{C}_n + \bar{C}_f)\,(\bar{\gamma}/\gamma)^2 \qquad [3]$$

where $\bar{C}_f$ and $\bar{C}_n$ are the concentrations of fixed ion and co-ion, respectively. γ and $\bar{\gamma}$ are the activity coefficients in the external and membrane phase, respectively.

Figure 3 indicates a plot of $\bar{C}_n$ *vs.* C for N-form Nafion in HCl electrolyte. The solid curves are calculated by Eq. [3] based on $\bar{C}_f$ given in Fig. 2 and on the basis that the activity coefficient ratio in Eq. [3] is unity. For estimation of co-ion concentration, this assumption seems useful as the agreement with the experimental data is reasonable. Besides, the same assumption has also been employed successfully in many membrane systems which differ considerably in structure (43, 44). The dashed line is for the case in which there is no Donnan exclusion effect for the membrane ($\bar{C}_f = 0$). A similar plot for E-form Nafion in HBr electrolyte is given in Fig. 4.

The data strongly support the suggestion that Nafion possesses ion-cluster morphology and is not a homogeneous medium. Furthermore, the materials exhibit a Donnan exclusion effect, which decreases significantly when the material is boiled, primarily due to the lower concentration of fixed ion, resulting from dilution by absorbed water. An extremely high Donnan exclusion effect in Nafion has also been found for the case of NaOH electrolyte (45).

Conductivity of hydrated membrane.—Figure 5 represents the membrane conductivity of Nafion in water as a function of water content (in terms of H_2O/SO_3^-).

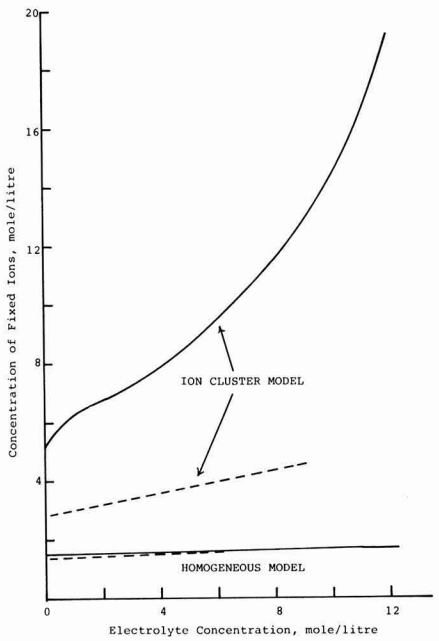

Fig. 2. Calculated concentration of fixed ion for Nafion of 1200 *EW* in various HCl electrolyte at 25°C. —— N-form, --- E-form.

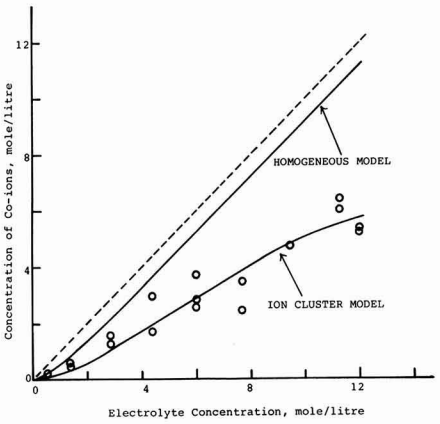

Fig. 3. Concentration of co-ion for N-form Nafion of 1200 *EW* in equilibrium with various HCl electrolytes at 25°C. Dashed curve, no Donnan effect; solid curves, calculated from Eq. [3].

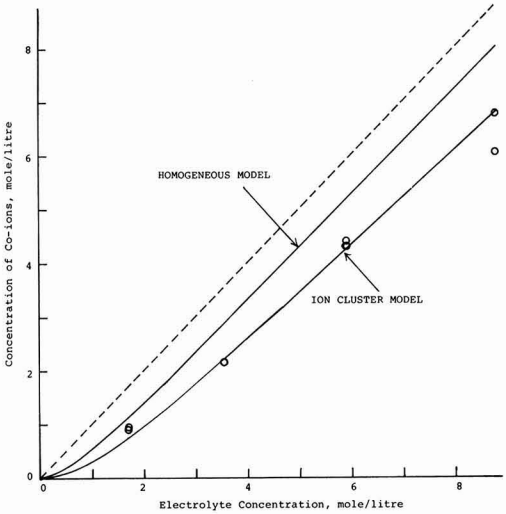

Fig. 4. Concentration of co-ion for E-form Nafion of 1200 *EW* in equilibrium with various HBr electrolytes at 25°C. Dashed curve, no Donnan effect; solid curves, calculated from Eq. [3].

Due to the strong acidity of the sulfonic acid groups (as shown by the dashed curve), the membrane is highly conductive to protons. The solid curve is calculated from the following equation

$$\kappa = A\kappa_e\,(1 - \theta)^{1.5} \qquad [4]$$

where θ is the volume fraction of polymer and κ_e is considered as the conductivity of sulfuric acid with concentration equal to that of the sulfonic acid group of the ion-clustered membrane. The pre-exponential factor $A = 0.54$ is observed. This factor could be ascribed to both the physical shape of the conductivity cell as well as the deviations from the assumption made on κ_e.

It has been reported (2, 3) that the conductivity of Nafion in concentrated acid electrolytes is one order of magnitude smaller than the electrolyte conductivity. However, the membrane conductivity is higher than the electrolyte conductivity in the case of very dilute electrolytes or nonaqueous solvents (7, 46) because the intrinsic conductivity (42) of the membrane becomes important.

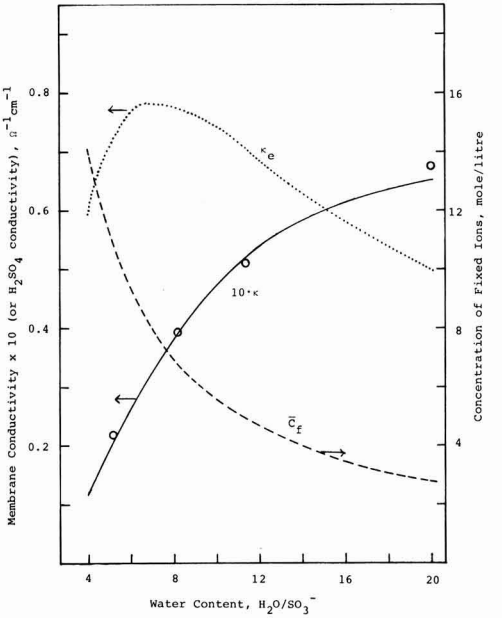

Fig. 5. Membrane conductivity of Nafion 1200 *EW* with various water content at 25°C. Solid curve, calculated from Eq. [4]; dashed curve, concentration of fixed ions as a function of water content; dotted curve, the conductivity of sulfuric acid with concentration equal to $\bar{C}_f$.

Hsu *et al.* (14) reported that the membrane conductivity of Nafion in alkaline electrolyte exhibits ion percolative behavior and can be given by

$$\kappa = \kappa_e (1 - \theta - \phi)^{1.5} \quad [5]$$

where ϕ is the threshold volume fraction of the aqueous phase and κ_e is the electrolyte conductivity. There is an (ionic) insulator-to-conductor transition in Nafion around ϕ. Based on the percolation theory, ϕ is 0.15 whereas the experimental value of 0.10 for Nafion in NaOH electrolyte is observed.

In order to explore the relationship between the membrane conductivity and the volume fraction of the polymer phase, the conductivity results on other systems are of interest. The conductivity of composite materials can be related to the volume fraction of nonconducting particles by the following equation

$$\kappa = \kappa_e (1 - \theta)^n \quad [6]$$

where n is an empirical exponent, which Archie (47) found to be applicable to unconsolidated sand (n = 1.3) and sandstones (n = 1.8-2.0).

Equation [6] becomes the well-known Bruggemann equation (48) if n = 1.5. Tobias *et al.* (49) have shown that the Bruggemann equation can be used to describe the conductivity of random dispersions of spherical insulators with a large size range of spheres, such as occurs in gas-electrolyte emulsions. More recently, Hino *et al.* (50) have reported that the superficial conductivity of the NaOH solution containing gas bubbles also agreed well with the Bruggemann equation.

There is a strong similarity between these different systems. The relationship between the conductivity and the volume fraction of nonconducting media can be very well described by different forms of the Bruggemann equation.

The Bruggemann equation was derived with the assumption that the nonconducting particles are spherically shaped. It is generally not applicable, particularly not if the particles are greatly elongated or when they contain cavities.

The conductivity of membranes with various water content and at various temperatures has been measured. Figure 6 shows a plot of log κ *vs.* $1/T$. The behavior is of the Arrhenius type, the activation energy for conduction is 2.25 kcal/mol, smaller than that for the case of HCl electrolytes (2).

Sorption of HCl by Nafion membrane.—For short times, the amount of electrolyte M_t absorbed by the polymer film in time t is given by the following equation (51)

$$\frac{M_t}{M_\infty} = 4\left(\frac{Dt}{l^2}\right)^{1/2}\left[\frac{1}{\pi^{1/2}} + 2\sum_{n=0}^{\infty}(-1)^n \text{ierfc}\frac{nl}{2(Dt)^{1/2}}\right] \quad [7]$$

where D is the diffusion coefficient, l is the thickness of the sheet, n is a positive integer, and ierfc X = $(1/\pi^{1/2})$ exp $(-X^2)$ − X erfc X, where erfc X is 1 − erf X, erf being the error function.

Figure 7 shows the typical sorption curves for various HCl concentrations. The linearity of the plots below M_t/M_∞ = 0.5 suggests that the diffusion is Fickian and that a constant diffusion coefficient is operative. The values of D were calculated from the initial slope of the plots, *i.e.*, by setting tthe second term in the bracket equal to zero (52, 53).

Figure 8 shows a plot of log D as a function of HCl concentration. It is clear that the diffusion of HCl electrolyte in Nafion is fast. For dilute electrolytes, it is one order of magnitude smaller than the self-diffusion of HCl.

Ion mobility in Nafion membrane.—Ion mobility can generally be calculated from conductivity and diffusivity data. The results of these calculations are summarized in Table I. The conductivity test measures the sum of proton mobility and co-ion (OH^- and Cl^-) mobility. On the other hand, the ion mobility obtained from the diffusivity study is ascribed to the "combined" mobilities of the HCl molecules and water molecules. It is largely attributed to the co-ion mobility as the proton mobility is relatively high. Furthermore, the results in Fig. 3 indicate that the Donnan effect of the membrane could make the mobility of HCl in the membrane slower than that for the water molecule. The diffusion coefficient obtained from the sorption method can be considered only as an "apparent" value because of these complications. It is thus meaningless to estimate the transport numbers

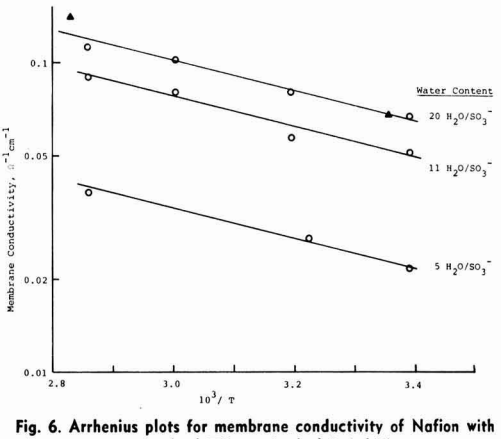

Fig. 6. Arrhenius plots for membrane conductivity of Nafion with various water contents. (○) This study; (▲) Ref. (41).

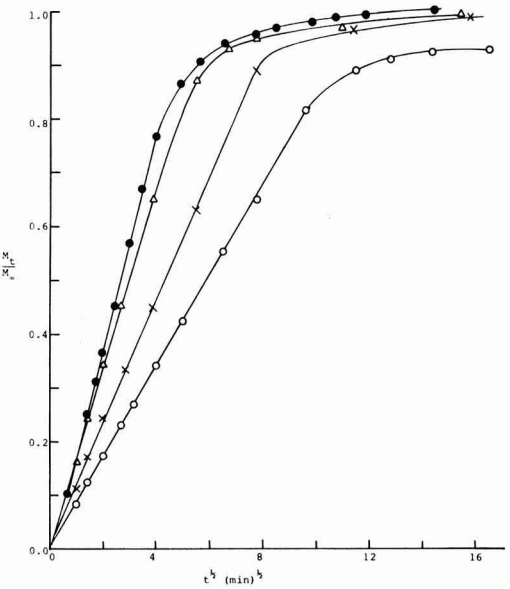

Fig. 7. Plot of M_t/M_∞ vs. $\sqrt{t}$ for Nafion of 1200 *EW*. (•) H_2O, (△) 10% HCl, (×) 20% HCl, (○) 25% HCl.

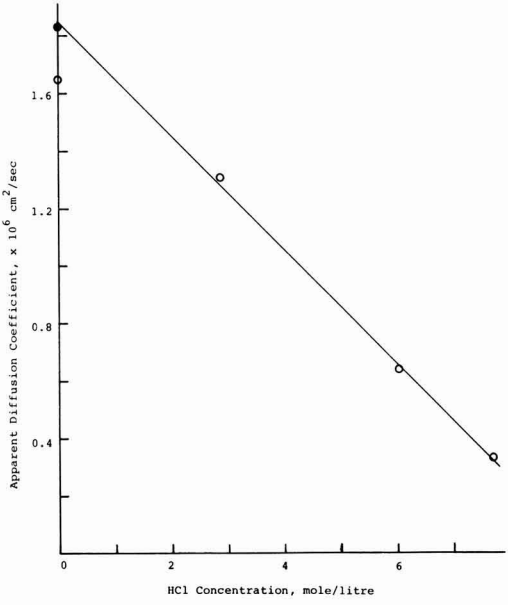

Fig. 8. Apparent diffusion coefficient of HCl electrolyte in Nafion of 1200 *EW* as a function of HCl concentration at 25°C. (○) This study, (•) Ref. (1).

of various ions in the membrane by combining the two sets of mobility data despite that they are in the same order of magnitude and follow the same trend with electrolyte concentrations.

Applications of Nafion as solid polymer electrolyte.— High ion mobility, together with strong acidity and hydrophilicity, makes this membrane a good "electrolyte" for many electrochemical applications. This perfluoro sulfonic acid polymer has recently been shown to have potential for use as a solid "superacid" catalyst for many electro-organic syntheses (54) as well as a semisolid proton conductor in WO_3-based electrochromic displays (55). The concept of using an ion exchange membrane as "electrolyte" in fuel cells was introduced by Grubb (56) in the early sixties.

Table I. Ion mobilities calculated from conductivity and diffusivity data

Electrolyte concentration (w/o HCl)	κ (Ω^{-1} cm^{-1})	$\bar{C}_t$ (mol/liter)	$U_\kappa \times 10^{5a}$ (cm^2 V^{-1} sec^{-1})	$D \times 10^6$ (cm^2 sec^{-1})	$U_D \times 10^{5b}$ (cm^2 V^{-1} sec^{-1})
0	0.051	5.21	10.1	1.66	6.53
10	0.06	7.13	8.72	1.31	5.15
20	0.028	9.40	3.09	0.64	2.52
25	0.016	11.21	1.48	0.33	1.30

[a] U_κ: ion mobility calculated from conductivity data.
[b] U_D: ion mobility calculated from diffusivity data.

The beauty of using Nafion membranes in electrochemical cells can be witnessed by the uniqueness of the solid polymer electrolyte (SPE) cells, which are being developed at various industrial laboratories (12, 57). The catalytic particles are bonded to the membrane that also serves as both the cell separator and the sole "electrolyte." Although deionized water is the only fluid circulated through the SPE water electrolyzer, the environment that the electrodes encounter is highly acidic. The sulfonic acid groups at the membrane surfaces produce an acidity equal to 20 w/o sulfuric acid. Because of this acidic media, acid resistant noble metals or their oxides are used as anode materials (13, 58) while platinum serves as the cathode material.

The relationship between the morphology and properties of the permselective membrane and its implication to the electrochemical application is rather complicated (59). It is desirable for the membrane to have the ion cluster morphology such that the concentration of fixed ion is higher, which, in turn, yields a higher Donnan effect. Consequently, a better current efficiency in electrochemical cells can be realized. This is particularly true for chlor-alkali cells, hydrogen-bromine cells, and zinc bromine cells. However, this ion cluster morphology may introduce poor conductivity as ion percolation occurs at low volume fraction of aqueous phase. On the other hand, the homogeneous morphology is desirable if one requires good conductivity while sacrificing current efficiency. Of course, it is essential that the membrane is macroscopically homogeneous, free of pinhole and defects, such that an even current distribution across the cell can occur.

The current efficiency of a cell utilizing a Nafion membrane can be facilitated by the ion-clustering effect of the membrane. Also, the conductivity of this membrane is rather high because of its fast ion transport properties. In most cell operating conditions, the percolation effect in Nafion disappears as the volume fraction of the aqueous phase is in excess of the threshold value. For the case of alkaline solutions, a volume fraction of more than 0.1 is required (14). For the case of acid electrolytes, it is likely there is no percolation effect in the proton transport since the threshold volume fraction is almost zero, as indicated by Eq. [4]. These results strongly suggest that Nafion can provide good current efficiency and voltaic efficiency in electrochemical applications. Of course, for chlor-alkali cells, the carboxylic analogue, such as Nafion 900 series (60) and Flemion (61), etc., are better than conventional Nafion as regards to the current efficiency.

Acknowledgment

The author is grateful to Dr. K. C. Tsai and Dr. J. Lee Morris of Pinnacle Research Institute for helpful discussions.

Manuscript submitted July 12, 1982; revised manuscript received Sept. 16, 1982.

Any discussion of this paper will appear in a Discussion Section to be published in the December 1983 JOURNAL. All discussions for the December 1983 Discussion Section should be submitted by Aug. 1, 1983.

REFERENCES

1. R. S. Yeo and A. Eisenberg, *J. Appl. Polym. Sci.*, **21,** 875 (1977).
2. R. S. Yeo and J. McBreen, *This Journal*, **126,** 1682 (1979).
3. R. S. Yeo and D-T. Chin, *ibid.*, **127,** 549 (1980).
4. R. S. Yeo, J. McBreen, G. Kissel, F. Kulesa, and S. Srinivasan, *J. Appl. Electrochem.*, **10,** 741 (1980).
5. R. S. Yeo, *Polymer*, **21,** 432 (1980).
6. R. S. Yeo, S. F. Chan, and J. Lee, *J. Membrane Sci.*, **9,** 273 (1981).
7. R. S. Yeo, in "Ion Exchange: Transport and Interfacial Properties," R. S. Yeo and R. P. Buck, Editors, pp. 235-248, The Electrochemical Society Softbound Proceedings Series, Pennington, NJ (1981).
8. R. S. Yeo and H. L. Yeager, in "Modern Aspects of Electrochemistry," J. O'M. Bockris, B. E. Conway, and R. E. White, Editors, Plenum Press, New York, In press.
9. H. L. Yeager, Z. Twardowski, and L. M. Clarke, *This Journal*, **129,** 324 (1982).
10. Z. Twardowski, H. L. Yeager, and B. O'Dell, *ibid.*, **129,** 328 (1982).
11. F. G. Will, *ibid.*, **126,** 36 (1979).
12. R. S. Yeo, in "Perfluorinated Ionomer Membranes," A. Eisenberg and H. L. Yeager, Editors, p. 453, American Chemical Society Symposium Series (1982).
13. J. L. Weininger and R. R. Russell, *This Journal*, **125,** 1482 (1978).
14. W. Y. Hsu, J. R. Barkley, and P. Meakin, *Macromolecules*, **13,** 198 (1980).
15. T. D. Gierke, G. E. Munn, and F. C. Wilson, *J. Polym. Sci., Polym. Phys. Ed.*, **19,** 1687 (1981).
16. E. J. Roche, M. Pineri, and R. Duplessix, *ibid.*, **20,** 107 (1982).
17. C. Heitner-Wirguin *et al.*, *Polymer*, **21,** 1327 (1980).
18. M. Falk, *Can. J. Chem.*, **58,** 1495 (1980).
19. P. K. Ng and D. D. Snyder, *This Journal*, **128,** 1714 (1981).
20. N. Sivashinsky and G. B. Tanny, *J. Appl. Polym. Sci.*, **26,** 2625 (1981).
21. K. Erdmann and A. Narebska, *Bull. Acad. Polon. Sci.*, **27,** 589 (1979).
22. W. G. F. Grot, G. E. Munn, and P. N. Walmsley, Paper 154 presented at the Electrochemical Society Meeting, Houston, Texas, May 7-11, 1972.
23. T. Takamatsu and A. Eisenberg, *J. Appl. Polym. Sci.*, **24,** 2221 (1979).
24. Symposium on "Perfluorocarbon Ion Exchange Membranes," The Electrochemical Society Meeting, Atlanta, Georgia, Oct. 9-14, 1977.
25. A. Eisenberg, Editor, "Ions in Polymers," American Chemical Society Symposium Series (1979).
26. R. S. Yeo and R. P. Buck, Editors, "Ion Exchange: Transport and Interfacial Properties," The Electrochemical Society Softbound Proceedings Series, Pennington, NJ (1981).
27. Workshop on Structure and Properties of Solid Ion-containing Polymers, M. Pineri, Chairman, Villard de Lans, France, June 1981.
28. Symposium on Electrochemical Membrane Technology, R. S. Yeo and H. L. Yeager, Chairmen, American Institute of Chemical Engineers Meeting, Orlando, Florida, February 1982.
29. A. Eisenberg and H. L. Yeager, Editors, "Perfluorinated Ionomer Membranes," American Chemical Society Symposium Series (1982).
30. R. S. Yeo, D-T. Chin, and T. Katan, Editors, "Transport Processes in Electrochemical Systems," The Electrochemical Society Softbound Proceedings Series, Pennington, NJ (1982).
31. A. Eisenberg and M. King, "Ion-containing Polymers," Academic Press, New York (1977).
32. T. C. Ward and A. V. Tobolsky, *J. Appl. Polym. Sci.*, **11,** 2403 (1967).
33. A. Eisenberg and M. Navratil, *J. Polym. Sci.*, **B10,** 537 (1972).
34. E. J. Roche, R. S. Stein, T. P. Russell, and W. J. MacKnight, *J. Polym. Sci., Polym. Phys. Ed.*, **18,** 1497 (1980).
35. C. L. Marx, D. F. Caulfield, and S. L. Cooper, *Macromolecules*, **6,** 3 (1973).
36. R. Longworth and D. J. Vaughan, *Nature (London)*, **2,** 85 (1968).
37. A. Eisenberg, *Macromolecules*, **3,** 147 (1970).
38. E. P. Otocka and T. K. Kwei, *ibid.*, **1,** 401 (1968).
39. E. P. Otocka and D. D. Davis, *ibid.*, **2,** 437 (1969).
40. E. P. Otocka, M. Y. Hellman, and L. L. Blyler, *J. Appl. Phys.*, **40,** 4221 (1969).
41. A. B. LaConti, A. R. Fragala, and J. R. Boyack, in "Electrode Materials and Processes for Energy Conversion and Storage," J. D. E. McIntyre, S. Srinivasan, and F. G. Will, Editors, p. 354, The Electrochemical Society Softbound Proceedings Series, Princeton, NJ (1977).
42. R. S. Yeo, in "Transport Processes in Electrochemical Systems," R. S. Yeo, T. Katan, and D-T. Chin, Editors, pp. 178-204, The Electrochemical Society Softbound Proceedings Series, Pennington, NJ (1982).
43. T. R. E. Kressman, P. A. Stanbridge, F. L. Tye, and A. G. Wilson, *Trans. Faraday Soc.*, **59,** 2133 (1963).
44. T. R. E. Kressman, P. A. Stanbridge, and F. L. Tye, *ibid.*, **59,** 2139 (1963).
45. R. S. Yeo, Unpublished data.
46. R. S. Yeo, in "Perfluorinated Ionomer Membranes," A. Eisenberg and H. L. Yeager, Editors, p. 65, American Chemical Society Symposium Series (1982).
47. G. E. Archie, *Trans. AIME*, **146,** 54 (1942).
48. D. A. G. Bruggemann, *Ann. Phys.*, **24,** 636 (1935).
49. R. E. De La Rue and C. W. Tobias, *This Journal*, **106,** 827 (1959).
50. F. Hino and K. Murakami, *ibid.*, **127,** 292 (1980).
51. J. Crank and G. S. Park, in "Diffusion in Polymers," J. Crank and G. S. Park, Editors, p. 16, Academic Press, New York (1968).
52. G. S. Park, in "Diffusion in Polymers," J. Crank and G. S. Park, Editors, p. 141, Academic Press, New York (1968).
53. G. J. van Amerongen, *Rubber Chem. Technol.*, **37,** 1065 (1964).
54. G. A. Olah, J. Kaspi, and J. Bakala, *J. Org. Chem.*, **42,** 4187 (1977).
55. J. P. Randin, *This Journal*, **129,** 1215 (1982).
56. W. T. Grubb, *ibid.*, **106,** 275 (1959).
57. A. B. LaConti, E. N. Balko, T. G. Coker, and A. G. Fragala, in "Ion Exchange," R. S. Yeo and R. P. Buck, Editors, p. 318, The Electrochemical Society Softbound Proceedings Series, Pennington, NJ (1981).
58. R. S. Yeo, J. Orehotsky, W. Visscher, and S. Srinivasan, *This Journal*, 128, 1900 (1981).
59. R. S. Yeo, in "Ion Exchange," R. S. Yeo and R. P. Buck, Editors, p. 311, The Electrochemical Society Softbound Proceedings Series, Pennington, NJ (1981).
60. H. L. Yeager, J. D. Malinsky, and R. L. Dotson, in "Transport Processes in Electrochemical Systems," R. S. Yeo, T. Katan, and D-T. Chin, Editors, pp. 215-222, The Electrochemical Society Softbound Proceedings Series, Pennington, NJ (1982).
61. M. Suhara and Y. Oda, in "Transport Processes in Electrochemical Systems," R. S. Yeo, T. Katan, and D-T. Chin, Editors, pp. 223-234, The Electrochemical Society Softbound Proceedings Series, Pennington, NJ (1982).

A Zinc Paste Primary Battery

Raymond Jasinski,* Robert McCarron,*,[1] and George Brilmyer*,[2]

Occidental Research Corporation, Irvine, California 92713

ABSTRACT

Zinc metal pastes can be electrolytically discharged in a concentrated caustic electrolyte. The ease with which a paste can be pumped is determined by the relative ratios of liquid, zinc, and a smaller particle size phase such as ZnO. These ratios are not arbitrary but are predictable via a model based on the packing of spherical particles. The depth of discharge is limited in part by the original liquid content of the paste.

Zinc/air batteries could, in principle, be used to power electric vehicles. One scheme for enhancing the practical performance of this battery system has been to separate energy density factors from power density factors. This can be accomplished by employing the active negative plate material in the form of a zinc slurry (1, 2) to be circulated from a reservoir through the negative electrode compartment. In this manner, the battery per se, *i.e.*, the current collectors, membranes, leads, frames, etc., are sized for the maximum required power. Only the zinc paste storage reservoir is sized for the required vehicle range. Obviously, the zinc loading per unit volume of fluid should be as high as possible for maximum range. State-of-the-art slurries contain nominally 0.27g of usable zinc per milliliter of slurry.

An extension of this fuel cell-battery concept is to use the active material as a pumpable paste rather than as a slurry (3). Much higher loadings of zinc were reported, *e.g.*, 1.9 g/ml, as well as, high zinc discharge efficiencies, *e.g.*, 85% depth of discharge for 1.6g of active zinc per milliliter of paste. The solid zinc was kept in suspension with Teflon particles; gelling agents were not needed (3).

In this paper, we discuss preliminary experiments on formulating and characterizing pumpable zinc/zinc oxide pastes in the context of a primary zinc/oxygen battery. A "paste" is defined here as a thick viscous mass of solid, uniformly and semipermanently dispersed in a liquid phase.

Not all mixtures of Zn, ZnO, and electrolyte are pumpable. First, we discuss the physical basis for predicting those solid/liquid mixtures that are pumpable pastes. Then, we show that this model has a basis in fact, and that the pastes so formed are indeed electroactive.

Experimental

The zinc dust, obtained from Mallinkrodt, had a mean particle size of 7 microns. Zinc oxide, also obtained from Mallinkrodt, had a mean particle size of 0.3 microns. This was determined from SEM photographs, since agglomeration effects caused sedimentation experiments to overestimate the particle size (0.75 microns). "Fluoroglide" Teflon powder and du Pont 15162 Teflon had average particle sizes of 0.4 microns. All zinc metal-KOH pastes were prepared and handled in a glove box under a nitrogen atmosphere. The silicate-containing pastes (nominally 1M SiO_2) were easier to handle, in that air oxidation appeared to be slower. The ratio "vol. ZnO/100g Zn" was particularly convenient for preparing and identifying pastes, and the data herein is, therefore, presented according to this ratio.

Viscosity measurements were made with a Brookfield viscometer and a "flow apparatus." The flow system, using gas pressure to force paste from a reservoir through the sample tube, was particularly well suited for characterizing paste flow through tubing, bends, and constrictions.

The electromechanical functions of the plate-and-frame cell were first established with static zinc paste mixtures painted into the grooves of the negative plate. The flow patterns of paste were first established with ZnO/KOH mixtures. A plexiglass cover was placed over the current collector so that stagnant areas would be visible; air bubbles were helpful in following paste flow.

The electrochemical capacity of the pastes ("depth of discharge") was the total number of coulombs passed to 70% of open-circuit voltage. The 5 × 5 mm negative electrode channels machined from steel blocks were gold plated to reduce ohmic resistance. The paste was delivered at typically 20 ml/min, into a plenum, through the channels, down the face of the current collector, and was collected at an exit plenum. The positive current collector used 2 × 2 mm silver plated channels with commercial platinum-on-carbon oxygen cathodes (Giner Incorporated, Waltham, Massachusetts). Electrode active area was 100 cm^2.

The anode compartment was separated from the cathode by a Celgard microporous polypropylene separator. Electrolyte was continuously circulated with a peristaltic pump through the cathode compartment. Flow through the membrane was minimal. A double junction reference electrode (SCE) was placed in the cathode compartment.

The equipment used for the paste discharge and polarization studies was of conventional design. A d-c power supply (Hewlett-Packard Model 6267B) was used to operate the zinc paste/oxygen battery under constant current conditions. The applied current was measured with a Keithley Model 179-20A digital voltamp meter. Cell voltages were monitored with a high impedance Keithley digital electrometer and displayed on a Linear Instruments/Strip Chart recorder. A slight positive pressure (nominally 2 in. of H_2O) was maintained across the oxygen cathodes. The electrolyte reservoir was continuously purged with nitrogen. Potential measurements were also made with an interruputer bridge of conventional design, at an interruption frequency of 1000 Hz.

Results

Mixtures of zinc powder and water, or caustic, could not be readily pumped through Tygon, glass, or Teflon-lined glass tubing by either peristaltic or piston pumps. Mixtures of zinc, caustic, and Teflon prepared according to the recipe of Ref. (3) were paste-like initially, but quickly separated into a Teflon phase and a zinc/caustic phase, and could not be pumped. However, mixtures of zinc plus zinc oxide in water and in caustic could be pumped, but only if the proper combination of ingredients was used. The following model, based on paint technology (4), was developed to predict those combinations of fluid, zinc, and zinc oxide which would be pumpable with a peristaltic pump. Commercial metallic zinc paints used for corrosion

* Electrochemical Society Active Member.
[1] Present address: Maintex Incorporated, El Monte, California 91734.
[2] Present address: Johnson Controls, Milwaukee, Wisconsin 53201.
Key words: mixing spherical particles, paste rheology, zinc slurries, critical pigment volume composition.

protection are made with pigments of 80% zinc and 20% zinc oxide.

The basis of the model is that the solid portion of the paste must consist of particles with significantly differing particle diameters, so that the small particles fill the voids between the large particles. Consider mixtures of noninteracting large and small spherical particles. (Photomicrographs indicated that the zinc and zinc oxide particles as received were substantially spherical in shape.) These are five different types, or stages, of mixing spherical particles with differing sizes: (*i*) dense random packing of the large spheres, (*ii*) dense random packing of the large spheres with some interstitial space filled with small spheres, (*iii*) dense random packing of large spheres with maximum filling of interstitial space by dense random packed small spheres, (*iv*) large spheres in a matrix of dense random packed small spheres, and (*v*) dense random packed small spheres. The equations relating the void volume of these mixtures (Q) to the packing fraction of the pure powders (ϕ) are listed in Table I and are derived in the Appendix. For present purposes, the void volume is taken to be that of the electrolyte fluid. The (V) terms are the volumes of the solids only (exclusive of void space). ϕ_A and ϕ_B are measured according to standard techniques (4). Equations [4] and [5] are indeed identical. Q_C can also be expressed by the same equation (see Appendix 1).

The equations of Table I were combined with these data to develop the plot in Fig. 1. The data are plotted out in terms of liquid-to-(solid + liquid) volume ratio *vs.* ZnO to Zn ratio (vol. ZnO/100g Zn).

Mixtures below the solid line have insufficient liquid to completely fill the void space. The circles indicate specific mixtures of zinc, zinc oxide, and water used to establish that these pastes were not pumpable. The "critical pigment volume composition" is the standard term to describe paint mixtures on the line.

The minimum in the curve is a unique ZnO/Zn ratio for given values ϕ_A and ϕ_B. The maximum amount of ZnO fills the interstices of the random close packed zinc, without disturbing the packing of the zinc. The remaining void space is filled with the maximum amount of fluid, again without disturbing the packing of the zinc particles. Increasing either the ZnO or liquid content must force some of the zinc particles apart, increasing the ohmic resistance of the paste. Increasing the liquid content did decrease paste viscosity so that the mixtures were more readily pumped. Mixtures with ZnO/Zn ratios lower than the curve minimum were difficult to pump, and had the appearance of wet gray sand. Mixtures above the dashed line in Fig. 1 were poorly dispersed, in that free-standing electrolyte was visible. With 12*N* KOH and 10*N* NaOH, the upper limit ratio was about 6.

The squares in Fig. 1 represent pumpable zinc pastes with zinc metal loadings of 1.5-2.8 g/ml of paste. These pastes were pseudoplastic; the viscosity decreased with time of mixing and rate of mixing. Figure 2 shows a plot of paste viscosity *vs.* zinc metal loading, in 12M KOH with a constant weight ratio of 0.45 for ZnO to Zn. The viscosity numbers are steady-state readings off the Brookfield viscometer at a constant rotation rate of 30 rpm.

Stable pumpable pastes were also formed with TiO_2 and zinc metal powder. These pastes followed the same model as the zinc oxide pastes (Fig. 1), adjusted for

Table I. Relationships of void volume to packing fractions

1. Dense random packing large spheres	$Q_A = V_A\left(\frac{1}{\phi_A} - 1\right)$
2. Some interstitial small spheres	$Q_B = V_A\left(\frac{1}{\phi_A} - 1\right) - V_B$
3. Maximum filling of interstices	$Q_C = (1 - \phi_B)\left(\frac{1}{\phi_A} - 1\right)V_A$
4. Large sphere in small sphere matrix	$Q_D = V_B\left(\frac{1}{\phi_B} - 1\right)$
5. Dense random packing of small spheres	$Q_E = V_B\left(\frac{1}{\phi_B} - 1\right)$

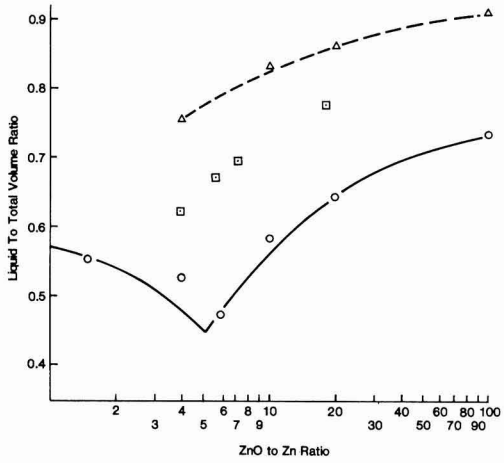

Fig. 1. Plotted are the ratio, liquid volume-to-total paste volume *vs.* volume ZnO(ml)/100g zinc powder forming the paste. Compared are the predictions of the packing model (the curved solid line) with experiment (the data points). The solid line represents the calculated CPVC. The dashed line represents the experimental ratio at which clear fluid separates from the paste. The points represented by squares are readily pumpable.

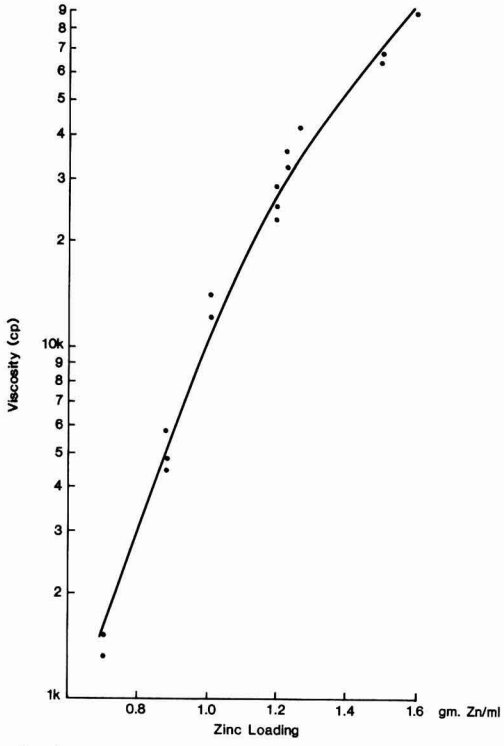

Fig. 2. Viscosity (kcp) readings of a Brookfield viscometer at a constant 30 rpm are plotted for pastes, *vs.* their zinc loading (g Zn/ml). The fluid phase was 12M KOH. The weight ratio ZnO/Zn was 0.45.

the different packing fraction of the particular titanium dioxide used.

Stable pastes could be formed with carbon and zinc, but only if the trace metal content of the carbon was low enough to maintain a low rate of hydrogen evolution. Otherwise, the mix would froth rapidly. Shown in Table II are the hydrogen evolution rates for a variety of zinc/carbon pastes. Considerable frothing was observed with the XC 72 and vitreous carbon materials but not with the Ultra F. Successful pastes were constructed with Ultra carbons. The packing fractions of these carbons were not determined.

Surfactants were tested as a means of decreasing paste viscosity. Fluorosurfactants did decrease viscosity but they invariably resulted in separation of the liquid and solid phases, especially under pressure. Including sodium silicate with the paste mixture significantly decreased viscosity. Silicates are used for this purpose in commercial zinc paint formulations. At high head pressure, liquid separation was again observed. Shown in Table III are Brookfield viscosity data at 30 rpm for zinc/ZnO/OH^- pastes with and without silicate present (1M SiO_2). Different electrolytes and concentrations were used than those for the data of Fig. 2. However, since the relative viscosity of 10M NaOH (16.8) is higher than the relative viscosity of 20M KOH (6.5), it is clear that sodium silicate does decrease paste viscosity.

The pastes made, according to the model of Fig. 1, are electroactive even well away from the CPVC line. Shown in Fig. 3 are the IR free zinc electrode potentials as a function of current density for 2 pastes. These rate data and the following capacity data were carried out with the "static" test cell. The ZnO/Zn mix (x points) had a liquid/solid ratio of 0.98, for a ZnO/Zn ratio (as defined for Fig. 1) of 28. The zinc/carbon mixture had a liquid/solid ratio of 3.4. Zinc/ZnO/KOH, silicate pastes gave similar performance data.

In all electrolytes, the discharge product was initially a blue-colored solid. Microscopic observation of this material indicated zinc metal coated by a waxy gelatinous mass which we presumed to be zinc hydroxide A white translucent material coating a gray mass will give the illusion of a blue-colored solid.

While the initial current/voltage profiles were essentially independent of paste composition and electrode configuration, paste capacity was significantly dependent upon these factors. It is to be expected from Ohm's law considerations that narrow channels, as well as the presence of an inert conductor (carbon) within the mix, would increase utilization of the zinc component. Indeed, this was the case. Shown in Table IV, as a function of channel depth, are discharge capacities for zinc pastes containing zinc oxide and carbon. The data shown are for equal weight ratios of zinc to carbon and to zinc oxide. Since the graphite is 2.5 times less dense

Table II. H_2 evolution rate from zinc-carbon pastes (2.9g carbon + 11g Zn + 11g KOH)

Carbon	Rate (ml/min)
None	0.006 ± 0.003
Vitreous carbon	1.45
Cabot XC 72	0.66
Ultra F	0.014

Table III. Effect of silicate on paste viscosity

Zinc loading (g/ml)	Paste viscosity (10^{+3} cp) 12M KOH	Silicate* + 10M NaOH
0.84	6.2	1.8
1.01	12	4.3
1.2	26	8.0

* Nominally 1M as SiO_2.

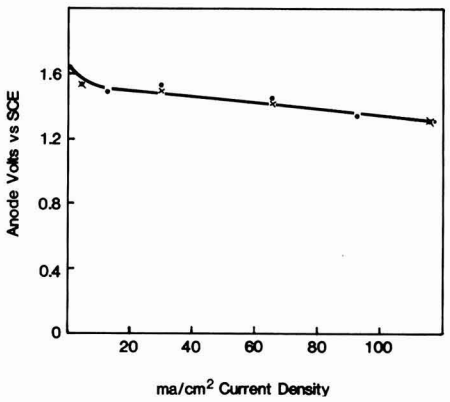

Fig. 3. Shown are the initial internal resistance-free potentials for the zinc electrode (SCE) vs. current density (mA/cm^2) for two pastes ZnO/Zn (×) and graphite/Zn (°).

than ZnO, the volume content of the conducting phase is much larger. At equal volume ratios, the depth of discharge of the 2.8g Zn/ml paste was 26% with graphite and 9% with ZnO (5 × 5 mm channels).

A preliminary study was made of pumping paste through an electrochemical cell. The major considerations in system design were to avoid constrictions and to avoid stagnant zones. With the appropriate cell design, we were able to sustain a current density of 10 mA/cm^2 at 1.1V (including internal resistance losses) pumping a Zn/ZnO/silicate-caustic paste for 18 hr over a 3 day period. In this case, the cell electrolyte was immobilized and not circulated; the pumping was deliberately semicontinuous to simulate on/off operation, and nominally 2% of the paste capacity was discharged. Eventual deterioration of the cell was due to oxygen electrode poisoning.

Half-cell measurements indicated a fall off in cell voltage above 50 mA/cm^2 due primarily to the effects at the oxygen electrode. Rotating disk studies confirmed an increase in platinum oxygen electrode overvoltage due to dissolved silicate.

Discussion

It is indeed possible to formulate metal/electrolyte pastes that are stable with time, pumpable, have high metal loadings, and are also electroactive. The ratios of the components within such pastes are not arbitrary, but approximate values calculated from a model based on the following precept. It is necessary that there be two solid particle size distributions within the paste, and sufficient smaller particles so that they at least completely pack within the spaces between the larger particles. The required ratio of fine particles to large particles is then readily determined by simple measurements of the packing density of the individual solids. This concept is classic to preparing metal paints (4).

We have shown herein that electroactive pastes can be formulated according to this model from binary mixtures of zinc dust, with ZnO, or TiO_2 powders. Satisfactory (as defined above) graphite/zinc pastes could also be formed. Presumably, finely divided zinc could

Table IV. Depth of discharge vs. channel size (at 10mA/cm^2)

Paste (gram Zn/ml)	Channel size	Depth of discharge (%)
2.48 + ZnO	5 × 5 mm	9.4
	1.5 × 1.5 mm	35
1.05 + graphite	5 × 5 mm	40
	1.5 × 1.5 mm	49

have been substituted for the oxides. The smaller particle size component, in principal, need not be a different chemical than the larger particle size material. This particular variant on the concept was not tested.

These pastes were pumpable but had high viscosities. The addition of surfactants lowered the viscosities, but also had an adverse effect on the flow characteristics at high head pressures. The flow patterns chosen for the pastes must avoid stagnant regions, such as found at abrupt constrictions. Pumping through glass tubes and bends was possible; pumping through Teflon-lined tubing required a lower pressure. It is to be expected that the half-cell potentials governing the rate at which electrical charge can be exchanged between the paste and current collector will be influenced by particle-particle contact (metal/oxide ratio) and the particle-collector contact. Indeed, the depth of discharge (to a preselected cutoff voltage) was found to increase by using more narrow channels surrounding the paste. Pastes containing conductive graphite rather than insulating ZnO gave higher depths-of-discharge.

In principle, this model can also predict the maximum depth of discharge for the electroactive paste. The half-cell reactions, the packing density of the discharge product(s), and the packing density of the partially discharged starting material (here Zn) must be known. Rigorous values for these parameters are not available for the zinc/oxygen system. Nevertheless, an approximate depth of discharge can be calculated. Assuming the cell reaction to be

$$Zn + \tfrac{1}{2}\,O_2 + H_2O = Zn(OH)_2$$

and assuming zinc particles are replaced by zinc hydroxide particles of the same packing density as the ZnO used to make the paste, the maximum capacity for the 2.48 g/ml paste described above is 20%. This is 0.5g active zinc per milliliter of paste. The 2.48g Zn/ml paste discharged to 35% had no fluid properties. The 9% depth of discharge material (originally 2.43g Zn/ml) had a solid crust, coating a paste-like material. It is inferred that the approximation is not totally unreasonable. Thus, this 2.48g Zn paste could have a capacity significantly higher than zinc/caustic slurries (0.28 g/ml).

Manuscript submitted July 22, 1982; revised manuscript received Sept. 28, 1982.

Any discussion of this paper will appear in a Discussion Section to be published in the December 1983 JOURNAL. All discussions for the December 1983 Discussion Section should be submitted by Aug. 1, 1983.

Publication costs of this article were assisted by Occidental Research Corporation.

APPENDIX

Derivation of Table I

1. Define the packing fraction as $\phi_A = V_A/V_T$ and $\phi_B = V_B/V_T$. V_A, V_B are the volumes of the particulate substances, exclusive of the void volume. These can be calculated from the density and the weight of the particles. V_T is the total volume actually occupied by the powder. In this discussion (A) represents the large particles, and (B) represents the smaller particles.

2. Thus, $V_{void} = V_T - V_A$, and $V_{void} = V_T(1 - \phi_A)$. Here, V_{void} is the space occupied by the liquid, *i.e.*, Q_A. Hence, $Q_A = (V_A/\phi_A)(1 - \phi_A) = V_A(1/\phi_A - 1)$.

3. The most dense packing occurs when V_{void} is V_T for the smaller particles. Thus, with V_{void} defined as above

$$V_B = \phi_B\, V_{void}$$

The volume of liquid Q_C is, by definition

$$Q_C = V_{void} - V_B$$

$$Q_C = V_{void}(1 - \phi_B) = V_T(1 - \phi_A)(1 - \phi_B)$$

$$V_T = V_A/\phi_A$$

$$Q_C = V_A\left(\frac{1}{\phi_A} - 1\right)(1 - \phi_B)$$

Q_C can also be expressed in terms of ϕ_B and V_B as follows

$$V_B = \phi_B\, V_{void}$$

$$Q_C = \frac{V_B}{\phi_B}(1 - \phi_B) = V_B\left(\frac{1}{\phi_B} - 1\right)$$

This relationship deserves some explanation. Q_C is the volume of liquid to be added. All the space among the large particles that can be occupied by smaller particles is occupied by smaller particles. The void space left over is that associated with the smaller particles only. The total volume of spheres plus liquid is now larger because of the larger particles, but the liquid volume is the same as with the smaller particles alone. For the same reason Q_D lacks a contribution from V_A.

REFERENCES

1. A. J. Appleby and M. Jacquier, *J. Power Sources*, **1**, 17 (1976).
2. H. Baba, SAE Tech. Paper 71-02-37 (1971).
3. B. Warszawski, U.S. Pat. 4,172,924 (1979).
4. T. Patton, "Paint Flow and Pigment Dispersion," John Wiley & Sons, New York (1979).

Incorporation of Chloride Ion in Passive Oxide Films on Nickel

B. MacDougall,* D. F. Mitchell, G. I. Sproule, and M. J. Graham

National Research Council of Canada, Division of Chemistry, Ottawa, Ontario, Canada K1A 0R9

ABSTRACT

Auger electron spectroscopy and secondary ion mass spectrometry, in conjunction with ion sputtering, have been used to demonstrate that chloride is incorporated in anodic oxide films formed on nickel in Cl^--containing, *p*H 4.0 Na_2SO_4 solutions. X-ray photoelectron spectroscopy indicates that this chloride is present as Cl^-. Cl^- is found in the first two layers of the four layers of the oxide, with the amount in the second layer being about twice that in the outermost layer. The extent of Cl^- incorporation is dependent on the $[Cl^-]$ in solution, electrode pretreatment (whether electropolished or cathodically reduced), and the potential and time of anodization. The amount of Cl^- in the oxide can thus be carefully controlled and varied. Cl^- incorporation does not occur when electropolished nickel is cathodically reduced in a 1.0M Cl^- solution and then air-exposed; anodic polarization in the passive potential region is necessary to fix Cl^- in the oxide lattice. Cl^- is incorporated when passive oxide films are formed in non-Cl^- solutions and then exposed to Cl^--containing electrolytes with an applied anodic potential. This incorporation is most probably associated with local breakdown-repair events at defects in the film as the rate of incorporation decreases with increasing perfection of the oxide.

It is well known that aggressive anions like Cl^- cause pitting of metals such as nickel, iron, and the stainless steels. The rapid metal dissolution associated with pitting appears to be due to the ability of the Cl^- to interfere with formation of the passive oxide film at localized surface sites. The importance of the oxide film in pit initiation and propagation is recognized and some of the pitting work in the literature has been specifically concerned with the influence of Cl^- on the nature of passive oxide films (1-13). In this previous work, there has been considerable disagreement as to whether Cl^- is incorporated in the oxide film prior to pitting. Ellipsometric studies on both iron and stainless steel suggest that incorporation of Cl^- is an integral part of the pitting process and may even determine the induction time for pitting (3-5). On the other hand, analyses (using UHV surface analytical techniques) of passive films formed in Cl^- solutions, both before and after pit initiation, appear to indicate that Cl^- is only adsorbed on the oxide surface, no detectable Cl^- being found in the oxide film (7-13). The present paper employs both Auger electron spectroscopy (AES) and secondary ion mass spectrometry (SIMS) to establish that Cl^- is incorporated in passive oxide films on nickel. The influence of the $[Cl^-]$ in solution, potential and time of anodization, and electrode pretreatment on the extent of incorporation is studied.

Experimental

Polycrystalline nickel specimens, 1 × 2.5 cm, were prepared as described previously (14). Potentials are referred to the saturated calomel reference electrode. Experiments were conducted at 25°C in a deaerated solution of 0.15*N* Na_2SO_4 at *p*H 4.0. In one series, nickel samples electropolished (EP) in 57 volume percent sulfuric acid were cathodically reduced (CR) at 20 $\mu A\ cm^{-2}$ and then were passivated in solutions of various $[Cl^-]$ using the potential step technique. The same solution was used for both CR of the prior oxide and the anodic passivation treatment. In a second series of experiments, electropolished nickel was immersed directly in the electrolyte with the anodic potential applied, *i.e.*, with no CR of the prior oxide. In a third series, nickel samples were passivated in non-Cl^- solutions and then transferred to Cl^--containing solutions for further anodic polarization. In all cases, samples were extensively flushed with doubly distilled water after the anodic treatment to ensure that all of the Cl^--containing electrolyte was removed from the surface. They were then dried with compressed air before installing in a Physical Electronics Incorporated Model 590 System for analysis by AES, SIMS, and x-ray photoelectron spectroscopy (XPS). Xenon ion sputtering at 0.5 kV was used to obtain both Auger and SIMS depth profiles through the oxide films (15-17), and the Auger sputter profiles were evaluated to give a layer-by-layer composition using the quantitative approach previously described (18).

* Electrochemical Society Active Member.

Key words: corrosion, passivity, surfaces.

Results and Discussion

AES and SIMS analyses of oxide films.—Figure 1 shows Auger spectra of EP nickel electrodes passivated at 0.3V for 15 sec in *p*H 4.0 Na_2SO_4 solutions of various $[Cl^-]$, both with and without CR of the prior oxide. Principal Auger electron signals associated with chlorine, carbon, oxygen, and nickel are indicated; of particular interest is the Cl signal at 181 eV. While little or no Cl is evident for the sample passivated in the Cl^--free solution, *i.e.*, Fig. 1(a), the samples treated in Cl^--containing solutions show a distinct Cl Auger signal. XPS spectra showed that the chlorine is present as Cl^- rather than as an oxychloride such as ClO_3^- and ClO_4^-. The Auger signals in Fig. 1 indicate homogeneous atomic concentrations of Cl^- of 1.0

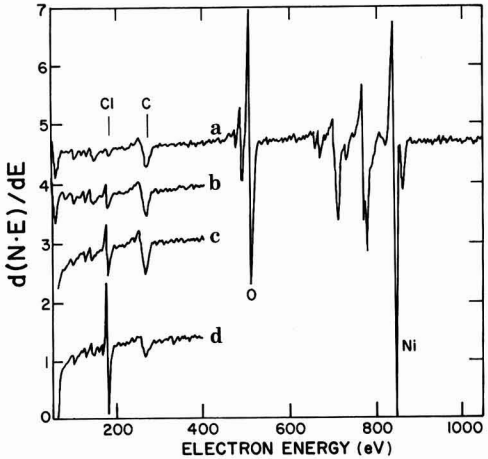

Fig. 1. Auger electron spectra of electropolished (EP) nickel passivated, either with or without cathodic reduction (CR) of the prior film, at 0.3V for 15 sec in *p*H 4.0 $NaSO_4$ solutions with different $[Cl^-]$. (a) CR and passivation in a solution with $[Cl^-] = 0$; (b) no CR and $[Cl^-] = 1.0M$; (c) CR and $[Cl^-] = 0.1M$; (d) CR and $[Cl^-] = 1.0M$. Above ~400 eV, spectrum (a) is typical of the other three spectra. (Electron beam 5 keV with a current ~0.3 μA; modulation 4 eV peak-to-peak.)

atomic percent (a/o) in Fig. 1(b), 1.8 a/o in (c), and 4.4 a/o in (d); the oxygen signal corresponds to ~30 a/o in each case and this represents an average oxide thickness of ~9Å, *i.e.*, the usual value for the passive film on nickel (14, 16, 17). The homogeneous atomic percent of Cl^- is defined as the concentration present if the chloride was uniformly distributed within the analysis volume.

While the Auger analyses indicate the presence of Cl^- in the surface regions of nickel passivated in Cl^--containing solutions (most of the signal comes from the top 15Å), they do not indicate how the Cl^- is distributed through the oxide. In fact, different concentrations of Cl^- within the analysis volume could give the same homogeneous atomic concentration simply by being distributed differently throughout the ~4 layers of nickel oxide. This situation arises because the contribution of any species to its overall measured Auger signal decreases exponentially with increasing distance from the outer surface. A layer-by-layer distribution of Cl^- can, however, be determined when the Auger analysis is performed in conjunction with ion beam sputtering (18).

An Auger sputter profile for a nickel oxide film with a homogeneous atomic concentration of Cl^- of 4.4% is shown in Fig. 2. The peak-to-peak (P/P) signal heights are plotted (cf. Fig. 1) for the various species through the film. The carbon signal falls off rapidly with most disappearing before the equivalent of one oxide layer has been sputtered, indicating that the carbon is an adsorbed surface contaminant. On the other hand, the Cl^- signal initially increases and then falls off slowly as the oxide is removed. While the initial increase is at least partly due to the removal of the carbon contamination which absorbs some of the Cl^- signal, it appears that Cl^- is incorporated or buried in the film rather than simply adsorbed on the surface. The Auger sputter profile in Fig. 2 quantitatively analyzed on a layer-by-layer basis (18) gives the elemental compositions listed in Table I. While the Cl^- is concentrated in the outer layers of the oxide, the increase from 6 a/o in the outermost layer to ~14 a/o in the second layer suggests that the Cl^- is incorporated in the oxide lattice. These calculated concentrations best fit the experimental profiles of Fig. 2; noticeable differences between calculated and experimental values occur if some of the Cl^- of layer 2 is put into layer 3. It should be further noted that the depth distribution given in Table I is independent of the total amount of Cl^- incorporated in the oxide. Also, similar layer-by-layer analysis of

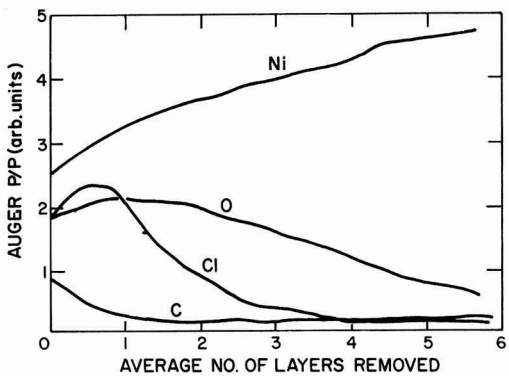

Fig. 2. Auger peak-to-peak (P/P) sputter profiles of various species in a nickel oxide film formed at 0.3V in 1.0M Cl^- solution. (Film corresponds to spectrum (d) in Fig. 1 and has a homogeneous Cl^- concentration of 4.4 a/o.) Sputter rate using 0.5 kV xenon is 0.6 layer min^{-1}; 1 layer $\simeq$ 2Å of NiO. (Each profile drawn through ~60 data points.)

Table I. Layer-by-layer composition (18) of the oxide formed by anodizing cathodically reduced (CR) nickel at 0.3V for 15 sec in pH 4.0 Na_2SO_4 + 1.0M Cl^- solution. Electron neutrality is maintained in each layer. (1 layer $\equiv$ 1.6 $\times$ 10^{15} atoms $cm^{-2} \simeq$ 2Å NiO).

Layer	Atomic composition (%) Ni	O	Cl	C
1	0.37	0.34	0.06	0.24
2	0.47	0.40	0.14	0.00
3	0.50	0.50	0.00	0.00
4	0.50	0.50	0.00	0.00

the oxide film on Fe-26Cr electropolished in $HClO_4$/CH_3COOH shows that substantial amounts of Cl^- are also incorporated in the outer 6 layers of the ~10 layers of oxide (18).

The anodic oxide films formed with various [Cl^-] were also analyzed by SIMS which has a very high sensitivity for Cl^- detection; the sputter profiles for films corresponding to (a), (b) and (d) in Fig. 1, are shown in Fig. 3. The curve shown for oxygen is representative of the O^- SIMS profile in each case. The SIMS profiles also indicate that Cl^- is incorporated in the oxide, the maximum Cl^- SIMS signal occurring after ~1 layer has been removed. The passive film gives only a very small Cl^- signal as anticipated for a film formed in a non-Cl^- solution. This Cl^- is thought to be due to system contamination and like C is on the sample surface. The film formed in 1.0M Cl^- solution after CR of the prior oxide gives a substantially higher maximum Cl^- signal than the film formed without CR, in agreement with the Auger analysis in Fig. 1. Indeed, the maximum SIMS signal for Cl^- may be correlated with the homogeneous atomic percent concentration of Cl^- determined by AES over a wide range of incorporated Cl^- levels. This is shown in Fig. 4 and Table II for samples prepared at different potentials and with different [Cl^-] in solution.

As indicated by the data in Table II, the Auger analysis is not reliable below a Cl^- level of ~0.5 a/o, but SIMS can detect very small amounts of Cl^- in

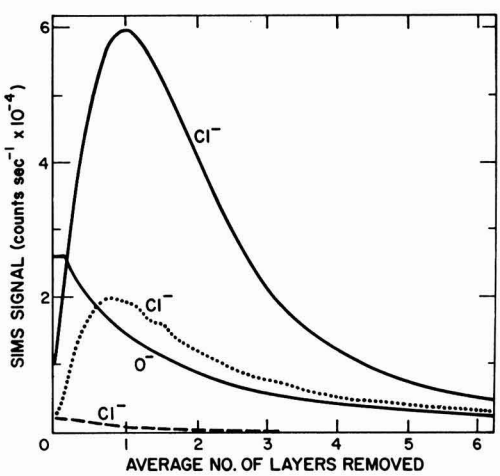

Fig. 3. SIMS Cl^- (mass 35) sputter profiles of electropolished (EP) nickel, passivated either with or without cathodic reduction (CR) of the prior film, at 0.3V for 15 sec in pH 4.0 Na_2SO_4 solutions with different [Cl^-]. (i) CR and passivation in a solution with [Cl^-] = 0 (---); (ii) no CR and [Cl^-] = 1.0M (●●●); (iii) CR and [Cl^-] = 1.0M (——). Also shown is a representative sputter profile for O^- (mass 16). Sputter rate using 0.5 kV xenon is 0.6 layer min^{-1}; 1 layer $\simeq$ 2Å of NiO. (Each profile drawn through ~60 data points.)

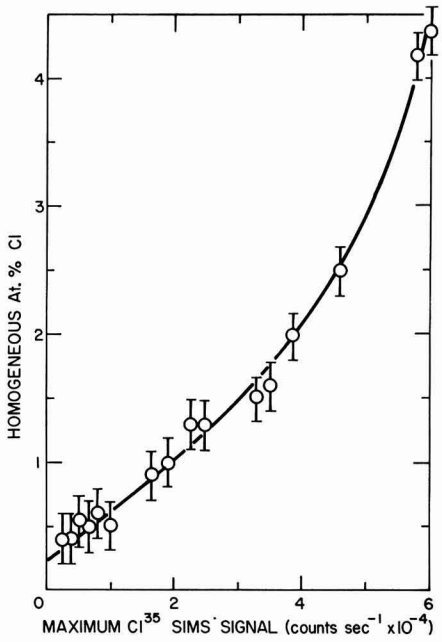

Fig. 4. Correlation between the homogeneous atomic percent concentration of Cl^- determined by AES and the maximum SIMS signal for Cl^- obtained during sputtering of anodic oxide films containing various incorporated Cl^- concentrations. (Error bars represent a 95% confidence level determined from five measurements.)

the oxide film. As the Cl^- level increases above ~5 a/o, the SIMS signal (Fig. 4) becomes less sensitive to changes in $[Cl^-]$ so that at these higher concentrations AES is the preferred method of analysis. At intermediate Cl^- levels both SIMS and Auger can be effectively used to study Cl^- incorporation into anodic oxide films on nickel.

Factors influencing the extent of Cl^- incorporation. —Figure 5 shows the influence of bulk $[Cl^-]$ in pH 4.0 Na_2SO_4 solution on the amount of Cl^- in the anodic oxide film formed at 0V. This amount increases logarithmically with increasing bulk $[Cl^-]$. Figure 6 shows the influence of anodic potential on the extent of Cl^- incorporation in solutions containing 0.1 and 1.0M Cl^-. The amount of Cl^- in the film increases with potential, the data generating an S-shaped profile

Table II. Comparison of SIMS and Auger signals for Cl^- in oxide films formed on nickel after different electrochemical treatments in pH 4.0 Na_2SO_4 solutions with various $[Cl^-]$ (EP, electropolished; CR, cathodically reduced). The SIMS signal quoted is the maximum obtained during sputter etching by 0.5 kV Xe ions.

Treatment		Counts (Cl-) by SIMS (±10%)	Homogeneous a/o Cl- by Auger (±0.2%)
Anodized in Cl-free solution		2,000	0.4
EP + CR in 0.1M Cl- + air exposure		2,800	0.4
EP + CR in 1.0M Cl- + air exposure		3,500	0.4
CR and anodized at 0V in:	0.025M Cl-	7,800	0.6
	0.1M Cl-	16,000	0.9
	1.0M Cl-	37,000	1.8
CR and anodized in 1.0M Cl- at:	−0.3V	8,400	0.6
	0V	37,000	1.8
	0.3V	60,000	4.4
Anodized at 0.2V in 0.1M Cl- after:	CR	33,600	1.5
	No CR	10,000	0.5
Anodized at 0.3V in 1.0M Cl- after:	CR	60,000	4.4
	No CR	19,000	1.0

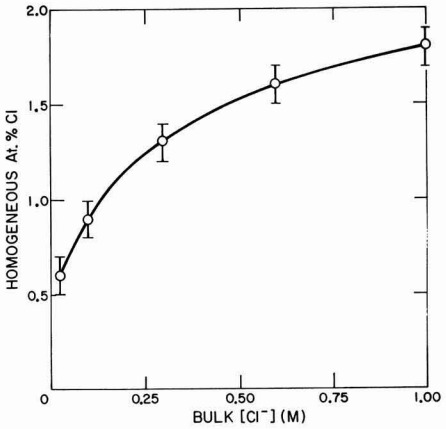

Fig. 5. Dependence of amount of Cl^- in oxide film, determined by AES, on bulk $[Cl^-]$ in pH 4.0 Na_2SO_4 solutions. In each case, electropolished nickel was cathodically reduced (CR) to remove the prior oxide film; the potential was then stepped to 0V and held there for 15 sec. (Error bars for the 95% confidence level are smaller than in Fig. 4 and 6 since all samples were analyzed during same machine loading.)

often found for adsorption isotherms [cf. Ref. (19)]. (Experiments cannot be performed beyond 0.5V with 1.0M Cl^- since pitting starts almost immediately under these conditions.) The results in Fig. 5 and 6 indicate that the amount of Cl^- incorporated in the passive oxide film on nickel can be controlled and varied through the bulk $[Cl^-]$ in solution and the anodic potential.

To check the influence of time of anodization on the amount of incorporated Cl^-, samples were prepared at 0V (in both 0.1 and 1.0M Cl^-) for 3 sec, 60

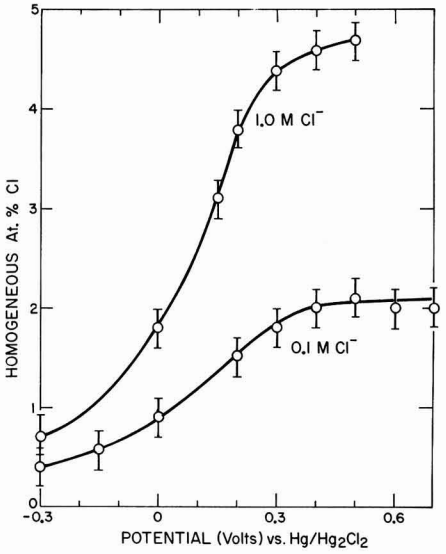

Fig. 6. Dependence of amount of Cl^- in the oxide film, determined by AES, on anodizing potential in pH 4.0 Na_2SO_4 solutions containing 0.1M Cl^- and 1.0M Cl^-. Electropolished nickel was cathodically reduced (CR); the potential was then stepped to the desired value and held there for 15 sec. At potentials above 0.4V with 0.1M Cl^- and 0.3V with 1.0M Cl^-, the holding time was only 3 sec since pitting began at longer times. (Error bars represent a 95% confidence level determined from five measurements.)

sec, and 1 hr and then analyzed for Cl^- by AES. The amount of incorporated Cl^- was independent of anodizing time at each solution [Cl^-], indicating that Cl^- incorporates rapidly. This is not surprising since most of the Cl^- should incorporate while the film is forming and most of the oxide forms during the first few seconds after the potential is stepped into the passive region (14, 20). Thus, the extent of Cl^- incorporation determined at higher potentials (>0.4V), using shorter anodization times to avoid pitting, can be compared with the data obtained at lower potentials where somewhat longer anodizing times are used (cf. Fig. 6).

To determine the extent of Cl^- incorporation in the absence of an applied anodic potential, electropolished electrodes were immersed in 0.1 and 1.0M Cl^- pH 4.0 Na_2SO_4 solutions, the prior oxide was cathodically reduced and the electrodes were then exposed to the air, immediately flushed with doubly distilled water, and dried. The results of the Cl^- analysis indicate that very little Cl^- is incorporated in the oxide in the absence of an anodizing potential (Table II). While an oxide is formed immediately on the oxide-free nickel surface upon exposure to the air, Cl^- in the electrolyte remaining on the surface is not substantially incorporated into the film.[1] This indicates that most of the Cl^- present in the film is fixed in the film during the passivation treatment and is not due to the specimen either being cathodically reduced in the Cl^- solution or being briefly in contact with the Cl^--containing electrolyte after removal from the cell prior to washing. Table II also shows that the extent of Cl^- incorporation is substantially decreased if the prior oxide on the electropolished electrode is not cathodically reduced before the anodic passivation (see also Fig. 1). The increase in oxide film thickness upon passivation of electropolished samples is only ~30% (17), and the small amount of Cl^- that is incorporated in the oxide may be associated with this increase in film thickness.

Finally, the kinetics of Cl^- incorporation into passive oxide films were studied by initially preparing the oxide in a Cl^--free solution followed by polarization for different times in a Cl^--containing solution. The results obtained with a 10 min prior passivation at 0.2V and subsequent polarization at this potential for different times in 1.0M Cl^- are shown in Table III. The amount of incorporated Cl^- increases with time of polarization in 1.0M Cl^- solution and eventually approaches the value expected if the film had been prepared in the 1.0M Cl^- solution (cf. Fig. 6). The results can be explained in terms of the "defect model" of the passive oxide film and the breakdown-repair events that occur at local sites within the film (13, 17, 20-22). When the film is polarized in Cl^- solution, local breakdown of the oxide (by, *e.g.*, chemical dissolution) is followed by its reformation, and thus Cl^- is locally incorporated into the film. Breakdown-repair events occur at random on the surface and, if the time period is sufficiently long, all of the surface will experience these events and the level of incorporated Cl^- will eventually reach a steady value appropriate for that solution [Cl^-] and anodic potential. The rate of increase of incorporated Cl^- is not constant with time because the oxide film perfects with time of anodization, even in a Cl^--containing solution. This means that there are fewer defects to break down and thereby lead to Cl^- incorporation in the film. The kinetics of Cl^- incorporation are also highly dependent on the defect state of the prior oxide since this determines the frequency of breakdown-repair events. The rate of incorporation is understandably higher with the electropolished film (Table III) since this oxide is more defective than the anodic film formed after 10 min at 0.2V. On the other hand, a highly perfect passive film like that formed by a 50 hr anodization at 0.2V has few defects and consequently, as seen in Table III, the rate of Cl^- incorporation is low.

Local incorporation of Cl^- into passive oxide films may be important in the initiation of pitting on previously passive metal surfaces and more work along these lines is underway. It should be noted, however, that while the present work shows that considerable Cl^- can be incorporated into the oxide lattice, this does not mean that such incorporation is a necessary precursor to pit initiation.

[1] The same result is obtained if the flushing of the Cl^--containing electrolyte from the sample with doubly distilled water is delayed for ~5 sec after air exposure.

Table III. Extent of Cl^- incorporation (as determined by AES) into preformed Cl^--free oxide films as a function of time of exposure to 1.0M Cl^- pH Na_2SO_4 solutions at 0.2V (EP, electropolished).

Prior treatment	Time of exposure to 1.0M Cl^- at 0.2V	Homogeneous a/o Cl^- (±0.2%)
Anodized at 0.2V for 10 min	60 sec	0.5
Anodized at 0.2V for 10 min	10 min	0.8
Anodized at 0.2V for 10 min	24 hr	2.7
Anodized at 0.2V for 50 hr	24 hr	0.6
EP	15 sec	1.0
EP	10 min	2.1

Manuscript submitted May 10, 1982; revised manuscript received Sept. 2, 1982.

Any discussion of this paper will appear in a Discussion Section to be published in the December 1983 JOURNAL. All discussions for the December 1983 Discussion Section should be submitted by Aug. 1, 1983.

Publication costs of this article were assisted by the National Research Council of Canada.

REFERENCES

1. M. E. Curley-Fiorino and G. M. Schmid, *Corros. Sci.*, **20**, 313 (1980).
2. G. Okamoto and T. Shibata, in "Passivity of Metals," R. P. Frankenthal and J. Kruger, Editors, p. 646, The Electrochemical Society Inc., Princeton, NJ (1979).
3. J. R. Ambrose and J. Kruger, in "Proceedings of Fourth International Congress on Metal Corrosion, Amsterdam, 1969," p. 698, NACE, Houston (1972).
4. S. Matsuda, K. Sugimoto, and Y. Sawada, in "Passivity of Metals," R. P. Frankenthal and J. Kruger, Editors, p. 699, The Electrochemical Society, Inc., Princeton, NJ (1979).
5. C. L. McBee and J. Kruger, in "Proceedings of U.R. Evans International Conference on Localized Corrosion, 1971," p. 252, NACE, Houston (1974).
6. T. P. Hoar, D. C. Mears, and G. P. Rothwell, *Corros. Sci.*, **5**, 279 (1965).
7. Z. Szklarska-Smialowska, H. Veifhaus, and M. Janik-Czachor, *ibid.*, **16**, 649 (1976).
8. M. Janik-Czachor, A. Szummer, and Z. Szklarska-Smialowska, *ibid.*, **15**, 775 (1975).
9. M. Janik-Czachor, *Werkst. Korros.*, **30**, 225 (1979).
10. M. Janik-Czachor, *Corrosion*, **35**, 360 (1979).
11. M. da Cunha Belo, B. Rondot, F. Pons, and J. P. Langeron, *This Journal*, **124**, 1317 (1977).
12. A. E. Yaniv, J. B. Lumsden, and R. W. Staehle, in "Passivity and its Breakdown on Iron and Iron Base Alloys," R. W. Staehle and H. Okada, Editors, p. 72, NACE, Houston (1976).
13. B. MacDougall, *This Journal*, **126**, 919 (1979).
14. B. MacDougall and M. Cohen, *ibid.*, **121**, 1152 (1974).
15. D. F. Mitchell, G. I. Sproule, and M. J. Graham, *J. Vac. Sci. Technol.*, **18**, 690 (1981).
16. B. MacDougall, D. F. Mitchell, and M. J. Graham, *This Journal*, **127**, 1248 (1980).
17. B. MacDougall, D. F. Mitchell, and M. J. Graham, *Corrosion*, **38**, 85 (1982).

18. D. F. Mitchell, *Appl. Surf. Sci.*, **9**, 131 (1981).
19. G. Horanyi, J. Solt, and F. Nagy, *J. Electroanal. Chem. Interfacial Electrochem.*, **31**, 95 (1971).
20. B. MacDougall, D. F. Mitchell, and M. J. Graham, *Israel J. Chem.*, **18**, 125 (1979).
21. B. MacDougall and M. Cohen, *This Journal*, **124**, 1185 (1977).
22. B. MacDougall, *ibid.*, **125**, 1183 (1978).

Experimental Determination of the Passive-Active Transition for Iron in 1M Sulfuric Acid

Philip P. Russell* and John Newman**

Department of Chemical Engineering, University of California, Berkeley, California 94720

ABSTRACT

Current-voltage curves from three iron rotating disks are obtained using a polarization device which permits determination of the transition region between the active and passive states. Diameters of the three electrodes are 0.494, 0.298, and 0.0986 cm, respectively. Results from the smallest electrode have the least amount of ohmic distortion. Trends in the data, which are observed as the electrode size is decreased, form the basis for the conclusions that are drawn from this work. Analysis of these trends indicates that the active-passive transition is characterized by a nearly vertical line on a current *vs.* potential plot. The Z-shaped nature of the current-voltage curves, reported by Epelboin *et al.*, is entirely due to ohmic potential drop in the solution. Analysis of the data, within the framework of a mathematical model presented by Law and Newman, indicates that the average current density on the active portion of the disk increases as the size of the active area decreases during the passivation process.

Passivation of iron in sulfuric acid was first observed by Flade (1). More recently, it has been shown that polarization curves for iron rotating disk electrodes, obtained with a potentiostat, in 1M sulfuric acid have displayed a hysteresis loop that obscured the current-voltage behavior of the active-passive transition. Epelboin *et al.* (2) have shown how this obscured current-voltage behavior can be traced in a stable manner using a polarization device known as a Negative Impedance Converter. Because of their characteristic shape, current-voltage curves obtained with this device were termed Z-shaped curves. Law and Newman (3) developed a mathematical model describing the passivation process. This model qualitatively duplicated the Z-shaped passivation curves that were experimentally obtained by Epelboin *et al.* The model indicates that the Z-shape is due entirely to ohmic potential drop. The resistance between the disk and the counterelectrode increases as the active area of the electrode decreases during the passivation process, resulting in a complication of the analysis.

The purpose of this paper is to present and analyze a series of experimentally determined passivation curves, each having a different amount of distortion due to ohmic potential drop. Results of this analysis indicate that the underlying assumptions in Law and Newman's mathematical model are correct. Specifically, the important assumption that the local passivation behavior of iron can be represented by a vertical transition on a current density *vs.* $(V - \Phi_0)$ plot is verified. Here, V is the electrode potential and Φ_0 is the potential in the solution just outside the electric double layer.

Three rotating disk electrodes, each having a different diameter, were used in this study. The smallest of these electrodes passed the least amount of total current; therefore, it rendered results that had the least amount of ohmic distortion. Conclusions were drawn from trends in the experimental results that were observed as the degree of ohmic distortion was reduced.

The active area of the disk decreases as the disk goes from the active to the passive state. The mathematical model of Law and Newman (3) indicates that the average current density on the active portion of the electrode should increase as the active area decreases. Using optical microscopy to determine the active area, Epelboin *et al.* (2) reported the opposite phenomenon; current density on the active area decreased as the active area decreased. Analysis of our experimental results, in a manner similar to that developed by Law and Newman, indicates that the average current density on the active area of the electrode increases as the active area decreases during the passivation process.

The principles governing a polarization device that provides a load line with a positive slope have been presented by Epelboin *et al.* The reasons why such a device must be used for polarization control of a passivating system are briefly reviewed.

Assume the I *vs.* $(V - \Phi_{RE})$ characteristics of an electrochemical system that undergoes passivation can be represented as in Fig. 1. If a polarization device with a vertical load line, such as a potentiostat, is used to polarize this cell, the curve a-b-c-d-e will be obtained for a positive voltage sweep. For a negative voltage sweep, the curve e-d-f-b-a is obtained. Curve c-f, which is of interest, is obscured within the hysteresis loop. The special polarization device produces a positive sloping load line, represented by L. This allows determination of a stable data point at (V^*, I^*). Adjustment of the potential, E, and the slope of line L allows determination of the curve c-f. A polarization device with this capability was used to

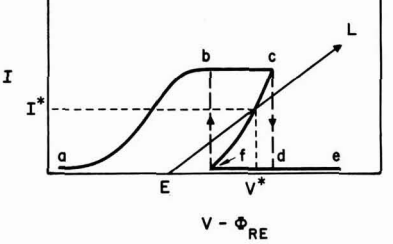

Fig. 1. Current vs. $(V - \Phi_{RE})$ characteristics for a passivating electrochemical system.

* Electrochemical Society Student Member.
** Electrochemical Society Active Member.
Key words: rotating disk electrode, ohmic potential drop, voltammetry.

study the three different sized iron rotating disk electrodes in the active-passive transition region.

Experimental

The rotating disk electrodes were the cross sections of different diameter iron rods (Johnson-Matthey, Puratronic). Three electrodes, each with a different diameter, were used in this work. Table I gives the radius and the cross-sectional area of each electrode. The electrodes were embedded in an insulating cylinder that was 1.95 cm in diameter. The insulating cylinder was composed of a 6:5 mix of Shell Epon 826 epoxy resin and Versamid 140 polyamid hardener.

Electrode surface preparation was carried out on a polishing wheel obtained from Buehler, Limited. Initially, 600 grit silicon dioxide abrasive paper was used on the wheel. This step rendered a matte finish on the iron surface. Next, a polishing cloth was used with 9, 3, and 1 micron diamond pastes. The electrodes were then carefully rinsed in distilled water. Initial surface preparation with abrasives finer than 1 micron was not necessary because the surface of the electrode was rapidly dissolved during the experiments.

The glass cell that was used is shown schematically in Fig. 2. Separate compartments were provided for both the reference electrode and the counterelectrode. Each compartment had two connections to the central portion of the cell. The upper connection had an inner diameter of approximately 0.6 cm and contained a porous glass frit. The lower connection was an open glass tube with an inner diameter of approximately 1 cm.

Nitrogen (Liquid Carbonic, "High Pure") was bubbled through the 1M sulfuric acid electrolyte for at least 1 hr before the experiments were begun. Nitrogen bubbling was continued during the experiments. The cell was placed in a constant temperature bath that was controlled to 25.0° ± 0.5°C. Polarization of the cell was controlled with a potentiostat (Stonehart Model BC 1200) that had auxiliary circuitry providing a load line with a positive slope.

Two different types of experiments were carried out. The first type, which is referred to as potentiodynamic sweeps, were runs where the load line of the potentiostat was vertical. The potential of the disk was varied from −1.0 to 0.6V with respect to a mercury-mercurous sulfate reference electrode. Slow sweep rates of 20-40 mV/sec were used. The sweep generator was a Princeton Applied Research, Model 175, Universal Programmer. Current-voltage plots were recorded on a Hewlett-Packard, Model 7047A, X-Y Recorder. Transients associated with the active-passive and passive-active transitions exceeded the time response capabilities of the X-Y recorder. These transients were accurately monitored with a Nicolet Instrument Corporation, Model 206, Digital Storage Oscilloscope.

The second type of experiment incorporated the use of the potentiostat circuitry that provided a positive sloping load line. By choosing a base potential, E, which was usually −0.27V with respect to the mercury-mercurous sulfate reference electrode, the Z-shaped part of the polarization curve (c-f) could be traced out by decreasing the slope of the load line.

A schematic diagram of the experimental apparatus is given in Fig. 3. All runs were made at a disk rotation speed of 1600 rpm (167.6 rad/sec).

Table I. Values of the radius and the cross-sectional area for each electrode

Electrode	Radius r_0 (cm)	Cross-sectional area (cm²)
A	0.247	0.1917
B	0.149	0.06984
C	0.0493	0.00763

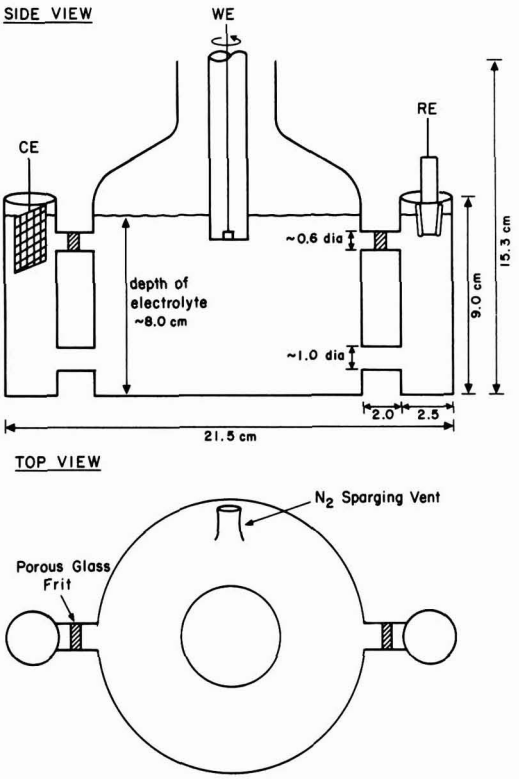

Fig. 2. Schematic diagram of the experimental cell. All dimensions are given in centimeters and are approximate. The electrodes are indicated in their usual operating positions: WE, working electrode; RE, reference electrode; and CE, counterelectrode.

Two different purities of the 1M sulfuric acid electrolyte were used. One solution was prepared using Mallinckrodt Sulfuric Acid, "Analytical Reagent," and distilled water. The second solution, which was composed of J. T. Baker Sulfuric Acid-Ultrex and purified water having a specific resistance of 17 MΩ-cm, was much lower in contaminants than the first solution. There was no apparent change in the results due to the difference in these solutions.

Results and Discussion

Figure 4, which is taken from Epelboin *et al.*, shows a hysteresis loop in the current-voltage curve observed when a potentiostat (vertical load line) is

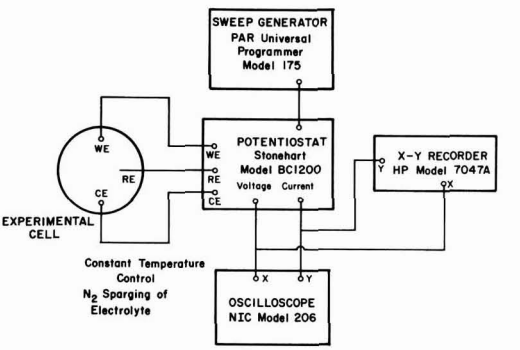

Fig. 3. Schematic diagram of the experimental apparatus

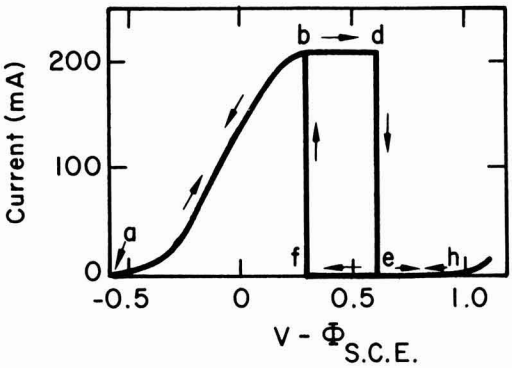

Fig. 4. Current-voltage curve for a 5 mm diam iron disk in 1M sulfuric acid, rotating at 750 rpm, taken from Epelboin *et al.*

used to polarize a 5 mm iron disk in 1M sulfuric acid at 750 rpm. A saturated calomel reference electrode was used in their work.

The total current is reduced when an electrode with smaller cross-sectional area is used. A reduction in current will cause the ohmic potential drop in solution to decrease, even though the resistance increases. This should result in a decrease of the width of the hysteresis loop. Figure 5 shows potentiodynamic sweep results for the three different sized electrodes. The current is reported as the average current density, $\bar{i} = I/\pi r_0^2$, where r_0 for each electrode is given in Table I. As expected, electrode C has the narrowest hysteresis loop because it passed less current than either electrode A or electrode B. The width of the hysteresis loop for electrode B is narrower than for electrode A for the same reason.

A limiting current plateau was observed on all of these runs. Epelboin *et al.* observed the same phenomenon in their experiments. A limiting current density of 1350 mA/cm^2 was observed for electrodes A and B. The limiting current density for electrode C was 8% lower than that for the larger electrodes. A possible explanation for the lower current density on electrode C could involve disruption of the known disk hydrodynamics. As the electrodes dissolve they recede up into the insulating disk. As this recess becomes deeper we would expect an increased resistance to mass transfer. This effect will be the greatest for electrode C because the ratio of depth of recess to r_0 will be the largest for this electrode.

For electrodes B and C we see an overshoot above the limiting current that is observed only on the potential sweep in the positive direction. This current overshoot has been previously observed and is considered to be an experimental artifact due to the finite voltage sweep rate (2). As evidence of this, consider the curve for electrode C in Fig. 5. If the positive sweep is stopped at point *s*, the current will fall to the limiting value at point *t*. The current will remain there so long as the potential is held at V_t. As further evidence, the current followed the curve through point *t* on the negative sweep. Similar phenomena were observed for electrode B; however, the negative sweep is not included in Fig. 5 to minimize confusion. This overshoot was not observed with electrode A because the sweep rate was only 20 mV/sec as compared to 40 mV/sec for the other two electrodes.

An unexpected feature of this plot is the difference in potentials at which the passive-active transitions occur for the three electrodes. For electrodes A, B, and C the transition occurred at $V - \Phi_{Hg/Hg_2SO_4} = -0.170$, -0.185, and -0.192V, respectively. Epelboin *et al.* (4) obtained a value of $V - \Phi_{Hg/Hg_2SO_4} = -0.17$ for a 5 mm diam disk, which is in precise agreement with our results for electrode A. The dependence of this potential on electrode size indicates that the change from passive to active states does not occur precisely at the Flade potential, but instead at a slightly more positive potential. A definition of the Flade potential is best delayed until the results obtained using the positive sloping load line have been discussed.

The determination of the current-voltage behavior of a passivating system requires the use of a polarization device having a load line with a positive slope. The positive feedback circuit on the Stonehart potentiostat provided this capability. Figure 6 presents these experimental results; again, the current is expressed in terms of the average current density based on the cross-sectional area of each electrode. The most important feature of Fig. 6 is the shape of the curves during the transition between the active state and the passive state. The Z-shape for electrode A is most prominent. However, the transition for electrode C is more closely characterized by a vertical line. The curve for electrode C has less ohmic distortion than the curves for either electrodes A or B.

From the progressive changes observed in these three curves, it is concluded that, in the limit of zero electrode size, both the active-passive and passive-active transitions are characterized by a nearly vertical line on an I *vs.* $(V - \Phi_{RE})$ plot. The voltage at which this transition would occur is the Flade potential. The determination of this potential and the generation of the dotted portions of the curves in Fig. 6 are discussed later in this section. Some difficulties associated with ohmic compensation and a discussion of some of the other features of Fig. 6 are now taken up.

Attempting to compensate for the ohmic resistance in solution by subtracting IR_Ω, using a constant R_Ω, is not valid for the passivation process. As the disk passivates, the active area decreases. This leads to a

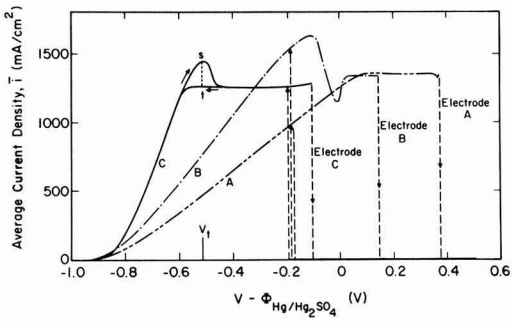

Fig. 5. Potentiodynamic sweep results. Note the different potentials at which the passive-active transition occurs for the three electrodes.

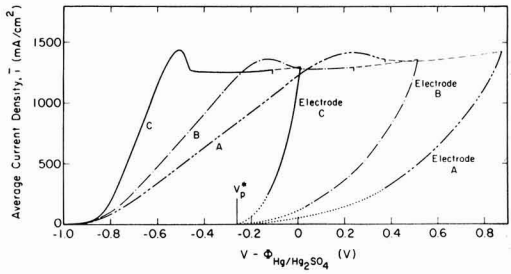

Fig. 6. Current-voltage curves for the three electrodes obtained using a polarization device having a load line with a positive slope. Electrode C has signifcantly less ohmic distortion than the two other electrodes. Anodic sweep rates: electrode A, 20 mV/sec; electrode B, 40 mV/sec; electrode C, 30 mV/sec.

continuous increase in the ohmic resistance. This can be seen more clearly by recalling the formula for the ohmic resistance between the edge of the active portion of the disk and a hemispherical counterelectrode located at infinity given by Law and Newman

$$R_\Omega = \frac{\epsilon}{4\kappa r_p} \quad [1]$$

where ϵ is a number which varies from 1 for a primary current distribution to $8/\pi^2$ for a uniform current distribution. Interpreted physically, ϵ is the ohmic potential drop to the edge of the disk at the given current distribution divided by the potential drop to the edge of the disk which would exist for a primary current distribution, assuming I and r_p are constant. Therefore, ϵ can be thought of as a dimensionless ohmic potential drop, scaled by the primary current distribution case. The passivation radius, r_p, is defined in the following way. For $r > r_p$, the disk is passivated; for $r < r_p$, the disk is active.

In Fig. 6, the dashed portions of the limiting current curves represent an unstable region in which the current could not be controlled. In certain potential ranges of this unstable region the current oscillated in a sustained manner. The average value of these oscillations is represented by the dashed line. This effect is different from the rather slow fluctuations which were described by Epelboin *et al.* in the same region of the curve.

The current overshoot above the limiting current is again seen for the positive voltage sweep. The cause and associated phenomena are the same as for the curves which were obtained under potentiodynamic control.

The determination of the Flade potential, which will be denoted as V_p^*, is now made. The basic procedure involves fitting the current-voltage data to a theoretically based equation. The extrapolation of this equation to the point of zero current will then yield the Flade potential.

Extrapolation of the Z-shaped curve.—The dotted portions of the curves in Fig. 6 could not be obtained with our polarization device because the minimum load line slope that the potentiostat could provide had been reached. The dotted portions of the curves were extrapolated from a least squares curve fit (5) through the data.

To begin, the following equation is recalled from Law and Newman

$$V - \Phi_{RE} = V_p^* + \frac{\epsilon\sqrt{\pi I i_{avg}^*}}{4\kappa} - \Phi_{RE} \quad [2]$$

This equation describes the current-voltage behavior during the passivation process. The Flade potential, V_p^*, is the point at which the local current density, i, goes to zero. It is presumed that the Flade potential prevails at the edge of the active portion of the disk. When the Flade potential reaches the center of the disk the entire surface is passive, and the total current falls to zero. It is important to understand the difference between $\bar{i}$ and i_{avg}^*. The average current density, $\bar{i}$, is defined as the total current divided by the cross-sectional area of the electrode, $\bar{i} = I/\pi r_o^2$. The quantity i_{avg}^* is the total current divided by the active area of the electrode, $i_{avg}^* = I/\pi r_p^2$. Equation [2] can be rearranged to give

$$I = b(V - V_p^*)^2 \quad [3]$$

where

$$b = \left(\frac{4\kappa}{\epsilon}\right)^2 \frac{1}{\pi i_{avg}^*} \quad [4]$$

If ϵ and i_{avg}^* are constants, then a plot of I *vs.* $(V - V_p^*)^2$ should be a straight line passing through the origin. Table II is a representative set of I *vs.* V data from the three electrodes. The electrode from which each data point was taken is noted. Extensive work with the data indicated that a plot of I *vs.* $(V - V_p^*)^2$ would not be linear for any reasonable value of V_p^*. This indicated that the quantity $(\epsilon^2 i_{avg}^*)$ was varying as the passivation process occurred. In order to account for these variations the data were fit with the following equation

$$I = a_0 + a_1(V - V_p^*)^2 + a_2(V - V_p^*)^4 \quad [5]$$

The current must be zero when $V = V_p^*$ because the disk becomes fully passivated at that point; therefore, $a_0 = 0$.

The computer program which determined V_p^* worked in the following way. An initial value of V_p^* was provided. A least squares curve fit program then generated values of a_0, a_1, and a_2 that were based on the 18 data points in Table II. If a_0 was not equal to zero, then a new value of V_p^* was determined, and the least squares program recalculated a_0, a_1, and a_2. This process was repeated until a_0 was sufficiently close to zero. The final values obtained for a_0, a_1, a_2, and V_p^* are shown in Table III. Figure 7 is a plot of the current against $(V - V_p^*)^2$, where $V_p^* = -0.26168$V. The computer generated curve (Eq. [5]) is shown as the solid line for comparison with the data.

The value of the passive-active transition potential depends on the passive film stability. A smaller disk electrode has smaller potential and concentration fluctuations over its surface. If such fluctuations lead to breakdown of the film, then it is reasonable to expect that the passive film will remain stable at a more negative potential on a smaller electrode.

In the potentiodynamic sweep experiments, the passive-active transition potential becomes more negative as the electrode size decreases. The result from the curve fit procedure is equivalent to obtaining the passive-active transition from a potentiodynamic sweep experiment for an electrode of infinitesimal area.

This explains the range of transition potentials varying from a calculated value of −0.2168V for an infinitesimally small electrode to an observed value of −0.17V for the largest electrode.

The dotted portions of the curves in Fig. 6 were obtained in the following way. From a given value of $(V - V_p^*)^2$, Eq. [5] estimates the total current, I.

Table II. Values of the current at various potentials for the three electrodes

Electrode	Potential $(V - \Phi_{RE})$ (V)	Current (mA)
C	−0.125	1.78
C	−0.100	2.61
C	−0.075	3.59
C	−0.050	4.80
C	−0.025	6.20
C	0.000	7.95
B	0.040	10.5
B	0.100	14.5
B	0.200	24.0
B	0.300	38.0
A	0.370	56.0
B	0.400	57.0
A	0.400	62.0
B	0.450	69.0
A	0.500	90.0
A	0.600	125
A	0.650	143
A	0.700	164

Table III. Values of the parameters in Eq. [5] determined by the least squares fit

Variable	Dimension	Least squares result
V_p^*	V	−0.26168
a_0	mA	0.00040397
a_1	mA/V²	99.737
a_2	mA/V⁴	86.525

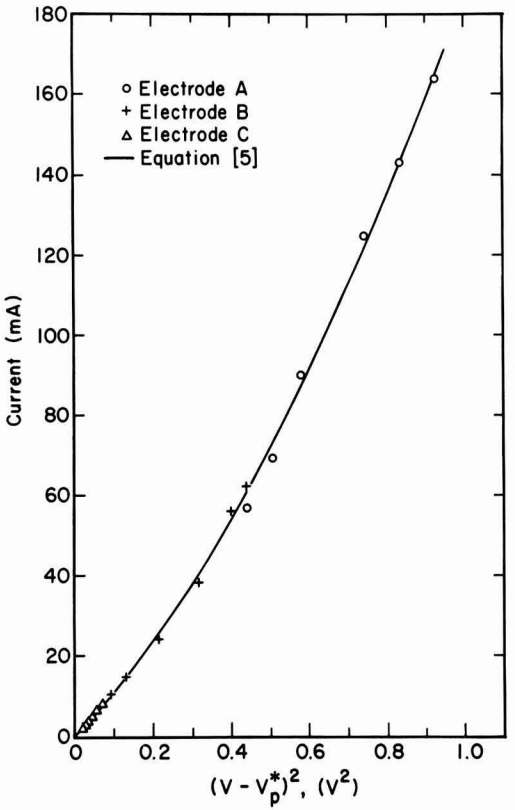

Fig. 7. Experimental values of I plotted against $(V - V_p^*)^2$. Equation [5] is shown as the solid line for comparison with the data.

This value was divided by the appropriate cross-sectional areas (see Table I) to obtain the corresponding average current densities for each electrode. This procedure was used to extrapolate from the point of zero current at $V = V_p^*$ up to the first data point for each electrode.

Determination of i_{avg}^*.—We now determine the variations in i_{avg}^* as the electrode passivates. This is accomplished within the framework of the model presented by Law and Newman. The curvature in Fig .7 indicates that ϵ and or i_{avg}^* are changing during passivation. Equations [3] and [4] can be combined to give

$$\epsilon^2 i_{avg}^* = \left(\frac{4\kappa}{\pi}\right)^2 \frac{(V - V_p^*)^2}{I} \qquad [6]$$

At this point, Eq. [5] indicates how I varies with $(V - V_p^*)$; therefore, i_{avg}^* could be determined from Eq. [6] if the dependence of ϵ on $(V - V_p^*)$ was also known. Previous results obtained for a nonpassivating disk electrode by Newman (6) indicate the complexity of this dependence. We now apply these results on the active portion of the electrode to calculate how ϵ depends on $(V - V_p^*)$. This procedure is now developed.

In general, the current distribution will depend on the parameters J, δ, α_a, and α_c. For the passivation problem

$$J = \frac{i_0 r_p n\mathbf{F}}{RT\kappa} \qquad [7]$$

Law and Newman give a value of 9.1×10^{-5} A/cm^2 for the exchange current density when the ferrous ion concentration is 4.0 mol/liter. Hurlen (7) indicates that the dependence of the exchange current density on hydroxide and ferrous ion concentrations is

$$\log (i_0)\,[\text{A/cm}^2] = 3.58 - \text{pOH} - \text{pFe} \qquad [8]$$

Because only small amounts of iron were dissolved during the experiments, the ferrous ion concentration can be considered negligible. Equation [8] indicates that the exchange current density was very small for our experimental conditions. From this reasoning, it was concluded that the approximation $J = 0$ was valid in the analysis of this work.

The second parameter is given by

$$\delta = \frac{\alpha_a \mathbf{F} r_p i_{avg}^*}{RT\kappa} \qquad [9]$$

In 1M sulfuric acid κ is 0.40 $(\Omega\text{-cm})^{-1}$ at 25°C (8), and α_a is 1.0 for the anodic dissolution process (3). The dependence of $(i/i_{avg}^*)|_{r=0}$, the current density at the center of the disk divided by i_{avg}^*, on δ is illustrated in Fig. 8. Focusing attention on the curve for $J = 0$, we see that as $\delta \to \infty$, $(i/i_{avg}^*)|_{r=0}$ approaches a value of 0.5 and a primary current distribution is obtained. Under these conditions $\epsilon = 1.0$.

At the other extreme when $\delta \to 0$, a uniform current distribution is obtained. For this case $(i/i_{avg}^*)|_{r=0}$ has a value of 1.0. Under these conditions $\epsilon = 8/\pi^2$.

With the relationship

$$I = i_{avg}^* \pi r_p^2 \qquad [10]$$

it is possible to eliminate r_p from Eq. [9] and obtain

$$\delta = \frac{\alpha_a \mathbf{F}}{RT\kappa} \sqrt{\frac{i_{avg}^* I}{\pi}} \qquad [11]$$

Substitution of Eq. [2] into Eq. [11] gives

$$\delta = \frac{4\alpha_a \mathbf{F}}{\epsilon \pi RT} (V - V_p) \qquad [12]$$

Equation [11] can be rearranged to give

$$i_{avg}^* = \delta^2 \left(\frac{RT\kappa}{\alpha_a \mathbf{F}}\right)^2 \frac{\pi}{I} \qquad [13]$$

In order to evaluate δ from Eq. [12] we must once again face the problem of determining how ϵ varies with $(V - V_p^*)$. A computer program describing the secondary current distribution on a disk electrode, developed by Newman (6), was available to calculate ϵ and δ for given values of J and the potential. Results from this program are given in Fig. 9. This plot indicates how ϵ varies with the parameter $\alpha_a \mathbf{F}(V - V_p^*)/RT$, when $J = 0.1$. The program could be rerun with $J = 0$; however, the change in results would be insignificant, as can be seen from Fig. 8.

The remaining steps in the determination of i_{avg}^* as a function of r_p were as follows. First, a value of $(V - V_p^*)$ was selected. With $\alpha_a = 1.0$ (3), a value

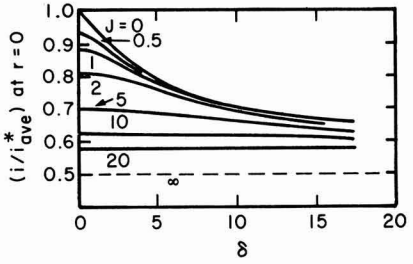

Fig. 8. Current density at the center of the disk as a function of δ.

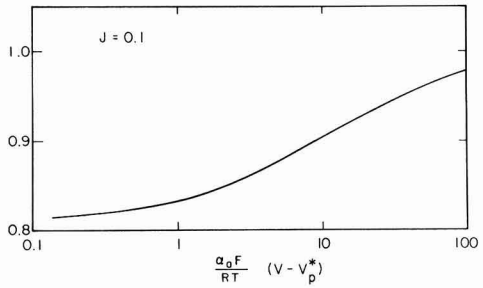

Fig. 9. Plot of ϵ vs. the parameter $\alpha_a F/RT(V - V_p^*)$ from Newman.

of ϵ was obtained from Fig. 9. The parameter δ was then determined from Eq. [12]. The total current, I, at the given value of $(V - V_p^*)$ was given by Eq. [5]; ultimately, i_{avg}^* was obtained from Eq. [13]. These results are presented in Table IV. The first two columns were taken directly from the computer program used to generate values plotted in Fig. 9. The values of δ and i_{avg}^* were computed according to the method outlined above. The radial point of passivation, r_p, was obtained from Eq. [10], using the known values of I and i_{avg}^*.

The calculations used to determine δ, i_{avg}^*, and r_p were repeated for the extreme cases of a primary and a uniform current distribution. For a primary distribution, ϵ is taken as 1, while for the uniform distribution, ϵ is taken as $8/\pi^2$ in the procedure outlined above. These results are shown as a plot of i_{avg}^* *vs.* r_p in Fig. 10. When the active portion of the disk was small, the calculated curve for i_{avg}^* approached the value corresponding to a uniform current distribution. As the active area increased, the calculated value of i_{avg}^* decreased rapidly and approached the primary distribution asymptotically.

For values of $r_p > 0.077$ mm, the calculations which generated the curves in Fig. 10 are based on the experimental data. For $r_p < 0.077$ mm the curves have been extrapolated. This region of extrapolation corresponds to the dotted portions of Fig. 6.

Table IV. Values of ϵ, δ, i_{avg}^*, and r_p at various potentials calculated from the experimental data

$\frac{\alpha_a F}{RT}(V - V_p^*)$	ϵ	δ	i_{avg}^* (A/cm^2)	r_p (mm)	Source[a] of data	r_o (mm)
0.02752	0.811	0.04321	12.47	0.000357	Extrap.	—
0.05504	0.811	0.08653	12.45	0.000714	Extrap.	—
0.08703	0.812	0.1365	12.40	0.00113	Extrap.	—
0.1231	0.814	0.1925	12.33	0.00161	Extrap.	—
0.2752	0.820	0.4276	12.16	0.00361	Extrap.	—
0.3892	0.822	0.6029	12.09	0.00513	Extrap.	—
0.8703	0.831	1.334	11.83	0.0116	Extrap.	—
1.231	0.837	1.873	11.66	0.0165	Extrap.	—
1.741	0.844	2.626	11.45	0.0236	Extrap.	—
2.462	0.853	3.677	11.21	0.0337	Extrap.	—
3.015	0.860	4.466	11.00	0.0417	Extrap.	—
3.481	0.864	5.130	10.87	0.0485	Extrap.	—
3.892	0.868	5.713	10.76	0.0545	Extrap.	—
4.262	0.871	6.230	10.65	0.0601	Extrap.	—
4.768	0.875	6.938	10.54	0.0677	Extrap.	—
5.321	0.879	7.707	10.41	0.0761	C	0.493
6.294	0.886	9.045	10.18	0.0913	C	0.493
7.267	0.892	10.38	9.98	0.107	C	0.493
8.240	0.896	11.71	9.80	0.123	C	0.493
10.19	0.905	14.34	9.43	0.156	C	0.493
14.08	0.916	19.57	8.74	0.230	B	1.49
21.86	0.932	29.87	7.38	0.416	B	1.49
25.76	0.938	34.96	6.73	0.534	A	2.47
27.70	0.941	37.50	6.42	0.601	B	1.49
33.54	0.948	45.05	5.53	0.837	A	2.47
37.43	0.952	50.09	5.01	1.03	A	2.47
41.34	0.955	55.14	4.54	1.25	Extrap.	—

[a] The symbol "Extrap." indicates that this data point was obtained by an extrapolation of Eq. [5]. A capital letter identifies the electrode from which the given data point was obtained. For these cases, the corresponding electrode radius is given for comparison with r_p.

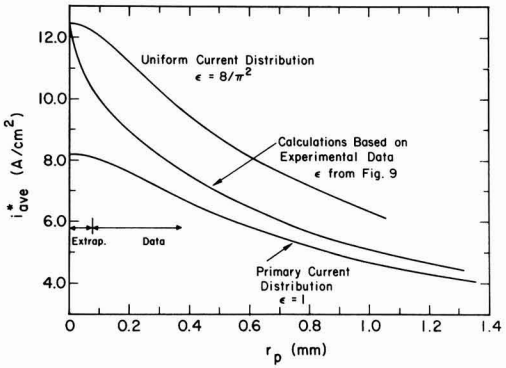

Fig. 10. Average current density on the active portion of the disk plotted against r_p.

The results obtained in this work are qualitatively similar to those presented by Law and Newman in their mathematical model describing the kinetically limited case. Both indicate that i_{avg}^* increases as the active electrode area decreases. As $r_p \to 0$ (complete passivation), the value of i_{avg}^* based on these experiments reaches a value of 12.44 A/cm^2, this compares with a value of 17.1 A/cm^2 estimated by Law and Newman. The qualitative agreement of these results was expected. The same model was used in both cases; however, the data bases were different.

The continuous increase in i_{avg}^* as r_p decreases can be explained in the following way. First, assume that the current density at $r = r_p$ is constant. For the experimental results obtained here, $i|_{r=r_p} = 12.44$ A/cm^2. For a large active area the primary current distribution is approached. Under these conditions $i|_{r=0} < i_{avg}^* << i|_{r=r_p}$, which is consistent with experimental observation. As the active area decreases and $r_p \to 0$, we approach a uniform current distribution, for which $i|_{r=0} \approx i_{avg}^* \approx i|_{r=r_p}$.

Law and Newman also calculated a value for the limiting current. Their calculations were based on a disk rotation speed of 4500 rpm. Since these experiments were carried out at 1600 rpm, it was necessary to correct for the difference in rotation speeds by using the Levich relationship (9)

$$I_{lim} = \beta\sqrt{\Omega} \qquad [14]$$

The adjusted value was 1.64 A/cm^2, which is to be compared with a value of about 1.35 A/cm^2 obtained in this work (see Fig. 5 and 6).

Conclusions

Experimental results obtained from three iron rotating disk electrodes indicate that the local passivation phenomenon can be represented as a nearly vertical line on a current *vs.* $(V - \Phi_o)$ plot. If it is assumed that the active portion of the electrode always has a disk configuration, then this work has shown that the Z-shaped polarization curve, obtained with a Negative Impedance Converter, is due only to ohmic potential drop in solution. This effect is complicated because the active area of the electrode decreases during the passivation process, resulting in a continuously increasing ohmic resistance to the disk. Analysis of the data obtained in these experiments, within the framework of the Law and Newman model, indicates the average current density on the active area of the electrode increases as the size of the active area decreases during passivation.

Recall that Epelboin *et al.* have observed the opposite phenomenon; current density on the active area decreased as the active area decreased. This difference can be explained if the local current density *vs.* poten-

tial behavior is assumed to be different, as explained in the following example.

Consider two cases: (*i*) the local current density monotonically increases as $V - \Phi_o$ increases toward V_p^* and (*ii*) the local current density monotonically decreases as $V - \Phi_o$ increases toward V_p^*. The value of i_{avg}^* is obtained by averaging the current density contributions over the values of $(V - \Phi_o)$ that exist on the active area. The variation in $(V - \Phi_o)$ from the center to the edge of the disk becomes smaller as the active area decreases. For case (*i*), a large active area implies that current densities considerably below $i|_{r=r_p}$ will be included in the average; for small active areas only current densities slightly below $i|_{r=r_p}$ will be included. The result is an increasing value of i_{avg}^* as r_p decreases. For case (*ii*), a large active area implies that current densities considerably above $i|_{r=r_p}$ will be included in i_{avg}^*; for small active areas only current densities slightly above $i|_{r=r_p}$ are included. The result is a decreasing value of i_{avg}^* as r_p decreases.

In this work we have measured $\epsilon^2 i_{avg}^*$ and calculated ϵ. This permits i_{avg}^* to be determined as a function of active area. This procedure indicates that i_{avg}^* increases as r_p decreases. Our results would have been stronger if i_{avg}^* itself had been experimentally measured, instead of relying on calculations. The apparent value of the current density at the point of passivation, $i|_{r=r_p}$, obtained from this study is 12.44 A/cm^2. Our local current density-potential relationship corresponds to case (*i*).

The result of Epelboin *et al.* corresponds to case (*ii*).

Further work is presently underway to determine the cause of the limiting current for the anodic dissolution of iron. Previous observation (2) has shown that the limiting current for this process obeys the Levich relation (9). In the unstable region of the limiting current curve it is observed that $i_{avg}^* > i_{lim}$ and $i|_{r=r_p} > i_{lim}$. We also see that $r_p < r_o$ for all data points listed in Table IV. This situation is unstable; the electrode may jump between states that have different active areas. This jumping explains the observed rapid current oscillations. Further study is needed to determine the triggering mechanism for the active-passive jumping.

The principal result of this work is Fig. 7. Having the active-passive transition data for the three electrodes fall on the same curve indicates that the passivated portion of the disk does not affect the active portion. This verified a major hypothesis in Law and Newman's model.

Acknowledgment

This work was supported by the Solar Energy Research Institute. The suggestions and comments of the reviewers are gratefully acknowledged.

Manuscript submitted April 30, 1982; revised manuscript received Sept. 5, 1982.

Any discussion of this paper will appear in a Discussion Section to be published in the December 1983 JOURNAL. All discussions for the December 1983 Discussion Section should be submitted by Aug. 1, 1983.

LIST OF SYMBOLS

a_0, a_1, a_2 constants in Eq. [5]
A electrode with diameter of 0.494 cm
B electrode with diameter of 0.298 cm
C electrode with diameter of 0.0986 cm
E base potential, Fig. 1, V
F Faraday's constant, 96,487 C/equiv.
i local current density, A/cm^2
i_0 exchange current density, A/cm^2
$\bar{i}$ average current density based on entire electrode area, A/cm^2
i_{avg}^* average current density based on active electrode area, A/cm^2
i_{lim} limiting current density, A/cm^2
I total current on the disk, mA
I_{lim} limiting current, A
J kinetic parameter, see Eq. [7]
L load line with positive slope, Fig. 1
r radial coordinate, cm
r_o radius of the electrode, cm
r_p radial point of passivation, cm
R universal gas constant, 8.3143 J/mol-K
R_Ω ohmic resistance in solution, Ω
T absolute temperature, K
V_p^* passivation potential, V
V disk potential, V

Greek letters

α_a anodic transfer coefficient
α_c cathodic transfer coefficient
β constant in Eq. [14], A-sec$^{1/2}$
δ kinetic parameter, Eq. [9]
ϵ current distribution parameter, Eq. [1]
κ bulk solution conductivity, $(\Omega\text{-cm})^{-1}$
π 3.14159
Φ_{Hg/Hg_2SO_4} potential of saturated mercurous sulfate reference electrode, V
Φ_o potential in solution just outside the electric double layer, V
Φ_{RE} reference electrode potential, V
Φ_{SCE} potential of saturated calomel electrode, V
Ω disk rotation speed, sec^{-1}

REFERENCES

1. Fr. Flade, *Z. Phys. Chem.*, **76**, 513 (1911).
2. I. Epelboin, C. Gabrielli, M. Keddam, J. C. Lestrade, and H. Takenouti, *This Journal*, **119**, 1632 (1972).
3. C. G. Law and J. Newman, *ibid.*, **126**, 2150 (1979).
4. I. Epelboin, C. Gabrielli, M. Keddam, and H. Takenouti, in "Comprehensive Treatise of Electrochemistry. Vol. 4: Electrochemical Materials Science," J. O'M. Bockris, B. E. Conway, E. Yeager, and R. E. White, Editors, pp. 151-192, Plenum Press, New York (1981).
5. R. Hornbeck, "Numerical Methods," pp. 122-125, Quantum Publishers, Inc., New York (1975).
6. J. Newman, *This Journal*, **113**, 1235 (1966).
7. T. Hurlen, *Acta Chem. Scand.*, **14**, 1533 (1960).
8. T. W. Chapman and J. Newman, "A Compilation of Selected Thermodynamic and Transport Properties of Binary Electrolytes in Aqueous Solution," UCRL-17767 (1968).
9. V. G. Levich, "'Physicochemical Hydrodynamics," p. 70, Prentice-Hall, Inc., Englewood Cliffs, NJ (1962).

Laser-Enhanced Electroplating on Good Heat-Conducting Bulk Materials

H. K. Kuiken

Philips Research Laboratories, 5600 MD Eindhoven, The Netherlands

F. E. P. Mikkers

Philips Sub-components Development Center, Elcoma, Eindhoven, The Netherlands

and P. E. Wierenga

Philips Research Laboratories, 5600 MD Eindhoven, The Netherlands

ABSTRACT

Laser-enhanced electroplating on good heat-conducting bulk materials is not very effective, as laser-beam irradiation results in a limited temperature rise only. It is shown, both experimentally and theoretically, that the application of a thin layer of a relatively poor heat-conducting material may lead to a considerable local temperature increase. The dimensionless parameter determining this effect is given by the product of the ratio of the thermal conductivities of bulk and layer material and that of layer thickness to laser-spot diameter.

Laser-enhanced electroplating has been shown to be a promising technique for maskless selective plating (1, 2). By focusing a laser beam onto the surface of an optically absorbing substrate in a plating solution, the plating rate at the laser spot and in the area surrounding it can be increased significantly. For relatively low laser intensities the temperature of the solid-liquid interface in the irradiated area will remain below the boiling temperature of the solution. Under such circumstances the temperature dependence of the rate of the electrode reaction mainly determines the locally increased plating rates. At temperatures below the boiling point microconvection cannot significantly contribute to the enhanced plating phenomenon, as the Grashof numbers involved are far too small (3). With a heated area of 200 microns only, a maximum temperature difference of 80 K, a thermal expansion coefficient of 10^{-4} K^{-1}, and a kinematic viscosity of $4 \cdot 10^{-7}$ m^2/sec, the Grashof number will have the value 4. Thus, only a very modest contribution can be expected from ordinary convection.

At increasing intensity of the laser beam, the local temperature of the electrode surface will eventually exceed the boiling temperature of the liquid. In this case, "local boiling" occurs, *e.g.*, nuclei (cavities) at the heated spot on the electrode surface are activated to generate vapor bubbles periodically. These bubbles grow (at the side facing the electrode) and implode (at the opposite side facing the bulk liquid) simultaneously; *i.e.*, if the bulk liquid is at room temperature, the bubbles adhere to the electrode surface during their entire short lifetime (4). This bubble behavior causes very rapid oscillatory motions (and pressure waves) in the liquid adjacent to the electrode. Ultimately, the result of the periodical action of the bubbles is a considerable enhancement of the convective transport at the electrode surface up to an order of magnitude.

At sufficiently high laser power densities, a relatively large liquid region in the immediate vicinity of the electrode, and surrounding the heated spot, will be heated to temperatures considerably above the original bulk temperature. In this case tiny bubbles depart from the electrode, and bubble jets are ejected in a direction normal to the surface. It should be noted that local boiling differs from what is commonly known as "pool boiling." As the latter occurs in any tea kettle, it is the more familiar kind of boiling. Its main characteristic is that the bulk is first raised to the boiling temperature before actual boiling occurs at the heated surface. In that case bubbles are ejected almost right from the start of the boiling process.

Key words: boiling, electrodeposition, films, metals.

Bubble ejection leads to considerable stirring near the irradiated area and therefore to increased local transport of reactants toward the electrode. Moreover, forced convection causes a narrowing of the temperature profile in the irradiated area. This will yield a more selective plating and therefore a more discrete metal deposition.

Von Gutfeld *et al.* describe experiments in which various metals are deposited selectively on substrates (1, 2) consisting of thin metallic films on glass. If the layer thickness is very much smaller than the laser-spot diameter, laser-enhanced plating yields metal spots with sizes comparable to the size of the laser spot itself. Very discrete spots can be obtained with relatively low laser-power densities. However, for thicker films the radial heat flux through the film surface increases. This causes the plated spot to become larger and less discrete. Besides, more laser power is needed to reach the boiling point at the hot spot.

In electronics the application of laser-enhanced electroplating offers distinct advantages over other plating techniques, if it can be applied to selective metal deposition on bulk metals or metal alloys, especially for plating relatively expensive metals such as gold. We have carried out laser plating experiments with gold on nickel-iron and copper-zinc alloy substrates. On the nickel-iron substrates a continuous incident laser power of 4W (power density at laser spot of the order of 50 $kW \cdot cm^{-2}$) is found to be sufficient to cause local boiling and to deposit well-localized gold spots, *e.g.*, with a diameter of 400 μm and a height of 1 μm. The plated spot diameter increases as a function of time, mainly due to lateral heat diffusion through the gold deposit. The maximum deposition rate is of the order of 5 $\mu m \cdot sec^{-1}$.

However, the thermal conductivities of our copper-zinc substrates are about four times higher than the conductivity of nickel-iron. As a consequence, it is impossible to deposit discrete gold spots of the above-mentioned geometry on bare copper-zinc substrates with a continuous laser, even at a laser-power density as high as 250 $kW \cdot cm^{-2}$. It is true that discrete spots can be obtained by the application of very short light pulses from a pulsed laser (1), but the disadvantage

of such a method is the low duty cycle, which means that the effective deposition rate will decrease considerably. Indeed, growth will be minimal during the larger part of the cool-down period and in the initial stages of the power-on phase.

We have found that the problems with laser-enhanced plating on a good heat-conducting bulk metal can be solved by covering the substrate with a thin, optically absorbing, metallic layer of relatively low thermal conductivity. The relevant theory behind this result is described in this paper and illustrated by some experimental observations.

Temperature Calculation

If a good heat-conducting bulk substrate is irradiated by a laser beam, the temperature rise at the laser-impact area may be quite limited. In this section we show, using a simple mathematical model, that a considerable temperature rise can be achieved at the laser-heated spot when the substrate is covered with a thin film of a relatively poor heat-conducting material. In this model we avoid complicating factors, such as boiling heat transfer and lateral thermal conduction through the plated spot.

We are allowed to make these assumptions as we have a limited goal in mind. Indeed, we only wish to show that the thin film allows temperatures to be reached at which the enhanced plating effect can be observed. Below a given temperature there will be no boiling of the electrolyte and consequently heat transfer will occur mainly through conduction. If the thermal conductivity of the substrate material is considerably higher than that of the electrolyte, conductive and convective heat transfer toward the latter may be disregarded. As a result most of the dissipated laser power will be conducted into the substrate.

Let us consider a semi-infinite region bounded by an infinite plane surface (Fig. 1). We use Cartesian coordinates (x, y, z), denoting the bounding plane by $z = 0$. The semi-infinite region shall be that of positive z, and this region is occupied entirely by two heat-conducting materials of different thermal properties. The first material (thermal conductivity k_1) fills the layer denoted by $0 \leq z < \delta$, while the second (k_2) is to be found in $z > \delta$. The two materials are thought to have a perfect bond in the plane $z = \delta$ resulting in the absence of any additional thermal resistance.

The heat-conducting region described above is heated by a Gaussian laser beam which has its axis centered on the line $r = 0$, where $r = (x^2 + y^2)^{1/2}$. Assuming a negligible penetration depth for the absorbed laser power a continuous heat input at $z = 0$ is obtained

$$k_1 \frac{\partial T}{\partial z} = -\frac{Q}{\pi a^2} e^{-r^2/a^2} \qquad [1]$$

where T is the temperature and Q denotes the absorbed power of the laser. Clearly the parameter a is a measure of the width of the laser beam (63% of the laser power is expended in the interval $0 \leq r \leq a$).

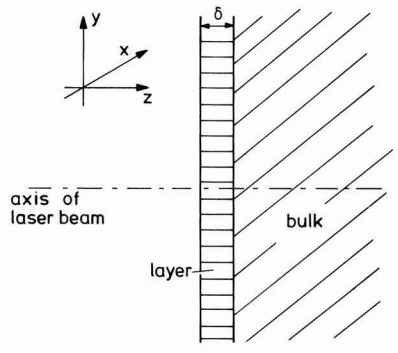

Fig. 1. Geometrical configuration

Transient effects may be neglected as the characteristic time $t_c = a^2/\kappa$ is much less than the time the laser is in operation, which is of the order of one second; κ is the thermal diffusivity of the bulk material. Since $a \sim 10^{-4}$m and $\kappa \sim 10^{-4}$ m$^2 \cdot$ sec^{-1}, we have $t_c \sim 10^{-4}$ sec, so that the investigations may be limited to the steady-state situation. We shall consider the Laplace equation

$$\nabla^2 \theta = 0 \qquad [2]$$

in the region $z \geq 0$, where θ denotes the temperature rise above the ambient level. At the interface $z = \delta$ the temperature and the heat flux ought to be continuous, which leads to the conditions

$$\theta|_{z=\delta-0} = \theta|_{z=\delta+0}, \quad k_1 \frac{\partial \theta}{\partial z}\bigg|_{z=\delta-0} = k_2 \frac{\partial \theta}{\partial z}\bigg|_{z=\delta+0} \qquad [3]$$

Finally

$$\theta \to 0 \text{ if } x^2 + y^2 + z^2 \to \infty \qquad [4]$$

The solution to the mathematical problem defined by the equations and boundary conditions given by Eq. [1]-[4] will be derived in the Appendix. In this section we concentrate on the final results. Although the general solution describes the temperature field in the complete domain, we are here only interested in the temperature distributions in the planes $z = 0$ and $z = \delta$. If the ratio of the thermal conductivities is denoted by

$$\gamma = k_2/k_1 \qquad [5]$$

and if it is assumed that

$$\gamma >> 1 \quad \text{and} \quad \delta/a << 1 \qquad [6]$$

we may derive the following approximate expression for the temperature in the plane $z = 0$

$$\frac{\pi a k_2}{Q}\theta(x,y,0) \sim \frac{\pi^{1/2}}{2} e^{-\frac{1}{2}r^2/a^2} I_0(\tfrac{1}{2} r^2/a^2) + \gamma \frac{\delta}{a} e^{-r^2/a^2} \qquad [7]$$

where I_0 is a modified Bessel function [Ref. (5), Chap. 9.6]. To the same level of approximation we have

$$\frac{\pi a k_2}{Q}\theta(x,y,\delta) = \frac{\pi^{1/2}}{2} e^{-\frac{1}{2}r^2/a^2} I_0(\tfrac{1}{2} r^2/a^2) \qquad [8]$$

where $\theta(x, y, \delta)$ is the temperature distribution in the plane $z = \delta$.

The conditions of [6] are actually in conformity with what we set out to investigate, namely, the influence of a thin layer of poor heat-conducting material on the temperature distribution in the laser-impact area. The second of the two conditions merely expresses that the laser beam is much wider than the layer is thick. It is Eq [7] that presents the answer to our question. Indeed, if the thickness of the layer tends to zero, the difference between [7] and [8] vanishes. This shows that Eq. [8] gives the temperature distribution at the outer surface in the absence of the poor heat-conducting skin. However, if the thickness of the layer increases, the importance of the second term on the right-hand side of [7] grows in relation to that of the first. Now a situation may arise where the second term is actually dominant, which is when the parameter

$$F = \gamma\delta/a > 1 \qquad [9]$$

Of course, in this model, the thickness of the poor heat conductor may not grow indefinitely, as the second condition of [6] would then be violated. In that case the layer itself would become a bulk material, so that it would no longer be justified to call it thin. However, it is perfectly obvious that values may be chosen for the parameters γ and δ/a that satisfy [6], but which yield a value of F in the range defined by [9]. This, then, leads to the temperature increase that we have

been trying to achieve by the application of the poor heat-conducting skin, which is the central theme of our paper.

It is interesting to note that the temperature in the good heat-conducting bulk is hardly affected by the presence of the layer. Indeed, the temperature in $z = \delta$, its bounding plane (Eq. [8]), is practically the same as that which would have existed in the absence of the skin.

In Fig. 2a the two terms on the right-hand side of Eq. [7] are shown separately. Clearly, the first term is represented by a much wider curve than the second. This can be attributed to the fact that the mathematical structures of the two terms are quite different. The second term reflects the power-input function of Eq. [1] with its typical rapid exponential decay. The first term, on the other hand, is a slowly decaying function. Using the asymptotic representation of the function I_0, valid for large values of the argument (5), we may find

$$\frac{\pi^{1/2}}{2} e^{-\frac{1}{2}r^2/a^2} I_0(\tfrac{1}{2} r^2/a^2) \sim \tfrac{1}{2} a/r \quad \text{if } r >> a \quad [10]$$

This suggests that spots plated on homogeneous substrates tend to be much wider than the laser spot itself (Eq. [1]). If [9] is satisfied we may expect a spot the width of which more or less reflects the lateral extent of the laser beam. Therefore, as a consequence of the enhanced temperature effect, the application of a thin film of poor heat-conducting material permits the plating of spots of limited size.

Unfortunately, should the material of the plated spots have a high thermal conductivity, the lateral spreading of injected heat through the spot tends to obscure this effect. Indeed, a high thermal conductivity results in elevated temperatures at the rim of the spot. Despite its low conductivity, the layer in the immediate neighborhood of the periphery will have a high temperature over a distance outside the spot which is of the order of δ. Since high temperatures at the outer surface of the film lead to increased plating rates, the spot will continue to grow until the temperature at its periphery drops below a critical value. The higher the conductivity of the plated material, the wider the spot will grow.

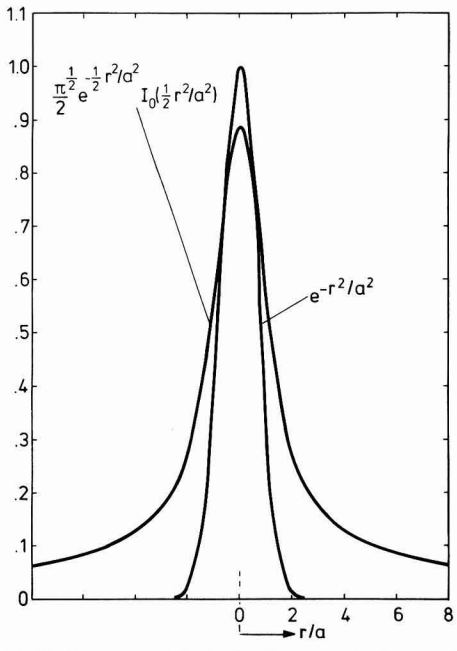

Fig. 2a. Comparison of the two functions appearing in Eq. [7]

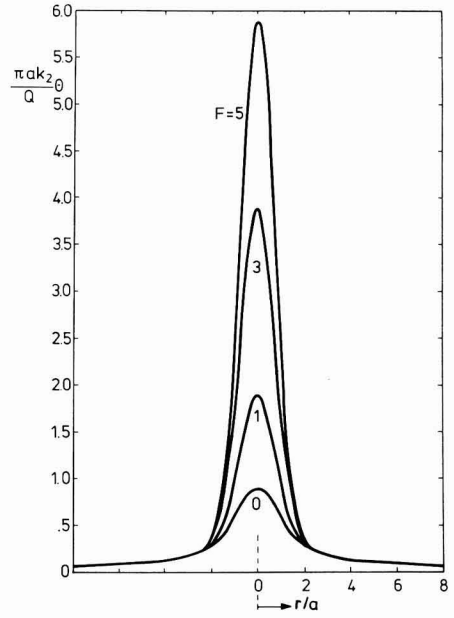

Fig. 2b. Temperature enhancement due to the presence of a layer of poor heat-conducting material.

Figure 2b presents the two terms of Fig. 2a, but now their effects are added up for various values of F. These graphs clearly indicate that the influence of the layer increases rapidly with F. Finally, from Fig. 3 one may obtain the temperature enhancement as a function of layer thickness at the center of the laser-impact area for various conductivity ratios.

Temperature distributions in laser-heated layered materials have been studied before, *e.g.*, in connection with laser welding (6), machining (7), and hole burning (8). It is difficult, however, to apply the general results obtained in these papers to the special case considered in our work. To obtain the temperature distributions ([A-8] and [A-9] of Appendix) a rederivation seemed justified.

Experimental

The experimental setup is shown in Fig. 4. The beam of a continuous argon-ion laser (Spectra Physics. Model 171; maximum output power 20W; wavelength region 450-510 nm) is focused onto the substrate sur-

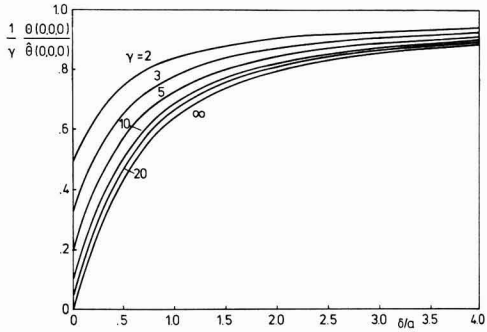

Fig. 3. Temperature enhancement as a function of layer thickness at the center of the laser-impact area for various conductivity ratios.

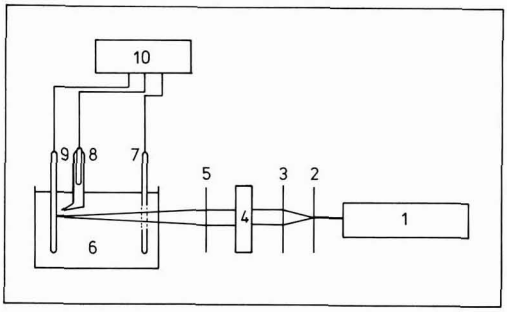

Fig. 4. Experimental set-up: 1, laser; 2-4, optical lenses; 5, photographic shutter; 6, electroplating cell; 7, anode; 8, reference electrode; 9, cathode; 10, potentiostat.

face by means of an optical lens system. A photographic shutter is applied to facilitate irradiation of the substrate during well-defined periods of time. The substrate is vertically mounted as the cathode in an electroplating cell. A saturated calomel electrode (SCE) is used as the reference electrode and a gold-plated titanium gauze functions as the anode. The electroplating voltage is set by a potentiostat.

The potential of the cathode with respect to the SCE is set at −800 mV. Our plating solution contains 100 g · dm^{-3} $KAu(CN)_2$ and 90 g · dm^{-3} citric acid. The pH of the solution is adjusted to 5.9 with KOH. Substrates of copper-zinc alloy (Tombak; 85% copper, 15% zinc), covered with nickel-phosphorous layers of variable thickness, are used for laser-enhanced electroplating. All experiments are carried out at ambient bath temperature.

Results and Discussion

The experimental results for Tombak substrates, covered with nickel-phosphorous layers of variable thickness, are shown in Fig. 5 and 6. The photographs were made through an optical microscope. For comparison, Fig. 6a shows the rather poor result for a substrate covered with a nickel layer. The explanation for this is that the thermal conductivity for nickel is almost 20 times higher than that for nickel-phosphorous. From Fig. 5 it appears that the critical layer thickness is about 4 μm. Inserting this value in Eq. [9], together with the thermal conductivities of Tombak ($k_2 \sim 160$ W · m^{-1} · K^{-1}) and nickel-phosphorous ($k_1 \sim 4$ W · m^{-1} · K^{-1}) and the laser-spot diameter of 50 μm, as used in the experiments, yields a value for the parameter F which is of the order of 3. This means that the temperature increase in the irradiated area of the surface is four times as high as for a substrate without a nickel-phosphorous layer. These two situations are shown in Fig. 5a and c, respectively. Well-localized gold spots of good quality are achieved for layer thicknesses above 4 μm with deposition rates on the order of 2 μm/sec.

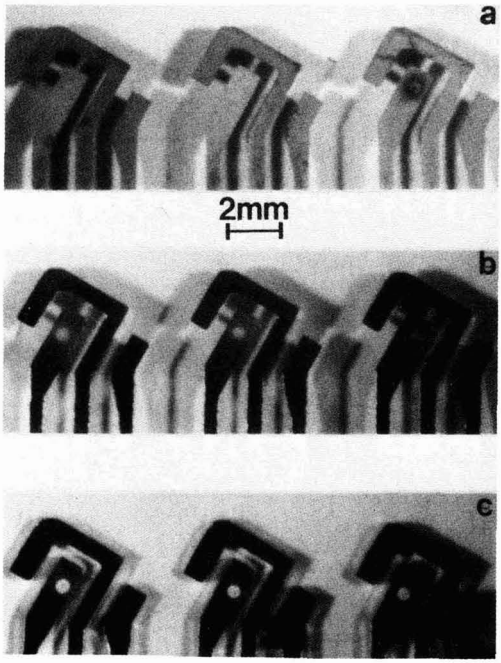

Fig. 6. The effect of a thermal film for laser-enhanced gold plating on Tombak; laser power 20W, irradiation time 2 sec. (a) 2 μm Ni; (b) 2 μm NiP; (c) 4 μm NiP.

The effect described above is very interesting from a physical point of view. The incident laser power will partly be absorbed and dissipated at the surface of the nickel-phosphorous layer. Most of this heat takes the shortest route through the poor heat conductor toward the region where the thermal conductivity is high. The influence of the thin layer on the temperature profile in the Tombak substrate is thus negligible. In the layer itself, however, a very definite and concentrated high temperature region is created. It is the combination of the poorly conducting film and the high conductivity bulk which is responsible for this effect. Should the substrate have consisted entirely of a poor heat conductor, the temperature concentration effect would have been absent.

Summarizing we may conclude that the selectivity and the plating rate of laser-enhanced electroplating on substrates that conduct heat well can be improved significantly by applying a thin film of a poor heat

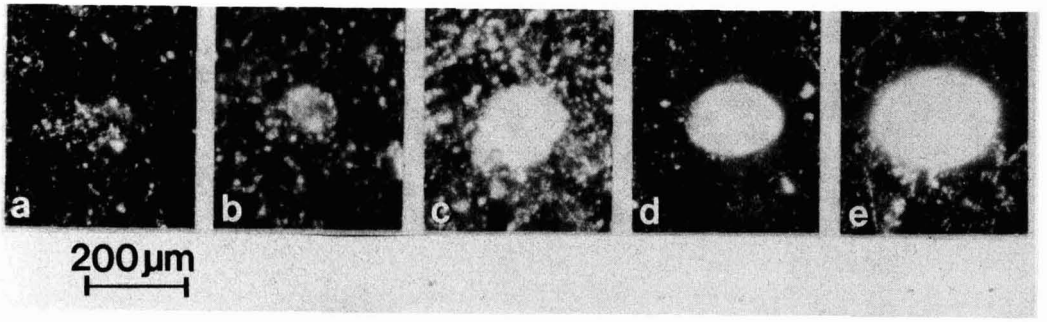

Fig. 5. The influence of the film thickness on the selectivity of laser-enhanced gold plating on Tombak; laser power 5W, irradiation time 32 sec. (a) NiP strike; (b) 1 μm NiP; (c) 4 μm NiP; (d) 8 μm NiP; (e) 16 μm NiP.

conductor on top of the substrate. In this way discrete metal spots can be obtained without the need of extremely high laser-power densities.

Acknowledgment

The authors wish to thank Dr. S. J. D. van Stralen of the University of Technology at Eindhoven for helpful advice on boiling phenomena.

Manuscript submitted May 11, 1982; revised manuscript received Sept. 27, 1982.

Any discussion of this paper will appear in a Discussion Section to be published in the December 1983 JOURNAL. All discussions for the December 1983 Discussion Section should be submitted by Aug. 1, 1983.

Publication costs of this article were assisted by Philips Research Laboratories.

APPENDIX

To solve the problem defined by Eq. [1]-[4], the double-Fourier transform

$$\bar{\theta}(\xi, \eta, z) = \int_{-\infty}^{\infty}\int e^{i(x\xi+y\eta)}\theta(x, y, z)\,dxdy \quad [A\text{-}1]$$

reduces the problem to

$$\frac{d^2\bar{\theta}}{dz^2} - (\xi^2 + \eta^2)\bar{\theta} = 0 \quad [A\text{-}2]$$

$$\frac{d\bar{\theta}}{dz} = -\frac{Q}{k_1}\exp\left[-\frac{a^2}{4}(\xi^2+\eta^2)\right] \quad \text{if } z=0 \quad [A\text{-}3]$$

with three conditions that are similar to those of Eq. [3] and [4]; a simple calculation yields

$$\bar{\theta} = \frac{Q}{k_1\alpha}\cdot\frac{1-Ne^{-2\alpha(\delta-z)}}{1+Ne^{-2\alpha\delta}}\cdot\exp(-\alpha z - a^2\alpha^2/4) \quad \text{if } 0\le z<\delta \quad [A\text{-}4]$$

and

$$\bar{\theta} = \frac{2Q}{(k_1+k_2)\alpha}\cdot\frac{\exp(-\alpha z - a^2\alpha^2/4)}{1+Ne^{-2\alpha\delta}} \quad \text{if } z>\delta \quad [A\text{-}5]$$

with

$$\alpha = (\xi^2+\eta^2)^{1/2} \quad \text{and} \quad N = \frac{k_2-k_1}{k_2+k_1} \quad [A\text{-}6]$$

Employing the inverse Fourier transform

$$\theta = \frac{1}{4\pi^2}\int_{-\infty}^{\infty}\int e^{-i(\xi x+\eta y)}\bar{\theta}(\xi, \eta, z)\,d\xi d\eta \quad [A\text{-}7]$$

using polar coordinates in the (ξ, η) plane we obtain finally

$$\theta(x, y, z) = \frac{Q}{2\pi ak_1}\int_0^{\infty} J_0\left(\frac{r}{a}\sigma\right)\frac{1-Ne^{-2(\delta-z)\sigma/a}}{1+Ne^{-2\delta\sigma/a}}\exp\left(-\frac{z}{a}\sigma - \frac{\sigma^2}{4}\right)d\sigma, \quad \text{if } 0\le z<\delta \quad [A\text{-}8]$$

and

$$\theta(x, y, z) = \frac{Q}{\pi a(k_1+k_2)}\int_0^{\infty} J_0\left(\frac{r}{a}\sigma\right)\frac{\exp\left(-\frac{z}{a}\sigma - \frac{\sigma^2}{4}\right)}{1+Ne^{-2\delta\sigma/a}}d\sigma, \quad \text{if } z>\delta \quad [A\text{-}9]$$

In deriving [A-8] and [A-9] we used the following relationship (3)

$$\int_0^{2\pi} e^{-i\sigma\cos\phi}\,d\phi = 2\pi J_0(\sigma) \quad [A\text{-}10]$$

The temperature distribution $\hat{\theta}$ that would have existed in the absence of the layer can be obtained from Eq. [A-9] by putting $\delta = 0$

$$\hat{\theta}(x, y, z) = \frac{Q}{2\pi ak_2}\int_0^{\infty} J_0\left(\frac{r}{a}\sigma\right)\exp(-z\sigma/a - \sigma^2/4)\,d\sigma \quad [A\text{-}11]$$

For convenience, it is assumed that the absorption coefficient of the bare substrate is equal to that of the substrate covered with a thin layer. This assumption does hardly influence experimental results, Q being determined by the optical properties of the plating material immediately after the initial plating step. We may now define the temperature-enhancement effect by considering the ratio

$$\frac{\theta(0,0,0)}{\hat{\theta}(0,0,0)} = \frac{\gamma}{\pi^{1/2}}\int_0^{\infty}\frac{1-Ne^{-2\delta\sigma/a}}{1+Ne^{-2\delta\sigma/a}}e^{-\sigma^2/4}\,d\sigma \quad [A\text{-}12]$$

Finally, it will be useful to know the temperature distributions in the planes $z = 0$ and $z = \delta$. In $z = 0$ we have

$$\frac{\pi ak_2}{Q}\theta(x, y, 0) = \tfrac{1}{2}\gamma\int_0^{\infty} J_0\left(\frac{r}{a}\sigma\right)\frac{1-Ne^{-2\delta\sigma/a}}{1+Ne^{-2\delta\sigma/a}}e^{-\sigma^2/4}\,d\sigma \quad [A\text{-}13]$$

When $\gamma >> 1$ and $\delta/a << 1$, we may simplify this expression as follows

$$\frac{\pi ak_2}{Q}\theta(x, y, 0) \sim \tfrac{1}{2}\gamma\int_0^{\infty} J_0\left(\frac{r}{a}\sigma\right)\left[\frac{1-N}{1+N} + \frac{4N}{(1+N)^2}\frac{\delta\sigma}{a}\right]e^{-\sigma^2/4}\,d\sigma \sim \frac{\pi^{1/2}}{2}e^{-\frac{1}{2}r^2/a^2}I_0(\tfrac{1}{2}r^2/a^2) + \gamma\frac{\delta}{a}e^{-r^2/a^2} \quad [A\text{-}14]$$

A similar expression valid in the plane $z = \delta$ is given by Eq. [8]

REFERENCES

1. R. J. von Gutfeld, E. E. Tynan, R. L. Melcher, and S. E. Blum, *Appl. Phys. Lett.*, **35**, 651 (1979).
2. J. Cl. Puippe, R. E. Acosta, and R. J. von Gutfeld, *This Journal*, **128**, 2539 (1981).
3. S. Ostrach, in "Theory of Laminar Flows," F. K. Moore, Editor, Vol. IV of "High Speed Aerodynamics and Jet Propulsion," Princeton, NJ (1964).
4. S. van Stralen and R. Cole, "Boiling Phenomena," (see pp. 29, 200, and 691 on local boiling), Hemisphere Publishing Corp., McGraw-Hill (1979).
5. M. Abramowitz and I. A. Stegun, "Handbook of Mathematical Functions," Dover Publishers, New York (1965).
6. N. N. Rykalin, A. A. Uglov, and N. I. Makarov, *Sov. Phys. Dokl.*, **11**, 632 (1967).
7. K. Takamoto and S. Nakayama, *Rev. Electr. Comm. Labs.*, **21**, 647 (1973).
8. P. Kivits, R. de Bont, and P. Zalm, *Appl. Phys.*, **24**, 273 (1981).

Current Distribution during Electroplating Within a Tubular Electrode of High Ohmic Resistance

Mordechai Ben-Porat

Department of Chemical Engineering, Technion-Israel Institute of Technology, Haifa, Israel

Joseph Yahalom*

Department of Materials Engineering, Technion-Israel Institute of Technology, Haifa, Israel

and Eliezer Rubin

Department of Chemical Engineering, Technion-Israel Institute of Technology, Haifa, Israel

ABSTRACT

Current distributions during electroplating within a tubular electrode were studied. A theoretical model was developed taking into account the various factors influencing the current distribution: metal electrode resistance, electrolyte phase resistance, mass transfer resistance, charge transfer resistance, as well as geometrical parameters and the applied potential. The model enables the prediction of the relative importance of each of these factors in obtaining uniform current distribution inside the holes. Criteria for obtaining uniform metal thickness inside holes based on limiting values of four dimensionless parameters are presented and discussed.

Knowledge of the current distribution in various geometrical configurations in electrolytic cells is important both for the analysis of data obtained in electrochemical experiments and for the design and scale-up of useful plating tanks in the electroplating industry.

Tubular geometry has a particular importance in the printed circuit industry and the production of millimeter waveguides. For example, production of multilayer printed circuits requires careful electroplating of copper in holes drilled through boards in order to provide electrical connection between various circuit layers.

In millimeter waveguides complex forms that are basically cylindrical in shape are produced by electroplating on a die. In the case of a printed circuit the diameter and depth of the holes are in the order of magnitude of millimeters, whereas in the case of millimeter waveguides the dimensions may be much larger.

Knowledge of the parameters which influence the current distribution within tubular electrodes is important in finding the optimal plating condition in the electroplating processes. The current distribution depends on many factors such as cell and electrode geometry, electrolyte conductivity, electrode kinetics, mass transfer, and electrode resistance.

The mathematical analysis of the electrochemical system, and specifically the solution of the equations, are very complex.

Owing to the complexity of the problem of current distribution within electrolytic cells only relatively few specific cases for given geometries have been solved.

Newman (1) and Parrish and Newman (2) analyzed current distribution in laminar forced convection electrodes having various two-dimensional slots. Alkire and Mirarefi (3) analyzed current distribution within a tubular electrode under unidirectional flow. Newman (4) solved the probelm of current distribution on rotating disk electrode. However, none of these investigators considered the possible initial ohmic resistance of the metallic electrode. Alkire and Varjian (5) developed a mathematical model which simultaneously takes account of the concentration field and the potential field in both the electrode and electrolyte phases for a resistive wire electrode moving at a steady speed through an electrolysis cell. The transient behavior was treated by Alkire (6) for electrodeposition onto a metal strip of high ohmic resistance, and by Alkire and Tvarusko (7) for current distribution along high resistance wire electrode during unsteady-state diffusion. However, in these two studies a uniform primary current distribution was assumed to be formed along the electrode, and the electrolytic solution ohmic resistance was neglected.

In many electroplating processes such as those mentioned above, a thin metallic layer is first deposited chemically followed by electrochemical plating. In these cases, both initial ohmic resistance and mass transfer may be of considerable importance in current distribution.

The object of the present work was to study current distributions during electroplating within a tubular electrode taking into account both initial ohmic resistance and mass transfer effects.

Consideration was also given to a periodic fluctuation in the liquid flow fluid similar to those encountered in the plating through holes in printed circuit board fabrication.

Mathematically, the problem to be solved invokes coupling of the Laplace equation for the electrolyte solution, mass transfer equations and the electrode kinetics equation occurring near an electrode surface, together with a nonuniform electrode potential distribution due to the initial high ohmic resistance of the thin metal electrode. The latter introduces transient effects.

Mathematical Model

The electrochemical system under consideration is shown schematically in Fig. 1. An electrically insulated tube of length $2l$ and of radius r_0 is inserted in an electrolyte solution and positioned between two parallel counterelectrodes. The inside wall of the tube is initially plated with a thin metal layer of thickness a_0. This initial layer is obtained by chemical deposition prior to the onset of the electrochemical process.

The tube openings $z = 0$ and $z = 2l$ are cathodically connected to a power supply, while the parallel electrodes are connected anodically. The electric potential between the cathode and anode is kept constant. Therefore, it can be assumed that the potential difference between the electrical contact point at the tube openings ($z = 0$, $r = r_0$, and $z = 2l$, $r = r_0$) and the electrolytic solution near this point is also constant.

* Electrochemical Society Active Member.

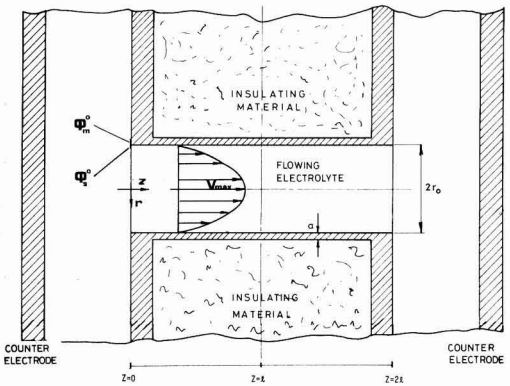

Fig. 1. Schematic diagram of the electrochemical system

The following simplifying assumptions are used:

I. Only one electrode reaction occurs and the reversible reaction rate has the form given by Eq. [1] in accordance with Butler-Volmer kinetics.

II. The electrical double layer and the mass transfer diffusion layer attain pseudo steady-state conditions relative to the rate of the electrode ohmic resistance changes.

III. The surface of the electrode remains smooth during the course of metal deposition. The electrode thickness change is small compared to the tube diameter, and therefore no significant geometric changes occur during the electrolysis.

IV. The reactive solution species are present in a dilute concentration. Therefore, because of the presence of a relatively high concentration of the supporting electrolyte, the effect of reactive species on the electric field is negligible.

V. The electrolyte flows through the tubular electrode in a fully developed laminar flow. Edge effects at the hole entrance are neglected.

VI. The dimensionless Péclet number, $2r_o\,\bar{v}_z/D$, is large. Therefore, the concentration differences in the electrolyte caused by the electrochemical reaction are confined to a very thin layer near the tube wall. Outside this layer the electrolytic solution is of uniform composition so that the potential distribution obeys the Laplace equation.

Assumption I requires further clarification and elaboration. 100% cathodic current efficiency is to be expected of a copper acid plating bath at the practical current densities, *e.g.*, Ref. (8). The local electrochemical reaction rate $j(z)$ proceeds at the tubular electrode wall ($r = r_o$) and is given by the Butler-Volmer expression

$$j(z) = i_o\left[\exp\left(\alpha_a\frac{n\mathbf{F}}{RT}\eta_s\right) - \exp\left(-\alpha_c\frac{n\mathbf{F}}{RT}\eta_s\right)\right] \quad [1]$$

The exchange current density i_o is related to the reactant cation concentration by an empirical expression

$$i_o(c = c_s) = \left(\frac{c_s}{c_b}\right)^{\gamma} i_o(c = c_b) \quad [2]$$

Since it is difficult to measure the local surface overpotential it is convenient to relate the reaction rate to the potential difference between metal and solution phase, thus including the concentration overpotential

$$\eta_T = (\phi_m - \phi_s) - E_{eq} = \eta_s + \eta_c \quad [3]$$

where the concentration overpotential is given by

$$\eta_c = \frac{RT}{n\mathbf{F}}\ln\frac{c_s}{c_b} \quad [4]$$

Substitution of Eq. [2], [3], and [4] in [1] relates the reaction rate to the local surface concentration and potential difference

$$j(z) = i_o(c = c_s)\left[\left(\frac{c_s}{c_b}\right)^{\gamma-\alpha_a}\exp\left(\frac{\alpha_a n\mathbf{F}}{RT}\eta_T\right) - \left(\frac{c_s}{c_b}\right)^{\gamma-\alpha_c}\exp\left(-\frac{\alpha_c n\mathbf{F}}{RT}\eta_T\right)\right] \quad [5]$$

We may relate the potential difference between the metal and the solution to the applied potential

$$\phi_m - \phi_s = (\phi_m^\circ - \phi_s^\circ) + (\phi_m - \phi_m^\circ) - (\phi_s - \phi_s^\circ) \quad [6]$$

and by subtracting E_{eq} from both sides and rearranging

$$[(\phi_m^\circ - \phi_s^\circ) - E_{eq}] = (\phi_m^\circ - \phi_m) + \eta_s + \eta_c + (\phi_s - \phi_s^\circ) \quad [7]$$

The quantity on the left side of Eq. [7] is the applied potential between the electrode and the solution at the tube openings. This potential consists of four irreversible phenomena, namely, ohmic losses ($\eta_{\Omega m}$) in the electrode phase, surface (activity) overpotential (η_s), concentration overpotential (η_c), and ohmic losses ($\eta_{\Omega s}$) in the electrolyte phase.

Thus we see that the system may be conveniently divided into three regions: (*i*) the electrode phase, (*ii*) a thin diffusion layer near the electrode surface within which a concentration variation takes place, and (*iii*) the bulk solution, of uniform composition, which fills the tubular electrode.

The Bulk Region

The potential distribution in the bulk region obeys the Laplace equation. In cylindrical coordinates this is given by [9]

$$\frac{1}{r}\frac{\partial}{\partial r}\left(r\frac{\partial\phi_s}{\partial r}\right) + \frac{\partial^2\phi_s}{\partial z^2} = 0 \quad [8]$$

With reference to Fig. 1, the boundary conditions are

$$\phi_s = f(r) \text{ for } z = 0 \text{ and } 0 \leq r \leq r_o$$

$$\phi_s = \phi_s^\circ \text{ for } z = 0 \text{ and } r = r_o \quad [9a]$$

$$\frac{\partial\phi_s}{\partial z} = 0 \text{ for } z = l \text{ and } 0 \leq r \leq r_o \quad [9b]$$

$$\frac{\partial\phi_s}{\partial r} = -\frac{j}{\kappa} \text{ for } r = r_o \text{ and } 0 \leq z < 2l \quad [9c]$$

The function $f(r)$ which describes the potential distribution at the tube openings ($z = 0$, $z = 2l$) should be found experimentally, however, we shall assume a uniform potential distribution, namely

$$f(r) = \phi_s^\circ \text{ for } z = 0 \text{ and } 0 < r < r_o$$

The Electrode Phase

Figure 2(a) describes schematically the metal layer on the tube wall. The current density is given by Ohm's law

$$i_m = -\sigma\frac{d\phi_m}{dz} \quad [10]$$

The current density in the metal phase varies with position owing to the electrode reaction. From a current balance on an element of length dz in the metal layer [Fig. 2(b)] a differential equation can be obtained describing the variation of the current density in the electrode phase

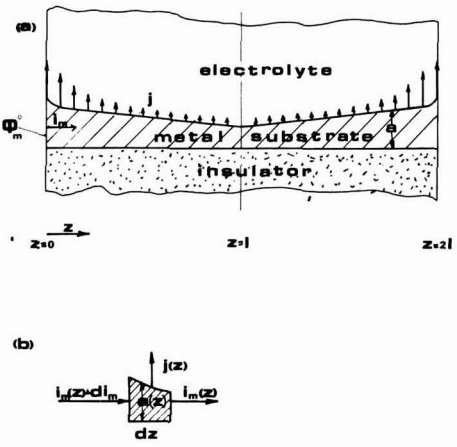

Fig. 2. (a) Schematic representation of the metal substrate on the tube wall. (b) Current balance on an element of length dz in the metal substrate.

$$\frac{d[i_m \cdot a]}{dz} = -j \qquad [11]$$

Substituting i_m from Eq. [10] in [11] gives a differential equation which describes the variation of the electrode potential

$$\frac{d}{dz}\left[a \cdot \frac{d\sigma_m}{dz}\right] = \frac{j}{\sigma} \qquad [12]$$

There are two boundary conditions

$$\phi_m = \phi_m^\circ \text{ at } z = 0 \text{ (and } z = 2l)$$

$$\frac{d\phi_m}{dz} = 0 \text{ at } z = l \qquad [13]$$

The local deposit thickness is obtained by integration of the local current density over the period of electrolysis

$$a(z,t) = a_o + \int_o^t \frac{M}{dn\mathbf{F}}|j|dt \qquad [14]$$

The Diffusion Layer

In accord with the assumption that the Péclet number is large, the steady-state equation of laminar convective diffusion in the tube is

$$v_s(r)\frac{\partial c}{\partial z} = D\left[\frac{\partial^2 c}{\partial r^2} + \frac{1}{r}\frac{\partial c}{\partial r}\right] \qquad [15]$$

The diffusion layer under this condition is very thin and the velocity distribution is approximately linear with distance from the wall; for small values of z provided that $(zD)/(2\bar{v}_z r_o^2) << 0.01$, Lévêque (9) recognized that there is a diffusion layer near the wall and derivatives with respect to r become large, thus the following approximations apply

$$\frac{1}{r}\frac{\partial c}{\partial r} << \frac{\partial^2 c}{\partial r^2} \qquad [16]$$

and

$$v_z = \frac{4\bar{v}_z}{r_o}y; \quad y << 1 \qquad [17]$$

where y is the distance from the tube wall

$$y = r_o\left(1 - \frac{r}{r_o}\right) \qquad [18]$$

By inserting these approximations in Eq. [15] one obtains

$$\frac{4\bar{v}_z}{r_o}y\frac{\partial c}{\partial z} = D\frac{\partial^2 c}{\partial y^2} \qquad [19]$$

At the limiting current condition the surface concentration of the solute is zero, and Eq. [19] can be solved using the similarity transformation

$$r_1 = y\left(\frac{4\bar{v}_z}{9zDr_o}\right)^{1/3} \qquad [20]$$

The concentration profile given by the solution of [19] is

$$\frac{c}{c_b} = \frac{1}{\Gamma(4/3)}\int_o^\eta e^{-\eta^3}d\eta \qquad [21]$$

The limiting current distribution is therefore

$$j_{lim} = n\mathbf{F}D\left.\frac{\partial c}{\partial y}\right|_{y=0} = \frac{n\mathbf{F}Dc_b}{\Gamma(4/3)}\left(\frac{4\bar{v}_z}{9Dr_o z}\right)^{1/3} \qquad [22]$$

In this electrochemical system the surface concentration of solute is not zero. Smyrl and Newman (10) solved Eq. [19] for currents below the limiting current. They obtained a relation between the surface concentration distribution and the current distribution by applying Duhamel's theorem to Eq. [22]

$$j = \frac{n\mathbf{F}D}{\Gamma(4/3)}\left(\frac{4\bar{v}_z}{9Dr_o}\right)^{1/3}\int_o^z \frac{dc_s(z')}{dz'}\cdot\frac{dz'}{(z-z')^{1/3}} \qquad [23]$$

Equation [23] gives the local electrochemical reaction rate.

The electrolyte velocity, $v(z)$, and therefore the local surface concentration, $c(z)$, are changing periodically due to the "side to side" tube motion caused by the cathode rod reciprocation agitation.

The theoretical prediction of the electrolyte velocity profile and the surface concentrations is exceedingly difficult under these circumstances. Edge-effects caused by the sharp-edged tube entrance, phase shift between the flow in the tube, and the cathode motion generated by the oscillating flow field are some of the considerations which indicate that fully developed laminar flow constitutes the conservative bound for the mixing in the mass diffusion layer at the tube surface [Engelmaier and Kessler (11)].

To avoid the mathematical difficulties we shall use an approximate value for the local surface concentration by defining the arithmetic mean of two surface concentration distributions: $\vec{c}_s(z)$ which would be if the electrolyte flows in the tube under fully developed laminar regime to one side and $\overleftarrow{c}_s(z)$ which would be if the electrolyte flows in the opposite direction, and assuming that the change in the electrode thickness during one cycle does not significantly affect the electrode potential.

This means, $\bar{c}_s(z)$, given by [24]

$$\bar{c}_s(z) = \frac{\vec{c}_s(z) + \overleftarrow{c}_s(z)}{2} \qquad [24]$$

gives an approximation to the effective local surface concentration.

Since the system is symmetrical around $z = l$ and if we assume that during one cycle the potential distribution, ϕ_m and ϕ_s do not change, one gets

$$\vec{c}_s(z) = \overleftarrow{c}_s(2l - z) \qquad [25]$$

and

$$\bar{c}_s(z) = \frac{\vec{c}_s(z) + \overleftarrow{c}_s(2l - z)}{2} \qquad [26]$$

The mean concentration calculated by Eq. [26] will be used in the subsequent analysis.

Dimensionless Equations

Complying with the assumptions of the model, the potential and the current distributions, as well as the concentration distribution inside the tubular electrode, may be determined from the solution of coupled differential Eq. [8] and [12], algebraic Eq. [5], and integral Eq. [14] and [23]. Before conducting the calculations, it is convenient to transform the equations into dimensionless form.

By introducing the following dimensionless variables

$$\zeta = \frac{z}{l} \qquad \rho = \frac{r}{l} \qquad \rho_o = \frac{r_o}{l}$$

$$\phi_m^* = \frac{n\mathbf{F}}{RT}[\phi_m - \phi_m^\circ] \qquad \phi_s^* = \frac{n\mathbf{F}}{RT}[\phi_s - \phi_s^\circ]$$

$$\phi_a^* = \frac{n\mathbf{F}}{RT}[\phi_m^\circ - \phi_s^\circ - E_{eq}]$$

$$\eta_T^* = \frac{n\mathbf{F}}{RT}\eta_T = \phi_m^* + \phi_s^* + \phi_a$$

$$c = \frac{\bar{c}_s}{c_b} \qquad a^* = \frac{a}{a_o} \qquad J = \frac{j}{i_{av}} \qquad [27]$$

where i_{av} is defined by [27]

$$i_{av} = \frac{\int_o^l j\,dz}{l} \qquad [28]$$

the number of independent system parameters is reduced to four independent dimensionless quantities

$$\xi_s = \frac{n\mathbf{F}}{RT}\frac{l^2}{r_o}\cdot\frac{i_o}{\kappa}$$

$$\xi_m = \frac{n\mathbf{F}}{RT}\frac{l^2}{a_o}\frac{i_o}{\sigma}$$

$$N = \frac{n\mathbf{F}}{\Gamma(4/3)}\frac{Dc_b}{i_o}\left(\frac{4\bar{v}_z}{9Dr_o l}\right)^{1/3}$$

$$\beta = \frac{i_{av}}{i_o} \qquad [29]$$

The dimensionless equations which describe the model are

$$\frac{\partial^2\phi_s^*}{\partial\zeta^2} + \frac{1}{\rho}\frac{\partial\phi_s^*}{\partial\rho} + \frac{\partial^2\phi_s^*}{\partial\rho^2} = 0 \qquad [30]$$

$$\phi_s^*(0,\rho) = f(\rho), \quad \phi_s^*(0,\rho_o) = 0$$

$$\frac{\partial\phi_s^*}{\partial\zeta}(1,\rho) = 0$$

$$\frac{\partial\phi_s}{\partial\rho}(\zeta,\rho_o) = \rho_o\xi_s\beta J \qquad [31]$$

$$\frac{d}{d\zeta}\left[a^*\frac{d\phi_m^*}{d\zeta}\right] = \xi_m\beta J \qquad [32]$$

$$\phi_m^*(0) = \frac{d\phi_m^*}{d\zeta}(1) = 0 \qquad [33]$$

$$J = \frac{1}{\beta}[c^{\gamma-\alpha_a}\exp(\alpha_a\eta_T^*) - c^{\gamma+\alpha_c}\exp(-\alpha_c\eta_T^*)] \qquad [34]$$

$$J = \frac{1}{\beta}N\int_o^\zeta \frac{dc(\zeta')}{d\zeta'}\frac{d\zeta'}{(\zeta-\zeta')^{1/3}} \qquad [35]$$

$$a^* = 1 + \int_o^t \frac{Mi_o}{dn\mathbf{F}a_o}J\beta dt \qquad [36]$$

Boundary conditions [31] as well as Eq. [32] are nonlinear and therefore Eq. [30] and [32] cannot be solved analytically.

Method of Solution

The solution of the set of equations and boundary conditions which describe the model, Eq. [30]-[36], was carried out using an iterative procedure as described in Appendixes A and B.

The calculations were carried out on an IBM 370 digital computer at the Technion Computer Center.

Results presented in this work were determined with the use of 50 ξ_m increments in the axial direction in the interval $0 < \zeta < 1$ and time increment of

$$\Delta = \frac{1}{10}\frac{dn\mathbf{F}a_o}{Mi_o}$$

For the range of parameters studied here, there was no appreciable improvement in the numerical results by the use of smaller steps. A run consists of calculations of metal and solution potential distribution for a particular set of parameter values, during the transient time of electroplating. The calculations were terminated when "practically" steady-state conditions were attained, that is, when ξ_m was below 0.001.

A typical run for one set of parameters was found to take approximately 30 sec on an IBM 360 computer when the program is compiled in FORTRAN X.

Results and Discussion

According to the model described here the applied potential drops over four resistances: metal (electrode) resistance, electrolyte resistance, charge transfer reaction resistance, and mass transfer resistance. The relative share of each is indicated by three dimensionless parameters

$$\xi_m = \frac{n\mathbf{F}}{RT}\cdot\frac{l^2}{a_o}\cdot\frac{i_o}{\sigma}$$

This is proportional to the rate of the cathodic reaction rate divided by the metal conductivity

$$\xi_s = \frac{n\mathbf{F}}{RT}\cdot\frac{l^2}{r_o}\cdot\frac{i_o}{\kappa}$$

which in turn is proportional to the rate of the cathodic reaction rate divided by the solution conductivity, and

$$N = \frac{n\mathbf{F}}{\Gamma(4/3)}\frac{Dc_b}{i_o}\left(\frac{4\bar{v}_z}{9Dr_o l}\right)^{1/3}$$

indicating the ratio between rate of mass transfer to the cathode surface and the cathodic reaction rate. The value of the gamma function $\Gamma(4/3)$ is 0.893. An additional parameter defines the geometric configuration of the tubular electrode

$$\rho_o = \frac{r_o}{l}$$

Calculations based on the theoretical model have been conducted in order to predict several essential features of the tubular electrode of high ohmic resistance. All calculations have been conducted for cathodic deposition with use of symmetric transfer coefficient ($\alpha_a = \alpha_c = 0.5$) and $n = 2$.

The dimensionless parameters employed in the following analysis should permit the application of the results to a wide variety of actual systems (*e.g.*, the printed circuit industry).

First consider the four overpotentials which constitute the applied potential.

Figure 3 illustrates how these overpotentials vary with distance along a tubular electrode for one typical situation ($\xi_s = 0.1$, $\xi_m = 0.1$, $N = 100$, $\phi_a^* = -9$, and $\rho_o = 0.1$). Note that the sum of the four overpo-

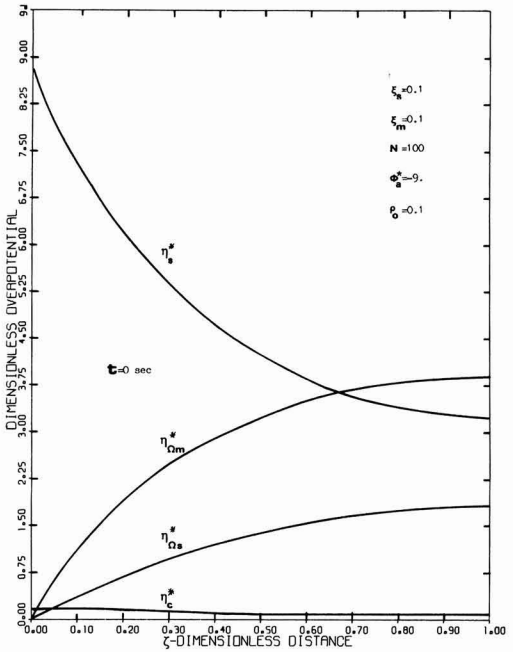

Fig. 3. Overpotential partition within a tubular electrode at the onset of electrodeposition.

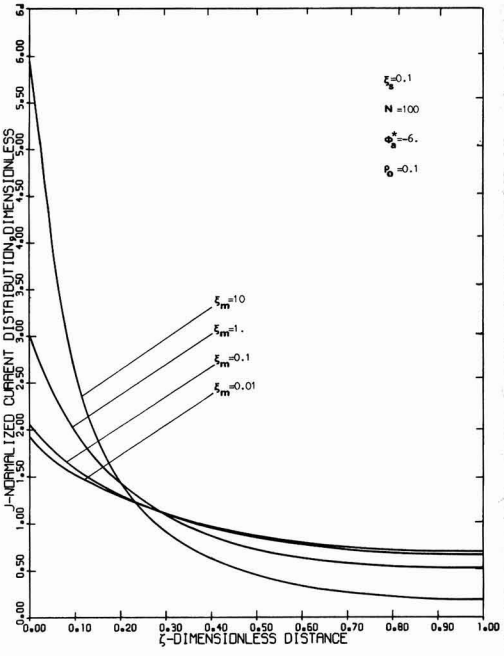

Fig. 4. Distribution of current density for different contributions of metal resistance, parameter ξ_m.

tentials is always a constant and equal to the applied potential.

Thus at the tubular electrode edge ($z = 0$), the only components of the applied potential are the charge transfer overpotential and the concentration overpotential (which is relatively small for this typical example). As we move inside the tube, the ohmic resistances of the metal and of the electrolyte, $\eta_{\Omega m}$ and $\eta_{\Omega s}$, respectively, act to consume an ever increasing proportion of the applied potential, decreasing the charge transfer overpotential. The variation of charge transfer overpotential along the tube length lead to a nonuniform current distribution Thus the local reaction rate is always the highest at the tube edge and decreases with distance inside the tube. The uniformity of the current distribution depends on the values of the parameters mentioned earlier.

Let us consider the influence of each of these parameters. Figure 4 illustrates the current density distribution dependence on parameter ξ_m.

If ξ_m is large, the ohmic loss in the metal is large and the current distribution is nonuniform; as the value of ξ_m decreases, the current distribution tends to be more uniform. When ξ_m is less than 0.01, the metal (electrode) resistance is negligible and the other overpotentials predominate. A similar behavior is described by Fig. 5 which shows the current density distribution dependence on the parameter ξ_s.

Again if ξ_s is large, there is a large ohmic loss, this time, in the electrolyte solution, and the current distribution is nonuniform. As the value of ξ_s decreases the current distribution becomes more uniform. At very low values of ξ_s (say, $\xi_s < 0.01$), the electrolyte ohmic resistance is very small and its value has no influence on the current distribution.

Let us now consider the influence of the third parameter, N. The current density distribution in the tubular electrode is shown in Fig. 6 for several values of N. For a large value of N the mass transfer resistance is small compared with charge transfer near the electrode.

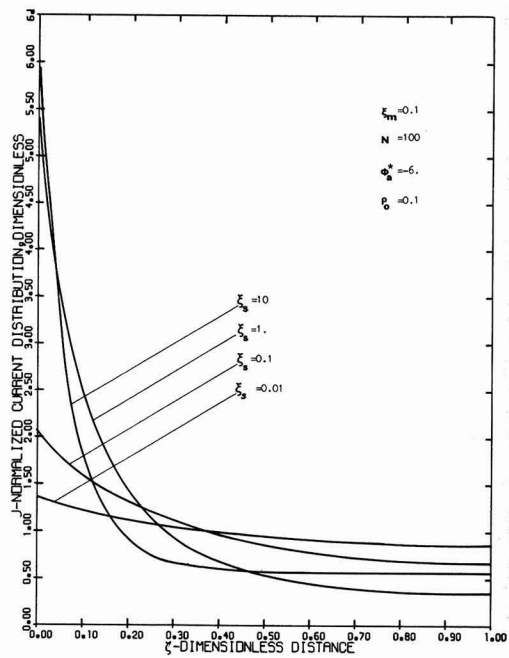

Fig. 5. Distribution of current density for different contributions of electrolyte resistance, parameter ξ_s.

Thus the current distribution depends merely on the charge transfer overpotential near the electrode (assuming that the electrolyte and metal ohmic resistance are small) and is relatively uniform. For small values of N, the mass transfer process tends to be rate limiting, the concentration overpotential predominates, and the current distribution is nonuniform.

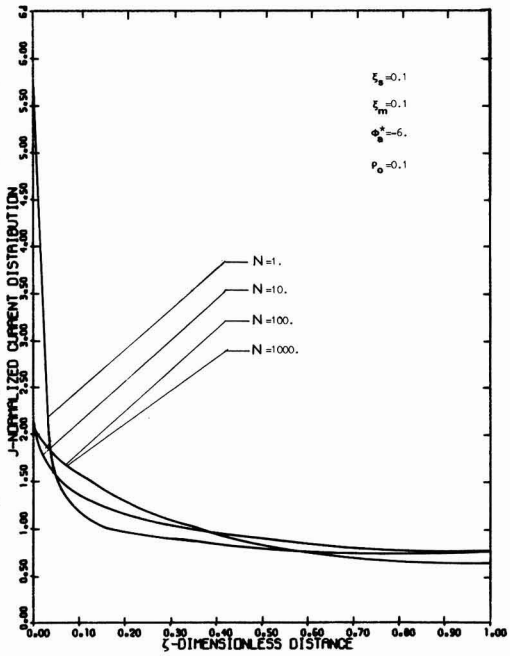

Fig. 6. Current density distribution for different mass transfer to charge transfer resistance ratios, parameter N.

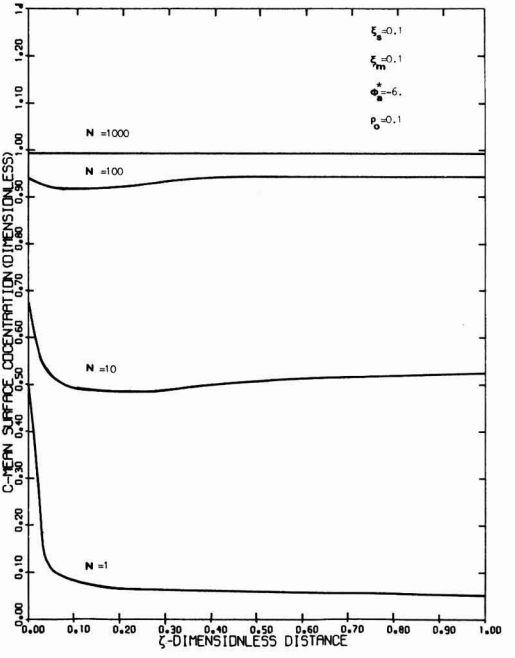

Fig. 7. Dependence of the mean surface concentration on the parameter N.

The concentration of reactive species near the tubular wall varies along the tube axis. Figure 7 illustrates the mean surface concentration dependence on parameter N. (The tube is placed between two counter-electrodes and is periodically moved to the left and to the right.)

When N has large values, mass transfer resistance is small and the surface concentration approaches that of the bulk. Note that surface concentration distribution is uniform. As N decreases the mass transfer resistance increases and lower surface concentrations are encountered. The surface concentration distribution tends to be nonuniform. For intermediate values of N at the tubular edge, the electrochemical reaction rate is high and also the reactive species is accessible; on the other hand, at the tube center the reactive species is less accessible but also the reaction rate is slower.

These phenomena cause the mean surface concentration to be higher at the tubular electrode edge and center than in intermediate points between them. They do not occur when N is small ($N < 1$) or large ($N > 100$).

The current density distribution varies with geometric configuration of the tubular electrode.

Figure 8 illustrates the effect of the geometric parameter ρ_o on the current density distribution.

If ρ_o is small, *i.e.*, the tube diameter is small compared to the tube length, ohmic resistances of the metal and the electrolyte are high (large values of ξ_m and ξ_s), the current distribution is very nonuniform. On the other hand, if ρ_o is large, *i.e.*, the tube diameter is large compared to the tube length, the current distribution becomes uniform as on a flat electrode.

An important factor in the electroplating industry is the rate of plating which is proportional to the total current consumed by the electrochemical reaction. We refer here to the average current density which is obtained by integrating the local current density over the entire tubular electrode.

The dependence of the average current density β on the applied potential is illustrated in Fig. 9, for several values of parameter ξ_m.

For large values of ξ_m, most of the applied potential falls over an ohmic loss in the metal electrode, the charge transfer overpotential is small and therefore the electrochemical reaction rate which varies with charge transfer overpotential according to Eq. [1] is low and depends linearly on the applied potential. On

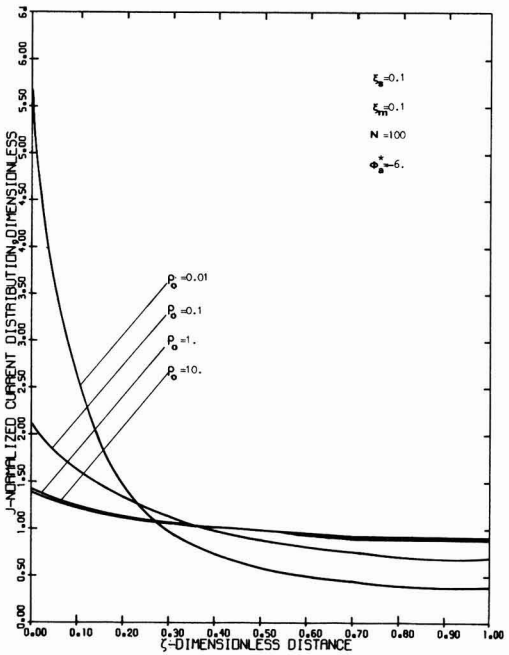

Fig. 8. Dependence of the current density distributions on the geometric parameter, ρ_o.

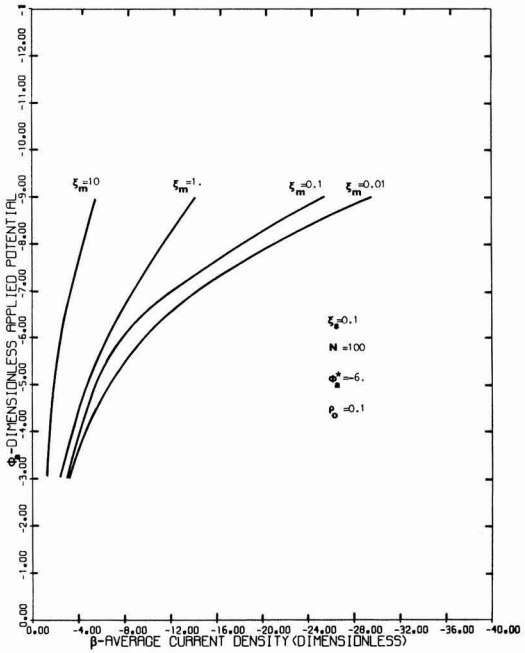

Fig. 9. Dependence of the average current density on applied potential for different metal resistance, parameter ξ_m.

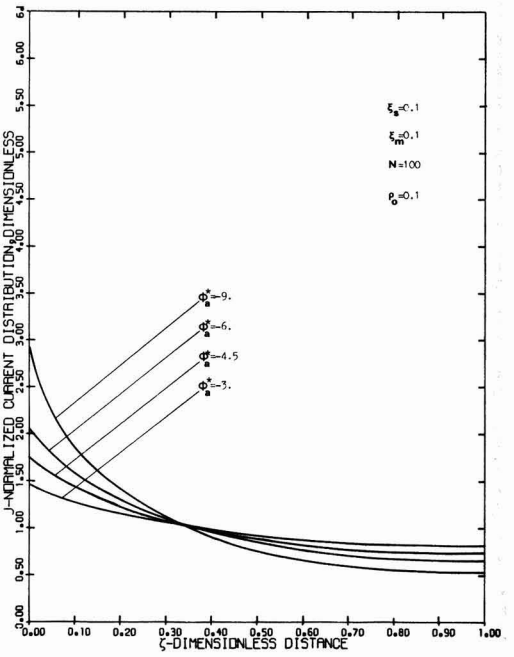

Fig. 10. Dependence of the current density distribution on the distance at different applied potentials ϕ_a^*.

the other hand, when ξ_m is small, the ohmic loss is negligible, the charge transfer overpotential dominates, and we obtain a Tafel-like (exponential) dependence of the reaction rate on the applied potential.

The applied potential also influences the current density distribution. An increase in the applied potential causes a more nonuniform current distribution within the tubular electrode. This phenomenon is shown in Fig. 10.

Finally, let us consider the transient behavior which occurs during the electroplating process (which causes thickening of the metal electrodes and lowers the ohmic resistance).

We turn back to the typical situation illustrated in Fig. 3 ($\xi_s = 0.1$, $\xi_m = 0.1$, $N = 100$, $\phi_a^* = 9$, $\rho_o = 0.1$): consider copper deposition from an acidified sulfate bath for which $M = 63.57$, $d = 8.9$ g/cm^3, $i_o = 10^{-3}$ A/cm^2, $a_o = 5 \times 10^{-5}$ cm (a typical electroless deposit thickness).

Figure 11 illustrates how the four overpotentials vary with distance along a tubular electrode after a long period of electroplating (in this situation after 2000 sec). ξ_m is small and thus the ohmic loss in the metal electrode is negligible, the charge transfer overpotential increases (by more than 50% at the tube center) and the electrochemical reaction is enhanced.

The electrolyte ohmic overpotential increases moderately (following an increase in the current density) while the concentration overpotential practically does not change, since for this typical example the mass transfer resistance is low ($N = 100$).

Variation of the current density distribution during electroplating is described in Fig. 12 for the same situation mentioned earlier but with $\xi_m = 1$.

The current distribution which is very nonuniform at the initial stage of the plating process becomes more uniform as the coating thickens and eventually attains the so-called "primary current distribution which is determined by the electrolyte properties (described by ξ_s) and the electrochemical cell geometry (ρ_o). For this typical example the mass transfer resistance is negligible.

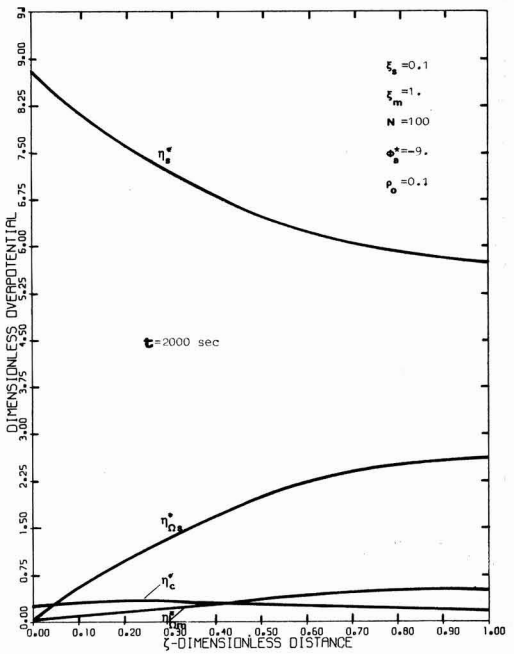

Fig. 11. Overpotential partition within a tubular electrode after a long period of time of electrodeposition.

Conclusions

A theoretical model has been developed which takes into account the various factors influencing the current distribution: metal electrode resistance, electrolyte phase resistance, mass transfer resistance, charge transfer resistance, as well as geometrical parameters

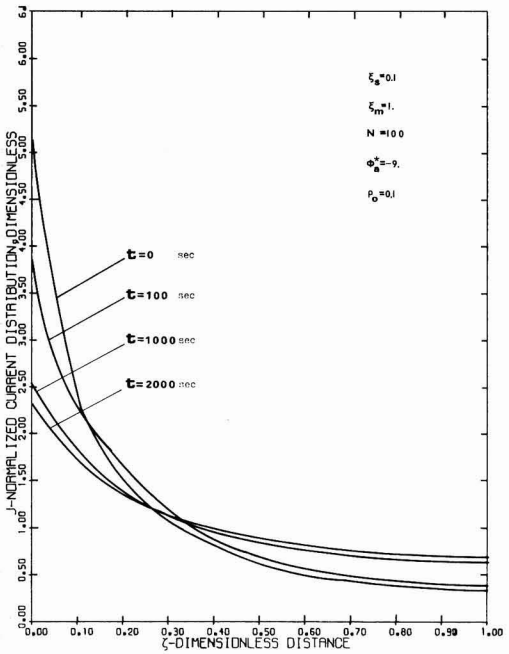

Fig. 12. Current density distribution during electroplating

and the applied potential. The model enables the prediction of the relative importance of each of the above-mentioned factors in obtaining uniform current distribution (*i.e.*, uniform metal thickness inside the holes).

It is shown that in order to obtain a uniform current distribution each one of the following dimensionless parameters:

ξ_m—proportional to the ratio of cathodic reaction rate to metal conductivity

ξ_s—proportional to the ratio of cathodic rate to solution conductivity

N—indicating the ratio between rate of mass transfer to the cathodic surface and the cathodic reaction rate

ϕ_a^*—dimensionless applied potential

should be in the following range: $\xi_m < 0.01$; $\xi_s < 0.01$, $N > 100$, $|\phi_a^*| < 3$. Also, it is desirable that the geometrical parameter ρ_o should be above 0.1. However, if this criteria for ρ_o cannot be met, it is possible to improve the current distribution by changing the other parameters as indicated below.

In industrial electroplating two effects are required: uniform metal thickness and high deposition rate. These two desired effects usually work in opposite directions when applied to planar surfaces. The present general model, through the above-mentioned dimensionless parameters, makes it possible to predict as well as to make the proper decision with respect to the optimal conditions for electroplating. The usual practical condition is that the geometrical factors, ρ_o, are given. ξ_m is dependent on the initial metal thickness and, after a short period of electroplating, its influence tends to become negligible. If the initial ξ_m is too large and it is not feasible to increase a_o during the metal deposition processes, the situation can be remedied by decreasing the initial applied potential (*i.e.*, decreasing ϕ_a^*). Once the value of a_o has increased enough due to thickening which occurs during electroplating process and ξ_m has reached a value below 0.01, the applied potential can be increased in order to speed up electroplating.

The value of ξ_s determines the primary current distribution. Small enough values of ξ_s can be achieved by increasing the electrolyte conductivity, *i.e.*, increasing κ.

Large enough values of N can be achieved by increasing the electrolyte flow velocity through the hole v_z, the metal ion concentration c_b, and the diffusion coefficient D. The latter can be obtained by increasing the temperature.

Manuscript submitted July 27, 1981; revised manuscript received July 1, 1982.

Any discussion of this paper will appear in a Discussion Section to be published in the December 1983 JOURNAL. All discussions for the December 1983 Discussion Section should be submitted by Aug. 1, 1983.

APPENDIX A

Iterative Solution of the Model Equations

(*i*) Make some initial guess of the potential distributions $\phi_s^*(\zeta, \rho_o)$ and $\phi_m^*(\zeta)$.

(*ii*) Calculate the concentration distribution $c(\zeta)$ (from Eq. [34] and [35].

(*iii*) Calculate $\phi_m^*(\zeta)$ by solving Eq. [32].

(*iv*) Calculate $\phi_s^*(\zeta, \rho_o)$ by solving Eq. [30].

(*v*) Using the calculated ϕ_m^* and ϕ_s^* return to iteration (*ii*) and repeat the sequence of operations until convergence is achieved.

(*vi*) Calculate the current density distribution $J(\xi)$ using the values of ϕ_s^*, ϕ_m^*, and C which were calculated previously. This is the initial current distribution through the hole (at $t = 0$).

(*vii*) Calculate the metal thickness which will be electrodeposited during a short time interval Δt at the calculated current density $J(\xi)$ (according to Eq. [36]).

(*viii*) Having the new metal thickness distribution repeat the sequence of calculations (*ii*-*vi*), this time the values are computed for Δt sec after the start of the electroplating. These values are used to calculate the metal deposit during the period of time of Δt sec from time Δt to $2\Delta t$.

(*ix*) The calculation is continued until the system arrives at a steady state and the change in the values of the variables from time t to $t + \Delta t$ is less than a small chosen value.

APPENDIX B

Mathematical Solution Details

By extracting J from Eq. [34] and [35], an algebraic-integral equation is obtained which may be evaluated by the method of Acrivos and Chambre (12), thus, for known values of ϕ_s^* and ϕ_m^* it is possible to calculate the concentration distribution inside the tube.

The potential distribution in the metal layer $\phi_m^*(\xi)$ is found by solving Eq. [32] and its boundary condition (given by Eq. [33]). This is a second-order, nonlinear equation which is solved numerically. The equation is linearized and then solved by using finite difference.

The potential distribution in the electrolyte solution ϕ_s^* is calculated from Eq. [30] and the set of boundary conditions given by Eq. [31].

The second-order partial differential equation with a nonlinear boundary condition is solved by a pseudo-analytical method. $\phi_s^*(\xi, \rho)$ is assumed to have a solution of the form

$$\phi_s^*(\zeta, \rho) = \frac{2}{\rho_o^2} \sum_{n=1}^{N} \frac{\sinh[\alpha_n(1-\xi)]}{\sinh(\alpha_n)} \frac{J_o(\alpha_n \rho)}{J_o^2(\alpha_n \rho_o)} \int_0^{\rho_o} \rho f(\rho) J_o(\alpha_n \rho)\, d\rho + \sum_{n=1}^{n=N} A_n \frac{1}{\lambda_n} \sin(\alpha_n \rho) \frac{I_0(\lambda_n \rho)}{I_1(\lambda_n \rho_o)}$$

where α_n, $n = 1$, and N are N roots of the equation

$$J_1(\alpha_n \rho_o) = 0$$

and λ_n are eigenvalues given by

$$\lambda_n = [2(m-1)+1]\pi/2$$

The coefficients A_n, $n = 1$, and N were calculated numerically using Grey's algorithm (13) for nonlinear optimization.

LIST OF SYMBOLS

a metal electrode layer thickness, cm
a^* metal electrode layer thickness a/a_o, dimensionless
a_o initial metal electrode layer thickness, cm
c_b concentration of reactant in bulk electrolyte, gmol/cm^3
$\vec{c}_s$ reactant concentration at electrode surface when the electrolyte is moving to the right, gmol/cm^3
$\overleftarrow{c}_s$ reactant concentration at electrode surface when the electrolyte is moving to the left, gmol/cm^3
c mean reactant concentration at electrode surface, gmol/cm^3
C mean reactant concentration at electrode surface c/c_b, dimensionless
D diffusion coefficient, cm^2/sec
d density of electrode metal, g/cm^3
E_{eq} potential difference between electrode and electrolyte at equilibrium, V
$\mathbf{F}$ Faraday's constant, 96,500 C/g-equiv.
i_m current density in metal electrode, A/cm^2
i_{av} average current density (Eq. [28]), A/cm^2
i_o exchange current density, A/cm^2
j_{lim} local limiting current density, A/cm^2
j local reaction rate along electrode, A/cm^3
J local reaction rate along electrode, dimensionless
$2l$ tube length, cm
M atomic weight of electrode metal, g/g-atom
n number of electrons taking part in the electrode reaction, g-eq/mol
N ratio of mass transfer resistance to charge transfer resistance, $\dfrac{n\mathbf{F}}{\Gamma(4/3)}\dfrac{Dc_b}{i_o}\left(\dfrac{4\bar{v}_z}{9Dr_o\bar{l}}\right)^{1/3}$, dimensionless
Pe Péclet number, $2r_o\bar{v}_z/D$, dimensionless
r special variable in radial direction, cm
r_o radius of tubular electrode, cm
R gas constant, 8.31 J/gmol K
Re Reynolds number, $2r_o\bar{v}_z/\nu$, dimensionless
R_o radius of multilayer board hole, cm
Sc Schmidt number, ν/D, dimensionless
t time, sec
t_B multilayer board thickness, cm
T temperature, K
v_{max} electrolyte velocity along tube axis, cm/sec
v_z electrolyte velocity in z direction, cm/sec
y special variable normal to electrode surface, cm
z special variable parallel to the tube axis, cm
α_a anodic transfer coefficient in reaction rate expression, Eq. [1]
α_c cathodic transfer coefficient in reaction rate expression, Eq. [1]
β average current density, i_{av}/i_o, dimensionless
γ constant in Eq. [2], dimensionless
$\Gamma(4/3)$ gamma function of 4/3
ξ special variable in axial direction, dimensionless
η similarity transformation, $y(4v_z/9zDr_o)^{1/3}$, dimensionless
η_c concentration overpotential, V
η_c^* concentration overpotential, $(n\mathbf{F}/RT)\eta_c$, dimensionless
η_s charge transfer overpotential, V
η_s^* charge transfer overpotential, $(n\mathbf{F}/RT)\eta_s$, dimensionless
$\eta_{\Omega m}$ metal ohmic overpotential, V
$\eta_{\Omega m}^*$ metal ohmic overpotential, $(n\mathbf{F}/RT)\eta_{\Omega m}$, dimensionless
$\eta_{\Omega s}$ electrolyte ohmic overpotential, V
$\eta_{\Omega s}^*$ electrolyte ohmic overpotential, $(n\mathbf{F}/RT)\eta_{\Omega s}$, dimensionless
η_T total overpotential, V
η_T^* total overpotential, $(n\mathbf{F}/RT)\eta_T$, dimensionless
κ electrolyte conductivity, $(\Omega\text{-cm})^{-1}$
ν kinematic viscosity, cm^2/sec
ξ_m ratio of metal ohmic resistance to charge transfer resistance, $\dfrac{n\mathbf{F}}{RT}\dfrac{l^2}{a_o}\dfrac{i_o}{\sigma}$, dimensionless
ξ_s ratio of electrolyte ohmic resistance to charge transfer resistance, $\dfrac{n\mathbf{F}}{RT}\cdot\dfrac{l^2}{r_o}\dfrac{i_o}{\kappa}$, dimensionless
ϕ_a^* applied potential, dimensionless (Eq. [27])
ϕ_m potential in metal electrode, V
ϕ_{sm}° potential in the metal electrode at the tube entrance, V
ϕ^* potential in the metal electrode, $n\mathbf{F}/RT$ $(\phi_m - \phi_m^\circ)$, dimensionless
ϕ_s potential in the electrolyte (outside the diffusion layer), V
ϕ_s° potential in the electrolyte, at the tube entrance, V
ϕ_s^* potential in the electrolyte, $n\mathbf{F}/RT$ $(\phi_s - \phi_s^\circ)$, dimensionless
ρ special variable in radial direction, r/r_o, dimensionless
ρ_o geometric parameter, r_o/l, dimensionless
σ metal conductivity $(\Omega\text{-cm})^{-1}$

Subscripts

m pertains to metallic electrode phase
s pertains to electrolytic solution phase
r in r-direction
y in y-direction
z in z-direction

REFERENCES

1. J. Newman, *Int. J. Heat Mass Transfer*, **10**, 983 (1967).
2. W. R. Parrish and J. Newman, *This Journal*, **116**, 169 (1969); **117**, 43 (1970).
3. R. Alkire and A. A. Mirarefi, *ibid.*, **120**, 1507 (1973).
4. J. Newman, *ibid.*, **113**, 1235 (1966); **114**, 239 (1967).
5. R. Alkire and R. Varjian, *ibid.*, **124**, 388 (1977).
6. R. Alkire, *ibid.*, **118**, 1935 (1971).
7. R. Alkire and A. Tvarusko, *ibid.*, **119**, 340 (1972).
8. R. A. Lowenheim, "Modern Electroplating," 3rd ed., p. 185, John Wiley & Sons, Inc., New York (1974).
9. M. A. Lévêque, *Ann. Mines Memoires, Ser. 12, 13*, 201 (1928).
10. W. H. Smyrl and J. Newman, *This Journal*, **119**, 212 (1972).
11. W. Engelmaier and T. J. Kessler, *ibid.*, **125**, 36 (1978).
12. A. Acrivos and P. L. Chambré, *IEC*, **49**, 1025 (1957).
13. L. W. Cornwell, R. J. Pegis, A. K. Rigler, and T. P. Vogl, *J. Opt. Soc. Am.*, **63**, 576 (1973).

A Preparation of Perpendicular Magnetic Recording Media by an Electroless Plating Method

Tetsuya Osaka,* Naoki Kasai, and Ichiro Koiwa

Department of Applied Chemistry, Wasada University, Okubo Shinjuku-ku, Tokyo 160, Japan

and Fumio Goto and Yoji Suganuma

Nippon Electric Company Limited, Microelectronics Research Laboratories, Miyazaki, Takatsu-ku, Kawasaki 213, Japan

ABSTRACT

The perpendicularly oriented crystal structure conditions of electroless plated film for high density perpendicular recording media were investigated mainly by (002) plane rocking curves and cross sectional SEM observation. A highly oriented narrow dispersion of c-axis orientation normal to the surface plane was consequently obtained, and the columnar structure of hcp crystal with *ca.* 0.05 μm diam was confirmed. As a result of preparing disks A and B, which were chemically plated from an optimum bath and a more improved bath, respectively, the recording characteristics with a combination of ring head were obtained as recording densities of D_{50} = 18,500 FRPI for disk A and 25,000 FRPI for disk B, in spite of a relatively thick magnetic medium. The di-pulse waveforms, which are characterized with perpendicular recording, were observed at low bit recording density. It was indicated by the above results that the chemically plated Co alloy films are applicable as a perpendicular recording medium.

Perpendicular magnetic media for high density recording have been studied by many workers (1), since a proposal regarding its recording system by the Iwasaki school (2, 3). In a previous paper (4), the authors reported the development of electroless cobalt alloy plating bath for a perpendicular recording medium. The crystal structure for film plated from the electroless bath is reported in the present paper.

Recording and reproducing characteristics for a perpendicular Co-Cr flexible disk medium were first tried by using a single-pole head (3). The combination of a perpendicular medium with a ring head, which might be a first step toward practical use of a perpendicular recording system, was also reported by several workers (5, 6). This paper reports 8 in. diam disk media and their recording characteristics using a ring head.

Experimental

Plating conditions for Co alloy films and determining several properties for their films were the same as shown in a previous paper (4). The film cross section was observed by scanning electron microscopy. Two kinds of magnetic films for plated disks were prepared from electroless plating baths A and B, shown in Table I. Figure 1 demonstrates the disk structure, using a structure similar to that for 8 in. longitudinal high density recording plated disk (7) developed by Nippon Electric Company Limited. The magnetic films have a 5 μm plating for disk A or a 3 μm plating for disk B on a polished Ni-P substrate, which was chemically plated on an aluminum alloy plate. The SiO_2 (8) protective overcoat, 0.1 μm for disk A and 0.02 μm for disk B, was formed by heat-treatment at 200°C after being covered with tetrahydroxy silane alcohol solution by a spin-coat method. Disk and head properties for a read/write measurement are shown in Table II.

* Electrochemical Society Active Member.
Key words: electroless, ferromagnetism.

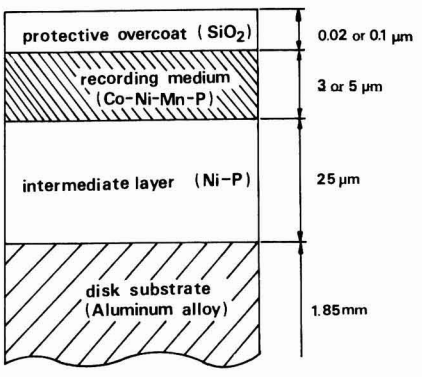

Fig. 1. Plated disk structure for perpendicular recording medium

Results and Discussion

Investigation on c-axis orientation normal to surface plane.—The effects of three factors in the bath (*i.e.*, $MnSO_4$ concentration, bath pH, and $NiSO_4$ concentration) on c-axis orientation were studied by rocking curves for the (002) plane. The $MnSO_4$ concentration effect on c-axis orientation is demonstrated in Fig. 2, where the $\Delta\theta_{50}$ value means the peak breadth at half-maximum intensity for (002) plane peak in rocking curve. The $\Delta\theta_{50}$ value represents the c-axis orientation

Table I. Electroless plating bath compositions and operating conditions

Chemicals	Bath A	Bath B
$NaH_2PO_2 \cdot H_2O$	0.20 M · 1^{-1}	0.20 M · 1^{-1}
$(NH_4)_2SO_4$	0.50	0.50
$CH_2(COONa)_2 \cdot H_2O$	0.50	0.50
$C_2H_5OH(COONa)_2$	0.05	0.05
$CoSO_4 \cdot 7H_2O$	0.025	0.035
$NiSO_4 \cdot 6H_2O$	0.01	0.01
$MnSO_4 \cdot 4 \sim 5H_2O$	0.04	0.04
Bath temperature	85°C	80°C
pH adjusted by NH_4OH	9.6	9.6

Table II. Disk and head characteristics

	Disk A	Disk B
Medium material	Co-Ni-Mn-P	Co-Ni-Mn-P
Medium thickness/μm	5.0	3.0
Coercivity, $Hc(\perp)$/Oe	1530	1040
Overcoat thickness/μm	0.10	0.02
Substrate material	Polished Ni-P on Al alloy	Polished Ni-P on Al alloy
Core material	Mn-Zn ferrite	Mn-Zn ferrite
Gap length/μm	1.0	0.5
Track width/μm	50	30
Flying height/μm	0.2 at 22 m/sec	0.1 at 7.89 m/sec

degree normal to the surface plane. In the 0 ~ 0.015M $MnSO_4$ range, the hexagonal crystal for plated films reaches an in-plane orientation. The c-axis orientation changes from in-plane to perpendicular form, with the increase in $MnSO_4$ concentration. From the 0.025M $MnSO_4$ point, the hexagonal crystal c-axis orients completely to the perpendicular. The $\Delta\theta_{50}$ value becomes minimum at 0.04M $MnSO_4$. This condition corresponds well to the x-ray diffraction patterns and magnetic properties shown in the previous paper (4). In Fig. 2, the results for two kinds of substrates, Cu and polished Ni-P, were plotted as a function of $MnSO_4$ concentration. The $\Delta\theta_{50}$ values for Ni-P substrate are always lower than those for Cu substrate. The substrate roughness effect on magnetic properties was previously discussed (9). It was concluded that the larger variation in surface roughness, obtained by an emery paper, for example, is too large to affect the magnetic properties. It was also concluded that the smaller variation, produced by such a crystallite grain size, greatly influences magnetic properties (9). The above fact may be due to the small difference in surface roughness produced by such a crystallite grain size (*cf.*, the mean surface roughness values for Cu and polished Ni-P are 0.1 and 0.015 μm, respectively). The most uniformly perpendicular-oriented condition for hcp crystals is obtained at the 0.04M $MnSO_4$ point, where $\Delta\theta_{50}$ reproducibly shows a minimum value of *ca.* 10°. This minimum value was always reproducibly obtained, but a more highly uniform structure, *ca.* 6°, was occasionally obtained. The plots in the figures do not show the best data indicating less than 10°. Instead, the plots show typical data reproducibly obtained. The $\Delta\theta_{50}$ value is very sensitive to surface roughness. Different values appear even in the case of a little difference, such as crystallite sizes in the order of, at least, less than 0.1 μm. Therefore, the surface flatness for such a little difference is also an important factor, which must be paid attention to in obtaining a more highly uniform c-axis orientation normal to the surface plane.

The bath *p*H effect on $\Delta\theta_{50}$ is shown in Fig. 3, where the $\Delta\theta_{50}$ value for Ni-P substrate is also always lower. There is a minimum $\Delta\theta_{50}$ value at bath *p*H 9.6 for Cu substrate. However, for Ni-P substrate, the $\Delta\theta_{50}$ values become the lower constant value for *ca.* 10.5° at the *p*H 9.4 ~ 9.8 range. The results for Cu substrate correspond well to those for x-ray diffraction patterns and magnetic properties described in a previous paper (4).

In order to get a perpendicular anisotropy it is also necessary to lower the saturation magnetization, *Ms*, for film as well as to make the c-axis orientation normal to the surface plane. An attempt was made to codeposit nickel into films for this purpose. The $NiSO_4$ concentration effect on $\Delta\theta_{50}$ was demonstrated in Fig. 4. When Cu substrate is used, the $\Delta\theta_{50}$ value gradually becomes larger with the increase in $NiSO_4$ concentration. For Ni-P substrate, the $\Delta\theta_{50}$ value gives a lower constant value, even with the increase in $NiSO_4$ concentration up to 0.01M $NiSO_4$ concentration. From that point on, it gradually becomes larger. Since the perpendicular orientation uniformity on the Ni-P substrate is retained up to 0.01M $NiSO_4$ concentration, as seen in Fig. 4, the $NiSO_4$ addition into the bath solution can be allowed up to 0.01M, in order to decrease *Ms* in the film.

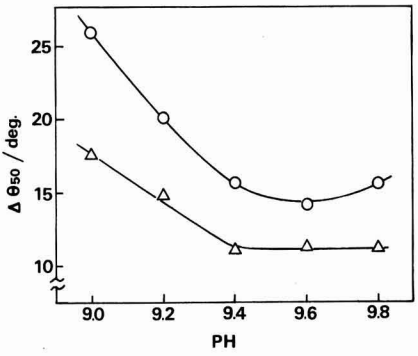

Fig. 3. Bath *p*H effect on $\Delta\theta_{50}$ for plated films. ○: Cu substrate, △: Ni-P substrate.

SEM observation on crystal structure for film plated under optimum conditions.—Figure 5 shows a typical cross section of Co alloy film plated under optimum plating condition shown in Table I-A. The most typical cross section micrograph is shown in Fig. 5(a), where the 11.6 μm thick cross section is shown inclined 60° from the substrate plane. In Fig. 5(a), the Co-Ni-Mn-P film cross section indicates a uniform columnar growth structure with *ca.* 0.2 μm diam in appearance, which is composed of pole-like crystals. Since the plated film surface gives fairly rough conditions, the surface was polished to mirror conditions when making disk B. In order to confirm columnar crystals in detail, a Co alloy film cross section containing part of the broken columnar crystals, produced during the cutting process, is demonstrated in Fig. 5(b). The arrow in Fig. 5(b) indicates the position revealed under magnification shown in Fig. 5(c). Since the columnar structures are composed of pole-like crystal with *ca.* 0.05 μm diam, as seen in Fig. 5(c), the apparent columnar structure with *ca.* 0.2 μm diam, shown in Fig. 5(a) or (b), is in a state of aggregation for column-like crystals with *ca.* 0.05 μm diam. Film made from such columnar crystals with *ca.* 0.05 μm diam is consid-

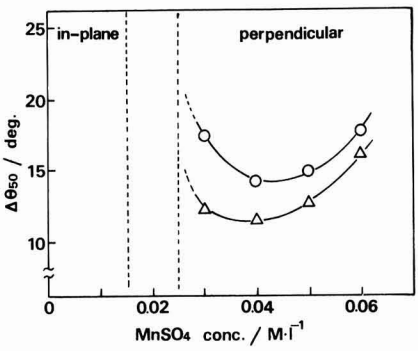

Fig. 2. $MnSO_4$ concentration effect on $\Delta\theta_{50}$ for plated films. ○: Cu substrate, △: Ni-P substrate.

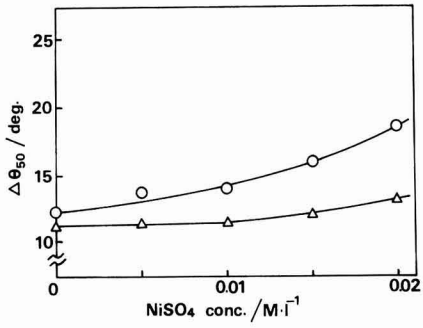

Fig. 4. $NiSO_4$ concentration effect on $\Delta\theta_{50}$ for plated films. ○: Cu substrate, △: Ni-P substrate.

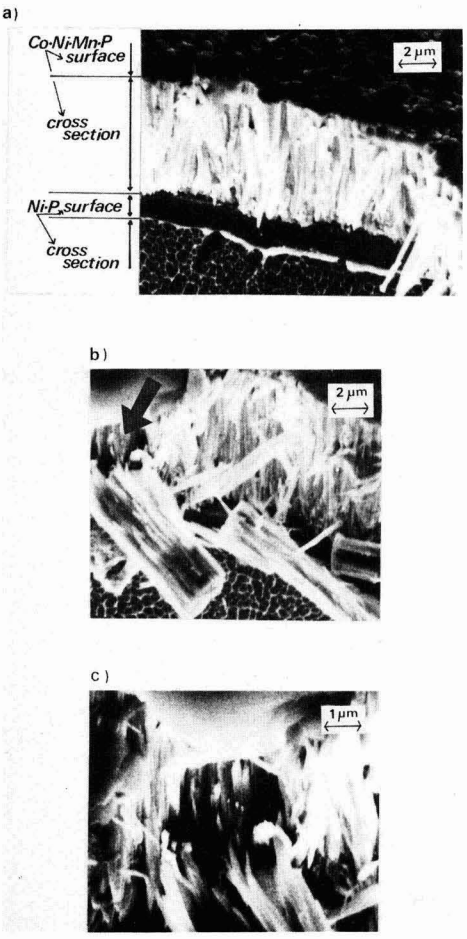

Fig. 5. Scanning electron micrographs showing a cross section of film plated under optimum condition listed in Table I-A using Ni-P substrate. (a): Typical cross section for plated film using Ni-P substrate (×5,000), (b) and (c): Other cross section parts of plated film containing broken columnar crystals, which are produced during cutting, [×5,000 for (b)] and [×10,000 for (c)]. The arrow shown in (b) indicates the part corresponding to the enlarged section shown in (c).

ered to be suitable for a high density perpendicular recording medium (*e.g.*, the 100,000 FRPI recording density corresponds to 0.25 μm length for one bit).

Magnetic disks preparation and their read/write properties.—Two kinds of 8 in. diam disks, A and B, were prepared from baths A and B shown in Table I. The composition and operation conditions for bath A for disk A were determined and reported in the previous paper (4). The conditions for bath B for disk B were improved for the higher density recording. The recording density naturally depends not only on disk properties, but also on read/write conditions, especially depending on gap length of ring head and head-medium spacing (5). Since the higher *Hc* for disk A has to be lowered, in order to be able to use a ring head with narrower gap length for establishing higher density recording, the bath B conditions were improved to obtain a lower *Hc* film than that plated from bath A. Improved bath B, with higher $CoSO_4$ concentration and lower bath temperature, makes it possible to combine ring head conditions for a narrower gap length. The protective overcoat for disk B is also made thinner, 0.02 μm, for lowering the head-medium spacing. The characteristics for disk media A and B and their read/write conditions are shown in Table II. The plated magnetic film polishing process was added only for disk B, using the head with lower spacing conditions.

Reproduced waveforms, low bit density (740 FRPI) and high bit density (23 KFRPI) for the read/write conditions in Table II-A, were shown in Fig. 6. Since an output voltage waveform at low bit density, in perpendicular magnetic recording using a ring head, is confirmed by the Iwasaki school (11) to show a dipulse shape, the dipulse waveforms shown in Fig. 6(b) is considered to be produced by the perpendicular recording results. It also supports the perpendicular recording performance wherein the waveforms at high bit density, 23 KFRPI, are produced by using the thicker magnetic medium, 5 μm thick, because such a high density recording is performed only in the case of very thin magnetic medium (less than *ca.* 0.1 μm) in the case of a longitudinal recording system.

Figure 7 demonstrates the recording characteristics for Co alloy magnetic disks A and B, which were measured under the disk and head conditions shown in Table II. The recording densities for D_{50}, which means the recording density at half the maximum output voltage value, are observed to be 18,500 FRPI for disk A and 25,000 FRPI for disk B, respectively.

The authors have studied the use of an electroless cobalt alloy magnetic medium for a perpendicular recording medium, considering that magnetic films showing incompletely perpendicular magnetic anisotropy can also be used for this medium, as well as when

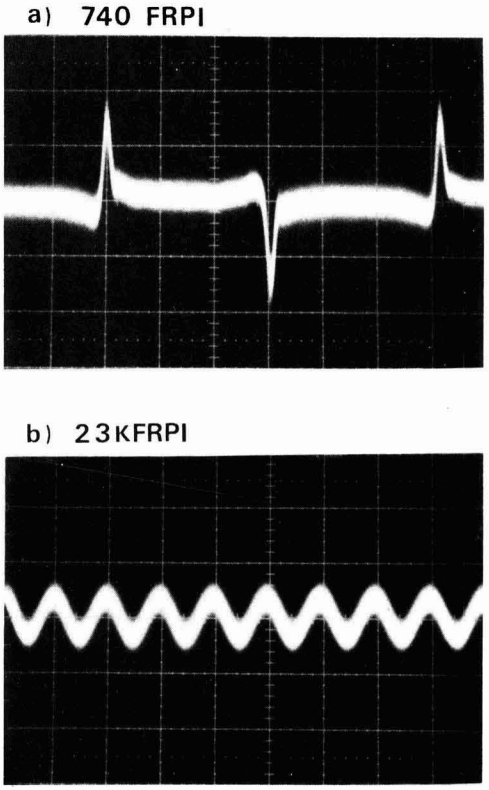

Fig. 6. Reproduced waveforms, (a) low density of 740 FRPI (b) high density of 23,000 FRPI. The disk and ring head are used with the condition shown in Table II-A.

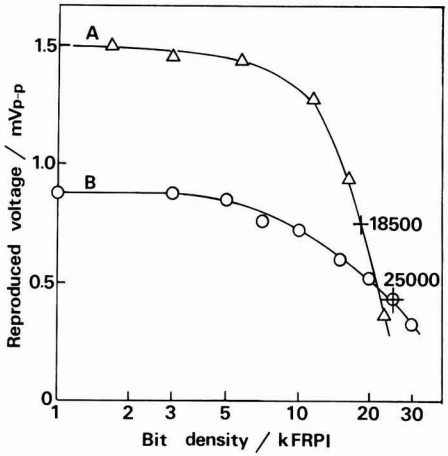

Fig. 7. Recording characteristics for Co alloy disks. A and B characters represent the data using disks A and B, respectively.

using complete perpendicular magnetic anisotropy media, such as an rf sputtered Co-Cr film. The possibility of a perpendicular recording medium is consequently confirmed by using disks A and B whose magnetic films do not show a complete perpendicular magnetic anisotropy (12), such as an rf sputtered film. Finally, it can be concluded that chemically plated Co alloy magnetic film is applicable as a high density perpendicular recording medium.

Acknowledgments

The authors would like to thank Professor Emeritus Dr. Tadashi Yoshida, Waseda University, and Dr. Takashi Furuoya, Dr. Daisaburo Shinoda, and Mr. Koichi Matsumi, Microelectronics Research Laboratories, Nippon Electric Company Limited, for their encouragement during the research. The authors also would like to thank Messrs. Hideo Tanaka, Masahiro Yanagisawa, and Morishige Aoyama for their assistance in read/write tests and in forming the protective overcoat.

Manuscript submitted May 20, 1982; revised manuscript received Nov. 12, 1982.

Any discussion of this paper will appear in a Discussion Section to be published in the December 1983 JOURNAL. All discussions for the December 1983 Discussion Section should be submitted by Aug. 1, 1983.

Publication costs of this article were assisted by Nippon Electric Company, Limited.

REFERENCES

1. *e.g.*, Proceedings of 1982 Sendai Symp. on Perpendicular Magnetic Recording, Research Institute of Electrical Commun., Tohoku University, Japan (1982).
2. S. Iwasaki and K. Takemura, *IEEE Trans. Magn.*, **mag-11**, 1173 (1975).
3. S. Iwasaki and Y. Nakamura, *ibid.*, **mag-13**, 1272 (1977).
4. T. Osaka, K. Kasai, I. Koiwa, and F. Goto, *This Journal*, In press.
5. T. Suzuki and S. Iwasaki, IECE Tech. Group Meeting of Magn. Rec., Japan, MR81-8 (1981).
6. K. Kobayashi and G. Ishida, *J. Appl. Phys.*, **52**, 2453 (1981).
7. M. Nagao, Y. Suganuma, H. Tanaka, M. Yanagisawa, and F. Goto, *IEEE Trans. Magn.*, **mag-15**, 1543 (1979).
8. M. Yanagisawa and F. Goto, Ann. Conf. in IECE, Japan, 1-189 (1980).
9. T. Osaka, H. Nagasaka, and F. Goto, *This Journal*, **128**, 1686 (1981).
10. T. Osaka, K. Kasai, I. Koiwa, F. Goto, and Y. Suganuma, The 65th Conf. of Metal Finishing Soc. of Japan, p. 136 (1982).
11. S. Iwasaki, *IEEE Trans. Magn.*, **mag-16**, 71 (1980); S. Iwasaki and M. Suzuki, Ann. Conf. in IECE Japan, 1-199 (1980).
12. F. Goto, T Osaka, N. Kasai, I. Koiwa, H. Tanaka, M. Aoyama, and Y. Suganuma, Proc. of 1982 Sendai Symp. on Perpendicular Magn. Recording, Research Institute of Electrical Commun., Tohoku Univ., Japan (1982), p. 197.

Electric Field Enhanced Diffusion in Trans-$(CH)_x$

J. H. Kaufman, E. J. Mele, and A. J. Heeger

Department of Physics, University of Pennsylvania, Philadelphia, Pennsylvania 19104-3895

and R. Kaner* and A. G. MacDiarmid

Department of Chemistry, University of Pennsylvania, Philadelphia, Pennsylvania 19104

ABSTRACT

A theory is developed which shows how high power and high current densities can be generated by a $(CH)_x$ battery cell despite the slow diffusion and low conductivity characteristic of ionic motion in polyacetylene. The presence of a small driving potential (or a load) causes current to flow and generates a large electric field within the fibrils. This field dramatically increases the ion transport rate when the electronic screening length is comparable to or greater than the radius of a fibril.

Polyacetylene, $(CH)_x$, is the prototype example of a conducting polymer (1). Recent studies have demonstrated that after synthesis, $(CH)_x$ can be oxidized or reduced chemically (1, 2) or electrochemically (3) at room temperature. As a result of these controlled doping procedures, increases in electrical conductivity of over twelve orders of magnitude have been observed (4). Doping to high levels results in a semiconductor-metal transition (5-7), giving a whole new class of highly conducting "plastic" metals with a wide range of electronegativity. The partly oxidized material is relatively electronegative and exists as a stabilized polycarbonium ion, $(CH^{+y})_x$, in combination with the corresponding number of monovalent counterions, A^-, such that the overall composition is $(CH^{+y}A_y^-)_x$. Similarly, the partly reduced material is relatively electropositive and exists as a polycarbanion, $(CH^{-y})_x$, in combination with the corresponding number of monovalent countercations, M^+, such that the

* Electrochemical Society Active Member.

Key words: conducting polymer batteries $(CH)_x$, polyacetylene ionic diffusion.

overall composition is $(M_y{}^+CH^{-y})_x$. Since reversible electrochemical oxidation and reduction (*i.e.*, doping and "undoping") have been demonstrated, the possibility of using polyacetylene as an electrode in an electrochemical cell has been proposed (8-10). Indeed, in earlier experimental studies it has been demonstrated (8-10) that films of partly oxidized or reduced $(CH)_x$ can be used as the cathode and anode materials in lightweight rechargeable storage batteries.

Electron microscopy studies (11, 12) show that the as-grown $(CH)_x$ films consist of randomly oriented fibrils with typical fibril diameter ~200Å. The diameter can be reduced significantly with different polymerization conditions (13). The bulk density is about 0.4 g/cm^3 compared with 1.2 g/cm^3 as obtained by flotation techniques, indicating that the polymer fibrils fill only about 1/3 of the total volume, and that the effective surface area in contact with the electrolyte is quite high, ~60 m^2/g.

During the doping and undoping processes which accompany battery charge and discharge, the ions from the electrolyte must diffuse into and out of the $(CH)_x$ fibrils, *i.e.*, between the individual $(CH)_x$ polymer chains. However, since the solid-state ionic mobility in $(CH)_x$ is much smaller than the ionic mobility in the electrolyte, the short-circuit current and power density of an electrochemical cell might be expected to be limited by the slow diffusion of ions through the polyacetylene fibrils.

In fact, recent measurements (14) of free diffusion of Li^+ ions into $(CH)_x$ fibrils in electrochemical cells reveal diffusion constants of $D \simeq 4 \times 10^{-18}$ cm^2/sec. The diffusion of ClO_4^- during p-doping is of the same order of magnitude. On the same cells, however, high short-circuit currents and high power densities are obtained (8-10, 15). An explanation of this apparent contradiction is necessary, and it is the subject of this paper.

Summary of Experimental Results

A detailed description of the diffusion studies will be presented elsewhere (10, 14). We briefly summarize the experimental results here as background information for quantitative input into the calculations which follow and which are the principal point of this paper. A battery cell is constructed by pressing $(CH)_x$ film (~0.1 mm thickness by ~1 cm^2; ~3 mg) onto platinum mesh to act as the working electrode (9). Lithium metal embedded in nickel mesh (Delker Corporation) acts as the counterelectrode and is separated from the $(CH)_x$ by a kiln-dried piece of glass filter paper. A second (identical) lithium electrode is used as the reference electrode. Basic activated alumina serves as a scavenger for impurities. One molar $LiClO_4$/tetrahydrofuran is added as the electrolyte-solvent system for n-type doping of $(CH)_x$, while 1M $LiClO_4$/propylene carbonate is used for p-type doping. Prior to use, the $LiClO_4$ is melted under dynamic vacuum. Tetrahydrofuran (Fischer Scientific Company) is kept in sodium benzophenone, while propylene carbonate (Aldrich Chemical Company) is spin band distilled and stored over lithium chips. The cell is encased in rectangular glass and sealed under vacuum across platinum wires which are spot welded to the electrode. This construction yields stable cells with internal resistance which is typically about 100Ω.

Measurements of the diffusion time, τ_o, and the diffusion constant for Li^+ ions were made by monitoring the recovery of the open-circuit voltage (V_{oc}) after step potential changes in charging. In a typical experiment, the applied voltage was stepped by 0.1V and held at the new potential until the current fell (during about 20 min) to ~1/10 of its initial value. The power supply was then disconnected, and the open-circuit voltage was monitored by periodically connecting the cell to a high input impedance digital voltmeter. For example, at 3% doping, after an initial transient of about 1.5 hr, the open-circuit voltage approached its equilibrium value exponentially with a time constant τ_o of about 12 hr. Initial experiments yield a time constant of the same magnitude for p-doping (with ClO_4^-). During this time, no current was flowing; the change in V_{oc} occurs as the dopant ions freely diffuse into the fibrils in response to the concentration gradient imparted by the step change in applied voltage. Assuming cylindrical geometry for the $(CH)_x$ fibrils, the diffusion constant can be obtained from the exponential part of the curve (16)

$$D_o = r_o{}^2/((2.405)^2)\tau_o \qquad [1]$$

where r_o is the radius of the $(CH)_x$ fibril, $r_o \simeq 100$Å. From this expression, a time constant of 12 hr corresponds to a diffusion constant $D_o \simeq 4 \times 10^{-18}$ cm^2/sec. On the same cells, short-circuit currents were typically as high as 100 mA/cm^2 of $(CH)_x$ film with maximum power densities, for $(CH(ClO_4)_y)_x$ *vs.* Li, of 30 kW/kg (excluding weight of electrolyte, current collectors, and container (10).

To further quantify the anomaly of high current and power densities in spite of small free diffusion rates, we use the measured free diffusion constants to estimate the internal resistance of the cell. The ionic conductivity is given by $\sigma_I = ne\mu$ where $\mu = eD/kT$ is the ionic mobility. For 1% doping, $n = 2 \times 10^{20}$ ions/cm^3; using $D_o = 10^{-18}$ cm^2/sec, one obtains for the ionic conductivity $\sigma_I = 10^{-15}$ Ω^{-1}-cm^{-1}. For a 1 cm^2 piece of $(CH)_x$ film, 0.01 cm in thickness, the effective surface area is $A_s = 2.5 \times 10^3$ cm^2. Using $R_I = \rho_I r_o/A_s$ to estimate the total resistance, we obtain $R_I = 4 \times 10^5\Omega$, three orders of magnitude greater than the value measured from the current (typically in the range 10-100 mA/cm^2) through a series of known load resistors.

Field Enhanced Diffusion in $(CH)_x$

The failure of this calculation stems from ignoring the effect of the electric field on the ionic transport. For example, after a voltage step, ΔV, current flows and an electric field exists; $E \sim \Delta V/r_o$ where r_o is the radius of a fibril. Taking $V = 0.5$V, and $r_o = 10^2$Å, $E = 5 \times 10^5$ V/cm. Such enormous electric fields will literally drive the ions into (or out of) the fibrils leading to significant enhancement of the net ion transport rate.

To understand this effect in more detail, we first consider the free diffusion equation describing mass transport due to a concentration gradient

$$\frac{\partial C_I}{\partial t} = -D_o \nabla^2 C_I \qquad [2]$$

where C_I is the ion concentration, which will in general vary across the thickness of a fibril. This equation has been solved for the cylindrical geometry appropriate to polyacetylene fibrils (16). After a short transient, the time dependence of the concentration gradient becomes exponential, with time constant τ_o given by Eq. [1]. Under conditions of current flow, an electric field exists in the $(CH)_x$ fibrils, and a second term must be added to the first integral of the diffusion equation

$$\vec{J}_I = -D_o \vec{\nabla} C + \bar{\sigma}_I \vec{E}/e \qquad [3]$$

where $\vec{J}_I$ is the ion current density in the $(CH)_x$ electrode, and $\bar{\sigma}_I$ is the average ionic conductivity in the absence of a field. Assuming that ion motion into (or out of) the fibril limits the kinetics, the local concentration of ions will differ from that of electrons while current is flowing, thereby, giving rise to the electric field term in Eq. [3]. Since this electric field can be screened by a redistribution of the electronic density, it will be important only under conditions when the electronic screening length transverse to the $(CH)_x$ chains is comparable to a fibril radius, ~50-100Å. This

will certainly be the case at low doping levels, *i.e.*, below the semiconductor-metal transition. Moreover, because of the highly anistropic electronic properties (implying a highly anisotropic effective mass), this condition should be satisfied well into the metallic regime. We note, however, that the existence of a significant electric field effect is directly related to the existence of the fibrillar morphology with fibril dimensions of the same magnitude as electronic screening lengths.

Differentiating Eq. [3] $(\vec{\nabla} \cdot \vec{J}_I)$ and using the continuity equation for the ion current $(\vec{\nabla} \cdot \vec{J}_I = \partial C_I/\partial t)$ and the Maxwell equation $[\vec{\nabla} \cdot \vec{E} = 4\pi e\ (C_I - C_e]$ leads to a "forced" transport equation

$$\frac{\partial C_I}{\partial t} = -D_o \nabla^2 C_I + 4\pi\bar{\sigma}_I (C_I - C_e) \qquad [4]$$

In the above, we have used the fact that the net charge density is $e(C_I - C_e)$ where e is the electronic charge, and C_I and C_e are the local concentrations of ions and electrons (or holes in the case of p-doping), respectively. Note that rigorously σ_I is proportional to C_I. In writing Eq. [4], we have linearized the equation by keeping only the leading term, *i.e.*, the dependence on $(C_I - C_e)$.

Under open-circuit conditions, no current flows and $C_I = C_e$. If the applied voltage differs from V_{oc}, or if the cell is placed under load, current flows from Ohm's law

$$\frac{V_{oc} - V_{ext}}{R_i} = evd \frac{\partial}{\partial t} (C_I - C_e) \qquad [5]$$

where V_{ext} is the external cell voltage (*i.e.*, the voltage at the polymer electrolyte interface), v is the volume of the $(CH)_x$ electrode, d is the number density of (CH) units, and R_i is the measured internal resistance of the cell. Although Eq. [5] applies to the sample as a whole, we can use it to calculate the local concentration within a fibril. This follows since the electrolyte is in contact with all the fibril surfaces. Moreover, even though electron injection into the $(CH)_x$ occurs only at the contact, the electronic resistivity is sufficiently small along the chain direction that all of the fibrils are at a common average electrical potential.

Assuming C_I and C_e have the same time dependence $(e^{-t/\tau})$, Eq. [4] can be linearized using Eq. [5] and the empirical relation[1] found for V_{oc} *vs.* Q for $(CH)_x$ (*vs.* Li)

$$V_{oc} \simeq A \pm bQ^\gamma = A \pm Bv^\gamma C_I^\gamma \qquad [6]$$

where A, B, and γ are fitting parameters. In Eq. [6], the + and − signs refer to p-type and n-type doping, respectively. From Eq. [4] and Eq. [5]

$$\frac{\partial C_I}{\partial t} = -D_o \nabla^2 C_I + 4\pi\sigma_I \left[\frac{\tau}{evdR_i} (V_{oc} - V_{ext})\right] \qquad [7]$$

and from [6]

$$-D_o \nabla^2 C_I = -\frac{1}{\tau} - \left(\frac{4\pi\bar{\sigma}_I}{edR_i}\right) \tau \left[(A - V_{ext}) \left(\frac{B}{A - V_{oc}}\right)^{1/\gamma} - B \left(\frac{B}{A - V_{oc}}\right)^{1/\gamma - 1} \right] C_I \qquad [8]$$

With the above assumption of an exponential dependence for C_I, this equation has the form of the free diffusion equation (Eq. [2]) implying an effective decay rate given by

$$\frac{1}{\tau} = \frac{1}{\tau_o} + \left(\frac{4\pi\bar{\sigma}_I}{edR_i}\right) \tau \left[(A - V_{ext}) \left(\frac{B}{A - V_{oc}}\right)^{1/\gamma} - B \left(\frac{B}{A - V_{oc}}\right)^{1/\gamma - 1} \right] \qquad [9]$$

where $1/\tau_o$ is given by Eq. [1]. This expression is only valid for $\Delta V \equiv |V_{ext} - V_{oc}|$ small; for ΔV large, the change in V_{oc} over a time τ is too large, and the equation cannot be linearized.

Although Eq. [8] has the form of an effective diffusion equation, it should not be interpreted as implying an increase in the ionic conductivity. The entire analysis was carried out in the linear response regime, *i.e.*, σ_I was assumed to be field independent. The increased transport rate does not arise from an increase in σ_I, but from the internal electric field generated during current flow (see Eq. [3] and [4]). In obtaining Eq. [8] and [9], we assumed a simple exponential decay toward equilibrium for C_I. The true time dependence implied by simultaneous solution of Eq. [4], [5], and [6] in the cylindrical geometry appropriate to the $(CH)_x$ fibrils is more complex so that the result (Eq. [9]) is only approximate. We note, however, that the experimental results yield an exponential decay after an initial transient, suggesting that the assumption is reasonable. We have, furthermore, ignored any intrinsic dependence of D_o (and σ_I) on the dopant concentration. Therefore, Eq. [9] does not predict any fine structure arising from the dependence of τ_o on concentration.

Figures 1a and b show the dependence of τ on $V = |V_{ext} - V_{oc}|$ for different values of σ_I and V_{oc} (n-type doping) calculated from Eq. [9]. From the figures, it is evident that a small driving potential greatly reduces the ionic transport time. For example, at $V_{oc} = 1.7$V and $\sigma_I = 10^{-16}\ \Omega^{-1}\text{-cm}^{-1}$, an external potential $V_{ext} = 1.75$V decreases the diffusion time from 4×10^4 sec ($V_{ext} = V_{oc}$) to ~125 sec ($|V_{ext} - V_{oc}| = 0.05$V). The increase in ionic transport rate of $\sim 10^3$ indicated in Fig. 1a and b provides the explanation of the large values observed for short-circuit currents (and power density) in electrochemical cells using $(CH)_x$ electrodes.

When $V_{ext} = V_{oc}$, the potential dependent term vanishes, Eq. [10] becomes $\tau^{-1} = \tau_o^{-1}$, and the free diffusion behavior is recovered. We note that in absence of current flow, the electric field inside a fibril is zero (whether or not the doping is uniform). The sharp drop in τ due to small displacements from the equilibrium V_{oc} (resulting from current flow) is due directly to the unique morphology of polyacetylene and the large resulting potential gradients that occur within the fibrils.

Quantitative measurements of τ as a function of V are underway. Preliminary results are in order of

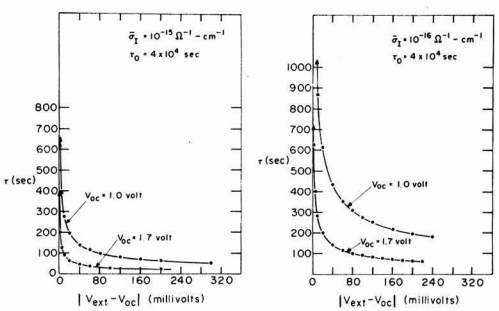

Fig. 1. τ *vs.* $|V_{ext} - V_{oc}|$ for $\sigma_1 = 10^{-15}\Omega^{-1}\text{-cm}^{-1}$ (Fig. 1a), and $\sigma_I = 10^{-16}\Omega^{-1}\text{-cm}^{-1}$ (Fig. 1b). Curves corresponding to two values of V_{oc} are shown (1.0 and 1.7V). The internal resistance is taken to be 100Ω.

[1] Equation [6] provides an excellent empirical fit to the V *vs.* Q data for both p-type (Ref. 10) and n-type (Ref. 15) doping. Typical values (*e.g.*, for n-type) are $A = 1.9$V, $B = 0.75$, and $\gamma = 2/3$.

magnitude agreement with the behavior predicted above.

Conclusion

The theory developed in this paper shows how high power densities and current densities can be generated by a $(CH)_x$ battery cell despite the slow free diffusion and low conductivity characteristic of ionic motion in polyacetylene. The presence of a small driving potential (or a load) causes current to flow and generates a large electric field within the $(CH)_x$ fibrils. This field increases the effective ion transport rate by several orders of magnitude.

Other mechanisms may also contribute. For example, enhancement of diffusion can also arise from the change in electrochemical potential with concentration (17). Although this mechanism may play a role at the most dilute doping levels, it will not be important above about 0.5% where the V_{oc} *vs.* y curve is relatively flat (10). More rapid ionic diffusion might be expected in amorphous regions as compared to crystalline regions. However, this cannot explain the apparent contradiction (high measured short-circuit currents and slow measured free diffusion) outlined at the beginning of the paper. On the other hand, the electric field enhancement mechanism presented in this paper provides the explanation of the unusual result reported earlier (10) that one obtains higher Coulomb efficiency with a faster discharge. Under rapid discharge conditions, $V_{oc} - V_{ext}$ is large so that the field enhanced ion transport mechanism is most effective.

In conclusion, the fibrillar morphology of polyacetylene is critically important to the potential use of this polymer as a battery electrode in two ways: (*i*) the fibrils provide a microgrid such that ions from the electrolyte need to traverse distances no greater than about 100Å, and (*ii*) the small diameter of the fibrils provides an enhancement of the local electric field (during charging and discharging) which increases the ionic transport rate by several orders of magnitude over that obtained from free diffusion.

Acknowledgments

We thank Dr. K. Kaneto for many valuable discussions. This work was supported by DOE Advanced Energy Projects, DE-AC02-81ER10832.

Manuscript submitted July 29, 1982; revised manuscript received Oct. 6, 1982.

Any discussion of this paper will appear in a Discussion Section to be published in the December 1983 JOURNAL. All discussions for the December 1983 Discussion Section should be submitted by Aug. 1, 1983.

Publication costs of this article were assisted by the University of Pennsylvania.

REFERENCES

1. A. G. MacDiarmid and A. J. Heeger, in "The Physics and Chemistry of Low Dimensional Solids," L. Alcacer, Editor, p. 353, 393, Reidel, Dordecht (1980); S. Etemad, A. J. Heeger, and A. G. MacDiarmid, "Annual Reviews of Physical Chemistry," Vol. 33, p. 443, In press.
2. T.-C. Chung, A. Feldblum, A. J. Heeger, and A. G. MacDiarmid, *J. Chem. Phys.*, **74**, 5504 (1981).
3. P. J. Nigrey, A. G. MacDiarmid, and A. J. Heeger, *J. Chem. Soc. Chem. Commun.*, 594 (1979).
4. Y. W. Park, A. J. Heeger, M. A. Druy, and A. G. MacDiarmid, *J. Chem. Phys.*, **73**, 946 (1980).
5. C. K. Chiang, C. R. Fincher, Jr., Y. W. Park, A. J. Heeger, H. Shirakawa, E. J. Lowis, S. C. Gau, and A. G. MacDiarmid, *Phys. Rev. Lett.*, **39**, 1098 (1977).
6. D. Moses, A Feldblum, E. Ehrenfreund, A. J. Heeger, T.-C. Chung, and A. G. MacDiarmid, *Phys. Rev. B*, **26**, 3361 (1982).
7. A. Feldblum, J. H. Kaufman, S. Etemad, A. J. Heeger, T.-C. Chung, and A. G. MacDiarmid, *ibid.*, **26**, 815 (1982).
8. D. MacInnes, Jr., M. A. Druy, P. J. Nigrey, D. P. Nairns, A. G. MacDiarmid, and A. J. Heeger, *J. Chem. Soc. Chem. Commun.*, 317 (1981).
9. P. J. Nigrey, D. MacInnes, Jr., D. P. Nairns, A. G. MacDiarmid, and A. J. Heeger, *This Journal*, **128**, 1651 (1981).
10. K. Kaneto, M. Maxfield, D. P. Nairns, A. G. MacDiarmid, and A. J. Heeger, *J. Chem. Soc. Faraday Trans.*, **78**, 3417 (1982).
11. T. Ito, H. Shirakawa, and S. Ikeda, *J. Polym. Sci.*, **13**, 1943 (1975); H. Shirakawa and S. Ikeda, *Synthetic Metals*, **1**, 175 (1979/80).
12. F. E. Karasz, J. C. W. Chien, R. Galkiewicz, G. E. Wnek, A. J. Heeger, and A. G. MacDiarmid, *Nature*, **282**, 286 (1979).
13. M. Aldissi, Ph.D. Thesis, Montpellier, France (1981).
14. R. Kaner, A. G. MacDiarmid, and A. J. Heeger, Paper 27 presented at The Electrochemical Society Meeting, Detroit, Michigan, October 17-21, 1982.
15. J. H. Kaufman, J. W. Kaufer, A. J. Heeger, R. Kaner, and A. G. MacDiarmid, *Phys. Rev. B*, Rapid Communications, **26**, 2327 (1982).
16. W. Jost, "Diffusion in Solids, Liquids and Gases," Academic Press, New York (1960).
17. W. Weppner and R. A. Huggins, *Ann. Rev. Mater. Sci.*, **8**, 269 (1981).

Studies of the Reduction of Oxygen on Gold in Molten Li_2CO_3-K_2CO_3 at 650°C

W. M. Vogel,* S. W. Smith,* and L. J. Bregoli

United Technologies Corporation, Power Systems Division, South Windsor, Connecticut 06074

ABSTRACT

Limiting currents obtained with rotating gold wire cathodes indicate that oxygen dissolves in Li, K carbonate melt predominantly as superoxide. The reduction of dissolved oxygen proceeds at polarizations only moderately larger than the diffusion overvoltage for the complete reduction of superoxide. The remaining polarization can be rationalized as mostly ionic concentration overvoltage. In some experiments, a second wave is observed which appears to be due to some cathodic process which does not involve oxygen.

A summary of previous work on the reduction of oxygen in molten carbonates has been given by Appleby and Nicholson (1). The same workers also studied the reaction in Li_2CO_3 on gold (1) and in the ternary Li, Na, K eutectic on gold and on silver (2, 3). Silver is a rather special case, presumably because of the large solubility of oxygen in this metal. The essential findings were that dissolved molecular O_2 can be neglected as primary (diffusing) species. The cath-

* Electrochemical Society Active Member.

odic current was stated to be due to successive reduction of peroxide and superoxide formed by chemical reaction of oxygen with the melt. The reaction was reported to be further complicated by the slow reaction of oxide ions with dissolved CO_2 to $CO_3^=$. The cation composition was of major importance for the kinetics of the reaction. The present work was undertaken to further elucidate the oxygen reduction mechanism with the binary melt 62 mol/percent (m/o) Li_2CO_3-38 m/o K_2CO_3 because of the importance of this electrolyte for molten carbonate fuel cells. Because of the indicated complex nature of the dissolved reactant, particular attention was paid to the control and selection of the O_2-CO_2 mixtures.

Separate studies of the oxygen solubilities (4) have quantified the findings of Appleby and Nicholson with regard to the nature of oxygen dissolved in this melt at 650°C. The total solubility should obey Eq. [1]

$$S = kP_{O_2} + 0.5\,K_1 P_{O_2}^{0.5}/P_{CO_2} + 0.75\,K_2 P_{O_2}^{0.75}/P_{CO_2}^{0.5}, \quad \text{equiv. mol } O_2/\text{cm}^3 \quad [1]$$

In Eq. [1], k is the Henry's law constant for molecular O_2, and K_1 and K_2 are equilibrium constants for the formation of peroxide and superoxide, respectively

$$K_1 \equiv (O_2^=)\,P_{CO_2}/P_{O_2}^{0.5}, \quad K_2 \equiv (O_2^-)\,P_{CO_2}^{0.5}/P_{O_2}^{0.75} \quad [2]$$

The solubility data was explained nearly equally well with

$$k_1 \sim 0, \quad K_1 \sim 3.2 \cdot 10^{-8}\ \text{mol atm}^{0.5}/\text{cm}^3, \quad K_2 \sim 1.5 \cdot 10^{-7}\ \text{mol/cm}^3\ \text{atm}^{0.25} \quad [3a]$$

or with

$$k \sim 0, \quad K_1 << K_2 \sim 2.5 \cdot 10^{-7},\ \text{mol/cm}^3\ \text{atm}^{0.25} \quad [3b]$$

These results indicate that superoxide is the reactive oxygen species in the melt under most conditions according to

$$(O_2^-)/(O_2^=) = \frac{K_2}{K_1}\,(P_{O_2}^{0.5}\,P_{CO_2})^{0.5} \geq 4.7\,(P_{O_2}^{0.5}\,P_{CO_2})^{0.5}, \text{ equiv./equiv.} \quad [4]$$

The present experiments were extended to very small reactant pressures in order to vary the ratio of reactants.

Experimental

The apparatus used is shown schematically in Fig. 1a. The electrolyte (approx. 300 cm³) is contained in an alumina beaker (99.8% Al_2O_3), which is placed inside an Incoloy 800 container. A cover for the container carries all of the cell components and is sealed with a graphite gasket. The apparatus is heated in a crucible furnace controlled by a thermocouple between the container wall and the furnace elements; the temperature of the melt is measured by a thermocouple in an Al_2O_3 tube immersed in the melt.

The design of the working electrode is shown in Fig. 1b. It is rotated by a belt drive apparatus to a maximum capability of 10,000 rpm. Several electrode shapes were evaluated, with the one shown giving the most consistent results and used to take the data reported here. Because of the lack of strength of Au at operating temperature, it was necessary to use a relatively short electrode of large diameter (1 cm × 0.1 cm). Formation of a meniscus electrode inside the tube was prevented by choosing the wire and tube diameter such that a solid plug was formed which sealed the system.

The reference electrode and counterelectrode were both contained in Al_2O_3 tubes which communicate with the solution through a packed bed of crushed Al_2O_3 and a small slit cut in the side of the tube. The reference electrode consisted of a partially immersed gold-

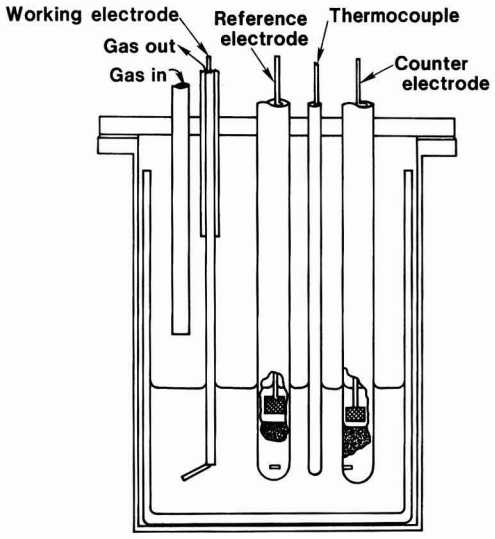

Fig. 1a. Schematic description of test apparatus

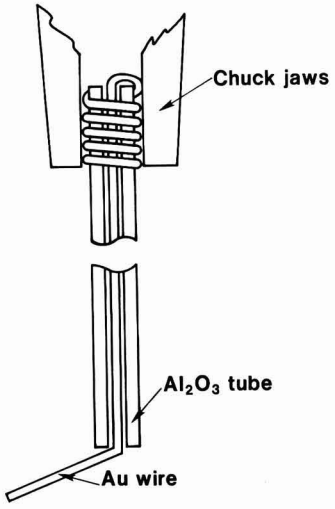

Fig. 1b. Details of electrode construction

wire under 1/3 atm O_2-2/3 atm CO_2. The furnace, rotator, and electrochemical cell were all attached to a common frame which made a solid connection from the working electrode to the rotator possible.

All experiments were conducted at 650°C in 62 m/o Li_2CO_3-38 m/o K_2CO_3. The salts used were reagent grade and were further purified to remove iron and sulfur. The iron was removed by treating the melt with O_2 to precipitate an insoluble oxide which was removed from the solid mass after freezing. The solids were crushed, remelted, and treated with H_2 for several days to remove sulfur. The gases were primarily of "high purity" grade, although several grades of CO_2 were evaluated to obtain minimum residual currents. Gas mixing was done with a Matheson Model 8249 mass flow controller.

The polarization data were taken at a sweep rate of 100 mV/min or with each point held for 5 min. These two techniques gave the same results. Higher rotation rates were not used because of the problem of keeping the wire shape constant.

Results and Discussion

The steady-state polarization curves show essentially two waves, the second one barely observable in some experiments, see Fig. 2. The first wave starts at the thermodynamic potential of the oxygen electrode and has a polarization not much larger than the concentration overvoltage for a two or three electron process

$$\eta_c = \frac{RT}{nF} \ln (1 - i/i_{lim}) \quad n = 2 \text{ or } 3 \qquad [5]$$

The limiting current of the first wave varied accurately with square root of rotational speed and is therefore diffusion controlled.

Values of limiting currents at 1600 rpm of the first wave are given in Table I. The currents in this wave are related to oxygen reduction since the wave disappears under oxygen-free CO_2 as is shown in Fig. 3.

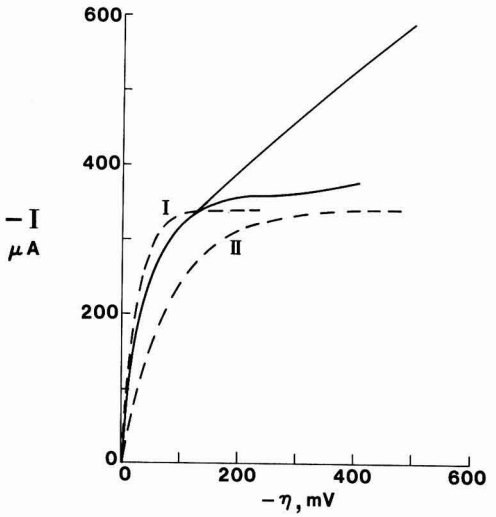

Fig. 2. Irreproducibility of second wave. Two experiments in supposedly similar melt batches. $P_{O_2} = 0.04$ atm, $P_{CO_2} = 0.0004$ atm, 400 rpm. Dashed lines: (I) calculated from Eq. [5] with n = 3, (II) with n = 1.

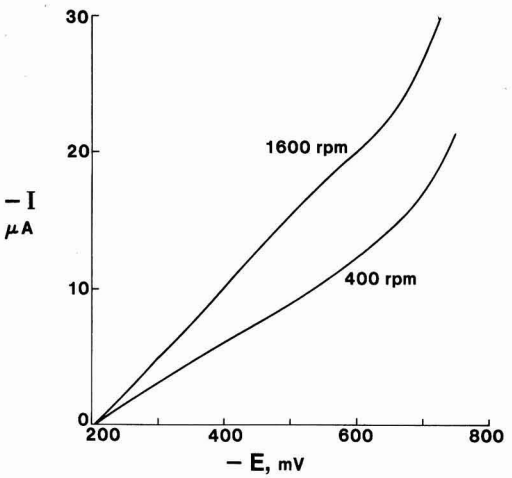

Fig. 3. Currents at $P_{CO_2} = 1$ atm, after best efforts to eliminate oxygen traces.

Table I. Limiting currents at 1600 rpm

P_{O_2} (atm)	P_{CO_2} (atm)	$-I_{lim}$ (1600 rpm)
0.64	0.0016	2290
0.64	0.0019	2030
0.33	0.67	80
0.296	0.096	106
0.16	0.0008	1260
0.16	0.0011	1070
0.16	0.0032	390
0.101	0.0016	615
0.0635	0.0008	750
0.074	0.098	48
0.04	0.0004	960
0.04	0.0007	670
0.04	0.0016	300
0.04	0.0032	200
0.04	0.0064	135
0.04	0.0256	68
0.04	0.1025	37
0.03	0.20	26
0.0076	0.01	40
0.0076	0.10	16
0.003	0.063	12

If the ocp for this case is assumed to be the equilibrium O_2 potential, the gas used would be calculated to contain about 5 ppm O_2. The corresponding oxygen concentration in the melt would be of the order $5 \cdot 10^{-11}$ mol O_2/cm^3 according to Eq. [1]. The data in Fig. 3 represent the best effort to eliminate all potential sources of trace oxygen from the counterelectrode, the reference electrode, and air leaks.

The limiting currents of the first wave could be due to the reduction of O_2^-, of $O_2^=$, or of both species simultaneously. In the latter case, a plot of the data in the table according to Eq. [6] should yield a straight line

$$I_{lim} P_{CO_2}/P_{O_2}^{0.5} = \text{const.} [K_1 \cdot D_{O_2^=} + K_2 D_{O_2^-} \cdot P_{O_2}^{0.25} P_{CO_2}^{0.5}] \qquad [6]$$

The plot is shown in Fig. 4. Not shown in the figure is the point for $P_{O_2} = 0.33$, $P_{CO_2} = 0.67$, which lies on the straight line at $P_{O_2}^{0.25} P_{CO_2}^{0.5} = 0.62$. From the slope and ordinate intercept of the line

$$K_2 \cdot D_{O_2^-} >> K_1 \cdot D_{O_2^=} \qquad [7]$$

This result indicates that superoxide is the predominant diffusing and electroactive species in the first wave. Equation [7] does not indicate if peroxide is present in the bulk melt in significant concentration, but is not reduced in the first wave.

The reduction of O_2^- appears to be complete in the first wave. If O_2^- were reduced to peroxide, it should be completely reduced at larger polarization in a second wave, and the latter should increase in proportion to the first wave. This has not been observed. Furthermore, the oxidant diffusion overvoltage due to partial reduction of O_2^- can be calculated from the observed limiting currents, using Eq. [5] with $n = 1$. An example is given in Fig. 2 as dashed line II. The calculated

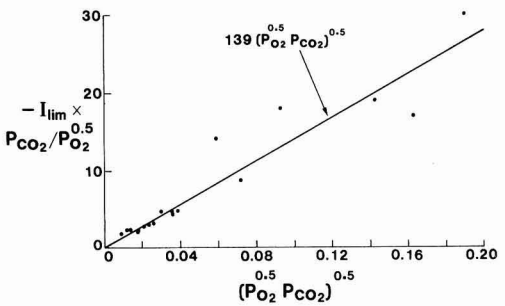

Fig. 4. Limiting currents at 1600 rpm, plotted assuming O_2^- and $O_2^=$ as diffusing species.

overvoltage is larger than the observed one, which makes no sense. Using the value $n = 3$ for complete reduction of O_2^- results in curve I in Fig. 2. Thus, the first wave is explained by essentially diffusion controlled and complete reduction of superoxide.

As has been mentioned, the resulting Eq. [7] leaves open the possibility that peroxide is present in the bulk melt, but that it is not reduced in the first wave. If this is true, $O_2^=$ should be reduced at larger polarization, *i.e.*, in a second wave. If P_{CO_2} is increased at constant P_{O_2}, the equilibrium concentrations of O_2^- and $O_2^=$ decrease, with the decrease in $(O_2^=)$ being more pronounced according to Eq. [4]. If the observed second wave were due to bulk peroxide reduction, it should decrease more than the first wave on such variation in gas composition. Results of relevant tests are shown in Fig. 5 for $P_{O_2} = 0.04$ atm. The first wave varies with $P_{CO_2}^{0.5}$, *i.e.*, with the superoxide concentration. The second wave should decrease with $P_{CO_2}^{-1}$, *i.e.*, by the factor 64 in the sequence $P_{CO_2} = 0.0016$ to 0.1024 atm. In actual fact, it remained approximately constant, indicating that the second wave does not represent the reduction of bulk peroxide. These results suggest that the second wave is not due to peroxide reduction, be it bulk peroxide or $O_2^=$ produced by partial reduction of O_2^- in the first wave.

The second wave in fact is very difficult to explain. It was found to be very irreproducible unless the same batch of the same age was used. It was essentially absent in some tests, but very pronounced in others as can be seen in Fig. 2. When observed, the second wave showed large polarization and no limiting current to potentials where CO_2 reduction commences. It is concluded that this wave is due to some other process not involving oxygen. This would also explain the results in Fig. 3 for extremely small O_2 and large CO_2 pressures.

Neglected in the discussion so far has been the very important role of CO_2 in the oxygen reduction. Owing to the small solubility of molecular CO_2, molten carbonate can be compared with a salt solution of small *p*H-buffer capacity. In such a solution, an H^+-consuming reaction such as the evolution of H_2 does not yield a cathodic H^+-limiting current. Rather, the polarization curve shows an inflection which corresponds to the change from the acidic to the alkaline hydrogen reaction (5). Similarly, CO_2-diffusion too slow to sustain the formation of carbonate should not result in a CO_2-limiting current, but in an inflection corresponding to the change from Eq. [8] to [9]

$$O_2^- + 2CO_2 + 3e^- = 2CO_3^= \quad [8]$$

$$O_2^- + 3e^- = 2\,O^= \quad [9]$$

Equations [8] and [9] are coupled by the acid/base reaction

$$O^= + CO_2 = CO_3^= \quad [10]$$

The combined oxidant and ionic diffusion overvoltage is derived by assuming equilibrium of Eq. [8]-[10]. The overvoltage is now

$$\eta_d = \frac{RT}{3F} \ln \frac{(O_2^-)}{(O_2^-)_o} \left[\frac{(O^=)_o}{(O^=)} \right]^2 = \frac{RT}{3F} \ln \frac{(O_2^-)}{(O_2^-)_o} \left[\frac{(CO_2)}{(CO_2)_o} \right]^2 \quad [11]$$

The index/suffix (o) indicates the values in the bulk melt. The ratio $(O_2^-)/(O_2^=)_o$ is calculated from the observed limiting current using Fick's law

$$\frac{(O_2^-)}{(O_2^-)_o} = 1 - \frac{i}{i_{lim}} \quad [12]$$

The ratios $(O^=)_o/(O^=)$ and $(CO_2)/(CO_2)_o$ are equal and are derived as follows. The current density is equal to the combined fluxes of $O^=$ and CO_2

$$i = \frac{1.5FD_{O^=}}{\delta} [(O^=)_o - (O^=)] + \frac{1.5FD_{CO_2}}{\delta} [(CO_2) - (CO_2)_o] \quad [13]$$

Introducing the following formal limiting currents

$$i_{O^=} = \frac{1.5FD_{O^=}}{\delta} (O^=)_o \quad [14]$$

$$i_{CO_2} = \frac{-1.5FD_{CO_2}}{\delta} (CO_2)_o \quad [15]$$

Equation [13] can be written in the form

$$i = i_{O^=} \left[1 - \frac{(O^=)}{(O^=)_o} \right] + i_{CO_2} \left[1 - \frac{(O^=)_o}{(O^=)} \right] \quad [16]$$

Equation [16] yields

$$2\frac{(O^=)}{(O^=)_o} = 1 + \frac{i_{CO_2}}{i_{O^=}} - \frac{i}{i_{O^=}} + \left[\left(1 + \frac{i_{CO_2}}{i_{O^=}} - \frac{i}{i_{O^=}} \right)^2 - 4\frac{i_{CO_2}}{i_{O^=}} \right]^{1/2} \quad [17]$$

The polarization curve for pure diffusion overvoltage can be calculated from Eq. [11] using Eq. [12] and [17] provided $i_{O^=}$ and i_{CO_2} are known. For certain combinations of the three limiting currents, single waves are calculated, for other values a double wave. All curves end in the O_2^- limiting current.

Such changes had been expected in the tests which produced the curves in Fig. 5. In these tests, the ratio of superoxide to CO_2 concentration in the melt varied from 170 (at 0.0004 atm CO_2) to 0.04 (at 0.1024 atm CO_2). These values were calculated with the value of Eq. [3b] for K_2, and the Henry's law constant of CO_2, $k = 10^{-5}$ mol/cm³ atm (6, 7). Despite the very large range of the ratio $(O_2^-)/(CO_2)$, little change and certainly no inflection is seen in the shape of the curves in Fig. 5. The reason, presumably, is that changes in P_{CO_2} at constant P_{O_2} do not simply change i_{CO_2} and $i_{O^=}$ in opposite directions, but that the superoxide concentration also changes. Because of this, the transition from a single wave at low P_{CO_2} (Eq. [9]) to a single

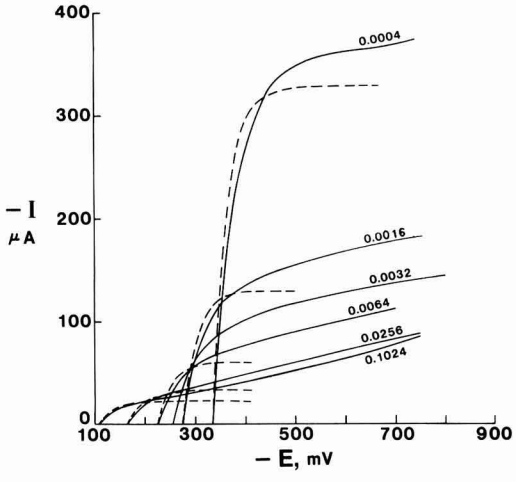

Fig. 5. Steady-state polarization curves at 400 rpm. $P_{O_2} = 0.04$ atm, P_{CO_2} as indicated. Dashed lines calculated from Eq. [5] with $n = 3$.

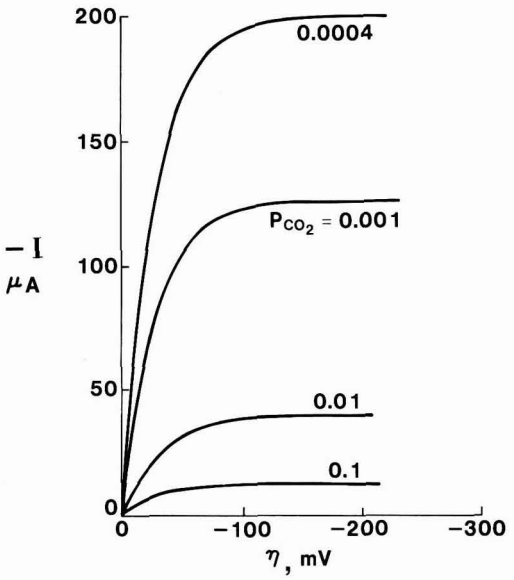

Fig. 6. Concentration overvoltage calculated from Eq. [11], [12], and [17] with $i_{CO_2} = 1500\ P_{CO_2}$, $i_{O^=} = 1.5/P_{CO_2}$, $i_{O_2^-} = 4/P_{CO_2}^{1/2}$ for $P_{O_2} = 0.04$ atm.

wave at large P_{CO_2} (Eq. [8]) may have occurred without a noticeable double wave at intermediate CO_2 pressures. This possibility is demonstrated in Fig. 6 which was calculated from Eq. [11], [12], and [17] with the following assumed values

$$\mathbf{F}/\delta = 10^{13},\ \mu\text{A sec/cm equiv.}$$

$$D_{CO_2} k_{CO_2} = 10^{-10},\ \text{mol/cm sec atm}$$

$$K_2 \cdot D_{O_2^-} = 1.5 \times 10^{-12},\ \text{mol/cm}^3\ \text{sec atm}^{1/4}$$

$$K_B \cdot D_{O^=} = 10^{-13},\ \text{mol atm/cm sec}$$

where K_B is the equilibrium constant of Eq. [10]. The curves in Fig. 6 resemble the experimental ones in Fig. 5. No attempts at better fitting the latter were made because of the large number of unknown constants which have to be used. An experimentally determined value is available only for K_2 (Eq. [3]). Values for k_{CO_2} (6) and K_B (8) apply to ternary melts containing Li, Na, K-carbonate.

Conclusions

Oxygen dissolves in fused Li, K-carbonate (62 m/o Li) primarily as superoxide with some peroxide present at very small CO_2 pressures. Molecular O_2 is negligible in the melt. The dissolved oxygen is reduced completely on gold in a single wave. The polarization is moderately larger than the superoxide diffusion overvoltage. The difference appears to be mainly ionic concentration overvoltage for submerged electrodes.

Acknowledgments

The present study was supported by the Electric Power Research Institute under contract RP-1085-4. Dr. A. J. Appleby was the EPRI Project Manager for this contract; his suggestions and support are appreciated.

Manuscript submitted Aug. 3, 1981; revised manuscript received April 23, 1982.

Any discussion of this paper will appear in a Discussion Section to be published in the December 1983 JOURNAL. All discussions for the December 1983 Discussion Section should be submitted by Aug. 1, 1983.

Publication costs of this article were assisted by United Technologies Corporation.

REFERENCES

1. A. J. Appleby and S. B. Nicholson, *J. Electroanal. Chem.*, **53**, 105 (1974).
2. A. J. Appleby and S. B. Nicholson, *ibid.*, **83**, 309 (1977).
3. A. J. Appleby and S. B. Nicholson, *This Journal*, **127**, 759 (1980).
4. S. W. Smith, W. M. Vogel, and S. M. Kapelner, *ibid.*, In press.
5. See *e.g.*, K. Vetter, "Electrochemical Kinetics," Academic Press, New York (1967); E. Lange and H. Göhr, "Thermodyamische Electrochemie," p. 251, A. Huthig Verlag, Heidelberg (1962).
6. G. H. J. Broers, M. Schenke, and H. J. J. van Ballegoy, Ext. Abstr. No. II 77, 20th ISE Meeting, Druzhba, Bulgaria, Sept. 1977.
7. A. J. Appleby and C. van Drunen, *This Journal*, **127**, 1655 (1980).
8. N. Busson, S. Palous, J. Millet, and R. Buvet, *Electrochim. Acta*, **12**, 1609 (1967).

Structural and Compositional Characterization of Mixed CdS-CdSe Films Grown by Cathodic Electrodeposition

Andrzej S. Baranski, W. Ronald Fawcett,* Kazimierz Gatner, and Alex C. McDonald*

The Guelph-Waterloo Centre for Graduate Work in Chemistry, Department of Chemistry, University of Guelph, Guelph, Ontario, Canada N1G 2W1

and Jack R. MacDonald and Mats Selen

Department of Physics, University of Guelph, Guelph, Ontario, Canada N1G 2W1

ABSTRACT

Mixed CdS-CdSe films have been electrodeposited cathodically from DMSO solutions containing cadmium chloride, elemental sulfur and elemental selenium. The mixed films were characterized structurally using x-ray diffraction, scanning electron microscopy, and Rutherford backscattering spectrometry. The photoelectrochemical response of the CdS-CdSe material was studied in a photoelectrochemical cell with a sulfide-polysulfide electrolyte. It has been found that the composition and optical bandgap of the CdS-CdSe films can be varied by changing the composition of the deposition solution. However, the films with higher CdSe content are amorphous, and have a higher resistivity than pure CdS.

The cathodic electrodeposition of thin films of CdS and other metal chalcogenides on metal substrates from nonaqueous electrolyte solutions has been discussed previously (1, 2). This simple technique allows one to fabricate CdS films exhibiting a high degree of crystallinity and continuity, in a physical configuration suitable for direct incorporation into photovoltaic and photoelectrochemical cells (PEC). Since the bandgap of CdS is rather large (2.4 eV) for efficient utilization of incident solar radiation, it is desirable to examine composite CdS-CdSe materials with smaller bandgaps (1.7-2.4 eV).

There has been some interest in mixed n-type CdS-CdSe (3, 4) and CdSe (5) electrodes for incorporation into PEC's. The maximum theoretical efficiency of a PEC for illumination with light at the bandgap energy (6) can be expressed as

$$\eta = \frac{(V_{redox} - V_{FB})\mathbf{F}}{E_g} = \frac{V_{oc}\mathbf{F}}{E_g} \qquad [1]$$

where V_{redox} is the equilibrium potential of the redox couple in the electrolyte, V_{FB}, the flatband potential of the semiconductor in the electrolyte, V_{oc}, the open-circuit voltage, E_g, the bandgap of the semiconductor, and **F**, the Faraday. Both the maximum open-circuit voltage and the efficiency of the device are functions of V_{FB} and E_g. It has been shown that V_{FB} of CdX films can be shifted significantly in the cathodic direction in aqueous electrolytes containing S^{2-} (7), and that the degree of shift is a function of the composition of the mixed CdS-CdSe material (3, 4). Thus, the efficiency of such a solar device may be optimized by the manipulation of the composition of the semiconductor electrode, and hence V_{FB} and E_g. It has also been suggested that high efficiency PEC's could be obtained through the use of CdS-CdSe electrodes with a gradient composition as a function of depth (3). This gradient may allow a maximization of V_{oc} through an advantageous shift in V_{FB} achieved by altering the surface composition of the film, and a minimization of E_g on the basis of optimizing the composition of the bulk of the film.

It has been found that smooth coherent polycrystalline and amorphous films of CdS_xSe_y can be cathodically electrodeposited on metal substrates from a dimethylsulfoxide (DMSO) electrolyte solution containing cadmium chloride, elemental sulfur, and elemental selenium. The composition of the mixed semiconductor films may be altered, by varying the parameters controlling the electrodeposition of the films, and the concentration of Se in the electrolyte solution. The results of a characterization of the structural properties of the electrodeposited CdS_xSe_y films and measurements of E_g in aqueous electrolytes containing Na_2S and elemental S are presented in this paper.

* Electrochemical Society Active Member.

Key words: electrodeposition of semiconductors, CdS-CdSe films, semiconductor films.

Experimental

All CdS_xSe_y films were electrodeposited on smooth substrates of high purity Pt sputtered on glass. The preparation of the Pt substrate has been described elsewhere (2). The configuration of the cell and the procedure used for the electrolysis were identical to those described for the electrodeposition of the CdS films (1, 2). The electrolyte solution consisted of 0.055M $CdCl_2$, and 0.19M S with a varying concentration of Se in reagent grade DMSO. The temperature of the electrolyte solution was held constant by immersing the cell in an oil bath whose temperature was maintained at 110°C by a temperature controller/circulator.

The structural properties and composition of deposited SdS_xSe_y films were examined using electron microscopy, x-ray crystallography, Rutherford backscattering spectroscopy, and thickness measurements as described previously (2). Selected CdS_xSe_y films were incorporated into a photoelectrochemical cell, using a Pt counterelectrode and saturated calomel electrode reference. The aqueous electrolyte solution contained 1.0M NaOH, 1.0M Na_2S and 0.01M S. The cells were illuminated with a 1000W xenon lamp through a 7.0 cm H_2O infrared filter. All photocurrent outputs were corrected for the power against wavelength output of the lamp. For comparison purposes, the photoresponse for a CdSe film electrodeposited from an aqueous solution was also measured. In this case, the electrodeposition solution consisted of 2g $CdSO_4$, and ~1g H_2SeO_3 in 100 ml of 0.1M H_2SO_4 (9); the film was deposited at a current density of 15 mA cm^{-2} for 600 sec, the temperature of the bath being 60°C. It was annealed in argon for 1 hr at 400°C. No attempt was made to anneal films electrodeposited from DMSO because of problems with cracking.

Results and Discussion

The CdS_xSe_y films electrodeposited by the method described above appeared very smooth and uniform and exhibited extremely good adhesion to the Pt substrate. The color of the films was a function of the Se concentration in the electrolyte solution, ranging from the familiar yellow-gold of CdS for [Se] = 0 to a dark reddish-purple for films deposited from the solution saturated with Se (approximately 0.01M Se) at 110°C.

Electron micrographs of typical films grown from electrolyte solutions containing a range of Se concentrations are shown in Fig. 1. A transition from crystalline, highly cracked films (Fig. 1a) to smooth, glass-like films (Fig. 1d) was observed as the Se concentration in the electrolyte solution was increased from 0.0025M to saturation. This transition from a highly structured to an amorphous film upon incorporation of Se is also evident from the x-ray diffractometer pattern of the same series of films (Fig. 2a-2d). As the Se concentration was increased, the intense peak at $2\theta \simeq 32°$, which is attributed to CdS,[1] became less intense, until it disappeared for a film grown from a solution saturated with Se. The extraneous peaks at 36.5° and 38° are due to a limited degree of orientation of the underlying substrate Pt.

Plots of the voltage applied to the cell during deposition against the time of deposition are shown in Fig. 3. The increase in the slope of the V against t plots with

[1] Further x-ray analysis of the electrodeposited CdS films described in Ref. (2) has indicated that the CdS has a hexagonal structure. The intense peak in the x-ray pattern (see Fig. 2) at $2\theta \simeq 32°$ is due to secondary reflection from the 001 planes indicating that the crystallites are oriented with their c-axes perpendicular to the substrate.

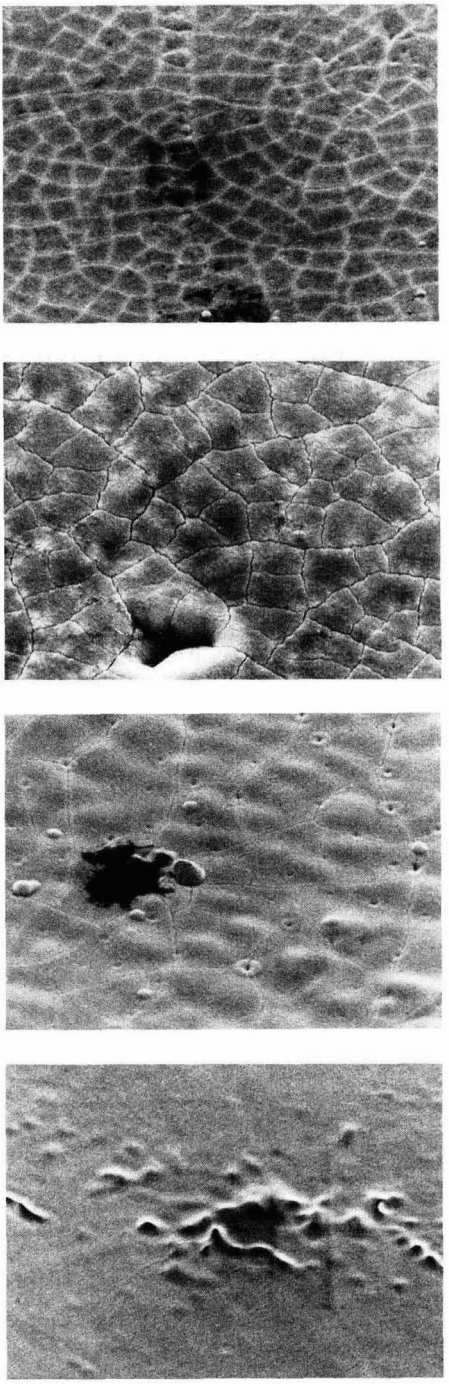

Fig. 1. Electron micrographs of CdS_xSe_y films deposited on Pt from DMSO electrolyte solutions containing 0.020M sulfur, 0.055M $CdCl_2$, and (a) 0.0025M Se (mag 5000×); (b) 0.0040M Se (mag 7900×); (c) 0.0050M Se (mag 5230×); (d) sat. Se at 110°C (mag 5340×).

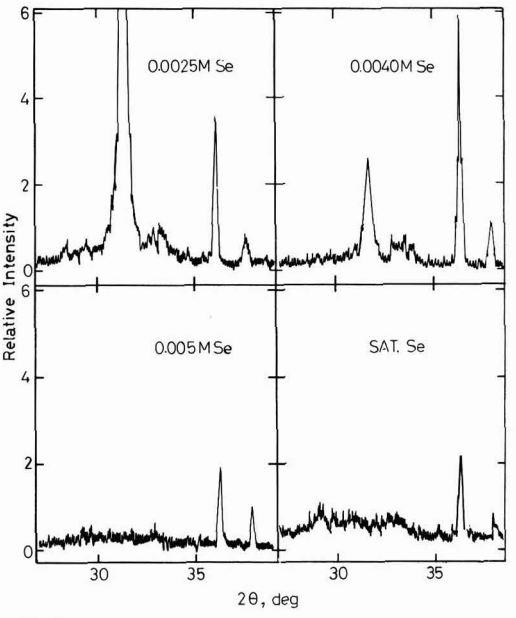

Fig. 2. X-ray diffractometer patterns of CdS_xSe_y films deposited on Pt from DMSO electrolyte solutions, containing various concentrations of Se as indicated (Co, K_α emission).

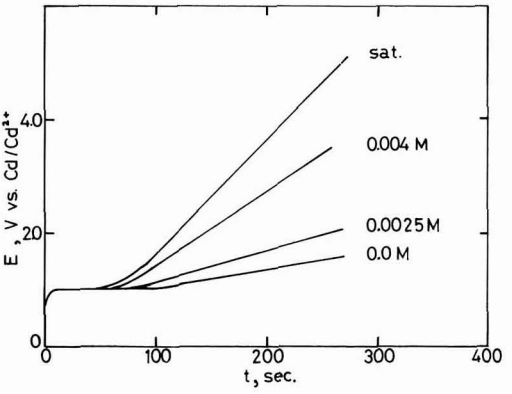

Fig. 3. Voltage against deposition time during deposition of CdS_xSe_y on Pt from electrolyte solutions, containing various concentrations of Se as indicated. The current density was 2.5 mA cm^{-2} and the temperature, 110°C.

increase in the Se concentration in the electrolyte indicates that the resistivity of the films also increases. This result is also consistent with the decrease in the degree of crystallinity of the CdS_xSe_y deposit with increasing Se concentration. Attempts to measure resistivities were not successful, due to the difficulty in making ohmic contacts to the thin films. The average film thickness as a function of applied current density during deposition and as a function of the time of deposition is shown in Fig. 4 for varying Se concentrations. The decrease in slope at both long deposition time and high current density with increasing Se concentration probably reflects a lower efficiency of deposition of CdS_xSe_y, with respect to that for CdS. These results suggest that the rate of film formation depends on the nature of the chalcogen involved.

A plot of the average CdS_xSe_y film thickness against the solution temperature during deposition for films grown from the electrolyte solution saturated with Se is shown in Fig. 5. The composition of the same series of films as determined by Rutherford backscattering spectrometry (8) is summarized in Table I (see also Fig. 6). The films grown at temperatures in the range from 350-390 K appeared to have the highest quality and uniformity, and exhibited good adhesion to the substrate. It is significant that the ratio of total chalcogen to cadmium in these films remains approximately constant and stoichiometric over this temperature range.

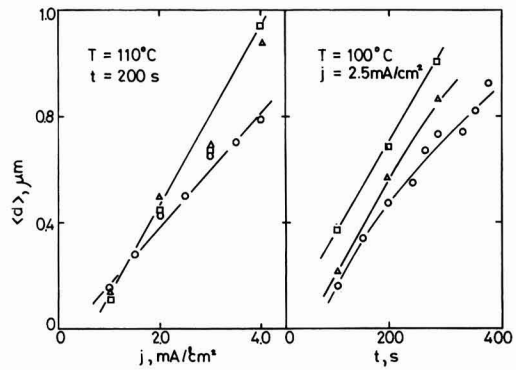

Fig. 4. Average thickness of CdS_xSe_y films deposited on Pt from electrolyte solutions containing 0.020M sulfur, 0.055M $CdCl_2$, and 0.0025M Se (□), 0.0040M Se (△), or sat. Se (○) at 110°C against current density, j. Deposition time and solution temperature were held constant as indicated.

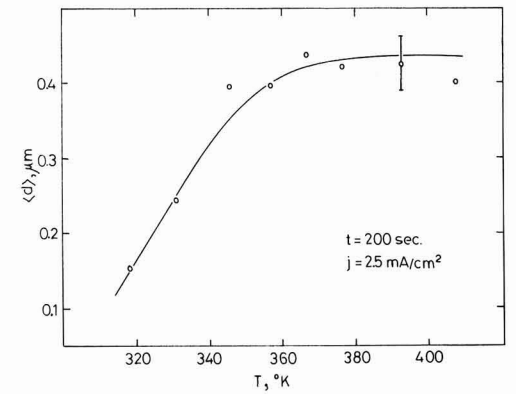

Fig. 5. Average thickness of CdS_xSe_y films deposited on Pt from electrolyte solutions containing 0.020M sulfur, 0.055M $CdCl_2$, and saturated with Se against solution temperature. Current density and deposition time were held constant as indicated.

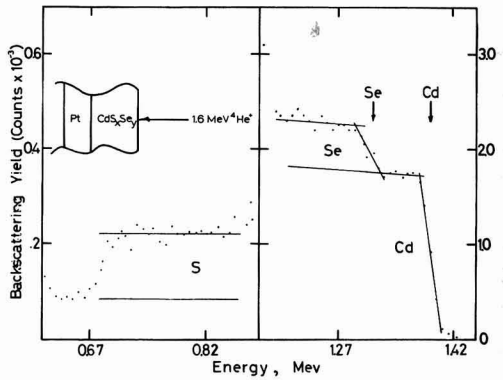

Fig. 6. Rutherford spectrum of backscattered α particles from a CdS_xSe_y film on Pt in the energy ranges 0.60-0.85 MeV and 1.15-1.43 MeV, corresponding to scattering from S and Se, Cd atoms respectively.

In Fig. 7, the S/Cd ratio is plotted against the Se/Cd ratio for a variety of CdS_xSe_y films grown from solutions with a range of Se content. Although there is considerable scatter in these results, there is a general trend of increasing Se/Cd ratio with decreasing S/Cd ratio. This result may indicate that the mechanisms by which the chalcogens, S and Se, are incorporated into the film are similar. A graph of the Se/Cd concentration ratio in the CdS_xSe_y films is plotted against Se content in the electrolyte solution in Fig. 8. It is apparent that the Se content of the semiconductor can be varied over a wide range by varying its concentration in the electrodeposition solution.

Typical plots of photoresponse against wavelength for selected electrodes in PEC's illuminated by the xenon lamp at 100 mW cm^{-2} are shown in Fig. 9. It was noted that films deposited from aqueous solution had a black porous appearance, as opposed to the

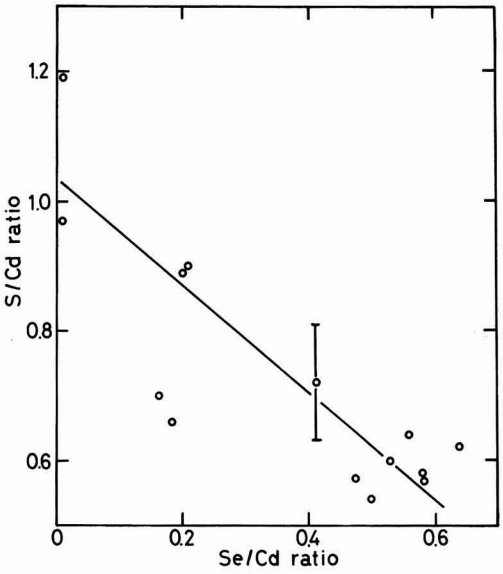

Fig. 7. S/Cd ratio against Se/Cd ratio for CdS_xSe_y films deposited on Pt, from electrolyte solutions containing various concentrations of Se, and at several current densities (from Rutherford backscattering spectrometry).

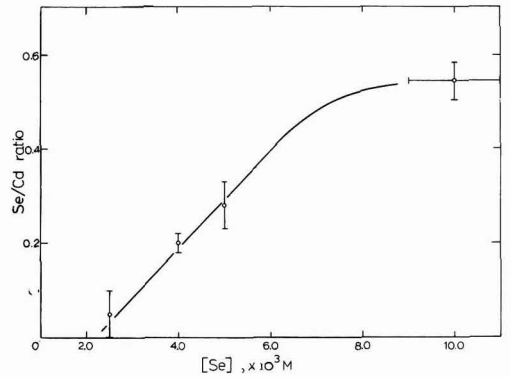

Fig. 8. Se/Cd ratio of CdS_xSe_y films deposited on Pt against Se concentration in electrolyte solution (from Rutherford backscattering spectrometry).

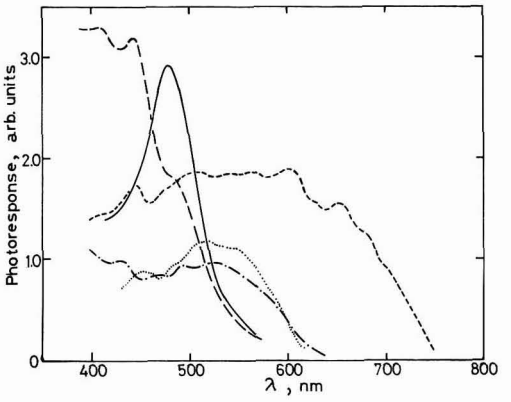

Fig. 9. Relative photoresponse of CdS_xSe_y electrodes in an aqueous solution containing 1.0M NaOH, 1.0M Na_2S, 0.01M S against wavelength of illuminating light: --- CdSe (deposited from aqueous solution), ... CdSe (deposited from DMSO solution saturated with Se at 110°C), — · — $CdS_{0.5}Se_{0.5}$, — — — — $CdS_{0.9}Se_{0.1}$, ——— CdS (deposited from DMSO solution).

smooth glassy appearance of CdSe films deposited from the nonaqueous bath. In recording the photoresponse curve for the sample grown from the aqueous medium, the wavelength was swept rapidly (1 nm sec^{-1}) to prevent any significant effect from surface degradation of the sample, due to S-Se exchange. Values of the bandgap, E_g, estimated from the onset of photoanodic current are summarized in Table II. The decrease in relative photoresponse with increasing Se content is probably due to the increasing resistivity of the films. The reason for the discrepancy between the estimate of E_g for CdSe deposited from DMSO (1.94 eV) and from aqueous solution (1.74 eV) is unclear, but it probably results from the great structural difference between the two materials. Moreover, the estimated bandgaps for all the CdS_xSe_y films are larger than expected on the basis of previously reported data for mixed films (4, 5). This result is probably due to the amorphous character of the electrodeposited material, and may also reflect some incorporated impurities, such as solvent molecules which may be trapped in the film during deposition.

The flatband potential, V_{FB} of the electrodeposited CdS films in the aqueous electrolyte used in the PEC, was determined to be −1.35V against a saturated calomel electrode on the basis of Mott-Schottky plots. Values of V_{FB} for the graded composition CdS_xSe_y

Table I. Composition of CdS_xSe_y films as a function of deposition temperature*

T, K	[Se]/[Cd]	[S]/[Cd]	[Se + S]/[Cd]	[S]/[S + Se]
353	0.55	0.55	1.10	0.50
363	0.48	0.58	1.06	0.55
373	0.54	0.56	1.10	0.51
383	0.52	0.55	1.07	0.51

* The deposition solution contained 0.187M S and 0.055M $CdCl_2$, and was saturated with Se; the current density was 2.5 mA cm^{-2} and the growth time, 200 sec.

Table II. Variation in the estimated bandgap, E_g for Cd_xSe_y films in a PEC configuration as a function of film composition*

[Se], M	x	y	E_g, eV
0	1.0	0	2.34
0.0025	0.1	0.9	2.25
0.0040	0.2	0.8	2.25
0.0060	0.4	0.6	2.10
0.0080	0.5	0.5	2.00
Sat.	0.5	0.5	2.00
Sat. ([S] = 0)	0	1.0	1.94

* The deposition solution contained 0.187M Se and 0.055M $CdCl_2$; the current density was 2.5 mA cm^{-2}, growth time, 200 sec and temperature, 383 K. The electrolyte solution in the PEC contained 1.0M NaOH, 1.0M Na_2S, and 0.10M S.

material could not be determined precisely in the aqueous electrolyte. It is possible that H_2O interacts strongly with DMSO or its decomposition products incorporated in the films during deposition, thereby altering the adsorption characteristics of the system and making the determination of V_{FB} difficult. A slight negative shift in the onset potential of the PEC's from −1.2 to −1.3 *vs.* SCE was observed as the composition of the anode was changed from CdS_xSe_y to CdS. This shift may be due to a shift in V_{FB} to more negative values as the S content of the films is increased. As pointed out by Noufi *et al.* (3), a film of graded composition with high CdSe content in the bulk to achieve a low bandgap, and high CdS content at the surface to achieve a more negative flatband potential, would be more efficient according to Eq. [1]. The present electrodeposition technique would be ideally suited to the fabrication of such films.

In conclusion, the cathodically electrodeposited CdS_xSe_y films, despite their amorphous nature and high resistivity, are promising materials for incorporation into PEC devices. The films show excellent mechanical stability, and are photoconductive with a composition and bandgap which can be controlled by varying the Se content in the electrodeposition solution. The technique therefore lends itself well to the fabrication of composite electrodes.

Manuscript submitted June 1, 1982; revised manuscript received Sept. 30, 1982.

Any discussion of this paper will appear in a Discussion Section to be published in the December 1983 JOURNAL. All discussions for the December 1983 Discussion Section should be submitted by Aug. 1, 1983.

Publication costs of this article were assisted by the University of Guelph.

REFERENCES

1. A. S. Baranski and W. R. Fawcett, *This Journal*, **127**, 766 (1980).
2. A. S. Baranski, W. R. Fawcett, A. C. McDonald, R. M. de Nobriga, and J. R. MacDonald, *ibid.*, **128**, 963 (1981).
3. R. N. Noufi, P. A. Kohl, and A. J. Bard, *ibid.*, **125**, 375 (1978).
4. R. C. Kainthla, D. K. Pandya, and K. L. Chapra, *ibid.*, **129**, 99 (1982).

5. M. A. Russak, J. Reichman, H. Witzke, S. K. Deb, and S. N. Chen, *ibid.*, **127**, 725 (1980).
6. M. D. Archer, *J. Appl. Electrochem.*, **5**, 17 (1975).
7. T. Inoue, T. Wanatabe, A. Fujishima, and K. Honda, *Bull. Chem. Soc. Jpn.*, **52**, 1243 (1979).
8. W. K. Chu, J. W. Mayer, and M. A. Nicolet, "Backscattering Spectrometry," Academic Press, New York (1978).
9. G. Hodes, J. Manassen, and D. Cahan, *Nature*, **261**, 403 (1976).

Filtration Coefficient and Hydraulic Permeability of Nafion 125 Membranes in Metal Alkali Solutions

C. Fabiani, S. Scuppa, L. Bimbi, and M. De Francesco

E.N.E.A., Divisione Chimica, Laboratorio Chimica Fisica, CRE Casaccia, Rome, Italy

ABSTRACT

Membranes based on Nafion (trademark of E. I. du pont de Nemours & Company), a copolymer of tetrafluorethylene and a vinylsulfonic acid, have received to date a great deal of experimental work (1-6) because of their very interesting characteristics for use in electrolysis (7, 8), fuel cells (9), and batteries (10, 11). Experimental results on mechanical (2), structural (4), chemical (6, 10), and transport properties (5, 8) of Nafion membranes demonstrate that their peculiarity depends mainly on the ion sequestering structure (clusters) and swelling properties. The water content and salt up-take of the membrane exposed to electrolyte solutions are of fundamental importance for the membrane transport properties (7, 12). Among the transport coefficients, the hydraulic permeability and filtration coefficient have been less extensively studied despite the useful correlations which can be stated between them and the electroosmotic permeability, pore diameter, and solvation (13). In this paper experimental results on the hydraulic and filtration coefficients of Nafion 125, an homogeneous 5 mils thick membrane of 1200 equivalent weight, are presented. The dependence of these parameters on the applied pressure difference, salt concentration, and counterion nature is discussed.

Experimental

Membranes were activated according to the following procedure: equilibration in 0.1M HCl (~24 hr) and in boiling water (for 72 hr). Swelled membranes in the H^+ form are then equilibrated in the desired electrolyte solution until complete exchange is obtained. The hydraulic permeability (when membranes are exposed to pure water) and the filtration coefficient (when membranes are exposed to salt solutions) K_s, (both in $m^3\ N^{-1}\ sec^{-1}$ units), were determined, in a two chamber cell made of Perspex [a poly(methyl methacrylate)resin] and thermostated at 20° ± 0.5°C, by measuring the liquid meniscus displacement in a calibrated pipette (Δh) when a ΔP pressure difference is imposed between the two half-cells. The presence above and below the polymeric film of two rigid perforated stainless steel disks prevent the membrane from deforming. The two half-cells are filled with water or with identical solutions. The volume flow rate $\alpha = s\Delta h/t$ [with s (cm^2) the pipette cross section and t (sec) the experimental time interval] becomes a constant after some time, *i.e.*, a linear $s\Delta h$ *vs.* t plot is obtained. The hydraulic or filtration coefficient for a membrane of area A in cm^2 (we have assumed A = 7.08 cm^2, the geometrical membrane surface) is given by

$$K_s = (J_v/\Delta P) = (\Delta h/t)\,(s/A)/\Delta P = (\alpha/\Delta P)\,(1/A) \quad [1]$$

The independence of K_s on the applied pressure difference has been tested in the ΔP = 13.3-80.0 kPa range with all the examined NaCl solutions. Results for some of these solutions are reported in Fig. 1. The water permeability in any other system (*i.e.*, in the alkali hydroxide solutions) was measured at a fixed ΔP = 50.7 kPa value.

The filtration coefficient K_s is defined as

$$K_s = (J_v/\Delta P)_{\Delta E=0,\,\Delta C=0} \quad [2]$$

where E = electrical potential; C = concentration; J_v is the volume flow given by $J_v = \Sigma_i J_i V_i + J_w V_w$ (J_i and J_w are the fluxes of the ith species and water; V_i and V_w are partial molar volumes). Theoretically when a solution containing charged species is forced across a charged membrane, a streaming potential shows up. Therefore since $\Delta E \neq 0$, the experimental conditions of the K_s definition are not fulfilled. However, it has been demonstrated (14) that in charged membranes this contribution is less than 1% and therefore

$$(J_v/\Delta P)_{\Delta E=0,\,\Delta C=0} \cong (J_v/\Delta P)_{I=0,\,\Delta C=0} \quad [3]$$

(I = current density) and conditions $I = 0$, $\Delta C = 0$ correspond to our experimental arrangement.

It must be noted that the filtration coefficient represents also an hydraulic permeability (15) of the membrane exposed to salt solutions when the salt flow under an applied pressure is practically zero, *i.e.*

$$J_v = \Sigma_i J_i V_i + J_w V_w \cong J_w V_w \quad [4]$$

These conditions are obtained with highly charged and permselective membranes exposed to aqueous, nonconcentrated solutions (no salt up-take in the membrane phase and Donnan co-ion exclusion). In fact it is known (16) that Nafion 125 membranes are

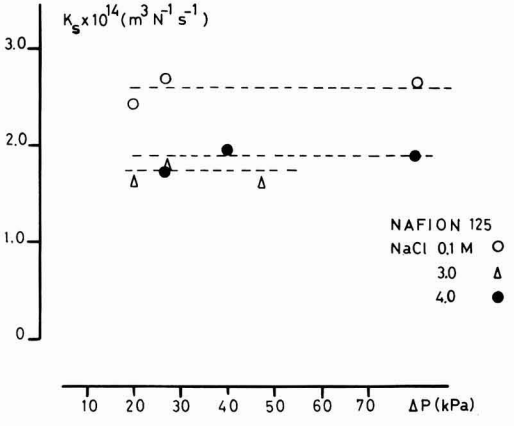

Fig. 1. Filtration coefficients, K_s, for Nafion 125 membranes in NaCl solutions at different concentrations as a function of the applied pressure difference ΔP (kPa).

Key words: applied pressure difference, salt concentration, counterion nature.

permselective in alkali chloride and hydroxide solutions for concentrations as high as 1-2M.

Results

The hydraulic and filtration coefficients, K_s, should depend on the water content of the membrane, w % (dry polymer), which is a function of the external solution concentration C (mols liter^{-1}). These effects are shown in Fig. 2 for Nafion 125 in NaCl solutions. The w % in the membrane phase was measured according to a procedure already reported (17). The pronounced decrease in K_s values above C = 1M corresponds to the observed drastic reduction in water content above this concentration (Fig. 2) which is also reflected in the decrease in cationic selectivity (t_{Na^+}, counterion transport number in NaCl solutions, decreases from C = 0.90 at 1M down to 0.72 at 4M) and electrical resistance (from 4.1 Ω-cm^2 in NaCl 1M to 2.0 Ω-cm^2 in NaCl 5.0M at 25°C) (18).

The water content and dependent membrane properties, such as the electrical resistance, depend on the counterion present in the external solution (18). This counterion dependence should also be expected in the filtration coefficient values. To show this effect the filtration coefficient in the alkali hydroxide series LiOH, NaOH, KOH, and CsOH has been measured at a fixed concentration 0.1M (Fig. 3). The K_s value still decreases as the membrane water content decreases. Moreover, as for other membrane transport properties dependent on the membrane solvation [for example the membrane resistance (7, 18)] a straight correlation between the filtration coefficient and the counterion hydration exists in Nafion membranes exposed to alkali hydroxide solutions. The correlation follows the series (Fig. 3)

$$M^+ (n_{hyd.}): \quad Li(4.25) > Na(2.9) > K(1.2) > Cs(0)$$

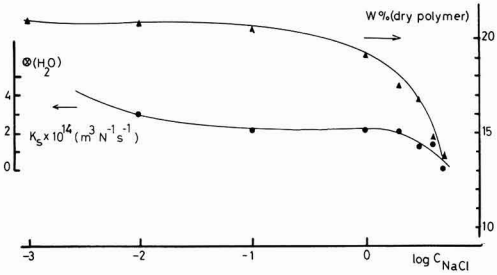

Fig. 2. Dependence of the filtration coefficient K_s and membrane water content, w % (referred to the dry polymer weight), on the salt concentration C for Nafion 125 membranes in NaCl solutions. The point x (H_2O) represents the membrane hydraulic permeability. All measurements were made at T = 20.0° ± 0.5°C.

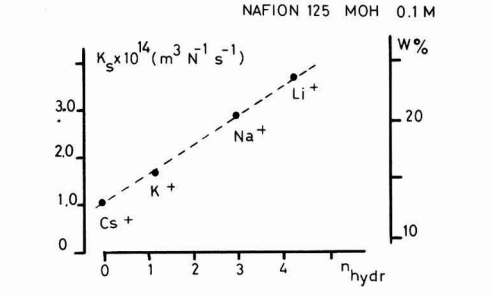

Fig. 3. Correlation between filtration coefficients and counterion hydration number, $n_{hyd.}$, for Nafion 125 membranes in alkali hydroxide 0.1M solutions at T = 20° ± 0.5°C. The membrane water content w % (referred to the dry polymer weight) is also shown.

Table I. Evaluation of the pore radius, r_p (Å) in Nafion 125 membranes by using Eq. [5]: with l = 0.013 cm and d = 47.3Å [from Ref. (20)]

Electrolyte (mols liter^{-1})		η(cP)*	$K_s \times 10^1$ (m^3 N^{-1} sec^{-1})	r_p (Å)
H_2O		1.002	5.33	7.89
NaCl	0.001	1.388	4.04	7.99
	0.010	1.424	3.17	7.57
	0.100	1.436	2.53	7.17
	1.00	1.589	2.48	7.31
	2.00	1.707	2.53	7.48
	3.00	1.974	1.79	7.12
	4.00	2.284	1.94	7.53
	5.00	2.609	0.97	6.55

* η(cP) in membrane has been calculated according to the method of Ref. (21).

[$n_{hyd.}$ are taken from Ref. (19)]. However, no difference in the filtration coefficients appears in electrolytes with a common counterion (Na^+) and different co-ions (Cl^-, OH^-) at a given concentration (0.1M). In fact K_s (NaCl 0.1M) = 2.53 × 10^{-1} and K_s (NaOH 0.1M) = 2.92 × 10^{-1} both in m^3 N^{-1} sec^{-1}.

Evaluation of membrane pore radius, r_p.— It seems interesting to evaluate the membrane pore radius from filtration coefficient data. Gierke (20) reports a pore diameter ($2r_p$) of 12Å (from water diffusion measurements) and 13Å (from hydraulic permeability data) for Nafion 120, a membrane which differs only in thickness (10 mils) from Nafion 125. These values were calculated by means of the equation (20)

$$r_p = (8/\pi l \eta K_s d^2)^{1/4} \qquad [5]$$

with l the membrane thickness (0.013 cm), K_s the hydraulic permeability, η the viscosity of the membrane interstitial solution, and d the Bragg distance between clusters in the Nafion structure. By means of Eq. [5] and the water permeabilities reported in Fig. 2 as K_s, the pore radius values for Nafion 125 in NaCl solutions in the concentration range 10^{-3}-5M have been obtained and are reported in Table I. These values do not seem to depend strongly on the membrane solvation as they change from 6.5 to 8.0Å. As compared with Gierke's data values reported in the table are very similar. In fact the two comparable quantities are 13Å (Gierke) and 2 × 7.9 = 16Å (from the K_s value reported in the table in the case of a membrane exposed to water).

From the above discussion we may conclude that the water permeability through Nafion 125 membranes depends on the membrane water content and on the electrolyte concentration. Moreover, a linear correlation between filtration coefficients and counterion hydration has been observed in the alkali hydroxide series. However, the membrane pore radius does not seem to depend on the membrane solvation.

Manuscript submitted March 15, 1982; revised manuscript received Oct. 7, 1982.

Any discussion of this paper will appear in a Discussion Section to be published in the December 1983 JOURNAL. All discussions for the December 1983 Discussion Section should be submitted by Aug. 1, 1983.

Publication costs of this article were assisted by CRE Casaccia.

LIST OF SYMBOLS

d	Bragg distance between clusters in Nafion structure (Å)
h	meniscus level in the cell capillary (cm)
l	membrane thickness (cm)
$n_{hyd.}$	counterion hydration number
r	membrane pore radius (Å)
s	capillary cross section (cm^2)
t	time (sec)
A	geometrical membrane area
C	concentration (mols liter^{-1})

J_v volume flow ($m^3 m^{-2} sec^{-1}$)
J_i, J_w fluxes of ith species and water, respectively, (mols $m^{-2} sec^{-1}$)
K_s hydraulic or filtration coefficient ($m^3 N^{-1} sec^{-1}$)
P pressure (Pa)
V_i, V_w partial molar volume of ith species and water, respectively, (cm^3)
w % water content (in weight) of the swelled membrane as referred to the dry polymer weight
α volume flow rate ($m^3 sec^{-1}$)
η viscosity of the membrane interstitial solution (cP)

REFERENCES

1. "Symposium on Fluorocarbon Ion Exchange Membranes," The Electrochemical Society Meeting, Atlanta, Georgia, Oct. 9-14, 1977.
2. A. Eisenberg and M. King, "Ion Containing Polymers," Polymer Physics, Vol. 2, R. S. Steiner, Editor, Chap. IV, pp. 162-169, Academic Press, New York (1978).
3. W. G. F. Grot, *Chem. Ind. Techn.*, **50**, 295 (1978).
4. R. S. Yeo and A. Eisenberg, *J. Appl. Polym. Sci.*, **21**, 875 (1977).
5. C. Heitner-Wirguins, in "Proceedings of the Symposium on Ion Exchange," R. S. Yeo and R. P. Buck, Editors, The Electrochemical Society Softbound Proceedings Series, Pennington, NJ (1981).
6. H. L. Yeager and B. Kipling, *J. Phys. Chem.*, **83**, 1653 (1979).
7. R. S. Yeo, J. McBreen, G. Kissel, F. Kulesa, and S. Srinivasan, *J. Appl. Electrochem.*, **10**, 741 (1980).
8. H. L. Yeager, B. Kipling, and R. L. Dotson, *This Journal*, **127**, 303 (1980).
9. R. S. Yeo, J. McBreen, A. C. C. Tseung, S. Srinivasan, and J. McElroy, *J. Appl. Electrochem.*, **10**, 393 (1980).
10. F. G. Will, *This Journal*, **126**, 36 (1979).
11. F. G. Will and H. S. Spacil, *J. Power Sources*, **5**, 173 (1980).
12. C. Fabiani, M. DeFrancesco, and L. Bimbi, Comitato Nazionale Energia Nucleare, Rome, Italy, Technical Report/Chemistry No. 10, (1979).
13. B. R. Breslau and I. F. Miller, *Ind. Eng. Chem. Fundam.*, **10**, 554 (1971).
14. Y. Kobatake, M. Yuasa, and F. Fujita, *J. Phys. Chem.*, **72**, 1752 (1968).
15. N. Lakshminarayanaiah, "Transport Phenomena in Membranes," Chap. 6, Academic Press, New York (1969).
16. B. Scuppa, L. Bimbi, M. DeFrancesco, and F. Croce, Comitato Nazionale Energia Nucleare, Rome, Italy, Technical Report/Chemistry No. 2 (1980).
17. C. Fabiani, B. Scuppa, M. DeFrancesco, and L. Bimbi, *ibid.*, No. 15 1981).
18. G. Scibona, C. Fabiani, and B. Scuppa, *J. Memb. Science*, To be published.
19. C. B. Monk, "Electrolytic Dissociation," Academic Press, New York (1961).
20. T. D. Gierke, Paper 438 presented at The Electrochemical Society Meeting, Atlanta, Georgia, Oct. 9-14, 1977.
21. B. R. Breslau and I. F. Miller, *J. Phys. Chem.*, **74**, 1056 (1970).

Cyclic Voltammetry in Solutions of Aluminum Bromide and KBr in Aromatic Hydrocarbons

II. The Behavior of Pb and Sn

M. Elam, E. Peled,* and E. Gileadi*

Institute of Chemistry, Tel Aviv University, Ramat Aviv, Israel

ABSTRACT

The electrochemical behavior of dilute solutions of $SnBr_2$ and $PbBr_2$ in a nonpolar solvent system consisting of solutions of 1.0M Al_2Br_6 and 0.80M KBr in ethylbenzene was studied. Cyclic voltammograms show well defined peaks for the deposition and dissolution of the divalent metal. Oxidation to the tetravalent state could not be detected in the available potential region. The diffusion coefficients were 1.1×10^{-6} cm^2/sec for lead and 2.7×10^{-6} cm^2/sec for tin. Lead ions inhibit the electrodeposition of aluminum while tin ions seem to have little or no effect. An overpotential associated with initial nucleation on a platinum electrode is observed for both metals and electrodeposition does not start until η reaches a value of about 30-40 mV. Formation of a thermodynamically unstable Al/Pb alloy at sufficiently cathodic potentials in solutions containing $PbBr_2$ is indicated.

In the first paper in this series (1) the surface processes taking place on three types of electrode materials (Pt, Au, and glassy carbon) were studied in solutions containing Al_2Br_6 and KBr in aromatic hydrocarbons (mostly ethylbenzene). On glassy carbon no surface phenomena were observed in the available potential region (*ca.* 1.4V in ethylbenzene) between aluminum deposition on the cathodic side and bromine evolution on the anodic side. When platinum is used as the working electrode in the same solvent, a clear anodic adsorption peak is observed, at about 1.0V *vs.* RAlE (reversible aluminum electrode in the same solution). Analysis of the peak (2-4) shows that it corresponds to the formation of a monovalent surface species, which was identified as adsorbed bromine atoms. Conductivity and transference number measurements in this system showed (5) that the ionic species existing in solution are rather complex, but a simple reaction corresponding to the transfer of a single electron per atom of bromine adsorbed on the surface can nevertheless be written (1).

The initial potential for bromine evolution was found to depend significantly on the solvent, ranging from 1.20V for mesitylene to 1.45V RAlE for benzene. Good correlation was observed (1) between this potential and the rate constant for halogenation of the solvent molecules.

The cyclic voltammograms on gold electrodes are more complex. The formation of several types of surface compounds such as $AuBr_3$, AuBr, and possibly $AuBr_4^-$ was assumed to account for the observed peaks.

In a subsequent paper (6) the behavior of iodide ions in the same type of solutions was studied, employing platinum working electrodes and a number of different solvents.

The half-wave potential for oxidation of iodide was found to be *ca.* 1.10V RAlE (compared to 2.20V RAlE in aqueous solutions). Perhaps the most striking result of these experiments is that iodine produced electrochemically (or introduced as such) can oxidize

* Electrochemical Society Active Member.

Key words: electrodeposition, overpotential, reversibility, nucleation.

bromide. The bromine liberated reacts with the solvent, shifting the equilibrium in the direction of further oxidation of bromide. This process can take place as a result of the relatively small difference in potential between iodine and bromine evolution (0.1V when mesitylene is employed as the solvent, compared to *ca.* 0.50V in aqueous solutions) and the fact that the solvent molecules act as scavengers for the bromine formed.

In the present work the behavior of $SnBr_2$ and $PbBr_2$ in solutions of Al_2Br_6 and KBr in ethylbenzene was studied. The standard reversible potentials, which are essentially equal for these two elements in aqueous solutions (1.54 and 1.53V RAlE for Pb and Sn, respectively) are different in the present solvent system (0.16 and 0.29V RAlE for Pb and Sn) and both are much closer to the reversible potential for aluminum deposition, as discussed elsewhere (1, 7, 8).

Experimental

The cell, electrodes, and electronic equipment employed for measurements of cyclic voltammograms were described in the first paper in this series (1). Potentiostatic transients were performed with a PAR Model 173 potentiostat and the currents were recorded on a Yokogawa Type 3077 X-Y-t recorder. All experiments were performed employing a Pt working electrode, unless otherwise specified.

All experiments were performed inside a glove box filled with pure argon (9, 10), in rigorously dried solutions of 1.0M Al_2Br_6 and 0.80M KBr in ethylbenzene. The methods of preparation of the solutions and the purification and drying of the compounds have been described elsewhere (1, 7, 9). Lead bromide (BDH, 98%) was dried by heating overnight at 250°C in vacuum. Stannous bromide (ROC/RIC, anhydrous 99.5%) was used without further purification. All potentials reported were measured against a reversible aluminum electrode in the same solution (RAlE).

Results and Discussion

Cyclic voltammograms for $SnBr_2$.—Typical cyclic voltammograms for a solution containing $SnBr_2$ are shown in Fig. 1 for two sweep rates. The reversible potential for tin in the same solution is 0.227V (11). The anodic peak corresponds to the oxidation of metallic Sn to Sn^{++} and has a characteristic shape corresponding to such processes, as is discussed below. A second anodic peak which would correspond to the oxidation of divalent to tetravalent tin could not be detected in the whole potential region up to bromine evolution.

The cathodic peak current $i_p(c)$ is proportional to the concentration of $SnBr_2$ up to a concentration of about 80 mM. At higher concentrations deviations occur. The same behavior was observed for $PbBr_2$ and is discussed below (cf. Fig. 5). The peak potential $E_p(c)$ changes by about 28 mV/decade for sweep rates ($v = dE/dt$) above 10 mV/sec as seen in Fig. 2. This behavior corresponds to an irreversible reaction with a Tafel slope of $2.3RT/F$ (12-14). On the other hand, $E_p(c)$ depends on the concentration of $SnBr_2$ (*ca.* 33 mV/decade) as shown in Fig. 3, as would be expected for a two-electron reversible process. The complexity of the reaction is further indicated by the fact that $i_p(c)$ is not proportional to $v^{1/2}$ and the coefficient $d \log i_p(c)/d \log v$ is about 0.36.

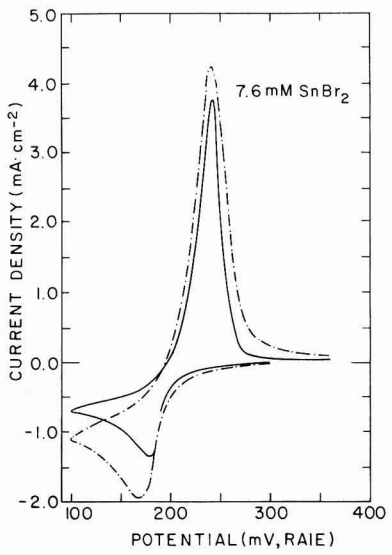

Fig. 1. Cyclic voltammogram of $SnBr_2$. Solid line: $v = 21$ mV/sec; broken line: $v = 55$ mV/sec.

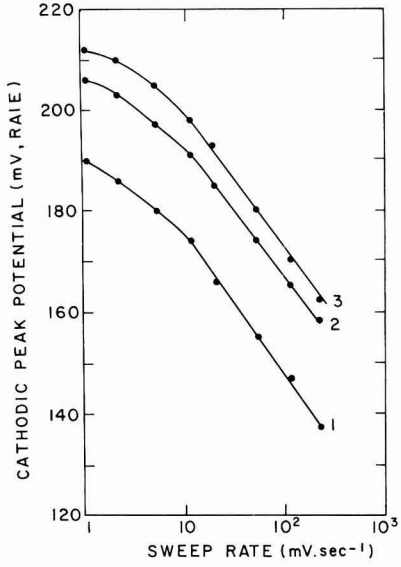

Fig. 2. Cathodic peak potential *vs.* log *(v)* for reduction of Sn^{++}. Concentration of $SnBr_2$: curve 1, 3.9; 2, 10.2; 3, 17.6 (mM).

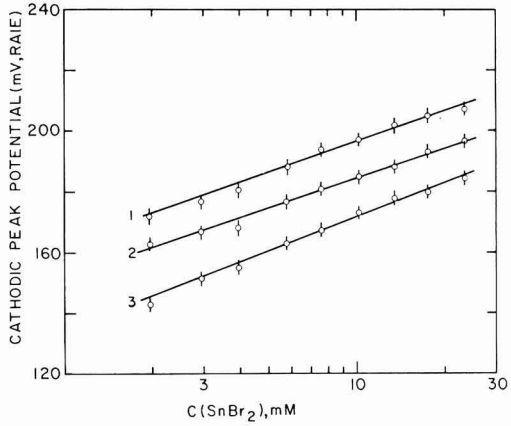

Fig. 3. Cathodic peak potential plotted as a function of log C ($SnBr_2$). Sweep rate: curve 1, 5.5; 2, 21; 3, 55 (mV/sec).

As the concentration of $SnBr_2$ was increased above 0.10M, the conductivity decreased significantly. Since $SnBr_2$ is not soluble in the pure aromatic solvent but dissolves well if aluminum bromide is added and, moreover, the conductivity of a solution of aluminum bromide in ethylbenzene is increased by several orders of magnitude on the addition of tin or lead bromide, it is reasonable to assume that these salts are complexed with aluminum bromide to form $[Sn(Al_2Br_7)_2]$, which is analogous to $[K(Al_2Br_7)]$ (5). Solution of 1.0M aluminum bromide and 0.80M KBr can accommodate no more than 0.10M tin or lead bromide before a significant change in the nature of the dissolved species must occur. This can account for the lower conductivity and also for the deviation from linearity of the $i_p(c)$ *vs.* $C(SnBr_2)$ relationship observed at higher concentrations. A similar deviation from linearity of the Nernst plots at high concentration of $SnBr_2$ and $PbBr_2$ was also observed (11).

Cyclic voltammetry for $PbBr_2$.—Two voltammograms taken in a solution containing $PbBr_2$ are shown in Fig. 4. The reversible potential for lead in this solution is 97 mV RAlE (11). Because of significant nucleation overpotential, the onset of lead deposition is delayed and the cathodic peak occurs at potentials negative to that of reversible aluminum. However, as a result of an inhibition effect, aluminum deposition does not commence in solutions containing Pb^{++} ions until much more negative potentials are reached.

The cathodic peak current is proportional to the concentration of $PbBr_2$ up to *ca.* 0.10M and then tends to level off, as seen in Fig. 5. As in solutions containing $SnBr_2$, this behavior is attributed to the fact that new types of species must be formed in solution above this concentration. These may allow deposition of the metal only at higher cathodic potentials and may have a smaller diffusion coefficient, which would explain the observed deviation from linearity in Fig. 5.

The cathodic peak potential shifts with concentration (implying reversibility) and with sweep rate (implying irreversibility) as in solutions containing Sn^{++} ions. The dependence of peak current on sweep rate is given by $(d \log i_p(c)/d \log v) = 0.41$, which deviates significantly from the value of 0.50 expected for a simple charge transfer process (12), indicating that a complex process takes place.

A second anodic peak, which would correspond to the oxidation of divalent to tetravalent lead, was not observed throughout the potential region up to bromine evolution.

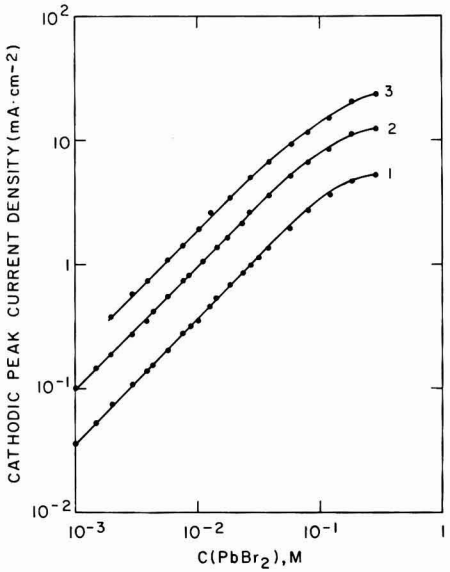

Fig. 5. Cathodic peak current density as a function of concentration of $PbBr_2$, on a log-log scale. Sweep rate: curve 1, 1.1; 2, 12; 3, 55 (mV/sec).

Aluminum deposition in the presence of $PbBr_2$.—In Fig. 6 three voltammograms, all started at +0.25V RAlE and taken under identical conditions, except for the extreme cathodic potential reached, are shown. The solid line, which ends at −50 mV RAlE (common to all three sweeps), is very similar to the voltammograms shown in Fig. 4. Aluminum deposition is completely inhibited by the presence of 2.0 mM $PbBr_2$ in solution. When the cathodic limit is extended to −70 mV RAlE, a nucleation loop, evidenced as a cathodic peak current during the anodic sweep, is clearly

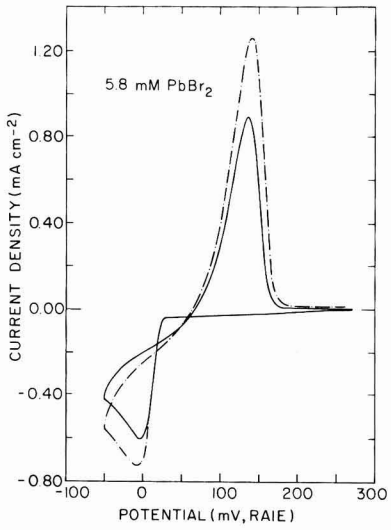

Fig. 4. Cyclic voltammogram of $PbBr_2$. Solid line: $v = 12$ mV/sec; broken line: $v = 21$ mV/sec.

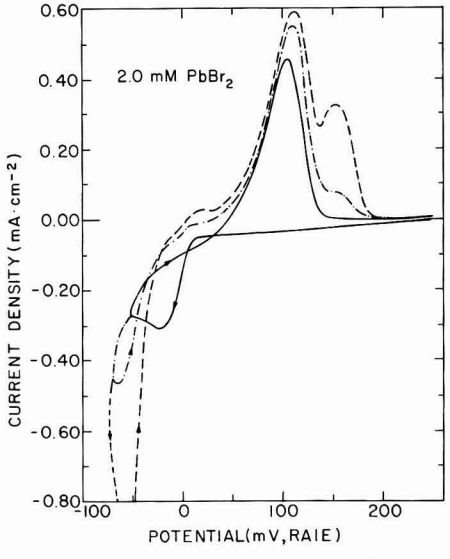

Fig. 6. Aluminum deposition and dissolution in the presence of $PbBr_2$. Sweep rate: 21 mV/sec.

seen. On the anodic branch, a small shoulder can be observed at the potential corresponding to the dissolution of aluminum (a few mV positive to zero). More significantly, a new anodic peak appears at a potential of *ca.* 0.15V, beyond the peak corresponding to the dissolution of lead. Extending the cathodic limit by a mere 5-75 mV causes a very large increase in the cathodic current, yet the aluminum dissolution peak at +10 mV stays very small. The new anodic peak at 0.15V increases fourfold while the main peak due to lead dissolution increases by less than 10%, showing that the new peak is to be associated with the dissolution of aluminum. Close examination of the voltammogram shows that, while the potential is swept anodically, lead deposition continues after aluminum deposition has stopped, so that most of the aluminum is buried under layers of lead and cannot be dissolved until most of the lead has been dissolved. The position of the dissolution peak at 0.15V probably indicates the formation of a Pb/Al alloy which dissolves anodically at a higher potential than lead itself. Although equilibrium phase diagrams show no Pb/Al alloy (15), it is well known (16-18) that supersaturation and formation of unstable phases can occur in electrodeposited alloys.

In Fig. 7 two voltammograms are shown, one in the presence of a low concentration of lead (0.5 mM $PbBr_2$) and the other in its absence.

With the sweep ending at −40 mV RAlE, cathodic deposition and anodic dissolution of aluminum are observed. The low concentration of $PbBr_2$ used clearly inhibits this process. The current loops formed in the cathodic region in Fig. 6 and 7 are characteristic of crystal growth requiring nucleation (19).

The inhibition effects discussed above were not observed in solutions containing $SnBr_2$ instead of $PbBr_2$.

Reversibility.—In metal deposition, the potential difference between the cathodic and anodic peaks cannot serve as a criterion for reversibility (20). The anodic peak depends on the amount of metal deposited in the previous cathodic sweep. This is demonstrated in Fig. 8 which shows that $i_p(a)$ increases and $E_p(a)$ moves to more positive potentials as the potential is swept to more cathodic values in the previous half-cycle, *i.e.*, as more metal is deposited.

When the dissolved metal ion is not stable in solution and must be complexed (as is the case in the present system), a diffusion limitation may be observed in the anodic peak as a result of depletion of the complexing agent near the electrode surface. Such behavior was observed for solutions containing $SnBr_2$ or $PbBr_2$, as seen in Fig. 9, where the function i/c is plotted *vs.* potential. A distinct broadening of the peak is observed at higher concentration on the descending part of the peak. The width of the peaks at half-height, $\Delta E_{1/2}$, is independent of concentration, while $\Delta E_{1/4}$ increased from 34 to 42 mV and further to 47 mV as the concentration of $SnBr_2$ is increased from 3.9 to 13.6 mM and further to 23.6 mM.

A convenient criterion for establishing reversibility in metal deposition is to examine the difference between the cathodic peak potential $E_p(c)$ and the value

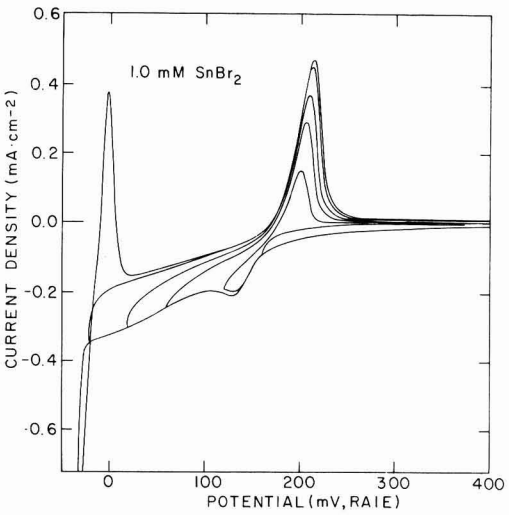

Fig. 8. The effect of the extreme cathodic potential reached on the anodic peak of Sn dissolution. Sweep rate: 12 mV/sec.

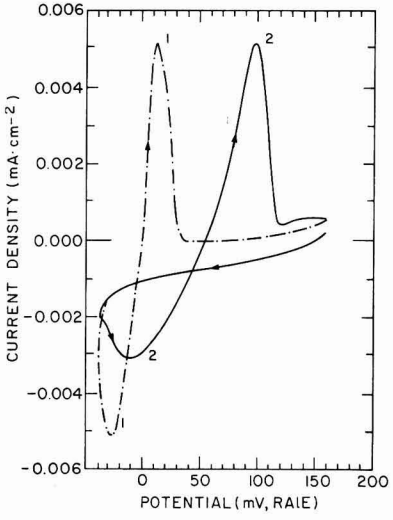

Fig. 7. The inhibiting effect of a low concentration of $PbBr_2$ on aluminum deposition. Broken line: no $PbBr_2$; solid line: 0.5 mM $PbBr_2$. Sweep rate: 1.1 mV/sec.

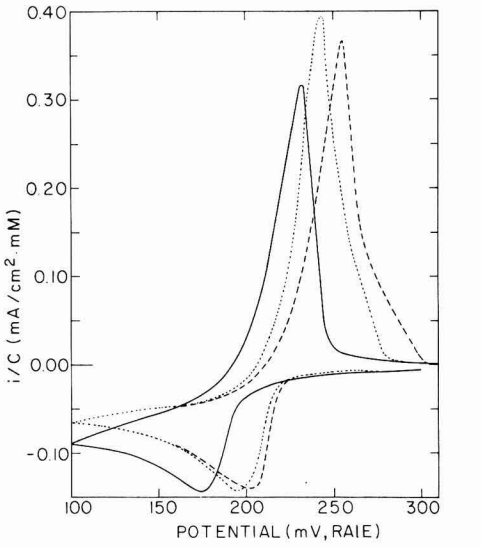

Fig. 9. Plots of the function i/C at constant $v = 12$ mV/sec for different concentrations of $SnBr_2$, showing broadening of the anodic dissolution peak due to diffusion-limitation at higher concentrations. Solid line: 3.9 mM; dotted line: 13.6 mM; broken line: 23.6 mM.

of the potential $E_{p/2}$ at $i = i_p(c)/2$. The difference

$$\Delta E = E_p - E_{p/2} \quad [1]$$

should be $-0.77RT/n\mathbf{F} = -0.020/n$ V at 25°C for the reversible deposition of an insoluble substance (21). A value of $\Delta E = 10$ mV was observed in our experiments only for solutions of $PbBr_2$ at the lowest sweep rate tested (1.1 mV/sec). Assuming reversibility, one can estimate the diffusion coefficient from the relationship (22)

$$i_p(c) = 3.67 \times 10^5 n^{3/2} D^{1/2} C^\circ v^{1/2} \quad [2]$$

The value obtained for lead at 25°C is

$$D(Pb^{++}) = (1.1 \pm 0.1) \times 10^{-6} \text{ cm}^2/\text{sec}$$

This should be compared to values of 0.8×10^{-6} and 4.0×10^{-6} cm²/sec found for Hg^{++} in mesitylene and toluene, respectively, in somewhat more concentrated solutions (Al_2Br_6 1.15M; KBr 0.76M) (23).

The viscosity of solutions of Al_2Br_6 and KBr in different aromatic solvents was studied recently in our laboratory (24, 25). The results show that the value of $D(Hg^{++})$ in toluene quoted above was taken at nearly the same viscosity as in the present system, while in mesitylene the viscosity was *ca.* 80% higher. Thus the solvation radius of Pb^{++} calculated from the relationship

$$D = kT/6\pi r\eta \quad [3]$$

is comparable to that of Hg^{++} in mesitylene (5-6Å).

The value of the diffusion coefficient for Sn^{++} could not be determined accurately but was estimated to be

$$D(Sn^{++}) = (2.9 \pm 0.6) \times 10^{-6} \text{ cm}^2/\text{sec}$$

This estimate agrees well with a value of 2.7×10^{-6} obtained from potentiostatic transients, as is shown below.

The variation of $E_p(c)$ with concentration of either $PbBr_2$ or $SnBr_2$ would indicate reversible behavior, while the dependence of $E_p(c)$ on sweep rate shows lack of reversibility (22). At the same time, the plot of log $i_p(c)$ *vs.* log v is linear over three orders of magnitude of sweep rates (0.001-1.0 V/sec), but the slope deviates significantly from a value of 0.50 predicted for a simple charge-transfer reaction. Combining the above observations suggests that a preceding or following chemical step may be involved (12). This could be the decomposition or reforming of a complex ion of the type $[Pb(Al_2Br_7)]^+$ or $[Pb(Al_2Br_7)_3]^-$ or a surface process such as adatom formation or nucleation.

Nucleation.—The deposition of a metal on a foreign substrate is often controlled by the rate of nucleation (26-30). Figure 10 shows this type of behavior for both lead and tin. Curve No. 1 is taken in both cases on a Pt electrode freshly coated with the respective metal, while curve 2 is taken on a bare Pt electrode. Deposition of lead (or tin) on Pt does not start until a significant overpotential (*ca.* 30 mV) is reached. At this point the current rises very rapidly.

A different experiment depicting the same type of phenomenon is shown in Fig. 11, where current/time transients following a potential step from 0.30V RAlE to the values marked, are plotted. At the most cathodic potential (155 mV RAlE), the current decays in a regular manner with $t^{-1/2}$. At more anodic potentials, the current on the bare Pt electrode first decreases but as soon as a sufficient layer of Sn is formed, nucleating overpotential disappears and the current rises to the value it would have on a freshly deposited Sn electrode.

This behavior is further exemplified in Fig. 12, where the shapes of the transients obtained on Pt electrodes (broken lines) are compared to those obtained on freshly deposited tin electrodes. This type of behavior has been observed before for different

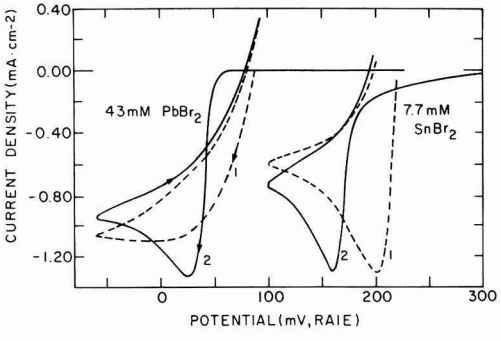

Fig. 10. Comparison of initial potential for deposition of Sn or Pb on Pt and on the respective metal. Curve 1, Pb deposited on Pb (or Sn on Sn); 2, Pb (or Sn) deposited on Pt. Sweep rate: 1.1 mV/sec for $PbBr_2$, 21 mV/sec for $SnBr_2$.

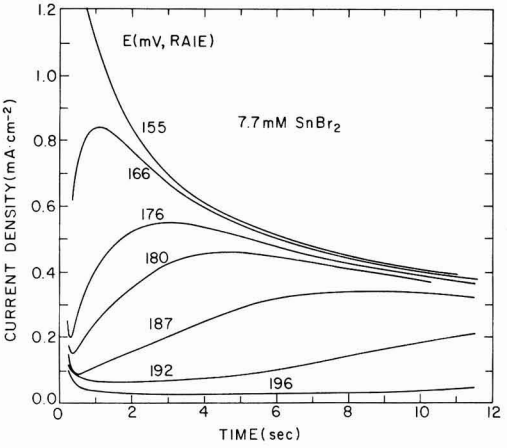

Fig. 11. Potentiostatic transients for deposition of Sn on Pt. Initial potential: +300 mV RAlE in all cases. Final potential as marked.

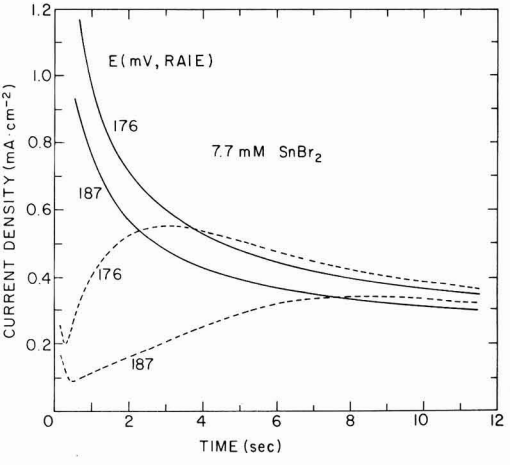

Fig. 12. Comparison of potentiostatic transients for deposition of Sn on Pt (broken line, same as in Fig. 11) and on Sn (solid line). In the latter the initial potential was the open-circuit reversible potential.

metals deposited from aqueous (26) solutions as well as from molten-salt systems (27-30) and has probably little to do with the nature of the solvent.

Replotting the uppermost curve in Fig. 11 as $1/i$ *vs.* $t^{1/2}$ yields a straight line. The diffusion coefficient of tin calculated from the slope is 2.7×10^{-6} cm²/sec, in excellent agreement with the value of $(2.9 + 0.6) \times 10^{-6}$ cm²/sec obtained above from cyclic voltammograms.

Conclusions

Lead and tin can be deposited from solutions of Al_2Br_6 and KBr in ethyl benzene and similar aromatic hydrocarbons. In the presence of lead, aluminum deposition is inhibited and does not occur until an overpotential of *ca.* −70 mV is reached.[1] Tin, which is deposited at a more anodic potential, does not exert a similar inhibition effect.

The anodic peak depends on the amount of metal deposited in the previous cathodic half-cycle and cannot be used to analyze the course of the reaction. When the potential is allowed to reach a sufficiently cathodic potential to deposit aluminum in the presence of lead, a second anodic peak appears, which can probably be associated with the formation of an Al/Pb alloy.

On platinum electrodes a nucleation process takes place and deposition of both Sn and Pb requires a threshold overpotential of *ca.* 30 mV for deposition to start. The diffusion coefficients of lead and tin were found to be 1.1×10^{-6} and 2.7×10^{-6} cm²/sec, respectively, as compared to a value of 4.0×10^{-6} cm²/sec for mercury in solutions of toluene of nearly the same viscosity (23-25).

Acknowledgments

Financial support by the "Foundation for Industrial-Applied Research at the Universities" of the Planning and Grants Committee of the Council for Higher Education is gratefully acknowledged.

Manuscript submitted June 7, 1982; revised manuscript received Sept. 20, 1982.

Any discussion of this paper will appear in a Discussion Section to be published in the December 1983 JOURNAL. All discussions for the December 1983 Discussion Section should be submitted by Aug. 1, 1983.

[1] The potential at which Al deposition starts moves to more negative values as the concentration of lead is increased. The value of −70 mV RAlE was observed for a concentration of 2.0 mM $PbBr_2$.

REFERENCES

1. M. Elam and E. Gileadi, *This Journal*, **126**, 1474 (1979).
2. S. Srinivasan and E. Gileadi, *Electrochim. Acta*, **11**, 321 (1966).
3. E. Gileadi and B. E. Conway, in "Modern Aspects of Electrochemistry," Vol. III, J. O'M. Bockris and B. E. Conway, Editors, Chap. 5, Butterworths, London (1964).
4. H. Angerstein-Kozlowska, J. Klinger, and B. E. Conway, *J. Electroanal. Chem. Interfacial Electrochem.*, **75**, 45 (1977).
5. A. Reger, E. Peled, and E. Gileadi, *J. Phys. Chem.*, **83**, 869, 874 (1979).
6. M. Elam and E. Gileadi, *This Journal*, **127**, 815 (1980).
7. E. Peled, A. Mitavski, A. Reger, and E. Gileadi, *J. Electroanal. Chem. Interfacial Electrochem.*, **75**, 677 (1977).
8. E. Gileadi, "Proceedings of 3rd Symposium on Electrode Processes," S. Bruckenstein, J. D. E. McIntyre, B. Miller, and E. Yeager, Editors, p. 366, Boston (1979).
9. A. Reger, E. Peled, and E. Gileadi, *This Journal*, **123**, 638 (1976).
10. S. Ziegel, E. Peled, and E. Gileadi, *Electrochim. Acta*, **23**, 363 (1978).
11. M. Elam, E. Peled, I. Bahatt, and E. Gileadi, In preparation.
12. R. S. Nicholson and I. Shain, *Anal. Chem.*, **36**, 706 (1964).
13. E. Gileadi, E. Kirowa-Eisner, and J. Penciner, "Interfacial Electrochemistry—An Experimental Approach," pp. 109-111, Addison-Wesley Publishing Co., Reading, MA (1975).
14. P. Delahay, "New Instrumental Methods in Electrochemistry," pp. 115-129, Interscience Publishers Inc., New York (1954).
15. M. Hansen and K. Anderko, in "Constitution of Binary Alloys," 2nd ed., p. 122, McGraw-Hill, New York (1958).
16. A. Brenner, in "Electrodeposition of Alloys," Vol. I, pp. 195-198, Academic Press, New York (1963).
17. K. M. Gorbunova and Yu. M. Polukarev, in "Electrodeposition of Metals and Alloys," N. E. Khomutov, Editor, p. 28, Israel Prog. Sci. Translations, Jerusalem (1969).
18. E. Raub, *Metalloberflache*, **7A**, 17 (1953).
19. J. N. Jovicevic, A. R. Despic, and D. M. Drazic, *Electrochim. Acta*, **22**, 577 (1971).
20. N. White and F. Lawson, *Electroanal. Chem.*, **26**, 113 (1970).
21. G. Mamantov, D. L. Manning, and D. M. Dale, *J. Electroanal. Chem. Interfacial Electrochem.*, **9**, 253 (1965).
22. T. Berzins and P. Delahay, *J. Am. Chem. Soc.*, **75**, 555 (1953).
23. E. Peled, A. Mitavski, and E. Gileadi, *Z. Phys. Chem.*, **98**, 111 (1975).
24. E. Peled, M. Brand, and E. Gileadi, *This Journal*, **128**, 1697 (1981).
25. E. Peled and E. Gileadi, in Proceedings of 1st International Symposium on Electrodeposition of Aluminum, G2, American Electroplaters Society, Boston, June 1981.
26. G. J. Hills, D. J. Shiffrin, and J. Thompson, *Electrochim. Acta*, **19**, 657 (1974).
27. B. Gilbert, G. Mamantov, and K. Fung, *Inorg. Chem.*, **14**, 1802 (1975).
28. P. Roland and G. Mamantov, *This Journal*, **123**, 1299 (1978).
29. C. L. Hussey, L. A. King, and J. K. Erbacher, *ibid.*, **125**, 50 (1978).
30. C. L. Hussey, L. A. King, and R. A. Carpio, *ibid.*, **126**, 1029 (1979).

Application of the "Swiss-Roll" Electrolysis Cell in Vitamin-C Production

P. M. Robertson*

Technisch Chemisches Labor, Swiss Federal Institute of Technology, 8092 Zurich, Switzerland

P. Berg and H. Reimann

F. Hoffmann-LaRoche Limited, Grenzach, Germany

and K. Schleich and P. Seiler

F. Hoffmann-LaRoche and Company Limited, 4002 Basel, Switzerland

ABSTRACT

The "Swiss-roll" cell was developed in 1973. This paper is concerned with the most important application of the cell; the oxidation of DAS to DAG, which is one of the steps in the synthesis of vitamin-C. For proprietary reasons the details of this work have not been divulged until now. Because of the differing factors involved, but more especially to give an insight into how the project developed, the material is presented in more or less chronological order.

Origin of the "Swiss-Roll" Design

The development of cell designs to make use of new materials took on a surge of activity in the 70's, mostly due to the impetus of the Southampton and Newcastle schools. An effort in this direction was needed since it was true to say that much of the resistance to organic electrosynthesis stems from the unsuitability of existing electrolysis cells or electrodes, mostly because of economics. The design of the "Swiss-roll" electrolysis cell came as a result of a consideration of electrode materials and also the electrode reaction rate. Up to that time, apart from a few isolated examples, the most commonly used electrode materials for anodes were platinum, graphite, or lead dioxide. These materials all have some disadvantages. Platinum is very expensive, graphite often undergoes severe erosion, and PbO_2 is also prone to stability problems. In contrast to many other materials they are all stable in acidic solutions. There are, however, many processes that can be carried out in alkaline solution, in which some very inexpensive metals are quite stable.

The Pourbaix diagrams for copper and nickel show that in the alkaline range and anodically polarized the oxides are the stable form present. These oxides are electronically conducting. In 1971 our attention was caught by the publication of Fleischmann *et al.* on the oxidation of alcohols and amines at nickel anodes in KOH (1). Although this was to be expected on the basis of early literature [Fichter (2)], it was seen as a confirmation that useful results could be obtained with inexpensive materials.

The oxidation of amines to nitriles, primary alcohols to acids, and secondary alcohols to ketones were all shown to give almost quantitative yields even before optimization of the oxidation conditions (Table I). The mechanism of the oxidation was proposed to go through a nickel (III) species which acts as a hydrogen abstractor

$$Ni(OH)_2 + OH^- \rightleftharpoons NiOOH + H_2O + e$$

$$NiOOH + R_1R_2CHOH \rightleftharpoons Ni(OH)_2 + R_1R_2\dot{C}OH$$

$$R_1R_2\dot{C}OH \xrightarrow{\text{further oxidation}} \begin{cases} \text{primary alcohol} \rightarrow \text{acid} \\ \text{secondary alcohol} \rightarrow \text{ketone} \end{cases}$$

The organic compound is thereby oxidized and the nickel (III) species reduced back to $Ni(OH)_2$ which at a suitable potential (~400 mV *vs.* Ag/AgCl) is immediately reoxidized to nickel (III). The nickel hydroxide is formed as a thin film on a nickel surface when placed in an alkaline solution. This film is stable as well as the oxidized form under normal conditions. Corrosion problems, however, occur with "obvious" agents such as chloride ions.

The oxidation rates measured by Fleischmann were found to lie well under the diffusion-controlled limit. The rate-controlling step was therefore the hydrogen atom abstraction. The oxidation currents for 0.1M substrates at polished nickel electrodes were well under 1 mA/cm^2.[1] This implies a factor of about 100 or more under the limiting current. This has very negative implications for a proposed industrial synthesis, since for operation at such a current density an excessively high electrode area would be needed (Table II). Despite the originally reported low oxidation rates, the oxidations with nickel anodes were regarded as important enough to warrant the development of a compact cell based on nickel sheet electrodes. The cell that

[1] Later work showed that the pretreatment of the anode allows significant higher current densities to be attained. Other factors that can increase the current are a higher substrate concentration and a higher temperature.

Table I. Percent current yield of products from the anodic oxidation of organic substrates at a nickel anode in 1M KOH

Substrate	Product*
n-Propylamine	Ethyl cyanide (84), propionaldehyde (11)
n-Butylamine	Propyl cyanide (85), n-butyraldehyde (6)
Ethanol	Acetic acid (98)
Propanol	Propionic acid (95)
Isopropanol	Acetone (90)

* Percent current yield in parentheses.

Table II. Anodic oxidation of alcohols

Substrate	Current for 0.1M substrate in 0.87M KOH at polished Ni (mA/cm^2)	Electrode area for production of 1 ton/day (m^2)
Methanol	0.24	29,100
Ethanol	0.34	14,300
n-Propanol	0.21	17,700
Isopropanol	0.08	46,500
Sec-butanol	0.07	43,100

* Electrochemical Society Active Member.

evolved was not far removed from the form of the nickel sheet received from the supplier, a roll. The electrochemical cell took the form of a rolled-up sandwich and thereby had a form very similar to that of the "Swiss-roll," the English name for the pastry shown in Fig. 1. (Incidentally, building instructions are widely available in books other than electrochemical ones!) The electrochemical equivalent of this structure is shown schematically in Fig. 2.

The main components of the "Swiss-roll" electrolysis cell are: two separator cloths, 1, which serve to electrically isolate the anode, 2, and cathode, 3, from each other and also to provide an electrolysis chamber. These layers are arranged as a sandwich, rolled up around an axis (often acting as a current feeder to one of the electrodes), and pressed into a cylindrical container with the necessary inlet and outlet for the electrolyte, which is pumped through. The main properties of the cell are a high specific electrode area, a very high mass transfer rate, constructional simplicity, and ease of scale-up. This then was the basic "Swiss-roll" cell as used in the laboratories at the ETH for the oxidation of organic substrates (3). At about the same time Williams and co-workers at du Pont had developed a very similar "Jelly-roll" cell (4). In future work (1975-1980) the components of the cell were studied in some detail and even new concepts in cell construction developed (5).

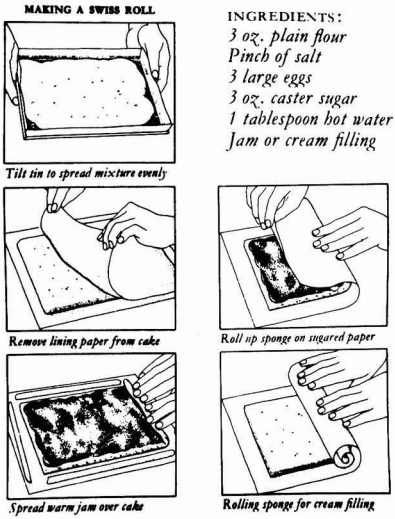

Fig. 1. The "original" "Swiss-roll" with "building" instructions!

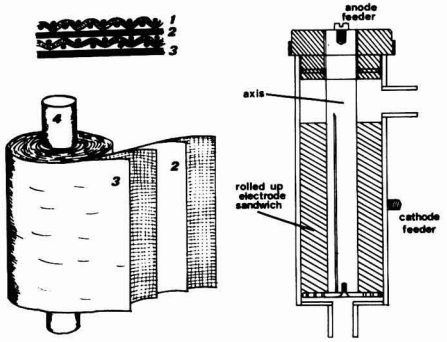

Fig. 2. The "Swiss-roll" electrolysis cell. The main components are: 1, separator net; 2, anode sheet; 3, cathode sheet.

As shown in Fig. 3 there are various components that can be incorporated into the "Swiss-roll" cell: sheet or net electrodes (6-8), turbulence promoting separator cloths (9), and "convection dampers" to reduce the extent of diffusion-controlled loss reactions at the counterelectrode (10, 11). So much for the developments that followed. Back in 1973 the "Swiss-roll" cell had merely been used to repeat the results of Fleischmann with alcohols and amines, which for industry were of little importance. The reaction that turned out to be the launching pad for the "Swiss-roll" cell was a step in the synthesis of vitamin-C.

Application of the "Swiss-Roll" Cell in Vitamin-C Synthesis

This industrial process is carried out on the scale of several 10,000 tons per year world-wide. It is a six step process (scheme 1). The first step, a hydrogenation, was carried out electrochemically between 1937 and 1948 (12) but is now superseded by a catalytic reaction. It was, however, the fourth step that was for us of interest. This is the oxidation of a primary alcohol to a carboxylic acid. The publication that turned our attention to it was that of Vertes *et al.* (13). They showed that high yields could be obtained by the direct electrolytic oxidation at nickel. Preliminary experiments with the "Swiss-roll" cell indeed confirmed the results of Vertes. A 95% material yield of diacetone-2-keto-L-gulonic acid (DAG) was obtained in an 11 batch oxidation of 10% diacetone-L-sorbose (DAS) in 1M KOH electrolyte.

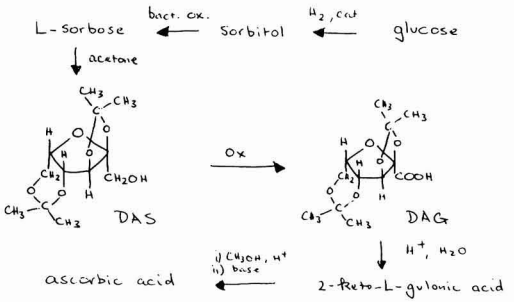

Scheme 1

The current industrial processes for the oxidation of DAS to DAG are a catalytic air oxidation or a sodium hypochlorite oxidation. Looking more closely at the sodium hypochlorite route in Fig. 4 it is obvious that it is similar to the direct electrolytic route in that an electrolysis step is involved as well as a nickel catalyst. The sodium hypochlorite oxidation may therefore be regarded as a very indirect electro-oxidation.

A comparison of both routes involving nickel would, at least in terms of the number of process steps in-

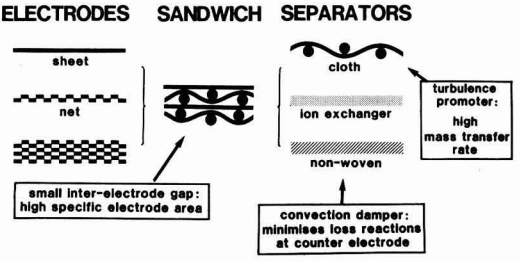

Fig. 3. Building blocks of the electrode sandwich

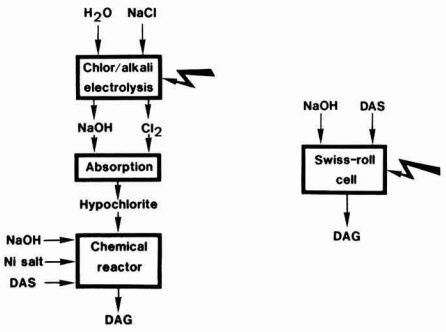

Fig. 4. Industrial routes for the oxidation of DAS to DAG. Left: hypochlorite oxidation with Ni catalyst; right: direct electro-oxidation at a nickel anode.

volved, appear to come out in favor of the direct electrochemical oxidation. At this stage of the work Hoffman-LaRoche showed an interest and thereafter carried out the bulk of the work on the direct electrolytic oxidation of DAS and the scale-up of the "Swiss-roll" cell to production size.

The work at the ETH concentrated on investigating various aspects of the behavior of nickel anodes and the mechanism of the oxidation of organic substrates at them. This served in most cases as confirmation of the results being obtained in Basel. For this work we were particularly fortunate in having a computerized instrument which allowed complex testing programs to be run (often simultaneously with 6 electrolysis cells). The main features of it are shown in Fig. 5. It is composed of a PAR polarograph which had been modified for remote control, an HP IEEE-interface and digital plotter and a Commodore PET "home" computer.

Questions of importance for the synthesis in Basel, such as "what is the best pH to oxidize at?," "what conditions lead to corrosion of the electrodes?," or "what are the factors having an influence on the activity of the electrodes?" were answered with the help of this equipment. The reinvestigation of the oxidation of organic compounds at nickel anodes in fact revealed some features that had not previously been reported.

Current/potential plots as a function of pH showed that the oxidation rate was not independent of pH as reported by Fleischmann, but a linear function of c_{OH^-} up to a critical c_{OH^-} beyond which the oxidation rate of the alcohol remained constant. In Fig. 6 the well-known features of the nickel electrode in alkaline solution are visible, namely, the oxidation of the $Ni(OH)_2$ to NiOOH at about 450 mV and its back reduction at 350 mV (here the computer was programmed so as to separate the forward and reverse scans, although they were obtained without any pause between). The linear dependence of the current on c_{OH^-}, its diffusion-controlled characteristic at lower c_{OH^-} values, and the formation of a steady-state oxidation peak beyond the diffusion-controlled region (kinetic control-hydrogen abstraction) came as a surprise (14).

The practical significance of these results was, in the first instance, to define the minimum OH^- concentration necessary to achieve the maximum limiting oxidation rate for a given DAS concentration. The results are summarized in Fig. 7, which shows the peak oxidation current as a function of c_{OH^-} for various DAS concentrations. The linear portion of the curve had more or less the same slope regardless of substrate or its concentration. Apparently in this region the oxidation is limited by the flux of OH^- to the electrode. These currents were diffusion-controlled as substantiated by rotating disk electrode experiments. The magnitude of the currents corresponded to those expected for a diffusion of the OH^-.

With regard to the oxidation rate, Vertes in his experiments prepared the nickel anodes by cathodic deposition of a nickel hydroxide layer from a solution of a nickel salt. By this means thick layers of hydroxide may be built up, which are apparently porous and offer a large active area for the oxidation of DAS to DAG. Much higher current densities may thereby be attained. We have also investigated this, in fact the data in the last two figures were obtained at "thick" nickel oxide electrodes.

Figure 8 compares electrodes that have been pretreated by varying amounts. Again the peak current for the oxidation of the organic substrate (in this case ethanol) is plotted as a function of c_{OH^-}. Longer deposition times give a thicker $Ni(OH)_2$ layer which is immediately obvious from the height of the peak for

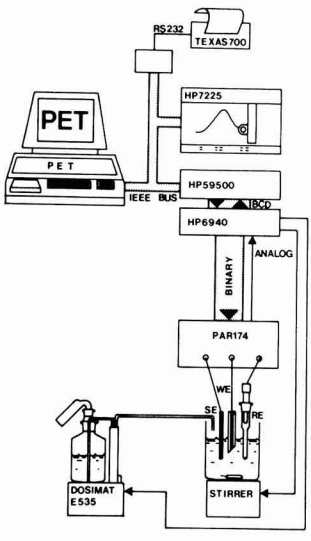

Fig. 5. Schematic of the computer-controlled instrumentation used for the study of the nickel anode behavior and the oxidation kinetics of DAS.

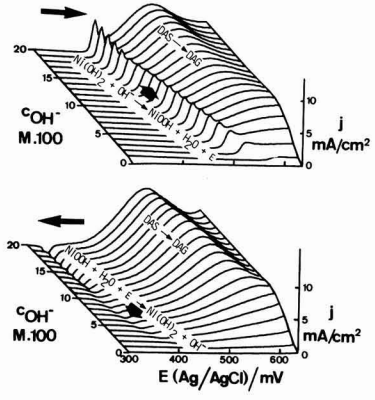

Fig. 6. Current potential sweep measurements for the oxidation of DAS at a nickel anode. Top: forward scan; bottom: backward scan (both at 5 mV/sec) at several different hydroxyl ion concentrations.

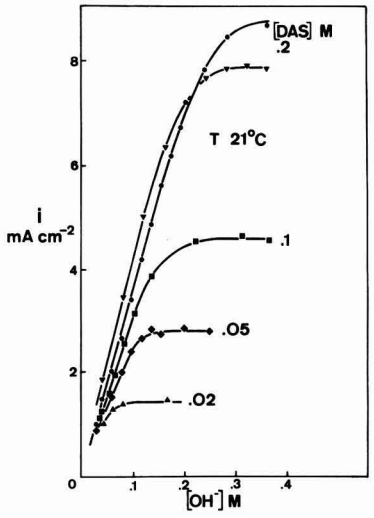

Fig. 7. Peak current for the oxidation of DAS on an etched nickel anode at various concentrations as a function of hydroxyl concentration.

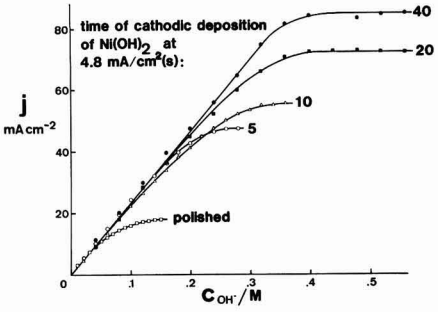

Fig. 8. Activity of a nickel oxide electrode as a function of the oxide layer thickness and hydroxyl concentration as manifest by the peak oxidation current for 0.17M EtOH. The following electrode pretreatments were employed: (a) polished; (b) 5 sec cathodic deposition of nickel at 4.8 mA/cm² from a 0.1M $Ni(NO_3)_2$ solution; (c) 10 sec; (d) 20 sec; (e) 40 sec.

the oxidation of Ni(II) to Ni(III) and from the increased activity for the oxidation of the organic substrate. Current increases of the order of about 10 (in comparison to the polished electrode) may be realized.

Scale-Up of the Process in Size and Time

In the meantime Roche had advanced to a somewhat larger synthesis setup with a "Swiss-roll" cell of area 3 m² and radial electrolyte flow. This equipment, which allowed continuous operation, is shown schematically in Fig. 9. The main features are: centrifugal pump, rotameter, mono-polar "Swiss-roll" cell, heat exchanger, electrolyte reservoir, and oxygen meter.

At first, batch experiments were carried out with a 12 liter charge of 10% DAS solution. About 500g of DAG could be prepared per hour. During the reaction only NaOH was added to maintain constant *p*H. In order to determine the behavior of the system over long periods of time, the first continuous experiment was planned. It was intended to run the experiment for 100 hr from Monday to Friday. The first phase of the experiment went very satisfactorily. After 5 hr a steady state was reached and all experimental parameters such as DAS, DAG, and NaOH concentration,

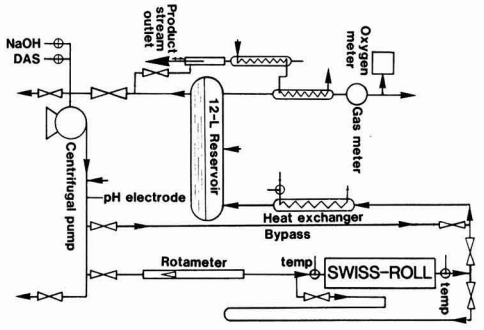

Fig. 9. Schematic diagram of flow system used for the batch and continuous oxidation of DAS with a "Swiss-roll" cell with anode area of 3 m².

current, cell potential, and oxygen content in the vent gas stayed constant. On the recorder hours and hours of straight lines were registered so that one almost had to fight against boredom. However, after 40 hr the anode became progressively deactivated, the degree of oxidation sank as well as the current and selectivity. The scale-up in time had encountered the first problems. The answer to this problem was luckily already at hand from previous work by Roche in Nutley and more recently published confirmation by Fioshin and co-workers who in the first half of the 70's were also working intensively on the electrolytic oxidation of DAS (15). The addition of catalytic amounts of a nickel salt effectively suppressed the deactivation. This phenomenon was studied at the ETH to define more precisely, using instrumental methods, the conditions leading to and the extent of the problem. These results confirmed those of Roche which were based more on the preparative experiments. The electrode activity was ascertained from current/potential curves obtained periodically during an electrolysis of DAS at 530 mV. The observations from the preparative experiments were confirmed (Fig. 10): the decrease of the peak height for DAS oxidation and the increased rate of oxygen production.

The addition of a small amount of nickel brought a stable activity to the nickel anode and, more strikingly, complete inhibition of oxygen evolution. The results shown in Fig. 11 are in the first 3 hr life of the electrode. The positive effect of the nickel salts was also confirmed over a 60 hr period (Fig. 12). Passivation would always set in if a nickel-free electrolyte was employed. In the diagram the results of such a test are also shown. After 60 hr successful

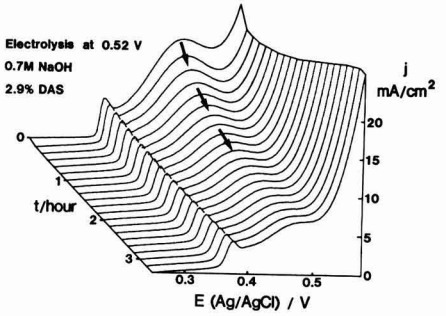

Fig. 10. Current/potential sweeps obtained during the electrolysis of DAS at 520 mV (*vs.* Ag/AgCl) as a function of electrolysis time. Note the decrease of DAS oxidation current and the increase (at end of scan) of the oxygen evolution.

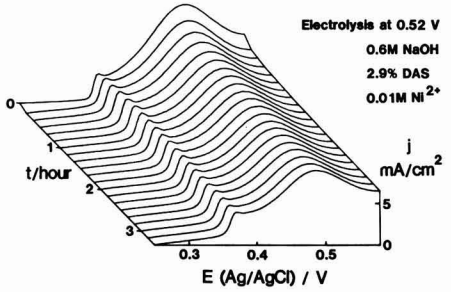

Fig. 11. As for Fig. 10 except that the electrolyte contains 10 mM nickel salt. The loss of electrode activity for the oxidation of DAS is not observed.

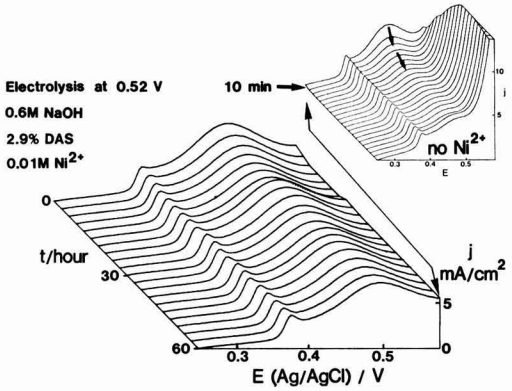

Fig. 12. As for Fig. 11 except over an extended electrolysis time of 60 hr. The insert figure shows the behavior of the 60 hr old electrode when the electrode is changed to no-nickel composition, the electrode deactivates.

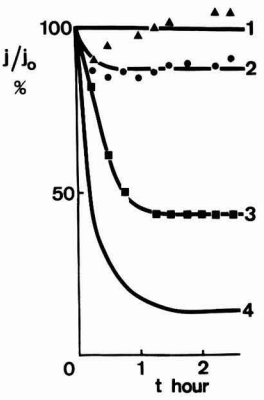

Fig. 13. Peak oxidation current normalized with respect to the initial value (new electrode) for the electro-oxidation of a 10% DAS solution in 0.1M NaOH as a function of time for different concentrations of nickel. 1, 1 mM; 2, 0.1 mM; 3, 0.01 mM; 4, 0.

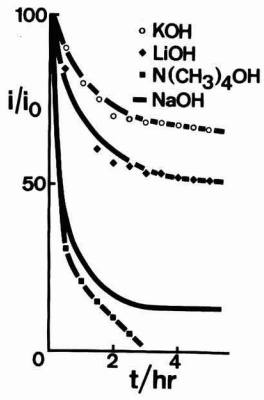

Fig. 14. Peak oxidation current normalized with respect to the initial value (new electrode) for the electro-oxidation of a 10% DAS solution in 0.1M NaOH as a function of time for different support electrolytes.

operation in a nickel-containing electrolyte, the solution was changed to a nickel-free system and immediately the passivation, typified by a decrease of the DAS oxidation current and the onset of oxygen evolution, set in. A restoration of the original state proceeded only partly on addition of a nickel salt.

Because the solubility of nickel salts in such an alkaline solution is low it is to be expected that small amounts of nickel are sufficient to bring the beneficial effect. The activity of nickel anodes is expressed in Fig. 13 as the peak current for DAS oxidation normalized with respect to its initial value. It is plotted as a function of time for different values of the total nickel concentration. Already at 0.001M the problem of passivation is solved.

Interestingly the cation of the support electrolyte also influences the passivation behavior. In Fig. 14, which is similar to the previous, the effect of the cation of the support electrolyte (in the absence of a nickel salt) on the anode activity is shown. Potassium gives the least loss of activity, while a quaternary ammonium salt is the most serious offender.

All of the observations obtained here on the oxidation of DAS at nickel, of course, have implications on the reaction mechanism. It appears doubtful that the Ni(III) species is really the active species since the oxidation occurs in the range where Ni(III) is oxidized further, and cations are incorporated into the oxide film (perhaps explaining the sensitivity of the electrodes to cations and the observed passivation effects).

During this phase two complex questions had to be answered in Basel: (*i*) the process conditions for optimal operation (yield, current efficiency, energy consumption per kilo DAG, NaOH consumption as a function of the current density, temperature, NaOH concentration, pumping rate and so on, and (*ii*) the reaction conditions that led to a drop in yield! The latter seems to be a strange form of occupational therapy but, in fact, it was of considerable importance to define to the production engineers conditions that were to be avoided. The process, in fact, turned out to be extremely uncritical. In the continuous operating mode with recycling of the electrolyte a high conversion of DAS to DAG can only be realized with minimum electrode area when a cascade of reactors is operated in series. The next stage of the piloting was therefore to simulate a two-stage cascade of reactors. In this test the processed solution from a first pass in which a 90% conversion had been obtained was collected and then with conditions simulating a second stage re-electrolyzed to 99% conversion. The electrolysis conditions and the results obtained are given in Table III. In long-term experiments these conditions could be realized for several weeks.

Scale-Up to the Commercial Cell Size

The work in Basel was more or less complete. The development of the "Swiss-roll" cell and the process

Table III. Oxidation of DAS in mini-pilot plant

	Stage 1	Stage 2	Total
Current, A	120	18	
Cell potential, V	2.2	1.9	
NaOH conc, M	0.3	0.2	
Degree of oxidation, %	90	99	99
DAG production rate, kg/hr			0.26
Energy requirement, kW-hr/kg			1.2
Current efficiency, %			70
Isolated yield, %			93

for the oxidation of DAS was then transferred to Grenzach (the site of Roche Vitamin-C production in Europe). At first a "Swiss-roll" cell of anode area 30 m^2 was put into service (Fig. 15). The results obtained in the laboratory were reproduced or even bettered. The performance of bipolar "Swiss-roll" cells was also successful. The electrolytically produced DAG matched all production requirements and passed all quality controls. As a result a full scale unit was constructed, whereby through replication a production capacity of several thousand tons per year could be realized. The principles of the mini-pilot plant could be carried over to the large system with very little modification. The main features of the large plant were several bipolar "Swiss-roll" cells operating in a cascade at currents from 20 kA down in steps to 1 kA. Each "Swiss-roll" had several hundred m^2 anode area. One of these units is shown in Fig. 16. With this oxidation stage more than 2 tons of DAG could be produced daily. The cells have already been operating successfully for several thousand hours. A close investigation of the electrodes and the separator nets revealed that no corrosion had occurred.

Conclusions

The direct electrolytic oxidation has already been compared with the hypochlorite route. What can be said now that the process has been brought to the production stage? Although the production costs for the two routes do not greatly differ, the electrochemical route uses less electrical energy (mainly on account of the lower cell voltage of 2V in comparison to the 4V of a chlor/alkali electrolysis) and gives less NaCl-loaded waste water.

In terms of the criteria that are often used to point to profitable electrochemical routes, the DAS/DAG oxidation involves: (*i*) fewer processing steps, (*ii*) a product is produced on the anode and on the cathode (H_2 is used in the hydrogenation of the glucose), (*iii*) few scale-up difficulties were encountered, (*iv*) the stability of the electrodes was tolerable, (*v*) the electrolyte conductivity was high, (*vi*) DAS and DAG are very soluble in the electrolyte, (*vii*) there is no need for an expensive supporting electrolyte, and (*viii*) there was no special requirement for the feedstock and the product work-up was as for the conventional process.

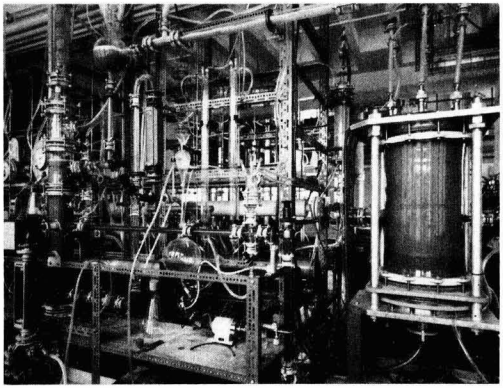

Fig. 15. Pilot-plant with 30 m^2 "Swiss-roll" electrolysis cell (left) for the continuous oxidation of DAS.

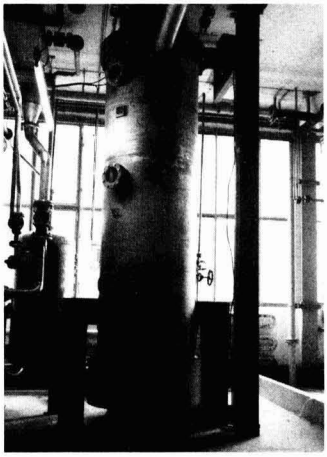

Fig. 16. One of the commercial size "Swiss-roll" cells used by Roche in a cascade of reactors for the production of 2 ton/day DAG.

Manuscript received July 16, 1982. This was Paper 586 presented at the Montreal, Quebec, Canada, Meeting of the Society, May 9-14, 1982.

Any discussion of this paper will appear in a Discussion Section to be published in the December 1983 JOURNAL. All discussions for the December 1983 Discussion Section should be submitted by Aug. 1, 1983.

Publication costs of this article were assisted by the Swiss Federal Institute of Technology.

REFERENCES

1. M. Fleischmann, K. Korinek, and D. Pletcher, *J. Electroanal. Chem. Interfacial Electrochem.*, **31**, 39 (1971).
2. F. Fichter, "Organische Elektrochemie," Steinkopff, Leipzig (1942).
3. P. M. Robertson, F. Schwager, and N. Ibl, *J. Electroanal. Chem. Interfacial Electrochem.*, **65**, 883 (1975); P. M. Robertson (Assignee: Roche) U.S. Pat. 4,040,938; P. M. Robertson (Assignee: Roche) U.S. Pat. 4,097,346.
4. J. M. Williams, U.S. Pat. 3,859,195 (to E. I. du Pont de Nemours).
5. P. M. Robertson, P. Cettou, D. Matic, F. Schwager, A. Storck, and N. Ibl, *AIChE Symposium Series No. 185*, **75**, 115 (1979).
6. P. Gallone, P. L. DeAnna, and P. L. Bonora, *Mater. Chem.*, **3**, 285 (1978).
7. A. Storck, P. M. Robertson, and N. Ibl, *Electrochim. Acta*, **24**, 373 (1978).
8. B. Scholder, ETH Dissertation, In preparation.
9. F. Schwager, P. M. Robertson, and N. Ibl, *Electrochim. Acta*, **25**, 1655 (1980).
10. D. Matic, P. M. Robertson, and N. Ibl, *ibid.*, **25**, 487 (1980).
11. P. M. Robertson, R. Oberlin, and N. Ibl, *ibid.*, **26**, 941 (1981).
12. C. L. Mantell, "Electro-organic Chemical Processing," Noyes Development Corp., Park Ridge, NJ, p. 147 (1968).
13. G. Horanyi, G. Vertes, and F. Nagy, *Acta Chim. Acad. Sci. Hung.*, **67**, 357 (1971).
14. P. M. Robertson, *Electrochim. Acta*, **22**, 411 (1977).
15. T. E. Mulina, I. A. Avrutskaya, M. Ya. Fioshin, and T. A. Malakhova, *Sov. Electrochem.*, **10**, 467 (1974); M. Ya. Fioshin, I. A. Avrutskaya, T. A. Malakhova, and T. E. Mulina, *ibid.*, **10**, 760 (1974); I. A. Avrutskaya, M. Ya. Fioshin, T. E. Mulina, and T. A. Arkhinova, *ibid.*, **12**, 1176 (1976).

Electrochemical Determination of Cation Radical Stabilities of Monomethylbenzo[a]pyrenes

Donald A. Tryk,* Su-Moon Park,* and Guido H. Daub

Department of Chemistry, University of New Mexico, Albuquerque, New Mexico 87131

ABSTRACT

All twelve monomethylbenzo[a]pyrenes were studied using cyclic voltammetry and single- and double-potential-step chronoamperometry at a platinum electrode in acetonitrile, in order to determine the kinetic stability of the cation radicals, and to obtain information on the decay reaction mechanisms. For most of the compounds there may be more than one mechanism operating in parallel, but single-potential-step chronoamperometric data were amenable to calculation of rate constants for the reaction of cation radical with water. With some exceptions, larger rate constants correlate with lower calculated localization energies. There are some parallels between the kinetic results and animal carcinogenicity data reported eleswhere.

Polycyclic aromatic hydrocarbons (PAH's) have long been studied with a view towards correlating physical properties and theoretical parameters with carcinogenicities. Examples of attempts at correlations of carcinogenicities with electrochemical properties can be found (1, 2). Ionization potentials and polarographic half-wave potentials (2, 3) yield fair correlations with carcinogenicities, and have led some to propose that cation radicals are involved as intermediates in carcinogenesis (4). More easily formed cation radicals should be more potent carcinogens. However, if there is a cellular oxidizing agent sufficiently strong to oxidize most PAH's, the next most important criterion should be the kinetic stability of the cation radical (5). This stability must fall within a certain range: too low a stability will not allow the species to reach a DNA molecule unchanged, whereas too high a stability will not allow it to react even after reaching a DNA molecule.

A theoretical measure of kinetic stability is the localization energy for the reaction of cation radical with nucleophile, a reaction in which charge becomes localized at a particular carbon in the PAH upon binding with the nucleophile. For most groups of related PAH's, a larger localization energy and consequently higher stability would mean greater carcinogenicity.

Caspary *et al.* (5) describe an experiment which measures such a kinetic stability, in which they determine the steady-state ESR signal of a frozen benzene solution containing iodine and PAH. The correlation is quite good for 14 compounds, with the exception of perylene, which probably falls into the too-stable category, and of dibenz[a,c]anthracene and dibenz[a,h]anthracene (discussed below).

An alternate method of determining cation radical stabilities is a transient electrochemical experiment, such as cyclic voltammetry or chronoamperometry (6). The advantages of such techniques are (*i*) that the potential can be controlled and (*ii*) that the cation radical decay mechanisms can be determined. Iodine activation is not a true test of radical stability because the yield of radicals varies with the redox potential of the compound in question. Dibenz[a,h]anthracene and dibenz[a,c]anthracene are relatively difficult to oxidize, and this fact may account for the low ESR signals observed (5). Both compounds are either mutagenic or carcinogenic, however (5, 7).

We have studied the monomethyl derivatives of benzo[a]pyrene (BaP) using cyclic voltammetry, and single- and double-potential-step chronoamperometry in order (*i*) to obtain information about the overall electron transfer/chemical reaction mechanisms, (*ii*) to obtain chemical reaction rate constants, (*iii*) to compare the latter with cation radical charge distributions and localization energies calculated using simple MO theory, and (*iv*) to compare all of these results with known carcinogenic properties. The numbering system for BaP is

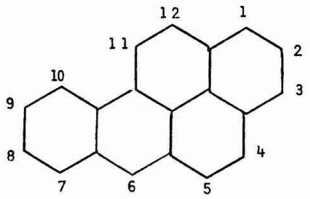

Experimental

Monomethylbenzo[a]pyrenes.—1-, 2-, 3-, 4-, 5-, 11-, and 12-methylbenzo[a]pyrenes (MeBaP's) were synthesized and purified by one of the authors (GHD) and co-workers (8-12). Syntheses for 3- and 5-MeBaP's have been reported (13-15). The remaining MeBaP's were obtained from the National Cancer Institute Chemical Repository and used as received. Syntheses have been reported (14, 16-19).

Reagents.—Eastman spectrograde acetonitrile was distilled on a high vacuum line three times from P_2O_5 and then stored under vacuum. The background water concentration has been estimated to be approximately 4 mmol on the basis of measured rate constants (k_1 in Eq. [1]) with standard additions of water. Polarographic grade tetrabutylammonium perchlorate (TBAP) from Southwestern Analytical Chemicals, Austin, Texas, was dried on a vacuum line overnight at 90°-100°C.

Preparation of electrochemical cell.—A three-electrode cell adapted for use on a vacuum line was used. The cell and its use have been described previously (20). The TBAP and MeBaP concentrations were 0.1M and approximately 0.5 mmol, respectively. The platinum working electrode (0.0228 cm^2) was polished with Fisher grade B gamma alumina (<0.1 μm particles), and placed in concentrated HNO_3 for 1 min. The reference electrode was an Ag wire pseudo reference, which was approximately +0.16V with respect to a saturated calomel electrode. Water was added to the cell while helium was flowing to minimize contact with air.

Electrochemical experiments.—Cyclic voltammetry (CV) and single- and double-step chronoamperometry (CA1 and CA2) were performed using a Princeton Applied Research Model 175 Universal Programmer and Model 173 galvanostat-potentiostat. For pulse widths less than 1 sec, a Tektronix Model 5115 storage oscilloscope was used and, for pulse widths of 1 sec or longer and for CV, a Houston Model 2000 X-Y recorder

* Electrochemical Society Active Member.

Key words: monomethylbenzo[a]pyrenes, cation radical, carcinogenicity, HMO calculation.

was used. For CA1 and CA2 experiments, the cell solution was manually stirred and then potentiostated at 0V for 10 sec prior to activation. At activation the potential was stepped to a value at which the concentration of electroactive material at the electrode surface would be reduced to zero, approximately 100 mV positive of the first oxidation CV peak. The first oxidation peak occurred at a potential at least 250 mV negative of the second oxidation peak, except in the case of BaP, where the separation was 200 mV. For CA2, the potential was then stepped after the nominal pulse width to a point at which the concentration of cation radical at the electrode surface would be reduced to zero, 100 mV negative of the re-reduction peak potential. *IR* compensation was not used; instead, current values were corrected by substracting background currents at various pulse widths, which were measured in a cell prepared without electroactive material and subjected to similar potentials. At 0.1 sec the correction was on the order of 10% of the total current. The n_{app} values were computed for the MeBaP's assuming that diffusion coefficients were the same as those reported by Jeftic and Adams for BaP (21).

MO calculations.—A standard Hückel MO program (22) was employed, in which an h value of -0.5 (inductive model) was used for the carbon at which a methyl group was attached (23). Charges were computed for the cation radicals by summing the squares of the AO coefficients, and localization energies were calculated by computing the difference in total binding energy between the cation radical and the conjugated system formed when the charge is localized at C-6. Both systems contain 19π electrons.

Results and Discussion

Electrochemical experiments.—In the presentation of results it will be helpful to refer to an anodic oxidation scheme for benzo[a]pyrene (BaP) itself based on the one developed by Jeftic and Adams (21). This scheme is in the form of a series of six electron transfer/chemical reaction (EC) steps. *R* refers to BaP without two of its hydrogen atoms. The groups represented without parentheses are attached at the 6-carbon, while the groups within parentheses can be attached at the 1-, 3-, or 12-carbons

$$E_1:\ R(H)H \overset{-e^-}{\rightleftharpoons} R(H)H^{\cdot +} \xrightarrow{H_2O,k_1} R(H)HOH^{\cdot} + H^+ \qquad [1]$$

$$E_2:\ R(H)HOH^{\cdot} \overset{-e^-}{\rightleftharpoons} R(H)HOH^{+} \xrightarrow{k_2} R(H)OH + H^+ \qquad [2]$$

$$E_3:\ R(H)OH \overset{-e^-}{\rightleftharpoons} R(H)OH^{\cdot +} \overset{k_3}{\rightleftarrows} R(H)O^{\cdot} + H^+ \qquad [3]$$

$$E_4:\ R(H)O^{\cdot} \overset{-e^-}{\rightleftharpoons} R(H)O^{+} \xrightarrow{H_2O,k_4} R(OH)OH + H^+ \qquad [4]$$

$$E_5:\ R(OH)OH \overset{-e^-}{\rightleftharpoons} R(OH)OH^{\cdot +} \overset{k_5}{\rightleftarrows} R(OH)O^{\cdot} + H^+ \qquad [5]$$

$$E_6:\ R(OH)O^{\cdot} \overset{-e^-}{\rightleftharpoons} R(OH)O^{+} \overset{k_6}{\rightleftarrows} R(O)O + H^+ \qquad [6]$$

Thus the final product $R(O)O$ is a mixture of the BaP diones, 1,6-dione, 3,6-dione, and 6,12-dione. Also, some of the chemical steps may be reversible, especially [3], [5], and [6].

Reaction [1] is shown diagrammatically below, broken into elementary steps.

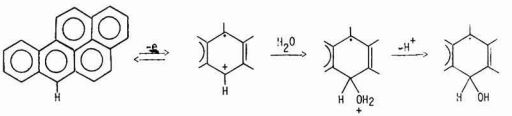

Cyclic voltammograms for BaP are shown in Fig. 1 before and after the addition of enough water to bring the concentration to 39.0 mmol. In this and other voltammetry shown, the initial positive potential scan is reversed after the cation radical is produced; the second scan is reversed after dication is produced at more positive potentials. In Fig. 1a, formation of cation radical is seen at +1.09V and formation of anion radical is seen at −2.09V, both *vs.* Ag. Two fused peaks corresponding to reduction of products with the main peak at +0.58V have been associated with the reduction of 6-oxo-BaP cation to its free radical (reaction [4]) and the reduction of 6-OH-BaP cation radical to 6-OH-BaP (reaction [3]) (21). After the addition of water (Fig. 1b) a peak corresponding to reduction of BaP dione appears at +0.27V (21).

Methylated BaP cation radicals are on the whole more stable than that of BaP, as can be seen in Fig. 2, showing CV of 3-MeBaP. Voltammograms for the other MeBaP's are fairly similar except for variations in peak shapes due to adsorption and kinetics. The most pronounced example of adsorption is 6-MeBaP, whose CV is shown in Fig. 3. Here the cation radical adsorbs, and its reduction is seen as a small spike when no water has been added. Note that the decay of cation radical gives rise to no clearly defined product peaks while the decay of dication gives rise to two clearly defined peaks. The second product peak, here seen at +0.23V, is much more pronounced than it was for any of the other compounds. This peak could again correspond to reduction of a dione. In support of this, there is a strong similarity between the CV for 6-MeBaP observed with added water (Fig. 3b) and that for BaP with added water (Fig. 1b).

CA2 current ratios ($R_i \equiv i_2\tau/i\tau$, where τ is the pulse width) are shown for representative MeBaP's in Fig. 4. It has been helpful to compare these results with

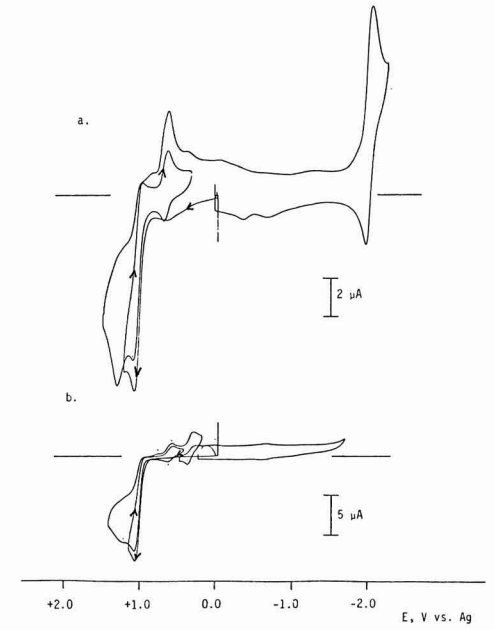

Fig. 1. CV of BaP (0.49 mmol) at 100 mV sec^{-1} in acetonitrile. The arrow marks indicate the potential scan corresponding to the cation radical generation. a. No H_2O added. b. 39.0 mmol H_2O.

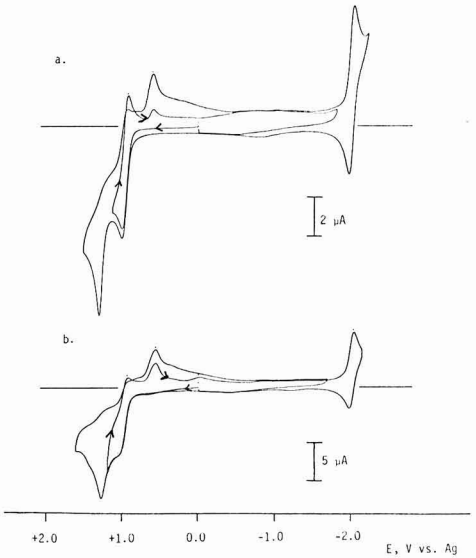

Fig. 2. CV of 3-MeBaP (0.46 mmol) at 100 mV sec^{-1} in acetonitrile. a. No H_2O added. b. 10.2 mmol H_2O.

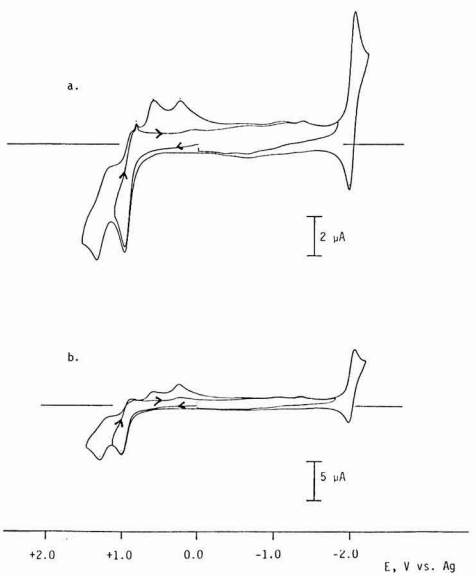

Fig. 3. CV of 6-MeBaP (0.49 mmol) at 100 mV sec^{-1} in acetonitrile. a. No H_2O added. b. 13.5 mmol H_2O.

the comprehensive set of digitally simulated working curves published by Hanafey *et al.* (24). The behavior of 11-MeBaP indicates that it has the most stable cation radical, and the curve approaches the first-order EC working curve shown for comparison at large τ values. However there are about ten other possible mechanisms which give similar working curves, including ECE, ECEC, and ECC mechanisms. All of these exhibit the approach at small τ values of R_i to the value of 0.293, which is predicted for a simple diffusion-controlled electron transfer uncomplicated by chemical reactions (25). The explanation for the fact that R_i is less than expected is that adsorption equilibrium is not being established at short times (26).

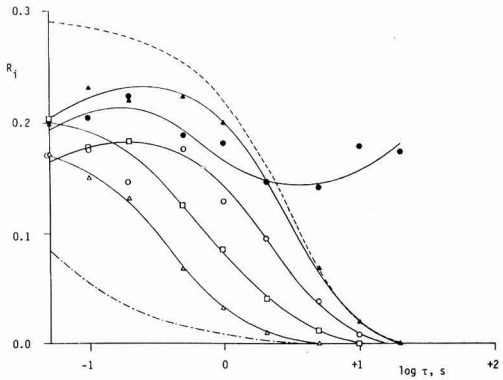

Fig. 4. CA2 current ratios as a function of pulse width for several MeBaP's in anhydrous acetonitrile. (○) 1-MeBaP; (△) 2-MeBaP; (□) 3-MeBaP; (●) 6-MeBaP; and (▲) 11-MeBaP. Points are averaged from two experimental values. All concentrations were approximately 0.5 mmol. Dashed line: first order EC working curve; dotted and dashed line: EC, radical-radical coupling working curve (37).

1-MeBaP has a somewhat stable cation radical according to its R_i *vs.* log τ behavior. Less stable are the cation radicals of 3-MeBaP and 2-MeBaP. 6-MeBaP exhibits unique behavior and is discussed below. All of the other MeBaP's not represented in Fig. 4 (4, 5, 7-10, and 12) exhibited plots intermediate between those of 2- and 3-MeBaP. As the stability of the cation radicals decreases, R_i seems to fall off more gradually, as in the case of 2-MeBaP. This kind of behavior is indicative of a second-order process for the decay of cation radicals. Hanafey *et al.* present working curves for five such possible mechanisms, all involving the coupling of two electrogenerated species (24). Two possible mechanisms which have relevance in the present case are (*i*) EC, radical-radical coupling and (*ii*) ECC, second-order disproportionation. The first possibility can be represented as follows

$$2R(H)H^{+\cdot} \rightarrow (H)R\text{—}R(H) + 2H^+ \qquad [7]$$

Here the coupling occurs at the 6-position, as has been documented for BaP (21). BaP, 8-MeBaP, and 11-MeBaP all experienced irreversible adsorption of product, which in the case of BaP has been found to be composed mainly of BaP dimer (21). A film coats the electrode as current is passed for extended periods. Thus for these compounds, reaction [7] is probably a significant pathway.

The second possibility can be represented as follows

$$2R(H)H^{+\cdot} \rightarrow R(H)H + R(H)H^{2+} \qquad [8]$$

$$R(H)H^{2+} + H_2O \rightarrow R(H)OH + 2H^+ \qquad [9]$$

Supporting evidence for this mechanism is the fact that when the potential is swept in the C-V to values at which dication can be formed (Fig. 1 and 2), there is more efficient production of products. Both mechanisms have virtually identical working curves (24), and the curve corresponding to reaction [7] is shown for comparison in Fig. 4.

For most of the MeBaP's the current ratio plots lie somewhere between the first-order EC-type and the second-order-type working curves. The reason is probably that reactions [1]-[6], [7], and [8]-[9] are occurring in parallel but in various proportions for the different MeBaP's.

After water was added to the level of about 10 mmol, the R_i plots for most of the compounds shifted to the left, indicating a lessening of cation radical stability.

Also, for all compounds except 1- and 11-MeBaP (and 6-MeBaP, to be discussed below) the second-order character of the plots increased. This phenomenon could be consistent with radical-radical coupling (reaction [7]) if one assumed that water, even while accelerating the decay of cation radical through reaction [1], was enhancing the adsorption of both parent compound and cation radical, and thus increasing the concentration of cation radicals near the electrode. The assumption is valid because the presence of 5.2 mmol water increased the surface excess of 1-MeBaP from 6.8×10^{-10} to 1.2×10^{-9} mol cm^{-2}, and that of 1-MeBaP cation radical from 2.1×10^{-10} to 4.6×10^{-10} mol cm^{-2}, as determined from chronocoulometric measurements. This phenomenon could also be consistent with disproportionation (reactions [8]-[9]) for the same reason. The R_i plot for 6-MeBaP (Fig. 4) shows values less than expected at the shorter pulse widths probably again due to adsorption of compound. As was seen with cyclic voltammetry, there is also adsorption of cation radical, which definitely accounts for the large R_i values at the longer pulse widths.

Representative results for single-potential-step chronoamperometric (CA1) experiments done without added water are presented in Fig. 5. All of the data are characterized by a monotonic increase in n_{app} as time proceeds. Results for the MeBaP's not presented in the figure are very similar in shape to those for 1- and 2-MeBaP. The plot for 6-MeBaP has been fit assuming $n_2 = 0.5$ and that for 11-MeB has been fit assuming $n_2 = 1$. Those compounds will be discussed in more detail below. At times shorter than 0.1 sec, all of the n_{app} values rise with decreasing time due to adsorption of compound at the electrode surface, as discussed above.

For simple ECE mechanism, n_{app}, the apparent number of electrons transferred should rise to a plateau value according to the number of electrons involved in the second electron transfer [6] based on the equation $n_{app} = n_1 + n_2 (1 - e^{-kt})$. Here n_1 and n_2 are the number of electrons transferred before and after the chemical step, and k is the rate constant for the chemical step. The lower portion of the experimental curves (Fig. 5a and b) can be fit reasonably well to the ECE working curve in which $n_1 = 1$ and $n_2 = 2$. Over the region where n_{app} is $2 \sim 3$ the curves start deviating due probably to the operation of further electron transfer steps. Finally at much longer times (<60 sec), the actual current reached a steady-state value in every case, and thus the n_{app} values began to increase steeply. It is probable that this phenomenon is due in part to a catalytic mechanism because the time at which steady state was reached depended on the compound. However, it is difficult to separate the contribution of steady-state currents brought on by radial diffusion and by natural convection from such a catalytic current.

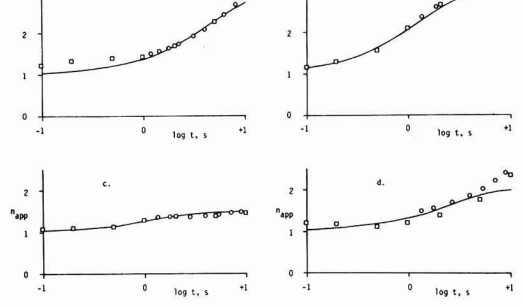

Fig. 5. CA1 n_{app} values as a function of time for (a) 1-MeBaP, (b) 2-MeBaP, (c) 6-MeBaP, and (d) 11-MeBaP in anhydrous acetonitrile. Concentrations were approximately 0.5 mmol. ECE working curves are shown which assume $n_1 = 1$ and (a) $n_2 = 2$, (b) $n_2 = 2$, (c) $n_2 = 0.5$, and (d) $n_2 = 1$. Squares and circles designate points obtained using an oscilloscope and an x-y recorder, respectively.

It has been shown using cyclic voltammetry and chronopotentiometry that several dimethylbenzo[a]-pyrenes exhibit catalytic or regenerative behavior in the presence of water (27). A possible mechanism would be

$$R(H)H^{+\cdot} + H_2O \rightarrow R(H)H + \text{products} \quad [10]$$

It appears that whatever mechanism is involved, it holds at long times for all of the compounds except for 6-MeBaP.

An ECE mechanism with $n_1 = 1$ and $n_2 = 2$ would be consistent with reactions [1]-[6] if k_2 were relatively large. Effectively then, reactions [2] and [3] would be combined

$$R(H)HOH\cdot \overset{-2e^-}{\rightleftharpoons} R(H)OH^{+\cdot} + H^+ \quad [11]$$

The resulting cation radical (derived from BaP) has been shown in our laboratory to be stable on the cyclic voltammetric time scale (100 mV sec^{-1} scan rate). Thus, the rate constant k_3 seems to be rather small. The product of reaction [3], the 6-oxo-BaP free radical, is also a stable species which can undergo further oxidation (reaction [4]) to form 6-oxo-BaP cation (21). Nucleophilic attack upon this cation by water (reaction [4]) is relatively slow, as seen by the fact that in the CV not much current is observed for reduction of further products, especially with the MeBaP's (Fig. 2). Thereafter the last two electron transfers seem to blend smoothly in the n_{app} *vs.* log t curves (Fig. 5b).

It is difficult simply by monitoring current to distinguish ECE from ECC-heterogeneous disproportionation, in which the electron transfer in reaction [2] is effected in solution by BaP cation radical, instead of at the electrode (24)

$$R(H)H^{+\cdot} + R(H)HOH\cdot \rightarrow R(H)H + R(H)HOH^+ \quad [12]$$

Parent compound is regenerated and thus this mechanism is similar to one-half-order regeneration (28). Amatore and Saveant (29) predict a distinguishing feature in the CA2 behavior between ECE and disproportionation, but it is not applicable here because of the existence of further chemical steps. ECEC and disproportionation can have very similar CA2 behavior (24). The CA1 behavior for the two mechanisms is also quite similar (30), and the calculation of k values should yield similar values in both cases.

It is also difficult in single-potential-step experiments to distinguish between ECE and ECC, second-order disproportionation (reactions [8] and [9]). Marcoux (31) predicts a slightly less steeply rising n_{app} *vs.* log t curve for the latter mechanism. However, the pronounced effect of a second-order mechanism which was seen in double-potential step experiments (Fig. 4) is not evident in the CA1 data (Fig. 5). Thus, the calculation of k values from CA1 data based on an initial ECE mechanism seems valid.

Rate constants for all compounds except for 6-MeBaP and 11-MeBaP have been determined by fitting the data to an ECE working curve in which $n_1 = 1$ and $n_2 = 2$; they are tabulated in Table I. For 6- and 11-MeBaP, values of n_2 of 0.5 and 1.0, respectively, were used for the calculation. The rate constants calculated, assuming $n_2 = 2$ will be controlled by both k_1 and k_2 and will be designated as k', although $k' \approx k_1$. The ranking of stabilities of cation radicals based on Table I generally follows the ranking based on CA2 results as well as that based on CA1 results with added water.

Table I. Pseudo-first order rate constants (sec^{-1}) for reaction of BaP and MeBaP cation radicals, based on CA1 data, assuming $n_1 = 1$

	k, sec^{-1}	n_2
BaP	1.12	2
1-MeBaP	0.21	2
2-MeBaP	0.76	2
3-MeBaP	0.63	2
4-MeBaP	0.32	2
5-MeBaP	0.71	2
6-MeBaP	0.72	0.5
7-MeBaP	0.36	2
8-MeBaP	0.60	2
9-MeBaP	0.20	2
10-MeBaP	0.26	2
11-MeBaP	0.37	1
12-MeBaP	0.32	2

The n_{app} values for 6-MeBaP plateau at around 1.5 electrons (Fig. 5c), indicating a different mechanism at work, as was hinted at by the CA2 results. Coupling of cation radicals is probably occurring as in reaction [6], but possibly through the methyl group. Interestingly, however, when the dication is produced in a CV experiment, highly efficient formation of a dione seems to occur (Fig. 3). This dione could be a 1,3 type.

In any case, 1-MeBaP has a rather reactive cation radical. In comparing rate constants in Table I, the fact that the decay rate for 6-MeBaP cation radical is second order in hydrocarbon makes it appear more stable than it actually is. Note that the concentration of hydrocarbon is about 0.5 mmol while the estimated concentration of background water is 4 mmol. Thus a comparison based on second-order rate constants would show this cation radical to be the most reactive.

The 11-MeBaP cation radical is the most stable, based on CV and CA2 data. The CA1 data points, if they are fit to an ECE working curve in which $n_1 = 1$ and $n_2 = 2$, also show a very low decay rate constant. However, the fit is better for $n_2 = 1$ (Fig. 5d), indicating that the k_2 value is small. Thus the calculated rate constant represents a true k_1 value.

Summarizing the mechanistic results for the MeBaP's there are several pathways which can operate in parallel: (*i*) ECEC . . . EC. (*ii*) ECC . . ., heterogeneous disproportionation. Here the successive electron transfers can be mediated by solution species, principally the cation radical. It is impossible at this point to determine the relative contributions of mechanisms [1] and [2], but calculated k values are virtually identical. (*iii*) EC, radical-radical dimerization. This pathway is important for the three compounds which undergo filming of the electrode, BaP, 8-MeBaP, and 11-MeBaP, as well as for 6-MeBaP. (*iv*) ECC . . ., second-order disproportionation. This pathway is important for all of the compounds except 1-MeBaP and 11-MeBaP, especially with added water. Mechanisms [3] and [4] affect the CA2 behavior much more than they affect the CA1 behavior. Therefore, k values can be calculated on the basis of mechanism [1] using CA1 data. (*v*) EC . . ., second-order regenerative. At long electrolysis times, this pathway predominates for all compounds except 6-MeBaP.

MO calculations.—HMO calculations give the result that the 6 carbon of the cation radical BaP and of the MeBaP's has the highest positive charge as well as the lowest localization energy. Thus it should be the most reactive, according to considerations of both the initial state in a potential energy diagram and of the activated complex with water. Values are given in Table II. For most of the MeBaP's there is an inverse relationship between charge and localization energy, except for 5- and 7-MeBaP. They have high charges but also high localization energies.

Table II. Charges and localization energies for MeBaP cation radicals

	$q_r\,[R(H)^{+\cdot}]$[a]	ΔE_{loc}[b] in β units	r
BaP	0.1884	1.5893	6
1-MeBaP	0.1611	1.6479	6
2-MeBaP	0.1877	1.5914	6
3-MeBaP	0.1628	1.6417	6
4-MeBaP	0.1675	1.6271	6
5-MeBaP	0.1821	1.6361	6
6-MeBaP	0.4132	1.2416	6
6-MeBaP	0.0903	1.8681	1
7-MeBaP	0.1854	1.6349	6
8-MeBaP	0.1835	1.5917	6
9-MeBaP	0.1746	1.6217	6
10-MeBaP	0.1807	1.6057	6
11-MeBaP	0.1765	1.6098	6
12-MeBaP	0.1679	1.6343	6

[a] This quantity is the charge at the r position, where r is listed in the fourth column.

[b] This quantity is the localization energy or the energy difference between the cation radical and the cation radical plus water

$$\Delta E_{loc} = -\{E[R(H)HOH_2^{+\cdot}] - E[R(H)H^{+\cdot}]\}_r$$

β unit $\approx$ 18 kcal/mol.

Support for the concept of addition of water to the cation radical as a rate-determining step is given by a potential energy diagram (Fig. 6). HMO total binding energies were calculated for the species involved in reactions [1]-[3], in addition to the activated state itself, cation radical plus water. The fact that there is a plateau at the highest potential energy (lowest binding energy) is misleading however: the chemical transformations are occurring outside the conjugated system and thus do not affect the total energy.

If the logarithm of the rate constant k' is plotted against localization energy (Fig. 7), one sees a basic trend, but with several exceptions. 1-, 7-, 12-, 4-, 8-, and 2-MeBaP follow the expectation that lower localization energies are correlated with larger rate constants. The cation radicals of 5- and 7-MeBaP were predicted to have relatively large positive charges at the 6-carbon, but relatively high localization energies. The rate constant for 7-MeBaP seems to fit better with the localization energy, while that of 5-MeBaP fits better with the charge.

For 10- and 11-MeBaP there should be some steric hindrance between the methyl group and the neighboring hydrogen atom. By analogy with several meth-

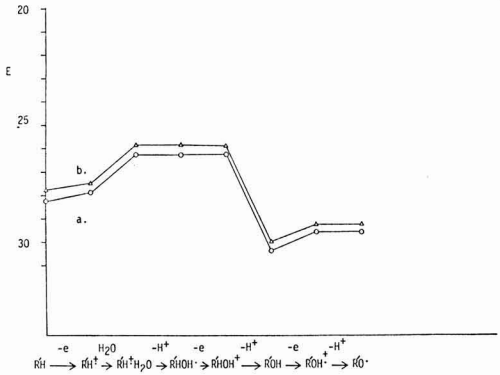

Fig. 6. Total HMO binding energies in β units for oxidation products and intermediates of BaP (○) and 1-MeBaP (△). *R'* refers to BaP or 1-MeBaP without a hydrogen atom at the 6 position.

ylbenz[a]anthracenes and methylchrysenes, there should also be a deviation from planarity for such compounds (32-34). Perhaps such an effect could explain the larger than expected stability of the cation radical if a thermodynamic argument were used: destabilization due to nonplanarity might affect the neutral molecule more unstable than the cation radical, leading to a lowered redox potential. Rough measurements using a saturated calomel reference electrode and correcting for following reactions indicate that 10- and 11-MeBaP do indeed have more negative potentials for oxidation. However, the apparent difference in k_2 value between 11-MeBaP and, say, 1-MeBaP remains to be explained. It implies something surprising, *i.e.*, that a dearomatized intermediate, $R(H)HOH^+$ in reaction [2], is stabilized for 11-MeBaP. Perhaps there is an interaction between the nonplanarity mentioned above and an enhanced resonance stabilization through a mechanism such as hyperconjugation.

Carcinogenicity.—Carcinogenicity data have been gathered from the literature and are given in Table III. Data in the lefthand column tend to support the theory of diolepoxide intermediacy (35), which would predict no activity for 7-, 8-, 9-, or 10-MeBaP, although the nonzero activities for 7- and 10-MeBaP suggest that there might be another mechanism at work (3). The lack of activity for 8- and 9-MeBaP is at complete variance with the theory of cation radical intermediacy, however.

Data in the righthand column of Table III for a limited group of MeBaP's show that methylation at some positions leads to enhanced carcinogenicity. This fact is consistent with the assumption that compounds with more stable cation radicals (within limits) should be more active. 2-MeBaP has greater radical stability than BaP, but has the lowest of the MeBaP's and also shows a slightly lower carcinogenic activity. 11-MeBaP has the highest cation radical stability and shows a slightly higher activity.

Even these very limited parallels should encourage further work along these lines, given the complex nature of the carcinogenic process. Since many biological testing systems may involve several simultaneous pathways, it may be useful to devise systems which involve only one pathway, such as that involving the cation radical. Such an approach is being taken by Cavalieri and co-workers (36, 37).

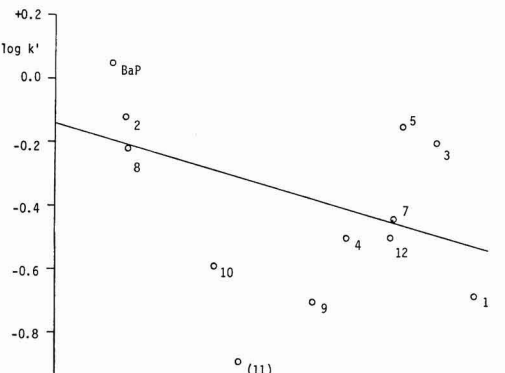

Fig. 7. Log of the ECE rate constant computed from CA1 data (see Table I) *vs.* the localization energy for C-6 in β units. Log k' = −0.89 for 11-MeBaP assuming n_2 = 2 (see text). A least squares line is plotted based on all points except that for 11-MeBaP.

Table III. Carcinogenicities of MeBaP's

	No. of pulses (+)[a]	Iball index[b]
BaP	4	69
1-MeBaP	—	—
2-MeBaP	4	92
3-MeBaP	4	95
4-MeBaP	4	95
5-MeBaP	2	—
6-MeBaP	4	—
7-MeBaP	2	—
8-MeBaP	0	—
9-MeBaP	0	—
10-MeBaP[c]	1	—
11-MeBaP	4	103
12-MeBaP	4	97

[a] The number of pluses (+) is based on Badger's system (38). Data for 5- through 9-MeBaP are also from Badger. Data from Lacassagne *et al.* (39) for the remaining compounds were converted to this scale.

[b] The Iball (40)

$$\text{carcinogenicity index} = \frac{\%\ \text{tumors} \cdot 100}{\text{avg latency period in days}}$$

Indexes were computed using data from Lacassagne *et al.* (39).

[c] Data from Harvey (41) indicate that 10-MeBaP is less than 1/10 as potent as BaP, while that from Hecht *et al.* (33) indicates that it is roughly 1/2 as potent as BaP.

Acknowledgments

We would like to express our appreciation to Dr. J. N. Keith, NCI Chemical Repository, IIT Research Center, Chicago, for supplying samples of 6-, 7-, 8-, 9-, and 10-MeBaP. We would also like to acknowledge helpful discussions with Dr. Kenneth Wiberg, Yale University and with Dr. Tsutomu Ohzuku, Okayama University.

Manuscript submitted June 7, 1982; revised manuscript received *ca.* Oct. 10, 1982.

Any discussion of this paper will appear in a Discussion Section to be published in the December 1983 JOURNAL. All discussions for the December 1983 Discussion Section should be submitted by Aug. 1, 1983.

REFERENCES

1. A. C. Allison, M. E. Peover, and T. A. Gough, *Nature*, **197**, 764 (1963).
2. V. Podany, E. Rezabkova, and L. Bahna, *Neoplasma*, **25**, 57 (1978).
3. E. Cavalieri, R. Roth, C. Grandjean, J. Althoff, K. Patil, S. Liakus, and S. Marsh, *Chem.-Biol. Interactions*, **22**, 53 (1978).
4. M. Wilk, W. Bez, and J. Rochlitz, *Tetrahedron*, **22**, 2599 (1966).
5. W. Caspary, B. Cohen, S. Lesko, and P. O. P. Ts'o, *Biochem.*, **12**, 2649 (1973).
6. D. D. MacDonald, "Transient Techniques in Electrochemistry," Plenum Press, New York (1977).
7. J. McCann, E. Choi, E. Yamasaki, and B. N. Ames, *Proc. Nat. Acad. Sci. USA*, **72**, 5135 (1975).
8. J. L. Adelfang and G. H. Daub, *J. Am. Chem. Soc.*, **77**, 3297 (1955).
9. J. L. Adelfang and G. H. Daub, *ibid.*, **79**, 1751 (1957).
10. J. W. Patton and G. H. Daub, *ibid.*, **79**, 709 (1957).
11. J. L. Comp and G. H. Daub, *ibid.*, **80**, 6049 (1958).
12. C. Doyle, Jr. and G. H. Daub, *ibid.*, **80**, 5252 (1958).
13. J. M. L. Cameron, J. W. Cook, and R. Schoental, *J. Chem. Soc.*, 257 (1952).
14. L. F. Fieser and E. B. Hershberg, *J. Am. Chem. Soc.*, **60**, 2542 (1938).
15. R. S. Bodine and G. H. Daub, *J. Org. Chem.*, **44**, 4461 (1979).
16. L. F. Fieser and E. B. Hershberg, *J. Am. Chem.*

Soc., **60**, 1658 (1938).
17. L. F. Fieser and M. Fieser, *ibid.*, **57**, 782 (1935).
18. M. S. Newman and S. Kamer, *J. Org. Chem.*, **42**, 3284 (1977).
19. W. E. Bachmann and M. J. Carmack, *J. Am. Chem. Soc.*, **63**, 2494 (1941).
20. S.-M. Park, *This Journal*, **125**, 216 (1978).
21. L. Jeftic and R. N. Adams, *J. Am. Chem. Soc.*, **92**, 1332 (1970).
22. K. B. Wiberg, "Computer Programming for Chemists," pp. 215-225, W. A. Benjamin, New York (1965).
23. A. Streitwieser, Jr., "Molecular Orbital Theory for Organic Chemists," p. 135, John Wiley & Sons, New York (1961).
24. M. K. Hanafey, R. L. Scott, T. H. Ridgway, and C. N. Reilley, *Anal. Chem.*, **50**, 116 (1978) and supplementary material.
25. A. J. Bard and L. R. Faulkner, "Electrochemical Methods: Fundamentals and Applications," p. 182, John Wiley, New York (1980).
26. R. H. Wopshall and I. Shain, *Anal. Chem.*, **39**, 1514 (1967).
27. S.-M. Park, J. J. Michnovicz, and G. H. Daub, *Anal. Biochem.*, **90**, 374 (1978).
28. T. H. Ridgway, R. P. Van Duyne, and C. N. Reilley, *J. Electroanal. Chem.*, **67**, 1 (1976).
29. C. Amatore and J. M. Saveant, *ibid.*, **107**, 353 (1979).
30. C. Amatore and J. M. Saveant, *ibid.*, **102**, 21 (1979).
31. L. Marcoux, *J. Am. Chem. Soc.*, **93**, 537 (1971).
32. D. W. Jones and J. M. Sowden, *Cancer Biochem. Biophys.*, **4**, 43 (1979).
33. S. S. Hecht, N. Hirota, and D. Hoffman, *Cancer Lett.*, **5**, 179 (1978).
34. S. S. Hecht, M. Loy, R. Mazzarese, and D. Hoffman, *J. Med. Chem.*, **21**, 38 (1976).
35. D. M. Jerina, R. Lehr, M. Schaefer-Ridder, H. Yagi, J. M. Karle, D. R. Thakker, A. W. Wood, A. Y. H. Lu, D. Ryan, S. West, W. Levin, and A. H. Conney, in "Origins of Human Cancer," H. Hiatt, J. D. Watson, and I. Winsten, Editors, pp. 639-658, Cold Spring Harbor Laboratory, Cold Spring Harbor, NY (1977).
36. E. Cavalieri, E. Rogan, and R. Roth, in "Free Radicals and Cancer," R. Floyd, Editor, Marcel Dekker, New York (1982), In press.
37. E. Rogan, R. Roth, E. Cavalieri, P. Katomski, and J. Benderson, *Chem.-Biol. Interactions*, **22**, 35 (1978).
38. G. M. Badger, *Brit. J. Cancer*, **2**, 22 (1948).
39. A. Lacassagne, F. Zajdela, N. P. Buu-Hoi, O. Chalvet, and G. H. Daub, *Int. J. Cancer*, **3**, 238 (1968).
40. J. Iball, *Am. J. Cancer*, **35**, 188 (1939).
41. R. G. Harvey and F. B. Dunne, *Nature*, **273**, 566 (1978).

Crystallographic Anisotropies in Electrochemical Etching of Pt

R. Caracciolo and L. D. Schmidt

Department of Chemical Engineering and Materials Science, University of Minnesota, Minneapolis, Minnesota 55455

ABSTRACT

Single crystal microspheres of Pt are examined by scanning electron microscopy following electrochemical and chemical etching in chloride and cyanide solutions. In all cases, a single major crystal plane is formed which is not the close packed (111) plane. Rates of dissolution and facet formation also vary among planes and with etching conditions. The largest anisotropy occurs with aqua regia where initial attack is exclusively near (210) but only (110) facets are formed. The (111) and (100) planes are attacked in aqua regia only from their edges, but eventually these orientations are transformed completely into (110) facets. Electrochemical chloride etching with a-c potentials produces large smooth planes near (100), and the (111) plane is attacked readily to form (100) facets. Electrochemical cyanide etching produces the most rapid attack of the (111) orientation to produce facets of (110). Possible mechanisms for these processes and implications for preparation of Pt electrodes are discussed.

Platinum, the standard electrode in most electrochemical processes (1), derives its usefulness from its high reactivity in electrode reactions combined with inertness towards erosion and deactivation through solid compound formation. Because of these properties, Pt electrodes exhibit a reproducibility unequaled by any other electrode materials. On the other hand, Pt does erode electrochemically in some solutions, and faceting and recrystallization produce changes in properties with time. Platinum electrodes must be prepared and treated in a specified manner to obtain quantitative reproducibility.

Different crystal planes of Pt behave quite differently in adsorption and reactions. The variations in H_2 and O_2 evolution with crystallographic orientation have been particularly well documented (2-6). It has typically been assumed that polycrystalline wires or foils facet into the close packed (111) plane because this is the lowest free energy plane at the metal-vacuum interface. However, it is not obvious that this plane is most stable in electrolyte solutions because rates of surface dissolution and rearrangement processes influence which planes are formed.

Many years ago Gwathmy and co-workers (7, 8) introduced the use of polished single crystal spheres to study crystallographic anisotropies. They examined the thickness of oxide films on ~1 cm diam Cu spheres and also studied faceting produced by H_2 oxidation on Cu and Ni spheres. In this laboratory (9), smaller spheres of Pt have been used to study catalytic etching, the faceting which occurs in catalytic reactions of gases at high temperatures. We showed that the rates of etching and the stable planes depended strongly on crystallographic orientation. We also found that the stable plane is frequently not the (111), and that each reaction produces different morphologies. Single crystal spheres <1 mm in diameter are very easily prepared by melting of a wire in a torch, and these sizes are convenient for examination in the scanning electron microscope (SEM).

The objective of this research is to determine the role of crystallographic orientation in faceting of Pt in specimens which are free of grain boundaries and stresses, because both of these effects can compete with crystallographic anisotropies in influencing erosion processes.

There have been many studies of erosion of Pt electrodes (10-13). It is widely recognized that rates vary with crystal plane and conditions, and the mechanisms of etching have been discussed (10, 11). However, to our knowledge, the crystal plane dependence of rates of etching and stabilities have not yet been identified.

Experimental

The electrodes for these experiments were platinum single crystal microspheres, ~0.02 cm diam, prepared

by melting the ends of high purity (99.9+%) 0.006 cm Pt wires in a CH_4-O_2 torch as described previously (9). The surface of these spheres after solidification appears spherical and smooth except for flat (111) and smaller (100) facets. These planes are identified by their three- and four-fold symmetries, respectively. This is probably the high temperature equilibrium form in which the flat areas are orientations with minimum surface free energy which form cusps in a Wulff plot (9). The stereographic triangle, the "unit cell" of possible orientations on a curved surface, can be identified on a single crystal sphere by symmetry to give a complete characterization of the surface. Several spheres were spot welded to one larger wire so that a number of spheres could be treated and examined simultaneously.

Throughout this manuscript we shall use the notation (h, k, l) to designate the family of crystal planes with this Miller index. The same notation will be used for both the description of a crystal plane (smooth surface or orientation of facet planes), as well as for the nominal orientation of a surface. For example, the (111) orientation of the original sphere is in some cases etched into small (110) facets while the nominal orientation of the region can still be identified as (111).

For electrochemical etching, 2V a-c at 60 Hz was used with a Pt or carbon counterelectrode. Current density was maintained below 4 A/cm². The electrolyte for chloride etching was a solution of aqueous HCl, 20% by volume, with KCl added to saturation. For cyanide etching, the electrolyte was a mixture of 0.1M KCN and 0.1M KOH. Etching times varied from several minutes to several hours. Dissolution of Pt in cyanide solution was more rapid, resulting in the destruction of the electrode assembly in less than 10 min at this voltage. The reagent for chemical etching was boiling aqua regia. (HCl, HNO_3, H_2O in a 3-1-4 volume ratio). Etching times varied from 10 to 35 min.

The resulting surface morphologies were examined by SEM in either a Cambridge Instruments SEM or a JEOL JEM 100CX STEM with resolutions of 300 and 30Å, respectively. Some samples were also examined using a Perkin-Elmer Physical Electronics scanning electron microprobe (SAM) with a lateral resolution of 500Å. No nonmetallic impurities were present on the surfaces at levels up to 1%. The surfaces contained primarily C, O, N, and Cl, although no significant variations in composition between facets could be detected. Sputter depth profiling indicated that the spheres were pure Pt for depths > 10Å below the original surfaces.

Results

Chloride electrochemical etching.—Figure 1 shows spheres after etching in HCl/KCl under conditions just described. The original sphere transforms into a slightly deformed cube whose (100) facets bulge slightly and whose (111) corners remain flat. Figure 1a shows a complete sphere, while Fig. 1b, c, and d show another sphere at increasing magnifications.

The only stable planes are within 10° of (100), with this orientation being smooth except for a square of shallow curved pyramids at ~5° from (100). The region closer to (100) is again smooth, but a pointed cusp occurs exactly at the (100) poles.

The (111) is not smooth, but is completely broken into triangular etch pits which are between 0.1-3μ across. Examination of these facets shows that they are exclusively (100) planes.

The edges of the cube, with Miller indices (1, 1, x) with $0 < x < 1$, is constructed from the intersection of the large sharp smooth faces near (100). Thus, the (110) and its vicinals disappear completely. The only exception is a small flat facet on the edge near (331) which is visible in Fig. 1b and c.

We have examined ~50 spheres following 5 similar etching procedures, and all exhibited morphologies

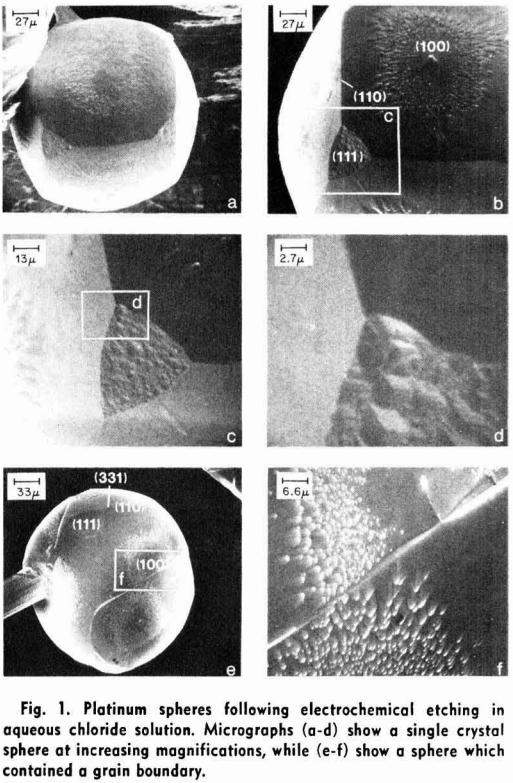

Fig. 1. Platinum spheres following electrochemical etching in aqueous chloride solution. Micrographs (a-d) show a single crystal sphere at increasing magnifications, while (e-f) show a sphere which contained a grain boundary.

essentially identical to those shown in Fig. 1, except for the extent of etching which varied somewhat among spheres.

Figures 1e and f show a sphere which illustrates etching at a grain boundary and earlier stages of etching than Fig. 1a-d. In this sphere, the edges have not yet become sharp, but the (100) and (111) regions can be identified by symmetry. Pyramids near (100) and etch pits on (111) are also observed to form after short times.

This sphere exhibits two grain boundaries which are formed on ~20% of spheres and are caused by nucleation of several crystals during solidification. These micrographs and others of spheres with grain boundaries show that no preferential etching occurs at grain boundaries. The boundary of Fig. 1f is between crystals which are near (100) as identified from cusps in each crystal. The walls of the grain boundary also appear to be near (100), and no evidence of extensive grain boundary grooving is noted.

Chloride chemical etching.—Figure 2 shows several Pt spheres after etching in boiling aqua regia. Extensive etching transforms the sphere into roughly a cubic shape, just as with chloride electrochemical etching. However, the morphology is quite different with the cube faces broken into microfacets of (110) planes.

Figure 2a shows the entire cube in nearly its final configuration. The corners of the cube are flat triangles, whose three-fold symmetry identifies them as (111) planes while the rest of the sphere is faceted. The corners are still smooth and unetched due to the progression of etching as will be explained below. Figures 2b and c show regions which include the (111) and (110) nominal orientations, respectively. One can determine the crystallographic orientation of the facets by examining the facets along the edge of the cube. These facets are parallel to the (110) nominal orienta-

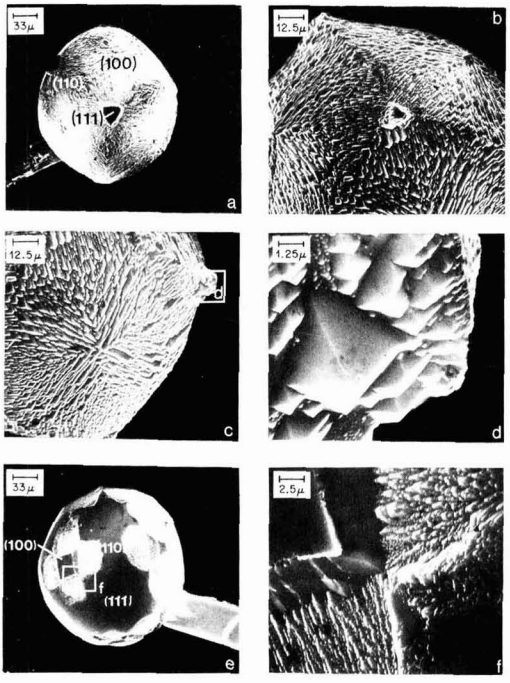

Fig. 2. Platinum spheres following chemical etching in aqua regia. Micrograph (a) shows the entire sphere while (b, c and d) show various regions of another sphere. Micrographs (e and f) show a sphere in initial stages of etching which shows that the (210) region is the first to be attacked.

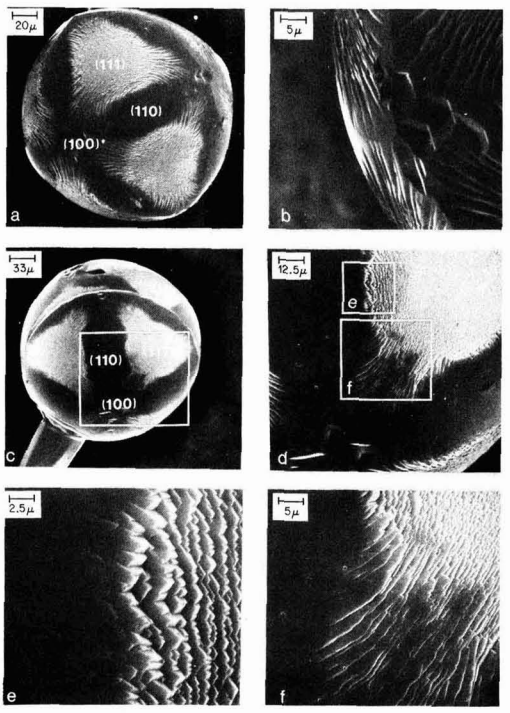

Fig. 3. Platinum spheres following electrochemical etching in aqueous cyanide solution. Micrographs (a and b) show one sphere while (c-f) show another sphere at increasing magnifications.

tion, and all facets on the rest of the sphere are parallel to them. Figure 2d is a high magnification of the corner of the cube on which is a small projection. Facets in this region are variable in size, but all facets have (110) orientation. At the end of the projection is the original (111) orientation which has shrunk and almost disappeared.

The progress of the dissolution process can be seen from Fig. 2e and f. Initial stages of attack show that chemical etching is more anisotropic than chloride electrochemical etching. The four-lobed depressions around the (100) poles indicate that etching initiates near the (210) regions and spreads until the entire sphere is eventually faceted. The wall around the (100) poles (upper left corner of Fig. 2f) is fairly large and smooth and consists of the relevant (110) planes. The original (110), (111), and (100) orientations are not attacked initially. These surfaces are only affected by the etching process as the "front," originating from the (210) orientation, spreads to finally envelop them from their edges. These edges are entirely (110) planes.

As noted previously, the (111) orientations at the corners of the cubes are resistant to the dissolution process. As a result, the sphere in its final configuration has projections at the corners (Fig. 3c and d), because as the sphere is dissolving and decreasing in size, the (111) planes are resistant to dissolution and do not disappear until they shrink to zero size.

In summary, faceting in aqua regia originates at the (210) orientation, spreads to envelope the (110), then the (100), and finally the (111). The final shape of the sphere is a cube covered with (110) facets which are 0.5-1μ across.

Electrochemical etching in cyanide solution.—Figure 3 shows micrographs of Pt spheres following a-c electrochemical etching in basic 0.1M KCN solution. It is found that platinum is removed more rapidly in this solution than in either aqua regia or electrolytic chloride solutions, since the support wires are etched away within several minutes. Examination of Fig. 3a and c shows that etching is most rapid near (111) and less on (110) and (100). The erosion of the (111) to produce nearly flat (but heavily faceted) regions causes the original sphere to transform into the shape of an octahedron with (100) at its corners and (110) at its edges. The (110) remains curved and smooth, while the (100) orientation becomes pointed but with large etch pits near the (100) pole.

The 0.5-2μ facets on the (111) region appear to consist exclusively of planes near (110). All walls in the sawtooth pattern at the right side of Fig. 3e and the triangular etch pits near the center (111) are exclusively (110) planes.

Towards (110), Fig. 3e, the facets disappear, and the surface is smooth with a large radius of curvature, showing that regions within ~10° of (110) are smoothly and uniformly etched.

Surrounding the (100) vertices at the corners of the octahedron are smooth partially faceted planes as shown in Fig. 3b. However, the angle between these nearly flat planes is not large enough to be (111) planes, and we estimate them to be approximately (211) or (311) planes. The vertices themselves are decorated with large (~5μ across), triangular etch pits which appear to have walls near (110).

Etching in other solutions.—Electrochemical etching in chloride or cyanide with d-c potentials produced no visible etching; after 1 hr with 2V applied, no etch patterns or sphere size reduction were evident with the spheres at either the anode or the cathode even though vigorous bubbling occurred.

Etching was attempted under similar experimental conditions using a-c and d-c potentials in 10% by volume sulfuric and phosphoric acid electrolytes. Although reconstruction or dissolution of platinum is re-

ported to occur (3, 14), no visible etching patterns could be detected after 1 hr.

Discussion

Etching is obviously a very complicated process, and our discussion will be limited to a survey of behavior, qualitative comments on the probable processes, and a summary of implications for Pt electrodes.

Table I summarizes these results for the three etching situations. After sufficient time, only a single plane exists on the sphere (two planes in cyanide). This is the "stable" plane, although it is not clear that it is the minimum free energy or equilibrium plane but merely the one which is formed under these etching conditions. The identification of the plane attacked most rapidly comes from noting which regions lose metal most rapidly. This may or may not be the crystallographic orientation which forms. The planes attacked most slowly are identified as those on which metal loss is least and which do not rapidly form facets. In aqua regia, the (111) and (100) planes are totally inert except for attack from their edges which eventually causes their complete disappearance.

The overall shape of the resultant single crystals is a result of the rapid erosion of (100) or (111) to form cubes and octahedra, respectively. It is evident that the shape does not necessarily correlate with the planes which form, because the regions attacked readily also facet except in the case of electrochemical chloride etching.

Crystallographic anisotropies involve: (*i*) relative rates of etching and (*ii*) relative stabilities of planes. In practice, these are intricately coupled because etching is a rate process in which the approach to equilibrium in various steps is unknown. The equilibrium configuration of a surface is determined by the surface free energy γ *vs.* crystallographic orientation. A crystalline solid may exhibit faces exposing one or more flat crystal planes, both flat and curved surfaces, or only curved surfaces, depending on the anisotropy in γ with orientation (15, 16). If γ exhibits cusps on a plot of γ *vs.* orientation (the Wulff plot), then those planes will exhibit flat faces while otherwise a range of orientations will be stable. Clean platinum exhibits large crystallographic anisotropies in γ with $\gamma_{(111)} < \gamma_{(100)} < \gamma_{(110)}$. A clean platinum crystal would form a cubo-octahedron exposing only (111) and (100) planes, and other orientation should form facets of these planes only.

However, with adsorbates, there is at present no way to predict the ordering of γ on different planes or the size of its anisotropies. If the stable planes observed in these experiments were controlled by equilibrium considerations, then the results imply that (100) or (110) and their vicinals have much lower γ than do other orientations including the close packed (111) plane.

Kinetics of dissolution and transport should be equally important in controlling morphologies and stabilities in an etching situation. It should also be noted that etching may involve both dissolution and deposition, particularly with a-c potentials. Thus, in some situations, material may be removed from some planes and deposited on adjacent facets, while in others, metal may be dissolved from all regions but at different rates. Calculations of concentration gradients parallel to the surface with reaction indicate that lateral transport in the boundary layer and by surface diffusion may be important (15).

Etching of a metal must involve formation of a soluble metal ion, and the inertness of Pt is associated with the instability and insolubility of most ions containing Pt. Chloroplatinate $PtCl_6^=$ and cyanoplatinate $Pt(CN)_4^=$ are the most stable aqueous ions of Pt, and these species are almost certainly formed in electrochemical and chemical etching as discussed by many authors (10-12). In any situation, dissolution involves oxidation of Pt at the surface to Pt^{+2} or Pt^{+4}, its complexing with Cl^- and CN^- at the surface, and the dissolution of the stable anion. In each solution, distinct processes should occur for each step.

Aqua regia.— Oxidation of Pt is probably by attack of Cl atoms generated in solution. A possible sequence of reactions is

$$Cl(sol'n) \rightarrow Cl(s)$$

$$4Cl(s) + Pt(s) \rightarrow PtCl_4(s)$$

$$PtCl_4(s) + 2Cl^- \rightarrow PtCl_6^=(sol'n)$$

although the oxidation states and complexes of Pt intermediates on the surfaces are of course unknown.

Etching in aqua regia exhibits the greatest crystallographic anisotropy with only the (210) orientation attacked initially to form (110) facets. The (111) and (100) planes are not attacked directly until facets of (110) have formed. This suggests that these planes either do not adsorb Cl atoms, that Cl is not capable of oxidizing Pt atoms, or that the complex does not dissolve. The hexagonal and square close packed planes of Pt are apparently inert toward direct attack. It is also possible that a monolayer or multilayer film such as oxide, carbide, or an impurity acts to passivate these planes.

Electrochemical chloride.—This process is probably similar to that in aqua regia, except now the Cl is deposited electrochemically at the surface

$$Cl^-(sol'n) \rightarrow Cl(s) + e^-$$

The electrochemical potential, thus, may induce Cl^- adsorption and Pt oxidation on planes where the Cl atom in solution will not react. The fact that a-c potentials are necessary for erosion has been suggested to arise from the necessity to remove adsorbed oxygen or oxide before Cl^- attack is possible (10-13). Evidence on the existence and nature of such oxides is not sufficient to decide this issue. An alternative is that, in the cathodic cycle, the adsorbed $PtCl_6^=$ species is desorbed into solution to allow attack of the underlying Pt metal. The etching rates also suggest that Pt metal may be redeposited on some crystals planes in Cl^- solutions.

Electrochemical cyanide.—Presumably, this process is similar to that in Cl^- except the anion involves Pt^{+2}. However, a different plane is formed, and dissolution is much more rapid in CN^- solution. Significant differences must, therefore, exist in the various steps leading to dissolution.

Table I. Comparison of crystallographic anisotropies in etching

Etching method	Planes formed	Overall shape	Planes attacked most rapidly	Planes attacked most slowly
Aqua regia	(110)	Cube	(210) (100)†	(111)* (100)*
A-C Cl- electrolysis	Near (100)	Cube	(100) (111)	(110)
A-C CN- electrolysis	(110) Near (221)	Octahedron	(111)	(110)

* Inert except for attack from edges.
† The (100) plane is initially inert, but once attack from edges is complete, this region erodes more rapidly than any others.

Summary

The most important conclusions from these experiments are that etching produces predominantly one crystal plane, that the plane formed is different for each situation, and that it is not the close packed (111) plane. Electrolytic treatment of polycrystalline Pt wires, foils, and single crystals is highly effective in transforming surfaces into these orientations. This transformation is much faster in a-c chloride and cyanide solutions than with d-c etching or in other electrolytes. However, our criterion is the formation of facets $\gtrsim$ 1000Å in size, shorter times, and milder con-

ditions may still readily produce microfacets. We suggest that the standard procedures prescribed for "cleaning" Pt surfaces are probably highly effective in forming facets of another crystallographic orientation. We know of no straightforward technique to detect formation of microfacets except by the chemistry they produce.

Adsorption studies on single crystal planes of Pt imply that the adsorption and reaction properties of each crystal plane are quite distinct. For CO (17), H_2 (18), and NO (19) on all of the major planes, results can be summarized as indicating much higher heats of adsorption and reactivities on those planes, exposing four-fold adsorption sites on (100) than the two- and three-fold sites on (110) and (111). The (111) and (110) planes exhibit similar behavior in most respects, and behavior on high index and stepped planes generally appears to be correlated with the existence of several types of sites. It is interesting to note that stepped planes, associated with curved surfaces near a high density orientation, do not appear to form in our experiments except for the (100) plane in chloride solution; this plane is itself highly reactive. Stepped planes are predicted to be highly unstable if the high density plane exhibits a cusp in its Wulff plot (15, 16).

While we have only attempted to offer qualitative explanations of the molecular processes responsible for these phenomena, detailed studies of these processes are obviously necessary to explain this behavior. Crystallographic anisotropies play a dominant (and unavoidable) role in all electrochemical processes. The use of additional analytical techniques and detailed modeling will be necessary to explain these situations and to exploit them to control processes at electrode surfaces.

Acknowledgments

This research was partially sponsored by the University of Minnesota Corrosion Center funded by the Department of Energy. Surface analysis was obtained through the Electron Microscopy Center and the Regional Instrumentation Facility for Surface Analysis.

Manuscript submitted April 12, 1982, revised manuscript received Sept. 20, 1982.

Any discussion of this paper will appear in a Discussion Section to be published in the December 1983 JOURNAL. All discussions for the December 1983 Discussion Section should be submitted by Aug. 1, 1983.

REFERENCES

1. Ronald Woods, in "Electroanalytical Chemistry," Vol. 9, p. 2, A. Bard, Editor, Marcel Dekker, New York (1976).
2. P. N. Ross, Jr., *This Journal*, **126**, 67 (1979).
3. K. Yamamoto, D. M. Kolb, R. Kotz, and G. Lehmpfuhl, *J. Electroanal. Chem.*, **96**, 233 (1979).
4. A. T. Hubbard, R. M. Ishikawa, and J. Katekaru, *ibid.*, **86**, 271 (1978).
5. L. D. Schmidt, in "Topics in Applied Physics," Vol. 4, p. 63, R. Gomer, Editor, Springer-Verlag, New York (1975).
6. E. Yeager, W. E. O'Grady, M. Y. C. Woo, and P. Hagans, *This Journal*, **125**, 348 (1978).
7. A. T. Gwathmey and A. F. Benton, *J. Chem. Phys.*, **8**, 431 (1940).
8. A. T. Gwathmey and R. E. Cunningham, *Adv. Catal.*, **10**, 57 (1948).
9. M. Flytzani-Stephanopoulos, S. Wong, and L. D. Schmidt, *J. Catal.*, **49**, 51 (1977).
10. J. Llopis and A. Sancho, *This Journal*, **108**, 720 (1961).
11. J. A. Bittles and E. L. Littauer, *Corros. Sci.*, **10**, 29 (1970).
12. M. Pourbaix, "Atlas of Electrochemical Equilibria in Aqueous Solutions," Pergamon Press, Oxford, New York (1966).
13. R. Juchniewicz, *Corros. Sci.*, **6**, 69 (1966).
14. P. Bindra, S. J. Clouser, and E. Yeager, *This Journal*, **126**, 1631 (1979).
15. M. Flytzani-Stephanopoulos and L. D. Schmidt, *Prog. Surf. Sci.*, **9**, 83 (1979).
16. C. Herring, *Phys. Rev.*, **82**, 87 (1951).
17. A. Crossley and D. A. King, *Surf. Sci.*, **95**, 131 (1980).
18. K. E. Lu and R. R. Rye, *ibid.*, **45**, 677 (1974).
19. R. J. Gorte, L. D. Schmidt, and J. L. Gland, *Surf. ibid.*, **109**, 367 (1981).

The Electroreduction of Carbon Dioxide and Formic Acid on Tin and Indium Electrodes

S. Kapusta* and N. Hackerman†

Chemistry Department, Rice University, Houston, Texas 77251

ABSTRACT

The electrochemical reduction of carbon dioxide and formic acid has been studied in aqueous solutions on tin and indium electrodes using a-c impedance and photoemission techniques. Carbon dioxide reduction to formic acid (or the formate ion) proceeds with high current efficiencies (about 95%) although the overall power efficiency is low due to the high overpotential of the reaction. The reaction mechanism on tin and indium is similar to that postulated on mercury cathodes (17). The reaction rates are higher than on mercury and are affected by adsorption of intermediates and kinetics complications due to side reactions. Reduction of formic acid was only observed on tin cathodes at low current densities. The poor efficiency of this reaction is related to the formation of organometallic complexes on the electrode surface that accelerate the rate of hydrogen evolution.

The cathodic reduction of carbon dioxide has attracted considerable attention in recent years, especially as an alternative to photosynthesis for the production of organic raw materials or fuels [Ref. (1-7) and references therein]. The main reaction product in aqueous solutions is formic acid (or the formate ion), with faradaic efficiencies of over 90% on metal electrodes. The reduction of formic acid is more difficult. The best electrocatalyst materials are metals with high hydrogen overpotential (lead, tin, indium) and low pzc (3, 7). This latter condition may be related to the adsorption and desorption of reaction intermediates.

In this paper we report on the reduction of both carbon dioxide and formic acid in aqueous solutions on tin and indium cathodes. Both a-c impedance and photoemission techniques have been used in addition

* Electrochemical Society Active Member.
† Electrochemical Society Honorary Member.
Key words: tin, indium, reduction, carbon dioxide, formic acid, photoemission.

to electrochemical measurements to determine the reaction kinetics and mechanism.

Experimental

All measurements were performed in a standard, three compartment, all-glass cell at 23° ± 0.2°C. The cell was fitted with a quartz window to allow illumination of the electrodes. Preparation of the electrodes has been described elsewhere (8). Solutions were made from analytical grade reagents and conductivity water (8) and were deaerated by continuous bubbling of purified nitrogen. Nitrous oxide was used as a standard to calibrate the photoemission currents (9). The concentration of carbon dioxide was altered by changing the ratio of N_2 to CO_2 in the gas flowing through the solution and was calculated from standard thermodynamic data (10). The partial currents of the CO_2 electroreduction were determined by subtracting the hydrogen evolution current measured in solutions saturated with nitrogen from the current measured in a CO_2/N_2 atmosphere. It was assumed that, as a first approximation, the partial currents of hydrogen deposition and CO_2 reduction were additive, *i.e.*, there is no catalytic acceleration or inhibition of the hydrogen evolution process in the presence of CO_2. The partial current of formic acid reduction was calculated from the charge consumed in methanol production during long-term electrolysis experiments, following the procedure described in Ref. (2).

The circuits and techniques used for electrochemical, photoelectrochemical, and impedance measurements were described earlier (8, 11). All results are referred to the geometrical electrode area (1 cm²), although roughness factors of 2 for tin and 1.4 for indium were estimated from the capacitance results. All potentials are referred to the saturated calomel electrode (SCE).

Results and Discussion

Reduction of Carbon Dioxide

Electrochemical reduction.—The polarization curves of the electroreduction of CO_2 on tin and indium cathodes in a 0.95 KCl + 0.05 $NaHCO_3$ solution saturated with CO_2 are shown in Fig. 1, together with the results reported on mercury under similar conditions (7). The effect of concentration polarization has been eliminated using the values of $[i \cdot i_d/(i_d - i)]$ as ordinates, where i_d is the limiting diffusion current in unstirred solutions and i is the cathodic current measured at any potential E.

Two Tafel regions are observed in the case of tin. The first one, at potentials $E > -1.45$V, has a slope of 115 mV/decade and extends over approximately two orders of magnitude of current. The second region, at $-1.45\text{V} > E > -1.8$V, has a slope of 320 ± 20 mV. The partial current of the CO_2 reduction is difficult to estimate in this second region, since the hydrogen evolution currents are high and depend on both stirring and the buffer capability of the solution. In the case of indium, a single Tafel line, with a slope of 140 mV/decade, is observed over the entire potential range studied.

Within experimental accuracy, the partial CO_2 reduction current in the first Tafel region does not depend on solution *p*H, in the range 1-6.5. In the second region, the current tends to increase slightly with *p*H, although, as mentioned above, the experimental error is large at these large negative potentials. The partial current is also independent of solution composition, *i.e.*, similar results are obtained in carbonate, phosphate, acetate, and borate buffer solutions. Some experiments were performed using tetramethyl ammonium chloride instead of KCl as supporting electrolyte. In all cases, formate ions are the main product of the reaction. In fact, oxalate, mallate, or glycollate were not detected by careful analysis of the solution

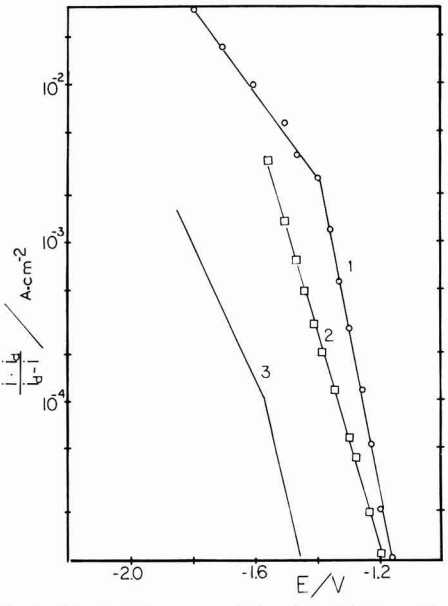

Fig. 1. Potentiostatic current, i (for Sn and Hg) or $[(i \cdot i_d)/(i_d - i)]$ (for In), vs. potential, E, polarization curves of the partial current of carbon dioxide reduction measured on tin (curve 1), indium (curve 2), and mercury (curve 3) electrodes in a 0.95 KCl + 0.05M $NaHCO_3$ solution saturated with CO_2 at 1 atm. Results for mercury taken from Ref. (7).

following the procedure described in Ref. (12). The reaction order with respect to CO_2 is 1 over the entire potential range. These results are in excellent agreement with previous reports (6, 13).

The CO_2 reduction process can be represented by two successive electron transfer reactions, preceded by an adsorption equilibrium

$$CO_{2\,aq} \rightleftharpoons CO_{2\,ads} \qquad [1]$$

$$CO_{2\,ads} + e^- \rightleftharpoons CO_2^{\cdot-}{}_{ads} \qquad [2]$$

and

$$CO_2^{\cdot-}{}_{ads} + AH + e^- \rightarrow HCO_2^- + A^- \qquad [3]$$

where AH is the proton donor and ads indicates an adsorbed species.

Both capacitance and potential decay measurements indicate that coverage of the electrode by adsorbed species is small ($< 5\%$). Assuming Langmuir conditions, the Tafel slopes of ~120 mV/decade and the independence of the cathodic currents on *p*H indicate that step [2] is the rate-determining step (rds) of the reaction on both electrodes, at least at the more positive potentials. The change to a Tafel slope of ~340 mV/decade at more negative potentials ($E < -1.4$V) on tin cathodes can be taken as an indication of a change in the rds.

Extrapolating the Tafel lines measured at the more positive potentials in Fig. 1 to the reversible potential of the reaction under these experimental conditions (*p*H ~ 7), *i.e.*

$$CO_2 + H_2O + 2e^- \rightarrow HCO_2^- + HO^- \quad E_r = -0.76\text{V} \qquad [4]$$

the approximate values of the exchange current densities i_o for Hg = 5×10^{-11} A/cm², Sn = 1×10^{-9} A/cm², and In = 1×10^{-8} A/cm² can be calculated. Even though current efficiencies as high as 99% can be obtained, the overall power efficiency of the reduction process is low because of the low i_o (or high overvoltages) of the reactions involved.

Photoelectrochemical reduction.—Further information about these reactions can be obtained from photoemission experiments. The irradiation of a polarized metal surface in contact with aqueous electrolytes with light of a certain energy (wavelength) leads to the photoemission of electrons into the solution (9, 14). In the presence of an appropriate electron scavenger, capture of the photoemitted electrons results in generation of radical anions at or near the electrode surface. The measured photocurrent depends on the decay mechanism of these radicals: photocurrents can be observed only if they decay to electroinactive species either through dimerization or reduction at the electrode.

Figure 2 shows the potential dependence of the photocurrents measured on a tin electrode in a 0.95M KCl + 0.05M $NaHCO_3$ solution, saturated with N_2O and CO_2. In the first case a photocurrent i_p is observed at all potentials $E < -0.9$V. The shape of the i_p *vs.* E curve differs from that measured, *e.g.*, on mercury, since electrochemical reduction decreases the concentration of N_2O at the surface at high negative potentials (8). In the solutions containing CO_2 as electron scavenger, a photocurrent appears only at $E < -1.2$V. The ratio of the photocurrents, $i_p(CO_2)/i_p(N_2O)$, first increases with potential, but then remains constant for $-1.4 > E > -1.6$V. Once again, the decrease in $i_p(CO_2)$ at large negative potentials is due to the depletion of CO_2 by electrochemical reduction. Similar results were obtained on indium electrodes.

A parameter usually employed for analyzing the results of photoemission experiments is the stoichiometric number, ν. This number represents the total number of electrons transferred from the electrode for each successful act of photoelectron capture in solution. For instance, $\nu_{N_2O} = 2$. For any scavenger S, and using N_2O as calibration standard, the value of ν_S can be calculated from (15, 16)

$$\nu_S = \frac{2i_p(S)}{i_p(N_2O)}\left[\frac{k_{N_2O}\cdot C_{N_2O}}{k_S\cdot C_S}\right]^{1/2} \qquad [5]$$

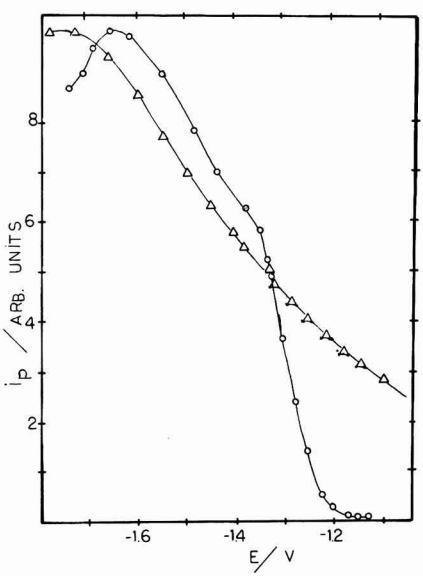

Fig. 2. Potential dependence of the photocurrent i_p measured on a tin electrode under periodic illumination. 0.95M KCl + 0.05M $NaHCO_3$ solution saturated with N_2O (△) or CO_2 (○). Chopping frequency 17 Hz. Wavelength = 410 nm. Light intensity ~10 mW/cm².

where k_S and k_{N_2O} are the rate constants for the homogeneous reaction of solvated electrons, e_{aq}, with S and N_2O, respectively, and C_S and C_{N_2O} are the corresponding concentrations. At potentials where the photocurrents are diffusion limited, the dependence of i_p on the concentration of scavenger, S, can be approximated by (9, 16)

$$i_p = i_e\delta\left[\frac{k_S\cdot C_S}{D_e}\right]^{1/2} \qquad [6]$$

where i_e is the total photoemission current, D_e is the diffusion coefficient of e_{aq}, and δ is a parameter that depends on the function used to describe the solvated electron redeposition. Therefore

$$\frac{i_p(CO_2)}{i_p(N_2O)} = \left[\frac{k_{CO_2}\cdot C_{CO_2}}{k_{N_2O}\cdot C_{N_2O}}\right]^{1/2} \qquad [7]$$

Figure 3 shows the dependence of the constant photocurrent ratio (see above) on the square root of the CO_2 concentration. From the slope of this line, the rate constant for the homogeneous reaction of hydrated electrons with CO_2 can be calculated. A value of $k_{CO_2} = 7 \times 10^9$ M^{-1} sec^{-1} is obtained, in excellent agreement with previous reports on Hg (15). This independence of the reaction rate on electrode material is typical of homogeneous reactions.

The following mechanism has been proposed to account for the photocurrents observed in CO_2 solutions (15)

$$CO_2 + e^-_{aq} \rightarrow CO_2^- \qquad [8]$$

followed by

$$CO_2^- + AH + e^-_M \rightarrow HCO_2^- + A^- \qquad [9]$$

and/or

$$CO_2^- \rightarrow CO_2 + e^-_M \qquad [10]$$

Here the subscripts aq and M indicate electrons that are hydrated in solution or in the metal, respectively. Some of these species may be adsorbed on the electrode surface (see below). This mechanism shows that a photocurrent will be observed only if the radical anion formed after capture of e_{aq} by CO_2, Eq. [8], is further reduced at the electron through step [9] ($\nu_{CO_2} = 2$). Otherwise, if the radical is re-oxidized through step [10], no photocurrent should appear ($\nu_{CO_2} = 0$). From the results in Fig. 2, we conclude that ν_{CO_2} goes from 0 to 2 over a narrow potential range (~150 mV).

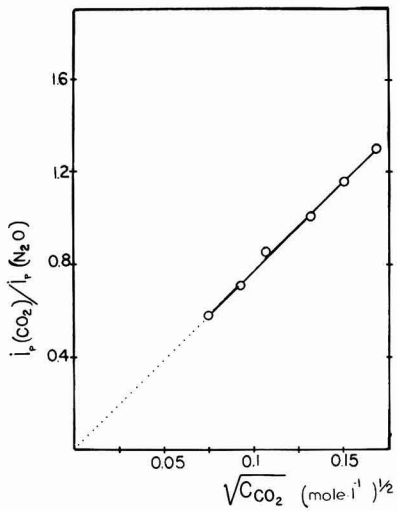

Fig. 3. Dependence of the ratio of the photocurrents, $i_p(CO_2)/i_p(N_2O)$, on the square root of the CO_2 concentration. Potential range −1.5 to −1.65V. Other conditions as in Fig. 2.

Considering Eq. [8]-[10], the steady-state photocurrent is given by (14, 15)

$$i_p = \frac{2i_o k_{o9} C_{AH} \exp[-\alpha f(E - E_{o9})]}{k_{o10} \exp[\beta \mathbf{F}(E - E_{o10})] + k_{o9} C_{AH} \exp[-\alpha f(E - E_{o9})]} \quad [11]$$

where i_o is the electron photoemission current after subtraction of the redeposition current of electrons that do not react with the CO_2 scavenger molecule, $f = \mathbf{F}/RT$, C_{AH} is the concentration of the proton donor AH, k_{o9} and k_{o10} are the rates of reactions [9] and [10], respectively, at the corresponding standard potentials E_{o8} and E_{o9}, and α and β are the charge transfer coefficients. The factor 2 in Eq. [11] represents the stoichiometric number for the total photoelectrochemical reduction of CO_2. From Eq. [11], the photocurrent goes to 0 at the more positive potentials ($E - E_{o10} >> 0$), and to $2i_o$ at more negative potentials ($E - E_{o9} << 0$).

Equation [11] can be rearranged to give

$$E = 1/f(\alpha + \beta)\{\ln[(2i_o/i_p) - 1] + \ln(k_9/k_{10}) + \ln C_{AH}\} \quad [12]$$

Here $k_9 = k_{o9} \exp(\alpha f E_{o9})$ and $k_{10} = k_{o10} \exp(-\beta f E_{o10})$.

The product of solvated electron capture by N_2O (*i.e.*, $HO\cdot$) is completely reduced at potentials $E < -0.9$V. Therefore (14)

$$2i_o = i_p(N_2O) \times \left[\frac{k_{CO_2} \cdot C_{CO_2}}{k_{N_2O} \cdot C_{N_2O}}\right]^{1/2} \quad [13]$$

Figure 4 shows the results of plotting the experimental data obtained on tin and indium electrodes according to Eq. [12]. The value of $(2i_o/i_p - 1)$ gives the ratio between the rates of $CO_2^{\cdot-}$ reduction and oxidation according to Eq. [9] and [10], respectively. This ratio is equal to 1 at a potential $E^{\neq} = -1.35$V on tin, -1.25V on indium, and -1.5V on mercury (15). At more positive potentials, corresponding to the first Tafel region of the polarization curves of tin in Fig. 1, the oxidation rate of $CO_2^{\cdot-}$ is higher than its reduction rate. At potentials $E < -1.35$V, *i.e.*, in the second Tafel region in Fig. 1, the reduction of $CO_2^{\cdot-}$ predominates over its oxidation. From the slope of the lines in Fig. 4, the value $\alpha + \beta = 0.6$ for both tin and indium can be calculated. On mercury, on the other hand, this value is *ca.* 0.9. The values of $E^{\neq}$ are independent of pH above 5.5, indicating that water molecules act as proton donors. As expected from Eq. [11], $E^{\neq}$ are also independent of the CO_2 concentration.

The differences between the values of overpotential for CO_2 reduction on Hg and Sn in the dark (~0.25V) and under illumination (~0.15V) are almost equal. We can thus assume that the reaction mechanism on both metals is the same, as described by Eq. [1]-[3]. Step [2] is the rds at $E > -1.4$ (in the first Tafel region). At more negative potentials, step [3] determines the reaction rate. The small potential dependence of the current in this region may be due to a decrease in the surface concentration of $CO_2^{\cdot-}$ as the electrode potential is made more negative. As mentioned earlier, the partial current of CO_2 reduction increases slightly with pH in the second Tafel region, a result that is at variance with the postulated rds. This apparent contradiction arises from the assumption that the background current due to hydrogen ion reduction remains constant in solutions saturated with CO_2 or N_2. This assumption may not be valid in acid solutions (see below). The dependence of the reaction rate (and $E^{\neq}$) on the nature of the cathode indicates that the reaction intermediates are adsorbed on the surface. The surface coverage, however, is very small.

Some photoelectrochemical experiments were performed in 1M KCl solutions saturated with either N_2 or CO_2 and containing 1×10^{-3}, 2×10^{-3}, 5×10^{-3}, and 2×10^{-2}M HCl to adjust the solution pH. Since two electron scavengers, H^+ and CO_2, are present, the resulting photocurrents are determined by the electrochemical behavior of the primary products formed, H· atoms and $CO_2^{\cdot-}$ radicals. In a first approximation, we can neglect any secondary reactions between the radicals initially formed and the scavengers in solution. Thus, the photocurrent measured with two competing scavengers, A and B, is related to that produced by a single species by (9)

$$\frac{i_p(A + B)}{i_p(A)} = \frac{\nu_A k_A C_A + \nu_B k_B C_B}{\nu_A (k_A C_A)^{1/2} (k_A C_A + k_B C_B)^{1/2}} \quad [14]$$

Figure 5 shows some typical results obtained on tin electrodes in acid solutions saturated with N_2O, N_2,

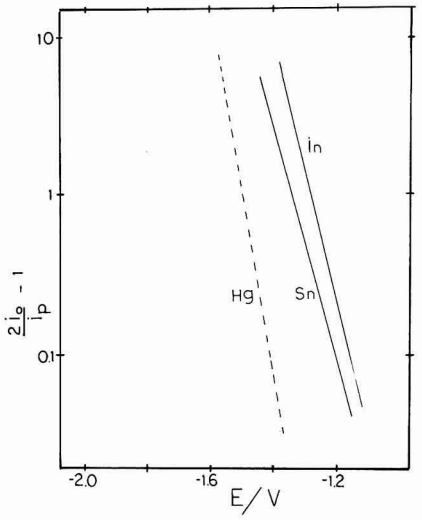

Fig. 4. Results of plotting the data from Fig. 2 according to Eq. [12]. Results for Hg taken from Ref. [15].

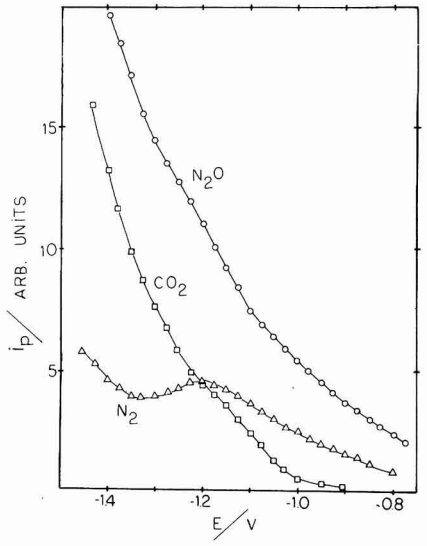

Fig. 5. Potential dependence of the photocurrents i_p measured on a tin electrode under periodic illumination in a 1M KCl + 0.001M HCl solution, pH = 3.0, saturated with N_2O (○), N_2 (△), and CO_2 (□). Other conditions as in Fig. 2.

and CO_2. A completely similar behavior was observed on indium cathodes. The constant ratio $i_p(H)/i_p(N_2O)$ at potentials $E > -1.2V$ indicates that oxidation of the H· atoms formed after the initial electron capture by H^+ does not occur within the potential range considered here. Thus, the photoelectrochemical reduction of H^+ can be described by

$$H^+ + e_{aq} \rightarrow H\cdot \quad [15]$$

$$H\cdot + H^+ + e_M^- \rightarrow H_2 \quad [16]$$

From the dependence of the photocurrent ratio on the hydrogen ion concentration, a value of $k_H = 1.3 \times 10^{10}\ M^{-1}\ sec^{-1}$ can be calculated, in good agreement with previous reports (9). The decrease in $i_p(H)$ at high negative potentials is caused by the depletion of H^+ ions due to their electrochemical reduction.

When the results obtained in the CO_2-saturated solution are analyzed using Eq. [14], negative values of ν_{CO_2} are calculated at $E > -1.1V$. The failure of this model to describe the behavior of acid CO_2 solutions arises from the assumption that there is no interaction between the radicals and the scavengers in solution. This interaction may be stated in terms of the reaction between a fraction of the H· atoms produced through Eq. [15] with CO_2 molecules in solution (15, 16)

$$H\cdot + CO_2 \rightleftharpoons COOH \quad [17]$$

or

$$H\cdot + CO_2 \rightleftharpoons CO_2^{\tau} + H^+ \quad [18]$$

If the COOH or CO_2^{τ} radicals thus formed are oxidized there will be a net decrease in the photocurrent as compared with CO_2-free solutions. The ratio of photocurrents will then be given as (15, 16)

$$\frac{i_p(H^+ + CO_2)}{i_p(H^+)} = \frac{\nu_{CO_2}(k_{CO_2}C_{CO_2} + \delta Q_H k_H C_H) + \nu_H(1 - \delta Q_H)k_H C_H}{\nu_H(k_H C_H + k_{CO_2}C_{CO_2})^{1/2}(k_H C_H)^{1/2}} \quad [19]$$

where $Q_H = (k_H \cdot C_{CO_2}/D_H)^{1/2}$, k_H· is the rate constant of the reaction of H· with CO_2, D_H is the diffusion coefficient of H·, and $\delta Q_H k_H C_H$ accounts for the reactivity of H· atoms toward CO_2. The parameter $(1 - \delta Q_H)$ can be calculated from the photocurrent ratio at potentials $E > -1.1V$ (15) and is equal to 0.7. Equation [19] can be used to determine the potential dependence of ν_{CO_2} in acid solutions. However, it is simpler to analyze the data in terms of an equation equivalent to Eq. [12], namely

$$\ln[(2/\nu_{CO_2}) - 1] = \ln(k_9/k_{10}) + f[E(1 - \alpha + \beta) - (1 - \alpha)E_{o9} - \beta E_o] - \ln C_H \quad [20]$$

where β and E_o are the transfer coefficient and standard potential of the reduction of CO_2^{τ} radicals in acid solutions, *i.e.*

$$CO_2^{\tau} + H^+ + e_M^- \rightarrow HCO_2^- \quad [21]$$

or

$$CO_2^{\tau} + H^+ \rightarrow COOH$$
$$COOH + e_M^- \rightarrow HCO_2^- \quad [22]$$

Figure 6 shows the result of plotting the photocurrent data obtained on a tin electrode in acid solutions saturated with CO_2 according to Eq. [20]. Measurements at $pH < 2$ are difficult because the dark currents become high and the electrode surface is covered with hydrogen bubbles. An average value of $\alpha + \beta = 0.5$ can be calculated from the slope of the lines, as compared with 0.6 on mercury. As expected from Eq. [20], $E^{\pm}$ shifts toward more positive potentials with an increase in the hydrogen ion concentration. From the limited data available it is not possible to determine the pH at which the reaction mechanism changes from that described by Eq. [9]-[10] to that of Eq. [21]-[22].

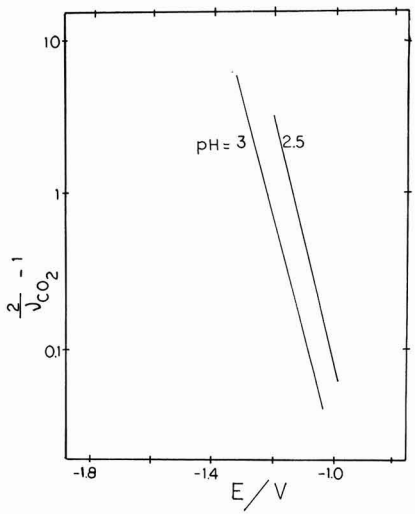

Fig. 6. Results of plotting the data from Fig. 5 according to Eq. [20].

Hydrogen atoms can also be formed during the electrochemical reduction of H^+ in the dark, *i.e.*, $H^+ + e_M^- \leftrightarrow H\cdot$. These atoms can then react with adsorbed CO_2 molecules, following a mechanism equivalent to Eq. [18]. The result of this process would be the "chemical" reduction of CO_2, with simultaneous elimination of H· atoms. For this reason, the partial current of hydrogen evolution may decrease in the presence of CO_2. The experimental procedure used to determine the partial CO_2 reduction current was based on the assumption that the hydrogen current remains constant in both N_2- and CO_2-saturated solutions. Therefore, coupling of the two reactions leads to erroneous conclusions regarding the pH dependence of the CO_2 reduction rate. A similar explanation was advanced in the case of mercury cathodes (15).

Reduction of Formic Acid

Electrochemical reduction.—The electrochemical reduction of formic acid on both tin and indium electrodes is a slow process. Solution analysis (2) revealed that methanol was the only detectable reaction product. During long-term electrolysis experiments (48 hr at currents between 1 and 50 μA), the highest current efficiency (~95%) was measured on tin cathodes in a 0.5M HCOOH + 0.5M HCOONa solution at $i \sim 5\ \mu A$, corresponding to a potential $E = -0.95V$. The efficiency fell quickly at more negative potentials.

At constant potential ($-0.85V > E > -1.2V$) the current increased slowly with time due to an acceleration of the hydrogen evolution process. A similar behavior was observed during electrolysis of formaldehyde solutions (8) and ascribed to the formation of tin complexes on the surface that reduce the hydrogen overpotential. The low efficiencies for formic acid reduction can thus be attributed to the competition of the hydrogen evolution reaction.

Further information about the system can be obtained from electrode impedance measurements.

Photoelectrochemical reduction.—The primary product formed after capture of e_{aq} by HCOOH may decompose according to (15)

$$HCCOH^{\tau} \rightarrow HCOO^- + H\cdot \quad [23]$$

or

$$HCOOH^{\tau} \rightarrow HCO\cdot + HO^- \quad [24]$$

H· atoms may also react with the formate ion

$$H\cdot + HCOO^- \rightarrow H_2 + CO_2^{-\cdot} \quad [25]$$

The photoelectrochemical behavior of formic acid solutions should be similar to that of CO_2-saturated solutions, with the additional complication introduced by reaction [24]. This has been shown to be the case on mercury electrodes (15): the potential dependence of the photocurrent exhibited a prewave, due to the reduction of $CO_2^{-\cdot}$ radicals following Eq. [23] and [25] and a main wave due to the reduction of HCO· radicals. On tin and indium, on the other hand, a single wave is found. The ratio $i_p(HCOOH)/i_p(N_2O)$ is constant over the entire potential range considered, indicating that reduction of the HCO· radical is a diffusion-limited process. Figure 7 shows the HCOOH concentration dependence of this constant ratio, from which a value of $k_{HCOOH} = 1.4 \times 10^9\ M^{-1}\ sec^{-1}$ can be calculated. This value is one order of magnitude larger than the one reported by Gordon *et al.* (18), which seems too low, and similar to the one measured on mercury (15). From these results we conclude that the rds of HCOOH reduction on both tin and indium is the transfer of the first electron to the HCOOH molecule. The reaction mechanism involves HCO· radicals as an adsorbed intermediate. The differences observed with respect to mercury electrodes can be ascribed to the higher rate of H· and $CO_2^{-\cdot}$ reduction on these metals. It is also possible that the electrode surface has a significant influence on the way the initially formed radical decomposes, *i.e.*, the ratio of H· to HCO· produced.

Impedance measurements.—Impedance measurements have been extensively used in the study of electrochemical reactions [*e.g.*, Ref. (19) and references therein]. Figure 8 shows the frequency response of the impedance measured on a tin electrode in a 1M HCOOH + 0.1M HCOONa solution at pH = 3.5. Similar results were obtained on indium electrodes. The complex plane spectrum (CPS) shows a single loop within the frequency range 10 kHz-2 Hz that can be analyzed on the basis of a Randles equivalent circuit (19). It is then possible to calculate the double layer capacitance, C_{dl}, the charge transfer and electrolyte resistances, R_{ct} and R_e, and the Warburg impedance, R_w. Figure 9 shows the potential dependence of the electrode capacitance, C_s (series equivalent circuit), and C_{dl} obtained from the CPS analysis.

The low values of C_{dl} are usually taken as an indication of adsorption, in this case of HCOOH. Desorption of this species was not observed. The product

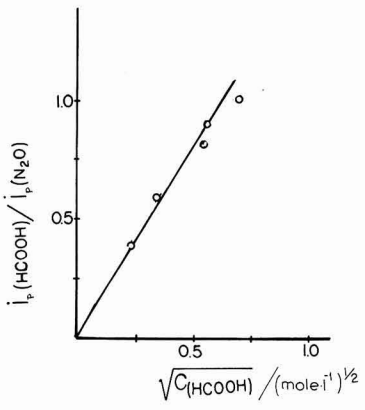

Fig. 7. Dependence of the photocurrent ratio $i_p(HCOOH)/i_p(N_2O)$ on the square root of the HCOOH concentration. Tin electrode. $E < -1.0V$.

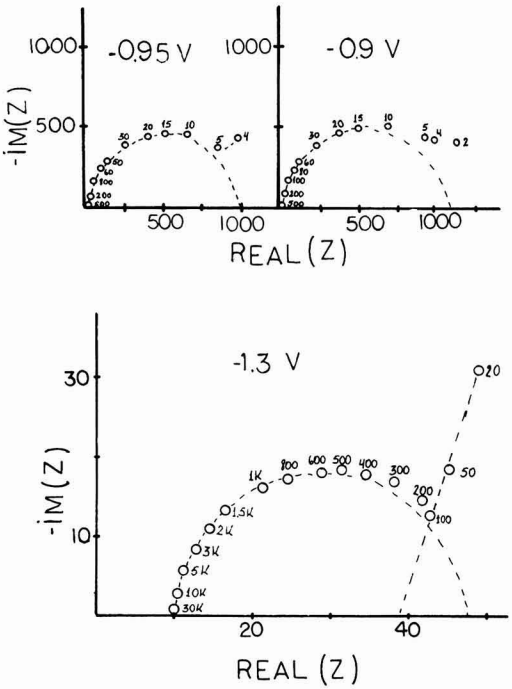

Fig. 8. Complex impedance $Z = Real(Z) - j \times Imaginary(Z)$ of a tin electrode measured in a 1M HCOOH + 0.1M HCOONa solution at the potentials indicated. Experimental points correspond to frequencies in Hz. Dotted lines show the best fitting to the results expected from a Randles equivalent circuit.

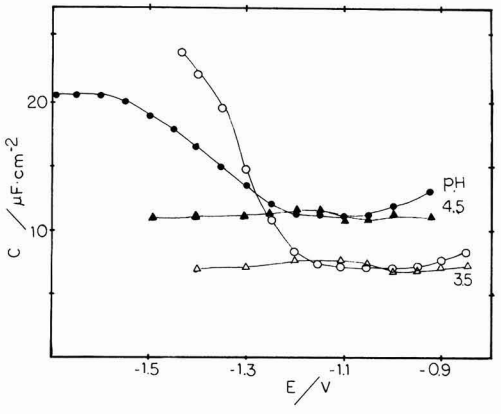

Fig. 9. Potential dependence of the series capacitance, C_s, measured at 1 kHz (○), and double layer capacitance, C_{dl}, determined from CPS (△), of a tin electrode in 1M HCOOH + 0.1M HCOONa, pH = 3.5 (open symbols) and 0.1M HCOOH + 1M HCOONa, pH = 4.5 (full symbols) solutions.

$R_{ct} \times i$ (where i is the cathodic current measured under potentiostatic conditions) is constant over the entire potential range here considered. Under these conditions it is not possible to separate the contribution of the HCOOH reduction reaction to the overall current. Future work will involve extending the low frequency limit below 1 Hz in order to observe slow processes, *e.g.*, desorption of HCOOH.

Acknowledgment

The financial support of the Robert A. Welch Foundation of Houston, Texas, is gratefully acknowledged.

Manuscript submitted May 20, 1982; revised manuscript received Oct. 18, 1982.

Any discussion of this paper will appear in a Discussion Section to be published in the December 1983 JOURNAL. All discussions for the December 1983 Discussion Section should be submitted by Aug. 1, 1983.

Publication costs of this article were assisted by Rice University.

REFERENCES

1. T. E. Teeter and P. Van Risselberghe, *J. Chem. Phys.*, **22**, 759 (1954).
2. F. H. Meller, Final Report (Phase II), Contract No. N00014-66-C0139, Office of Naval Research, Washington, DC (1968).
3. K. S. Udupa, G. S. Subramanian, and H. V. K. Udupa, *Electrochim. Acta*, **16**, 1593 (1971).
4. V. Kaiser and E. Heitz, *Ber. Bunsenges. Phys. Chem.*, **77**, 818 (1973).
5. J. Ryu, T. N. Andersen, and H. Eyring, *J. Phys. Chem.*, **76**, 3278 (1972).
6. A. V. Zakharyan, N. V. Osetrova, and Yu. B. Vasilev, *Sov. Electrochem.*, **13**, 1568 (1978).
7. P. G. Russell, N. Kovac, S. Srinivasan, and M. Steinberg, *This Journal*, **124**, 1329 (1977).
8. S. Kapusta and N. Hackerman, *J. Electroanal. Chem. Interfacial Electrochem.*, **138**, 295 (1982).
9. Yu. Ya. Gurevich, Yu. V. Pleskov, and Z. A. Rotenberg, "Photoelectrochemistry," Consultants Bureau, New York (1980).
10. "International Critical Tables," McGraw Hill, New York and London (1982).
11. S. M. Cai, C. Y. Liu, S. M. Wilhelm, and N. Hackerman, Abstract 697, p. 1115, The Electrochemical Society Extended Abstracts, Montreal, Quebec, Canada, May 9-14, 1982.
12. A. Bewick and G. P. Greener, *Tetrahedron Lett.*, **53**, 4623 (1969) **54**, 391 (1970).
13. A. V. Zakharyan, Z. A. Rotenberg, N. V. Osetrova, and Yu. B. Vasilev, *Sov. Electrochem.*, **14**, 1317 (1978).
14. Yu. V. Pleskov, Z. A. Rotenberg, V. V. Eletsky, and V. I. Lakomov, *Faraday Discuss. Chem. Soc.*, **56**, 52 (1974).
15. D. Schiffrin, *ibid.*, **56**, 75 (1974).
16. G. C. Barker, A. W. Gardner, and D. C. Sammon, *This Journal*, **113**, 1182 (1966).
17. W. Paik, T. N. Andersen, and H. Eyring, *Electrochim. Acta*, **14**, 1217 (1969).
18. S. Gordon, E. J. Hart, M. S. Matheson, J. Rabani, and K. J. Thomas, *Discuss. Faraday Soc.*, **36**, 193 (1963).
19. C. Gabrielli, "Identification of Electrochemical Processes by Frequency Response Analysis," Solartron Instrumentation Group, Irvine, CA (1980).

Polymer Films on Electrodes

XI. Electrochemical Behavior of Polymer Electrodes Produced by Incorporation of Tetrathiafulvalenium in a Polyelectrolyte (Nafion) Matrix

Timothy P. Henning* and Allen J. Bard**

Department of Chemistry, University of Texas, Austin, Texas 78712

ABSTRACT

The electrochemical behavior of the cation exchange polymer Nafion containing tetrathiafulvalenium (TTF^+) on a platinum substrate is described. The polymer electrode shows cyclic voltammetric behavior similar to that of solid films of TTF on platinum. In 1.0*M* KBr the oxidized form of the electroactive molecules in the polymer (TTF^+) forms nonstoichiometric complexes with Br^-. The peak potentials in cyclic voltammetry shift with changes in concentration of supporting electrolyte, temperature, and anion of the supporting electrolyte. Very narrow cyclic voltammetric waves are observed that result in part from attractive interactions between the electroactive molecules. The separation in peak potential of the reduction and oxidation waves is explained by formation of $TTFBr_{0.7}$ which stabilizes the oxidized form (TTF^+) and makes it harder to reduce. Peak potentials for the oxidation and reduction shift closer together as the scan rate is lowered, which is explained by a "square (reaction) scheme."

The electrochemistry of layers on electrode surfaces, both solids and polymers, has been investigated by many research groups. The cyclic voltammetric behavior of the surface-confined layers frequently deviates from the theoretical "thin film" behavior of a one-electron nernstian reaction at 25°C; *i.e.*, peak width at half-height ($\Delta E_{1/2}$) of 90.6 mV and no splitting between the anodic and cathodic peaks ($\Delta E_p = E_{pa} - E_{pc} = 0$) (1). Relatively few films show a $\Delta E_{1/2}$ significantly smaller than 90.6 mV (2). These narrow cyclic voltammetric (CV) waves were attributed to interactions among the electroactive molecules and phase formation in the layer. Large peak separations observed in cyclic voltammetry at fast scan rates (1 V/sec and larger) have been attributed to slow heterogeneous kinetics and resistance effects in the layer. Even at slow scan rates, where heterogeneous kinetics and resistance usually are not of importance, finite ΔE_p values have been observed. These have been explained by kinetic effects associated with phase formation (nucleation overpotential) (2d) and interconversion between different forms of the polymer-confined electroactive molecules with different standard potentials (3).

We recently described unusual CV behavior of a polymer electrode in which tetrathiafulvalenium ion (TTF^+) was incorporated into a layer of the perfluorinated sulfonate polymer, Nafion (NAF) (4). This polymer electrode exhibited narrow ($\Delta E_{1/2} < 20$ mV) CV waves and ΔE_p of $\sim$ 150 mV at intermediate scan rates (*e.g.*, 10 mV/sec). This is remarkably similar to the electrochemical behavior of solid films of TTF. In this paper we describe more detailed studies of the electrochemical behavior of the TTF/NAF polymer electrode, examining the effects of supporting electrolyte concentration, different supporting electrolytes, temperature, and different scan rates in cyclic voltammetry. We also obtained absorption spectra of the TTF polymer on SnO_2 transparent conducting electrodes, which yielded information about the nature of the electroactive TTF molecules in the polymer. In a related paper the behavior of solution redox species on the TTF polymer electrodes is described (5).

* Electrochemical Society Student Member.
** Electrochemical Society Active Member.
Key words: cyclic voltammetry, scan rate, chronoamperometric behavior.

Experimental

Materials.—TTF (Aldrich) was purified by several vacuum sublimations. TTFCl was synthesized by dissolving TTF in benzene and adding dropwise a benzene solution which was saturated with chlorine. The purple TTFCl precipitate was washed with ether and air dried. The supporting electrolytes were used as purchased. The 970 eq wt Nafion dissolved in ethanol was a gift from the E. I. du Pont de Nemours & Company.

Apparatus.—All electrochemical experiments employed a Princeton Applied Research (PAR) Model 175 universal programmer, Model 173 potentiostat, and Model 179 digital coulometer. Slow potential scans (< 1 mV/sec) were accomplished by introducing a voltage divider between the programmer and potentiostat. The working electrode used in all the electrochemical experiments was a Pt disk (area = 0.027 cm^2) embedded in a glass rod. A Pt mesh was used as a counterelectrode and a saturated calomel electrode (SCE) was used as a reference. Resistance compensation was used at all scan rates faster than 10 mV/sec by adjusting the amount of positive feedback just short of oscillation.

Procedure.—The electrodes were prepared by covering the Pt disk with 10 μliter of an EtOH solution of Nafion (2% by weight) and allowing the EtOH to evaporate. The dry thickness of the resulting films (typically 1 μm) was determined with a Sloan Dektak surface profile measuring system. The TTF^+ was incorporated into the Nafion film by immersing the electrode in an aqueous solution of ~ 1 m*M* TTFCl for 10 min. The electrode, denoted Pt/NAF,TTF^+, turned a golden color after immersion in the TTF^+ solution, indicating the incorporation of TTF^+. The average concentration of electroactive TTF in the electrode was typically about 0.3*M* as determined by the integrated charge under a steady-state CV wave.

Results

Cyclic voltammetry.—The behavior of a freshly formed Pt/NAF,TTF^+ electrode in aqueous 1.0*M* KBr is shown in Fig. 1. The first reduction scan of the electrode to TTF produced a broad cathodic wave. The oxidation of the electrode back to TTF^+ produced a sharp anodic wave which shifted toward less positive potentials with further cycling. The second reduction scan produced a sharp cathodic wave; this wave shifted very little in potential with further cycling. The Pt/NAF, TTF^+ electrode, which was originally golden in color, became colorless when the film was reduced in 1.0*M* KBr and then purple when the film was oxidized. After about 10 cycles the anodic wave attained a constant shape and peak potential. The integrated charge under the CV waves decreased for the first 4-5 cycles after which the integrated charge was about half that of the first reduction and then remained essentially constant. After about 2 hr the peak currents for the CV waves slowly decreased with continuous scanning and after about 12 hr the waves had disappeared.

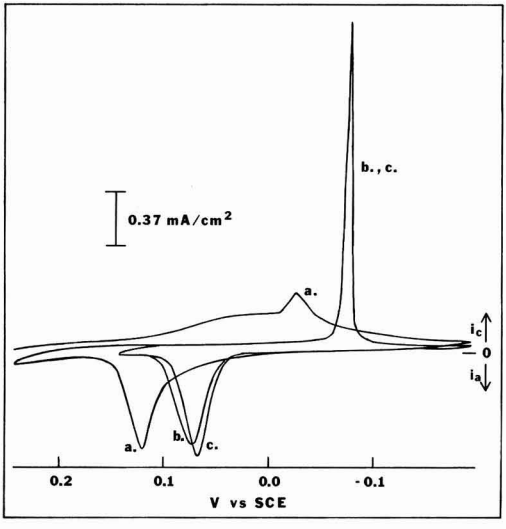

Fig. 1. Cyclic voltammogram of a Pt/NAF,TTF^+ electrode in 1M KBr at 10 mV/sec, (a) initial CV, first cycle; (b) third cycle; (c) fifth cycle. Integrated charge under the anodic wave, Q_t = 74 μC.

While the first CV reduction wave (Fig. 1) was a broad, drawn-out wave with a slowly decaying (diffusive) tail, which is characteristic of the CV waves seen for other electroactive molecules bound into Nafion polymer layers (6), the subsequent oxidation and reduction waves had shapes different from those previously seen in polymer electrodes. The purple color of the oxidized form of the electrode after the first and subsequent reductions has been ascribed to the formation of a $TTFBr_{0.7}$ complex, rather than the original golden material, where the TTF^+ ion is associated with the sulfonate group on the polymer. The stability of the freshly formed electrode was also very different from the electrochemically cycled electrode. When a freshly formed Pt/NAF,TTF^+ electrode was taken out of the aqueous TTFCl solution in which incorporation of TTF^+ took place, the golden-colored electrode could be immersed in water at open circuit for at least one week without any apparent effect on the subsequent electrochemistry of the polymer. If the electrode was immersed in 1.0*M* KBr, however, colored material diffused out of the polymer into the solution. Within a few minutes the amount of electroactive TTF^+ remaining in the polymer was greatly reduced over that which would have been found if the electrochemical cycling of the polymer had begun immediately. This experiment indicated that TTF^+ was indeed electrostatically bound into the Nafion polymer from the aqueous TTFCl solution and the stability of the polymer in water can be attributed to the absence of cations in solution capable of exchanging with the TTF^+ on the polymer sites. In 1.0*M* KBr, K^+ can replace TTF^+ on the polymer sites. Note, however, that after a few reduction or oxidation cycles, the electrode could be immersed at open circuit in 1*M* KBr in either the TTF^+ or TTF form with little loss of electroactive material over 1 hr. The difference in stability between the initially formed golden TTF^+ electrode and the electrochemically oxidized purple electrode in 1.0*M* KBr indicated that the electrochemically oxidized form of the polymer was very different from the initially formed material.

The steady-state cyclic voltammogram of a Pt/NAF, TTF^+ electrode is shown in Fig. 2a. For comparison, a cyclic voltammogram for a nernstian one-electron reaction showing thin layer behavior (7) with the same area under the waves is shown. This theoretical CV wave emphasizes both the unusual sharpness of the peaks and the nature of the peak separation at this scan rate. Also included in Fig. 2 is the CV of a solid film of TTF on a Pt electrode, denoted Pt/TTF. This film was formed by placing a drop of benzene containing dissolved TTF on a Pt electrode and allowing the benzene to evaporate. The similarities between the solid and polymer layers of TTF suggest that the TTF species in the polymer after cycling resembled the solid TTF and TTF^+-Br^- phases. However, while the Pt/NAF,TTF^+ electrode was reproducible and stable upon cycling for hours, the Pt/TTF electrode was less reproducible and became irreversibly oxidized in less than 1 hr of electrochemical cycling.

CV: effect of scan rate.—The CV behavior of a Pt/NAF,TTF^+ electrode was studied in 1*M* KBr for scan

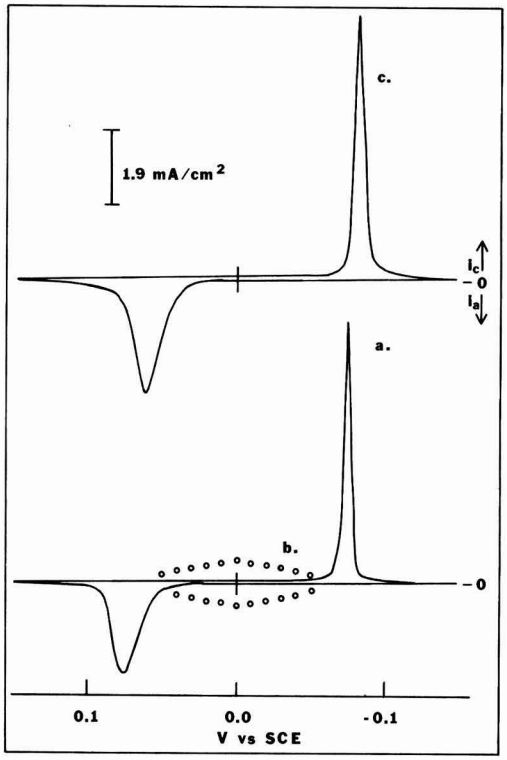

Fig. 2. Cyclic voltammogram at 10 mV/sec of (a) Pt/NAF, TTF^+ electrode in 1M KBr, $Q_t = 147$ μC; (b) ideal $1e^-$ thin layer electrode using Q_t as in (a) and an $E°$ of 0.0V; (c) Pt/TTF electrode (~800Å thickness) in 1M KBr.

rates (v) of 0.02-10 V/sec (Fig. 3-5). With increasing v, the peak potential of the anodic wave (E_{pa}) shifts toward more positive values and that of the cathodic wave (E_{pc}) toward more negative values (Fig. 6). In investigations at $v < 1$ mV/sec (Fig. 3), the electrode was scanned at 1 mV/sec until ~ 150 mV before the CV wave and then v was decreased to the desired value until the peak was traversed, then increased to 1 mV/sec again until the opposite peak was reached. Although both waves shifted with increasing v, the behavior of the anodic and cathodic waves with v was

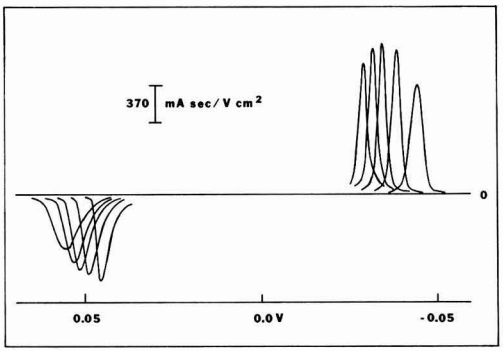

Fig. 3. Cyclic voltammogram (i_p/vA vs. E) of a Pt/NAF,TTF^+ electrode in 1M KBr at various sweep rates. The outside cathodic and anodic peaks correspond to a sweep rate of 0.5 mV/sec with subsequent anodic and cathodic peaks corresponding to sweep rates of 0.2, 0.1, 0.05, and 0.02 mV/sec. $Q_t = 152$ μC.

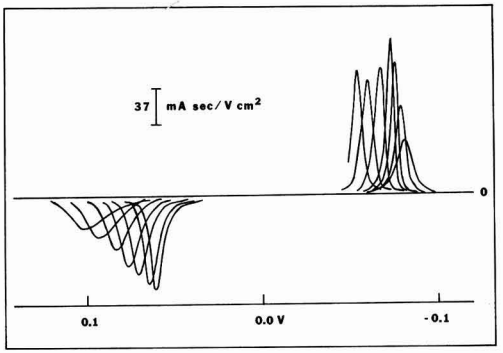

Fig. 4. Cyclic voltammogram (i_p/vA vs. E) of a Pt/NAF,TTF^+ electrode in 1M KBr at various sweep rates. The outside cathodic and anodic peaks correspond to a sweep rate of 100 mV/sec with subsequent anodic and cathodic peaks corresponding to sweep rates of 50, 20, 10, 5, 2, and 1 mV/sec. $Q_t = 44$ μC.

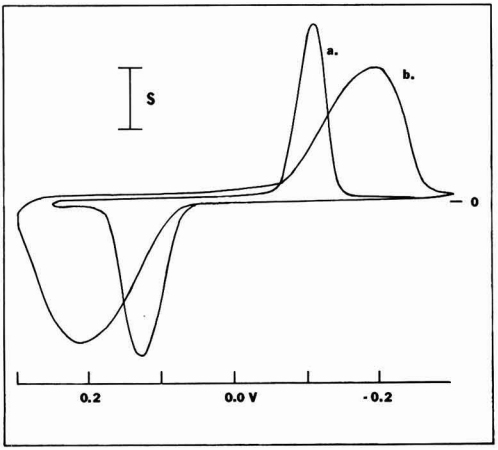

Fig. 5. Cyclic voltammogram of a Pt/NAF,TTF^+ electrode in 1M KBr at sweep rates of (a) 1 V/sec, $S = 14$ mA/cm², $Q_t = 55$ μC; (b) 10 V/sec, $S = 74$ mA/cm².

different. The anodic peak shifted out and became broader and i_{pa}/v decreased with increasing v. The cathodic peak shifted out but maintained roughly the same shape, and for $v < 50$ mV/sec, i_{pc}/v was nearly the same (Fig. 4). The integrated charges under the oxidation and reduction waves were within 5% of each other and constant for the range 1-10 V/sec. The integrated charge at $v < 1$ mV/sec was not measured, but the constant shape of the waves suggests that the charge was the same for all scan rates. The electrode deteriorated more rapidly at 10 V/sec than at slower scan rates, probably because of the large current density (0.16 A/cm²) being passed through the film at this v (Fig. 5).

The shape of the CV waves of Pt/NAF,TTF^+ electrodes varied slightly from electrode to electrode; the peak currents were directly influenced by the amount of TTF^+ incorporated into the polymer layer. The examples given in the figures represent typical behavior. Because the life of any single electrode was limited, the data represent the behavior from several different electrodes. The integrated charge under a steady-state wave in cyclic voltammetry is included with each figure to make comparisons between figures easier. The CV behavior for the Pt substrate was not unique. The CV waves of the NAF-TTF polymer on Au, pyrolytic

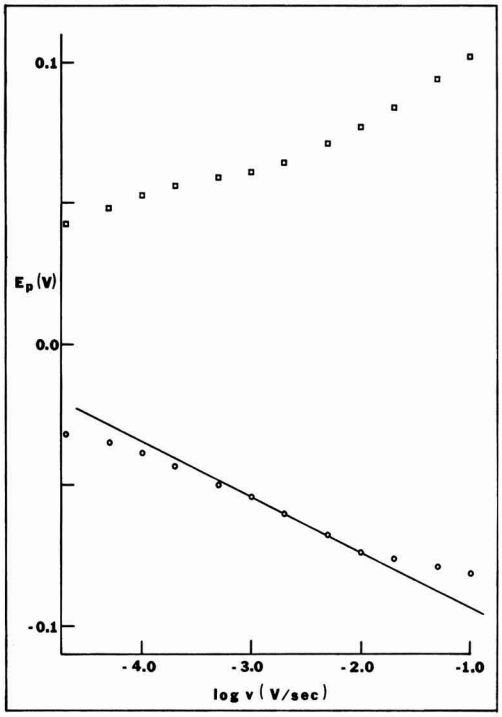

Fig. 6. Plot of E_{pc} (○) and E_{pa} (□) *vs.* log v. Same electrode as used in Fig. 4.

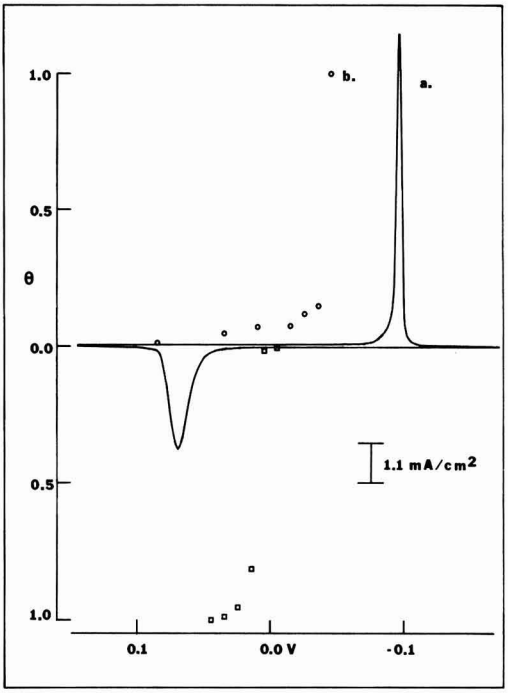

Fig. 7. (a) Cyclic voltammogram of a Pt/NAF,TTF^+ electrode in 1*M* KBr at 10 mV/sec, Q_t = 159 μC; (b) (circles and squares) electrochemical isotherm of the same electrode as shown in (a), showing total charge passed at given potential normalized to 159 μC.

graphite, optically transparent SnO_2-coated glass, and Ta substrates were very similar to that on a Pt substrate.

Equilibrium behavior.—To investigate whether the peaks would shift in and exhibit the same E_p value as equilibrium was approached, the potential was scanned to a given potential and held there until the current dropped below 1.5 nA (*i.e.*, 0.1 μC of charge per min). The ratio of the charge passed at a given potential to that needed for complete reduction or oxidation of the film, θ, as a function of E, is shown in Fig. 7. This CV isotherm taken at essentially an infinitesimal scan rate showed a sharp break in both the cathodic and anodic branches which occurred well before the peaks in the cyclic voltammogram at 10 mV/sec. If the time required for establishment of equilibrium was decreased by setting higher current limits, the effect on the isotherm was to shift the breaks in the isotherm to more negative and more positive potentials; this is the same effect as seen for the peak potentials in cyclic voltammetry with faster scan rates. The potential of the break was invariant with the amount of electroactive material reduced or oxidized in the layer during the break in the isotherm. If the potential was shifted to less negative potentials during the break in the cathodic isotherm the reaction immediately ceased. The cathodic isotherm had a long slow rise before the sharp break in the isotherm which possibly resulted from the existence of other forms of TTF^+, such as bound to the SO_3^- groups in the polymer.

CV: effect of scan reversal.—Reversal in the direction of a potential scan at different points along the CV wave was suggested by Conway *et al.* (8) to be a useful way of determining the effect of interactions among the molecules in the surface layer. The effect of scan reversal into both the oxidation and reduction waves of a Pt/NAF,TTF^+ electrode is shown in Fig. 8. The current after reversal of the scan was larger than that seen before the potential direction was reversed with this effect being more pronounced for the reduction wave. This effect is not usually seen with polymer or modified electrodes and points to strong positive (attractive) interactions among the oxidized molecules in the polymer with a smaller positive interaction among the reduced molecules. The potential of the reverse peak also showed a much larger shift for the reduction wave as compared to the oxidation wave.

CV: effect of supporting electrolyte concentration.—The concentration of supporting electrolyte was varied to determine the effect of changes in Br^- concentration on the cyclic voltammogram of a Pt/NAF,TTF^+ electrode. The results of varying the KBr concentration from 3.5 to 0.1*M* are shown in Fig. 9 for the same electrode. A plot of the shift in peak potential of both the cathodic and anodic waves *vs.* the log of the KBr concentrations for all concentrations investigated is shown in Fig. 10. The fact that the CV waves of the Pt/NAF,TTF^+ electrode responded to changes in the supporting electrolyte concentration was not surprising, because it has already been established that the oxidized form of the electrode involved formation of a TTF^+-Br^- complex. The shift in potential was close to the expected −59 mV per tenfold change in Br^- concentration. A significant deviation in the shape of the waves occurred at the lowest concentration, 0.1*M*. At this concentration each wave looked to be two waves, a broad diffusional looking wave with a sharper wave superimposed. Significantly, the color of the oxidized form of the wave at the lowest concentration was no longer purple but golden. The average molar concentration of electroactive TTF molecules in the polymer films, as was stated earlier, was typically 0.3*M*. The concentration of KBr present in the polymer after im-

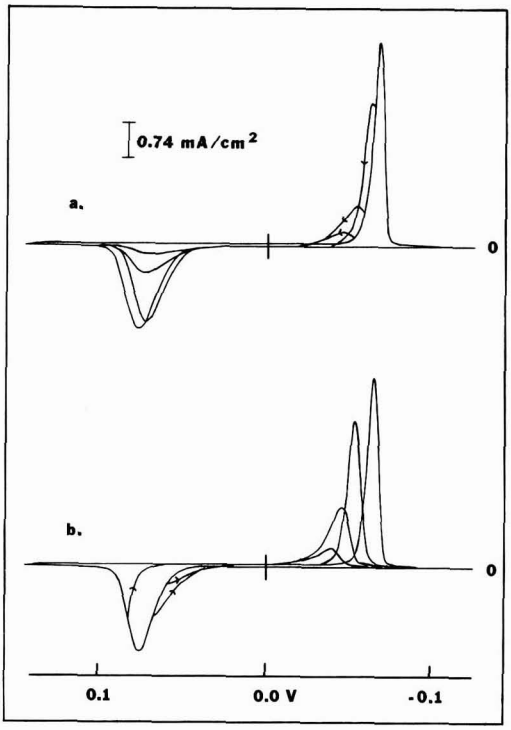

Fig. 8. Cyclic voltammogram of a Pt/NAF,TTF+ electrode in 1M KBr at 10 mV/sec with (a) scan reversal into the cathodic wave; and (b) scan reversal into the anodic wave; $Q_t = 90\ \mu C$.

mersion in a KBr solution is unknown, but examination of the polymers coated on Pt in a scanning electron microscope using energy dispersive spectroscopy showed

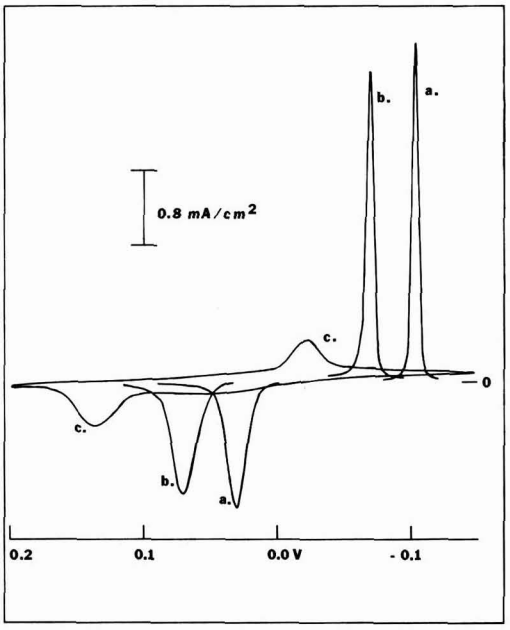

Fig. 9. Cyclic voltammogram of a Pt/NAF,TTF+ electrode at 10 mV/sec in (a) 3.48M KBr; (b) 1.0M KBr; $Q_t = 108\ \mu C$; (c) 0.1M KBr.

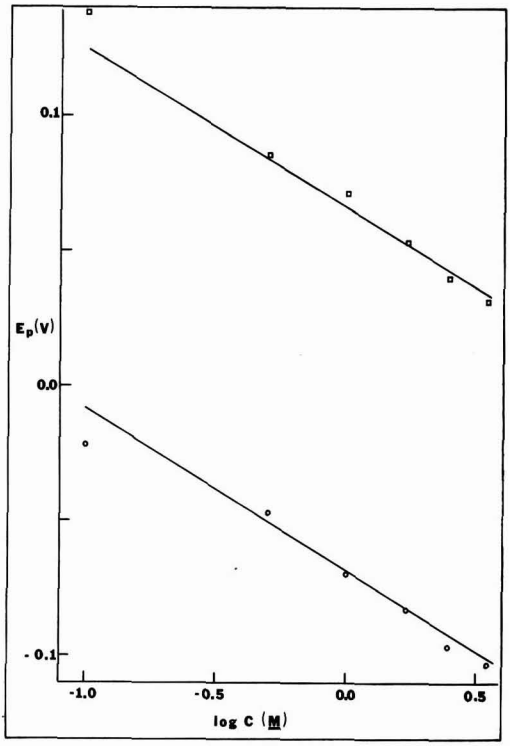

Fig. 10. Peak potential vs. log KBr concentration from the experiment shown in Fig. 9. Lines are drawn with a slope of −59 mV.

that after soaking in a KBr solution, Br was present in the polymer. Experiments using NaOH showed that after equilibration the Nafion achieved nearly the same concentration of NaOH as that present in solution (9). These facts suggested that the electrochemical process changed at the lowest concentration because of an excess in electroactive TTF over bromide ion present in the polymer.

CV: temperature effects.—The effect of varying the temperature on CV waves has been used to obtain information about the kinetics of reactions coupled to electron transfer reactions (10). Unusual temperature effects on the CV waves of TTF-TCNQ pressed pellet electrodes were previously observed (11). The temperature of the Pt/NAF,TTF+ electrode immersed in the solution was held at a given value by placing the electrochemical cell in a water bath. The SCE reference electrode remained at room temperature throughout the experiment with only the reference electrode tip in the solution. The CV waves of a Pt/NAF,TTF+ electrode were strongly temperature dependent as is shown in Fig. 11. Both the cathodic and anodic waves shifted closer together with increasing temperature. The reduction waves at the higher temperatures (36° and 55°C) were initially sharper than those at lower temperatures but within a few cycles broadened out to the shape shown in Fig. 11. The shift in peak potential with temperature was greater for the reduction wave as is shown in the plots of reduction and oxidation peak potentials *vs.* temperature (Fig. 12) which were linear over the temperature range studied.

CV: effect of different halide ions.—The halide ion in the supporting electrolyte was varied to determine the effect of the counterion on the CV waves of a Pt/NAF,TTF+ electrode (Fig. 13). The CV peaks shifted to more negative potentials in the order $Cl^- < Br^-$

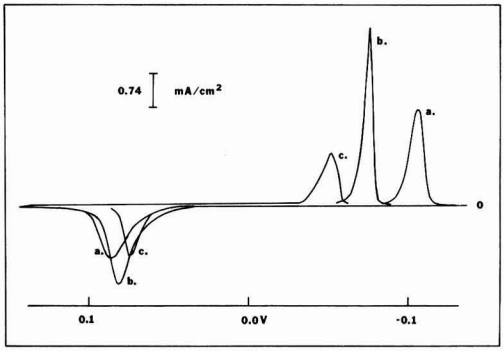

Fig. 11. Cyclic voltammogram of a Pt/NAF,TTF$^+$ electrode in 1M KBr at 10 mV/sec and at a temperature of (a) 1.5°C; (b) 21°C; $Q_t = 97\ \mu C$; (c) 36°C.

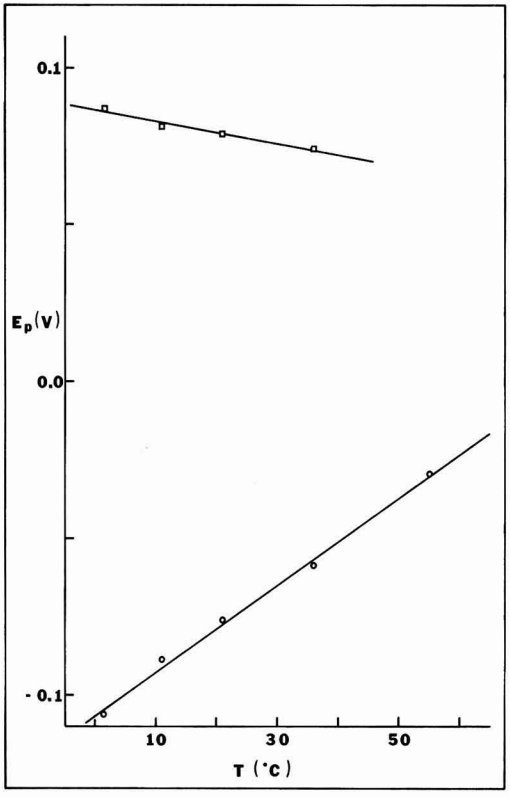

Fig. 12. Peak potential vs. temperature from the experiment shown in Fig. 11.

< I^- and the oxidized form of each electrode was purple. In KF the CV waves were broad and had a shape similar to that of other electroactive molecules observed in Nafion. The shape of the CV waves and the color of the oxidized form of the electrode, golden, in KF was identical to the electrode behavior observed using potassium acetate and potassium sulfate as supporting electrolytes. TTF$^+$ is known to form one-dimensional conducting complexes with Cl^-, Br^-, and I^-, but no conducting complexes have been reported using F^-, acetate, or sulfate. If the same electrode was used in different supporting electrolytes, the behavior was unaffected by the order in which the different solutions were investigated. No effect on the cyclic voltammogram of a Pt/NAF,TTF$^+$ electrode in a Br^- solution was seen when the cation of the supporting electrolyte was changed from potassium to sodium.

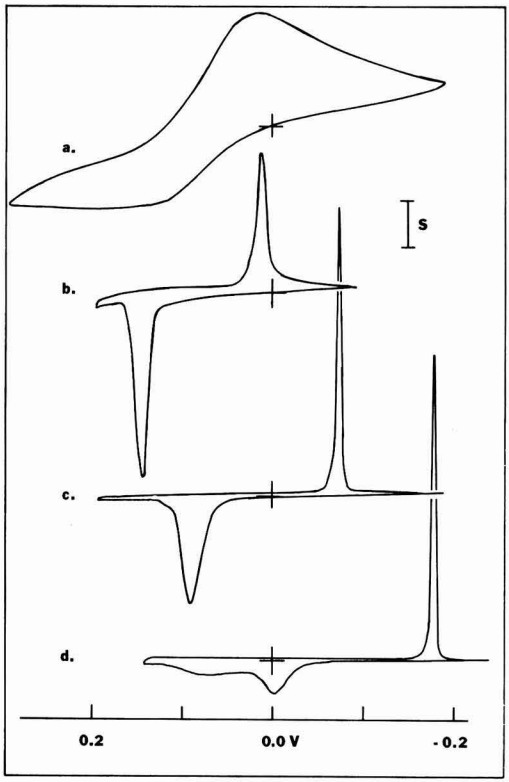

Fig. 13. Cyclic voltammogram of a Pt/NAF,TTF$^+$ electrode at 10 mV/sec in various supporting electrolytes: (a) 1M KF, S = 74 $\mu A/cm^2$; (b) 1M KCl, S = 740—(>40) $\mu A/cm^2$; (c) 1M KBr, S = 740 $\mu A/cm^2$, $Q_t = 137\ \mu C$; (d) 1M KI, S = 740 $\mu A/cm^2$.

Chronoamperometric behavior.—Chronoamperometric methods can be useful in determining the apparent diffusion coefficient, D_{app}, of a species confined to a layer on an electrode surface. When D_{app} is measured using chronoamperometric methods, the value may be associated with a specific ion diffusion through the polymer, an electron hopping process, or both, depending on what process limits the current (12). A potential step (0-0.25V) was applied to a reduced Pt/NAF, TTF$^+$ electrode in a 1*M* KBr solution and the current-time (i-t) transient recorded. The plot of i *vs.* $t^{-1/2}$ (Fig. 14) shows a linear region with zero intercept (Cottrell region). The slope of the linear region yielded D_{app} of 8×10^{-7} cm^2/sec based on the Cottrell equation and assuming an average concentration of the electroactive TTF molecules uniformly distributed throughout the film and a one-electron process. Based on the thickness of the layer and D_{app}, the onset of deviations from Cottrell behavior which occur at longer times due to thin layer effects occurred at approximately the expected time. The current from the i-t trace for the reduction of the electrode using a potential step from 0.2 to −0.4V decayed rapidly after 2 msec, presumably showing the effect of reduction of the bulk of the TTF$^+$. The processes by which the electrode reduced and oxidized during a potential step were clearly different.

Spectroscopy.—Electrodes were formed on a transparent SnO_2 glass conducting substrate so that ab-

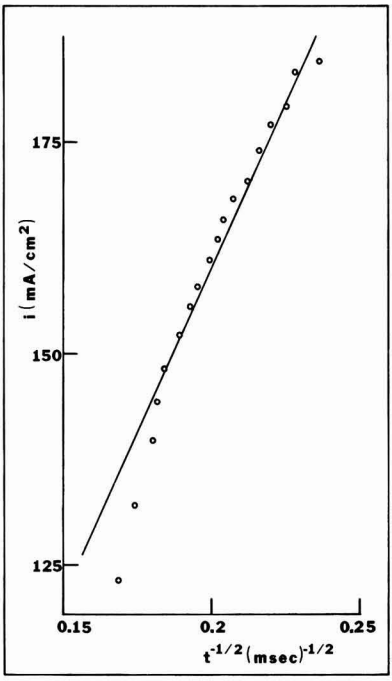

Fig. 14. Current vs. $t^{-1/2}$ for the oxidation of a Pt/NAF,TTF$^+$ electrode in 1M KBr. The potential was stepped from 0.0 to 0.25V.

sorption spectroscopy could be used to identify the form of the oxidized and reduced molecules in the polymer. The electrochemistry of the SnO_2/NAF,TTF$^+$ electrodes was similar to that of electrodes using Pt substrates. The vis-near infrared spectra of dry electrodes were recorded with a Cary 14 spectrophotometer for electrodes before electrochemical cycling and after electrochemical cycling with the electrode left in the reduced or oxidized forms (Fig. 15). The results from these spectra are shown in Table I along with results from previous studies of $TTFBr_{0.79}$ and TTFCl crystals (13). The spectrum of the electrode before electrochemical cycling was close to that of the dimer dication of TTF$^+$ as observed for TTFCl crystals (13). The peak at 790 nm (λ_{CT}) corresponds to an intermolecular electronic transition between the molecules of the dimer. The spectrum of the reduced form of the electrode did not show any peaks in the visible region; this corresponds to published spectra of TTF (13) where only an absorption peak in the u.v. was seen. The surface of the reduced form of the electrode

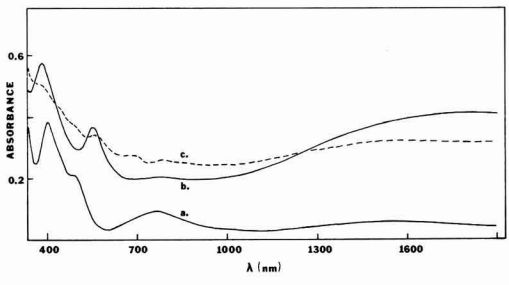

Fig. 15. Absorption spectrum of a dry glass-SnO_2/NAF,TTF$^+$ electrode (a) freshly formed; (b) after electrochemical cycling in 1M KBr, removed from solution in the oxidized state; (c) after electrochemical cycling in 1M KBr, removed from solution in the reduced state.

Table I. Absorption maxima of SnO_2/NAF,TTF$^+$ electrodes

	λ_{max} (nm)	λ_{sh} (nm)	λ_{CT} (nm)
Fresh SnO_2/NAF,TTF$^+$ electrode	400	490	760
TTFCl (dimer)*	380	530	790
Oxidized SnO_2/NAF,TTF$^+$ electrode	397	561	1890
$TTFBr_{0.79}$*	374	537	1970

* Absorption spectrum of powdered samples dispersed in KBr [from Ref. (13)].

was partially covered with the nonelectroactive crystals of $TTFBr_{0.7}$ (5), but the absence of any peaks in the spectra due to the nonelectroactive crystals means they contributed very little to the absorption spectrum. The spectrum of the electrode in the oxidized form also was similar to that for crystals of $TTFBr_{0.79}$, where the peak present in the near-infrared was shown to correspond to intermolecular electronic transitions along the conducting axis of the crystal. The presence of the near-infrared peak leads to the conclusion that the oxidized form of the electroactive molecules in the electrode was $TTFBr_{0.7\text{-}0.8}$.

Discussion

The electrochemical investigation of Pt/NAF,TTF$^+$ electrodes leads to the following model for the oxidation and reduction of the electroactive TTF molecules in the polymer layer. The consistency of the experimental results to this model is discussed below. Incorporation of TTF$^+$ into the Nafion layer produces a golden-colored film in which TTF$^+$ has no special structural arrangement and exists predominantly as TTF$^+$,$-SO_3^-$ pairs. However, upon several reduction and oxidation cycles, counterions from the electrolyte (*e.g.*, Br^- and K^+) are incorporated into the layer and the oxidized form of the layer is now purple and has an organized TTF$^+Br^-$ structure (probably in the conductive nonstoichiometric form, $TTFBr_{0.7}$). The overall redox reaction upon cycling can then be written as

$$TTFBr_{0.7} + 0.7e \rightleftharpoons TTF + 0.7Br^- \quad E^\circ_1 \qquad [1]$$

However, the structural changes that occur during these redox reactions cause the electrochemical behavior to deviate from that expected when all processes and elementary steps are rapid and reversible. Neutral TTF has a crystal structure in which the flat TTF molecules lie parallel to one another, forming stacks of TTF with each molecule assuming a staggered (st) configuration with respect to the one below it (14). The crystal structure of $TTFBr_{0.7}$ also involves stacks of TTF$^+$ molecules, but these assume an eclipsed (ec) position with respect to one another (13). The reduction of the film involves loss of Br^- and structural rearrangement of the molecules from the ec TTF$^+$ form to the st configuration of the neutral TTF molecules. The stabilization of the TTF$^+$ molecules by formation of the Br^- complex makes the complexed form of TTF$^+$ harder to reduce than the uncomplexed one. The reaction then occurs by a "square scheme" mechanism (3)

$$\begin{array}{ccc} \underline{TTFBr_{0.7}(ec)} & + 0.7e - & TTF\ (ec) + 0.7Br^- \\ \uparrow k' & & \downarrow k \end{array} \qquad [2]$$

$$TTFBr_{0.7}(st) + 0.7e - \underline{TTF\ (st)} + 0.7Br^- \qquad [3]$$

(where the underlined forms are the stable ones). The E° for reaction [2] is more negative than E°_1 by an amount related to the energy difference between the ec and st forms of neutral TTF, and E° for reaction [3] is more positive than E°_1 by an amount related to the energy difference between the st and ec forms of the TTF$^+$ species. The different E°-values for oxidation and reduction result in the peak splitting shown in

the CV waves. However, the peaks do not occur at potentials governed by their respective E^{o}'s because the following irreversible reactions cause the peaks to shift in (toward E^{o}_{1}). This behavior is characteristic of reversible electron transfers followed by irreversible following reactions of solution species (an E_rC_i reaction) (1b, 15) and of surface monolayers (16). The extent of the shift in the CV peaks depends on the rate constants of the following reactions (k and k') and the scan rate (v) in a manner consistent with the behavior shown in Fig. 3 and 4. The rapidity and irreversibility of the structural rearrangements is shown by the rapid scan (v = 10 V/sec) experiments, where no reversal peaks corresponding to either reaction [2] or [3] are observed (Fig. 5). At essentially infinitesimal scan rates (Fig. 7), the behavior approaches that governed by the overall reaction, (Eq. [1]); the results suggest that $E^{o}_{1} = 0.00 \pm 0.02$V *vs.* SCE.

The model is consistent with the 59 mV shift of both peaks per tenfold change in Br^- concentration (Fig. 10). The shifts in E^{o}_{1} with supporting electrolyte anion (Fig. 13) point to stronger complexation of TTF^+ by I^- ($E^{o}_{1} \sim -0.1$V *vs.* SCE) and weaker complexation by Cl^- ($E^{o}_{1} \sim +0.05$V *vs.* SCE). Fluoride ion does not form a conductive complex, so the wave loses its thin-layer shape in a F^- medium and the structural reorganization effects are absent (Fig. 13a).

The quantitative electrochemical behavior and the detailed shapes of the waves depend on other factors, such as attractive interactions within the film which cause the extreme narrowness of the reduction peak. A digital simulation treatment of this system will be discussed elsewhere (17). However, thin layer E_rC_i behavior (16) probably is a reasonable approximation for both parts of the square scheme. The reaction of the Pt/NAF,TTF^+ electrode is considered to be thin layer at scan rates below 10 V/sec because the integrated charges under the CV waves are independent of v. The theory predicts that in the scan rate regime where the rate of the following reaction is much larger than the scan rate and the electron transfer is reversible (*i.e.*, where $(RT/n\mathbf{F})(k/v) > 10$), no peaks are observed for the unreacted form of the molecules and the variation in peak potential is described by Eq. [4] (16)

$$E_{pc} = E^{o} + (2.3RT/n\mathbf{F}) \log (RTk/n\mathbf{F}v) \qquad [4]$$

The plot of E_{pc} *vs.* log v for a Pt/NAF,TTF^+ electrode (Fig. 6) was linear over the intermediate range of scan rates ($\sim 10^{-4}$ to 10^{-2} V/sec). The slope of the line (−19.4 mV) is much smaller than that predicted by Eq. [4] for a one-electron transfer. The predicted value of $\Delta E_{1/2}$, the width at half-height, for a thin layer E_rC_i reaction is $66/n$ mV (16). The width of the anodic wave is ~20 mV but the cathodic wave is much narrower. The narrowness of the reduction wave can be explained by attractive interactions among the oxidized molecules in the polymer; these are also responsible for the unusual behavior found for scan reversal at different points into the cathodic wave, where the cathodic current increases on reversal (Fig. 8). This is explained as follows. The oxidized electrode is initially hard to reduce because the attractive interactions must be overcome; this causes the cathodic wave to be shifted to more negative potentials. As the electrode is partially reduced the retarding effect of the interactions is decreased because of the smaller concentration of oxidized molecules within the film, so the reduction rapidly accelerates, producing a narrow, tall reduction wave. This effect is less pronounced for the oxidation wave indicating that the attractive interactions among the reduced molecules are smaller than among the oxidized ones. Similarly, the $\Delta E_{1/2}$ of the oxidation wave is apparently less affected by attractive interactions than the reduction wave. If the E_rC_i model is valid for this system, the slope of the E_p *vs.* log v line suggests an n-value of 3 (*i.e.*, 3 electrons transferred per molecule). One can speculate that the critical lattice unit is $(TTF)_4Br_3$ and the overall reaction is

$$(TTF)_4Br_3 + 3e \rightleftharpoons (TTF)_4 + 3Br^- \qquad [5]$$

The deviations at high scan rates can be attributed to the onset of the significance of heterogeneous kinetics.

The effect of varying the temperature on the CV peak potentials of a Pt/NAF,TTF^+ electrode (Fig. 11) showed that the change in entropy (ΔS) for the reduction and oxidation processes were not of equal magnitude and, furthermore, did not have the same sign. This result can be explained by first assuming the cathodic and anodic processes are E_rC_i reactions in a thin layer, and then examining the temperature dependence of the peak potential for such a reaction (Eq. [4]). This is done by expressing E^{o} as a function of its enthalpic (ΔH^{o}) and entropic (ΔS^{o}) contributions and the rate constant, k, by the Arrhenius equation in terms of the activation enthalpic ($\Delta H^{\neq}$) and entropic ($\Delta S^{\neq}$) contributions. The result is Eq. [6] where h is Planck's constant and N_A is Avogadro's number. The sign is plus for a reduction and minus for an oxidation

$$n\mathbf{F}E_p = -\Delta H^{o} + T\Delta S^{o} \pm (T\Delta S^{\neq} - \Delta H^{\neq} + R \ln (RT^2/N_A n\mathbf{F}hv)) \qquad [6]$$

The derivative of Eq. [6] with respect to temperature is given by Eq. [7]

$$n\mathbf{F}\frac{dE_p}{dT} = \Delta S^{o} \pm (\Delta S^{\neq} + R \ln (R^2T^2/N_A n\mathbf{F}hv) + 2R) \qquad [7]$$

Over the experimental temperature range, dE/dT should be constant to within 2%. The experimental peaks shifted linearly with temperature (Fig. 12), with a cathodic peak slope of 1.44 mV/K, and an anodic peak slope of −0.34 mV/K. There are four terms in Eq. [7] which contribute to the slope, one of which, ΔS^{o}, has been extensively studied for solution redox species (18). The change in entropy for the reduction of a cation in solution is generally positive with dE/dT in the range 0.2-2.0 mV/K. The peak potentials of both the oxidation and reduction waves should shift to more positive potentials with increasing temperature as a result of the ΔS^{o} term. The other three terms in Eq. [7] result from the perturbation caused by the following reaction. While $\Delta S^{\neq}$ is unknown for the reaction, the other two terms can be estimated and yield ±2.79 mV/K for n = 1 (T = 298 K, v = 0.01 V/sec) and ±0.90 mV/K for n = 3 (T = 298 K, v = 0.01 V/sec) (+ for reduction, − for oxidation). The two terms cause a shift in the reduction wave to more positive potentials and the oxidation wave to more negative potentials with increasing temperature. The two calculated terms are in the same direction as the effect ΔS^{o} for the reduction peak, but are opposite to the ΔS^{o} term for the oxidation peak. This could explain why the cathodic process has a larger positive slope than the anodic process and why the anodic process has a slope with a sign opposite to that of the reduction process.

We do not believe that other explanations of the observed CV peak separations and narrow waves for Pt/NAF,TTF^+ electrodes are as reasonable. For example, resistance effects can cause peak separations in cyclic voltammetry (19), but a large resistance ($R >$ 0.1 MΩ) would be needed to cause the peak separations observed in the slow scan rate experiments, because of the small currents being passed. The cell resistance of a Pt/NAF,TTF^+ electrode in 1.0*M* KBr

was small (20Ω) as determined by observing the charging of the double layer in response to a potential step in a nonfaradaic region. A small heterogeneous electron transfer rate constant can produce peak splittings in cyclic voltammetry. However, the peak separation found at 0.02 mV/sec would yield (with $\alpha = ½$ and $n_a = 1$) a rate constant, k^o, of 2×10^{-8} cm/sec (20). This seems unreasonably small compared to other values reported for electroactive molecules in Nafion (6b, c). Attractive interactions between reduced and oxidized molecules will not normally produce CV peak splittings. Large attractive interactions that occur with the onset of phase transitions can produce CV peak splittings; however, the isotherm under those conditions would not have the shape found for Pt/NAF, TTF^+ electrodes.[1]

Conclusion

A freshly formed Pt/NAF,TTF^+ electrode contains TTF^+, probably as TTF_2^{2+}, electrostatically bound on the $-SO_3^-$ cation exchange sites of the polymer. After electrochemical cycling the electroactive molecules in the polymer form small domains of solid which show similar behavior to electrodes made from thin films of TTF. This aggregation occurs within the polymer film, where the reduced form of the electroactive molecules is neutral TTF and the oxidized form is $TTFBr_{0.7}$. The sharp, narrow CV waves for the oxidation of TTF and reduction of $TTFBr_{0.7}$ are split by over 100 mV; this can be explained by structural transitions between the oxidized and reduced forms. The shape and hysteresis found on scan reversal demonstrates that attractive interactions which are greater for the oxidized form exist between the electroactive molecules.

Acknowledgment

The support of this research by the National Science Foundation (CHE 7903729) and the Robert A. Welch Foundation (F-079) is gratefully acknowledged.

Manuscript submitted April 26, 1982; revised manuscript received *ca.* Sept. 14, 1982.

Any discussion of this paper will appear in a Discussion Section to be published in the December 1983 JOURNAL. All discussions for the December 1983 Discussion Section should be submitted by Aug. 1, 1983.

Publication costs of this article were assisted by the University of Texas at Austin.

[1] For a detailed discussion of peak splittings in cyclic voltammetry resulting from phase transitions, see Ref. (2d and 8).

REFERENCES

1. (a) A. J. Bard and L. R. Faulkner, "Electrochemical Methods," p. 522, John Wiley & Sons, Inc., New York (1980); (b) A. J. Bard and L. R. Faulkner, "Electrochemical Methods," Chap. 11, John Wiley & Sons, Inc., New York (1980).
2. (a) P. Daum and R. Murray, *J. Electroanal. Chem. Interfacial Electrochem.*, **103**, 289 (1979); (b) F. B. Kaufman, A. H. Schroeder, E. M. Engler, S. R. Kramer, and J. Q. Chambers, *J. Am. Chem. Soc.*, **102**, 483 (1980); (c) D. Ellis, M. Eckhoff, and V. D. Neff, *J. Phys. Chem.*, **85**, 1225 (1981); (d) A. Bewick and B. Thomas, *J. Electroanal. Chem. Interfacial Electrochem.*, **85**, 329 (1977).
3. P. Peerce and A. J. Bard, *J. Electroanal. Chem. Interfacial Electrochem.*, **114**, 89 (1980).
4. T. P. Henning, H. S. White, and A. J. Bard, *J. Am. Chem. Soc.*, **103**, 3937 (1981).
5. T. P. Henning, H. S. White, and A. J. Bard, *ibid.*, **104**, 5862 (1982).
6. (a) I. Rubinstein and A. J. Bard, *J. Am. Chem. Soc.*, **102**, 6641 (1980); (b) I. Rubinstein and A. J. Bard, *ibid.*, **103**, 5007 (1981); (c) C. Martin, I. Rubinstein, and A. J. Bard, *ibid.*, **104**, 4812 (1982).
7. A. J. Bard and L. R. Faulkner, "Electrochemical Methods," p. 410, John Wiley & Sons, Inc., New York (1980).
8. (a) E. Laviron, *J. Electroanal. Chem. Interfacial Electrochem.*, **63**, 245 (1975); (b) H. Angerstein-Kozlowaska, J. Klinger, and B. E. Conway, *ibid.*, **75**, 45 (1977); (c) E. Laviron, *ibid.*, **122**, 37 (1981).
9. T. D. Gierke, Paper 438 presented at The Electrochemical Society Meeting, Atlanta, Georgia, Oct. 9-14, 1977.
10. R. P. Van Duyne and C. N. Reilley, *Anal. Chem.*, **44**, 153 (1972).
11. C. D. Jaeger, Ph.D. Dissertation, University of Texas at Austin, 1979.
12. (a) D. A. Buttry and F. C. Anson, *J. Electroanal. Chem. Interfacial Electrochem.*, **130**, 333 (1981); (b) H. S. White, J. Leddy, and A. J. Bard, *J. Am. Chem. Soc.*, **104**, 4811 (1982).
13. J. B. Torrance, B. A. Scott, B. Welber, F. B. Kaufman, and P. E. Seiden, *Phys. Rev. B*, **19**, 730 (1979).
14. W. F. Cooper, J. W. Edwards, F. Wudl, and P. Coppers, *Cryst. Struc. Commun.*, **3**, 23 (1974).
15. R. S. Nicholson and I. Shain, *Anal. Chem.*, **36**, 706 (1964).
16. (a) E. Laviron, *J. Electroanal. Chem. Interfacial Electrochem.*, **35**, 333 (1972); (b) E. Laviron, *ibid.*, **39**, 1 (1972).
17. T. P. Henning, Ph.D. Dissertation, University of Texas at Austin, 1982.
18. E. L. Yee, R. J. Cave, K. L. Guyer, P. D. Tyma, and M. J. Weaver, *J. Am. Chem. Soc.*, **101**, 1131 (1979).
19. R. S. Nicholson, *Anal. Chem.*, **37**, 1351 (1965).
20. A. J. Bard and L. R. Faulkner, "Electrochemical Methods," p. 412, John Wiley & Sons, Inc., New York (1980).

Different Aging Effects of Electrosorbed Oxygen Monolayers. The Polycrystalline Platinum/Molten Potassium Acid Sulfate Interface

M. E. Folquer, N. R. de Tacconi, and A. J. Arvía*

Instituto de Investigaciones Fisicoquímicas Teóricas y Aplicadas (INIFTA), Sucursal 4, C.C. 16, 1900 La Plata, Argentina

ABSTRACT

Molten $KHSO_4$ offers the possibility of studying the electrochemical process related to the electroadsorption and electrodesorption of the O-containing species on Pt, under a large concentration of ionic species and a low possibility of impurity interference. The potentiodynamic response of the corresponding interface with different complex potential/time perturbation functions, as well as the potential decay at open circuit, indicates the existence of at least three different aging effects of the O-electrosorbed species. Each aging effect can be related to a particular energetic configuration of the electrosorbed layer.

The electrochemical kinetics of the O-electroadsorption and O-electrodesorption in noble metal electrodes both in aqueous and in molten salt electrolyte is explained through a complex reaction pattern where various electron transfer and structural reactions related to aging effects of the O-electroadsorbed species, at the monolayer level are involved (1-6). Different configurations of the O-electroadsorbed species can be achieved through either short or long range term transformations involving as possible contributing processes, dehydration, *i.e.*, a change of interaction between the electroadsorbed species and surrounding water (7-9), surface reaccommodation of the O-containing layer (8, 9), restructuring of the metal substrate (12, 13), ionic specific adsorption (14), changes in the film stoichiometry related to possible disproportionation reactions occurring therein (2) and possible formation of peroxidic-type structures (15-17). This paper attempts to contribute to the understanding of the aging processes through the electrochemical behavior of the Pt/$KHSO_4$ (melt) interface, a system where the aging effect under open-circuit conditions was first determined (18).

Experimental

The experimental arrangement is similar to the one described in previous publications (18, 19). The working electrodes are made of polycrystalline Pt wires (spectroscopic quality) of apparent area in the 0.15-0.49 cm^2 range. The potential of the working electrode was measured against a reversible hydrogen electrode in molten $KHSO_4$ at 1 atm H_2 saturation. The smooth working electrode was cleaned in 1:1 H_2SO_4-HNO_3 mixture, and rinsed with triply distilled water. This procedure was repeated for each new experiment.

Molten AR (Merck) $KHSO_4$ was used as electrolyte. O_2 was carefully removed from the melt following the usual procedures. Runs were made at 245°C. Three different potential perturbation programs were used. Program A (Fig. 1) involves the potential sweep from $E_{s,c}$ to $E_{s,a}$ and backward until the null net current potential ($E_{i=0}$) is reached. At this potential the current is interrupted leaving the system under open circuit during the time τ_{oc}. After τ_{oc}, the open-circuit potential shifts to E_τ and immediately afterward the potential scan is continued to reach $E_{s,c}$. Program B (Fig. 2) involves a preset potential holding (for instance, at $E_{s,a}$) during the time τ_p. Program C (Fig. 3) corresponds to that already described to promote the potentiodynamic aging of the layer forming species (3). In this case $E'_{s,c}$ can be either more positive or more negative than the potential of the O-electrodesorption current peak (E_p). The nomenclature used in the present work to identify the different charges playing part in the potentiodynamic aging is the same as that already described in a recent publication (3).

* Electrochemical Society Active Member.

Key words: metal, electrode, voltammetry, chemisorption.

Results

Electroreduction profiles obtained with program A.—The electroreduction E/I displays obtained with program A (Fig. 1) when $\tau_{oc} = 1.5$ min start from a common potential ($E = 0.32$V). The electroreduction charge at any v remains constant and the first portions of the electroreduction profiles are coincident. At τ_{oc} larger than 10 min, the electroreduction charge decreases (18). For a constant electroreduction charge, the potential of the electroreduction peak at 50 mV/sec is shifted 25 mV more negative than the potential of the electroreduction peak recorded under comparable repetitive triangular potential sweeps (RTPS). The kinetic analysis of these profiles were already discussed in Ref. (18).

Electroreduction profiles run with program B.—The electroreduction E/I displays resulting after holding the potential at $E_{s,a}$ during a time τ_p ($0 < \tau_p < 30$ min) (Fig. 2) show a progressive increase in charge and a gradual shift of the potential of the electroreduction peak toward negative potentials as τ_p increases. The potential holding at $E_{s,a}$ involves the aging of the film and its subsequent growth beyond the monolayer thickness. In this case, a partial dissolution of the oxide film is probably also involved in the overall process occurring at $E_{s,a}$.

Electroreduction profiles after perturbation program C.—The intermediate repetitive triangular potential sweeps (IRTPS) in program C involve the periodical

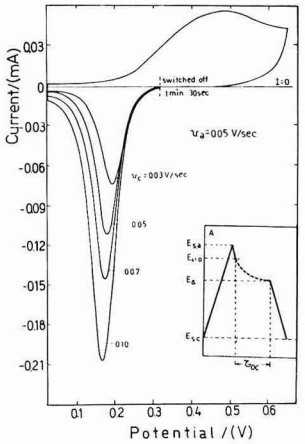

Fig. 1. Potentiodynamic E/I profiles run at a constant anodic potential sweep rate; $v_a = 0.05$ V/sec and at different cathodic potential sweeps; v_c after the current interruption at the null current potential. Apparent area = 0.49 cm^2.

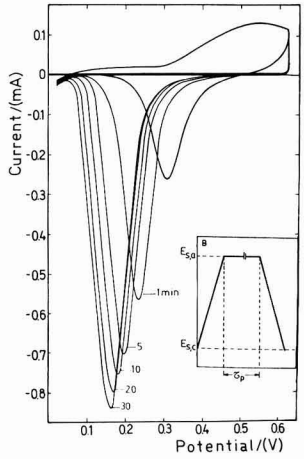

Fig. 2. Potentiodynamic *E/I* profiles run at 0.4 V/sec. Potentiostatic aging at $E_{s,a} = 0.62$V. Influence of τ_p, $\theta_i = 0.68$. Apparent area = 0.18 cm².

removal and rebuilding a fraction of the O-containing surface species initially produced. The electroreduction displays (Fig. 3) run at 0.4 V/sec IRTPS during a preset number of cycles depend quite remarkably on $E'_{s,c}$. The splitting of the electroreduction profile is only noticed when $E'_{s,c}$ is slightly more negative than E_p in the conventional RTPS display (3). The time required to attain a definite splitting in the electroreduction profile increases as $E'_{s,c}$ is increasingly more negative. The optimal splitting condition (OSC) corresponds to an $E'_{s,c}$ value involving the removal (θ_r) and rebuilding of about 70% of the initial O-containing surface species (θ_i) during the first IRTPS. Then, the potential difference of the two electroreduction peaks attained after $\tau_i = 4$ min is slightly larger than 0.1V.

When $E'_{s,c}$ is more positive than E_p (Fig. 4) and only 30-40% of the O-surface coverage is involved in the IRTPS, a single electrodesorption peak is observed afterward. The potential of the broad electroreduction peak becomes gradually more negative and simultaneously the cathodic charge increases accordingly with τ_i, exceeding that in the conventional RTPS profile when τ_i is greater than 10 sec. In this case, during the IRTPS most of the surface is covered by the O-species. The shift of the electroreduction peak potential after $\tau_i = 30$ min is *ca.* 0.20V (Fig .4).

When $E_{s,a}$ is such that only a fraction of the O-monolayer is formed, an increasing inhibition of the O-electroadsorption during the IRTPS is observed. This suggests a probable competition effect between

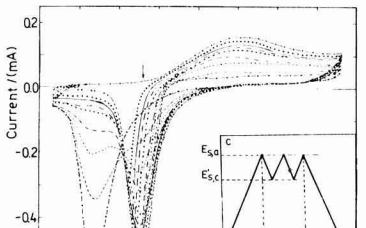

Fig. 3. Potentiodynamic *E/I* profiles run at 0.4 V/sec. IRTPS at 0.4 V/sec (100 cycles). Influence of $E'_{s,c}$. Apparent area = 0.18 cm².

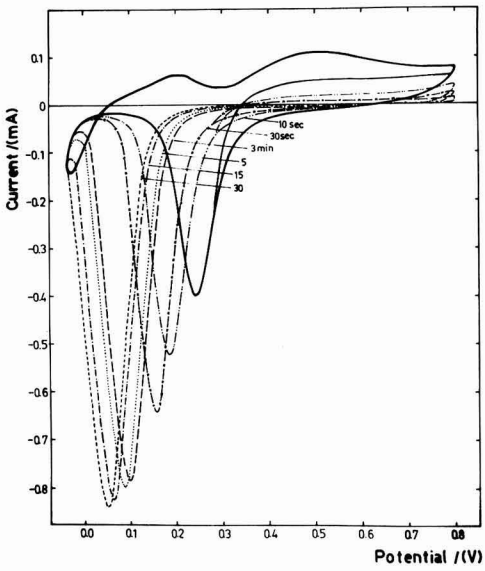

Fig. 4. Potentiodynamic *E/I* profiles run at 0.4 V/sec. IRTPS at 0.4 V/sec between $E'_{s,c} = 0.29$V, $E_{s,a} = 0.80$V. Influence of τ_i; ($\theta_r/\theta_i \approx 0.35$). Apparent area = 0.15 cm².

the restructuring of the O-containing species and the adsorption of anions on the available free metal sites (14).

Aging and film growth processes.—The charge of the O-containing species, Q_T, and the charge associated with aged O-species, Q_{ag}, increase proportionally to ln τ (Fig. 5). The potentiostatic O-layer growth fits a good linear Q_T *vs* ln τ relationship, whose slope increases with the initial amount of O-containing species at the metal surface. Otherwise, the accumlation of the

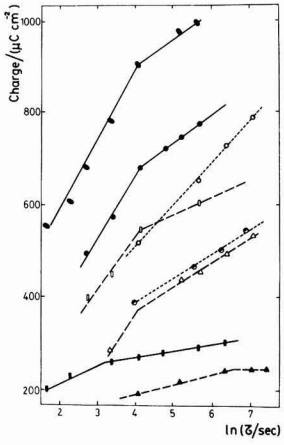

Fig. 5. Accumulated charge *vs.* ln τ plot for the potential perturbation programs B and C. ----- Potentiostatic aging, ——— potentiodynamic aging with $\theta_r/\theta_i < 0.5$, —·—·— potentiodynamic aging with $\theta_r/\theta_i > 0.5$, ○○○ Q_T *vs.* ln τ_p with $\theta_i = 0.68$ (potentiostatic aging), ◓◓◓ Q_T *vs.* ln τ_p with $\theta_i = 0.46$ (potentiostatic aging), ●●● Q_T *vs.* ln τ_i with $\theta_i = 1.2$ and IRTPS at 0.4 V/sec, ●●● Q_T *vs.* ln τ_i with $\theta_i = 0.98$ and IRTPS at 0.4 V/sec, ■■■ Q_T *vs.* ln τ_i with $\theta_i = 0.46$ and IRTPS at 0.4 V/sec, □□□ Q_{ag} *vs.* ln τ_i with $\theta_i = 0.61$ and IRTPS at 4 V/sec, △△△ Q_{ag} *vs.* ln τ_i with $\theta_i = 0.5$ and IRTPS at 0.4 V/sec, ▲▲▲ Q_T *vs.* ln τ_i with $\theta_i = 0.40$ and IRTPS at 0.4 V/sec.

O-containing species during the potentiodynamic aging also fits either a Q_T or Q_{ag} *vs.* ln τ_p plots but involving two linear regions. In the first region, at values of ln $\tau < 4$, the slope increases with θ_i and, at $\theta_i > 0.6$ approaches the slope of O-layer growing process under potentiostatic conditions. In the second region, at values of ln $\tau > 4$, the slope is lower than in the first region but increases on θ_i, for $\theta_i < 0.5$. It should be borne in mind that under potentiodynamic aging perturbation conditions, the smaller θ_i is, the smaller the average potential related to the IRTPS.

Runs using the potential perturbation program B (Fig. 2) at low values of v show the occurrence of two different processes when the potential is held at any $E_{s,a}$ lying within the range of the potential corresponding to the formation of the O-electroadsorbed monolayer and the equilibrium potential of the Pt/PtOH couple (1, 2). These processes can be related to the restructuring of the fraction of the O-monolayer initially formed and the competition between the O-electroadsorption and the anion adsorption for the sites available at the metal surface.

For the potentiodynamic aging at large values of v (high frequencies), a single O-electroreduction profile is recorded, its potential being shifted toward more negative values than that of the corresponding conventional RTPS profile. The potential shift (ΔE_p) is, however smaller than that observed when the splitting of the peak takes place. This suggests that at the largest frequency the reaccommodation of the O-species at the surface is to a large extent hindered, and as practically no free sites for the location of new species through the O-electroadsorption process become available.

For a constant percentage of the O-containing species removed and rebuilt in the IRTPS, ΔE_p increases as θ_i increases (Fig. 6) because as the amplitude of the IRTPS depends on θ_i, the time available to promote the restructuring of the surface species increases. Likewise, for a constant number of IRTPS cycles, ΔE_p increases as v increases, as in this case the formation of more stable O-containing species is assisted. On the other hand, when the electroreduction charge of the O-species involved in the IRTPS is lower than that corresponding to the OSC value, ΔE_p is sensitive to $E'_{s,c}$. But, when $E'_{s,c}$ is more cathodic than the OSC value, ΔE_p becomes independent of $E'_{s,c}$. The amount and degree of stabilized O-containing species decreases as the frequency of the IRTPS decreases.

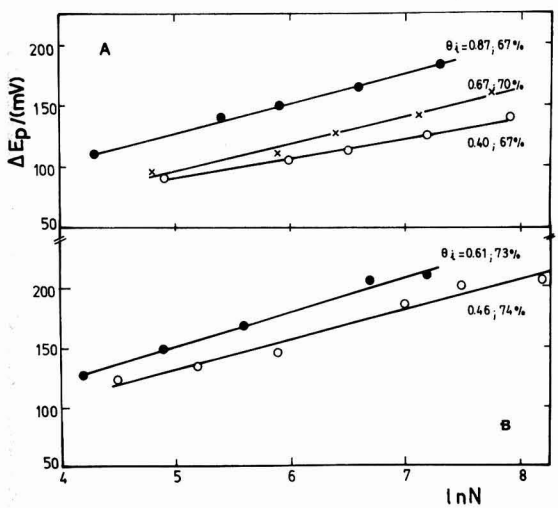

Fig. 6. ΔE_p *vs.* ln N (number of cycles) for different $E_{s,a}$ and $E'_{s,c}$. (a) $v = 0.4$ V/sec and (b) $v = 4$ V/sec.

Change of the open-circuit potential.—The decay of the open-circuit potential from $E_{s,a}$ was determined in the following different ways (Fig. 7); (*i*) after obtaining the stabilized *E/I* profile under RTPS, (*ii*) after the IRTPS during either 100 or 300 cycles, covering a potential range where 65% of the O-containing monolayer is initially removed and rebuilt, (*iii*) the same as (*ii*) but covering a potential range involving only 30% of the surface coverage, (*iv*) after holding the potential at $E_{s,a}$ during preset times which are the same as those used in (*iii*).

For case (*i*), (*iii*), and (*iv*) a single transition time was observed. The fastest potential decay corresponds to case (*i*). In case (*ii*) a complex potential decay is shown, where two relatively poorly defined transition times (at $E_r^{(1)}$ and $E'_r{}^{(1)}$, respectively) are apparently observed. In cases (*i*), (*iii*), and (*iv*) the potential decay plateau ($E_r^{(1)}$) is located between 0.30-0.35V. The final potential ($E_r^{(2)}$) which is the same for cases (*i*) to (*iv*), is located at 0.1V. The results from (*ii*) indicate the existence of at least two coupled reactions related to the potential decay. The time required to attain $E_r^{(2)}$ increases with the number of IRTPS.

Activation of the O_2 and H_2 evolution reactions.—Modifications in the electrolytic activity of the electrode surface is envisaged from the potentiodynamic *E/I* displays when the electrode is subjected to a combined potential perturbation program, covering the initial portions of both the H_2 and O_2 evolution reactions (Fig. 8) at $v = 0.3$ V/sec, adjusting later $E_{s,c}$ to a new $E'_{s,c}$ value to remove and rebuild about 90% of the O-containing species during each potential sweep at the same v and immediately afterward, applying an RTPS during 5-15 min at a greater v. Finally, the RTPS is again run in the $E'_{s,c}$ to $E_{s,a}$ range at the initial v.

Under these circumstances the O_2-evolution reaction is enhanced and the O-electroreduction charge is remarkably smaller than the one initially formed in the same potential range. A further potential cycling produces a gradual increase of the O-electroreduction peak, but the activity for the O_2 evolution reaction remains practically the same. At the final stage when $E'_{s,c}$ is changed to $E_{s,c}$, there is a remarkable electroreduction current at the low potential region. This perturbation procedure induces a drastic temporary activation of the electrode surface for both the H_2 and O_2 evolution potential ranges. On further cycling, the *E/I* profile approaches slowly that initially depicted under RTPS. The largest transient electrocatalytic activation of the O_2 evolution reaction is related to a set of optimal values ($E'_{s,c}$, f, and $E_{s,a}$) (Fig. 9).

Discussion

The application of each perturbation tehnique produces a definite shift of the O-electroreduction current peak toward the negative potential side which is interpreted in terms of aging of the O-electroformed

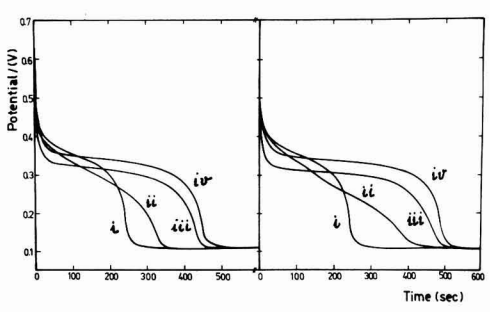

Fig. 7. Open-circuit potential decay curves. (a) IRTPS 100 cycles; (b) IRTPS 300 cycles. The identification of the curves is given in the text.

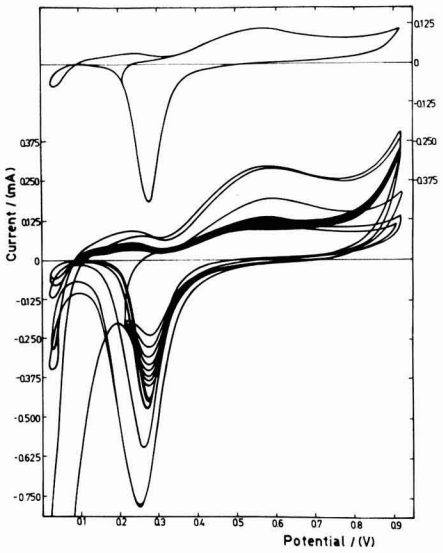

Fig. 8. Potentiodynamic *E/I* profile run at 0.3 V/sec. Initial RTPS, $E_{s,c} = 0.02V$ and $E_{s,a} = 0.92V$. Afterward $E_{s,c}$ was changed to 0.22V, and *v* was increased to 26 V/sec and the IRTPS was maintained during 15 min. Immediately after the IRTPS was repeated at the same *v* initially used. After 10 cycles $E_{s,c}$ was extended again to 0.02V. The initial *E/I* profile is shown in the upper part of the figure. Apparent area = 0.18 cm^2.

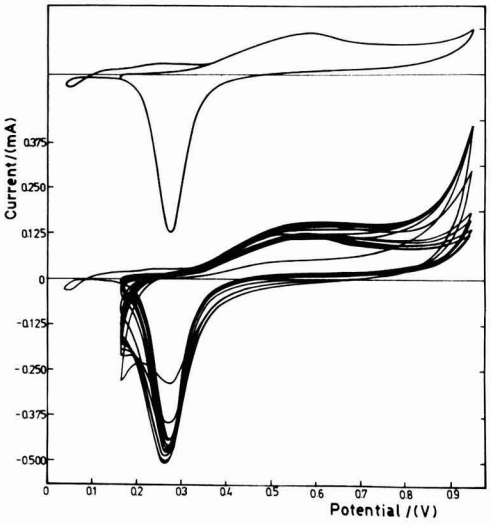

Fig. 9. Potentiodynamic *E/I* profile run at 0.3 V/sec with the same conditions described in Fig. 8, but the IRTPS was made at 115 V/sec during 4 min. Under these circumstances the largest increase in current at $E_{s,a}$ is obtained. Apparent area = 0.18 cm^2.

layer on platinum. In this case, however, the platinum electrode in $KHSO_4$ melt exhibits under perturbation programs B and C, an accumulation of charge larger than that found in 3.7M H_2SO_4 (3). A comparison of runs made for a constant number of potential sweeps (100 cycles) at 0.4 V/sec, is shown in Table I. The ΔE_p values resulting under perturbation programs B and C in any case are remarkably larger than

Table I. Potential shifts (ΔE_p) of the O-electroreduction current peak at 0.4 V/sec as compared to the peak potential of the stabilized *E/I* profile after 100 IRTPS cycles

θ_T/θ_1	IRTPS amplitude/ (V)	Splitting	ΔE_p/ (V)	Q_{as} after IRTPS (mC/cm^2)	Perturbation program
—	—	No	0.025	—	A
~0	0.25	No	0.090	1.16	B
~0.35	0.52	No	0.150	1.03	C
~0.67	0.56	Yes	0.163	1.76×10^{-1}	C
~0.85	0.59	Yes	0.163	3.88×10^{-2}	C

those resulting from the O-electrodeposition profile after open-circuit aging (18). This shift is related to the overall energy change occurring at the surface after aging either because of rearrangement of the surface species or by accumulation of the O-containing species.

The ΔE_p obtained under open circuit is the same found for the aging of metal hydroxide multilayers in acid and alkaline electrolytes at room temperature (20). Its magnitude is close to that of hydrogen bonding energy. In these circumstances it appears that the energy does not depend on the type of film formed neither on the metal substrate. Hence, the main process under open-circuit aging, should be associated with either a dehydration of the O-containing layer or a structural change involving a shift of water through hydrogen bond breakage.

The electroreduction profile resulting after potentiodynamic perturbation program C exhibits two different behaviors depending whether the $E'_{s,c}$ during the IRTPS is more anodic or more cathodic than E_p in the conventional RTPS display. When $E'_{s,c}$ is more anodic than E_p, the accumulated charge increases exceeding the monolayer charge, and simultaneously, there is no splitting of the O-electroreduction peak, but a single peak progressively shifted to negative potentials. In this case, as $E'_{s,c}$ becomes more positive, the following features should be distinguished: (*i*) the decrease of the average area available for reaccommodation of the O-species during the IRTPS, as the average potential perturbing the interface during each cycling in the IRTPS becomes more positive; (*ii*) the greater possibility of producing higher oxidation states at the metal surface; (*iii*) the incorporation of anions either on or in the O-containing layer; (*iv*) the thickening of the film; (*v*) the possible dehydration of the film through electrochemical deprotonation. These contributions which are related to continuous and monotonous changes of the surface film properties should be magnified by both the high temperature and high ionic concentration in the molten electrolyte. Therefore, under these conditions no splitting of the O-electroreduction current peak should be expected.

As $E'_{s,c}$ approaches to $E_{s,a}$, the response of the *E/I* profile after the IRTPS tends to that obtained after holding the potential at $E_{s,a}$ for a certain time (program B). On the other hand, when $E'_{s,c}$ is more cathodic than E_p so that the charge playing part during the IRTPS is relatively large, the surface reaccommodation of the O-species becomes then possible as well as the simultaneous restructuring of the metal surface. Under these circumstances the Pt/$KHSO_4$ (melt) interface approaches the characteristics of the Pt/H_2SO_4 3.7M interface at 55°C, as previously discussed (3).

The ΔE_p corresponding to the potentiostatic and potentiodynamic aging for $E'_{s,c}$ not far from $E_{s,a}$ are nearly the same. The largest peak potential shifts are related to the more stable structure of the O-containing layer as well as to the thickening of the film. In this case, the stabilization of the film forming species could be assisted by anion adsorption. When the electrode potential in the melt is maintained at a value sufficiently positive during a relatively prolonged time,

then anion adsorption on the O-containing film would assist the stabilization of the O-containing film under a relatively strong electric field. The thickening of the film can then be conceived in terms of a place exchange mechanism assisted by the electrical field set up between the metal plane and the plane of anion adsorption. The O-containing layer should acquire a more compact structure because of the electrostriction effects produced through the adsorption of anions at the layer-electrolyte plane. Therefore, in this case the ΔE_p values may be considered a direct measure of the electrostriction effect.

The ΔE_p found for the potentiodynamic aging for $E'_{s,c}$ more cathodic than E_p implies a more remarkable change in the structure of the surface species. The main process has been assigned to a change in position of the O-species in relation to the metal lattice (3). This change also should imply a change in position of the atoms in the first metal plane and to a lesser extent in other metal planes in depth which may be comparable to the reorganization of the O-coverage in oxygen adsorption on Pt (10, 11). The overall process should include the participation of the solvent both as a constituent of the electrochemical interface and through its direct interaction with the O-containing film. The existence of the two surface species which are involved in this case is also revealed through the E/t curve at open circuit.

The existence of two well-defined O-species on Pt, depending on the aging conditions, is also clearly revealed through the Tafel plots (Fig. 10) of the initial portion of the electroreduction profiles shown in Fig. 4. A constant Tafel slope of about 1.5 times larger than the RT/F ratio is obtained for short aging times. Conversely, for aging times larger than 1 min a second constant Tafel slope results whose value is close to the RT/F ratio. Taking into account that the decrease in the Tafel slope follows the corresponding cathodic charge increase, the effect is justly the reverse of the effect predicted for this type of processes where any aging effects are disregarded (21).

The film growth process follows apparently the same form of rate law already established for anodic film growth on various metals (22), but the rate depends whether the growth occurs potentiostatically or it is produced potentiodynamically. For the latter, at $\theta_i < 0.4$, the low growth rate should be appreciably influenced by anion adsorption (14). The change of slope in the Q_T *vs.* ln τ plots occurred at a τ value in the 30 sec $< \tau_t <$ 1 min range, and it is associated with the existence of at least two different O-containing species independently of the amount of O-containing species at the metal-solution interface.

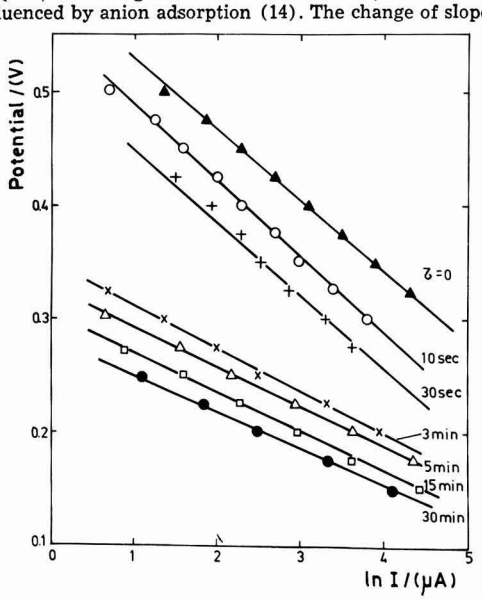

Fig. 10. Tafel plots obtained from the initial portion of the E/I cathodic profiles when $\theta_r/\theta_i \approx 0.35$. Data taken from Fig. 4.

The difference in the kinetics of film growth correlates with the $E/\ln I$ plots for the electroreduction of O-containing layer after different aging times (Fig. 10). In this case, the time range for the transition in the $E/\log I$ slope coincides with that related to the change of the slope in the $Q_T/\ln \tau$ plots.

The existence of different O-containing species is also deduced from the open-circuit potential decay. The different species involved in the potential decay process should be related to the values of the arrest potentials. The first arrest potential ($E_r^{(1)}$) obtained after the different aging conditions from the potential decay curves is practically the same, $E_r^{(1)} = 0.340 \pm 0.005$V while the final rest potential ($E_r^{(2)}$) is lower, $E_r^{(2)} = 0.110 \pm 0.005$V.

The contribution of each O-containing species during the electrochemical process associated with the potential decay at open circuit depends on the extent of the aging reached at the interface for the O-electroadsorbed species (Fig. 7).

Acknowledgment

INIFTA is sponsored by the Consejo Nacional de Investigaciones Científicas y Técnicas, the Universidad Nacional de La Plata, and the Comisión de Investigaciones Científicas (Provincia de Buenos Aires). This work was partially supported by the Regional Program for the Scientific and Technological Development of the Organization of American States.

Manuscript submitted July 30, 1981; revised manuscript received Oct. 11, 1982. This was Paper 504 presented at the Minneapolis, Minnesota, Meeting of the Society, May 10-15, 1981.

Any discussion of this paper will appear in a Discussion Section to be published in the December 1983 JOURNAL. All discussions for the December 1983 Discussion Section should be submitted by Aug. 1, 1983.

Publication costs of this article were assisted by Instituto de Investigaciones Fisicoquímicas Teóricas y Aplicadas (INIFTA).

REFERENCES

1. N. R. de Tacconi, J. O. Zerbino, and A. J. Arvía, *J. Electroanal. Chem.*, **79**, 287 (1977).
2. J. O. Zerbino, N. R. de Tacconi, A. J. Calandra, and A. J. Arvía, *This Journal*, **124**, 475 (1977).
3. M. E. Folquer, J. O. Zerbino, N. F. de Tacconi, and A. J. Arvía, *ibid.*, **126**, 592 (1979).
4. B. E. Conway and S. Gottesfeld, *J. Chem. Soc. Faraday Trans.*, **69**, 1090 (1973).
5. B. E. Conway, H. Angerstein-Kozlowska, F. C. Ho, J. Klinger, B. MacDougall, and S. Gottesfeld, *Discuss. Farad. Soc.*, **56**, 210 (1973).
6. A. J. Arvía, *Israel J. Chem.*, **18**, 89 (1979).
7. G. B. Fisher and B. A. Sexton, *Phys. Rev. Lett.*, **44**, 683 (1980).
8. B. A. Sexton, *Surf. Sci.*, **94**, 435 (1980).
9. G. B. Fisher and J. L. Gland, *ibid.*, **94**, 446 (1980).
10. S. K. Shi, J. M. White, and R. L. Hance, *J. Phys. Chem.*, **84**, 2441 (1980).
11. H. Niehus and G. Comsa, *Surf. Sci.*, **93**, L147 (1980).
12. M. Salmeron and G. A. Somorjai, *ibid.*, **91**, 373 (1970).
13. J. P. Biberian, *ibid.*, **97**, 257 (1980).
14. I. I. Labkovskaya, V. I. Luk'yanyacheva, and V. S. Bagotskii, *Elektrokhimiya*, **5**, 580 (1969).
15. S. Shibata, *Bull. Chem. Soc. Jpn.*, **38**, 1330 (1965).
16. A. Hickling and G. Vrojosek, *Trans. Faraday Soc.*, **57**, 123 (1951).
17. M. I. Florit. M. E. Martins, and A. J. Arvía, *J. Electroanal. Chem.*, **126**, 255 (1981).
18. N. R. de Tacconi, A. J. Calandra, and A. J. Arvía, *ibid.*, **51**, 25 (1974); **57**, 325 (1974).
19. J. O. Zerbino, N. R. de Tacconi, and A. J. Arvía, *This Journal*, **125**, 1266 (1978).

20. M. E. Martins, R. Córdova O., and A. J. Arvía, *Eleetrochim. Acta*, **25**, 453 (1980).
21. K. J. Vetter and J. W. Schultze, *J. Electroanal. Chem.*, **34**, 131 (1972); **34**, 141 (1972).
22. M. J. Dignan, in "Compressive Treatise of Electrochemistry," J. O'M. Bockris, E. B. Conway, E. Yeager, and R. E. White, Editors, Vol. 4, p. 247, Plenum Press New York (1981).

Technical Notes

A Lithium Electrode with a Zinc Substrate for Secondary Batteries

Yoshiharu Matsuda,* Masayuki Morita, and Hidenori Katsuma

Department of Industrial Chemistry, Faculty of Engineering, Yamaguchi University, Tokiwadai, Ube, Yamaguchi, Japan

The development of a lithium secondary battery using an organic electrolyte has been actively pursued in recent years (1, 2). An efficient Li electrode is required to realize such rechargeable batteries. Some Li negatives with metal substrates have been proposed in order to obtain good efficiency of charge-discharge cycling (3-9). Especially, it is worth noting that high coulombic efficiency was achieved by using an Al substrate, which forms an alloy with deposited Li during the period of the charging (8, 9). Previously, the authors pointed out the importance of the correlation between the alloy formation of the substrate metal and the charge-discharge efficiency on the substrate (10). Furthermore, it was found that Zn, as well as Al, is a promising substrate for secondary lithium electrodes (10). The present note shows the charge-discharge characteristics of the Li electrode with a Zn substrate in propylene carbonate (PC) solution containing lithium perchlorate ($LiClO_4$) or lithium tetrafluoroborate ($LiBF_4$). The results are briefly discussed by comparing the characteristics with those obtained on the Al substrate.

Experimental

The substrates used in this work were high purity (>99.9%) Zn and Al disks (12.5 diam, 0.5 mm thick). After having been polished with emery papers, these were thoroughly washed with acetone in an ultrasonic cleaner. The substrates were then fitted to Teflon holders; the effective surface area of the resulting substrate was 0.95 cm^2. The electrolyte was PC containing $LiClO_4$ or $LiBF_4$ (1 mol dm^{-3}). The solvent and the salts were purified and dehydrated by usual methods (11, 12). Water content of the solution was less than 80 mg · dm^{-3}. The charge-discharge characteristics were evaluated by half-cell tests. A platinum sheet having a large surface area was used as the counter-electrode. The reference electrode was a saturated calomel electrode (SCE), which was connected to the test electrode by a Luggin capillary filled with the organic solution being investigated. The charge-discharge test was carried out by a cycling procedure in which Li was charged at a constant current of 0.10 mA (0.11 mA/cm^2) for 1 hr followed by a discharge at the same current density until the electrode potential was −1.0V *vs.* SCE. The current-potential curves were measured after the fourth charge. These measurements were conducted under a dry N_2 atmosphere at 25°C.

Results and Discussion

Typical charge and discharge curves are shown in Fig. 1. In any case, the coulombic efficiency (ampere-hours discharged/ampere hours charged) tends to decrease slightly with cycling after the fourth discharge. The charge-discharge characteristics of the Zn substrate are almost similar to those of the Al substrate after several cycles, but the discharge potential of Li on Zn is a little lower than that on Al. This is because the potential of the alloy formation in the Li-Al system is more positive than that in the Li-Zn system (10, 13). On the Zn substrate, moreover, a little potential step is observed at the first stage of the discharge, which corresponds to the transition in the anodic dissolution from the metallic Li to the Li-Zn alloy. One of the advantages in the use of a Zn substrate is that the charge-discharge performance is little affected by a small amount of water in the electrolyte as compared with the case using an Al substrate (10). The cycling characteristics obtained in the $LiBF_4$ solution is almost the same as those in the $LiClO_4$ solution. From the viewpoint of solution stability (1), however, it would be preferable to use the $LiBF_4$ solution.

Figure 2 shows the polarization curves of the Li electrodes with Zn and Al substrates after the fourth charging. The polarization characteristics on the Al substrate in the $LiBF_4$ solution are almost equivalent to those in the $LiClO_4$ solution. On the Zn substrate, the potential in the $LiClO_4$ solution is generally more negative than that in the $LiBF_4$ solution, and the maximum current density in the former is also higher than that in the latter solution. Current shoulders, which resulted from the heterogeneous dissolution of the

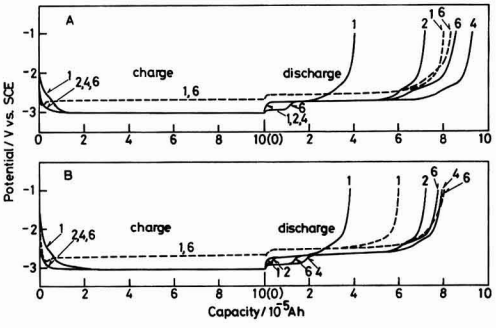

Fig. 1. Charge and discharge curves of Li negative electrodes with Zn and Al substrates, i = 0.10 mA (0.11 mA/cm^2), A: 1 mol dm^{-3} $LiClO_4$ in PC, B: 1 mol dm^{-3} $LiBF_4$ in PC, ———: Zn substrate, – – – –: Al substrate, (Figures on the lines denote cycling numbers).

* Electrochemical Society Active Member.

Key words: lithium cell, cycling, negative electrode, alloy formation.

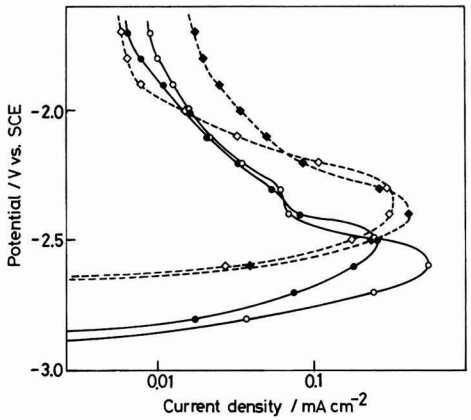

Fig. 2. Anodic polarization curves of Li electrodes with Zn and Al substrates, open symbols: 1 mol dm^{-3} $LiClO_4$ in PC, closed symbols: 1 mol dm^{-3} $LiBF_4$ in PC, ○, ●: Zn substrate, ◇, ◆: Al substrate.

alloy, are observed in both solutions at about −2.3V on the electrode with the Zn substrate while the anodic dissolution on the Al substrate seems to occur homogeneously. It is apparent from the current-potential curves that good discharge performances can be expected in the potential region from −2.7 to −2.4V at the Zn substrate. For both of the substrates, however, deep discharges should be avoided because of the lowering of the current density at more positive potentials.

The efficiency of the charge-discharge cycling on the Zn substrate, which alloys easily with deposited Li, is as high as that on the Al substrate. The present results hint on how to develop an efficient negative electrode for secondary lithium batteries. However, it is further necessary to examine the corrosion resistance of the substrates and the combination with other solvents, in connection with the durability of the cycling over a longer period of time.

Acknowledgment

The authors would like to acknowledge that this work was supported by the Grants in Aid for Scientific Research (No. 505577 and 56850187) by Japan Ministry of Education.

Manuscript submitted Feb. 16, 1982; revised manuscript received Oct. 19, 1982.

Any discussion of this paper will appear in a Discussion Section to be published in the December 1983 JOURNAL. All discussions for the December 1983 Discussion Section should be submitted by Aug. 1, 1983.

Publication costs of this article were assisted by Yamaguchi University.

REFERENCES

1. V. R. Koch, *J. Power Sources*, **6**, 357 (1981).
2. K. M. Abraham, *ibid.*, **7**, 1 (1982).
3. J. O. Besenhard and G. Eichinger, *J. Electroanal. Chem.*, **68**, 1 (1976).
4. F. W. Dampier and S. B. Brummer, *Electrochim. Acta*, **22**, 1339 (1977).
5. V. R. Koch and S. B. Brummer, *ibid.*, **23**, 55 (1978).
6. T. Takei, *J. Appl. Electrochem.*, **9**, 587 (1979).
7. V. R. Koch and J. H. Young, *Science*, **204**, 499 (1979).
8. I. Epelboin, M. Froment, M. Garreau, J. Thevenin, and D. Warin, *This Journal*, **127**, 2100 (1980).
9. Y. Takada, *Denki Kagaku*, **49**, 96 (1981).
10. Y. Matsuda, M. Morita, and H. Katsuma, *ibid.*, **49**, 537 (1981).
11. Y. Matsuda, Y. Ouchi, and H. Tamura, *J. Appl. Electrochem.*, **4**, 53 (1974).
12. Y. Matsuda, H. Nakashima, M. Morita, and Y. Takasu, *This Journal*, **128**, 2552 (1981).
13. A. N. Dey, *ibid.*, **118**, 1547 (1971).

Lithium Cycling in Polymethoxymethane Solvents

J. S. Foos* and J. McVeigh

EIC Laboratories, Incorporated, Newton, Massachusetts 02158

During the past few years, several Li battery electrolytes have been reported which allow the plating and stripping of Li in greater than 95% efficiency at 25°C. Newman reported the use of $LiClO_4$ in dioxolane in Li/TiS_2 cells (1). The cycling efficiency in these cells is very good, but unfortunately they are susceptible to detonation (2). Koch has reported the use of 2-methyltetrahydrofuran (2Me-THF) (3) and diethyl ether blends (4) as solvents for $LiAsF_6$ in Li half-cells. The conductivity of these electrolytes is low.

The solution of $LiAsF_6$ in dioxolane is an electrolyte with good conductivity but is reported to polymerize readily (5). Ring strain may contribute to the reactivity of dioxolane. It might be anticipated that the open-chain analogues of dioxolane might be less reactive. Dimethoxymethane (DMM) I and trimethoxymethane (TMM) II were investigated as solvents for possible use with $LiAsF_6$ in Li batteries

$CH_2(OMe)_2$ (I) $\qquad$ $CH(OMe)_3$ (II)

We wish to report that these solvents produce conductive solutions with $LiAsF_6$, show good stability at 70°C, and cycle Li well in half-cell tests.

* Electrochemical Society Active Member.
Key words: electrolyte, organic, battery, conductance.

Experimental

The solvents, DMM and TMM (trimethyl orthoformate), were obtained from the Aldrich Chemical Company. Before use, the solvents were purified first by preliminary drying using $MgSO_4$ and /or molecular sieves (3 or 4A) for DMM; and molecular sieves (3 or 4A) only for TMM. Subsequently, they were distilled from Na benzophenone ketyl (6). Some difficulty was encountered in forming the blue ketyl in TMM. This was attributed to surface films on the Na which can be disrupted by placing the reaction flask in an ultrasonic bath.

The electrolytes for cycling and storage tests were prepared using $LiAsF_6$ (U.S. Steel, as-received) with cooling, using Cu shot previously cooled by Dry Ice. The solvents, if treated with alumina, were passed through a column of activated alumina (Woelm N-Super 1) and the first 10% discarded. Where applicable, pre-electrolyses were done by passing a current (1 mA/cm^2) between two Li metal electrodes (~30 cm^2) suspended in the electrolyte (100 ml) for ~16 hr.

Conductivities were obtained using dried distilled DMM and TMM. The conductivities were determined in conductivity cells with cell constants determined using aqueous KCl. An a-c conductivity bridge (YSI

Model 31) was used to measure the cell resistance. The conductivities were determined at, or corrected to, 25°C with a precision of ~5%. The storage tests were done in screw cap (Teflon-lined) glass vials. These were stored at 70°C.

The Li cycling was done in prismatic glass cells containing 15-20 ml electrolyte. This experiment, described previously (7), involves making a preplate of 4.5 C/cm² of Li on an Ni substrate (Ni shim) followed by stripping and then replating 1.1 C/cm² on the preplated Li. The average efficiency for cycle E, is calculated in Eq. [1]

$$E = \frac{Q_s - \frac{Q_{ex}}{n}}{Q_s} \quad [1]$$

where n is the number of apparent "100%" cycles, Q_s is the charge stripped (1.1 C/cm²), and Q_{ex} is the charge in the excess Li (3.4 C/cm²) at the start of the experiment.

Solution preparation and the electrochemical experiments themselves were conducted at room temperature under an Ar atmosphere in a Vacuum-Atmospheres Corporation dry box equipped with a Model HE-493 Dri-Train.

Results

Conductivity of electrolytes.—In order to minimize electrolyte IR drop, the electrolyte in a battery should show maximum conductivity. The solvents I and II give electrolytic solutions with greater conductivities than most other noncyclic ethers.

The conductivities of solutions of $LiAsF_6$ in ethers are generally high as compared to solutions of other salts such as $LiClO_4$, $LiBF_4$, etc. For instance, the maximum conductivity of $LiAsF_6$ in THF is 0.017 Ω^{-1} cm^{-1} (7) as compared to 0.006 and 0.004 for $LiClO_4$ (8) and $LiBF_4$ (9), respectively. The ethereal solutions of $LiAsF_6$ previously known to cycle Li with high efficiency, *i.e.*, 2Me-THF and DEE blends, have maximum specific conductivities in the 0.002-0.004 Ω^{-1} cm^{-1} range.

Conductivity *vs.* concentration profiles for $LiAsF_6$ in DMM and TMM are shown in Fig. 1. The conductivity profiles are typical for solutions of $LiAsF_6$ in ethers and show maximum conductivities of ~0.0065 Ω^{-1} cm^{-1} for DMM and ~0.008 Ω^{-1} cm^{-1} for TMM.

Lithium cycling in half-cells.—The plating and stripping of Li at 25°C is a rigorous test of electrolyte stability. Electrolytes were evaluated for half-cell cycling efficiency using electrolytes prepared using distilled solvent (D), distilled solvent treated with alumina (DA), and electrolytes that were additionally pre-electrolyzed (DP).

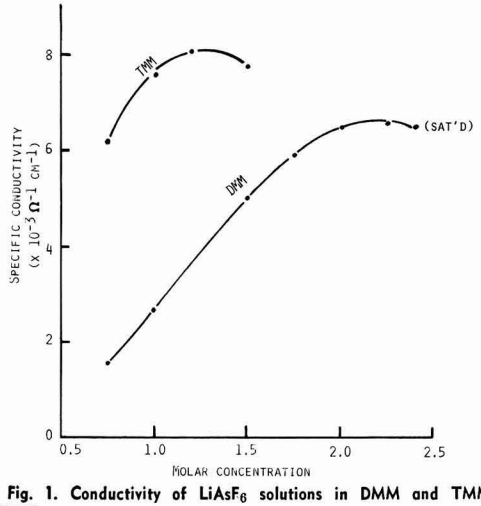

Fig. 1. Conductivity of $LiAsF_6$ solutions in DMM and TMM (25°C).

The freshly plated Li, generated during pre-electrolysis, should be especially reactive. It was hoped that this Li would react with impurities in the electrolyte giving insoluble reaction products and thereby purify the electrolyte. The results for DMM and TMM electrolytes are shown in Table I. This table shows representative cycling efficiencies which illustrate the effect of different purification on Li cycling. In these tests, both electrolytes show high cycling efficiency.

Electrolyte stability at 70°C.—The cycling test above allows the evaluation of room temperature stability of the electrolyte towards freshly plated Li over the period of the experiment, one or two days. An accelerated test for long term stability is the storage of electrolytes at 70°C in the presence and absence of Li. A solvent, 2Me-THF, which has proved useful in Li/TiS_2 cells shows excellent stability when stored with Li at 70°C (7).

Stability tests were conducted by storing samples of 1.5M $LiAsF_6$ in DMM and TMM in the presence and absence of Li at 70°C. The results are shown in Table II. The TMM appears more stable with no apparent reaction noted at 20 days at 70°C. These tests may be somewhat misleading. Although no reaction was observed visually, the TMM electrolyte stored at 70°C with Li subsequently failed completely to cycle Li. The DMM results were variable, with the results reported typical of several tests. Despite the apparent lack of stability in DMM electrolytes, the samples stored with Li retained moderate cycling ability.

Discussion

The conductivity of the electrolytes studied makes them interesting candidates for Li battery use. However, the stability of the electrolytes under actual cell conditions is of primary concern. This includes stability towards reduction by Li and to thermal decomposition in the bulk electrolyte. The half-cell cycling results indicate a relatively high degree of stability of electrolyte towards Li. However, this test is somewhat insensitive to electrolyte decomposition due to the large excess of electrolyte present. The variation of the cycling efficiency with purification appears to be reproducible. It is attributed to variations of the levels of impurities. What is not clear is the nature of the impurities and whether they improve half-cell and storage test behavior. It may be that the electrolyte containing only pure solvent and salt would give the best results. On

Table I. Half-cell cycling tests using DMM and TMM electrolytes

		%
1.5M $LiAsF_6$ in DMM	(D)	97.3
	(DA)	97.5
	(DP)	96.5
1.5M $LiAsF_6$ in TMM	(D)	93.2
	(DP)	95.1

Table II. Storage tests and cycling after storage using DMM and TMM electrolytes at 70°C

Solvent	With Li	Without Li
DMM (D)	Electrolyte clear with a small amount of Li corrosion at 10 days	Electrolyte clear >10 days then darkened rapidly
DMM (D)	Cycled after 10 days storage with Li → 87.5%	
DMM (DA)	Electrolyte clear with a small amount of Li corrosion, > 1 month	Electrolyte dark at 6 days
DMM (DA)	Cycled after 10 days storage with Li → 86.9	
TMM (D)	No reaction at 20 days	No reaction at 20 days
TMM (DP)	Cycled after 14 days with Li (no reaction) → 0%	

the other hand, perhaps small amounts of impurities may scavenge undesirable reactive intermediates. Differentiating between these possibilities is difficult.

In this work, electrolytes which were optimized in half-cell work were chosen for storage tests and cycling after storage. The DMM electrolytes (D and DA) gave similar cycling efficiencies before storage and similar, though decreased, efficiencies after storage. The electrolyte purified with alumina (DA) gave contradictory results in that it appeared more stable than the DMM (D) in the presence of Li and less stable in the absence of Li. The TMM electrolyte also gave contradictory results by showing no apparent reaction in stability tests and yet failing to cycle after storage.

The above observations illustrate the difficulty in evaluating electrolytes for Li batteries using half-cells and the appearance of storage tests. Further investigation of these electrolytes in Li/TiS_2 test cells as well as a more thorough chemical analysis of the storage tests is in progress.

Acknowledgment

We wish to acknowledge the support of the Office of Naval Research for this research.

Manuscript received Sept. 23, 1982. This was Paper 38 presented at the Detroit, Michigan, Meeting of the Society Oct. 17-21, 1982.

Any discussion of this paper will appear in a Discussion Section to be published in the December 1983 JOURNAL. All discussions for the December 1983 Discussion Section should be submitted by Aug. 1, 1983.

REFERENCES

1. G. H. Newman, in "Lithium Nonaqueous Battery Electrochemistry," E. B. Yeager, B. Schumm, Jr., G. Blomgren, D. R. Blankenship, V. Leger, and J. Akridge, Editors, p. 143, The Electrochemical Society Softbound Proceedings Series, Pennington, NJ (1980).
2. G. H. Newman, R. W. Francis, L. H. Gaines, and B. M. L. Rao, *This Journal*, **127**, 2025 (1980).
3. V. R. Koch and J. H. Young, *Science*, **204**, 499 (1979).
4. V. R. Koch, J. L. Goldman, C. J. Mattos, and M. Mulvaney, *This Journal*, **129**, 1 (1982).
5. P. G. Glugla, in "Power Sources for Biomedical Implantable Applications and Ambient Temperature Lithium Batteries," B. B. Owens and N. Margalit, Editors, p. 407, The Electrochemical Society Softbound Proceedings Series, Pennington, NJ (1980).
6. V. R. Koch, *This Journal*, **126**, 181 (1979).
7. J. L. Goldman, R. M. Mank, J. H. Young, and V. R. Koch, *ibid.*, **127**, 1461 (1980).
8. P. Jagodzinski and S. Petrucci, *J. Phys. Chem.*, **78**, 917 (1974).
9. S. D. James, *J. Chem. Eng. Data*, **23**, 313 (1978).

Electrodeposition of Calcium and Strontium Ions on Carbon Electrode

H. J. Huang

Department of Chemistry, National Sun Yat-Sen University, Kaohsiung, Taiwan 800, China

Electrodeposition is one of the versatile electrochemical techniques used in different fields for various purposes, *e.g.*, electroplating of Ag, Cd, Ni, and Cr for practical decorating and protection purpose, electrowinning and electrorefining of certain special metals for metallurgical purpose, electrogravimetry and coulometry for analytical purpose. But so far, the application of electrodeposition technique is limited to those electroactive species. In this experiment, the application of cathodic precipitation method for the deposition of certain electroinactive species (*i.e.*, the alkaline earth metal ions) was studied. Basically, instead of the electroinactive metal ion, an electroactive reagent can be reduced on electrode surface, and if the reduced species is subsequently able to form an insoluble compound with the inactive metal ion in solution, the inactive metal ion then becomes possible to be deposited on the electrode surface. The deposition processes can be expressed by following equations

$$R_{soln} + pe^- \rightleftharpoons R^{p-}{}_{elde} \quad [1]$$

$$M^{n+}{}_{soln} + qR^{p-}{}_{elde} \rightarrow MR_{q,elde} \quad [2]$$

Where $M^{n+}{}_{soln}$, R_{soln} are the inactive metal ion and the reducible reagent in solution, respectively, $R^{p-}{}_{elde}$ is the electrochemically generated species on electrode surface, $MR_{q,elde}$ is the insoluble metallic compound formed on electrode surface, and $q \cdot p = n$.

Experimental

The electrolysis was accomplished either potentiostatically or galvanostatically by PAR 173 Potentiostat/Galvanostat. The working electrode was prepared from spectroscopic carbon rod with a diameter of 0.78 cm (purchased from the National Carbon Company, division of Union Carbide and Carbon Corporation, New York, New York). A Tracor Northern NS-880 x-ray fluorescence (XRF) spectrometer was used for the determination of Ca^{2+} and Sr^{2+} deposition on carbon electrode. After polishing and cleaning, the electrode was inserted into a cylindric Teflon electrode holder which ensured a watertight fit and prevented seepage of electrolyte along the inner side of the cylinder.

Ammonium nitrate was used as the supporting electrolyte, and the ionic strength of the electrolytic solution was kept at 0.2. The *p*H of the solution was adjusted to 8.5 by the addition of NaOH solution. The polarization potential was set against a saturated calomel electrode (SEC). The electrodeposition was performed in stirred solutions at ambient temperature. On completion of each deposition, the carbon electrode with its holder was removed from the electrolytic solution with potential or current applied. The electrode holder was rinsed carefully with distilled-deionized water. After air drying, the carbon electrode with its holder was covered with a piece of KAPTON film (from SPEX Industries, Incorporated) and screwed onto a Teflon ring which has an outer dimension just fitted into the sample cell of the XRF spectrometer. Accumulated counting time used for collecting the XRF data was 500 sec. The data were obtained from the digitized spectra by a computer-assisted integration of the analytical peak. In order to eliminate the interference from absorbing gases and x-rays emitted by atmospheric argon, the XRF measurement of Ca^{2+} deposit was done in vacuum.

Key words: electroinactive, cathodic precipitation, diffusion control, dioxane.

Results and Discussion

A simple system consisting of Ca^{2+} in aqueous solution was chosen for demonstration. The electrolytical solutions contained various concentrations of Ca^{2+} and fixed amount of supporting electrolyte. During electrolysis, the water molecule in solution (corresponds to R_{soln} in Eq. [1]) was decomposed to generate hydroxide ion OH^- (corresponds to $R^{p-}{}_{elde}$ in Eq. [1]) on

carbon electrode. The electrochemical reaction proceeded on carbon electrode is

$$2H_2O + 2e^- \rightarrow H_{2,gas} + 2\,OH^- \quad [3]$$

Afer sufficient amount of OH^- has been generated, the Ca^{2+} started to react with the hydroxide ion and form the insoluble $Ca(OH)_2$ compound on electrode surface

$$Ca^{2+}{}_{soln} + 2\,OH^-{}_{elde} \rightarrow Ca(OH)_{2,elde} \quad [4]$$

The amount of Ca^{2+} deposited on electrode was determined by the XRF spectrometric method. The obtained XRF data were normalized and expressed as the number of counts per unit area (cm^2) of electrode surface per 500 sec of accumulated counting time. Due to the difficulty of reproducing exactly the same electrode surface, a 10% error was estimated for the variation of electrode surface area even if the same polishing procedures were followed.

Different from the conventional electrodeposition of metal ions, several steps are involved in the deposition processes of Ca^{2+} (Eq. [3], [4]) on electrode. They are (*i*) transport of the reducible reagent H_2O and the metal ion Ca^{2+} from solution bulk to electrode surface, (*ii*) transfer of electrons (preceding of electrochemical reaction), (*iii*) removal of the generated species OH^- from electrode surface to solution bulk, (*iv*) nucleation of insoluble compound $Ca(OH)_2$ on electrode surface or in the solution near electrode, and possibly, (*v*) diffusion of the insoluble compound from electrode to solution. After the beginning of electrolysis, the concentration of $OH^-{}_{elde}$ will increase rapidly, but no insoluble compound can be formed until the concentration of Ca^{2+} and OH^- is larger than certain supersaturation value. Whenever the solution is beyond the metastable supersaturation state, it is regarded as labile and is subjected to spontaneous deposition of the insoluble $Ca(OH)_2$ compound (1). After the initiation of nucleation, the insoluble compound $Ca(OH)_2$ will be formed spontaneously as long as the concentration product of (Ca^{2+}) and $(OH^-)^2$ is larger than the K_{sp} of $Ca(OH)_2$. During electrolysis if the applied potential or current density is large enough, Eq. [3] will proceed rapidly, and the reduced species OH^- is generated at a fast rate, therefore, the transport of H_2O or Ca^{2+} from solution bulk to electrode surface will dominate the whole deposition processes and become the rate-controlling step (for simplicity, the effect of the step (*iii*) and step (*v*) are assumed to be negligible). Since the concentration of the reducible species H_2O in solution is much larger than that of the metal ion Ca^{2+}, the diffusion of Ca^{2+} becomes the rate-determining step after the nucleation of the insoluble compound has been initiated.

For a diffusion controlled process, the rate of deposition and the total amount of deposit can be derived easily by following the same procedures as that of the conventional semi-infinite linear diffusion (2). The resulting equation describing the amount of insoluble compound $Ca(OH)_2$ formed on electrode surface $N_s(0, t)$ with electrolysis time, t is

$$N_s(0,t) = \frac{D_o A (C^\circ - C')t}{\delta} \quad [5]$$

for deposition in stirred solution. Where C° represents the Ca^{2+} concentration before electrolysis, C' represents the surface concentration of Ca^{2+} at time t, is equal to $K_{sp,Ca(OH)_2}/(OH)^2$, A is the geometric area of electrode, δ is the thickness of diffusion layer. Both C° and C' are in unit of mol cm^{-3}, while A is in cm^2, D_o is in $cm^2\,sec^{-1}$, t is in sec, δ is in cm, N_s is in mol.

According to Eq. [5], the amount of insoluble compound $Ca(OH)_2$ deposited on electrode surface is directly proportional to the concentration of Ca^{2+} in solution and to the electrolysis time t. The relationships between solution concentration (from 2.5×10^{-4} to 1.25×10^{-3}M) and the amount of Ca^{2+} deposit (electrolyzed at −1.6V for 30 min) are shown in Fig. 1. The intercepts obtained from extrapolation (as calculated by the linear regression method) is 0.28×10^{-4}M. This value is, therefore, equal to C' in Eq. [5] and represents the Ca^{2+} concentration on electrode surface during electrolysis. Since the deposition time used in this experiment is 30 min which is believed to be much longer than the possible induction period for nucleation of $Ca(OH)_2$ (3), the nucleation process would become unimportant and the diffusion process would thus dominate the whole deposition processes and become the rate-determining step. The dependence of the amount of Ca^{2+} deposit upon the time of electrolysis is shown in Fig. 2. The straight line obtained confirmed the existing linear relationship between the amount of deposit and the electrolysis time described by Eq. [5].

Since the formation of insoluble compound on electrode surface also depends on the magnitude of solubility product, the change of dielectric constant (also polarity) in electrolytic solution would affect the deposition processes. The influence of solvent on deposition efficiency was studied by adding an increasing amount of dioxane (from 10 to 50%) to

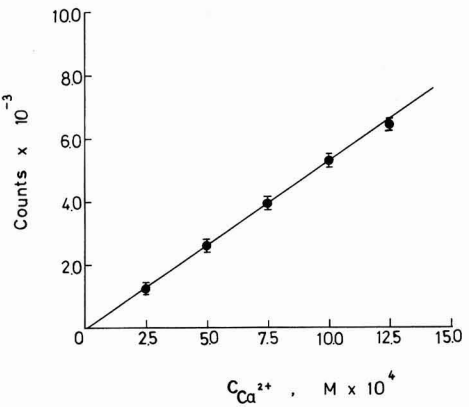

Fig. 1. Amount of Ca^{2+} deposit *vs.* Ca^{2+} concentration in solution. Electrodeposition was conducted potentiostatically at −1.6V for 30 min.

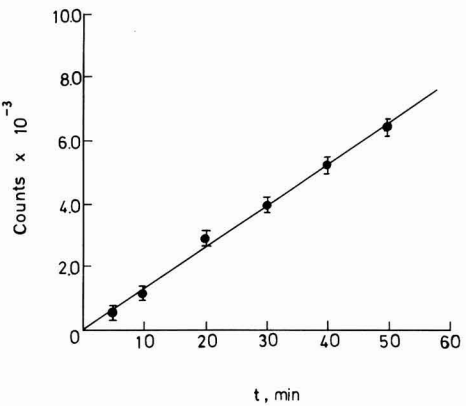

Fig. 2. Amount of Ca^{2+} deposit *vs.* electrolysis time. Electrodeposition was run potentiostatically at −1.6V with 7.5×10^{-4}M of Ca^{2+} in solution.

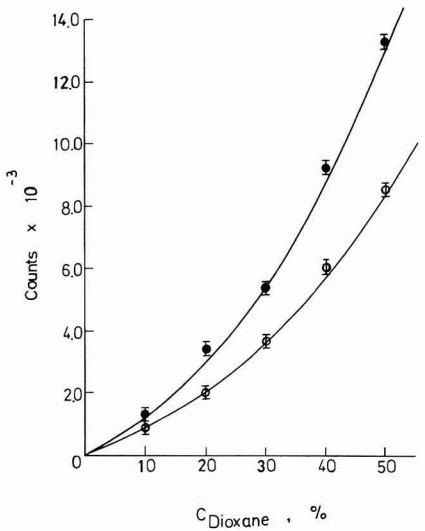

Fig. 3. Plots of the amount of Ca^{2+} (●) and Sr^{2+} (○) deposit vs. the dioxane concentration in solution. Solutions used contained 1.0×10^{-5}M of Ca^{2+} and 5.0×10^{-6}M of Sr^{2+}, respectively.

the aqueous electrolytic solution. Depositions were run galvanostatically with a current density of 1.0 A/cm^2 in vigorous stirring solution. Figure 3 shows the increment of the amount of Ca^{2+}, Sr^{2+} deposit in accordance with the change of dioxane concentration in solution. The relationships between the amount of Ca^{2+}, Sr^{2+} deposit and solution concentration, electrolysis time in dioxane solution were found to be similar to those shown in Fig. 1 and 2. Thus, the deposition processes in mixed solvent system follow the same behavior as that of aqueous. The deposition efficiency in 40% (arbitrarily selected) dioxane solution was found to increase approximately with an order of two in comparison with that of aqueous.

From the results of this investigation, deposition of other electroinactive species on appropriate substrate can be achieved easily if proper reagent (by Eq. [1]) has been chosen. Further exploration of this technique might lead to some useful applications. For example, thin films (with known quantity) of radioactive Sr^{2+} or Ba^{2+} (both are strong β-emitting species) ion can be prepared on suitable substrate and thus serve as a calibrated standard for radioactivity measurement. The possible simultaneous deposition of alkaline earth metal ion with other electroactive species might induce some interesting techniques for the deposition of binary metal oxides (or hydroxides), such as $SrTiO_3$, $BaTiO_3$ which are solar energy conversion related compound (4, 5). Also, the quantitative deposition of Ca^{2+}, Sr^{2+} on electrode can be used as a preconcentration step and, thus, might become a useful analytical procedure for trace analysis of these species.

Acknowledgment

The author wishes to thank UIRL in Hsinchu, Taiwan for the full support of this work.

Manuscript submitted March 18, 1982; revised manuscript received *ca.* Nov. 5, 1982.

Any discussion of this paper will appear in a Discussion Section to be published in the December 1983 JOURNAL. All discussions for the December 1983 Discussion Section should be submitted by Aug. 1, 1983.

Publication costs of this article were assisted by National Sun Yat-Sen University.

REFERENCES

1. H. A. Laitinen and W. E. Harris, "Chemical Analysis," 2nd ed., pp.142-149, McGraw-Hill Book Company, New York (1975).
2. P. Delahay, "New Instrumental Methods in Electrochemistry," p. 47, Interscience, New York (1954).
3. V. K. La Mer, *Ind. Eng. Chem.*, **44**, 1270 (1952).
4. M. S. Wrighton, A. B. Ellis, P. T. Wolczanski, D. L. Morse, H. B. Abrahamson, and D. C. Ginley, *J. Am. Chem. Soc.*, **98**, 2774 (1976).
5. R. D. Nasby and R. K. Quinn, *Mater. Res. Bull.*, **11**, 985 (1976).

Mechanism of Hole Injection on Ferric Oxide Photoelectrodes

Tamás Pajkossy

Hungarian Academy of Sciences, Central Research Institute for Physics, Budapest, H-1525, Hungary

It seems that ferric oxide is advantageous as a semiconductor photoelectrode for utilizing solar energy (1-10). Ferric oxide is an n-type semiconductor, its bandgap is reasonable for such purposes, it can be manufactured easily and cheaply, and it is reasonably stable. It does, however, suffer from the disadvantage of low quantum efficiency. The efficiency can be increased if the surface processes are understood, and it is known how to suppress surface recombination.

Recently, analysis of phototransients was used by Iwanski *et al.* to investigate processes taking place on illuminated ferric oxide electrodes (8). The results of similar experiments are presented here. Our aim was to determine whether hole injection at the interface proceeds directly from the valence band or via surface states. With this in mind, the photocurrent was measured on ferric oxide electrodes at constant electrode potential and slightly modulated illumination as a function of reducing agent concentration. The average value of the photocurrent was measured directly, and the current transients due to light modulation were recorded, using the signal averaging technique.

Key words: photoelectrochemistry, hole injection, ferric oxide, semiconductor.

Experimental

Ferric oxide electrodes made by thermal oxidation of iron specimens were used. The details of preparation and characterization of these electrodes are reported elsewhere (10). The electrodes behave similarly to those reported in Ref. (4 and 7); from the conventionally determined Mott-Schottky plots a donor density of 10^{18}/cm^3, and a flatband potential of around -0.35V *vs.* saturated calomel electrode (SCE) at *p*H 9.0 were evaluated. The long wavelength edge of the spectral response of the photocurrent was found to be around 610 nm, indicating that the bandgap of the semiconductor is about 2.1 eV. The overall oxide thickness was 0.15 mm.

The solutions were 0.2M borate buffers of pH 9.0 with different concentrations of KI (0-22 mM). These solutions were carefully deaerated before and during experiments by means of bubbling high purity nitrogen. The electrode potential was maintained at 0.2V *vs.* SCE, since at this potential only KI is oxidized under illumination (10).

The measurements were made using a standard three-electrode cell, whose overall resistance is around 30Ω, determined by extrapolation of high frequency impedance data. From the same impedance data the cell capacitance was also evaluated; it was found to be less than 1 μF, thus, the cell response time is less than 30 μsec. (The change in KI concentration of the solution had only a minor effect on the cell time constant.)

A medium speed potentiostat (AFKEL 415.5 μsec rise time) and a current amplifier of 30 μsec rise time range (Keithley 427) were applied. The electrode was steadily illuminated by a 150W tungsten lamp, fed from a d-c power supply, and by a smaller lamp (50W), whose light was interrupted by a rotating sector. This sector gave rectangular light pulses of 60 μsec rise time and about 5 msec duration every 30 msec. The light modulation depth was about 1%. (The use of white light may seem inexact in photoelectrochemical measurements; however, as our preliminary experiments revealed, the measured transients were of the same shape at any wavelength, they differed from each other only in height.)

It is seen from the above data that the time constants of the cell, electronics, and shutter are much smaller than 10 msec, this value being a characteristic decay time found in the experiments.

The current transients were recorded by means of an averaging transient digitizer (KFKI, Hungary). The number of the transients repeated and averaged was usually $2^{12} = 4096$.

Theory

As has been shown in detail elsewhere (10) the steady state photocurrent on ferric oxide at constant potential is highly influenced by the concentration of the reducing substances, *i.e.*, hole acceptors in the solution. The difference between the photocurrent and dark current, which we call excess photocurrent, j', depends on the concentration of reducing agent in the solution in steady state according to Eq. [1]

$$1/j_s' = (1/j_h)\,(1 + k_1/k_2 c_{red}) \qquad [1]$$

where j_h is the hole flux to the surface, and k_1 and k_2 are phenomenological rate coefficients for recombination and injection, respectively; j_s' is the steady-state excess photocurrent; and c_{red} is the concentration of the reducing agent at the interface.

Equation [1] was obtained taking into account the following (10): Photogenerated charges in the semiconductor space charge layer are separated by transport processes, the details of which are beyond our present scope. A hole flux reaches the surface of the semiconductor, where holes are either injected into the solution and react with a hole acceptor, or recombine with electrons in the semiconductor. At medium electrode potentials, holes react only with strongly reducing substances (*e.g.*, $[Fe(CN)_6]^{4-}$, I^-), not with water molecules. At these electrode potentials there is competition between hole injection and recombination; the competition between the different hole acceptors can be neglected. By means of Eq. [1], from the dependence of excess photocurrent on reducing agent concentration the hole flux and the ratio of the rate constants can be obtained.

A number of kinetic models can be formulated for steady state leading to Eq. [1] (11-14). The surface processes invclved in these models can be summarized as follows:

Hole injection proceeds either directly (model B) or via surface states (model A). Recombination is assumed to proceed via surface states only (15). These two alternative kinetic models are illustrated in Fig. 1. In order to be able to decide which of the two simplified models is more suitable for the illuminated ferric oxide electrode, rate equations are established and compared with light modulation experiments for both cases.

Let us suppose, for both cases, that hole current j_h arriving at the surface responds immediately to the change of illumination intensity, because the charge carrier transport in this semiconductor is considered to be very fast in comparison with surface processes. This can be supported by the results of photocurrent rise time calculations given in Ref. (13), being in the order of magnitude of 10^{-6}-10^{-3} sec. The characteristic decay time presented here, and ascribed to surface processes, is at least one order of magnitude longer.

On the other hand, the diffusion of hole acceptors in the liquid phase can also be considered to be very fast. This was elsewhere demonstrated (10) as a consequence of the measurements being carried out, using an illuminated rotating ferric oxide electrode.

Thus, the transport processes in both phases can be regarded as not to be rate determining and may be ignored, allowing our attention to be centered on the surface processes. The role of surface states in our models is to act as intermediate states of charge. Their physical and/or chemical nature is not known, and from the present point of view their nature is quite irrelevant.

Let us suppose for both models that the partial order for every reaction partner in the surface processes is one. A remark needs to be made concerning this assumption: The surface concentration of the hole acceptor in the liquid phase is considered to be proportional to the bulk concentration. In Ref. (10) it has been shown that the competition kinetics, expressed in the form of Eq. [1], holds only if the surface and bulk concentrations of the reducing substance are proportional to each other, *i.e.*, weak adsorption occurs.

In both models the measured excess photocurrent is the difference between the hole flux, j_h, and the electron flux due to recombination, j_r

$$j' = j_h - j_r \qquad [2]$$

In the following the rate equations are presented. We calculate the current response of suddenly increasing illumination for both models.

Model A (Fig. 1A)

Let the surface charge density of holes captured by surface states be denoted by p, then

$$dp/dt = + j_h - k_i c_{red}\, p - k_r n_e p \qquad [3]$$

where k_r is the rate coefficient of surface recombination, n_e the electron density at the interface, and k_i

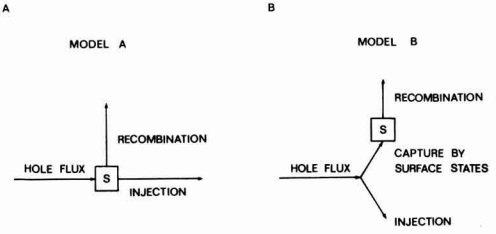

Fig. 1. Two possible kinetic schemes of surface reactions. Surface states are denoted by "S".

the rate coefficient of hole injection into the solution. Since both k_r and n_e are thought to be constant at constant electrode potential, $k_r n_e$ will be constant and denoted by k_r'. If, at $t = 0$, the light intensity is increased instantaneously from I to I + ΔI, then the hole flux, j_h, increases from $j_h°$ to $j_h° + \Delta j_h$. The latter change will be considered as an increase of step function form. In this case Eq. [3] has the form after rearrangement

$$dp/dt + (k_i c_{red} + k_r')p = j_h° + \Delta j_h \cdot u(t) = 0 \quad [4]$$

where $u(t)$ is the unit step function (16).

Since under steady illumination $dp/dt = 0$, the initial condition is given as the steady-state solution of Eq. [4], *i.e.*

$$p(t < 0) = j_h°/(k_i c_{red} + k_r') \quad [5]$$

Thus the solution to Eq. [4] equals

$$p(t) = (k_i c_{red} + k_r')^{-1} \cdot \{j_h° + \Delta j_h \cdot u(t) \cdot [1 - \exp(-(k_i c_{red} + k_r') \cdot t)]\} \quad [6]$$

The electron flux due to recombination, j_r', is equal to $k_r'p$, so for $t > 0$, j_A', the excess photocurrent from model A, using Eq. [2] and [6], is given as

$$j_A' = [k_i c_{red}/(k_i c_{red} + k_r')]\{j_h° + \Delta j_h(1 + (k_r'/k_i c_{red}) \cdot \exp[-(k_i c_{red} + k_r') \cdot t])\} \quad [7]$$

Model B (Fig. 1B)

For the analogous derivation we have to take it into account that only the $\xi = k_i c_{red}/(k_i c_{red} + k_a)$ fraction of the hole flux is injected into the solution, the remaining $(1 - \xi)$ fraction is captured by surface states. The phenomenological rate coefficient of capture is denoted by k_a. Generally the rate of hole capture by surface states is proportional to the occupancy of these states by electrons (15). In view of the small light perturbation applied, the occupancy can be regarded as constant, and therefore in the expression of ξ, it is incorporated into the phenomenological rate coefficient k_a. In this case for the surface charge density of holes, the following balance equation holds

$$dp/dt = j_h(1 - \xi) - k_r'p \quad [8]$$

Similarly to the derivation applied for model A, using illumination of the same step form, and taking initial condition for $t < 0$

$$p(t < 0) = (j_h/k_r')$$

one gets for the excess photocurrent from this model, j'_B, for $t > 0$

$$j' = \xi \cdot \{j_h° + \Delta j_h [1 + (1/\xi)(1 - \xi) \cdot \exp(-k_r' \cdot t)]\} \quad [9]$$

If the illumination of the electrode is modulated by small rectangular pulses, the photocurrent transients can be compared with Eq. [7] and [9]. Right at the start of the light pulses an immediate increase of photocurrent is expected. The increase for both models is the same, and equals Δj_h. Just after the photocurrent jump a decay portion is expected. The initial slope of the transients for model A is

$$dj_A'/dt \approx -j_h \cdot k_r' \quad [10]$$

which is seen to be independent of c_{red}.

For model B, however, one finds

$$dj_B'/dt \approx -j_h \cdot k_r' \cdot (1 - \xi) = -j_h \cdot k_r' \cdot k_a/(k_i c_{red} + k_a) \quad [11]$$

Introducing the notation

$$\tau = -(1/\Delta j_h)(dj'/dt)_{t \to 0} \quad [12]$$

one finds for model A the expression

$$\tau_A = 1/k_r' \quad [13]$$

whereas the same time constant for model B is

$$\tau_B = (1/k_r')(1 + k_i c_{red}/k_a) \quad [14]$$

If the modulation depth is very small, that is, $\Delta I << I$ hence $\Delta j_h << j_h°$, then the average value of j' under modulated illumination can be considered to be the same as that under constant illumination, that is, $\bar{j}' \approx j_s'$ so the average excess photocurrent for model A can be calculated as

$$1/\bar{j}_A' = (1/j_h°)(1 + k_r'/k_i c_{red}) \approx 1/j_s' \quad [15]$$

for model B, $\bar{j}'$ is given by

$$1/\bar{j}_B' = (1/j_h°)(1 + k_a/k_i c_{red}) \approx 1/j_s' \quad [16]$$

Both Eq. [15] and [16] are of the same form as Eq. [1]; but the physical meaning of the two former equations is more specified.

Results and Discussion

The transients in solutions containing different concentrations of KI can be seen in Fig. 2. The descending part of the transients depends on KI concentration. Consequently model A must be inadequate (cf. Eq. [10]).

The comparison between model B and experiments was as follows: Since the rise time of the transients is about 1 msec (not zero as in our oversimplified model), the initial slope of the descending part can be determined with limited accuracy only. However, the experimental values, according to Eq. [14], depend linearly on c_{red} (Fig. 3). From the slope and intercept of the τ *vs.* c_{red} plot, k_a/k_i can be determined. According to least squares fit $k_a/k_i = 23 \pm 6$ mM. As said above, k_a/k_i can be determined independently from the j_s' *vs.* c_{red} curve (Eq. [16]). From the steady-state measurement, $k_a/k_i = 36 \pm 1$ mM (Fig. 4). Given the simplifications of the model, these two values agree reasonably well.

Qualitatively, the same tendency of initial slopes was observed in the solutions of two other reducing substances, $K_4[Fe(CN)_6]$ and Na_2SO_3; the characteristic time of the decay of the transient, τ, significantly increased with their concentration in the solution,

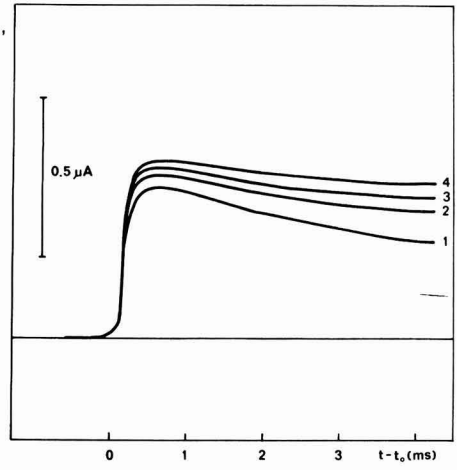

Fig. 2. Some representative current transients for different concentrations of KI in 0.2M borate buffer of pH 9.0 (1-0 mM, 2-9.5 mM, 3-16.3 mM, 4-18.2 mM). In each case the base lines are made to coincide.

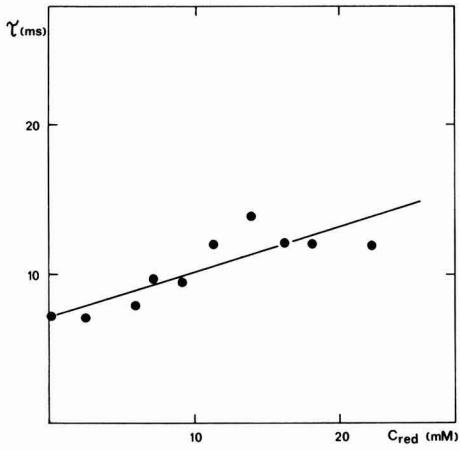

Fig. 3. Dependence of τ on c_{red}. The straight line is the least squares fit (cf. Eq. [14]).

indicating that model A is inappropriate also with these solutes.

Consequently, model B appears to be the more suitable for describing hole injection from ferric oxide, *i.e.*, holes are injected into the solution directly from the valence band, not via surface states.

This statement seems to be reasonable if we consider the energetics of the surface processes. The location of the valence bandedge of ferric oxide is 2.2 eV at pH 9.0 (17), the redox potential of the I^-/I_2 couple is 0.62 eV on the hydrogen scale. (The $E°_{redox}$ values for the two other redox systems, $[Fe(CN)_6]^{4-}/[Fe(CN)_6]^{3-}$ and SO_3^{2-}/SO_4^{2-} at pH 9.0, are 0.36 eV and −0.60 eV, respectively). Taking these data into consideration, hole injection from the valence band, since this process is highly exothermic, is energetically possible. It is not possible in view of there being insufficient data, however, to give any estimate of the phenomenological rate coefficients as they depend upon many factors: electrode potential, illumination intensity, nature of solute, etc. Our further work is aimed at the investigation of these dependences.

Acknowledgments

The author is indebted to Dr. R. Schiller and to Dr. L. Nyikos for stimulating discussions and help.

Manuscript submitted March 30, 1982; revised manuscript received Nov. 3, 1982.

Any discussion of this paper will appear in a Discussion Section to be published in the December 1983 JOURNAL. All discussions for the December 1983 Discussion Section should be submitted by Aug. 1, 1983.

Publication costs of this article were assisted by the Central Research Institute for Physics.

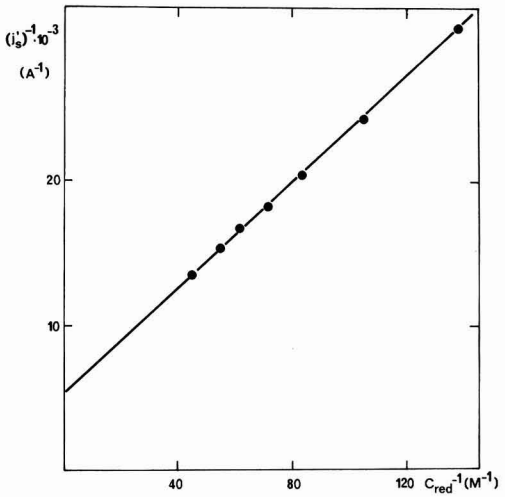

Fig. 4. Dependence of average excess photocurrent on c_{red}. The straight line is the least squares fit (cf. Eq. [16]).

REFERENCES

1. K. L. Hardee and A. J. Bard, *This Journal*, **124**, 215 (1977).
2. J. H. Kennedy and K. W. Frese, *ibid.*, **125**, 709 (1978).
3. L. R. Yeh and N. Hackerman, *ibid.*, **124**, 833 (1977).
4. S. M. Wilhelm, K. S. Yun, L. W. Ballanger, and N. Hackerman, *ibid.*, **126**, 419 (1979).
5. R. K. Quinn, R. D. Nasby, and R. J. Baughman, *Mater. Res. Bull.*, **11**, 1011 (1976).
6. A. F. Sammels and P. G. P. Ang, *This Journal*, **126**, 1831 (1979).
7. J. S. Curran and W. Gissler, *ibid.*, **126**, 56 (1979).
8. P. Iwanski, J. S. Curran, W. Gissler, and R. Memming, *ibid.*, **128**, 2128 (1981).
9. T. Pajkossy, I. Molnár, M. Pálfy, and R. Schiller, *Acta Chim. Acad. Sci. Hung.*, **101**, 93 (1979).
10. T. Pajkossy, *ibid.*, In press.
11. P. A. Kohl and A. J. Bard, *J. Am. Chem. Soc.*, **99**, 7531 (1977).
12. S. N. Frank and A. J. Bard, *ibid.*, **99**, 4667 (1977).
13. D. Laser, *This Journal*, **126**, 1011 (1979).
14. R. H. Wilson, in "Semiconductor Liquid Junction Solar Cells," A. Heller, Editor, pp. 67-83, The Electrochemical Society Softbound Proceedings Series, Princeton, NJ (1977).
15. V. A. Myamlin and Yu. V. Pleskov, "Electrochemistry of Semiconductors," Plenum Press, New York (1967).
16. Handbook of Mathematical Functions with Formulas, Graphs and Mathematical Tables, M. Abramowitz and I. A. Stegun, Editors, Dover Publications Inc., New York (1972).
17. S. R. Morrison, "Electrochemistry at Semiconductor and Oxidized Metal Electrodes," Plenum, New York-London (1980).

Reliable Glass-Polyethylene Dropping Mercury Electrode for Electrocapillary Measurements

M. Carlá and G. Aloisi

Universitá di Firenze–Istituto di Chimica Fisica, 50121 Firenze, Italy

The drop-time method is an attractive technique for interfacial tension measurements both because it is intrinsically simple and because it lends itself to automation.

Measurements are usually performed using drawn and internally siliconized glass capillaries. However, a high degree of training and skill is required to draw a good capillary. Moreover, measurements are unreliable in several electrolytic solutions, some of which are particularly useful for adsorption studies (say, HF, NaOH, diluted NaF (1, 2), etc.). Teflon tips joined to a glass capillary have been proposed for polarographic measurements (3, 4), but they are mechanically or electrically bored, and do not offer the geometrical regularity needed for accurate drop-time measurements; besides, they require a complex machines for construction. Polyethylene tips have been reported to give good results in drop-time measurements because of their accuracy, stability, and chemical inertness. However, following the construction procedure outlined in Ref. (2), we were unable to obtain fully satisfactory results.

In this communication, we describe in detail a very simple procedure for the construction of a composite glass-polyethylene dropping mercury electrode from readily available laboratory materials.

Capillary Construction

The polyethylene tip is drawn from a piece of 3 × 0.9 mm tube, about 8 cm long.[1] The tube is drawn by holding it in a vertical position under a 10g tension (applied through a silk wire to avoid tube bending), and by warming it locally at about 1/3 of its length with a flow of air heated to 200°C. As soon as the polyethylene tube reaches the softening temperature the air flow is removed, and the tube elongation is mechanically stopped at 3.5 cm. The polyethylene tube is allowed to cool before removing it, then it is frozen with liquid nitrogen together with a razor blade, and finally cut with the blade normal to its axis at its smallest cross section. The orifice which results has a very sharp and clean edge, with an internal diameter ranging from 200-300 μm.

The polyethylene tip is then joined, through an inox Swagelock (1/8-3/16) adapter with Teflon cones, to a standard glass capillary for polarography, whose internal diameter and length are chosen to provide the desired drop time. The electrode is connected to a mercury reservoir and filled, while keeping it in a vertical position with the tip upward. It is not necessary to connect the electrode to a vacuum system. If proper care is taken in cutting the polyethylene tube normal to its axis, the above procedure results in almost one working electrode for each attempt, with a limited scatter of characteristics.

Results

Several electrodes with drop times in the range from 10 to 20 sec were tested, and in all cases reproducibility in drop time of the order of 1 msec during a several hours' run was obtained. The instrument was calibrated against a Vos and Los electrocapillary curve for 0.1M KCl (5), the only available electrocapillary curve obtained entirely by an absolute method.

Key words: interfacial tension, drop time.

[1] We used the internal insulator of RG 58/U cable from Fabbrica Milanese Conduttori, Milano.

Electrocapillary curves for 0.1M $HClO_4$ and 1M KCl as measured with one of these electrodes are shown in Fig. 1 and 2. These figures also show that agreement with other authors' data (6, 7) is quite satisfactory, discrepancies being no greater than 0.6 dyne cm^{-1}. Data scatter between two different runs is better than 0.2 dyne cm^{-1} for any measured value.

One of these electrodes has been working for several months for adsorption measurements of aliphatic compounds from 0.1M NaOH solutions. As an example, Fig. 3 shows the electrocapillary curves of n-hexylamine solutions of different concentrations, as obtained by measuring three consecutive drop times for each applied potential at 25 mV intervals. The data are very regular even though no smoothing process was used. Even in these NaOH solutions, where the reproducibility attainable with conventional glass electrodes is

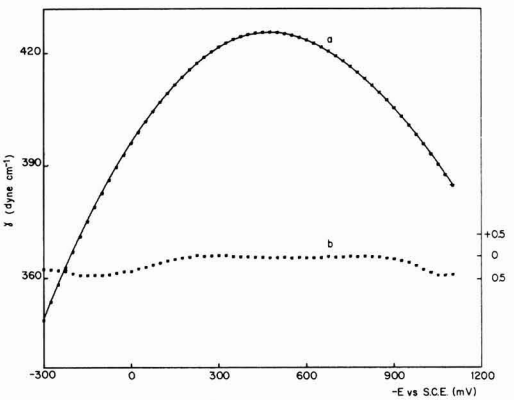

Fig. 1. Electrocapillary curve of 0.1M $HClO_4$: a) solid line: our data; squares: data from Ref. (6). b) Difference between the two sets of data.

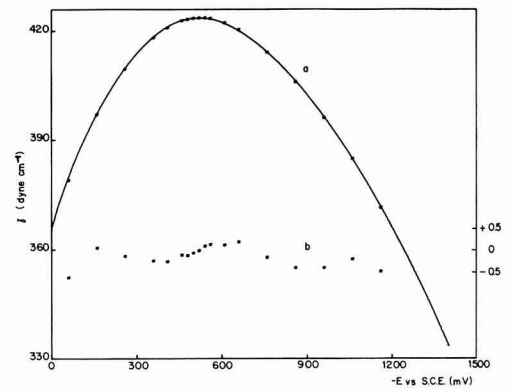

Fig. 2. Electrocapillary curve of 1M KCl: a) solid line: our data; squares: data from Ref. (7). b) Difference between the two sets of data.

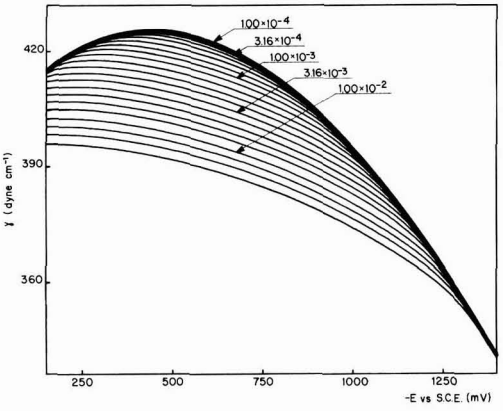

Fig. 3. Electrocapillary curves of N-hexylamine in 0.1M NaOH. Amine concentration ranges from 1.0 × 10^{-4}M to 2.0 × 10^{-2}M with 0.1 decimal logarithmic step.

very poor, a reproducibility of 0.2 dyne cm^{-1} was observed between different runs.

Acknowledgments

The authors thank Prof. S. Bordi and Prof. G. Papeschi for helpful discussions. Financial support of this work was granted by Menestro della Publica Intruzione.

Manuscript received Sept. 21, 1982.

Any discussion of this paper will appear in a Discussion Section to be published in the December 1983 JOURNAL. All discussions for the December 1983 Discussion Section should be submitted by Aug. 1, 1983.

Publication costs of this article were assisted by the Universita di Firenze.

REFERENCES

1. R. Payne, *J. Electroanal. Chem.*, **41**, 277 (1973).
2. L. Novotný, J. Kůta, and I. Smoler, *ibid.*, **88**, 161 (1978).
3. H. P. Raaen, *Anal. Chem.*, **34**, 1714 (1962).
4. A. M. Bond, T. A. O'Donnel, and A. B. Waugh, *J. Electroanal. Chem.*, **39**, 137 (1972).
5. H. Vos and J. M. Los, *J. Colloid Interface Sci.*, **74**, 360 (1980).
6. K. G. Baikerikar, J. Buckfelder, and R. S. Hansen, *J. Electroanal. Chem.*, **108**, 17 (1980).
7. R. G. Barradas and F. M. Kimmerle, *Can. J. Chem.*, **45**, 110 (1967).

Erratum

In the paper "Electron Traps in SiO_2 Grown in the Presence of Trichloroethylene" by A. B. Bhattacharyya and L. Manchanda which appeared on pp. 2772-2778 in the December 1982 JOURNAL, Vol. 129, No. 12, Fig. 9 should read as follows

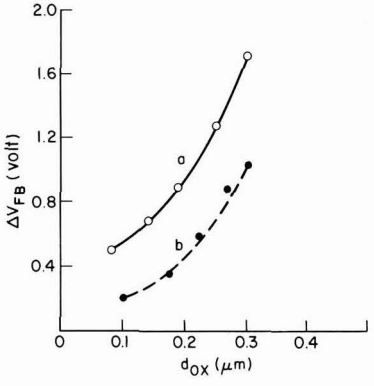

JOURNAL OF THE ELECTROCHEMICAL SOCIETY

SOLID-STATE SCIENCE AND TECHNOLOGY

MARCH 1983

Low Temperature Deposition of Silicon Nitride by Reactive Ion-Beam Sputtering

D. Bouchier, G. Gautherin, C. Schwebel, and A. Bosseboeuf

Institut d'Electronique Fondamentale, Bâtiment 220, Université Paris XI, 91405 Orsay-Cédex, France

and B. Agius* and S. Rigo

Groupe de Physique des Solides, E.N.S.-Université Paris VII, Tour 23, 2 Place Jussieu, 75221 Paris-Cédex, France

ABSTRACT

The deposition mechanism of reactive ion beam sputtered silicon nitride was studied. Using RBS analysis, the composition of Si_xN_y layers deposited at room temperature has been investigated as a function of different parameters. Irrespective of the nitrogen partial pressure, ranging from 10^{-4} to 0.2 Pa, the stoichiometry of the film depends only on the sputtering yield of silicon in the range 0.4-20 keV. Si_3N_4 layers can be obtained at low voltage, but only with a low deposition rate (typically 1 nm/min at our experimental conditions). In order to obtain Si_3N_4 films with higher deposition rates, we increased the nitridation of deposited silicon, either by introducing in the deposition chamber a highly reactive molecule such as NH_3, or by using electronic bombardment, which stimulates the adsorption of N_2 on the growing film.

Although the electrical characteristics of silicon oxide films and of their interface with silicon substrate are good enough to allow MIS silicon devices to be widely used, there are no commercially available MIS devices on GaAs or InP substrates. Direct oxidation of GaAs substrates can be performed by thermal oxidation (1), chemical anodization (2, 3), or plasma oxidation (4); however, up to now, these techniques led to a high value of interfacial trap density ($\simeq 10^{12}$ cm^{-2} eV^{-1}) and to various stoichiometries. Deposition of different dielectric layers has not given any significantly better results (5); following Wieder (6) this behavior seems to be inherent in using GaAs material. However, good MIS characteristics may be achieved when the natural oxide layer has been removed from the substrate before deposition of the dielectric layer, especially for pure Si_3N_4, as shown earlier by Bayraktaroglu (7). Another important use of Si_3N_4 is as an encapsulating layer: it has been shown that silicon nitride becomes an effective diffusion barrier for Ga atoms when its oxygen content is lower than 1% (8, 9).

Various nitride deposition techniques have been developed such as d-c and rf sputtering, ion plating, chemical vapor deposition (CVD), thermally initiated, catalyzed, or assisted by an rf plasma (10). The incongruent evaporation of Ga and As from GaAs at temperatures higher than 600°C (11) prohibits the use of thermally initiated CVD (at 900°-1100°C), while rf plasma deposition (at 200°-350°C) produces highly pure Si_3N_4 films (7, 8). Reactive d-c sputtering can be carried out at nearly room temperature and can lead to layers with suitable composition, but this method needs very careful handling (12). To avoid the complex phenomena arising from the presence of the plasma, which makes *in situ* characterizations more difficult, it is possible to use a variation of the basic sputtering method, ion beam sputtering, which was first proposed by Weissmantel (13).

In our case, reactive ion beam sputtering uses the interaction of a monoenergetic nitrogen ion-beam, generated in a separate duoplasmatron ion-source, with a silicon target situated in the deposition chamber which can be maintained at the required very low pressure ($< 10^{-2}$ Pa). Sputtered atoms are deposited on a substrate in front of the target. In this range of pressure, the mean free path is very large in comparison with the distance between the target and the substrate. We are concerned with the mechanisms of reactions occurring on the surfaces of the target, and of the growing film. A number of authors have shown that the bombardment of a silicon target by a nitrogen ion beam leads to the formation of a nitride layer at the surface of the target (14, 15).

The deposition mechanisms which may be considered to explain the composition of the nitride films are those we have previously discussed for ion-beam sputtered Nb-Ti thin films (16). The incorporation of nitrogen into the layer can occur according to three processes: (a) Nitrogen ions, after implantation into the target, are then sputtered, linked or not with silicon atoms, by subsequent ion bombardment. In the steady state, the sputtering yield of implanted nitrogen per impinging atomic ion is obviously equal to one, if the fraction of scattered ions can be neglected. Therefore, the corresponding ratio N/Si of the deposited layer should be in inverse ratio to the sputtering yield of silicon "S." For identical angular distributions and the same sticking coefficient on the deposition substrate for sputtered silicon and sputtered and/or reflected nitrogen species, the contribution of this process is equal to $1/S$. In any case, it is a function only of the ion energy. (b) Molecular nitrogen would be absorbed on the surface of the target and then sputtered as single or linked atoms towards the growing film. The contribution of this process depends on the nitrogen partial pressure and on the current density of ions which can produce two opposed effects such as ion stimulated desorption and a possible increase of the reactivity of adsorbed nitrogen with

* Electrochemical Society Active Member.

Key words: dielectric, films, stoichiometry, adsorption.

silicon. (c) Molecular nitrogen would be adsorbed on the thin film itself during its formation; this process contributes to the N/Si ratio, as a term proportional to the flow rate of nitrogen towards the growing film, and to the sticking coefficient of N_2 on it, for a given deposition rate of silicon.

The stoichiometry of the deposits is determined by the sum of the effects of these three mechanisms. The purpose of the present work is to evaluate each of their respective contributions. As our ion beam consists of both N^+ and N_2^+ ions, we first try to determine the contribution of each kind of ions during the stationary interaction of the beam with the silicon target. In a second part, we study the effect of the nitrogen partial pressure which was varied over a large range of pressure. Moreover, to try to evaluate the sticking coefficient of molecular nitrogen on the growing film, some deposits were made under a molecular beam bombardment of the substrate. In a third part, the effect of the ion-energy is shown and discussed. Finally, we propose two methods for obtaining stoichiometric silicon nitrides by increasing the nitridation of deposited silicon: (*i*) by introducing in the deposition chamber a highly reactive molecule such as NH_3, for example, and (*ii*) by using electronic bombardment (17) for dissociating or for exciting the molecular nitrogen.

Experimental Procedure

Deposition.—The experimental setup has been described elsewhere (16); however, some improvements have been included to make it suitable for this study (Fig. 1): (*i*) an electrostatic lens which allows us to lower the accelerating voltage down to 0.4 kV with a beam current up to 1.5 mA. (*ii*) a molecular beam generator made out of a multichannel nozzle with about 900 channels of 0.1 mm diam and 2.5 cm length. It provides on the substrate surface a molecular flow equivalent to a calculated (18) local pressure up to 0.2 Pa. A liquid He cryogenic pump with a pumping speed of 5000 l/sec for nitrogen gives a maximum isotropic pressure $P_I = 5 \times 10^{-3}$ Pa during the experiments with the molecular beam generator. (*iii*) a tungsten-rhenium ribbon which is positioned in front of the substrate. This simple electron gun delivers an electronic current up to 50 mA under an accelerating voltage of 150V. It may induce some tungsten incorporation in the deposit, but this does not change anything in the mechanisms we want to study.

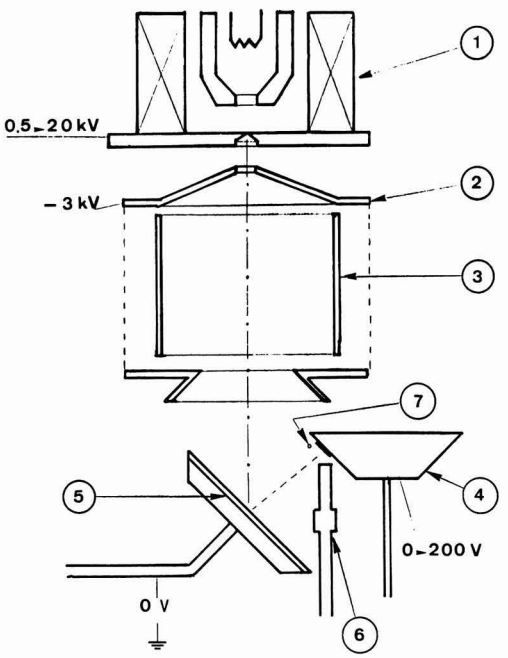

Fig. 1. Experimental setup used for silicon nitride deposition: 1. duoplasmatron ion source, 2. extractor, 3. electrostatic lens, 4. substrate-holder, 5. target, 6. molecular beam generator, 7. tungsten-rhenium filament.

High purity vitreous carbon substrates provided by Carbone Lorraine were used in order to obtain directly by MeV ^4He backscattering the composition of the deposits. These substrates were chemically cleaned by immersing them in trichloroethylene, ethanol, and acetone successively, rinsed in deionized water, and baked out at 160°C *in vacuo*. All the films described in this paper were deposited at room temperature.

During deposition, the isotropic pressure of N_2 can vary from 7×10^{-5} Pa to 5×10^{-3} Pa according to the different experiments. A gas analyzer gives a continuous monitoring of partial pressures: 2.4×10^{-3} Pa of N_2, 1.7×10^{-6} Pa of H_2O, and 5×10^{-7} Pa of CO_2 are typical values measured during a deposition process.

A separate apparatus was used to make N^+ or N_2^+ implanted silicon samples; it consisted of a duoplasmatron ion source and a magnetic mass separator. The energy of the ions can be varied from 4 to 10 keV, the current density on the sample being typically equal to 50 $\mu A/cm^2$.

Nuclear microanalysis.—The experiments were carried out on the 2 MeV Van der Graaf accelerator of the Groupe de Physique des Solides de l'E.N.S.

The composition and stoichiometry measurements by MeV ^4He backscattering have been described generally (19), and more accurately in the case of silicon nitride deposited on silicon and carbon substrates (12). The absolute determination of the numbers of atoms/cm^2 is made using a tantalum thin film standard (20).

The total amount of nitrogen N^+ or N_2^+ implanted in silicon samples has been determined by comparison with a standard (21), using the nuclear reaction $^{14}N(d, \alpha)^{12}C$ initiated by a deuteron beam with an energy of 1300 keV.

Results and Interpretation

Study of the implanted target.—During the ion bombardment of a solid, a steady state is reached when the surface of the solid has been etched further than the particle projected range R_p. The total amount of implanted atoms becomes constant, and their depth distribution in the target is stationary. If no diffusion occurs, the steady state implies that the sputtering yield of implanted atoms is equal to one atom per impinging atomic ion. Moreover, Biersack has calculated (22): (*i*) the total amount N_N of implanted nitrogen given by

$$N_N = \frac{q R_p}{v}$$

where q is the implantation rate (atoms cm^{-2} sec^{-1}) and v, the speed of surface erosion (nm sec^{-1} if R_p is expressed in nm). (*ii*) the maximum concentration, C_N, of implanted nitrogen, near the surface in our case, given by

$$C_N = \frac{q}{v}$$

If we neglect the reflected ions, this relationship may be expressed as N/Si = n/S where S is the sputtering yield of silicon per molecular ion, constituted of n atoms (in our case, $n = 1$ or 2 for N^+ or N_2^+ respectively). We have to make some remarks about the dependence of N_N on the energy: N_N is propor-

tional to R_p and in inverse ratio to S. LSS theory (23) shows that R_p is nearly proportional to the energy E. Therefore, N_N would be linear with E in a range of energy where S is nearly constant: in our case, between 2 and 20 keV. This range has been determined using Sigmund's theory (24) for pure silicon sputtered by N^+ ions. We try now to use this argument in order to determine the effect of N_2^+ ions in comparison with that of N^+. A simple hypothesis which can be made about the behavior of N_2^+ as bombarding particle is that this ion with an energy E has its N—N bond broken when impinging on the surface of the solid, and can be then considered as two N^+ ions with the energy $E/2$. Therefore, the total amount of implanted nitrogen, in the steady state, would be lower by half for N_2^+ ions than that obtained for N^+ with the same energy.

Our experimental results seem to verify this hypothesis; some implantations at normal incidence have been made on (111) silicon targets with ion beam energies ranging from 4 to 10 keV, and with bombardment doses up to 10^{18} ions cm^{-2} of N_2^+ or N^+, respectively. Figure 2 shows that the implanted doses are nearly proportional to the accelerating voltage with slopes equal to 2.40×10^{16} atoms cm^{-2} keV^{-1} and 1.16×10^{16} atoms cm^{-2} keV^{-1} for N^+ and N_2^+, respectively.

The same experimental setup (25) permits us to measure the composition (N^+, N_2^+) of the ion beam delivered by the duoplasmatron source according to its discharge conditions. We were able to determine the values of the parameters, which give a composition of the ion beam stabilized at 80-90% of N_2^+. In the following text we call this value β. These experimental conditions were used to obtain the deposited films we study in this work.

Effect of nitrogen pressure.—Assuming the deposition conditions previously defined for Nb-Ti films (16) to be available for silicon-nitride film, we first tried to deposit Si_3N_4 films with an ion beam energy of 10-20 keV. Figure 3a shows the RBS spectrum obtained for a typical layer deposited on a carbon substrate with a beam energy of 10 keV at a nitrogen pressure $P_I = 10^{-4}$ Pa. The thickness of the deposit is about 65 nm. There is a slight oxygen peak near the surface, corresponding to about 10^{16} atoms cm^{-2}, the remainder being uniformly distributed. The analysis of this spectrum yields the following composition, expressed in atomic ratios: N/Si = 0.53 and O/Si ~ 0.01 in the depth of the film. Therefore, these deposition conditions lead to a film with an N/Si ratio much less than for stoichiometric nitride films (N/Si = 1.33 for Si_3N_4 films).

In order to evaluate the effect of molecular nitrogen, some deposits have been made with increasing pressures of N_2 ranging from $P_I = 10^{-4}$ Pa to $P_I = 7 \times 10^{-3}$ Pa. The results are presented in Table Ia: no significant increase of N/Si ratio can be noted in this range of pressure. Thus, a higher pressure is needed to determine the sticking coefficient of molecular nitrogen, but 7×10^{-3} Pa seems to be the maximum value compatible with a well-defined ion beam in our apparatus, because the scattering of ions by gas molecules becomes important at higher pressure. A molecular beam generator, in our case a multichannel nozzle, pointed at the surface of the film, allows us to avoid this difficulty. The flow rate of N_2 impinging on

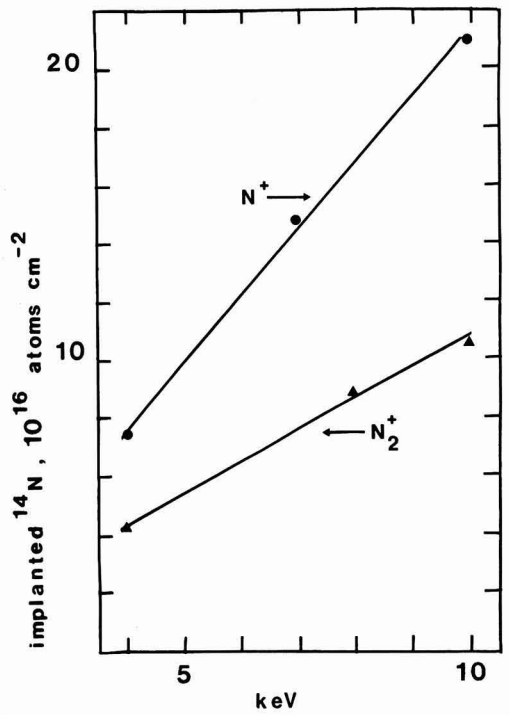

Fig. 2. Amount of nitrogen in (111) silicon target implanted with N^+ and N_2^+ beams expressed as a function of energy. Dose used: 10^{18} ions/cm^2.

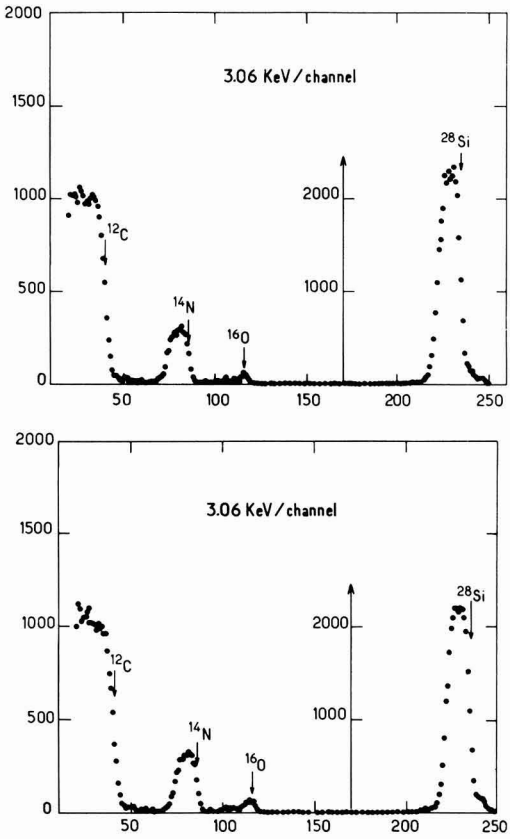

Fig. 3. Energy spectra of ^4He particles backscattered at 150° from a 1.8 MeV $^4He^+$ beam by Si_xN_y films deposited on carbon substrates: (a) $P_{N_2} = 10^{-4}$ Pa; (b) $p_{N_2} \sim 0.2$ Pa. Beam energy = 10 keV. Ion beam current 3 mA. Thickness of the deposits: ~65 nm.

Table I. Stoichiometry of nitride layers deposited at nearly constant deposition rate of silicon expressed as a function of

(a) the isotropic pressure of nitrogen P_I

P_I (10^{-4} Pa)	Ion-beam current (mA)	Deposition rate of silicon (10^{15} atoms cm^{-2} sec^{-1})	N/Si
1.0	6	1.0	0.49 ± 0.02
2.7	6	0.9	0.50 ± 0.02
13.3	6	1.0	0.51 ± 0.02
24.0	3	0.3	0.53 ± 0.02
70.0	6	0.7	0.48 ± 0.02

(b). The input pressure P_I in the molecular beam generator

Input pressure P_I (10^2 Pa)	Calculated local pressure (Pa)	Deposition rate of nitrogen (10^{15} atoms cm^{-2} sec^{-1})	Deposition rate of silicon (10^{15} atoms cm^{-2} sec^{-1})	N/Si
0	0.002	0.18	0.34	0.53 ± 0.02
1.6	0.02	0.18	0.32	0.57 ± 0.02
6.0	0.08	0.18	0.31	0.60 ± 0.02
13.4	0.18	0.20	0.34	0.59 ± 0.02
16.0	0.21	0.19	0.27	0.72 ± 0.02

the surface of the film has been calculated as a function of the dimensions of the channels and of the input pressure, P_I, according to numerical results (18) derived from Zugenmaier's theory.

The RBS spectrum shown on Fig. 3b corresponds to a layer deposited with a nitrogen molecular beam directed towards the film surface, the nitrogen beam being produced with an input pressure of 1300 Pa. The other deposition conditions are those described above for Fig. 3a. There is no difference between the two spectra: the amount of nitrogen is nearly the same, and furthermore, the oxygen peak in spectrum 3b corresponds to a small proportion of oxygen (~3%).

Table Ib shows the values of the deposition rates of nitrogen and silicon as a function of the input pressure P_I. No significant effect of nitrogen pressure is observed; however, if such an effect exists, the maximum increase of the nitrogen incorporation rate would be $\sim 2 \times 10^{13}$ atoms cm^{-2} sec^{-1} for a localized surface nitrogen pressure of $\sim 2 \times 10^{-1}$ Pa, corresponding to a sticking coefficient of N_2 on the growing film equal to $\sim 2 \times 10^{-5}$.

Other results (Fig. 4) obtained for a nitrogen partial pressure of 10^{-4} Pa and various ion beam intensities suggest that N/Si may be correlated to the deposition rate of silicon, N_{Si}. Figure 4 shows an increase of N/Si from 0.5 to 0.7 when N_{Si} decreases from 10×10^{14} to 1.6×10^{14} atoms cm^{-2} sec^{-1}; dividing N_{Si} by 6 induces much more effect than multiplying the pressure by 70. This can be explained by process (b). As we have shown that N/Si does not depend on the pressure from 10^{-4} to 10^{-2} Pa, the contribution of this process seems to be fixed only by the current density in this pressure range.

Effect of the beam energy.—We have assumed the stoichiometry of the nitride films to be determined by the sum of three contributions: the first (*i*) depends on the energy, the second (*ii*) is more difficult to evaluate but is certainly a function of the current density, and the third (*iii*) is proportional to the N_2 pressure. The latter has been found to be negligible and (*ii*) is of little influence. Study of the first one is the purpose of this section where we show the effect of the beam energy.

The RBS spectrum shown on Fig. 5 relates to a 70 nm thick nitride layer deposited with an accelerating voltage value of 500V, and a beam current of 1.5 mA. The N/Si ratio is found equal to 1.16, and the oxygen content in the depth of the layer does not exceed 2%.

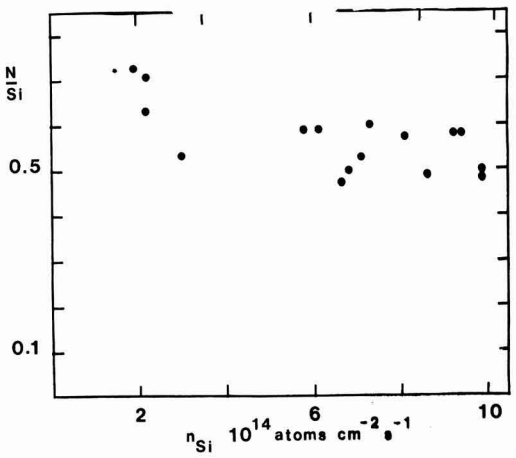

Fig. 4. Stoichiometry of Si_xN_y films expressed as a function of the deposition rate of Si. The nitrogen pressure is equal to 10^{-4} Pa. Ion beam energy = 10 keV. Current intensity varies from 1-6 mA.

Experiments have been made with ion beam energies ranging between 0.4 and 10 keV, and for two values of the beam intensity 1.5 and 0.75 mA. The focusing conditions have been adjusted to ensure the same divergence of the ion beam for each value of the current. For a given accelerating voltage, the average current densities could be roughly evaluated equal to 150 and 75 μA/cm^2 for 1.5 and 0.75 mA values, respectively. Figure 6 shows the normalized deposition yields of nitrogen and silicon N_{Si} (Fig. 6a), and N_N (Fig. 6b), respectively, and the N/Si ratio (Fig. 6c) expressed as a function of the accelerating voltage V. The N/Si ratio depends sharply on V in the range 0.4-1 kV, and for the lowest values the Si_3N_4 stoichiometry is nearly reached. The points corresponding to the lowest current density are slightly above the average curve. Above 5 kV, N/Si ratio is constant and equal to ~ 0.5. The value of N_{Si} increases linearly with log V up to 4-5 kV and becomes constant above this value, while N_N increases with V in a 0.4-0.9 keV range and then remains constant. In order to explain these results, we have to formulate the dependence of N_N and N_{Si} on the sputtering process itself: (*i*) assuming the sticking probability of silicon

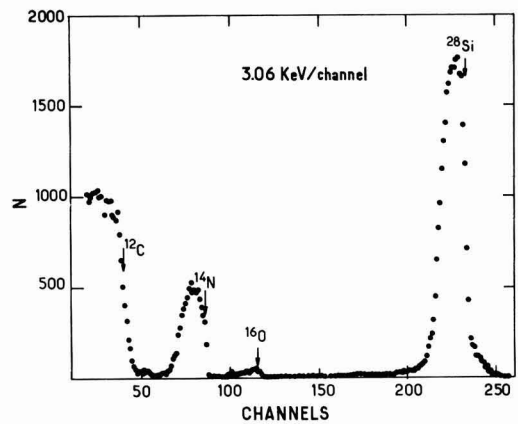

Fig. 5. ^{4}He backscattering spectrum for a 70 nm thick ion-beam sputtered silicon nitride film deposited with an ion beam energy of 500 eV at a current of 1.5 mA. The film observed here is slightly under stoichiometric.

to be equal to one, the deposition yield of the silicon by unity bombardment dose is given by

$$N_{Si} = K \cdot S \cdot I \cdot t \qquad [1\text{-a}]$$

where S is the sputtering yield of silicon, t the deposition time corresponding to the unity dose, I the beam intensity expressed in ions/sec, and K a geometrical coefficient. This formula summarizes the complete expression we have previously used (16)

$$N_{Si}/t = \int_s S \cdot j(x,y) \cdot \cos\theta/\pi \cdot \Omega(x,y)\,dx\,dy \qquad [1\text{-b}]$$

where s is the surface of the target, $j(x,y)$ the current density, $\cos\theta/\pi$ the proportion of sputtered atoms emitted in direction θ, measured from the normal to the surface, and $\Omega(x,y)$ is the solid angle under which the substrate is seen from point (x,y).

Assuming the ion beam has a gaussian spatial distribution of half-width δ, we can deduce the values of K as a function of δ [Eq. 1-b] and then evaluate S from the measurement of N_{Si} [Eq. 1-a]. The spot of the ion beam on the surface of the target gives a value of δ ranging from 2 to 3.5 cm; for instance, $S = 1$ atom/ion corresponds to $N_{Si} = 10.5 \times 10^{16}$ and 9×10^{16} atoms cm^{-2} coulomb^{-1} for 2 and 3.5 cm, respectively. (*ii*) We have previously seen that an N_2^+ ion beam of energy E may be considered as an N^+ ion beam with the energy $E/2$ and a doubled current density. If the proportions of N^+ and N_2^+ in the ion beam are respectively α and β, S must be written as

$$S = \alpha S'(E) + 2\beta S'(E/2) \qquad [2]$$

where S' is the sputtering yield of Si by N^+ ion. The β value is in the range 0.8-0.9 (25). (*iii*) The sputtering yield of implanted nitrogen must be equal, in the steady state, to one atom/atomic ion if the fraction of reflected ions may be neglected; following the theoretical calculations of Bottiger (26), this fraction is equal to about 10% with our experimental conditions, a value which seems to be more likely at high energies (27). But, if the angular distribution of reflected ions is nearly the same as that of sputtered nitrogen the latter cannot be differentiated from the reflected species. So, N_N must be written as

$$N_N = a(\alpha + 2\beta)\, I \cdot t \cdot K \qquad [3\text{-a}]$$

where a is the sticking probability of sputtered nitrogen on the growing film. Assuming that sputtered nitrogen has the same angular distribution as sputtered silicon, we can use the same value of K for these various species. Considering our experimental value of β, [3-a] can be written

$$N_N \sim 2a \cdot I \cdot t \cdot K \qquad [3\text{-b}]$$

From Eq. [1-a] and [3-a], we obtain for N/Si ratio

$$\frac{N}{Si} = a(\alpha + 2\beta)/S \qquad [4\text{-a}]$$

If α can be neglected and if $S'(E/2) \simeq S'(E)$, Eq. [4-a] becomes

$$\frac{N}{Si} \simeq a/S'(E/2) \qquad [4\text{-b}]$$

Let us discuss the results of Fig. 6 using the above considerations. The first feature to examine is N_{Si} increasing with log V (Fig. 6-a). From this dependence and considering Eq. [1-a], we can deduce that S increases linearly with log V when V varies from 0.4 to about 5 kV. For higher values of V, S remains practically constant and equal to about 2. This kind of behavior is in good agreement with Sigmund's theory (24). Nevertheless, in the logarithmic domain, the variation of S with log V is two times larger than that

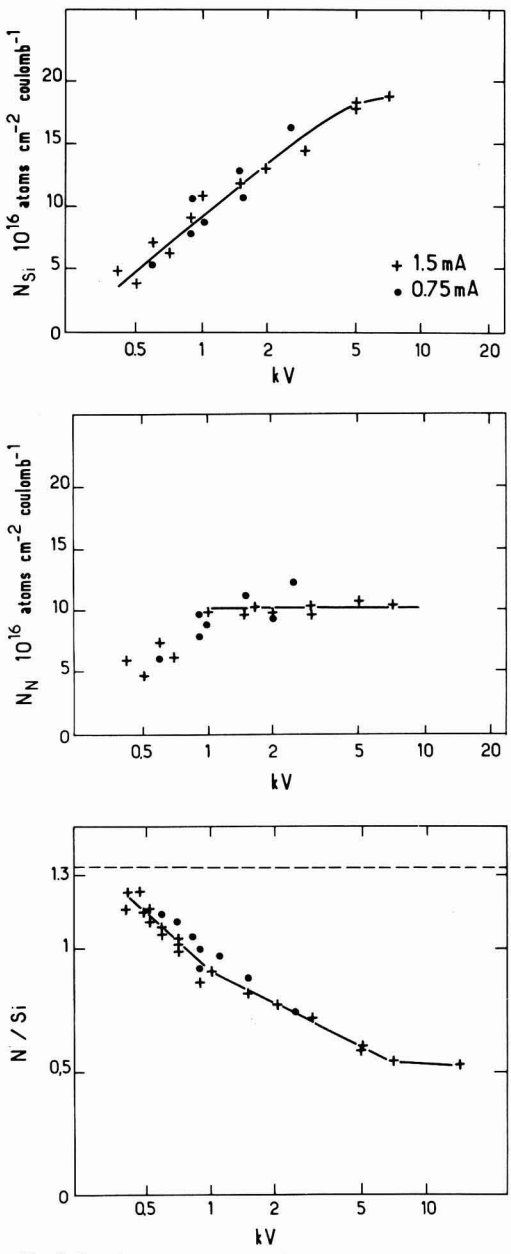

Fig. 6. Deposition yields of silicon N_{Si} (Fig. 6a), of nitrogen N_N (Fig. 6b) expressed in atoms cm^{-2} coulomb^{-1}, and the atomic ratio N/Si (Fig. 6c) as a function of the accelerating voltage V.

predicted by Sigmund. This unexplained result has already been reported in the case of a noble gas ion beam (24). If we took for the theoretical energy a value equal to half the experimental one, a satisfactory agreement would be obtained between the energy position of the maximum of S in the theoretical curve, and that of N_{Si} (*i.e.*, of S) in the experimental one. This is in agreement with the hypothesis we have made about the behavior of N_2^+ ions, which are the main component of the nitrogen beam. The theoretical value of the maximum of $S'(E/2)$ is found equal to 1.3, assuming a bond energy of 7.8 eV which is that of pure silicon, and con-

sidering a 45° angle of incidence. It appears that the experimental value of S maximum is in agreement with the theoretical one if $S \simeq 2S'(E/2)$.

Next, we shall discuss the variation of N_N with energy (Fig. 6-b). In the voltage range 1-10 kV and from Eq. [3-b], we deduce that a, sticking probability of sputtered nitrogen on the growing film, is equal to about 0.5. This is a large value in comparison with that of the sticking coefficient of molecular nitrogen, which has been estimated above to be lower than about 10^{-5}. This confirms that implanted nitrogen would be sputtered as atoms linked with silicon or as highly reactive single atoms. Let us note that the proportion of sputtered Si_xN_y clusters would depend on the density of damage induced by the impinging ions; consequently, the coefficient a is a function of the current density, and then varies with the focusing and the composition (N_2^+/N^+) of the ion beam.

Below 900V, N_N decreases with V. This can be explained by two processes: (*i*) the maximum concentration of nitrogen at the target surface is given by $N/Si = 2/S$ for N_2^+ impinging ions, if the fraction of reflected ions still may be neglected at low energy. (See section on study of the implanted target.) The surface of the target is then very over-stoichiometric when S is lower than 1, as is true in this range of energy (Fig. 6-a), and nitrogen in excess may be sputtered (or desorbed) as N_2 molecules with a low sticking probability. (*ii*) The fraction of reflected nitrogen ions increases with decreasing energy, as has been reported for inert gas (27) and nitrogen ions (17), and their angular distribution is very different than that of the sputtered species. In these conditions, an important part of emitted nitrogen does not reach the growing film.

For low values of V, giving nearly stoichiometric Si_3N_4 layers, the balance we can make for deposited silicon and incorporated nitrogen—~ 0.5 Si and ~ 0.6 N atoms for one N_2^+ ion—is in good agreement with the formal equation proposed by Weissmantel (13) for a sputtering yield of 0.48.

Deposition of stoichiometric Si_3N_4.—Stoichiometric nitride layers can be obtained in our apparatus with the required energy of the ions (Fig. 6), but with a very low deposition rate, typically 1 nm/min. In order to obtain Si_3N_4 films with higher deposition rates, we used two different methods. The first one consists of introducing a partial pressure of ammonia in the deposition chamber. This molecule being much more unstable that N_2 should be a more efficient nitriding agent. The sticking probability of N_2 has such a low value that the production of an intense molecular beam towards the growing film does not significantly change its stoichiometry (second section). The assumption that atomic nitrogen has a very different behavior suggests the second method, which consists of depositing a nitride layer with a significant flow rate of N_2 and a simultaneous electronic bombardment on the growing film. The following results were obtained:

Effect of a partial pressure of ammonia.—Typical results are presented in Fig. 7. They are for layers deposited with an ion beam of 6 keV energy and of 3 mA intensity, the partial pressure of ammonia $P(NH_3)$ being varied from 0 to 5×10^{-3} Pa. The N/Si ratio, N_N and N_{Si} are plotted *vs.* the pressure of NH_3. N/Si increases strongly with $P(NH_3)$ and reaches a saturation value greater than 1.33 for a pressure equal to 2×10^{-3} Pa. N_N also increases and reaches an asymptotic value, but at a lower pressure value ($\sim 3 \times 10^{-4}$ Pa), while N_{Si} shows an unexpected decrease in the same range of pressure.

The behavior of N_N and N_{Si} cannot be entirely explained by process (c) (direct adsorption of NH_3 on the growing film) as this process cannot induce a decrease of N_{Si}. So we have to take into account the process (b)

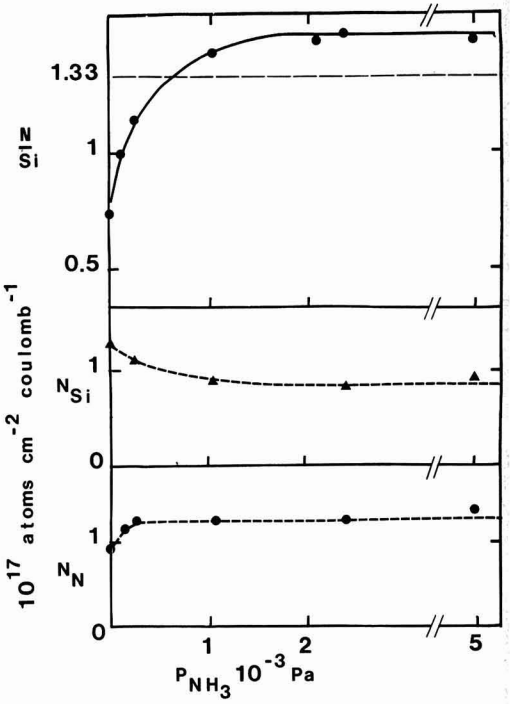

Fig. 7. Deposition yields of silicon and nitrogen and stoichiometry of ion-beam sputtered silicon nitride films deposited with an nitrogen ion-beam energy of 6 keV at a current of 3 mA expressed as a function of the partial pressure of ammonia.

which is related to the adsorption of NH_3 on the target: this adsorption should change the composition of the target surface and thus lower the sputtering yield of silicon. Moreover, over-stoichiometric nitride films were obtained for higher pressures of NH_3; nitrogen in excess may be incorporated as N-H radicals. We are studying this possible effect.

Effect of electron bombardment combined with N_2 molecular beam.—Layers were deposited with a beam of energy equal to 10 keV and of intensity equal to 3 mA. The input pressure in the molecular beam generator was maintained equal to 1600 Pa and the calculated value of the corresponding local pressure of N_2 was equal to 0.2 Pa (18). The intensity of the electronic bombardment ranged from 0 to 50 mA with 150V applied to the substrate. Figure 8 shows the N/Si ratio as a function of the electronic current: it increases and nearly reaches the Si_3N_4 stoichiometry for intensities higher than 30 mA. The oxygen content can be reduced to less than 3% (Fig. 3b) when great care has been taken for the gas entry system.

From the slope of this curve, at $I = 0$, and knowing the deposition rate of silicon, we obtain a value

$$\frac{dn_N}{dI} = 2.9 \times 10^{13} \text{ atoms cm}^{-2} \text{sec}^{-1} \text{mA}^{-1}$$

From this, we can deduce the increase of the sticking probability of N_2 with electronic bombardment

$$da/dI = 7 \times 10^{-5}/\text{mA}$$

To explain this increase we assume the following process: nitrogen molecules are adsorbed on the growing films and then are dissociated by the electronic bombardment; this atomic nitrogen is the reactant for nitridation of unbound silicon. We can also determine the

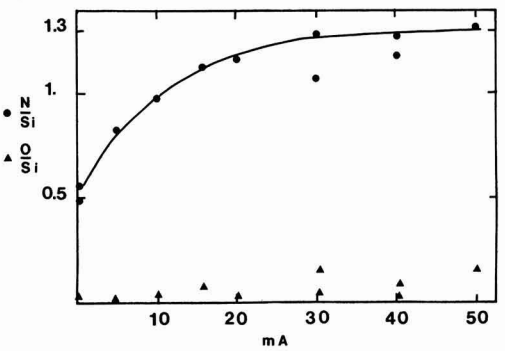

Fig. 8. N/Si ratio as a function of the electronic bombardment intensity corresponding to ion-beam sputtered silicon nitride films deposited under an N_2 molecular beam (local pressure: 0.2 Pa) with an ion-beam energy of 10 keV and a current intensity of 3 mA.

coverage density of adsorbed N_2, assuming the dissociation cross section to be the same for adsorbed and free molecules [about 2×10^{-16} cm^2 at 150 eV (28)]; we find a value of about 10^{13} atoms/cm^2, equivalent to one-hundredth of a monolayer.

Conclusion

This study allowed us to determine the respective contributions of different mechanisms which take place during the deposition of silicon nitrides by ion beam sputtering. It has been shown that: (*i*) The sticking probability of molecular nitrogen on the growing film is negligible (less than 2×10^{-5} in 10^{-4} to 0.2 Pa pressure range), (*ii*) The incorporation in the growing film of nitrogen sputtered and/or reflected from the target is independent of the ion beam energy in 1-10 keV range. The corresponding sticking probability is equal to 0.5. Moreover the contribution of the adsorbed molecular nitrogen on the target seems to be limited by the current density and independent of the pressure for values greater than 10^{-4} Pa. The N/Si ratio is fixed by the sputtering yield of silicon: it is equal to about 1 for 0.9 keV and decreases linearly with log E, from 1 to 0.5 in the 1-5 keV energy range, while the sputtering yield S varies from 1 to 2 atom/ion. Note that S must be reduced if we want to reach the Si_3N_4 stoichiometry; we have obtained 1.25 for the N/Si ratio at 0.4 keV, for $S = 0.5$ atom/ion. (*iii*) Stoichiometric silicon nitrides were obtained by increasing the sticking probability of molecular nitrogen on the growing film by using electronic bombardment; with our experimental conditions the corresponding increase is equal to about 10^{-4}/mA. Another possibility is to use NH_3 as a highly reactive molecule: nitrogen-rich nitride is obtained from P_{NH_3} greater than 10^{-3} Pa.

Acknowledgments

The authors wish to thank E. d'Artemare for his assistance with the experiments carried out on the Van de Graaf accelerator. This work was supported by the Centre National de la Recherche Scientifique (RCP 157) and Délégation Générale à la Recherche Scientifique et Technique.

Manuscript submitted Dec. 30, 1981; revised manuscript received Nov. 8, 1982. This was Paper 37C presented at the Denver, Colorado, Meeting of the Society, Oct. 11-16, 1981.

Any discussion of this paper will appear in a Discussion Section to be published in the December 1983 JOURNAL. All discussions for the December 1983 Discussion Section should be submitted by Aug. 1, 1983.

REFERENCES

1. Z. Shoita, N. Miyamoto, and J. I. Nishizawa, *This Journal*, **124**, 1405 (1977).
2. J. M. Poate, P. J. Silverman, and J. Yahalom, *J. Phys. Chem. Solids*, **34**, 1847 (1973).
3. C. Cohen, M. Croset, A. V. Drigo, and J. Siejka, Proc. of the Eighth International Vacuum Congress, Vol. I, F. Abeles, and M. Croset, Editors, p. 586, Sept. 1980, Cannes, France.
4. R. P. H. Chang, J. J. Coleman, A. J. Polak, L. C. Fellman, and C. C. Chang, *Appl. Phys. Lett.*, **34**, 237 (1979).
5. D. L. Lile and D. A. Collins, *Thin Solid Films*, **56**, 225 (1979).
6. Wieder, in *Inst. Phys. Conf.* **50**, 234 (1979).
7. B. Bayraktaroglu, W. M. Theis, and F. L. Schuermeyer, *ibid.*, **50**, 280 (1979).
8. K. V. Vaidyanathan, M. J. Helix, D. J. Volford, B. G. Streetman, R. J. Blattner, and C. A. Evans, *This Journal*, **124**, 178 (1977).
9. M. J. Helix, K. V. Vaidyanathan, B. G. Streetman, H. B. Dietrich, and P. K. Chatterjee, *Thin Solid Films*, **55**, 143 (1978).
10. C. E. Morosanu, *ibid.*, **65**, 171 (1980).
11. S. T. Picraux, in "Ion Implantation in Semiconductors and Other Materials," B. L. Crowder, Editor, Plenum Press, New York (1975).
12. S. Rigo, G. Amsel, and M. Croset, *J. Appl. Phys.*, **47**, 2810 (1976).
13. C. Weissmantel, *Thin Solid Films*, **32**, 11 (1976); H. J. Erler, G. Reisse, and C. Weissmantel, *ibid.*, **65**, 233 (1980).
14. T. Tsujide, M. Nojiri, and M. Kitagawa, *J. Appl. Phys.*, **51**, 3 (1980).
15. A. D. Yadav and M. C. Joshi, *Thin Solid Films*, **59**, 313 (1979).
16. D. Bouchier, G. Gautherin, B. Agius, and S. Rigo, *J. Appl. Phys.*, **49**, 12 (1978).
17. H. F. Winters, in "Topics in Current Chemistry," Vol. 94, S. Veprek and M. Venugopalan, Editors, New York (1980).
18. C. B. Lucas, *Vacuum*, **23**, 11 (1972).
19. W. K. Chu, J. N. Mayer, M. A. Nicolet, T. M. Buck, G. Amsel, and F. Eisen, *Thin Solid Films*, **17**, 1 (1973).
20. S. Rigo, C. Cohen, A. L'hoir, and E. Backelandt *Nucl. Instr. Methods*, **149**, 721 (1978). New York (1973).
21. G. Amsel and D. David, *Rev. Phys. Appl.*, **4**, 383 (1969).
22. J. P. Biersack, "Ion Surface Interaction Sputtering and Related Phenomena," Gordon and Breach, New York (1973).
23. J. Lindhard, M. Scharff, and M. E. Schiott, *Mater. Fys. Medd.*, **33**, 14 (1963).
24. P. Sigmund, *Phys. Rev.*, **184**, 2 (1969).
25. D. Bouchier, Ph.D. Thesis, Université Paris XI Orsay, France (1977).
26. J. Bottiger, J. A. Davies, P. Sigmund, and K. B. Winterbon, *Radiat. Eff.*, **11**, 69 (1971).
27. C. Carter, D. G. Armour, S. E. Donnely, D. C. Ingram, and K. P. Webb, *ibid.*, **53**, 143 (1980).
28. H. F. Winters, *J. Chem. Phys.*, **44**, 1472 (1966).

Sputter-Etching Planarization for Multilevel Metallization

H. Kotani, H. Yakushiji, and H. Harada

Computer Development Laboratories Limited, 4-1 Mizuhara, Itami, Hyogo 664, Japan

and K. Tsukamoto* and T. Nishioka

Mitsubishi Electric Corporation, LSI Research and Development Laboratory, 4-1 Mizuhara, Itami, Hyogo 664, Japan

ABSTRACT

A simple process of sputter-etching planarization was developed for multilevel metallization, which utilized an angular dependence of sputter yield. Silicon nitride and phosphosilicate glass as interlevel insulators were planarized to a slope angle of 45° by using rf sputter etching with an argon gas. The surface topology was well predicted by computer simulation. The sputter-etching planarization was successfully applied to three-level metallization, resulting in very high yields of interconnection continuity, interlevel insulation, and via holes.

Planar surfaces become increasingly important in LSI's, especially in multilevel interconnections for the demand of higher packing density. Since the existence of topographic steps extremely restricts minimum feature size, and reduces metallization yield and reliability, extensive works have been devoted to achieve planarization (1, 2, 3). Among them, it is a well-known technique to flow phosphosilicate glass (1), which cannot, however, be applied to aluminum-aluminum interconnections because of its higher temperatures required. Recently, other methods have been studied for low-temperature processing. For example, films covering stepped surfaces were coated with photoresist and then removed by either plasma etching (2) or ion beam etching (3) under the same etching rate for the film and the resist. Although this process provides very smooth surfaces, it was complicated and difficult to control the etching condition which depends on the film material.

Sputter etching is a commonly used technique to delineate fine patterns. A number of papers have reported on the change of surface profiles by ion bombardment (4-10). The etched profiles are mainly determined by an angular dependence of sputter yield, which results in sloping walls. It is the purpose of this paper to provide a simple process for planarization utilizing the angular dependence of sputter etching. The evolution of surface profiles of silicon nitride and phosphosilicate glass films is presented and compared with the results of a computer simulation. In order to evaluate the planarization effect, the technique is then applied to three-level metallization.

Computational Model

The basic mechanism of the sputter-etching planarization is based on the fact that the sputter-etching rate depends on the angle of ion incidence. Since substrates are normally bombarded by ions in an rf sputtering system, the etching rate is different at various locations on the surface due to its original topology, which results in a continuous modification of the profile. A computer simulation of the surface profile was performed in a similar manner which Lehmann reported as follows (10).

The variation of the sputter yield, as a function of the angle of incidence with respect to the surface normal, is written by the following analytical expression

$$S(\theta) = \alpha \cos\theta + \beta \cos^2\theta + \gamma \cos^4\theta \qquad [1]$$

where α, β, and γ are the constants given by the boundary conditions as

$$S(0°) = 1, \frac{dS}{d\theta} = 0, \text{ and } S(45°) = Sp \qquad [2]$$

$$\theta = 45°$$

Key words: multilevel metallization, planar metallization, surface coverage, sputtering.

This function $S(\theta)$ has a maximum of Sp at an angle $\theta = 45°$. Figure 1 plots these functions for $Sp = 3.3$ and 5.0.

The original profile is expressed by the curve as shown in Fig. 2, where D is the step height, and the corners at the step region are approximated by circles

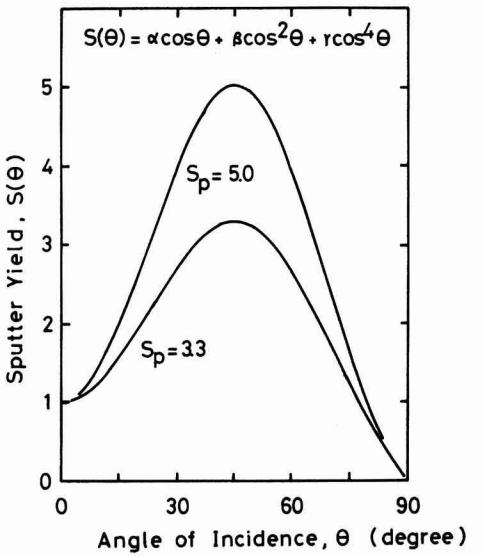

Fig. 1. Sputter yield as a function of angle of ion incidence for $Sp = 3.3$ and 5.0.

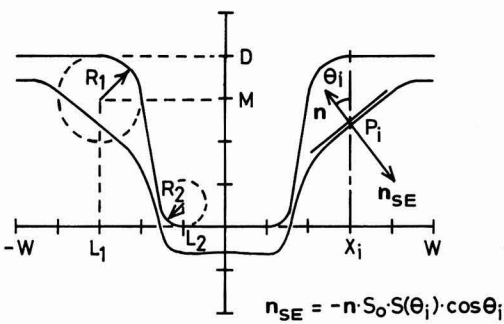

Fig. 2. Schematic illustration of evolution of surface profile due to sputter etching.

with radii R_1 at the top and R_2 at the bottom. These parameters, D, R_1, R_2, L_1, L_2, and M, are determined by tracing the original topology. The profile is approximated at all times by the same number of segments connecting a finite number of points P_i, where $i = 1, \ldots, 80$. As indicated in Fig. 2, the sputter etching causes the points P_i to move by the amount and the direction as

$$\mathbf{n}_{SE} = -\mathbf{n} \cdot S_0 \cdot S(\theta_i) \cdot \cos\theta_i \qquad [3]$$

where $\mathbf{n}$ is a unit vector of the surface normal and S_0 is the sputter yield for unit cycle when $\theta_i = 0°$. A new profile is then given by the shifted segments. In our simulations, the sputter-etched materials are assumed to be homogeneous and isotropic. Although the effect due to redeposition of sputtered materials might affect the etched profiles and become increasingly significant with decreasing feature size, the redeposition is a secondary effect, and is neglected in the present simulations. This point will be discussed later.

Experimental

Aluminum alloy films, Al-Si and Al-Si-Cu, were formed by d-c planar magnetron sputtering for interconnections. Silicon nitride films (P-SiN) and phosphosilicate glass films (LP-PSG) were utilized for interlevel insulators. P-SiN were deposited by a plasma CVD technique at 300°C, employing SiH_4 and NH_3 gases diluted with an inert gas. LP-PSG were deposited by a low pressure CVD technique at 430°C, using SiH_4, O_2, and PH_3 gases diluted with an inert gas. The via holes in P-SiN were opened by plasma etching employing a gas mixture of CF_4 and O_2, while those in LP-PSG by chemical wet etching using an HF solution. The surfaces were planarized by rf sputter etching using an Ar gas in the following conditions: a distance between parallel plate electrodes was 2.5 cm, an argon pressure was 1.7 Pa, and an rf power density was 0.5 W/cm². These conditions were mainly decided by the performance of the sputtering apparatus. The chosen argon pressure and the rf power density provided a stable rf plasma and uniform etching rates. The etching rates of Al, P-SiN, and LP-PSG were about 100, 70, and 60 A/min, respectively. During the sputter etching, the temperature of samples rose to above 200°C.

Results and Discussions

Figure 3 shows cross-sectional SEM pictures of as-deposited P-SiN, with a thickness of 1.47 μm covering 0.72 μm of patterned Al-Si, and those after sputter etching. It can be clearly seen that the facet with an angle of 45° develops and the surface is planarized. The etching rate of 67 A/min was obtained at the flat areas on metal lands.

The simulated profiles were then compared with the experimental ones as shown in Fig. 4, where we set $Sp = 3.3$ and $S_0 = 0.02$ μm, which corresponds to an etch time of 3 min. A fairly good agreement was obtained between the calculated and experimental results, which indicates that the analytical expression $S(\theta)$ employed is very similar to the actual sputter yield function. The only difference is observed at the bottom of the steps, where the actual etched depth is shallower than the calculated one. This would be attributed to redeposition of sputtered P-SiN, and was not observed when the width of the groove was larger than 5 μm. The effect of redeposition causes the limitation of ion etching, while it is advantageous for planarization because the step height decreases. In the case of the example shown in Fig. 4, the initial step height of 0.93 μm was reduced to 0.83 μm during sputter etching of 30 min by the redeposition effect.

Similar results were also obtained for LP-PSG. LP-PSG films exhibited poorer step coverage than P-SiN films, and the step angle made by the LP-PSG going over an Al step was larger than 90°, *i.e.*, a negative slope. Even if the slope angle was negative as in the

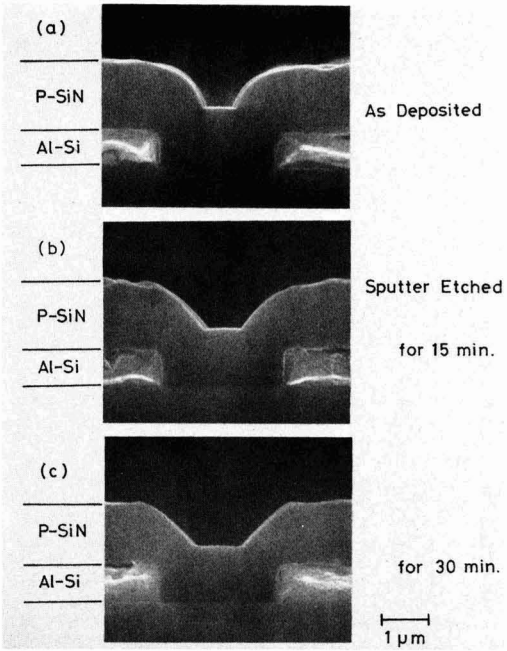

Fig. 3. Experimental evolution of profile for P-SiN covering patterned Al-Si steps. (a) Original profile. (b) After sputter etching for 15 min. (c) After sputter etching for 30 min.

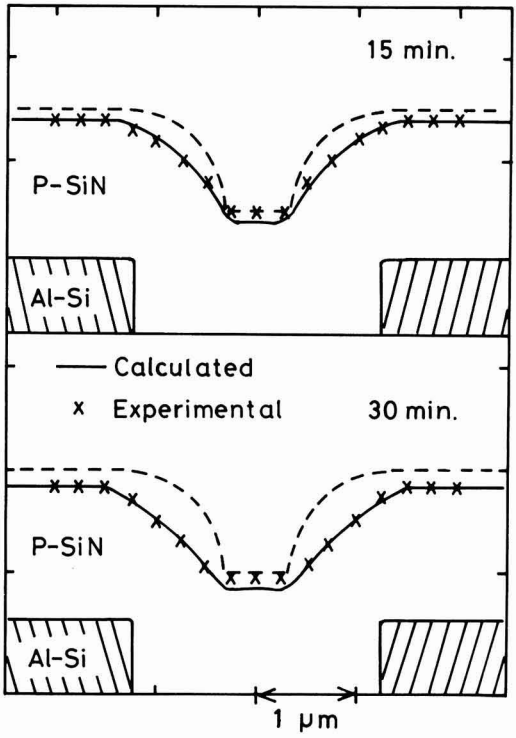

Fig. 4. Calculated evolution of profile corresponding to Fig. 3. Dotted line and X indicate original profile and experimental results on profile traces, respectively.

case of LP-PSG, sufficiently long etching time, say 60 min, resulted in a gentle slope with a step angle of 45°.

In order to evaluate the sputter-etching planarization, this technique was applied to three-level metallization. The process flow is summarized in Fig. 5. The deposition of sputtered Al films follows immediately after the sputter-etching process in the same apparatus, which leads to an additional advantage of a good step coverage of the metal, since the sputter etching causes the temperature rise of samples as mentioned above. Figure 6 shows a result of a test pattern of the three-level metal structure, where the coverage is relatively smooth due to the sputter-etching planarization. Figure 7 shows a cross-sectional SEM micrograph of a via hole between the first and second level metals. It can be seen that the sloped contour of the via sidewall provides a good step coverage of the second level conductor pattern. It also can be seen that the first level metal of about 0.3 μm is etched at the via by the planarization process.

The test chip was also used to determine crossover continuity yield, via hole yield and insulation yield. The structures and a typical set of results are listed in Table I, where the almost 100% yields have proved the usefulness of the planarization process. Although the

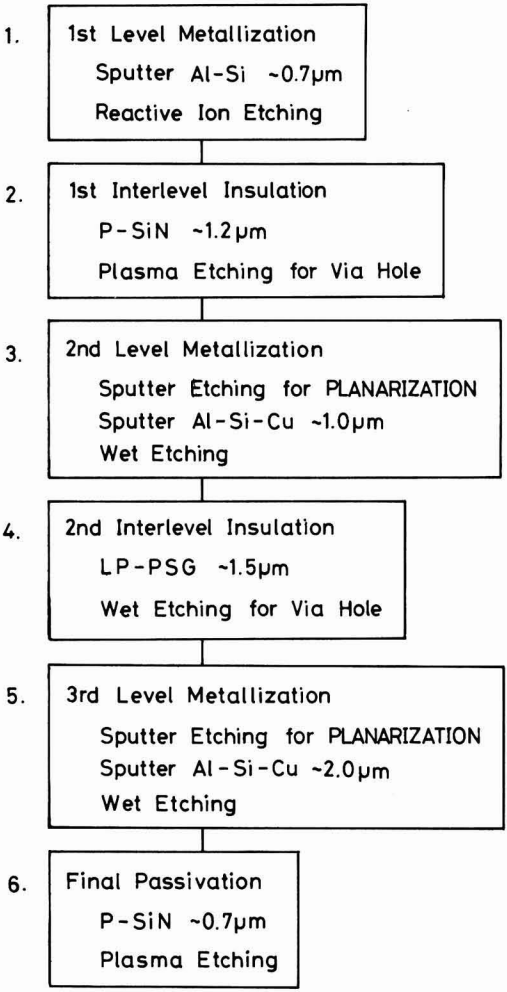

Fig. 5. Process flow and parameters for three-level metallization

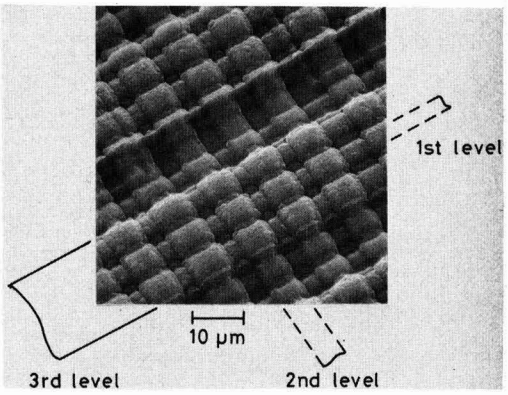

Fig. 6. 3rd-level metal coverage over 1st- and 2nd-level metals

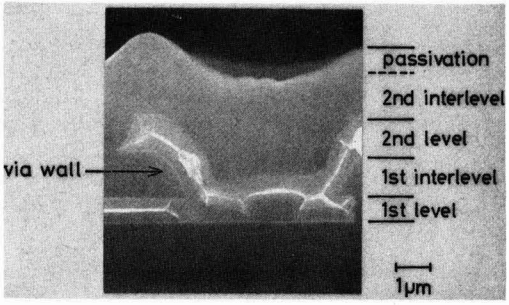

Fig. 7. 2nd-level metal coverage over via hole to 1st-level metal

size of the first via hole was 3 × 3 μm^2 and the contact resistance would be sensitive to the effect of redeposition, there was no difference observed between the contact resistances with and without the sputter-etching planarization. This is probably because the Al contact surface is sufficiently etched during the planarization process as mentioned above, so that the amount of the redeposited dielectrics onto the contact surface is negligible. The contact resistance of the second via hole, the size of which 10 × 10 μm^2, was not affected by the redeposition effect. The present sputter-etching planarization did not degrade the contact resistances of the via holes. Also the electrical characteristics of transistors were not affected by the sputter etching.

Summary

The angular dependence of rf sputter etching was utilized to achieve planarization. The slope angle of 45° was obtained for P-SiN and LP-PSG as interlevel insulation films by sputter etching with an argon gas, an angle of which was determined by the angular variation of the sputter yield for the materials. Also the step height was slightly reduced, due to redeposition when the width of the groove was narrower than a few μm. The sputter-etching process has been successfully applied to three-level metallization, resulting in very high yields for interconnection continuity, interlevel insulation, and via holes. No effect on device characteristics was observed after the planarization process.

Although the slope angle obtained is relatively large, around 45°, due to the physical properties of the sputtered materials, the sputter-etching planarization for multilevel metallization appears to be of great advantage. It should be noted that the planarization process is extremely simple, and the subsequent metallization could be continuously carried out after the planar-

Table I. Structures of test patterns and resultant yields

Test	Structure			Average resistance (Ω)	Yield (%)
Metal integrity	Width (μm)	Space (μm)	Length (cm)		
1st level	3	3	15	2740	99
2nd level	5	4	10	847	99
3rd level	20	10	3	33.4	100
Interlevel insulation	Area (mm^2)				
1st to 2nd	1.8				99
2nd to 3rd	1.7				96
Via hole	Area (μm × μm)	Number			
1st to 2nd	3 × 3	1600		372*	97
2nd to 3rd	10 × 10	300		11.6*	100

* The resistance of Al interconnection is included.

ization in the same sputtering apparatus. The technique should be applicable to a wide variety of materials.

Acknowledgments

The authors would like to thank Dr. H. Oka, Dr. H. Nakata and Mr. T. Etoh for their helpful discussions and encouragements.

Manuscript submitted July 12, 1982; revised manuscript received Nov. 12, 1982.

Any discussion of this paper will appear in a Discussion Section to be published in the December 1983 JOURNAL. All discussions for the December 1983 Discussion Section should be submitted by Aug. 1, 1983.

Publication costs of this article were assisted by Computer Development Laboratories, Limited.

REFERENCES

1. W. E. Armstrong, *This Journal*, **121**, 307 (1974).
2. A. C. Adams, *Solid State Technol.*, **24**, 178 (1981).
3. L. F. Johnson, K. A. Ingersoll, and D. Kahng, *Appl. Phys. Lett.*, **40**, 636 (1982).
4. A. R. Bayly, *J. Mater. Sci.*, **7**, 404 (1972).
5. C. Catana, J. S. Colligon, and G. Carter, *ibid.*, **7**, 467 (1972).
6. D. J. Barber, F. C. Frank, M. Moss, J. W. Steeds, and I. S. Tsong, *ibid.*, **8**, 1030 (1973).
7. G. Carter, J. S. Colligon, and M. J. Nobes, *ibid.*, **8**, 1473 (1973).
8. T. Ishitani, M. Kato, and R. Shimizu, *ibid.*, **9**, 505 (1974).
9. J. P. Ducommun, M. Cantagrel, and M. Moulin, *ibid.*, **10**, 52 (1975).
10. H. W. Lehmann, L. Krausbauer, and R. Widmer, *J. Vac. Sci. Technol.*, **14**, 281 (1977).

Langmuir Probe Measurements on CHF_3 and CF_4 Plasmas: The Role of Ions in the Reactive Sputter Etching of SiO_2 and Si

Ch. Steinbrüchel

Laboratories RCA Limited, CH-8048 Zürich, Switzerland

ABSTRACT

Langmuir probe measurements on CHF_3, CF_4, CF_4-H_2, and CF_4-O_2 plasmas with concurrent etch rate measurements on SiO_2 and Si have been made in a reactive sputter etching system. At an rf power of 300W and a pressure of 15 mTorr, the ion density is typically 1.5×10^{10} cm^{-3}, the electron temperature 2 eV, the plasma potential 30 eV, and the ion energy (*i.e.*, the sheath potential) of the order of 500 eV. The dependence of these parameters on rf power, pressure, reactor geometry, and plasma gas composition is investigated, as well as the spatial uniformity of the plasma. For SiO_2, etch rates vary essentially in proportion to ion densities with all the different plasmas. For Si in CF_4-O_2 plasmas, the anisotropic part of the etch rate also parallels the ion density. From the measured ion densities the ion flux to the substrate is estimated. Thus, etch rates per ion can be determined, which turn out to be similar to those in reactive ion beam etching, although in reactive sputter etching ion energies are much smaller.

Dry processing is replacing more and more wet chemical methods in the fabrication of microelectronic devices, the reason being that dry methods allow for better dimensional control of structures to be formed in different materials.

For Si-based materials, dry processing occurs in a plasma of a reactive gas such as CF_4 or CHF_3. A large number of processes have been developed to etch a particular material selectively over another, with etching being preferably anisotropic at the same time (1). Yet information on the details of the chemical mechanisms underlying the various processes is still rather incomplete (1-3).

Key words: semiconductor, integrated circuits, discharge, sputtering.

The main difficulty in understanding dry etching processes at the molecular level stems from the fact that a reactive plasma is a complex mixture of interacting chemical species. Ions may remove material physically from the substrate, or they may react chemically with the substrate, or they may promote chemical reactions of the substrate with other gas phase species such as atoms and radicals. Not only is it difficult to measure the concentrations and reactivities of the various species, but the plasma composition also depends in a complicated manner on the external operating parameters.

Nevertheless, a coherent picture is beginning to emerge of the important qualitative aspects of dry etching, mostly from relating etch rate data to optical

(4-9) and mass-spectrometric measurements (8-14) on plasmas. The connection between the state of an etched surface and etching conditions has also been investigated (15, 16). For Si and SiO_2, the major characteristics of dry etching may be summarized very briefly from the literature as follows (1-3): A dry-etch process must yield only volatile products. In a fluorine-based plasma, F atoms are the main etchant for Si, but are probably less important for the etching of SiO_2. Selective etching of SiO_2 over Si requires a fluorine-deficient plasma. Anisotropic etching is related to the impact of ions on the substrate. Plasma conditions must be chosen such that no deposition of polymeric material on the substrate can occur.

It is the purpose of this paper to establish more clearly the role of ions in reactive sputter etching (36) [sometimes also called reactive ion etching (1)]. To this end we present Langmuir probe measurements of ion densities and electron temperatures in etching plasmas, and we relate these to concurrent etch rate measurements. Specifically, we study the etching of SiO_2 and Si in CHF_3, CF_4, CF_4-O_2, and CH_4-H_2 plasmas. In the process we are able to estimate plasma potentials, average ion energies, and ion fluxes onto the substrates. We discuss our results in relationship to previous work using other plasma-diagnostic techniques, and in relationship to recent results on reactive ion beam etching.

Langmuir Probe Plasma Diagnostics

A Langmuir probe is a simple well-known device (17) consisting of a small electrode in contact with the plasma. The basic measurement involves recording the current to the probe, I_p, as a function of the applied potential, V_p. Fom this type of measurement, information can be gained on the plasma ion density and electron temperature.

In spite of their simplicity, Langmuir probes have been used only rarely in connection with sputtering-type plasmas. This is due partly to experimental difficulties in obtaining reliable measurements (see section on experimental arrangement), and partly to problems in interpreting such measurements (see below). Langmuir probe experiments have been reported to map out the dark space in a discharge (18), to demonstrate the effect on the plasma potential of a positive electrode in contact with the plasma (19), and to determine ion densities and electron temperatures in an Ar discharge (20, 21). Langmuir probes were used also to compare qualitatively CF_4 and NF_3 discharges (22), to determine electron temperatures and estimate ion fluxes in plasma mixtures of He with other gases including F_2 (12), and to obtain electron densities in CF_4 plasmas (37).

Qualitatively it is straightforward to explain the current *vs.* potential characteristic of a Langmuir probe (21, 23, 24) (see also Fig. 1 and 2). At large negative potential, a sheath of positive ions forms around the probe such that only ions are collected, and electrons are repelled. In the transition region of small negative potential where the slope of the characteristic changes rapidly, the probe acts as an energy selector for electrons, and ions and electrons contribute in comparable measure to the probe current. At large positive potential the probe current consists only of electrons. The electron saturation current is much larger than the ion saturation current because of the higher mobility of electrons.

For the purpose of quantitative description it is easiest to deal with the electron current in the transition region (23, 24). There the probe reduces the electron density in its vicinity such that for a thermal electron distribution at a temperature T_e

$$I_e = eN_eA\,(kT_e/2\pi M_e)^{1/2} \exp X \qquad [1]$$

In [1] N_e is the electron density in the bulk plasma, A the probe area, M_e the electron mass and X a dimensionless potential defined as

$$X = e(V_p - V_s)/kT_e \qquad [2]$$

where V_p is the potential applied to the probe, and V_s is the local plasma potential. Thus, a plot of log I_e *vs.* V_p should give a straight line with a slope inversely proportional to T_e.

It is much more difficult to describe quantitatively the ion saturation region, at large negative V_p (23, 24). The difficulty arises because the positive ion sheath shields the probe only incompletely. A small but significant tail of the probe potential extends to large distances. At the same time, the ion density at the sheath edge is depressed somewhat with respect to the bulk of the plasma, and ions enter the sheath with a mean energy of about kT_e. Consequently, the simple Langmuir theory for ion collection assuming a sharp sheath edge (23) does not hold, and one must resort to elaborate numerical computation for obtaining the ion current as a function of the probe potential.

Comprehensive numerical results have been presented by Laframboise in a form useful to the experimenter (24, 25). First we note that a typical plasma in reactive sputter etching is collisionless: the mean free path for charged particle-neutral collisions is of the order of 1 cm, and thus much larger than the Debye length λ_D

$$\lambda_D = (kT_e/4\pi N_e e^2)^{1/2} \qquad [3]$$

which turns out to be of the order of 10^{-2} cm. Furthermore, the ions in the bulk plasma are close to room temperature (~0.1 eV), whereas T_e is typically a few eV. For such a plasma and a cylindrical probe of radius r_p, Laframboise represented the ion current I_i as

$$I_i = eN_iA\,(kT_e/2\pi M_i)^{1/2} i_i \qquad [4]$$

where N_i is the ion density in the bulk plasma, A the probe area, M_i the ion mass, and i_i a dimensionless current depending on r_p/λ_D and on the potential X, but only weakly on the ion temperature T_i. Moreover, from Laframboise's results, one can infer that as long as $r_p/\lambda_D \lesssim 3$ and $T_i/T_e << 1$

$$i_i^2 = 1.27(-X) \qquad [5]$$

to within about 3%. Thus, from [4] and [5], I_i^2 will be a linear function of the probe potential V_p with a slope determined by the ion density N_i

$$-\Delta(I_i^2)/\Delta V_p = 0.20e^3N_i^2A^2/M_i \qquad [6]$$

The plasma potential V_s can be deduced if one notes that at the floating potential X_f, electron and ion currents to the probe are equal (23, 24). Upon combining [1], [4], and [5], and assuming $N_i = N_e$, one finds that X_f must satisfy the equation

$$1.1\,(M_e/M_i)^{1/2}(-X_f)^{1/2} = \exp X_f \qquad [7]$$

Hence, X_f can be calculated as the solution of [7]. [For example $X_f = -4.8$ for a CHF_3 plasma and $X_f = -5.0$ for a CF_4 plasma.[1]] Then from [2] with $X = X_f$ (at $I_p = 0$)

$$V_s = V_p(I_p = 0) - kT_eX_f/e \qquad [8]$$

where $V_p(I_p = 0)$ is the potential applied to the probe at which the net probe current is zero. (It should be mentioned that in [8] a d-c shift, induced by the rf component of the potential between the probe and the plasma, is neglected [Ref. (37)]. This would imply a too negative $V_p(I_p = 0)$ as compared to X_f, and thus a somewhat too small V_s calculated from [8].)

Experimentally, one proceeds as follows: Having recorded an $I_p(V_p)$ curve, one determines first N_i from a plot of I_p^2 *vs.* V_p at large negative V_p, where $I_p = I_i$ (see Eq. [6]). Next, one extrapolates I_i into the transition region of $I_p(V_p)$ to obtain $I_e(V_p)$ as the difference

[1] We assume that CF_3^+ is the major ion in a CF_4 plasma, and CHF_2^+ in a CHF_3 plasma [see Ref. (3, 26)].

of I_p and I_i. A plot of log I_e *vs.* V_p will yield T_e (see [1]). The plasma potential V_s then follows from Eq. [7] and [8], together with the experimental value for $V_p(I_p = 0)$.[2]

Experimental Arrangement

The main components of our setup are a stainless-steel vacuum chamber pumped by a 1800 l/sec oil diffusion pump, and rf electronics by MRC, operating at 13.56 MHz, for maintaining a discharge in the chamber. The chamber is 42 cm in diam, and 24 cm in height, and acts as the grounded electrode for the discharge. The rf-driven electrode (or cathode) is made of copper, is watercooled, and covered by an SiO_2 plate, and is usually 38 cm in diam. It is also shielded at the edge by a dark space shield. The rf-induced d-c voltage is measured directly at the copper plate, via a low-pass filter. Several gases can be admitted independently to the chamber via flow controllers (Tylan FC-260). The pressure is measured by a baratron cell (MKS Type 170 M-6B). The pumping speed at the chamber can be varied with a home-built iris diaphragm.

Our Langmuir probe is similar in design to one by Eser *et al.* (21). It consists of a short piece of tungsten wire of 0.25 mm diam, soldered to a long piece of tungsten wire of 1 mm diam which, near the soldering joint, is sealed into a Pyrex tube of 5 mm diam. The thin probe wire is partially shielded by the glass tube, such that its length exposed to the plasma is 1 cm. The probe is connected via a tuned filter to a set of batteries with a voltage-dividing network, so that $I_p(V_p)$ characteristics can be recorded directly on an X-Y recorder, the reference electrode being the grounded vacuum chamber in contact with the plasma [cf. Ref. (21)].

In order to get reliable probe measurements, one needs to take certain short as well as long term precautions. First, if the probe is exposed to the plasma at floating potential, contamination can be noticed within a few minutes in a CHF_3 plasma, and within an hour even in an Ar plasma, since the probe characteristic becomes distorted in the transition region.[3] This is caused, presumably, either by material sputtered from the SiO_2 cathode (in Ar) or by polymers deposited from the plasma (in CHF_3). But if the probe is held at −180V between taking $I_p(V_p)$ traces, then ion bombardment is apparently sufficient to keep it clean, or at least in a reproducible condition, indefinitely in an Ar or O_2 plasma. In a CHF_3 plasma contamination still becomes noticeable after about an hour, but then the probe, at −180V, can be cleaned easily in an O_2 plasma. (A probe made out of a platinum wire turned out to be much more prone to contamination and more difficult to regenerate than the tungsten wire probe.) Unfortunately, the procedure for maintaining a clean probe has a side effect, in that the probe wire itself is being etched slowly. This brings about a noticeable decrease of the wire diameter over an extended period of time, thus affecting the effective probe area.

Effects of geometry on the discharge are investigated by comparing plasmas with cathodes of 38 and 15 cm diam. Also, the probe can be positioned either 4 or 12 cm above the center of the cathode, or it can be moved in a horizontal direction. (The cathode dark space in our experiments is typically 1-2 cm high.)

Samples to be etched are small (~1 cm^2) pieces of steam-grown SiO_2 or poly-Si ($\gamma = 0.05$) placed directly on the SiO_2 cathode plate. Etch rates are measured interferometrically using an He-Ne laser.

[2] Values for V_s thus obtained roughly agree with those using the point of electron current saturation, although that point is not too well defined (the "knee" in the $I_p(V_p)$ is not very pronounced, and the electron current does not really saturate). Also, in that region the probe draws enough current so as to get hot quickly and disturb the plasma.

[3] Similar contamination problems have been noted before [Ref. (18, 24)].

Results

In Fig. 1 to 3 we illustrate how to obtain ion densities N_i and electron temperatures T_e from recorded $I_p(V_p)$ curves. Figure 1 shows a set of representative $I_p(V_p)$ curves for a CHF_3 plasma at 11 mTorr pressure, and 14 sccm flow, with the probe close to the SiO_2-covered cathode (4 cm above the center). From these curves one can construct plots of I_p^2 *vs.* V_p (Fig. 2) and log I_e *vs.* V_p (Fig. 3) as described above. Clearly, the postulated straight-line relationships (cf. Eq. [1] and [6]) determining N_i and T_e are well obeyed. Also, one notes immediately the higher ion density and lower electron temperature at higher power.

On this basis, etching plasmas of several gases have been examined under various conditions. The results for CHF_3 etching SiO_2 are summarized in Fig. 4 to 7. At constant pressure and flow (Fig. 4), the etch rate R_e depends linearly on the rf power applied. The ion density N_i varies less strongly, being proportional to the square root of the power. Also, with decreasing power the electron temperature T_e increases markedly, whereas the ion energy E_i decreases mark-

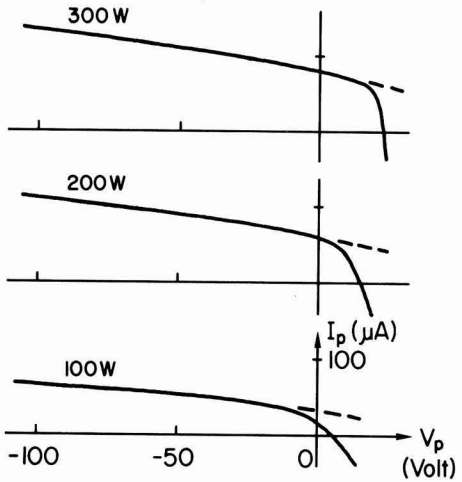

Fig. 1. Probe characteristics for CHF_3 at 11 mTorr and 14 sccm. Probe 4 cm above large cathode (see text). Dashed lines give extrapolated ion currents.

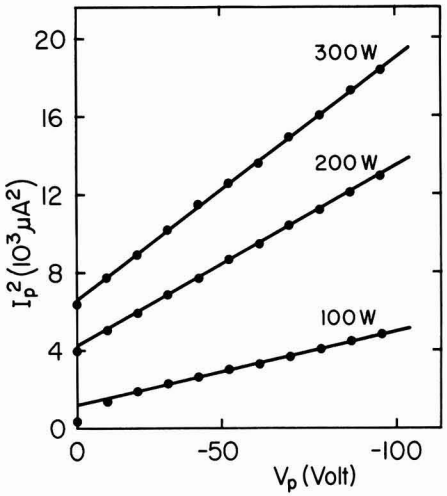

Fig. 2. Plots of I_p^2 *vs.* V_p from curves of Fig. 2

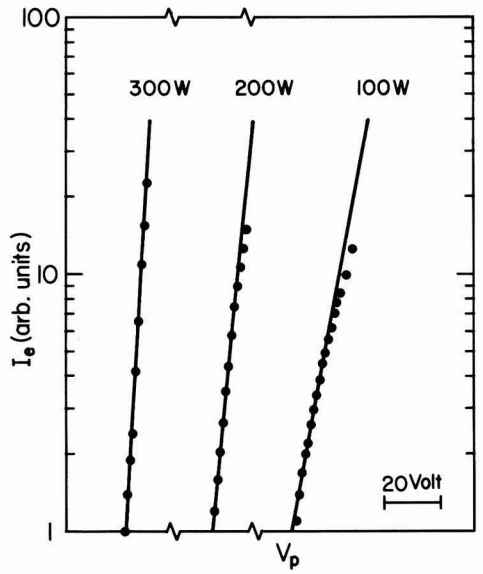

Fig. 3. Plots of log I_e (electron current) vs. V_p from curves of Fig. 1.

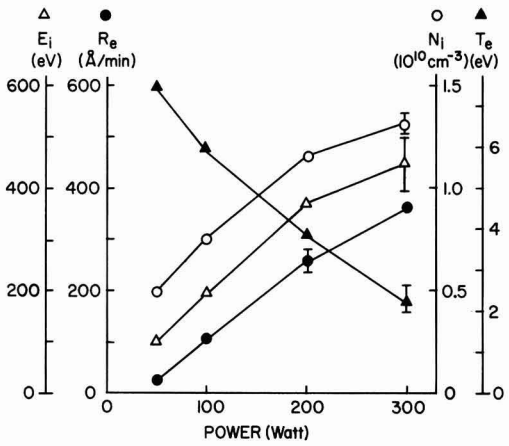

Fig. 4. Reactive sputter etching of SiO_2 in a CHF_3 plasma: plots of etch rate R_e, ion density N_i, electron temperature T_e, and ion energy E_i, vs. rf power. p = 10 mTorr, flow rate = 15 sccm. Probe 4 cm above large cathode.

edly. E_i is taken as the difference between the plasma potential V_s and the rf-induced d-c voltage at the cathode, V_{DC}. It is noteworthy that here, as well as in all other cases, variations in E_i are due mostly to changes in V_{DC}, V_s being quite constant. For the conditions of Fig. 4, V_s is about 30V, and V_{DC} varies between −400 and −70V, as the power varies from 300 to 50W. At constant power and flow but variable pressure, (Fig. 5), N_i, R_e, and E_i are fairly constant, whereas T_e increases strongly at lower pressure.

Certain geometrical aspects of the plasma are illustrated in Fig. 6 and 7. First, regarding the probe position, one consistently obtains somewhat higher values for N_i and T_e with the probe 4 cm rather than 12 cm above the center of the cathode (Fig. 6). Also, 4 cm from the edge of the cathode in the horizontal direction, N_i is typically 20% lower than in the center of the discharge. Figure 7 shows that for fixed external plasma parameters, R_e is considerably higher with the 15 cm than with the 38 cm diam cathode, even at a pressure where N_i is lower. Evidently, the major factor responsible for this difference is the ion energy which, in turn, is determined mostly by the induced d-c potential: For the small cathode $E_i \approx$ 1400V (V_{DC} = −1400V, V_s = 35V), and for the large cathode $E_i \approx$ 450V (V_{DC} = −400V, V_s = 30V), at 300W, regardless of the pressure. Interestingly, if with the small cathode the power is reduced (typically by a factor ~2.5) to the point where R_e is the same as with the large cathode, then N_i and E_i turn out to be very similar in the two cases.

Analogous results for a CF_4 plasma etching SiO_2 are displayed in Fig. 8 and 9. Overall, qualitative trends are very similar to those for a CHF_3 plasma.

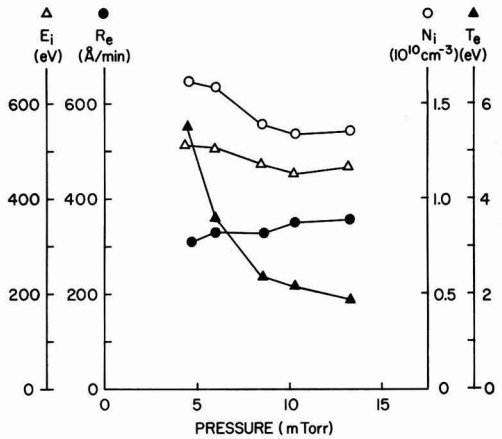

Fig. 5. Reactive sputter etching of SiO_2 in a CHF_3 plasma: plots of etch rate R_e, ion density N_i, electron temperature T_e, and ion energy E_i vs. pressure. RF power = 300W, flow rate = 15 sccm. Probe 4 cm above large cathode.

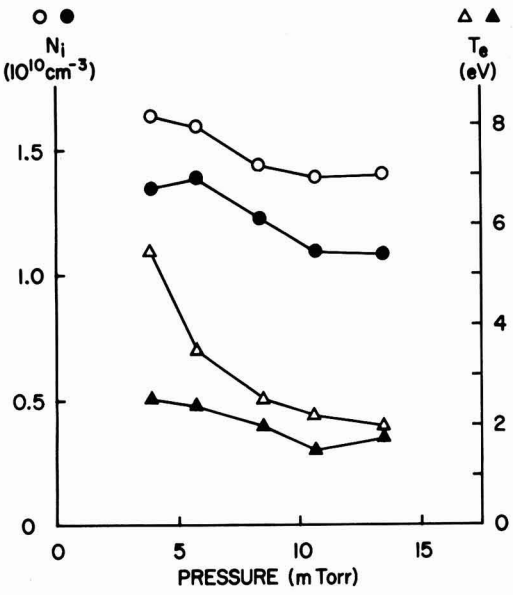

Fig. 6. Plots of ion density N_i and electron temperature T_e vs. pressure of CHF_3 with variable probe position. △, ○: probe 4 cm above large cathode; ▲, ●: probe 12 cm above large cathode. RF power = 300W, flow rate = 15 sccm.

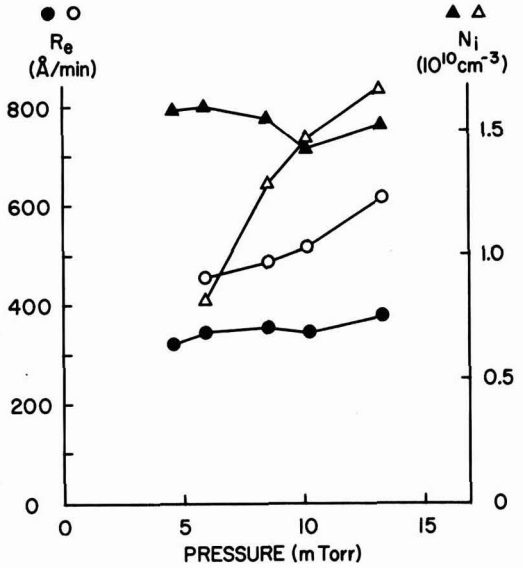

Fig. 7. Plots of ion density N_i and etch rate R_e of SiO_2 vs. pressure of CHF_3 with variable cathode size. ▲, ●: large cathode (38 cm diam); △, ○: small cathode (15 cm diam). RF power = 300W, flow rate = 15 sccm. Probe 4 cm above cathode.

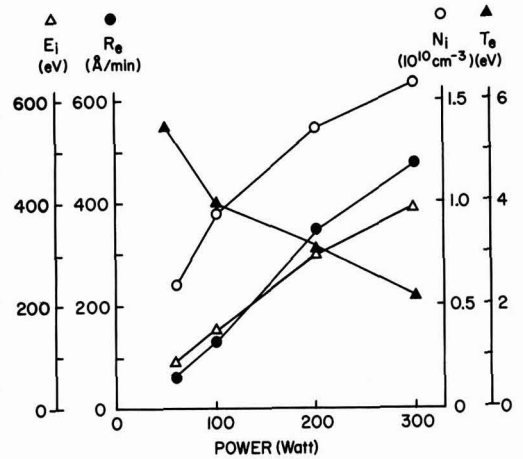

Fig. 8. Reactive sputter etching of SiO_2 in a CF_4 plasma: plots of etch rate R_e, ion density N_i, electron temperature T_e, and ion energy E_i, vs. rf power. p = 19 mTorr, flow rate = 19 sccm. Probe 4 cm above large cathode.

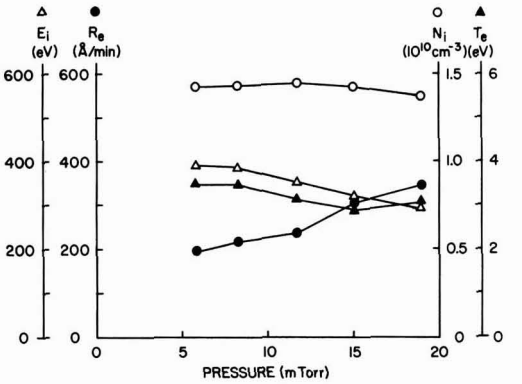

Fig. 9. Reactive sputter etching of SiO_2 in a CF_4 plasma: plots of etch rate R_e, ion density N_i, electron temperature T_e, and ion energy E_i vs. pressure. RF power = 200W, flow rate = 19 sccm. Probe 4 cm above large cathode.

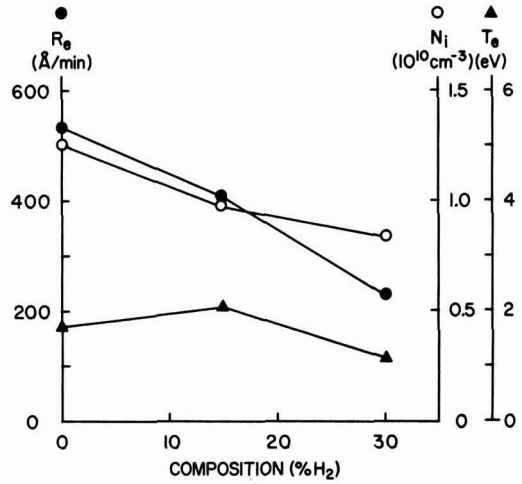

Fig. 10. Reactive sputter etching of SiO_2 in a CF_4-H_2 plasma: plots of etch rate R_e, ion density N_i, and electron temperature T_e vs. gas composition. RF power = 300W, p = 20 mTorr, flow rate = 24 sccm. Probe 12 cm above large cathode.

More specifically, with given external plasma parameters, R_e is about the same for the two gases, whereas N_i is slightly higher, and E_i slightly lower for CF_4 than for CHF_3. The effects in varying cathode size and probe position are the same as for CHF_3.

In Fig. 10-12 some mixtures of CF_4 with other gases are considered. In CF_4-H_2 mixtures, both N_i and R_e for SiO_2 decrease continuously with increasing H_2 content, whereas T_e is relatively constant (Fig. 10). On the other hand, in CF_4-O_2 mixtures N_i and R_e for SiO_2 exhibit a weak maximum at about 10% O_2 content, and T_e is increased markedly as soon as the plasma contains even a small amount of O_2 (Fig. 11). The etch rate for Si peaks much more sharply than that for SiO_2, but at about the same O_2 concentration (Fig. 12). Neither V_s nor E_i depend significantly on the gas composition. Our data on etch rates *vs.* composition agree with earlier work (8, 9, 27, 28).

Discussion

In the discussion of our work we wish first to address some practical issues related to obtaining reliable data. Second, we examine the properties of etching plasmas as they emerge from our results on the various microscopic plasma parameters. And third, we relate these parameters to etch rates, with a view on contributing to the ongoing discussion on etching mechanisms.

Experimental aspects.—Given a certain set of discharge parameters, the quantities best reproducible (*i.e.*, to within a few percent) are the ion density N_i and the etch rate R_e. Plots of I_p^2 *vs.* V_p determining N_i (Eq. [6]) indeed turn out to be accurately linear in the ion saturation region (cf. Fig. 2). A somewhat larger uncertainty is associated with the electron temperature T_e, a typical error being 10% for small values of T_e, less for larger values. Part of the reason for this is that T_e derives from the electron current I_e to the probe in the transition region (cf. Eq. [1]), where I_e is equal to the small difference $I_p - I_i$, and at the same time the probe is most sensitive to contamination (cf.

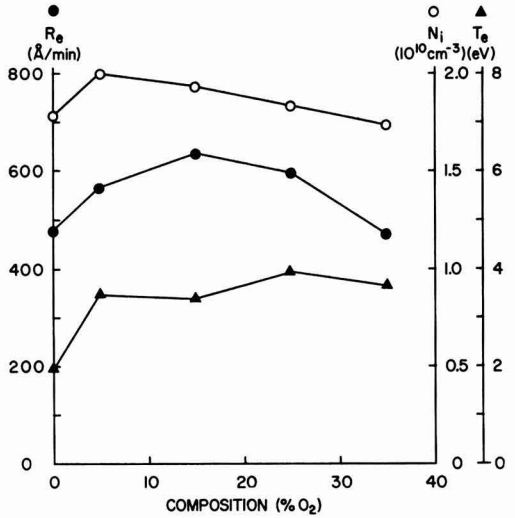

Fig. 11. Reactive sputter etching of SiO_2 in a CF_4-O_2 plasma: plots of etch rate R_e, ion density N_i, and electron temperature T_e vs. gas composition. RF power = 300W, p = 20 mTorr, flow rate = 20 sccm. Probe 4 cm above large cathode.

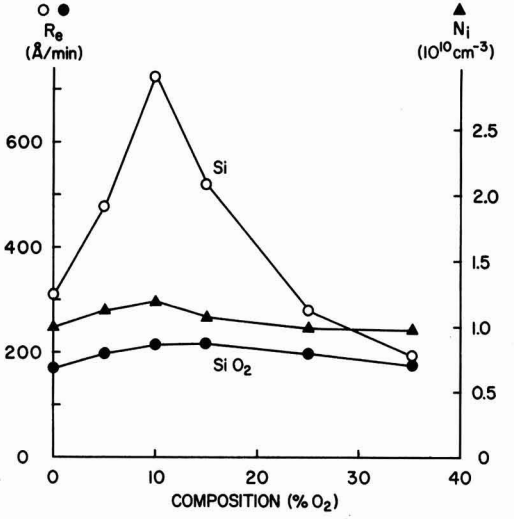

Fig. 12. Reactive sputter etching of SiO_2 and Si in a CF_4-O_2 plasma: plots of etch rates R_e and ion density N_i vs. gas composition. RF power = 100W, p = 20 mTorr, flow rate = 20 sccm. Probe 4 cm above large cathode.

Fig. 1). Nevertheless, log I_e usually is a linear function of V_p over at least a decade (cf. Fig. 3). The least reliable figures are those for the ion energy E_i, the reason being that E_i is largely a function of the induced d-c potential V_{DC} at the cathode, and the value of V_{DC} may vary appreciably on a day-to-day basis, depending on what gases have been used previously for etching, even though presputtering in O_2 is always done at the beginning of a run in order to clean the probe and the system. Furthermore, V_{DC} is measured at the copper cathode, whereas the sample is put on the SiO_2 plate on top of the copper cathode. However, the trends shown in the figures for the various quantities are observed consistently, and are thus believed to be representative of the plasma conditions investigated.

Plasma properties.—Our results show, as expected, that at a given pressure and flow, higher rf power leads to higher ion density N_i for both CHF_3 and CF_4 (Fig. 4 and 8). The highest values measured for N_i, around 1.5×10^{10} cm^{-3} at 300W, correspond to a degree of ionization of about 10^{-4}. Also, a high value for N_i always seems to go with a low value for T_e. This is somewhat contrary to expectations (1, 12), since ions are said to be produced by electrons from the high-energy tail of the distribution, and such electrons will be more numerous at higher T_e. The apparent contradiction may be resolved if one does not think in terms of a certain electron energy distribution giving rise to a certain ion density. Rather, one should see the plasma as maintaining a dynamic balance between electrons and ions, such that N_i, T_e, the sheath potential, as well as the cross sections and mean free paths for ionizing and other (inelastic or elastic) collisions, are all interdependent. Further insight into this contradiction might be gained from computational modeling, as described by Kushner (37).

With regard to the general validity of our analysis, we note that the plasma conditions investigated in our experiments typically range from $N_i = 1.5 \times 10^{10}$ cm^{-3}, $T_e = 2$ eV at high power (300W), to $N_i = 0.5 \times 10^{10}$ cm^{-3}, $T_e = 7$ eV at low power (50W). Thus the Debye length λ_D, Eq. [3], varies between 0.9×10^{-2} cm and 3×10^{-2} cm. and with the radius r_p of the probe wire equal to 0.0125 cm. one has $1.4 \geqq r_p/\lambda_D \geqq 0.4$. This means that the condition for I_i^2 to be proportional to X, $r_p/\lambda_D \lesssim 3$, is well fulfilled in all cases.

For fixed power and flow but variable pressure p, the ion density N_i, the plasma potential V_s, and the ion energy E_i are all fairly independent of p, whereas the electron temperature T_e tends to increase at lower p, particularly for CHF_3 (Fig. 5 and 9). Here again, a complicated interaction of various plasma processes manifests itself, in that a higher p does not necessarily produce a higher N_i (2) but, apparently, at lower p the increased mean free path of electrons, and thus the higher electron energy, compensate for the lower gas density as far as the creation of ions is concerned. It is worth noting that the behavior of T_e *vs.* p parallels the pressure-dependence of the excitation efficiency, as determined from optical emission measurements (5). Also, our values for the plasma potential V_s (~30V) are comparable to those observed in similar experiments at low p (~10 mTorr) (10, 12), but are much lower than values quoted for plasmas at higher p (>100 mTorr) (29).

In all experiments we have observed very little influence of the flow rate, at constant power and pressure, on the plasma parameters N_i, T_e, V_s, within a range of flow rates of 10-25 sccm.

Certain geometrical properties of the plasma can be inferred from the results obtained with different probe positions and different-sized cathodes. With the probe 12 cm away from the cathode, N_i and T_e are consistently lower than with the probe 4 cm from the cathode (Fig. 6). This slight inhomogeneity of the plasma can be explained if one notes that in the far position, the probe is certainly some distance into the negative glow, at which point electrons have undergone several more collisions than at the near position close to the dark space. If one moves the probe closer to the cathode yet, into the dark space, then a decrease of N_i becomes apparent.

The size of the cathode affects the plasma properties in subtle ways which cannot be explained easily. Whereas the plasma potential V_s is quite independent of cathode size, the induced d-c potential V_{DC} is considerably larger at the small cathode. However, the ratio of voltages at the powered and unpowered electrode varies much less strongly than the fourth power of the area ratio of the unpowered and powered electrode (29, 30). Also, with a small cathode, the ion density N_i changes roughly as the pressure p for both

CHF_3 (Fig. 7) and CF_4, but with the larger cathode, N_i is quite independent of p (Fig. 5-7, 9). Furthermore, we have seen evidence for an electron energy distribution corresponding to two different temperatures (~1 eV and ~4 eV) in a CF_4 plasma with the small cathode.

The most interesting features of CF_4-O_2 plasmas are a slight but clear maximum of N_i at around 10% O_2 content and a significant increase in T_e at even lower O_2 concentration (Fig. 11). At 35% O_2 N_i is still as high as in pure CF_4, and T_e is unchanged with respect to its value at 5% O_2 (Fig. 11). Thus, the addition of O_2 to CF_4 neither cools the electron distribution (5, 8), nor does it reduce the electron density if one assumes approximate charge neutrality (6). Furthermore, even at 35% O_2, the character of the plasma is still strongly determined by CF_4, in contrast to what was observed in the afterglow of a 2450 MHz discharge (13). (For a pure O_2 plasma at the conditions of Fig. 12 $N_i = 1.5 \times 10^{10}$ cm^{-3} and $T_e = 1.5$ eV.)

Etching mechanisms.—The importance of ions in many etching processes has, of course, been long recognized. In most instances, however, the evidence was indirect. For example, profiles etched in SiO_2 turned out to mirror the expected distribution of electric field lines in a reactor (31). Etching of Si and SiO_2 was typically faster and more anisotropic with the substrate on the driven, rather than on the grounded electrode (1, 10, 12), and was found also to depend on the coupling between the substrate and the electrode (32).

We believe that the present results establish, for the first time, a direct connection between ions in the plasma and etch rates for the case of SiO_2 etched in a CHF_3 or CF_4 plasma. The connection is simplest for CF_4-O_2 and CF_4-H_2 mixtures where, given no major variation of the relevant potentials, etch rates R_e and ion densities N_i (and thus ion fluxes) change proportionately (Fig. 10 and 12). The changes of R_e with rf power (Fig. 4 and 8) can also be understood via changes in N_i, if one allows for a slight dependence of R_e on the ion energy E_i (cf. also Fig. 7). For variable pressure p, the changes in R_e and N_i tend to be small although with opposite trends (Fig. 5 and 9), but one should keep in mind that varying p changes the spatial characteristics of the plasma (mean free paths, dark space height) so that the probe does not necessarily measure N_i at a uniform position relative to the dark space. As an aside, we note that the power density is not really relevant in characterizing an etching plasma, but the microscopic quantities N_i, T_e, and V_s are. Indeed we find that with the small cathode twice the power density is required to achieve the same R_e as with the large cathode, but conditions of equal R_e are always associated with very similar values for N_i, T_e, and V_s.

Of course, as one varies the composition of the plasma gas or other plasma parameters, additional changes in the plasma chemistry may occur. For example, it is well known (6-9, 11, 13) that adding O_2 to a CF_4 plasma will increase the F atom concentration but decrease the amount of CF and CF_2, whereas in CF_4-H_2 or CHF_3, just the opposite happens. Such changes seem to be of secondary importance, however, in light of the excellent correspondence between ion densities and etch rates of SiO_2.

The role of ions in the etching of Si is somewhat different as becomes evident from Fig. 12. The large increase in the etch rate with about 10% O_2 in CF_4 is not related to the ion density, but rather parallels the well-known increase in the concentration of F atoms (6, 8, 9). This additional etching is also essentially isotropic (9, 28). On the other hand, in pure CF_4 or at large O_2 concentration, the etching of Si has a considerable anisotropic component (9. 28. 32), and that again scales quite well with the ion density.

Since we can determine ion densities, plasma and sheath potentials, we are also able to estimate the ion flux to the substrate if we make a reasonable assumption about the ion velocity distribution at the probe position. Considering two extreme cases, we note that if the probe were sufficiently far away from the dark space, the distribution would be Maxwellian with temperature T_i (near room temperature). If the probe were at the edge of the sheath formed by the dark space, there would be a flux of ions with energy kT_e towards the cathode. Taking then typical conditions of $R_e = 140$Å /min and $N_i = 10^{10}$ cm^{-3} for CF_4 etching SiO_2 (Fig. 8), one finds that the ion fluxes to the substrate for the two velocity distributions are 0.012 mA/cm^2 and 0.29 mA/cm^2. Thus one obtains the following etch rates r_e per incoming ion in reactive sputter etching (RSE), which can be compared to values from ion beam experiments (RIBE)

SiO_2/CF_4	Ion energy (eV)	Etch rate r_e (atoms/ion)
RSE (100W, 20 mTorr)	120	$0.8 \leq r_e \leq 20$
RIBE: Ref. (33)	400	1.4
Ref. (34)	500	3

We note first that in our RSE experiments the probe is probably located near, but not at the dark space edge. Thus, r_e will probably be about 1, *i.e.* comparable to r_e in the RIBE mode. Also the values for r_e in RIBE are larger than expected for physical sputtering, the difference between the two figures probably being accounted for by variations in the ion beam composition, and in the flux of neutrals to the substrate.[4] From the above we conclude that etching of SiO_2, although induced by ions, is somewhat different in the two etching modes. In RIBE, etching results from the impact of ions on a surface whose state is also determined, to a considerable extent, by the ion beam, although neutral species participate significantly in the etching process. In RSE the etch rate per ion is of the same order as in RIBE, in spite of the ion energy being much lower. Because of the difference in pressure, in RSE neutral reactive species are present in abundance, essentially saturating the substrate surface, yet the overall etch rate is still determined largely by the ion flux to the substrate.

We also note the somewhat different selectivity for RSE and RIBE in etching Si over SiO_2 with CF_4. In RIBE the ratio of etch rates is typically 1:6 (33). In RSE, on the other hand, taking into account only the anisotropic (*i.e.* ion-induced) part of Si etching, the ratio of etch rates is about 2:1 (9, 28) (cf. also Fig. 12). For the etch rates r_e per incoming ion one finds

Si/CF_4	Ion energy (eV)	Etch rate r_e (atoms/ion)
RSE (100W, 20 mTorr)	120	$1.2 \leq r_e \leq 30$
RIBE: Ref. (15)	3000	1.5
(33)	1200	1.5
(35)	3000	1.7

Following arguments given above, we conclude that in the RIBE mode the etching of Si by CF_4 (*i.e.* CF_3^+) is mostly due to physical sputtering, whereas in the RSE mode the neutral species are responsible for etching, but etching is strongly ion-enhanced.

Summary

We have presented Langmuir probe measurements on low-pressure etching plasmas of CHF_3, CF_4, CF_4-H_2, and CF_4-O_2. Under conditions typical for reactive sputter etching, we find ion densities between 0.5×10^{10} cm^{-3} and 1.5×10^{10} cm^{-3}, and electron temperatures between 7 eV and 2 eV. We are also able to estimate plasma potentials, which turn out to be fairly low (~30 eV) and quite independent of the experimental conditions, as well as ion energies, which

[4] The ion composition of the beam depends on the ion source operating parameters, and different ions have different reactivities. Also, a dependence of the etch rate on pressure is observed [see Ref. (34)].

are 100-500 eV. For SiO_2 etch rates vary essentially in proportion to ion densities with all the different plasmas. In addition, there is evidence for a dependence of the etch rate on the ion energy. For Si in CF_4-O_2 plasmas of different composition, the anisotropic part of the etch rate also parallels the ion density. From an estimate of the ion flux to the substrate we are able to determine etch rates per ion in reactive sputter etching. These turn out to be comparable to, possibly even larger than, those in reactive ion beam etching, although in reactive sputter etching ion energies are much smaller.

Acknowledgments

I am grateful to H. W. Lehmann for suggesting this study, for useful discussions, and for a critical reading of the manuscript, and to K. Frick for technical assistance. I thank the referees for valuable comments.

Manuscript submitted Aug. 13, 1982; revised manuscript received Oct. 22, 1982. This was 361 RNP presented at the Detroit, Michigan, Meeting of the Society, Oct. 17-21, 1982.

Any discussion of this paper will appear in a Discussion Section to be published in the December 1983 JOURNAL. All discussions for the December 1983 Discussion Section should be submitted by Aug. 1, 1983.

Publication costs of this article were assisted by RCA Laboratories.

REFERENCES

1. L. M. Ephrath, *This Journal*, **129,** 62C (1982); C. J. Mogab, Inst. Phys. Conf. Series No. 53, 37 (1980).
2. J. W. Coburn and H. F. Winters, *J. Vac. Sci. Technol.*, **16,** 391 (1979).
3. J. Dieleman, Proc. Symp. Dry Processing, Tokyo, pp. I-1.1, October 26-27, 1981.
4. S. T. Griffin and J. T. Verdeyen, *IEEE Trans. Electron. Devices*, **ed-27,** 602 (1980).
5. J. W. Coburn and M. Chen, *J. Vac. Sci. Technol.*, **18,** 353 (1981).
6. R. d'Agostino, F. Cramarossa, S. De Benedictis, and G. Ferraro, *J. Appl. Phys.*, **52,** 1259 (1981).
7. M. M. Millard and E. Kay, *This Journal*, **129,** 160 (1982).
8. C. J. Mogab, A. C. Adams, and D. L. Flamm, *J. Appl. Phys.*, **49,** 3796 (1978).
9. M. Bolsen and D. Stephani, in Proc. Microcircuit Engineering 81, A. Oosenbrug, Editor, p. 467, Lausanne (Switzerland), September 28-30, 1981.
10. J. W. Coburn and E. Kay, *IBM J. Res. Develop.*, **23,** 33 (1979).
11. E. A. Truesdale and G. Smolinsky, *J. Appl. Phys.*, **50,** 6594 (1979).
12. M. J. Vasile, *ibid.*, **51,** 2503 and 2510 (1980).
13. C. I. M. Beenakker, J. H. J. van Dommelen, and R. P. J. van de Poll, *J. Appl. Phys.*, **52,** 480 (1981).
14. H. W. Lehmann, E. Heeb, and K. Frick, *Solid State Technol.*, **24,** 69 (1981).
15. J. W. Coburn, H. F. Winters, and T. J. Chuang, *J. Appl. Phys.*, **48,** 3532 (1977).
16. T. J. Chuang, *ibid.*, **51,** 2614 (1980).
17. I. Langmuir, in "Collected Works of Irving Langmuir," G. Suits, Editor, Vol. 4, Macmillan, New York (1961).
18. W. R. Larsen, C. W. Wilmsen, and P. W. Chan, *J. Appl. Phys.*, **44,** 2153 (1973).
19. H. Norstrom, R. Olaison, S. Berg, and L. P. Andersson, *This Journal*, **127,** 2680 (1980).
20. D. J. Ball, *J. Appl. Phys.*, **43,** 3047 (1972).
21. E. Eser, R. E. Ogilvie, and K. H. Taylor, *Thin Solid Films*, **68,** 381 (1980).
22. N. J. Ianno, K. E. Greenberg, and J. T. Verdeyen, *This Journal*, **128,** 2174 (1981).
23. F. F. Chen, in "Plasma Diagnostic Techniques," R. H. Huddlestone and S. L. Leonard, Editors, Chap. 4, Academic Press, New York (1965).
24. R. M. Clements, *J. Vac. Sci. Technol.*, **15,** 193 (1978).
25. J. G. Laframboise, Univ. of Toronto Inst. Aerospace Studies Rept. No. 100 (1966). (See also *Adv. Appl. Mech. Suppl.*, **3,** Vol. II, 1966).
26. S. G. Lias, J. R. Eyler, and P. Ausloos, *Int. J. Mass Spectrom. Ion Phys.*, **19,** 219 (1976).
27. L. M. Ephrath, *This Journal*, **126,** 1419 (1979).
28. J. Paraszczak and M. Hatzakis, *J. Vac. Sci. Technol.*, **19,** 1412 (1981).
29. J. L. Vossen, *This Journal*, **126,** 319 (1979).
30. H. R. Koenig and L. I. Maissel, *IBM J. Res. Develop.*, **14,** 276 (1970).
31. H. W. Lehmann and R. Widmer, *J. Vac. Sci. Technol.*, **15,** 319 (1978).
32. G. C. Schwartz, L. B. Rothman, and T. J. Schopen, *This Journal*, **126,** 464 (1979).
33. B. A. Heath, *ibid.*, **129,** 396 (1982).
34. T. M. Mayer and R. A. Barker, *ibid.*, **129,** 585 (1982).
35. S. Tachi, K. Mizake, and T. Tokuyama, Proc. Symp. Dry Processing, pp. I-3, 17, Tokyo, October 26-27, 1981.
36. N. Hosokawa, R. Matsuzaki, and T. Asamaki, *Jpn. J. Appl. Phys. Suppl.*, **2,** Pt. 1, 435 (1974).
37. M. J. Kushner, *J. Appl. Phys.*, **53,** 2923 and 2939 (1982).

A Laser Interferometer System to Monitor Dry Etching of Patterned Silicon

M. Sternheim and W. van Gelder*

Bell Laboratories, Murray Hill, New Jersey 07974 and Allentown, Pennsylvania 18103

and A. W. Hartman

National Bureau of Standards, Washington D.C. 20234

ABSTRACT

A laser interferometer system to monitor plasma etch rate, and to control etched depth of isolation areas in silicon for oxide isolated bipolar devices, is reported. The etching process is stopped as soon as the desired etched depth is achieved. The accuracy of the system is 4-6%, depending on the masking material. It is found that this method of laser interferometry can be particularly useful in process development for observations in real time of changes in etch rate.

Laser interferometers have been used in integrated circuit processing to monitor the etch rates of dielectric films in plasma etch processes (1, 2, 3). In particular the detection of the completion of the process, the so called end-point detection, is of high interest. This is because during an overetch period, undercutting may

* Electrochemical Society Active Member.
Key words: semiconductor, lasers, interferometry, etching.

occur as well as mask erosion, each causing undesirable loss of linewidth control. Also, etching through an underlying layer may occur as a result of poor selectivity between the etched film and the underlying layer.

In some processes, such as the planarization of phosphorous doped SiO_2 (4), and the etching of grooves or tubs in a silicon substrate, the etched material is not etched to completion. In these types of processes other methods of end-point detection, such as optical emission (5), mass spectroscopy (6), plasma impedance, and reactor pressure (7) cannot be used. But a laser interferometer can be used in these cases because it has the advantage of measuring the actual etched depth in real time.

In this paper we report the application of a laser interferometer system in monitoring the depth of plasma etched areas in a silicon substrate. The plasma etched regions are of the order of one micron deep, and are used as oxide isolation areas in "OXIL" bipolar device processing. The system monitors the etch rate by indicating at each moment in time how much "depth" has been etched. The plasma etching is stopped as soon as the required depth is reached.

Equipment and Experimental Setup

An interferometer that measures the distance between the etched surface and the unetched surface of a silicon wafer was chosen as the system to monitor the etched depth. A linearly polarized, 2 mW He-Ne laser was used as a light source with wavelength $\lambda = 6328$Å. (Shorter wavelength laser light sources would be desirable for higher fringe resolution, but are not as conveniently available.)

At first we built a two beam interferometer into a parallel-plate silicon plasma etcher. The principal of operation is shown in Fig. 1. This system is a simplified version of a double beam, double pass, step height polarization interferometer with one nanometer resolution, designed and built by Hartman (8). The laser light is split into two parallel beams (2 mm apart) by a beam splitter. The two beams pass through an optical window W in the top electrode and are then reflected from each side of a growing step in silicon. The reflected beams are brought together by the same beam splitter with a small offset, so that the reflected light can be collected by prism P and directed towards photocell F. The output of the photocell shows the normal interference response as a function of the growing step height d. With this system we have done real-time step height measurements in silicon using aluminum as a mask. The etching conditions were: pressure 0.4 Torr; power 1.5 kW 13.6 MHz, flow rate 100 ml/min CF_3Cl, electrode spacing 1 in., 22 in. diam, parallel plate plasma etching machine with a hole in the top electrode to admit the laser light. A typical fringe response curve is shown in Fig. 2. The agreement between the step height calculated from the interference fringes and the step height obtained by an "alpha" step profilometer was typically better than 2%.

But this system had some serious drawbacks. It requires large areas, approximately 2 × 2 mm, next to each other to reflect the two laser beams. Each laser beam is ~1 mm in diam and both beams have to be accurately positioned, so that one beam reflects from the masked (unetched) area and the other beam reflects from the unmasked (etched) area. This turned out to be a cumbersome and tedious procedure, which can be avoided by using a single beam system in which one beam is reflected from a closely spaced repeated number of steps in the silicon. This is basically reflection from a relief diffraction grating, where we only consider the central image reflection (or zero order diffraction). This single beam laser interferometer is similar to those described in (1) and (3), and was mounted on a parallel plate plasma reactor as well as in a reactive sputter etch (RSE) reactor. The principle of operation is shown in Fig. 3. A 2 mW linearly polarized He-Ne laser emits light into a polarizing beam splitter. With the polarization plane adjusted as shown almost all the light is reflected to the left. It passes a quarter wave retardation plate and an optional beam expander BE. The grating type sample is located in the plasma region behind an optical window. The reflected light is split into various diffraction angles, but we only collect the zero order reflected light. At 0° angle of incidence, the light passes back onto itself through the quarter wave plate. The plane of polarization is turned 90° as a result of double passage

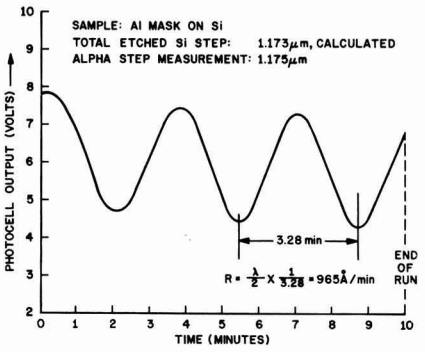

Fig. 2. Typical response curve with double beam interferometer

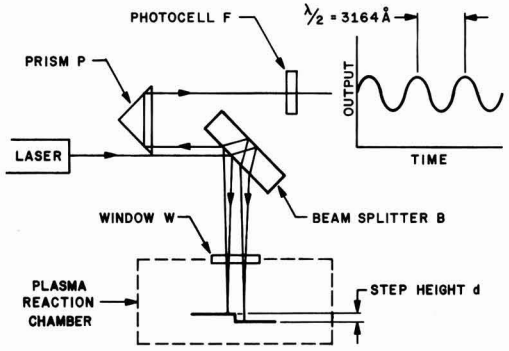

Fig. 1. Double beam laser step height interferometer

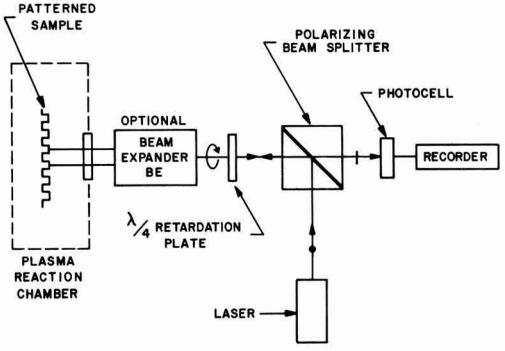

Fig. 3. Single beam grating step height interferometer

through the $\lambda/4$ plate, and the beam passes through the polarizing beam splitter into a photocell. The output of the photocell is recorded as a function of time. It appears that most integrated circuit patterns form a a grating during etching so that no extra test patterns are needed. For perpendicular illumination (0° angle of incidence), whenever the groove depth d satisfies the relation, $2d = \lambda/2, 3\lambda/2, 5\lambda/2, \ldots$, the reflected intensity of the central diffraction image will be at a minimum. On the other hand, when $2d = 0, \lambda, 2\lambda, \ldots$, the reflected light is at a maximum. During the etching process, the depth of the Si trenches increases and the light intensity in the zero order of the diffraction pattern changes periodically. In an ideal case where the etch mask itself has zero etch rate, the voltage output of the photocell will be sinusoidal. This happens when aluminum is used as a mask. In most practical cases, a dielectric film and/or a photoresist film is used as a masking material, which has itself a measurable etch rate. The output voltage of the detector in these cases is periodical but not purely sinusoidal. The period of the voltage waveform corresponds to a change of $d = \lambda/2$ in the depth of the etched trenches. A detailed treatment of a grating test pattern is given by Kleinknecht and Meier (3).

In order to make the system compatible with automatic process control, the voltage output signal $v(t)$ has to be processed. The signal must be smoothed and the time derivative calculated using a desk top computer. The zero crossings of the time derivative of the voltage function $v'(t)$ corresponds to the maxima and minima of the light intensity in the zero order of the diffraction pattern. The etched depth between two zero crossings of $v'(t)$ corresponds to $\lambda/4 = 1582$Å, and the average etch rate for a particular period can be calculated, knowing the period of $v'(t)$. The averaged etch rate per period can be integrated to calculate the total etched depth, and the process can be stopped when the preset depth is reached.

Experimental Results

The samples were silicon wafers patterned using 7000Å Al as a mask for experiments in a parallel plate plasma reactor, and using 4000Å SiO_2 as a mask for experiments in Reactive Sputter Etching (RSE) and other plasma reactors. The etched depth calculated from the etch rate was compared to Talystep or alphastep measurements. The etched area was reduced below 25% of the total area, without affecting the signal to noise ratio or the accuracy of determined depth. Figure 4 demonstrates the method for an Al mask on single crystal silicon in a plasma process. The etch conditions used were 100 ml/min CF_3Cl at 0.4 Torr and 1.5 kW; the average silicon etch rate was 1000 Å/min, and the aluminum was not etched. It is apparent from the voltage waveform that the optical properties of the surfaces are nearly constant during the process. The accuracy of the method in determining the etch rate is better than 4%. Figure 5 shows the results for an SiO_2 mask over silicon. The selectivity of the silicon etch rate over the SiO_2 etch rate was deliberately reduced to 5:1, and the accuracy was still better than 6%. The changes in the amplitude of the voltage signal correspond to beats because of the relative etch rates of the dielectric film and the silicon.

For an alignment free system a beam expander is used. An $\times 8$ expansion covers a full chip. There is no effect on the signal to noise ratio, or on the accuracy of the results when an expanded beam is used instead of the original beam size.

It was observed that when the selectivity of mask to substrate is further reduced to values approaching 1:1, the accuracy decreases fast and the method reaches its limit of usefulness.

Conclusions

A simple interferometric method to monitor the etch rate of patterned silicon layers was developed, to control the etched depth of isolation areas for bipolar technology. The accuracy of the method is better than 6%, even if the selectivity of silicon over the masking material is as low as 5:1. When the selectivity approaches a value as low as 1:1, the accuracy decreases

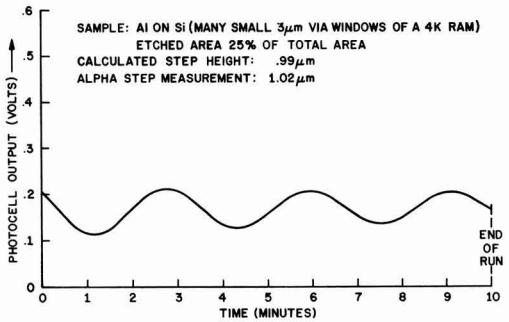

Fig. 4. Response from single beam grating interferometer

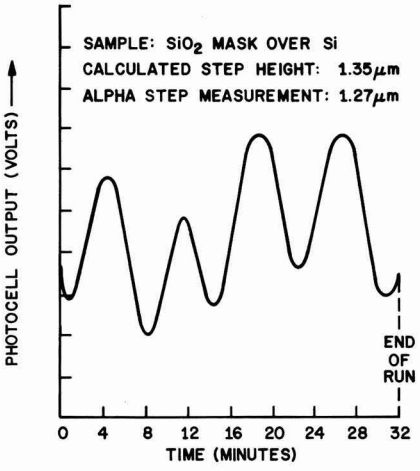

Fig. 5. Response from single beam grating interferometer

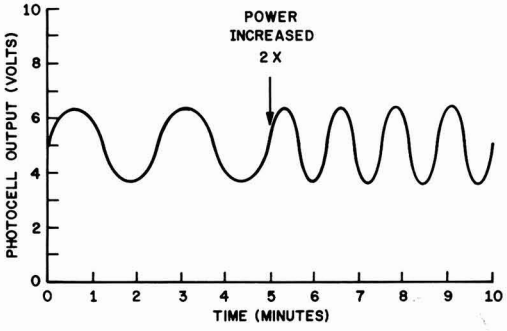

Fig. 6. Response curve showing real time result of power increase: etch rate increased ~2×.

and the method reaches its limit of usefulness. An accuracy of better than 4% is achieved for an infinite selectivity with the use of aluminum as a mask.

It was found that this method of laser interferometry can be particularly useful in process development. For instance, it can be observed in real time how etch rates change *in situ*, while process parameters such as pressure, power, and flow rate are changed (*e.g.*, Fig. 6).

The method is compatible with an automatic process control system. It can also be used to monitor the etch rates of patterned metals like Al. In order for the method to be reasonably accurate, the total etched depth has to be more than $\lambda/2$, where λ = laser wavelength. It should be noted that the interferometer system described herein is readily usable for the more conventional end-point detection of dielectric layers, where an optical grating is not needed (1, 2, 3, 9).

Acknowledgments

We would like to thank H. J. Levinstein, D. A. McGillis, and E. F. Labuda for their encouragement, M. Feldman, A. White, and S. D. Steenwyk for their helpful discussions, and A. C. Adams for correcting the manuscript.

Manuscript received June 1, 1982. This was Paper 294 presented at the Denver, Colorado, Meeting of the Society, Oct. 11-16, 1981.

Any discussion of this paper will appear in a Discussion Section to be published in the December 1983 JOURNAL. All discussions for the December 1983 Discussion Section should be submitted by Aug. 1, 1983.

Publication costs of this article were assisted by Bell Laboratories.

REFERENCES

1. J. A. Bondar, W. R. Case, and H. A. Clark, Abstract 303, p. 760, The Electrochemical Society Extended Abstracts, Seattle, Washington, May 21-26, 1978.
2. H. H. Busta, R. E. Lajos, and D. A. Kiewit, *Solid State Technol.*, **22**, 61 (1979).
3. H. P. Kleinknecht and H. Meier, *This Journal*, **125**, 798 (1978).
4. A. C. Adams, *ibid.*, **128**, 423 (1981).
5. R. G. Poulsen and G. M. Smith, in "Semiconductor Silicon 1977," H. R. Huff and E. Sirtl, Editors, p. 1058, The Electrochemical Society Softbound Proceedings Series, Princeton, NJ (1977).
6. G. B. Bunyard and B. A. Ruby, *Solid State Technol.*, **20**, 53 (1977).
7. M. L. Hitchman and V. Eichenberger, *J. Vac. Sci. Technol.*, **17**, 1378 (1980).
8. A. W. Hartman, *Opt. Eng.*, **15**, 180 (1976).
9. P. J. Marcoux and Pang Dow Foo, *Solid State Technol.*, **24**, 115 (1981).

Control of Silicon Dioxide Properties by RF Sputtering

M. K. Lee,* C. Y. Chang,* J. S. Tzeng, and Y. K. Su

Research Institute of Electronics and Electrical Engineering, National Cheng Kung University, Tainan, Taiwan, China

ABSTRACT

We have examined the effect of simultaneously sputtered Teflon on the properties of sputtered silicon dioxide films. C-V measurements show that positive ions in sputtered silicon dioxide can be compensated. It also shows that the compensation effect can be controlled by the negative voltage of bias sputtering during deposition.

Silicon dioxide films are extensively used in semiconductor device technology. They perform many functions such as surface passivation, impurity masking, active device dielectric, etc. SiO_2 films deposited by sputtering have many advantages over thermally grown films; for example, the former can be prepared at relatively low temperature. However, the resulting films show instability due to ionic contamination. Positive charges degrade SiO_2 films. The reduction of positive charges is an important factor in determining the quality of semiconductor devices. In this report, the effect of fluorine ions (1) sputtered into SiO_2 films to compensate positive charges was studied.

Experimental

An MRC SEM-8620 sputtering system was used for the deposition of SiO_2 films. It has a 1½ kW rf power generator, and provides the user with all rf sputtering functions, sputter-etching, and rf bias sputtering The space between target and substrate holder was adjusted to 5 cm in the experiments. The target, IC grade SiO_2, 6 in. in diam and 3/16 in. in thickness, was also supplied by MRC. It is water cooled via a cathode plate. The vacuum system consisted of an oil diffusion pump and a rotary pump. In an MRC 8620 sputtering system, the cathode head is insulated from its mounts by Pyrex glass. In a typical run, however, the Pyrex glass was substituted by Teflon ($CF_2 = CF_2$) in our experiments for comparison. High purity (5*N*) argon, purified by the inert gas purifier and filtered through millipore gas line filter (0.25 μm pore size), was fed into the chamber during deposition.

The silicon wafers are n-type <111> oriented, and have resistivities of 3-5 Ω-cm. Before being loaded onto the substrate holder, the silicon wafers were cleaned sequentially in TCE, ACE, H_2SO_4:H_2O_2 = 3:1, HF:H_2O = 1:10, then rinsed in deionized water.

The copper plating technique (2) was used for the pinhole test. MIS structure was adopted for the study of electrical properties of SiO_2 film. An aluminum (99.9%) electrode was evaporated over the oxide film through a metal mask. The thickness and area of Al films were 3000Å and 0.01 cm^2, respectively. For measurement of the breakdown strength, the polarity of Al electrode is positive. Capacitance was measured at 10 kHz with SANWA Type M1-316B capacitance meter.

Results and Discussion

In order to study the effects of Teflon simultaneously sputtered on the properties of SiO_2 film, three different sputtering processes were tried and compared. In process I, Teflon was used as insulator of the electrode. The initial pressure of the system was pumped down to less than 4×10^{-6} Torr. Prior to deposition, the target was presputtered under argon pressure of 5×10^{-3} Torr, then pumped down again to 4×10^{-6} Torr. The argon pressure was kept at 5×10^{-3} Torr during sputtering. The sputtering power was 300W.

In process II, Pyrex glass was used as insulator of the electrode. The substrates were sputter-etched at 400W under argon pressure of 3×10^{-3} Torr for about 1 μm. To minimize radiation damage, the rf power was de-

* Electrochemical Society Active Member.
Key words: sputtering, SiO_2, fluorine, doping.

Table I. Properties of sputtered SiO_2 films of three processes

Table I. Properties of films of three processes.

	Pinhole density ($1/cm^2$)	P etch rate (A/min.)	breakdown strength (V/cm)
Process I	26	132	3×10^6
Process II	18	140	7.5×10^6
Process III	12	128	1×10^7

creased toward the end in steps of 6 min at 50, 40, 15, and 10W (3). The other conditions were the same as that of process I.

In process III, bias sputtering was used. The Si substrate was negatively biased with bias voltage (4) of −40V for Teflon as insulator of electrode. The other conditions were the same as that of process II.

The quality of the SiO_2 films prepared from above three processes was examined by pinhole test, P etch rate (5), and breakdown strength. The results are summarized in Table I. Obviously, process III gives the best quality in all three measurements. The breakdown strength obtained is higher than those of previous reports. This may be due to the effect of F^- ion from the Teflon.

The C-V curves of MIS samples obtained from the above three processes are shown in Fig. 1. For Fig. 1b, Pyrex glass was used as insulator; the C-V curve is like that of a thermally oxidized one. The imbedded

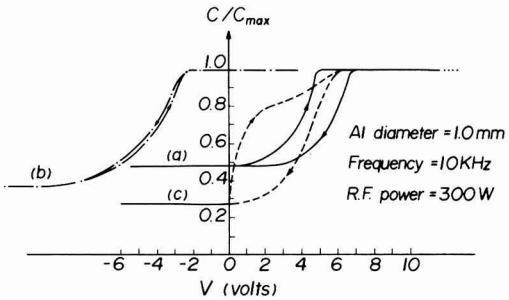

Fig. 1. (a) C-V curve for Teflon as insulator of electrode. SiO_2 film thickness is 1500Å. (b) C-V curve for Pyrex glass as insulator of electrode. SiO_2 film thickness is 1500Å. (c) C-V curve with bias voltage −40V for Teflon as insulator of electrode. SiO_2 film thickness is 1200Å.

charges are positive as usually reported (6). When Pyrex glass was substituted by Teflon, the C-V curve shifted toward the right as shown in Fig. 1a. It appears that negative charges are imbedded in the sputtered SiO_2 film, contrary to process II. It can be presumed that the negative charges were related to the Teflon. The negative charges might come from the F^- ions of Teflon, and the trapped F^- ions could compensate the effect of positive charges. If the Si substrate is negatively biased during bias sputtering, the negative bias voltage would retard the trapping of the negative charges. Figure 1c shows that the C-V curve shifted toward left with −40V bias voltage during bias sputtering. That is to say, the concentration of negative charges in SiO_2 film could be decreased by the negative bias voltage of the Si substrate during bias sputtering. This phenomenon could also prove the fact that the trapped charges are negatively charged. As to the sense of the hysteresis, Fig. 1a, c indicate charge exchange across the silicon dioxide-silicon interface. That is opposite to the sense of Fig. 1b. This phenomenon is usually referred to as Si injection (7). It could be associated with the trapped negative charges.

Conclusion

We conclude that if Teflon is simultaneously sputtered with the SiO_2 target, it can reduce positive charges in MOS device. The compensation effect could be related with the F^- ions.

Manuscript submitted April 4, 1981; revised manuscript received Nov. 2, 1982.

Any discussion of this paper will appear in a Discussion Section to be published in the December 1983 JOURNAL. All discussions for the December 1983 Discussion Section should be submitted by Aug. 1, 1983.

Publication costs of this article were assisted by Cheng Kung University.

REFERENCES

1. M. K. Lee, C. Y. Chang, and J. S. Tzeng, Paper 614 presented at The Electrochemical Society Meeting, Los Angeles, California, October 14-19, 1979.
2. W. J. Shannon, *RCA Rev.*, **31**, 431 (1970).
3. H. U. Schreiber and E. Fröschle, *This Journal*, **123**, 30 (1976).
4. J. S. Logan, *IBM J. Res. Develop.*, **14**, 172 (1970).
5. W. A. Pliskin and R. P. Gnall, *This Journal*, **111**, 872 (1964).
6. J. S. Logan, F. S. Maddocks, and P. D. Davidse, *IBM J. Res. Develop.*, **14**, 182 (1970).
7. S. M. Hu, D. R. Kerr, and L. V. Gregor, *Appl. Phys. Lett.*, **10**, 97 (1967).

Island Stage of InP Anodization

W. H. Makky and C. W. Wilmsen

Department of Electrical Engineering, Colorado State University, Fort Collins, Colorado 80523

ABSTRACT

The island growth of anodic oxides on InP has been studied with transmission electron microscopy. The islands appear smooth for all growth conditions tested in contrast to the rough edge anodic oxide islands of GaAs. Changing the pH, electrolyte, or illumination did not significantly change the island shape. The islands were often observed to form in closely spaced rows indicating a heterogeneous nucleation. Coalescence appeared to be caused by a rapid growth in the regions between the touching islands.

Recently we reported on a transmission electron microscope (TEM) study of the island growth of anodic oxides on GaAs (1). It was found that the islands on GaAs varied in size, had very rough and pitted edges, and had a distinct boundary between coalescing islands until the neck region was completely filled in. In this paper we briefly report on a similar TEM study of the anodic oxide islands of InP.

The growth and properties of anodic oxides on InP have been investigated by numerous authors (2-9)

who have reported the chemical composition, growth characteristics, and electrical properties of the oxides. The oxides appear to be a mixture of In_2O_3 and P_2O_5, with the ratio being dependent upon the electrolyte and electrolyte *p*H (6, 7). Based on the voltage *vs.* time curve during anodization it was previously suggested (5) that the oxide growth was initiated by a nucleation and island growth stage as is the case for the anodization of GaAs.

The present paper shows that the islands on InP differ from those on GaAs and that the island characteristics did not change for electrolyte *p*H equal to 2.7 and 7.0, the amount of illumination, the electrolyte, and rinsing with water or methanol.

Experimental Technique

The InP wafers were (100) undoped, n-type with carrier density of 4×10^{16} cm^{-3} from Crystal Communications, Incorporated. The samples were etched in 10% HCl for 10 min, rinsed with deionized (DI) water, and then blown dry with N_2. The surface was chemomechanically polished using 1% Br/methanol and a Pellon Pan-W polishing pad, rinsed thoroughly with methanol, then rinsed with acetone to remove the

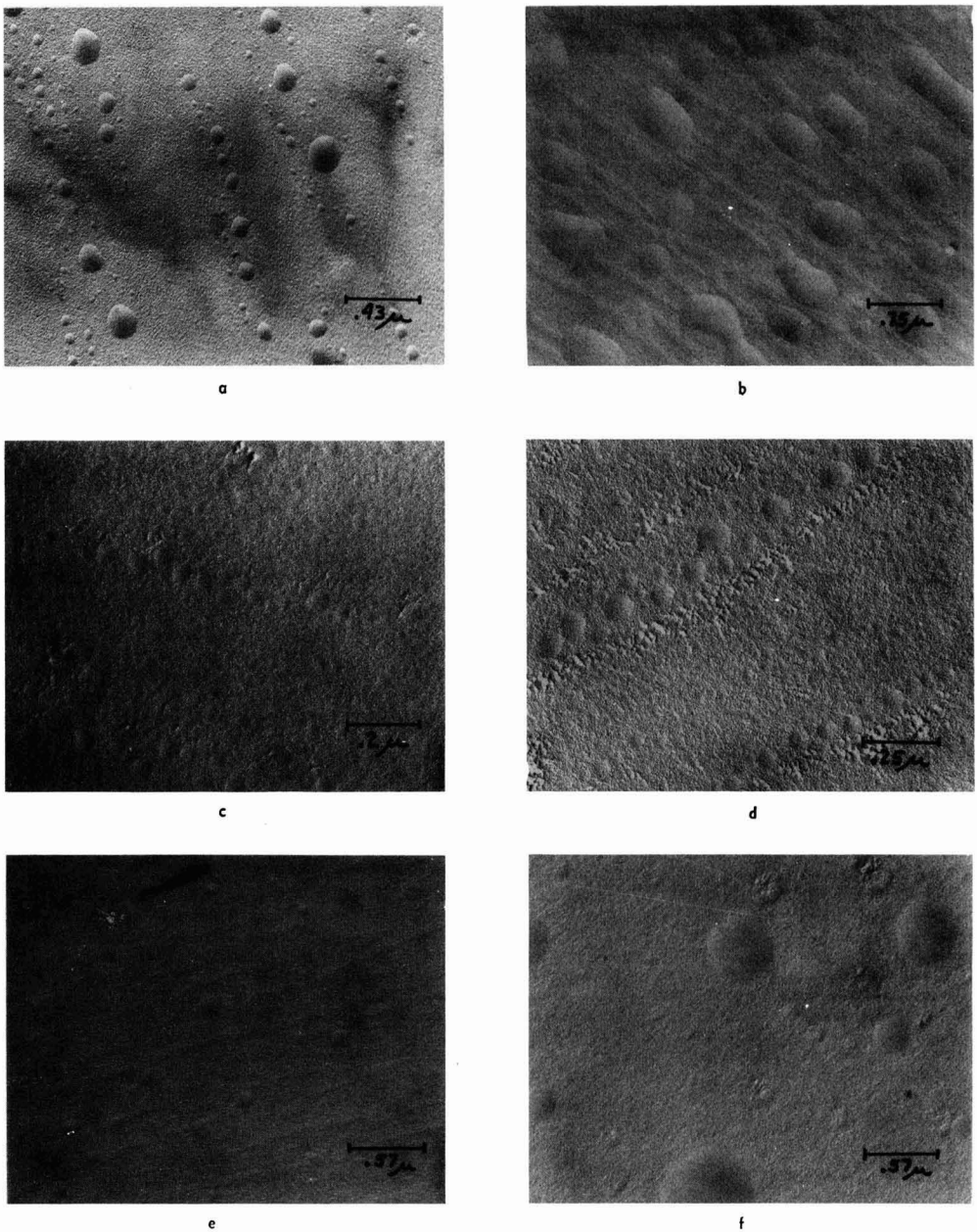

Fig. 1. Anodic oxide islands on InP formed with different growth conditions; (a) dipping in a tartaric acid electrolyte at a *p*H = 7, (b) growth in tartaric acid, *p*H = 7 with a strong light, (c) growth in phosphoric acid, *p*H = 2.7 with strong light, (d) same as (b) except in the dark, (e) same as (c) except in the dark, and (f) same as (b) except rinsed with methanol.

Crystal Bond, and blown dry with N_2. The surfaces of the bare substrates were replicated using a 4% collodion solution in amyl acetate. The collodion was left to dry at room temperature. The collodion replicas were then removed with the help of DI water vapor. The samples were then anodized with a constant current density of approximately 0.2 mA/cm^2. The anodization process was stopped before the passivation time was over, *i.e.*, somewhere during the "flat" portion of the voltage-*vs.*-time curve. Some samples were anodized in the dark while the others were anodized under a strong light. Electrolytes of a 3% phosphoric acid solution (pH = 2.7) mixed 1:1 with propylene glycol, and a 3% tartaric acid solution (pH = 7) mixed 1:6 with propylene glycol were used. The effect of rinsing the samples with methanol and DI water for a few seconds after anodization was examined. The surfaces of the anodized samples were replicated in the same way as discussed above.

The collodion replicas were then shadowed with Pt at an angle of 25° and coated with 200Å of carbon using a "Balzers 301 Evaporator." To eliminate possible variations in the shape of the TEM pictures of the sample before and after anodization due to the shadowing process, the collodion replicas of each sample before and after anodization were shadowed together. The Pt-C secondary replicas were obtained by placing the shadowed collodion replicas on SPI (400 mesh-3 mm) Cu TEM specimen grids and then digesting the collodion with amyl acetate.

Results

Nucleation and island growth.—The six photomicrographs of Fig. 1 illustrate the primary island structure of anodic oxides on InP. While the samples for Fig. 1 were prepared in different ways, each one has the same smooth, round islands which we believe to be the basic island shape. The smooth edged islands of the InP oxide are much different than the ragged and pitted edges of GaAs anodic oxide island shown in Fig. 2 and discussed in detail in a previous publication (1). The InP islands often (but not always) form rows $\approx$ 0.2-0.6μ apart. The lining up of the islands imply that there are lines of preferred nucleation sites which could be the result of mechanical damage due to sawing or polishing, steps on the surface, or doping striations. Saw damage is expected to be much more widely spaced and much larger in extent. Polishing scratches should have more random directions. Both sawing and polishing damage should be removed by deep polishing but this did not appear to be possible with these samples. Doping striations should not appear in low doped material such as was used in this investigation. Thus, surface steps appear to be the most likely cause of lines of preferred nucleation.

The islands shown in Fig. 1a were formed by dipping the InP in the electrolyte for 10 min without connecting any leads. The fact that the islands formed means that the contact potential between the InP and the electrolyte was sufficient to initiate the nucleation and growth process as we previously suggested for GaAs (5). There is a distribution of island sizes which suggests that the nucleation process occurs over a period of time. However, the islands' size of the other photomicrographs have a much smaller spread and most of the islands are approximately the same size on a given sample. This is different from GaAs anodic islands and may in part be due to the preferred nucleation sites on InP. The smallest island found on the sample of Fig. 1a had a diameter of $\approx$250Å and the largest was $\approx$5000Å.

The islands of Fig. 1b and c were grown under strong illumination while those of Fig. 1d and e were grown in the dark. The same basic island shape is observed for all growth conditions. The rough background (probably an oxide) seen in Fig. 1c cannot be attributed solely to the state of illumination since identical results were obtained with growth under strong light, Fig. 1d. We believe that the rough background seen in Fig. 1c and d is caused by a rough native oxide which sometimes grows on the InP and has occasionally been observed during the course of our work on thin plasma (10, 11), thermal (11), and anodic (12) oxides of InP, but the cause is not presently known.

The sample for Fig. 1f was grown under strong illumination and was rinsed with methanol instead of water as were the samples for Fig. 1a-e. It is seen that methanol rinsing produces the same type of smooth island as does a water rinse. The islands shown in Fig. 1f are randomly distributed and are all approximately the same size. The smaller dimpled "islands" seen in between the smooth islands were also observed with other growth conditions.

The approximate height of the islands was estimated by measurement of the shadow length and knowing the angle at which the samples were shadowed. The shadows on the InP replicas were not as distinct as those on GaAs (1), which reduces the accuracy of the measurement and prevents estimation of shadow length of the smaller islands. For the larger islands this method yields a height of $\approx$200Å, which is similar to that obtained on GaAs (1).

Coalescence.—Some coalescence is seen in the islands of Fig. 1b in which islands in the same line form elongated islands. Similar coalescence is seen in the islands of Fig. 3. The coalesced islands are all smooth with no distinct boundary between them, as is the case with GaAs (1). However, as with GaAs, the islands appear stationary with the neck regions filling in by a fast growth process due to electric field enhancement

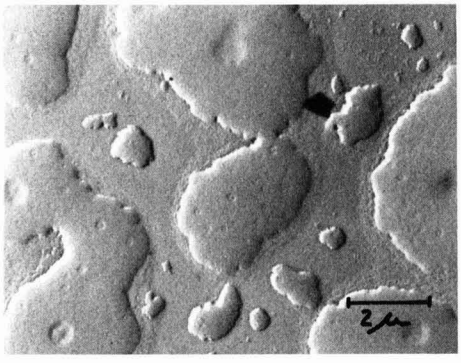

Fig. 2. Anodic oxide islands on GaAs grown in tartaric acid, pH = 7 with strong light.

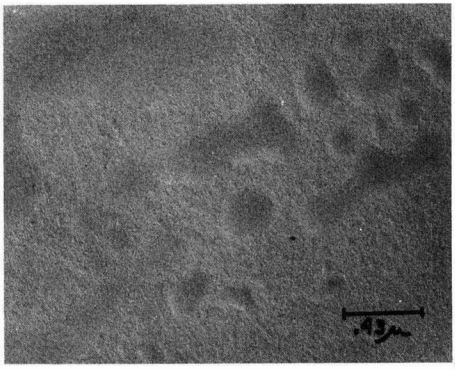

Fig. 3. Anodic oxide islands on InP showing coalescence. Growth in tartaric acid, pH = 7 in the dark.

in these regions. The elongated and irregular island shapes argue against a liquid-like coalescence due to surface migration of molecules as discussed previously for GaAs (1).

Summary

The TEM micrographs show that the anodic oxidation of InP is initiated by nucleation and island growth. In contrast to GaAs, the islands on InP are smooth without rough edges. However the islands on InP are approximately the same height and area as those observed on GaAs. The same basic island shape of the InP islands was observed for all growth conditions tested. Some variation from run to run was observed but this was not consistent and could not be attributed to the electrolyte, electrolyte pH, or intensity of illumination. It is believed that the observed variations were due to the quality of the substrate polish and not the changes in the growth conditions. On many of the samples, the islands were in rows separated by ≈ 0.2-0.6μ. These are thought to be due to surface steps which cause a heterogeneous nucleation.

The coalescence of the islands appeared to be caused by rapid growth in the neck region between the two touching islands similar to that observed for GaAs.

Acknowledgments

We wish to thank Kent Geib for his help with sample preparation and Dr. Morita for his assistance with the electron microscope. This work was supported by ARO.

Manuscript submitted June 15, 1982.

Any discussion of this paper will appear in a Discussion Section to be published in the December 1983 JOURNAL. All discussions for the December 1983 Discussion Section should be submitted by Aug. 1, 1983.

Publication costs of this article were assisted by the Colorado State University.

REFERENCES

1. W. H. Makky, F. Cabrera, K. M. Geib, and C. W. Wilmsen, *J. Vac. Sci Technol.*, **20**, 417 (1982).
2. D. L. Lile and D. A. Collins, *Appl. Phys. Lett.*, **28**, 554 (1976).
3. C. W. Wilmsen and R. W. Kee, *J. Vac. Sci. Technol.*, **14**, 953 (1977).
4. K. P. Pande and G. G. Roberts, *ibid.*, **16**, 1470 (1979).
5. K. M. Geib and C. W. Wilmsen, *ibid.*, **17**, 952 (1980).
6. D. H. Laughlin and C. W. Wilmsen, *Appl. Phys. Lett.*, **37**, 915 (1980).
7. D. A. Baglee, D. H. Laughlin, C. W. Wilmsen, and D. K. Ferry, "The Physics of MOS Insulators," G. Luscovsky, S. T. Pantelides, and F. L. Galeener, Editors, Pergamon, New York (1980).
8. A. A. Studna and G. J. Gualitieri, *Appl. Phys. Lett.*, **39**, 965 (1981).
9. A. Yamamoto and C. Uemura, *Electron. Lett.*, **18**, 63 (1982).
10. J. F. Wager, W. H. Makky, and C. W. Wilmsen, *Thin Solid Films*, **95**, 343 (1982).
11. J. F. Wager and C. W. Wilmsen, *J. Appl. Phys.*, To be published.
12. W. H. Makky, Unpublished.

The A-C Conductivity of Polycrystalline LISICON, $Li_{2+2x}Zn_{1-x}GeO_4$, and a Model for Intergranular Constriction Resistances

P. G. Bruce[1] and A. R. West

University of Aberdeen, Department of Chemistry, Meston Walk, Old Aberdeen AB9 2UE, Scotland

ABSTRACT

The a-c conductivity of a polycrystalline, Li^+ ion conducting solid electrolyte, LISICON, $Li_{2+2x}Zn_{1-x}GeO_4$, has been measured over the frequency range 10^{-3}-10^7 Hz and attention focused on the methods of data analysis. The data show intragranular (bulk) and grain boundary effects in which, for a given sample, both effects are characterized by a similar activation energy; a constriction resistance model for the latter is proposed based on air gaps existing in polycrystalline sinters of less than theoretical density. The data only crudely fit a Debye-like equivalent circuit, composed of frequency independent resistors and capacitors, but fit well an equivalent circuit that contains Jonscher elements, *i.e.*, frequency dependent admittances, in addition to normal R and C elements. Two such Jonscher elements are needed, one for the grain boundary and one for the intragranular contribution. With this circuit, departures from ideality in, *e.g.*, the complex impedance, admittance, and electric modulus planes are accounted for.

The a-c conductivity of solid electrolytes is generally analyzed in terms of equivalent circuits composed of frequency independent resistors and capacitors. Very often, however, the a-c response does not correspond to that predicted by simple, ideal circuits; for instance, semicircles in the complex impedance Z^* plane are often broadened and distorted into asymmetric arcs. Various attempts have been made to deal with this problem: empirical functions based on the Cole-Cole (1-3) or Cole-Davidson (4) expressions have been used to fit the experimental results; a distribution of hopping processes leading to a distribution of relaxation times has also been postulated (5). Such nonideal response is only observed in electrolytes with a high concentration of charge carriers. These are just the systems in which cooperative interactions are manifest.

[1] Present address: Department of Inorganic Chemistry, University of Oxford, Oxford OX1 3QR, England.

A recent approach which is gaining increasing acceptance is based on Jonscher's "universal law of dielectric response" (6, 7), which, unlike the above approaches, can be derived from theories of cooperative migration (8-11). When this theory is applied to a-c conductivity, frequency dependent elements must be introduced into the equivalent circuit. This approach, utilizing one frequency dependent element, has been used by Jonscher (7, 12), Huggins and others (13-15) to model the a-c response of polycrystalline materials. We have shown (16) that the bulk a-c response of single crystal β-alumina can be treated in the same way, and that the observed large departures from Debye-like behavior can be fitted to a relatively simple equivalent circuit. In this paper, we discuss the application of Jonscher circuits to a polycrystalline Li^+ ion conducting electrolyte LISICON, and show how both the grain boundary and bulk regions may be satisfactorily described, extending previous approaches by utilizing

two frequency dependent elements. We also show how the departures from Debye-like response are manifested in all four complex formalisms, the admittance (Y^*), impedance (Z^*), permittivity (ϵ^*), and modulus (M^*), which are interrelated (17)

$$Y^* = (Z^*)^{-1} = j\omega Co(M^*)^{-1} = j\omega Co\epsilon^* \quad [1]$$

where ω is the angular frequency, $2\pi f$, and Co is the vacuum capacitance of the conductivity cell.

In addition to the above-mentioned representation of grain boundary response, the origin of such grain boundaries in LISICON is discussed and a model for them presented.

Experimental

The synthesis of lithium zinc germanate phases and their analysis by x-ray diffraction has been discussed previously (18). Pellets for conductivity measurements were prepared by cold-pressing powders of the γ_{II}-type solid solutions at 45,000 psi, followed by sintering at temperatures between 1000° and 1100°C for 1-2 hr. A few pellets were covered with powder of the same composition to reduce lithia loss and sintered at 1200°C for 5-10 hr. Pellet densities were typically 75-80% of the theoretical values. In some cases, unsintered pellets were partially melted by heating in closed Pt envelopes for 10-15 min at temperatures above the solidus. No significant distortion of the pellets occurred. This gave densities ~ 85% of the theoretical value.

Gold electrodes were applied to opposite pellet faces, generally by vapor deposition. Care was taken to mask the edges of the pellet to prevent penetration of the gold onto the sides of the pellet. In other cases, gold electrodes were applied with Englehard paste, heated at 150°-500°C in successive steps to remove the organic solvent, decompose the organo-gold complex, and harden the metallic residue. In some instances, before the electrodes were applied, the pellet surfaces were polished with successively finer grades of silicon carbide paper, using ethanol as lubricant, and finally with a rotary polisher using 1 μm diamond paste. The internal microstructure and composition of some pellets were examined by scanning electron microscopy combined with microprobe analysis.

The conductivity jig took the form of a stainless steel G-clamp, Fig. 1. The cell was held between high purity silica glass disks and pressure maintained by a spring loaded plunger (evaporated electrodes). Connection was made to the measuring apparatus by inserting gold foil strips between each silica disk and cell face. Each gold foil strip was wrapped around a platinum wire mounted within a stainless steel cylinder, from which it was insulated by a concentric silica glass tube. Internal surfaces of the jig head were lined with an insulating material (pyrophyllite). The temperature was measured with a Chromel/Alumel thermocouple, the tip of which was maintained in close proximity to the cell for maximum accuracy. The jig was mounted in a silica glass tube, thus permitting measurements to be made in vacuum or different atmospheres. The entire assembly was clamped centrally inside a noninductively wound, horizontal tube furnace attached to a Eurotherm P.D.I. controller. Temperatures were controlled and measured to ±2°C.

Two terminal a-c measurements were conducted over the frequency range 10^{-3}-10^7 Hz, using a combination of bridge and automated phase sensitive detection techniques. For the range 100 Hz-70 kHz, a Wayne Kerr B224 bridge was used with a Brookdeal 9472 signal source and 9654 null detector. The signal generator output was maintained at 25 mV rms throughout; however, the voltage output from the bridge depended on the particular admittance range selected. An accuracy, in the measured admittance values, of better than 3% was typically obtained.

For the range 70 kHz-7 MHz, a B602 rf bridge and combined source/detector unit, SR268L, were used al-

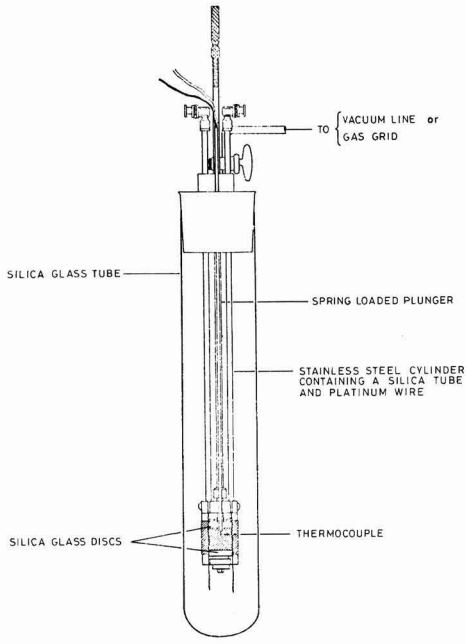

Fig. 1. A-C conductance jig

though at the extremes of this frequency range, the experimental data points showed some scatter. The applied voltage was 25 mV rms. For the frequency range 10^{-3}-10^4 Hz, a Schlumberger Solartron Frequency Response Analyzer (F.R.A.) Model 1170 was used. Normally 500 mV rms was applied across a standard resistance and the cell, which were connected in series; only a proportion of this applied voltage appeared across the cell therefore, and this proportion varied with frequency, since the cell impedance was frequency dependent.

Generally, the matching and continuity of results from the F.R.A. and the two bridges was good.

Results

Impedance data—general comments.—Three typical sets of a-c data, in the form of complex impedance plane plots, are given in Fig. 2 for Au/LISICON/Au cells. The LISICON solid electrolyte composition was $Li_{2+2x}Zn_{1-x}GeO_4$: $x = 0.55$; similar behavior was observed for other x values. The data separate clearly into a high frequency region, which contains two semicircles, and a low frequency region, which contains a spike that was sometimes linear and sometimes curved. The spike was associated with the electrode-electrolyte interface since it was sensitive to polishing of the pellet surface prior to application of the electrodes. The high frequency region was assigned to the a-c response of the electrolyte itself, since it was independent of the magnitude of the applied electric field, at least up to 9.0V rms.

Within the high frequency region, Fig. 2, two slightly distorted semicircles are present, but their relative sizes are different in the three cases. The magnitude of the low frequency semicircle varied considerably from cell to cell and at the same temperature. In some cases it was the larger of the two (c) and in others it was the smaller (a, b). This indicates that the two semicircles had a different origin.

The high frequency semicircle, which passes through the origin, was associated with the intragranular or bulk response of the solid electrolyte. The intercept, R_g, on the Z' axis gives the resistance of the grains.

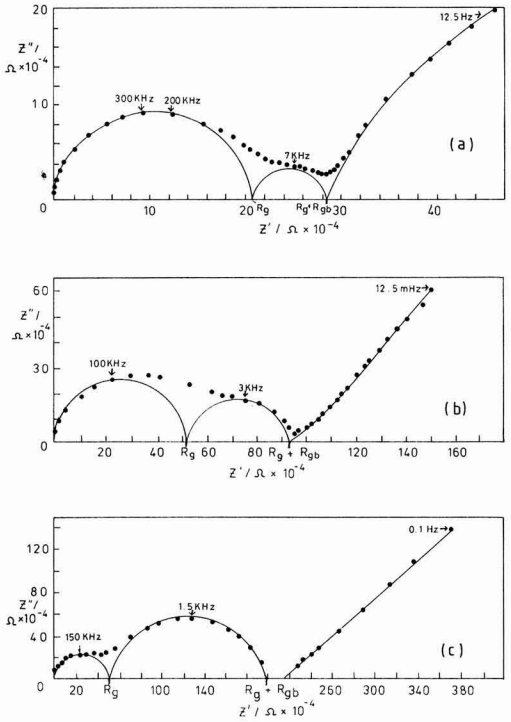

Fig. 2. Typical complex impedance plots for three Au/LISICON/Au cells, at 59°C: a) cell constant, $k = 0.55$ cm^{-1}; b) cell constant, $k = 0.47$ cm^{-1}; c) cell constant, $k = 0.64$ cm^{-1}.

For a given composition, x, and temperature, the value of R_g was the same, within a factor of 2-3, in all samples studied [large changes in R_g occurred on prolonged aging of samples, however (24): see later]. Using the relation $\omega RC = 1$, which holds at the maximum of an ideal semicircle, the capacitance of the high frequency semicircle was evaluated as ~1-2 pf cm^{-1}. This corresponds with that expected from the dielectric polarization of the crystals, assuming a typical bulk dielectric constant of ~5-25.

The second, low frequency semicircle is attributed to a grain boundary impedance in series with the intragranular impedance. The value of its capacitance, C_{gb}, calculated from the maximum of the second semicircle is in the range 10-400 pf cm^{-1} and represents charge polarization at the grain boundaries. These C_{gb} values are relatively small compared with grain boundary capacitances observed in solid electrolytes, such as Na β-alumina [800 pf cm^{-1} (Ref. 19) 21, nf cm^{-1} (Ref. 20)], and doped CeO_2 [50 nf cm^{-1} (Ref. 21)]. The magnitude of the grain boundary resistance, R_{gb}, varied from sample to sample at the same composition and was usually in the range $0.2\ R_g < R_{gb} < 8R_g$.

Although the magnitudes of R_g and R_{gb} were normally different, an important result is that, for a given sample, they appeared always to have the same activation energy, in contrast to the results of Bayard (22). Typical results are shown in Fig. 3 for a pellet in which both R_g and R_{gb} could be determined over a range of temperatures. The two sets of data fall on straight lines that are parallel within experimental error. Similarly, parallel sets of data were obtained: (*i*) for a variety of compositions, x; (*ii*) for samples that had undergone a phase transition to give one of various γ-derivative phases; (*iii*) for samples that had aged, *i.e.*, had undergone a marked decrease in conductivity on annealing (24).

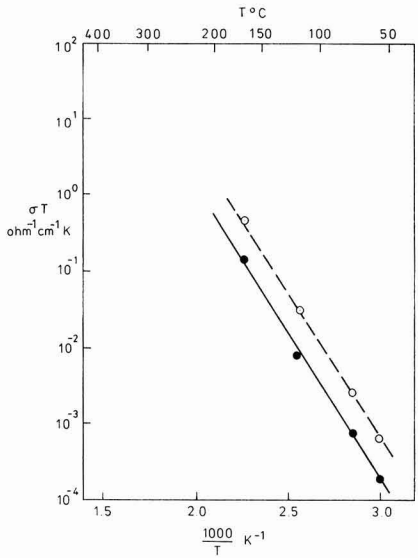

Fig. 3. Arrhenius plot of the intracrystalline conductivity ($1/R_g$)—⊙ and intercrystalline conductivity ($1/R_{gb}$)—● of an LISICON solid solution.

The similarity in the activation energies of R_g and R_{gb} indicates that charge migration in the intracrystalline and grain boundary regions occurred by the same process. In particular, the grain boundary effect is believed to be associated with a constriction of current pathways at the necks between crystals. A model for this is presented in the third section.

Various alternative explanations for the occurrence of more than one semicircle were considered but were rejected. These alternative explanations, with reasons for their rejection are as follows: (*i*) The presence of a surface layer on the electrolyte at the interface with the electrode, arising from, *e.g.*, surface attack (23) or electrochemical reactions. This layer would have a different structure and composition to the bulk, and probably, therefore, a different activation energy for conduction, in contrast to the results. (*ii*) If the crystal conductivity was markedly anisotropic, the presence of crystals in different orientations could possibly give rise to broadening of, or resolution into, two complex impedance semicircles. Again, however, it is likely that the two associated resistances would have different activation energies. (*iii*) Compositional variations between or within the crystallites (*i.e.*, a variation in x) could give rise to the appearance of more than one complex impedance semicircle. However, the activation energy for conduction in these LISICON solid solutions is very composition dependent (24), and any additional semicircles arising from compositional inhomogeneities should have different activation energy from the bulk. (*iv*) Dielectric relaxation may occur due to the formation of dipoles between, *e.g.*, substitutional and interstitial Li^+ ions. If this was the cause of the appearance of two semicircles, it can be shown that the dielectric relaxation time, which should be a fundamental property for each composition, in fact varied from sample to sample. This possibility is discounted, therefore. Details of the analysis and an equivalent circuit which may be used to represent a solid electrolyte that contains both free ions and dipoles, is given in the Appendix.

The intracrystalline (bulk) a-c response.—In the above analysis, it was assumed that the bulk properties could be approximated by a parallel combination

of a resistance and a capacitance. In fact, departures from this ideal behavior occurred, as shown in Fig. 4a, where data are presented as spectroscopic plots of M'' and Z'' against frequency. In the ideal case, the M'', Z'' peaks should be similar-shaped, Debye peaks ($\frac{1}{2}\Delta = 1.14$ decades) with their maxima occurring at the same frequency (17). In fact, the peak maxima occur at different frequencies in Fig. 4a, and the M'' peak is noticeably broadened on the high frequency side. The Z'' peak shows a spur on the low frequency side which is due to the onset of polarization associated with the grain boundary effect.

In order to analyze further these nonideal data, use is made of an equivalent circuit that contains a frequency dependent admittance, $Y^*(\omega)$, in parallel with the normal R and C elements, Fig. 5b. This circuit was also used to analyze data for single crystal beta alumina (16). The method of data analysis is as follows:

First, the impedance data are replotted in the admittance formalism, on logarithmic scales. This is done in Fig. 4b for one data set. The Y' plot shows two steps, or frequency independent plateaus, one below ~ 300 Hz and one between $\sim 10^4$ and 10^5 Hz, and a high frequency dispersion, above $\sim 10^5$ Hz. The low frequency plateau represents the overall electrolyte conductivity and after correction for the cell constant, is given by $(R_g + R_{gb})^{-1}$. The high frequency plateau represents the bulk, intracrystalline conductivity, $(R_g)^{-1}$. The Y'' plot shows an apparent plateau between 10^3 and 10^4 Hz, with a steep ramp at higher frequencies and another dispersion at lower frequencies. At this stage we are concerned with the bulk response only, which is given by the data above $\sim 10^4$ Hz.

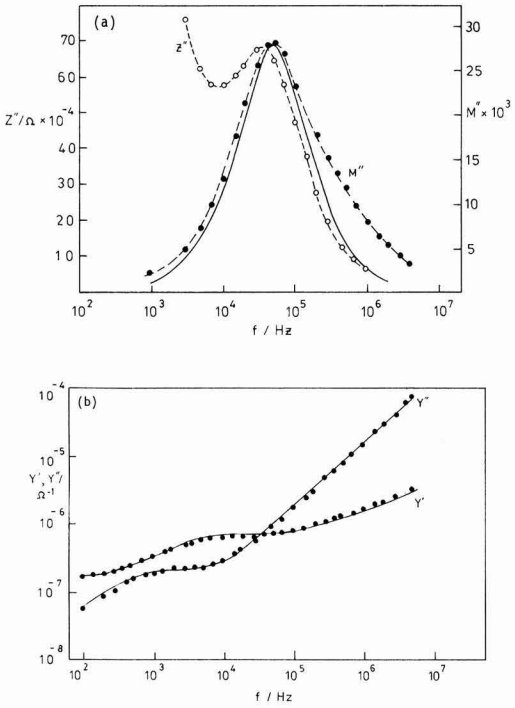

Fig. 4. (a) Z''-log f and M''-log f plots for an LISICON solid solution, $x = 0.55$, cell d, $k = 0.55$ cm^{-1}. The solid line represents an ideal Debye peak. Temperature: 39°C. (b) Log Y' and log Y''-log f plots of the data in (a). Solid circles are experimental points. Solid lines are calculated admittances.

The bulk admittance data, above $\sim 10^4$ Hz, can be represented by circuit (b), Fig. 5 whose complex admittance is

$$Y^* = R_g^{-1} + j\omega C_\infty + (A\omega^n + jB\omega^n) \quad [2]$$

The term in brackets is $Y^*(\omega)$, where A, B, and n are constants, $B = A\tan(n\pi/2)$ and $\omega = 2\pi f$: this describes the nonideal features of the response. Therefore

$$Y' = R_g^{-1} + A\omega^n, \quad Y'' = B\omega^n + \omega C_\infty \quad [3]$$

since

$$Y^* = Y' + jY'' \quad [4]$$

The equation for Y' contains two terms; R_g^{-1} is the value of the bulk conductivity and gives rise to the plateau in Y' between $\sim 10^4$-10^5 Hz; $A\omega^n$ represents the conductance ramp above $\sim 10^5$ Hz. The equation for Y'' also contains two terms; ωC_∞ gives the limiting slope of unity observed above $\sim 10^4$ Hz. The term $B\omega^n$ should give a low frequency slope of n, but below $\sim 10^4$ Hz, grain boundary phenomena influence the Y'' data and the region corresponding to $B\omega^n$ is not clearly distinguished. Values of the various parameters, extracted from Fig. 4b by curve fitting, are given in Table I. A test of the quality with which Eq. [2]

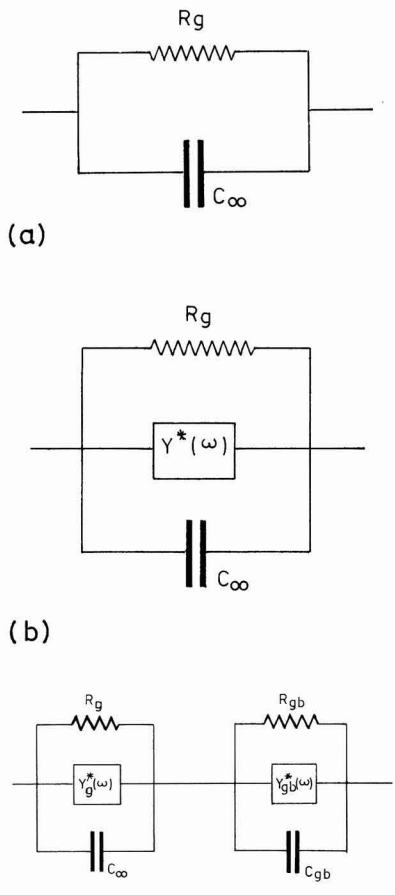

Fig. 5. Traditional (a) and new (b) equivalent circuits for the intracrystalline a-c response of a polycrystalline electrolyte. (c) Equivalent circuit for the entire a-c response of polycrystalline LISICON.

Table I. Equivalent circuit parameters extracted from Fig. 4b

	Bulk region	Grain boundary region
R^{-1}	3.9×10^{-7} ohm^{-1} cm^{-1}	1.2×10^{-7} ohm^{-1} cm^{-1}
A	4.3×10^{-11} ohm^{-1} cm^{-1} rad^{-n}	8.7×10^{-11} ohm^{-1} cm^{-1} rad^{-n}
B	5.9×10^{-11} ohm^{-1} cm^{-1} rad^{-n}	2.3×10^{-10} ohm^{-1} cm^{-1} rad^{-n}
n	0.60	0.77
C	1.3×10^{-12} F cm^{-1}	1.9×10^{-11} F cm^{-1}
k	0.55 cm^{-1}	0.55 cm^{-1}

models the experimental data is given by the closeness of the agreement between calculated and experimental admittance data. This is described in section below, in which the total admittance of the electrolyte, including both intragranular and grain boundary effects, is calculated and compared with the experimental results. The solid line in Fig. 4b represents calculated values and it can be seen that the agreement with the experimental data is good.

The complex admittance of circuit [Fig. 5(b)] may be converted into the three other complex formalisms using Eq. [1] and hence, the response of the equivalent circuit in all four formalisms may be calculated. The limiting high and low frequency expressions for each of the four formalisms are given in Table II. Equations [1] and [2] permit a better understanding of the different expressions of nonideality seen in the various formalisms and plots. For instance, the M'' peak, on a logarithmic scale, has a limiting slope of 1 at frequencies below the peak maximum, but a limiting slope of $n - 1$ ($0 < n < 1$) at frequencies above the peak maximum. In contrast, the Z'' peak has limiting slopes of n and -1 at low and high frequencies, respectively, Table II. This accounts for the marked tendency, noted in various ionic conductors and Fig. 4a, for the M'' peak to be broader than the Z'' peak at frequencies above the peak maximum. Further, the simulations show that the maxima of the M'' and Z'' peaks are not coincident, but that the M'' spectrum always peaks at higher frequencies than the Z'' spectrum. The present results on LISICON show smaller departures from Debye response than observed in β-alumina (16). This may be because the mobile ion concentration in LISICON is considerably less than expected, in keeping with a model of ion trapping to be discussed elsewhere (25).

Grain boundary effects.—Polycrystalline LISICON sinters gave complex impedance plane plots that showed two semicircles, Fig. 2; the high frequency semicircle is attributed to the bulk response and the low frequency one to an intergranular or grain boundary effect. Since the resistances determined from the intercepts of the two semicircles on the Z' axis have similar activation energies in all samples studied, the origin of the low frequency semicircle is believed to be in the constriction of the current pathways at the necks which connect adjacent grains. These necks are clearly seen in a scanning electron micrograph, Fig. 6, and the porous nature of the sinter is also apparent. While, in some systems, an intergranular blocking phase of different composition to the bulk crystals may give rise to a constriction and a second semicircle in the a-c data (26), there is no evidence for such a second phase here: on extended exposure, Guinier x-ray powder diffraction photographs of powdered pellets, there was no evidence of a second phase. In addition, electron microprobe analysis of materials such as those shown in Fig. 6a, showed no difference in Zn,Ge content between the bulk and intergranular regions. It is believed, therefore, that the necks or intergranular regions are composed of material of the same composition and structure as the bulk of the crystals. In the following, a model is proposed to show how constriction of current pathways by the presence of air gaps between grains can lead to an extra semicircle in the complex impedance plane.

A schematic, idealized constriction between two grains is shown in Fig. 7a and a model equivalent circuit in Fig. 7b. The essential difference between grain and constriction regions lies in their relative cross-sectional area. It is assumed that there are no extra resistances at the contact points between grains, and that the crystal structure passes continuously from one grain to the next via the constricted region; it is also assumed that conduction is isotropic, and that differences in grain orientation do not affect the behavior. The grain and constriction resistances are set equal to R_1 and R_2 (the resistivities, ρ_1 and ρ_2, are equal, but the two regions have a different effective cell constant). The capacitances of the two regions are C_1 and C_2; C_1 corresponds to the bulk capacitance of the grains, C_2 represents the combination of the capacitance of the constriction region, C_c and the capacitance of the air gap, C_a. The Maxwell relaxation times, τ, of the grain and constriction regions are given, assuming simple geometries, by

$$\tau_1 = R_1C_1 = \rho\epsilon' e_o$$

$$\tau_2 = R_2C_2$$

where ϵ' is the bulk dielectric constant and e_o the permittivity of free space. But

$$C_2 = C_c + C_a$$

$$= \epsilon'\epsilon_o \frac{A_c}{l_c} + \epsilon_o \frac{(A_g - A_c)}{l_c}$$

where A_c, A_g, and l_c are defined in Fig. 7(a). Assuming that $A_g >> A_c$

$$C_2 = \epsilon'\epsilon_o \frac{A_c}{l_c} + \epsilon_o \frac{A_g}{l_c}$$

$$\therefore \tau_2 = \left(\rho \frac{l_c}{A_c}\right)\left(\epsilon'\epsilon_o \frac{A_c}{l_c} + \epsilon_o \frac{A_g}{l_c}\right)$$

Hence

$$\tau_2 = \tau_1 + \tau_1 \frac{A_g}{A_c} \cdot \frac{l}{\epsilon'} \qquad [5]$$

As an order of magnitude calculation, if $\epsilon' = 10$ and $A_g = 90\ A_c$, then $\tau_2 = 10\tau_1$. In complex impedance plots, semicircle maxima occur when $\omega\tau = 1$, and therefore, two semicircles separated by one decade in frequency would be expected.

In order to try and modify the constriction resistances, some pellets were partially melted and their a-c conductivity measured. SEM photographs are shown in Fig. 6b, c for a pellet of composition $x = 0.55$, which was partially melted at $\sim$1350°C and subsequently annealed at 1150°C for 1 hr. Electrodes were then applied and the a-c response of this cell determined. After conductivity measurements, the electrodes were removed, the pellet crushed to a fine powder, repelleted, and sintered at 1150°C for 1 hr; an SEM micrograph is given in Fig. 6d. The two pellets should differ only in their texture, therefore. It can be seen that the partially melted pellet, Fig. 6b, c, had a much larger average grain size than the reground

Table II. Limiting high and low frequency expressions calculated for the Jonscher circuit, Fig. 5(b)

	Y'	Y''	ϵ'	ϵ''	Z'	Z''	M'	M''
$\omega \to 0$	$1/R$	$B\omega^n$	$(B\omega^{n-1})/C_o$	$1/\omega RC_o$	R	$R^2B\omega^n$	$R^2C_oB\omega^{n+1}$	$RC_o\omega$
$\omega \to \infty$	$A\omega^n$	ωC_∞	C_∞/C_o	$(A\omega^{n-1})/C_o$	$(A\omega^{n-2})/C_\infty^2$	$1/\omega C_\infty$	C_o/C_∞	$(C_oA\omega^{n-1})/C_\infty^2$

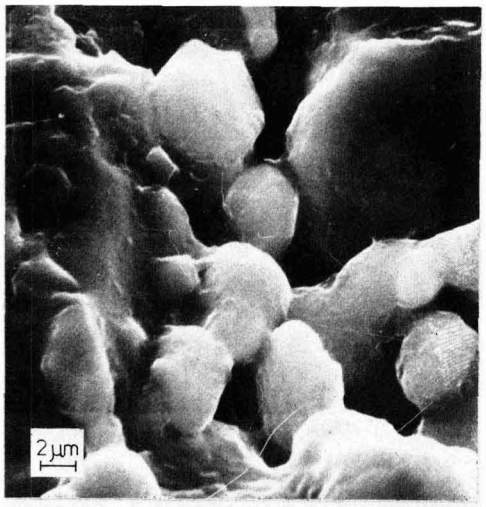

(a)

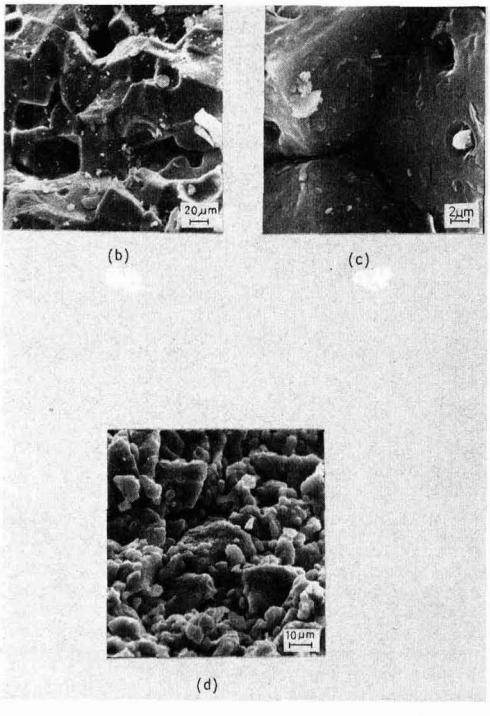

(b) (c)

(d)

Fig. 6. Scanning electron micrographs of a) a sintered polycrystalline LISICON electrolyte, $x = 0.55$, fracture surface. b) and c) A partially melted electrolyte, $x = 0.55$, fracture surface. The micrograph (c) is a 10× magnification of the central region of (b). d) Sample (b, c) after grinding, repelleting, and sintering.

and sintered pellet, Fig. 6d. The partially melted pellet also had lower porosity, as confirmed by measurements of the densities of the two pellets: the partially melted electrolyte was 30% less porous than the reground sinter. The a-c response of the two pellets was markedly different, especially that part associated with the low frequency, grain boundary semicircle. In

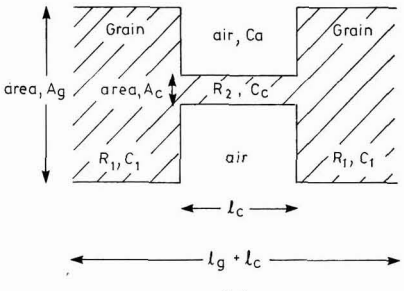

(a)

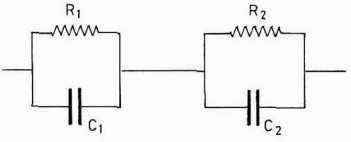

(b)

Fig. 7. (a) Schematic diagram of an intergranular constriction resistance. R_1—resistance of the grain region, R_2—resistance of the constriction region, C_1—capacitance of the grain region, C_c—capacitance of the constriction region, C_a—capacitance of the air gap, A_g—cross-sectional area of the grain region, A_c—cross-sectional area of the constriction region, l_g—length of the grain region, l_c—length of the constriction region. (b) The equivalent electrical representations. $C_2 = C_a + C_c$.

particular, C_2, the capacitance associated with the intergranular constriction was about ten times larger in the partially melted pellet than in the reground and sintered pellet. This is because the constriction resistances still exist but are now much thinner, Fig. 6c: the SEM micrographs show that in the partially melted sample, cracks run through some crystals and narrow gaps exist between grains.

It is concluded qualitatively that constriction resistances in porous sinters may be treated as separate *RC* elements in the equivalent circuit and, depending on the relative magnitudes of τ for the bulk and constriction regions, a separate or partly resolved second semicircle may be present in, *e.g.*, the complex impedance plane. The relative magnitudes of τ_g and τ_{gb} depend on the magnitude of the constriction capacitance C_a. This, in turn depends on: (*i*) the geometry, and (*ii*) the permittivity of the constriction region. For an air gap, ϵ' is approximately one tenth that expected for a second phase (which could also give rise to a constriction resistance). This contributes to the relatively low grain boundary capacitances observed here.

Quantification of the above model for constriction resistances is difficult because of the highly heterogeneous nature of polycrystalline sinters. However, account must also be taken of the nonideal response of the constriction region, in the same way that the bulk response is not Debye-like. In the next section, an analysis of the constriction region in terms of frequency dependent admittances is presented.

Analysis of grain boundary a-c data using a circuit containing a frequency dependent admittance.—It was shown in the section above that the intracrystalline response could be represented by an equivalent circuit, Fig. 5b, that incorporated a frequency dependent ad-

mittance. It is expected that a similar circuit may be of use in representing the constriction region. In order to analyze the data in this way, it was first necessary to subtract that component due to the intracrystalline response from the experimental data. Since the grain and constriction resistances are in series, this subtraction was made using corresponding impedance data

$$Z^*(gb) = Z^*(t) - Z^*(b) \qquad [6]$$

where $Z^*(gb)$ is the residual impedance that is left after subtracting the intragranular impedance, $Z^*(b)$, calculated using the parameters given in Table I, from the total experimental impedance, $Z^*(t)$. Results are shown in Fig. 8b for $Z^*(gb)$, which was obtained by processing the data given in Fig. 8a. The $Z^*(gb)$ data fall on a distorted semicircle. These data were converted back into the Y^* formalism, replotted on logarithmic scales, Fig. 8c, and analyzed as described in the section above. The data again fit Eq. [2] but in this case, C_∞ is replaced by C_{gb}, and R_g by R_{gb}. In contrast to the intracrystalline response, C_{gb} is dominated by the expression $B\omega^n$ (Y'' data). The Y' data cover the frequency region over which both the terms R_{gb}^{-1} and $A\omega^n$ are significant. The values extracted from Fig. 8c are given in Table I.

Modeling the overall a-c response of LISICON polycrystalline electrolytes.—It has been shown that both the intragranular and constriction regions give an a-c response that may be described by an RC circuit containing an additional, frequency dependent admittance element. The total a-c response of the pellet may be represented by assuming that these two regions occur in series, with the equivalent circuit shown in Fig. 5c. Simulations based on this circuit are shown in Fig. 4b, 8a, d, and e for the parameters listed in Table I. The calculated response (solid curves) agrees very well with the experimental data points within the limits of error inherent in the use of log-log plots to extract parameter values. It is particularly reassuring to note good agreement in all four formalisms, since each places a different emphasis

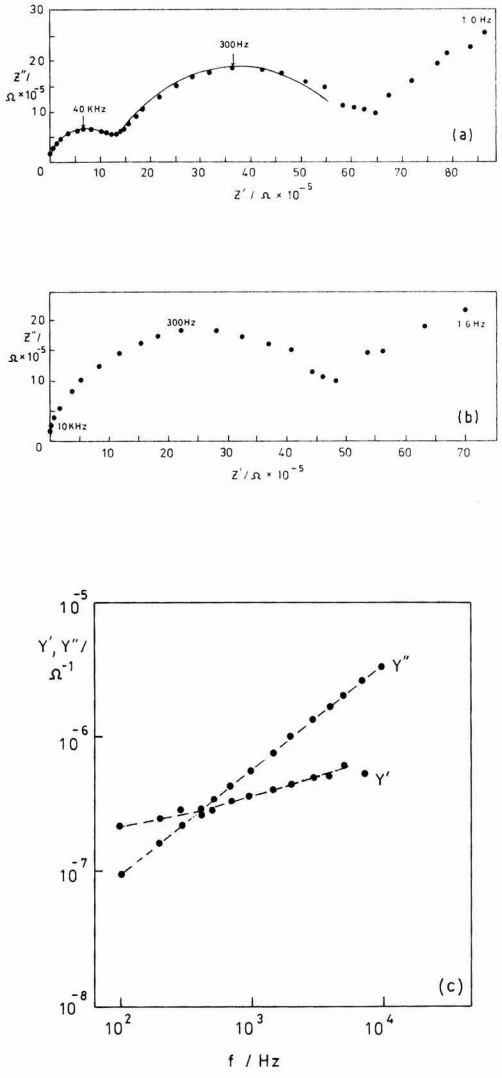

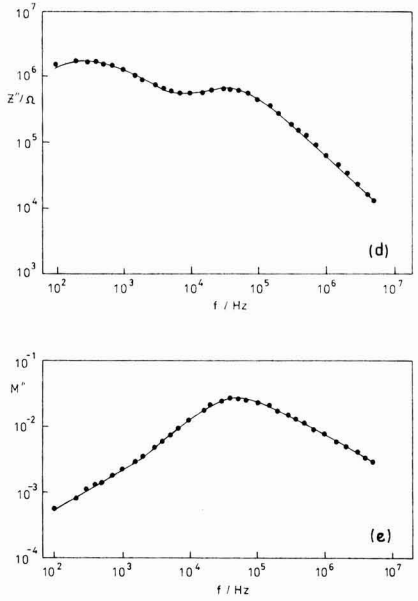

Fig. 8. (a) Complex plane plot of the total impedance, $Z^*(t)$, of cell d. The solid line represents the calculated total electrolyte impedance. (b) Complex plane plot of the grain boundary impedance, $Z^*(gb)$, of cell d, after subtracting the simulated intracrystalline impedance, $Z^*(b)$, from the total a-c response, $Z^*(t)$. At the lowest frequencies the data in (a) and (b) are significantly affected by the electrode impedance. (c) Log Y'-log f and log Y''-log f plots for the data in (b). Intra- and intercrystalline a-c response of cell d expressed as plots of: (d) log Z'' against log f for data in a), (e) log M'' against log f for data in a). In d) and e) solid circles represent experimental data and solid lines the calculated a-c response.

on the form of the a-c response. The use of a series circuit to model the total a-c response does not, of course, preclude the possibility of alternate parallel pathways. However, the current is likely to follow the parallel pathways of least impedance so that, to a first approximation, more than one parallel pathway need not be considered. The circuit then reduces to a series distribution of bulk and grain boundary elements.

The successful modeling of the overall electrolyte response, using circuit 5(c), is achieved without specifically taking into consideration any variation in the aspect ratio of crystal and neck geometries, which must inevitably be present in the pellets. It is possible that the difference in n between the two regions is related in some way to the considerable distribution in the geometries of the grain boundary regions. More work is clearly needed on different types of grain boundary in order to determine the factors that are important in controlling the a-c response.

The electrode-electrolyte interface.—Ideal blocking behavior at the electrode-electrolyte interface, which is signified by a limiting low frequency, vertical spike in the complex impedance plane, was not observed with the present materials. Instead, the electrode spike was inclined to the Z' axis at an angle of much less than 90° and, particularly at low frequencies, showed evidence of a downward curvature, Fig. 2a. A detailed study of the electrode-electrolyte response has not been made although some preliminary observations were made. The nonvertical nature of the spike was not associated simply with roughness of the electrolyte surface: although the spike was somewhat sensitive to polishing, a vertical spike was never obtained. It has been shown in other systems that a Jonscher expression, containing a frequency dependent admittance, may be used to model nonideal electrode-electrolyte response (12-14); it could probably also be relevant to the present, low frequency data.

APPENDIX

A Model for Dielectric Relaxation

Dielectric relaxation in solid electrolytes may occur if dipoles, formed by the pairing of ions, exist. In the LISICON solid solutions, dipoles may feasibly form by the pairing of substitutional and interstitial Li^+ ions, whch carry effective charges of -1 and $+1$, respectively. An equivalent circuit representation of a solid electrolyte that contains both mobile (*i.e.*, "free") ions and dipoles is given in Fig. 9. It is assumed that the dipole reorientation processes, represented by R_D and C_D, occur in parallel with the long range ionic motion, represented by R_g. The limiting, high frequency capacitance of the material is given by C_∞.

In the complex impedance plane, the circuit given in Fig. 9 would in principle give rise to two semicircles, due to the coupling of R_g, C_D and R_D, C_∞. The two semicircles can be resolved provided their time constants,

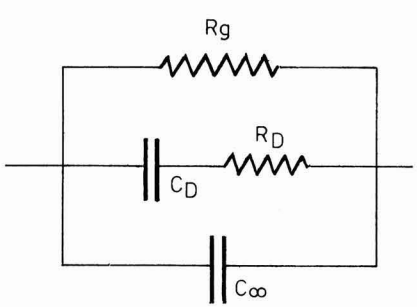

Fig. 9. Equivalent circuit for a solid electrolyte containing dipoles which give rise to dielectric relaxation. R_g—long range ionic migration, C_∞—high frequency polarization of the electrolyte, C_D, R_D—dipole reorientation process.

given by the magnitude of the products RC, are quite different and $R_D < R_g$. However, although these time constants may be defined for the complex impedance plane, the dielectric reorientation process has a different time constant τ_D, given by the product, R_DC_D. τ_D is a fundamental property of the reorientation process and should have an Arrhenius temperature dependence $\tau_D = \tau_0 \exp(E/kT)$, that is expressed in the temperature dependence of R_D. The dielectric relaxation process, which is represented by a series element, R_D and C_D, would not therefore be observed directly in the complex impedance plane, since semicircles arise from parallel R, C combinations. However, the relevant parameters may be extracted, R_D from the high frequency semicircles and C_D from the low frequency semicircle.

Acknowledgments

We thank SERC and Tioxide International Limited for a research studentship to PGB and SERC for a research grant to ARW. Dr. W. McHardy of the Macaulay Soil Research Institute, Aberdeen kindly provided facilities and assistance with the scanning electron microscopy. We thank Mr. A. Barclay for help with the design and fabrication of the conductivity jig.

Computing facilities were provided by the University of Aberdeen, Computing Centre.

Manuscript submitted Jan. 21, 1982; revised manuscript received Oct. 25, 1982.

Any discussion of this paper will appear in a Discussion Section to be published in the December 1983 JOURNAL. All discussions for the December 1983 Discussion Section should be submitted by Aug. 1, 1983.

REFERENCES

1. K. S. Cole and R. H. Cole, *J. Chem. Phys.*, **9**, 341 (1949).
2. D. Ravaine and J-L. Souquet, *J. de Chemie Physique*, **11**, 693 (1974).
3. E. Schouler, A. Hammou, and M. Kleitz, *Mater. Res. Bull.*, **71**, 693 (1976).
4. D. W. Davidson and R. H. Cole, *J. Chem. Phys.*, **18**, 1417 (1951).
5. I. M. Hodge, Unpublished work.
6. A. K. Jonscher, *Nature*, **267**, 673 (1977).
7. A. K. Jonscher, *J. Mater. Sci.*, **13**, 553 (1978).
8. K. L. Ngai, *Comments Solid State Phys.*, **9**, 127 (1979).
9. K. L. Ngai, A. K. Jonscher, and C. T. White, *Nature*, **277**, 185 (1979).
10. L. A. Dissado and R. M. Hill, *ibid.*, **279**, 685 (1979).
11. L. A. Dissado and R. M. Hill, *Philos. Mag.*, **B41**, 625 (1980).
12. A. K. Jonscher and J-M. Reau, *J. Mater. Sci.*, **13**, 563 (1978).
13. I. D. Raistrick, C. Ho, Y. W. Hu, and R. A. Huggins, *J. Electroanal. Chem.*, **77**, 319 (1977).
14. T. M. Gur, I. D. Raistrick, and R. A. Huggins, *Solid State Ionics*, **1**, 251 (1980).
15. I. D. Raistrick, C. Ho, and R. A. Huggins, *This Journal*, **123**, 1469 (1976).
16. P. G. Bruce, A. R. West, and D. P. Almond, *Solid State Ionics*, **7**, 57 (1982).
17. I. M. Hodge, M. D. Ingram, and A. R. West, *J. Electroanal. Chem.*, **74**, 125 (1976).
18. P. G. Bruce and A. R. West, *Mater. Res. Bull.*, **15**, 379 (1980).
19. E. Lilley and J. E. Strutt, *Phys. Status Solidi, A*, **54**, 629 (1979).
20. R. W. Powers and S. P. Mitoff, *This Journal*, **122**, 226 (1975).
21. D. Y. Wang and A. S. Nowick, *J. Solid State Chem.*, **35**, 325 (1980).
22. M. L. Bayard, in "Fast Ion Transport in Solids," P. Vashishta, J. N. Mundy, and G. K. Shenoy, Editors, North-Holland, Amsterdam (1979).
23. E. N. Boulos, A. V. Lesikar, and C. T. Moynihan, *J. Non-Cryst. Solids*, **45**, 419 (1981).
24. P. G. Bruce and A. R. West, *J. Solid State Chem.*, **44**, 354 (1982).
25. P. G. Bruce and A. R. West, In preparation.
26. J. E. Bauerle, *J. Phys. Chem. Solids*, **30**, 2657 (1969).

Lattice Parameter Changes in $Al_{0.39}Ga_{0.61}As$ Due to O, Ge, Si, and S Doping

W. R. Wagner, N. E. Schumaker,* J. L. Zilko, P. J. Anthony,* and V. Swaminathan

Bell Laboratories, Murray Hill, New Jersey 07974

ABSTRACT

The change in lattice parameter of epitaxial films of $Al_{0.39}Ga_{0.61}As$ was investigated as a function of growth solution doping. With the lattice constant of GaAs as the reference constant, it was found that the presence of either O_2 in the growth ambient or Ge in the growth solutions dilated the lattice. Growth solution doping with Si was found to initially dilate the lattice while further Si doping resulted in a lattice contraction. Sulfur doping contracted the lattice. It was found that the lattice dilation due to O_2 in the growth ambient principally resulted from a reduction in the background S contamination of the epitaxial films.

The purposeful addition of selected impurities is central to semiconductor materials technologies. The measurement of dopant incorporation into such materials is commonly limited to electrically active species since the measurement of total dopant incorporation is more difficult. Secondary ion mass spectroscopy (SIMS), radioisotope, and neutron activation techniques are the usual techniques used to monitor their incorporation. Insights into both dopant incorporation and dopant behavior can be provided by combining electrical measurements and less direct techniques such as precision lattice parameter measurements. The determination of dopant-induced or process-induced lattice parameter changes can provide a direct measurement of the effective size of an impurity or vacancy in the lattice. If the effective sizes are known, low impurity concentrations can be measured. Also, the defect chemistry of dopants can be investigated by measuring lattice parameter changes as a function of dopant incorporation. For instance, in GaAs, the incorporation of electrically active Te saturates at approximately 8×10^{18} free carriers/cm^3 (Ref. 1), but radiotracer techniques indicate that Te continues to be incorporated until at least 10^{20}/cm^3 (Ref. 2). When the effective Te distribution coefficient decreased, a relatively large lattice dilation was measured that increased directly with increased Te doping (3). This indicated the formation of strain centers such as high concentrations of interstitial defects or precipitates. Transmission electron microscopy revealed that these defects were nucleated by GaTe microprecipitates that were presumably the strain centers first detected with the x-ray lattice parameter measurement.

The lattice constant of GaAs has been measured often (4, 5). It is known as a function of the growth technology (5), *i.e.*, LPE, VPE, Bridgeman, and Czochralski, and as a function of doping (4, 5), and ranges from 5.65317 to 5.65333Å. On the other hand, only powder measurements of the lattice constant of AlAs exist (6, 7, 8), with $a = 5.6605 \pm 0.0005$Å. Also it has been shown that the lattice constant of $Al_xGa_{1-x}As$ alloys followed Veygard's law (6, 9, 10), such that

$$a_{(Al_xGa_{1-x}As)} = a_{(GaAs)} + x[a_{(AlAs)} - a_{(GaAs)}]$$

Lattice parameter measurements of $Al_xGa_{1-x}As$ alloys other than determinations of the lattice mismatch between a heteroepitaxial film and its substrate have not been made.

In this paper we report double-crystal x-ray diffractometric measurements of lattice parameter changes of LPE $Al_{0.39}Ga_{0.61}As$ films resulting from the addition of Si, Ge, and S to the growth solution and from the presence of O_2 in the growth ambient. Growth conditions resembled the multiple growth well, multiple layer growth environment used for manufacturing double heterostructure laser crystals. Selected contaminants were increased to identify their effects on a laser structure. This was deemed desirable because the reproducibility of the electrical characteristics of individual $Al_{0.4}Ga_{0.6}As$ films is excellent, while the electron transport properties of the same film grown from the same growth solution in a multiple growth well environment is not (11).

* Electrochemical Society Active Member.

Key words: double crystal x-ray diffractometry, thin films, liquid phase epitaxy, growth solution doping, lattice parameter, AlGaAs.

Fundamental Considerations

The underlying principle of the lattice parameter measurements is naturally Bragg's law

$$n\lambda = 2d \sin\theta$$

and its differential

$$\frac{\Delta d}{d} = \Delta\theta \cot\theta$$

where λ is the incident x-ray wavelength, d is the interplanar spacing of the diffracting planes, and θ is the angle of incidence of the x-rays. Implicit in the statement of Bragg's law is the assumption of a single incident x-ray wavelength and a single angle of incidence, *i.e.*, a plane wave. Real x-ray sources, however, generate polychromatic spherical waves. The double-crystal x-ray experimental arrangement (12) transforms this radiation into a good approximation to a plane wave such that the fundamental Darwin-Prins (12) linewidths can be closely realized. The incident radiation is first collimated, then diffracted from a highly perfect monochromator crystal. If the diffraction condition is arranged to be asymmetric, *i.e.*, the diffracting planes are not parallel to the surface, the divergence of the diffracted beam can easily be reduced by another factor of 10 (12)

$$b = \frac{\sin(\theta - L)}{\sin(\theta + L)}$$

where b is the asymmetry factor, θ is the Bragg angle, and L is the angle between the surface and the diffracting planes.

If a plane wave of x-rays is incident on a heterostructure consisting of an $Al_xGa_{1-x}As$ film on a GaAs substrate, the Bragg condition will be satisfied for two angles of incidence for every set of diffracting planes arising from the two different interplanar spacings. In practice, the sample is approximately aligned to the Bragg angle, then rotated slowly and precisely through both Bragg angles. The diffracted intensity is recorded as a function of rotation angle generating a "rocking" curve consisting of two peaks separated by an angle $\Delta\theta$ that defines the difference in interplanar spacing between the substrate and the epitaxial film.

The difference in interplanar spacing measured in this manner is a measurement of a stressed elastically deformed heterostructure. When a film of a different lattice constant is grown on a substrate, the resultant structure is stressed in such a way that the unit cell of the epitaxial film is tetragonally deformed (13, 14). Compared to the deformation of the epitaxial film the deformation of the substrate is negligible because (15)

$$\sigma_{sub} = -\frac{t_l}{t_{sub}}\sigma_l$$

where the ratio of epi-thickness t_l to substrate thickness t_s, t_l/t_s, is typically 1/50. In the epitaxial film, the planes parallel to the growth interface are constrained elastically to have the same interatomic spacings as the substrate. The lattice then deforms in the direction of growth. The relaxed lattice constant of the epitaxial film was derived by Hornstra and Bartels (16) and by Estop and Sauvage (6). For {100} growth interfaces

$$\frac{\Delta d}{d_{relax}} = 0.525\frac{\Delta d}{d_{stressed}}$$

This elasticity correction from the experimental values is indeed significant.

The tetragonal deformation of the unit cell is easily observed with x-ray diffractometry. Because of the deformation, lattice planes that are not parallel or perpendicular to the growth interface will not be parallel to corresponding planes in the epitaxial film. With a <511> diffraction condition and a (001) interface

$$\Delta\theta(\bar{1}15) \approx 2\Delta\theta(1\bar{1}5)$$

If a <511> diffraction condition is used to determine $\Delta a/a$, then the arithmetic mean of the two $\Delta\theta$ measurements (9) has to be used to compute $\Delta a/a$.

Experimental Arrangement

Double-crystal x-ray diffractometry.—The white Cu radiation (emitted by a 6 kW Rigaku rotating anode generator) is first collimated, then diffracted from a highly perfect Ge monochromator crystal. The monochromator had polished {111} faces and was aligned to the incident x-rays to excite the <511> reflection. This alignment corresponds to an asymmetry factor $b = 0.107$, indicating that the reflected beam will be roughly ten times wider than the incident beam while the angular dispersion is one-tenth its original value. A second slit was used to reduce the width of the reflected beam because samples were curved as a result of heteroepitaxial stresses and thereby dispersed the Bragg condition. Samples were aligned in a +-geometry to again excite the <511> reflection.

The possible Bragg reflections of a heterostructure wafer were examined by scanning a small angle near $\theta_B = 45.2°$ about an axis perpendicular to the x-ray beam. Specimens could be translated parallel to the {100} surface to examine the uniformity of alloy composition. The x-ray intensities reflected from the specimen wafer were measured with an LiF scintillation counter and plotted against the rocking angle in 0.25 sec/step increments.

Liquid phase epitaxy.—Great care was taken with the LPE growth of our specimens to insure that the reproducibility of the Al alloy compositions of the resultant epitaxial films was within ±0.25% Al. The basic LPE technique was patterned after Dawson's (17) source-seed-slider method. All LPE reactors were standardized to a common 780°C temperature with a single Pt-Pt 10% Rh thermocouple. The growth schedules were rigorously duplicated as were the basic compositions of the growth solutions. Several growths were made with varying amounts of Ge, Si, and S introduced into each melt and with a flowing growth ambient of pure He (<1 ppb O_2) or He containing 0.7 ppm O_2. In every growth, at least one melt composition of a previous experiment was duplicated as a check on reproducibility. With our growth technology, six different epitaxial films could be grown simultaneously on six different substrates. Twelve substrates from three adjacent wafers of the same Si doped ingot were used to assure a uniform substrate lattice constant. In all growth solutions used in this experiment, the Al content was 6.43 mg with a standard deviation of ±0.04 mg in an 8 ± 0.05g Ga growth solution. In the direction of the flowing ambient, the first growth solution remained undoped, the second contained 50 mg Ge as did the next four solutions. The third solution also contained 50 μg Si, the fourth 500 mg Si, the fifth 5 mg Si, and the sixth 50 mg Si, all in addition to the 50 mg Ge. A single layer of $Al_{0.39}Ga_{0.61}As$ approximately 3 μm thick was grown on every substrate. In all, three different epitaxy reactors supplied samples for this experiment.

Results

A pair of diffractometric plots of the <511> diffraction condition were obtained from every $Al_{0.39}Ga_{0.61}As$-GaAs heterostructure; one plot for the 29° angle of incidence (Fig. 1) and the other for the 61° angle of incidence (Fig. 1). From these, the relaxed ($\Delta a/a$) were computed. These values are plotted against the growth solution composition in Fig. 2 and listed in Table I. The addition of 0.7 ppm of O_2 to the growth ambient was found to uniformly dilate the lattice by 14 ± 4 ppm, as compared to films grown in the pure He ambient, regardless of the Ge or Si doping of the growth solution. Doping the growth solution with 0.6 atom percent (a/o) Ge was found to dilate the resultant $Al_{0.39}Ga_{0.61}As$ lattice compared to undoped films by 15 ± 4 ppm. Si doping to the level of 1.6×10^{-3} a/o was found to dilate the lattice by 3-10 (±4) ppm beyond the lattice constant of the Ge-doped films, while additional Si doping contracted the lattice by 13 ppm for each order of magnitude increase in the Si doping of the growth solution, a total decrease of 45 ppm between 1.6×10^{-3} to 1.6 a/o Si in the growth solution.

The incorporation of sulfur in the $Al_{0.39}Ga_{0.61}As$ lattice was found to result in a significant lattice contraction also. As little as 6.4×10^{-5} a/o S in the growth solution was found to contract the $Al_{0.39}Ga_{0.61}As$ lat-

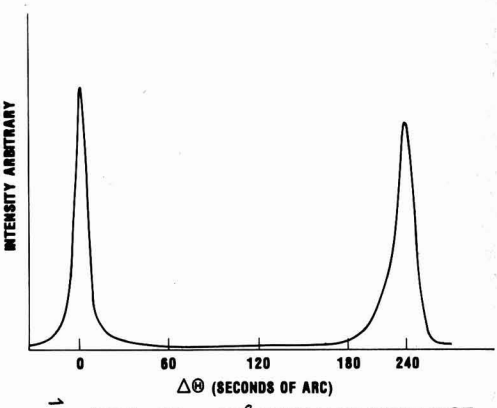

Fig. 1. Typical diffractometric plot of an $Al_{0.39}Ga_{0.61}As$ heteroepitaxial film on a GaAs substrate. The diffraction peak arising from the film is at the right.

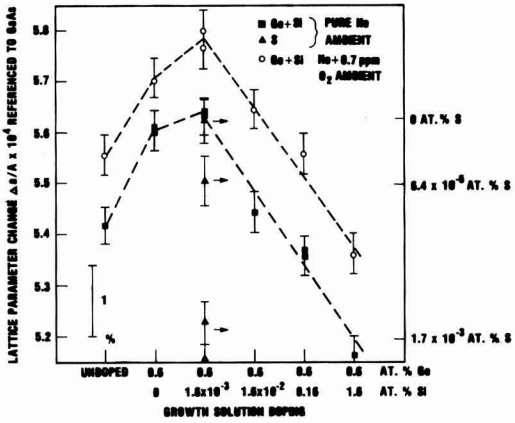

Fig. 2. Plot of the lattice changes $\Delta a/a$ as a function of growth solution doping and growth ambient.

tice by 14 ± 4 ppm from the Ge- and Si-doped level. Furthermore, 1.7×10^{-3} a/o S in the growth solution contracted the lattice by 44 ± 4 ppm. Separate samples reproducing earlier growths were found to have the same lattice constant well within the estimated limits of error of this experiment.

Discussion

Sources of error.—The measurement of dopant-induced lattice parameter changes on $Al_{0.4}Ga_{0.6}As$ films with double-crystal x-ray diffractometry requires two constants. The lattice parameter of the substrates used had to be uniform on the scale of the lattice parameter changes to be measured, and the Al content of the epitaxial films had to be reproducible and uniform to substantially better than 1%. The importance of reproducible Al concentrations is illustrated by the length of the 1% Al bar in Fig. 2. Lattice parameter fluctuations in melt-grown GaAs were studied extensively by Mullin *et al.* (5). Samples doped to 2×10^{18} free carriers/cm³ with a variety of dopants ("Te and other dopants") as a group fluctuated by $\Delta a/a = \pm 4 \times 10^{-6}$. The subgroup of Si-doped samples was not separately identified, but it can be expected to fluctuate even less. Furthermore, the electrical characteristics of the substrates used for our study were quite homogeneous, 1.5×10^{18} free carriers/cm³ and 2700 cm² V-sec mobilities at room temperature. Electrolytic etching of typical substrates indicated also that doping levels were homogeneous even on a small scale. It could, therefore, be presumed that the lattice parameter of the substrates used in this experiment was constant to 1 ppm. Included in this consideration were thermal expansion effects during the x-ray measurement. The thermal expansion coefficients of GaAs and AlAs lie between $5\text{-}6 \times 10^{-6}/(K^{-1})$ (17, 18). A 1°C temperature gradient in the 25 μm penetration depth of the x-ray beam is possible only for a 10°C temperature gradient in the entire sample. The thermal conductivity of the material (0.37 W/cm K) and the long equilibration time of each specimen indicate that even a 1°C temperature gradient in the sample was unlikely. Thermal expansion effects were then much less than 1 ppm.

A significant source of error consisted of the measurement of the angle $\Delta\theta$. This angle was generated with a differential micrometer, 100 divisions per 0.005 in., and 1.2 divisions per sec of arc. The repeatability of measurement was found to be ±1 div, *i.e.*, ±0.8 sec. The accuracy of the micrometer was found to be at least ±0.001 ($\Delta l/l$). Mechanical error should then be of the order of ±0.8 sec, corresponding to $\Delta a/a = \pm 3.8 \times 10^{-6}$ for the <511> reflection used. The accuracy in determining the center of mass of the diffraction peaks was substantially better. Rocking curves that did not result in two symmetric peaks of better than 10 sec half-maximum widths were repeated with better specimen alignments. The midchord peak construction (19) was used to determine the center of mass. For each diffraction peak, this determination was accurate to at least ±0.1 sec. The total error in $\Delta\theta$ was conservatively estimated to be ±1 sec of arc. The data, in fact, indicated a better degree of reproducibility. Repeated measurements of different areas of the same sample wafer at different times agreed to better than 1 sec of arc.

The reproducibility of the Al alloy compositions of the heteroepitaxial films was the most important consideration in assessing the validity of these results. An evaluation of this was, in fact, the secondary goal of this experiment. As already mentioned, considerable care was taken in the LPE growths to achieve reproducible growth conditions. Unfortunately, the determination of absolute Al compositions to the $x = \pm 0.001$ accuracy necessary to differentiate between alloy and doping effects appears impossible. Photoluminescence measurements of the completely undoped film and the equivalent film grown in the 1 ppm O_2 ambient indicated equivalent Al alloy compositions. Certainly, a $\Delta x = 0.03$ decrease in the alloy content of lightly and heavily Si-doped films did not occur. To an accuracy of $x = 0.01$, these measurements indicated that the Al compositions remained constant. The data listed in the

Table I. Data summary of growth solution doping, impurities, and lattice change

Wafer No.		Growth solution doping (a/o) x_e (Al)	x_e (Ge)	x_e (Si)	x_e (S)	Impurities in the solid ($\times 10^{-17}$/cm³) Ge	Si	S	Lattice change measurements ($\Delta a/a$) $\times 10^4$ First	Second
426	—1	0.208	0.6	1.6	0.0	20•	500•	1•	5.16	
	—2	0.206	0.6	0.16	0.0	20•	50•	1•	5.36	5.37
	—3	0.204	0.6	0.016	0.0	20•	5•	1•	5.44	
	—4	0.209	0.6	0.0016	0.0	20•	0.5••	1••	5.64	5.63
	—5	0.207	0.6	0.0	0.0	20•	<0.1•	1•	5.61	5.60
	—6	0.208	0.0	0.0	0.0	<1•	<0.1•	1•	5.42	5.44
83	—1	0.208	0.6	1.6	0.0	20•	300•	0.3•	5.37	
	—2	0.209	0.6	0.16	0.0	20•	30•	0.3•	5.56	
	—3	0.206	0.6	0.016	0.0	20•	3•	0.3•	5.65	
	—4	0.208	0.6	0.0016	0.0	20•	0.3••	0.3••	5.80	5.77
	—5	0.209	0.6	0.0	0.0	20•	<0.1•	0.3•	5.71	
	—6	0.208	0.0	0.0	0.0	<1•	<0.1•	0.3•	5.55	
45	—3	0.208	0.6	0.0013	1.7×10^{-5}	20•	0.9••	300••	5.15	
46	—3	0.209	0.6	0.0013	1.7×10^{-5}	20•	1.2••	270••	5.23	5.20
	—6	0.209	0.6	0.0013	0.0	20•	0.5••	0.5••	5.64	5.62
48	—6	0.209	0.6	0.0013	6.4×10^{-5}	20•	0.4••	10••	5.48	5.52

• Estimated concentration.
•• Concentration measured by SIMS.

table indicate an alloy reproducibility better than $\Delta x = 0.002$. Unquestionably, this data proves a satisfying degree of repeatability in our epitaxial growth technology. Two different LPE reactors on several occasions produced films with the same lattice constant from growth solutions of the same composition.

Without a precise determination of the Al alloy compositions of the epitaxial films, the data may be interpreted in two ways: either the distribution coefficient for Al in doped GaAs solutions changes systematically at low dopant concentrations, or the incorporation of impurities in $Al_{0.39}Ga_{0.61}As$ systematically changes the lattice constant. We support the latter view. It is difficult to accept that 0.7 ppm of O_2 in the growth ambient, the accepted background contamination of most LPE reactors, would increase the distribution coefficient of Al. This level is significantly below the solubility limit for oxygen in Ga; both Ga_2O_3 and GaO in Ga solutions are reduced in such an ambient. The level of oxygen in the growth solutions will be too small to result in any change in the distribution coefficient. Furthermore, a possible oxygen reaction with Al would tend to reduce the effective distribution coefficient. The same argument can be applied to the effects of S on the distribution coefficient of Al. It is not reasonable that 1.7×10^{-3} a/o S in the growth solution could reduce the Al concentration by $\Delta x = 0.03$. In fact, photoluminescence spectroscopy indicates that x changed by less than 0.01. In the case of Ge doping of $Al_xGa_{1-x}As$ films, an electron beam determination of Al compositions indicated a decrease in the Al distribution coefficient only for a/o Ge greater than 1% in the growth solution (20). Our result could be interpreted only in terms of an increase in the distribution coefficient. The Si doping of the growth solutions is more extensive, ranging from 1.6×10^{-3} to 1.6 a/o. While it is not inconceivable that 1.6 a/o Si in the growth solution might alter the Al distribution coefficient, the change must be less than $x = 0.01$, but then two and three orders of magnitude lower Si doping cannot be expected to have a significant effect.

The best argument for constant Al compositions and dopant-induced lattice changes lies in the self-consistent nature of the data as a set as shown in Fig. 2. The symmetry of the figure is a strong argument for the occurrence of dopant-induced lattice changes rather than changes in the Al distribution coefficient. Dilute dopants at concentrations of roughly one impurity atom per 1000 unit cells can be expected to behave as single strain centers with clearly differentiable ϵeffects for each dopant species. On the other hand, changes in the Al distribution coefficient with respect to the composition of the growth solutions can be expected to be interactive such that one species is predominant. A parallelism such as appears in this data where the effects of oxygen, Ge, Si, and S are clearly differentiated would be surprising.

The significance of the results.—The knowledge of the precise impurity concentration of the epitaxial films would be of great aid in the interpretation of the results. Hall measurements can give only an order of magnitude estimate of the total impurity concentration in this alloy because so many carriers enter the (L and X indirect) conduction bands. Actual impurity concentrations may be deduced from other data. There exists good evidence indicating that the distribution coefficient of Ge does not change in $Al_xGa_{1-x}As$ alloys at low doping levels (21). The observed lattice dilations due to Ge doping may then be compared to similar measurements in GaAs. According to Ketchow (22), our doping of 0.6 a/o Ge should be equivalent to 2×10^{18} free carriers/cm^3 (in GaAs). Two other lattice parameter measurements are known to us. Mullin *et al.* (5) measured $\Delta a/a = 1.5 \times 10^{-5}$ for 2×10^{18} free carriers/cm^3, Ge-doped, Bridgeman grown GaAs, also by x-ray techniques. Rode *et al.* (23) measured a dilation of $\Delta a/a = 4 \times 10^{-6}$ in a film doped to 4×10^{18} free carriers/cm^3 by curvature measurements of epitaxial bilayers. In this experiment, we measured a somewhat larger dilation of $\Delta a/a = 1.5 \times 10^{-5}$ in Ge-doped $Al_{0.39}Ga_{0.61}As$. There exists then a consensus that Ge-doping dilates both the GaAs and $Al_xGa_{1-x}As$ lattice, indicating again that Ge is incorporated into the As sublattice. However, the observed magnitude of this effect is at least one order of magnitude higher than can be calculated using Veygard's law and Pauling's covalent radii (5). Rode *et al.* (23) suggested that the principal source of this lattice dilation consisted of bond-breaking by free holes, but the lattice change calculated with his model is also significantly less than was observed here.

With Si doping, in addition to the "background" Ge doping, an initial slight lattice dilation was followed by a more severe contraction at higher growth solution doping. In four samples, the Si content of the epitaxial film was measured to be near 0.5×10^{17}/cm^3 by SIMS using a Cs^+ beam and negative ion spectroscopy, yielding an atomic distribution coefficient of 0.14, the published value (25) for an effective acceptor distribution coefficient for Si in GaAs is 8×10^{-2} at 800°C. If the assumption is made that the Si distribution coefficients for GaAs and $Al_xGa_{1-x}As$ are relatively insensitive to x, our data can be compared to the existing results of lattice changes in Si-doped GaAs. In Bridgeman-grown GaAs doped with Si to a level of 2×10^{18} free carriers/cm^3, a lattice contraction of approximately $\Delta a/a = 4 \times 10^{-6}$ was reported. This doping level would correspond to our growth solution doping of 0.16 a/o resulting in extrapolated Si levels of 5×10^{18}/cm^3 and 3×10^{18} free carriers/cm^3. The lattice change measured in this experiment was substantially greater than the reported value, namely, a contraction of $\Delta a/a = -2.5 \times 10^{-5}$. In view of the amphoteric nature of Si, this discrepancy is not surprising. During Bridgeman growth, Si is predominantly incorporated as a donor, while in LPE growth Si enters predominantly as an acceptor. The actual site distribution should be very complex, as is indicated by the great disparity between the estimated atomic and free-carrier distribution coefficient. These Si-doped films are certainly heavily compensated (26). For both Si and Ge doping in GaAs, it was suggested (26) that the incorporation of the impurity proceeds simultaneously with the incorporation of compensating centers that were presumed to be impurity-vacancy complexes. The lattice effects arising from these compensating centers cannot be identified at this time but they are certain to be a major cause of the discrepancy between measured and calculated lattice changes.

Qualitatively, the data suggest that the lattice dilation due to Ge doping should be principally an electronic effect while lattice changes due to the incorporation of Si will arise both from electronic effects and effects due to the smaller covalent radius of Si relative to Ge and As. The initial lattice dilation is probably an electronic effect akin to the bond breaking suggested by Rode (23). At higher doping levels, the electronic effects can be expected to diminish due to the increase in self-compensation (25). Then, covalent bond effects predominate to contract the lattice. With the simple model used by Mullin *et al.* (5), qualitative agreement with the measured lattice contraction is reached with the estimated 3×10^{18} free donors/cm^3 and 5×10^{19} atoms/cm^3 resulting from 0.16 a/o Si in the growth solution. Setting

$$N_a + N_d = N_a \text{ (Si on As sites)}$$

$$+ N_d \text{ (Si on Ga sites)} = 3.6 \times 10^{19}/\text{cm}^3$$

and

$$N_a - N_d = 3 \times 10^{18}/\text{cm}^3$$

a lattice contraction of $\Delta a/a = -9.5 \times 10^{-5}$ is cal-

culated and a contraction of $\Delta a/a = -4.5 \times 10^{-5}$ was measured.

The incorporation of S into the $Al_{0.39}Ga_{0.61}As$ lattice can be expected to contract the lattice solely on the basis of sulfur's small covalent radius, 14% smaller than that of As. SIMS measurements (24) of films grown from solutions containing 6.4×10^{-5} a/o S and 1.7×10^{-3} a/o S were found to contain 1×10^{18} and 3×10^{19} atoms S/cm^3, respectively. The corresponding lattice contractions were measured to be $\Delta a/a = -1.4 \times 10^{-5}$ and -4.5×10^{-5}. These results are at variance with the results of Mullin *et al.* (5) of Bridgeman-grown S-doped GaAs. At a presumed S level of 2×10^{18}/cm^3, a contraction of $\Delta a/a = -3.5 \times 10^{-6}$ was measured, and at a level of 4×10^{18}/cm^3, a dilation of $\Delta a/a = 7 \times 10^{-6}$ was measured. Their results are internally inconsistent and, thus, cannot be used as a reference standard.

The calculation of the expected sulfur concentration in the epitaxial films from our data based on covalent radii (5) results in a value of 5.2×10^{18}/cm^3 and 1.7×10^{19} impurities/cm^3 (as compared to the measured values of 1×10^{18}/cm^3 and 3×10^{19}/cm^3) for the two doping levels. As was the case with Si, at low doping levels the measured lattice change was too large to be explained with this simple model. At the higher doping levels, this model appears to hold up much better, but this is probably fortuitous. The unknown lattice effects of the high concentration of compensating centers (26) combined with the likely presence of structural defects (27, 28) should make the prediction of lattice changes at high doping levels a very difficult task.

Based on its very small covalent radius, the incorporation of oxygen in GaAs or $Al_{0.39}Ga_{0.61}As$ is expected to contract the lattice as sharply as sulfur. Indeed, in Bridgeman-grown O-doped GaAs, Mullin *et al.* (5) measured a contraction of $\Delta a/a = -1.2 \times 10^{-5}$ for only 1×10^{17} presumed oxygen doping. This contraction was more than one order of magnitude greater than could be expected based on covalent radii.

Quite different from their findings, our results clearly indicate a uniform lattice dilation, irrespective of growth solution doping, presumably the result of the presence of the intentional 0.7 ppm O_2 in the growth ambient. The observed lattice dilation is certainly not an ionic effect, but it could be an electronic effect if oxygen is thought to result in acceptor levels (29). But since oxygen has virtually the same covalent radius as sulfur, identical lattice effects should be expected. To explain this, the key findings resulted from SIMS. The expected increase in the background concentration of oxygen was not found. The oxygen content of all samples was found to be less than 3×10^{17}/cm^3, below the instrumental detection limit for the oxygen species. On the other hand, in the samples grown in an ambient of pure He plus 0.7 ppm O_2, the sulfur concentration decreased from 1×10^{17} to 3×10^{16}/cm^3. The observed lattice dilation could then be due in part to the decrease in the sulfur-based contraction and in part to the lattice dilation resulting in the increased concentration of free holes, *i.e.*, broken bonds arising from the decreased concentration of donors associated with sulfur (30). Reproducibly low film resistivities were achieved in the P-ternary layer ($Al_{0.4}Ga_{0.6}As$) of AlGaAs-GaAs laser heterostructures with the combination of O_2, Si, and Ge in the growth environment.

The incorporation of dopants into GaAs or $Al_xGa_{1-x}As$ is basically not understood. It seems fairly certain that high concentrations of compensating centers are formed readily (26), but it is not really known if they are impurity-vacancy complexes or interstitial clusters. The surprisingly large lattice dilations or contractions which were found here and by Mullin (5) indicate that simple substitutional incorporation, perhaps occasionally on the wrong sublattice, may not be the major mode of incorporation. Calculations based on simple electron bonding will be in error for the same reason. As long as the lattice effect of the compensating centers are unknown, computations based on covalent radii will be at best estimates.

Conclusion

With the demonstration that $Al_xGa_{1-x}As$ films could be reproducibly grown by LPE, lattice changes due to impurity incorporation have been measured. The observed lattice changes can be attributed to both electronic bonding effects and ion size effects, but the lack of the detailed knowledge of self-compensation effects makes it impossible at this time to reach more than a qualitative understanding of these changes.

Acknowledgments

The authors wish to thank D. Van Haren and S. M. Woelfer for their substantial assistance during this work.

Manuscript submitted May 27, 1981; revised manuscript received Sept. 23, 1981. This was 555 RNP presented at the Minneapolis, Minnesota, Meeting of the Society, May 10-15, 1981.

Any discussion of this paper will appear in a Discussion Section to be published in the December 1983 JOURNAL. All discussions for the December 1983 Discussion Section should be submitted by Aug. 1, 1983.

Publication costs of this article were assisted by Bell Laboratories.

REFERENCES

1. W. R. Wagner, *"Inst. Phys. Conf. Ser. #33b,"* L. F. Eastman, Editor, 65 (1977).
2. H. C. Casey, Jr. and M. B. Panish, *J. Cryst. Growth*, **13/14,** 818 (1972).
3. G. M. Kuznetsov, O. V. Pelevin, A. D. Barsukov, V. V. Olenin, and Savel'eva, *Jzv. Akad. Nowk. SSR Neorg. Mater.*, **9,** 759 (1973).
4. J. F. C. Baker, M. Hart, M. G. Halliwell, and R. Heckingbottom, *Solid State Electron.*, **19,** 331 (1976).
5. J. B. Mullin, B. W. Straughan, C. M. H. Driscoll, and A. F. W. Willoughby, *CRC Crit. Rev. Solid State Sci.*, 441 (Nov. 1975).
6. E. Estop, A. Izrael, and M. Saurage, *Acta Crystallogr.*, **A32,** 627 (1976).
7. M. Ettenberg and R. J. Paff, *J. Appl. Phys.*, **41,** 3926 (1970).
8. J. Whitaker, *Solid State Electron.*, **8,** 649 (1965).
9. W. J. Bartels and W. Nijman, *J. Cryst. Growth*, **44,** 518 (1978).
10. M. C. Rowland and D. A. Smith, *ibid.*, **38,** 143 (1976).
11. J. Zilko and P. J. Anthony, *This Journal*, **128,** 871 (1981).
12. R. W. James, "The Optical Principles of the Diffraction of X-Ray," Cornell U. Press, Ithaca, New York (1965).
13. M. C. Rowland and D. A. Smith, *J. Cryst. Growth*, **38,** 143 (1976).
14. C. Schiller, "Inst. Phys. Conf. Ser. #33a," C. Hilsum, Editor, p. 25 (1977).
15. F. K. Reinhart and R. A. Logan, *J. Appl. Phys.*, **44,** 3171 (1973).
16. J. Hornstra and W. J. Bartels, *J. Cryst. Growth*, **44,** 513 (1978).
17. L. Dawson, *ibid.*, **27,** 86 (1974).
18. E. D. Pierron, D. L. Parker, and J. B. McNeely, *J. Appl. Phys.*, **38,** 4669 (1967).
19. T. W. Baker, J. D. George, B. A. Bellamy, and R. Causer, *Nature*, **210,** 720 (1966).
20. H. T. Minden, R. Premo, and C. V. Collins, *J. Cryst. Growth*, **27,** 316 (1974).
21. A. J. Springthorpe, F. D. King, and A. Becke, *J. Electron. Mater.*, **4,** 101 (1975).
22. D. R. Ketchow, *This Journal*, **121,** 1237 (1974).
23. D. L. Rode, R. L. Brown, and M. A. Aframowitz, *J. Cryst. Growth*, **30,** 299 (1975).
24. Charles Evans and Associates, San Mateo, CA.

25. H. G. Hicks and P. D. Greene, "Inst. Phys. Conf. Ser. #9," 92 (1971).
26. C. M. Wolfe and G. E. Stillman, *Appl. Phys. Lett.*, **27**, 564 (1975).
27. H. Kressel, *J. Appl. Phys.*, **40**, 3587 (1969).
28. N. S. Belyaskaya, *Sov. Phys. Crystallography*, **17**, 129 (1972).
29. A. Fazzio, L. M. Brescansin, M. J. Caldas, and J. R. Leito, *J. Phys.*, **12**, L831 (1979).
30. P. J. Anthony, J. L. Zilko, V. Swaminathan, N. E. Schumaker, W. R. Wagner, and J. C. Norberg, *Appl. Phys. Lett.*, **38**, 434 (1981).

Deposition of GaAs Epitaxial Layers by Organometallic CVD

Temperature and Orientation Dependence

D. H. Reep* and S. K. Ghandhi*

Department of Electrical, Computer and Systems Engineering, Rensselaer Polytechnic Institute, Troy, New York 12181

ABSTRACT

Epitaxial layers of GaAs have been grown in an atmospheric organometallic CVD system, for a wide variety of gas phase reactant partial pressures and over a broad range of temperature (450°-1050°C). The growth rates for (100), (100) + 3° → <110>, (110), (111)Ga, and (111)As substrates are reported as functions of temperature and gas composition. Three distinct temperature dependent regions of growth are identified, corresponding to a mid-temperature mass transport limited range, a low-temperature kinetic controlled regime, and a high-temperature desorption limited region. The growth rate is studied as a function of the growth parameters and substrate orientation, and is related to the decomposition of the two reactants trimethylgallium and arsine. A model for the epitaxial growth of GaAs by the organometallic process is proposed, based on these findings.

The growth of thin epitaxial layers of GaAs, by the organometallic CVD technique, has received much attention recently. In particular, the use of such layers for optoelectronic (1, 2), microwave (3, 4), and high speed digital circuits (4) has given promising results. This technique has also produced layers approaching the purity and mobility of the best layers grown by the halide or hydride techniques, and has generated much interest due to its simplicity and flexibility.

Compared to the halide and hydride growth systems, little has been published in regard to the mechanisms of growth by the organometallic process. While it is considered to be a "simple" pyrolysis of trimethylgallium (TMG) and arsine, the growth of GaAs films by this technique certainly involves complex processes. This is, in part, due to the nature of the pyrolytic reaction, which occurs far from equilibrium and precludes reversal of the deposition reaction. Hence, there is no possibility of any "reordering" of the deposited GaAs film, in the sense of the reversible halide/hydride reactions, owing to the absence of an etching halogenic species in the deposition zone. This effect is most pronounced in terms of the resulting epitaxial layer morphology, as detailed in our earlier work (5).

In this paper, we report on the growth of GaAs epitaxial layers on a variety of substrate orientations [(100), (100) + 3° → <110>, (110), (111)Ga, and (111)As faces], and over a wide range of deposition temperatures and reactant partial pressures. We describe three distinct regions of growth: a mid-temperature mass transport limited region, a low temperature kinetically controlled growth regime, and a high temperature surface species desorption limited range. The dependence of the observed GaAs deposition rate on gas phase reactant partial pressures and substrate orientations is considered in conjunction with the activation energies of deposition that are associated with the three growth regions. A simple growth model is proposed, based on these observations.

Experimental Procedure

Epitaxial layers of GaAs were grown by the pyrolysis of arsine and TMG, using hydrogen as the carrier gas. Anhydrous hydrogen chloride was available for *in situ* etching of the GaAs substrates prior to epitaxial layer growth. The layers were deposited at temperatures ranging from 450° to 1050°C, with the input TMG partial pressure varying from 4.6-37 × 10^{-5} atm. Arsine flows were also varied over a wide range, corresponding to AsH_3/TMG ratios of 4.7-75 at the reactor inlet. The hydrogen carrier gas flow was fixed at 5 liters/min for all of the growth runs carried out for this study.

The single crystal semi-insulating GaAs substrate material that was used in this study was obtained from either Crystal Specialties, Incorporated, Monrovia, California or Cambridge Instruments, Incorporated, Monsey, New Jersey. The wafers were purchased lapped and chem-mechanically polished on one side, and were oriented (100), (100) + 3° → <110>, (110), or (111)As.

The (111)Ga substrates were prepared at our facility, by mechanically polishing the reverse side of (111)As wafers with successively finer grits, to a final 0.05 μm alumina (Buehler, Limited, Lake Bluff, Illinois) polish. After demounting from polishing slugs, the wafers were cleaned sequentially in baths of methanol, acetone, and trichloroethylene. A chemical polishing etch of 5 min duration, in a solution consisting of 11HNO_3 (70%): 49H_3PO_4 (85%) at 60°C, produced mirror-like, damage free (111)Ga surfaces (6).

The (100), misoriented (100), (110), and (111)As wafers were degreased as described earlier, and given a 1 min free etch in hot Caro's acid [3H_2SO_4 (97%): 1H_2O_2 (30%): 1H_2O, at 60°C], to remove any residual surface damage. This procedure gave mirror-like surfaces on all of these substrate orientations, and removed 15-25 μm from their surfaces.

The epitaxial reactor consisted of an atmospheric pressure, horizontal, rf heated, cold wall system as described earlier (7). Gases were delivered to the 50 mm ID quartz reaction chamber through 316 stainless steel or Monel tubing. The substrate temperature was monitored with a type R thermocouple (Pt/Pt-13% Rh), sheathed in quartz, and inserted into a well in the back of the graphite susceptor.

TMG (Alpha Products, Danvers, Massachusetts) vapor was introduced into the reactor by bubbling hydrogen through the liquid, which was held at 0°C in a stainless steel bubbler. An LED grade, 10% mixture of

* Electrochemical Society Active Member.
Key words: organometallic, OMVPE, OMCVD, epitaxy, gallium arsenide.

arsine in hydrogen (Air Products, Tamaqua, Pennsylvania), was used to provide AsH_3 in concentrations necessary for good epitaxial layer growth. A 1% mixture of electronic grade hydrogen chloride in hydrogen (Air Products, Tamaqua, Pennsylvania) was available for *in situ* etching of the substrate when required. Ultrapure hydrogen carrier gas was obtained by passing commercial grade hydrogen (Air Products, Tamaqua, Pennsylvania) through a Pd-Ag alloy purifier. In all cases, the reactants were mixed just prior to entry into the reaction chamber.

The substrates were loaded into the reactor immediately after chemical etching and microscopic inspection of their surfaces. The reactor was evacuated, and then purged with commercial grade argon (Air Products, Tamaqua, Pennsylvania), followed by hydrogen. After sufficient purging, the desired flows of hydrogen and arsine were set. For those experiments involving an *in situ* etch prior to growth, the susceptor was heated and allowed to stabilize at the etch temperature, typically 945°C. After a period of 5 min which was considered sufficient to remove any oxide on the GaAs surface left from the chemical free etch (8), the substrates were given an *in situ* etch of the type previously detailed (9). The susceptor temperature was then reset and allowed to stabilize at the growth temperature for 2 min prior to the commencement of TMG flow.

For experiments where no *in situ* etch was performed, the susceptor was heated to the growth temperature[1] and stabilized for 5 min, before the TMG flow was terminated, and the system maintained at the growth temperature for an additional 3 min. The susceptor was then allowed to cool in the AsH_3/H_2 atmosphere, followed by an argon purge after the temperature fell below 200°C.

The growth rate of the epitaxial layer was determined either by weight change, when no *in situ* etch was performed, or by cleaving and staining, followed by optical microscope inspection using Nomarski differential interference contrast. Scanning electron microscopy was employed to study the surface morphology.

The (100) + 3° → <110> orientation is often used in commercial practice. Consequently, an initial series of experiments were carried out with side-by-side growth on (100) and (100) + 3° → <110> oriented substrates for purposes of comparison. In all cases, these gave identical growth rates and morphology, which were dependent only on the growth parameters. Subsequently, the remaining experiments were conducted with simultaneous growth on (110), (111)Ga, and (111)As substrates, in addition to the (100) + 3° wafers, since they were more readily available for this study.

Results

All of the (100) layers (oriented as well as misoriented) showed good surface quality over a wide range of growth temperatures. Furthermore, the morphology was found to be essentially independent of the TMG or arsine flows for these samples as detailed earlier (5) for film growth at 700°C. However, layers grown on (110), (111)Ga, and (111)As faces showed a strong dependence of morphology on both the arsine and TMG flows. In the earlier study, it was also shown that for all growth conditions, the best morphology for these orientations was obtained with a gas phase AsH_3/TMG ratio at the reactor inlet in the 18-37 range. Consequently, the bulk of the growth rate data reported here will fall in this range as well.

The growth rate for the (100), (110), (111)Ga, and (111)As samples, plotted *vs.* reciprocal temperature, can be seen in Fig. 1 for inlet partial pressures of TMG equal to 1.8×10^{-4} atm and AsH_3 equal to 3.3×10^{-3} atm (AsH_3/TMG = 19). The apparent activation energies are shown for each orientation and for each of the three distinct growth regions. These are identified as a mid-temperature mass transport limited region, a low temperature kinetically controlled regime, and a high temperature desorption limited range.

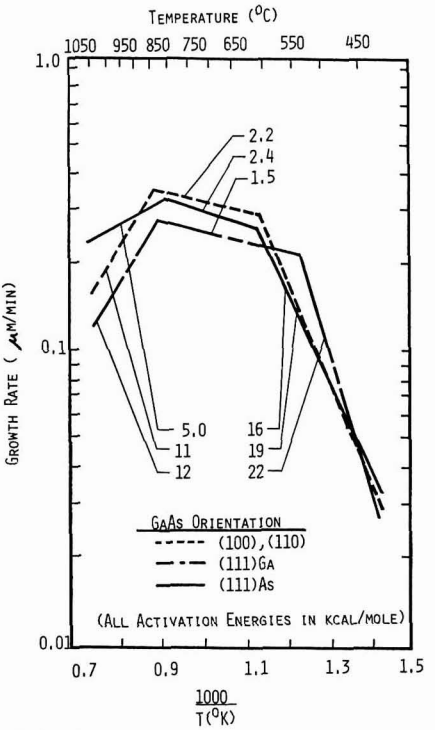

Fig. 1. Growth rate *vs.* reciprocal temperature for epitaxial layers on (100), (110), (111)Ga, and (111)As oriented GaAs substrates with $P_{TMG} = 1.8 \times 10^{-4}$ atm and $P_{AsH_3} = 3.3 \times 10^{-3}$ atm (AsH_3/TMG = 19).

Singling out one particular deposition temperature in each of the three growth regions, the effect of varying the TMG or AsH_3 partial pressures is seen in Fig. 2-4, as a function of substrate crystallographic orientation. Each of these regions will be considered separately, with the important features of each noted.

Mid-temperature, mass transport limited growth.— As seen from Fig. 1, the growth is weakly dependent on the deposition temperature between 600°-850°C. Here, the apparent activation energy ranges from 1.5 to 2.4 kcal/mol as is expected for diffusion controlled mass transport limited film growth (10). Additionally, the growth rate is relatively insensitive to the substrate orientation in this temperature region, with the maximum variation between the highest and lowest values shown being approximately 20%.

Figures 2a and b show the growth rate *vs.* P_{TMG} and P_{AsH_3}, respectively, at 700°C. Here, all substrate orientations used show the same linear variation in growth rate with P_{TMG}, and independence of growth rate (within the limits of experimental error) on P_{AsH_3}, as has been commonly reported in the literature (11-13). Moreover, in this mass transport limited regime, the nature of the growth mechanisms is masked since the growth rate is limited by the diffusion of the minority species in the gas stream to the growing crystal surface.

[1] A minimum of 700°C was used for the pregrowth heat-treatment, as this is just sufficient to rapidly remove any trace surface oxide (8). Thus, for those depositions performed below 700°C, the susceptor temperature was restabilized as appropriate following this deoxidation treatment.

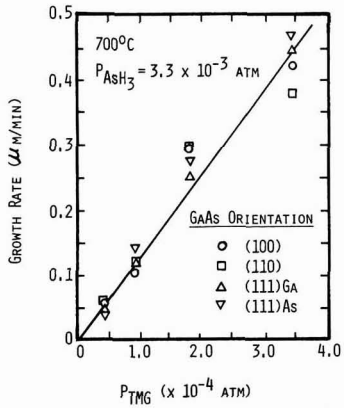

Fig. 2a. Growth rate vs. partial pressure of TMG for GaAs epitaxial layers at constant $P_{AsH_3} = 3.3 \times 10^{-3}$ atm and 700°C.

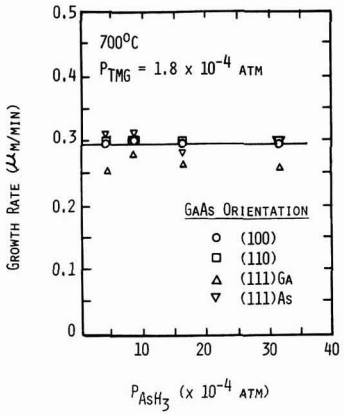

Fig. 2b. Growth rate vs. partial pressure of AsH_3 for GaAs epitaxial layers at constant $P_{TMG} = 1.8 \times 10^{-4}$ atm and 700°C.

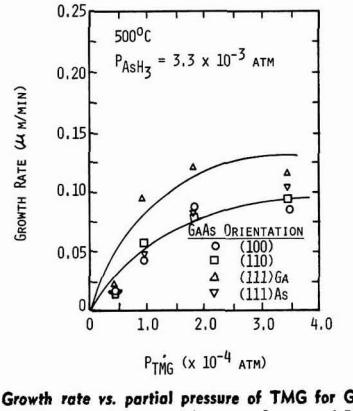

Fig. 3a. Growth rate vs. partial pressure of TMG for GaAs epitaxial layers at constant $P_{AsH_3} = 3.3 \times 10^{-3}$ atm and 500°C.

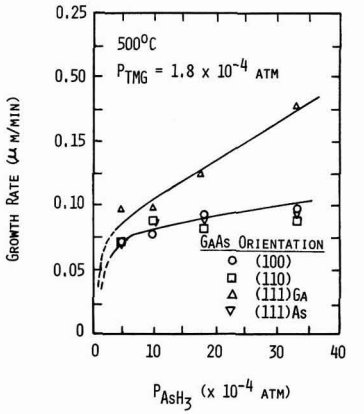

Fig. 3b. Growth rate vs. partial pressure of AsH_3 for GaAs epitaxial layers at constant $P_{TMG} = 1.8 \times 10^{-4}$ atm and 500°C.

Low temperature, kinetic controlled growth.—The deposition rate is kinetically limited at temperatures below approximately 600°C (550°C for the (111)Ga face), showing an overall activation energy for the deposition process ranging from 16 kcal/mol for the (111)As to 22 kcal/mol for the (111)Ga (Fig. 1). Figure 3a shows the effect of varying the TMG partial pressure while holding P_{AsH_3} constant at 500°C, while Fig. 3b shows the case for varying P_{AsH_3} at constant P_{TMG} again at 500°C. From these graphs, one can see that the (100), (110), and (111)As oriented layers all behave in a very similar manner, showing a slight sublinear variation of growth rate with P_{TMG} and weak dependence of the deposition on P_{AsH_3}. In contrast to this, the (111)Ga face shows strongly nonlinear behavior of the growth rate with P_{TMG}, and a significant dependence of growth rate on the magnitude of P_{AsH_3}.

High temperature, desorption limited growth.—For epitaxial deposition at temperatures greater than 850°C, the growth rate falls off with increasing temperature at a rate which is highly orientation sensitive (Fig. 1). The lowest fall off is seen for the (111)As face at 5 kcal/mol, whereas the (100), (110), and (111)Ga faces show a fall-off "activation energy" of 11-12 kcal/mol. The growth rate on the various orientations is also quite different, with growth on (111)As face being approximately 42% faster than the (111)Ga at 1000°C.

Finally, Fig. 4a and b show the growth rate *vs.* P_{TMG} and P_{AsH_3}, respectively, at 1000°C. Here, the deposition rate was found to be linear with P_{TMG}, with growth being fastest on the (111)As face, and slowest for the (111)Ga orientation, with intermediate values for the (100) and (110) faces. The deposition rate was also found to be independent of P_{AsH_3} at this temperature, for fixed P_{TMG}, but varied with crystallographic orientation in the same order as above.

Discussion

This section interprets our experimental results in terms of classical growth mechanisms which have been described in the literature. For simplicity, reacting species are written as TMG and AsH_3. However, the actual surface species which lead to GaAs growth are considerably more complex in organometallic CVD. Although their nature is uncertain, some conjectures will be made based on the available studies of decomposition of the reactants.

In previous studies, the pyrolysis of TMG and AsH_3 has been modeled both with a Langmuir-Rideal mechanism (14) where gas phase gallium species react with surface adsorbed arsenic, and by a Langmuir-Hinshelwood mechanism (15) where TMG and AsH_3 adsorb on the surface prior to partial decomposition and reaction. These two heterogeneous reaction mechanisms should be distinguishable by the dependence of the growth rate on the partial pressures of TMG and AsH_3 in the gas phase.

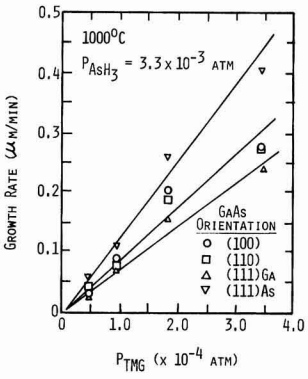

Fig. 4a. Growth rate vs. partial pressure of TMG for GaAs epitaxial layers at constant $P_{AsH_3} = 3.3 \times 10^{-3}$ atm and 1000°C.

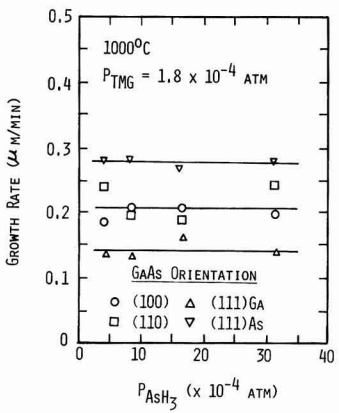

Fig. 4b. Growth rate vs. partial pressure of AsH_3 for GaAs epitaxial layers at constant $P_{TMG} = 1.8 \times 10^{-4}$ atm and 1000°C.

For the Langmuir-Rideal case, assuming AsH_3 is adsorbed prior to decomposition, the growth rate, R, is given by

$$R = K_1 \theta_{AsH_3} P_{TMG}$$

where K_1 is a rate constant, P_{TMG} is the gas phase TMG partial pressure, and θ_{AsH_3} is the surface coverage of arsine as predicted by the Langmuir adsorption isotherm (after (10))

$$\theta_{AsH_3} = \frac{\beta_{AsH_3} P_{AsH_3}}{1 + \beta_{AsH_3} P_{AsH_3}}$$

Here, P_{AsH_3} is the arsine gas phase partial pressure and β_{AsH_3} is the ratio of the rate constant for adsorption of arsine to the rate constant for desorption. If $\beta_{AsH_3} P_{AsH_3} >> 1$ due to strong arsine adsorption, then this equation reduces to

$$R = K_1 P_{TMG}$$

so that the predicted growth rate is linearly dependent on the partial pressure of TMG, and independent of the AsH_3 overpressure.

The Langmuir-Hinshelwood model for noncompetitive adsorption of TMG and AsH_3 [2] followed by surface reaction predicts that

$$R = K_2 \theta_{AsH_3} \theta_{TMG}$$

[2] Noncompetitive surface adsorption is expected, due to the strong Lewis acid-Lewis base interaction of AsH_3 with a Ga surface atom, or of an As surface atom with TMG. Thus, a two site adsorption mechanism is probable, as a result of this complexing of the reactants with the surface (16).

where the terms are analogous to those defined for the Langmuir-Rideal case, and

$$R = \frac{K_2 \beta_{AsH_3} \beta_{TMG} P_{AsH_3} P_{TMG}}{(1 + \beta_{AsH_3} P_{AsH_3})(1 + \beta_{TMG} P_{TMG})}$$

so that the predicted growth rate is sublinear in both TMG and AsH_3. This equation also assumes no hindering effect of desorption of reaction by-products such as CH_4 as has been experimentally verified (16).

Mid-temperature, mass transport limited region.— In the temperature range from 600°-850°C, the observed growth rate is linearly dependent on the TMG partial pressure and independent of the AsH_3 partial pressure. This is as expected for growth which is limited by diffusion of the less abundant species to the crystal surface. Moreover, the surface reactions proceed faster than this diffusion process, so that information on the growth rate gives little insight with respect to the mechanisms of reaction in this temperature range. Independence of growth rate on crystallographic orientation is also observed, since the surface dependent processes are effectively masked by the nature of the mass transport limited growth.

Low temperature, kinetically controlled growth.— Our results show that, over this temperature range, the growth of GaAs is sublinear with respect to both TMG and AsH_3 for all substrate orientations (Fig. 3a and b). Thus, the Langmuir-Hinshelwood model can be used to describe the growth process. Here, the adsorption of both arsenic and gallium species plays a role in this deposition. However, we propose that processes associated with arsenic adsorption dominate, since the growth rate on the (111)Ga face is higher than that on the (111)As face.

In this region, the measured activation energy for the deposition of GaAs on the (111)Ga face is 22 kcal/mol. Since this is very nearly the same as the energy measured for the heterogeneous decomposition of AsH_3 (23.2 kcal/mol, (17)) corresponding to rapid removal of the first H atom subsequent to adsorption, we postulate that the adsorption and rapid decomposition of arsine on the growing surface is the dominant process. Further, the lower value for the activation energy on the (111)As face (15 kcal/mol) suggests that the presence of the Ga-bearing reactant enhances the probability of chemisorption of AsH_2, probably as a result of coordination with these species. We expect this coordination to follow the gas phase partial pressure of the minority species (TMG), such that the decomposition remains a strong function of the minority reactant, as is verified by the experimental results of Fig. 3a.

The availability of many coordination sites for AsH_3 on the (111)Ga face should result in the growth being a function of the AsH_3 partial pressure, as seen in Fig. 3b. On the (111)As face, however, the growth should be relatively independent of the AsH_3 overpressure, since this surface provides an abundance of As atoms.

In the previous study (15), an activation energy of 13 kcal/mol was measured for the low temperature, surface catalyzed reaction of TMG and AsH_3, where no oriented single crystal substrate was present. A value of 13 ± 5 kcal/mol was reported previously (14), for the growth on (100)GaAs substrate material. Both of these values compare favorably with our results.

Thus, the growth of GaAs films at low temperatures is aided by the adsorption of both reactants leading to significant deposition even at low temperatures, where homogeneous AsH_3 decomposition cannot take place to any significant extent (18). Finally, comparison of the value for the third $GaCH_3$ bond dissociation energy (77.5 kcal/mol) (19) and the observed activation energy of GaAs deposition indicates that no gas phase reactions are expected to occur in this temperature range.

High temperature, desorption limited region.—In this region (>850°C), the growth rate falls off with in-

creasing temperature. This can be caused by gas phase depletion effects (which were not observed at the flow rates used in our experiments) or by increased desorption of reactant species. We note, however, that the growth rate varies linearly with P_{TMG} and is independent of the arsine overpressure to temperatures as high as 1050°C. This would indicate that the dominant factor controlling growth in the high temperature range is the desorption of the gallium species and not the arsenic species (14). Following this line of reasoning, we would expect the gallium species to be more strongly adsorbed on the (111)As face, resulting in a slower fall off with temperature than for the (111)Ga orientation. Moreover, we would expect the growth rate to be higher on the (111)As face due to the larger number of available gallium kink sites. Both of these observations were noted in our experiments (see Fig. 1 and 4).

Although desorption of the gallium species is the controlling factor, an important consideration is that growth takes place in an excess arsenic overpressure. Thus, the observed growth behavior may be explained by the Langmuir-Hinshelwood model (both species surface adsorb prior to reaction), where

$$\beta_{AsH_3} P_{AsH_3} >> 1 \text{ and } \beta_{TMG} P_{TMG} << 1$$

Under these conditions of relatively strong As adsorption, and increasing Ga-species desorption

$$R = K_2 P_{TMG}$$

as seen in our experimental results.

We have ruled out depletion reactions as a cause for the observed high temperature growth rate fall off for three reasons. First, we observed no gas phase reaction products either in the gas stream or on the reactor walls in the vicinity immediately preceding the hot susceptor, at the gas flows used in our work (total flow $\simeq$ 5 liters/min). Second, we observed no dependence of the fall off in growth rate on the AsH_3 partial pressure. This rules out gas phase TMG-AsH_3 coordination reactions of the type reported for the growth of GaInAs, where depletion of In from the gas phase increased monotonically with P_{AsH_3} (20). Third, the possibility of partial gas phase decomposition of TMG leading to polymers of the form $(GaCH_3)_n$ seems unlikely, since these polymers should react readily with AsH_3 at low temperatures (15, 16).

Nature of the surface species.—The form of the gallium and arsenic bearing species on the crystal surface has not yet been explicitly determined. However, several studies of the kinetics of TMG decomposition (19), the decomposition of arsine (17), the interaction of TMG with an arsenic film (21), and the surface interaction of TMG with AsH_3 (15, 16) can be used to gain some insight into their nature.

The study of the decomposition kinetics of TMG (19) gave dissociation activation energies of 59.5, 35.4, and 77.5 kcal/mol for the first, second, and third $GaCH_3$ bonds, respectively. For the temperature range of 400°-800°C, decomposition led to only formation of Ga-bearing polymers, presumably $(GaCH_3)_n$, in addition to CH_4, C_2H_6, and to a much smaller extent, several more complex hydrocarbons. Moreover, the rate constant for the dissociation of the first $GaCH_3$ bond was considerably higher than that of the second bond, even though its activation energy was higher. Thus, the rate limiter for the thermal decomposition of TMG is in all probability the breaking of the last $GaCH_3$ bond.

A study performed on the decomposition of AsH_3 (17) suggested that the rate limiter in this case is the removal of the first hydrogen atom or the energy for direct chemisorption onto the surface. Moreover, the chemisorption onto an As surface

$$AsH_3\ (g) \rightarrow AsH_2{}^* + H^*$$

(where the * denotes surface-adsorbed species) has been found to proceed with a relatively low activation energy of 23.2 kcal/mol, with subsequent hydrogen release being more rapid. In a later study (16), AsH_3 was found to decompose over GaAs at 172°C by a surface catalyzed reaction, lending support to the notion of its easy chemisorption followed by rapid decomposition.

A recent study detailing the homogeneous breakdown of AsH_3 using mass spectroscopy showed that the prevalent breakdown products are As and H_2 below 620°C, with As_2 and As_4 formation occurring only at higher temperatures (22). A study of the AsH_3 content of the gas stream of a cold wall organometallic CVD reactor near the end of the decomposition zone has also demonstrated significant amounts of undecomposed AsH_3 are present for a susceptor temperature of 700°C (23). This study provided additional evidence of enhanced AsH_3 breakdown in the presence of a GaAs substrate. Thus, at the growth temperatures commonly used for organometallic deposition of GaAs, the limited communication between the gas stream and hot susceptor at typical flow rates combined with the surface catalyzed breakdown of AsH_3 would suggest that the amount of As_2 and As_4 present will be less than that predicted by thermodynamics.

The interaction of TMG and AsH_3 enhances the breakdown of the Ga-bearing reactant. Support of this comes from the observation that heated mixtures of TMG and AsH_3 give products of the form $(CH_3)_{3-x}$-$GaAsH_{3-y}$ which eventually evolve to GaAs by 420°C (15). Moreover, these partial decomposition products react with AsH_3 at temperatures as low as 364°C to give GaAs (16), and TMG breaks down in the presence of an arsenic-coated surface at temperatures in the vicinity of 285°C (21). In contrast, the decomposition of TMG to gallium in the absence of an As-bearing species has not been observed below 800°C (19).

Based on these observations, we propose that the most probable situation is that $GaCH_3$* and AsH* are the primary reactant species on the growing surface. Moreover, the abundance of hydrogen ($P_{H_2} \simeq 1$ atm) in our system should lead to a large surface population of AsH*, and promote dissociation of As_2 and As_4 species. The deposition reaction may follow

$$GaCH_3{}^* + AsH^* \rightarrow (CH_3Ga - AsH)^*$$

$$(CH_3Ga - AsH)^* \rightarrow GaAs_{(s)} + CH_{4(g)}$$

Thus, at growth temperatures above 420°C, the sequential demethylation of $(CH_3)_{3-x}GaAsH_{3-y}$ seems unlikely, in view of the probable surface catalyzed formation of CH_3Ga-AsH.

An alternate viewpoint is that $GaCH_3$* is chemisorbed on the surface and diffuses to a gallium kink site where it eventually forms GaAs. This process is enhanced by the presence of arsenic, so that this reaction most probably proceeds as follows

$$AsH^* \rightarrow As_{As} + H^*$$

$$GaCH_3{}^* + As_{As} + H^* \rightarrow GaAs_{(s)} + CH_{4(g)}$$

where As_{As} denotes arsenic on an arsenic lattice site. Finally, the reaction may be aided by the formation of C_2H_6, as detected both in the absence of AsH_3 (19) as well as in its presence (24). This would correspond to

$$2AsH^* \rightarrow 2As_{As} + H_{2(g)}$$

$$2GaCH_3{}^* + 2As_{As} \rightarrow 2GaAs_{(s)} + C_2H_{6(g)}$$

We note, however, that this situation is less probable than the previous, since TMG is the lesser reactant and much less abundant than hydrogen. Moreover, the excess of the As-species would suggest that interaction of the adsorbed Ga- and As-bearing reactants would occur faster than the Ga-species would find a lattice kink site. The distinction here is whether mobile Ga- and As-bearing reactants diffuse to their appropriate kink sites prior to decomposing, or whether these

species interact to form a mobile $(CH_3Ga\text{-}AsH)^*$ complex[3] which diffuses to the growing crystal step. Neither of these cases greatly alters the growth model, as both should fit a Langmuir-Hinshelwood type reaction and will be indistinguishable based on studies of the reactant input partial pressures and overall deposition process.

The gas phase complexing of AsH_3 with TMG has not been detected (15); however, the possibility of such a complex diffusing to the crystal surface and heterogeneously decomposing cannot be entirely ruled out.

In summary, therefore, the actual gas phase and surface reaction processes are quite complex. However, the primary result of these processes is the strong adsorption of $GaCH_3$* and AsH* on the surface of the gallium arsenide over the useful practical range of growth temperatures.

Conclusions

We conclude that the deposition of GaAs epitaxial layers by the pyrolysis of TMG and AsH_3 most probably occurs following a Langmuir-Hinshelwood type reaction. That is, both the gallium- and arsenic-bearing reactants are expected to adsorb on the growing crystal face prior to reaction. Furthermore, such a reaction is heterogeneous in nature, and no evidence of gas phase reactions was found even in the high temperature range.

Three distinct growth regions were identified as the deposition temperature was increased from 450°-1050°C. The low temperature kinetically controlled growth regime was characterized by an orientation dependent deposition rate and activation energy that suggest the chemisorption and subsequent decomposition of the As-bearing species is essential to the growth in that region. Furthermore, the deposition in this range was found to vary sublinearly with the gas phase partial pressures of both the Ga- and As-bearing reactants, as predicted by the Langmuir-Hinshelwood model. From approximately 600°-850°C, a mass transport limited growth region was observed. Here, the apparent activation energy for the deposition of GaAs epitaxial layers corresponded to growth which was limited by reactant diffusion through a stagnant boundary layer. Finally for temperatures above 850°C, a decrease in the layer growth rate with increasing temperature was noted. This was explained on the basis of $GaCH_3$ desorption, since even in that region, the growth was independent of the gas stream partial pressure of AsH_3. The substrate orientation dependence of the observed high temperature fall off in deposition rate was used to provide evidence of a lack of significant depletion effects for our reported flow conditions, and to give further support to the Langmuir-Hinshelwood growth model.

[3] This case is essentially analogous to that suggested to explain experimental results for the halide growth of GaAs, where AsGaCl is thought to be the mobile reactant responsible for deposition (25).

Acknowledgments

The authors wish to thank R. Reep and A. Hayner for manuscript preparation. This work was supported by the Solar Energy Research Institute, Golden, Colorado, under Contract No. XS-0-9002-4.

Manuscript submitted Sept. 3, 1982; revised manuscript received Oct. 22, 1982.

Any discussion of this paper will appear in a Discussion Section to be published in the December 1983 JOURNAL. All discussions for the December 1983 Discussion Section should be submitted by Aug. 1, 1983.

Publication costs of this article were assisted by Rensselaer Polytechnic Institute.

REFERENCES

1. R. R. Bradley, *J. Cryst. Growth*, **55**, 223 (1981).
2. J. P. André, P. Guittard, J. Hallais, and C. Piaget, *ibid.*, **55**, 235 (1981).
3. M. Bonnet, N. Visentin, G. Bessonneau, and J. P. Duchemin, *ibid.*, **55**, 246 (1981).
4. T. Nakanisi, T. Udagawa, A. Tanaka, and K. Kamei, *ibid.*, **55**, 255 (1981).
5. D. H. Reep and S. K. Ghandhi, *ibid.*, Submitted.
6. D. J. Stirland and B. W. Straughan, *Thin Solid Films*, **31**, 139 (1976).
7. K. P. Pande, D. H. Reep, S. K. Shastry, A. S. Weiner, J. M. Borrego, and S. K. Ghandhi, *IEEE Trans. Electron Devices*, **ed-27**, 635 (1980).
8. M. Otsubo, T. Oda, S. Mitsui, and H. Miki, *This Journal*, **124**, 1907 (1977).
9. R. Bhat, B. J. Baliga, and S. K. Ghandhi, *ibid.*, **122**, 1378 (1975).
10. D. W. Shaw, in "Crystal Growth," Vol. I, C. H. L. Goodman, Editor, p. 1, Plenum Press, New York (1974).
11. H. M. Manasevit and W. I. Simpson, *This Journal*, **116**, 1725 (1969).
12. A. L. Lin, V. Dao, and L. F. Donaghey, in "Chemical Vapor Deposition 1977," L. F. Donaghey, P. Rai-Choudhury, and R. N. Tauber, Editors, p. 264, The Electrochemical Society Softbound Proceedings Series, Princeton, NJ (1977).
13. S. J. Bass, *J. Cryst. Growth*, **31**, 172 (1975).
14. W. H. Petzke, V. Gottschalch, and E. Butter, *Krist. Tech.*, **9**, 763 (1974).
15. D. J. Schlyer and M. A. Ring, *This Journal*, **124**, 569 (1977).
16. D. J. Schlyer and M. A. Ring, *J. Organomet. Chem.*, **114**, 9 (1976).
17. K. Tamaru, *J. Phys. Chem.*, **59**, 777 (1955).
18. V. S. Ban, *This Journal*, **118**, 1473 (1971).
19. M. G. Jacko and S. J. W. Price, *Can. J. Chem.*, **41**, 1560 (1963).
20. J. S. Whiteley and S. K. Ghandhi, Submitted to *This Journal*.
21. D. J. Schlyer and M. A. Ring, *J. Organomet. Chem.*, **71**, C25 (1974).
22. A. R. Calawa, *Appl. Phys. Lett.*, **38**, 701 (1981).
23. M. R. Leys and H. Veenvliet, *J. Cryst. Growth*, **55**, 145 (1981).
24. N. N. Travkin, B. G. Gribov, C. P. Rumyantseva, I. G. Tonoyan, and E. N. Zorina, *J. Gen. Chem. USSR*, **45**, 316 (1975).
25. J. L. LaPorte, M. Cadoret, and R. Cadoret, *J. Cryst. Growth*, **50**, 663 (1980).

The Uranyl Ion, Fluorescent and Fluorine-Like: A Review

Christian K. Jørgensen

Département de Chimie Minérale, Analytique and Appliquée, Université de Genève, CH 1211 Geneva 4, Switzerland

and Renata Reisfeld

Enrique Berman Professor of Solar Energy, Department of Inorganic Chemistry, Hebrew University, Jerusalem, Israel

ABSTRACT

The uranyl ion has rather unique stereochemistry, and its ultraweak electron transfer bands are compared with other transition-group spectra. The 6 most recent MO calculations are shown to be inconclusive about the distribution of the many excited levels. The first excited state has very different chemical properties compared with the ground state, reacts with polarizable cations and anions, and shows a potent photochemistry of electron and of hydrogen atom abstraction. Its fluorescence (with much higher quantum yield in glasses than in aqueous solution) can be used for flat-plate concentrators of solar energy.

The fluorescence of uranyl compounds first studied by Brewster 1833 allowed Stokes to formulate his law (of photon energies lower or equal to the beginning of the first absorption band) in 1852 and played an incidental (but fate-changing) role in Becquerel's discovery of radioactivity in 1896. Contrary to absorption spectra approximately following Beer's law, the study of luminescence lacks notoriously a proportional (or even a monotonic) dependence of intensity on concentration, and in many cases, a tiny concentration of an "activator" (frequently of unknown constitution) provides the fluorescence. On the other hand, efficient energy transfer to quenchers, or concentration quenching due to cross-relaxation (1) may prevent the light emission. The first inorganic stoichiometric compound not needing a trace activator was a uranyl salt. This does not prevent that also uranium(VI) frequently acts as activator (1-6) in vitreous and crystalline solids.

The interpretation of excited states of luminescent species usually goes through a preliminary study of the absorption spectrum. In most of this century, there has been general agreement that the narrow absorption bands of trivalent lanthanides (of which the positions hardly depend on the ligating atoms) represent transitions to excited J-levels of a partly filled 4f shell (1), and in 1933, the same proposition was made for green $5f^2$ uranium(IV) compounds, which recently (7) could be compared with U^{+4}. This is so much more remarkable as the only gaseous M^{+3} of the 4f group with identified J-levels are Ce^{+3}, Pr^{+3}, and Yb^{+3}. On the other hand, the assignment of the (usually broader) absorption bands of d-group compounds only developed after 1954 (8, 9). The two main categories are "ligand field" transitions (9, 10) between approximately nonbonding and antibonding orbitals belonging to the partly filled d-shell, and electron transfer spectra (8, 11) of which the most common type involves one (or several) reducing ligands loosing one electron to empty or partly filled d-like orbitals centered on an oxidizing atom.

Since cerium(IV) is a closed-shell system isoelectronic with xenon, there was no doubt that the broad absorption bands in the near ultraviolet, providing the orange to yellow colors, are due to electron transfer, and the high wave-numbers for 4f → 5d excitation (1) in cerium(III) and the detection (12, 13) of electron transfer bands in $4f^6$ europium(III), $4f^{13}$ ytterbium (III), $4f^5$ samarium(III), and $4f^{12}$ thulium(III) left no doubt that the electron goes to the 4f shell. In view of the ground states of U(V) and U(IV) belonging to $5f^1$ and $5f^2$, it was highly likely that the yellow colors of uranyl compounds are due to electron transfer to the empty 5f shell.

Key words: inorganic, solar, visible, quantum theory.

The crystal structures (14) frequently show a linear OUO^{+2} group, with the U-O distance as short as 1.7-1.8Å, to be compared with distances between 2.2 and 2.5Å to 6 or 5 oxygen or fluorine atoms in the equatorial plane. Like CO_2 and CO, the uranyl ion lacks proton affinity in solution, and the very slow ^{18}O exchange shows that tautomeric rearrangement to $U(OH)_4^{+2}$ does not occur. At this point, the chemistry of U(VI) is strikingly different from Cr(VI), Mo(VI), and W(VI) but shows some similarity (15) with *trans*-dioxo octahedral complexes of the diamagnetic (two electrons in a nonbonding xy-orbital) $4d^2$ ruthenium (VI), $5d^2$ rhenium (V), and $5d^2$ osmium(VI).

Seen from a spectroscopic point of view, it is surprising that the first electron transfer band of uranyl ions occurs already close to 20,000 cm^{-1} (2.5 eV) when compared with molybdate (43,200 cm^{-1}) and tungstate (50,300 cm^{-1}) of similar chemically oxidizing character. These tetroxo complexes (16, 17) also show unexpected trends compared with hexahalide complexes (11). Though the orange CrO_3X^- have their first electron transfer band earlier than the unsubstituted chromate, the wave number hardly depends on X = F, Cl, Br, or OH, and the usual treatment of optical electronegativities (9, 11) useful not only for halides, but also for many other ligands, is not as convincing for oxide (1, 18). It may be noted that the parameter 30,000 cm^{-1} (allowing x_{opt} for halides to have the Pauling values of the electronegativity x) most unexpectedly has shown up (19, 20) as the product of 3.7 eV and x_{opt} being roughly 1 eV lower than the lowest ionization energy I of gaseous halide molecules, and 0-1 eV higher than I of solid halides. The apparently excessive oxidizing character of U(VI) is also remarkable (6, 21) by comparison of UF_6 and WF_6.

It is very characteristic for uranyl complexes that they are highly anisotropic (22), the (much broader, and relatively more intense) electron transfer bands due to reducing ligands in the equatorial plane have wave numbers in much better agreement with x_{opt} determined from many other complexes. Thus, the fox-red color, of uranyl complexes of sulfur-containing ligands and of ferrocyanide, and orange $UO_2I_4^{-2}$, indicate x_{opt} of U(VI) as low as 1.8; whereas, x_{opt} = 3.1 for the two oxo ligands would provide x_{opt} = 2.4 for U(VI) to be compared with 1.8 (1.5, when corrected for spin-pairing energy) for U(IV) in UI_6^{-2} (22).

The anomalous low wave number of the electron transfer band due to the two ligands with exceptionally short U-O internuclear distances is not the only enigmatic aspect of the uranyl ion. The oscillator strength P (called f by many authors) is $4.32 \cdot 10^{-9}$ times the integrated area of the molar extinction coefficient as a function of the wave number, and is 7.2

$\cdot 10^{-5}$ for the whole blue and violet region between 20,000-25,000 cm^{-1} (23) now known to represent at least four electronic transitions as discussed below. This value is only one order of magnitude higher than for the narrow bands of trivalent lanthanides (1) and is much smaller than 10^{-3} characterizing parity-forbidden transitions (8) from even MO to d-like orbitals in hexahalide complexes, or 0.02-0.5 for corresponding parity-allowed transitions from odd MO.

In so far as the excitations are manifestly localized within the triatomic uranyl group, there is no longer any doubt that these ultraweak transitions are all parity-forbidden and, hence, go from π_u or σ_u orbitals formed mainly from oxygen 2p orbitals on a LCAO picture (6) to the empty 5f shell. There are certainly no parity-allowed transitions below 30,000 cm^{-1}; whereas, a rather indefinite background slope is raising at higher energies (2). It has been noted for a long time (23, 24) that the absorption spectrum consists of a roughly equidistant series of maxima with the distance around 700 cm^{-1}. The fluorescence emission spectrum typically shows 5-6 approximately equidistant peaks (one coinciding with the Stokes threshold at 20,600 cm^{-1} or 485 nm in the aqua ion) with a separation close to 850 cm^{-1}. This increased difference is interpreted as vibrational structure, the electronic ground state having a higher force constant than the excited state. The large Stokes shift indicates the equilibrium internuclear distances to be considerably elongated in the excited state.

However, it cannot be justified to speak about one excited state. It seems to be a numerical accident that the energy differences between several electronic states happen to be close to a multiple of the lower vibrational wave number, and still the intensity distribution and the variation of subsequent distances are perceptibly irregular. This situation was clarified by the careful study of $Cs_2UO_2Cl_4$ at liquid helium temperature by Denning, Snellgrove, and Woodwark (25) using isotopic ^{18}O substitution to shift the vibrational structure and identify 11 electronic origins between 20,096 and 27,758 cm^{-1}. It had previously been noted (24, 26) that the appropriate quantum number (besides even or odd parity) to use in the linear uranyl ion is Ω being O^+, O^-, or a positive integer (10, 27) having the same relation to J in spherical symmetry as Λ has to L. In particular, states with well-defined M_J have $\Omega = |M_J|$. The excited states of the uranyl ion are rather unique by combining strong effects of spin-orbit coupling ($^2F_{7/2}$ of $5f^1$ is situated (28) 7609 cm^{-1} above $^2F_{5/2}$ in gaseous U^{+5}, and the absorption spectrum of aqueous uranyl perchlorate (24) seems to repeat itself after 7900 cm^{-1} above the first origin) with almost coinciding energy of at least four 5f-like orbitals with symmetry types ϕ_u and δ_u. One corollary (26) is that it has no meaning to discuss whether the excited states (14) are triplet ($S = 1$) or singlet. The two MO of symmetry type π_u are expected to have the component $\omega = 3/2$ at slightly higher energy than $\omega = 1/2$. This separation is hardly due to spin-orbit coupling operating close to the oxygen nuclei, but could be a few thousand cm^{-1} by participation of the empty U7p or filled U6p in LCAO descriptions. The σ_u has exactly $\omega = 1/2$. Each of such two ω values provides 16 Ω values by transfer of an electron to the 5f shell. The lowest excited state (25) has selection rules in polarized light clearly indicating $\Omega = 1$. This can be interpreted as transfer of π_u ($\omega = 3/2$) to the lowest ($\Omega = 5/2$) component of $^2F_{5/2}$ representing about equal squared amplitude (24) of ϕ_u and δ_u. Another alternative is transfer of σ_u ($\omega = 1/2$) to the ($\Omega = 3/2$) component of $^2F_{5/2}$ expected (29, 30) to be some 2000 cm^{-1} above the ($\Omega = 5/2$) component. However, it is conceivable that the ligands in the equatorial plane destabilize ϕ_u to a slightly larger extent than δ_u. Denning *et al.* (25) assign six Ω values to the 11 origins found in $Cs_2UO_2Cl_4$, the tetragonal symmetry induced by the four equatorial chloride ligands splitting positive even Ω value by several hundred cm^{-1}. Denning prefers the second alternative, but this question is by far not resolved (6). It is beyond dispute that several (of at least 16) Ω values correspond to weak transitions hidden in the background.

One might have hoped that MO calculations might throw light on the problem whether σ_u or π_u is most readily excited. There have been several previous attempts (14), but Table I gives the predicted ionization energies I in eV (= 8065.48 cm^{-1}) of four relativistic calculations (31-34) at a high level of sophistication, and of one parameterized extended Hückel calculation (35). Wadt (36) is interested in the gaseous molecule ThO_2 (known to be bent at 122°), and Table I includes the results for linear ThO_2 with the distance $R = 1.92$Å and for the isoelectronic UO_2^{+2} assuming the short $R = 1.64$Å. Both Walch and Ellis (31) and Boring and Wood (33, 34) agree with the Denning hypothesis (that σ_u is the highest occupied MO), but in all three cases, even MO occur less than 1 eV below σ_u. This difficulty does not occur for Pyykkö and Lohr (35) nor for the ThO_2 calculation (36); whereas, the two other uranyl calculations (32, 36) have an even MO highest. The precision of these results does not seem better than 2 eV, making them inconclusive for the description of the electron transfer spectrum. It must be said in all fairness that the order of MO energies is more significant than the zero-point of energy. The neglect of a background Madelung potential for the uranyl cation has increased the four first lines of Table I by a contribution of the order 10 eV, but four calculations (on a comparable level of sophistication) of the neutral molecule UF_6 (33, 37-39) also scatter by several eV (6) though much better agreement exists about the order of MO energies, and the result that the highest occupied MO are the t_{1u} in contradistinction to t_{1g} in all other neutral hexafluorides and hexahalide anions. The dispersion of results for the uranyl ion in Table I is comparable to the effect of throwing dice.

A very interesting aspect of the calculations is that the squared amplitude of U5f character in the highest filled σ_u orbital is 0.87 by Pyykkö and Lohr (35), 0.59 by Boring and Wood (33), and in the results of Wadt (36) 0.57 for UO_2^{+2} (though here, σ_g is the highest MO), and 0.25 for linear ThO_2. A squared U5f amplitude well above ½ would mean that the visible absorption of uranyl compounds is not strictly speaking due to electron transfer, but to an electron jumping from a bonding to approximately nonbonding 5f-like orbitals, and also that the conditional oxidation state (9) of the ground state is U[IV]. This hypothesis has been further analyzed (40), and it is argued that if Denning's proposal of lower excitation energy of σ_u than of π_u is valid, it is rather due to "pushing from below" by the filled U6p orbitals having moderate I. The latter explanation is recognized in UF_6 (33, 38)

Table I. Calculated molecular orbital (MO) ionization energies in eV

Ref.	5f (ω = 3/2)	5f (ω = 5/2)	σ_u	π_u	π_g	σ_g
(31)	22.0	22.2	22.5	25.3	24.5	23.5
(32)	24.0	24.3	26.5	25.6	24.6	26.3
(33)	—	19.6*	23.1	23.6	23.5	24.9
(34)	19.38	19.52	23.0	23.3	23.2	24.6
(35)	—	—	10	12	13	13
(36), UO_2^{+2}	—	—	29.5	29.4	29.5	28.7
(36), linear ThO_2	—	—	8.8	10.7	11.9	12.3

* This value is obtained by correcting I = 19.09 eV reported for ϕ_u and δ_u by the spin-orbit stabilization 0.54 eV in gaseous U^{+5}.

where the squared U6p amplitude in the highest occupied MO (t_{1u}) is 0.09 and 0.07, and the large calculated spin-orbit coupling corresponds to about a-tenth U6p character (6). By the same token, Wadt (36) finds 0.09 in UO_2^{+2} and 0.15 Th6p character in linear ThO_2. Several authors (34, 36) point out that the U6p character increases strongly as a function of decreasing R. Hence, the high energy of σ_u is a specific effect of very short R.

This whole grid of rationalizations may have a weak point. All MO calculations tend to overestimate the extent of covalent bonding, when the d- or f-shell of a transition-group central atom has the same (or slightly higher) ionization energy I as the loosest bound orbitals of the ligands. A closer analysis (41-43) shows that this paradox has its root in the electron affinity of the partly filled shell (being much smaller than I in the case of small average radii) being the significant quantity to be compared with I of the ligands. It would seem that the calculations (33, 35, 36) predicting the squared amplitude of U5f in σ_u to be above ½ are influenced by the somewhat accidental coincidence of (predicted) I (U5f) and I (O2p). At this point, it should not be neglected that I (O2p) of solid oxides is known from photoelectron spectra (19, 20, 41) to fall in the interval 10-11 eV in most cases, and I (F2p) of solid fluorides usually between 12-13 eV.

The first excited state of the uranyl ion is notable both for its fluorescence and for its extensive photochemistry (2, 14, 44, 45). An excited state living for longer than some 10^{-9} sec looses its vibrational energy to the thermal reservoir of the surrounding condensed matter, and remains in the vibrational ground state (if the frequencies are much higher than kT) of the electronically excited state. Adamson (46, 47) calls such thermally equilibrated excited states "thexi" states. Frequently, their chemistry is highly different from the electronic ground state, corresponding to noble-metal central atoms with conspicuous chemical polarization (48). The excited state is simultaneously much more reducing and much more oxidizing than the ground state, by having its free energy increased by the Stokes threshold $h\nu$. Thus, the standard oxidation potential $E°$ for ionization $G \rightarrow G^+$ of the ground state is decreased to $(E° - h\nu)$ for the oxidation of the thexi state $T \rightarrow G^+$; $E_*°$ of the process $G^- \rightarrow G$ expressing the oxidizing character of G is increased to $(E_*° + h\nu)$ for $G^- \rightarrow T$. This argument is slightly modified by the Franck-Condon co-excitation of vibrations, but it is true within 1/10 eV that $E°$ for $UO_2^+ \rightarrow UO_2^{+2} = +0.06V$ (relative to the standard hydrogen electrode; it is (20, 48) +4.5V relative to vacuo) is increased by $h\nu = 2.56$ eV to close to +2.6V indicating an oxidizing character of the excited uranyl ion (in the following $*UO_2^{+2}$) almost as strong as of free fluorine. Seen from this point of view, one would have expected the photolysis of water to $2H_2 + O_2$ by visible light to have been much easier than it seems to be in practice (49, 50). It is also clear that the redox reactions of a thexi state during its lifetime are more determined by kinetic activation energy than by considerations of free energy.

Einstein proposed in 1917 a formula for the radiative half-life of an excited state (1, 6) being inversely proportional to the product $P(h\nu)^2$. The first ($\Omega = 1$) state of the uranyl ion has (at most) $P = 5 \cdot 10^{-6}$ corresponding to a mean lifetime (equal to 1.44 times the half-life for exponential decay) of 1.4 msec. Such lasting luminescence is known for several crystalline uranyl salts, and glasses; whereas, the lifetime is close to 10^{-6} sec for aqua ions (51, 52) though slightly dependent on pH and temperature. However, 0.67-15M phosphoric acid increases the lifetime to values between 0.2-0.02 msec, to be compared with 0.4 msec in phosphate glass of stoichiometry $NaPO_3$ (29, 51, 53). Since a single anion bound in the equatorial plane in many cases stretch the lifetime by a factor of 20-100, it cannot be argued that the nonradiative de-excitation by ephemeral hydrogen atom abstraction from water molecules (52) is prevented by lack of coordinated H_2O, but it may suggest that the H atom is abstracted close to one of the oxygen atoms in $*UO_2^{+2}$. If the ground state has a charge distribution (9) close to $z = +3$ on U and -0.5 on O, the thexi state may have almost neutral oxygen atoms. It would be comparable to O_2^+ if $z = +2$ for uranium in the ground state.

Many reducing anions quench the uranyl fluorescence (14, 51, 53) show the two main reactions induced by $*UO_2^{+2}$, electron, and (of greater versatility in organic molecules) hydrogen atom abstraction. Flash photolysis of uranyl solutions containing $Mn(OH_2)_6^{+2}$ produces purple manganese(III) aqua ions (54). Several other cations, usually with high chemical polarizability (48), quench, and it can be shown (55, 56) that $*UO_2^{+2}$ binds one silver(I), and one or two thallium(I) cations. The $5f^2$ system neptunium(V) NpO_2^+ reacts already in its ground state (57) with Al(III), Fe(III), In(III), Th(IV), and many other aqua ions, and it is possible (58) to isolate $ONpOM(OH_2)_5^{+4}$ with M = Cr and Rh. A comparable U(V) and Cr(III) adduct is formed (59) by reducing UO_2^{+2} with chromium(II) aqua ions. Both UO_2^+ and NpO_2^+ form adducts with UO_2^{+2} which were recently reviewed (6, 60). It is not surprising that $*UO_2^{+2}$ shows even more complicated behavior; Marcantonatos (52, 61) argues that exciplexes such as $*UO_2HUO_2^{+4}$ are formed, with the emission spectrum slightly different from $*UO_2^{+2}$. Oligomeric hydroxo-bridged complexes might form (6) at slightly higher pH.

The 10^{-8}M uranyl carbonate complexes present in sea water (and sometimes higher concentrations in rivers and lakes) are excited, on the average, every 10 min, when the sun stands in zenith. It is possible (15) that this catalyst (with rapid turn-over) photooxidizes otherwise nonbiodegradable organic compounds arriving in the ocean from the large Amazon and Zaire rivers.

The fluorescence of uranyl glasses (62) and subsequent energy transfer (1, 63) to neodymium(III) and holmium(III) has been applied in flat-plate luminescent concentrators, trapping the radiation by a sequence of total reflections and, hence, diminishing the area of photovoltaic silicon on the rim of the plate an order of magnitude, relative to the plate area (64).

$*UO_2^{+2}$ is dark blue, having an intense broad band in the yellow (14). Among its other unusual physical properties is the Becquerel effect (65) of imperfectly understood differences between electrode potentials in illuminated and dark volumes of a uranyl solution. We have been speaking as if $*UO_2^{+2}$ is represented exclusively by the first excited state. Actually, it seems as if the previous reports about fluorescence originating in a second state have been reinterpreted as traps in cooled $Cs_2UO_2Br_4$ crystals (66) and as vibrational structure (67). Nevertheless, it is true (68) that all excited states start immediately to luminesce, with an integrated quantum yield which is the ratio between the observed and the (Einstein) radiative lifetime. The 48 Ω levels due to transfer of an electron from the odd MO to the 5f shell (they would split into 84 electronic origins in sufficiently low symmetry of the equatorial plane) must decay very rapidly to the ($\Omega = 1$) origin. If these levels have a radiative half-life of 1 msec, a higher level with the half-life 10^{-8} sec would have the quantum yield of 10^{-5}.

Besides the fascinating spectroscopic and photochemical properties, the inexpensive ^{238}U available as by-product from isotope separation may help the uranyl fluorescence contributing to utilization of solar energy (64, 69).

Acknowledgment

This work was made possible by the grant no. 2.841-080 from the Swiss National Science Foundation.

Manuscript received July 6, 1982. This was Paper 476 presented at the Montreal, Canada, Meeting of the Society, May 9-14, 1982.

Any discussion of this paper will appear in a Discussion Section to be published in the December 1983 JOURNAL. All discussions for the December 1983 Discussion Section should be submitted by Aug. 1, 1983.

Publication costs of this article were assisted by The University of Geneva.

REFERENCES

1. R. Reisfeld and C. K. Jørgensen, "Lasers and Excited States of Rare Earths," Springer-Verlag, Berlin (1977).
2. E. Rabinowitch and R. L. Belford, "Spectroscopy and Photochemistry of Uranyl Compounds," Pergamon Press, Oxford (1964).
3. G. Blasse, *This Journal*, **124**, 1280 (1977).
4. W. A. Runciman and E. Y. Wong, *J. Chem. Phys.*, **71**, 1838 (1979).
5. K. C. Bleijenberg, *Struct. Bonding*, **42**, 97 (1980).
6. C. K. Jørgensen and R. Reisfeld, *ibid.*, **50**, 121 (1982).
7. C. K. Jørgensen, *Chem. Phys. Lett.*, **87**, 320 (1982).
8. C. K. Jørgensen, *Adv. Chem. Phys.*, **5**, 33 (1963).
9. C. K. Jørgensen, "Oxidation Numbers and Oxidation States," Springer-Verlag, Berlin (1969).
10. C. K. Jørgensen, "Modern Aspects of Ligand Field Theory," North-Holland Publ. Co., Amsterdam (1971).
11. C. K. Jørgensen, *Prog. Inorg. Chem.*, **12**, 101 (1970).
12. C. K. Jørgensen, *Mol. Phys.*, **5**, 271 (1962).
13. J. L. Ryan and C. K. Jørgensen, *J. Phys. Chem.*, **70**, 2845 (1966).
14. H. D. Burrows and T. J. Kemp, *Chem. Soc. Rev. (London)*, **3**, 139 (1974).
15. C. K. Jørgensen, *Rev. Chim. Miner. (Paris)*, **14**, 127 (1977).
16. A. Müller, E. Diemann, and C. K. Jørgensen, *Struct. Bonding*, **14**, 23 (1973).
17. G. Blasse, *ibid.*, **42**, 1, (1980).
18. J. A. Duffy, *ibid.*, **32**, 147 (1977).
19. C. K. Jørgensen, *ibid.*, **24**, 1 (1975); **30**, 141 (1976).
20. C. K. Jørgensen, *Comments Inorg. Chem.*, **1**, 123 (1981).
21. R. McDiarmid, *J. Chem. Phys.*, **65**, 168 (1976).
22. J. L. Ryan and C. K. Jørgensen, *Mol. Phys.*, **7**, 17 (1963).
23. J. T. Bell and R. E. Biggers, *J. Mol. Spectrosc.*, **18**, 247 (1965).
24. C. K. Jørgensen, *Acta Chem. Scand.*, **11**, 166 (1957).
25. R. G. Denning, T. R. Snellgrove, and D. R. Woodwark, *Mol. Phys.*, **32**, 419 (1976); **37**, 1109 (1979).
26. C. K. Jørgensen and R. Reisfeld, *Chem. Phys. Lett.*, **35**, 441 (1975).
27. G. Herzberg, "Electronic Spectra and Electronic Structure of Polyatomic Molecules," Van Nostrand, Princeton (1966).
28. V. Kaufman and L. J. Radziemski, *J. Opt. Soc. Am.*, **66**, 599 (1976).
29. N. Lieblich-Sofer, R. Reisfeld, and C. K. Jørgensen, *Inorg. Chim. Acta*, **30**, 259 (1978).
30. C. K. Jørgensen, *J. Lumin.*, **18**, 63 (1979).
31. P. F. Walch and D. E. Ellis, *J. Chem. Phys.*, **65**, 2387 (1976).
32. C. Y. Yang, K. H. Johnson, and J. A. Horsley, *ibid.*, **68**, 1001 (1978).
33. M. Boring and J. H. Wood, *ibid.*, **71**, 392 (1979).
34. J. H. Wood, M. Boring, and S. B. Woodruff, *ibid.*, **74**, 5225 (1981).
35. P. Pyykkö and L. L. Lohr, *Inorg. Chem.*, **20**, 4405 (1981).
36. W. R. Wadt, *J. Am. Chem. Soc.*, **103**, 6053 (1981).
37. D. D. Koelling, D. E. Ellis, and R. J. Bartlett, *J. Chem. Phys.*, **65**, 3331 (1976).
38. P. J. Hay, W. R. Wadt, L. R. Kahn, R. C. Raffenetti, and D. C. Phillips, *ibid.*, **71**, 1767 (1979).
39. D. A. Case and C. Y. Yang, *ibid.*, **72**, 3443 (1980).
40. C. K. Jørgensen, *Chem. Phys. Lett.*, **89**, 455 (1982).
41. C. K. Jørgensen, *Chimia*, **27**, 203 (1973); **28**, 6 (1974).
42. C. K. Jørgensen, *Struct. Bonding*, **22**, 49 (1975).
43. R. Ferreira, *ibid.*, **31**, 1 (1976).
44. A. W. Adamson, W. L. Waltz, E. Zinato, D. W. Watts, P. D. Fleischauer, and R. D. Lindholm, *Chem. Rev.*, **68**, 541 (1968).
45. V. Balzani, F. Bolletta, M. T. Gandolfi, and M. Maestri, *Top. Curr. Chem.*, **75**, 1 (1978).
46. R. T. Walters and A. W. Adamson, *Acta Chem. Scand.*, **A33**, 53 (1979).
47. A. W. Adamson and A. R. Gutierrez, *J. Phys. Chem.*, **84**, 2492 (1980).
48. C. K. Jørgensen, *Top. Curr. Chem.*, **56**, 1 (1975).
49. J. Kiwi, K. Kalyanasundaram, and M. Grätzel, *Struct. Bonding*, **49**, 37 (1982).
50. H. Tributsch, *ibid.*, **49**, 127 (1982).
51. M. Moriyasu, Y. Yokoyama, and S. Ikeda, *J. Inorg. Nucl. Chem.*, **39**, 2199, 2205, and 2211 (1977).
52. M. D. Marcantonatos, *J. C. S. Faraday Trans. I*, **75**, 2273 (1979); **76**, 1093 (1980).
53. R. Matsushima, H. Fujimori, and S. Sakuraba, *ibid.*, **70**, 1702 (1974).
54. H. D. Burrows, S. J. Formosinho, M. da G. Miguel, and F. Pinto Coelho, *ibid.*, **72**, 163 (1976).
55. M. D. Marcantonatos and M. Deschaux, *Chem. Phys. Lett.*, **76**, 359 (1980); **80**, 327 (1981).
56. M. Deschaux and M. D. Marcantonatos, *J. Inorg. Nucl. Chem.*, **43**, 2915 (1981).
57. J. C. Sullivan, *J. Am. Chem. Soc.*, **84**, 4256 (1962).
58. R. K. Murmann and J. C. Sullivan, *Inorg. Chem.*, **6**, 892 (1967).
59. T. W. Newton and F. B. Baker, *ibid.*, **1**, 368 (1962).
60. B. Guillaume, G. M. Begun, and R. L. Hahn, *ibid.*, **21**, 1159 (1982).
61. M. Deschaux and M. D. Marcantonatos, *J. Inorg. Nucl. Chem.*, **43**, 361 (1981).
62. R. Reisfeld and S. Neuman, *Nature*, **274**, 144 (1978).
63. R. Reisfeld and Y. Kalisky, *ibid.*, **283**, 281 (1980).
64. R. Reisfeld and C. K. Jørgensen, *Struct. Bonding*, **49**, 1 (1982).
65. I. Lifschitz and S. B. Hooghoudt, *Z. Phys. Chem.*, **A146**, 145 (1930).
66. C. D. Flint and P. A. Tanner, *Inorg. Chem.*, **20**, 4405 (1981).
67. C. D. Flint, P. Sharma, and P. A. Tanner, *J. Phys. Chem.*, **86**, 1921 (1982).
68. C. D. Flint, *Chem. Brit.*, **14**, 223 (1978).
69. C. K. Jørgensen, in "Photochemical Conversion and Storage of Solar Energy," J. S. Connolly, Editor, p. 79, Academic Press, New York (1981).

Contact Angles Between III-V Melts and Several Substrates

U. König and W. Keck

AEG-TELEFUNKEN, Forschungsinstitut Ulm, D 7900 Ulm, Germany

ABSTRACT

The wetting behavior of several melts with different III-V compound semiconductors is studied. The characteristic parameter measured is the contact angle of a melt drop with a solid. It is evaluated by a geometrical measurement of the melt drop. The importance of clean surfaces of drop and solid is shown. Contact angles between 20° and 60° are found, depending on the type and composition of the melt and substrate. The temperature dependence amounts to about −4° per 100 K increase. In addition, the contact angle varies with the substrate orientation. The (100) orientated substrates are wetted better than (111) A orientated ones.

In liquid phase epitaxy (LPE) of a III-V compound semiconductor, a metallic melt is in contact with a solid substrate and a crucible, usually graphite. The wetting behavior of a III-V melt influences the carryover of melt, and by this the epitaxial quality with respect to unintentionally grown layers [*e.g.*, (1)].

The quality of the wetting may also affect the crystalline perfection of an epitaxial layer along the melt meniscus due to surface tension (2). When removing the melt from the semiconductor, it moves by a "stick-slip" motion. This forms the well-known meniscus lines (3).

The representative parameter for wetting is the contact angle at the melt meniscus between the melt surface and the substrate surface covered by the melt [*e.g.*, (4)]. The better the wetting, the smaller the contact angle is. The literature data for Ga on GaAs with contact angles >90°, from Munir and co-workers (5, 6), do not agree with the phenomenological experience of capillary ascension at LPE of III-V compounds. When melt and substrate are brought into contact, one usually observes a creeping of the melt on the substrate under the melt chamber walls. Very recently, Small and Potemski (7) reported on smaller angles for GaAs and $Ga_{0.4}Al_{0.6}As$, when regarding a microscopical deformation of the solid around the periphery of the drop. We have evaluated contact angles in a macroscopical measure of melt and solid to find representative data for LPE. Several III-V compound systems and different substrate orientations have been studied in a hydrogen atmosphere.

Experimental

We have used a horizontal LPE apparatus, consisting of a movable heat pipe furnace, a quartz reaction tube, a Pd diffusion cell, and a crucible of high purity graphite with fixed melt chambers, and a sliding substrate holder. A side-wall of one melt chamber was omitted in order to directly observe the melt contact angles. During a 3 hr heat cleaning at 1145 K in purified hydrogen, the melt drop, of about 5 mm diam, lies on the graphite slider within the chamber of 24 × 24 mm^2 separated from the substrate. The substrate is protected by a graphite cover. The sliding mechanism allows us to roll the melt drop on the graphite slider so that its surface can be exposed to reducing hydrogen, even its incipient contact area. Only after the heat cleaning is the substrate rapidly moved under the melt drop. The drop spreads on the substrate surface without touching the chamber walls, and forms an equilibrium contact angle. For making a photograph, the furnace is moved partially away from the crucible. Moving of the melt and photographing did not last more than 10 sec in order to avoid a temperature decrease larger than 20 K (measured beneath the melt chamber with a thermocouple and deduced from the shiny drop surface free of crystallization). The photographs had to be corrected for the viewing angle to determine the contact angles.

In the case of a $Ga_{1-x}Al_xAs$ semiconductor which tends to form stable surface oxides, the wetting experiment takes place just after depositing an epitaxial $Ga_{1-x}Al_xAs$ layer under an appropriate melt in a separate chamber of the crucible. This may provide an oxide-free semiconductor surface when one brings the melt drop into contact with the solid.

The GaAs substrates are heavily Zn doped ($\approx 2 \cdot 10^{18}$ cm^{-3}). The doping level of the epitaxial layers $Ga_{0.35}Al_{0.65}As$ and $Ga_{0.96}In_{0.04}As$ are around $5 \cdot 10^{17}$ cm^{-3}.

To avoid the formation of a thermally stable oxide film on a drop containing Al, which would not allow representative wetting, a heat cleaning step at 750 K is introduced. This temperature is sufficient to liberate contaminations from the drop and low enough to prevent rapid Al oxidation (8).

The compositions of the melt drops are determined from their respective phase diagrams (9, 10). They correspond to a temperature a few degrees below our typical drop temperature. This avoids spontaneous crystallization within or on the melt drop, as well as, a severe melt back of the substrate. As a further preventive measure, the time period between the first contact of the drop with the substrate and the photograph is chosen as short as possible (see above).

Different cleaning precautions are used for the growth system and the components. The LPE reaction tube is heated under hydrogen flow for about 4 hr at 1150 K. The crucible is baked out in high vacuum for 8 hr at about 1400 K in a special reactor, followed by a gettering procedure for several hours at 1150 K with a hydrogen flow and with Ga filled melt chambers within the LPE system. The melts are composed of 6*N* metal components, wet chemically cleaned. All substrates are given a standard preepitaxial cleaning process.

Results and Discussion

The contact angles found for several III-V compound systems, *i.e.*, for (111) A orientated GaAs substrates, $Ga_{0.96}In_{0.04}As$ and $Ga_{0.35}Al_{0.65}As$ epitaxial layers with Ga, In, Ga-As, Ga-In-As, and Ga-Al-As, are listed in Table I. Because of the important influence of the wetting behavior with the crucible material during LPE, graphite is also regarded as a substrate. Contact angles above 140° are found (Table I). This angle depends on the graphite type and the machined surface roughness. Clean III-V semiconductors are better wetted by III-V liquids according to contact angles between 20° and 63°. Indium containing melts form the smallest contact angles with the GaAs and $Ga_{1-x}In_xAs$ substrates. For liquid compositions from $x_{As} = 0$ to $x_{As} = 3.16$ a/o, Table I, the contact angle is found to increase with the amount of the solute.

Special considerations are required for Al containing systems. An insufficiently heat cleaned Ga-Al-As melt forms no definite drop. In addition, a $Ga_{1-x}Al_xAs$ semiconductor will be poorly wetted (large contact

Key words: wetting, orientation dependence, gallium arsenide, liquid phase epitaxy.

Table I. Contact angles at 1125 K for several melt compositions with (111) A orientated III-V compound semiconductors and with two types of graphite, typically used in LPE

Substrate	Melt	Contact angle (°)
GaAs	Ga	28 ± 1
	In	20 ± 2
	Ga-As 3.16 a/o As	40 ± 2
	Ga-In-As 70 a/o In 11 a/o As	32 ± 2
	Ga-Al-As 0.8 a/o Al 1.29 a/o As	51 ± 1
$Ga_{0.99}In_{0.01}As$	Ga-In-As 70 a/o In 11 a/o As	34 ± 1
$Ga_{0.35}Al_{0.65}As$ oxidized	Ga-As 3.16 a/o As	126 ± 4
$Ga_{0.35}Al_{0.65}As$ fresh	Ga-Al-As 0.8 a/o Al 1.29 a/o As	53 ± 3
Graphite FE 49	Ga-As 3.16 a/o As	63 ± 3
Graphite Poco		140 ± 3
		153 ± 2

angle, see Table I), when the semiconductor is grown in a preceding LPE process, or well wetted (small contact angle, see Table I), when the $Ga_{1-x}Al_xAs$ layer is freshly deposited just before the wetting with the test drop. Apparently, there is a thermally stable oxide coating on the $Ga_{1-x}Al_xAs$ surface which prevents wetting.

The contact angles found at 1125 K, Table I, are for a typical LPE process temperature. For a wetting experiment with the Ga/GaAs (111) A-system at 570 K, we obtained a contact angle of 48° ± 2°. This indicates a contact angle decrease of about 3.6° for a 100 K increase.

The orientation dependence of the contact angle obtained for (111) A and (100) orientated GaAs and $Ga_{1-x}Al_xAs$ substrates is presented in Table II. The (100) orientated substrates are better wetted. This agrees with the observation of a stronger capillary ascension on (100) orientated substrates under melt chamber walls in an LPE-crucible. The contact angles seem to be independent of the orientations in the substrate surface, according to the circular contact areas of the drops.

Contrary to our low values <63° in hydrogen, and those <83° of Small and Potemski (7), contact angles around 110° were reported for a III-V system in high vacuum and inert gases (5, 6). The question is whether the different surrounding atmospheres can be responsible for such differences. Principally, a difference can be expected according to Young's law, which relates the contact angle with the surface tensions between

Table II. Dependence of the contact angle on the substrate orientation for two systems at 1125 K

Melt	Orientation	Substrate	Contact angle (°)
Ga-As 3.16 a/o As	(111) A	GaAs	40 ± 2
		$Ga_{0.35}Al_{0.65}As$	53 ± 3
	(100)	GaAs	35 ± 1
		$Ga_{0.35}Al_{0.65}As$	48 ± 3

solid-vapor (or vacuum), liquid-vapor (or vacuum), and solid-liquid [*e.g.*, (4)]. However, the surface tensions of the known liquid and solid elements (11, 12) and also of some compounds (13) are nearly unaffected by the ambient gas or vacuum. Presuming this for III-V compounds, too, the contact angles observed here and in (5, 6) should not differ so much. Even the lower temperatures (<752 K) of Ref. (5) cannot be responsible for this discrepancy, for we have found much lower angles also in this temperature range (see above). One should consider that, in Ref. (5, 6), melt and substrate were already brought into contact a few degrees above the melting point, where Ga oxides strongly affect the melt meniscus. The following heating up in vacuum is not sufficient to produce an oxide-free Ga drop like a reducing hydrogen atmosphere. Therefore, in Ref. (5, 6), the contact angle of the initial melt meniscus is given, which remains fixed on the substrate by oxides on the drop. In experiments with insufficiently cleaned Ga drops, we have obtained comparable large angles.

Conclusion

We have evaluated some quantitative dependences of the contact angle on the type of the III-V solid, on the type and composition of III-V melts, on the temperature, and on the substrate orientation. An estimation of contact angles by means of comparison with Young's law fails because of the poor knowledge of surface tension data for III-V components. Particularly, the solid-vapor and the solid-liquid surface tensions are very uncertain (14) or even unknown.

The carry-over of melts, undesirable during LPE, is probably due to the good wetting, particularly for In melts and (100) orientated III-V semiconductors. The knowledge of the contact angles will help to overcome these problems by adapting the crucible material and construction to the respective wetting behavior of the system melt/substrate.

Manuscript submitted July 20, 1982; revised manuscript received Oct. 7, 1982.

Any discussion of this paper will appear in a Discussion Section to be published in the December 1983 JOURNAL. All discussions for the December 1983 Discussion Section should be submitted by Aug. 1, 1983.

Publication costs of this article were assisted by AEG-TELEFUNKEN.

REFERENCES

1. M. B. Panish, S. Sumski, and I. Hayashi, *Met. Trans.*, **2**, 795 (1971).
2. M. B. Small, K. H. Bochem, and R. M. Potemski, *J. Cryst. Growth*, **39**, 216 (1977).
3. M. B. Small, A. E. Blakeslee, K. K. Shih, and R. M. Potemski, *ibid.*, **30**, 257 (1975).
4. H. Mykura, "Solid Surfaces and Interfaces," Routledge and Kegan Paul Ltd., London (1966).
5. B. E. Liebert and Z. A. Munir, *J. Cryst. Growth*, **118**, 368 (1971).
6. J. Y. Kashkooli, Z. A. Munir, and L. Williams, *J. Mater. Sci.*, **9**, 538 (1974).
7. M. B. Small and R. M. Potemski, Paper presented at SPIE Conference Semiconductor Growth Technology, Los Angeles, CA, Jan. 1982.
8. P. E. Blackburn and E. A. Gulbransen, *J. Mater. Sci.*, **107**, 944 (1960).
9. R. N. Holl, *ibid.*, **110**, 385 (1963).
10. T. Y. Wu and G. L. Pearson, *J. Phys. Chem. Solids*, **33**, 409 (1972).
11. G. Lang, "Handbook of Chemistry and Physics," 53rd ed., p. 15, CRC Press, Cleveland, OH (1972/73).
12. W. R. Tyson, *Can. Metal. Quarterly*, **14**, 307 (1975).
13. A. Bondi, *Chem. Rev.*, **52**, 417 (1953).
14. J. M. Blakely, "Introduction to the Properties of Crystal Surfaces," p. 116, Pergamon Press, Elmsford, NY (1973).

Effects of Ion Implantation on the Thermal Growth of Pt and NiPt Silicides

T. W. Orent,* C. I. Knudson, and J. A. Sartell

Honeywell Corporate Technology Center, Bloomington, Minnesota 55420

and S. Lee[1] and T. L. Brewer[2]

Honeywell Solid State Development Center, Plymouth, Minnesota 55441

ABSTRACT

The effects of low-dose ion implantation of inert gas ions, prior to thermal annealing on the interactions between Pt and NiPt thin films with various forms of silicon, have been investigated. Specimens were implanted with Kr^{2+} and then annealed along with unimplanted samples in the temperature range 350°-650°C. The extent of silicide formation and the phases formed were determined by Auger electron spectroscopy (AES), x-ray diffraction, and transmission electron microscopy (TEM). The unimplanted Pt films reacted to form complete layers of Pt_2Si which then continued to react to form highly textured layers of PtSi. However, in the implanted samples, no distinct Pt_2Si layers were observed, and the final PtSi phases were fine grained and polycrystalline. In the case of NiPt films, ion implantation inhibited the formation of the distinct Pt silicide layers found during the early stages of the reaction in unimplanted samples. The differences between implanted and unimplanted NiPt samples became progressively smaller with increasing annealing temperature. The final phase formed in both types of specimens was the ternary silicide, $Ni_xPt_{1-x}Si$.

Metal silicides are physically and chemically compatible with integrated circuit fabrication processing and are used currently as Schottky barriers, ohmic contacts and low-resistivity gates, and interconnects (1-4). There is interest in the use of silicides in VLSI devices since they can be processed to form self-aligning shallow contacts with fine-grained structures that are suitable for submicron patterning. There are several possible ways to adjust the Schottky-barrier heights of metal silicides in order to tailor them for a specific application, including ion implanting a thin p- or n-type layer at the interface between the metal and the silicon before forming the silicide (5, 6), by using parallel contacts (7), or by using two metals to form an alloyed silicide (8-10).

In the case of alloyed-silicide diodes, silicides formed by thermal annealing of platinum and nickel layers on silicon have received the most attention (8-10). Measured barrier heights on n-type silicon were between 0.66-0.87 eV, which are the values for NiSi and PtSi, respectively. There also appeared to be a correlation between the barrier height and the Pt content (8). While the system does appear to have highly desirable electrical characteristics, thermal annealing produced multilayer structures with nonuniform compositions (8, 10). This is a very undesirable characteristic since each diode has to be mechanically and electrically stable to further processing.

In order to form uniform stable alloy silicides, the nucleation processes and the growth kinetics must be modified in order to alter the composition, the uniformity, and the grain size. Nucleation is usually an activated process with an activation energy that is higher than that for subsequent growth of the new phase. As a result, while a highly energetic process must be used to initiate compound formation, a less energetic method can be employed to complete the growth. In the case of Pt silicides, Pt_2Si and PtSi have been the only two phases detected when thin films of Pt on Si have been thermally annealed (11). However, ion implantation of inert gas ions through the Pt into the Si prior to thermal annealing caused the formation of the metastable phase Pt_2Si_3 (12).

* Electrochemical Society Active Member.
[1] Present address: Magnetic Peripherals, Incorporated, Bloomington, Minnesota 55435.
[2] Present address: Brewer Science, Rolla, Missouri 65401.
Key words: silicides, interdiffusion, ion implantation.

We investigated the structures formed when a combination of low-dose ion implantation followed by thermal annealing was used to form the silicides from double layers of nickel and platinum on various forms of silicon. The low ion dose should modify the nucleation process because of the resultant collision-cascade mixing and enhanced solid-state diffusion while producing minimal damage, and the subsequent thermal annealing should improve the thermal stability and reduce stresses in the silicide.

Experimental

Thin layers of Pt and Ni were sequentially deposited by rf sputtering at rates of 20Å/min onto several types of chemically cleaned and backsputtered substrates. Both n- and p-type Si(100), poly-Si, and SiO_2 were coated, and the substrate temperatures remained below 100°C during deposition. After deposition, some samples were ion implanted to a dose of 5×10^{14} cm^{-2} with 600 keV Kr^{2+} ions at room temperature. Krypton implantation into Au under these conditions would produce a broad profile peaked about 900Å below the surface (13). In order to insure that the ions penetrated into the substrate and caused the atomic mixing necessary for silicide formation (11, 12), the total metal thickness for the implanted specimens was kept less than 800Å.

Both implanted and unimplanted specimens were annealed in a tube furnace in flowing nitrogen at temperatures between 350° and 650°C for various times. The processed samples were analyzed by Auger electron spectroscopy (AES) to determine compositions as functions of depth, by x-ray and electron diffraction to determine the phases formed, and by transmission electron microscopy (TEM) to examine the microstructures of some of the Pt silicides. The wafers were not patterned to form diodes, and no electrical measurements were made.

Auger analysis showed the presence of carbon and oxygen on all surfaces and more oxygen present after annealing. Since the presence of impurities in the metal film has been shown to alter reaction rates and the phase growth sequence, the carbon and oxygen Auger peaks were monitored in all depth profiles; but, since these levels were less than 1 atomic percent (a/o) in both the as-deposited metals and the silicides, the traces were not included in the figures. No buildup of impurities was found at any interface in the as-depos-

ited or annealed specimens. The peak Kr concentration was about 3×10^{19} cm^{-2} or about 0.05 a/o which was too low to be detected.

Results and Discussion

Pt/Si.—The as-deposited Pt layers had strong (111) textures. Texturing has been observed not only in thicker sputter-deposited Pt layers (14) but also in E-beam evaporated layers on Si(100) (15). Even though no interfacial mixing was apparent in AES depth profiles, selected-area electron diffraction data from a specimen thinned for TEM analysis did show the presence of both Pt_2Si and PtSi near the Pt/Si interface. When unimplanted samples were annealed at 350°C, Pt_2Si formed at the interface and grew rapidly consuming all of the Pt in a few minutes as shown in Fig. 1a (16-19). Continued annealing at 350° resulted in a slow conversion of the Pt_2Si to PtSi. The conversion rate was much faster at higher temperatures, but PtSi was still the final phase formed at temperatures up to 650°C.

Both silicides had uniform textures with grain sizes about 500Å, and both had sharp interfaces with the Si substrate. The systematic absence of lines in the x-ray diffraction data indicated that both silicides were highly oriented. The data for the PtSi were very similar to those of Joubert, Auvray, and Henry (14) who determined that their sample had a (101) texture. Other dominant orientations, such as (002) (20) or a mixture of (110) and (121) (15), have been reported also. The discrepancies have been attributed to different film thicknesses (20). There were no obvious differences in the sequence of phases formed, the rates of growth, or film morphology among the various types of substrates used, except for the SiO_2 where no reaction was observed at 350°C.

Auger depth profiles of the ion-implanted Pt/Si samples showed that the elements had been intermixed over a distance of several hundreds of angstroms. While no new phases could be detected in the x-ray diffraction pattern, high resolution AES spectra of the Si LVV region revealed the additional fine structure characteristics of Pt silicides (8, 21) throughout the mixed region. Thermal annealing at 350°C caused additional intermixing with the Pt to Si atomic ratio decreasing monotonically with depth (Fig. 1b).

The transmission x-ray diffraction patterns for unimplanted and implanted samples that had been annealed at 350°C for 10 min are shown in Fig. 2. The unimplanted sample (Fig. 2a) was Pt_2Si, and the discontinuous diffraction rings indicated that there was a preferred orientation for the grains. The implanted specimen (Fig. 2b) contained PtSi as well as Pt_2Si, and the grains were oriented randomly. This compound layer eventually formed a uniform layer of PtSi, but the rate of growth was much slower than that of thermally generated PtSi, and the grain size was much smaller. No macroscopic region of Pt_2Si was detected during growth.

Since ion implantation causes lattice damage as well as atomic mixing, a wafer was implanted with Kr^{2+}

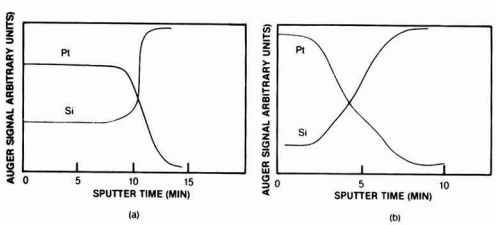

Fig. 1. Auger depth profiles (5 keV, 5 μA, 100 Å/min) of 500Å Pt/Si(100) after (a) annealing at 400°C for 10 min and (b) ion implantation (5×10^{14} cm^{-2} with 600 keV Kr^{2+}) followed by annealing at 350°C for 5 min.

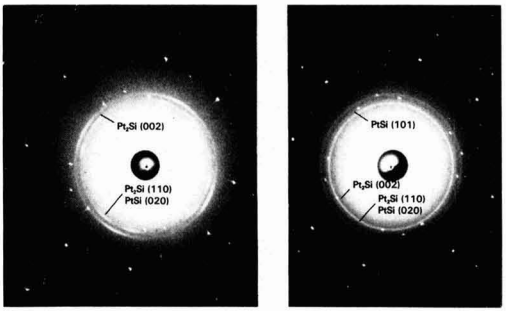

Fig. 2. Transmission x-ray diffraction patterns (Co radiation, 35 keV) of 500Å Pt/Si(100) samples annealed at 350°C for 10 min: (a) as deposited and (b) implanted with Kr^{2+} before annealing. Discontinuous diffraction rings indicate that the silicide film had a preferred orientation.

before Pt deposition in order to determine the relative importance of these effects for silicide growth. There were no differences in phase growth sequence, growth rate, or interface width between unimplanted samples and those implanted before metallization. As a result, the observed differences between unimplanted specimens and those implanted after metal deposition were due primarily to atomic mixing.

The results for the unimplanted Pt/Si samples are in good agreement with the fairly extensive literature on the thermal growth of Pt silicides from thin films deposited on Si (14-21). Both the reactions

$$2Pt + Si \rightarrow Pt_2Si \quad [1]$$

$$Pt_2Si + Si \rightarrow 2PtSi \quad [2]$$

are diffusion controlled with reproducible activation energies but with kinetics that were highly dependent upon impurity content (16-19). Rapid atomic diffusion at low temperatures can be strongly suppressed by the segregation of impurities along the fast diffusion paths. Very low levels of impurities decorating the silicide grain boundaries are the most probable cause for the large variation in observed Pt diffusivities (16, 17, 19). In fact, silicide growth can be inhibited completely by the formation of very thin layers of silicon oxides or nitrides (14, 19, 22, 23). The kinetics of Pt silicide formation are not yet established clearly, but several mechanisms have been proposed (2). The low temperature needed to initiate the reaction (19), the parabolic growth rate (16-19), and the radiotracer data that indicate that Pt is the dominant diffusing species (24) all favor a model in which interstitial diffusion of Pt into the Si is responsible for the release of Si atoms from the lattice.

Previous studies on the effects of ion implantation through Pt films on Si have shown that continued implantation resulted first in the formation of a complete layer of Pt_2Si followed by pure atomic mixing with no detectable silicide formation (11). The phase PtSi was not observed, and, in fact, it was shown to be unstable to ion bombardment (12). For low-dose ion implantation, both Pt_2Si and PtSi were observed after thermal annealing for a short time. In this case, microcrystallites of both phases were randomly generated throughout the intermixed region, and then the subsequent thermal growth produced a fine-grained, randomly oriented final phase of PtSi with no distinct intermediate layers ever being formed. The slow growth of the mixed phases indicated a reduced supply of reactant which prevented the predominant growth of Pt_2Si at the expense of PtSi. The reduced diffusion rate was similar to that observed for high levels of impurities (19); however, in this case, no excessive contamination was detected in the Pt film or at the Pt/Si interface.

The slower reaction rate was not due to the presence of Kr which is inert but rather to a change in the growth mechanism. Instead of the formation of a single phase along a uniform growth front, there was competitive growth of two Pt silicides from a large number of randomly distributed microcrystallites.

Ni/Pt/Si.—The presence of Ni over the Pt did not have any detectable effect on the initial Pt-Si interaction. Annealing an unimplanted sample at 350°C produced first a complete layer of Pt_2Si (25) via reaction [1]. No Ni/Pt interdiffusion was apparent in the AES depth profiles during this stage of growth. The next step was the formation of PtSi by reaction [2] at the Pt_2Si/Si interface. The growth rate of the PtSi was much slower than that observed in Pt/Si samples. The onset of PtSi formation was accompanied by the diffusion of Ni through the Pt silicides toward the Si substrate. Ni-rich layers were eventually formed at both the Pt_2Si/PtSi and PtSi/Si interfaces as seen in Fig. 3a.

Continued annealing produced the layered structure indicated by the spectrum shown in Fig. 3b. The presence of Pt silicides in these structures was confirmed by x-ray analysis, but no Ni silicides could be identified because the layers were so thin. The Ni to Si atomic ratio determined by AES suggested the formation of NiSi which is the end phase formed from Ni/Si couples at temperatures between 350°-750°C (26, 27).

Annealing at higher temperatures caused a reaction among the Ni remaining at the surface, the PtSi layer, and additional Si

$$Ni + PtSi + Si \rightarrow Ni_xPt_{1-x}Si \qquad [3]$$

The resultant $Ni_xPt_{1-x}Si$/NiSi layered structure has been observed previously (8, 10). Raising the annealing temperature even higher resulted in additional redistribution of the Pt and Ni to form a homogeneous layer of the ternary as shown in Fig. 3c. Concentration gradients were usually observed in the high temperature specimens with the Ni concentration highest near the substrate (22, 28). The x-ray diffraction data from several samples with different Ni to Pt atomic ratios correlated very well with the results reported for the proposed ternary silicide $Ni_xPt_{1-x}Si$ (25).

Ion implantation through a 400Å Ni/150Å Pt/Si sample (Fig. 4a) resulted in atomic mixing at both interfaces as shown in Fig. 4b. High-resolution Auger spectra again indicated silicide formation in the region near the Pt/Si interface. Annealing at 400°C for a short time (Fig. 5) did not produce the distinct Pt silicide layers that were evident in unimplanted samples annealed under the same conditions (Fig. 3a). Long-term annealing at 400°C eventually resulted in the formation of the layered $Ni_xPt_{1-x}Si$/NiSi structure. No uniform layers of Pt silicides were ever detected. Increasing the annealing temperature decreased the differences in annealing times needed to produce similar structures in the implanted and unimplanted specimens. The only detectable differences in the depth profiles were much longer Ni diffusion tails into the substrate in the implanted samples. It was not possible to ascertain if the Ni in the diffusion tail had reacted to form a silicide, because there is no fine structure in the Si LVV Auger peak for the Ni silicides and Ni diffusion into Si without silicide formation has been reported (29).

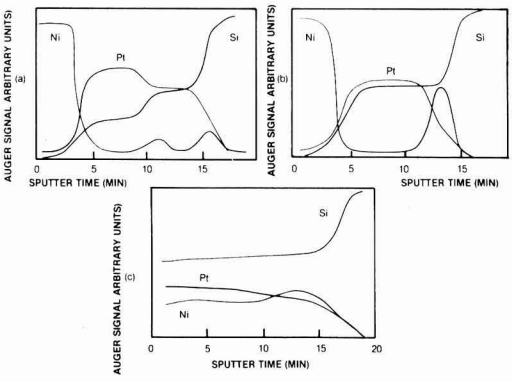

Fig. 3. Auger depth profiles of 400Å Ni/400Å Pt/Si(100) annealed for 30 min at (a) 350°C, (b) 400°C, and (c) 600°C.

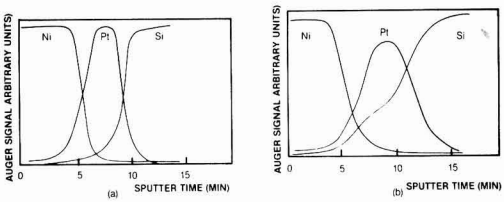

Fig. 4. Auger depth profiles of 400Å Ni/150Å Pt/Si(100) (a) as deposited and (b) after ion implantation with Kr^{2+}.

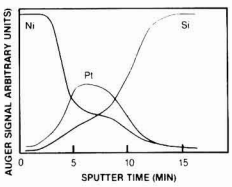

Fig. 5. Auger depth profile of an ion implanted sample of 400Å Ni/150Å Pt/Si(100) annealed at 400°C for 10 min.

The growth of silicides from Ni and Pt layers on Si will be described in terms of the relative interdiffusion coefficients, their temperature dependences, and the ability of some phases to act as diffusion barriers to some species. The initial stage in the thermal growth, *i.e.*, the formation of a complete layer of Pt_2Si below the Ni, occurred because of the rapid diffusion of Pt through Pt_2Si at temperatures as low as 200°C and because of the very slow interdiffusion of Pt and Ni at temperatures below 500°C (30).

Once all of the Pt had been converted to Pt_2Si, both Pt and Ni began to diffuse through that layer to form PtSi at the Pt_2Si/PtSi interface and NiSi between the PtSi and the substrate. This simultaneous diffusion resulted in different kinetics from those observed for either metal alone. The growth rate of PtSi was much slower than that observed in Pt/Si samples because the Ni in the grain boundaries probably interfered with the Pt diffusion. In the case of the Ni, no first phase of Ni_2Si (26, 2) was observed either because the Ni_2Si reacted very quickly to form NiSi or the Pt restricted the supply of Ni enough to alter the first phase formed. Implantation of nitrogen has been reported (23) to cause such an alteration in Ni silicide growth kinetics. The depth profile shown in Fig. 3a indicates that Ni diffuses faster through Pt_2Si than through PtSi. The relative growth rates of Pt_2Si and PtSi samples indicates that Pt also diffuses faster through Pt_2Si than PtSi.

Once the Pt_2Si had been completely converted to PtSi, no more Ni diffused into the substrate to form NiSi. In the thicker Pt samples, there was still a distinct layer of Ni at the outer surface along with some Ni in the PtSi (Fig. 3b). Since PtSi is clearly not a diffusion barrier to Ni, another phase must have begun to form at this point. A likely candidate is $Ni_xPt_{1-x}Si$ formed at the PtSi/NiSi interface by reaction [3].

The existence of this monosilicide as well as PdNi and PtPd ternary silicides has been proposed on the basis of x-ray data (25, 31). The additional Si could be supplied by either diffusion of Si atoms from the substrate through the NiSi or by the decomposition of NiSi at the PtSi/NiSi interface followed by Ni diffusion toward the substrate where it formed NiSi. These possibilities cannot be distinguished readily, and the slow reaction rate is consistent with both mechanisms.

These data indicate that the reaction of Si with Pt_2Si to form PtSi was favored over the reaction of Si with PtSi and Ni to form $Ni_xPt_{1-x}Si$, and that the formation of $Ni_xPt_{1-x}Si$ was favored subsequently over the reaction of the remaining outer layer of Ni with the PtSi to form NiSi and Pt. The ternary silicide continued to form until it consumed the Ni and PtSi layers resulting in a $Ni_xPt_{1-x}Si$/NiSi structure with some PtSi decorating the NiSi grains. This structure could be converted to a uniform layer of the ternary monosilicide by annealing above 500°C where Pt/Ni interdiffusion (23) and Si mobility (32) are known to be high. The gradients in the Ni and Pt concentrations would persist until complete interdiffusion of the monosilicide and the NiSi had occurred.

Electrical measurements have been made by others (8-10, 28) on layered structures with various Ni/Pt atomic ratios formed at temperatures below 500°C. The barrier heights were between 0.66-0.87 eV, which are the values for NiSi and PtSi, respectively; they appeared to vary smoothly with the Pt content. It has been suggested (25) that the amount and distribution of Pt (or a Pt silicide) among the NiSi grains controlled the barrier height. These data are in agreement with the previous observations. The reported stability of diodes annealed below 500°C may be related to the ability of the monosilicide to act as a diffusion barrier. The Pt distribution in the NiSi phase did not appear to change until the outer layers had been converted completely to the ternary monosilicide which is a slow process at temperatures below 500°C.

Comparison of Fig. 3a and 5 clearly show that ion implantation greatly reduced the amount of interdiffusion in Ni/Pt/Si samples during the initial stage of annealing. Analogous to the Pt/Si case, the most likely cause of the reduced silicide formation rate was the competitive growth of several phases that had been randomly nucleated as a result of the ion implantation. Even though Pt, Ni, and Si were intimately mixed at this stage and the Si Auger peak indicated the formation of a silicide, no detectable amount of the ternary silicide was formed. Continued annealing resulted in the eventual diffusion of Ni to the substrate where it formed NiSi.

Once an appreciable amount of NiSi had been formed, there were no differences between the implanted and unimplanted specimens with further annealing except for the deeper penetration of Ni into the substrate in the implanted samples. Berning and Levenson (29) proposed that, when Ni was deposited on defect-free Si, interdiffusion occurred without silicide formation. Comparison of the results for the implanted and unimplanted samples suggests the opposite conclusion. In the unimplanted samples, the near surface region of the Si substrate was first converted to PtSi; and then Ni diffused through that layer to form NiSi in the defect-free region and below the original surface. In the implanted samples, no distinct Pt layers were formed, and the Ni diffused into the damaged region where it not only formed some silicide but also continued to diffuse deep into the substrate.

Conclusions

Ion implantation of inert gas ions through Pt thin films into the Si resulted in the random nucleation of both Pt_2Si and PtSi and the subsequent formation of a layer containing both phases during thermal annealing instead of a layer of Pt_2Si. Continued annealing of an implanted specimen produced a final phase of PtSi that was fine-grained and randomly oriented instead of highly textured as found in unimplanted samples.

Unimplanted NiPt layers on Si formed multilayer structures when annealed at temperatures below 500°C. This nonuniformity may have resulted from the formation of a ternary silicide, $Ni_xPt_{1-x}Si$, which may be an effective diffusion barrier for Ni at low temperatures.

Ion implantation through NiPt thin films caused atomic mixing at both interfaces and inhibited the formation of distinct Pt silicide layers during thermal annealing at low temperatures possibly due to the random nucleation of several phases.

There were no major differences between implanted and unimplanted NiPt samples when they were annealed at high temperatures. The final phase formed in both types of specimens was the ternary silicide, $Ni_xPt_{1-x}Si$.

Note: G. Ottaviani *et al.* [*J. App. Phys.*, **53**, 4903 (1982)] observed the formation of NiSi at the metal/Si interface after annealing NiPt alloy films on Si(100) at low temperatures (300°-350°C).

Acknowledgments

The authors wish to thank D. W. Paananen and T. G. Gruchow for depositing the metal films, B. T. McClure and S. J. Tibbetts for doing the ion implantations, and A. D. Beck for helping with the Auger analysis.

Manuscript submitted Aug. 2, 1982; revised manuscript received Nov. 11, 1982. This was Paper 288 presented at the Minneapolis, Minnesota, Meeting of the Society, May 10-15, 1981.

Any discussion of this paper will appear in a Discussion Section to be published in the December 1983 JOURNAL. All discussions for the December 1983 Discussion Section should be submitted by Aug. 1, 1983.

Publication costs of this article were assisted by Honeywell, Incorporated.

REFERENCES

1. J. M. Andrews, *J. Vac. Sci. Technol.*, **11**, 972 (1974).
2. K. N. Tu and J. W. Mayer, in "Thin Films—Interdiffusion and Reactions," J. M. Poate, K. N. Tu, and J. W. Mayer, Editors, Chap. 10, Wiley, New York (1978).
3. F. Mohammadi, *Solid State Technol.*, **24**, 65 (1981).
4. A. K. Sinha, *J. Vac. Sci. Technol.*, **19**, 778 (1981).
5. J. M. Shannon, *Solid-State Electron.*, **19**, 537 (1976).
6. R. L. Thornton, *Electron. Lett.*, **17**, 485 (1981).
7. K. N. Tu, *J. Vac. Sci. Technol.*, **19**, 766 (1981).
8. S. Thomas and L. E. Terry, *J. Appl. Phys.*, **47**, 301 (1976).
9. L. E. Terry and J. Saltich, *Appl. Phys. Lett.*, **28**, 229 (1976).
10. A. Shepela, R. Phaneuf, and E. F. Kennedy, *J. Appl. Phys.*, **51**, 2928 (1980).
11. B. Y. Tsaur, Z. L. Liau, and J. W. Mayer, *Appl. Phys. Lett.*, **34**, 168 (1979).
12. B. Y. Tsaur, J. W. Mayer, and K. N. Tu, *J. Appl. Phys.*, **51**, 5326 (1980).
13. B. Smith, "Ion Implantation Range Data for Silicon and Germanium Device Technologies," Research Studies Press, Forest Grove, Oregon (1977).
14. P. Joubert, P. Auvray, and L. Henry, *Thin Solid Films*, **79**, 235 (1981).
15. H. B. Ghozlene, P. Beaufrere, and A. Authier, *J. Appl. Phys.*, **49**, 3998 (1978).
16. J. M. Poate and T. C. Tisone, *Appl. Phys. Lett.*, **24**, 391 (1974).
17. C. Canali, C. Catellani, M. Prodenziati, W. H. Wadin, and C. A. Evans, Jr., *Appl. Phys. Lett.*, **31**, 43 (1977).
18. C. Canali, F. Catellani, G. Ottaviani, and M. Prudenziati, *Appl. Phys. Lett.*, **33**, 187 (1978).
19. C. A. Crider, J. M. Poate, J. E. Rowe, and T. T. Sheng, *J. Appl. Phys.*, **52**, 2860 (1981).
20. J. Angilello, F. D'Heurle, S. Peterson, and A. Segmuller, *J. Vac. Sci. Technol.*, **17**, 471 (1980).

21. A. Roth and C. R. Crowell, *J. Vac. Sci. Technol.*, **15**, 1317 (1978).
22. R. J. Blattner, C. A. Evans, Jr., S. S. Lau, J. W. Mayer, and B. M. Ullrich, *This Journal*, **122**, 1732 (1975).
23. L. Wielunski, D. M. Scott, M. A. Nicolet, and H. von Seefeld, *Appl. Phys. Lett.*, **38**, 106 (1981).
24. R. Pretorius, A. P. Botha, and J. C. Lombaard, *Thin Solid Films*, **79**, 61 (1981).
25. T. G. Finstad, *ibid.*, **51**, 411 (1978).
26. K. N. Tu, E. I. Alessandrini, W. K. Chu, H. Krautle, and J. W. Mayer, *Jpn. J. Appl. Phys.*, Supple. **2-1**, 669 (1974).
27. D. J. Coe and E. H. Rhoderick, *J. Phys. D*, **9**, 965 (1976).
28. R. Pretorius, A. P. Botha, and J. C. Lombaard, *Thin Solid Films*, **79**, 61 (1981).
29. G. I. P. Berning and L. L. Levenson, *ibid.*, **55**, 473 (1978).
30. C. Chang and W. K. Chu, *J. Appl. Phys.*, **52**, 512 (1981).
31. T. G. Finstad and M. A. Nicolet, *ibid.*, **50**, 303 (1979).
32. R. Pretorious, J. O. Olowolafe, and J. W. Mayer, *Philos. Mag. A*, **37**, 327 (1978).

Compositional Depth Profile of a Native Oxide LPCVD MNOS Structure Using X-Ray Photoelectron Spectroscopy and Chemical Etching

J. A. Wurzbach[1] and F. J. Grunthaner

Jet Propulsion Laboratory, California Institute of Technology, Pasadena, California 91109

ABSTRACT

A compositional profile of a native oxide LPCVD MNOS structure has been obtained by x-ray photoelectron spectroscopy used in conjunction with a stopped-flow chemical etching procedure. A depth resolution of 5-10Å was achieved. Stoichiometric Si_3N_4 was found in the bulk with about 0.4 atomic percent (a/o) oxygen impurity. In contrast to profiles completed by other techniques, SiO_2 was found intact at the interface; complete conversion of oxide to oxynitride during LPCVD did not occur. The oxide/nitride interface is best described as sharp; the oxygen concentration drops by 80% in less than 8Å. There is also a diffuse oxynitride gradient extending into the film, but the oxygen concentration in this region is quite low. Evidence was also found for an 8Å layer containing excess bonds to silicon between the oxide and nitride layers. Possible charge trap structures that might limit device performance are discussed along with processing suggestions aimed at minimizing the formation of traps.

Studies of the composition and interfaces of silicon nitride on oxidized silicon have been driven by the wide application of these structures in electrically alterable, nonvolatile MNOS memory devices (1). Many of the electrical properties of these devices are related to the structure and composition of the nitride-oxide and oxide/silicon interfaces. Charge storage in MNOS structures involves modified Fowler-Nordheim tunneling across the thin oxide layer to traps at or beyond the nitride/oxide interface (2). Shifts in the logical voltage window have been related to states at the oxide/substrate interface (1). Endurance and retention problems (1) manifest themselves after repeated write/erase cycling moves charge across MNOS interfaces. It is, therefore, desirable to achieve an accurate understanding of the structure and composition of MNOS systems in the bulk region and particularly at the interfaces.

Numerous techniques have been applied to the characterization of silicon nitride and MNOS interfaces including: Auger electron spectroscopy (AES) (3-9), energy-loss spectroscopy (ELS) (10), spectroscopic ellipsometry (SE) (8, 11), Rutherford backscattering (RBS) (5c, 8, 12, 14), nuclear-reaction analysis (5c, 13, 15), secondary ion mass spectroscopy (SIMS) (9b), multiple internal reflection (MIR) (5c, 15, 16), and x-ray photoelectron spectroscopy (XPS) (17).

AES work has been done in conjunction with argon ion sputtering to obtain profiles of composition *vs.* depth. Early work (3) suggested an apparent width of 20-30Å FWHM, or 50Å 10/10%, for the interface between bulk silicon nitride and the silicon substrate of memory-type MNOS structures. These estimates were not corrected for the broadening effects of differential mean-free-paths and ion knock-on. More recent AES work (7, 8) also shows an apparent 20Å interface, but in recognition of sputter-broadening effects, 20Å is quoted only as an upper limit of interdiffusion and not as a defined width (8). Similar results were obtained by ELS (10).

All of this work has failed to show any evidence of interfacial SiO_2. This fact, together with the apparently broad interfaces seen by these techniques, has been interpreted in terms of complete conversion of SiO_2 to SiO_xN_y during nitride deposition (3, 10). However, Frenzel and Balk (9) have demonstrated that the broad interfaces observed by AES are experimental artifacts rather than the results of chemical reaction, diffusion, or nonuniform thickness. They show that sputtering induces surface roughness on the order of 20Å in SiO_2 (9a). In MNOS structures, they show that preferential sputtering (4, 9b) and bond cleavage lead to atomic mixing when sputtering across the interface of a double layer. Broadening due to these effects was calculated to be 45Å. Accordingly, an upper limit of 8 ± 4Å was placed on the actual width of the nitride/oxide interface (9b). These authors conclude that reliable information about interface structure can only be obtained by methods that do not require sputter profiling (9a).

SE has been shown to be an effective method of nondestructively detecting buried layers in thin films; however, the analysis of these layers must be inferred from least-square regression calculations. For example, SE data have identified an optically absorbing region between the oxide and nitride layers (11). This region has been modeled as a 12Å layer of amorphous silicon. However, the authors (11) caution that this model may not be quite realistic; they suggest only that the amorphous silicon dielectric function is a useful prototype for describing this region, and that this region must, therefore, contain Si-Si bonds. The oxy-

Key words: silicon nitride etching, charge trap structures, traps.

[1] Present address: General Dynamics Corporation, Pomona, California 91769.

gen analysis from SE refers to effective "SiO_2" volume fractions without implying an actual oxygen content.

RBS results have shown that bulk silicon nitride is stoichiometric (5c, 8, 12, 14), but the depth resolution (~ 40Å) was not adequate to quantify the oxide interface.

Thus, despite their technological importance, there has not been an unambiguous analysis of the composition and interfacial structure of MNOS systems. In this paper, we present the results of depth-profiling an MNOS structure by combining x-ray photoelectron spectroscopy (XPS) with a controlled stopped-flow chemical-etching procedure. XPS is sensitive to the structure of surface layers, while stopped-flow etching permits the controlled removal of overlying material on a scale of atomic layers (19), to expose new surface layers as a function of thickness. Therefore, with careful analysis of observed intensities at measured depths, this combination of techniques affords depth resolution between 5 and 10Å. Thus, direct observations can be made about the details of the composition and stoichiometry of the nitride/oxide/silicon interfaces and the transition to the bulk nitride in MNOS structures. The data show intact SiO_2 at the substrate interface and some evidence strongly suggestive of a thin layer containing excess bonds to silicon on top of the SiO_2. Although an oxynitride gradient is found to extend into the film from the oxide/nitride interface, the oxygen concentration is so low that the interface is still best described as sharp.

Experimental

Samples for the depth profile were prepared by LPCVD (750°C, 0.5 Torr, $NH_3/SiH_2Cl_2 = 9$) of silicon nitride onto crystalline silicon substrates (n-type, 4-8 Ω-cm, [100]) in a hot wall tube reactor. The final thickness was 483Å, measured ellipsometrically (6328Å, refractive index 1.99). The nitride was deposited directly onto the native oxide resulting from wet chemical processing of the substrate wafer. No thermal oxide was intentionally grown. The thickness of the native oxide has been estimated by ellipsometry to be 5-7Å. These dimensions correspond to a typical native oxide MNOS structure for memory applications.

Thin nitrides were prepared as control samples. Some were fabricated on native oxides, exactly as described above, to a nitride thickness of ~ 40Å. A second set was deposited over intentionally grown thermal oxides 22Å thick (steam, 700°C, 9.5 min). These 22Å oxides were then covered with ~ 20Å silicon nitride by LPCVD (800°C, $NH_3/SiH_2Cl_2 = 5$).

The etchant used is a modification of the patent by Loic (18). It consists of HF (48%), H_3PO_4 (85%), and ethanol (absolute) mixed in the ratio 15:10:60 by volume. Ethanol is used as a solvent instead of water because it films over silicon nitride more uniformly, it dries quickly, and it is relatively more inert. This etchant is nearly anhydrous; it contains about 9% water from the concentrated liquid acids, HF, and H_3PO_4.

A strictly anhydrous rinse was prepared by bubbling HCl gas through absolute ethanol. Sufficient HCl was dissolved in the ethanol to give an apparent "pH" of ~ 1.

Details of the stopped-flow etching procedure are described elsewere (19). In summary, the etchant is applied dropwise on a ⅜ in. square sample which is spinning at 12,000 rpm. The etch is done at room temperature in an inert N_2 ambient. Each etching step is followed by an ethanol/HCl rinse or a rinse with absolute ethanol, or both. The observed etch rate is 100-150Å nitride/ml. Many variables affect the etch rate. Some, such as temperature, are obvious; others which are related to the specific experimental geometry include: drop size (0.01-0.02 ml), dropping rate (~ 12 drops/min), rpm, and humidity in the N_2 ambient (ideally zero).

Uniformity of material removal was checked ellipsometrically and by C-V measurements. After etching ~ 300Å of the nitride, the remaining film thickness was found by ellipsometry to be uniform within ± 5Å at the center of the ⅜ in. square sample and within 10-15Å going from one corner to the opposite corner. Since the XPS experiment measures only a limited portion of the center of the sample, this uniformity was more than adequate. As an independent second check, mercury probe C-V measurements were performed. The results corroborated the ellipsometric findings of local uniformity and a slight thickness gradient across the sample diagonal.

Film thickness was measured ellipsometrically until about 60Å of the film remained. At that point, the Si2p signal from the substrate was detectable, and the film thickness could be determined from the ratio of the integrated Si2p signals from the nitride/oxide and substrate (20, 28).

The conversion of the nitride/oxide: substrate intensity ratio to a thickness requires a knowledge of the photoelectron mean-free-path λ through the overlying film material. Taylor *et al.* (21) have derived an estimate of λ_{Si2p} ~ 36Å in Si_3N_4. The data in this work are consistent with somewhat lower values ranging from the low to high twenties. Film thickness is the only calculated parameter which depends on λ_{Si2p}, the value of which is currently tentative. Therefore, to be technically correct, the thickness coordinate in figures relevant to the interface has been given in multiples of λ_{Si2p}. However, as an intuitive aid, a thickness scale is also given in angstroms, based on λ_{Si2p} selected at 30Å as a reasonable average of the available estimates. All other calculations are based on mean-free-path ratios, which can be calculated quite accurately (24) without any dependence on a specific choice of λ_{Si2p}.

To obtain accurate intensities for this study, it was necessary to account for residues left on the surface by the etching procedure. The dominant residues are surface reaction products of ethanol and ethyl fluoride, which form spontaneously at room temperature in acidic, alcoholic fluoride solutions. These species are tightly bound to the surface; in control experiments, temperatures exceeding 100°C failed to desorb them into the UHV environment. O1s from residual ethanol reaction products interfered with the O1s from impurities in the bulk nitride. It was possible to correct for this problem by estimating the magnitude of the ethanol contribution from a fit of the C1s spectrum. Additionally, a small peak was often observed 4 eV from the main N1s peak (see Fig. 1a). In control experiments, this feature disappeared after the sample was warmed to 50°C in vacuum; simultaneously, the F1s signal decreased by ~ 10%. These results are best interpreted as fluorine, probably in the form of HF, loosely bound to nitrogen lone pairs projecting from the surface. Therefore, we might use HF as a convenient marker for the fraction of surface nitrogen atoms with exposed lone pairs. The data in Fig. 1a, for example, suggest that HF is bound to the lone pairs of ~ 10% of the surface nitrogen atoms. Figure 2 shows that residual sodium, probably from trace amounts of sodium phosphate in the phosphoric acid, was effectively removed by a rinse with the anhydrous ethanol/HCl described above. Fewer sweeps were accumulated on the sample after the rinse than before, which resulted in a relatively higher noise level. After the data were scaled to the same number of sweeps, it was found that the sodium level had been reduced by at least an order of magnitude. A sodium 1s contribution equal to 10% of the original intensity would still be detectable despite the noise in the after-rinse spectrum. In a more sensitive test, the after-rinse data were smoothed by cross correlation with the initial sodium 1s signal. The result indicated a virtually complete elimination of sodium.

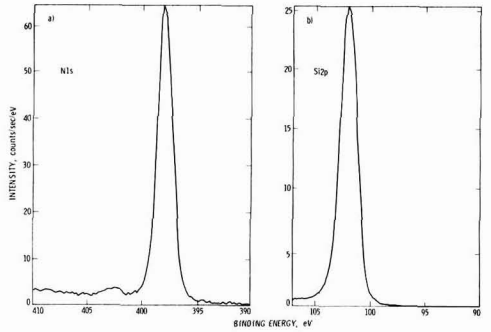

Fig. 1. (a) Nitrogen 1s spectrum from the bulk of the nitride film. These data show the most pronounced example of a peak shifted 4 eV to high binding energy, probably by HF loosely bound to surface nitrogen lone pairs. (b) Typical Si2p spectrum from the bulk of the nitride film.

Results and Discussion

Bulk film composition.—Typical N1s and Si2p lineshapes from the bulk nitride are shown in Fig. 1. The results (22) of a chemical depth profile are shown in Fig. 3. Integrated intensities corrected for relative photoemission cross sections (23), but not corrected for escape-depth differences (24), are shown in Fig. 3a. The N1s and Si2p signals correlate with one another, especially through the bulk region of the film from about 400 down to 75Å. Fluctuations of N1s and Si2p through this region are generally anticorrelated with the C1s intensity, which strongly suggests that the fluctuations are due to variations in a carbonaceous surface overlayer.

The data in Fig. 3a clearly show an oxynitride gradient extending from the surface into the bulk of the film. This familiar feature has already been well documented [Ref. (17, 3, 6, 8, 10, 11, 13, and 15)]. The O1s intensity drops off rapidly toward the bulk O1s value while the N1s intensity rises correspondingly. The width of the gradient at half-height can be estimated from the O1s data to be about 25Å, which is consistent with previous estimates of 6Å equivalent of SiO_2 (XPS on LPCVD nitride) (17), 8Å equivalent of SiO_2 (RBS on LPCVD nitride) (8), and ~30Å (AES on plasma nitride) (4). The O1s data points at 436 and 392Å suggest the possibility that the tail of the gradient may extend deeply, but at low concentration, into the bulk of the nitride film. If this deep penetration truly exists, it probably results from exposing the nitride film to the atmosphere while it is still hot from the furnace.

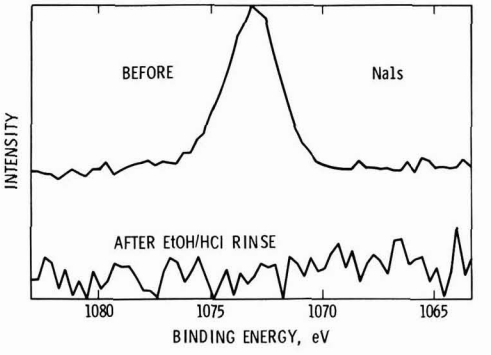

Fig. 2. Sodium 1s etchant residue was effectively removed by an anhydrous ethanol/HCl rinse. Fewer sweeps were accumulated in the lower spectrum, which resulted in a higher noise level relative to the upper spectrum. Smoothing of the lower spectrum by cross-correlation with the upper spectrum indicated the virtually complete removal of sodium.

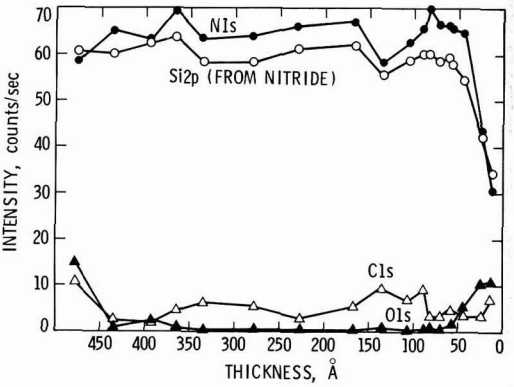

Fig. 3a. Intensities from a chemical depth profile of a nitride/native oxide/silicon structure. Intensities are corrected for cross sections, but not for escape-depth differences. Si2p refers to the contribution from silicon atoms in the silicon nitride film. Substrate was observed when the film was etched to less than 80Å; however, no Si2p intensity from the substrate is shown in the graph.

Within the bulk of the nitride film, the O1s intensity drops to a level indicative of 0.4 ± 0.2 atomic percent (a/o) oxygen. This level, and significantly higher levels, of oxygen incorporation within the bulk are also well documented in the literature (3, 5, 6, 8, 13), and it has been attributed to oxygen-containing impurities in the NH_3 stream by correlating oxygen intensity with with the NH_3/SiH_4 ratio (3, 6).

Using published procedures (24c, d), the integrated intensities in Fig. 3a were converted to the atomic ratio of nitrogen/silicon as a function of depth through the bulk. The integrated intensities of Fig. 3a were already corrected for relative photoionization cross section (23). Corrections for mean-free-path were made by taking $\lambda_{N1s}/\lambda_{Si2p} = (E_{N1s}/E_{Si2p})^{0.75}$ (24a, b, d), where λ is the mean-free-path and E is the photoelectron kinetic energy. This simple expression gave results which agreed within $< 1\%$ with the theoretical calculations of Penn (24c). These corrections are all based on a homogeneous film with a thickness much greater than the mean-free-path. Figure 3a shows that the composition of the film is rather uniform over hundreds of angstroms. Thus, the use of these corrections within the bulk seems justified. The results are replotted in Fig. 3b where the ordinate is now the atomic ratio of nitrogen/silicon corrected for cross section and mean-free-path.

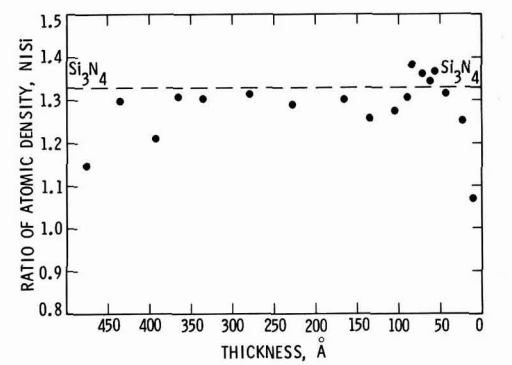

Fig. 3b. Atomic ratio of N/Si *vs.* depth, corrected for cross sections and mean-free-path. Dotted lines shows the ratio for Si_3N_4.

Figure 3b shows that the composition of the film is nearly stoichiometric Si_3N_4, in agreement with AES (6) and RBS analyses of CVD silicon nitride (5c, 8, 12). The average N/Si ratio through the bulk region is 1.31, compared to the stoichiometric ratio, 1.33. The agreement is good, and it lends confidence to the cross-section and mean-free-path corrections. The slight deviation below 1.33 may even suggest a small contribution from Si-Si bonding (12, 15a). Figure 3b also shows that the composition is more uniform than it would seem from Fig. 3a; the fluctuations in Fig. 3a are less significant when ratios are taken for Fig. 3b. The corrections leading to Fig. 3b are only valid within the bulk of the film. The compositional gradients at the interface require a more detailed treatment, which is given below.

Interfacial SiO_2.—It has generally been believed that nitridation converts the tunneling oxide of MNOS structures completely to a graded composition of oxynitride, with no SiO_2 surviving the nitridation process intact (3, 6, 10). We have observed a region of graded oxynitride in this work, but in addition, we have unambiguously identified SiO_2 at the substrate interface.

Figures 4a and b show, respectively, the N1s and Si2p regions after the final etch. These spectra represent a nitride + oxide film with a nominal thickness of 12Å, as determined by the ratio of nitride and oxide Si2p to substrate Si2p. The Si2p data show asymmetry at 103-105 eV, where SiO_2 contributes (25), and not the various forms of oxynitride (17). This asymmetry does not exist in the Si2p spectra of the bulk silicon nitride (Fig. 1b). It is possible to estimate the contribution of silicon nitride in Fig. 4b, subtract it, and analyze the region of asymmetry in detail. The result is in Fig. 4c, which shows the Si2p data of Fig. 4b with an overlay of a Si2p nitride signal from the bulk. The overlay has been scaled to represent the equivalent amount of nitride Si2p intensity corresponding to the nitride N1s intensity in Fig. 4a. Subtracting the overlay gives the result shown in Fig. 4d.

The small peak in Fig. 4d has the characteristics of an Si2p signal from amorphous SiO_2. The separation between the small peak and the substrate Si2p peak is 4.2 eV. Thin films of a-SiO_2 show a separation ranging from 3.9-4.3 eV (25b), depending on film thickness. The energy separation between the small Si2p peak and the corresponding O1s peak is 429.7 eV, which agrees exactly with the O1s-Si2p separation found for 1-2 monolayer films of a-SiO_2 [Fig. 2 in Ref. (25b)]. (O1s from residual ethanol does not interfere with the determination of this separation because it accounts for only 10% of the intensity in the O1s peak corresponding to Fig. 4d. It is only a minor perturbation in the spectra at the interface.) Finally, the atomic

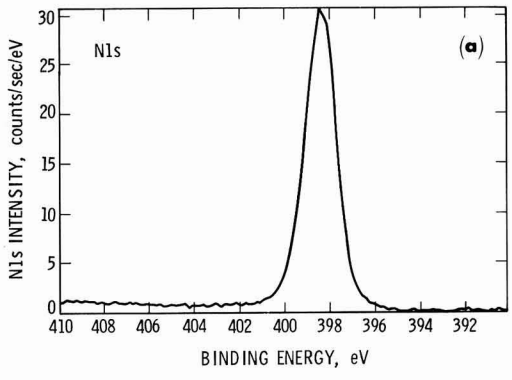

Fig. 4a. N1s signal from a nitride/oxide film with a nominal thickness of 12Å.

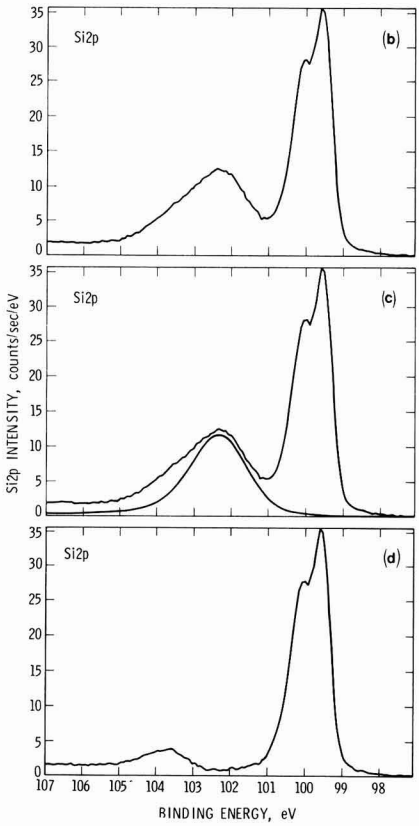

Fig. 4b. The corresponding Si2p signal from the same film as 4a. Fig. 4(c) 4b overlayed with an Si2p nitride spectrum from the bulk. Overlay has been scaled to represent that amount of nitride which would be necessary to account for the N1s intensity in 4a. Fig. 4(d) 4b minus the nitride contribution. Shows the interfacial SiO_2 contribution clearly.

ratio of O/Si for the 104 eV peak corrected for cross section and escape depth is 2.44, *i.e.*, SiO_2 with a small amount of oxygen available for some oxynitride formation and possibly SiOH species. Since this small peak in Fig. 4d appears where SiO_2 is expected, beyond the region where oxynitride is found (17), and since it shows the characteristics determined from pure a-SiO_2 films (25), it is clear that this peak represents SiO_2 still intact at the interface after nitridation. Taking the ratio of this SiO_2 peak to the substrate peak, it was found that this peak represents a thickness of a-SiO_2 equivalent to 4-5Å of SiO_2, approximately 0.8 monolayer. It is, therefore, likely that the SiO_2 layer is not continuous, and that nitrogen-containing species may extend all the way to the interface. The ratio of oxide to substrate intensities is independent of the thickness of an overlayer. Both intensities will be attenuated by the same factor after passing through the overlayer, and the ratio will remain unchanged. Therefore, the thickness of the interfacial SiO_2 layer, which is derived directly from the oxide to substrate ratio, can be determined more accurately than the depth resolution would ordinarily allow. There are, however, limits to the uniformity of the etching; consequently we allow for the possibility of a full monolayer of SiO_2, but certainly less than two monolayers.

The SiO_2 thickness observed here is then compared to estimates of a 15-20Å equivalent thickness of "SiO_2" in other nitride samples (11). First, it must be remem-

bered that the MNOS structure profiled in this work includes only a native oxide estimated by single wavelength ellipsometry to be approximately 5Å thick before the silicon wafer was placed in the reactor. A much stronger SiO_2 peak would be expected for a MNOS structure made with an intentionally grown thermal oxide. Second, the 15-20Å "SiO_2" estimate from SE results (11) is explained to be a virtual thickness which refers only to the silicon-oxygen content in a given nitride film, and not the identification of the specific chemical state of stoichiometric SiO_2. Finally, it is conceivable that the native oxide on this sample may have been partially etched at the start of LPCVD by chlorine-free radicals released from the pyrolysis of SiH_2Cl_2.

The existence of interfacial SiO_2 was strongly suggested by earlier experiments on specially prepared control samples (26). The samples were thin (20-40Å) layers of LPCVD silicon nitride on both native and thermally grown tunneling oxides. The deposited nitride films were intentionally made thinner than a few photoelectron mean-free-paths, so that XPS could be used to study the nitride/oxide and oxide/substrate interfaces simultaneously without the requirement of etching. The results are shown in Fig. 5, which compares the Si2p data for a 20Å nitride/22Å thermal oxide/silicon structure (Fig. 5a) with Si2p data from a 16Å film of thermal SiO_2 (Fig. 5b). A resolution enhancement algorithm based on maximum entropy spectral estimation has been applied to each set of data; this algorithm and its applications have been described in detail elsewhere (27). The results of the resolution enhancement are overlayered on the data in Fig. 5. Extensive work (25) has lead to a detailed understanding of the Si2p spectrum of SiO_2, such as the data in Fig. 5b. Three peaks are conspicuous near 104 eV in the resolution-enhanced SiO_2 spectrum in Fig. 5b. This triad is reproducibly found in all such enhanced SiO_2 spectra; it has been suggested (25) that these peaks reflect Si-O-Si bond angles of approximately 120, 144, and 160-180 degrees. The a-SiO_2 peaks in Fig. 5b are labeled with the bond angles which they represent. In the absence of gross interference, this triad can be taken as an identifying characteristic of a-SiO_2 in XPS Si2p data.

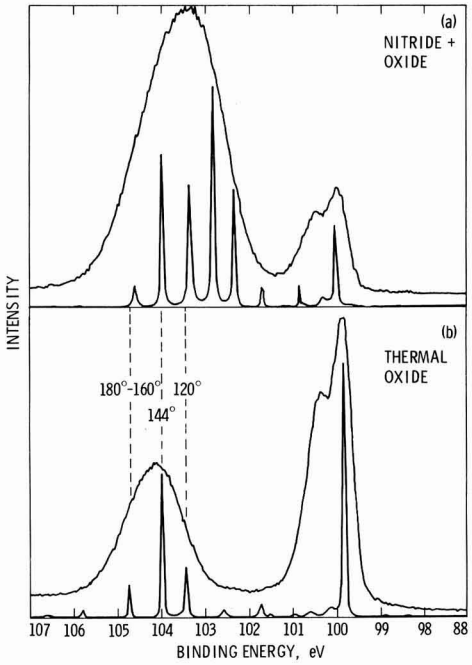

Fig. 5. (a) Si2p data from a 20Å LPCVD silicon nitride/22Å thermal oxide/silicon (100) structure. (b) Si2p data from a 16Å thermal oxide. Both data sets are shown with the results of resolution enhancement. [See Ref. (25 and 27).] The triad of oxide peaks is shown with each peak labeled according to the Si-O-Si bond angle which it represents (25, 27). Spectrum (a) has been shifted to align the 144° oxide peaks for clarity. It then appears that the substrate signals near 100 eV differ by 0.2 eV. This difference is within the errors of computation, doping differences, and surface potentials.

In the thin nitride/thermal oxide data of Fig. 5a, the energy regime where SiO_2 Si2p photoelectrons are found is chemically shifted beyond the region where the nitride and oxynitride Si2p contribute (17). Thus, the oxide region of the spectrum is relatively free of interference, and we can look for the a-SiO_2 triad in the resolution-enhanced spectrum as evidence of a-SiO_2 in the film. In the SiO_2 region of Fig. 5a, the resolution-enhanced data show a three-peak structure which closely corresponds to the triad in the SiO_2 model spectrum in Fig. 5b. This agreement was not built into either spectrum by any manipulation of the algorithm. Similar results on two other samples led us to conclude that a-SiO_2 was a component of these thin nitride control samples. Beyond the identification of a-SiO_2, the enhanced spectrum of Fig. 5a becomes difficult to interpret. Within the binding energy region of 101-102 eV, one expects a multiplicity of chemical states due to oxynitride, nitride, and hydrogen bonding. An extensive enhancement calculation would be required to resolve the diversity of subtly shifted chemical states in this region. Therefore, the peaks observed in this region of Fig. 5a are only representative of the possible contributions; these peaks cannot be assigned unambiguously. These complications were not present in the enhancement of SiO_2 data such as in Fig. 5b.

Interface composition.—The calculation of the N/Si atomic ratio in Fig. 3b was done assuming a thickness much greater than the mean-free-path with a uniform composition within the film. This reasoning was only valid in the bulk of the film; analysis of atomic ratios within a few mean-free-paths of the interface must account for the compositional gradients in this region. The method for calculating atomic ratios in this region is a straightforward adaptation of the calculation by Vasquez (28) on the SiO_2/Si interface.

The region of variable composition is modeled as a stack of thin layers, with each layer having a uniform composition. The intensity (normalized with respect to relative cross section) from a stack of n layers, $I(n)/\sigma$ is related to the intensity from $n-1$ layers, $I(n-1)/\sigma$ by Eq. [1a]

$$\frac{I(n)}{\sigma} = \frac{I(n-1)}{\sigma} \exp(-d/\lambda \sin\theta) + I_x A T \rho \lambda \sin\theta [1 - \exp(-d/\lambda \sin\theta)] \quad [1a]$$

where I is the observed intensity of photoelectrons from a given orbital of a given atom, σ is the relative cross section for photoemission, ρ is the atomic density of the atom being measured, λ is the photoelectron mean-free-path, d is the thickness of one of the hypothetical layers, and $I_x A T \sin\theta$ are the instrument parameters representing x-ray intensity, sample area, spectrometer transmission, and photoelectron takeoff angle $\theta = 38.5°$. Equation [1a] can now be solved for ρ, the atomic density. If this procedure is followed for two components, *e.g.*, nitrogen and silicon, a ratio of atomic densities can be derived in which the instrumental parameters cancel to a close approximation

$$\frac{\rho_N}{\rho_{Si}} = \frac{[I(n)_{N1s} - I(n-1)_{N1s} \exp(-d/\lambda_{N1s} \sin\theta)]\ \sigma_{Si2p}\lambda_{Si2p}\,[1 - \exp(-d/\lambda_{Si2p} \sin\theta)]}{[I(n)_{Si2p} - I(n-1)_{Si2p} \exp(-d/\lambda_{Si2p} \sin\theta)]\ \sigma_{N1s}\lambda_{N1s}\,[1 - \exp(-d/\lambda_{N1s} \sin\theta)]} \quad [1b]$$

The intensities are measured, and ratios of cross section (23) and mean-free-paths (24) can be obtained to sufficient accuracy. The use of $\lambda_{Si2p} = 30$Å causes $< 2\%$ error in the calculation of ρ_N/ρ_{Si}, because Eq. [1b] depends only weakly on the choice of λ_{Si2p}. Ratios of N/Si and O/Si were calculated, from which an N/O ratio could be derived. From these data, atomic fractions of O, N, and Si could be derived as a function of thickness, as shown in Fig. 6. These atomic fractions do not include a contribution from hydrogen, which cannot be directly measured by XPS.

The oxygen profile shown in Fig. 6 decreases rapidly at the interface, and the oxygen concentration drops to 20% of its initial value within a few angstroms, in general agreement with the conclusion reached independently by Frenzel and Balk (9). Over the next 16Å, the concentration decreases slightly and is approximately constant. After 24Å, the oxygen concentration declines until it merges with the bulk concentration of 0.4 ± 0.2 a/o. There is no apparent evidence of SiO_2 in this region; therefore, it is likely that the composition is best described in terms of a low concentration oxynitride gradient. Within 45Å, the oxygen level drops below 2 a/o; the bulk composition is reached at a thickness between 50-60Å. The amount of oxygen in this gradient is represented pictorially in Fig. 9.

The nitrogen profile is consistent with the oxygen results, showing the likelihood of nitrogen-containing species extending to the interface. The rest of the profile is consistent with the low concentration oxynitride gradient, which reaches nearly pure Si_3N_4 at ~45Å.

The silicon profile in Fig. 6 shows a conspicuous increase at a thickness of 4-8Å. To interpret this increase, we invoke the same bonding model described by Philipp (29) and Raider (17), that all silicon is bonded tetrahedrally by single bonds to other silicon, oxygen, and nitrogen (29), and that all oxynitride bonding occurs in the form of siloxane (Si-O-Si) and silazane (Si-N-Si) bridges (17). Within the context of this model, the total number of available silicon single bonds must equal the combined numbers of oxygen and nitrogen single bonds. In Fig. 7 we divide the number of available silicon single bonds (4× atomic fraction of Si) by the sum of oxygen and nitrogen single bonds (2× oxygen fraction + 3× nitrogen fraction). Where this fraction deviates from unity, we must consider some deviation from the simple oxynitride model, such as Si-Si or Si-H bonding. Figure 7 shows a layer of excess bonds to silicon about 8Å thick. The ratio in Fig. 7 peaks at 4-8Å, where there is found a clear excess of silicon bonds which cannot be accounted for by simple oxygen and nitrogen coordination. It seems that the excess exists on top of the native oxide layer.

Certain aspects of this observation are in qualitative agreement with results obtained by others (11). However, it is unlikely that this region contains any substantial amount of amorphous silicon. In the presence of oxygen and excess nitrogen at elevated temperatures, amorphous silicon would be unstable with respect to the formation of oxides and nitrides. Si-Si and Si-H bonding plus Si dangling bonds within an oxynitride framework are more plausible. Therefore, rather than speaking of excess silicon, we refer to this system in terms of excess bonds to silicon. Figure 7 indicates that as much as 90% of the silicon in the region of peak excess may have a bond not going to nitrogen or oxygen. A reasonable representation of this bonding arrangement is shown in Fig. 9.

It is important to emphasize that the excess bonds to silicon cannot be attributed to a spurious substrate silicon contribution due to nonuniform etching or some other artificial result. The substrate and nitride/oxide silicon form two distinct Si2p peaks resolved from one another. (See Fig. 4b.) Substrate Si2p appears at 99.5 eV; nitride/oxide Si2p appears at 102 eV. The substrate contribution was not included in taking Si2p intensities for the silicon profile.

While this evidence strongly suggests the existence of the excess bonds, full confirmation awaits the replication of these observations on other samples. The source of the excess also remains to be identified. Reaction products from etching are possible contributors. It is likely that etching leaves some surface silicon bonds hydrogenated after the elimination of nitrogen. The relative contribution of this surface layer becomes increasingly significant as the film thickness decreases; the apparent result would be a gradual increase in Si-H bonding as the etching approached the interface. However, the peak shown in Fig. 7 rises so sharply that one is led to also consider the LPCVD process as a source of the excess bonds to silicon. Perhaps the excess bonds hold clues about the mechanisms involved in the interaction of reactant gases with the native oxide during the initial stages of LPCVD.

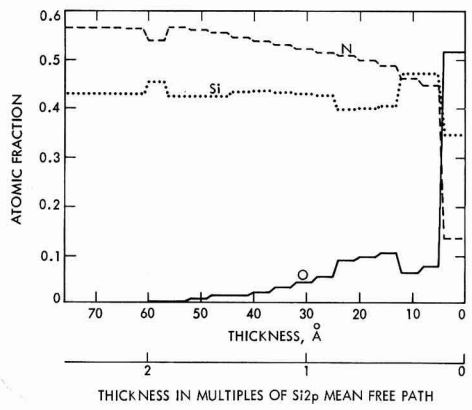

Fig. 6. Atomic fractions of oxygen, nitrogen, and silicon as a function of thickness. These atomic fractions do not include a contribution from hydrogen, which cannot be measured by XPS.

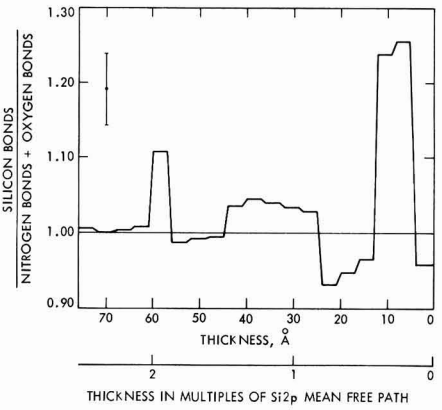

Fig. 7. Ratio of available silicon single bonds to the number of oxygen and nitrogen single bonds. vs. thickness. The excursion at 60Å represents the maximum limit of experimental error.

One possibility is the reduction of interfacial SiO_x and SiO_2 during the initial nitridation. This process was once used as a method of making silicon nitride according to the following reaction (30)

$$3SiO_2 + 6C + 2N_2 \xrightarrow[1200°\text{-}1500°C]{H_2} Si_3N_4 + 6CO \quad [2]$$

Many of the conditions of this reaction are satisfied by the system being considered here. Carbon is available as a contaminant found on the native oxide surface before deposition, and LPCVD conditions provide hydrogen and nitrogen species. Although reaction [2] could be run at 1200°C using oxide catalysts, the temperature still exceeds the LPCVD range of 750°C. However, the high temperature may only have been necessary to cleave the N_2 bond in reaction [2], and this step is not required in LPCVD using NH_3. Therefore, it is possible that, at lower LPCVD temperatures, a reaction would start, but not necessarily go to completion as in Eq. [2]. Instead, some mechanism similar to Eq. [2], and involving interfacial SiO_x, might govern a reaction which stops after consuming the carbon contaminant layer, and yields products of suboxides, subnitrides, and oxynitrides containing Si-Si and Si-H bonds.

Another possibility is a surge of SiH_2Cl_2 when the inlet valve is opened at the start of LPCVD. Other mechanisms are not as well defined. Nevertheless, under these conditions of deposition and etching, the data indicate the existence of one or two monolayers of oxynitride containing excess bonds to silicon on top of the native oxide.

Implications for Device Performance and Processing

Several features of the interfacial structure determined in this study may be significant in terms of MNOS endurance and retention effects. In particular, the region of excess bonds to silicon is likely to be chemically labile under electrical stress. A plausible bonding arrangement representative of this region is given schematically in Fig. 8. Two silicon atoms are connected to nitrogen and oxygen by single bonds. The silicons are also connected to one another through a single bond, which is one example of an excess bond to silicon not accounted for by nitrogen or oxygen. Other possibilities include Si-H and Si dangling bonds.

The Si-Si bond strength has been measured at various values ranging from 2-3 eV (31). Therefore, it is possible that during write/erase cycling, hot electrons (or holes) could cleave Si-Si bonds near the interface. Recombination is expected, unless the broken bond is stabilized chemically, or unless lattice relaxation pulls the silicon atoms too far apart to reestablish a bond, thus forming Si dangling bonds. Relief of lattice strain is, therefore, a central theme in this proposal. The strain concept has already been successful in providing a basis for understanding the formation of Si^{+3} sites at the SiO_2/Si interface (32); the Si dangling bond sites formed in Fig. 8 are analogous to the Si^{+3} formed in the SiO_2/Si system.

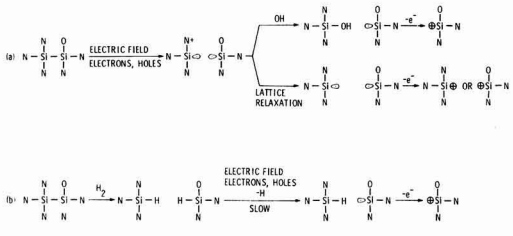

Fig. 8. Representation of Si—Si bond cleavage in an oxynitride structure to yield trapped positive charge at the interface after write/erase cycling.

During further write/erase cycling, electron impact may ionize the Si dangling bonds and leave a positive charge at the interface. The net effect observed electrically would be a shift in the logical voltage window. It is expected that, as an intrinsic result of the LPCVD process, some Si dangling bonds exist in the film even before write/erase cycling; they should behave the same way as the Si dangling bonds produced in Fig. 8.

Si-H bonds are also subject to cleavage and the formation of Si dangling bonds. It has, in fact, been shown that electron irradiation under a negative bias condition is capable of converting interfacial Si-H to Si^0 in native oxide MNOS structures; it is possible to interpret the Si^0 observed in this conversion as an Si dangling bond (35). Following hydrogen removal, an Si dangling bond is left to be ionized, again leaving a fixed charge at the interface.

In these terms, a mechanism can be proposed to explain recent experience in hydrogen annealing (34). In this case, Si-Si linkages would be converted to Si-H. No additional dangling bonds would be formed; those dangling bonds which exist intrinsically after LPCVD would also be converted to Si-H. There would be a substantial reduction in the number of Si dangling bonds remaining to be ionized by electron impact. Since the bond energies of Si-H and Si-Si are comparable (31), the cleavage of Si-Si bonds by H_2 is probably assisted by lattice strain. Thus, the hydrogen annealing process may also be interpreted as a strain relief mechanism. It is found that hydrogen annealing mitigates the endurance problem, but does not eliminate it. Therefore, we must propose that strained Si-Si bonds, which may exist before hydrogen annealing, cleave more readily than unstrained Si-H bonds after hydrogen annealing.

Si dangling bonds are not limited to a role as electron donors leading to interfacial positive charge. A singly occupied dangling orbital can also accept an electron. Therefore, dangling bonds are expected to be amphoteric, *i.e.*, having the ability to act as an electron acceptor as well as an electron donor. As electron acceptors, Si dangling bonds could receive electronic charge from the bulk and trap it near the interface, where it could tunnel out of the film. Thus, Si dangling bonds can function as "hopping" sites for electrons to leak back into the substrate, resulting in a loss of retention. Si dangling bonds resulting from the dehydrogenation of Si-H centers have been proposed as the cause of increased conductivity in thermally annealed silicon nitride films (37).

The silicon nitride, oxynitride, and oxide are also sources of dangling bonds and other amphoteric sites. Although Si-N and Si-O bonds are stronger than Si-Si and Si-H bonds, they are still subject to cleavage during electrical stress, particularly in the presence of a strained lattice. The cleavage of Si-O bonds in SiO_2 under electron bombardment has already been documented (32). The resulting Si^{+3} sites and nonbridging oxygen sites have been described in terms of being amphoteric, self-annealing charge traps. In silicon nitride, Si-N bond cleavage leading to amphoteric, annealable charge traps has also been proposed (36). The low-level oxynitride gradient extending into the film may, therefore, be a source of "hopping" sites for the dissipation of charge from the bulk back into the substrate.

The native oxide layer, which was found intact at the interface in this work, represents a system which has been shown to contain strained bonds and silicon suboxides (25, 32). Suboxides of silicon, especially Si^{+3}, have been found to be active as interface states (25, 32) which are capable of amphoteric charge trapping behavior. Si^{+3} has also been shown to disproportionate into Si^{+4} and Si^0 under electron irradiation (33); the Si^0 then becomes available for the formation of Si-Si and Si-H bonds, which have al-

ready been discussed in terms of charge trapping. These considerations are particularly relevant in the case of native oxide MNOS structures, because the conditions which exist at the interface during deposition (hydrogen, surface carbon, high temperature) would promote the reduction of the oxide to suboxides.

These results prompt the consideration of processing steps aimed at minimizing the formation of trap sites which limit device performance. The potential sources of traps implicated in this work include the excess bonds to silicon, lattice strain, intermediate oxidation states of silicon in the native oxide, and the oxynitride gradient extending into the film. This study suggests that excess bonds to silicon may be due to the interaction between the LPCVD reactant gases, surface carbon, and the native oxide; a momentarily high partial pressure of SiH_2Cl_2 may also contribute. Accordingly, control of surface carbon contamination and the elimination of an SiH_2Cl_2 pressure surge at the start of deposition might limit the formation of excess bonds to silicon.

Intermediate oxidation states, oxynitride, strained bonds, and excess bonds to silicon are all related to the native oxide. Therefore, it may also be desirable to eliminate the native oxide layer with an *in situ* HCl etch in the reactor tube. Pyrolysis of SiH_2Cl_2 probably contributes toward the removal of some native oxide; the brief addition of HCl to the gas stream immediately prior to SiH_2Cl_2 should complete the removal process.

Any or all of these processing changes may assist in producing more effective native oxide MNOS devices.

Conclusions

Stopped-flow chemical etching has been used in conjunction with XPS to obtain a detailed compositional profile of a native-oxide LPCVD MNOS structure. Numerous surface and bulk features were observed, including a surface oxynitride gradient and stoichiometric nitride in the bulk film. The bulk stoichiometry was essentially equal to the ideal Si_3N_4 with a 0.4 a/o oxygen impurity and possibly an observable contribution from Si-Si bonding.

The interfacial region has been revealed at a high level of detail and depth resolution. The essential features of the interface are summarized in Fig. 9. Some SiO_2 has been found intact at the interface after nitridation. The total amount present is approximately a monolayer, and probably about 0.8 monolayer. Therefore, it is likely that the SiO_2 is not continuous, and that nitrogen-containing species may reach all the way to the interface. This thin coverage is consistent with the fact that only a native oxide was present before nitridation.

On top of the native oxide, there is a layer containing excess bonds to silicon. The thickness of this region is about 8Å. The excess bonds do not imply a distinct phase of amorphous silicon. Instead, it is most likely that the excess bonds represent Si-Si and Si-H bonds plus Si dangling bonds in an oxynitride framework. These three possibilities cannot be distinguished easily because XPS cannot measure hydrogen directly. The mechanism of the formation of the excess bonds has not been confirmed. Etching by-products may account for some of the bonds, but the initial reaction of the LPCVD gases with the native oxide surface must also be involved. A reduction mechanism and an SiH_2Cl_2 surge are also proposed as possible explanations.

The oxide/nitride interface is characterized by both sharp and diffuse features. Within less than 8Å, the oxygen concentration drops off to one fifth of the initial concentration at the substrate interface. Thereafter, an oxynitride gradient does indeed exist. However, the amount of oxygen incorporation is quite modest, never exceeding 10 a/o, and dropping below 2 a/o within 45Å. At 50-60Å, the composition of the film is indistinguishable from the bulk within the detection limits of this technique. Thus, at least in this case of a native-oxide MNOS structure, the oxide/nitride interface is best described as being sharp with only a low concentration of oxygen extending into the LPCVD film.

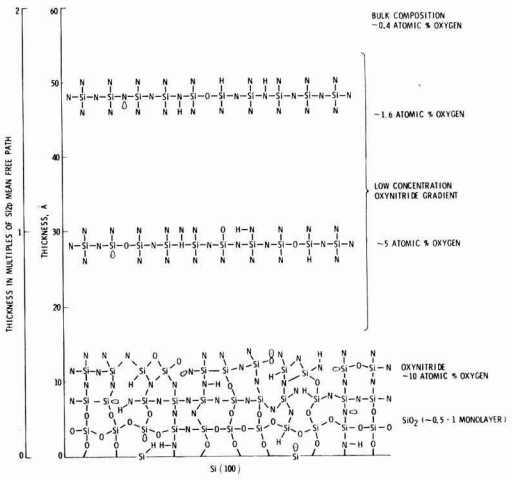

Fig. 9. Schematic diagram showing the essential features of a native-oxide LPCVD MNOS interface determined from this study. The bonding arrangement shown is one example of a geometry which would be consistent with the atomic fractions and chemical shifts observed in this work. Specific examples are given for excess bonds to silicon, strained bonds, and oxynitride. To maintain clarity in this 2-dimensional representation of a 3-dimensional situation, some of the bonds to nitrogen and oxygen have not been included. Also, for simplicity, strain is not shown explicitly in the oxynitride gradient, although it is believed to exist. The hydrogen bonds have been drawn from inference because hydrogen cannot be measured directly by the techniques used in this work.

The excess bonds to silicon, the Si-O and Si-N bonds, and intermediate oxidation state of silicon may be sources of endurance and retention problems. Under the influence of lattice strain, these systems may undergo bond cleavage resulting in amphoteric trap sites. Some suggestions are proposed for processing steps directed at minimizing the formation of these trap structures.

Acknowledgments

LPCVD nitride samples were kindly provided with helpful discussion and explanation by J. R. Cricchi and F. L. Hampton of Westinghouse, M. C. Peckerar at the Naval Research Laboratory, and M. Beguwala and F. Erdmann of Rockwell International. J. Maserjian has also provided beneficial advice. The authors thank P. Chimiklis for assistance with the chemical etching, and C. Akers for help with data reduction. Thanks also to M. Brandenberg for manuscript preparation.

This work was supported by the U.S. Air Force, Rome Air Development Center, Deputy for Electronic Technology, Hanscom Air Force Base, and was monitored by Dr. P. Vail and Mr. H. DeAngelis. Instrument support was provided by the National Aeronautics and Space Administration under Contract NAS7-100. The work was performed at the Jet Propulsion Laboratory, California Institute of Technology.

Manuscript submitted Nov. 30, 1981; revised manuscript received April 12, 1982.

Any discussion of this paper will appear in a Discussion Section to be published in the December 1983 JOURNAL. All discussions for the December 1983 Discussion Section should be submitted by Aug. 1, 1983.

Publication costs of this article were assisted by the Californa Institute of Technology.

REFERENCES

1. P. Balk, in the "Proceedings of the 8th International Vacuum Congress," Vol. I, F. Abélès and M. Croset, Editors, p. 525, Cannes, France (1980).
2. (a) J. J. Chang, *IEEE Trans. Electron Devices*, **ed-24**, 511 (1977); (b) A. V. Ferris-Prabhu, *ibid.*, p. 524.
3. J. S. Johannessen, C. R. Helms, W. E. Spicer, and Y. E. Strausser, *IEEE Trans. Electron Devices*, **ed-24**, 547 (1977).
4. S. Thomas and R. J. Mattox, *This Journal*, **124**, 1942 (1977).
5. (a) P. H. Holloway, *Surf. Sci.*, **54**, 506 (1976); (b) P. H. Holloway and H. J. Stein, *This Journal*, **123**, 723 (1976); (c) H. J. Stein, S. T. Picraux, and P. H. Holloway, *IEEE Trans. Electron Devices*, **ed-25**, 1008 (1978).
6. V. J. Kapoor, R. S. Bailey, and S. R. Smith, *J. Vac. Sci. Technol.*, **18**, 305 (1981).
7. A. Van Oostrom, *Surf. Sci.*, **89**, 615 (1979).
8. F. H. P. M. Habraken, A. E. T. Kuiper, A. Van Oostrom, Y. Tamminga, and J. B. Theeten, To be published.
9. (a) H. Frenzel and P. Balk, in "The Physics of MOS Insulators," "Proceedings of the International Topical Conference, Raleigh, North Carolina," G. Luscovsky, S. T. Pantelides, and F. L. Galeener, Editors, p. 246, Pergamon Press, Inc., New York (1980); (b) H. Frenzel and P. Balk, in the "Proceedings of the 8th International Vacuum Congress," Vol. I, F. Abélès and M. Croset, Editors, p. 538, Cannes, France (1980).
10. R. Hezel and N. Lieske, in the "Proceedings of the Conference on Insulating Films and Semiconductors," Durham, 1979, Institute of Physics Conference Series No. 450, G. G. Roberts and M. J. Morant, Editors, p. 206.
11. J. B. Theeten, D. E. Aspnes, F. Simondet, M. Erman, and P. C. Mürau, To be published.
12. J. Gyulai, O. Meyer, J. W. Mayer, and V. Rodriguez, *J. Appl. Phys.*, **42**, 451 (1971).
13. S. Rigo, G. Amsel, and M. Croset, *J. Appl. Phys.*, **47**, 2800 (1976).
14. A. K. Sinha and E. Lugujjo, *Appl. Phys. Lett.*, **32**, 245 (1978).
15. (a) H. J. Stein and H. A. R. Wegener, *This Journal*, **124**, 908 (1977); (b) P. S. Peercy, H. J. Stein, B. L. Doyle and S. T. Picraux, *J. Electron. Mater.*, **8**, 11 (1979).
16. P. C. Mürau and B. Singer, in Proceedings of the International Electron Devices Meeting, Washington, D.C., 1978, p. 452.
17. S. I. Raider, R. Flitsch, J. A. Aboaf, and W. A. Plişkin, *This Journal*, **123**, 560 (1976).
18. H. Loic, "Method of Etching a Pattern in a Silicon Nitride Layer," U.S. Pat. 3,867,218 (1975); German Pat. 2,321,013 (1974); British Pat. 1,420,155 (1976).
19. F. J. Grunthaner, P. J. Grunthaner, C. Butler, R. P. Vasquez, and J. A. Wurzbach, Submitted to *This Journal*.
20. T. A. Carlson and G. E. McGuire, *J. Electron Spectrosc. Rela. Phenom.*, **1**, 161 (1972/1973).
21. J. A. Taylor, G. M. Lancaster, A. Ignatiev, and J. W. Rabalais, *J. Chem. Phys.*, **68**, 1776 (1978).
22. Preliminary results were presented at the Non-Volatile Semiconductor Memory Workshop, Vail, Colorado, August 1980.
23. J. H. Scofield, Lawrence-Livermore Laboratory Report No. UCRL-51326 (1973), and *J. Electron Spectrosc. Rela. Phenom.*, **8**, 129 (1976).
24. (a) C. J. Powell, *Surf. Sci.*, **44**, 29 (1974); (b) Handbook of X-Ray Photoelectron Spectroscopy, G. E. Muilenberg, Editor, p. 5, Perkin-Elmer Corp., Eden Prairie, Minnesota (1979); (c) D. R. Penn, *J. Electron Spectrosc. Rela. Phenom.*, **9**, 29 (1976); (d) C. D. Wagner, *Anal. Chem.*, **49**, 1282 (1977).
25. (a) F. J. Grunthaner and J. Maserjian, in "The Physics of SiO_2 and Its Interfaces," S. T. Pantelides, Editor, p. 389, Pergamon Press, Inc., New York (1978); (b) F. J. Grunthaner, P. J. Grunthaner, R. P. Vasquez, J. Maserjian, and A. Madhukar, *J. Vac. Sci. Technol.*, **16**, 1443 (1979); (c) R. N. Nucho and A. Madhukar, *Phys. Rev. B*, **21**, 1576 (1980); (d) F. J. Grunthaner, P. J. Grunthaner, R. P. Vasquez, B. F. Lewis, J. Maserjian, and A. Madhukar, *Phys Rev. Lett.*, **43**, 1683 (1979).
26. J. A. Wurzbach and F. J. Grunthaner, "Examination of Thin Silicon Nitride Layers on MNOS Tunneling Oxides by X-Ray Photoelectron Spectroscopy," Presented at the IEEE Semiconductor Interface Specialists Conference, New Orleans, 1979.
27. R. P. Vasquez, J. D. Klein, J. J. Barton, and F. J. Grunthaner, *J. Electron Spectrosc. Rela. Phenom.*, **23**, 63 (1981).
28. R. P. Vasquez and F. J. Grunthaner, *Surf. Sci.*, **99**, 681 (1980).
29. H. R. Philipp, *This Journal*, **120**, 295 (1973).
30. E. Friederich and L. Sittig, *Z. Anorg. Chem.*, **65**, 38 (1925).
31. E. Hengge, "Silicon Chemistry II, Topics in Current Chemistry," Vol. 51, p. 52, Springer-Verlag, New York (1974).
32. F. J. Grunthaner, B. F. Lewis, R. P. Vasquez, J. Maserjian, and A. Madhukar, in "The Physics of MOS Insulators," "Proceedings of the International Topical Conference, Raleigh, North Carolina, June 1980," G. Lucovsky, S. Pantelides, and F. Galeener, Editors, p. 290, Pergamon, New York (1980).
33. (a) J. A. Wurzbach, *ibid.*, p. 172; (b) P. J. Grunthaner, F. J. Grunthaner, and J. W. Mayer, *J. Vac. Sci. Technol.*, **17**, 924 (1980).
34. (a) F. L. Hampton and J. R. Cricchi, Private communication; (b) M. C. Peckerar and N. Bluzer, *IEEE Trans. on Nucl. Sci.*, **ns-27**, 1753 (1980).
35. (a) J. Wurzbach, F. Grunthaner, and J. Maserfian, Presented at the Semiconductor Interface Specialists Conference, Ft. Lauderdale, Fla., Dec. 1980. Manuscript in preparation; (b) F. Grunthaner, P. Grunthaner, R. Vasquez, J. Wurzbach, B. Lewis, and J. Maserjian, Presented at the same conference.
36. C. T. Kirk, Jr., *J. Appl. Phys.*, **50**, 4190 (1979).
37. H. J. Stein, *J. Electron. Mater.*, **5**, 161 (1976).

A Study of Impurities and Traps in Liquid Phase Epitaxial InP in Relation to Melt Prebaking

Jin K. Rhee and Pallab K. Bhattacharya

Department of Electrical and Computer Engineering, Oregon State University, Corvallis, Oregon 97331

ABSTRACT

Deep- and shallow-level defects in liquid phase epitaxial InP have been detected and characterized by transient capacitance, Hall transport, and photoluminescence measurements. The background impurity levels in the undoped crystals were varied by varying the period of prebaking of the In melt. A single deep electron trap with activation energy $\Delta E_T = 0.38 \pm 0.02$ eV is present dominantly with a concentration almost three orders lower than the background carrier concentration in the layers. From electron capture measurements, the electron capture cross section is found to obey the law $\sigma_n(T) = 4.78 + 10^{-15} \exp(-0.13/kT)$. The consistency of its concentration, irrespective of the purity of the crystal, and its removal after short-term heat-treatment leads us to believe that the trap is related to native defects. A hole trap with an activation energy of 0.22 eV was detected in some samples at low temperatures.

The fabrication of InP microwave and millimeter wave devices necessitates the growth of active layers of high purity. Liquid phase epitaxy (LPE) is a widely used technique for growing device quality InP. High-purity epitaxial InP and InP-based compounds are also being considered as an alternate host material for the fabrication of ion-implanted devices (1, 2). The presence of unintentional impurities in the melt, substrate, source materials, and growth ambient have plagued the growth of LPE InP with reproducible purity. It has now been recognized that Si and S are the two major background donor impurity species present in the In and InP used to form the growth solution, and C is the principal acceptor, originating from the graphite boat.

In addition to impurities giving rise to shallow donor and acceptor levels, there may also be present deep levels arising from impurities or grown-in and propagating native defects. There has not been any report of a detailed study of trap levels in LPE InP, except that of the presence of a 0.36 eV electron trap in such material by Nickel and Kuphal (3).

In this paper, we report the LPE growth of undoped single layers of InP which are suitable for a detailed study of traps. The layers were grown with varying periods of prebaking of the In melt in an ultrapure H_2 ambient. Prolonged prebaking of the melt is one of the most successful methods utilized to grow high-purity crystals (4, 5). Silicon present in the melt is converted to SiO_2 by minute traces (<0.1 ppm) of H_2O present in the H_2 ambient according to

$$Si(l) + 2H_2O(g) \rightleftarrows SiO_2(s) + 2H_2(g)$$

SiO_2 does not affect the purity of the crystal. Other techniques which are now being used to achieve high purity are: introduction of controlled amounts of H_2O in the growth ambient (6), use of epitaxial InP grown on dummy substrates as the source material (7), growth in a PH_3 atmosphere (8), and extended prebaking of the melt in high vacuum ($\sim 10^{-6}$ Torr) (9). The last method is claimed to be particularly effective for the removal of S. It has also been found that the intentional introduction of H_2O can lead to inferior surface morphology and the creation of O-related traps (9). The electrical and optical quality of the layers grown by us were evaluated from analysis of temperature dependent Hall-effect data and high-resolution photoluminescence (PL) spectra, respectively. We find that layers with reasonable purity ($n_{300\,K} = 4 \times 10^{15}$ cm^{-3}, $\mu_{77\,K} = 30{,}000$ cm^2/V · sec) can be grown with only 20 hr prebaking of the In melt in our growth system.

Detailed transient thermal emission and capture measurements were performed to determine the trap spectra in undoped LPE InP of reasonable purity. We find that the 0.36 eV electron trap reported by Nickel and Kuphal (3) is also dominant in our layers. We have studied the physicochemical origin of this trap by varying the growth conditions and by performing postgrowth annealing. An additional hole trap, located 0.22 eV above the valence band, was detected in some layers at low temperatures, but was not a dominant center. Our results lead us to conclude that the dominant electron trap in LPE InP is related to a native defect. Transitions involving acceptor impurities were detected in the low-temperature PL spectra.

Experimental

Liquid phase epitaxial growth of InP.—Single layers of LPE InP, 5-7 μm thick, were grown on nominally (100)-oriented InP:Fe substrates in a horizontal graphite sliding boat system. The reaction tube was made of suprasil quartz. The graphite boat was first heated at 1000°C for 4 hr under a vacuum of 2×10^{-7} Torr and then back-filled with He. The boat was then loaded in the reaction tube, and all the grooves were loaded with 99.9999% In (Johnson Matthey) and baked at 730°C for 72 hr under Pd-diffused H_2 flow. This purging step is crucial for the removal of residual impurities in the walls of the boat. The boat was cooled to room temperature and loaded with 4g In for the *in situ* melt-etch and 2.5g In for the growth melt which were then baked at 730°C for periods ranging from 10-70 hr. The system was again cooled and an appropriate amount of polycrystalline source InP ($\mu_{77\,K} = 75{,}000$ cm^2/V · sec) was added to the growth melt to form the growth solution. The time-temperature cycle for a typical epitaxial growth run is depicted in Fig. 1. The reaction tube was sealed and purged with purified H_2 for at least 2 hr (A to B). The In-InP solution was baked at 730°C for 10 hr (C to D). During this period, the solution was covered with a graphite cap to prevent evaporation of P atoms. At time E, the polished and cleaned substrate was loaded into the boat at room temperature. The growth system was again purged

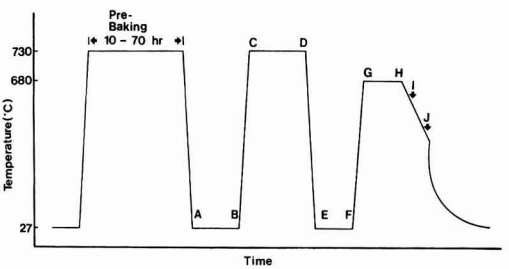

Fig. 1. Time-temperature cycle for a typical epitaxial growth run with ramp-cooling and *in situ* meltback etching.

with H_2 for 2 hr (E to F). The temperature was then raised to and held at 680°C for 30 min. During this time (G to H), the substrate was covered with a graphite cap to minimize loss of P from its surface. A ramp-cooling was then set in the programmer-controller, and the boat with its contents were cooled at 1°C/min. It is our experience that ramp-cooling gives better surface morphology than step-cooling for the growth of single InP layers. When the temperature of the growth melt reached 675°C (time I), *in situ* etching of the substrate was accomplished by sliding the pure In melt on top of the substrate for a few seconds. Epitaxial growth was then initiated by pulling the In-InP saturated melt on the substrate. Growth was terminated at time J by sliding the melt away from the grown epitaxial layer. The growth time varied typically from 15 to 20 min. Figure 2 depicts the surface morphology of a layer grown after 20 hr prebaking of the melt. The features are characteristic of LPE InP grown on (100)-oriented substrates and are similar to earlier reports (10).

Successful epitaxial growth largely depends on the availability of defect-free and clean substrates. A rigid procedure was followed to minimize the damage introduced into the substrate during substrate preparation and handling. The etch-pit density in the InP:Fe substrates, grown at Varian by the liquid encapsulation Czochralski technique, was less than 5×10^3 cm^{-2}. The surface morphology of the polished substrates were further improved by chemimechanical polishing with bromine methanol in stages. The final polish was achieved with a 0.5% solution. The polished substrate was degreased by boiling sequentially in high-purity trichloroethylene, acetone, and isopropyl alcohol (IPA). This was followed by a 30 sec etch in aqueous HCl (1:1) and a final rinse in IPA. The substrate was finally dried in IPA vapor and loaded in the growth cell. The same procedure was used to clean the polycrystalline InP source material. Indium for the melt was etched in aqueous HNO_3 (1:1) for 1 or 2 min immediately before each growth sequence.

The purity of the samples was greatly influenced by the ambient and flow rate of the purified H_2. It was ensured that the reaction tube was leak-proof to the extent that it could hold a vacuum of at least 10^{-5} Torr. A flow rate of ~15 liters/hr was maintained during epitaxial growth. The temperature profile along the entire length of the boat was uniform and was controllable within ±0.1°C.

Photoluminescence measurements.—Photoluminescence spectra of the LPE InP samples mounted in a strain-free manner were recorded at 4.2 K. Excitation was provided by the second harmonic (5300Å) line of a CW Nd:YAG laser. The focused beam at the sample surface had a diameter of ~0.1 mm, and the power absorbed by the sample was between 0.10 and 0.15W. The intensity of the light could be varied by neutral density filters. The luminescence was collected and analyzed by a double monochromator (SPEX 1402) with a resolution of 2Å or better.

Low temperature PL spectra of LPE InP have been recorded and analyzed by several authors (11-13). Their results were used as the basis for identification and comparison of our data. The main features in the PL spectra of our samples are observed in Fig. 3, where the bandedge luminescence of a layer grown after 10 hr prebaking of the melt is shown. The strong emission at 1.4168 eV is believed to arise from excitons bound to neutral donors (D°X) (11, 12). A shoulder to this peak on the high-energy side at 1.4184 eV has been identified as the free exciton-polaritron emission (11, 12). The peak at 1.38 eV, observed by several authors (13-15), is ascribed to band-to-acceptor (BA) and donor-to-acceptor (DA) transitions involving shallow acceptor impurities. It is recognized that C is the most dominant background acceptor impurity in LPE InP and peaks at 1.3803, and 1.3832 eV have been ascribed to DA and BA transitions involving C (13). No other acceptor species were detected in the layers. However, the peak at 1.38 eV, shown in Fig. 3, was the strongest observed in our samples and was undetectable in layers grown with longer prebaking intervals of the In melt. This strongly suggests that the peaks observed in our samples may not be due to C. It was also observed that in general the intensity of the free exciton peaks increased with increased durations of prebaking in the range 10-70 hr. Measurements at several points on the surface confirmed the spatial homogeneity of the layers.

Transport measurements.—The free-carrier concentration and Hall mobility in the undoped epitaxial layers were measured in the temperature range 77-300 K. Hall measurements were performed with a magnetic field of 0.5 Tesla and with the lowest possible current. The free-electron concentration at room temperature in the samples studied is listed in Table I.

The measured variation of the free-electron concentration (n_H) and the Hall mobility μ_H with temperature in a layer grown after 20 hr prebaking of the In melt are shown in Fig. 4. The data are representative of more than one sample grown under identical conditions. It might be noted that mobility at 77 K in our samples are lower than the highest values measured in undoped LPE InP (4, 9), but are still of the order of values claimed to be reasonably good (5).

The temperature dependence of the electron mobility in the different samples was analyzed by fitting the measured values with theoretically computed ones. These latter values were calculated by considering the mobilities limited by ionized-impurity, polar-optical phonon, piezoelectric, and deformation potential scattering. The temperature dependence of the carrier

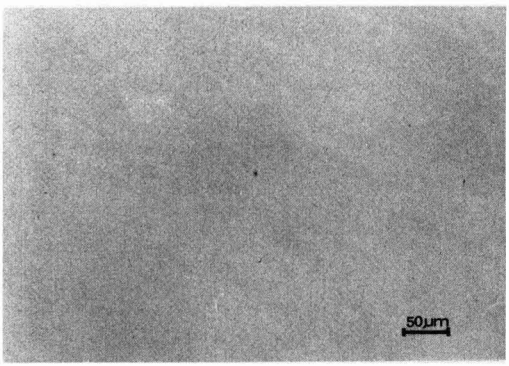

Fig. 2. Photomicrograph of an epitaxial layer grown on (100)-InP substrate after 20 hr melt prebaking.

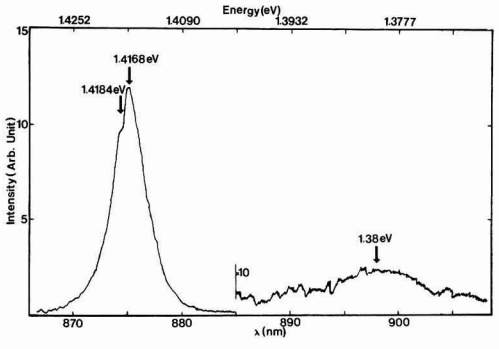

Fig. 3. Edge photoluminescence spectrum at 4 K of an epitaxial layer grown after 10 hr prebaking of the melt.

Table I. Variation of electrical properties and relative trap densities with duration of melt baking in LPE InP. The data indicate that the 0.38 eV trap concentration is almost independent of background doping

Melt baking time (hr)	n_H at 300 K ($\times 10^{15}$) (cm^{-3})	μ_H at 100 K ($cm^2/V \cdot sec$)	N_T/n ($\times 10^{-3}$)
10	14.0	11,041	0.6
20	4.5	26,331	1.9
30	4.3	21,128	1.9
40	6.1	14,972	0.7
50	1.6	6,601	4.1
60	9.5	14,008	0.6
70	10.0	16,761	0.8

concentration was fitted by taking charge-neutrality conditions into account. The continuous lines in Fig. 4 indicate the average fitting to the data. Values of $N_D = 5.3 \times 10^{15}$ cm^{-3} and $N_A = 8.0 \times 10^{14}$ cm^{-3} were obtained from the fits to the concentration and mobility data for this particular layer. It was observed that $(N_D - N_A)$ in the layers decreased, in general with longer prebaking of the melt. We believe that the values of N_A and N_D are representative of the concentrations of acceptors and Si and S as donors, respectively, in the LPE material. The low value of n_H in the sample grown after 50 hr melt-baking and the slight increase in its value in the samples grown after 60 and 70 hr melt-baking are attributed to additional impurity incorporation and compensation.

Trap measurements.—Transient capacitance measurements were performed with Schottky diodes made on the n-InP layers with Au dots and In-Sn ohmic contacts. In brief, the measurement procedure is as follows. The diode is normally reverse-biased in the quiescent state. Electron traps in a portion of the depletion region are filled by applying a majority-carrier pulse to the diode. The traps then thermally re-emit the captured electrons to the conduction band with a characteristic time constant dependent on temperature. Similarly, hole trap emission to the valence band can be observed after filling the traps with intrinsic photoexcitation. The resulting capacitance change is monitored by a 1 MHz capacitance bridge and recorded. The incremental capacitance change ΔC_o due to trap-filling is a measure of the trap density N_T by virtue of the approximate relation

$$N_T = (N_D - N_A)^2 \Delta C_o / C_\infty \quad [1]$$

where C_∞ is the quiescent reversed bias capacitance of the diode. Other expressions for calculating the trap density more accurately have been given by one of us (PKB) in earlier publications (16, 17). The thermal activation energy of the trap level ΔE_T, inclusive of the barrier to carrier capture, ΔE_B, is determined from the measured thermal emission rates by detailed balance considerations (16). The electrical field values in the depletion region should be kept at a low value to minimize the effects of field-enhanced trap emission. In our experiments, the quiescent bias was adjusted so that the electric field in the region of the depletion region, where trap capture and emission processes are operative, was less than 10^5 V/cm.

The thermal capture cross section of the trap can be estimated from the emission rate prefactor in the detailed balance equation (16), but a more accurate value can be obtained from direct measurements of electron capture rates. The capture cross section to electrons, σ_n, is related to the capture rate, c, by

$$c = \sigma_n v_{th} n \quad [2]$$

where v_{th} and n are, respectively, the thermal velocity and concentration of electrons in the conduction band.

The temperature dependence of the emission time constant for the only electron trap detected in all our layers is shown in Fig. 5. The activation energy obtained from a regression analysis of the data is $\Delta E_T = 0.38 \pm 0.02$ eV. An electron trap with $\Delta E_T = 0.36 \pm 0.005$ eV in the same temperature range was reported by Nickel and Kuphal (3). The temperature dependence of the capture cross section, σ_n, is also depicted in Fig. 5. The data can be fitted by the equation $\sigma_n(T) = \sigma_\infty \exp(-\Delta E_B/kT)$ and values of $\Delta E_B = 0.13 \pm 0.02$ eV and $\sigma_\infty = 4.78 \times 10^{-15}$ cm^2 are obtained. A value of $\sigma_\infty = 1.44 \times 10^{-15}$ cm^2 is obtained from the emission rate prefactor of the detailed balance equation (16).

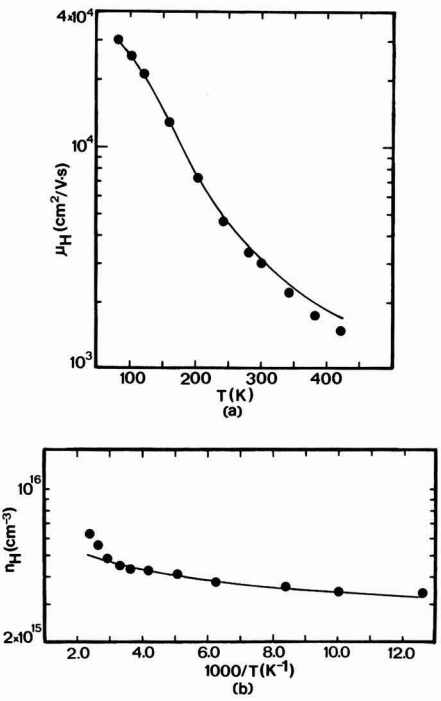

Fig. 4. Typical variation of the Hall mobility μ_H and Hall electron concentration n_H in undoped LPE InP. The solid lines are theoretical fits to the data.

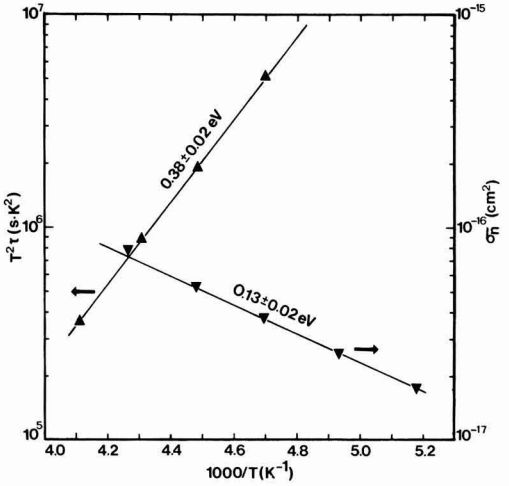

Fig. 5. Variation of the thermal emission time constant and thermal electron capture cross section of dominant traps in LPE InP. The slopes of the plots give the thermal activation energy and the barrier energy, respectively.

The ratio N_T/n in the different samples are listed in Table I. It is apparent that the absolute trap density is almost constant and thus independent of the baking period (purity) of the sample. A hole trap with $\Delta E_T = 0.22 \pm 0.01$ eV and $\sigma_\infty = 1.5 \times 10^{-23}$ cm^2 was observed in some layers in the temperature range 190-220 K. This center has not been detected before and more work on it is in progress in our laboratories.

Heat-treatment.—A few layers of as-grown InP were heat-treated in an LPE furnace under H_2-flow at 470°C for 15 min by placing the sample in the growth cell. The exposed surface morphology was severely degraded, and no device could be made without removal of this portion. By covering the sample with a piece of InP during the anneal, such degradation of the surface morphology could be avoided. It was observed that the 0.38 eV electron trap was removed at the surface. Considering a certain amount of P evaporation to be operative in our mode of heat-treatment the formation of, or an increase in, P-vacancies near the surface can be assumed. The possibilities of outdiffusion of impurities towards the surface or any indiffusion that might take place from spurious impurities from the surface cannot be ruled out.

Discussion

Our results clearly indicate that the 0.38 ± 0.02 eV electron trap is a dominant center in LPE InP. We have intentionally varied the purity of the crystals by varying the prebaking time of the growth melt. The concentration of the residual impurities, particularly S, Si, and C, are greatly altered and subsequently the background impurity concentrations in the crystals are also different. The trap concentration, however, remains almost invariant. This indicates that the center probably originates from native defects.

It is likely that in our mode of heat-treatment, with a proximity cap of InP, there is still a slight loss of P-atoms from the surface. In other words, the slight overpressure of P provided by the InP cap only helps to maintain the surface morphology, but does not enhance the P/In ratio at the surface. If this is true then the trap is related to an In site. Possibilities other than an isolated vacancy are an antisite defect P_{In}, in-site impurities, or V_{In}-impurity complexes. The possible source of some of these impurities have been mentioned in the previous section. However, if during the heat-treatment, there is enough overpressure of P, the trap could be related to P. These aspects are being studied by varying the conditions of heat-treatment.

The characteristics of the trap detected in our crystals is similar to those of the trap observed by Nickel and Kuphal (3), and we believe that they are the same centers. Our measurements have also revealed some of the electron capture properties of the trap. It is clear that the thermal capture cross-section for electrons is thermally activated with a barrier energy of 0.13 ± 0.02 eV. This value is about the same as for most dominant traps in GaAs and GaP (18). It is of interest to note that McAfee *et al.* (19) have reported an electron trap with an activation energy of 0.35 ± 0.03 eV (level E2) to be present in bulk LEC-grown InP. However, the temperature range in which level E2 was detected is much lower than the range in which the electron trap was detected in our samples.

Since the concentration of the 0.38 ± 0.02 eV electron trap is generally low, and it is detected at temperatures much lower than 300 K, it is expected that the performance of devices made from such layers will not be affected. And even if it did, our experiments show that defect-annealing can be achieved by a simple heat-treatment. In addition, LPE InP should prove to be a trap-free host material for ion-implantation.

Summary

We have grown high-purity undoped LPE InP with varying pregrowth conditions, which altered the purity of the layers. The electrical and optical properties of the layers were determined from temperature dependent Hall and low-temperature PL measurements. Detailed capacitance transient emission and capture measurements were performed on Au Schottky diodes made on the epitaxial layers. A single electron trap, with a thermal activation energy of 0.38 ± 0.02 eV has been consistently detected in all the crystals. Its capture cross section is thermally activated, with a barrier energy $\Delta E_B = 0.13 \pm 0.02$ eV and its concentration is $\sim 10^{12}$ cm^{-3} irrespective of the unintentional background doping. Short-term heat-treatment at 470°C anneals the trap completely in regions close to the surface of the layers. These facts point to the association of the traps with native defects.

Acknowledgments

The authors are grateful to T. Matsumoto for useful discussions and a critical reading of the manuscript and J. Staehli (Lausanne) for performing the photoluminescence measurements. The work was supported by the National Science Foundation under Grant ECS-8011917.

Note added in proof: Nakajima *et al.* [J. Crystal Growth, **59**, 572 (1982)] have recently reported that the intensity of the 1.38 eV PL peak decreases with baking, which agrees with our observations.

Manuscript submitted July 26, 1982; revised manuscript received Oct. 5, 1982.

Any discussion of this paper will appear in a Discussion Section to be published in the December 1983 JOURNAL. All discussions for the December 1983 Discussion Section should be submitted by Aug. 1, 1983.

Publication costs of this article were assisted by National Science Foundation.

REFERENCES

1. J. J. Berenz, F. B. Fank, and T. L. Hierl, *Electron. Lett.*, **14**, 683 (1978).
2. K. Tabatabaie-Alavi, A. N. M. M. Choudhury, N. J. Slater, and C. G. Fonstad, *Appl. Phys. Lett.*, **40**, 517 (1982).
3. H. Nickel and E. Kuphal, *Phys. Status Solidi A*, **65**, 583 (1981).
4. V. L. Wrick, K. T. Ip, and L. F. Eastman, *J. Electron Mater.*, **7**, 253 (1978).
5. E. Kuphal, *J. Cryst. Growth*, **54**, 117 (1981).
6. D. E. Holmes and G. S. Kamath, *ibid.*, **54**, 51 (1981).
7. L. F. Eastman, Presented at the NATO InP Workshop, June 1980.
8. M. G. Astles, F. G. H. Smith, and E. W. Williams, *This Journal*, **120**, 1750 (1973).
9. E. Kunphal and A. Pöcker, Presented at the Electronic Materials Conference, Fort Collins, June 1982.
10. T. Nishinaga, K. Pak, and S. Uchiyama, *J. Cryst. Growth*, **42**, 315 (1977).
11. A. M. White, P. J. Dean, L. L. Taylor, R. C. Clarke, D. J. Ashen, J. B. Mullin, and P. D. Green, *J. Phys.*, **C5**, 1727 (1972).
12. J. U. Fischbach, G. Benz, N. Stath, M. H. Pilkuhn, and K. W. Benz, *Solid-State Commun.*, **11**, 721 (1972).
13. K. Hess, N. Stath, and K. W. Benz, *This Journal*, **121**, 1208 (1974).
14. R. C. C. Leite, *Phys. Rev.*, **157**, 672 (1967).
15. U. Heim, *Solid-State Commun.*, **7**, 445 (1969).
16. P. K. Bhattacharya, J. W. Ku, S. J. T. Owen, C. B. Cooper, and R. L. Moon, *Appl. Phys. Lett.*, **36**, 304 (1980).
17. P. K. Bhattacharya, J. K. Rhee, S. J. T. Owen, J. G. Yu, K. K. Smith, and R. Y. Koyama, *J. Appl. Phys.*, **52**, 7224 (1981).
18. C. H. Henry and D. V. Lang, *Phys. Rev. B*, **15**, 989 (1977).
19. S. R. McAfee, F. Capasso, D. V. Lang, A. Hutchinson, and W. A. Bonner, *J. Appl. Phys.*, **52**, 6158 (1981).

Evaluation and Control of Resistivity in N^-/N^+ Epitaxial Depositions

J. L. Sachitano* and V. C. Kannan*[1]

Tektronix, Incorporated, Tektronix Laboratories, Beaverton, Oregon 97077

ABSTRACT

Autodoping from 0.001 Ω-cm arsenic-doped wafers interferes with the use of 10 Ω-cm P-type wafers for evaluating epi resistivities. A diffused layer is formed in the test wafers by arsenic atoms that evaporate from the N^+ wafers during the post-HCl bake prior to deposition. This layer leads to an erroneous four-point probe measurement of the epi-layer sheet resistance on the test wafer. A model is given that describes the formation of the diffused layer and its dependence upon the number of N^+ wafers. The model accounts for the epi resistivity as determined from the test water. A two-step epi procedure is described that allow the use of this type of test wafer for evaluating resistivities up to ≈30 Ω-cm.

A growing epi layer has many sources of dopants whose relative magnitudes influence the ability to control epi resistivity. The generally recognized sources are purposely introduced gas-phase dopants (inject), dopant evaporation from front and back sides of the substrates, solid-state diffusion of dopant from the substrate into the epi layer, and extraneous dopant evaporation from other surfaces such as the bell jar or susceptor. Extraneous sources can be ignored when the background resistivity can be controlled to greater than 100 Ω-cm by careful cleaning of the reactor surfaces and by proper treatment of the susceptor, such as etching and coating between runs. The contribution of solid-state diffusion (1, 2) is described by an erfc distribution with effects localized to the epi-substrate interface. Dopant evaporation from the front, back, and sides (3-8) of the substrate add to the inject dopant in the gas phase during the deposition cycle. Prior to the deposition, the substrate is at growth temperature with dopant evaporating and approaching a steady-state concentration in the stagnant layer above the substrate surface (9). When the deposition begins, the front surface is effectively sealed off and no longer contributes to the gas phase because the epi growth rate is greater than the dopant diffusion rate (1). However, in the case of antimony, surface adsorption and redistribution at the growing interface have been shown to occur (10). The back side may continue to contribute dopants throughout the deposition cycle. Various reports (3, 5, 7) demonstrate that sealing the back side, *e.g.*, with oxide (3), can reduce this contribution to autodoping. A comprehensive review (11) of autodoping in a horizontal epi reactor has considered the above effects in structures with buried layers (12).

We investigated the effect of autodoping on lightly doped P-type test wafers used to monitor the resistivity of high-resistivity arsine-doped $SiCl_4$ epi on N^+ arsenic-doped wafers in a vertical reactor. The extent of autodoping during the bake was correlated with the number of N^+ wafers, and the subsequent diffused layer is shown to dominate the test-wafer resistivity (4). A model that relates the surface area and concentration of the N^+ wafers to the diffused layer accounts for the measured resistivities. A two-step procedure, which reduces the front- and back-surface concentrations of the N^+ wafers before the test wafer is introduced, greatly reduces the autodoping and results in measured resistivity as high as 30 Ω-cm.

Experimental

The epi depositions ($SiCl_4$) were done in an Applied Materials AMV-800 vertical reactor. The test wafer was ≈10 Ω-cm, P type, <111>, and the run wafers were ≈0.001 Ω-cm, arsenic doped, <111>, and 2 in. in diam. The test wafer was actually quartered, and two chips were placed on the susceptor as shown in Fig. 1. (From here on, "P-type test wafer" means a quarter of a wafer.) The substrate placements for one-, four-, and eight-wafer runs are indicated. The epi sheet resistance was measured with a four-point probe, and junction depths were determined with a groove-and-stain technique using a sodium light source for interferometry. The spreading-resistance profiles were measured on an ASR-100 spreading-resistance probe.

A description of typical process conditions is given in Table I. To begin the procedure, the susceptor is etched with HCl, and a thick layer of polysilicon is coated onto it. An intrinsic run with only a test wafer is done to verify the background doping level of the system (typically 50-150 Ω-cm). The reactor is targeted for a specific resistivity in a test run using the above procedures to evaluate resistivity. After a satisfactory target run, N^+ wafers and test wafers are added to the reactor and a deposition using the doping conditions of the test run is done. The susceptor is etched and coated prior to subsequent depositions.

Results

Following these procedures, a series of depositions was done with differing numbers of wafers but with all other conditions held constant. The test run resistivity was 6.5 Ω-cm, and the results (Fig. 2) show that the test-wafer resistivity decreased as the number of N^+ wafers increased.

To aid in determining the cause of these effects, a scheme using three test wafers was introduced. The procedure, outlined in Table II, involves interrupting the process after the post-HCl bake. Test wafer 1 (TW1) is removed after the bake, TW2 remains and goes through the entire process, and TW3 is inserted after the bake and has only the epi deposition. A run using this procedure with four N^+ wafers was targeted for 5.1 Ω-cm. The results, summarized in Table III, indicate that the test wafer is affected before the epi deposition. An N-type layer is present after the bake, and the test wafer that has gone through the entire process shows a lower resistivity than the one that has only the epi deposition. A subsequent run substituted a 4 Ω-cm N-type test wafer in place of the usual 10 Ω-cm P type. This wafer was removed after the bake (*e.g.*, TW1), and a spreading-resistance profile (Fig. 3) shows a diffused layer at the surface.

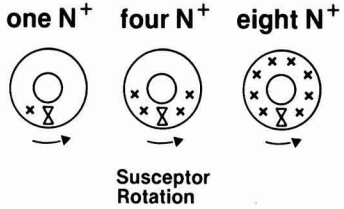

Fig. 1. Schematic representation of test-wafer (△) and run-wafer (×) placements on the susceptor.

* Electrochemical Society Active Member.
[1] Present address: Bell Laboratories, Allentown, Pennsylvania 18103.

Table I. Typical conditions for high-resistivity epi process on N⁺ substrates

Step / Conditions	Warm Up	Etch	Bake	Dep $SiCl_4$
Time (min)	5	1	10	10
Temperature (°C)	23 - 1200	1200	1180	1180
H_2 (main)	38 l/pm	38 l/pm	38 l/pm	38 l/pm
$SiCl_4/SiH_4$	—	—	—	0.25 l/pm
HCl	—	0.67 l/pm	—	—
AsH_3 (source) ≈ 50 ppm in H_2	—	—	—	0.028 l/pm
H_2 (diluent)	—	—	—	3.98 l/pm
AsH_3 (inject)	—	—	—	0.021 l/pm

Table II. Sequence to evaluate process effects on test-wafer resistivities

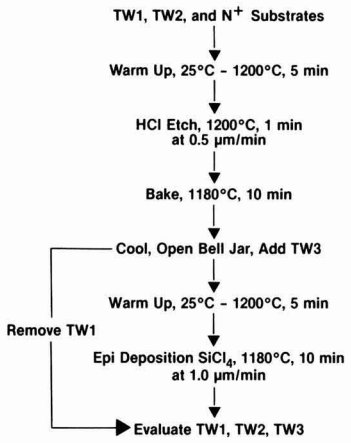

Table III. Test-wafer evaluation of epi process

Number of N⁺ Substrates	TW Resistivity (Ω-cm)		
	Warm Up to Bake (TW1)	Full Process (TW2)	Epi Only (TW3)
0	—	5.1	—
4	1.4	3.7	5.1

Model for Test-Wafer Resistivity

The essential features of the model are that arsenic evaporates from the N⁺ wafers and diffuses into the test wafer during the post-HCl bake, which results in an erfc distribution (dep) with a surface concentration that is dependent upon the number of N⁺ wafers present. This diffused layer then redistributes to a near-Gaussian profile during the epi deposition. The measured test-wafer conductance results from the sum of the conductances of the epi layer, the dep diffusion into the epi, and the dep diffusion into the substrate. The structure is shown schematically in Fig. 4.

Following Skelly and Adams (5), the amount of arsenic evaporating from the N⁺ wafer (13, 14) for the case of uniform initial dopant concentration C_0 and zero gas-phase concentration, is given by

$$\bar{C}(t) = 2C_0(Dt)^{1/2} \left\{ \frac{1}{(\pi)^{1/2}} - \frac{[1 - \exp(Z^2)\,\mathrm{erfc}\,(Z)]}{2Z} \right\} \quad [1]$$

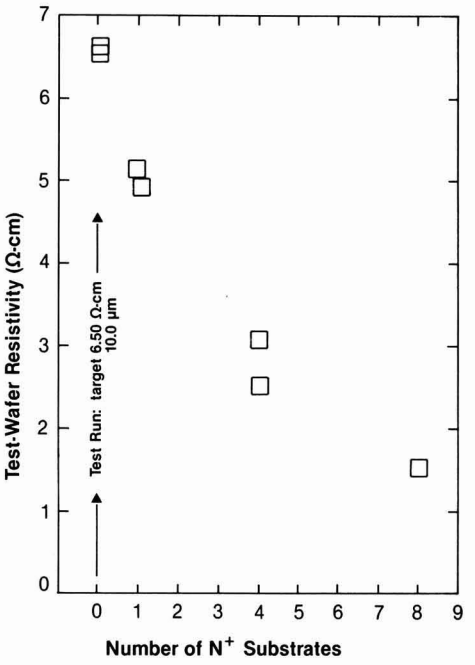

Fig. 2. Dependence of test-wafer resistivity on the number of N⁺ wafers in the epi run. Gas-flow settings, temperatures, and times were held constant for all data points. The epi targets were 6.5 Ω-cm and 10.0 μm.

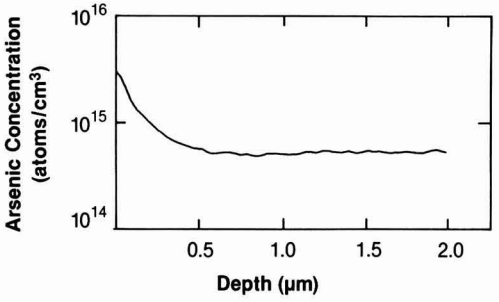

Fig. 3. Spreading-resistance profile of 4 Ω-cm N-type test wafer after post-HCl bake showing diffused layer at surface.

where $Z = Kt/(Dt)^{1/2}$. The arsenic diffusion coefficient is D, and the evaporation coefficient is K. In the following calculations, the diffusivity data of Masters and Fairfield (15) were used to calculate outdiffusion from the N⁺ substrates and the diffusion into the test wafer. Abe's (2) value of K at 1250°C, 7×10^{-9} cm sec^{-1}, was adjusted to 1200°C assuming that the temperature dependence of K is the same as that of D (16). Equation [1] gives the total number of evaporated atoms per unit surface area for a given time. In this way, the effect of varying the number of N⁺ substrates can be accounted for. Using this equation, the average rate of evaporation is just $\bar{C}(t)/t$.

The test-wafer surface concentration of arsenic during the bake can be calculated from Henry's law. If the maximum dopant concentration is $<10^{18}$ atoms/cm³, then the activity coefficient of arsenic can be approximated to unity (17), and Henry's law becomes $C_0 = HP_{As}$, where H is Henry's law constant, P_{As} is the partial pressure of arsenic, and C_0 is the arsenic con-

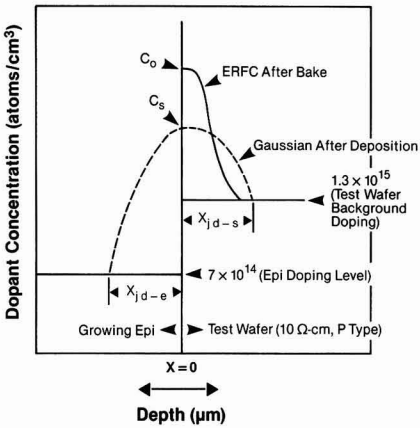

Fig. 4. Schematic illustration used for calculating test-wafer resistivity.

centration in the wafer. The arsenic partial pressure can be estimated from $P_{As} = R_{As}/R_{H_2}$, where R_{As} is the average rate of arsenic evaporation from Eq. [1], and R_{H_2} is the flow rate of hydrogen in the reactor. This estimation assumes complete mixing in the system, which gives the lowest estimate of P_{As}. Evaporation of arsenic occurs from both sides of the N^+ wafers, but the back side contribution is less effective because of transport limitations. This factor is estimated by assuming that the effective surface area of the back side is equal to 10% of the front. Henry's law constant was obtained from a plot, Fig. 5, of the partial pressure of arsine *vs.* the arsenic concentration in epi layers. This plot gives a value of $H = 3.2 \times 10^{24}$ atoms cm^{-3} atm^{-1} at 1200°C with a slope of 0.98. The resulting diffusion into the test wafer is described by

$$\frac{C(x,t)}{C_0} = \text{erfc}\,(y) - \exp\,(Z^2)\exp\,(yz)\,\text{erfc}\,(y+Z) \qquad [2]$$

where $y = x/2(Dt)^{1/2}$ and $Z = Kt/(Dt)^{1/2}$. This equation converges to a simple error function when $Kt > (Dt)^{1/2}$.

The predeposition cycle is divided into 3 time segments: warm up (5 min from room temperature to 1200°C), HCl etch (1 min), and bake (10 min). It is possible that some diffusion into the test wafer could occur before the HCl etch and remain after the etch. However, in our case, $(Et/Dt)^{1/2} \geq 12$, we have assumed that no diffusion remains after the etch, so only diffusion during the bake is considered.

Since the epi layer grows fast compared with the diffusivity of arsenic, the redistribution of the diffused layer can be treated as a thin source diffusing from two sides into an infinite body. This redistribution is analogous to a dep and drive in which the dep length $(D_1t_1)^{1/2}$ is small compared with the drive length $(D_2t_2)^{1/2}$, and the dep is then represented by a delta function. In the present case, $D_1t_1/D_2t_2 \approx 1$ and the distribution is better represented by solutions for the two-step diffusion (18). However, the assumption of a Gaussian distribution does not lead to an error greater than ≈25% in estimating conductance. This assumption was made to reduce the computational burden by using Irvin's curves (19). The resulting depth of diffusion into the wafer or into the epi layer is

$$x_j^2 = 4D_2t_2 \ln\left[\frac{C_0}{\pi C_B}\left(\frac{D_1t_1}{D_2t_2}\right)^{1/4}\right] \qquad [3]$$

where C_B is the appropriate background concentration. The conductance of the diffused layers can be estimated by using x_j calculated from Eq. [3]. The diffused-layers plus the epi-layer conductance then gives the total conductance $\sigma_T = \sigma_{d-s} + \sigma_{d-e} + \sigma_{epi}$. The resistivity is then $\rho = x_j/\sigma_T$. In Eq. [1]-[3], we used $K = 1.63 \times 10^{-7}$ cm sec^{-1}, $D_{ex} = 5.078 \times 10^{-12}$ cm^2 sec^{-1}, $D_{in} = 2.59 \times 10^{-13}$ cm^2 sec^{-1} (1200°C), $D_{in} = 1.64 \times 10^{-13}$ cm^2 sec^{-1} (1180°C), and $C_0 = 1.92 \times 10^{17}$ atoms cm^{-3}, where D_{ex} is for N^+ wafers and D_{in} is for test wafers.

The results of these calculations are shown as the solid line in Fig. 6 superimposed on the experimental results of Fig. 2. Given the simplifications made in the model, it reasonably accounts for the observed results.

Modified Epi Process

In order to use a P-type test wafer in the presence of N^+ wafers, the diffused layer must be eliminated. The rate of arsenic evaporation is proportional to the surface concentration of the N^+ substrates (5). Reducing the front- and back-surface concentrations before the test wafer is put in place should reduce the extent of the diffused layer. A procedure for doing this, outlined in Table IV, involves sealing the back surfaces by transferring polysilicon from the susceptor to the back of the wafer (6) during the HCl etch and the short epi ($SiCl_4$) deposition. The front surface is also sealed by the short deposition. Spreading-resistance profiles, Fig. 7, of the front and back surfaces of an N^+ wafer after this treatment show several orders of magnitude reduction in surface concentrations.

The process is interrupted at this point; the test wafer is inserted, and the epi deposition follows. The short HCl etch included at this step is necessary in order to maintain good surface quality. Autodoping should now be reduced as a result of the low surface concentration of arsenic in the coated N^+ wafers. This reduction was verified by spreading-resistance profiles (Fig. 8) of intrinsic epi on ≈4 Ω-cm N-type test wafers

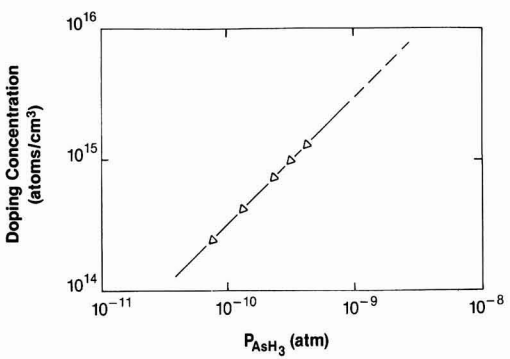

Fig. 5. Variation of doping concentration in the epi layer with arsine partial pressure for $SiCl_4$ epi.

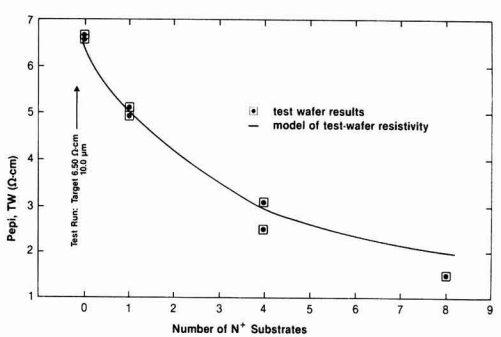

Fig. 6. Effect of number of N^+ substrates on test-wafer resistivity as predicted by the model (solid line).

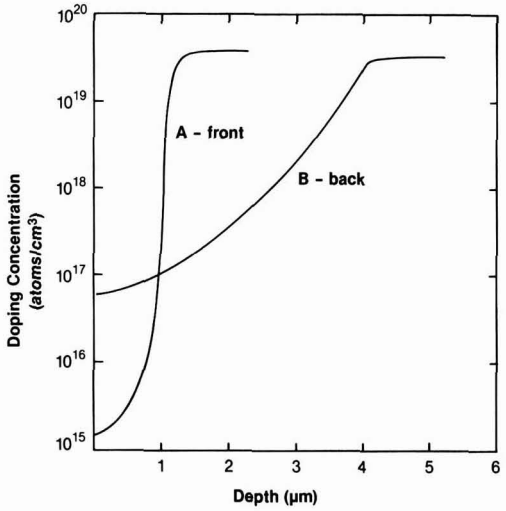

Fig. 7. (A) Front side concentration profile after a 1 min epi deposition, and (B) back side profile after HCl etch and 1 min epi deposition.

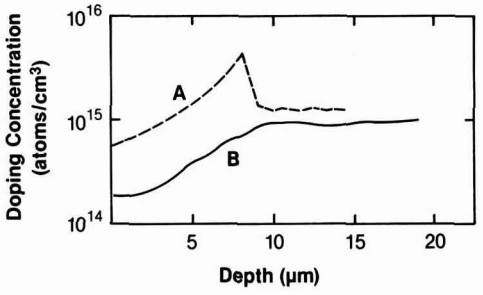

Fig. 8. Doping profiles of intrinsic epi layers obtained for (A) one-step and (B) two-step deposition processes. The test wafers were 4 Ω-cm, N type.

in the presence of seven N^+ wafers. The original single-step process clearly gives a diffused layer, but none is apparent in the modified two-step process.

In order to estimate the upper limit of resistivity obtainable with this process, the procedure was repeated using 10 Ω-cm P-type test wafers and intrinsic epi. The results of several runs with either 4 or 8 N^+ wafers are listed in Table V. Some residual autodoping effects are apparent since all results are less than the typical background resistivity (≥50 Ω-cm). A comparison of the results of 4 and 8 wafers also indicates a loading effect. These effects may have been reduced if the system had been cleaned and the susceptor etched and coated after the bell jar was opened.

Summary

The use of a 10 Ω-cm P-type test wafer to evaluate N^-/N^+ epi resistivities is inappropriate because of a diffused layer formed during the post-HCl bake. Arsenic out-diffusion and evaporation from the N^+ wafers is the source of the diffused layer, and the extent of the diffusion depends upon the number of N^+ wafers present. The diffused layer leads to erroneous resistivity evaluations. A model was given that relates the autodoping process and the resulting diffused layer to the observed resistivity evaluations. A two-step process in which the N^+ wafer surfaces are sealed before the test wafer is inserted has given 20-30 Ω-cm resistivity measurements.

Table IV. Sequence for the two-step process

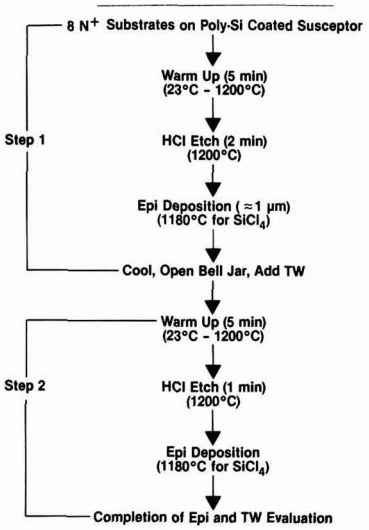

Table V. Test-wafer resistivities with intrinsic $SiCl_4$ epi using the two-step process

	Resistivity (Ω-cm)	
# Wafers	TW2 (complete)	TW3 (epi only)
4	5.7	27.3
4	5.1	32.4
8	2.7	20.3

Acknowledgments

The authors thank Mrs. I. Cady for assisting with the epi experiments and Mr. R. Osterman for the spreading-resistance measurements.

Manuscript submitted Jan. 28, 1980; *revised manuscript received* Sept. 20, 1982.

Any discussion of this paper will appear in a Discussion Section to be published in the December 1983 JOURNAL. All discussions for the December 1983 Discussion Section should be submitted by Aug. 1, 1983.

Publication costs of this article were assisted by Tektronix, Incorporated.

REFERENCES

1. S. D. Grove, A. Roder, and C. T. Sah, *J. Appl. Phys.*, **46**, 802 (1965).
2. T. Abe, Y. Nishi, K. Sato, and N. Oi, *Denki Kagaku*, **35**, 142 (1967).
3. B. A. Joyce, J. C. Weaver, and D. J. Maule, *This Journal*, **112**, 1100 (1965).
4. W. H. Shepard, *ibid.*, **115**, 652 (1968).
5. G. Skelly and A. C. Adams, *ibid.*, **120**, 116 (1973).
6. C. O. Bozler, *ibid.*, **122**, 1705 (1975).
7. P. H. Langer and J. I. Goldstein, *ibid.*, **124**, 591 (1977).
8. D. C. Gupta and R. Yee, *ibid.*, **116**, 1561 (1969).
9. T. Ishii, K. Takahashi, A. Kondo, and K. Shirahata, *ibid.*, **122**, 1523 (1975).
10. P. H. Langer and C. L. Paulnack, Abstract 295, p. 737, The Electrochemical Society Extended Abstracts, Vol. 78-1, Seattle, WA, May 21-26, 1978.
11. G. R. Srinivasan, *This Journal*, **127**, 1334 (1980).
12. G. R. Srinivasan, *ibid.*, **125**, 146 (1978).
13. F. M. Smits and R. C. Miller, *Phys. Rev.*, **104**, 1252 (1956).
14. R. N. Goshtagore, *Solid-State Electron.*, **15**, 1113 (1972).
15. B. J. Masters and J. M. Fairfield, *J. Appl. Phys.*, **40**,

2390 (1969).
16. K. Lehovec, K. Schoenic, and K. Zuleeg, *ibid.*, **28**, 420 (1957).
17. P. Rai-Choudhury and E. I. Salkovitz, *J. Cryst. Growth*, **1**, 361 (1970).
18. D. P. Kennedy and P. C. Murley, *Proc. IEEE*, **52**, 620 (1964).
19. J. C. Irvin, *Bell Syst. Tech. J.*, **41**, 387 (1962).

Some Illumination on the Mechanism of SiO_2 Etching in HF Solutions

Henry Nielsen and David Hackleman*

Hewlett-Packard Company, Corvallis, Oregon 97330

ABSTRACT

The etching of SiO_2 in aqueous buffered HF solutions can be impeded or stopped through the application of an electric field. In CMOS fabrication, very low levels of light can cause the effect. Parallel reaction paths are proposed for the dissolution process, coupled with the electric field's ability to stop or redirect the reaction at an intermediate step.

The dissolution of SiO_2 in HF solutions is a fundamental step in the fabrication of integrated circuits The overall chemical reaction involved is normally understood as

$$SiO_2 + 6HF \rightarrow 2H^+ + SiF_6^= + 2H_2O \qquad [1]$$

Etch rates and etch profiles are controlled by buffering and/or diluting the HF solution (1, 2) and by doping or damaging the glass layer via thermal diffusions (2) or ion implantation (3). Based on the knowledge behind these techniques, etching the structure shown in Fig. 1 should occur isotropically, with only a modest decrease in the etch rate of the boron doped glass found over the p+ region when compared to the phosphorus doped material above the n+ area. A slight overetch on the p+ side of the hole may occur due to the differential in oxide thickness, but this would be a minor difficulty.

Under some conditions of high n+ and p+ doping concentrations, shallow junctions, and very low silicon surface defect densities, when the structure in Fig. 1 is etched in the yellow light present in most integrated circuit processing photomasking areas, it has been observed that the n+ side will not clear regardless of the overetch time. In some cases, a brightly colored layer is visible over the n+ oxide. This layer is insoluble in nonoxidizing HF solutions. On the other hand, if the etch is performed in absolute darkness, the oxide dissolves uniformly over both n+ and p+ silicon. This light sensitivity indicates possible photocharging of the junction structures. Experiments were set up to investigate the effect of an applied E-field on the etching of SiO_2 layers. The effect of varying the junction structure was also examined. Lastly, Auger and SEM analyses of the material remaining in actual contact hole etches on integrated circuits were performed.

Experimental

Wafers, with the structure shown in Fig. 1, with varying junction depths were etched in ambient light, 405 nm light, and total darkness. The wafers etched in darkness or 405 nm light produced no HF-insoluble layer. Wafers etched in the yellow ambient light generated the HF-insoluble layer. The junction depths ranged from 500 to 1000 nm. Changing the junction depth had no discernable influence on the etching behavior.

The effect of changing the overlap of the n+ and p+ junctions shown in Fig. 1 was examined using an alignment monitor test cell. The alignment monitor, shown in Fig. 2, consists of a series of p-well regions, each split into an n+ and a p+ diffusioin. The cross sections of these regions look similar to Fig. 1 except that the masks for the diffusions are drawn to give 0, ±1, ±2, and ±3 microns overlap of the n+ and p+ diffusions. (These values change somewhat in practice, due to thermal side-diffusion of the dopants during activation of the implants and also due to photomasking misalignments.) When these arrays are etched in ambient light, the oxide over both the n+ and p+ silicon is removed uniformly, provided the diffusions do not over-

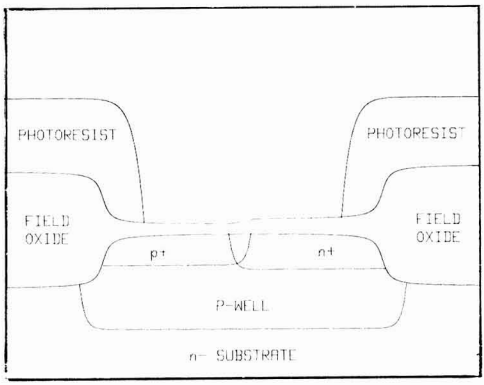

Fig. 1. Overlapped n+ and p+ diffusions in a CMOS p-well (vertical scale exaggerated for clarity). The oxide thickness over the n+ is 75 nm; over the p+, it is 50 nm.

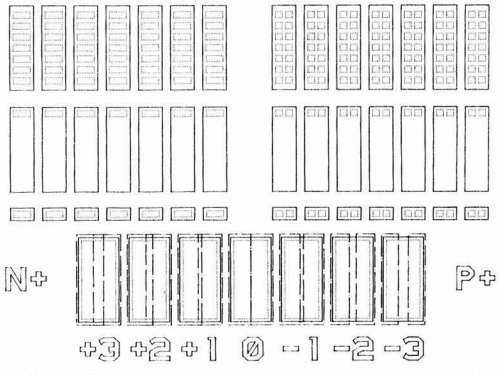

Fig. 2. N+/p+ diffusion overlap test structures. Solid lines designate islands; dotted lines are contacts; dot-dash lines are diffusions, as labeled. Diffusions are shown only on the bottom row for clarity; cross sections are similar to Fig. 1.

* Electrochemical Society Active Member.
Key words: glass, integrated circuits, photoelectricity, kinetics.

lap. If there is any overlap of the diffusions, the n+ oxide will not be removed. When an oxidant, such as oxalic acid, is added to the etchant, then diffusions that overlap only slightly will also clear uniformly in ambient light. When the same arrays are etched in total darkness with no oxidant in the etchant, the oxide is removed uniformly over both n+ and p+ silicon regardless of the diffusion overlap.

If the cross-sectional area of the hole being etched in the ambient light is small (10-40 μm^2), the n+ oxide appears highly colored. If the hole is larger (up to 1000 μm^2), a slight coloration may or may not be visible. In all cases, however, an insoluble film is present on the outer surface of the oxide, as shown in Fig. 3. The amount of coloration depends on the position of the hole with respect to the n+ diffusion and the amount of diffusion area attached to it. The pattern and degree of coloration are precisely that of the E-field that would exist if the n+ and p+ diffusions were being held at different potentials.

Samples were prepared for potentiostat experiments by growing 100 nm of oxide on n<100> silicon wafers, $\rho = 5\ \Omega$-cm, in a steam ambient. After a 1000°C, 30 min anneal in nitrogen, the wafers were diced and attached to IC lead frames. A wire was attached to the lead frame, and the samples were sealed in an electrically insulating plastic, leaving only the oxidized front surface exposed. The samples were then mounted on Plexiglas supports with epoxy.

The potentiostat samples were etched in a buffered HF solution (10.3M NH_4F, 1.2M HF) under an applied potential for 300 sec. The potential was maintained with respect to an Ag|AgF reference electrode using an EG&G Model 173 Potentiostat/Galvanostat. After the 300 sec etch, the residual oxide thickness measurements were obtained by using a Nanospec/AFT system. To obtain repeatable measurements, a 10 sec polysilicon etch (4) was necessary to remove the HF-insoluble layer. These results are shown in Fig. 4. Samples with no applied potential were found to etch completely in 180 sec, indicating an etch rate of 0.56 nm/sec. This etch rate did not change when the etchant was allowed to contact the back-side of the silicon substrate during the etch of samples with no applied potential.

The current required to maintain the applied potential on the samples was stable initially at approximately 5 nA. At 180 sec of etch time, the current rose sharply from the initial level to a second stable level which depended on the applied potential. This second current level is shown as a function of the applied potential in Fig. 5. The current seems to be limited by ionic transport between −1 and −2V, and surface limited at voltages more negative than this.

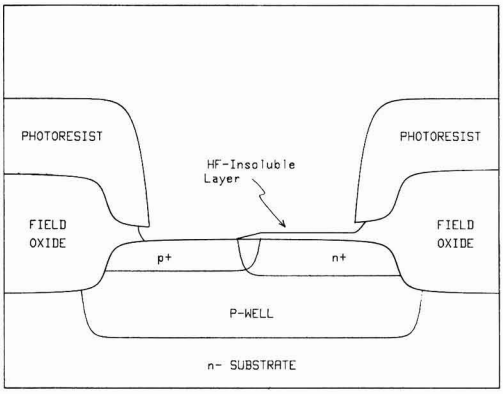

Fig. 3. Structure of Fig. 1 after etch in ambient yellow light

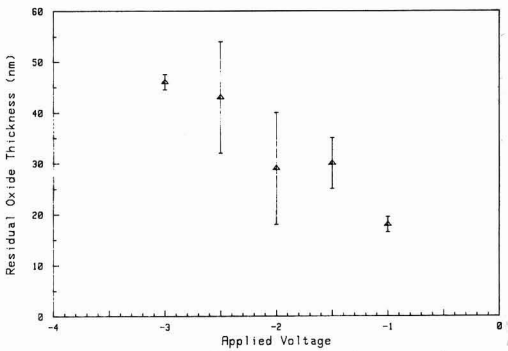

Fig. 4. Residual oxide thickness on potentiostat samples as a function of applied voltage.

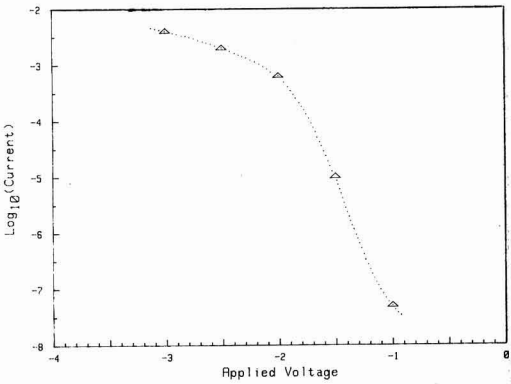

Fig. 5. Current required after 180 sec of etching to sustain a potentiostatic condition as a function of desired potential (Si with respect to AgF|Ag). Area of samples was constant at approximately 10 mm^2.

Auger and SEM analyses were performed on integrated circuit samples topologically similar to Fig. 6 directly after etching in ambient light. An overall line scan of the surface along line A of Fig. 6, after 5 nm of sputtering to remove contamination, is shown in Fig. 7. Note the sharp drop in the Si-O signal inside the contact hole even though the oxygen signal is not negligible over the n+ half of the contact. Figure 8 demonstrates the intermediate nature of the silicon peak found in the Pt 1 region (see Fig. 6). Pt 2 may be considered to represent an Si-Si bond, with Pt 3 an Si-O bond as in SiO_2. An Auger sputter profile of Pt 1, calibrated to SiO_2 yields a layer thickness of about 45 nm, in good agreement with the 40 ± 5 nm Nanospec readings obtained after removal of the HF-insoluble layer.

Discussion

The environmental lighting experiments show that the etch stopping effect occurs when photons with wavelengths longer than that of blue visible light are present. Changing the junction structure to allow a larger depletion region (more efficient photon absorption) enhances the effect, suggesting that the p+ and n+ diffusions are photocharged causing an electric field across the oxide. The potentiostat experiments, summarized in Fig. 4, show that an E-field across the oxide is capable of stopping the etch.

Referring to Fig. 1, note that the n+ oxide is thicker than the p+ oxide by about 15 nm. If both oxides etch at approximately the same rate, the p+ silicon will be in direct contact with the solution while 15 nm of ox-

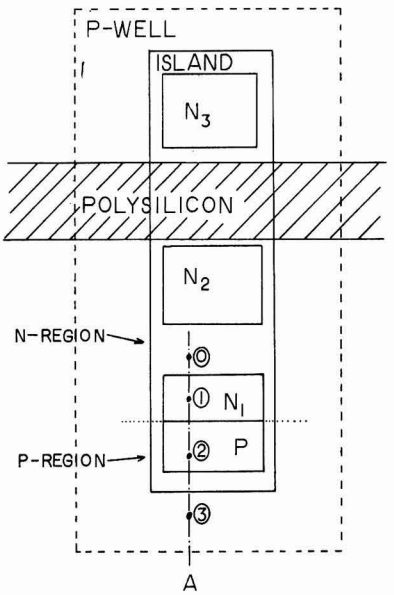

Fig. 6. Portion of CMOS IC used for Auger line scan and depth profiling. (Cross section similar to Fig. 1.) Under standard etching conditions, P clears; N1 does not clear; N2 may not clear; N3 does clear.

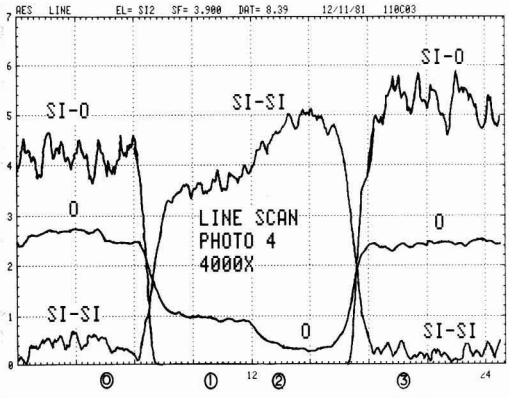

Fig. 7. Auger line scan along line A of Fig. 6

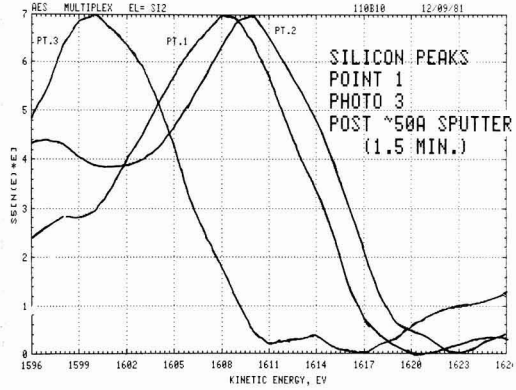

Fig. 8. Auger energy spectra from points 1, 2, and 3 of Fig. 6

ide remains over the n+ silicon. (The doping levels in the oxides are low enough that they do not affect the oxide etch rates). If there is a photoinduced potential difference between the p+ and n+ diffusions, a similar potential will appear across the n+ oxide when the p+ side clears. The E-field from the charged junctions may also impede the etching of the oxide over the n+ silicon before the p+ side clears. From Fig. 4, a potential difference of 0.5V is sufficient to stop the etching of SiO_2 at 10-15 nm. As long as this potential difference exists, no amount of overetch will clear the n+ oxide. The apparent thickness by Auger and Nanospec readings on actual contact holes of 40 nm are significantly greater than the 10-15 nm Nanospec readings on potentiostat samples from Fig. 4. The actual contact holes were etched for 150 sec while the potentiostat samples were etched for 300 sec. It is possible that the contact holes, if etched for 300 sec, would have oxide thicknesses nearer 15 nm. While this measurement was not made, it is known that no amount of overetch will completely clear the n+ side of the contact hole.

It is believed from the Auger analysis that the HF-insoluble layer formed on the outer surface of the oxide is a thin layer of partially reduced SiO_2 (SiO_x, where $x < 2$). Oxides such as this are believed to be insoluble in HF solutions unless an oxidant, such as HNO_3, is present (2). The observed films are soluble in HF/NHO_3 solutions. This identification of the insoluble layer is further supported by the results of the oxalic acid addition to the etchant. Slightly overlapped junctions, which have smaller depletion regions and subsequently smaller charging, clear uniformly in ambient light with oxalic acid in the etchant. The same junction structures do not clear in ambient light without the oxalic acid.

Mechanisms

The mechanism for SiO_2 dissolution in HF solutions is not known entirely. Bridging oxygen bonds are probably converted to silanol bonds which are then replaced by Si-F bonds, but the reactive species and mechanistic steps have not been isolated to our knowledge. The etch rate is not a strong function of the F^- concentration (5), but F^- may be indirectly involved in preventing the precipitation of silicon compounds from the solution. For solutions up to 10M in HF, this leaves HF_2^- and HF as the only appreciable fluoride species. Above 10M HF, more complicated H-F complexes have been implicated in the dissolution process (5).

For 1M ionic strength HF solutions, the etch rate is a linear function of the HF_2^- and HF molar concentrations (5)

$$\text{Etch rate (Å/sec)} = 9.66[HF_2^-] + 2.50[HF] - 0.14 \quad \text{(23°C)} \quad [2]$$

Equation [2] implies at least two parallel reaction paths where either reactive species can replace an Si-OH bond with an Si-F bond, as depicted in Fig. 9a. Silanol formation is not considered by this model. Silanol bond formation is most probably due to reaction of a bridging oxygen with H_2O or H^+, but the parallel reaction of HF with a bridging oxygen gives a silanol bond on one silicon and fluorinates the other (Fig. 9b). Thus, HF appears to have a dual function, reacting with either Si-OH bonds or bridging oxygens. Lowering the pH increases the HF concentration and probably enhances its action as a direct fluorinating agent.

The overall reaction given in Eq. [1] does not require either reduction or oxidation of silicon. However, the creation of the insoluble layer in all of the experiments performed suggests that the normal dissolution process involves steps that approach reduction of the

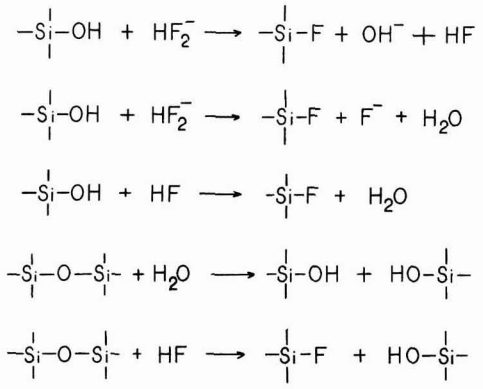

Fig. 9. (a, top) Reactions fluorinating silanol bonds by HF_2^- and HF. (b, bottom) Reactions creating silanols and silicon fluoride from bridging oxygen bonds in silicon dioxide.

SiO_2. The presence of an electric field then shifts the local chemical potential so that reduction is favored.

The dissolution of SiO_2 can be mechanistically modeled using only HF_2^- ions as in Fig. 10a. An alternative model using only HF is shown in Fig. 10b. Due to the similarity in the intermediate silicon structures, numerous combinations of the two distinct paths are possible, such as in Fig. 10c. The sum of all the possible combinations with the different rate constants for HF_2^- and HF at each step reduces to an expression for the etch rate of the form given in Eq. [2].

The insoluble layer formation can occur in the presence of an electric field from the initial steps of any

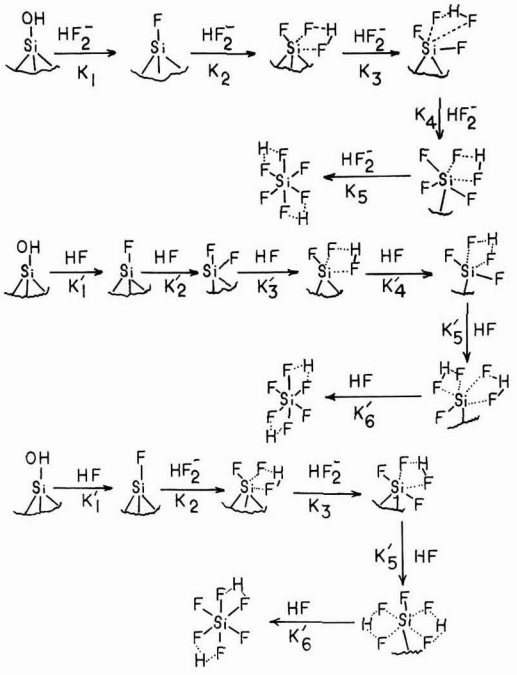

Fig. 10. (a, top) A dissolution model for SiO_2 employing only HF_2^-. (b, middle) A dissolution model for SiO_2 employing only HF. (c, bottom) A dissolution model for SiO_2 employing both HF and HF_2^-.

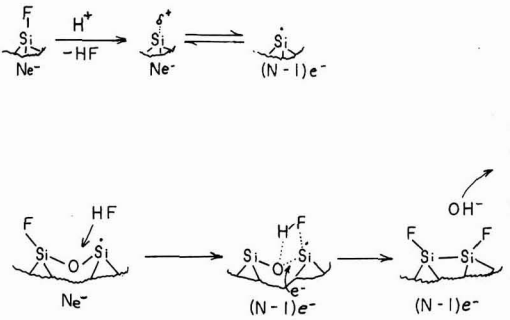

Fig. 11. (a, top) Reduction of a surface Si atom by H^+. (b, bottom) Formation of an Si—Si surface bond.

of the pathways shown in Fig. 10. Figure 11a shows the formation of a reduced Si surface atom, and Fig. 11b shows the formation of an Si-Si surface bond. The Auger energy scan of Fig. 8 suggests the surface region of the insoluble layer has bonds with an energy greater than a standard Si-Si but less than Si-O, which is consistent with the structure shown in Fig. 11b. Si-Si double bonds have been reported (6), but the expected energy in the Auger spectra would be closer to an Si-O bond than an Si-Si single bond. Also, the surface would need to reorganize substantially to allow silicon double bonds because one bridging oxygen would need to be removed from each of the participating silicons. This suggests the surface reduction as the more likely event. The reduction of the silicon surface below valence 4 could occur in a manner similar to the alleged behavior of silicon monoxide, a mixture of Si(O) and Si(IV). The only other explanation is that the silicon actually is in a reduced state, an unexpected, but nonexcludable possibility.

Conclusion

The dissolution of SiO_2 in HF solutions can be stopped by the application of an electric field across the SiO_2. The field strength required is small enough to be generated in shallow-junction CMOSC circuits through photon absorption. In some CMOS structures, it is possible to generate an HF-insoluble layer at the SiO_2|solution interface. This layer is most probably a film of partially reduced SiO and is soluble in HF/HNO_3 solutions.

Acknowledgments

The authors wish to thank Marzio Leban for useful discussions and help with the electrochemical system apparatus, and Ellen Tappon for SEM and Auger analysis.

Manuscript submitted Jan. 25, 1982; revised manuscript received Aug. 17, 1982.

Any discussion of this paper will appear in a Discussion Section to be published in the December 1983 JOURNAL. All discussions for the December 1983 Discussion Section should be submitted by Aug. 1, 1983.

Publication costs of this article were assisted by the Hewlett-Packard Company.

REFERENCES

1. G. Parisi, S. Haszko, and G. Rozgonyi, *This Journal*, **124**, 917 (1977).
2. W. Kern, in "Proc. Symp. Etching for Pattern Definitions," H. G. Hughes and M. J. Rand, Editors, pp. 1-18, The Electrochemical Society, Princeton, NJ (1976).
3. F. Schwettman, R. Dexter, and D. Cole, *This Journal*, **120**, 1566 (1973).

4. 200:80:1 by volume, Reagent grade HOAc:HNO_3:HF.
5. J. Judge, in "Proc. Symp. Etching for Pattern Definitions," H. G. Hughes and M. J. Rand, Editors, pp. 19-36, The Electrochemical Society, Princeton, NJ (1976).
6. R. West, M. Fink, and J. Michl, *Science*, **214**, 1343 (1981).

Amorphous Silicon Photovoltaic Modules

Y. Uchida, H. Sakai, N. Furusho, M. Nishiura, and H. Haruki

Fuji Electric Corporate Research and Development Limited, 2-2-1, Nagasaka, Yokosuka 240-01, Japan

ABSTRACT

In hydrogenated amorphous silicon solar cells of 100 cm^2, the conversion efficiency of more than 6% has been obtained for the cells with metal/n-i-p/ITO/glass and ITO/n-i-p/SS structures under AM1 (100 mW/cm^2) illumination. The module structure and encapsulating materials suitable for a-Si solar cell were investigated to make a low cost module. Typical output power under AM1 illumination is 16W for the module composed of 40 sheets of ITO/n-i-p/SS cells with 10×10 cm^2 area. The a-Si modules have been tested in various environments. The results show that the a-Si solar cells are highly resistive to high and low temperature, high humidity environments, and thermomechanical stress.

Hydrogenated amorphous silicon (a-Si:H) produced by glow discharge decomposition of silane has been shown to possess desirable properties for thin film solar cell (1). Because of the excellent photoconductive property and the high optical absorption coefficient of a-Si:H over the visible region of the solar spectrum, an efficient solar cell can be constructed with a 1 μm thick a-Si:H film. Amorphous silicon shows economical advantage in cell fabrication processes over conventional crystalline solar cells: lower growth temperature, capability of forming junction during the deposition process, and the easy production of large area cells.

Most of the previously reported discussions on the structure and performance of a-Si:H solar cell were concerned with small area cells (2). From a practical point of view, our efforts have been concentrated on the development of large area a-Si:H solar cell (3). We have developed a series of a-Si:H solar cells for consumer electronics like hand-held calculators, and put them on the market for the first time, in the summer of 1980 (4). For practical application of the cell to photovoltaic power generation, the cell performance under the sunlight must be further improved. In a-Si:H solar cells the conversion efficiency measured under the sunlight depends on the cell area, and decreases with increasing cell area (5). We have studied the causes of this cell area dependence of the cell performance, and have found that the conversion efficiency degradation is caused mainly by series resistance in the electrodes (6, 7). By employing these results, we have improved the performances of a-Si:H solar cells, prepared on stainless steel and glass substrates with an area of 100 cm^2, as a part of this work. Prior to applying the a-Si:H solar cell to practical power generation, the optimum module structure and encapsulating material must be developed to make a low cost module. The cell performance should be reasonably retained when the a-Si:H solar cell is assembled into a module. Furthermore, the module should stand for long-term use. We reported the module composed of 36 sheets of 7×7 cm^2 area a-Si:H solar cells, and a solar cell array which consisted of 108 pieces of the modules (4). These modules had the conventional glass/silicone/metal plate structure.

In this paper, we present a-Si photovoltaic modules with simpler structure. This paper also describes the environmental test results of the a-Si:H solar cells, encapsulating materials, and the photovoltaic modules.

Performance of Large-Area a-Si:H Solar Cell

The structures of a-Si:H solar cells discussed in this study include ITO/p-i-n/stainless steel (SS), ITO/n-i-p/SS, and metal/n-i-p/ITO/glass. The a-Si:H was prepared by glow discharge decomposition of silane in capacity coupled rf systems. The window-side a-Si:H layer is p-type in ITO/p-i-n/SS cell and n-type in ITO/n-i-p/SS cell. A 500Å thick phosphorous (or boron)-doped a-Si:H layer was deposited on an SS-substrate at first. Then 0.5 μm thick undoped a-Si:H layer and a 100Å thick boron (or phosphorous)-doped a-Si:H layer were successively deposited. Finally, a transparent conductive ITO film and metal grid electrodes were formed. In metal/n-i-p/ITO/glass cell, a 100Å thick boron-doped a-Si:H layer was deposited on a glass plate coated with a transparent conductive ITO film. Then 0.5 μm thick undoped and a 500Å thick phosphorous-doped a-Si:H layer were successively deposited. And finally metal film back-contact electrodes were formed. This type of solar cell was illuminated through glass-substrate. Since the excellent window-effect of a-SiC:H was reported by Tawada *et al.* for small-area cells (8), we have applied a-SiC:H film to a window-side layer in the large-area glass-substrate cell.

For practical application of the a-Si solar cell, enlargement of cell area without conversion efficiency degradation is required. However, the short-circuit current (*Jsc*) and the fill factor (*FF*) tend to decrease with increasing cell area. We proposed a method for analyzing the cell area dependence of *Jsc* and *FF* in the SS-substrate a-Si solar cell, and reported the results for a 7×7 cm^2 cell (6). By applying this technique, we have estimated degradation in the performance of the ITO/n-i-p/SS cell associated with the increase of cell area from 1.2 to 100 cm^2. The estimation has been done on a 100 cm^2 cell [Fig. 1(a)] in which the sheet resistance of ITO film is 50 $\Omega/\square$, and the grid electrodes are formed by 1.0 μm thick Ti-Ag layer of which resistivity is 2×10^{-6} Ω-cm. Table I summarizes the cell performances for the 1.2 and 100 cm^2 cells, and the factors influencing the cell area dependence of *Jsc* and *FF*. According to the results shown in Table I, half the decrease in *FF* associated with the increase in cell area from 1.2 to 100 cm^2 is caused by a series resistance, which consists of resistances of the grid electrodes and ITO. About 80, 10, and 10% of the decrease are caused by the power losses due to the series resistances in the stem and branch parts of grid electrodes, and the ITO film, respectively. About one third of *FF* degradation is caused by a contact resistance at the ITO and metal interface, and 10% is due to shunt resistance of the solar cell, which was measured as 40Ω from dark current-voltage characteristics. The rest (10%) is caused by an inhomogeneity of a-Si layer. Therefore, suppressing the series resistance offers an effective measure for improving *FF*.

Key words: amorphous semiconductor, solar cell, reliability.

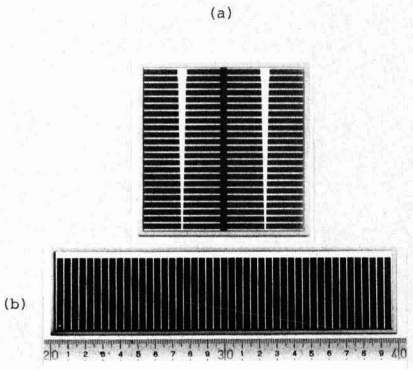

Fig. 1. Grid electrode configurations of two types SS-substrate solar cells with 100 cm² area.

Figure 2 shows *FF* in the 100 cm² cell as a function of grid electrode thickness calculated by considering a cell configuration shown in Fig. 1(a). By doubling the thickness of grid electrodes from 1 to 2 μm, we will be able to obtain 0.58 as the value of *FF* in type (a). However, Fig. 2 shows that the thickness of grid electrodes must be increased to over 10 μm in order to improve *FF* to more than 0.60. We designed and prepared another type of 100 cm² cell shown in Fig. 1(b).

For electrical interconnections of this type of cells, pieces of metal ribbons or wires can be soldered on any part of the stem without shadowing the active area of the cell, to make power loss in the stem part of grid electrodes negligible. In such cell, *FF* of 0.60 is expected.

The similar calcualtion was conducted in the design of a metal/n-i-p/ITO/glass cell in which unit cells formed on a glass-substrate are connected in series on the same substrate. The key parameters to determine the *FF* of such a cell include the length of a unit cell and the sheet resistances of ITO and metal electrodes. The power loss in ITO and metal electrodes is shown in Fig. 3. The power loss was calculated as a function of photogenerated current, with respect to the length *L* of the unit cell, indicated in the inset of Fig. 3. The sheet resistances of the metal and the ITO film were assumed to be 0.05 and 10 $\Omega/\square$, respectively. We found that the length of the unit cell should be limited within 15 mm to retain the *FF* degradation within 10% of the ideal *FF*, when the sheet resistance of a transparent conductive film is 10 $\Omega/\square$. The power loss decreases with decreasing *L*, while the active area of the solar cell decreases. To use more than 80% of the substrate area as an active area, *L* should be more than 7 mm. Two types of a-Si solar cells on glass-substrate shown in Fig. 4 were fabricated. In Fig. 4(a), 10 cells formed on a glass-substrate of 10 × 10 cm² were connected in series, and in Fig. 4(b), 6 cells formed on a glass-substrate of 11 × 12 cm² were connected in series.

Table I. Factors influencing the cell area dependence of short-circuit current (*Jsc*) and fill factor (*FF*) for ITO/n-i-p/SS solar cell

Cell area	*FF*	*Jsc* (mA/cm²)
1.2 cm²	0.659	11.2
100 cm²	0.549	10.6
Difference	0.110	0.6
Contribution to *FF* and *Jsc* lowering		
Shunt resistance	10%	
Series resistance	50%	
Inhomogeneity	10%	100%
Contact resistance	30%	

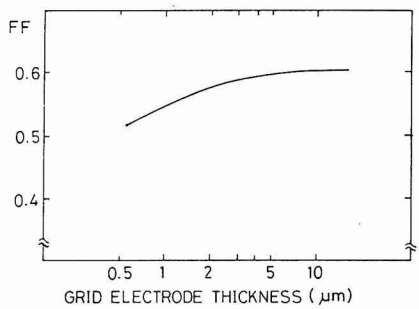

Fig. 2 Grid electrode thickness dependence of fill factor (*FF*) in a 100 cm² area cell [Fig. 1(a)]. In the calculation, the resistivity of the grid electrode is assumed to be 2 × 10^{-6} Ω-cm.

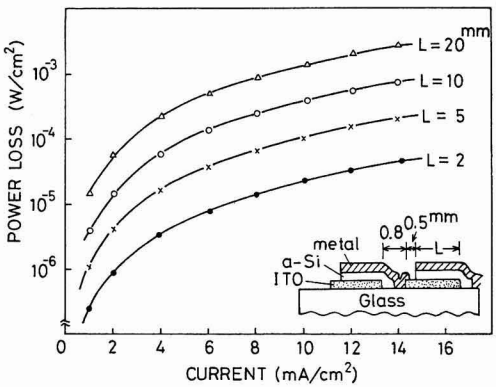

Fig. 3. Power loss *vs.* generated current with respect to the length of the unit cell (*L*) of a metal/n-i-p/ITO/glass cell.

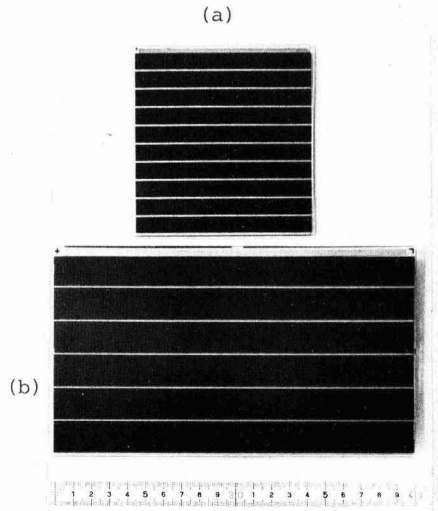

Fig. 4. Two types of glass-substrate cells: (a) 10 series connected cell with 10 × 10 cm² area, (b) 6 series connected cell with 11 × 20 cm² area.

Output characteristics of large area a-Si solar cells on SS- and glass-substrates are summarized in Table II. The *Jsc* and the conversion efficiency η in Table II

Table II. Output characteristics of large area solar cells under AM1 (100 mW/cm²) illumination

Cell structure	Cell area (cm²)	Voc (V)	Jsc (mA/cm²)	FF	η (%)
ITO/n-i-p/SS	10 × 10 (a)	0.88	11.4	0.58	5.8
	5 × 20 (b)	0.86	11.8	0.60	6.0
Metal/n-i-p/ITO/glass	10 × 10 (a)	8.5	12.3	0.59	6.2
	11 × 20 (b)	5.28	12.7	0.54	6.0

are active area values. The solar cell on SS-substrate shown in Fig. 1(a), in which the grid electrodes were 2 μm in thickness, gives the conversion efficiency of 5.8% and *FF* of 0.58. In the 5 × 20 cm² solar cell [(b) in Fig. 1], conversion efficiency of 6.0% was obtained. The *FF* for this cell was 0.60. These observed *FF*'s show fair agreement with the expected values proposed in the foregoing section.

The conversion efficiency of 6.2% was obtained in the a-Si solar cell formed on a 100 cm² glass-substrate [(a) in Fig. 4]. For larger solar cells, conversion efficiency of 6.0% has been obtained in an 11 × 20 cm² cell [(b) in Fig. 4]. The *FF* of the former cell is 0.59, and that of the latter cell is 0.54. This difference in *FF* between the 100 cm² cell ($L = 8$ mm) and the 11 × 20 cm² cell ($L = 15$ mm) is due to the difference in the unit cell length L as discussed above.

Photovoltaic Module for Power Application

The a-Si photovoltaic cells can be made on several kinds of substrate, such as metal, glass, and polymer film. Module structure should be chosen by considering the substrate used. We have conducted an investigation on module fabrication process for SS-substrate cells and glass-substrate cells.

For SS-substrate cells, semitempered soda-lime glass plate, silicone resin, and polyvinyl fluoride (PVF) film were used for a front cover, encapsulant, and a back cover, respectively. Figure 5 shows the module composed of 40 cells with 10 × 10 cm² area. These 40 cells were wired in 4 parallel strings of 10 cells wired in series.

When SS-substrate cells are assembled into a module, they show a definite advantage over other photovoltaic cells, because SS-substrate cells are resistive against mechanical shock, such as striking of hail or small stones. Another advantage is that positive and negative electrodes can be made on the same plane of substrate, as shown in Fig. 6. This cell structure makes wiring process easy. In order to make a low cost module, we will examine possibilities to replace the semitempered glass plate for a front cover by thin polymer film in the near future.

There is another possibility to make a low cost module with a glass-substrate cell. Since electrically separated unit cells are connected in series on a glass-substrate, high output voltage can be obtained from a glass-substrate cell. Moreover, the substrate glass plate may also play as the front cover of a module. Therefore, we proposed the "single substrate module," which is composed of a large area glass-substrate cell with resin coating and a metal or plastic frame, as schematically shown in Fig. 7(a). Figure 7(b) shows the prototype of the "single substrate module" with a 15 × 22 cm² glass-substrate cell.

We have tested applicabilities of various materials to front cover, encapsulant, and back cover. Table III shows the change in transparency of several candidate materials for encapsulant, under environmental test conditions. Two types of specimens, glass/polymer/glass (type 1), and PVB film/polymer/glass (type 2), were used for the test. After heat-treatment at 80°C for 500 hr, silicone resin, polyvinyl butyral (PVB), and ethylene vinylacetate copolymer (EVA) showed little change in transparancy, even when they were employed for the type 1 specimen. Under high humidity condition at 60°C, 95% RH for 500 hr, silicone resin and PVB showed little change in transparency when they were employed for the type 1 specimen. However, when the type 2 specimen was tested, PVB became opaque. In heat shock test (high temperature condition 80°C, 1 hr: low temperature condition −20°C, 1 hr: 10 cycles), unsaturated polyester resins showed severe change in their appearance, but the other materials shown in Table III showed no change. From the above

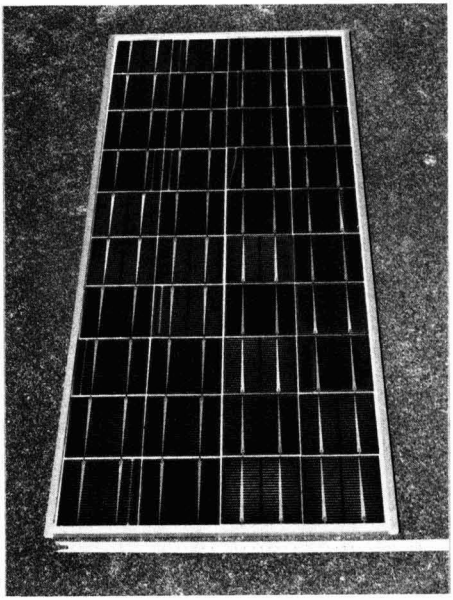

Fig. 5. a-Si photovoltaic module composed of 40 pieces of 10 × 10 cm² SS-substrate cells.

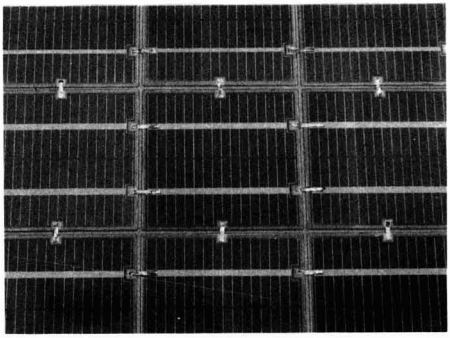

Fig. 6. SS-substrate cells connected with the same plane of each substrate.

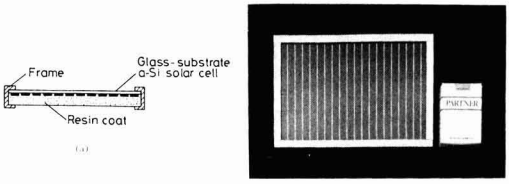

Fig. 7. Schematics of "single substrate module" (a) and the prototype with a 15 × 22 cm² glass-substrate cell (b).

Table III. Change in transparency of several materials under the environmental tests

Test condition	High temperature 80°C, 500 hr		High humidity 60°C, 95% RH, 500 hr	
Specimen construction	Type 1	Type 2	Type 1	Type 2
Silicone resin	96	94	97	97
PVB	100	95	100	80
EVA	98	98	—	—
Epoxy resin	94	85	91	89
Unsaturated polyester resin	87	80	90	90

results, it has been found that encapsulating materials are much affected by water vapor permeation, oxygen permeation, and mechanical stress in their life. Therefore, at selecting encapsulating materials, module structure should be considered at the same time.

To obtain maximum output power of photovoltaic module from incident solar energy, transparency of a front cover and reflection at a module surface are key parameters. As a front cover, semitempered soda-lime glass plate was found to be usable instead of semitempered low iron glass plate, which is generally used in single crystalline Si photovoltaic module, because the wavelength of the maximum sensitivity of a-Si photovoltaic cells lies near 550 nm, which is in the lowest optical loss region for soda-lime glass.

In order to reduce the reflection at the module surface, the wavelength dependence of surface reflectance was measured on an air/ITO/n-i-p/SS cell, and a glass/silicone resin/ITO/n-i-p/SS module. The wavelength for the minimum reflectance depends on ITO film thickness. The thickness which obtains the minimum reflectance at the wavelength of 550 nm is 750Å. Figure 8 shows reflectance of the cell and module when the thickness of ITO film is 750Å. The surface reflectance of the cell at 550 nm (curve a) is about 5%, and increases to 18% by impregnating a silicone resin between a semitempered glass plate cover and the cell (curve b). Thus, the conversion efficiency of SS-substrate cells decreases by about 10% when they are assembled into a module.

The output characteristics of the modules composed of 40 cells of 10 × 10 cm² have been measured with a large area solar simulator. Typical electric output power under AM1 (100 mW/cm²) illumination is 12 and 16W, for the modules using ITO/p-i-n/SS and ITO/n-i-p/SS cells, respectively. Figure 9 shows the typical output characteristics of the latter module.

Reliability of a-Si:H Solar Cell

An a-Si solar cell is composed of several layers with different thermal expansion coefficients, and also subjected to various temperatures in wiring, encapsulating, and servicing. Thermomechanical stress due to

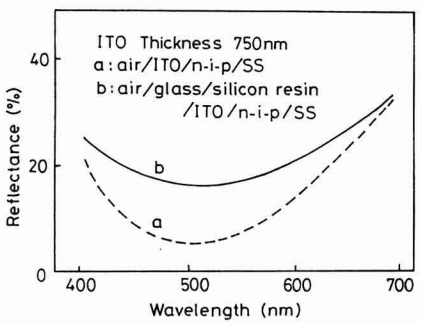

Fig. 8. Surface reflectance of SS-substrate cell (a) and module (b).

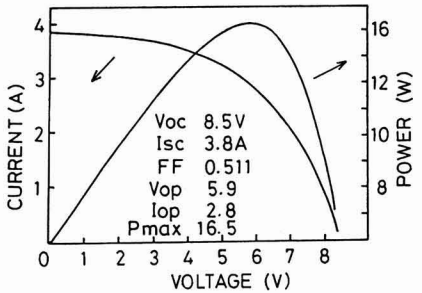

Fig. 9. Output characteristics of the module composed of 40 cells with 10 × 10 cm².

these temperature changes must affect the cell characteristics. To evaluate this effect, a heat cycle test was conducted on SS-substrate (0.5 mm thick) cells of 10 × 10 cm².

The cell performance before and after 10 heat cycles did not show any noticeable difference, as shown in Table IV. The cell appearance also showed no change under the usual test conditions. Only a bit of peeling-off in the a-Si:H film was observed after 10 cycles, under the unusually severe test condition (−200°C ↔ 200°C). In the bending test (center load up to 5 kg, two end supports), no crack and peeling-off in the a-Si film occurred, and the cells have retained their original performance.

Reliability tests for the modules composed of 36 sheets of ITO/p-i-n/SS cells with 7 × 7 cm² area were carried out under conditions listed in Table V. No change in the output characteristics and the appearance of modules was found, not only in the heat cycle test, but also in other tests listed in the Table.

A slight decrease in the conversion efficiency was found under continuous illumination of AM1 spectrum (100-1000 mW/cm²). Figure 10 shows the results under continuous illuminations of various light intensity. After 240 hr of illumination, the conversion efficiency

Table IV. Cell characteristics and appearance before and after heat cycle test for SS-substrate cells

Test condition	Cell characteristics: Initial	Cell characteristics: After 10 cycles	Appearance
100°C 30 min ↑ ↓ (1 min) −40°C 30 min ↓	100	102	No change
200°C 30 min ↑ ↓ (1 min) −40°C 30 min ↓	100	110	No change
200°C 30 min ↑ ↓ (1 min) −75°C 30 min ↓	100	100	No change
200°C 30 min ↑ ↓ (1 min) −200°C 30 min ↓	100	96	A bit of peeling

Table V. Reliability test conditions for the modules with glass/silicone/PVB film configuration

Tests	Present test level
Humidity cycling	80°C, 95% RH, −20°C, 10 cycles
Heat cycle	−20°C ↔ 80°C (50°C/hr), 50 cycles
Voltage loading	AC 2000V, 1 min
Cyclic pressure loading	Positive + 150 kg/m² + 300 kg/m², 2 sec interval, 1800 cycles Negative − 150 kg/m² − 300 kg/m², 2 sec interval, 1800 cycles
High humidity	70°C, 95% RH, 2000 hr
High temperature	80°C, 1000 hr
Cold temperature	−40°C, 1000 hr
Salt spray	5% NaCl solution, 35°C, 500 hr

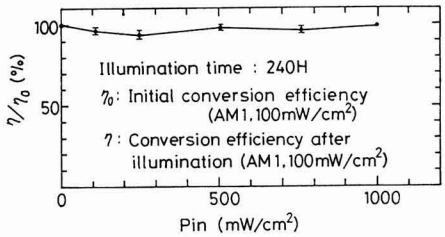

Fig. 10. Conversion efficiency of modules (ITO/p-i-n/SS) after 240 hr continuous illumination normalized by the initial value. The axis of abscissa is the incident power density of the continuous illumination.

of the module remained above 90% of the initial value η_0 under all the applied illuminances.

Conclusion

A considerable progress has been achieved in cell performances of large area a-Si:H solar cells. In the ITO/n-i-p/SS cell, the grid electrode configuration was designed by considering reduction of power loss, and consequently the conversion efficiency of 6.0% has been obtained for the 100 cm^2 cell. Intending to reduce the power loss and keep the active area of the cell above 80% of the substrate, we have fabricated 100 cm^2 cell in which 10 cells were connected in series, and obtained conversion efficiency of 6.2%.

The module structure for the a-Si solar cell was studied. By assembling 40 pieces of 100 cm^2 SS-substrate cells, we fabricated a-Si photovoltaic modules with glass/silicone/PVB film configuration. Typical output powers of the modules under AM1 illumination are 12 and 16W for ITO/p-i-n/SS and ITO/n-i-p/SS cells, respectively. We proposed the "single substrate module" and demonstrated the prototype with a 15 × 22 cm^2 glass-substrate cell.

The a-Si modules composed of SS-substrate cells have been tested under various conditions, including temperature, heat cycle, humidity, and bending load. The results show that the a-Si solar cells are highly resistive to high temperature, low temperature, high humidity environments, and thermomechanical stress. The remaining problem is the slight decrease in the conversion efficiency under continuous illumination of the sunlight.

Acknowledgment

The authors are grateful to Dr. A. Shimazaki, Dr. S. Fushimi, and Dr. H. Fujino for their helpful advice. This work was supported by the Agency of Industrial Science and Technology under the contract of the Sunshine Project.

Manuscript submitted June 17, 1982; revised manuscript received Oct. 15, 1982. This was Paper 44 presented at the Montreal, Que., Canada, Meeting of the Society, May 9-14, 1982.

Any discussion of this paper will appear in a Discussion Section to be published in the December 1983 JOURNAL. All discussions for the December 1983 Discussion Section should be submitted by Aug. 1, 1983.

Publication costs of this article were assisted by Fuji Electric Corporation.

REFERENCES

1. D. E. Carlson and C. R. Wronski, *Appl. Phys. Lett.*, **28**, 671 (1976).
2. D. E. Carlson, *Sol. Energy Mater.*, **3**, 503 (1980).
3. Y. Uchida, H. Sakai, and M. Nishiura, *Jpn. J. Appl. Phys.*, **20**, Suppl. 20-2, 191 (1981).
4. Y. Uchida, H. Sakai, T. Ichimura, M. Nishiura, and H. Haruki, *Fuji Electric Rev.*, **27**, 34 (1981).
5. Y. Uchida, H. Sakai, M. Nishiura, M. Miyagi, and K. Maruyama, Proc. 8th Int. Vacuum Congress, p. 699, Cannes, 1980.
6. Y. Uchida, H. Sakai, M. Nishiura, and H. Haruki, Conf. Rec. 15th IEEE Photovoltaic Specialists Conf., p. 922, Florida, 1981.
7. H. Haruki, Y. Uchida, H. Sakai, M. Nishiura, and M. Kamiyama, *Jpn. J. Appl. Phys.*, **21**, Suppl. 21-1, 283 (1982).
8. Y. Tawada, M. Kondo, H. Okamoto, and Y. Hamakawa, *J. Phys. (Paris)*, **42**, Suppl. 10, C4-471 (1981).

Technical Note

Incidence Angle Dependence of Planar Channeling in Boron Ion Implantation into Silicon

Masayasu Miyake, Masahiro Yoshizawa, and Hiroyuki Harada

Nippon Telegraph and Telephone Public Corporation, Musashino Electrical Communication Laboratory, Musashino, Tokyo, 180 Japan

Ion implantation has been widely used in LSI fabrication process due to its superiority in impurity concentration controllability and reproducibility. In order to achieve reproducible doping into single crystal silicon by the ion implantation, channeling effects must be avoided (1-4). For axial channeling, which is channeling along a low index axis, a number of reports have been published about depth profiles for channeled ions and the incidence angle dependence of the channeling (2-5). However, few such experimental reports have been published for planar channeling, which is channeling along a low index plane, in boron implantation into silicon. In order to avoid the channeling, it is important to reveal the channeling effect incidence angle dependence. In the present work, a new method for estimating the

Key words: pulsed MOS C-V technique, doping uniformity, critical angle.

channeling incidence angle dependence using C-V profiling technique was developed. Using this method, the incidence angle dependence of (110) planar channeling in boron implantation into silicon was studied.

CZ, p-type, 75 mm diam, <001> oriented silicon wafers with 30 ~ 50 Ω cm resistivity were used. Boron was implanted into the wafers at 40 ~ 150 keV energy and 1×10^{12} cm^{-2} dose. Figure 1 shows the relationship between the ion beam incidence direction and the wafer orientation. Tilt angle ψ is defined as the angle between the <001> axis and the ion beam direction to the center of the wafer as shown in Fig. 1. In order to avoid <001> axial channeling, boron implantations were accomplished at 8° misalignment from the <001> axis, *i.e.*, at $\psi = 8°$. A well-focused ion beam was scanned over a wafer using an electrostatic deflection system. The wafers have (110) orientation flat. Rotation angle θ is defined as the angle between the <1$\bar{1}$0> orientation and the horizontal plane, as shown in Fig. 1. Boron implantations were accomplished at $\theta = 0°$ so that planar channeling along the (110) plane might occur. The planar channeling ion beam incidence angle dependence was estimated from the variation in the implanted boron depth profiles in a wafer, since the ion beam incidence angles to the (110) plane vary in a wafer because of the ion beam electrostatic deflection system. The implanted boron depth profiles were measured by pulsed MOS C-V technique (6, 7) using the MOS diodes fabricated as follows. After boron ion implantation, the wafers were oxidized in dry O_2 ambient at 1000°C for 60 min to form 500Å thick gate oxide. Evaporating Al electrode, 0.5 × 0.5 mm square shaped MOS diodes were delineated by photolithography. MOS diodes were spaced 1.5 mm apart in a wafer.

Figure 2 shows boron depth profiles implanted at 150 keV energy measured by the pulsed MOS C-V technique for position A, which is the center of the wafer, and for position B, which is near the orientation flat. If the x-y orthogonal coordinate system is defined as shown in Fig. 2, position A is represented as (0 mm, 0 mm), and position B is represented as (0 mm, 24 mm). It can be seen that implanted boron penetrates deeper at the center of the wafer, A, than at the edge of the wafer, B, due to the planar channeling effect along the (110) plane. The profiles are not "as implanted" profiles, but are redistributed profiles due to diffusion, since the oxidation was performed at 1000°C for 60 min after implantation. Though the measured profiles are not "as implanted" profiles, the planar channeling effect can be estimated from the profiles, since the diffusion does not so seriously cause a redistribution (8). Penetration depth, R_{pe}, is defined as the depth where boron concentration is equal to 10^{16} cm^{-3}

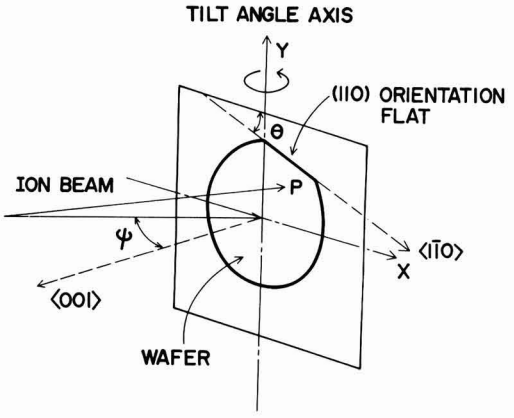

Fig. 1. Ion beam incidence direction and wafer orientation

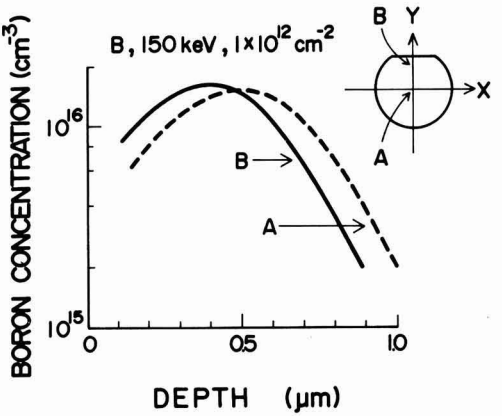

Fig. 2. Boron depth profiles measured by pulsed MOS C-V technique for position A, which is the center of the wafer, and position B, which is near the orientation flat.

(deeper one). The (110) planar channeling effect was estimated by measuring the penetration depth distribution in the wafer. Figure 3 shows the penetration depth dependence on the position along the y axis. As can be seen, the penetration depth has a maximum value of 7300Å at $y = -3$ mm. That is, the planar channeling along the (110) plane most remarkably occurred at $y = -3$ mm, which indicates that ion beam incidence direction was parallel to the (110) plane at $y = -3$ mm for the wafer. In Fig. 4, x direction dependence of the penetration depth is shown at $y = -3$ mm. As can be seen, the penetration depth does not vary with x direction, since ion beam incidence angle to the (110) plane is 0°, and does not vary with x direction at $y = -3$ mm. On the other hand, the ion beam incidence angle to the (110) plane varies with y direction. Angle ϕ between ion beam incidence direction and the (110) plane is represented as follows along the y axis

$$\phi = \tan^{-1}(y/l) - \tan^{-1}(y_0/l) \qquad [1]$$

where l is the distance from the electrostatic scanner to the wafer in the ion implanter (l is 100 cm in the present work), and y_0 is the position where the planar channeling most markedly occurs (y_0 is −3 mm in Fig. 3). Using Eq. [1] and the measured depth profile variation in the wafer, the channeling effect incidence

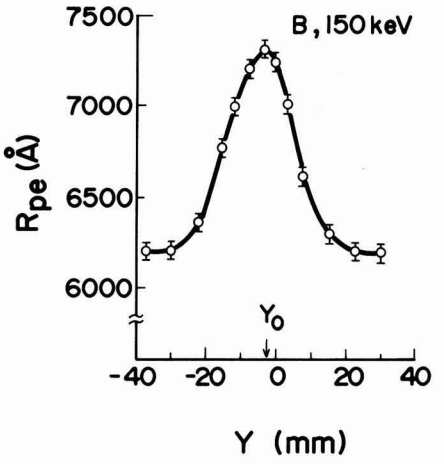

Fig. 3. Penetration depth dependence on the position along the y axis.

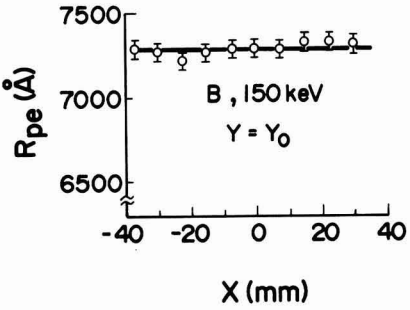

Fig. 4. Penetration depth dependence on the position along the x axis at y = −3 mm.

angle dependence can be estimated easily. The incidence angle dependence for the (110) planar channeling is shown in Fig. 5, which was deduced from the data shown in Fig. 3, using Eq. [1]. It can be seen that increase in the penetration depth due to the planar channeling is about 20%, and that the penetration depth decreases with increasing the incidence angle to the (110) plane. It can be also seen that the planar channeling does not occur for larger ϕ than 1.5°. It was confirmed that the projected range, R_p, agrees well with the LSS theory range for a larger ϕ than 1.5° (9). Cutoff angle, ϕ_{co}, is defined as the minimum angle that ensures a random equivalent implantation. The cutoff angle in the (110) planar channeling for 150 keV boron was estimated as 1.5°. Figure 6 shows boron ion energy dependence of the cutoff angle. It is seen that ϕ_{co} slightly decreases with increasing boron energy. The (110) planar channeling can be avoided by setting ϕ larger than about 2° for the boron energy range used for LSI fabrication. The dashed line in Fig. 6 represents the critical angle, ϕ_c, for (110) planar channeling calculated on the basis of the continuum potential model using screened Coulomb potential, which was described in Ref. (10). The critical angle is the maximum angle within which the continuum potential approximation holds. Slight channeling effect occurs even for $\phi > \phi_c$ (quasi-channeled case) (11). Therefore, the cutoff angle is considered to be slightly larger than the critical angle. It is seen from Fig. 6 that boron energy dependence of the cutoff angle obtained in the present work agrees well with boron energy dependence of the critical angle, and that the cutoff angle is slightly larger than the critical angle. The difference between

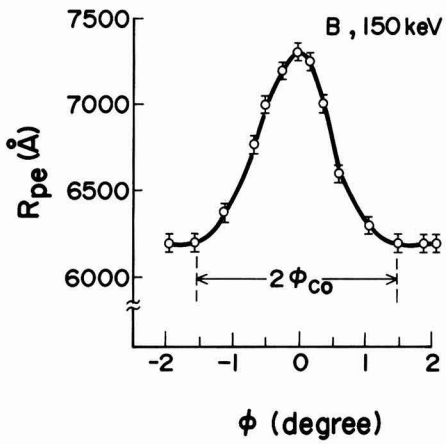

Fig. 5. Ion beam incidence angle dependence for (110) planar channeling.

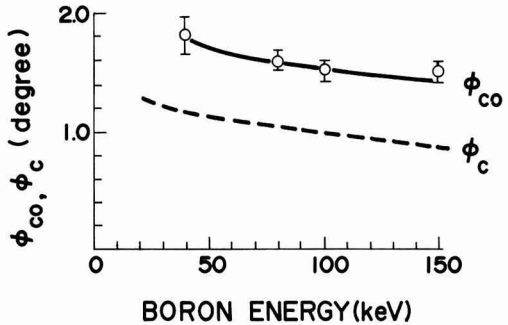

Fig. 6. Boron energy dependence of the cutoff angle for (110) planar channeling. Dashed line represents boron energy dependence of the calculated critical angle.

the cutoff angle and the critical angle probably arises from the above-mentioned quasi-channeling effect.

Next, we consider how the condition of $\phi > \phi_{co}$ can be achieved in a practical ion implantation. The incidence angle to the (110) plane, ϕ, for a point $P(x,y)$ in a wafer is represented as follows, referring to Fig. 1

$$\phi = \sin^{-1}\{|(x + 1\sin\psi)\sin\Theta + y\cos\Theta|/\sqrt{(x + 1\sin\psi)^2 + y^2 + l^2\cos^2\psi}\} \quad [2]$$

The incidence angles in a 75 mm diam wafer were calculated using Eq. [2] for $\psi = 8°$ and various values of Θ. The calculated result indicated that the condition of $\phi > 2°$ can be achieved by setting Θ larger than 30° for any point in a 75 mm diam wafer. That is, uniform and reproducible implantation can be accomplished by setting $\psi = 8°$ and $\Theta = 30°$ for a 75 mm diam wafer. This result was also confirmed experimentally.

In summary, the incidence angle dependence of the (110) planar channeling was studied by measuring depth profile variation in a silicon wafer, into which boron was implanted using the ion implanter with an electrostatic scan system. The depth profile variation in the wafer was measured by the pulsed MOS C-V technique. The cutoff angle for 40 ~ 150 keV boron was estimated as 1.8 ~ 1.5°. It was found that the cutoff angle slightly decreases with increasing boron energy. Consequently, a random equivalent implantation, or uniform and reproducible implantation can be accomplished by setting ϕ larger than about 2° for boron energy range used for LSI fabrication. The condition of $\phi > 2°$ can be achieved by setting $\psi = 8°$ and $\Theta = 30°$ for a 75 mm diam wafer.

Acknowledgments

The authors express deep appreciation to Dr. H. Mukai, Dr. M. Kondo, and Dr. E. Arai for their advice and encouragement.

Manuscript submitted April 26, 1982; revised manuscript received Nov. 1, 1982.

Any discussion of this paper will appear in a Discussion Section to be published in the December 1983 JOURNAL. All discussions for the December 1983 Discussion Section should be submitted by Aug. 1, 1983.

Publication costs of this article were assisted by Nippon Telegraph and Telephone Public Corporation.

REFERENCES

1. F. H. Eisen, *Can. J. Phys.*, **46**, 561 (1968).
2. G. Dearnaley, J. H. Freeman, G. A. Gard, and M. A. Wilkins, *ibid.*, **46**, 587 (1968).
3. T. E. Seidel, in Second International Conference on Ion Implantation in Semiconductors, p. 47, Springer-Verlag, New York (1971).
4. V. G. K. Reddi and J. D. Sansbury, *J. Appl. Phys.*, **44**, 2951 (1973).
5. J. Comes and R. G. Wilson, *J. Appl. Phys.*, **51**, 3697 (1980).

6. W. van Gelder and E. H. Nicollian, *This Journal*, **118,** 138 (1971).
7. K. Ziegler, E. Klausmann, and S. Kar, *Solid-State Electron.*, **18,** 189 (1975).
8. M. Miyake and H. Harada, *This Journal*, **129,** 1097 (1982).
9. J. F. Gibbons, W. S. Johnson, and S. W. Mylroie, "Projected Range Statistics," 2nd ed., Dowden, Hutchinson and Ross, Inc., 1975, Distributed by Halsted Press.
10. D. V. Morgan and D. van Vliet, *Can. J. Phys.*, **46,** 503 (1968).
11. D. van Vliet, in "Channeling," Chap. 2, D. V. Morgan, Editor, John Wiley & Sons, London (1973).

The Electrochemical Society, Inc.
10 South Main Street, Pennington, New Jersey 08534-2896 • Telephone: 609-737-1902

Instructions to Authors

The **JOURNAL OF THE ELECTROCHEMICAL SOCIETY** is the official monthly journal of the Society. It contains three sections: Electrochemical Science and Technology, Solid-State Science and Technology, and Reviews and News. Technical Papers, Technical Notes, and Accelerated Brief Communications are published in the first two sections and Review Papers in the third. All manuscripts submitted are considered for publication, with the understanding that they have not been submitted, accepted for publication, or published elsewhere. A wide range of subject matter is acceptable. Manuscripts can be handled promptly and efficiently if these instructions are followed.

TYPES OF PAPERS

Technical Papers describe fundamental or applied studies in depth. They contain new data and/or new interpretations of existing data. Abstracts summarizing the results are required.

Technical Notes report briefly on limited research or development that is not being pursued further. No abstracts are required.

Accelerated Brief Communications present, in camera-ready format of limited length, scientific or technological information warranting rapid dissemination. No abstracts are required.

Review Papers furnish critical analyses of topical subjects. Abstracts are required.

SUBMISSION

Submit three complete, clear copies of each manuscript and the originals of all figures and illustrations to:

Editorial Office
The Electrochemical Society, Inc.
10 South Main Street
Pennington, New Jersey 08534-2896

A letter accompanying the manuscript should give (a) the name and mailing address of the author to whom correspondence should be sent, (b) reference to any presentation of the work at a meeting of The Electrochemical Society, (c) the Division or Group of the Society or the Divisional or Group Editor (both are listed in the front of each issue of the Journal) whose interests are most closely related to the work being discussed, (d) the section of the Journal in which the work should appear, and (e) the names and addresses of people able to act as reviewers.

EDITORIAL PRACTICES

Following receipt by the Editorial Office, each manuscript is sent to a Divisional or Group Editor with knowledge of the subject matter. This editor arranges for review of the manuscript and communicates with the author(s) regarding revisions. Final acceptance or rejection of a manuscript is determined by the Editor.

Accelerated Brief Communications are handled as rapidly as possible, ordinarily with a response to the author(s) from the Divisional Editor, the Group Editor, or the Editor within three weeks of their arrival at Pennington. Response to the authors of other manuscripts usually takes place within six weeks. Following acceptance, authors are notified of the Journal issue in which publication is scheduled; about one month before publication, page proofs and an order blank for reprints are provided. Proofs must be promptly corrected and returned. Extensive alterations by the author may delay publication; their cost will be billed to the author(s).

PUBLICATION CHARGE

To help meet publication costs, a payment of $65.00 per printed page is requested for the publication of technical material. If at least one author is a Society member or an employee of a Patron or Sustaining member, a 10% reduction is allowed. Acceptance of manuscripts for publication is, however, based on merit and is in no way dependent on such payment, which may be waived in individual cases upon request.

PRESENTATION

Organization and clarity are essential elements of successful written communication. Identify the subject matter in the title, using words useful in indexing. State the purpose of the work early in the text. Avoid introductory and explanatory material that is overly familiar to those in the field. Present the work and the arguments in an order that leads naturally to clearly specified conclusions. Provide enough information for the work to be reproduced and the logic behind it to be understood. Identify and justify any assumptions that are made; avoid tacit assumptions. Omit details that are generally known or that can be covered by reference to other publications. Give the magnitude and define the significance of experimental errors. Use headings and subheadings as appropriate. Avoid proprietary and trade names, but capitalize them where their use is necessary. Define unusual technical terms and abbreviations. Where symbols are used extensively, list them with their definitions at the end of the paper. Avoid repetition in the text and duplication of material in figures and tables. Be brief but clear.

Edit and proofread the manuscript carefully; these are not the responsibilities of the editors or reviewers.

KEY-DESCRIPTORS

To aid in indexing, authors must supply standard key-descriptors, preferably four of them, from a list with instructions published annually in the December issue of the Journal and available from the Editorial Office. These key-descriptors must appear at the bottom of the first page of the manuscript.

MANUSCRIPT PREPARATION

Accelerated Brief Communications must be typewritten or printed on standard forms obtained, with detailed instructions for their use, from the Pennington Editorial Office.

All other manuscripts must be typewritten or printed, double-spaced throughout, on one side only of white 21.6 x 27.0 cm paper, with 2.5-3.8 cm margins. Do not use single spacing anywhere, in title, abstract, text, references, tables, or figure captions.

For general matters of style and format, see papers in recent issues of the **Journal** and consult a style manual such as that of the American Chemical Society or that of the American Institute of Physics. These also provide lists of common abbreviations and units. The following specific items should be noted:

(a) Système Internationale (SI) units are to be used; a description may be found in NBS Special Publication 330 or ASTM Metric Practice Guide E-380-72.

(b) The signs of cell and electrode potentials are to follow the IUPAC conventions of 1953.

(c) **Mathematical equations** should be written on a single line, if possible, using parentheses, brackets, the solidus, negative exponents, etc.

(d) **References** are to be listed separately at the end of the paper in the order they are cited in the text, being sure that each listed reference is cited. Authors' initials must be given, and Chemical Abstracts abbreviations must be used. Citations of other than the generally available literature should be avoided if possible.

(e) **Tables** are to be presented on individual sheets, with both captions and body double-spaced.

(f) **Figure captions** and numbers are to be included on a separate sheet and must not appear in the body of any figure or illustration.

(g) **Drawings** and **graphs** will ordinarily be reduced to column width (8.3 cm) and after such reduction should have lettering at least 0.15 cm high. Lettering must be of letter-guide quality. Originals in India ink on tracing cloth or paper are preferred, but India ink on coordinate paper with blue ruling is acceptable. When several curves are shown, each may be lettered and identified in the caption. The Editorial Office will not make corrections or additions to figures.

(h) **Photographs** should be used sparingly. The originals supplied must be glossy prints and should be protected against bending. Micrographs must have a labeled unit length within the body of the picture; reduction for printing makes magnifications meaningless.

Revised December 1, 1980

Printed in the United States of America

JOURNAL OF THE ELECTROCHEMICAL SOCIETY

ACCELERATED

—BRIEF COMMUNICATIONS—

MARCH 1983

Phenomenological Model for Silicon Oxidation in Dry Oxygen in the Presence of HCl

A. I. Ellis,* K. M. Gardiner, and T. E. Cyr

Solid State Electronics Division, Honeywell Incorporated, Plymouth, Minnesota 55441

INTRODUCTION

Thermal oxidation of silicon to form a thin SiO_2 layer is one of the most important processes in VLSI and VHSIC technology. Presently, some commercially available, high performance MOS memory circuits use gate oxides as thin as 400 Å. There is a wide body of experimental evidence which indicates that such thin layers of SiO_2 are substantially different from thicker layers. These differences include growth kinetics, optical properties, breakdown characteristics, and physical structure. In spite of the pioneering studies of Deal and Grove [1] and several other authors [2-4], the growth of the first several hundred angstroms of oxide has not yet been quantitatively explained. In this paper we propose a conceptually simple modification of the Deal -Grove model based on the assumption that the oxygen atoms impacting the oxide surface have a definite probability of penetrating to a certain depth. Expressions useful for data analysis and simulation (SUPREM II and III) are given.

DRY OXIDATION MODEL

Blanc [3] proposed a simple model which explains well the anomalously high oxidation rate of thin oxide. This model assumes that although oxygen diffuses molecularly during the dry oxidation, the actual oxidant is atomic oxygen; this leads to a conceptually simple modification of the Deal-Grove model. Blanc's model was tested in both the thin and thick oxide regions and was found inadequate for the simulation of both oxide regimes. Therefore, here we suggest a semiempirical modification of the Deal-Grove formula. It was assumed after Deal and Grove, that the oxidation mechanism arises from the diffusion transport of oxidant through the growing amorphous SiO_2 layer followed by the reaction of Si with oxidant at the advancing interface. The equation of Deal and Grove which describes the change of oxide thickness, Z_{ox}, with the oxidation time, t, has the following form:

$$\frac{dZ_{ox}}{dt} = \frac{K_l K_p}{2K_l Z_{ox} + K_p} \qquad (1)$$

Here K_l and K_p are the linear and parabolic growth rates respectively. They are related to the linear and parabolic rate constants A and B by $A = K_p/K_l$ and $B = K_p$. We suggest that for thin oxides the linear growth rate K_l should be replaced by K_n, where

$$K_n = K_l (1 + Z_f \exp(-Z_{ox}/Z_l)) \qquad (2)$$

The new model parameters are: Z_f the growth acceleration factor, and Z_l the effective penetration depth. Their temperature dependences (for dry O_2) as determined by comparison to experimental data are:

$$Z_f = 39.965 - .08145 + 4.2552 \times 10^{-5} T^2 \qquad (3)$$

$$Z_l = 1/(692 - 1.3641T + 6.876 \times 10^{-4} T^2) \text{ (microns)} \qquad (4)$$

where T is in °C.

Integrating equation (1) one obtains the well known dependence (Grove's equation):

$$t = \frac{Z_{ox}^2}{K_p} + \frac{Z_{ox}}{K_l} \qquad (5)$$

This equation will take the following form if K_n is substituted for K_l in Eq (1):

---

* Electrochemical Society Active Member.

Key words: oxidation, growth, kinetics.

$$t = \frac{Z_{ox}^2}{K_p} + \frac{Z_{ox}}{K_1} + \frac{Z_1}{K_1} \ln \left[\frac{1 + Z_f e^{-Z_{ox}/Z_1}}{1 + Z_f} \right] \quad (6)$$

Equation (6) differs from equation (5) by an additional term which causes faster growth for thin oxides but is negligible for oxides 3 to 4 times thicker than Z_1.

The SUPREM II-05 program models the oxide growth by employing approximate empirical correction factors to the usual linear parabolic growth law. The model proposed here improves the predictive capabilities of SUPREM. In Fig.1 we compare the oxide growth rate dZ_{ox}/dt calculated from the Deal and Grove model with that predicted by the new model. Also shown is the growth rate which was used in the SUPREM II-05 program. Note the sharp discontinuity in the SUPREM II-05 curve. This is due to the attempt to fit the experimental data with a constant acceleration factor.

The analysis of the data [1,2,4,5] at 700, 780, 893, 980 and 1100°C further confirm the validity of the proposed model. Figure 2 shows the comparison of the theory with experimental data for oxidation in dry O_2 at 893°C. The dashed curve is the result of the SUPREM II-05 calculations and the solid curve shows that the new model provides a smooth transition from the accelerated to the linear growth regions while maintaining a good fit to experimental data for thick oxides. Such a good fit, over the entire oxide thickness range was not possible with Deal and Grove model.

Equation (10) was solved numerically for each of the A coefficients using least squares, and the following parametric equations were obtained

$$A_f = 69.79 + 0.150P - 0.13682T + 6.838 \times 10^{-5}T^2 + 5.18 \times 10^{-5}PT - 8.54 \times 10^{-3}P^2 \quad (11)$$

$$A_1 = -12.20 - 0.198P + 3.221 \times 10^{-2}T - 1.871 \times 10^{-5}T^2 + 1.636 \times 10^{-4}PT - 1.92 \times 10^{-3}P^2 \quad (12)$$

$$A_p = -51.12 + 0.182P + 0.10414T - 5.143 \times 10^{-5}T^2 - 1.059 \times 10^{-4}PT + 2.55 \times 10^{-3}P^2 \quad (13)$$

where T is in °C.
Equations (3-5), (7-9), (11-13) were directly implemented into the SUPREM II program (Subroutine OXDEP) to account for the effect of chlorine in the dry O_2 oxidizing gas.

To verify our phenomenological model we have calculated the oxide thickness as a function of the oxidation time for dry O_2 oxidation of <100> silicon at 975°C and with 4% HCl. The calculation is compared with the measured values [12] in Figure 3. It is seen that our oxidation model agrees closely with the experimental data in both the linear and parabolic regimes. The dashed curve represents the calculations done assuming that there is no oxide present on the silicon surface at time t = 0. Usually however there is initially a thin layer of oxide present and this can easily be included in the calculations by using the DEPOSITION step in the SUPREM Input Data File before the OXIDATION steps are simulated. The full curve represents results of calculations for initial oxide thickness of 25 Å with a 9 minute push-in simulated prior to the high temperature oxidation. Incorporation of these two processing steps brings the theory into much closer agreement with the experimental data, especially in the thin oxide regime. The growth of the initial 25 Å of oxide can be easily associated with the standard R.C.A. cold clean process through which wafers went before high temperature oxidation.

CONCLUSION

The phenomenological model presented here should be useful for most (chlorine) oxidations of practical interest, within the range of conditions for which data is currently available. Better understanding of the mechanisms involved will be necessary, however, for complete predictive capability particularly outside the available data range.

ACKNOWLEDGMENT

The authors are indebted to J. S. T. Huang for comments and helpful suggestions. Special thanks are due to D. Suhl, S. Peck and G. Kirchner for supplying us with their experimental data and for helpful discussions.

REFERENCES

1. B.E. Deal and A.S. Grove, J. Appl. Phys., 36, 3770 (1965)
2. E.A. Irene and Y.J. Van der Meulen, J. Electrochem. Soc, 23, 1380 (1976)
3. J. Blanc, Appl. Phys. Lett. 33, 424 (1978)
4. E.A. Irene J. Electrochem. Soc. 125, 1708 (1978)
5. G. Wright, Private Communication
6. D.W. Hess and B.E. Deal, J. Electrochem. Soc. 124, 735 (1977)
7. B.E. Deal, J. Electrochem. Soc. 125, 576 (1978)
8. C. Hashimoto, S. Muramoto, N. Shiono, and O. Nakajima, J. Electrochem. Soc. 127, 129 (1980)
9. R.W. Dutton et. al. "Oxidation and Epitaxy", Tech. Report No. 5021-1, Stanford University, Stanford, California (1977)
10. J.R. Monkowski, J. Stach, and R.E. Tressler "A Model of Silicon Oxidation in Chlorine-Containing Ambients: Competition between two oxidants", IEEE Proc. Electron. Components Conf.,San Francisco, Calif., 61 (1980)
11. B.E. Deal, L.N. Lie and R.R. Razouk "Characterization of Silicon Oxidation in High Pressure Dry O_2", Technology Modeling Seminar, Stanford University, Stanford, California (1981)
12. G. Kirchner, S. Peck and D. Suhl, Private Communication
13. E.A. Irene, J. Electrochem. Soc., 121, 1631 (1974)

Manuscript submitted June 1, 1982; revised manuscript received Sept. 10, 1982.

Publication costs of this article were assisted by Honeywell Incorporated.

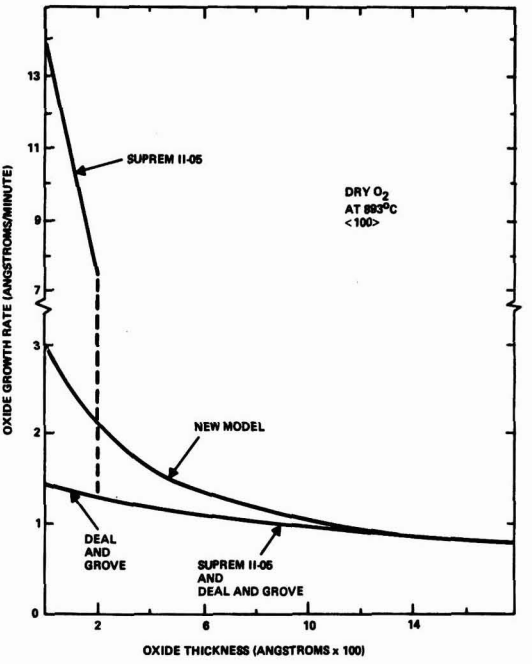

Fig. 1. Comparison of the predicted oxide growth rate for the new dry oxidation model with that of Deal and Grove and that used in SUPREM II-05.

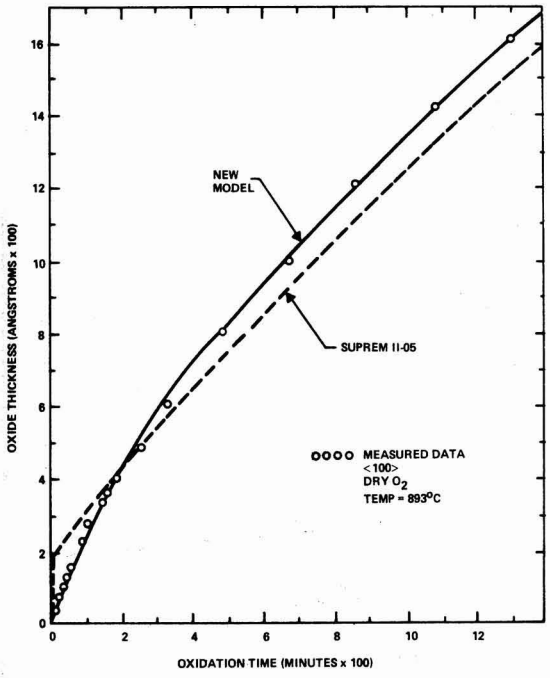

Fig. 2. Comparison of the theory with experimental data[1,2,4,5] for <100> silicon oxidation in dry O_2 at 893°C.

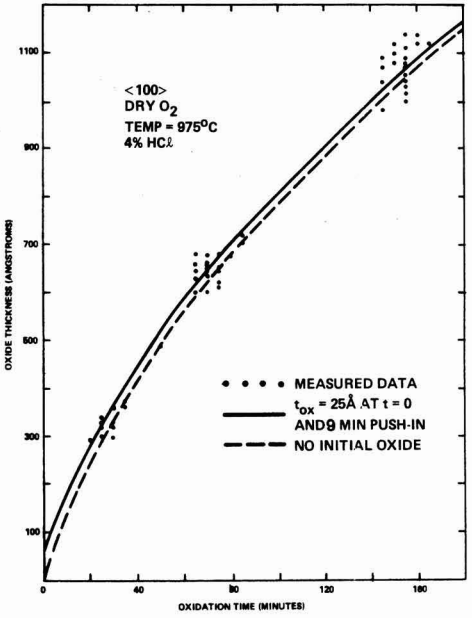

Fig. 3. Comparison of the theory with experimental data[12] for <100> silicon oxidation in dry O_2 with 4% HCl at 975°C. The dashed curve was calculated assuming that t_{ox} = 0 at t=0. The full curve represents results of calculations for initial oxide thickness of 25 Å with a 9 minute push-in simulated before the high temperature oxidation.

The Growth of Zn_3P_2 by Metalorganic Chemical Vapor Deposition

Judith Long

Bell Laboratories, Murray Hill, New Jersey 07974

INTRODUCTION

Recent studies resulting from the interest in developing new materials for low-cost photovoltaic devices have shown zinc phosphide (Zn_3P_2) to be a promising candidate for such applications. Amongst its advantages are a direct band gap of 1.5 eV and relatively cheap and abundant constituent elements. Previously, Zn_3P_2 for device applications has been grown principally by close space vapor transport (1,2). This paper reports the first growth of Zn_3P_2 by the method of metalorganic chemical vapor deposition. The metalorganic technique possesses the advantage that relatively low growth temperatures may be used in conjunction with the independent regulation of the Group II and Group V sources. Since the reactor contains only one hot zone, in the substrate region, the cold reactor walls do not interfere with the growth, which occurs only on the heated substrate. In addition, the apparatus may be easily scaled to accommodate large-area substrates.

EXPERIMENTAL

The growth apparatus, shown in Fig. 1, consisted of a vertical, water-cooled, quartz reactor tube, 50 mm in diameter, containing a molybdenum or silicon carbide coated graphite susceptor on which the substrate was mounted. The temperature was monitored by a thermocouple embedded in the susceptor and heating accomplished by means of an r.f. coil. The zinc source consisted of either of the two volatile metal-organic compounds diethylzinc or the considerably more volatile dimethylzinc (vapor pressures at 25°C = 16.0 torr and 369.1 torr respectively). These were contained in stainless steel bubblers held at room temperature. The metalorganic vapor was transported by passing a hydrogen gas stream through the bubbler. This was then mixed with a stream of phosphine gas in hydrogen, diluted with extra hydrogen and introduced into the reactor where decomposition of the reactants occurred at the heated substrate.

The effects of growth conditions, in particular, temperature, zinc source and P/Zn mole fraction ratio were examined in detail. Growth times were typically on the order of 30 minutes with a total gas flow of 3500 cm^3/min. The zinc mole fraction was generally kept at ~9 x 10^{-4}, whereas the phosphorus mole fraction was varied over the range 1 to 9 x 10^{-3}.

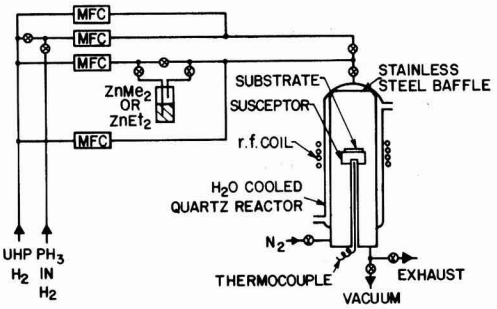

Fig. 1 Simplified schematic of the MOCVD apparatus.

Key descriptors: semiconductor, photovoltaic

RESULTS AND DISCUSSION

Initial growth studies employed $ZnEt_2$ as the zinc source and Carbone-Lorraine 5890-PT high-density graphite as the substrate. Although growth of Zn_3P_2 could be accomplished over the rather wide temperature range of 300 to 500°C, the layers were non-uniform and partially covered with a brown deposit. Positioning a stainless steel baffle, containing many small circular perforations, in the reactor tube, directly below the gas inlet greatly improved growth uniformity and eliminated the brown deposit, presumably as a result of more efficient mixing of the reactant gases.

Using $ZnEt_2$, and a P/Zn mole fraction ratio of 1.1:1 the Zn_3P_2 growth rate was examined as a function of temperature. As shown in Fig. 2, the growth rate was found to increase with increasing temperature, from a value of 3μm/hr at 300°C to one of 10μm/hr at 420°C, where it remained relatively constant over the next 70°. This dependence of the growth rate on temperature in the lower temperature range implies that kinetic control is in effect with the overall growth limited by some relatively slow surface process. For temperatures above 500°C the growth rate decreased rapidly, dropping to 3μm/hr at 550°C, suggesting that the reacting species may be re-evaporating off the substrate surface coupled with parasitic nucleation on the reactor walls.

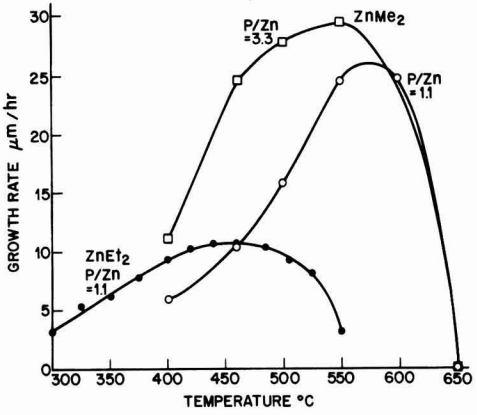

Fig. 2 Zn_3P_2 growth rate as a function of temperature.

Fig. 2 also shows the results obtained using $ZnMe_2$ as the zinc source with the same zinc mole fraction. Although the overall growth pattern was similar, with an initial growth rate increase with temperature followed by a rapid decrease, the highest rates were obtained in the 550 to 600°C range. This shift of the growth region to higher temperatures is in keeping with the higher decomposition temperature of $ZnMe_2$ compared with that of $ZnEt_2$ (3). A notable difference between the two sources was the value of the growth rate which reached a maximum of 25μm/hr with $ZnMe_2$ but only 10μm/hr using $ZnEt_2$. One possible explanation is that reaction at the substrate surface is less favorable for $ZnEt_2$ due to the greater steric bulk of the ethyl groups compared with the methyl. Parasitic nucleation on the reactor walls, which depletes the zinc source, may also be more of a problem for $ZnEt_2$, particularly since the growth occurs at lower temperatures.

Dependence of the growth rate on the P/Zn mole fraction ratio was also examined for the $ZnMe_2$ source. As shown in Figs. 2 and 3, the growth rate increased with increasing P/Zn ratio until a ratio of ~6:1 was reached. Above this value the rate became independent of the P/Zn ratio.

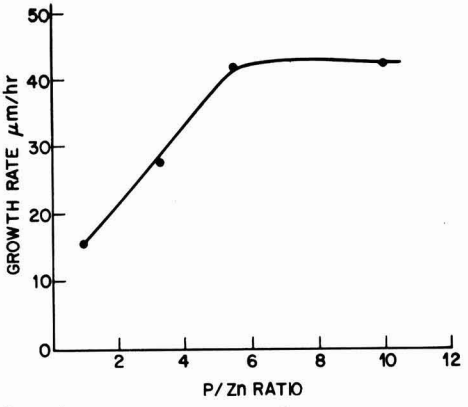

Fig. 3 Zn_3P_2 growth rate as a function of the P/Zn mole fraction ratio.

The Zn_3P_2 samples, however, were all found to exhibit p-type conductivity irrespective of the V/II ratio.

Fig. 4 shows the effect of varying the P/Zn ratio on the surface morphology. An increase in the ratio from 1:1 in a) to 10:1 in b) reduced the tendency for growth of isolated blocks of Zn_3P_2 crystals to occur at the surface. In addition, the grain size was found to be larger at the higher ratios, increasing from 2 to 3μm in a) to 5 to 10μm in b). A similar increase in grain size was also observed on increasing the substrate temperature from 400°C to 550°C.

Graphite was originally the substrate of choice because of its relatively low cost, in addition to several other desirable properties such as thermal stability and chemical inertness. However, despite the large variety of graphite types available, the high thermal expansion coefficient of Zn_3P_2 ($14 \times 10^{-6} °C^{-1}$) made it impossible to find one with a suitably closely-matched coefficient. As a result of this mismatch there was a problem with the occurrence of microcracks and pinholes in the Zn_3P_2 layers, which provide current leakage paths through the material. The cracks were particularly evident in the samples grown at higher temperatures. Previous workers have grown Zn_3P_2 successfully on mica and silicon steel substrates (4), both of which are compatible with the metalorganic technique. Thus, in order to improve the quality of the Zn_3P_2 layers we grew several samples on both mica and silicon steel. The growth conditions were essentially unchanged from those used with graphite substrates. The Zn_3P_2 layers were found to be highly resistive, those grown on mica having sheet resistances of 1 to 2×10^6 Ω/[]. Figure 5 shows SEM photographs of two samples grown on silicon steel, with P/Zn ratios of 1:1 in a) and 10:1 in b). No sign of microcracks was evident in these samples, nor in those grown on mica, and the improvement in surface morphology at higher P/Zn ratios was again observed.

CONCLUSIONS

The growth of undoped, polycrystalline Zn_3P_2 by the method of metal-organic chemical vapor deposition has been demonstrated for the first time and the growth characteristics determined as a function of growth conditions. The quality of the layers was observed to be highly dependent on the substrate material. The samples grown on graphite exhibited microcracks due to a mismatch of the thermal expansion coefficient of Zn_3P_2 with that of the graphite. This problem was eliminated by use of mica or silicon steel as the substrate.

ACKNOWLEDGEMENTS

The author would like to thank W. D. Johnston, Jr., H. J. Leamy and A. Heller for their help and encouragement and M. Bhushan for providing the silicon steel substrates.

REFERENCES

[1] A. Catalano, M. Bhushan, and N. Convers-Wyeth, Proceedings of the 14th. IEEE Photovoltaic Specialists Conference, San Diego, 1980, p. 641.

[2] M. P. Bendett and R. G. Hunsperger, J. Electron Mater., 10, 559 (1981).

[3] G. A. Razuvaev, R. F. Galiulina, and G. G. Petukhov, Zh. Obsh. Khim., 38, 3 (1968).

[4] M. Bhushan and A. Catalano, Proceedings of the 15th. IEEE Photovoltaic Specialists Conference, Orlando, 1981.

Manuscript received Oct. 19, 1982.

Publication costs of this article were assisted by Bell Laboratories.

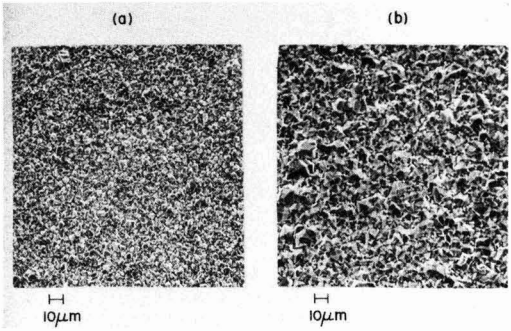

Fig. 4 SEM photographs of Zn_3P_2 growth on graphite a) P/Zn mole fraction ratio = 1:1, b) P/Zn = 10:1.

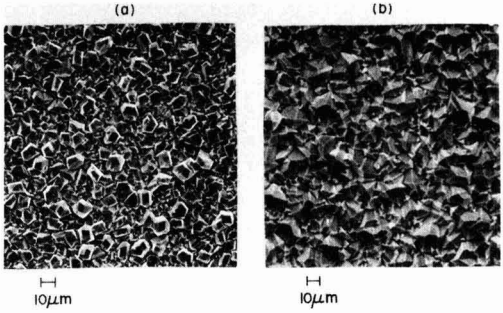

Fig. 5 SEM photographs of Zn_3P_2 grown on silicon steel a) P/Zn mole fraction ratio = 1:1, b) P/Zn = 10:1.

Metal Oxidation as a Heat Pump

Daniel Cubicciotti*

Electric Power Research Institute, Palo Alto, California 94303

The oxidation of a metal is generally an exothermic process, and the rate of heat release is slow enough in most cases that the detailed location of the site of heat evolution is not important. Heat transfer processes, under these conditions, are usually rapid enough to dissipate temperature gradients. Thus, other than being associated with the formation of oxide, the details of heat generation are not important in such situations.

During a rapid oxidation however, it is interesting to consider the detailed processes of heat generation. For example, rapid oxidation of Zircaloy by steam can occur during a nuclear reactor accident involving core dry out such as occurred at TMI-2, and the rate of heat generation from that oxidation can be larger than other heat sources such as radioactive decay. The locus of the heat generation can be important for calculating heat transfer rates and thus local, transient temperatures in a nuclear core during an accident.

The overall process of oxidation of a metal such as zirconium to form a coherent, protective oxide can be divided into three sets of reactions occurring in the following localized regions: (a) at the interface between the metal and the oxide layer, (b) transport of species through the oxide layer, and (c) at the interface between the oxide and the oxidizing gas.

For the oxidation of zirconium by steam, which is a case of interest in nuclear accidents, the reactions occuring in those locations can be represented as follows:

(A) $Zr\ (metal) = Zr^{+4}\ (oxide) + 4e\ (oxide)$

(B) $4e\ (in\ oxide\ at\ metal\ interface) = 4e\ (in\ oxide\ at\ gas\ interface)$

$O^{-2}\ (in\ oxide\ at\ gas\ interface) = O^{-2}\ (in\ oxide\ at\ metal\ interface)$

(C) $2H_2O\ (gas) + 4e\ (oxide) = O^{-2}\ (oxide) + 2H_2\ (gas).$

The heat effects associated with those reactions must be evaluated. The reactions in B have relatively small heats, which will be assumed equal to zero in the present treatment. To evaluate the heat associated with the reaction at A, the reaction will be represented as the sum of four reactions for which enthalpy changes can be evaluated:

(A1) $Zr\ (metal) = Zr\ (gas);\quad \Delta H(A1) = 143.7\ kcal$

(A2) $Zr\ (gas) = Zr^{+4}\ (gas) + 4e\ (gas);\quad \Delta H(A2) = 1783\ kcal$

(A3) $Zr^{+4}\ (gas) = Zr^{+4}\ (oxide);\quad \Delta H(A3) = -1320\ kcal$

(A4) $4e\ (gas) = 4e\ (oxide);\quad \Delta H(A4) = -287\ kcal$

The values quoted were obtained as follows: The value of $\Delta H(A1)$ was taken from Ref. 1. $\Delta H(A2)$ is the sum of the ionization potentials for the first four ionizations of gaseous zirconium, which is given in Ref. 2 as 1783 kcal. $\Delta H(A3)$ was assumed to be the negative of half of the lattice energy, that is, half of the enthalpy change for the reaction:

$$Zr^{+4}\ (gas) + O^{-2}\ (gas) = ZrO_2\ (solid);\quad \Delta H = -2640\ kcal$$

which was calculated from the enthalpy changes of the following reactions:

$Zr(s) = Zr(g);\quad \Delta H = 143.7\ kcal$ (Ref. 1)

$Zr(g) = Zr^{+4}(g) + 4e(g);\quad \Delta H = 1783\ kcal$ (Ref. 2)

Manuscript submitted Oct. 22, 1982; revised manuscript received Nov. 24, 1982.

Publication costs of this article were assisted by Electric Power Research Institute.

*Electrochemical Society Active Member,

Key words: metal oxidation, zirconium.

$1/2O_2(g) = O(g)$; $\Delta H = 59.2$ kcal (Ref. 3)

$O(g) + 2e(g) = O^{-2}(g)$;
$\Delta H = 166$ kcal (Ref. 4)

$\Delta H(A4)$ is equal to four times the negative of the work function of ZrO_2 which is given in Ref. (5) as 3.12 eV.

The sum of the enthalpy changes for reactions A1 to A4 is 320 kcal. This is, per mole of zirconium oxidized, 320 kcal of heat are absorbed at the metal-oxide interface (location A) for a constant pressure oxidation of one mole of zirconium.

At location C (the oxide gas interface), the enthalpy change is the sum of the following reactions:

(C1) $2\,H_2O\,(gas) + 4e\,(gas) = 2O^{-2}\,(gas) + H_2\,(gas)$;
$\Delta H\,(C1) = 566$ kcal

(C2) $2O^{-2}\,(gas) = 2O^{-2}\,(oxide)$;
$\Delta H(C2) = -1320$ kcal

(C3) $4e\,(oxide) = 4e\,(gas)$;
$\Delta H(C3) = 287$ kcal

For reaction C1, the enthalpy of formation of $H_2O(g)$ is -57.8 kcal (Ref. 1), and that of O^{-2} (g) is 225 kcal (Ref. 3 and 4). In reaction C2 the enthalpy change was assumed to be the negative of half of the lattice energy, and $\Delta H(C3)$ is four times the work function of ZrO_2.

The sum of the enthalpy changes for reactions C1 to C3 is -467 kcal per mole of zirconium oxidized. Thus, 467 kcal of heat are evolved at the metal-gas surface (location C) for a constant pressure oxidation of one mole of zirconium by steam.

Thus, at the metal-oxide interface 320 kcal of heat are absorbed due to the oxidation reaction and 467 kcal of heat are liberated at the oxide-gas surface when a mole of zirconium reacts with steam. That is, the oxidation process acts like a heat pump which transfers 320 kcal away from the metal-oxide surface and to the oxide-gas surface where it is evolved together with the net heat of reaction.

This rather surprising result means that during the rapid oxidation of zirconium, there should be a temperature gradient through the thickness of the oxide. The metal side should be cooler than the gas side of the oxide. If the zirconium were in a fast flowing stream of gas which could effectively remove the heat pumped through the oxide layer to the oxide-gas surface, then the substrate metal would be cooled by the oxidation process and the temperature of the metal would fall below its initial value.

It should be noted that there may be relatively large uncertainties in the values used for the reaction enthalpies. For instance the value used for the enthalpy of attachment of two electrons to an oxygen atom is the average of two indirectly obtained values that differ by 26 kcal. The work function of ZrO_2 in the literature has values that differ by 10 kcal and it enters as the fourfold product. Also the chemical states of the reactants are probably different from those assumed. For instance zirconium metal at the interface with oxide probably is a solution of the metal containing oxide. The oxide at the metal interface is probably substoichiometric in oxygen. Thus, the present treatment is only approximate. However, because the amounts of heat calculated to be transferred by the oxidation reaction are large, the conclusions are expected to be at least qualitatively correct.

The phenomenon can have some impact on the temperatures of the UO_2 in fuel rods during a nuclear power reactor accident. In such accidents, there is substantial gas flow past the Zircaloy cladding which is being oxidized, rapidly at times. Under those conditions, the above analysis would predict that the Zircaloy oxidation reaction should pump heat out of the fuel rods into the flowing gas stream.

Acknowledgment -- The author is indebted to Professor Leo Brewer, of the University of California, for helpful suggestions.

REFERENCES

1) O. Kubaschewski and C. B. Alcock, "Metallurgical Thermochemistry", Pergamon Press, NY, 1979.

2) C. Moore, "Ionization Potentials and Ionization Limits Derived from the Analyses of Optical Spectra", NSRDS-NBS34, U.S. Government Printing Office, Washington, D.C., 1970.

3) JANAF Thermochemical Tables, The Dow Chemical Company, Midland, Michigan, 1981.

4) P. J. Durrant and B. Durrant, "Advanced Inorganic Chemistry", p 356, Longmans Green & Company, London, 1962.

5) G. V. Samsonov, "The Oxide Handbook", 2nd Edition, Plenum Press, NY, 1982.

Activated Ir: An Electrode Suitable for Reversible Charge Injection in Saline Solution

L. S. Robblee,* J. L. Lefko, and S. B. Brummer*

EIC Laboratories, Incorporated, Newton, Massachusetts 02158

INTRODUCTION

Electrical stimulation of the nervous system with metal electrodes requires reversible charge injection processes to mediate the change in charge carriers at the metal/solution interface and to avoid the formation of toxic electrochemical reaction products (1). Reversible charge injection is possible either by a capacitive process, e.g., double layer charging, or by faradaic reactions involving species that remain bound to the electrode surface.

The multilayer oxide film that is formed on Ir by repetitive potential cycling may produce as much as a 100-fold increase in the charge capacity of the surface (2-4). The increased capacity of so-called "activated" Ir is the result of highly reversible H^+ or OH^- transfer reactions and valence transitions within the oxide layer (4-7). These reactions may provide an ideal mechanism for reversible charge injection providing they proceed reversibly in the in vivo saline environment and occur without excessive dissolution of the oxide. This paper describes the results of our initial evaluation of activated Ir for use as a stimulation electrode.

EXPERIMENTAL

Cyclic voltammetry was carried out with an Amel Model 551 potentiostat programmed with a Bromberg sweep generator, or a Bioanalytical Systems CV-1B voltammetry unit. Potentials were measured against a saturated calomel reference electrode and are reported vs. the reversible hydrogen electrode (RHE).

Iridium electrodes, 0.04 to 0.09 cm^2 geom., consisted of 0.05 cm diameter Ir wire (>99.9% Ir) sealed into Pyrex glass tubing. To obtain an oxide-free, deactivated surface, these electrodes were held for 5 to 10 minutes at 1.9V in 1M H_2SO_4 (3). Iridium microelectrodes, approximately 10^{-6} cm^2 geom., were supplied by M. Bak, National Institute of Neurological and Communicative Disorders and Stroke, NIH. These consisted of 25 μm Ir wire insulated with Parylene-C and having exposed tips of bare Ir 8 to 20 μm in length (8). Electrodes were activated by repetitive potential cycling at 100 mV sec^{-1} between 0.05V and 1.45V in 1M H_2SO_4, as described by others (4). Phosphate-buffered saline (PBS) was also investigated as an alternative electrolyte for activating Ir, particularly for use with the Parylene-insulated microelectrodes. The saline electrolyte contained 0.14M NaCl in 0.1M Na_2HPO_4/NaH_2PO_4 buffer, pH 7.4. In order to standardize our procedures, all electrodes activated for subsequent tests were cycled until the charge capacity in the oxide potential region, 0.4 to 1.4V, approximated 10 $mC \cdot cm^{-2}$.

Biphasic pulse tests and dissolution measurements of activated and deactivated Ir were carried out in 1 ml volume of PBS containing 0.02 wt% human serum albumin (PBS-protein) as described previously for Pt electrodes (9). Because of the low dissolution rates found for Ir, aliquots of pulse solution were analyzed only at the termination of the experiment and not at various time intervals as was done for Pt. Metal analysis was performed by flameless atomic absorption spectrometry. Analytical detection limits for Ir in PBS-protein were determined to be 0.03 to 0.06 μg/ml. Detection limits for Pt in the same solution were 0.01 to 0.02 μg/ml.

The charge limits for water electrolysis were determined with Ir microelectrodes. These were used "as received" or they were activated in PBS as described above. Monophasic, capacitively-coupled stimulation pulses (0.1 ms pulse width, 400 Hz) were applied to microelectrodes in PBS-protein while observing them at 100X magnification for gas bubble formation. The pulse waveform was monitored on an oscilloscope. The stimulation and monitoring circuits are described elsewhere (10). The pulse current

*Electrochemical Society Active Member

Key words: dissolution, microelectrode, electrochemistry of stimulation electrodes, electrical stimulation.

was increased very slowly until a gas bubble was observed to form at the electrode tip, at which time the current was decreased quickly to about one-half the gassing level. Pulsing was continued for several minutes after which the current was again slowly increased until bubble formation was observed. This procedure was repeated several times to evaluate the reproducibility of the determination. Both anodal and cathodal current pulses were evaluated.

RESULTS AND DISCUSSION

Activation of Ir.--Activation of Ir by repetitive cycling of the potential between 0.05V RHE and 1.45V RHE in PBS produced a progressive increase in charge capacity in the potential region above 0.4V RHE similar to what was observed in 1M H_2SO_4 (Fig. 1). In the saline electrolyte, the main anodic and cathodic current peaks occurred at slightly lower potentials and were less symmetrical about the current axis than in acid solution. However, when an electrode activated in PBS was placed in 1M H_2SO_4 for cyclic voltammetry, the resulting i vs. E curve was typical of Ir that had been activated in H_2SO_4 initially. The shift of peak potentials in the neutral saline is probably an effect due to electrolyte composition and pH (5) rather than due to differences in the oxide film itself. The buffered saline solution, therefore, should be an appropriate electrolyte for activating the type of Ir electrodes designed for in vivo use, such as the microelectrodes evaluated here.

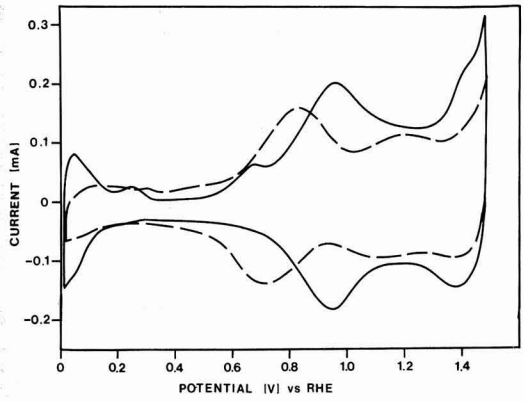

Fig. 1. Cyclic voltammetry curves for Ir after 60 min repetitive potential cycling in 1M H_2SO_4 (solid line) and PBS (dashed line). Scan rate: 100 mV sec^{-1}. Electrode area: 0.09 cm^2 geom. T = 25°C.

Dissolution Tests.--The results of comparative dissolution tests of Ir, Pt and Pt:30% Ir electrodes are shown in Table 1. No dissolution was detected for any of the activated Ir electrodes subjected to anodic-first (AF) biphasic pulses of varying current and charge densities. Deactivated Ir had a significantly greater dissolution than activated Ir with AF pulses of high current and charge density. However, with lower current and charge densities there was no detectable dissolution. Ir dissolution from the Pt:30% Ir alloy was higher than from 100% Ir; Pt dissolution from the alloy was comparable to that from 100% Pt. On the basis of dissolution behavior alone, activated Ir would seem to be the preferred metal for use as a stimulation electrode. The Pt:30% Ir alloy, which is frequently used in stimulation electrodes in place of pure Pt because of its greater mechanical strength, is at a disadvantage due to the likelihood of two metal dissolution products rather than just one.

Gassing Limits.--The evaluation of anodal and cathodal gassing limits for microelectrodes indicated that activation of the Ir surface extended the useful charge injection limits for anodal pulses as much as tenfold (Table 2). There was not as dramatic an effect on charge limits for cathodal pulses, consistent with the charge capacities seen in cyclic voltammograms. For instance, the cathodic charge between 0.7V and 0.0V on a cyclic voltammogram (the possible potential excursion experienced by an electrode during a cathodal pulse) is much less than the anodic charge between 0.7V and 1.45V (the possible potential excursion of an electrode during an anodal pulse).

CONCLUSIONS

Reversible charge injection requires that no new chemical species be produced in solution. With Pt, up to 400 $\mu C \cdot cm^{-2}$ of real area can be injected before the onset of water electrolysis, but a small amount of the injected charge is always lost to metal dissolution (9,11). The results of these initial studies of activated Ir indicate that the charge injection limits for water electrolysis might be increased by a factor of 10 or greater, and that little or no charge is lost to metal dissolution. We conclude that activated Ir is an exceptionally promising material for use as a stimulation electrode. The high capacity for reversible charge injection is of great advantage for applications such as intracortical stimulation of single neurons (12) where the small size of the stimulation electrode, $<10^{-6}$ cm^2 geom., may result in charge densities up to 10 $mC \cdot cm^{-2}$ geom. Moreover, the superior

corrosion resistance of activated Ir, compared to Pt or Pt:Ir alloy, will significantly extend the useful lifetime of a chronically implanted neural prosthesis.

ACKNOWLEDGMENT

The authors gratefully acknowledge the support of this work by the National Institute of Neurological and Communicative Disorders and Stroke, National Institutes of Health, under Contract N01-NS-9-2315.

REFERENCES

1. S. B. Brummer and M. J. Turner, IEEE Trans. Biomed. Eng., BME-24, 59 (1977).
2. D. A. J. Rand and R. Woods, Electroanal. Chem. Interfacial Electrochem., 55, 375 (1974).
3. D. N. Buckley and L. Burke, J. Chem. Soc., 71, 1447 (1975).
4. J. O. Zerbino, N. R. deTacconi, and A. J. Arvia, This Journal, 125, 1266 (1978).
5. S. Gottesfeld and J. D. E. McIntyre, This Journal, 126, 742 (1979).
6. G. Beni, C. E. Rice, and J. L. Shay, This Journal, 127, 1342 (1980).
7. W. C. Dautremont-Smith, Displays, 3, 67 (1982).
8. M. Salcman and M. J. Bak, Med. and Biol. Eng., 14, 42 (1976).
9. L. S. Robblee, J. Marston, J. McHardy, and S. B. Brummer, Biomaterials, 1, 135 (1980).
10. L. S. Robblee, E. M. Kelliher, M. E. Langmuir, H. Vartanian, and J. McHardy, J. Biomed. Mat. Research, in press.
11. S. B. Brummer and M. J. Turner, IEEE Trans. Biomed. Eng., BME-24, 440 (1977).
12. E. Schmidt and J. McIntosh, Exptl. Neurol., 63, 485 (1979).

TABLE 1. SUMMARY OF DISSOLUTION STUDIES OF Ir, Pt:30% Ir AND Pt ELECTRODES

Experimental Conditions: Continuous Charge-Balanced Biphasic Pulses; 50 Hz; PBS-Protein Pulse Solution

Electrode Type	Number of Tests	Current Density ($mA \cdot cm^{-2}$)	Charge Density ($\mu C \cdot cm^{-2}$)	Total Time (hr)	Aggregate Charge[1] (coul)	Ir Dissolution (μg)	Pt Dissolution (μg)
Activated Ir (0.04 to 0.09 cm^2 geom)	2	± 800	± 800	66 and 168	931 and 2080	N.D.[2]	
	2	± 400	± 100	48	35	N.D.	
	2	± 200	± 50	48	40	N.D.	
Deactivated Ir (0.04 to 0.09 cm^2 geom)	2	± 800	± 800	48	636	0.16 ± 0.04	
	1	± 800	± 800	24	297	0.46	
	2	± 400	± 100	48	35	N.D.	
	2	± 200	± 50	48	40	N.D.	
Pt:30% Ir (0.09 cm^2 geom)	4	± 800	± 800	48	648	1.85 ± 1.68	2.45 ± 2.24
Pt (0.06 cm^2 geom)	4	± 800	± 800	24	207		1.50 ± 0.16

[1]Charge per phase (anodic or cathodic) x total number of biphasic pulses.
[2]N.D. = None detected. With present analytical detection limits, this may be 0.06 μg or less.

TABLE 2. GASSING LIMITS FOR MICROELECTRODES

Experimental Conditions: Continuous Monophasic Capacitively-Coupled Pulses; 100 μsec Pulse Width; 400 Hz; PBS-Protein Pulse Solution

Electrode Type	Anodic Charge ($mC \cdot cm^{-2}$ geom)	Cathodic Charge ($mC \cdot cm^{-2}$ geom.)
Pt:30% Ir	1.2-1.3	5-5.3
∿3% x 10^{-6} cm^2 geom.	1.3-2.0	0.7-3.3
Ir, As Received	2.0-9.0	1.4
0.8-2 x 10^{-6} cm^2 geom.	1.0-7.0	1.9
Ir, Activated	31-40	3.0-4.0
0.8-1 x 10^{-6} cm^2 geom.	29-30	5.0

Manuscript submitted Sept. 13, 1982; revised manuscript received ca. Nov. 29, 1982.

Dinitrogen Electrochemical Reduction to Ammonia over Iron Cathode in Aqueous Medium

A. Sclafani, V. Augugliaro, and M. Schiavello

Istituto di Ingegneria Chimica, Università di Palermo, Palermo, Italy

The ammonia synthesis is one of the most important and best established catalytic industrial processes. Neverthless fundamental and applied research is still carried out on this subject with the objective of finding processes which can occur in milder conditions and in the more general field of dinitrogen fixation with the aim to discover new routes for transforming dinitrogen into ammonia.

In this latter field the attempts move along several paths. One tries to simulate the mechanism of biochemical processes carried out by dinitrogen fixing microbes, which operate at atmospheric pressure and room temperature. Indeed precise knowledge about the mechanism of operation of the nitrogenase enzyme will give in future substantial progress to this way. A second utilizes activating complexation of dinitrogen molecule with transition metals such as Ti, Ru, Os, Rh, Re, Mo, Co, etc. and subsequent reduction with very strong reducing compounds. Reviews on this matter have been reported by Kuchynka (1) and Venuto (2).

Recently a completely new route has been suggested by Schrauzer and Guth (3), which produced ammonia from water and dinitrogen on wet TiO_2 powder. Various photocatalysts have been used (4) and a correlation between semiconductors properties and the yield of ammonia has been found (5). Ammonia has been also obtained from dinitrogen and water vapour by heterogeneous photoassisted catalysis utilizing iron doped titanium oxides (6-9) and titanium exchanged zeolites (10, 11).

A method of electrolytic and chemical reduction of molecular dinitrogen has been presented by Van Tamelen and Akermark (12) and Van Tamelen and Seeley (13), which used the electrolytic cell as a chemical reducing agent. Dinitrogen fixation, at room temperature and atmospheric pressure, by a photoenhanced reduction process has been carried out in a photoelectrochemical cell containing a p-GaP cathode and an Al metal anode immersed in a nonaqueous electrolyte (14). An electrochemical reduction, catalyzed by the $Ti(OH)_3$ - Mo(III) system, has been performed by Gorodyskii et al. (15) on a mercury cathode in an alkaline methanol solution under mild conditions.

In this communication preliminary results of a study concerning the direct electrochemical reduction of dinitrogen over iron cathode, at atmospheric pressure and low temperatures, are reported. It must be outlined that at this stage of the research only the feasibility of dinitrogen reduction to ammonia has been studied by the use of an electrochemical cell with aqueous electrolyte at suitable values of cathodic potential.

EXPERIMENTAL

The experiments have been carried out in an electrochemical cell maintained at constant temperature by means of a thermostatic chamber. Three series of experiments at the temperatures of 25, 35 and 45 °C have been performed. An iron cathode with a surface area of 0.25 m^2 was utilized while the anode was a sheet of AISI 316 stainless steel. The electrolyte was a 6 N KOH aqueous solution and the cathodic compartment was separated from the anodic one by means of a porous polyethylene membrane.

Pure dinitrogen (99.99 % purity) was con-

Key words: dinitrogen electrochemical reduction, ammonia production, iron cathodes.

For all the experiments performed at cathodic potential values below that of hydrogen discharge, the values of faradic yield, calculated with respect to ammonia, were of the order of magnitude of a percent. It has been also found that these values decreased by increasing the absolute value of cathodic potential as well as the gas flow rate, at equal temperature and potential. Indeed these very low values are explainable by considering that the relevant process that occurs in the cell consists in the redox process of iron ions (17, 18), as expected. Moreover, as the agitation of the electrolytic solution increases by increasing the gas flow rate, the transport rates of iron ions increase and therefore, being the ammonia production constant at equal temperature and potential, the faradic yield lowers.

Concluding, the feasibility of direct electrochemical reduction of molecular dinitrogen to ammonia, probably without the aid of activating complexes in the electrolytic solution, seems well proved. On the ground of all the previous considerations, one may hypothesize that the dissolved dinitrogen undergoes the following reaction:

$$N_{2(d)} + 3H_2O_{(l)} \rightarrow 2NH_{3(d)} + 1.5O_{2(g)} \cdot (E_{25°C} = 1.14\ V)$$

The observed decrease of the ammonia production when the cathodic potential is in the region of hydrogen discharge, can be explained by the occurrence of a competitive adsorption between dinitrogen and hydrogen species on the cathodic surface.

REFERENCES

1. K. Kuchynka, Catal. Rev., 3, 111 (1969).
2. R. H. Fischer and P. B. Venuto, Bull. New Jersey Acad. Sci., 15, 1 (1970).
3. G. N. Schrauzer and T. D. Guth, J. Am. Chem. Soc., 99, 7188 (1977).
4. A. Fujishima, T. Inoue, S. Konishi, C. P. Weber, and K. Honda, The Annual Meeting of the Chemical Society of Japan, Nagoya, Japan, Oct. 17 1978.
5. H. Miyama, N. Fuji, and Y. Nagae, Chem. Phys. Letters, 74, 523 (1980).
6. V. Augugliaro, A. Lauricella, L. Rizzuti, M. Schiavello, and A. Sclafani, Int. J. Hydrogen Energy, 7, 845 (1982).
7. V. Augugliaro, F. D'Alba, L. Rizzuti, M. Schiavello, and A. Sclafani, Int. J. Hydrogen Energy, 7, 851 (1982).
8. M. Schiavello, L. Rizzuti, A. Sclafani, I. Majo, V. Augugliaro, and P. L. Yue, In T. N. Veziroglu, W. D. Van Vorst, J. H. Kelley (Eds.). Hydrogen Energy Progress IV, Pergamon Press, Oxford 1982, vol. 2 p. 821.
9. A. Brucato, I. Majo, A. Sclafani, and M. Schiavello, Proc. 4th Int. Conf. on Photochemical Conversion and Storage of Solar Energy, Jerusalem, August 8-13 1982, p. 116.
10. F. Khan, P. L. Yue, L. Rizzuti, V. Augugliaro, and M. Schiavello, J. C. S. Chem. Comm., 1050 (1981).
11. F. Khan, P. L. Yue, L. Rizzuti, V. Augugliaro, and A. Brucato, Ind. Eng. Chem. Prod. Res. Dev., submitted (1982).
12. E. E. Van Tamelen and B. Akermark, J. Am. Chem. Soc., 90, 4492 (1968).
13. E. E. Van Tamelen and D. A. Seeley, J. Am. Chem. Soc., 91, 5194 (1969).
14. C. R. Dickson and A. J. Nozik, J. Am. Chem. Soc., 100, 8007 (1978).
15. A. V. Gorodyskii, V. V. Danilin, O. N. Efimov, N. E. Nechaeva, and V. N. Tsarev, React. Kinet. Catal. Lett., 11, 337 (1979).
16. J. M. Henry, M. M. Cannon, and T. A. Winkelmann, "Clinical Chemistry: Principles and Techniques", Harper and Row, New York (1978).
17. L. Ojefors, This Journal, 123, 1691 (1976).
18. R. S. Schrebler Guzmàn, J. R. Vilche, and A. J. Arvìa, Electrochim. Acta, 24, 395 (1979).

Manuscript submitted July 20, 1982; revised manuscript received Nov. 10, 1982.

Publication costs of this article were assisted by the University of Palermo.

tinously fed to the cathodic compartment by means of properly positioned spargers so that the whole cathode was hit by the gas bubbles. Different values of the gas-solid interface have been obtained by using the following values of the gas flow rate: 1.1, 2.3, 3.7 and 8.3 cm^3/s. To decrease the dinitrogen concentration in the electrolytic solution, some runs have been performed by using dinitrogen-argon mixtures, 10 and 50 % in N_2, at the flow rate values previously reported.

The gas outlet contained the produced ammonia that was continuously stripped from the cell. The ammonia-dinitrogen mixture was bubbled in a 0.01 N HCl aqueous solution, which fixed all the ammonia. A standard colorimetric method (16), specific for ammonia and able to appreciate ten parts per billion, was used. Before starting the runs, the solutions have been carefully tested to check the total absence of ammonia.

The electrolytic process has been performed at potentiostatic conditions by using an Amel potentiostat mod. 551. The cathodic potential values, measured with reference to SCE, ranged from -920 to -1210 mV, for all the temperatures used. In order to calculate the values of faradic yield with respect to ammonia, the quantities of charge passed during the runs have been measured by an Amel integrator mod. 731. Each experiment lasted several hours; during the run, the ammonia fixing solution was replaced every two hours and tested. When the analysis of some consecutive samples gave the same figures, thus indicating steady state conditions in the cell, the run was stopped and the last figure was taken as indicative of the ammonia production.

RESULTS AND DISCUSSION

For the used temperatures the experimental results, obtained by feeding the cell by pure dinitrogen at a flow rate value of 2.3 cm^3/s, are reported in Fig. 1 as ammonia production, μmol/h, vs. cathodic potential, referred to SCE.

It has been found that, by varying gas flow rate and gas composition, the ammonia production, at equal temperature and cathodic potential, did not appreciably change. This behaviour suggests the following general considerations. The independence of ammonia production from the gas-solid interface indicates a transport of dinitrogen towards the cathodic surface which occurs through the liquid phase; moreover, the independence of ammonia production from dinitrogen concentration in the liquid phase suggests that the mass transfer resistances play a negligible, if any, role.

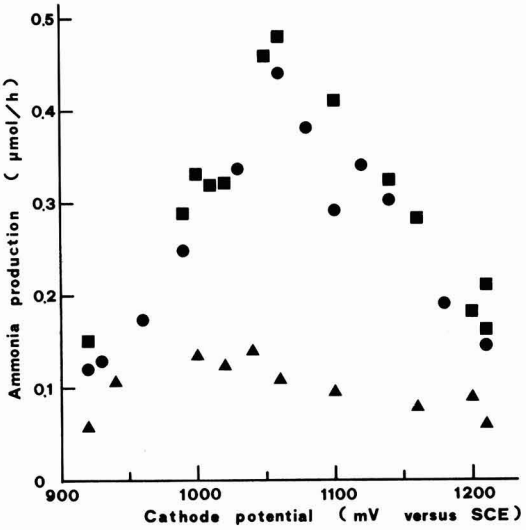

Fig. 1 - Experimental results of ammonia production per unit time vs. cathodic potential, referred to SCE, for the three temperatures used: ▲, 25 °C; ●, 35 °C; ■, 45 °C.

From the results reported in Fig. 1 the following considerations can be made:

a) ammonia is produced throughout the explored range of cathodic potential;
b) ammonia production is enhanced by increasing the temperature;
c) for each temperature ammonia production increases by increasing the cathodic potential; but, when the values of the cathodic potential are in the region of hydrogen discharge, ammonia production decreases.

JOURNAL OF THE ELECTROCHEMICAL SOCIETY

REVIEWS AND NEWS

MARCH 1983

San Francisco— The Great City of the Golden Hill

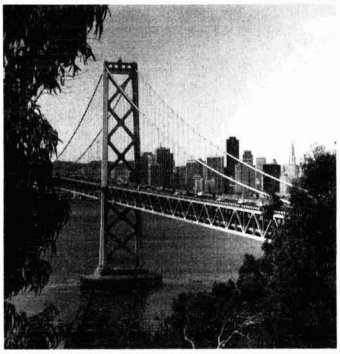

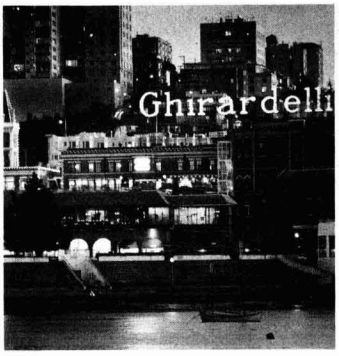

Photos courtesy of the San Francisco Visitors Bureau

Welcome to Gum San Dai Foo, the Great City of the Golden Hill, for the 163rd Meeting of the Society. San Francisco, penned by John Steinbeck as "a golden handcuff with the key thrown away" is a 47-square mile city of hills, skyscrapers, Victorian houses, ferries, and cabarets that offers something to everyone. Attendees will be staying at the elegant Westin St. Francis, the Sir Francis Drake Hotel, the San Francisco Hilton, or the Hyatt on Union Square.

Surrounded on three sides by the Bay and spread amidst some 40 hills, San Francisco boasts of 700,000 residents and 4.8 million people in the Bay area. Settled in 1776, the city became famous in the Gold Rush of 1849, which brought 40,000 fortune seekers to the area from all over the country and the world. Since that time it has been a bustling metropolitan center of business and cultural activity. The city has many sights to see, so bring comfortable walking shoes! Temperatures for May range between 50°-64°F, with the average temperature about 55°F, so it is advisable to bring a light weight coat.

Just looking at San Francisco is an experience in itself. One glance takes in metropolitan downtown, with its shops, hotels, and skyscrapers, scattered churches, and Victorian row houses, all surrounded by the Bay. Famed for its varied and beautiful architecture, San Francisco's Victorian houses, built between 1850 and 1900, give a quaint aura to the city. These houses have been preserved or restored by public groups as well as private entrepreneurs, especially west of Van Ness and in the Spanish Mission District. Walking through the District, you will enjoy the stained glass, rosettes, friezes, and fans of Victorian ornamentation against a background of glittering water and high-rise buildings.

Cultural attractions abound in San Francisco. For those who enjoy shops, restaurants, and galleries, Ghirardelli Square. at the foot of Russian Hill, is a perfect site for an afternoon excursion. The Westin St. Francis, one of our host hotels, is located in Union Square, which is the center of San Francisco's shopping district. The Square, situated in a beautiful park, has many import specialty stores and fine hotels. North Beach, the center of night life, offers theatres, cabarets, restaurants, jazz clubs, and cappucino houses for evening entertainment.

For registrants who have a touch of the seafarer's spirit, Fisherman's Wharf is a must. Here you may take a cruise of the Bay, visit the Wax Museum, have some sourdough French bread and Bay shrimp or crab cocktails ($1.00!), or visit the Del Monte Cannery. Nearby is the famous Pier 39 shopping complex. And whether you are simply a seafood lover or an international cuisine gourmet, San Francisco offers over 2,600 restaurants of every nationality from which to choose!

A city encompassing many ethnic and cultural heritages, San Francisco offers international attractions that shouldn't be missed. From Fisherman's Wharf you can walk straight to Little Italy, and enjoy the incomparable delicatessens of the Italian District. Next door is the world-famous Chinatown, the largest Chinese settlement outside of Asia. Take in the exotic shops, temples, and museums, not to mention the delicious (but inexpensive) oriental cuisine. And for Japanese food lovers, there is the Nihonmachi section as well.

For those who wish to escape the bustle of city life, the Golden Gate Park offers a backpacker's haven, with its 1017 acres of lawns, flowers, and bridle paths. Here also you can visit the Asian Art Museum, the de Young, and the California Academy of Sciences. The Parks' most famous attraction is the Japanese Tea Garden, with its authentic streams, shrubs, buddhas, and thatched tea house. The exquisitely ordered gardens provide a serene escape from the busy city into a quiet world of beauty. And of course there is the magnificent Golden Gate Bridge to tread—toll free to pedestrians!

Finally there is the world-famous Alcatraz to visit, as well as St. Mary's Cathedral, the wine country, and, of course, the San Francisco Zoo. Or if the thought of all of this sight-seeing is too wearing, simply take an elevator up to the top of your hotel and take in the whole metropolis from a breathtaking view. Whatever you do, you are sure to enjoy your stay in the Great City of the Golden Hill. San Francisco is a concourse of scenery, activity, and excitement, a city which you will not forget.

The Electrochemical Society, San Francisco Meeting, May 8-13, 1983
St. Francis Hotel

		Monday May 9	Tuesday May 10	Wednesday May 11	Thursday May 12	Friday May 13
Grand Ballroom Mezzanine	A.M.	**D&I/Electronics—** 4th International Symposium on Plasma Processing	**D&I/Electronics—** 4th International Symposium on Plasma Processing	**D&I/Electronics—** 4th International Symposium on Plasma Processing	**D&I/Electronics—** 4th International Symposium on Plasma Processing	**Electronics/D&I—** Joint Recent News Papers
	P.M.					
Colonial Ballroom Mezzanine	A.M.	**Electronics/D&I—** Joint General Session	**Electronics/D&I—** Joint General Session	**Electronics/D&I—** Joint General Session	**Electronics/D&I** Joint General Session	**Electronics/D&I—** Joint General Session
	P.M.					
California West 2nd Floor	A.M.	**ETG/Battery/D&I—** Conducting Organic Polymers in Energy Conversion and Storage	**ETG/Battery/D&I—** Conducting Organic Polymers in Energy Conversion and Storage	**D&I/Electronics—** Silicon Nitride Thin Insulating Films	**D&I/Electronics—** Silicon Nitride Thin Insulating Films	**D&I/Electronics—** Silicon Nitride Thin Insulating Films
	P.M.					
California East 2nd Floor	A.M.	**Electronics—** Computer Controlled IC Processing and Monitoring	**Electronics—** Computer Controlled IC Processing and Monitoring	**D&I/Electronics/Corrosion/ HTM/ETG—** Materials and New Processing Techniques for Photovoltaics	**D&I/Electronics/Corrosion/ HTM/ETG—** Materials and New Processing Techniques for Photovoltaics	**D&I/Electronics/Corrosion/ HTM/ETG—** Materials and New Processing Techniques for Photovoltaics
	P.M.					
	Evening		Informal Discussion on Computer Controlled IC Processing and Monitoring			
Georgian Room Mezzanine	A.M.	**Electronics—** III-V Opto-Electronic Epitaxy and Device Related Processes	**Electronics—** III-V Opto-Electronic Epitaxy and Device Related Processes	**Electronics—** III-V Opto-Electronic Epitaxy and Device Related Processes	**Electronics—** III-V Opto Electronic Epitaxy and Device Related Processes	
	P.M.				**Electronics/D&I** Joint Recent News Papers	
	Evening			Informal Discussion on Future Choices for III-V Opto-Electronic Epitaxy		
Elizabethan Room D 2nd Floor	A.M.	**Organic & Biological Electrochemistry—** Mechanisms and Modeling of Electrochemical Membrane Processes	**Organic & Biological Electrochemistry—** Mechanisms and Modeling of Electrochemical Membrane Processes	**Organic & Biological Electrochemistry—** Mechanisms and Modeling of Electrochemical Membrane Processes	**Organic & Biological Electrochemistry** Structure and Reactivity in Organic Chemistry and Electrochemistry	**Organic & Biological Electrochemistry—** Structure and Reactivity in Organic Chemistry and Electrochemistry and General Session
	P.M.			**Organic & Biological Electrochemistry—** Structure and Reactivity in Organic Chemistry and Electrochemistry		
Elizabethan Room C 2nd Floor	A.M.	**HTM—** High Temperature Materials Chemistry	**HTM—** High Temperature Materials Chemistry	**HTM—** High Temperature Materials Chemistry	**HTM—** High Temperature Materials Chemistry	**HTM—** High Temperature Materials Chemistry
	P.M.					
Elizabethan Room A and B 2nd Floor	A.M	**Electronics—** Defects in Silicon	**Electronics—** Defects in Silicon	**Electronics—** Defects in Silicon	**Electronics** Defects in Silicon	
	P.M.					

Borgia Room Mezzanine	**A.M.**	**Battery—** Cell Testing and Reliability	**Battery—** Cell Testing and Reliability	**Battery—** Cell Testing and Reliability	**Battery—** Cell Design and Optimization	
	P.M.			**Battery—** Cell Design and Optimization		
Olympic Room 2nd Floor	**A.M.**	**ETG—** Novel Photoelectrochemical Synthetic Routes	**ETG—** Novel Photoelectrochemical Synthetic Routes	**Organic & Biological Electrochemistry—** Ions and Electrochemical Control of Cell Functions	**Organic & Biological Electrochemistry—** Ions and Electrochemical Control of Cell Functions	**Organic & Biological Electrochemistry—** Ions and Electrochemical Control of Cell Functions
	P.M.					
Oxford Room 2nd Floor	**A.M.**	**D&I/Electronics—** Dielectric Isolation	**HTM/Physical Electrochemistry/ Battery/ETG—** New Solid Electrolytes for Energy Conversion	**HTM/Physical Electrochemistry/ Battery/ETG—** New Solid Electrolytes for Energy Conversion	**D&I/HTM—** High Temperature Adhesives	
	P.M.					
Yorkshire Room 2nd Floor	**A.M.**	**Corrosion—** General Session	**Corrosion—** General Session	**Corrosion—** General Session	**ETG—** General Session	**ETG—** General Session
	P.M.					
Victorian Room 2nd Floor	**A.M.**	**Industrial Electrolytic/ Corrosion/ Electrodeposition—** Anode and Cathode Materials	**Industrial Electrolytic/ Corrosion/ Electrodeposition—** Anode and Cathode Materials	**Luminescence & Display Materials—** Display Technology	**Luminescence & Display Materials** General Session	**Luminescence & Display Materials—** Phosphor Synthesis and Characterization
	P.M.					
Essex Room 2nd Floor	**A.M.**				**Industrial Electrolytic—** Science and Engineering of Membranes and Separators	
	P.M.			**Industrial Electrolytic—** Science and Engineering of Membranes and Separators		

Sir Francis Drake Hotel

Empire Room 2nd Floor	**A.M.**	**Physical Electrochemistry—** Chemistry and Physics of Electrocatalysis	**Physical Electrochemistry—** Chemistry and Physics of Electrocatalysis	**Physical Electrochemistry—** Chemistry and Physics of Electrocatalysis	**Physical Electrochemistry—** Chemistry and Physics of Electrocatalysis	
	P.M.					
Franciscan Room Mezzanine	**A.M.**	**Physical Electrochemistry—** 4th International Symposium on Molten Salts	**Physical Electrochemistry—** 4th International Symposium on Molten Salts	**Physical Electrochemistry—** 4th International Symposium on Molten Salts	**Physical Electrochemistry—** 4th International Symposium on Molten Salts	**Physical Electrochemistry—** 4th International Symposium on Molten Salts
	P.M.					
Tudor Room 2nd Floor	**A.M.**	**Physical Electrochemistry—** General Session	**Physical Electrochemistry—** General Session	**Physical Electrochemistry—** General Session	**Physical Electrochemistry—** General Session	
	P.M.					

Program
San Francisco, California, Meeting
THE ELECTROCHEMICAL SOCIETY, INC.
May 8-13, 1983
Sunday through Friday

HOTEL INFORMATION

The 1983 Spring Meeting will be held at The Westin St. Francis Hotel, Union Square, San Francisco, California. The telephone number is 415-397-7000. The convention rate is $80.00 to $115.00 single and $100.00 to $135.00 double or twin. Hotel Reservation Cards will be sent to all members, authors of papers, and Technical Session Chairmen and Vice-Chairmen. If you call for a reservation you **must** mention that you are attending The Electrochemical Society Meeting to obtain the special convention rate.

Additional rooms have been reserved at the Sir Francis Drake Hotel, just ½ block away on Powell at Sutter Street. The telephone number is 415-392-7755 or 800-227-5480 outside of California. The convention rate at this hotel is $69.00 to $89.00 single and $79.00 to $99.00 double. You **must** mention that you are attending The Electrochemical Society Meeting to obtain the special convention rate.

Additional rooms have been reserved at The San Francisco Hilton, one and a half blocks away on O'Farrell Street. Call Hilton Reservation Service in your city or call the hotel directly at 415-771-1400. The convention rate is $67 to $90 single and $87 to $110 double or twin. You **must** mention that you are attending The Electrochemical Society Meeting to obtain the special convention rate.

Also, in order to accommodate anticipated attendance, additional rooms have been reserved at Hyatt on Union Square, 345 Stockton Street. This hotel is one block away from The Westin St. Francis Hotel. The telephone number is 415-398-1234. The convention rate is $85.00 to $150.00 single and $110.00 to $180.00 double. You **must** mention that you are attending The Electrochemical Society Meeting to obtain the special convention rate.

If you plan to stay at the Headquarters Hotel, The Westin St. Francis, it is suggested that you use the special reservation card. If you plan to stay at one of the overflow hotels you may make your reservation directly by telephone.

All hotel rooms are subject to a City Hotel Tax which is 9.75% at press time.

TRAVEL INFORMATION

In order to reduce expenses for attendees, United Airlines has been named the "official carrier" for this Spring Meeting. Arrangements have been made for attendees to obtain the lowest available air fare.

To obtain the lowest available air fare you can call United Airlines directly at 800-521-0810, except for Michigan. The number for Michigan residents is 800-482-0243. You may also make your reservation and obtain the lowest available air fare by calling Fugazy International Travel of New Jersey at 201-828-4488.

In either case you **must** mention that you are attending The Electrochemical Society Meeting.

Bus service is available from the lower level of both the North and South terminals of the San Francisco Airport to a terminal downtown, two blocks from The Westin St. Francis. The service is provided by the Airporter Bus, which is painted orange and blue, for $4.00 (at press time).

REGISTRATION

The registration area will be located in the Italian Room, Mezzanine, on Sunday and Monday until 10:30 A.M.

Beginning Monday at 10:30 A.M. the registration area will be relocated to the Convention and Registration Center, also on the Mezzanine near the elevators.

Advance Registration

Advance registration is suggested if you plan to attend the Spring Meeting. Forms are available from The Electrochemical Society, Inc., 10 South Main Street, Pennington, New Jersey 08534-2896 or call 609-737-1902. Deadline for receipt of advance registration including payment is April 23, 1983. Requests for refunds will be honored if received at Society Headquarters in Pennington before May 7, 1983.

Registration at the Meeting

The registration hours are:

Sunday, May 8	2:00 P.M. to	8:00 P.M.
Monday, May 9	7:30 A.M. to	3:30 P.M.
Tuesday, May 10	8:00 A.M. to	4:00 P.M.
Wednesday, May 11	8:00 A.M. to	4:00 P.M.
Thursday, May 12	8:00 A.M. to	4:00 P.M.
Friday, May 13	8:00 A.M. to	10:00 A.M.

REGISTRATION FEES

All participants and attendees are required to pay a registration fee. Payment can be made by cash, check or travelers checks in U.S. funds. Credit cards are **not** accepted. The schedule of fees is as follows:

Technical Session Registration Fees

Members	$65.00
Nonmembers	$90.00*
Emeritus, Honorary and Student Members	Complimentary
Members (not currently employed)	$ 2.00
Student Nonmembers	$ 5.00

Last Day Registration

Members	$20.00
Nonmembers	$30.00

Nontechnical Registrants Fee	$15.00

***If a nonmember submits an Application for Admission within four months of the meeting and is subsequently elected to membership in the Society, the difference between the nonmember and member registration fee will be applied to the first year's dues.**

MEETING INFORMATION

Technical sessions will be held in both The Westin St. Francis and the Sir Francis Drake Hotels. Divisional Luncheons and Business Meetings are also scheduled for both hotels. Committee meetings will be at The Westin St. Francis. Check the detailed program for the room and the hotel. Also at The Westin St. Francis Hotel are:

Information/Message Center	Registration Area
Nontechnical Registrants Headquarters	Oz
Society Headquarters Office	Sussex Room-2nd Floor

GENERAL FUNCTIONS

Sunday Evening Get Together

An informal Sunday Evening Get-Together will be held in the Grand Ballroom from 8:00 to 10:00 P.M. All meeting registrants are invited to attend.

Monday—Plenary Session

At 9:00 A.M. the Plenary Session will be held in the Grand Ballroom. C. Lester Hogan, Director and Consultant, Fairchild Camera & Instrument Corporation will deliver The Electrochemical Society Lecture, "VLSI Processes-and the Future."

Monday Evening Mixer

An informal gathering will be held in the Grand Ballroom from 6:00 to 7:15 P.M. Beer, soft drinks, and snacks will be served on a complimentary basis. In addition, there will be a cash bar for those who prefer mixed drinks or wine. All meeting registrants are invited to attend.

Tuesday

Awards and Recognition Session

The Awards and Recognition Session will begin at 4:30 P.M. in the Grand Ballroom. Several divisional awards will be presented, including the Thomas D. Callinan Award of the Dielectrics and Insulation Division to Laurence Young, the Electronics Division Award to Don W. Shaw, and the David C. Grahame Award of the Physical Electrochemistry Division to Fred C. Anson.

The Solid State Science and Technology Award will be presented to Nick Holonyak, Jr., Professor, Department of Electrical Engineering, University of Illinois.

Solid State Science and Technology Award Address

Immediately following the Awards and Recognition Session, Nick Holonyak, Jr. will deliver the Solid State Science and Technology Address entitled, "From Silicon to III-V Compounds."

Solid State Science and Technology Award Reception

Immediately following the Award Address, there will be a reception in the Colonial Room honoring Nick Holonyak, Jr. All those attending the Awards and Recognition Session and the Solid State Science and Technology Award Address are invited to attend and greet the medalist.

AN EVENING OUT IN SAN FRANCISCO

By special arrangement with The Gray Line, Inc. several evening tours are offered at reduced rates.

Monday and Wednesday—"San Francisco-Night on the Town." This tour includes dinner in Tiburon for $31 per person.

Tuesday and Thursday—"Night Club Tour." This tour includes visits to several night clubs and with dinner is $47. per person; tour without dinner is $33. per person.

Call for reservations from 7:30 A.M. until 10:00 P.M.; in San Francisco, the number is 771-4000. If you prefer to make reservations before arrival in San Francisco, call 800-227-4152 and ask for "night life reservations." To obtain the special reduced rates, you **must** mention The Electrochemical Society.

COMMITTEE MEETINGS

ALL COMMITTEE MEETING ROOMS ARE ON THE SECOND FLOOR OF THE WESTIN ST. FRANCIS UNLESS NOTED OTHERWISE.

Sunday, May 8, 1983

3:00 P.M.	Vittorio de Nora-Diamond Shamrock Award Subcommittee	Parlor A
3:30 P.M.	Electronics Division VLSI Materials Subcommittee	Windsor Room
3:30 P.M.	Electronics Division Compound Semiconductor Subcommittee	Parlor B
4:30 P.M.	Electronics Division VLSI Processing Subcommittee	Victorian Room

5:00 P.M.—Electronics Division Award Subcommittee		Board Room
5:30 P.M.—Electronics Division Symposia Planning Committee		Oxford Room
5:30 P.M.—Energy Technology Group Executive Committee		Essex Room
7:00 P.M.—Electronics Division Audit/Budget/Finance Subcommittee		Windsor Room
7:00 P.M.—Carl Wagner Memorial Award Subcommittee		Parlor B
7:00 P.M.—Council of Local Sections		Kent Room
8:00 P.M.—Electronics Division Executive Committee		Victorian Room

Monday, May 9, 1983

7:15 A.M.—High Temperature Materials Division Executive Committee		Parlor A
7:15 A.M.—Dielectrics & Insulation Division Long Range Planning Committee		Windsor Room
7:30 A.M.—Physical Electrochemistry Division Executive Committee		Parlor B
10:00 A.M.—Education Committee		Board Room
10:00 A.M.—Olin Palladium Medal Award Subcommittee		Parlor B
1:30 P.M.—Society Meeting Committee		Board Room
2:00 P.M.—New Technology Subcommittee		Parlor A
4:00 P.M.—Electronics Division Planning Committee on Informal Discussions		Parlor B
4:00 P.M.—Honors and Awards Committee		Board Room
4:30 P.M.—Division/Group/Local Section Representatives to Individual Membership Committee		Windsor Room

Tuesday, May 10, 1983

7:30 A.M.—Symposium Subcommittee		Windsor Room
8:00 A.M.—Editorial Committee		Essex Room
9:00 A.M.—Publication Committee		Board Room
1:30 P.M.—Technical Affairs Committee		Board Room
8:00 P.M.—Luminescence and Display Materials Group Executive Committee		Parlor B

Wednesday, May 11, 1983

7:30 A.M.—Solid State Divisions Chairmen's Breakfast		Parlor A
7:30 A.M.—Council of Past Presidents Breakfast		Parlor B
7:30 A.M.—Finance Committee		Board Room
8:00 A.M.—Industrial Electrolytic Division Executive Committee		Windsor Room
10:00 A.M.—Ways and Means Committee		Board Room
1:30 P.M.—Contributing Membership Committee		Board Room
1:30 P.M.—Financial Policy Advisory Committee		Parlor A

Thursday, May 21, 1983

9:00 A.M.—Board of Director's Meeting		Monterey Room 2nd Floor Sir Francis Drake Hotel

LUNCHEONS AND BUSINESS MEETINGS

Monday, May 9, 1983

12:15 P.M.—Electronics Division		Italian Room Mezzanine
12:15 P.M.—High Temperature Materials Division		The City Club 12th Floor
12:15 P.M.—Physical Electrochemistry Division		Monterey Room Sir Francis Drake Hotel

Tuesday, May 10, 1983

12:15 P.M.—Annual Society Luncheon & Business Meeting		Italian Room Mezzanine

Wednesday, May 11, 1983

12:15 P.M.—Energy Technology Group		The City Club 12th Floor
12:15 P.M.—Industrial Electrolytic Division		Monterey Room Sir Francis Drake Hotel
12:15 P.M.—Organic and Biological Electrochemistry Division		Italian Room Mezzanine

Thursday, May 12, 1983

12:15 P.M.—Dielectrics and Insulation Division		Grand Ballroom (rear section) Mezzanine
12:15 P.M.—Luminescence and Display Materials Group		Italian Room Mezzanine

TECHNICAL SESSION CHAIRMEN ORIENTATION

All Session Chairmen and Vice-Chairmen are required to attend a breakfast meeting at 8:00 A.M. on the day of their participation in the Kent Room, Second Floor.

NONTECHNICAL REGISTRANTS PROGRAM

For details of the evening social events, please refer to the category, GENERAL FUNCTIONS.

The headquarters for the nontechnical registrants will be in the Oz, 32nd floor. This will be the starting point for daily activities. The nontechnical registrants are cordially invited to visit here in the morning to meet old friends and make new ones.

Monday, May 9—Coffee and rolls will be available in the Oz, 32nd floor of The Westin St. Francis Tower from 9:00 A.M. to 10:00 A.M.

At 10:00 A.M. buses will depart from the entrance of The Westin St. Francis for a "Legendary Landmarks" tour of San Francisco. Discover the sights and sounds that have made it the "jewel of the West." The tour includes the majestic Golden Gate Bridge and breathtaking view of the Bay from Vista Point; exotic Chinatown, "the city-within-the-City"; "Painted Ladies"—the colorful, restored Victorian Homes; the serene lawns and lakes of Golden Gate Park; panoramic views from Twin Peaks; historic Cliff House overlooking the Pacific Ocean and landmark skyscrapers of the Financial District: Transamerica Pyramid and Bank of America World Headquarters.

Lunch will be on your own at bustling Fisherman's Wharf with its steaming crab cauldrons, colorful fishing boats and seafood restaurants overlooking the Bay. After lunch you will reboard your motorcoach to continue your tour.

A famous writer once declared, "Everyone should be allowed to love two cities—his own, and San Francisco." Today, you'll discover for yourself why this is true. Return to the hotel about 3:00 P.M. The cost of tickets is $13.00 each excluding lunch.

Tuesday, May 10—Coffee and rolls will be available in the Oz, 32nd floor, of The Westin St. Francis Tower 9:00 A.M. to 10 A.M.

Today, choose one of two tours:

Performing Arts Center—This morning you will have the unique opportunity to visit the three centers of San Francisco's musical performing arts. While many cities have built new performing art centers in recent years, San Francisco has not only built a new center specifically for the symphony, it is keeping the original building as the home of the remaining arts, The San Francisco Ballet and the Opera.

The tour program this morning will take you through the original buildings, the San Francisco Opera House and the War Memorial Building. These two buildings were erected in the early 30's and are representative of gothic architecture common from that era. Since San Francisco's opera and ballet perform simultaneously, you will learn the secret of how staging is reproduced and moved to accommodate these two arts. Then it is on to the Louise M. Davies Symphony Hall, the newest structure for the performing arts in California. This hall has been designed by the top acoustical engineers and is laid out specifically for the San Francisco Symphony. The stage and seating is located in the center of the building in an inner core, totally protected from sound of any kind from the outside world. After the tour, you will have lunch on your own in the Civic Center area. Then you will be returned to your hotel about 3:00 P.M. The cost of tickets is $17.00 each excluding lunch.

The other tour is:

Accent on Art—San Francisco has frequently been accused of being a culture snob; her citizens find this difficult to refute, because it happens to be true. San Francisco is outmatched only by New York, boasting three top-class art museums and literally strings of art galleries whose works range from Mexican muralists to whimsical West Coast ceramicists.

Today, you will discover why painting and sculpture are probably the Bay City's greatest cultural contribution. With the accent on contemporary works, you will visit the most progressive of the "Big Three" museums, the Museum of Modern Art whose abstract expressionism exhibits and other major schools of the 20th Century have given it world class status. Next, you will visit a most unusual gallery, the walls of the Mission District. This impressive "art of the streets" includes murals in the tradition of Diego Rivera and Orozco with their "people-oriented" wide canvas of color and representation. Your last stop will be made at the Vorpal Gallery whose elegantly renovated building displays the best avant-garde artists of the West Coast with every medium represented, from steel to soft sculpture. Luncheon, at your own expense, will be available during the tour. Return to the hotel about 3:00 P.M. The cost of tickets is $16.00 each, excluding lunch.

Wednesday, May 11—Coffee and rolls will be available in the Oz, 32nd floor, of The Westin St. Francis Tower from 9:00 A.M. to 10:00 A.M.

Orient Express—Discover San Francisco's rich Oriental heritage. Today, your excursion will begin with a visit to a fabled San Francisco landmark, the Japanese Tea Garden in Golden Gate Park. The Tea Garden, with its winding paths, tranquil pools and miniature gardens, has delighted visitors since its opening in 1894. While in Golden Gate Park, you will enjoy a docent-guided tour of the Asian Art Museum whose magnificant jades are exhibited in their own opulent gallery. The main floor galleries are devoted to objects of Chinese origin, while the second floor galleries are divided among the diverse arts of the Middle East, Southeast Asia, and Japan.

From Golden Gate Park, you will go to "Nihonmachi" or Japantown, center for the Japanese community. There will be time to visit the galleries, showrooms, and craft shops that reflect the gentle ambience of Japanese culture.

Next, you will visit exuberant Chinatown, "the city within the City." In the largest community outside Asia, you will explore the exotic shops, temples, museums, food markets, and apothecaries. You can stop for an authentic Chinese luncheon at your own expense. Afterward, you may wish to remain in Chinatown to browse and shop or return in your motorcoach to your hotel about 3:00 P.M. The cost of tickets is $17.00 each, excluding lunch.

Thursday, May 12—Coffee and rolls will be available in the Oz, 32nd floor, from 9:00 A.M. to 10:30 A.M.

There are no scheduled tours on this day, to permit you to visit that special place, museum, gallery, or browse in the hundreds of shops.

COST OF VARIOUS FUNCTIONS
(Other than Registration)

Sunday Evening Get-Together	Complimentary
Monday Evening Mixer	Complimentary
Tuesday Evening Reception	Complimentary
Society, Divisional and Group Luncheons (each)	$ 8.00

Nontechnical Registrants Activities

Monday Tour of San Francisco	$13.00
Tuesday Tour Performing Arts Center	17.00
Accent on Art	16.00
Wednesday Tour Orient Express	17.00

(Luncheon each day is at your own expense).

DISCUSSION

No recording will be made of oral discussion. Those contributing to the discussion of a paper and desiring their remarks to be published should send the discussion to the Publication Editor of the **Journal of The Electrochemical Society,** 10 South Main Street, Pennington, New Jersey 08534-2896. The discussion will then be referred to the author for reply. Publication of the discussion and the comment of the author(s) depends on publication of the paper in the **Journal.**

Written discussion of a published paper should be submitted within two months following publication of the article.

Employment Posters

There will be a special bulletin board in the Registration Area for employment posters. Companies desiring to recruit employees are requested to place their announcement on this special board. These announcements should be no larger than 8½" × 11".

NOTE

Photographing of lantern slides, charts, etc., will be permitted unless specifically prohibited by the speaker. PHOTO FLASH AND PHOTO FLOODS ARE PROHIBITED. Tape recordings, except on behalf of the Society, are prohibited.

TECHNICAL SESSIONS

Monday, May, 9, 1983

9:00 A.M. Society Plenary Session, Grand Ballroom, Mezzanine, St. Francis Hotel. C. Lester Hogan will deliver The Electrochemical Society Lecture, "VLSI Processes and the Future."
12:15 P.M. Electronics Division Luncheon and Business Meeting, Italian Room, Mezzanine, St. Francis Hotel
12:15 P.M. High Temperature Materials Division Luncheon and Business Meeting, The City Club, Twelfth Floor, St. Francis Hotel
12:15 P.M. Physical Electrochemistry Division Luncheon and Business Meeting, Monterey Room, Second Floor, Sir Francis Drake Hotel

BATTERY
Cell Testing & Reliability
S. C. Levy, Chairman; B. B. Owens, Vice-Chairman
Borgia Room, Mezzanine

10:00 Introductory Remarks by S. C. Levy
10:15 The Reliability of Primary Batteries: A General Assessment by P. Bro — 1
11:00 Testing of Advanced Lithium Batteries to Establish Performance and Reliability Characteristics for Navy Applications by J. A. Barnes, R. F. Bis, F. C. DeBold, G. F. Hoff, J. D. Jensen, L. A. Kowalchik, and D. L. Warburton — 2
11:20 A Statistical Study of Sources of Variation in Battery Testing by K. Y. Cheung and W. S. Lindsay — 3
11:40 Characterization Testing of Alkaline Batteries by S. Gross — 4

C. F. Holmes, Chairman; D. F. Untereker, Vice-Chairman

2:00 Nondestructive Tests for Predicting Battery Reliability by S. C. Levy, N. H. Hall, and P. Bro — 5
2:20 Microcalorimetric and A-C Impedance Studies of Anode Stability in Lithium-Sulfuryl Chloride by J. C. Hall — 6
2:40 The Use of Complex Impedance Analysis in Predicting Reliability of Li/SO_2 Primary Cells by C. D. Jaeger, and J. C. D'Angelo — 7
3:00 Analysis of Thionyl Chloride Electrolyte by Gas Chromatography by S. Solomon — 8
3:20 Fifteen-minute intermission
3:35 Nondestructive Control of Highest Quality Defense and Medical Li/$SOCl_2$ Batteries by N. Marincic, J. Epstein, and P. Kane — 9
3:55 Performance Data Base for Li/$SOCl_2$ Cells Acquired by Means of a Computer Controlled Data Acquisition System by R. Szwarc and F. M. Kline — 10
4:15 Capacity Losses in Li/SO_2 Cells due to Chemical Reactions at High Rate, High Temperature Discharges by W. Bowden, R. H. Holmes, L. Chow, and D. Demuth — 11
4:35 Voltage Compatible Lithium Cells by F. Bonino, M. Lazzari, A. Padula, and B. Scrosati — 12

CORROSION
General Session
F. Mansfeld, Chairman; M. C. H. McKubre, Vice-Chairman
Yorkshire Room, Second Floor

10:00 The Dissolution and Passivation of Iron in Concentrated Alkali by M. C. H. McKubre, M. J. Madou, and K. Kinoshita — 53
10:25 Mechanism of Passive Film Formation and Reduction on Iron by Gh. Nazri, and E. Yeager — 54
10:50 A New Mossbauer Conversion Electron Detection Technique for In Situ Passivation Studies on Iron by M. E. Kordesch, J. Eldridge, D. Scherson, and R. W. Hoffman — 55
11:15 An In Situ Technique for the Decoration of Defects in Passive Films by X. Wu, Y. K. Hong, and R. A. Oriani — 56
11:40 Active-Passive Transition Study of Titanium-Molybdenum Alloy by Y. K. Hong, and R. S. Glass — 57

M. C. H. McKubre, Chairman; F. Mansfeld, Vice-Chairman

2:00 Breakdown of Passive Films on Iron in Chloride Solutions by O. J. Murphy, T. E. Pou, and J. O'M. Bockris — 58
2:25 Effect of Focused Ultrasound on Depassivation of Iron in Sulfuric Acid by R. Alkire, and S. Perusich — 59
2:50 Influence of Anions on the Dissolution of Titanium in Acidic Aqueous Solution by G. M. Brown — 60
3:15 Mechanism of Transpassive Dissolution of Titanium-Molybdenum Alloys by R. S. Glass, and Y. K. Hong — 61
3:40 Ten-minute intermission
3:50 An Electrochemical and ESCA Study of Titanium Dissolution in Acidic Sulfate Solutions Containing CrII/CrIII Ions by A. L. Bacarella, J. M. Dale, and L. D. Hulett, Jr. — 62
4:15 Corrosion Behavior of Ion-Implanted Amorphous Alloys by N. R. Sorensen, and S. T. Picraux — 63
4:40 On the Interpretation of Cyclic Voltammograms of Iron Electrode in Alkaline Solutions at Various Temperatures by A. Wieckowski and E. Ghali — 64

DIELECTRICS AND INSULATION/ELECTRONICS
Dielectric Isolation
B. M. Kemlage, Chairman; J. E. Berthold, Vice-Chairman
Oxford Room, Second Floor

10:00 Thermal Oxidation of Sputtered Silicon Carbide Thin Films by W. J. Lu, T. P. Chow, A. J. Steckl, and W. Katz — 86
10:20 Planarization of Isolation Oxide by Argon Ion Sputtering by Y. Mashiko, H. Koyama, S. Kawazu, T. Nishioka, H. Yakushiji, and H. Harada — 87
10:40 A Model for the Two-Dimensional Thermal Oxidation of Silicon Cylindrical Geometries by G. Oleszek, K. Kasley, R. Jones, and D. Granteer — 88
11:00 Multiwafer-Plasma Oxidation System by A. K. Ray, A. Reisman, and M. Berkenblit — 89
11:20 Interpoly Oxides for EEPROM Devices by H. L. Peek and J. F. Verwey — 90
11:40 Deposition and Reflow of Phosphosilicate Glass by R. A. Bowling, G. B. Larrabee — 91

J. E. Berthold, Chairman; B. M. Kemlage, Vice-Chairman

2:00 Observations of the Temperature Gradient Zone Melting Process for Isolating Small Geometry Devices by D. J. Lischner, H. Basseches and F. A. D'Altroy — 92
2:20 The Effects of Insulator Thickness and Small Changes in Seed Orientation on the Defect Structure of Silicon SOI Films Grown by Epitaxial Lateral Overgrowth Techniques by J. T. McGinn, L. Jastrzebski, and J. F. Corboy — 93
2:40 Cap Layers for Silicon-on-Insulator Films Produced by Laser or Strip Heater Recrystallization by P. G. McMullin and S. Dutta — 94
3:00 Dielectric Isolation by Lateral Epitaxial Growth by McD. Robinson, G. K. Celler, and D. J. Lischner — 95
3:20 Effect of Laser Annealing on Conventional and High Pressure Thermal Oxides of Silicon by A. A. Naem, A. R. Boothroyd, S. P. Tay, I. D. Calder, and H. M. Naguib — 96
3:40 Electrical Properties of Thermal Tantalum Oxide Films Incorporating Silicon by H. Hasegawa, T. Ogawa, K. Wada, and M. Nakano — 97
4:00 Properties of Tantalum Pentoxide Thin Films on Silicon by G. S. Oehrlein and A. Reisman — 98
4:20 Microstructure and Surface Characterization of Plasma-Polymerized Styrene Films on Silicon Substrates by O. K. T. Wu and D. M. Chen — 99
4:40 The Effect of Oxidation Rate on the Characteristics of Anodically Oxidized GaAs Samples by P. Das, B. Davari, and M. Tabib-Azar — 100

Fourth Symposium on Plasma Processing
Deposition
G. C. Schwartz, Chairman; J. Amouroux, Vice-Chairman
Grand Ballroom, Mezzanine

10:00 Interaction of Plasma Oxide Deposition Variables by E. Sabin, and C. Ramiller — 141
10:20 A Plasma Oxide Interlayer Dielectric for use in Two Layer Metallization by S. S. Dottarar — 142
10:40 Plasma Deposition of Dielectric Polymer Films for High-Voltage Insulation of Devices by D. M. Chen — 143
11:00 Plasma-Enchanced Chemical Vapor Deposition of Epitaxial Silicon from Silane by S. R. Shanfield, and R. Reif — 144
11:20 Characterization of PdO Formed by D-C Generated Oxygen Plasma by V. A. Karagounis, C. C. Liu, M. R. Newman, and L. T. Romankiw — 145
11:40 Lift Off Lithography Using Low-Frequency Plasma Buffer Layers by D. M. Dobkin, B. D. Cantos, and D. B. Deal — 146

Etching; Dielectrics and Silicon
G. Turban, Chairman; D. M. Chen, Vice-Chairman
Grand Ballroom, Mezzanine

2:00 Characterization of Silicon Nitride Dry Etching in SF_6/He Mixtures by E. Laes, F. Coopmans, P. Verdonck, G. Declerck, and G. Peeters — 147
2:20 Dry Etched Vias for Two Layer Interconnect on High Density Bipolar IC's by D. R. Evans — 148
2:40 High Temperature Plasma Etching of Silicon and Silicon Dioxide by W. R. Snow and K. C. Ray Chiu — 149

Monday continued

3:00 Anisotropic Etching of Polycrystalline Silicon by M. Yoneda, H. Itakura, M. Hatanaka, T. Shibano and H. Abe 150
3:20 RIE Etching of Poly-Si by CCl_4+O_2 by A. I-T. Pan 151
3:40 Silicon Etch Rate as a Function of Dopant Concentration in a CF_3Cl Plasma by M. F. Leahy and D. J. Tanguay 152
4:00 Fabrication of Submicrometer Structures in Si Using $SiCl_4/O_2$ Reactive-Ion Etching by S. M. Cabral, D. D. Rathman, and N. P. Economou 153
4:20 A Controllably Anisotropic, High Rate, Polysilicon Plasma Etch Process with Very High Selectivity Against SiO_2 and Photoresist by C. B. Zarowin and J. Dalle Ave 154
4:40 Reactive Sputter Etching of Single Crystal Silicon with Cl_2 and $SiCl_4$ by K. O. Park and F. C. Rock 155

ELECTRONICS
Computer Controlled IC Processing and Monitoring
E. H. Nicollian, Chairman; P. L. Castro, Vice-Chairman
California East, Second Floor

10:00 IBM's "QTAT" Experience: A Foundation for VLSI Manufacturing Control System Development in the 80's (FCMS) by T. Francis, D. Griffin, and P. Bhalla 251
10:20 Economic Justification for FCMS (Factory Control and Monitoring System) at IBM E. Fishkill: Yield Management by D. Griffin, P. Bhalla, and T. Francis 252
10:40 Successful Implementation of "FCMS" at IBM E. Fishkill: A Basis for Future VLSI Manufacturing Strength by P. Bhalla, T. Francis, and D. Griffin 253
11:00 Computer Aided IC Manufacturing at Hewlett-Packard Laboratories by M. Parikh 254
11:20 IC Fabrication Information Control via an Electronic Message System by D. K. Brotz 255
11:40 Digital Automation: The Slave of the Electrochemist by P. Rony, K. Mercure, I. Malkin, and V. Guruswamy 256

P. L. Castro, Chairman; E. H. Nicollian, Vice-Chairman

2:00 The Statisical Characterization of CMOS Inverters Using Noise Margins by M. G. Buehler and T. W. Griswold 257
2:20 Use of a Defect Monitor Test Structure for Optimizing Process Yield in VLSIC Manufacturing by R. Stanley, T. Hasan, V. Akylas, and E. Lee 258
2:40 Systematic Control of Epitaxial Deposition Processes with a Microcomputer System by M. E. McPherson, T. L. Carlson, and J. E. Chambers 259
3:00 Twenty-minute intermission
3:20 Monochromatic IR Reflectance Method for Thickness Measurement of Thin (1.0 μ m) Epitaxial Silicon Layers by S. P. Weeks and B. Senitzky 260
3:40 Measurement and Evaluation of Registration Errors of Step-and-Repeat Photolithographic Systems by H. S. David, J. A. Henson, and J. E. Heideman 261
4:00 Computerized Process Control via Shewhart Control Charting Techniques by J. J. Delgado and W. J. Daughton 262

Defects in Silicon
W. M. Bullis, Chairman; L. C. Kimerling, Vice-Chairman
Elizabethan Room A and B, Second Floor

10:00 Introductory remarks
10:10 Trends in Defect and Impurity Control for Fine Line Processing by G. A. Rozgonyi 269
10:50 Silicon Defects and Their Effect on Integrated Circuits by J. H. Matlock 270

Intrinsic Gettering

G. A. Rozgonyi, Chairman; L. Jastrzebski, Vice-Chairman

2:00 Oxygen Out-Diffusion Model for Denuded Zone Formation in Czochralski-Grown Silicon with High Interstitial Oxygen Content by J. Andrews 271
2:20 Gettering of P+ (100) Si Substrates for Epitaxial Growth by W. Dyson, L. Hellwig, J. Moody, and J. A. Rossi 272
2:40 Three-Step Anneals and Oxygen Precipitation in High Carbon CZ Silicon by C. Y. Kung, L. Forbes, and J. D. Peng 273
3:00 The Homogenization of Micro-Defects in the Bulk of Silicon Wafers by a 3-Step Thermal Heat-Treatment by J. O. Borland 274
3:20 Origins of Oxidation-Induced Stacking Faults in N-Type (100) - Oriented Silicon Wafers by S. Hahn, and D. Cheng 275
3:40 Ten-minute intermission

L. Jastrzebski, Chairman; G. A. Rozgonyi, Vice-Chairman

3:50 Generation Lifetime Improvement Through Intrinsic Gettering in n-Type <100> Si Wafers by E. M. Murray, M. P. Scott, and S. Hahn 276
4:10 Oxygen Precipitation, Denuded Zones, and Intrinsic Gettering Effects on Generation Lifetimes for (100) CZ Silicon by L. Forbes, C. Y. Kung, and J. D. Peng 277
4:30 Activation of the Intrinsic Gettering Mechanism by the Precipitation and Growth of Oxygen Related Precipitates in Cz-Grown Silicon Wafers by J. O. Borland 278
4:50 Dark Current Dependence on Denuded Zone Depth for Intrinsic Gettering of Silicon by D. N. Nichols 279

III-V Opto-Electronics Epitaxy and Device Related Processes
S. Mahajan, Chairman; V. G. Keramidas, Vice-Chairman
Georgian Room, Mezzanine

10:15 Introductory remarks by V. G. Keramidas
10:20 Challenges in III-V Semiconductor Compounds by H. C Gatos 320
11:05 III-V Optoelectronic Devices by H. Kressel 321

J. H. Wernick, Chairman; G. A. Antypas, Vice-Chairman

2:00 Liquid Encapsulated Czochralski (LEC) Growth of III-V Crystals by W. A. Bonner 322
2:30 Reduction of Dislocation Densities of LEC-Grown InP Crystals by Aid of Thermal Anaylsis by G. Muller, E. Tomzig, and J. Volkl 323
2:50 Ten-minute intermission
3:00 Horizontal Bridgman Growth of Optoelectronics Grade GaAs by S. Akai, K. Fujita, S. Nishine, N. Kito, Y. Sato, S. Yoshitake, and M. Sekinobu 324
3:30 The Effects of Melt Stoichiometry and Impurities on the Formation of Dislocations in Bulk GaAs by J. M. Parsey, Jr., J. Lagowski, and H. C. Gatos 325
3:50 Growth and Characterization of GaAs Single Crystal by Magnetic Field LEC Technique by K. Terashima, and T. Fukuda 326

Recent News Papers

4:10 Recent News Papers

ELECTRONICS/DIELECTRICS AND INSULATION
Joint General Session
Compound Semiconductors
J. M. Woodall, Chairman; C. M. Osburn, Vice-Chairman
Colonial Ballroom, Mezzanine

10:00 Characterization of II-VI Compounds by Electrochemical Photocapacitance Spectroscopy by R. Haak, and D. Tench 353
10:20 Characterization of GaAs by Electrochemical Photocapacitance Spectroscopy by R. Haak, and D. Tench 354
10:40 Anomalous Transient Response in Optically Excited GaAs MESFET's by T. K. Plant, and S. J. T. Owen 355
11:00 Long Wavelength Characterization of GeAs and SiAs: Two New Semiconductors by D. G. Mead 356
11:20 MOS Capacitors on CdTe by R. T. Talasek, and A. J. Syllaios 357
11:40 LPE Growth of $Hg_{.8}Cd_{.2}Te$ on Horizontal Rotating Substrates by W. L. Ahlgren 358

2:00 Electronic Conductivity of Li_2MnO_3 Doped with Aluminum, Magnesium, or Zinc by G. H. Kucera, J. W. Sim, and J. L. Smith 359
2:20 Deep Levels in Device-Quality Ion-Implanted GaAs by S. J. Prasad, P. K. Bhattacharya, M. V. Rao, J. K. Rhee, B. Venkatraman, and R. Y. Koyama 360
2:40 On The Redistribution of Implanted Be in Semi-Insulating InP After Annealing by B. Molnar, G. Kelnar, G. H. Morrison and G. Ramseyer 361

Joint General Session
Processing
M. Jones, Chairman; P. Rai-Choudhury, Vice-Chairman
Colonial Ballroom, Mezzanine

3:00 Chlorine Levels in MOS Gate Oxides by W. A. Bosenberg, and C. W. Magee 362
3:20 Annealing of Fixed Changes in Poly-Si Gate MOS by J. P. McVittie, G. Chang, D.-B. Kao, and G. L. Patton 363
3:40 Hydrogen Gettering Effect of Mo_2N/Mo MOS Process by M. J. Kim, and D. M. Brown 364
4:00 1.2 μ m Process Design for CMOS VLSI's by J. I. Matsunaga, N. Matsukawa, K. Hashimoto, M. Nakase, H. Nozawa, and S. Kohyama 365
4:20 Process for Borderless Source and Drain Contacts by R. C. Dockerty, G. T. Elie, and C. C. Hu 370
4:40 Characterization of the Self-Aligned $TiSi_2$ Process by C. K. Lau 371
5:00 Phosphosilicate Glass Flow Analysis and Experiments by J. B. Price, and E. Reed 372

ENERGY TECHNOLOGY
Novel Photoelectrochemical Synthetic Routes
H. Chum, Chairman; A. J. Nozik, Vice-Chairman
Olympic Room, Second Floor

10:00 Photoelectrochemical Synthetic Processes by M. S. Wrighton 504
10:30 Chemical Control of Fermi Levels of Platinum Group Metal Catalysts. Part I by A. Heller and E. Aharon-Shalom 505
10:45 Chemical Control of Fermi Levels of Platinum Group Metal Catalysts. Part II by A. Heller 506
11:00 The Role of Catalysts in Light-Induced Electrochemical Reactions at Semiconductors by R. Memming, D. Meissner, and B. Kastening 507
11:30 Hot Carrier Photoelectrochemistry by A. J. Nozik, G. Cooper, J. A. Turner, and B. A. Parkinson 508

A. J. Nozik, Chairman; H. Chum, Vice-Chairman

2:00 Organic Oxidative Cleavage on Irradiated Semiconductor Powders by M. A. Fox, M.-J. Chen, and C.-C. Chen 509
2:30 Photoelectrochemical Reactions of Lactic Acid on n-Type Semiconductor Powders by M. A. Ratcliff, and H. L. Chum 510

Monday continued

3:00 Photo-Oxidation of Organic Compounds at Doped α -Fe_2O_3 Electrodes by J. H. Kennedy, and D. Dunnwald 511
3:25 Fifteen-minute intermission
3:40 Oxidation Processes on CdSe and Se Electrodes by W. M. Sears and S. R. Morrison 512
4:05 A New Look at the Photo-Kolbe Reaction: Where Do We Go from Here? by R. E. Schwerzel 513
4:30 Photo-Kolbe Studies of Aromatic Acids Using Platinized Magneli Phases of TiO_x by J. S. Cantrell 514

ENERGY TECHNOLOGY/BATTERY/DIELECTRICS AND INSULATION
Conducting Organic Polymers in Energy Conversion and Storage
A. G. MacDiarmid, Chairman; A. F. Diaz, Vice-Chairman
California West, Second Floor

10:00 Synthesis and Chemical Doping of New Tractable Electrically Conducting Polymers by Y. S. Papir, V. P. Kurkov, and S. P. Current 543
10:40 Electrochemistry and Conductivity of New Tractable Electrically Conducting Polymers by A. H. Schroeder, Y. S. Papir, and V. P. Kurkov 544
11:15 Conducting Polymers Derived from Pyrroles by G. B. Street 545

W. M. Ayers, Chairman; L. W. Shacklette, Vice-Chairman

2:00 Electroactive Properties of Polyaromatic Polymer Films by R. J. Waltman, J. Bargon, S. Mohmand, and A. F. Diaz 546
2:35 Electrochemistry of Thin Film Heteroaromatic Ladder Polymers by R. J. Nowak, L. Polyak, and D. Rolison 547
3:05 In Situ Mossbauer Spectroscopy of Iron Complexes Incorporated into a Conducting Polymer Matrix by M. Daroux, H. Gerdes, D. Scherson, J. Eldridge, M. Kordesch, and R. Hoffman 548
3:35 Properties of Polyphenylene Films Deposited Electrochemically in HF-Benzene System by I. Rubinstein 549
4:05 Characteristics of Electrochemically Reduced Polyacetylene by R. B. Kaner and A. G. MacDiarmid 550
4:35 Electrochemical Characteristics of Chemically Doped Polyacetylene by W. H. Smyrl, S. R. Kurtz, C. D. Jaeger, J. M. Zeigler, and D. S. Ginley 551

Recent News Papers

5:05 Recent News Papers

HIGH TEMPERATURE MATERIALS
High Temperature Materials Chemistry
Vapor Species
D. L. Hildenbrand, Chairman; J. W. Hastie, Vice-Chairman
Elizabethan Room C, Second Floor

10:00 Introductory remarks by Z. A. Munir and D. Cubicciotti
10:15 Molecular Species in the As-O System by K. H. Lau, R. D. Brittain, and D. L. Hildenbrand 438
10:40 Transpiration Mass Spectrometry of Potassium Salt Systems by J. W. Hastie, K. F. Zmbov, and D. W. Bonnell 439
11:05 Nucleation and Condensation of Fe, Si, Fe/Si, FeO_x, and SiO_x Vapors by J. R. Stephens and S. H. Bauer 440

Recent News Papers

11:30 Recent News Papers

Synthesis and Thermodynamics
L. Brewer, Chairman; Z. A. Munir, Vice-Chairman

2:00 Preparation of Ductile Nickel Aluminides for High Temperature Uses by C. T. Liu, C. C. Koch, and C. L. White 441
2:30 Synthesis of Refractory Oxide Materials by Skull Melting by R. G. Behrens and C. C. Herrick 442
3:00 The Kinetics of the Gas/Solid/Liquid Reaction by M. Balooch, W. H. Siekhaus, and D. R. Olander 443
3:30 Fifteen-minute intermission
3:45 Thermodynamic Properties of Alkali Metal Zirconates by R. Kohli 444

Recent News Papers

4:15 Recent News Papers

INDUSTRIAL ELECTROLYTIC/CORROSION/ELECTRODEPOSITION
Anode and Cathode Materials
D. R. Turner, Chairman; J. B. Hoare, Vice-Chairman
Victorian Room, Second Floor

10:00 State of Oxidized Noble Metal Anodes by B. E. Conway 575
10:30 Fundamentals of the Behavior of Insoluble Oxide Anodes by S. Trasatti 576
11:00 Activated Carbon as a Fluidized-Bed Anode by H. H. Law and V. Tierney 577
11:30 Glassy Carbon Anodes and Air-Depolarized Cathodes for the Generation of Ozone by P. C. Foller, M. L. Goodwin, and C. W. Tobias 578

B. E. Conway, Chairman; H. Law, Vice-Chairman

2:00 Activated Lead Anode for Metal Electrowinning by H. B. Beer 579
2:30 Anode Materials for Electroplating by D. R. Turner 580
3:00 A Review of the Anodic Behavior of Nickel in Electroplating Solutions by G. A. DiBari 581
3:30 Five-minute intermission
3:35 Formation of Salt Films during Anodic Metal Dissolution in the Presence of Fluid Flow by R. Alkire and A. Cangellari 582
4:05 The Morphology of Copper Deposits Powder Deposition by A. Kindler and C. W. Tobias 583

Recent News Papers

4:35 Recent News Papers

ORGANIC AND BIOLOGICAL ELECTROCHEMISTRY
Mechanisms and Modeling of Electrochemical Membrane Processes
H. N. Blount, Chairman; H. B. Mark, Jr. Vice-Chairman
Elizabethan Room D, Second Floor

10:00 Introductory remarks
10:05 Biocatalytic Processes at Potentiometric Membrance Electrodes by G. A. Rechnitz 615
10:35 Electron Transfer across Biological Membranes: An Electrodic Model of Membrane-Solution Interface by J. O'M. Bockris and M. A. Habib 616
11:05 Noise in Ion Selective Field Effect Transistors under Nonequilibrium Conditions by J. M. Reijn, J. Janata, and J. J. Brophy 617
11:35 Proton Transfer in Artificial Membranes by J. H. Fendler 618

B. S. Pons, Chairman; P. P. Schmidt, Vice-Chairman

2:00 Induced Irreversibility of Ion Transfers across Liquid/Liquid Interfaces by R. P. Buck, J. D. Reid, O. R. Melroy, and W. E. Bronner 619
2:30 Transport Properties of Phospholipid Monolayer Membrane Models by D. J. Schiffrin, L. Berlouis, J. Chatham, and H. H. J. Girault 620
3:00 Ten-minute intermission
3:10 The Role of Surface Charge in Membrane Permeability Changes by M. Blank 621
3:40 Ion Gates. Electroactive Membranes with Embedded Electrodes by P. Burgmayer and R. W. Murray 622

PHYSICAL ELECTROCHEMISTRY
The Chemistry and Physics of Electrocatalysis
J. D. E. McIntyre, Chairman; R. A. Marcus, Vice-Chairman
Sir Francis Drake Hotel, Empire Room, Second Floor

10:00 Introductory remarks
10:10 Molecular Ingredients of Heterogeneous Catalysis by G. A. Somorjai 694
10:50 Lattice Models, Interactions, and Solvent Effects in Electrochemical Monolayer Formation by B. E. Conway, S. Marshall, and K. Tellefsen 695
11:25 The Bornian Hiatus in Electrode Kinetics by S. U. M. Khan and J. O'M. Bockris 696

E. B. Yeager, Chairman; P. N. Ross, Jr., Vice-Chairman

2:00 Structure of Metal and Semiconductor Surfaces and Chemisorption on These Surfaces by W. A. Goddard III 697
2:35 Surface Chemistry of Copper: Reactions of Small Molecules with and on Cu(110) by R. J. Madix 698
3:10 Electrocatalysis at Single-Crystal Electrodes. The Role of Surface Defects and Adatoms by J. D. E. McIntyre and W. F. Peck, Jr. 699
3:45 Ten-minute intermission
3:55 Electrodeposition at Well-Defined Electrode Surfaces by A. T. Hubbard, J. L. Stickney, S. D. Rosasco, and M. P. Soriaga 700
4:30 Crystal Face Specificity of Double Layer Structure and Electrocatalysis by S. Trasatti 701

Fourth International Symposium on Molten Salts
D. Newman, Chairman; J. Braunstein, Vice-Chairman
Sir Francis Drake Hotel, Franciscan Room, Mezzanine

10:00 Vibrational Spectra of Chloraluminates by E. Rytter 738
10:20 Molecular Dynamics Calculations of MAX_4 Melts by M.-L. Saboungi, M. Blander, and A. Rahman 739
10:50 The Coupling between Transport of Electric Charge and Chemical Reaction by T. Forland, A. A. Makange, and S. K. Ratkji 740
11:20 Characteristic Diffusion Phenomena of Fluorine in Molten LiF-BeF_2 and NaF-BeF_2 Systems by H. Ohno and K. Furukawa 741

Recent News Papers

11:40 Recent News Papers

G. P. Smith, Chairman; B. Tremillion, Vice-Chairman

2:00 Thermodynamic Properties of $AlCl_3$-Containing Melts by H. A. Oye and W. E. Wohnsiedler 742
2:40 An Interpretive Review of Some Unusual Properties of $SbCl_3$-$AlCl_3$ and $SbBr_3$-$AlBr_3$ Melts by C. P. Smith, M. Sorlie, and G. Mamantov 743
3:00 Thermodynamics of Evaporation of Melts of $LiAlCl_4$, $NaAlCl_4$, and $KAlCl_4$ by H. Wendt and U. Gesenhues 744
3:20 The Use of Lithium Aluminum Chloride Molten Salt as an Electrolyte in Lithium Cells by I. D. Raistrick and R. A. Huggins 745
3:40 The Fischer-Tropsch Reaction in Chloroaluminate Melts by G. Mamantov and S. E. Walters 746

Monday continued

4:00 The Role of Coupled-Transport Reactions in the Preparation of Metal Halides and Chalcides Using Molten Aluminum Halide Solvents by W. B. Jensen and E. M. Larsen 747
4:20 Molten Gallium Halides as Media for Reactions of Polycyclic Aromatic Hydrocarbons (PAH's) by A. S. Dworkin, A. C. Buchanan III, and G. P. Smith 748
4:40 Phase Diagram of LiCl-NaCl-$AlCl_3$ Ternary System by Y. Sato and T. Ejima 749

General Session
P. N. Ross, Jr., Chairman; M. J. Weaver, Vice-Chairman
Sir Francis Drake Hotel, Tudor Room, Second Floor

10:00 O_2 Reduction Kinetics in Deuterated Phosphoric Acid by M. Ghoneim, S. Clouser, and E. Yeager 801
10:20 Thermal Desorption and Auger Electron Spectroscopic Studies of Anodic Oxygen on Pt(100) by F. T. Wagner and P. N. Ross, Jr. 802
10:40 The Effect of H_2PO_4 Anion on the Kinetics of Oxygen Reduction on Pt by P. E. Andricacos and P. N. Ross, Jr. 803
11:00 Electrocatalysis for Oxygen Reduction by Adsorbed Dicobalt Cofacial Porphyrins by M. J. Weaver, H. Y. Liu, C.-B. Wang, and C. K. Chang 804
11:20 Spatio-Temporal Organization of the Adsorbates Involved in the Reduction of Dissolved Oxygen at the Titanium Acidic Media Interface by A. Caprani, J. P. Frayret, M. Keddam, and P. Morel 805
11:40 Low Energy Electron Diffraction (LEED) Characterization of Metal Electrode Surfaces by P. N. Ross, Jr. and F. T. Wagner 806

M. Solomon, Chairman; R. A. Osteryoung, Vice-Chairman

2:00 Conductivity Studies in Mixed Solvents by M. Salomon and E. Plichter 807
2:20 Electrochemical Behavior of Lithium Closoborane Electrolytes by H. H. Law, J. J. Auborn, and K. T. Ciemiecki 808
2:40 Raman Spectroscopic Studies of the Chemistry of SO_2 in the Solvents Pyridine and α -Picoline by W. A. Adams and L. A. Dierker 809
3:00 Voltammetric Reduction of Sulfur Oxychloride Solvents in the Presence of Calcium Tetrachloroaluminate by W. K. Behl 810
3:30 Fifteen-minute intermission
3:35 Factors Influencing Lithium Rechargeability in Aprotic Solvent Based Electrolytes by R. S. Salter, C. D. Desjardins, and T. Cadger 811
3:55 Study of Metal Solvent Interaction by XPS for the Case of Molybdene Napthalocyanine in the Prescence of $SOCl_2$: Application to the Reduction of $SOCl_2$ in Batteries by J. Riga, J. J. Verhist, M. Savy, G. Magner, and G. Scarbeck 812
4:15 Complex Inpedance Measurements of $SOCl_2$ Reduction by N. Doddapaneni and F. M. Delnick 813
4:35 Cathode Studies of a High Rate Li/$SOCl_2$ Cell by N. Doddapaneni and S. Szpak 814

Tuesday, May 10, 1983

12:15 P.M. Annual Society Luncheon and Business Meeting, Italian Room, Mezzanine, St. Francis Hotel
4:30 P.M. Awards and Recognition Session, Grand Ballroom, Mezzanine, St. Francis Hotel. Nick Holonyak, Jr. will deliver the Solid State Science and Technology Award Address, "From Silicon to III-V Compounds."

BATTERY
Cell Testing and Reliability
A. E. Verardo, Chairman; S. C. Levy, Vice-Chairman
Borgia Room Mezzanine

9:00 Introductory remarks by A. E. Verardo
9:15 A Failure Model for Secondary Power Sources by R. F. Fedors and S. Di Stefano 13
9:35 Real Time and Accelerated Geosynchronous Orbit Testing of Nickel-Cadmium Cells by P. G. Fougere, R. E. Corbett and J. Lovgren 14
9:55 Heat Flux Simulation during Battery Life Test by W. C. Hwang and C. C. Badcock 15
10:15 Fifteen-minute intermission
10:30 Assessing Battery Performance Through Examination of Cell Voltage Test Data by P. P. McDermott 16
10:50 Sealed Lead-Acid Battery Test Results by D. M. Bush, A. E. Verardo, D. W. Miller, and J. D. Sealey 17
11:10 Effect of Charge Acceptance on Life Performance of SLI Batteries by K. Abe, T. Yoshida, Y. Ohya, and H. Morimoto 18
11:30 Photoelectrochemical Properties of Lead Oxides by L. M. Peter, and N. Freeston 19

E. J. Cairns, Chairman; S. Gross, Vice-Chairman

2:00 Thermogravimetry-Envolved Gas Analysis of Silver Oxide Cathode Material by W. A. Parkhurst, S. Dallek, and B. F. Larrick 20
2:20 Effect of Adsorption Phenomena and Phase Transition on Electrochemical Behavior of Silver/Silver Oxides Electrodes in KOH Solutions by M. Hepel, and M. Tomkiewicz 21
2:40 Assurance of an Automatically Activated Silver-Zinc Battery by H. W. Ko 22
3:00 Correlation of Fuel Cell Performance with Fabrication Parameters by G. G. Barna, S. N. Frank, and L. D. Weedon 23
3:20 Testing and Evaluation of Prototype Zinc/Bromine Batteries by P. C. Butler, and D. W. Miller 24
3:40 Reliability Testing of Flowing Zinc-Bromine Batteries and Components by K. R. Newby, R. Bellows, H. Einstein, P. Grimes, E. Kantner, and P. Malachesky 25

CORROSION
General Session
M. Kendig, Chairman; R. C. Newman, Vice-Chairman
Yorkshire Room, Second Floor

9:00 Growth Kinetics of Single Pits in 304 Stainless Steel by R. C. Newman 65
9:25 Modeling of Film Formation and Oscillatory Instability in the Electrodissolution of Copper in Acidic Chloride Media by A. J. Pearlstein, H. P. Lee, and K. Nobe 66
9:50 Oscillatory Behavior in Copper Electrodissolution in Acidic Chloride Media by H. P. Lee, and K. Nobe 67
10:15 Corrosion of a Cupro-Nickel Alloy in Sulfide-Containing Solutions by H. S. Tong 68
10:40 Ten-minute intermission
10:50 Composition of Chromate Passivation Films on Aluminum-Zinc Alloy-Coated Sheet Steel by H. E. Townsend and R. G. Hart 69
11:15 Effect of Alternating Voltage on the Corrosion of Stainless Steels by J. L. Wendt and D-T. Chin 70
11:40 Influence of CO and CO_2 Partial Pressure on Electrochemical Behavior of Stainless Steels and Nickel Base Alloys in Carbonate Solutions by K. V. Quang, R. Sehil, N. Jallerat, F. Bourelier, and M. Fedoroff 71

R. C. Newman, Chairman; M. Kendig, Vice-Chairman

2:00 Evaluation of Structured Noise Techniques for the Measurement of Interfacial Impedance by D. D. Macdonald, and B. G. Pound 72
2:20 A-C Impedance Study of the Passivation of Mg, Al, and Mg Alloy AZ91B by P. L. Hagans 73
2:40 Impedance Spectra for Anodized Aluminum Alloys during Exposure to NaCl by F. Mansfeld, and M. Kendig 74
3:00 The Role of Polymer Adhesion and Cohesion on the Corrosion Protection of Polymer Coated Steel by M. Kendig, A. Aerora, and F. Mansfeld 75
3:20 Interference Problem Related to the Rotating Ring-Disk Electrode by Gh. Nazri, and B. D. Cahan 76
3:40 Carbon Corrosion by L. Berk, and D. Zuckerbrod 77

DIELECTRICS AND INSULATION/ELECTRONICS
Fourth Symposium on Plasma Processing
J. Dieleman, Chairman; B. R. Soller, Vice-Chairman
Grand Ballroom, Mezzanine

9:00 Magnetically Confined Discharge for Plasma Etching by T. D. Mantei and T. Wicker 156
9:20 A New, High Efficiency, Submegahertz Excitation Frequency, Inductively Coupled Plasma Generator for High Rate Downstream Photoresist Stripping and Isotropic Etching by C. B. Zarowin, G. N. Steinberg, and A. R. Reinberg 157
9:40 Magnetron-Enhanced Reactive Ion Etching of SiO_2 by I. Lin, D. Hinson, and W. Class 158
10:00 Automated Sequential Dry Processing: Develop, Etch, Ash by R. J. Mattox 159
10:20 Optical Etch Rate Monitoring: Computer Simulation of Reflectance by P. A. Heimann, and R. J. Schutz 160
10:40 Paper withdrawn 161
11:00 A Statistical Approach to Selective Etching Process Development by W. Ma, J. Bondur, and T. Krawiec 162
11:20 Tapering CVD SiO_2 Vias for Improved Metal Step Coverage Using RIE by E. Crabbe, and E. R. Sirkin 163
11:40 The Importance of Plasma Poly Etching Selectivites by P. C. Chang 164

R H. Burton, Chairman; W. Bienvogl, Vice-Chairman

2:00 Dry Etching of Dielectrics for VLSI by M. T. Duffy, R. A. Soltis, and A. Day 165
2:20 Polymer Formation and Reactor Cleaning during Silicon Oxide Etching by L. Peccoud, Ph. Laporte, and P. Lassagne 166
2:40 Controlled Film Formation during CCl_4 Plasma Etching by S. E. Bernacki and B. B. Kosicki 167
3:00 Plasma Metal Etching for High Yield in a Production Environment by S. Fouts and D. Vogel 168
3:20 Plasma Etching Techniques for SiO_2, Polysilicon, and Aluminum-Silicon (U) by R. W. Light 169
3:40 Positive and Negative Dry Development of Chalcogenide Optical Resists by J. M. Lavine, S. A. Lis, J. I. Masters, and G. M. Goldberg 170

Tuesday continued

ELECTRONICS
Computer Controlled IC Processing and Monitoring
A. Ipri, Chairman; M. Parikh, Vice-Chairman
California East, Second Floor

9:00 VLSI Yield Management in the '80's by T. Collopy, M. Cowan, W. Freitag, M. Lowe, D. Piscitelli, and E. Squarzini 263
9:20 Process Engineering Tools in a Distributed Software Environment by V. H. Brecher, and J. K. Siudut 264
9:40 Host Computer Controls Process Equipment by U. Kaempf 265
10:00 Twenty-minute intermission
10:20 Computer Aided Manufacturing (CAM) for Semiconductor Processing and Monitoring by D. L. Cole and I. Smethurst 266
10:40 Computer Model of Laser Target Link Explosion in Redundant Memories by J. D. Chlipala and L. M. Scarfone 267
11:00 APL Application for Plating Process Control of IC Substrates by S. A. McGarry 268

Informal Discussion
P. L. Castro, Chairman; E. H. Nicollian, Vice-Chairman

8:00 Informal Discussion on Computer Controlled IC Processing and Monitoring

ELECTRONICS
Defects in Silicon
Reactions and Diffusion
A. Reisman, Chairman; R. A. Craven, Vice-Chairman
Elizabethan Room A and B, Second Floor

9:00 Point Defect Complexing in Silicon by E. Sirtl 280
9:40 A Determination of Vacancy and Self-Interstitial Contributions to Dopant and Self-Diffusivities in Silicon by T. Y. Tan, F. Morehead, and U. Gosele 281
10:00 Diffusion of Impurities in Silicon and Defect Reactions by G. M. Bisio, S. De Pasquale, and P. G. Graglia 282
10:20 Ten-minute intermission

R. A. Craven, Chairman; A. Reisman, Vice-Chairman

10:30 Bore Diffusion in Heavily n-Doped Silicon by D. Tsoukalas, and P. Chenevier 283
10:50 Kinetics of Silicon Interstitial Defects from Oxidation Stacking Fault Observations by K. Taniguchi, and D. A. Antoniadis 284
11:10 Effect of Phosphorus Diffusion on Oxidation-Induced Stacking Faults by S. Matsumoto, and T. Niimi 285
11:30 Annealing of Interstitial Loops in As-Implanted Si by N. R. Wu, P. Ling, D. K. Sadana, and J. Washburn 286
11:50 Carbon Gettering in Silicon by W. E. Bailey, R. A. Bowling, and K. E. Bean 287

L. C. Kimerling, Chairman; W. M. Bullis, Vice-Chairman

Recent News Papers

2:00 Recent News Papers

III-V Opto-Electronics Epitaxy and Device Related Processes
G. Stillman, Chairman; A. SpringThorpe, Vice-Chairman
Georgian Room, Mezzanine

9:00 Theoretical Aspects of III-V Heterostructure Formation by LPE by R. Ghez 327
9:30 Unstable Region Behavior in Type $A_{1-x}B_xC_{1-y}D_y$ III-V Quaternary Solid Solutions with Short-Range Clustering by K. Onabe 328
9:50 An Experimental Investigation of the GaAs-InAs-GaP-InP Psuedo-Quaternary Phase Diagram by A. J. SpringThorpe 329
10:10 Ten-minute intermission
10:20 Experimental Studies on LPE of III-V Compound Semiconductors by E. Bauser 330
10:50 Zone-Melting Recrystallization of InSb with Planar Patterning by C. J. Keavney, H. A. Atwater, and H. I. Smith 331
11:10 Liquid Phase Epitaxy Growth of InGaAsP Double Heterostructure Laser Material by P. Besomi, R. B. Wilson, J. Degani, and R. J. Nelson 332
11:30 InGaAs Photodetector for the 1.8-2.0 Micron Region by C. B. Morrison, S. M. Bedair and K. J. Bachmann 333

D. M. Collins, Chairman; M. B. Panish, Vice-Chairman
Georgian Room, Mezzanine

2:00 The Current State of III-V Molecular Beam Epitaxy for Optoelectronics by M. B. Panish 334
2:30 Effect of Group V/III Flux Ratio on Optical and Electrical Properties of Si-Doped $Al_xGa_{1-x}As$ Grown by Molecular Beam Epitaxy by Y. Nomura, S. Naritsuka, M. Mannoh, K. Yamanaka T. Yuasa, M. Mihara, and M. Ishii 335
2:50 Ten-minute intermission
3:00 TEM Studies of Defects in MBE-GaAs by C. B. Carter 336
3:20 Growth of Single-Crystalline Epitaxial Group-II Fluorides Films on InP(001) by Molecular-Beam Epitaxy by C. W. Tu, T. T. Sheng, M. H. Read, A. R. Schlier, J. G. Johnson, W. D. Johnston, Jr., and W. A. Bonner 337

ELECTRONICS/DIELECTRICS AND INSULATION
Joint General Session
Processing
P. Rai-Choudhury, Chairman; M. Jones, Vice-Chairman
Colonial Ballroom, Mezzanine

8:40 Evidence of Surface State Induced Instability in NMOS-IGFET's and a Process for Its Suppression by P. K. Chaudhari 373
9:00 Lateral Epitaxial Growth of Si over SiO_2 Using Strip Electron Beam by Y. Hayafuji, T. Yanada, S. Usui, S. Kawado, A. Shibata, N. Watanabe, M. Kikuchi, and K. E. Williams 374
9:20 Low Voltage Programmable MNOS Process for VLSI Technology by A. El Dessouky 375
9:40 A Photoprocess and Test Results for a Two-Layer Metallization System for High Density Bipolar IC's by B. D. Ulrich, and D. L. Fehrs 376
10:00 Low Noise Bipolar Process Using Ion Implanation by T. Ajima, J. Ohshima, Y. Koshino, and T. Yonezawa 377
10:20 Base-Etched Transistor by G. R. Srinivasan, J. S. Lechaton, and S. P. Gaur 378
10:40 Aluminum Spike Problem in Bipolar IC and the Impact of Various Processing Technologies by A. Sharif 379

Silicon Reactions, Diffusion, and Silicides
H. R. Huff, Chairman; P. Marcoux, Vice-Chairman
Colonial Ballroom, Mezzanine

11:00 Annealing of Si Surfaces after Epitaxial Growth by C. H. Orner 380
11:20 The Influence of Oxygen Internal Gettering on the Quality of Epitaxial Layers by K. H. Yang, and C. Orner 381
11:40 The Effects of High Temperature Preannealing on the Formation of Oxygen Thermal Donors in Czochralski Silicon by B.-Y. Mao, J. Lagowski, and H. C. Gatos 382

ELECTRONICS DIVISION AWARD ADDRESS
R. E. Enstrom, Chairman
Colonial Ballroom, Mezzanine

2:00 Electronics Division Award Address, Kinetics and Mechanism of GaAs Vapor Phase Epitaxy by D. W. Shaw

ELECTORNICS/DIELECTRICS AND INSULATION
Joint General Session
Silicon Reactions, Diffusion, and Silicides
P. Marcoux, Chairman; H. R. Huff, Vice-Chairman
Colonial Ballroom, Mezzanine

2:40 Laser Crystallization of Silicon Films on $LiNbO_3$ by G. Goetz, M. Rivier, and A. Cserhati 383
3:00 Two-Dimensional Oxidation Mechanism in Local Oxidation Process by C.-H. Hui, and W. G. Oldham 384
3:20 Control of Staining in a High Temperature Diborane Diffusion Process by Hydrogen Injection by D. L. Meier, and P. Rai-Choudhury 385
3:40 Solid Phase Epitaxy of Amorphous Silicon Deposited over SiO_2 Windows by Y. Y. Wang, N. W. Cheung, D. K. Sadana, and M. Strattman 386

ENERGY TECHNOLOGY
Novel Photoelectrochemical Synthetic Routes
M. Wrighton, Chairman; N. N. Lichtin, Vice-Chairman
Olympic Room, Second Floor

9:00 Photoelectrochemical Reduction of CO_2 and Cleavage of H_2S: Catalytic Effects in Semiconductor Powder Suspensions and on Electrodes by A. Mackor, A. H. A. Tinnemans, and D. H. M. W. Thewissen 515
9:30 Photocatalyzed Light-Driven Reduction of CO_2 and N_2 on Semiconductor Surfaces by N. N. Lichtin and K. M. Vijayakumar 516
10:00 Reduction of CO_2 at n-Type Semiconductor Electrodes by K. W. Frese, Jr. and D. Canfield 517
10:30 Fifteen-minute intermission
10:45 Photo-Assisted Hydrogen Evolution at Platinized p-Type InP Electrodes - Effects of Methods of Platinization on the Electrode Properties by H. Tamura, H. Yoneyama, and M. Azuma 518
11:15 Water Cleavage Reaction via Polypyrrole and Ruthenium Oxide Modified CdS Photochemical Diodes by A. J. Frank and K. Honda 519

R. Memming, Chairman; M. A. Fox, Vice-Chairman

2:00 Silicon Electrodes Modified with Polymer Bound Metal Phosphine Complexes by D. L. DuBois 520
2:25 Organometallic Coatings for CdS by M. Cocivera, J. H. Reeves, and P. Szczecinski 521
2:50 Effects of Adsorbents on Photoelectrochemical Properties of MoS_2 by S. M. Ahmed 522
3:15 A Photoelectrochemical Comparison of Chloro-Gallium Phthalocyanine to Other Phthalocyanine Derivatives by C. A. Linkous and M. R. Armstrong 523
3:40 Efficient n-Type Gallium Arsenide Phosphide Anodes in Aqueous Electrolytes by N. S. Lewis and C. M. Gronet 524

ENERGY TECHNOLOGY/BATTERY/DIELECTRICS AND INSULATION
Conducting Organic Polymers in Energy Conversion and Storage
G. B. Street, Chairman; T. A. Skotheim, Vice Chairman
California West, Second Floor

9:00 The Kinetics and Properties of Doped Polyacetylene in 552

Tuesday continued

Nonqueous Electrolytic Solutions by W. H. Smyrl, S. R. Kurtz, and D. S. Ginley

9:35 Anodic Deterioration of Polyacetylene Film in Nonaqueous Electrolyte by K. Abe, F. Goto, T. Yoshida, and H. Morimoto 553

10:10 Kinetics of Electrochemical Doping and Undoping of Polyacetylene by F. G. Will 554

10:40 The Thermal and Oxidative Stability of Polyacetylene by F. G. Will 555

11:15 Solid Polymer Electrolyte Photovoltaic Cells by T. A. Skotheim, M. V. Rosenthal, and S. W. Feldberg 556

R. J. Nowak, Chairman; D. S. Ginley, Vice-Chairman

2:00 The Electrochemistry of Polyacetylene: Application in High Power Density Rechargeable Batteries by A. G. MacDiarmid, M. Aldissi, R. B. Kaner, M. Maxfield, and R. J. Mammone 557

2:40 Electrochemical Cells Based on the Reduction of Polyacetylene, Poly(p-Phenylene), and Polythiazyl by L. W. Shacklette, R. H. Baughman, and J. M. Sowa 558

3:20 An Approach to the Evaluation of Conductive Polymers for Batteries by B. L. McKinney, R. G. Burrow 559

HIGH TEMPERATURE MATERIALS
High Temperature Materials Chemistry
Electronics Materials I
R. Hiskeff, Chairman; R. A. Huggins, Vice-Chairman
Elizabethan Room C, Second Floor

9:00 Ternary Phase Equilibria Considerations in Solubility and Diffusivity Studies of Cr in GaAs by M. D. Deal and D. A. Stevenson 445

9:30 The Control and In Situ Monitoring of Oxygen in Liquid Phase Gallium Arsenide Growth by S. C. Chang and D. A. Stevenson 446

10:00 High Temperature Chemistry and Physics of Optical Fiber Fabrication by K. L. Walker and D. L. Wood 447

10:30 Fifteen-minute intermission

10:45 Spray Pyrolysis of Electronic Materials by J. B. Mooney and R. H. Lamoreaux 448

Recent News Papers

11:15 Recent News Papers

Electronic Materials II
D. A. Stevenson, Chairman; R. Hiskeff, Vice-Chairman

2:00 Relationships Exhibited Among Electrochemical, Thermodynamic, and Oxygen Potential Quantities in Lithium-Transition Metal-Oxygen Molten Salt Batteries by N. A. Godshall, I. D. Raistrick, and R. A. Huggins 449

2:30 Thermodynamic Studies of the Li-Al-Sb System by C. M. Luedecke, J. P. Doench, and R. A. Huggins 450

3:00 Ternary Alloys as Negative Electrodes in Lithium Systems by J. P. Doench and R. A. Huggins 451

3:30 Electrical Conductivity of Sulfur-Doped Stabilized Zirconia and Diffusion of Sulfur in Stabilized Zirconia by G. M. Mehrotra, A. Nakamura, and J. B. Wagner, Jr. 452

HIGH TEMPERATURE MATERIALS/PHYSICAL ELECTROCHEMISTRY/ BATTERY/ENERGY TECHNOLOGY
New Solid Electrolytes for Energy Conversion
J. Bates, Chairman; A. Hooper, Vice-Chairman
Oxford Room, Second Floor

9:00 What Factors May Increase Superionic Conductivity? by C. Delmas, A. Levasseur, M. Maazaz, J. M. Reau, and P. Hagenmuller 485

9:30 Na-Diffusion Paths and Na Potentials in NASICON by H. Kohler, and H. Schulz 486

10:00 Preparation of New Divalent Ion Conducting Beta" Aluminas by S. M. Griep, D. L. Yang, B. Dunn, B. Ghosal, and G. C. Farrington 487

10:20 Transport and Structural Properties of New Divalent Beta" Aluminas by G. C. Farrington, L. Cratty, B. Ghosal, D. L. Yang, B. Dunn, and J. O. Thomas 488

10:40 Ionic Transport in Ternary Di-Anionic Lithium Compounds by W. Weppner 489

G. C. Farrington, Chairman; R. A. Huggins, Vice-Chairman

2:00 Concentration Dependence of Ion Transport in Polymer Electrolytes by D. F. Shriver, R. Dupon, and M. Stainer 490

2:20 Fast Ion Conductors: Lithium Ionomers and Salts - Polymer Based Materials by J. R. Wasson, D. E. Bolster, and W. E. Hatfield 491

2:40 Limiting Current Effect in Poly(Ethylene Oxide) Based Solid Electrolytes by J. R. Owen, P. C. Spurdens, J. E. Shemilt, and B. C. H. Steele 492

3:00 Electrical Breakdown in Polyethylene Oxide-Based Lithium Ion Conducting Polymers by C. A. C. Sequeira and A. Hooper 493

3:20 Polymeric Electrolytes: Application to the Thermodynamics of the Lithium-Aluminum Electrode by M. Armand, B. Kapfer, A. Belanger, and M. Robitaille 494

3:40 Electrochemical Investigations of Conintercalated TiS_2 Using a Polymeric Electrolyte by W. B. Johnson and W. L. Worrell 495

INDUSTRIAL ELECTROLYTIC/CORROSION/ELECTRODEPOSITON
Anode and Cathode Materials
M. R. Tighe, Chairman; G. A. DiBari, Vice-Chairman
Victorian Room, Second Room

9:00 High Performance Electrode Materials for the Hydrogen Evolution Reaction from Alkaline Media by B. V. Tilak 584

9:30 Hydrogen Evolution Cathodes For Alkaline Electrolytes by D. E. Hall and V. R. Shepard, Jr. 585

10:00 Thermal Oxidation Effects on Nickel and Steel Cathodes by D. E. Hall 586

10:30 Five-Minute intermission

10:35 The High Rate Aqueous Anodic Oxidation of Carbonaceous Crude Fuels by R. L. Clarke, P. C. Foller, and R. J. Vaughan 587

11:05 An Electrochemical Investigation on Operational Parameters for Laminated Fuel Cell Cathodes by P. W. T. Lu 588

11:35 A Voltametric Study of the Reduction of Chromic Acid on Bright Platinum by J. P. Hoare 589

R. Alkire, Chairman; D. E. Hall, Vice-Chairman

2:00 A Protective Conducting Silica Film on n-Silicon by A. Q. Contractor and J. O'M. Bockris 590

2:30 Preparation of Transition Metal Phosphides with Varying Phosphide Contents by M. Robbins, J. T. Plewes, P. K. Gallagher, V. G. Lambrecht, and J. J. Auborn 591

3:00 Characterization of Transition Metal Phosphide Films with Varying Phosphide Contents by J. T. Plewes, M. Robbins, and R. C. Stoffers 592

ORGANIC AND BIOLOGICAL ELECTROCHEMISTRY
Mechanisms and Modeling of Electrochemical Membrane Processes
J. F. Evans, Chairman; M. Fleischmann, Vice-Chairman
Elizabethan Room D, Second Floor

9:00 Enhanced Charge Transport by Electron Exchange Between Redox Reagents Incorporated in Polymer Films by F. C. Anson and D. A. Buttry 623

9:30 Charge Transfer Reactions Involving Physically Constrained Molecules by B. S. Pons and J. F. McAleer 624

10:00 Characterization of Electrodes Coated with Polymer Networks Cross-Linked by Gamma-Irradiation by W. R. Heineman, E. S. DeCastro, D. A. Smith, D. Villarroel, and J. E. Mark 625

10:30 Ten-minute intermssion

10:40 Electron Transfer Reactions across the Polymer/Polymer Interface of Bilayer Electrodes by C. R. Leidner and R. W. Murray 626

11:10 Electrocatalysis at Modified Polysulfurnitride and Other Conducting Polymers by H. B. Mark, Jr., J. F. Rubinson, L. Laguren, K. Shenoy, D. Cunningham, and H. Zimmer 627

11:40 Photoelectrochemical Behavior of TiO_2 Pigmented Membranes by L. M. Peter and J. Li 628

R. P. Buck, Chairman; D. J. Schiffrin, Vice-Chairman

2:00 Theory of the Gated and Channelled Transfer of Ions across Lipid Membranes by P. P. Schmidt, S. Chang, and C. Korzeniewski 629

2:30 Dynamic Impedance Models for In Situ Determinations of Ion Binding and Transport Kinetics: Application to Living Cell Membranes by A. A. Pilla 630

3:00 Proton Transport in Beta" Alumina by G. C. Farrington, K. Frase, and J. Thomas 631

Recent News Papers

3:30 Recent News Papers

PHYSICAL ELECTROCHEMISTRY
The Chemistry and Physics of Electrocatalysis
M. J. Weaver, Chairman; J. O'M. Bockris, Vice-Chairman
Sir Francis Drake Hotel, Empire Room, Second Floor

9:00 Strong and Weak Overlap Reactions; Similarities and Differences by R. A. Marcus 702

9:35 Electron Transfer Through Intermediate States in Solid: Electrolyte and Solid:Solid Systems by J. Ulstrup and A. M. Kuznetsov 703

10:10 The Effect of Adsorbed Molecules on the Kinetics of Heterogeneous Electron Transfer by W. R. Fawcett 704

10:45 Ten-minute intermission

10:55 Redox Pathways. Applications in Catalysis by T. J. Meyer 705

11:30 Mechanistic Aspects of Oxygen Electrochemistry by E. Yeager, D. Scherson, and B. Simic-Glavaski 706

B. E. Conway, Chairman; L. R. Faulkner, Vice-Chairman

2:00 Potential Step Methods for the Study of the Electrocatalytic Reactions of Organic Molecules by D. Pletcher 707

2:30 Ad-Atom Coverage Studies during the Catalysis and Inhibition of Formic Acid Electro-Oxidation by Underpotential Deposition by M. Shabrang and S. Bruckenstein 708

3:00 Investigations of Adsorbed Species in Electrocatalytic Oxidations Using In Situ IR Spectroscopy by A. Bewick 709

3:30 New Approaches to Improving the Sensitivity and Generality of SERS by R. P., Van Duyne 710

Tuesday continued

Fourth International Symposium on Molten Salts
H. Oye, Chairman; G. Mamantov, Vice-Chairman
Sir Francis Drake Hotel, Franciscan Room, Mezzanine

9:00 Transition Metal Chloro Complex Formation in Room Temperature Chloroaluminate Melts by C. L. Hussey, T. B. Scheffler, and T. M. Laber 750
9:20 Prospect for Alkyl Pyridinium Chloride Aluminum Chloride Melts by C. D. Desjardins, T. Cadger, E. J. Casey, and R. S. Salter 751
9:40 Reduction of Aromatic Ketones in an Aluminum Chloride: Dialkylimidazolium Chloride Molten Salt System by R. Herzog and G. T. Cheek 752
10:00 Organic Reactions in Low Melting Chloroaluminate Molten Salts by J. A. Levisky, J. L. Pflug, and J. S. Wilkes 753
10:20 Ten-minute intermission
10:30 A Survey of the Electrochemistry and Spectroelectrochemistry of Some Arenes in $SbCl_3$-Rich Room Temperature Melts by D. M. Chapman, M. Sorlie, G. P. Smith, C. Petrovic, and G. Mamantov 754
10:50 Use of $AlCl_3$-Containing Molten Salts for Carbonization as Solvent and Catalyst by E. Ota and S. Otani 755

Recent News Papers

11:10 Recent News Papers

R. Osteryoung, Chairman; V. Maroni, Vice-Chairman

2:00 Influence of Redox and Lewis Acid Functions of $SbCl_3$-Rich Molten Salt Catalysts on the Reactions of Coal Model Compounds by A. C. Buchanan III, A. S. Dworkin, and G. P. Smith 756
2:40 Reactivity of Anthracene in a Novel Antimony Trichloride-Rich Room-Temperature Melt by S. P. Zingg, A. S. Dworkin, M. Sorlie, D. M. Chapman, A. C. Buchanan III, and G. P. Smith 757
3:00 Interaction Between Aromatics and Molten or Supported Zinc Chloride by M. Morita, K. Hirosawa, T. Sato, and K. Ouchi 758
3:20 Kinetics of Organic Substitution Reactions in Molten Acetate and Thiocyanate Salts by T. I. Crowell, E. H. Braue, Jr., and P. S. Hillery 759
3:40 Reactions of Ethane, Chloroethane, and Chloroethene with Chlorine in Molten Salts by M. Sorlie, P. G. Wahlbeck, and H. A. Oye 760

General Session
N. E. Vanderborgh, Chairman; W. Vielstich, Vice-Chairman
Sir Francis Drake Hotel, Tudor Room, Second Floor

9:00 On the Limitations of Stationary Methods for the Study of Fast Electrode Reactions by W. Vielstich 815
9:25 Information Sources for Electrochemistry by C. W. Moulton and H. D. Hannan 816
9:50 Proton and Water Transport Through SPE Membranes by N. E. Vanderborgh and T. Springer 817
10:15 Fifteen-minute intermission
10:30 Electrochemical and Radiotracer Study of Iron Electrode in CO_2 Saturated Neutral Electrolytes by A. Wieckowski, E. Ghali, M. Szklarczyk, and J. Sobkowski 818
10:50 Electrochemical Reduction of Ag_2CrO_2 in $LiClO_4$-PC Electrolyte by J.-Q. Wang and Y.-H. Sun 819
11:10 Effects of Chloride Ion Adsorption on Oxide Film Formation at Pt Electrodes as a Function of pH by C. Vielma, B. Scharifker, and J. Mozota 820
11:30 Behavior of Superacid Electrolytes in Fuel Cells by R. Atanasoski, W. O'Grady, and H. Olender 821

J. G. Gordon, Chairman; J. McBreen, Vice-Chairman

2:00 Effect of Rhodamine-B on Pb Electrodeposition on Ag and Cu by J. C. Farmer and R. H. Muller 822
2:20 Nucleation of Pb Electrodeposits on Ag and Cu by J. C. Farmer and R. H. Muller 823
2:40 Electrocrystallization of Zinc from Concentrated Zinc Solid Electrolytes by J. McBreen and E. Gannon 824
3:00 Study of Model Zinc Electrode Pores in Alkaline Electrolyte by J. H. Flatt, F. R. McLarnon, and E. J. Cairns 825
3:20 XPS and Electrochemical Characterization of Copper Electrodes in Aqueous Base by J. G. Gordon II and W. Kautek 826
3:40 Double-Layer Structure of Polycrystalline Electrodes by D. Larkin 827

Wednesday, May 11, 1983

12:15 P.M. Energy Technology Group Luncheon and Business Meeting, The City Club, Twelfth Floor, St. Francis Hotel
12:15 P.M. Industrial Electrolytic Division Luncheon and Business Meeting, Monterey Room, Second Floor, Sir Francis Drake Hotel
12:15 P.M. Organic and Biological Electrochemistry Division Luncheon and Business Meeting, Italian Room, Mezzanine, St. Francis Hotel

BATTERY
Cell Testing and Reliability
D. F. Untereker, Chairman; P. M. Skarstad, Vice-Chairman
Borgia Room, Mezzanine

9:00 Accelerated Testing of Batteries for an Implantable Insulin Pump by S. C. Levy, and C. C. Crafts 26
9:15 Determining the Reliability of Lithium/Iodine Pacemaker Cells Using a Life Test Sample by R. C. Stinebring, C. F. Holmes, and M. M. Safford 27
9:30 Design Testing and Reliability of Lithium-Iodine Pacemaker Batteries by W. D. Helgeson 28
9:45 Fifteen-minute intermission
10:00 Reliability of Glass Insulators in Lithium Ambient Batteries by C. Nelson, and B. C. Bunker 29
10:20 Glass Corrosion of Battery Headers in Ambient Temperature Lithium Batteries by B. C. Bunker, and C. Nelson 30
10:40 End-of-Life Testing of Lithium/Cupric Sulfide Cells - Battery Packs Designed with Mismatched Cells by D. Bump, H. Tataria, A. Nolton, and A. DeHaan 31
11:00 Elucidation of Current Drain History in Depleted Li/CuS Cells by D. L. Hart 32

Cell Design and Optimization
B. B. Owens, Chairman; S. C. Levy, Vice-Chairman
Borgia Room, Mezzanine

11:20 Lithium/Cupric Sulfide - Cell Design and Optimization by H. Tataria, D. Bump, and A. DeHaan 33
11:40 Development of MnO_2/Li Cells for Implantable Artificial Ear by H. Ikeda 34

H. J. Saxton, Chairman; S. C. Levy, Vice-Chairman

2:00 Lead Acid Maintenance Free Battery with Improved Storage Life by T. Palanisamy, and D. Cipris 35
2:20 A "Precharged" Positive Plate for the Lead-Acid Automotive Battery. I. Positive Plate Allowing Direct Incorporation of PbO_2 by E. J. Taylor, G. Shia, and D. T.Peters 36
2:40 A "Precharged" Positive Plate for the Lead-Acid Automotive Battery. II. Effect of various PbO_2 Types and Past Formulations of Precharged Positive Plate Peformance by E. J. Taylor, G. Shia, and D. T.Peters 37
3:00 Silver-Zinc Cell Design - A Survey by A. S. Berchielli 38
3:20 Physical Design Optimization of the Fiber Composite Nickel Plaque by W. A. Ferrando, W. W. Lee, and R. A. Sutula 39
3:40 High Efficiency Nickel Electrode by A. H. Zimmerman 40
4:00 Electrolyte Manifold Design for Batteries by J. B. Riggs 41
4:20 Zinc-Bromine Battery Design and Optimization - Decoupling of Hydraulic and Shunt Considerations by P. Grimes, R. Bellows, H. Einstein, E. Kantner, P. Malachesky, and K. Newby 42
4:40 Thermal Modeling of a Flowing Electrolyte Li/$SOCl_2$ Battery by D. W. Ernst 43

CORROSION
General Session
D. D. MacDonald, Chairman; R. A. Oriani, Vice-Chairman
Yorkshire Room, Second Floor

9:00 An Electrochemical Technique for Measuring Residual Stresses in Inconel 600 Tubes by R. Bandy, and T. Zemanian 78
9:20 The Open-Circuit Potential of Oxidized and Hydrided TiCode-12 by Y. J. Kim, Y. K. Hong, and R. A. Oriani 79
9:40 The Electrochemical Behavior of Aluminum Containing Al-Fe-Si Particles in Hydrochloric Acid by C. D. S. Tuck 80
10:00 Cathodic Protection of Above-Ground Structures by a Sparse Zinc Coating by P. J. Sides, and D. C. Prieve 81
10:20 Ten-minute intermission
10:30 Corrosion of Thin Film Cobalt Alloys in Variable Relative Humidity Atmospheres by R. R. Dubin, and K. D. Winn 82
10:50 Development of Protective Systems for Metallic Canisters by L. Gruss, and S. Kolodzey 83
11:15 Influence of Impurities on the Corrosivity of Industrial Phosphoric Acid by M. El Safty, F. Dabos, and N. Bui 84
11:40 Electrode Modification for Corrosion Control in FeS Electrodes by J. A. Smaga, and J. E. Battles 85

DIELECTRICS AND INSULATION/ELECTRONICS
Silicon Nitride Thin Insulating Films
Materials and Processing
H. J. Stein, Chairman; R. A. Turi, Vice-Chairman
California West, Second Floor

9:00 Introductory remarks
9:05 Materials Analysis of Silicon Nitride by P. S. Peercy and H. J. Stein 101
9:40 Materials Processing for MNOS Nonvolatile Memories by J. A. Topich 102
10:20 Compositional Depth Profiling of Silicon Nitride Interfaces by J. A. Wurzbach 103

R. A. Turi, Chairman; H. J. Stein, Vice-Chairman

11:00 Effects of Annealing in Different Ambients on the Hydrogen and Charge Distributions in CVD-Silicon Nitride Films by H. E. Maes, and J. Remmerie 104
11:20 The Physical Properties of LPCVD Si-N Films by P. Pan, I. Assur, W. Berry, and S. Burton 105

Wednesday continued

11:40 High-Temperature Hydrogen Anneal of MNOS Structures by H. E. Maes and G. Schols 106

Compoung Semiconductors - Plasma Nitrides
D. J. Connolly, Chairman; W. D. Brown, Vice-Chairman

2:00 Introductory remarks
2:05 Silicon Nitride Films on GaAs by F. L. Schuermeyer 107
2:40 Plasma Deposition of Silicon Nitride and Boron Nitride Films for Encapsulated Annealing of Implanted GaAs by G. J. Valco, and V. J. Kapoor 108
3:00 Plasma Deposited Nitride Films on GaAs and InP by D. C. Liu and V. J. Kapoor 109
3:20 One-Micron Lateral Diffusion of Beryllium Ion-Implanted Junctions in GaAs Using Si_3N_4 Encapsulation by P. M. Campbell and B. J. Baliga 110

W. D. Brown, Chairman; D. J. Connolly, Vice-Chairman

3:40 Comparison of Laser and Plasma Assisted Deposition of Silicon Nitride by W. H. Ritchie, W. Metz, P. K. Boyer and G. J. Collins 111
4:00 Physical and Electrical Properties of Plasma Deposited Silicon Nitride Films by T. E. Nagy, C. D. Fung, and W. H. Ko 112
4:20 Studies of Nitrogen Plasma in the Silicon Nitride Deposition Reaction by C. Y. Yang 113
4:40 Comparative Study of Plasma Enhanced Chemically Vapor Deposited (PECVD) Silicon Nitride Films for IC Passivation by H. E. Maes, G. L. Heyns, H. Loos, H. Pauwels, and A. Van Calster 114
5:00 Effect of Frequency on Plasma SiN Deposited in a Parallel Plate Radial Flow Reactor by F. Martinet and G. Quegan 115

Fourth Symposium on Plasma Processing
Plasma Induced Damage
G. Smolinsky, Chairman; M. F. Leahy, Vice-Chairman
Grand Ballroom, Mezzanine

9:00 Heavy Metal Contamination Caused by Reactive Sputter Etching by Y. Kawamoto 171
9:20 The Effect of Chamber Configurations and Bias Voltages on Damage Induced in Si by Reactive-Ion Etching by S. W. Pang, C. M. Horwitz, D. D. Rathman, S. M. Cabral, D. J. Silversmith, and R. W. Mountain 172
9:40 Solving the Problem of High Contact Resistance Observed in Reactive Ion Oxide Etching by J. S. Chang 173
10:00 Characterization of Post-RIE Damage Removal Techniques by C. M. Ransom, T. I. Chappell, A. Sugerman, R. S. Bennett, and L. Ephrath 174
10:20 Modification of Schottky Barriers in Silicon by Reactive Ion Etching in NF_3 Gas Mixtures by T. P. Chow, and S. Ashok 175
10:40 Twenty-minute intermission

Etching of Organics

11:00 Hydrogen-Plasma Etching of Organic Films by F. Robb 176
11:20 Dry Etching of Polyimide in O_2-CF_4 and O_2-SF_6 Plasmas by G. Turban, and M. Rapeaux 177
11:40 Via Profiling in Polyimide for a 3 Micron CMOS Array by C. J. Heslop, S. J. Wright, R. E. Hine, M. Gill, and A. Belka 178

Etching of Organics
R. D. Rust, Chairman; R. S. Horwath, Vice-Chairman

2:00 Plasma Etching of Vias in Polyimide Using Nonerodible Masks by T. O. Herndon, W. J. Landoch, and R. L. Burke 179
2:20 Application of Emission Spectroscopy for Profile Control during Oxygen RIE of Thick Photoresist by B. R. Soller, R. F. Shuman, and R. R. Ross 180
2:40 Plasma Photoresist Stripping: Variation in Mobil Ion Contamination across Wafer Diameter by D. Summers 181
3:00 Twenty-minute intermission

Printed Circuit Boards

3:20 Plasma Processing in the Printed Circuit Industry by R. D. Rust 182
3:40 The Mechanism of Plasma Etching of Multilayer Boards by A. A. Parker, R. J. Pachter, and R. D. Rust 183
4:00 Unique Reactor Geometry for Plasma Removal of Epoxy Smear in Multilayer Printed Wiring Boards by R. J. Rhodes 184
4:20 Polymer Interlayer Adhesion Enhancement Through Plasma Surface Modification by R. H. Wheater, F. Emmi, R. F. White, W. D. Bingle, and R. S. Horwath 185
4:45 Dielectrics and Insulation Division - Informal Idea Exchange Mixer. Meet, exchange ideas, discuss future plans with the Officers and Executive Committee of the Division.

DIELECTRICS AND INSULATION/ELECTRONICS/CORROSION/
HIGH TEMPERATURE MATERIALS/ENERGY TECHNOLOGY
Materials and New Processing Techniques for Photovoltaics
J. A. Amick, Chairman; V. K. Kapur, Vice-Chairman
California East, Second Floor

9:00 Recent Status of Solar Photovoltaic R&D in Japan by Y. Hamakawa 203
9:45 State of Photovoltaics Technology in the European Community by R. J. Van Overstraeten 204
10:30 Five-minute intermission
10:35 Photovoltaics in the U.S. by H. Ehrenreich 205
11:20 Compound Semiconductor Thin Films: A Solar Cell Research Opportunity by C. F. Gay and V. K. Kapur 206

R. R. Addis, Chairman; A. Sanjurjo, Vice-Chairman

2:00 Advances in the Refining of MG-Silicon by J. Dietl 207
2:35 Solar Cells from High-Purity Arc-Furnace Silcon by L. P. Hunt et al. 208
2:55 Boron and Phosphorus Determination in Low-Resistivity Solar-Grade Silicon by L. P. Hunt, R. W. Francis, and J. P. Dismukes 209
3:15 Ten-minute intermission
3:25 Rice Hulls as a Raw Material for Producing Silicon by L. P. Hunt, J. P. Dismukes, J. A. Amick, K. Larsen, and A. Schei 210
3:45 Silicon Electrorefining and the Transport Properties of Cu_3Si by J. M. Olson 211
4:20 Aerosol Reactor for Silicon Production by M. K. Alam and R. C. Flagan 212
4:40 Status and Potential of the EFG Technology for Low Cost Photovoltaics by K. V. Ravi 213

Phenomena and Crystal Growth
J. Mikkelsen, Chairman; W. T. Stacy, Vice-Chairman
Elizabethan Room A and B, Second Floor

9:00 Oxygen Aggregation and Diffusivity in Silicon by M. Stavola 288
9:40 Oxygen in Silicon by W. C. O'Mara 289
10:00 Photoluminescence Study of Oxygen Related Donors in Silicon by R. W. Shaw and R. A. Craven 290
10:20 Ten-minute intermission

W. T. Stacy, Chairman; J. Mikkelsen, Vice-Chairman

10:30 Local Phonon Mode Calculations for Point Defects in Si by R. J. Hauenstein, R. M. Feenstra, and T. C. McGill 291
10:50 Isotope Shifts of the P,Q,R Lines in Indium-Doped Si by T. E. Schlesinger, and T. C. McGill 292
11:10 Bulk Properties Improvement of CZ Silicon from Large Melts by Thermal Convective Flow Control by G. Fiegl 293
11:30 Defect Control for Silicon Epitaxial Processes Using Silane, Dichlorosilane, and Silicon Tetrachloride by H. R. Chang 294
11:50 Defect Reduction by Dichlorosilane Epitaxial Growth by S. B. Kulkarni 295

Defects in Silicon
Characterization
C. W. Pearce, Chairman; J. Das, Vice-Chairman
Elizabethan Room A and B, Second Floor

2:00 Precise and Rapid Measurement of Oxygen and Carbon Concentrations in Silicon by K. Krishnan 296
2:20 Characterization of Back Surface Damaged Wafers by Fourier Transform Infrared Spectroscopy by A. Baghdadi 297
2:40 Reproducibility of Oxygen and Carbon Determinations in Silicon from IR Absorbance Measurements by W. M. Bullis and W. C. O'Mara 298
3:00 The Effect of Striations on Compositional Analysis by R. A. Forman, M. I. Bell, S. Mayo, and A. H. Kahn 299
3:20 Conversion Coefficient for IR Measurement of Oxygen in Si by T. Iizuka 300
3:40 Ten-minute intermission

J. Das, Chairman; C. W. Pearce, Vice-Chairman

3:50 Improved Analysis Procedures for Deep-Level Measurements by Transient Capacitance by W. E. Phillips, W. R. Thurber, and J. R. Lowney 301
4:10 The Characterization of Heteroepitaxial Silicon by the Surface Photovoltage Technique: Improved Properties Resulting from Implant-Damage and Solid-State Regrowth by J. Lagowski, L. Jastrzebski, M. T. Duffy and G. W. Cullen 302
4:30 The Effects of Pressure, Temperature, and Time on the Annealing of Ionizing Radiation Induced Insulator Damage in N-Channel IGFET's by A. Reisman and C. J. Merz 303

III-V Opto-Electronics Epitaxy and Device Related Processes
M. Ludonise, Chairman; G. Stringfellow, Vice-Chairman
Georgian Room, Mezzanine

9:00 The Growth of III-V Compound Semiconductors by Metalorganic Chemical Vapor Deposition by R. D. Dupuis 338
9:30 OMVPE Growth of GaP, InP, and GaInP by C. C. Hsu, and G. B. Stringfellow 339
9:50 Preparation of Device Quality GaAs Using Plasma Enhanced Mo-CVD Technique by K. P. Pande, and A. Seabaugh 340
10:10 Ten-minute intermission
10:20 GaAs Millimeter Wave Mixer Diodes Grown by MOCVD by R. W. Glew and M. J. Sisson 341
10:40 Emission Spectra of Doped ZnSe Grown Epitaxially on GaAs by Organometallic Chemical Vapor Deposition by T. N. Chin 342
11:00 X-Ray Diffraction and Doping Studies of Strained-Layer Superlattices Grown by Metal Organic Chemical Vapor Deposition by R. M. Biefeld, G. C. Osbourn, P. L. Gourley, and I. J. Fritz 343

Wednesday continued

H. M. Cox, Chairman; B. W. Wessels, Vice-Chairman

2:00 Epitaxial Growth of InGaAs by the VPE-Hydride Technique Using a Ga-In Alloy As Source by T. E. Erstfeld and K. P. Quinlan 344
2:20 Growth and Characterization of High Purity VPE InP Prepared by the Hydride Process by B. W. Wessels, S. Y. Sun, and C. A. Adams 345
2:40 Morphological Study of Thermal Decomposition of InP Surfaces by S. N. G. Chu, C. M. Jodlauk, and W. D. Johnston, Jr. 346
3:00 Ten-minute intermission
3:10 Vapor Phase Deposition of Single Crystal GaAs Using the AsH_3-Ga-HCl Process by A. R. Sears, P. Menditto, and P. M. Campbell 347

Recent News Papers

3:30 Recent News Papers

Informal Discussion

S. Mahajan, Chairman

8:00 Informal Discussion on Future Choices for III-V Opto-Electronics Epitaxy

ELECTRONICS/DIELECTRICS AND INSULATION
Joint General Session
Silicon Reactions, Diffusion, and Silicides
P. L. Castro, Chairman; G. W. Cullen, Vice-Chairman
Colonial Ballroom, Mezzanine

9:00 Diffusion of Implanted Phosphorus in Polysilicon by D. L. Losee, J. P. Lavine, S. T. Lee, C. M. Jarman, and E. A. Trabka 387
9:20 Diffusion of Pd and Si Through Pd_2Si by E. C. Zingu, R. Pretorius, C. Comrie, and J. W. Mayer 388
9:40 A Comparative Study of Molybdenum Silicide Formation by F. Arnaud, D'Avitaya, G. Bomchil, and C. Arena 389
10:00 Oxygen Control and Intrinsic Gettering in CZ Silicon by R. B. Swaroop, and T. Fish 390
10:20 Short Time Annealing of Coevaporated Tungsten Silicide Films by T. O. Sedgwick, F. M. d'Heurle, and S. A. Cohen 391
10:40 Low Temperature Diffusion of Arsenic in Polycrystalline Silicon Films by M. Arienzo, Y. Komen, A. E. Michel, and R. H. Kastl 392

Measurement and Analysis

11:00 Accelerated Testing for Silicon Dioxide Breakdown by W. Weick 393
11:20 Charge Tunneling and Trapping and Trap Generation in Thin SiO_2 by C. Chang, M. S. Liang, C. Hu, and R. W. Brodersen 394
11:40 Generalized Technique for Measuring Specific Contact Resistance by D. L. Meier and P. Rai-Choudhury 395

G. W. Cullen, Chairman; P. L. Castro, Vice-Chairman

2:00 A Novel Method for Measuring Low-Dose Implants by M. J. Markert, D. S. Perloff, and E. Lee 396
2:20 Scanning Auger Microscopy for Surface Potential Profiling of HV Devices by D. M. Taylor, D. W. Tong, and W. R. Van Dell 397
2:40 Structural Analysis of Silicon Implanted Polymethyl Methacrylate Films on Glass by C. E. Bleil and B. A. MacIver 398
3:00 A Rapid Method of Sampling Polycrystalline Silicon for Determination of Phosphorus, Boron, Arsenic, and Alumium by Photoluminescence Analysis by W. F. Tucker, L. C. Winterton, P. L. Clem, Jr. and B. D. Stone 399
3:20 A Comparison of Donor and Acceptor Levels in Silicon as Determined by Infrared and Photluminescence Analyses by L. Shive and H. Mollenkopf 400
3:40 Relation Between Two-Probe and Four-Probe Resistances on Nonuniform Structures by H. L. Berkowitz and J. Albers 401
4:00 Terminator Open-Short Reliability Testing by S. Carbone, J. Granada, and A. Sarkhel 402
4:20 Infrared Studies of Silicon by D. G. Mead 403

HIGH TEMPERATURE MATERIALS
High Temperature Materials Chemisty
Evaporation and Decomposition
G. M. Rosenblatt, Chairman; A. W. Searcy, Vice-Chairman
Elizabethan Room C, Second Floor

9:00 Catalytic Effects in the Decomposition Behavior of Metal Sulfates by R. D. Brittain and D. L. Hildenbrand 453
9:30 Metastable Equilibrium in a Calcite Powder Bed by A. W. Searcy, D. Beruto, and M. G. Kim 454
10:00 The Determination of Carbon Thermochemical Properties by Laser Vaporization by R. L. Baker, M. A. Covington, and G. M. Rosenblatt 455
10:30 Laser Pulse Vaporization of Uranium Dioxide by C.-H. Tsai and D. R. Olander 456
11:00 Evaporation in the Presence of an Electrical Field by Z. A. Munir 457
11:30 The Relationship Between the Vaporization of Atoms and Electrons by E. Storms 458

Metal - Gas Reactions I
G. H. Meier, Chairman; J. B. Wagner, Jr., Vice-Chairman

2:00 Acoustic Emission Studies of High Temperature Oxidation by R. A. Perkins and G. H. Meier 459
2:25 The Use of Laser Raman Spectroscopy to Study the Hot Corrosion of Ni-Cr Alloys by J. J. Truhan and R. E. Benner 460
2:50 In Situ Oxidation of Iron at High Temperatures by T. L. Jungling and R. A. Rapp 461
3:15 The Affect of Hafnium on High Temperature Oxidation Resistance by J. G. Smeggil 462
3:40 Oxidation of Nickel Sulfides in Oxygen by G. M. Mehrotra, V. B. Tare, and J. B. Wagner, Jr. 463
4:05 Reaction of Nickel with SO_2 at Elevated Temperatures by W. L. Worrell and N. Jacobson 464
4:30 Effect of the Amount of Na_2SO_4 on the High Temperature Corrosion of U700 by A. K. Misra and F. J. Kohl 465

HIGH TEMPERATURE MATERIALS/PHYSICAL ELECTROCHEMISTRY/
BATTERY/ENERGY TECHNOLOGY
New Solid Electrolytes for Energy Conversion
L. C. DeJonge, Chairman; W. Johnson, Vice-Chairman
Oxford Room, Second Floor

9:00 Electrochemical Studies of the Conuctivity in Oxide-Doped CaF_2 by W. Weppner and T. L. Wen 496
9:20 Electrochemical Investigation of Electrode Processes on $PbSnF_4$ Electrolyte by E. Siebert and J. Fouletier 497
9:40 Ceramic-Metal Solid Electrolytes by R. J. Lauf and J. B. Bates 498
10:00 Adaptation of a Network Analyzer for Four-Point A-C Electrical Measurements of Ionic Conductors by J. B. Bates, N. J. Dudney, and S. M. Casey 499
10:20 D-C Polarization Measurements on Lithium Silicate-Based Solid Electrolytes by R. F. Aspandiar, I. D. Raistrick, and R. A. Huggins 500
10:40 Re-Examination of Beta-Alumina Doped with Chromium Using Photo-Acoustic Spectroscopy by J. H. Kennedy and A. M. Schuler 501
11:00 Use of Ca-β"-Alumina as a Solid State Electrolyte by E. E. Hellstrom 502
11:20 Fast Proton Conductivity in $H_3OTi_2NbO_7.H_2O$ by C. Schuler 503

INDUSTRIAL ELECTROLYTIC
Science and Engineering of Membranes and Separators
R. L. Dotson, Chairman; R. E. White, Vice-Chairman
Essex Room, Second Floor

2:00 Introductory remarks
2:05 A Simple Model of a Diaphragm-Type Chlorine Cell by R. E. White, J. S. Beckerdite, and J. Van Zee 560
2:30 A Simple Model of a Diaphragm-Type Chlorine/Caustic Cell with Acidified Brine Feed by J. Van Zee and R. E. White 561
2:55 Transport in a Chloroalkali Diaphragm by R. R. Chandran, D-T. Chin, and K. Viswanathan 562
3:20 Ten-minute intermission
3:30 Transport Through Charged Porous Membranes by G. B. Westermann-Clark 563
3:55 Influence of Cell Parameters on the Current Efficiency of a High Performance Chlor-Alkali Membrane by H. L. Yeager and J. D. Malinsky 564

LUMINESCENCE AND DISPLAY MATERIALS
Display Technology
S. Hackwood, Chairman; P. N. Yocom, Vice-Chairman
Victorian Room, Second Floor

9:00 Introductory remarks 593
9:05 Electrochemical Displays by G. Beni 594
9:55 Photoelectrochromism of Prussian Blue Films by A. Viehbeck and D. W. DeBerry
10:20 Ten-minute intermission
10:30 Improved Electrochromic Properties of Flash Evaporated High Density Tungsten Oxide Layers by P. Schlotter and L. Pickelmann 595
10:55 Spectroelectrochemical Properties of Polyheterocycles - Application to Electrochromic Display Devices by M. Gazard, J. C. Dubois, M. Champagne, F. Garnier, and G. Tourillon 596
11:20 Rapid Anisotropic Diffusion of Lithium in Electrochromic $Li_yK_xWO_3$ by S.-K. Joo, I. D. Raistrick, and R. A. Huggins 597

P. N. Yocom, Chairman; S. Hackwood, Vice-Chairman

2:00 Introductory remarks
2:05 Optimization of Electrochromics for Complex Displays by D. J. Barclay, C. L. Bird, A. C. Lowe, and D. H. Martin 598
2:40 Liquid Crystal Technology - A Review by G. J. Sprokel 599
3:15 Electrical Control of the Hysteresis Behavior in A-C Thin-Film Electroluminescent Devices by K. W. C. Yang and S. J. T. Owen 600

ORGANIC AND BIOLOGICAL ELECTROCHEMISTRY
Mechansims and Modeling of Electrochemical Membrane Processes
F. M. Hawkridge, Chairman; W. R. Heineman, Vice-Chairman
Elizabethan Room D, Second Floor

9:00 Adsorbed Proteins in Simulating Membrane Process by J. Haladjian and P. Bianco 632
9:30 An Electrochemical Investigation of the Reaction of Cytochrome c with Mitochondria and Models Thereof by F. A. Armstrong, H. A. O. Hill, and N. J. Walton 633

Wednesday continued

10:00 Electron Transfer Properties of Immobilized Cytochrome c by M. A. Schafer and G. S. Wilson 634
10:30 Ten-minute intermission
10:40 Photosynthetic Oxidation of Water to Dioxygen in Chloroplast Membranes by K. Sauer and J. L. Casey 635
11:10 Direct Observation by Laser Flash Photolysis of Light-Induced Electron Transfer Within and Across Chlorophyll-Containing Lipid Bilayer Vesicle Membranes by G. Tollin, W. E. Ford, and Y. Fang 636
11:40 Simularities in the Redox Behavior of Two Flavoprotein Oxidase Enzymes by M. Stankovich 637

Structure and Reactivity in Organic Chemistry and Electrochemistry
M. D. Hawley, Chairman; H. Lund, Vice-Chairman

2:00 Ring Forming Reactions Using Electrochemical and Nonelectrochemical Methods. II. Electrochemical Conversion of Secondary Nitroalkanes to Ketones by R. D. Little, M. M. Baizer, S. T. Nugent, W. T. Monte, and L. Moens 638
2:40 Cathodic Processes in Solutions Containing CO_2 and Aromatic Hydrocarbons by E. R. Gonzalez, L. A. Avaca, and E. A. Ticianelli 639
3:10 A Tetraalkylammonium Amalgam by E. Kariv-Miller and C. Nanjundiah 640
3:40 Mechanism of the Decomposition of Benzoate Ester Radical-Anions by J. H. Wagenknecht, R. D. Goodin, P. J. Kinlen, and F. E. Woodard 641
4:10 Relationship Between Electrochemical and Chemical Oxidation of Organic Sulfur Compounds by W. K. Musker 642

Ions and the Electrochemical Control of Cell Functions
A. Boynton, Chairman; A. A. Pilla, Vice-Chairman
Olympic Room, Second Floor

9:00 Molecular Considerations Relevant to the Mechanism of Active Transport by J. Kyte 659
9:30 Monoclonal Antibodies, Ion Flux Regulation, and the Control of Hepatocyte Proliferation by H. L. Leffert, K. S. Koch, D. Schenk, P. Shapiro, H. Skelly, and M. Schumaker 660
10:00 Is "Turned-On" (Na^++K^+) - ATPase of Mouse Embryonic Fibroblasts Secondary to Activation of a Protein Kinase by C. E. Wenner and K. J. Leister 661
10:30 Ten-minute intermission
10:40 Induced Pulsating Currents Affect Membrane Bound Enzyme Kinetics: Application to Na-K ATPase Using a New Flow System by A. A. Pilla, K. Gary, and C. Mayaud 662
11:10 Intracellular pH and Control of Cellular Proliferation by R. J. Gillies 663
11:40 Microenvironmental Changes Associated with Electrical Stimulation of Osteogensis by Direct Current by T. J. Baranowski, Jr., J. Black and C. T. Brighton 664

A. A. Pilla, Chairman; A. L. Boynton, Vice-Chairman

2:00 Why Use Ions to Regulate Cells? by R. A. Steinhardt 665
2:30 The Role of Electrogenic Sodium Transport in Early Embryonic Development by C. D. Stern 666
3:00 How a Transient Rise in Calcium Causes Activation of the Egg at Fertilization by D. Epel and M. Poenie 667
3:30 Ten-minute intermission
3:40 Injury, Electrical Fields, and Regeneration by R. B. Borgens 668
4:10 The Transducer System Activated by Nerve Growth Factor (NGF) by K. H. Pfenninger 669

PHYSICAL ELECTROCHEMISTRY

The Chemistry and Physics of Electrocatalysis
S. Bruckenstein, Chairman; A. T. Hubbard, Vice-Chairman
Sir Francis Drake Hotel, Empire Room, Second Floor

9:00 Influence of Crystallographic Orientation on the Electrochemical Properties of Some sp Metals by A. Hamelin 711
9:35 Electrocatalysis by Ad-Atoms by S. Motoo 712
10:10 Ten-minute intermission
10:20 Clusters and Surfaces in Catalysis by E. L. Muettepties 713
10:55 Determination of the Structure of Dispersed Metal Catalysts by the EXAFS Technique by F. W. Lytle, R. B. Greegor, E. C. Marques, D. R. Sandstrom, G. H. Via, and J. H. Sinfelt 714
11:30 Microstructure of Highly Dispersed Pt Cataylsts and the Relation to Activity for Oxygen Reduction by P. N. Ross, Jr. 715

The Chemistry and Physics of Electrocatalysis
R. A. Osteryoung, Chairman; E. J. Cairns, Vice-Chairman

2:00 Introductory remarks by R. A. Osteryoung

D. C. Grahame Award Address

2:10 D. C. Grahame Award Address, Adventures in Electrocatalysis: Acceleration of Electrode Reactions by Adsorbed Ions, Molecules, or Polymers by F. C. Anson 716

The Chemistry and Physics of Electrocatalysis

3:00 Ten-minute intermission
3:10 The Kinetics of Electron Transfer Reactions in and at Films of Electroactive Polymers by C. R. Leidner, R. H. Schmehl, P. Pickup, and R. W. Murray 717
3:45 Luminescence as a Means for Probing Model Electrocatalytic Systems In Situ by L. R. Faulkner, J. S. Pflug, and W. R. Seitz 718
4:20 Influence of Specific Reactant-Surface Interactions upon Electrochemical Reactivity by M. J. Weaver 719

Fourth International Symposium on Molten Salts
R. A. Huggins, Chairman; K. H. Stern, Vice-Chairman
Sir Francis Drake Hotel, Franciscan Room, Mezzanine

8:30 Molten Salt Batteries by E. J. Cairns 761
9:10 A Review of the Chemistry of Rechargeable Molten Salt Cells by G. Mamantov 762
9:50 Alkali Nitrite Molten Salt for Use in Intermediate Temperature Lithium Cells by J. Poris, I. D. Raistrick, and R. A. Huggins 763
10:10 Molten Onium Polyiodide Salt - Iodine Cathode Materials in Lithium Cells by P. M. Skarstad, T. G. Hayes, B. B. Owens, J. B. Phipps, and D. F. Untereker 764
10:30 Ten-minute intermission
10:40 Thermal Behavior of the Potassium-Sulfur Electrolyte in Advanced Battery Concepts by G. J. Janz and D. J. Rogers 765
11:00 Ceramic Oxides as Container/Current Collector Materials for the Sulfur Electrode by R. P. Tischer, H. Wroblowa, G. M. Crosbie, and G. J. Tennenhouse 766
11:20 Solubility of Li_2S in LiF-LiCl-LiBr Electrolyte: Measurements and Calculations by Z. Tomczuk, D. R. Vissers, and M. L. Saboungi 767
11:40 Electrolytic LiCl Precipitation from LiCl-KCl Melt in Porous Anodes by C. E. Vallet, D. E. Heatherly, J. Braunstein, and L. Heatherly 768

D. Inman, Chairman; K. E. Johnson, Vice-Chairman

2:00 Spectroscopic Studies of Solutions of Transition Metal Ions in Molten Alkali Metal Carboxylates by V. A. Maroni and M. L. Maciejewski 769
2:20 Spectroelectrochemistry of Molten Salts with an OMA-2 Optical Multichannel Analyzer by G. P. Smith, M. Sorlie, and S. P. Zingg 770
2:40 On the Thermodynamic Characteriestics of Water in Hydrated Melts of Magnesium Chloride by H. H. Emons and W. Voigt 771
3:00 Electroactivity of Water in Nitrate Melts: New Results and Remarks on Recent Literature Findings by P. G. Zambonin, E. Desimoni, F. Palmisano, and L. Sabbatini 772
3:20 The Behavior of Water in Molten Salts by U. M. Twardoch and S. H. White 773
3:40 Vapor Pressures of Hydrate Melts Containing Lithium Nitrate and Alkali Nitrites by T. B. Tripp 774
4:00 Vapor Pressures and Thermodynamics of Molten Halide Mixtures by H. H. Emons and W. Horlbeck 775

Recent News Papers

4:20 Recent News Papers

General Session
H. F. Gibbard, Chairman; B. Miller, Vice-Chairman
Sir Francis Drake Hotel, Tudor Room, Second Floor

9:00 Heats of Dilution of Aqueous Zinc Bromide by H. F. Gibbard 828
9:20 Bromine Complexing Agents for Energy Storage Applications by H. F. Gibbard 829
9:40 Electrochemical Measurements on Metal Oxide Electrodes by K. Kinoshita and M. Madou 830
10:00 Impedance Measurements on Nb-Doped Single Crystalline TiO_2 by M. Madou, K. Kinoshita and M. C. H. McKubre 831
10:20 Calorimetric Investigations on the AgI-AgBr System by A. Khandkar, V. B. Tare, A. Navrotsky, and J. B. Wagner, Jr. 832
10:40 Electrical Conduction in the Two-Phase $AgCl-Al_2O_3$ System by A. Khandkar and J. B. Wagner, Jr. 833
11:00 Enhanced Modes of Electroanalysis for Hydrodynamically Modulated Rotating Disk Electrodes by B. Miller and J. M. Rosamilia 834
11:20 Inelastic Neutron Scattering of Lead Dioxides by R. Varma, J. Eckert, J. A. Goldstone, A. D. Taylor, and J. Jorgensen 835
11:40 The Preparation and Behavior of Activated Tantalum Anodes by Ch. Comninellis and E. Plattner 836

W. A. Adams, Chairman; P. Bindra, Vice-Chairman

2:00 Heterogeneous Electrocatalysis of the Acidic Coal Slurries by S. B. Lalvani and R. W. Coughlin 837
2:20 On the Mechanism of Laser-Enhanced Copper Deposition by W. Stimming, G. Arbach, and P. Bindra 838
2:40 The Effect of Neutral Surface Active Additives on the Kinetics of the Cu(II)/Cu Electrode by P. Bindra, D. Light, and D. Rath 839
3:00 The Direct Measurement of Anionic Adsorption at Pt Electrodes by a High-Sensitivity Computer-Operated Automatic Ellipsometer by S. Gottesfeld, P. J. Hyde, C. J. Maggiore, and S. Srinivasan 840

Wednesday continued

3:20 Combined Ellipsometric and A-C Impedance Measurements of Porous Ruthenium Oxide Films by S. Gottesfeld, J. Rishpon, and I. Reshef 841
3:40 Ten-minute intermission
3:50 Electrode Kinetics in Nonaqueous Solvents by P. G. Pai and J. Jorne 842
4:10 The Reduction of Ni(II) on Hg in Uncomplexating Acetonitrile Solutions by E. R. Gonzalez, L. A. Avaca, and G. Tremiliosi-Filho 843
4:30 The Electrochemical Behavior of Macrocyclic Complexes of Ni(II) in Acetonitrile Solutions by E. R. Gonzalez, L. A. Avaca, and G. Tremiliosi-Filho 844

Thursday, May, 12, 1983

12:15 P.M. Dielectrics and Insulation Division Luncheon and Business Meeting, Grand Ballroom (rear section), Mezzanine, St. Francis Hotel
12:15 P.M. Luminescence and Display Materials Group Luncheon and Business Meeting, Italian Room, Mezzanine, St. Francis Hotel

BATTERY
Cell Design and Optimization
C. C. Liang, Chairman; B. B. Owens, Vice-Chairman
Borgia Room, Mezzanine

9:00 Lithium Anode Rechargeability and Design Considerations for Ambient Temperature Lithium Cells by M. Eisenberg 44
9:20 Changing the LiAl/FeS Cell Design to Include Excess FeS Capacity by T. D. Kaun 45
9:40 Test-Electrode Design and Method for Active Material Characterization by L. Redey, and D. R. Vissers 46
10:00 Power vs. Energy Trade-Off Studies for Lithium-Alloy/Iron Sulfide Cells by E. C. Gay, L. Redey, F. J. Martino, and P. A. Nelson 47
10:20 Prototype Aluminum - Air Cell by D. J. Levy, R. P. Hollandsworth, E. M. Gonzales, and E. L. Littauer 48
10:40 Reverse Voltage Protection in Lithium/Thionyl Chloride Cells by N. A. Godshall, J. K. Surprenant, and A. Zolla 49
11:00 Thermophysical Properties of Thionyl Chloride Based Electrolytes for Li/$SOCl_2$ Battery by H. V Venkatasetty, and S. Szpak 50
11:20 Low Temperature Performance Characterization of Lithium-Sulfuryl Chloride Cells by M. Binder, S. Gilman, and W. L. Wade, Jr. 51
11:40 Lithium/Sulfuryl Chloride Cell Optimization by K. A. Klinedinst 52

DIELECTRICS AND INSULATION/ELECTRONICS
Silicon Nitride Thin Insulating Films
Radiation, Transport, and Traps
V. J. Kapoor, Chairman; H. T. Weaver, Vice-Chairman
California West Second Floor

9:00 Introductory remarks
9:05 Radiation Hardened MNOS - A Review by P. J. Vail 116
9:40 Process Developments for a Radiation-Hard MNOS Memory by R. V. Jones and W. H. Dodson 117
10:00 Evaluation of MNOS Nonvolatile Memories for Space Applications by H. E. Maes, G. L. Heyns, and P. May 118
10:20 Space Charge Effects in Irradiated Si_3N_4 Films by R. C. Hughes 119

H. T. Weaver, Chairman; V. J. Kapoor Vice-Chairman

10:40 Trapping Kinetics in Insulators Having a High Charge Capture Probability by S. B. Bibyk and V. J. Kapoor 120
11:00 Charge Characteristics of Ion-Implanted and Annealed Nitride/Oxide/Si Structures by H. H. Stein 121
11:20 Origin and Characteriestics of Trap States in CVD Silicon Nitride by S. Fujita and A. Sasaki 122
11:40 Insulator Charges and Interface States in MNOS Structures with APCVD and PECVD Silicon Nitride by R. Hezel, K. Blumenstock, and R. Schorner 123

Thermal Nitrides and Ion Implantation
C. T. Kirk, Chairman; R. J. Sokel, Vice-Chairman
California West Second Floor

2:00 Introductory remarks
2:05 Effect of Nitridation of Thick Oxide on Its Infrared Spectrum by M. L. Naiman, C. T. Kirk, R. L. Aucoin, F. L. Terry, P. W. Wyatt, and S. D. Senturia 124
2:25 Low Pressure Direct Thermal Nitridation of Si in Nitrogen by R. V. Giridhar and K. Rose 125
2:45 Thermal Nitridation of Silicon in a Cold Wall Reactor by M. Moslehi and K. C. Saraswat 126
3:05 Composition, Electrical Conduction, and Trapping Properties of Nitrided-Oxide and Reoxidized Nitrided-Oxide by S. S. Wong, S. H. Kwan, H. R. Grinolds, and W. G. Oldham 127
3:25 Growth and Properties of Thermal Silicon Oxynitride Films and Device Applications of These Films by D. J. Dumin, K. Hollowell, K. P. Tsao, and R. Langlais 128

R. J. Sokel, Chairman; C. T. Kirk, Vice-Chairman

3:45 Low Energy Implantation of Nitrogen and Ammonia into Silicon by T. Y. Chiu and W. G. Oldham 129
4:05 Physical Properties of Low Energy Nitrogen Implantation into Silicon and Thermal Oxide Layer by S. Inoue, Y. Furumura, M. Maeda, and M. Takagi 130
4:25 Electrical Properties of Silicon Nitride and Silicon Oxide Thin Films Formed by the Low Energy Ion Implantation by Y. Furumura, S. Inoue, M. Maeda, and M. Takagi 131
4:45 Microstructure and Electrical Properties of Buried Silicon Nitride Layers in Silicon Formed by Ion Implantation by C. D. Fung, J. L. Liao, K. R. Elsayed, and J. J. Kopanski 132

Fourth Symposium on Plasma Processing
Mechanisms
R. Gottscho, Chairman; F. Robb, Vice-Chairman
Grand Ballroom, Mezzanine

9:00 The Reaction Probability of XeF_2 with Silicon by M. J. Vasile 186
9:20 Optical Emission from Reactive Fluorocarbon-Oxygen Plasma by Y. H. Lee and M. M. Chen 187
9:40 The Effect of Collisions in Anisotropic Plasma Etching and Its Relation to Reactive Ion Etching by C. B. Zarowin 188
10:00 Determination of Electric Fields in Plasma Etch Discharges from Observable Parameters by C. B. Zarowin 189
10:20 Influence of Electrode Material on the Etch Characteriestics of an Argon Plasma by W. G. M. van den Hoek 190
10:40 Studies on the Mechanism of Selective Isotropic Dry Etching of Si_3N_4 over SiO_2 by F. H. M. Sanders and J. Dieleman 191
11:00 Studies of Plasma Etching Mechanisms with Cantilever Structures by J. L. Reynolds, J. Hollins, and A. R. Neureuther 192
11:20 Plasma Etch Process Modeling by K. C. R. Chiu 193
11:40 A Review of Reactive Ion Beam and Ion-Assisted Chemical Etching by D. F. Downey and R. A. Powell 194

Etching of Metals
G. C. Schwartz, Chairman; S. W. Pang, Vice-Chairman

2:00 Plasma Etch Process Modeling: Application to Al Etch Process Development by K. C. R. Chiu 195
2:20 Use of Optical Emission from Cl_2, $SiCl_4$, and BCl_3 during Reactive Ion Etching of Aluminum by K. O. Park and F. C. Rock 196
2:40 Reactive Ion Etching of Aluminum in BCl_3-Cl_2 Mixtures by S. Schwarzl and W. Beinvogl 197
3:00 Process Integrity and the Role of $AlCl_3$ in the Plasma Etching of Aluminum by J. E. Spencer 198
3:20 Twenty-minute intermission
3:40 Variation of CF_4+O_2 Plasma Etch Rate of Ta Films on Ceramic with Flow, Pressure, and Exposed Area (Loading) by G. L. Dybwad 199
4:00 Contamination in AlSi Dry Etching by H. Itakura, T. Shibano, M. Yoneda, and H. Abe 200
4:20 After Corrosion Treatments in Aluminum Alloy Reactive Ion Etching by T. Tsukada, H. Takei, E. Wani, and K.Ukai 201
4:40 A Review of Plasma Etching of Refractory Metal Silicides by T. P. Chow and A. J. Steckl 202

DIELECTRICS AND INSULATION/ELECTRONICS/CORROSION/ HIGH TEMPERATURE MATERIALS/ENERGY TECHNOLOGY
Materials and New Processing Techniques for Photovoltaics
J. Dietl, Chairman; A. Morrison, Vice-Chairman
California East, Second Floor

9:00 Compositional Analysis of Silicon for Solar Cells by L. P. Hunt 214
9:35 Effective Segregation Coefficients of Impurities in Silicon Ingots Grown by Czochralski and Bridgeman Techniques by P. S. Ravishankar, L. P. Hunt, and R. W. Francis 215
9:55 Carrier Lifetime Measurements in Silicon Wafers by A. K. Ghosh, T. Tiedje, J. I. Haberman, and R. W. Francis 216
10:15 Characterization of Silicon Crystals Grown by the Heat Exchanger Method by S. Hyland, K. A. Dumas, G. H. Schwuttke, J. A. A. Engelbrecht, and D. Leung 217
10:35 Ten-minute intermission
10:45 Influence of Iron, Titanium, and Vandium on Photovoltaic Behavior of Polycrystalline Solar Cells by S. Pizzini, C. Calligarich, C. Chemelli, M. Gasnarini, P. Rava, and L. Sardi 218
11:20 Mechanisms Limiting Performance in Polycrystalline Silicon Solar Cells by J. H. Wohlgemuth, J. S. Culik, and P. Alexander Hydrogen Motion and Bonding in Silicon Grain 219
11:40 Boundaries by C. H. Seager, J. K. G. Panitz, and D. J. Sharp 220

A. Rohatgi, Chairman; C. Megerle, Vice-Chairman
California East, Second Floor

2:00 Low Energy NMA Ion Implantation for the Formation of Back Surface Fields by M. E. Brady and D. J. Fitzgerald 221
2:20 Low Cost, High Efficient and Reliable Silicon Solar Cells with Plasma-Deposited Silicon Nitride as Antireflective Coating by T. Kato, H. Morita, A. Sato H. Washide, A. Onoe F. Fujimoto, K. Komaki, A. Ootuka, and Y. Iwata 222

Thursday continued

2:40 Application of Thermonanalysis to Thick Film Materials Development by J. Parker and B. Gallagher 223
3:00 Development of a Contact End Resistance Approach to Contact Resistivity Measurement by D. R. Burger 224
3:20 Ten-minute break
3:30 High Efficiency Amorphous Silicon Solar Cells Fabricated by Reactive Sputtering by T. D. Moustakas 225
4:05 Optical and Structural Properties of LPCVD Silicon Films by N. Proust, R. Bisaro, J. Magarino, and K. Zellama 226
4:25 A Non-Noble Front Metallization Process Using Mo/Sn Screen Printed Pastes by A. Garcia III and B. D. Gallagher 227
4:45 Zinc Oxide Synergistic Systems for the Weathering Stabilization of Polyolefins by B. Baum and D. S. Carr 228

DIELECTRICS AND INSULATION/HIGH TEMPERATURE MATERIALS CHEMISTRY
High Temperature Adhesives
T. L. St. Clair, Chairman
Oxford Room, Second Floor

9:00 High Temperature Adhesives Study by R. J. Kuhbander and J. R. Rhodehamel 241
9:30 High Temperature Adhesives Based on Thermid-600-Acetylene Terminated Polyimide by T. J. Reinhart and R. J. Kuhbander 242
10:00 Polyquinoxaline (PQ) Adhesives - An Overview of Materials and Applications by M. G. Maximovich 243
10:30 Phthalonitrile Resins for High Temperature Adhesives by J. R. Griffith 244
11:00 High Temperature Space Film Adhesives by A. K. St. Clair and T. L. St. Clair 245

2:00 Inorganic Ceramic Cements, Their Properties, and Applications in Industry for High Temperature Adhesion by J. A. Crawford 246
2:30 An XPS and TEM Study of Adhesion Between Polyimide and Cr Metallurgy by N. J. Chou, D. W. Dong, and J. Kim 247
3:00 Anodized Titanium Immersed in Hot Water: Oxide Stability and Metal Corrosion by M. Natan and J. D. Venables 248
3:30 Characterization of Anodic Films on Titanium Using AES and STEM by M. Natan, and J. S. Ahearn 249
4:00 High Temperature Stability of a Polyimide Film by R. Ginsburg, and J. R. Susko 250

Recent News Papers

4:30 Recent News Papers

ELECTRONICS
Defects in Silicon
Contamination Gettering
J. Andrews, Chairman; S. Prussin, Vice-Chairman
Elizabethan Room A and B, Second Floor

9:00 Silicon Microdefects and Contamination Control in MOS Device Processing by J. R. Carruthers 304
9:40 Iron Contamination in Silicon Processing by K. G. Barraclough, and P. J. Ward 305
10:00 Prismatic Punching of Dislocations from NiSi2 Precipitates in Epitaxial Si by P. D. Augustus 306
10:20 Ten-minute intermission

S. Prussin, Chairman; J. Andrews, Vice-Chairman

10:30 Saucer Pit Defects in Silicon by C. W. Pearce and V. C. Kannon 307
10:50 Survey of Microdefects on the Surface of Oxidized Silicon Wafers by G. Keefe-Fraundorf and R. A. Craven 308
11:10 Thickness Dependences of Dielectric Breakdown Failure of Thermal SiO_2 Films by K. Taniguchi, K. Yamabe, and Y. Matsushita 309
11:30 The Microstructure of Polysilicon Backsurface Gettering by W. T. Stacy, K. N. Ritz, J. G. de Groot, M. C. Arst, and M. H. Norcott 310
11:50 Gettering of Gold in Silicon Wafers Using Various Backside Gettering Techniques by D. E. Hill 311

Device Processing
H. R. Huff, Chairman; K. E. Bean, Vice-Chairman
Elizabethan Room A and B, Second Floor

2:00 Internal Gettering in Bipolar Process. I. Effect on Circuit Performance by L. Jastrzebski, B. Goldsmith, and R. Soydan 312
2:20 Internal Gettering in Bipolar Process. II. Oxygen Precipitation Kinetics by L. Jastrzebski, R. Soydan, and B. Goldsmith 313
2:40 Sources of Emitter-Collector Shorts in Bipolar Transistors by M. E. Lunnon, D. A. Allison, and W. T. Stacy 314
3:00 Defect-Induced Leakage from Bipolar Transistor Isolation Processing by D. C. Ahlgren, A. C. Domenicucci, M. R. Poponiak, and S. R. Mader 315
3:20 Ten-minute intermission

K. E. Bean, Chairman; H. R. Huff, Vice-Chairman

3:30 Defect Formation for Ion Implantation by S. Prussin, D. I. Margolese, and R. N. Tauber 316
3:50 Understanding and Control of Residual Defects Generated by Implanted High Dose As^+ Bipolar Subcollectors by D. Hagmann 317
4:10 Electrical Properties of Silicon Implanted with 11 MeV Arsenic by P. F. Byrne, N. W. Cheung, and D. K. Sadana 318
4:30 Localized Lifetime Control by Argon Ion Implantation into Silicon by A. Morgro-Campero and R. P. Love 319

III-V Opto-Electronics Epitaxy and Device Related Processes
H. Temkin, Chairman; J. Narayan, Vice-Chairman
Georgian Room, Mezzanine

9:00 Toward Understanding of Schottky Barriers and Related Phenomena: III-V by W. E. Spicer, S. Eglash, D. Mo, P. Mahowald, S. Pan, W. Petro, and I. Lindau 348
9:30 An In Situ X-Ray Study of Metal-Semiconductor Interactions in the InGaAsP/InP System by J. M. Vandenberg and H. Temkin 349
9:50 Ten-minute intermission
10:00 Plasma Etching of III-V Compounds by D. L. Flamm 350
10:30 Dielectric III-V Semiconductor Interactions by H. H. Wieder 351
11:00 Surface Structural Damage Produced in InP(100) by RF Plasma or Sputter Deposition by W. C. Dautremont-Smith and L. C. Feldman 352

ELECTRONICS/DIELECTRICS AND INSULATION
Joint General Session
Silicon Devices
B. E. Deal, Chairman; E. H. Nicollian, Vice-Chairman
Colonial Ballroom, Mezzanine

8:40 On the Resistance Switching in Polycrystalline-Silicon Resistors by C. Y. Lu, N. C. C. Lu, C. C. Shih, M. K. Lee, and C. S. Wang 404
9:00 Threshold Shift from As-Implantation of SiO_2 by R. Kazerounian and W. G. Oldham 405
9:20 Very Shallow Ion-Implanted Boron Junction by T. M. Liu, and W. G. Oldham 406
9:40 A Process-Parameter Model for the Lateral Junction Contour of Double-Diffused Gaussian Profiles by J. P. Zigadlo, G. M. Oleszek, and K. L. Kasley 407
10:00 Avalanche Breakdown Voltages in Semiconductor Junctions by K. Shenai 408
10:20 Collector-Emitter Leakage Caused by Highly As-Doped Emitter and Recessed Oxide Isolation by M. Taguchi, G. Sasaki, A. Menjo, and K. Kanzaki 409
10:40 Empirical Relationships Between Carrier Mobility and Carrier Concentration in Arsenic-, Phosphorous-, and Boron-Doped Silicon by G. Masetti, M. Severi, and S. Solmi 410
11:00 Effect of Surface Beveling on Carrier Profiles by J. Albers, C. L. Wilson, and J. L. Blue 411
11:20 Effects of Autodoped Aluminum on MOSFET Characteristics in SOS Double Solid-Phase Epitaxy by S. Taguchi, M. Nakahara, T. Yoshii, K. Maeguchi, and H. Tango 412
11:40 Control of Polycrystalline-Silicon Resistor by Implanation of N_2^+ by H. Hayashi, H. Yamoto, and T. Ohshima 413

Chemical Vapor Deposition
E. H. Nicollian, Chairman; B. E. Deal, Vice-Chairman

2:00 The Effect of Deposition Temperature and Rate Upon the Structure of LPCVD Silicon by J. T. McGinn, H. F. Kuppert, L. Krausbauer, J. Shaw, and A. E. Widmer 414
2:20 High Quality Polysilicon by Amorphous LPCVD Growth by A. E. Widmer, G. Harbeke, and E. F. Steigmeier 415
2:40 LPCVD Deposition of P-Doped Polysilicon by D. L. Flowers 416
3:00 Continuous CVD: A New Type of Silicon Epitaxial Reactor by D. Bellavance and R. N. Anderson 417
3:20 Low Pressure CVD of a Stibinosilicate Glass by F. Pintchovski, P. J. Tobin, and J. B. Price 418
3:40 Metal-Organic Low Pressure Chemical Vapor Deposition of Al by M. L. Green, R. A. Levy, R. G. Nuzzo, and E. Coleman 419
4:00 Selective Low Pressure Chemical Vapor Deposition of Tungsten by E. K. Broadbent and C. L. Ramiller 420

Dielectrics

4:20 Limitationns of SIPOS-Insulator Passivation by R. D. Plummer 421
4:40 Electrical Properties of SIPOS-Si_3N_4 Bilayers by D. W. Tong, D. M. Taylor, and S. J. Rzad 422

ELECTRONICS/DIELECTRICS AND INSULATION
Joint Recent News Papers
P. L. Castro, Chairman; W. A. Pliskin, Vice-Chairman
Georgian Room, Mezzanine

2:00 Recent News Papers

ENERGY TECHNOLOGY
General Session
J. McBreen, Chairman; A. J. Nozik, Vice-Chairman
Yorkshire Room, Second Floor

9:00 Electric Birefringence and Elliposmetric Spectroscopy of the Semiconductor/Electrolyte Interface by P. G. P. Ang and A. F. Sammells 525

Thursday continued

9:25 Photoeffects at Semiconductor/Solid-Electrolyte Junction by A. F. Sammells and P. G. P. Ang 526
9:50 Stabilization of Semiconductor Photoanodes by Selective Electrodepositions by B. Scrosati and L. Fornarini 527
10:15 Fifteen-minute intermission
10:30 Photoelectrolysis at Ordered Polycrystalline GaPc-Cl Thin-Film Surfaces by P. Rieke, C. Linkous, and N. R. Armstrong 528
10:55 Investigation of Liquid Dopants for High Efficiency Solar Cell Production Using Silicon Dendritic Web Material by K. S. Tarneja, R. B. Campbell, and P. Alexander 529
11:20 Photoelectrochemical Activity of Solid Solutions of Lanthanum and Chromium Salts in Lanthanum Titanates by V. Guruswamy and S. Alexander 530
11:40 Electrodeposition of CdS from Diethylene Glycol Solutions by A. S. Baranski, M. Bennett, and W. R. Fawcett 531

J. McBreen, Chairman; A. J. Nozik, Vice-Chairman

2:00 Grain Boundary Passivation in Polycrystalline Silicon by D. S. Ginley, and D. M. Haaland 532
2:25 Iodidric Acid Photodecomposition on Layered-Type Transition Metal Dichalcogenides by L. Peraldo Bicelli and G. Pazzini 533
2:50 Interaction Plasma-Silicon Surface at Low and High Temperature - Application to the Modification of Surface Properties of the Material by J. Amouroux, D. Morvan, M. P. Bergougnan, and A. Salesse 534
3:15 Fifteen-minute intermission
3:30 Electroreduction of Oxygen by Cobalt Tetraazaannalene in Acid Media by H. P. Dhar, M. Yamana, R. Darby, and R. E. White 535
3:55 Transport Properties of Phosphoric Acid Fuel Cell Electrolytes by H. H. Chang, K-L. Hsueh, D-T. Chin, and S. Srinivasan 536
4:20 Electro-Oxidation of CO from Coal in Alkaline Media by E. Findl 537
4:40 Thermodynamics of Metallic Fission Products in Reactor Fuel Rods by R. Kohli 538

HIGH TEMPERATURE MATERIALS CHEMISTRY
High Temperature Materials Chemistry
Metal - Gas Reactions II
W. L. Worrell, Chairman; D. Cubicciotti, Vice-Chairman
Elizabethan Room C, Second Floor

9:00 Kinetics of Corrosion of CoCrAlY by SO_3-Na_2SO_4 by C. M. Kramer, and R. L. Jones 466
9:25 Reactions of NaCl with Gaseous SO_3, SO_2, and O_2 by W. L. Fielder, C. A. Stearns, and F. J. Kohl 467
9:50 Formation of Surface Layers during Oxidation of an Fe-Mn-Si Alloy by M. J. McNallan, J. M. Oh, and W. King 468
10:15 Oxidation of Cobalt-Chromium Alloys in Chlorine Contaminates Environments by M. J. McNallan, S. H. Kim, and W. W. Liang 469
10:40 A Model for the Growth of a Two-Phase Corrosion Scale by S. B. Sutton, J. J. Truhan, and D. W. Short 470
11:05 Analysis of Localized Heat Processes in Metal Oxidation by D. Cubicciotti 471

Coal Combustion I
R. W. Mar, Chairman; J. Stringer, Vice-Chairman

2:00 Use of the NASA CEC Code for the Prediction of Combustion Gas Deposit Compositions by F. J. Kohl, B. J. McBride, and F. J. Zeleznik 472
2:25 High Temperature Chemistry of Coal Ashing by R. W. Carling, R. W. Mar, and R. M. Allen 473
2:50 Behavior of Mineral Matter during Coal Combustion by R. J. Lauf, and L. A. Harris 474
3:15 Equilibrim Relations with a Bearing on Refractory Corrosion in Slagging Coal Gasifiers by A. Muan 475
3:40 Experimental and Modeling Studies of Coal Slag Vaporization and Phase Equilibria by J. W. Hastie, E. R. Plante, D. W. Bonnell, and W. S. Horton 476
4:05 Oxidation-Sulfidation Corroison in Fluidized Bed Combustor Environments by D. A. Stevenson, J. S. Lin, K. J. Mark, and J. Stringer 477
4:30 High Temperature Erosion and Erosion/Corrosion in Coal Combustion Systems by J. Stringer 478

INDUSTRIAL ELECTROLYTIC
Science and Engineering of Membranes and Separators
H. L. Yeager, Chairman; K. E. Woodard, Vice-Chairman
Essex Room, Second Floor

9:00 Solubility Characteriestics of Perfluorinated Polymers with Sulfonyl Fluoride Functionality by M. J. Covitch and G. H. McCain 565
9:25 Fluorescence Probe Studies of Solutions of Poly (Perfluorosulfonates) by C. R. Martin and N. E. Prieto 566
9:50 Electrochemical Generation and Characterization of Electrode Coatings Containing Molecular Sieve Particulates by D. R. Rolison, C. Murray, and R. J. Nowak 567
10:15 Ten-minute intermission
10:25 Structure Characterization of Sulfonated Polysulfone Membranes by W. Koh, K. Kem and H. Silverman 568
10:50 Supported Liquid Membrane Battery Separators by J. P. Pemsler and M. D. Dempsey 569
11:15 Equilibrium Parameters for a Sodium-Hydroxide-Water System in a Nafion Membrane by S. D. Bhakta and D. N. Bennion 570

D. Bennion, Chairman; M. J. Covitch, Vice-Chairman

2:00 Electrical Impedance of Electrodialysis Membranes by C. C. Herrmann 571
2:25 Pore Size Engineering of Separators for Nickel-Hydrogen Batteries by K. M. Abbey, D. L. Britton, and O. Gonzalez-Sanabria 572
2:50 In Situ Production of Ozone in Water Using an SPE Electrolyzer by S Stucki and G. Theis 573
3:15 Ten-minute intermission
3:25 Metal-Net-Backed Porous Oxide Ceramic Diaphragms: A Solution for the Separator-Problem of Caustic High Temperature (160°C) Water Electrolysis by H. Wendt and H. Hofmann 574

Recent News Papers

3:50 Recent News Papers

LUMINESCENCE AND DISPLAY MATERIALS
General Session
M. J. Brines, Chairman; R. Blonski, Vice-Chairman
Victorian Room, Second Floor

9:00 X-Ray Screen Performance Profile: Effect of Mechanical Energy during Phosphor Dispersion by P. De Maayer, W. Van Landeghem, and A. Neyens 601
9:25 Factors Influencing the Stability of Rare Earth Oxyhalides by J. G. Rabatin 602
9:55 Ten-minute intermission
10:05 Luminescence of ZnS:Tm, Ag Phosphors by T. E. Peters, J. R. McColl, and R. G. Pappalardo 603
10:30 The Saturation of Luminance in A-C Electroluminescent Thin Films by P. Thioulouse 604
10:55 A Special Mechanism of Depreciation in Reduced Wattage Fluorescent Lamps by F. M. Ryan and S. Sinharoy 605

G. R. Gillooly, Chairman; S. S. Trond, Vice-Chairman

2:00 Sensitization of Eu^{3+} Emission by Mn^{2+} in Fluoroapatites by R. G. Pappalardo, T. E. Peters, and R. B. Hunt, Jr. 606
2:25 New (Eu-Activated) Barium and Strontium Aluminates with Very Efficient Eu^{2+} Luminescence by J. T. C. van Kemenade and G. P. F. Hoeks 607
2:50 Rare Earth Activated Niobates by W. A. McAllister 608
3:15 Luminescence of (Sr,Ce)-Hexa-Aluminates by M. N. Alexander, A. G. Sigai, and C. W. Struck 609

Recent News Papers

3:50 Recent News Papers

ORGANIC AND BIOLOGICAL ELECTROCHEMISTRY
Structure and Reactivity in Organic Chemistry and Electrochemistry
P. Zuman, Chairman; M. Baizer, Vice-Chairman
Elizabethan Room D, Second Floor

9:00 Cation Radical Reactions by H. J. Shine 643
9:40 Electron-Transfer from Photo-Excited Ion Radicals by H. Lund and J. Eriksen 644
10:30 The Application of Electrocatalysis to Difficult Organic Conversions by P. J. Peerce-Landers 645
11:10 Chemical Events in Kinetically Heterogeneous Systems Involving Reactants All Dissolved in the Same Solvent by J. F. Bunnett 646

M. Baizer, Chairman; P. Zuman, Vice-Chairman

2:00 Electron-Transfer Mechanisms in Organic Chemistry by C. L. Perrin 647
2:40 Linear Free Energy Relationships in Organic Electrochemistry by P. Zuman 648
3:20 Electrochemistry of Absorbed Aromatic Intermediates by A. T. Hubbard, M. P. Soriaga, J. L. Stickney, and J. H. White 649
4:00 Electropolymerization Reactions of Aromatic Compounds by A. F. Diaz 650
4:30 Oxidative Electropolymerization of Aromatic Molecules by J. Bargon, S. Mohmand, and R. T. Waltman 651

ORGANIC AND BIOLOGICAL ELECTROCHEMISTRY
Ions and the Electrochemical Control of Cell Functions
L. Norton, Chairman; M. T. Corvol, Vice-Chairman
Olympic Room, Second Floor

9:00 Inorganic Ion Requirements for Proliferation of Normal Cells in Defined Media by R. G. Ham 670
9:30 Comparative Effects of Pulse Electromagnetic Fields and Growth Factors upon Culture Chondrocytes by M. T. Corvol, J. D. Monet, N. Dautigny, and J. Assailly 671
10:00 Calcium Activities Inside Small Intact Cells such as Lymphocytes by R. Y. Tsien, T. Pozzan, and T. J. Rink 672
10:30 Ten-minute intermssion
10:40 Human Lymphocytes Membrane Receptors, Lectins, and Electric Fields: Modeling and Experimental Results by M. Grattarola, A. Chiabrera, G. Bonanno, and A. Raveane 673
11:10 Calcium, Cyclic AMP, and Protein Kinases Combine to Trigger Chromosome Replication in Regenerating Liver by R. H. Rixon, J. F. Whitfield, and M. Sikorska 674

Thursday continued

11:40 The Extracellular Calcium Ion is Required for G1/S Transition of Non-Neoplastic Cells but Not Their Neoplastic Counterparts by A. L. Boynton, L. P. Kleine, and J. F. Whitfield 675

M. Corvol, Chairman; A. Gordzinsky, Vice-Chairman

2:00 Calplasin: A Growth-Sensitive Nucleolar Calmodulin Acceptor Protein by J. R. Dedman and M. A. Kaetzel 676
2:30 The Effect of PEMF on Cellular Control Mechanisms by D. B. Jones 677
3:00 The Effect of Selected Electromagnetic Fields on Protein Biosynthesis by R. Goodman, J. Ryaby, E. Zegarelli-Schmidt, C. A. L. Bassett, and A. S. Henderson 678
3:30 Ten-minute intermission
3:40 A Novel Approach to Augmenting Anticancer Chemoimmuno-therapy with Pulsatile Electromagnetically Induced Currents (PEMIC) by L. Norton, A. A. Pilla, S. Geller, and L. Tansman 679
4:10 Effect of Repetition Rate and Duty Cycle on Pulsed Magnetic Field Modulation of LSA Tumors in Mice by S. D. Smith and J. M. Feola 680
4:40 Ion-Induced Modifications in the Conformation of Chromatin, in Intact Cell Nuclei Measured by Means of Flow Microfluorimetry by M. Grattarola, A. Chiabrera, M. Parodi, P. Carle, and R. Finollo 681

PHYSICAL ELECTROCHEMISTRY
The Chemistry and Physics of Electrocatalysis
B. Miller, Chairman; J. D. E. McIntyre, Vice-Chairman
Sir Francis Drake Hotel, Empire Room, Second Floor

8:30 Catalysis of Redox Processes at Illuminated Semiconductor Electrodes by M. S. Wrighton 720
9:05 Photocatalysis with Colloidal Semiconductor Particles by M. Gratzel 721
9:50 Design of Efficient Semiconductor/Liquid Junction Solar Cells in Nonaqueous Solvents by N. S. Lewis and C. M. Gronet 722
10:15 Ten-minute intermission
10:25 Chemically Induced Interface States on Semiconductor Electrodes by M. A. Butler and D. S. Ginley 723
10:45 Structure-Property Behavior of Perovskite Oxide Electrocatalysts by E. J. Calvo, J. Drennan, J. A. Kliner, W. J. Albery, and B. C. H. Steele 724
11:05 Effect of Crystallographic Orientation of Single Crystal RuO_2 Electrodes on the Reversibility of the Electrochemical Hydrogen Adsorption Reactions by T. Hepel, F. H. Pollak, and W. E. O'Grady 725
11:25 Photocatalysis by Ruthenium Dioxide on P-Type Semiconductors by W. Gissler and A. J. McEvoy 726
11:45 Cobalt-Containing Mixed Oxides as Electrocatalysts for Anodic Oxygen Evolution. Preparation, Electrode Kinetics, and Their Use in Alkaline Water Electrolysis by H. Wendt and V. Plzak 727

E. B. Yeager, Chairman; M. J. Weaver, Vice-Chairman

2:00 In Situ X-Ray Absorption Spectra of Supported Platinum Electrodes by W. E. O'Grady, S. M. Heald, D. E. Sayers, and J. I. Budniek 728
2:20 Importance of Interatomic Spacing in Catalytic Reduction of Oxygen in Phosphoric Acid by V. Jalan and E. J. Taylor 729
2:40 Electrokinetics of Oxygen Reduction on Platinum in Trifluormethanesulfonic Acid by K-L. Hsueh, H. H. Chang, D-T. Chin, and S. Srinivasan 730
3:00 A New Look at the Kinetics and Mechanism of Oxygen Evolution at Pt in Alkaline Solutions by V. I. Birss and A. Damjanovic 731
3:20 On the Kinetice of Fast Redox Reaction Results Obtained with the Ring Electrode in Turbulent Pipe Flow by I. Iwasita, W. Schmickler, and J. W. Schultze 732
3:40 Five-minute intermission
3:45 Electrocatalytic Properties of Phthalocyanines by J. Zagal, P. Herrera, K. Brinck, and S. Ureta-Zanartu 733
4:05 Electrocatalysis Studies on the Cathodic Reduction of Thionyl Chloride by M. Madou, K. Kinoshita, M. C. H. McKubre, and S. Szpak 734
4:25 $SOCl_2$ Reduction on Rotating Disk and Stationary Electrodes by N. Doddapaneni 735
4:45 Electrochemical Reactions of Ethylene on Pt and Au in Sulfuric Acid by J. Heitbaum and G. Semrau 736
5:05 A Study of the Kinetics and Mechanisms of Anodic Oxidation of Carbonaceous Fuels by P. Bindra and J. Tweedie 737

Fourth International Symposium on Molten Salts
C. L. Hussey, Chairman; Z. Nagy, Vice-Chairman
Sir Francis Drake Hotel, Franciscan Room, Mezzanine

8:30 Performance of Al-Deposition from Chloride Melts by H. Wendt and K. Reuhl 776
8:50 Electrochemical Intercalation of Lithium into Transition Metal Compounds in Low Temperature Chloroaluminate Melts by J. Devynck, R. Messina, J. Pingaron, and B. Tremillon 777
9:10 Oxygen Evolution at Platinum and Ceramic Oxide Anodes in Cryolite-Alumina Melts by P. G. Russell 778
9:30 The Electrochemical Behavior of Sulfide Ions in Molten Cryolite by N. Q. Minhn and N. P. Yao 779
9:50 Corrosion of Metals and Alloys by Molten Salts Containing Aluminum Ions by T. R. Griffiths, K. King, and S. H. Marchant 780
10:10 Corrosion Studies of Iron, Nickel, and Incoloy 800 in Sodium-Potassium Nitrate Melts at 250°-550°C by H. Fernandez, M. Carter, and R. A. Osteryoung 781
10:30 Ten-minute intermission
10:40 Oxide Ion Chemistry and Corrosion in Molten Alkali Nitrates and Nitrites by N. Ramasubramanian 782
11:00 Solubility of the NiO Fuel Cell Cathode in Li_2CO_3-K_2CO_3 Melts as Determined by Cyclic Voltametry by T. D. Kaun 783
11:20 Solubility of Iron Disulfide in LiCl-KCl Eutectic Melts by R. A. Sharma and R. N. Seefurth 784
11:40 Metal Displacement Reactions by W. H. Smyrl 785

A. S. Dworkin, Chairman; T. R. Griffiths, Vice-Chairman

2:00 Measurements of the Partial Electronic Conductivity in Lithium Chloride-Potassium Chloride Molten Salts by G. J. Reynolds and R. A. Huggins 786
2:20 Cell Design Principles for the Measurement of Kinetics of Fast Electrode Reactions by Z. Nagy and J. L. Settle 787
2:40 The Electrocrystallization of Chromium from Molten LiCl-KCl at 450°C by D. Inman, T. Vargas, S. Duan, and P. Dudley 788
3:00 The Electrochemical Deposition of Refractory Metals from Chloride Melts by S. H. White and U. M. Twardoch 789
3:20 The Electrochemistry of Tungsten (V), (IV), and (III) in Molten LiCl-KCl Eutectic by D. Zuckerbrod and R. A. Bailey 790
3:40 Study of the Electrowinning of Lauthanum Nickel Alloys in LiCl + KCL Eutectic Melt by B. Tremillon, G. Picard, and Y. Mottot 791
4:00 Further Developments in Molten Salt Anodizing by D. G. Lovering and K. P. D. Clark 792
4:20 Electrodeposition of Tungsten Carbide Coatings from Molten Salts by K. H. Stern and S. G. Gadomski 793
4:40 Anode Depolarization by Coal in the Electrolysis of Calcium Nitrate Tetrahydrate Melts by K. E. Johnson and F. W. Yerhoff 794

General Session
M. Tomkiewicz, Chairman; B. E. Conway, Vice-Chairman
Sir Francis Drake Hotel, Tudor Room, Second Floor

9:00 Scanning and Transmission Microscopy Studies of Hyper-Extended Oxide Films at Ir and Ru by B. E. Conway, V. Birss, R. Myers, and H. Angerstein-Kozlowska 845
9:20 The Potential of Zero Charge of Oriented Single Crystal RuO_2 in Aqueous Electrolytes by M. Tomkiewicz, Y. S. Huang, and F. H. Pollak 846
9:40 Fuel Cell Performance under Extreme Operating Conditions by L. S. Joyce, A. A. Adams, A. J. Coleman, and J. A. Joebstl 847
10:00 Composite Electrocatalysts for Carbon Monoxide Resistant Fuel Cell Anodes by A. J. Coleman, A. A. Adams, J. A. Joebstl, and L. S. Joyce 848
10:20 Twenty-minute intermission
10:40 Electrosortion Characteristics of Thin Layers of Gold Deposited on Palladium Substrate by M. E. Gamboa and J. Genesca 849
11:00 Lateral Interactions of Adsorbed Species on Single Crystal Metal-Oxide Electrodes by T. Hepel 850
11:20 Kinetic Aspects of the New Adsorption Isotherm and the Approach to Dynamic Adsorption Equilibrium by R. Heyrovska 851
11:40 Determination of the Substrate and Adsorbate Characteristics from the Hg/aq. Solution Interfacial Tensions; Applicability of the New Isotherm for $0<\Theta<1$ by R. Heyrovska 852

Friday, May 13, 1983

DIELECTRICS AND INSULATION/ELECTRONICS
Silicon Nitride Thin Insulating Films
Plasma Nitrides and Analysis
M. C. Peckerar, Chairman; H. E. Maes, Vice-Chairman
California West, Second Floor

9:00 Introductory remarks
9:05 Electron and Ion Beam Effects in AES-Analysis of Silicon Nitride Thin Films by H. E. Maes, J. Remmerie, M. Hinoul, R. Vanden Berghe, and R. Viaeminck 133
9:25 Characterzation of Plasma Silicon-Nitride Layers by W. A. P. Claassen, W. G. J. N. Valkenburg, F. H. P. M. Habraken, and Y. Tamminqs 134
9:45 Nitriding in a Nonequilibrium Nitrogen, Nitrogen-Hydrogen, and Ammonia RF Plasma at Low Pressure (1-10 Torr)-Applications to W, Mo, and Si Surfaces by J. Amouroux, A. Gicquel, and M. P. Bergougnan 135
10:05 Plasma Deposition of Silicon Nitride and Silicon Oxynitride Using Inert Carrier Gases as Transport Agents by V. S. Nguyen 136

Friday continued

10:25 Irradiation-Induced Electrical Conduction in Silicon Nitride Thin Films by C. Gunkel, D. Schalch, and A. Scharmann 137

H. E. Maes, Chairman; M. C. Peckerar, Vice-Chairman

10:45 The Stability of Plasma Nitride Passivation Films on Plastic Encapsulated Devices in 85% Humidity/85°C by W. Baerg, S. Sachdev, P. Engel, and P. A. Gargini 138
11:05 Etching Rates of SiO_2 and Si_3N_4 Insulating Films in Ammonia-Hydrogen Peroxide Cleaning Process by M. Wantanabe, M. Harazono, Y. Hiratsuka, and T. Edamura 139
11:25 Synergetics of Insulating Silicon Nitride Thin Film Deposition Process Analysis and Control: Real Time Experimental Analysis by E. Siegel 140

DIELECTRICS AND INSULATION/ELECTRONICS/CORROSION/ HIGH TEMPERATURE MATERIALS/ENERGY TECHNOLOGY
Materials and New Processing Techniques for Photovoltaics
P. Rai-Choudhury, Chairman; V. Kapur, Vice-Chairman
California East, Second Floor

9:00 Transparent Conducting Oxide Films for Solar Cells by K. L. Chopra 229
9:35 Cadmium Telluride Solar Cells by R. H. Bube 230
10:10 High Efficiency Tandem Cells by J. C. C. Fan 231
10:45 Ten-minute intermission
10:55 Thin Film Compound Semiconductor Photovoltaic Devices by T. L. Chu 232
11:30 Thin Film Gallium Arsenide Solar Cells by S. S. Chu, T. L. Chu, F. S. Zhang, W. J. Chen, and Q. H. Wang 233

J. Thornton, Chairman; L. P. Hunt, Vice-Chairman

2:00 A Simplified Contacting Scheme for GaAs Solar Cells Using Silver by S. J. Hogan and K. Firor 234
2:20 Atomic Diffusion in Copper Indium Diselenide by S. Wagner 235
2:40 Preparation of $CuInSe_2$ Films by Reactive Co-Sputtering by J. A. Thornton, D. G. Cornog, R. B. Hall, and J. D. Meakin 236
3:00 Chemical and Optical Characterization of CuInSe2 Thin Films for Solar Cells by C. A. Megerle, R. K. Gupta, G. A. Pollock, S. A. Vasquez, W. A. Chesarek, M. B. Ammons, and V. K. Kapur 237
3:20 Five-minute intermission
3:25 Thin Film Cadmium Telluride Solar Cells by T. L. Chu, S. S. Chu, Y. T. Yang, X. J. Yi, and J. M. Yu 238
3:45 Zinc Sulfoselenide Thin Films for Photovoltaic Applications by B. W. Wessels, W. B. Leigh, and K. A. Christianson 239
4:05 Dust-Equivalent Series-Resistance of a Photovoltaic Concentrator by A. K. M. Zakzouk 240

Recent News Papers

4:25 Recent News Papers

ELECTRONICS/DIELECTRICS AND INSULATION
Joint General Session
Dielectrics
L. Rothman, Chairman; J. Maur, Vice-Chairman
Colonial Ballroom, Mezzanine

9:00 Structural and Electrical Properties of Photo-CVD Silicon Nitride Film by Y. Numasawa, K. Yamazaki, K. Hammano, and K. Kobayashi 423
9:20 Dielectric Relaxation and Charging and 1/f Flicker Voltage Noise in Silicon Nitride Thin Insulating Films by E. Siegel 424
9:40 Characterization of Dielectric $BaTiO_3$ Thin Films Using Electrolyte Contacts by T. L. Rose, E. M. Kelliher, A. N. Scoville, S. E. Stone, and S. B. Brummer 425
10:00 Electrochromism in the Anodic Oxides of Molybdenum and Tungsten by J. L. Ord 426
10:20 Silane Oxidation Studies: Analysis of LTCVD SiO_2 Films Deposition Data by C. Cobianu and C. Pavelescu 427

Sputtering and Deposition

10:40 Step Coverage Simulation and Measurement in a D C Planar Magnetson Sputtering System by H. A. Vander Plas and I. A. Blech 428
11:00 Reactively Sputtered Ti_xC Thin Films Preparation and Properties by M. Eizenberg and S. P. Murarka 429

J. Maur, Chairman; L. Rothman, Vice-Chairman

2:00 Dry Etching with U.V. Light Irradiation by H. Okano, Y. Horiike, and M. Sekine 430
2:20 Preferencial Etching of Multilayered Chromium and Copper Based on the Electrochemical Technology by M. Morijiri, M. Fuyama, and M. Hanazono 431
2:40 The Influence of Substrate Temperature and Annealing on AlN Films Deposited by Reactive RF Magnetron Sputtering by A. Fathimulla and A. A. Lakhani 432
Paper Withdrawn 433

Metallization

3:00 Electromigration Capacity and Microstructure of Layered Al/Ta Film Conductor by K. Hinode, S. Iwata, and M. Ogirima 434
3:20 A Two-Layer Gold Metallization Process by D. Summers 435
3:40 Thin-Film Interactions of Al and Al(Cu) on W and Ti by C. J. Palmstrom, I. Krafcsik, J. Gyulai, E. Colgan, E. Zingu, and J. W. Mayer 436
4:00 Aluminum Intrusions or "Rat Bites" by P. S. Gwozdz and H. M. Bath 437

Joint Recent News Papers
E. H. Nicollianan, Chairman; W. A. Pliskin, Vice-Chairman
Grand Ballroom, Mezzanine

9:00 Recent News Papers

G. C. Schwartz, Chairman; V. J. Silvestri, Vice-Chairman

2:00 Recent News Papers

ENERGY TECHNOLOGY
General Session
J. McBreen, Chairman; A. J. Appleby, Vice-Chairman
Yorkshire Room, Second Floor

9:00 $CuFeS_2$ a New Cathode Material for Lithium Secondary Cells by R. S. McMillan and R. R. Haering 539
9:25 Cycling Characteristics of the Lithium-Aluminum Electrode in Nonaqueous Solutions at Ambient Temperatures by A. S. Baranski, W. R. Fawcett, and T. Krogulec 540
9:50 Complex Impedance Methods for Study of the MoS_2/Electrolyte Interface by L. B. Anderson, and L. G. Thompson 541
10:15 Diffusion in Salt-Gradient Solar Ponds by C. C. Herrmann 542

Recent News Papers

10:40 Recent News Papers

HIGH TEMPERATURE MATERIALS
High Temperature Materials Chemistry
Coal Combustion II
F. J. Kohl, Chairman; R. W. Carling, Vice-Chairman
Elizabethan Room C, Second Floor

9:00 Materials Performance in Laboratory and Pilot Plant Coal Gasification Environments by V. L. Hill and B. A. Humphreys 479
9:25 High Temperature Materials for Gas-Fired Industrial Applications by C. J. Dobos and W. W. Liang 480
9:50 The Corrosion Behavior of Some Candidate Heat-Exchanger Alloys in the AFBC Environment by M. A. Rocazella and I. G. Wright 481
10:15 Studies of Pulverized Coal Combustion Using Fourier Transform Infrared Spectrometry by L. R. Thorne and D. K. Ottesen 482
10:40 Temperature Measurements of Single Pulverized-Fuel Particles by Two-Color Pyrometry by R. E. Mitchell, S. Niksa, and W. J. McLean 483
11:05 High Temperature Corrosion of Candidate Ceramic Heat Exchanger Materials by Coal Combustion Products by B. A. Nagaraj and J. R. A. Lowder 484

LUMINESCENCE AND DISPLAY MATERIALS
Phosphor Synthesis and Characterization
T. E. Peters, Chairman; M. Royce, Vice-Chairman
Victorian Room, Second Floor

9:00 Optical and Electronic Properties of ZnSe Luminescent Thin Films by B. W. Wessels, W. B. Leigh 610
9:25 Effects of Barium Fluoride on the Synthesis of $Y_3Al_5O_{12}$: Tb Phosphor by K. Ohno, T. Abe 611
9:50 An X-Ray Microanalysis Investigation of the Microhomogeneity of Garnet CRT Phosphors by S. E. Bulpett and B. J. Green 612
10:15 Synthesis of Eu^{2+}- Activated $MgO.CaO.2SiO_2$ and Terbium- and Cerium-Activated $ZnAl_2O_4$ by Y. Kotera, A. Ueno, K. Yamazaki, and M. Kage 613
10:40 Study on the Stability of Terbium-Activated Lanthanum Oxybromide by M. Z. Su and Y. J. Wang 614

ORGANIC AND BIOLOGICAL ELECTROCHEMISTRY
Structure and Reactivity in Organic Chemistry and Electrochemistry
H. Lund, Chairman; M. D. Hawley, Vice-Chairman
Elizabethan Room D, Second Floor

9:00 Neighboring Group Participation in Electron Transfer from Dialkyl Thioethers by R. S. Glass, B. R. Coleman, W. N. Setzer, and G. S. Wilson 652
9:40 Electrochemical Reduction of Dinitrotoluene Isomers by M. H. Miles and D. A. Fine 653
10:20 The Probable Condensed-Phase Preparation of the p-Nitrophenyl Nitrene Anion Radical by M. D. Hawley, D. E. Herbranson, and R. N. McDonald 654
10:50 Reaction Pathways of Aryl Ether Radical Anions by D. E. Bartak, M. D. Koppang, T. A. Thornton, and N. F. Woolsey 655
11:20 Photochemical and Electrochemical Generation and Reactions of Olefin Radical Cation-Superoxide Ion Pairs by C. S. Foote, K. J. Lee, and P. M. Allen 656

Friday continued

E. Kariv-Miller, Chairman; W. K. Musker, Vice-Chairman

2:00 Electro-Organic Reaction with A-C Electrolysis by C. Y. Cheng and D-T. Chin 657
2:30 The Chemical and Electrochemical Oxidation of Isoquinoline and Indole Derivatives by M. Sainsbury and A. Majeed 658

Ions and the Electrochemical Control of Cell Functions
A. Grodzinsky, Chairman; H. Pohl, Vice-Chairman
Olympic Room, Second Floor

9:00 Electrochemical Control of Membrane Premeability by A. J. Grodzinsky 682
9:30 Dielectrophoretic Cell Sorting by H. A. Pohl and K. Pollock 683
10:00 Electromagnetic Modulation of Biological Processes: Evidence for a Role of the Plasma Membrane in Signal Coupling by G. Colacicco and A. A. Pilla 684
10:30 Ten-minute intermission
10:40 Cellular Spin Resonance of Cells and Small Particles in Rotating Electic Fields by M. Mischel and H. A. Pohl 685
11:10 Electromagnetic Signal Analysis Applied to Controlling Cell Functions Electrically by B. R. McLeod 686
11:40 Electromagnetic Response of Cells and Tissues vs. Macroscopic Measurements by B. Tuerlinckx, M. Dierickx, L. Rybowski, M. Hinsenkamp, and F. Burny 687

H. Pohl, Chairman; A. A. Pilla, Vice-Chairman

2:00 Electrochemical Study of Chlorpromazine (CPZ) Effect on Platelet Membrane Potential (PMP) and the Ca^{2+} Level by A. Caprani and H. Vainer 688
2:30 A Potential Step Change Cause of Blood Clot Breakaway by V. Guruswamy and G. Helm 689
3:00 The Physiological Relevance of Laplace Plane Membrane Impedance Determinations by A. A. Pilla, G. Cerf, and C. Mayaud 690
3:30 An In Vivo A-C Impedance Measurement of the Cutaneous Effect of a Harsh Substance on the Dielectric Spectra of Human Skin by L. S. Lu, J. M. C. Roberts, W. I. Archer, and E. J. Lajiness 691

General Session
J. H. Wagenknecht, Chairman; H. N. Blount, Vice-Chairman
Elizabethan Room D, Second Floor

3:00 Detection and Measurement of Kolbe Electrolysis Products Using Permeable Membrane Mass Spectrometry by L. B. Anderson and T. J. Brockman 692
3:30 The Electrochemical Carbon-Carbon Bonding of CO_2 by V. Guruswamy and L. Pillis 693

Recent News Papers

4:00 Recent News Papers

PHYSICAL ELECTROCHEMISTRY
Fourth International Symposium on Molten Salts
D. G. Lovering, Chairman; S. N. Flengas, Vice-Chairman
Sir Francis Drake Hotel, Franciscan Room, Mezzanine

8:30 Equilibrium Measurements for the Adsorption of H_2S, COS and HCl by Alkali Metal Carbonates by S. E. Lyke, R. T. Hallen, and L. J. Sealock 795
8:50 Effect of Oxoacidity on the Thermochemical Stability of Molten Sodium Nitrate-Nitrite Mixtures by G. Picard, T. Flament, and B. Tremillon 796
9:10 Electrode Reactions Involving Lead or Cadmium Ions in Molten Nitrates by M. H. Miles, G. E. McManis, and A. N. Fletcher 797
9:30 Electrolysis Reactions in Inorganic Acetate Melts by E. Rhodes 798
9:50 Chlorinating Gaseous Mixtures in Molten Chlorides by G. Picard, F. Seon, and B. Tremillon 799
10:10 Standard Reference Electrode for Molten Salts by J. A. Plambeck 800

Recent News Papers

10:30 Recent News Papers

Abstracts*

BATTERY

Cell Testing and Reliability

1 The Reliability of Primary Batteries, A General Assessment: *P. Bro*, Southwest Electrochemical Company, Santa Fe, NM 87501

Reliability is vital for the medical implant applications of primary batteries, and, increasingly, the demand is growing for an improved reliability of batteries for various industrial and consumer applications. The emergence of long-life lithium batteries has given designers a wider choice from which to select systems with an improved intrinsic reliability of performance. Such a selection in combination with high reliability cell designs can lead to primary batteries with a substantially improved reliability. Concurrently, there is an increasing demand for rapid, efficient, and nondestructive methods to assess the long-term battery reliability to supplement the conventional methods of reliability assessment that involve real-time and accelerated testing. Such improved methods are now being developed and implemented.

2 Testing of Advanced Lithium Batteries to Establish Performance and Reliability Characteristics for Navy Applications: *J. A. Barnes,* R. F. Bis, F. C. DeBold, G. F. Hoff, J. D. Jensen, L. A. Kowalchik,* and *D. L. Warburton*, Electrochemistry Branch, Naval Surface Weapons Center, White Oak, Silver Spring, MD 20902

We are involved in a continuing program to evaluate the characteristics of lithium batteries in the areas of performance, reliability, and safety. This program is now focusing on commercially available cells containing lithium with $SOCl_2$, $SOCl_2$ plus additional reactants, or SO_2Cl_2. The tests include both destructive and nondestructive evaluation of the electrical and physical characteristics of the batteries. This paper describes the test program in detail with specific examples drawn from work now in progress.

3 A Statistical Study of Sources of Variation in Battery Testing: *K. K. Cheung** and *W. S. Lindsay*, Allied Chemical, Buffalo Research Laboratory, Buffalo, NY 14210

An analysis of variance experimental design has been utilized to quantify sources of variation in battery testing procedures. Factors investigated included: mixture preparations, electrode fabrication methods, and between and within run repeatabilities. Forty-eight experiments were run, and parameters measured were percent utilization and closed circuit voltage at various stages of discharge. Experimental data were analyzed using a program in the BMDP Statistical Software package (BMDP8V). The effect of the various factors on the measured parameters is discussed.

4 Characterization Testing of Alkaline Batteries: *S. Gross*, Boeing Aerospace Co., Seattle, WA 98124

A variety of novel tests are described which have been used successfully with alkaline cells and batteries. Special calorimeters have been built to determine heat generation in large primary and secondary batteries. Thermal tests have been developed to determine heat transfer behavior of battery packaging designs, including thermal conductance across critical paths. High speed test methods have been developed to determine fast transient behavior of batteries, such as with the breakdown of passivation overpotential. Tests have also been developed which can be used to help diagnose battery problems in spacecraft.

5 Nondestructive Tests for Predicting Battery Reliability: *S. C. Levy*, Sandia National Laboratories, Albuquerque, NM 87185, and *N. H. Hall*, Southwestern Electrochemical Company, Santa Fe, NM 87501

Several requirements for a primary battery with an active life greater than five years exist at Sandia National Laboratories. These batteries will be used in remote locations with limited accessibility, therefore, high reliability is required. At present, there is no satisfactory means of accurately predicting the reliability of batteries to be used for extended periods of time. An extensive program is underway to develop the methodology for predicting battery reliability. This program centers around the very sensitive techniques of microcalorimetry and complex impedance analysis coupled to a real time storage and discharge test. Initial data relating to the microcalorimetric study of Li/SO_2 cells are discussed.

6 Microcalorimetric and A-C Impedance Studies of Anode Stability in Lithium-Sulfuryl Chloride: *J. C. Hall*, Altus Corp., San Jose, CA 95112

Lithium-sulfuryl chloride is potentially an equally energetic and safer alternative to lithium-thionyl chloride. Reliable active electrolyte cells, however, require a minimum rate of lithium corrosion and voltage delay after storage. As a first step in the demonstration of such cells, investigations have been carried out of anode corrosion and film formation processes as a function of electrolyte composition and anode pretreatment. Initial results indicate substantial improvements in anode life and performance are possible by optimization of the electrolyte composition and pretreatment of the anode with cyanoacrylates.

7 The Use of Complex Impedance Analysis in Predicting Reliability of Li/SO_2 Primary Cells: *C. D. Jaeger* and *J. C. D'Angelo*, Sandia National Laboratories, Albuquerque, NM 87185

Presently at Sandia National Laboratories a study is being conducted to develop and evaluate methodology for predicting the reliability of ambient temperature lithium batteries (*i.e.*, the Li/SO_2 primary battery). One of the techniques being considered is the use of complex impedance analysis. The factors contributing to the total impedance of the Li/SO_2 battery are discussed as well as experimental data pertaining to the lithium anode, porous carbon cathode current collector, and Li/SO_2 D cell batteries.

8 Analysis of Thionyl Chloride Electrolyte by Gas Chromatography: *S. Solomon*, Cordis Corp., Miami, FL 33152

Thionyl chloride cell electrolyte has been quantitatively analyzed for the effects of moisture by determining its hydrolysis products, sulfur dioxide and hydrogen chloride, using gas chromatography with a gas density detector. Data obtained were correlated with infrared band assignments. The technique, not heretofore used extensively for analyses relating to cell systems, serves to assess electrolyte integrity prior to cell manufacture and provide insights to an understanding of cell electrochemistry, by examination of volatile discharge products such as sulfur monochloride and sulfur dioxide.

9 Nondestructive Control of Highest Quality Defense and Medical $Li/SOCl_2$ Batteries: *N. Marincic, J. Epstein,** and *P. Kane*, Battery Engineering Inc., Hyde Park, MA 02136

Quality control procedures are reviewed as practiced in the last five years in the production of cylindrical $Li/SOCl_2$ cells for use in medical implants and in high temperature memory circuits on aircrafts. A brief reference is made to the problems of materials traceability and component evaluation, followed by the applicability of specific military and FDA requirements to the oxyhalide type lithium batteries. Working statistics for rejection rates and reprocessing are discussed for materials, components, and critical steps of assemblage.

10 Performance Data Base for $Li/SOCl_2$ Cells Acquired by Means of a Computer Controlled Data Acquisition System: *R. Szwarc** and *F. M. Kline*, General Electric Co., St. Petersburg, FL 33542

The application of a number of new lithium anode based electrochemical systems for primary battery applications has prompted the need to generate a performance data base over a wide range of temperature and loading conditions. This base will be used to establish a useful range for each of the electrochemical systems investigated. This paper describes a sophisticated computer controlled tester and data acquisition system which is capable of testing numerous cells discharging simultaneously under varying loads and temperatures. The data are stored in magnetic mass storage disks for future processing, data reduction, and display. Data are presented for $Li/SOCl_2$ "D" cells which constitute a part of this data base.

11 Capacity Losses in Li/SO_2 Cells Due to Chemical Reactions at High Rate, High Temperature Discharges: *W. Bowden,* R. H. Holmes, L. Chow*, and *D. Demuth*, Duracell Inc., Duracell Laboratory for Physical Science, Burlington, MA 01803

The discharge capacity of Li/SO_2 cells was examined at high currents and temperatures. D cells rated at 8 A-hr delivered over 7 A-hr at 5A current and 55°C, while cells discharged at 72°C gave 7 A-hr at 3A. The cells were analyzed for residual lithium and sulfur dioxide. Spent cathodes were analyzed by infrared spectroscopy. A parasitic reaction was found in which $Li_2S_2O_4$ and S were formed, presumably by reaction of $Li_2S_2O_4$ with SO_2. This reaction became noticeable only under the extreme combination of high rate and temperature.

12 Voltage Compatible Lithium Cells: *F. Bonino, M. Lazzari*, Centro Studio Processi Elettrodici CNR, Polytechnic, Milan, Italy, and *A. Padula* and *B. Scrosati,** Instituto di Chimica Fisica, University of Rome, Rome, Italy.

Voltage compatible lithium batteries are of increasing interest as power sources for microelectronic devices. In this paper, the characteristics and performance of lithium organic electrolyte cells, having metal oxosalts as cathodes, are described.

13 A Failure Model for Secondary Power Sources: *R. F. Fedors* and *S. Di Stefano*, Jet Propulsion Laboratory, Pasadena, CA 91109

A model which had initially been developed to describe failure in sealed nickel-cadmium batteries has been applied to other secondary power sources, i.e., Pb-Acid, Ag-Zn. The model is derived from flaw theory and provides, in a natural way, for the statistical variability of battery lifetime into a physiochemical model. The model has been validated for sealed Ni-Cd batteries, [*J. Power Sources*, **8**, 369 (1982)]. When the model is applied to the Pb-Acid system, it indicates that the observed variability in battery life is due primarily to the statistical variability inherent in the battery itself. Application of the model as a tool for the determination of failure mechanisms and design of accelerated testing is discussed.

14 Real Time and Accelerated Geosynchronous Orbit Testing of Nickel-Cadmium Cells: *P. G. Fougere,** Societé Accumulateur Fixes et Traction, 93230 Romainville, France, and *R. E. Corbett* and *J. Lovgren*, Lockheed Missiles & Space Co., Inc., Sunnyvale, CA 94086

*** An asterisk by a name indicates which author will present the paper.**

SAFT and Lockheed have been engaged in an aerospace NiCd cell geosynchronous life test program since 1970, the purpose of which was to demonstrate cell life capability using the low charge rate (C/30-C/20) low temperature (0°C) operating method. Other goals of these tests were to elucidate the parametric performance dependency of temperature and depth of discharge, and to determine failure modes. Test results to date exceed 2100 cycles at 90% depth of discharge (DOD) and 3400 at 50% DOD for cells at 0°C. At this temperature fair correlation between cycle life of real time and accelerated tests has been observed.

15 Heat Flux Simulation during Battery Life Test: *W. C. Hwang** and *C. C. Badcock*, Aerospace Corp., Los Angeles, CA 90009

An adequate simulation of the radiative heat flux characteristics of a spacecraft battery during tests can be provided by using heat conduction. This procedure is demonstrated for a flight quality NiCd battery life test with simulation of fixed and louvered radiators. The computer controlled apparatus is described, and results are compared with orbital and modeling data. This method allows an accurate simulation of battery temperatures, temperature gradients, and their response to a variety of charge-discharge conditions.

16 Assessing Battery Performance Through Examination of Cell Voltage Test Data: *P. P. McDermott*, B-K Dynamics, Inc., Arlington, VA 22202

A number of charge and discharge curves from a life test of 12 A-hr nickel-cadmium cells were computer fitted utilizing the equation

$$\text{Voltage} = A \pm \frac{B}{(C - x)} \pm De^{-Ex}$$

where x is ampere hours and A, B, C, D, and E are fit parameters determined by means of a nonlinear regression program. When these parameters are plotted *vs.* cycles, definite trends are observed which can be related to previously derived equations relating cycle life to variables such as temperature and depth of discharge.

17 Sealed Lead-Acid Battery Test Results: *D. M. Bush,** *A. E. Verardo, D. W. Miller*, and *J. D. Sealey*, Sandia National Laboratories, Albuquerque, NM 87185

In early January of 1981, Sandia National Laboratories began testing sealed lead-acid batteries which were being developed under Sandia contracts. The goals for these contracts were to develop a totally maintenance-free sealed lead-acid battery capable of deep discharge operation in a photovoltaic power system. Sealed lead-acid batteries and a group of conventional flooded lead-acid batteries have been exposed to a matrix test plan with some approaching 1000 cycles. This paper describes the results of these tests.

18 Effect of Charge Acceptance on Life Performance of SLI Batteries: *K. Abe, T. Yoshida, Y. Ohya*, and *H. Morimoto*, Toyota Central Research and Development Laboratories, Inc., 41-1, Aza Yokomichi, Oaza Nagakute, Nagakute-cho, Aichi-gun, Aichiken, 480-11, Japan

The life of SLI batteries is largely affected by the charge acceptance. A poor charge acceptance would lead to formation of a vertical concentration gradient of the electrolyte which will shorten the life of the batteries. A new life testing method is proposed in due consideration of the charge acceptance of the batteries.

19 Photoelectrochemical Properties of Lead Oxides: *N. Freestone* and *L. M. Peter*,* Dept. of Chemistry, The University, Southampton, England SO9 5NH

The photoelectrochemical response of lead electrodes has been examined in a range of electrolyte solutions, including sulfuric acid. Analysis of the photocurrent excitation spectrum leads to the absorption spectrum of the photoactive oxide, and direct comparison with the absorption spectra of the known crystalline modifications of PbO shows that tetragonal lead dioxide is formed both by the oxidation of lead and by the reduction of αPbO_2. The potential dependence of the photocurrent is related to the electric field in the oxide, and the potential at which the photocurrent changes sign can give information about the local pH.

20 Thermogravimetry-Evolved Gas Analysis of Silver Oxide Cathode Material: *W. A. Parkhurst,** *S. Dallek*, and *B. F. Larrick*, Naval Surface Weapons Center, White Oak, Silver Spring, MD 20910

In this work, we report the development of a new, rapid, and precise thermogravimetry-evolved gas analysis (TG-EGA) method for the determination of the AgO, Ag_2O, Ag, and Ag_2CO_3 content of silver oxide cathodes. The analysis is important because the change in the chemical composition of these cathodes during storage affects battery capacity and performance. The results using this technique are given for silver oxide cathodes produced by various manufacturers and stored under different conditions.

21 Effect of Adsorption Phenomena and Phase Transition on Electrochemical Behavior of Silver/Silver Oxide Electrodes in KOH Solutions: *M. Hepel** and *M. Tomkiewicz*, Dept. of Physics, Brooklyn College of the City of New York, Brooklyn, NY 11210

Investigations of the electrochemical behavior of silver electrodes in aqueous alkaline solutions have been performed using linear potential scan voltammetry, chronamperometry and a-c impedance technique using full relaxation spectrum analysis. Three distinct potential regions are described: *i*) catalytic hydrogen evolution with kinetically controlled specific adsorption step, *ii*) lower oxide (Ag_2O) formation complicated by dissolution of silver in form of complexes $HAgO_2^{2-}$, and *iii*) higher oxide (AgO) nucleation, which is associated with its decomposition and oxygen evolution. From the experimental results, conclusions are presented regarding phase transition processes on porous silver electrodes occurring during charging and discharging of silver secondary battery.

22 Assurance of an Automatically Activated Silver-Zinc Battery: *H.-W. Ko*, Material Science Dept., Chung-Shan Institute of Science and Technology, Lung-tan, Taiwan 325, China

Requirement of destructive tests for an automatically activated silver-zinc battery demands a very high reliability. Performance is achieved by analyzing failure modes of many testing results. The problems of shorting, separator, activation system and its manifold, battery case and its reenforcement are among the items attracting most attention. A quality assurance program is set for manufacturing of electrodes, activation system, and assembly. No major defect has been detected after production of several hundred batteries, and only few minor defects occurred.

23 Correlation of Fuel Cell Performance with Fabrication Parameters: *G. G. Barna,** *S. N. Frank*, and *L. D. Weedon*, Texas Instruments Inc., Dallas, TX 75265

The primary measure of reliability of a fuel cell is its stability as a function of operating time. To analyze this time-dependent performance of an H_2/Br_2 fuel cell, a computerized lifetest system has been developed. The computer controls the load, while monitoring and recording the current/voltage/time parameters. In addition, data files are generated for each fuel cell, containing extensive documentation of the material and fabrication parameters for all the active components. A search routine then selectively retrieves the data, generating a correlation between the processing parameters, and the performance, of the fuel cells.

24 Testing and Evaluation of Prototype Zinc/Bromine Batteries: *P. C. Butler** and *D. W. Miller*, Sandia National Laboratories, Division 2525, Albuquerque, NM 87185

Sandia National Laboratories is the U.S. DOE lead center for the engineering development of advanced batteries. An in-house laboratory is operating to evaluate the technical status of four Exxon and one Gould/ERC zinc/bromine batteries. This paper presents the results of performance and cycle tests on these units. Available data from a four factor, two level factorial cycle test plan are presented. Failure analysis data are discussed.

25 Reliability Testing of Flowing Zinc-Bromine Batteries and Components: *K. R. Newby, R. Bellows, H. Einstein, P. Grimes, E. Kantner*, and *P. Malachesky*, Exxon Research and Engineering Co., Linden, NJ 07036

The flowing zinc-bromine battery has the advantage that by totally discharging the battery it is returned to an original state. Thus, the basic life and reliability requirements are found in the physical and chemical stability of the individual battery components. In the Exxon battery, the components of greatest concern are the bromine complexer, the carbon plastic, and the polyolefinic separator. Also of concern are impurities found in plastics such as Ziegler catalysts and antioxidants. Methods and data on individual component testing and on the complete battery system are presented.

26 Accelerated Testing of Batteries for an Implantable Insulin Pump: *S. C. Levy* and *C. C. Crafts*, Sandia National Laboratories, Albuquerque, NM 87185

Sandia National Laboratories in collaboration with the University of New Mexico Medical School has developed a programmable implantable insulin delivery system for use by diabetics. This system requires batteries to operate for three to five years with a high degree of reliability. An accelerated test was conducted using five types of battery from three different manufacturers. Four load profiles were included in the test to simulate different configurations of pump and electronics that might be used in future implants. The test design, computerized tester, and battery performance are discussed.

27 Determining the Reliability of Lithium/Iodine Pacemaker Cells Using a Life Test Sample: *C. F. Holmes, M. M. Safford*, and *R. C. Stinebring*,* Wilson Greatbatch Ltd., Clarence, NY 14031

A system has been developed for sampling, testing, and monitoring lithium/iodine cells for use in implantable cardiac pacemakers. Approximately 25,000 production lot samples representing numerous models are on life testing at simulated pacemakers loads and environment. A description is given of the computerized monitoring systems which are employed for evaluating the electrical performance as a function of time on test. From this large sample accurate measurements of reliability such as failure rate and cumulative survival probability can be made. The life-test sample also allows the accurate evaluation of the various cell designs thereby permitting improvements to be incorporated in new designs.

28 Design Testing and Reliability of Lithium-Iodine Pacemaker Batteries: *W. D. Helgeson*, Energy Technology, A Division of Medtronic, Inc., Brooklyn Center, MN 55430

Lithium-iodine batteries have proven to be highly reliable power sources for pacemakers and other implantable devices. Over

the past ten years, specialized testing techniques have evolved for lithium-iodine batteries, and based on those tests, the long-term reliability of a given battery design can be assessed with a high degree of confidence. The excellent long-term reliability of these batteries is illustrated by the results of over seven years of accelerated and real time discharge testing. Battery random failure rates of less than 0.01%/month, at 90% confidence, indicate the efficacy of the testing techniques.

29 Reliability of Glass Insulators in Lithium Ambient Batteries: *C. Nelson** and *B. C. Bunker*, Sandia National Laboratories, Albuquerque, NM 87185

A corrosion resistant, alumino-borosilicate glass, developed for use in glass-to-metal seals for lithium ambient temperature batteries, has been under test to determine the extent of production variability that can be tolerated during fabrication of battery headers. The effects of composition, preform type, and sealing procedure on the corrosion resistance of the glass are major concerns in developing reliable long-life lithium batteries. New glasses are also under development to extend battery life beyond ten years. (This work performed at Sandia National Laboratories supported by the U.S. Department of Energy under contract number DE-AC04-76DP00789.)

30 Glass Corrosion of Battery Headers in Ambient Temperature Lithium Batteries: *B. C. Bunker** and *C. Nelson*, Sandia National Laboratories, Albuquerque, NM 87185

Glass corrosion in the $Li/SOCl_2$ and $Li/SOCl_2$ + BrCl battery systems is shown to be similar to corrosion in the Li/SO_2 battery. Corrosion occurs when Li^+ is reduced to Li metal on glass which contacts the battery anode. A glass composition resistant to Li metal attack, TA-23, has been developed at Sandia which has a projected lifetime of over ten years in all three ambient temperature Li battery systems. Accelerated testing in liquid lithium is being used to select glass compositions which are even more corrosion resistant. (This work was performed at Sandia National Laboratories supported by the U.S. Department of Energy under contract number DE-AC04-76DP00789).

31 End-of-Life Testing of Lithium/Cupric Sulfide Cells—Battery Packs Designed with Mismatched Cells: *D. Bump,** *H. Tataria, A. Nolton,* and *A. DeHaan*, Cordis Corp., Miami, FL 33152-5700

The lithium/cupric sulfide cell discharges at two distinct voltage levels. Because these cells are matched with electronic systems designed to use the lower voltage level as a depletion indicator, detailed and reliable information concerning voltage, capacity, manufacturing variability, etc., is essential. A gentle stepwise discharge technique has been developed to minimize high-drain distortion while allowing precise data applicable to drain rates in the microampere range to be obtained in a reasonable time. The technique has become especially useful with the development of advanced electronic packages that give more than one depletion warning tripped by the multiple voltage levels resulting from deliberate mismatching of upper plateau capacities.

32 Elucidation of Current Drain History in Depleted Li/CuS Cells: *D. L. Hart*, Cordis Corp., Miami, FL 33152

Postmortem examination of cathodes in Li/CuS systems has revealed morphological and chemical variations inconsistent with present theory. Noted were distinct laminae occurring in cathodes from cells of two groups: i) laboratory controlled premature depletions and ii) those subjected to stepwise discharge. Models were produced, each being subjected to variable burn-in and drain rates. The laminae were physically characterized and identified using x-ray and microanalytical techniques. It was found that the occurrence of the laminae was proportional to the drain rate. Elemental analysis suggests that, at higher drain rates, there occur competing one- and two-electron reductions. The significance of these findings in elucidating current drain history of depleted cells and in selection of stepwise discharge rates is discussed.

BATTERY

Cell Design and Optimization

33 Lithium/Cupric Sulfide—Cell Design and Optimization: *H. Tataria, D. Bump,* and *A. DeHaan*, Cordis Corp., Miami, FL 33152-5700

The capacity density of the Cordis Li/CuS cell has been improved from 0.31 A-hr/cm^3 to 0.46 A-hr/cm^3. At the same time, the end-of-life impedance has been reduced by a factor of 4 (2000 to 500 Ω). These gains have been achieved by improvements in cathode purity, optimization of electrolyte ratios, and maximization of active volume. These characteristics make this system well suited for the new generation of physiological pacers.

34 Development of MnO_2/Li Cells for Implantable Artificial Ear: *H. Ikeda*, Sanyo Electric Co., Ltd., Director of Shioya Research Center, 809 Takamura, Higashitarumi, Tarumi-ku, Kobe 655, Japan

Recently, implantable artificial middle ear was investigated from standpoints of medical and engineering fields, and we have engaged in some parts of them. We selected MnO_2/Li cell as one of the most suitable cells for implantable artificial middle ear. This cell is sealed hermetically by laser weld, and several cell types such as flat, sheet, and square type cells are examined in accordance with the different implantable systems or surgical operations.

35 Lead Acid Maintenance Free Battery with Improved Storage Life: *T. Palanisamy** and *D. Cipris*, Allied Corp., Corporate Research and Development, Morristown, NJ 07960

Maintenance-free SLI batteries encounter performance problems after prolonged storage life (1-2 yr). This is attributed to the corrosion of grids, which progresses with time. A demarcation line is observed, which travels from the top to the bottom of the battery grid. The upper part of the grid may suffer severe corrosion to the extent of disappearance, if sufficient time is allowed. The cause and mechanism of the corrosion process were not known. The change in the concentration of sulfuric acid was suspected, but not a proven cause. We have studied the corrosion of the Pb-Ca-Sn and low Sb grid alloys as a function of the acid concentration. Strong dependence is observed in all studied cases with higher corrosion rates at lower acid concentrations. This finding is correlated with the processes taking place during battery storage which may cause lowering of the electrolyte concentration. Remedial measures are suggested to maintain uniform acid concentration throughout the battery storage. These call for a modification in cell design. Reduced corrosion rate and extended life should result.

36 A "Precharged" Positive Plate for the Lead-Acid Automotive Battery. I. Positive Plate Allowing Direct Incorporation of PbO_2: *E. J. Taylor, G. A. Shia,* and *D. T. Peters,** Inco Alloy Products Co. Research Center, Suffern, NY 10901

A process to manufacture the positive plate of the lead-acid battery that eliminates the conventional curing and formation steps via the direct incorporation of PbO_2 into the grid is described. "Precharged" plates made from a tetrabasic lead sulfate and PbO_2 mix were found to be strong and capable of delivering first cycle capacity at the automotive cranking rate (200 mA/cm^2) which was 35% of that of conventionally processed positive plates. PbO_2 obtained from electrochemically formed conventional positive plates was used in this study; the successful use of chemical PbO_2 is demonstrated in the following paper. This new process is simple and will allow manufacture of ready-to-use plates on modern automated expanded metal platemaking equipment.

37 A "Precharged" Positive Plate for the Lead-Acid Automotive Battery. II. Effect of Various PbO_2 Types and Paste Formulations of Precharged Positive Plate Performance: *E. J. Taylor,** *G. A. Shia,* and *D. T. Peters*, Inco Alloy Products Co. Research Center, Suffern, NY 10901

The performance of the "precharged" PbO_2 electrode formulated with PbO_2 from various sources is reported in this paper. PbO_2 samples were first characterized by several methods, and plates were constructed using tetrabasic lead sulfate (TTB) and other materials as binders according to the "precharged" plate concept described in the preceding paper. Performance of these plates correlates with active material morphology and PbO_2 particle size rather than intrinsic PbO_2 activity. TTB and $PbSO_4$ are shown to be the preferred binding materials. Plates made with about 30% TTB and strengthened with synthetic fibers for green strength exhibit superior cycle life performance on a simulated automotive cycle life test relative to conventionally prepared positive electrodes.

38 Silver-Zinc Cell Design—A Survey: *A. S. Berchielli*, Yardney Electric Corp., Pawcatuck, CT 02891

The silver-zinc system, although a mature technology, still maintains its place in many fields where high power loads must be supplied by a lightweight, reliable, portable energy source. Characteristics of the system design as they relate to power and energy densities are explored. Methods of fabrication and construction of both cells and batteries are reviewed. Examples of typical as well as extremes of hardware variations are shown and discussed.

39 Physical Design Optimization of the Fiber Composite Nickel Plaque: *W. W. Lee, W. A. Ferrando,** and *R. A. Sutula*, Naval Surface Weapons Center, Silver Spring, MD 20910

The fiber composite nickel plaques have been investigated with the aim of optimizing various physical properties through proper fabrication conditions. The design must combine the attributes of a lightweight porous electrode material having a strong sinter bond, while maintaining high electrical conductivity. The areas in which these plaques have been tested include: porosity, tensile strength, and active material utilization. Preliminary results indicate that the composite plaque has superior mechanical properties, wider range of available porosity, and greater ease of impregnating even thick plaques compared with conventional powder sinters.

40 High Efficiency Nickel Electrode: *A. H. Zimmerman*, Aerospace Corp., Los Angeles, CA 90009

The mechanisms of processes that control the rate at which the nickel electrode can be discharged have been evaluated. Premature electrode depletion during high rate discharge can result from the buildup of an insulating layer at the current collector/active material interface, and is exhibited as a discharge plateau at an unusually low voltage. A new nickel electrode fabrication technique controls the growth of the insulating layer during discharge, allowing improved efficiency at high discharge rates.

41 Electrolyte Manifold Design for Batteries: *J. B. Riggs*, Dept. of Chemical Engineering, West Virginia University, Morgantown, WV 26506

This paper considers practical and theoretical aspects of the manifold design for batteries that use forced convection electrolyte

systems. First, a theoretical model for calculating the flow distribution and pressure distribution for the four general types of manifolds is presented and analyzed with regard to manifold design. Then, a newly developed short-cut method for manifold design is presented and discussed. Finally, a review of common industrial practices for manifold design is presented and reviewed.

42 Zinc-Bromine Battery Design and Optimization—Decoupling of Hydraulic and Shunt Considerations: *P. Grimes, R. Bellows, H. Einstein, E. Kantner, P. Malachesky,* and *K. Newby,* Exxon Research and Engineering Co., Linden, NJ 07036

Many factors are involved in zinc-bromine battery designs. These include shunt current minimization, hydraulic and mass transfer uniformity, manufacturability, and system packaging. These factors are particularly true with high voltage high power systems with augmented conductivity electrolyte which requires careful consideration of the hydraulic and electrolytic shunt current protection networks, for minimal auxiliary power. The tunnel shunt current protection method has low power requirements for these conditions, and the manifold cross sections can be large leading to low pressure drops and uniform flows to each cell. A two piece unit cell construction with decoupled hydraulic and shunt protection factors has evolved. This leads to compact systems which are adaptable to various voltages and powers and should be easy to manufacture. The interaction and philosophy of design constraints are discussed.

43 Thermal Modeling of a Flowing Electrolyte Li/$SOCl_2$ Battery: *D. W. Ernst,* Naval Surface Weapons Center, White Oak, Electrochemistry Branch, Silver Spring, MD 20910

A computer program called HOT POT is being developed at NSWC to simulate heat generation in an Li/$SOCl_2$ battery utilizing a flowing electrolyte design. A finite element program called NACHOS is used as the basic program. NACHOS was developed for the analysis of two-dimensional, viscous incompressible fluid flow problems including heat transfer effects. To test the sensitivity of the program simulation runs were made for various current densities, electrode polarization values, electrolyte conductivity, and flow rates. The results obtained from this matrix study are reported.

44 Lithium Anode Rechargeability and Design Considerations for Ambient Temperature Lithium Cells: *M. Eisenberg,* Electrochimica Corp., Mt. View, CA 94040

The choice of the solvent system has a powerful effect on the rechargeability of lithium anodes in lithium ambient temperature cells. For instance, dioxolane based solvents are preferable to those employing 2-Me-Tetra Hydrofuran (2-Me-THF) on the basis of stripping efficiency studies in continuing cycling. If a reproducible minimum coulombic recharge efficiency of at least 95% can be obtained the designer of an ambient temperature lithium cell can then predict the number of cycles he will obtain either to a 100% of nominal capacity retention or to a specified drop in capacity retention or to a specified drop in capacity at the end of cycling on the basis of a set of simple relations to be presented. To avoid the use of very large excesses of capacity of lithium in a cell (which would dilute the practical energy density) the designer can calculate the initial lithium anode capacity ratio needed for a desired cycle life objective.

45 Changing the LiAl/FeS Cell Design to Include Excess FeS Capacity: *T. D. Kaun,* Argonne National Laboratory, Chemical Technology Div., Argonne, IL 60439

In prior art, cell capacity decline-phenomenon imposed restraints upon the LiAl electrode utilization requiring 20-35% excess LiAl capacity in the design. However, electrode development and cell diagnostics provided concurring results indicating cell performance limitations due to the FeS electrode. In response, tests of cells designed with excess FeS electrode capacity (15-20%) and stable LiAl electrodes are described. Here, cell internal resistance (about 0.75 Ω:cm^2 at 50% DOD), which had typically doubled between 50-80% depth of discharge, increased by only 20%. Consequently, this design change improved specific energy at 2-4 hr discharge rates, approximately 15%, and cell power at 80% depth of discharge, approximately 70%.

46 Test-Electrode Design and Method for Active Material Characterization: *L. Redey* and D. R. Vissers,* Argonne National Laboratory, Chemical Technology Div., Argonne, IL 60439

An electrode system which permits electrochemical investigation of active electrode-materials under one-dimensional current distribution has been developed. The design makes electrode bed characterization possible under a wide variety of conditions that include different forms of distributed current collection, isobaric or isometric material confinement, etc. Electrode processes which limit specific energy and power are studied by d-c current interruption, electrode potential relaxation, and current-pulse techniques. The method provides fundamental data elements for cell design and optimization. Results obtained on advanced battery system materials (Li-Al, Li-Si, FeS, FeS_2) are presented.

47 Power *vs.* Energy Trade-Off Studies for Lithium-Alloy/Iron Sulfide Cells: *E. C. Gay,* L. Redey, F. J. Martino,* and *P. A. Nelson,* Argonne National Laboratory, Chemical Technology Div., Argonne, IL 60439

Important factors in the design of batteries for electric-vehicle propulsion include battery capacity, specific energy, specific power, and power-to-energy ratio. One approach to power and energy trade-off is to vary the size of the current collector, interelectrode connectors, terminals, and thickness of the electrodes in the cell. A computer program for the design and optimization of Li-alloy/iron sulfide cells has been developed with the capability of calculating voltage losses across all of the current-carrying elements of the cell. These losses can be distributed as desired across the electrode current collectors, interelectrode connectors, and cell terminals. Ohmically and electrochemically related electrode bed resistances are calculated from equations derived from area-specific-resistance measurements from electrode polarization studies. Input to the program includes the usable capacity at a given discharge rate and the power-to-energy ratio.

48 Prototype Aluminum-Air Cell: *D. J. Levy,* R. P. Hollandsworth, E. M. Gonzales,* and *E. L. Littauer,* Lockheed Palo Alto Research Laboratory, Palo Alto, CA 94304

The Al-air battery is being developed as an automotive energy source for general purpose vehicles. Prototype cells, suitable for stacking, have been designed, constructed, and evaluated. The engineering design uses a novel anode current collector which avoids conventional attachment of electrical wire and enables rapid refueling. Details of two cell designs, power, electrode polarization, anode and electrolyte composition, and anode utilization are discussed. Cobalt-catalyzed air cathodes compare favorably with platinum-catalyzed cathodes.

49 Reverse Voltage Protection in Lithium/Thionyl Chloride Cells: *N. A. Godshall,* J. K. Surprenant,* and *A. Zolla,* Altus Corp., San Jose, CA 95112

Lithium/thionyl chloride cells can be internally protected against large reverse voltage excursions which normally occur whenever one cell, in a group of series-connected cells, reaches its end of discharge life before the others. The mechanism of this protection is internal to the cell, and causes the reverse voltage to remain smaller than −0.10V. It therefore offers several advantages over external diodes which do not protect the cell until the polarity reversal reaches −0.50-0.70V. The cell design required for this protection, and its theoretical basis, are discussed.

50 Thermophysical Properties of Thionyl Chloride Based Electrolytes for Li/$SOCl_2$ Battery: *H.V. Venkatasetty,* Honeywell Inc., Corporate Technology Center, Bloomington, MN 55420 and *S. Szpak,* Naval Ocean Systems Center, San Diego, CA 95152

Vapor pressure, heat capacity, and thermal conductivity of thionyl chloride based electrolyte solutions have been determined as a function of temperature. Vapor pressure is found to decrease with increasing concentration of the electrolyte. Heats of vaporization (ΔH_v) calculated also show increase with increasing concentration. These changes are interpreted in terms of ion-dipole interactions. Heat capacity data on these solutions show a gradual increasing trend with increasing temperature and the rate of increase is large at high temperature. Thermal conductivity data show that the electrolyte solutions have higher conductivity then pure thionyl chloride and thermal conductivity increases with increasing temperature particularly at high concentration of lithium chloride. These observed changes in the properties of electrolyte solutions are discussed in terms of their composition and structure.

51 Low Temperature Performance Characterization of Lithium-Sulfuryl Chloride Cells: *M. Binder,* S. Gilman,* and *W. L. Wade, Jr.,* Power Sources Division, Electronics Technology and Devices Laboratory (ERADCOM), Fort Monmouth, NJ 07703

Studies were performed to relate reduced operating voltages and capacities of Li/$LiAlCl_4$-SO_2Cl_2 cells to electrolyte concentration, measured electrolyte conductivity, and the composition and morphology of the solid cathodic discharge product phase. Over a wide temperature range, LiCl is the predominant solid cathodic product. Initial load voltages depend on the temperature dependent ability of the carbon cathode to catalyze the decomposition of SO_2Cl_2 to yield active chlorine. Decreased operating voltage at the end of cathode life is due to decreased transport of Li^+ and other electrolyte species through the LiCl product layer.

52 Lithium/Sulfuryl Chloride Cell Optimization: *K. A. Klinedinst,* GTE Laboratories, Inc., Waltham, MA 02254

It was noted nearly ten years ago that lithium/inorganic electrolyte cells with sulfuryl chloride-based electrolytes are potentially superior to similarly constructed lithium/thionyl chloride cells. Described here are some of the factors which formerly discouraged the development of a hermetically sealed lithium/sulfuryl chloride cell technology. Also described are recent improvements in cylindrical cell design and in electrolyte composition that have resulted from AA-size lithium/sulfuryl chloride cell optimization studies.

CORROSION

General Session

53 The Dissolution and Passivation of Iron in Concentrated Alkali: *M. C. H. McKubre,* M. J. Madou,* and *K. Kinoshita,* SRI International, Menlo Park, CA 94025

The passivation of iron in concentrated alkali proceeds through a number of stable surface oxide phases. These oxides may be formed *in situ* by solid phase reactions, or the reactions may involve dissolved intermediates. In this paper we describe the results of

rotating disk, rotating ring disk (RRDE), and a-c impedance studies of iron electrodes in 30 w/o KOH, in the temperature range 0°-100°C. RRDE results show clear evidence for dissolved phase reaction intermediates occurring within four well-defined regions of potential. The results of a-c impedance measurements to characterize the surface oxide, and cyclic voltammetry to identify the oxidation and reduction peaks of the rotating iron disk electrode, have enabled us to postulate a detailed mechanism for the formation and reduction of an oxide film on iron via a number of dissolved intermediate species.

54 Mechanism of Passive Film Formation and Reduction on Iron: *Gh. Nazri,** Lawrence Berkeley Laboratory, Materials and Molecular Research Div., Berkeley, CA 94720, and *E. Yeager* and *B. D. Cahan*, Dept. of Chemistry, Case Western Reserve University, CCES, Cleveland, OH 44106

Passivation was studied using linear sweep voltammetry, potential step measurements, and a rotating ring-disk electrode (RRDE) technique. Passive film reduction has also been studied by the same techniques. Data imply solid-state reduction followed by dissolution of the reduction products. Care was taken in electrode surface preparation and passive film formation to avoid formation of an overlayer on the passive film surface due to the oxidation of ferrous ions, which accumulate at the solid liquid interface during passive film formation.

55 A New Mossbauer Conversion Electron Detection Technique for *In Situ* Passivation Studies on Iron: *M. E. Kordesch,* J. Eldridge, D. Scherson*, and *R. W. Hoffman*, Case Center for Electrochemical Sciences and the Dept. of Physics, Case Western Reserve University, Cleveland, OH 44106

A system is described that allows the detection of conversion electrons through thin electrolyte layers, exploiting the increased surface sensitivity of electron detection Mossbauer measurements over conventional gamma-ray detection schemes. The substrate is a slowly rotating disk, where the upper emersed half is analyzed while the lower half remains submerged and under potential control. Spectra of the passive film on iron in buffered borate (pH 8.4) is presented and compared with conventional Mossbauer spectroscopy measurements of the passive film on iron in buffered borate and other electrolytes.

56 An *In Situ* Technique for the Decoration of Defects in Passive Films: *X. Wu, Y. K. Hong,** and *R. A. Oriani*, Corrosion Research Center, University of Minnesota, Minneapolis, MN 55455

Potentiostatic electrodeposition of silver has been employed to locate defects in passive films on stainless steel. The potential applied to form the passive film in 0.5M Na_2SO_4 of pH 2 is maintained during the subsequent injection of a dilute solution of silver ion. It was found that, within a certain film-forming potential and silver ion concentration, the number density of silver particles increases asymptotically with time to reach a plateau which increases with increasing silver ion concentration. At another range of potentials, a more-or-less continuous silver film is deposited on the passivating film. In both cases, resistance to pitting is increased. The significance of these results and the utility of the silver-deposition technique are discussed. (This work was done under the auspices of the Corrosion Research Center, supported by the Department of Energy, DOE/DE-AC02-79ER10450.)

57 Active-Passive Transition Study of Titanium-Molybdenum Alloy: *Y. K. Hong*, Corrosion Research Center, University of Minnesota, Minneapolis, MN 55455, and *R. S. Glass*, Sandia National Laboratories, Albuquerque, NM 87185

Electrochemical and surface analytical techniques (AES, XPS) have been used to study the active-passive transition in Ti-20Mo (w/o). The potential range from −1.2 to −0.9 V *vs.* SCE was examined electrochemically for the alloy in deaerated 2.5M NaOH at various temperatures ranging from 26° to 80°C. The results indicate that in the active region the surface oxide is enriched in Mo, and in the passive region it is depleted in Mo. The mechanisms for the active-passive transitions are discussed. (This research is supported by the Sandia National Laboratories, Contract No. 68-0273.)

58 Breakdown of Passive Films on Iron in Chloride Solutions: *O. J. Murphy,* T. E. Pou*, and *J. O'M. Bockris*, Dept. of Chemistry, Texas A and M University, College Station, TX 77843

The breakdown process of passive films formed on iron in chloride solutions is elucidated. Parameters investigated include passive film thickness, chloride ion concentration, solution pH, and electrode potential. Passive films were examined, prior to, and after, exposure to chloride ions by means of XPS, SIMS, and ISS. Differences in the nature of films are presented. Depassivation is discussed in terms of the water model for the passive film on iron.

59 Effect of Focused Ultrasound on Depassivation of Iron in Sulfuric Acid: *R. Alkire** and *S. Perusich*, Dept. of Chemical Engineering, Materials Research Laboratory, University of Illinois, Urbana, IL 61801

In one series of studies, a curved piezoelectric transducer (1.58 MHz) was used to create cavitation by focused ultrasound at the surface of an iron electrode immersed in 2N H_2SO_4 and held under controlled potential. In a second series of studies, a commercial sonicator was used to generate ultrasound. It was found that at high focal intensities (>1.5 kW/cm²) a single pulse (0.1 sec) of ultrasound produced immediate corrosion depassivation. At low focal intensities, continuous ultrasonic exposure led to depassivation after an induction period, which was found to depend upon potential. In all cases, depassivation was followed by precipitation of a metal salt film upon the surface before repassivation occurred.

60 Influence of Anions on the Dissolution of Titanium in Acidic Aqueous Solution: *G. M. Brown*, Oak Ridge National Laboratory, Chemistry Div., Oak Ridge, TN 37830

Titanium electrodes with an air-formed oxide film will not spontaneously activate in 1M aqueous perchloric or p-toluenesulfonic acid at 30°C. Addition 1×10^{-2} M H_2SO_4 or $Na_2C_2O_4$ allows dissolution of the air-formed oxide and spontaneous activation is observed. Detailed potentiostatic polarization studies of Ti in dilute solutions of sulfate in 1M chloride electrolyte at pH 1 show the influence of sulfate is to increase the anodic dissolution current with minor changes in the hydrogen evolution current. A similar mechanism is postulated in perchlorate or p-toluenesulfonate media. The quantitative aspects of the polarization curves are discussed. (Research sponsored by the Division of Materials Sciences, U. S. Department of Energy under contract W-7405-eng-26 with the Union Carbide Corporation.)

61 Mechanism of Transpassive Dissolution of Titanium-Molybdenum Alloys: *R. S. Glass,** Sandia National Laboratories, Albuquerque, NM 87175, and *Y. K. Hong*, Corrosion Research Center, The University of Minnesota, Minneapolis, MN 55455

Electrochemical and surface analytical techniques (AES) have been used to examine the mechanism of transpassive dissolution of Ti-Mo (5-30 w/o) alloys. The potential region from −0.3 to +0.4V *vs.* SCE has been examined electrochemically for the alloys in deaerated 1N HCl and H_2SO_4. The results indicate that in this region the β phase dissolves as an entity, *i.e.*, there is no preferential dissolution of Mo which might be anticipated from the anodic behavior of pure Mo in this potential region. The mechanisms for this transpassive behavior are discussed. (This work was supported by the U. S. Department of Energy (DOE), under Contract Number DE-AC04-76-DP00789.)

62 An Electrochemical and ESCA Study of Titanium Dissolution in Acidic Sulfate Solutions Containing CrII/CrIII Ions: *A. L. Bacarella,* J. M. Dale*, and *L. D. Hulett, Jr.*, Oak Ridge National Laboratory, Chemistry Div., Oak Ridge, TN 37830

An electrochemical and ESCA study is presented for titanium exposed to de-oxygenated acid sulfate solutions containing Cr(2)/Cr(3) ions. It is shown that the behavior is greatly different from the reported behavior in the presence of the Ti(3)/Ti(4) redox couple. Whereas with the higher valent Ti(4) ion passivation may occur, depending on the concentration and pH, here it is the lower valent Cr(2) ion, which provides an inhibition of dissolution over the entire potential range. (Research sponsored by the Division of Materials Sciences, U. S. Department of Energy under Contract W-7405-eng-26 with the Union Carbide Corporation.)

63 Corrosion Behavior of Ion-Implanted Amorphous Alloys: *N. R. Sorensen** and *S. T. Picraux*, Sandia National Laboratories, Albuquerque, NM 87185

A program is underway to study the corrosion behavior of amorphous alloys. Ion implantation has been used to produce both amorphous and crystalline surface layers on samples of an Fe-6Cr base alloy. Phosphorus has been implanted at various levels in order to gain insight into its role in the corrosion (passivation) process. Carbon is then implanted at the appropriate concentration to establish the structure (microcrystalline or amorphous) of the implanted layer. Potentiostatic current decay curves and potentiodynamic polarization techniques are used to study the corrosion/passivation behavior of these alloys in dilute sulfuric acid. In light of these experiments the relationship between structure and corrosion behavior of these alloys is discussed. (This work was supported by the U. S. Department of Energy (DOE), under Contract Number DE-AC04-76-DP00789.)

64 On the Interpretation of Cyclic Voltammograms of Iron Electrode in Alkaline Solutions at Various Temperatures: *A. Wieckowski** and *E. Ghali*, Faculté des Sciences et de Génie, Dépt. de Mines et Métallurgie, Université Laval, Laval, Qué., Canada G1K 7P4

Cyclic voltammetry of iron electrode in sodium hydroxide was made at various temperatures (from 25° to 95°C) and at scan rates (from 5 to 500 mV. sec^{-1}). Iron hydroxide formation is followed by a place exchange process which contributes to the establishing of the baseline current of all subsequent anodic peaks. The remaining processes identified are: active dissolution of iron, dissolution-precipitation (<55°C), oxidation of Fe(II) film to Fe(III) passive layer, two-steps (<55°C) or one-step (≥55°C) reduction of iron oxides. Diagrams summarizing voltammetric behaviour of iron at low and high temperatures are presented and conclusions concerning the diagnosis and prevention of SCC of carbon steel are drawn.

65 Growth Kinetics of Single Pits in 304 Stainless Steel: *R. C. Newman*, Corrosion Science Group, Brookhaven National Laboratory, Upton, NY 11973

Some aspects of pitting in Type 304 stainless steel have been examined using a neutral sodium chloride solution with a small addition of sodium thiosulfate. In this solution, single pits can readily be produced and subjected to various potential waveforms. The potential dependence of pit growth rate yields a resistance which is directly related to the rate of diffusion of corrosion products from the pit and thereby to the "protection potential" against pitting. The de-

pendence of protection potential on pit volume and solution resistance has been examined.

66 Modeling of Film Formation and Oscillatory Instability in the Electrodissolution of Copper in Acidic Chloride Media: *A. J. Pearlstein,* H. P. Lee,* and *K. Nobe,* School of Engineering and Applied Science, UCLA, Los Angeles, CA 90024

A simple model is proposed to describe anodic film formation and chemical dissolution at the surface of a rotating copper electrode. The model consists of a moving boundary problem for the diffusion of Cl^- in a porous CuCl film. The unique steady solution yields a nominally steady current and film thickness. A linear stability analysis is conducted to determine the conditions under which the steady solution is unstable. The results are compared to recent experiments.

67 Oscillatory Behavior in Copper Electrodissolution in Acidic Chloride Media: *H. P. Lee** and *K. Nobe,* Dept. of Chemical Engineering, UCLA, Los Angeles, CA 90024

The electrodissolution of copper in acidic chloride media has been studied by means of a rotating disk electrode. Current oscillations during the potentiostatic dissolution have been observed at potentials above the current minimum. The oscillatory behavior was found to depend on the chloride concentration, the potential, and the rotation rate. These oscillations are explained in terms of a mechanism involving film formation and electrodissolution.

68 Corrosion of a Cupro-Nickel Alloy in Sulfide-Containing Solutions: *H. S. Tong,* Revere Research, Inc., Edison, NJ 08837

The corrosion and electrochemical behavior of C71500 cupronickel alloy in deaerated 3.4% synthetic seawater and deionized water has been investigated as a function of dissolved sulfide concentration. The sulfide decay kinetics and its correlation with the pH of the electrolyte was also studied. Specimen surfaces were examined using scanning electron microscopy in conjunction with x-ray intensity mapping. It is shown that the presence of sulfide significantly changes the electrochemical characteristics of the alloy/media system. Possible mechanisms have been reviewed in terms of the present results.

69 Composition of Chromate Passivation Films on Aluminum-Zinc Alloy-Coated Sheet Steel: *H. E. Townsend** and *R. G. Hart,* Bethlehem Steel Corp., Homer Research Laboratories, Bethlehem, PA 18016

Chromate passivation is a surface treatment that is widely used to provide temporary protection to metallic-coated sheet steel against corrosion during shipment and storage. We studied the composition of films formed during chromate passivation of 55% aluminum-zinc alloy-coated sheet steel by use of Auger electron spectroscopy and x-ray photoelectron spectroscopy. The results show that the passivation film contains chromium oxide, aluminum oxide, and metallic chromium. We believe this composition accounts for unusually high resistances of the passivated sheet to wet-storage stain and atmospheric tarnishing.

70 Effect of Alternating Voltage on the Corrosion of Stainless Steels: *J. L. Wendt** and *D-T. Chin,* Dept. of Chemical Engineering, Clarkson College of Technology, Potsdam, NY 13676

The effect of square-wave alternating voltage (AV) on the corrosion of stainless steels in seawater and in aqueous solutions containing sulfate and nitrate ions has been examined with a potential step technique. The resulting d-c polarization curves exhibit an increase in the current density in the active and the passive regions and a shift of the passive/transpassive transitional potential toward the active direction. The incidence of pitting corrosion is greatly enhanced by the application of AV. A mathematical model is used to generate computer-simulated polarization curves and to explain the experimental results.

71 Influence of CO and CO_2 Partial Pressure on Electrochemical Behavior of Stainless Steels and Nickel-Base Alloys in Carbonate Solutions: *R. Sehil, N. Jallerat, F. Bourelier, M. Fedoroff,* and *K. Vu Quang,** Centre d'Etudes de Chimie Métallurgique, CNRS, 94400 Vitry, France

In an industrial process using hot concentrated potassium carbonate solution under 20 bar pressure of CO-CO_2 gas mixture, towers made of 316 Ti stainless steel underwent a severe corrosion. Pernicious effect of sulfide in solution has been pointed out (1). In the present study, the electrochemical behavior of AISI 304, 316 Ti, Inconel 600, 625, and Incoloy 800, 825 has been investigated, taking into account the partial pressure of CO and CO_2. CO_2 has been found to play a prevalent role and increase markedly the critical current of alloys, especially 304 SS in the range of 2-5 bar CO_2 partial pressure. Nickel base alloys, in particular alloy 800, showed very good behavior. Electrochemical data were in good agreement with analytical data obtained from tested solution and from alloy surface study.

1. K. Vu Quang *et al., Mét. Corros. Ind.,* **675,** 386 (1981).

72 Evaluation of Structured Noise Techniques for the Measurement of Interfacial Impedance: *B. G. Pound* and *D. D. Macdonald,** Fontana Corrosion Center, Dept. of Metallurgical Engineering, The Ohio State University, Columbus, OH 43210

Paper withdrawn during publication process.

73 A-C Impedance Study of the Passivation of Mg, Al, and Mg Alloy AZ91B: *P. L. Hagans,* The Dow Chemical Co., Central Research Inorganic Lab, Midland, MI 48640

Wide frequency a-c impedance measurements have been obtained on ultrapure Mg and AZ91B alloy (9% Al, 1% Zn) over the anodic range from open circuit to the onset of O_2 evolution and for Al from open circuit to +6.0V *vs.* α-PdH in a borate buffer solution. Two processes, dissolution at high frequency and passivation at low frequency, were observed from the Bode plots for each metal over the entire anodic range. Distinct differences in the dissolution-passivation mechanisms for each metal were detected.

74 Impedance Spectra for Anodized Aluminum Alloys during Exposure to NaCl: *F. Mansfeld** and *M. Kendig,* Rockwell International Science Center, Thousand Oaks, CA 91360

The corrosion resistance of various anodized Al alloys has been evaluated by measurements of the electrochemical impedance during exposure to 0.5*N* NaCl. The Al alloys 2024, 6061, and 7075 were tested, the anodizing treatments were carried out in sulfuric or in chromic acid, and hot water or dichromate sealing was used. The characteristic impedance parameters were compared with the corrosion behavior as determined by visual observation after the exposure test.

75 The Role of Polymer Adhesion and Cohesion on the Corrosion Protection of Polymer Coated Steel: *M. Kendig,** *A. Aerora,* and *F. Mansfeld,* Rockwell International Science Center, Thousand Oaks, CA 91360

Recent work in this laboratory showed that growing corrosion products decrease the pore resistance, R_{po}, of polymer coatings on steel. It is well known that cathodic reactions cause adhesive failure. The dependence of R_{po} on the elongation of polymer coated steel has been determined for coatings differing in ductility. Acoustic emission from polymer-coated steel specimens strained to failure at a constant rate quantifies the loss of adhesion and cohesion of the coatings due to exposure to 0.5M NaCl. The results are discussed in terms of substrate preparation and polymer properties. (This work was performed under Contract No. N00014-79-C-0437 with the Office of Naval Research.)

76 Interference Problem Related to the Rotating Ring-Disk Electrode: *Gh. Nazri,* Lawrence Berkeley Laboratory, Materials and Molecular Research Div., Berkeley, CA 94720, and *B. D. Cahan,** Dept. of Chemistry, Case Western Reserve University, CCES, Cleveland, OH 44106

The problem of ring-disk coupling in rotating ring-disk electrode due to the effect of disk current on ring potential as well as ring current on disk potential has been studied. We found that the way to solve this coupling effect, at least for primary current distribution, is by using two potentiostats with one feeding back partial voltage proportional to the current of the other electrode, when pulsing potential of one electrode and examining the response of the other. This procedure has been applied to the study of passivation of iron, which is still poorly understood, by using potential step and potential scan measurements. Our procedure has also been checked by using Au disk-Au ring electrode to compare our results with the literature. A new design for interchangeable ring-disk electrode was developed.

77 Carbon Corrosion: *L. Berk** and *D. Zuckerbrod,* Westinghouse Research and Development Center, Pittsburgh, PA 15235

Studies of carbon corrosion in both potassium hydroxide and phosphoric acid have been initiated. These are the first detailed studies of carbon at anodic potentials in base. The correlations of temperature, concentration, and surface area with the corrosion rate have been developed. Voltammetry of carbons in acid and bases has been used to develop corrosion models. The differences between corrosion in base at room temperature and in acid at 180°C are discussed.

78 An Electrochemical Technique for Measuring Residual Stresses in Inconel 600 Tubes: *R. Bandy** and *T. Zemanian,* Corrosion Science Group, Dept. of Nuclear Energy, Brookhaven National Laboratory, Upton, NY 11973

Residual stresses in Inconel 600 tubing have been determined using an electrochemical method of removing metal. Isotropic elasticity solution has been used to relate residual stresses in a thin layer of material removed from the inner surface of the tube to the resulting strains measured on the outer surface, and vice versa. The effect of cold working and stress relieving heat-treatments at several time-temperature combinations on the residual stresses, and the implication of the stress relief to stress corrosion cracking have been investigated.

79 The Open-Circuit Potential of Oxidized and Hydrided TiCode-12: *Y. J. Kim, Y. K. Hong,** and *R. A. Oriani,* Corrosion Research Center, University of Minnesota, Minneapolis, MN 55455

The open-circuit potential of TiCode-12 alloy immersed in neutral brine solution was measured as a function of time after a variety of pretreatments: (i) air exposure for various times, (ii) anodic oxidation in sulfuric acid for various times, and (iii) hydride formation at cathodic potentials in sulfuric acid. The open-circuit potential E_{oc} of case (iii) is more noble than (i), and case (ii) more noble than (iii). In all cases, $E_{oc} \alpha t^{1/2}$, where t = duration of immersion in the brine. The reasons for this behavior and the mechanisms for oxide-film thickening are discussed. (Research supported by the Sandia National Laboratories, Contract No. 68-0273.)

80 The Electrochemical Behavior of Aluminum Containing Al-Fe-Si Particles in Hydrochloric Acid: *C. D. S. Tuck*, Alcan International Ltd., Banbury, Oxon OX16 7SP, England

Aluminum-containing $FeAl_3$ and αAl-Fe-Si particles was electrolytically etched in 2% HCl and 2% HCl/3% acetic acid, and the various stages of etching were observed by scanning electron microscopy. $FeAl_3$ was more readily attacked in HCl than αAl-Fe-Si particles but in HCl/acetic acid, as well as a much shorter induction time for pitting, both the αAl-Fe-Si and $FeAl_3$ were attacked. The behavior is shown to indicate that the particles can display anodic or cathodic behavior depending on the degree of passivation of the aluminum matrix.

81 Cathodic Protection of Above-Ground Structures by a Sparse Zinc Coating: *D. C. Prieve* and *P. J. Sides*,* Dept. of Chemical Engineering, Carnegie-Mellon University, Pittsburgh, PA 15213

The effectiveness of a sparse zinc coating for cathodically protecting above-ground structures is theoretically analyzed. The radius of protection surrounding an individual zinc particle attached to a metal substrate and embedded in an ionically conducting coating is a function of a single parameter. For example, a 1 mm zinc dot embedded in a coating 1/10 mm thick and having a bulk conductivity of $0.001(\Omega\text{-cm})^{-1}$ protects an area 120 times larger than itself.

82 Corrosion of Thin Film Cobalt Alloys in Variable Relative Humidity Atmospheres: *R. R. Dubin** and *K. D. Winn*, Memorex Corp., Recording Technology Center, Santa Clara, CA 95052

The atmospheric corrosion behavior of several different cobalt based (Co, Co-Ni, and Co-Cr) thin film magnetic recording alloys was characterized after exposure to atmospheres containing up to 78% relative humidity at 85°C. Sulfur, chlorine, and oxygen penetration were measured and related to changes in magnetic properties. Surface characterization work showed that physical changes were localized at discrete points on the thin (1000Å to 1 micron) film surface. These sites generally contained high concentrations of the active chemical constituents present in the test atmosphere.

83 Development of Protective Systems for Metallic Canisters: *L. Gruss*, ARRADCOM, FSL, Dover, NJ 17801 and *S. Kolodzey*, Chemical Systems Laboratory, Aberdeen Proving Ground, MD 21010

A variety of metals, ceramics etc. were investigated for their electrochemical and corrosion behavior in methylphosphonicdifluoride (DF). Maximum exposure to DF was for a period of 26 weeks at 71°C in the concentration range of 97.1-99.2%. A scanning electron microscope (SEM) examination, energy dispersive x-ray (EDX), and energy dispersive system (EDS) analysis were performed on the exposed (to DF) and unexposed materials. Linear polarization, Tafel slope, and potentiodynamic anodic polarization measurements are described.

84 Influence of Impurities on the Corrosivity of Industrial Phosphoric Acid: *M. El Safty*,* *F. Dabos*, and *N. Bui*, Dept. of Chemical Engineering, Military Technical College, Kobry El Kobba, Cairo, Egypt

Industrial phosphoric acid produced by the wet method contains many impurities among which the Cl^- is the most dangerous. Egyptian phosphoric acid may contain 1000 ppm Cl^-, increasing the corrosivity of the acid specially in the units subjected to heat transfer conditions. In this paper, the electrochemical compartment of special alloys containing 20 Cr-25 Nr are studied and also the effect of temperature is illustrated. The influence of W on improving the corrosion resistance of these alloys is indicated.

85 Electrode Modification for Corrosion Control in FeS Electrodes: *J. A. Smaga* and *J. E. Battles*, Argonne National Laboratory, Argonne, IL 60439

The positive electrode hardware from Li-Al/FeS cells initially exhibits rapid corrosion which is characterized by grain fallout at the component surface. A transition to a lower rate of corrosion occurs within 250 days of operation. It was deduced from these post-test observations that corrosion of the low carbon steel hardware could be minimized with the addition of iron powder in excess of the amount required for a stoichiometric FeS electrode. Subsequent accelerated corrosion tests determined that the optimum concentration is 19 w/o iron powder of <150-μm size. A test cell which used this low-cost modification demonstrated a 70-75% reduction in corrosion of the steel current collector and framing with no loss in cell performance.

DIELECTRICS AND INSULATION/ELECTRONICS

Dielectric Isolation

86 Thermal Oxidation of Sputtered Silicon Carbide Thin Films: *W. J. Lu*, Rensselaer Polytechnic Institute, Center for Integrated Electronics, Troy, NY 12181, *T. P. Chow*, General Electric Corporate Research and Development, Schenectady, NY 12301, *A. J. Steckl*, Rensselaer Polytechnic Institute, Center for Integrated Electronics, Troy, NY 12181, and *W. Katz*, General Electric Corporate Research and Development, Schenectady, NY 12301

Silicon carbide thin films are being investigated as an alternative to silicon nitride in local oxidation (*e.g.*, LOCOS) processes. Silicon carbide thin films were deposited by rf sputtering at 300°C. Thermal oxidation was carried out in wet oxygen at 900°-1100°C for periods ranging from 20 to 120 min. The oxidation rate of silicon carbide was 3-4 times slower than that of single crystal, (100) Si. The refractive index of the carbide films (annealed at 1000°C in H_2) was approx. 2.55 *vs.* 2.65 for bulk SiC. Structural and compositional properties of these silicon carbide thin films and their grown oxide were studied by SIMS and x-ray diffraction.

87 Planarization of Isolation Oxide by Argon Ion Sputtering: *Y. Mashiko*,* *H. Koyama*, and *S. Kawazu*, Computer Development Lab. Ltd., Itami Hyogo 664, Japan, and *T. Nichioka*, *H. Yakushiji*, and *H. Harada*, Mitsubishi Electric Co., Hyogo 664, Japan

A high oxide step, or bird's head, resulting from the local oxidation of silicon degrades metal step coverages. This work describes planarization of the oxide topographies by an application of argon ion sputtering. The planarization process typically reduces step heights by more than 60%. Experimental results are compared with two dimensional model calculation, and the mechanism for the planarization is discussed. The advantages of this process over other isolation technologies are demonstrated in an actual ECL device.

88 A Model for the Two-Dimensional Thermal Oxidation of Silicon Cylindrical Geometries: *G. Oleszek*,* *K. Kasley*, Micro-Electronics Laboratory, Dept. of Electrical Engineering, University of Colorado, Colorado Srrings, CO 80933, *R. Jones*, Dept. of Physics, University of Colorado, Colorado Springs, CO 80933, and *D. Granteer*, Monsanto Corp., St. Louis, MO 63166

In the fabrication of high technology VLSI integrated circuits, the two-dimensional nature of thermal oxidation cannot be neglected. In high density bipolar and MOS technologies, for example, isotropically etched circular areas are thermally oxidized to provide isolation regions. In this paper, an analytical model for the two-dimensional oxidation of silicon cylindrical geometries is presented. The growth kinetics, applied to the case of cylindrical geometry, are based on the transport of the oxidant species from the gas to the outer surface of the oxide, and transport by diffusion toward the silicon surface, where the reaction proceeds to form SiO_2. It was found that the cylindrical growth rate expression differs from that of the planar case and depends on time in a more complex manner. Additionally, the growth rate depends on the surface topology, which is a function of the ductility of the growing oxide.

89 Multiwafer Plasma Oxidation System: *A. K. Ray*,* IBM T. J. Watson Research Center, Yorktown Heights, NY 10598, *A. Reisman*, Microelectronics Center of North Carolina, Research Triangle Park, NC 27709, and *M. Berkenblit*, IBM T. J. Watson Research Center, Yorktown Heights, NY 10598

An experimental system suitable for simultaneous oxidation of 8 silicon wafers in an oxygen or oxygen/argon plasma is described. Experiments were carried out at two different radio frequencies (3 MHz, 0.5 MHz). The rf coil design, plasma gas mixture, oxidation rate, and kinetics of oxidation were different at the two frequencies. At 3.0 MHz, the oxide thickness increases as $t^{0.5}$, but at 0.4 MHz it increases as $t^{0.3}$. The oxide thickness uniformity on a wafer and from wafer to wafer is within ± 5%. The properties of plasma oxides are comparable to thermal oxides grown at 1000°C.

90 Interpoly Oxides for EEPROM Devices: *H. L. Peek** and *J. F. Verwey*, Philips Research Laboratories, 5600 JA Eindhoven, The Netherlands

Oxides thermally grown on the poly-Si floating gate of EEPROM devices have a much lower resistance than oxides thermally grown on mono-Si. Therefore, deposited oxide layers were grown and their properties compared to thermal oxides on mono-Si. For the electrical characterization we used two methods, firstly the dielectric breakdown test and secondly, the oxide leakage test. The voltage is ramped and its value recorded when the current through the oxide in a MOS capacitor on poly-Si exceeds 10^{-6} A/mm² for the first and 10^{-11} A/mm² for the second method. The oxide field E_b (at 10^{-11} A/mm²) is considered as a measure of the oxide resistance at relatively low fields. The deposited oxides were obtained by CVD from SiH_2Cl_2 at 920°C (HTO) or from tetraethyl ortho silicate (TEOS) at 625°C. It has been observed for thermal oxides that E_b increases with decreasing oxide thicknesses. This can be explained in terms of decreasing asperity size on the poly-Si. The experimental results were verified by retention measurements in floating gate transistors.

91 Deposition and Reflow of Phosphosilicate Glass: *R. A. Bowling* and *G. B. Larrabee*, Texas Instruments Inc., Dallas, TX 75265

The phosphosilicate glass (PSG) chemical vapor deposition reaction from silane and phosphine has been simulated by SOLGAS thermochemical calculations. This equilibrium calculation method predicts stoichiometric conversion of silane and phosphine. In comparison to experimental determinations, it always underestimates the glass phosphorus content by about 1-3 w/o. Recent observations that the reflow of PSG is greatly enhanced by the presence of a steam ambient during heating have been examined. A mechanism of this reflow enhancement has been proposed, and experimental evidence is given which supports this mechanism.

92 Observations of the Temperature Gradient Zone Melting Process for Isolating Small Geometry Devices: *D. J. Lischner,* H. Basseches,* and *F. A. D'Altroy,* Bell Laboratories, Allentown, PA 18103

The temperature gradient zone melting process of aluminum has been studied for isolating triacs. The problems encountered when a square grid of aluminum metallization is migrated through a wafer is discussed. These include line breakup and lateral motion at the edge of the wafer. Techniques for minimizing these effects are described. Experiments associated with the heavy out diffusion of the aluminum into the SiO_2 passivation layer, as well as the enhanced diffusivity in the silicon, are discussed.

93 The Effects of Insulator Thickness and Small Changes in Seed Orientation on the Defect Structure of Silicon SOI Films Grown by Epitaxial Lateral Overgrowth Techniques: *J. T. McGinn,* L. Jastrzebski,* and *J. F. Corboy,* RCA Laboratories, Princeton, NJ 08540

Seeded films of monocrystalline silicon on insulator (SOI) grown via chemical vapor deposition have previously been shown to be sensitive to the major crystallographic orientation of the edge of the seed opening in the insulator. The highest quality epitaxial lateral overgrowth (ELO) films were found to occur when the edge of the seed opening ran approximately along the [001] direction on a (100) silicon surface. The defect structure of ELO films has been studied as a function of both insulator thickness and the misorientation of the seed edge about the [001].

94 Cap Layers for Silicon-on-Insulator Films Produced by Laser or Strip Heater Recrystallization: *P. G. McMullin* and *S. Dutta,* Westinghouse Research Laboratories, Pittsburgh, PA 15235

Dielectrically isolated silicon films on oxide can be made by recrystallization under laser or strip heater irradiation. A cap layer is used to stabilize the thin film and adjust optical characteristics. We have characterized thin and thick cap layers of oxide, nitride, and dual (oxide-nitride) dielectric structure for stability, surface reactions, and quality of the silicon film after recrystallization. Optical characteristics, damage thresholds, surface roughness, and crystal structures by TEM are reported.

95 Dielectric Isolation by Lateral Epitaxial Growth: *McD. Robinson** and *G. K. Celler,* Bell Laboratories, Murray Hill, NJ 07974, and *D. J. Lischner,* Bell Laboratories, Allentown, PA 18103

Dielectrically isolated single crystal silicon films with thickness >10 μm have been fabricated by lateral epitaxial growth over oxide (LEGO). The precursor structure is a combination of polycrystalline and single crystal epitaxial silicon grown over patterned oxide. This structure is melted by rapid thermal annealing (RTA) using uniform radiant heating from an extended array of tungsten-halogen lamps, and allowed to recrystallize. Heat flow, and therefore motion of the melt-solid interface, is controlled by the oxide/window pattern and the lamp cooling rate. The epitaxially regrown silicon is free of the low angle grain boundaries that have been reported in thin (<1 μm) silicon films melted by lasers and moving strip heaters.

96 Effect of Laser Annealing on Conventional and High Pressure Thermal Oxides of Silicon: *A. A. Naem** and *A. R. Boothroyd,* Dept. of Electronics, Carleton University, Ottawa, Ont., Canada K1S 5B6, *S. P. Tay,* Northern Telecom Elec, Ottawa, Ont., Canada K1Y 4H7, and *I. D. Calder* and *H. M. Naguib,* Bell-Northern Research, Ottawa, Ont., Canada K1Y 4H7

Capacitors of area 1 mm^2 were formed from 500Å films of atmospheric or high pressure (H i POx) thermal oxide with a polysilicon electrode. Measurements of leakage current, breakdown field strength, flatband voltage, and threshold voltage were made before and after CW laser annealing (LA) of the polysilicon. The characteristics of all unannealed oxides satisfy MOS device requirements. In the case of the H i POx samples, laser recrystallization of the polysilicon resulted in improvement of all measured parameters; in particular the breakdown field strength increased from 8.6 to 9.4 MV/cm. For the conventional oxides, the yield, leakage current, and breakdown field strength (8.5 MV/cm) were unchanged, while flatband and threshold voltages were improved. SEM analysis revealed no damage. Therefore LA of polysilicon gates is compatible with MOS technology. The applications of laser annealing and H i POx in stacked MOS structures are also discussed.

97 Electrical Properties of Thermal Tantalum Oxide Films Incorporating Silicon: *H. Hasegawa, T. Ogawa, K. Wada,* and *M. Nakano,* Fujitsu Ltd., IC Div., 1015 Kamikodanaka, Nakahara-ku, Kawasaki, Japan 211

The influence of silicon incorporated in thermally oxidized Ta films on Si substrates is studied in terms of the electrical properties. Ta films were deposited on Si substrates by electron beam evaporation, following a thermal oxidation to form Ta_2O_5 films. The amount of silicon incorporated in the Ta_2O_5 film was measured by ion microprobe analysis, and it was found that the content of silicon depends on the residual pressure during Ta evaporation. Electrical measurements were performed with an Al/Ta_2O_5/Si MOS structure. The relation between the electrical properties and the silicon incorporation is presented.

98 Properties of Tantalum Pentoxide Thin Films on Silicon: *G. S. Oehrlein** and *A. Reisman,* IBM Research Center, Yorktown Heights, NY 10598

The properties of tantalum pentoxide thin-films (approx. 50 nm) on silicon were studied. Tantalum pentoxide was formed by thermal oxidation of electron-beam evaporated or rf-sputtered Ta. Thin-film characterization was by ellipsometry, Rutherford backscattering, optical microscopy, and electrical measurements on Al/Ta_2O_5/Si capacitors. Of special interest was the influence of the oxidation conditions on the leakage through the dielectric films.

99 Microstructure and Surface Characterization of Plasma-Polymerized Styrene Films on Silicon Substrates: *O. K. T. Wu** and *D. M. Chen,* Gould Research Center, Rolling Meadows, IL 60008

Plasma-polymerized styrene films were deposited on silicon substrates in a rf glow discharge for high-voltage insulating applications. In this paper, scanning electron microscopy (SEM) and electron spectroscopy for chemical analysis (ESCA) were used to characterize the polymeric films before and after the electrical breakdown. Two distinct classes of as-deposited polymeric films were observed with reference to the surface texture, namely, glassy and "wormlike." It was found that the glassy film changed to a "wormlike" structure after a few thousand volts of breakdown. The breakdown process and the associated electrothermal effect on the modification of chemical composition and microstructure of these two classes of films are discussed.

100 The Effect of Oxidation Rate on the Characteristics of Anodically Oxidized GaAs Samples: *M. Tabib-Azar, B. Davari,* and *P. Das,** Dept. of Electrical, Computer, and Systems Engineering, Rensselaer Polytechnic Institute, Troy, NY 12181

The AGW solution is used for the anodic oxidation of GaAs samples. The oxide growth rate is controlled by the adjustment of the current density of the oxidation process. The anodic oxidation of GaAs has two distinct phases: (a) nucleation and island growth, (b) coalescence of islands and continuous growth. Different samples are oxidized using the following schemes: (*i*) low current in phase (a) followed by high current in phase (b), (*ii*) constant current in phase (a) and (b), (*iii*) high current in phase (a) and low current in phase (b). The oxidized samples are characterized by C-V and SAW techniques. The fast interface state density is obtained from the C-V data following Terman. Oxide bulk properties are monitored by the value of breakdown voltage and the density of slow interface states which is obtained from the C-V hysteresis data. The results of the measurements are compared for the different oxidation current density waveforms.

DIELECTRICS AND INSULATION/ELECTRONICS

Silicon Nitride Thin Insulating Films

101 Materials Analysis of Silicon Nitride: *P. S. Peercy** and *H. J. Stein,* Sandia National Laboratories, Albuquerque, NM 87185

The charge transport, trapping, and retention in silicon nitride films used in MNOS memories can be varied significantly by variations in the chemical vapor deposition conditions and by post-deposition treatments. Such variations also result in changes in the atomic composition and chemical bonding configurations in the films. In this paper, we will summarize results from a variety of materials analysis studies designed to establish relationships between electrical properties and silicon nitride. (This work performed at Sandia National Laboratories supported by the U. S. Department of Energy under contract number DE-AC04-76DP00789.)

102 Materials Processing for MNOS Nonvolatile Memories: *J. A. Topich,* NCR Corp., Microelectronics Div., Miamisburg, OH 45342

The electrical and charge retention characteristics of MNOS nonvolatile memory devices are affected by many factors, both during the growth and deposition of the silicon dioxide and silicon nitride layers, respectively, and in subsequent processing. The influence of the silicon dioxide and silicon nitride thicknesses, silicon nitride deposition temperature, gas composition during silicon nitride deposition, high temperature processing and hydrogen annealing on the Write/Erase, and charge retention characteristics of MNOS nonvolatile memory devices are discussed.

103 Compositional Depth Profiling of Silicon Nitride Interfaces: *J. A. Wurzbach,* General Dynamics Corp., Pomona, CA 91769

X-ray photoelectron spectroscopy has been used in conjunction with stopped-flow chemical etching and angular resolution to obtain compositional depth profiles of LPCVD MNOS structures and thermally grown silicon nitride films. MNOS data showed relatively sharp interfaces with a layer of SiO_2 intact after nitridation and evidence of silicon in a reduced oxidation state; thermal films

showed a compositional gradient ranging from oxide at the surface to nitride at the interface. Further work has implicated the cleavage of interfacial Si-H bonds in the stressing of MNOS memory structures. The combined results are related to interface state formation, mechanisms of MNOS memory degradation, film growth, and results from other techniques.

104 Effects of Annealing in Different Ambients on the Hydrogen and Charge Distributions in CVD-Silicon Nitride Films: *H. E. Maes** and *J. Remmerie*, ESAT Laboratory, Kardinaal Mercierlaan 94, B-3030 Heverlee, Belgium

Multiple internal reflection measurements on CVD (atmospheric pressure-, low pressure-, and plasma enhanced-) silicon nitride films, after successive post-deposition treatments (nitrogen and hydrogen anneals at different temperatures and for various times), in combination with electrical characterization of the stepwise back-etched films, reveal the effect of hydrogen diffusion at the two film boundaries. The results convincingly establish a correlation between the bonded hydrogen and the charge distribution within the bulk of the nitride, as well as at the interface.

105 The Physical Properties of LPCVD Si-N Films: *P. Pan**, *I. Assur*, *W. Berry*, and *S. Burton*, IBM General Technology Div., Essex Junction, VT 05452

With different NH_3/SiH_2Cl_2 gas ratios *(R)* ranging from 2 to 20, the LPCVD Si-N films were deposited at 770°C. The silicon and nitrogen concentration and their uniformity as a function of depth were measured by Auger electron spectroscopy (AES). By using infrared analysis, the N-H bonds were found to increase with increasing *R* values, but the Si-H bonds were not detected for all samples. The other physical properties, such as etch rate, stress, etc., were also studied and related to the film composition.

106 High-Temperature Hydrogen Anneal of MNOS Structures: *G. Schols*, BTMC-Ghent, Gasmeterlaan 106, B-9000 Ghent, Belgium, and *H. E. Maes*, ESAT Laboratory, Kardinaal Mercierlaan 94, B-3030 Heverlee, Belgium

The results of a detailed study of the high-temperature hydrogen anneal of MNOS structures are presented. This anneal which is currently being used by different manufacturers and which requires cutouts in the silicon nitride layer next to the active regions is shown to be a combined effect of a lateral hydrogen diffusion through the underlying thin oxide layer and a vertical diffusion through the silicon nitride film. Specially designed test devices have allowed the separation and modeling of both diffusion mechanisms.

107 Silicon Nitride Films on GaAs: *F. L. Schuermeyer*, Air Force Wright Aeronautical Labs., Wright-Patterson AFB OH 45433

Si_3N_4 films play an important part in the fabrication of GaAs devices and circuits. This paper reviews many of these applications, the results obtained, and deposition techniques used. Si_3N_4 films are used in ion implantation technology, both as an annealing cap and as a cover during implantation to alter the doping profile. These films are also used for GaAs surface passivation, for dielectric isolation between two conducting layers, for final circuit protection, as gate dielectric in insulated gate GaAs field effect transistors, and as dielectric of capacitors in GaAs monolithic circuits. The film deposition methods used are different from those commonly used in Si technology since GaAs decomposes at temperatures in excess of 600°C. The deposition methods used are based on low temperature processes such as plasma enhanced CVD. Excluded from this review are GaAs devices and circuits for optical applications.

108 Plasma Deposition of Silicon Nitride and Boron Nitride Films for Encapsulated Annealing of Implanted GaAs: *G. J. Valco** and *V. J. Kapoor*, Solid State Integrated Circuit Laboratory, Dept. of Electrical Engineering and Applied Physics, Case Western Reserve University, Cleveland, OH 44106

The plasma deposition of silicon nitride and boron nitride films for use as a post-ion implantation annealing encapsulant on GaAs substrates has been studied. The films were deposited in a planar system using SiH_4 and N_2 for the silicon nitride depositions and 0.5% B_2H_6 in N_2 and NH_3 for the boron nitride depositions. Properties and composition of the films as determined by ellipsometry, Auger electron spectroscopy (AES) and multiple internal reflection (MIR) spectroscopy were investigated as a function of gas composition, flow rates, pressure, substrate temperature, and rf power. The effects of films with various properties on the annealing of Si implanted GaAs are also presented. (This work was supported by NASA-Lewis Research Center.)

109 Plasma Deposited Nitride Films on GaAs and InP: *D. C. Liu** and *V. J. Kapoor*, NASA Lewis Research Center, Cleveland, OH 44135

Silicon nitride and boron nitride films are deposited on n- and p-type GaAs and InP substrates by plasma chemical vapor deposition process. The effect of growth conditions such as reaction gas ratio, growth rate, and substrate temperature are studied. The dielectric/III-V semiconductor structures are characterized by Auger electron spectroscopy (AES) profiling and x-ray photoelectron spectroscopy (XPS) analysis. Quality of the film and interface state density are determined by capacitance and conductance *vs.* voltage measurements at a series of frequencies and by ellipsometric analysis.

110 One-Micron Lateral Diffusion of Beryllium Ion-Implanted Junctions in GaAs Using Si_3N_4 Encapsulation: *P. M. Campbell** and *B. J. Baliga*, General Electric Co., Corporate R and D Center, Schenectady, NY 12301

We have made a comparative study of SiO_2, phosphosilicate glass, and low temperature plasma Si_3N_4 encapsulants for the high temperature annealing of Be implants in high purity ($10^{15}/cm^3$) LPE GaAs layers, which serve as a sensitive medium for the detection of surface lateral diffusion effects. The lateral diffusion was electrically measured by detecting the punch-through between diffusion islands of varied spacing, allowing measurement of the lateral diffusion to within 0.5 μm. Be implants annealed at 900°C for 30 min with an Si_3N_4 cap produced a 1 μm deep junction with a lateral diffusion of 1 μm. This direct electrical method of measuring lateral diffusion is more relevant to device fabrication than the commonly used angle lapping/staining method which does not detect the formation of thin conductive surface channels using the encapsulant. These implanted junctions exhibit nearly 100% electrical activation (p_{max} = $10^{18}/cm^3$) and low leakage currents (10^{-9} A) at reverse bias as high as 200V. These results are compared with junctions annealed with SiO_2 and phosphosilicate glass caps.

111 Comparison of Laser and Plasma Assisted Deposition of Silicon Nitride: *W. H. Ritchie** and *W. Metz*, NCR Microelectronics, Fort Collins, CO 80523, and *P. K. Boyer* and *G. J. Collins*, Dept. of Electrical Engineering, Colorado State University, Fort Collins, CO 80523

There is considerable interest in low temperature deposition of dielectric films to reduce defect generation and propagation, wafer warpage, and impurity redistribution that occurs at high temperatures. Laser and plasma assisted CVD reduce the processing temperature of silicon nitride by more than 300°C as compared to conventional LPCVD silicon nitride. These low temperature processes also have superior step coverage and stress characteristics. We will compare the physical, chemical, and electronic properties of both laser and plasma deposited silicon nitride on silicon and III-V substrates.

112 Physical and Electrical Properties of Plasma Deposited Silicon Nitride Films: *C. D. Fung*, *T. E. Nagy**, and *W. H. Ko*, Dept. of Electrical Engineering and Applied Physics and Engineering Design Center, Case Western Reserve University, Cleveland, OH 44106

Silicon nitride films were deposited using SiH_4 and NH_3 in a parallel plate plasma reactor. The rf frequency was 20 kHz with a power level around 40W. The physical characteristics of the films were evaluated. Nitride films near stoichiometric composition were employed to fabricate MNS and MNOS capacitors for electrical tests. Both I-V and C-V measurements were made to characterize the conduction mechanism and charge trapping phenomena. These devices indicate a flatband voltage shift in the same direction as the applied bias. This suggests that the interface trapping is the predominant charge instability mechanism in these devices.

113 Studies of Nitrogen Plasma in the Silicon Nitride Deposition Reaction: *C. Y. Yang*, Applied Materials Inc., Santa Clara, CA 95051

Silicon nitride films have been deposited by plasma CVD method with molecular nitrogen rather than ammonia as the primary source of active nitrogen. The purpose is to reduce the hydrogen content in the deposited thin films. The nitrogen plasma has been studied by using optical emission spectroscopy, mass spectrometry, and heterogeneous catalysis. The deposited films have been characterized with stress measurements, ellipsometric measurements, etch rates, hydrogen concentration, etc.

114 Comparative Study of Plasma Enhanced Chemically Vapor Deposited (PECVD) Silicon Nitride Films for IC Passivation: *H. E. Maes** and *G. L. Heyns*, ESAT Laboratory, Kardinaal Mercierlaan 94, B-3030 Heverlee, Belgium, and *H. Loos*, *H. Pauwels*, and *A. Van Calster*, BTMC Ghent, Gasmeterlaan 106, B-9000 Ghent, Belgium

A comparative study of the passivation properties of PECVD silicon nitride films has been performed. The films provided by different manufacturers of PECVD equipment were characterized both electrically and physically. The correlation between the composition and the passivation properties of the different films is studied in great detail using a specially designed test integrated circuit containing short channel devices, split gate MOS transistors, high voltage circuits, and many other test patterns.

115 Effect of Frequency on Plasma SiN Deposited in a Parallel Plate Radial Flow Reactor: *F. Martinet** and *G. Guegan*, IBM France, 91102 Corbeil Essones, France

Plasma-enhanced CVD silicon nitride has been studied using a conventional capacitively coupled radial flow reactor. Various mechanical, electrical, and chemical properties were investigated as a function of 2 different frequencies, rf power, gas composition, and temperature. Optical emission spectra of 13.56 MHz and 50 kHz glow discharges were investigated to explain the chemical film composition: for example Auger composition depth profile and hydrogen content measured with infrared spectra.

116 Radiation Hardened MNOS—A Review: *P. J. Vail*, Solid State Sciences Div. (ESR), Rome Air Development Center, Hanscom, AFB, MA 01731

The status of MNOS RAM and EAROM technology for application to nuclear weapon and space radiation environments is re-

viewed. Most of the problems encountered in developing radiation hardened MNOS result from the apparent incompatibility of processing radiation-hardened fixed-threshold MOS devices and processing variable-threshold MNOS memory devices with good memory properties on the same chip. Approaches for solving this incompatibility are described.

117 Process Developments for a Radiation-Hard MNOS Memory: *R. V. Jones** and *W. H. Dodson*, Sandia National Laboratories, Albuquerque, NM 87185

The design of a radiation-hard 128-word by 8-bit MNOS memory for an N-well CMOS metal-gate process required several process explorations to achieve the desired operating characteristics. Good memory transistors required thermal oxides because the LPCVD nitride consumed native oxides. Plasma etching of nitride from the control gates was necessary for radiation hardness, and required processing the memory gates before the control gates to prevent etching damage of control-gate oxides. A postnitride 800°C oxidation for the control transistors also created an MONOS memory structure which improved endurance and retention. Careful control of surface diffusion concentrations prevented premature breakdown and leakage caused by gated-diode structures.

118 Evaluation of MNOS Nonvolatile Memories for Space Applications: *G. L. Heyns* and *H. E. Maes*,* ESAT Laboratory, Kardinaal Mercierlaan 94, B-3030 Heverlee, Belgium and *P. May*, European Space Agency (ESA), Noordwijk, The Netherlands

In this paper the results of an extensive study on the commercially available 4 kbit GI 3400 p-channel metal-nitride-oxide-silicon (MNOS) part are presented. This study was performed in order to check whether these devices could be selected by the European Space Agency for space applications. The emphasis in this study was therefore on the temperature behavior of these MNOS devices and circuits and on their radiation hardness. It was found that the memory performance of the MNOS circuits was completely within specification over the total military temperature range (−55° to 125°C), and that the maximum total dose (using a Co 60 source) was about 30 kRad (Si), a limitation only imposed by the degradation of the peripheral MOS circuitry.

119 Space Charge Effects in Irradiated Si_3N_4 Films: *R. C. Hughes*, Sandia National Laboratories, Division 1132, Albuquerque, NM 87185

Irradiation of Si_3N_4 films on Si (MNOS devices) causes photoconductivity due to the production of electron-hole pairs. Since there are extremely large numbers of both electron and hole traps in Si_3N_4, this photocurrent is difficult to observe, but can result in charging of the Si_3N_4-Si interface. Solutions of the photoconductivity equations, including diffusion, recombination, drift, and trapping of the electron-hole pairs, are presented and compared with experimental data on the charging of MNOS devices under irradiation. (This work performed at Sandia National Laboratories supported by the U. S. Department of Energy under contract number DE-AC04-76DP00789.)

120 Trapping Kinetics in Insulators Having a High Charge Capture Probability: *S. B. Bibyk** and *V. J. Kapoor*, Solid State Integrated Circuit Laboratory, Dept. of Electrical Engineering and Applied Physics, Case Western Reserve University, Cleveland, OH 44106

The scaling of a silicon nitride film in nonvolatile memories is limited by the requirement to trap a significant amount of charge as free carriers drift through the nitride. A new u.v. photoinjection technique has been developed which injects carriers from the gate into the nitride and yields both the trapped charge density and the free carriers which are not trapped by measuring the flatband voltage shifts and the external current flow during charge trapping. The nitride thicknesses were varied from 1400 to 150Å. An analytical model based on multiple trap levels with large capture probabilities and field dependent emission rates was developed to determine the trap density, capture cross sections, and emission rates from the measurements. (This work was supported by U.S. Navy Office of Naval Research.)

121 Charge Characteristics of Ion-Implanted and Annealed Nitride/Oxide/Si Structures: *H. J. Stein*, Sandia National Laboratories, Division 1112, Albuquerque, NM 87185

The effects of $^{11}B^+$ and $^{14}N^+$ ion implantation on the C-V characteristics of CVD silicon nitride/native oxide/silicon structures have been investigated. C-V measurements were made as a function of ion energy, thermal annealing, u.v. exposure, and film etchback. Implantation increases u.v. and 650°C heating-induced charge accumulation in the structures. Implantation effects are ion independent, but dependent upon ion range. The data are discussed on the basis of ion-atom collisions and charge excitation. (This work performed at Sandia National Laboratories supported by the U. S. Department of Energy under contract number DE-AC04-76DP00789.)

122 Origin and Characteristics of Trap States in CVD Silicon Nitride: *S. Fujita** and *A. Sasaki*, Dept. of Electrical Engineering, Kyoto University, Kyoto, Japan

Origin of trap states in CVD silicon nitride is investigated by ESR and infrared absorption. The results suggest that variations of electron occupancy in silicon dangling bonds are responsible for nonvolatile memory behavior in MNOS structure, and that electron emission occurs more easily than capture process. Effects of oxygen doping and thermal annealing are also presented. Based on the results, write-in and retention characteristics of an MNOS device relating to preparation conditions are discussed.

123 Insulator Charges and Interface States in MNOS Structures with APCVD and PECVD Silicon Nitride: *R. Hezel,* K. Blumenstock*, and *R. Schörner*, Institut für Werkstoffwissenschaften VI, Universität Erlangen-Nürnberg, D 8520 Erlangen, Germany

The densities of grown-in insulator charges (Q_N) and interface states (N_{it}) in Al/Si-nitride/thin Si-oxide/p-Si(100) structures (MNOS) have been investigated as a function of the nitride deposition temperature and postdeposition annealing treatment for both atmospheric pressure CVD and plasma enhanced CVD Si-nitride films. Despite the two nitrides show a significantly different behavior, in contrast to MOS devices, no direct correlation between Q_N and N_{it} was observed. Very high densities of positive insulator charges (Q_N/q $10^{13}cm^{-2}$) could be obtained by incorporation of cesium into the nitride film, and their effect on the interface state density has been studied.

124 Effect of Nitridation of Thick Oxide on Its Infrared Spectrum: *M. L. Naiman,** *C. T. Kirk, R. L. Aucoin, F. L. Terry, P. W. Wyatt*, and *S. D. Senturia*, MIT Lincoln Laboratory, Lexington, MA 02173

Thick oxide films (~240 nm) have been nitrided heavily in ammonia. Infrared spectra before and after nitridation were compared. The following conclusions may be drawn from the spectra: nitrided oxide is not the same material as CVD silicon nitride, nitridation results in significant loss of Si-O asymmetric stretch intensity, and nitridation leads to the appearance of a spectral peak for planar triply bonded N-Si asymmetric stretch analogous to that in trisilylamine.

125 Low Pressure Direct Thermal Nitridation of Si in Nitrogen: *R. V. Giridhar** and *K. Rose*, Center for Integrated Electronics, Rensselaer Polytechnic Institute, Troy, NY 12189

The process of direct thermal nitridation of Si over the temperature range 900°-1200°C has been studied in a low pressure nitridation system using high purity nitrogen gas as a function of temperature, time, and gas flow rate. The films have been characterized using ellipsometry and infrared absorption spectroscopy. Results are presented on film properties such as etch rate and oxidation resistance.

126 Thermal Nitridation of Silicon in a Cold Wall Reactor: *M. Moslehi** and *K. C. Saraswat*, Integrated Circuits Laboratory, Stanford University, Stanford, CA 94305

Thermal nitridation of silicon in ammonia has been investigated. A cold wall rf heated reactor was used to minimize oxygen contamination from quartz tube. The physical characterization of the films was done by ellipsometry, Rutherford backscattering, and Auger electron spectroscopy. Electrical characterization of the thermally grown and chemically vapor deposited films was done by C-V and G-V techniques. Charge trapping was studied in the MNS capacitors. The details of this investigation are presented.

127 Composition, Electrical Conduction, and Trapping Properties of Nitrided-Oxide and Reoxidized Nitrided-Oxide: *S. S. Wong,** *S. H. Kwan*, and *H. R. Grinolds*, Hewlett Packard Laboratories, Palo Alto, CA 94304, and *W. G. Oldham*, University of California, Berkeley, CA 94720

Two reaction kinetics are involved in the nitridation of 10 nm SiO_2 in NH_3 or NH_4 plasma: (*i*) the conversion of surface layer of SiO_2 into silicon oxynitride and (*ii*) the direct nitridation of Si at the interface to form Si_3N_4-like structure. Annealing of the nitrided-oxide in O_2 first converts the surface layer back to SiO_2 and finally breaks through the nitrided interface. The dominant conduction mechanism of nitrided-oxide and reoxidized nitrided-oxide is Fowler-Nordheim tunneling of electrons with barrier height similar to that of SiO_2. Nitrided-oxide has slightly higher dielectric trap density (Not) than SiO_2; however, reoxidized nitrided-oxide has lower dielectric trap density than SiO_2.

128 Growth and Properties of Thermal Silicon Oxynitride Films and Device Applications of These Films: *D. J. Dumin,** *K. Hollowell, K.-P. Tsao*, and *R. Langlais*, Dept. of Electrical and Computer Engineering, Clemson University, Clemson, SC 29631

Thermally grown silicon-oxynitride films in the thickness range of 50-150Å have been used to fabricate MIS transistors. The growth process has been characterized, and the structure of the resulting film is complex. Tunneling currents have been measured and under certain operating conditions can lead to device instabilities. The device mobility decreases as normal electric field increases. Characterization of the films and devices are discussed.

129 Low Energy Implantation of Nitrogen and Ammonia into Silicon: *T.-Y. Chiu** and *W. G. Oldham*, Electronics Research Laboratory, University of California at Berkeley, Berkeley, CA 94720

Silicon nitride formation by low energy implantation of nitrogen or ammonia is performed. With a milling current of 0.2 mA/cm², the implantation is carried out in an ion milling system in 5 min. The nitride layer is about 10 nm thick at 1.9 keV implant energy. The material characteristics are studied by means of RBS, infrared, chemical etching, ellipsometry, AES, and XPS. The electrical properties are investigated using I-V and C-V measurements. The film can be used as local oxidation mask with reduced bird's beak. Its potential

as a gate dielectric with high breakdown strength (>10 MV/cm) and low defect density is examined.

130 Physical Properties of Low Energy Nitrogen Implantation into Silicon and Thermal Oxide Layer: *S. Inoue, Y. Furumura, M. Maeda,* and *M. Takagi,* Fujitsu Ltd., IC Process Engineering Div., 1015 Kamikodanaka, Nakahara-ku, Kawasaki, Japan 211

Silicon nitride and silicon oxynitride thin films were formed by low energy nitrogen implantation into silicon and thermal oxide layers. The implanted layers were analyzed by AES, XPS, and ultraviolet reflectivity spectra. By XPS analysis, Si-N bond is formed in the implantation into silicon, but Si-N bond is weak or not formed in the implantation into oxide. Implantation damage extends several hundred angstroms and is removed after high temperature annealing. This paper discusses the low energy implantation method and the physical properties of the films.

131 Electrical Properties of Silicon Nitride and Silicon Oxide Thin Films Formed by Low Energy Ion Implantation: *Y. Furumura,* S. Inoue, M. Maeda,* and *M. Takagi,* Fujitsu Ltd., IC Process Engineering Div., 1015 Kamikodanaka, Nakahara-ku, Kawasaki, Japan 211

The formation of silicon nitride and silicon oxide thin films were performed by the nitrogen or oxygen ion implantation at low energies below 20 keV into silicon substrates. The improvements of the electrical properties of the obtained films and the damaged layers were achieved by the conventional annealing techniques. The measurements of the current-voltage, capacitance-voltage, and breakdown voltage were carried out to investigate the electrical properties of the implanted films. MOS transistors using these films as gate dielectrics were fabricated, and the current-voltage characteristics were also investigated.

132 Microstructure and Electrical Properties of Buried Silicon Nitride Layers in Silicon Formed by Ion Implantation: *C. D. Fung,* J. L. Liao, K. R. Elsayed,* and *J. J. Kopanski,* Dept. of Electrical Engineering and Applied Physics, Case Western Reserve University, Cleveland, OH 44106

The formation of a buried insulating layer in silicon by ion implantation has a potential to achieve silicon-on-insulator structure. This can be used as an isolation method in very large scale integrations. The present paper reports implantation of N_2^+ and N^+ ions at 100 and 174 keV, respectively, followed by thermal anneal to form buried silicon nitride in silicon. Studies include the nitrogen distribution, the microstructure, and the electrical properties pertaining to the silicon/silicon nitride/silicon structure. The results indicate that as the ion dose approaches the required value for obtaining stoichiometric silicon nitride (approximately 0.25 and 1×10^{18} cm^{-2} for N_2^+ and N^+ ions, respectively, in this case) a continuous nitride film with good insulating property is formed. Measurements resulting from transmission electron spectroscopy and from depth profiles by Auger electron spectroscopy suggest, at higher doses, a possible nitrogen gas phase formation.

133 Electron and Ion Beam Effects in AES Analysis of Silicon Nitride Thin Films: *H. E. Maes** and *J. Remmerie,* ESAT Laboratory, Kardinaal Mercierlaan 94, B-3030 Heverlee, Belgium, and *M. Hinoul, R. Vanden Berghe,* and *R. Viaeminck,* BTMC-Ghent, Gasmeterlaan 106, B-9000 Ghent, Belgium

AES sputter-profiling can, under certain experimental conditions, lead to erroneous results even with respect to qualitative characterization of various CVD silicon nitride films. A simplified model, involving preferential sputtering as well as diffusion of N-species to the surface and formation of free silicon, due to the electron and ion beam impact, is proposed. This model satisfactorily explains the observed behavior of Si- and N-Auger intensities and gives rise to a renewed approach of AES for quantitative investigation of silicon nitride.

134 Characterization of Plasma Silicon-Nitride Layers: *W. A. P. Claassen, W. G. J. N. Valkenburg, F. H. P. M. Habraken,* and *Y. Tamminga,* Philips Research Laboratories, 5600 JA Eindhoven, The Netherlands

The authors have studied deposition of plasma silicon-nitride layers as a function of gas phase composition for the SiH_4-NH_3-X system, where X is N_2, Ar, or H_2. The deposited layers were characterized with Auger depth profiling, Rutherford backscattering, and infrared spectroscopy. The refractive index of the plasma silicon-nitride layer, deposited at 300°C, shows a linear behavior with both the Si/N ratio and the Si-H/N-H ratio. The layers contain about 2×10^{22} atoms hydrogen per cm^3, this content being nearly independent of the Si/N ratio of the plasma-silicon-nitride layer.

135 Nitriding in a Nonequilibrium Nitrogen, Nitrogen-Hydrogen, and Ammonia RF Plasma at Low Pressure (1-10 Torr)—Applications to W, Mo, and Si Surfaces: *J. Amouroux,* A. Gicquel,* and *M. P. Bergougnan,* Ecole Nationale Supérieure de Chimie de Paris, Equipe des réacteurs chimiques en phase plasma, 75231 Paris Cedex 05, France

The main aim of this work is the nitriding of materials by using an N_2, N_2-H_2, or NH_3 rf plasma at low pressure (1-10 Torr). The nonequilibrium plasma reactor is controlled by high resolution spectroscopy measurements in order to determine the rotational and vibrational temperature of the N_2 molecule. The surface of the target (W, Mo, Si) has been heated by the excited species and the ions of the plasma. A control of the temperature of the target and of the boundary layer permits a good understanding of the energy exchange between plasma and solid material. The evolution of the chemical properties of the surface is measured before and after the plasma treatment by ESCA technique, Vickers hardness, and resistivity. The main result is a better understanding of the energy and mass transfer in connection with the nature of the target. Specifically we have demonstrated the correlation between the energy level of the excited species of the boundary layer and the formation of the nitride layer.

136 Plasma Deposition of Silicon Nitride and Silicon Oxynitride Using Inert Carrier Gases as Transport Agents: *V. S. Nguyen,* IBM General Technology Div., Essex Junction, VT 05452

Silicon nitride and silicon oxynitride films with refractive indexes varying from 1.60 to 1.95, as desired, have been deposited on silicon and silicon dioxide substrates using the plasma enhanced chemical vapor deposition process. At low silane concentration (≤2.0%), helium was found to be a very efficient carrier gas in the plasma compared to other inert gases such as argon, krypton, xenon, and nitrogen, both from a mass transport and Penning reaction viewpoint. Excellent batch uniformity is achievable with this process.

137 Irradiation-Induced Electrical Conduction in Silicon Nitride Thin Films: *C. Gunkel,* D. Schalch,* and *A. Scharmann,* I. Physikalisches Institut der Universität Giessen, D-6300 Giessen, Germany

Field and temperature characteristics of charge transport in reactively sputtered silicon nitride irradiated with low energy electrons and ions were determined between $5 \cdot 10^6$ V/m < E < $2 \cdot 10^8$ V/m and LNT < T < 450 K, as well as the collected charge to dose ratios, space charge buildup, and current decay after cessation of irradiation. From carrier-type experiments it is concluded that electron and hole currents are comparable in magnitude. Additionally, TSC and optical transmission measurements are performed.

138 The Stability of Plasma Nitride Passivation Films on Plastic Encapsulated Devices in 85% Humidity/85°C: *W. Baerg,* S. Sachdev, P. Engel,* and *P. A. Gargini,* Intel Corp., Livermore, CA 94550

The failure rate of a plastic encapsulated static ram was investigated with regard to: (*i*) passivation composition, (*ii*) metallization composition, (*iii*) external sources of contamination. Silicon-rich nitride passivation films, silicon precipitate from aluminum-silicon metallization, and electrolyte migration from an experimental assembly process were all found to degrade the reliability of circuits in plastic. However, no failures after 2500 hr 85°C/85% RH were observed when these parameters were optimized.

139 Etching Rates of SiO_2 and Si_3N_4 Insulating Films in Ammonia-Hydrogen Peroxide Cleaning Process: *M. Watanabe,* M. Harazono, Y. Hiratsuka,* and *T. Edamura,* Hitachi, Ltd., Reliability Center, Production Engineering Research Laboratory, 292 Yoshidamachi Totsukaku Yokohama 244 Japan

Etching rates of thermally oxidized SiO_2, PSG, Si_3N_4, and Si wafer surface in NH_4OH-H_2O_2-H_2O cleaning process were measured at 20°-80°C. The dependence of etching rates both on cleaning temperature and concentration of cleaning chemicals was studied, and its mechanism was discussed. The etching amount of thermal oxide at 80°C for 10 min was more than 50Å, which might degrade the breakdown voltage of very thin insulating films used in MOS devices.

140 Synergetics of Insulating Silicon Nitride Thin Film Deposition Process Analysis and Control: Real Time Experimental Analysis: *E. Siegel,* San Francisco, CA 94118

Dielectric properties (complex: dielectric constant, impedance, reactance, conductance, capacitance, loss, dispersion and a-c and a-c electrical conductivity, charging time, discharging time, etc.) and 1/f flicker noise voltage power spectrum are reversibly connected in a synergetic experimental model between these functional properties and process-induced defect distribution disorder as measured by external radiation diffraction pattern static structure factor S(k). The confluence of the Jonscher (1) universal dielectric model with the Ngai (2) universal 1/f flicker noise model and the Siegel (3) universal collective-mode-softening driven by disorder via infrared divergence allows this universal reversible connection between functional properties and process induced morphology changes, *i.e.*, defect distribution. Rather than individual defect detailed mechanisms, synergetics concentrates on process-induced defect densities (defects per unit volume) measured by S(k) on the average to dominate various functional properties via linear densities of states of the complicated collective-modes for a particular material. The mathematical domination-slaving of these modes to infrared divergence makes the detailed microscopic defect types and mechanisms, and complicated collective-mode description average out and allows this type of real time synergetic analysis leading to process control of dielectric thin insulating film deposition in device manufacture, such as silicon nitride, as well as all other insulating, semiconducting, or metallic bulk or film materials of any type. Model-free process control is possible.

1. Jonscher, *Physics of Dielectric Solids*, I.O.P. **58,** 22 (1980).
2. K. L. Ngai, *Commun. Sol. State Phys.*, **4,** 127 (1979); **9,** 5, 141 (1980).
3. E. Siegel, J. *Non-Cryst. Solids*, **40,** 453 (1980).

DIELECTRICS AND INSULATION/ELECTRONICS

Fourth Symposium on Plasma Processing

141 Interaction of Plasma Oxide Deposition Variables: *E. Sabin** and *C. Ramiller*, Applied Materials, Inc., Santa Clara, CA 95051

The properties and uniformity of CVD silicon dioxide films have been characterized as a function of gas flows, system pressure, and rf power level, using a parallel plate plasma reactor. The plasma reactor is unique in that the gas is distributed across the platen, thus producing uniformities not possible in conventional systems. It has been found that increasing the flow will improve the uniformity to values less than ±5%. The refractive index varies with gas flow and nitrous oxide to silane ratio but is generally close to 1.47 and uniform to ±0.01.

142 A Plasma Oxide Interlayer Dielectric for Use in Two Layer Metallization: *S. S. Dottarar*, Tektronix, Inc., Beaverton, OR 97077

A low temperature, plasma oxide process has been developed for use as an interlayer dielectric on two layer gold metallization. Deposition parameters were evaluated with respect to uniformity and reproducibility, film composition, and electrical properties. Concurrently, variations in the metal side-wall profile and metallization processes were noted. The contribution of these variations to the final metal structure and plasma oxide step coverage is discussed.

143 Plasma Deposition of Dielectric Polymer Films for High-Voltage Insulation of Devices: *D. M. Chen*, Gould Research Center, Rolling Meadows, IL 60008

Plasma-polymerized styrene films deposited on silicon substrates were investigated for potential application as high-voltage (about 10,000 d-c V) insulating films used in electronic devices. The deposition process was carried out in a vertical parallel-plate glow-discharge reactor in an atmosphere of argon and styrene vapors. Dielectric breakdown tests were performed for films from submicron to 30-micron thicknesses. Results indicate that a 20 micrometer film of polystyrene is pinhole-free and will withstand the 10,000V; the dielectric strength of films ranged from 4 to 7 mV/cm. Thermal annealing of polymeric films significantly reduces the statistical spread of the breakdown data. Various microstructures were observed for films prepared under different process conditions. The plasma deposition system, process control parameters, and detailed results on the film properties are discussed in this paper.

144 Plasma-Enhanced Chemical Vapor Deposition of Epitaxial Silicon from Silane: *S. R. Shanfield*,* Spire Corp., Bedford, MA 01730, and *R. Reif*, Dept. of Electrical Engineering, Massachusetts Institute of Technology, Cambridge, MA 02139

Epitaxial silicon layers have been deposited from silane on (100) and (111) silicon substrates. The depositions are carried out at 700°-900°C in a low pressure plasma reactor. The dependence of the deposition rate, crystallinity, and thickness uniformity across a wafer upon deposition conditions have been investigated. Deposition rates of epitaxial layers are reported with and without plasma under otherwise identical deposition conditions.

145 Characterization of PdO Formed by D-C Generated Oxygen Plasma: *V. A. Karagounis*,* *C. C. Liu, M. R. Newman, and L. T. Romankiw*, Dept. of Chemical Engineering and Material Science in Syracuse University, Syracuse University, Syracuse NY 13210

Palladium oxide was formed in a d-c generated oxygen plasma in the pressure range from 15 to 50 mTorr. The substrate was biased for a range from 50 to 250V. The target voltage was also varied from 800 to 2000V. Oxide formation rate was studied as a function of pressure of oxygen, substrate bias, and target voltage. Palladium oxide formed by high temperature thermal oxidation and by reactive sputtering in oxygen plasma were characterized using electron spectroscopy for chemical analysis (ESCA), Auger spectroscopy and the sensitivity of their electrochemical potential to pH buffers was compared. The free energy of formation of palladium oxide formed in oxygen plasma is a strong function of the substrate bias and target voltage. The sensitivity of the electrochemical potential to pH buffers is affected from the target voltage and not from the pressure of oxygen or substrate bias. ESCA binding energy shifts correlate well with the sensitivity to pH. Increase in the binding energy shift correspond to a decrease in sensitivity.

146 Lift-Off Lithography Using Low-Frequency Plasma Buffer Layers: *B. D. Cantos, D. B. Deal*, and *D. M. Dobkin*,* Watkins-Johnson Co., Palo Alto, CA 94304

Lift-off lithography using multiple layers of positive resist separated by a plasma formed buffer layer has been previously reported. The buffer layers were susceptible to difficulties with adhesion, stress, and permeability. We have solved these problems through the use of a parallel-plate, low-frequency (40 kHz) plasma. We have studied both CF_4 and C_2F_6 plasmas, finding evidence for diffusion of F atoms in the resist. Various versions of this process have been used for small-scale production of GaAs MESFET's and monolithic circuits at W-J for more than a year. We have found it an inexpensive and reliable means of performing lift-off with submicron resolution and reasonable versatility.

147 Characterization of Silicon Nitride Dry Etching in SF_6/He Mixtures: *E. Laes*,* *F. Coopmans, P. Verdonck*, and *G. Declerck*, ESAT Laboratory, Katholieke Universiteit Leuven, Kardinaal Mercierlaan 94, Leuven, Belgium, B-3030, and *G. Peeters*, BTMC, Ghent, Belgium.

We report on the influence of the etch process parameters on the characteristics of Si_3N_4 dry etching with SF_6/He in a parallel plate reactor. The most striking result is the pronounced effect of the ion bombardment, leading to a uniform anisotropic etching with the same maximum selectivity over SiO_2 in both PE and RIE mode. A correlation of this behavior with the electrode potentials and the emission spectrum of the plasma is presented. Comparisons are made with polysilicon and silicon dioxide etching under the same conditions.

148 Dry Etched Vias for Two Layer Interconnect on High Density Bipolar IC's: *D. R. Evans*, Tektronix, Inc., Beaverton, OR 97077

The advent of VLSI bipolar IC's has necessitated the fabrication of small pitch two-layer metal interconnect. In the present application gold metallization with plasma oxide interlevel dielectric is used. A dry etching process has been developed which is anisotropic, uniform, reproducible, and has high selectivity for silicon dioxide over gold. It has been implemented on a commercially available single wafer at a time plasma etcher equipped with load locks. Yield analysis has been carried out and various yield loss mechanisms specific to this etching process are discussed.

149 High Temperature Plasma Etching of Silicon and Silicon Dioxide: *K. C. Ray Chiu*, Synertek, Inc., Santa Clara, CA 95051, and *W. R. Snow*,* Pacific Western Systems, Inc., Mountain View, CA 94041

An Arrhenius-like relationship between etch rate and temperature has been found for C_2F_6/O_2 and CF_4/O_2 mixtures in parallel plate etching of silicon and SiO_2, over a temperature range of 25°-700°C. High temperature operation was made possible by the use of graphite electrodes. The measurements, made at an rf power of 100 mW/cm² and pressure of 1.5 Torr, yield apparent activation energies of the order of 0.1 eV/mol for these systems.

150 Anisotropic Etching of Polycrystalline Silicon: *M. Yoneda, H. Itakura*, and *M. Hatanaka*, Mitsubishi Electric Corp., Computer Development Laboratories, Ltd., 4-1 Mizuhara, Itami, Hyogo, Japan 644, and *T. Shibano* and *H. Abe*,* Mitsubishi Electric Corp., LSI Research and Development Laboratory, 4-1 Mizuhara, Itami, Hyogo, Japan 664

Relations between the etching characteristics and the property of poly-Si film were investigated using $C_2Cl_2F_4$ gas plasma. The etching characteristics investigated here were the etch rate and the pattern size shift, $L_{poly\text{-}Si}$-L_{resist}. The property of poly-Si was changed by injecting some kinds of impurities and adding heat-treatment after that. We report that the grain size of poly-Si film is related to the etching characteristics, especially to anisotropic property.

151 RIE Etching of Poly-Si by CCl_4/O_2: *A. I-T. Pan*, Philips Research Laboratory-Sunnyvale, Signetics Corp., Sunnyvale, CA 94086

RIE etching of poly-Si by CCl_4 is enhanced by oxygen addition, which also changes the etch profiles from anisotropic to isotropic. Oxygen effects can be explained by higher active species concentrations and the removal of polymer films from etched surfaces. The etch rates of both poly-Si and thermal oxide increase with electrode spacings and resident times of etch gas in the chamber. Etching uniformities are also examined in his study.

152 Silicon Etch Rate as a Function of Dopant Concentration in a CF_3Cl Plasma: *M. F. Leahy* and *D. J. Tanguay*, RCA Laboratories, Princeton, NJ 08540

The etch rate of n-type polycrystalline sillicon is a strong function of the phosphorous concentration in a chlorotrifluoromethane (CF_3Cl) plasma. Etch differentials of 15 to 1 may be obtained for highly doped silicon *vs.* undoped or boron-doped silicon. Some implications of this phenomenon are discussed in relation to device fabrication.

153 Fabrication of Submicrometer Structures in Si Using $SiCl_4/O_2$ Reactive-Ion Etching: *S. M. Cabral*,* *D. D. Rathman*, and *N. P. Economou*, Lincoln Laboratory, Massachusetts Institute of Technology Lexington, MA 02173

Submicrometer structures have been reactive-ion etched in Si using $SiCl_4/O_2$ gas mixtures. $SiCl_4$ offers several advantages over Cl_2 and CF_4 as an etching gas: masking capabilities are improved, Si/SiO_2 selectivity is high, Si etch rates are greater than 1000 Å/min, and surface damage to the Si is reduced (1). Gratings of 3200Å period, which form the active region of the silicon permeable base transistor, are etched with an $SiCl_4/O_2$ ratio of 1/1. Anisotropic profiles and smooth, clean surfaces are obtained when Cr or SiO_2 is used as the etch mask. Selective deposition of SiO_x on Al during etching gives enhanced masking capabilities with Al, but results in a narrowing of the etched groove. This effect (insignificant for linewidths greater than 1 μm) can be minimized, by reducing the O_2 content. (This work was sponsored by the Department of the Air Force.)

1. S. Pang, D. D. Rathman, D. J. Silversmith, R. W. Mountain, and P. D. Degraff, Abstract 184, p. 289, The Electrochem. Soc. Extended Abstracts, Vol. 2, Detroit, MI, Oct. 17-22, 1982.

154 A Controllably Anisotropic, High Rate, Polysilicon Plasma Etch Process with Very High Selectivity Against SiO_2 and Photoresist: *C. B. Zarowin* and *J. Dalle Ave*, The Perkin-Elmer Corp., Wilton, CT 06897

We describe the plasma etching of doped polysilicon through a photoresist mask that permits continuous control of the etch process from anisotropic to isotropic, *i.e.*, from no mask undercut to that equal to the etch depth. This is controlled through the parameter $\sqrt{P_{rf}}/p$, where P_{rf} is the rf power and p is the etch gas pressure, shown elsewhere to control the ion energy and etch directionality. Under conditions that yield an etch undercut which is 10% of the etch depth, the polysilicon etch rate is about 0.5 microns/min while the photoresist (AZ1470) and SiO_2 rates are respectively less than 1/10 and 1/100 of the polysilicon. This process is particularly suitable for patterning of polysilicon over thick SiO_2 steps (0.3-1.0 microns) to very thin (100-500Å) gate oxides because it permits considerable over etch due to its anisotropy and selectivity.

155 Reactive Sputter Etching of Single Crystal Silicon with Cl_2 and $SiCl_4$: *K. O. Park** and *F. C. Rock*, GTE Laboratories, Waltham, MA 02254

The fabrication of certain silicon devices requires etching deep vertical trenches in the range of 3-5 μm in single crystal silicon. It has been reported that silicon can be plasma or reactively ion etched (RIE) with chlorine containing gases as well as some fluorine containing gases. It has been found, however, that gases like CCl_4 have limited usefulness in silicon plasma etching due to polymer formation during etching. It has also been found that Si RIE with fluorine containing gases normally results in unsatisfactory etch profiles when an etch proceeds deeper than 1 μm. Si RIE with Cl_2 at moderate levels of applied rf power (<0.4 W/cm²) produces an anisotropic profile, but its etch rate is very slow (<5 nm/min). However, at higher applied rf power, Si RIE with Cl_2 tends to produce a rough surface at the bottom of the trenches, which normally appears black under an optical microscope. In this paper, we report on the use of Cl_2 and $SiCl_4$ gases in reactive ion etching deep vertical trenches (>3.0 μm) in single crystal silicon using thermal oxide as an etch mask. It is shown that adding $SiCl_4$ to Cl_2 in RIE of silicon not only greatly enhances the etch rate, but also improves surface morphology. The results of optical emission spectroscopic studies of the reactant species as well as the etchant products are also presented, to elucidate the etching mechanism of these gas mixtures in the RIE mode.

156 Magnetically Confined Discharge for Plasma Etching: *T. D. Mantei** and *T. Wicker*, Dept. of Electrical and Computer Engineering, University of Cincinnati, Cincinnati, OH 45221

A plasma etching reactor has been developed which combines a primary electron source, surface magnetic field confinement, and independently controlled substrate biasing. Preliminary measurements show that the reactor produces a large volume of dense plasma (>10^{12} cm^{-3}) at very low pressure (~1.0 mTorr). The plasma parameters are uniform to within ±1% over the working volume, with no perturbing radio-frequency electric field. Profiles etched into Si and SiO_2 in CF_4 plasma are highly anisotropic with etch rates > 1000 Å/min.

157 A New, High Efficiency, Sub-megahertz Excitation Frequency, Inductively Coupled Plasma Generator for High Rate Downstream Photoresist Stripping and Isotropic Etching: *C. B. Zarowin, G. N. Steinberg*, and *A. R. Reinberg*, The Perkin-Elmer Corp., Wilton, CT 06897

We report a new generator for ion bombardment free, "downstream," photoresist "stripping" and isotropic etching. This generator is a gas discharge "loop" (torus) forming a one turn secondary of a transformer whose primary winding (about a magnetic core through the "loop") is driven by an rf power supply at about 300W and 400 kHz. This purely inductive coupling provides several advantages over other coupling schemes which result in the removal of photoresist at about 2 microns/min from a 100 mm diameter wafer. Because only the long-lived active species generated in the plasma reach the wafer located downstream, the chemiluminescence generated by the "stripping" reaction can be monitored without interference from the plasma emission. It is found that the "stripping" rate is proportional to the chemiluminescence intensity, providing a very convenient and reliable rate monitor.

158 Magnetron-Enhanced Reactive Ion Etching of SiO_2: *Lin I.**, *D. Hinson*, and *W. Class*, Materials Research Corp., Orangeburg, NY 10962

A magnetron-enhanced reactive ion etcher has been developed using a uniform magnetic field to produce a high flux (~40 mA/cm²) of low energy (≈100 eV) ions. The etch rate of SiO_2 is 3000 Å/min with a selectivity of 8:1 over Si at 1 W/cm² power density in a 10 mTorr CF_4/H_2 mixture. The high rate at low pressure gives a highly anisotropic etch, and the lower voltage can be expected to produce less radiation damage.

159 Automated Sequential Dry Processing: Develop, Etch, Ash: *R. J. Mattox*, Motorola, Inc. SPS, Process Technology Lab, SRDL, Phoenix, AZ 85008

As part of the continuing goal of our industry to increase the level of "hands-off" processing, the author has addressed the concept of combining photoresist dry developing, dry etching, and ashing in one system. This paper deals with that concept, specifically for the case of oxide patterning, utilizing a commercially available single wafer system. Data are presented concerning each step of the process, demonstrating that usable throughputs can be achieved.

160 Optical Etch Rate Monitoring: Computer Simulation of Reflectance: *P. A. Heimann** and *R. J. Schutz*, Bell Laboratories, Murray Hill, NJ 07974

We report on a numerical simulation of the signal from a laser etch rate monitor which utilizes changes in the optical reflectance of a multilayered structure while the top layer is being etched. The only required parameters are the wavelength of the light, and, for each layer, the indexes of refraction and absorption, the initial thickness, and the etch rate. It can also be applied to cases where portions of the film area are being etched at different rates, such as when part of the film is covered with photoresist. The simulation has been applied to several etch processes, including silicide-polysilicon gate and metallization etches, and good agreement is found between experimental and calculated data.

161 Paper withdrawn.

162 A Statistical Approach to Selective Etching Process Development: *W. Ma,** *J. Bondur*, and *T. Krawiec*, IBM General Technology Div., East Fishkill, NY 12533

This paper describes the method of, and results in, developing a selective etching process of SiO_2 over silicon using CHF_3 gaseous plasma. The experimental parameters were statistically selected with the aid of a computer program. This computer-aided parametric study allows an examination of the individual variable space of interest with a minimum set of experiments. This allows the optimum processing parameters to be rapidly defined, and the information can be used to scale-up the wafer batch size. The results showed that when wafers are coated with a resist pattern there is a well-defined relationship among etch rate, etch rate ratio, uniformity, and wafer loading. However, in the absence of photoresist, the relationships are not well defined.

163 Tapering CVD SiO_2 Vias for Improved Metal Step Coverage Using RIE: *E. Crabbé* and *E. R. Sirkin**, Xerox Palo Alto Research Center, Palo Alto, CA 94304

Tapered contact vias were etched through insulating CVD SiO_2 films using a "hexode" type reactive ion etcher. Sloped profiles in the SiO_2 films were controllably produced by altering photoresist and SiO_2 etch rates. The technique was demonstrated for photoresist defined by both proximity and projection aligners, and multilayer SiO_2 films consisting of thermal, P-doped CVD and/or undoped CVD SiO_2 films. The influence of different via profiles on the formation of microcracks in the subsequent metal film deposition is discussed.

164 The Importance of Plasma Poly Etching Selectivities: *P. C. Chang*, Monolithic Memories Inc., Sunnyvale, CA 94086

Plasma poly etch using various reactive gases has been investigated for several years; it is very important to obtain high selectivity against underlying films (*i.e.*, Si, or oxide) as well as photoresist. This report describes a special plasma poly etch, which not only increases dimensional control anisotropically, but also achieves high selectivity between those layers. A theoretical calculation of selectivity is also discussed.

165 Dry Etching of Dielectrics for VLSI: *M. T. Duffy** and *R. A. Soltis*, RCA Laboratories, Princeton, NJ 08540, and *A. Day*, RCA Solid State Division, Somerville, NJ 08876

Anisotropic etching in rf-generated plasmas is widely used for selectively defining contact openings with vertical walls in dielectrics during the fabrication of VLSI devices. Vertical wall profiles are produced under conditions intended to minimize lateral etching of small contact openings. However, subsequent step coverage over vertical walls presents some difficulties during metallization, especially in multilevel metal structures. It would be desirable, therefore, to control wall profiles by controlling vertical and lateral etch rates during the etching of contact openings or vias. This paper discusses the generation of vertical and tapered contact openings and vias in various dielectrics.

166 Polymer Formation and Reactor Cleaning during Silicon Oxide Etching: *L. Peccoud, Ph. Laporte*, and *P. Lassagne*, L.E.T.I., Commissariat à l'Energie Atomique, 38041 Grenoble Cedex, France

Polymer formation has been observed during silicon oxide etching by CHF_3, and it generally affects the reproducibility of the process. It can reduce etch rates and sometimes results in an incomplete removal of the oxide. The process is more or less critical in the reactor structure: electrode spacing, electrode configuration, and gas composition. The repetitivities of cleaning processes in various structure reactors are presented.

167 Controlled Film Formation during CCl_4 Plasma Etching: *S. E. Bernacki* and *B. B. Kosicki*, Sperry Research Center, Sudbury, MA 01776

Carbon tetrachloride plasma etching can be performed in a regime in which a film-like product is simultaneously formed on vertical surfaces but inhibited from forming on horizontal surfaces. If the photoresist profile is properly tailored this process is capable of etching polysilicon and layered molysilicide films with virtually no change in linewidth from the developed photoresist image. We discuss the influence of the masking profile on the etched film profile and present conditions necessary for controlled film formation.

168 Plasma Metal Etching for High Yield in a Production Environment: *S. Fouts** and *D. Vogel*, Intel Corporation, Santa Clara, CA 95051

Factors influencing the yield of VLSI devices with plasma etched metal are discussed. Emphasis is placed on those characteristics of etching desired for high volume manufacturing. A defect analysis chip for plasma metal etching is described. Reasons for the chip's construction and examples of findings from its use are detailed. Yield data is correlated to device topography and etching parameters. Mask reactivity in the plasma is shown to be particularly important.

169 Plasma Etching Techniques for SiO_2, Polysilicon, and Aluminum-Silicon (U): *R. W. Light*, Sandia National Laboratories, Albuquerque, NM 87185

Plasma etching processes suitable for fabrication of devices with 2 and 3 μm feature sizes are presented. The fluorine based polysilicon and silicon dioxide processes yield tapered profiles that enhance coverage by subsequent deposition steps. The degree of taper is a function of the photoresist profile and the relative etch rates of the photoresist and the film being etched. Al/Si is etched with a chlorine based reactive ion etching process and produces vertical profiles. Etch rate optimization and selectivity trends are discussed for each process.

170 Positive and Negative Dry Development of Chalcogenide Optical Resists: *S. A. Lis, J. M. Lavine,* J. I. Masters*, and *G. M. Goldberg*, GCA Corp., Bedford, MA 01730

Lithographic results and processing parameters are presented for the case of plasma development of Ag photodoped As_2S_3, As_2Se_3, and $GeSe_2$. The developing plasmas consisting of CF_4, H_2, and SF_6 were shown to be capable of generating submicron optical lithographic patterns. Also, positive image development in some of these chalcogenides is reported for the first time. Results of these various development methods are related to the nearly attained goal of an all dry (deposition and development) submicron lithographic process.

171 Heavy Metal Contamination Caused by Reactive Sputter Etching: *Y. Kawamoto*, Hitachi, Ltd., Central Research Laboratory, Kokubunji, Tokyo 185, Japan

Reactive sputter etching causes heavy metal contamination on Si surface. Minority carrier recombination lifetime of Si substrate is decreased by these contaminants. The degree of contamination depends on ion bombardment energy as well as the materials of plasma exposed surface in reaction chamber. Ions with a bombardment energy of more than 100 eV cause remarkable lifetime decrease even if the electrodes and chamber wall of etching apparatus are covered with quartz.

172 The Effect of Chamber Configurations and Bias Voltages on Damage Induced in Si by Reactive-Ion Etching: *S. W. Pang,** Lincoln Laboratory, Massachusetts Institute of Technology, Lexington, MA 02173, *C. M. Horwitz*, Dept. of Electrical Engineering, Massachusetts Institute of Technology, Cambridge, MA 02139, *D. D. Rathman, S. M. Cabral, D. J. Silversmith*, and *R. W. Mountain*, Lincoln Laboratory, Massachusetts Institute of Technology, Lexington, MA 02173

In this study, comparisons between damage in Si substrates caused by dry etching in different reactive-ion etching (RIE) chamber configurations and bias voltages are reported. The RIE chamber configurations used were as follows: *(i)* a stainless steel chamber with quartz plate on the powered electrode, (*ii*) a coating of amorphous SiO_x on the entire chamber applied by an rf discharge in $SiCl_4 + O_2 + Ar$, and *(iii)* various area ratios between the powered and ground electrodes. Damage in Si induced by RIE in CF_4 was evaluated by fabricating metal-oxide-semiconductor (MOS) capacitors on the etched Si surfaces. The increase of interface states and the degradation of generation lifetimes were found to depend on chamber conditions and bias voltages. (This work was sponsored by the Department of the Air Force.)

173 Solving the Problem of High Contact Resistance Observed in Reactive Ion Oxide Etching: *J. S. Chang*, STC Computer Research, Santa Clara, CA 95051

High contact resistance has been observed in reactive ion etching (RIE) of oxide with high bias voltage. To investigate this phenomenon, a MOS test device was used and the effects of etchant, power, and bias voltage were studied. Analytical methods were then applied to generate a model, included herein, that explains the phenomenon. Further, several techniques are presented to solve the problem.

174 Characterization of Post-RIE Damage Removal Techniques: *C. M. Ransom** and *T. I. Chappell*, IBM T. J. Watson Research Center, Yorktown Heights, NY 10598, and *A. Sugarman, R. S. Bennett*, and *L. Eprath*, IBM East Fishkill Facility, Hopewell Junction, NY 12533

Reactive ion etching (RIE) of an oxide to the silicon results in damage to the silicon surface. For applications such as Schottky barrier diode clamps in bipolar devices, RIE related interface damage could be significant if the barrier height shifts enough with respect to the pn junction. Post-RIE damage removal techniques are characterized by DLTS, CV, and IV measurements. The success of treatments involving oxidation of the damaged interface, wet chemical etching, and pre-metallization thermal anneals are compared. Speculations are made about RIE damage mechanisms.

175 Modification of Schottky Barriers in Silicon by Reactive Ion Etching in NF_3 Gas Mixtures: *T. P. Chow,** General Electric Corporate Research and Development, Schenectady, NY 12345, and *S. Ashok*, Engineering Science Program, The Pennsylvania State University, University Park, PA 16802

The surface properties of silicon after reaction ion etching (RIE) with various NF_3 gas mixtures has been studied with secondary ion mass spectrometry (SIMS) and Schottky diode characteristics. The parameters considered included applied rf power, etching time, d-c self-bias, pressure, and dilution with inert gases (argon and nitrogen). Generally, after RIE, the Schottky barrier height was decreased on n-type Si but increased on p-type Si, together with a marked increased of fluorine on the surface. The nature of Schottky barrier modification is discussed in terms of physical damage and chemical reactions.

176 Hydrogen-Plasma Etching of Organic Films: *F. Y. Robb*, Motorola, Inc. SPS, Process Technology Laboratory, SRDL, Phoenix, AZ 85008

The use of hydrogen plasma for reactive ion etching of organic films has been characterized. It was found that anisotropic etching could be easily achieved, but with relatively slow etch rates (<300 Å/min). The effect of reactor variables (such as pressure, temperature, and power) and chemistry changes (such as the addition of O_2, N_2, and Ar) were studied and are discussed. In addition, the applications of contact hole etching and trilevel resist processing are considered.

177 Dry Etching of Polyimide in O_2-CF_4 and O_2-SF_6 Plasmas: *G. Turban** and *M. Rapeaux*, Laboratoire de Physique Corpusculaire, E.R.A. 924, Université de Nantes, 44072 Nantes Cedex, France

The plasma etching of the polyimide kapton has been studied in a parallel plate reactor with two different gas mixtures: O_2-CF_4 and O_2-SF_6. A high etching rate has been obtained in both cases. At a pressure of 0.2 Torr, an anomalous loading effect is observed which is attributed to the nitrogen released by the polyimide. The gaseous effluents from etching have been studied by mass spectrometry and indicate that both atomic oxygen and atomic fluorine are involved in the etching process. A comparison with silicon etching in an SF_6-O_2 plasma permits us to propose a reactional scheme. XPS measurements of the polyimide surface before and after etching confirm the mass spectrometric observations.

178 Via Profiling in Polyimide for a 3 Micron CMOS Array: *C. J. Heslop,** *S. J. Wright, R. E. Hines, M. Gill*, and *A. Belka*, British Telecom Research Laboratories, Martlesham Heath, Ipswich Suffolk, England IP5 7RE

Planarization of a wafer by polyimide when used as an insulator for a two-level metal process is an advantage for subsequent step coverage, but imposes serious difficulties with dimensional control of the vias. Two techniques of profiling the vias while maintaining an upper limit on via size are described together with step coverage and contact resistance results. These are a two-layer recut process and a double etch using a metal mask.

179 Plasma Etching of Vias in Polyimide Using Nonerodible Masks: *T. O. Herndon,** *W. J. Landoch*, and *R. L. Burke*, MIT Lincoln Laboratory, Lexington, MA 02173

Techniques are under development for reliably etching high resolution vias in polyimide intermetal insulation. Problems due to nonselectivity of plasma etching using photoresist masking are aggravated by variations in underlying topography which cause peak thinning of resist and polyimide. Two types of nonerodible mask have essentially eliminated shorts due to overetching at peaks. Techniques for good via cleanout, and first metal surface preparation necessary for low first to second metal resistance have also been developed.

180 Application of Emission Spectroscopy for Profile Control during Oxygen RIE of Thick Photoresist: *B. R. Soller** and *R. V. Shuman*, Sperry Research Center, Sudbury, MA 01776, and *R. R. Ross*, College of the Holy Cross, Worcester, MA 01610

Oxygen reactive ion etching of the planarizing photoresist layer in a multilayer resist system was studied. The etch rate and the degree of isotropy were measured as functions of power density, d-c bias voltage, and pressure. In addition, the emission spectra of these plasma were recorded and interpreted. These spectra revealed the presence of O_2^+ molecules and O atoms. The ratio of their emissions is related to the degree of isotropy. With this information we were able to accurately control the profile of the resist system so it can be used as a mask for anisotropic etching of the substrate or for lift-off.

181 Plasma Photoresist Stripping: Variation in Mobil Ion Contamination across Wafer Diameter: *D. Summers*, Tektronix, Inc., Beaverton, OR, 97077

Mobil ion contamination caused by oxygen plasma removal of photoresist has been investigated. The variable of primary interest was the level of contamination as a function of position across the wafer diameter. Experimental system was a quartz chamber barrel reactor with wafers processed in a typical stand-up boat configuration. When multiple wafers are stripped, locations near the edge can have much greater contamination than those at the center. The effects of operating pressure, wafer to wafer spacing, and exposure time in the plasma were investigated.

182 Plasma Processing in the Printed Circuit Industry: *R. D. Rust*, Bell Laboratories, Whippany, NJ 07981

Plasma processing is under serious study for use in printed circuit board manufacturing. The removal of epoxy smear in the drilled holes of multilayer boards is one application of interest. This paper describes methods of characterizing and improving etch rate and uniformity over an 18 in. × 24 in. multilayer panel. Novel reactor features which enhance performance are also discussed.

183 The Mechanism of Plasma Etching of Multilayer Boards: *A. A. Parker,* R. J. Pachter,* and *R. D. Rust,* Bell Laboratories, Whippany, NJ 07981

We have developed a model for the etching process of an oxygen/freon plasma in printed circuit boards. This paper presents details of this model and describes a series of experiments whose results report the model. A good fit of the temperature dependence of the etch rate to an Arrhenius form was found. The etch rate as a function of pressure was found to be proportional to simple models for atomic oxygen and atomic fluorine concentration as functions of pressure.

184 Unique Reactor Geometry for Plasma Removal of Epoxy Smear in Multilayer Printed Wiring Boards: *R. J. Rhodes,* Bell Laboratories, Whippany, NJ 07981

An rf excited oxygen (O_2), Freon-14 (CF_4) plasma has been used as an alternative to concentrated sulfuric acid and vaporhone processes to remove epoxy smear from the holes in multilayer printed wiring boards (MLB's) generated during drilling. A commercially available reactor was modified to accept four MLB panels. The conductive surface layers of the drilled MLB's were used as the electrodes to generate the plasma resulting in effective smear removal. Dielectric field suppressors (DFS) positioned around the edges of the panels provided uniform treatment over the panel.

185 Polymer Interlayer Adhesion Enhancement Through Plasma Surface Modification: *R. H. Wheater,* F. Emmi, R. F. White, W. D. Bingle,* and *R. S. Horwath,* IBM Corp., Endicott, NY 13760

Parameters governing plasma modification of a phenoxy resin were correlated to the polymer's surface chemistry and the resultant polymer interlayer adhesion. An O_2/CF_4 plasma was explored with respect to plasma exposure time, gas composition, power density, and gas flow. Additionally, with a selected plasma condition process variables including material production lot, film thickness, film dryness, and mix methods were studied. XPS, SEM, and adhesion data were collected for the aforementioned variables in order to determine the key bonding mechanisms for the polymer layers in question. In all cases, the samples were evaluated for mechanical and chemical bonds.

186 The Reaction Probability of XeF_2 with Silicon: *M. J. Vasile,* Bell Laboratories, Murray Hill, NJ 07974

The plasma etching of silicon has been simulated with experiments using atomic fluorine sources or with the dissociative adsorption of XeF_2. It is reasonable to question whether XeF_2 and atomic fluorine are equivalent reactants with silicon. One means to compare these two reactants is through their reaction probabilities to form SiF_4 from a silicon surface. The reaction probability of XeF_2 with silicon was between $1\text{-}3 \times 10^{-3}$ under the conditions employed, and it is a factor of ten lower than the value obtained for atomic fluorine. Examination of the products obtained from the reaction of XeF_2 with silicon shows that there is a range in experimental conditions where the reaction probability is not a unique parameter. This occurs when the flux of XeF_2 or atomic fluorine is insufficient to fully fluorinate the silicon surface.

187 Optical Emission from Reactive Fluorocarbon-Oxygen Plasma: *M.-M. Chen* and *Y. H. Lee,** IBM T. J. Watson Research Center, Yorktown Heights, NY 10598

Optical emission and etch rates are measured for Si and Nb in the $CF_4 + O_2$, $C_2F_6 + O_2$, and $C_3F_8 + O_2$ plasma. A broad band at 350-450 nm is attributed to $CF_3{}^0$ and another band near 580 nm, only resolved in C_2F_6 and C_3F_8, to the triplet-to-singlet transition of $CF_2{}^0$. As O_2 is mixed, the F_1 intensity increases at the expense of $CF_2{}^0$ and $CF_3{}^0$. The lower the F/C ratio, the more O_2 is required for F to reach its maximum intensity, because of a higher generation rate of the fluorocarbon radicals in the gas with a lower F/C ratio. Chemical reaction between the fluorocarbon radicals and oxygen is slow, so that the F_1 intensity decreases with increasing total flow rate, while the O_1 intensity increases. Both Si and Nb etch rates directly follow the F intensity variation, reflecting that F is a dominant species responsible for the reactive etching in both materials. Also, we observe an Nb loading effect, different from that of Si

188 The Effect of Collisions in Anisotropic Plasma Etching and Its Relation to Reactive Ion Etching: *C. B. Zarowin,* The Perkin-Elmer Corp., Wilton, CT 06897

A model of plasma etch anisotropy is presented which shows that the ionic component of the chemical etch process produces etch profiles that vary with E/p, where E is the electric field controlling the ion transport to the etch surface and p is the etch gas pressure. This model predicts that the profiles will vary continuously from isotropically to anisotropically produced as E/p is increased. The one-to-one correspondence between ion energy and ion transport or etch directionality shown by this model clarifies the compromise required between etch anisotropy and the adverse effects of high ion energy, such as reduced resist survival and selectivity against other materials. Another consequence of this work is the establishment of a theoretical basis for extending the conventional wisdom that low pressures (<10 Pa) are required for anisotropic plasma etching to the more general requirement of a sufficiently high E/p ratio. It is shown that reactive ion etching (RIE) is a low pressure limiting case of plasma etching (PE), both capable of identically anisotropic etching, although the latter yields higher etch rates. Finally, this model predicts a dependence of the anisotropy on the ion-neutral collision cross section and mass ratio, which is experimentally confirmed by data given in this paper.

189 Determination of Electric Fields in Plasma Etch Discharges from Observable Parameters: *C. B. Zarowin,* The Perkin-Elmer Corp., Wilton, CT 06897

From a simple model of a two electrode rf discharge typically used for plasma/reactive ion etching, the relatively inaccessible electric fields in the plasma are related to the observable current or power densities. This model explains the differences in the electric fields produced at plasma excitation frequencies above and below a few MHz that yield different etch anisotropy at equal current densities and pressures. It also provides an explanation of the anisotropic etching occurring at the smaller area electrode and the isotropic etching at the larger. Finally, it shows that the fields in the plasma body are negligibly small compared to the sheath fields, so that the latter control the ion transport properties related elsewhere to the etch anisotropy and selectivity for a given etch chemistry and pressure.

190 Influence of Electrode Material on the Etch Characteristics of an Argon Plasma: *W. G. M. van den Hoek,* Philips Research Laboratories, Eindhoven, The Netherlands

The influence of electrode material on the etch characteristics of an argon plasma was investigated in a diode rf sputter etch system. The sputter etch rates of Au, Al_2O_3, AZ1375, and ferrite ($Ni_{0.64}Zn_{0.36}Fe_2O_4$) were determined in an argon plasma on Al_2O_3, Al, SiO_2, Cu, Au, and Mo electrodes. The sputter etch rates are observed to increase by a factor of 1.4 Au to 4 ferrite, changing the Al_2O_3 electrode for a Mo electrode. The sputter etch rates are also strongly dependent on the area of the electrode covered with wafers. Depending on the electrode material, both increasing and decreasing etch rates with increasing wafer area are found. These results are discussed in terms of secondary electron emission coefficients of the electrode materials, self-bias voltage, and argon flow.

191 Studies on the Mechanism of Selective Isotropic Dry Etching of Si_3N_4 over SiO_2: *F. H. M. Sanders** and *J. Dieleman,* Philips Research Laboratories, 5600 JA Eindhoven, The Netherlands

Selective isotropic dry etching of Si_3N_4 over SiO_2 in a barrel-type reactor can be accomplished by the addition of gases containing halogens, like chlorine, bromine, or iodine, to the well-known CF_4-O_2 mixture. Only small amounts of the additive gases are needed to improve the selectivity to a value higher than ten. Especially the use of gases containing bromine is advantageous, because high selectivity, good uniformity, and high etch rates are possible at the same time. Studies to elucidate the role of the additive gases in the etch mechanism are discussed.

192 Studies of Plasma Etching Mechanisms with Cantilever Structures: *J. L. Reynolds, J. Nollins,* and *A. R. Neureuther,* Dept. of Electrical Engineering and Computer Sciences, the Electronics Research Laboratory, University of California at Berkeley, Berkeley, CA 94720

Cantilevered structures are used to explore the relative importance of factors such as surface migration, ion directionality, and the basic isotropic and anisotropic components in plasma etching. Integrated cantilever structures were fabricated by overetching a supporting material (polyimide or SiO_x) beneath a non-eroding mask (titanium or hardened resist). This diagnostic structure is used in studies of silicon etching with SF_6/O_2, CF_4/O_2, and $CClF_3/CF_4/O_2$ under various powers, pressures, and flow rates. No surface migration or angularly distributed effects are found. However, accelerated etching and anisotropic undercutting are observed well into the shadowed region away from the mask edge. These experiments are being used to characterize the dominant etching mechanisms for incorporation into the profile simulation program SAMPLE. (This work was supported in part by Sandia National Laboratories (42-5874) and in part by the National Science Foundation (ECS-8106243-A01).)

193 Plasma Etch Process Modeling: *K. C. R. Chiu,* Synertek, Inc. Santa Clara, CA 95051

The plasma etch process has been modeled using optical emission spectroscopy. Plasma etch parameters such as gas mixtures, flow rates, pumping speed, operating pressure, rf power input, wafer loading, etc., have been quantitatively related to etch results and optical emission spectra. This has made more understandable the physics and chemistry involved in the plasma etch process and simplified the development of optimum conditions. The feasibility of scaling the process from one etcher to another of a different design has also been studied using this approach.

194 A Review of Reactive Ion Beam and Ion-Assisted Chemical Etching: *D. F. Downey,** Varian Associates, Extrion Div., Blackburn Industrial Park, Gloucester, MA 01930 and *R. A. Powell,* Varion Solid State Laboratories, Palo Alto, CA 94304

The use of reactive ions and ion beams in the dry etching of semiconductor devices is becoming an increasingly more important fabrication technology. This paper reviews the evolution and

significance of the energetic ion as a tool for the etching process where control, directionality, high resolution, and energetics are a prerequisite. Among the materials systems reviewed are Si, SiO_2, polysilicon, Al and its alloys, III-IV compound metal silicides, Si_3N_4, and standard masking materials.

195 Plasma Etch Process Modeling: Application to Al Etch Process Development: *K. C. R. Chiu*, Synertek, Inc., Santa Clara, CA 95051

A semiquantitative method for plasma process development was employed in the successful development of the Al etch process. The optical emission of the chlorinated plasmas was used not only as the end point indicator, but also to give a quantitative estimation of the etch results. By using the modeling procedure to guide process parameter selection, the process development can be simplified. The methodology used in the plasma process development is discussed.

196 Use of Optical Emission from Cl_2, $SiCl_4$, and BCl_3 during Reactive Ion Etching of Aluminum: *K. O. Park* and *F. C. Rock*, GTE Laboratories, Waltham, MA 02254

It is well known that aluminum can be reactively sputter etched with Cl_2, $SiCl_4$, and BCl_3, separately or in mixtures. In this paper, differences in the optical emission characteristic of reactive ion etching of aluminum are presented for several etchant gases. It is shown that intensities of Cl_2(I) and Cl_2(II) bands, which are initially very intense in Cl_2 plasmas, begin to reduce, accompanied by the growing appearance of molecular AlCl bands, as Al RIE proceeds. While Cl_2(I) and Cl_2(II) bands are not clearly seen in $SiCl_4$ plasma, intense SiCl bands are observed. As Al RIE proceeds in this system, AlCl(I) bands grow quickly. While BCl_3 spectra show weak Cl_2(I) emission bands and intense BCl(I) emission bands, during Al RIE AlCl(I) bands grow faster than in Cl_2 or $SiCl_4$ plasmas, indicating that BCl_3 is the least effected by native aluminum oxide. It is also shown that both Cl_2 and BCl_3 spectra are characterized by the presence of intense and well-resolved Al(I) emission lines during reactive ion etching of aluminum, in contrast to the situation for $SiCl_4$, where these lines are not discernible. The significance of the presence and behavior of these emission bands during Al RIE and the corresponding etching mechanism of aluminum in these gases is discussed. The suitability of molecular emission for end point detection is also discussed.

197 Reactive Ion Etching of Aluminum in BCl_3-Cl_2 Mixtures: *S. Schwarzl*,* Siemens AG, D-8000 München 80, Germany, and *W. Beinvogl*, Siemens AG, Research Laboratories, D-8000 München 83, Germany

Reactive ion etching of aluminum in BCl_3-Cl_2 mixtures was studied using a parallel-plate reactor without load look. Etching characteristics such as etch rate, loading effect, anisotropy, and uniformity are presented as functions of the process parameters. Reproducibility is not impaired by humidity and native oxide problems. Discussing the mechanism of anisotropy, special attention is paid to the influence of mask material. Strict anisotropy has been achieved down to submicron feature sizes.

198 Process Integrity and the Role of $AlCl_3$ in the Plasma Etching of Aluminum: *J. E. Spencer*, Texas Instruments Inc., Dallas TX 75265

A production-worthy aluminum etch process must enhance product manufacturability and yield. A major factor in the process integrity of aluminum plasma etching is the etch product $AlCl_3$. $AlCl_3$ represents a unique situation among plasma etching products due to its highly reactive nature. This reactivity must be carefully controlled during the etch process. Control of $AlCl_3$ requires a two level approach. The first level is to reduce the exposure of oxygen and moisture. The second level requires that the amount of $AlCl_3$ in the plasma must be minimized. High concentrations of $AlCl_3$ result in excessive photoresist degradation as well as high rates of SiO_2, the typical layer underlying aluminum on devices.

199 Variation of CF_4 + O_2 Plasma Etch Rate of Ta Films on Ceramic with Flow, Pressure, and Exposed Area (Loading): *G. L. Dybwad*, Bell Laboratories, Allentown, PA 18103

We are developing plasma etching for delineating tantalum based RC features on alumina for hybrid integrated circuits. We report here the variation of CF_4 + O_2 plasma etch rate of α-Ta films on alumina (Al_2O_3) with flow, chamber pressure, and area of exposed tantalum (loading effect). Also described is the effect of various areas of exposed circuit conductor gold and photoresist mask materials on etch rate. The data have aided optimization of dry processing of circuits. The results indicated that high pressure and flow increased the etch rate without forming chamber deposits as long as the residence time of the gas in the chamber, $t_r \geq 1.6$ sec. The loading effect was linear with exposed area. The presence of exposed photoresist inhibited Ta etching.

200 Contamination in AlSi Dry Etching: *H. Itakura*, *T. Shibano*, *M. Yoneda*, and *H. Abe*, Mitsubishi Electric Corp., Computer Development Laboratories Ltd., LSI R&D Laboratory, 4-1 Mizuhara, Itami, Hyogo, Japan 664

During the dry etching of AlSi by using CCl_4 + He mixed gas, the thin film deposits not only inside the chamber wall but also on the surface of the electrodes. There is a fear that the film makes reproducibility of etching characteristics worse, and causes redeposition on the sample. The formation of the film under some etching conditions and the composition of these films were investigated. When carbon was adopted as the material of the electrode, the thickness of the film was decreased, and redeposition was reduced.

201 After Corrosion Treatments in Aluminum Alloy Reactive Ion Etching: *T. Tsukada*,* *H. Takei*, *E. Wani*, *and K. Ukai* ANELVA Corp., 8-1 5-chome Yotsuya, Fuchu-shi, Tokyo, Japan 183

After corrosion treatments were studied in Al-1%Si-2%Cu reactive ion etching. Several kinds of gas species were investigated for the post treatments after aluminum etching. As the NH_3 gas or O_2 mixture gas plasma were not so effective for the corrosion, the post treatments of the fluorinated gas plasma were effective for the prevention of the corrosion. And the best treatment was more effective than the DI water rinse. The corrosion free process was made complete by using NH_3 water rinse. Using the surface analysis method, the post treatment mechanism is discussed.

202 A Review of Plasma Etching of Refractory Metal Silicides: *T. P. Chow*, General Electric, Corporate Research and Development Center, Schenectady, NY 12345, and *A. J. Steckl*, Rensselaer Polytechnic Institute, Center for Integrated Electronics, Troy, NY 12181

Refractory metal silicides are under active development as gate and interconnecting material in MOS integrated circuits. Fine line patterning of VLSI circuits necessitates the use of plasma etching techniques. In this paper, we review the status of plasma etching (including reactive ion etching) of various metal silicides (such as $MoSi_2$, WSi_2, and $TaSi_2$). Etching in both fluorine- and chlorine-based gas mixtures is discussed in terms of etch rate, anisotropy, selectivity with SiO_2, and photoresist. Key issues, such as control of edge profiles in silicide and polycide structures, are also addressed.

DIELECTRICS AND INSULATION/ELECTRONICS/CORROSION/ HIGH TEMPERATURE MATERIALS/ENERGY TECHNOLOGY

Materials and New Processing Technologies for Photovoltaics

203 Recent Status of Solar Photovoltaic R&D in Japan: *Y. Hamakawa*, Faculty of Engineering Science, Osaka University, Machikaneyama-cho 1-1, Toyonaka, Osaka, Japan

Current state of the art in Japanese domestic activities of the Solar Photovoltaic R&D project is reviewed. A revised new organizations for the accelerative promotion strategy in the Sunshine Project and its structure are also introduced. Materials science efforts and some key technologies for the cost reduction of the solar cells are described, and their industrializations including amorphous silicon solar cells are presented and discussed.

204 State of Photovoltaics Technology in the European Community: *R.J. Van Overstraeten*, ESAT Laboratory, Katholieke Universiteit Leuven, 3030 Heverlee, Belgium

Photovoltaic industry is developing in different countries of the European Community. The C.E.C. is now ending the second 4 year Research and Development program on energy and is preparing the third one. Substantial progress has been made on cell and module technology and on systems. The pilot projects give valuable information about all system aspects, such as power conditioning, inverters, structures, environmental conditions. . . . A lot of work remains to be done in reducing the cost of the starting semiconductor material.

205 Photovoltaics in the U.S.: *H. Ehrenreich*, Div. of Applied Sciences, Harvard University, Cambridge MA 02138

The development of U.S. photovoltaic technology during the past five years is reviewed by contrasting various approaches currently under assessment. These include: *(i)* silicon *vs.* thin film cells; *(ii)* single *vs.* multijunction cells; *(iii)* flat plate *vs.* concentrator systems; *(iv)* central *vs.* distributed power systems; and *(v)* U.S. *vs.* developing country applications. As had been supposed earlier, the development of the field has been evolutionary, with few exceptions. However, future significant U.S. utility applications depend on progressive intermediate market developments.

206 Compound Semiconductor Thin Films: A Solar Cell Research Opportunity: *C.F. Gay** and *V.K. Kapur*, ARCO Solar, Inc., Woodland Hills, CA 91365

Recent work with 2-6 compounds such as $CuInSe_2$ and CdTe indicates an excellent potential of meeting critical photovoltaic goals. Stability, efficiency over 10%, low sensitivity to lattice mismatch, and the favorable effect of oxygen should broaden the search for cell materials in this class. A promising and available technique for this search is reactive sputtering, in which multiple metallic targets and piped-in gases can contribute to the film. We urge an expanded effort on this basis.

207 Advances in the Refining of MG-Silicon: *J. Dietl*, Heliotronic GmbH, 8263 Burghausen, Germany D 8263

In the field of upgrading metallurgical grade silicon to solar grade quality, hydrometallurgical and pyrometallurgical treatments qualify themselves as effective purification steps. Impurities with favorable segregation coefficients can be eliminated by acid leaching down to low ppm and even sub-ppm levels. Liquid-liquid extraction, alone or in conjunction with liquid-gas extraction, completes the removal of individual impurities. Optimizing of such pyrometallurgical processes requires understanding of the operational systems on the basis of oxidative/reductive intractions.

208 Solar Cells from High-Purity Arc-Furnace Silicon: *J.A. Amick, J.P. Dismukes,* L.P. Hunt, R.W. Francis, P.S. Ravishankar,* and *M. Schneider,* Exxon Research and Engineering Company, Solar Electric Conversion Unit, Linden, NJ 07036, *R. Sylvain,* Solar Power Corporation, Woburn, MA 01801, and *K. Larsen* and *A. Schei,* Elkem a/s, R&D Center, P.O. Box 40, N-4620 Vaagsbygd, Norway

High purity sources of carbon black and silica are suitable for producing silicon that can be fabricated into high efficiency solar cells. These raw materials were agglomerated under noncontaminating conditions and smelted in experimental arc furnaces. Silicon produced in this manner has been converted into second-generation Czochralski ingots from which a series of 10-cm-diameter solar cells was fabricated, one-third of which had conversion efficiencies between 12 and 13%.

209 Boron and Phosphorus Determination in Low-Resistivity Solar-Grade Silicon: *L.P. Hunt,* R.W. Francis,* and *J.P. Dismukes,* Exxon Research and Engineering Company, Linden, NJ 07036

A technique was developed to determine the concentration of boron and phosphorus in purified metallurgical silicon (PMS). Net carrier concentrations were obtained from Hall-effect measurements made on Czochralski ingots grown from PMS. Good agreement was found between concentrations analyzed by this method and by multiple-pass float zoning. Concentrations were measured over the range of 1-30 ppma for boron and 0.1-20 ppma for phosphorus.

210 Rice Hulls as a Raw Material for Producing Silicon: *L.P. Hunt, J.P. Dismukes,* and *J.A. Amick,** Exxon Research and Engineering Co., Solar Electric Conversion Unit, Linden, NJ 07036, and *K. Larsen* and *A. Schei* (Elkem a/s), R&D Center, N-4620 Vaagsbygd, Norway

Rice hulls are a relatively high-volume low-cost by-product which contain the two basic components needed to produce silicon, namely, silica and carbon. Purified and unpurified coked rice hulls showed high reactivity with silicon monoxide. Unpurified, coked rice hulls were tested in a 50 kW arc furnace and the energy consumption per kg of silicon was very low. Boron content of the purified hulls appears satisfactory for preparing solar-grade silicon.

211 Silicon Electrorefining and the Transport Properties of Cu_3Si: *J.M. Olson,* Solar Energy Research Institute, Golden, CO 80401

The purification efficiency of a molten salt silicon electrorefining process is increased by more than two orders of magnitude by the use of a composite, Si:Cu_3Si anode. The enhancement is ostensibly due to the silicon permeability of Cu_3Si. We first review the basic workings of this novel purification technique with an emphasis on recent developments. The unique, mass transport properties of Cu_3Si are then examined. In particular, we present evidence which suggests that Cu and Si diffuse very rapidly and other elements (such as Al and Ti) diffuse very slowly in the high temperature polymorph of Cu_3Si. The implications of these results are discussed.

212 Aerosol Reactor for Silicon Production *M.K. Alam** and *R.C. Flagan,* Keck Laboratory, California Institute of Technology, Pasadena, CA 91125

A new chemical reactor for production of polycrystalline silicon by thermal pyrolysis of silane in a flow reactor is described. A seed aerosol ($d < 0.5\ \mu m$) is generated by homogeneous nucleation of silicon. By controlling the concentration of seed particles and the rate of silane decomposition, the silicon particles are grown to large size. The large size of the product aerosol facilitates separation of the particles from the gas flow by inertial or gravitational deposition. The theory of control of nucleation rates and results from an experimental system are discussed.

213 Status and Potential of the EFG Technology for Low Cost Photovoltaics: *K.V. Ravi,* Mobil Solar Energy Corp., Waltham, MA 01803

The edge-defined film fed growth (EFG) technology is the first of the new, low cost photovoltaic technologies to have reached a stage of commercialization. Photovoltaic modules and systems based on this technology are now being sold commercially. In this paper the current status of this technology including aspects of crystal growth, cell processing, and panel fabrication is discussed with examples of applications of the technology. Future developments and prospects are addressed.

214 Compositional Analysis of Silicon for Solar Cells: *L.P. Hunt,* Exxon Research and Engineering Company, Linden, NJ 07036

A review is given of techniques for determining the composition of silicon used for fabricating high-efficiency solar cells. Grades of silicon range from that exiting an arc furnace to ingots grown from the melt. Concentrations are measured for dopants (B and P), metals, and nonmetal (C, O, and SiC) impurities. Discussion of accuracy and precision is based upon practical experience gained from many analyses. Technique limitations are also reviewed.

215 Effective Segregation Coefficients of Impurities in Silicon Ingots Grown by Czochralski and Bridgman Techniques: *L.P. Hunt, P.S. Ravishankar,** and *R.W. Francis,* Exxon Research and Engineering Company, Linden, NJ 07036

Effective segregation coefficients were determined for impurities in specific Czochralski and Bridgman crystal growth systems used to produce crystalline silicon ingots which were subsequently fabricated into solar cells. Concentrations were plotted against fractional amounts of the solidified silicon according to the segregation equation $\ln C/C_0 = \ln k_{eff} + (k_{eff}-1) \ln (1-g)$. For the Czochralski system k_{eff} was 0.80 for single crystalline ingots. In the Bridgman system, k_{eff} for polycrystalline ingots were 0.8 for boron, 0.35 for phosphorus, and about 8×10^{-5} for iron.

216 Carrier Lifetime Measurements in Silicon Wafers: *A.K. Ghosh,* T. Tiedje, J.I. Haberman,* and *R.W. Francis,* Exxon Research and Engineering Co., Linden, NJ 07036

A contactless rf technique has been developed for measuring the minority carrier lifetime in silicon wafers from the photoconductivity decay. Surface recombination plays a dominant role in the measured decay time for typical wafer thickness (10-20 mils). For HF:HCOOH:HNO_3 etched surfaces, the best fit to the data is obtained with a surface recombination velocity of 10^5 cm/sec. The surface contribution depends on wafer thickness and carrier mobility and obviously on surface recombination center density. Experimental results on the effect of surface passivation with TiO_2 on the surface recombination velocity and on the role of dopant concentration in the bulk recombination lifetime are discussed.

217 Characterization of Silicon Crystals Grown by the Heat Exchanger Method: *S. Hyland,* K.A. Dumas,* and *G.H. Schwuttke,* Jet Propulsion Laboratory, Pasadena, CA 91103, *J.A.A. Engelbrecht,* University of Port Elizabeth, Port Elizabeth, South Africa, and *D. Leung,* Applied Solar Energy Corporation, City of Industry, CA 91700

Silicon ingots grown by the heat exchanger method (HEM) as large as 45 kg in mass (34 cm × 34 cm × 17 cm) are characterized electrically and structurally. The defect state in the crystal is correlated with the minority carrier diffusion length and related to the solar cell efficiency. Such characterization indicates that the solar cell efficiency of HEM crystals is limited by the crystal perfection. HEM silicon has the potential to yield silicon with quality comparable to Cz grown silicon. A new approach to grow HEM material of better quality is discussed.

218 Influence of Iron, Titanium, and Vanadium on Photovoltaic Behavior of Polycrystalline Solar Cells: *S. Pizzini,** Dipartimento di Chimicia Fisica ed Elettrochimica, Via Venezian 21, Milano, Italy, *C. Calligarich, C. Chemelli, M. Gasparini,* and *P. Rava,* HELIOSIL S.p.A., Via Franchetti 1/A, Milano, Italy, and *L. Sardi,* ANSALDO S.p.A., Via Nicola Lorenzi +, Genova, Italy

It has been already shown that the behavior of impurities in polycrystalline silicon solar cells presents atypical aspects, in comparison to those observed in single crystal silicon cells, essentially due to the additional presence of grain boundaries. It is, however, not completely understood how impurities interact with grain boundaries, as well as how carbon and oxygen influence the overall cell behavior. In order to get more insight into this problem, selected impurities have been incorporated at different levels in polycrystalline silicon ingots grown with the directional solidification and Czochralski techniques, and their influence on the structure, morphology, and electrical properties of solar cells has been determined. Results are discussed both in terms of their relevance to the physics of the recombination process of minority carriers in the simultaneous presence of impurities and grain boundaries, and to the growth technology of silicon crystals from heavy doped feedstocks.

219 Mechanisms Limiting Performance in Polycrystalline Silicon Solar Cells: *J.H. Wohlgemuth** and *J.S. Culik,* Solarex Corp., Rockville, MD 20850, and *P. Alexander,* Jet Propulsion Laboratory, Pasadena, CA 91109

This paper reports on a systematic study to determine exactly what factors are limiting the efficiency of polycrystalline silicon solar cells. Factors evaluated are grain boundary recombination, as it effects current collection and diode factors, bulk diffusion length in the grains as it effects current collection and open-circuit voltage, and the influence of a back surface field. Performance has been evaluated for a variety of materials, bulk resistivities, and substrate thickness as they relate to microscopic structure (*i.e.*, placement in the brick) and microscopic structure (*i.e.*, grain boundaries, twins, etc.).

220 Hydrogen Motion and Bonding in Silicon Grain Boundaries: *C.H. Seager, J.K.G. Panitz,* and *D.J. Sharp,* Sandia National Laboratories, Albuquerque, NM 87185

We have recently shown that very short exposures to an intense proton beam can result in removal of grain boundary electrical activity down to substantial depths in EFG ribbon silicon. We describe the results of recent "hydrogen masking" experiments that allow us to directly probe the effective passivation depth on a micron scale. The variation of this depth with ion beam conditions is described and correlated with the improvements seen in photovoltaic devices passivated under the same conditions. (This work was performed at Sandia National Laboratories supported by the U.S. Department of Energy under contract number DE-AC04-76DP00789.)

221 Low Energy NMA Ion Implantation for the Formation of Back Surface Fields: *M.E. Brady,** Boeing Aerospace Co., Pasadena, CA 91103 and *D.J. Fitzgerald*, Jet Propulsion Laboratory, California Institute of Technology, Pasadena, CA 91109

Low energy non-mass-analyzed (NMA) ion implantation has proved effective in the formation of solar cell junctions. A series of tests have been performed to evaluate the success of this implantation technique in forming back surface fields. Apparent dose varying from 5×10^{15} to 5×10^{16} ions/cm^2 were implanted at an energy of 15 keV using boron trifluoride as the dopant source. Various annealing cycles were investigated in order to provide activation of the doped region. The effects of thermally treating the silicon substrate prior to implantation were also investigated. The results of these tests are discussed and suggested methods for improvement described.

222 Low Cost, High Efficient and Reliable Silicon Solar Cells with Plasma-Deposited Silicon Nitride as Antireflective Coating: *T. Kato* and *H. Morita*, Toshiba Corp., 72 Horikawa-cho, Kawsaki City, Japan, *A. Sato*, Toshiba Battery Corp., 3-4-10 Minami-Shinagawa, Shinagawa-ku, Tokyo, Japan, *H. Washide* and *A. Onoe*, Toshiba Corp., 72 Horikawa-cho, Kawsaki City, Japan, and *F. Fujimoto, K. Komaki, A. Ootuka*, and *Y. Iwata*, Tokyo University, 3-8-1 Komaba, Meguro-ku, Tokyo 153, Japan

Vertical distribution of hydrogen in antireflective coatings for solar cells such as plasma-deposited Si_3N_4, SiO_2, and dip-coated Al_2O_3 were analyzed utilizing $^1H(15N, Alpha\ Gamma)12C$ reaction. Hydrogen depleted at Si_3N_4-Si interface while it accumulated at SiO_2-Si interface. These coatings, which then served as plating masks for fine electrodes, and shallow junction enabled low-cost, high efficient cells. Stability of hydrogen content in the above-metioned coatings during irradiation of corpuscular beam correlated to cell reliability under ultraviolet light exposure.

223 Application of Thermoanalysis to Thick Film Materials Development: *J. Parker,** Electrink, Inc., San Diego, CA 92121 and *B. Gallagher*, Jet Propulsion Laboratory, California Institute of Technology, Pasadena, CA 91109

A thermoanalytic approach to the characterization of thick film inks and to the optimization of firing processes was applied to the development of an all-metal electrode ink designed for use in silicon photovoltaic devices. Determinations of the likelihood of the occurrence of selected chemical reactions in the firing process were made using a combination of calculated reaction-heat data with thermogravimetric and differential thermal analyses. The influence of these reactions on the properties of the fired ink film discussed, and consequent composition and process recommendations presented.

224 Development of a Contact End Resistance Approach to Contact Resistivity Measurement: *D. R. Burger*, Jet Propulsion Laboratory, California Institute of Technology, Pasadena, CA 91109

A new approach to measurement of contact resistivity of production photovoltaics devices is presented. The transmission line model is the basis for the new approach which utilizes contact end resistance and sheet resistivity values. Test patterns can be quickly generated on standard devices removed from the production line. A simple measurement scheme is shown along with a graphical solution which allows rapid determination of the contact resistivity of the metal-semiconductor interface.

225 High Efficiency Amorphous Silicon Solar Cells Fabrication by Reactive Sputtering: *T.D. Moustakas*, Exxon Research and Engineering Company, Linden, NJ 07036

Amorphous silicon solar cells with efficiencies of 5-6% have been fabricated by the method of reactive sputtering. These cells have the configuration N-I-P/ITO and generate currents of 12-13 mA/cm^2, and voltages of 0.85-0.95V. The FF (~0.5) is the efficiency limiting parameter. In this paper we discuss the compositional and structural characteristics of the intrinsic (I) as well as of the doped (P,N) layers (i.e. hydrogen, phosphorus, and boron concentrations as well as film microstructure and degree of crystallinity). These findings are correlated with device parameters and trends to further improvements on the solar cell performance are suggested. [This work was supported partly by SERI (Contract No. XZ-0-9219).]

226 Optical and Structural Properties of LPCVD Silicon Films: *N. Proust,** *R. Bisaro, J. Magariño*, and *K. Zellama*, Thomson-CSF Laboratoire Central de Recherches, B.P. No. 10 91401 Orsay Cedex, France, and Groupe de Physique des Solides de l'E.N.S., Université Paris VII, 75221 Paris Cedex 05, France

We present here, optical and structural (x-rays and Raman scattering) results on low pressure CVD silicon films which are amorphous or polycrystalline, according to pressure and deposition temperature. Crystallization mechanisms are analyzed here by comparison with previous experiments on atmospheric pressure CVD. The implications of these results for photovoltaics application are discussed.

227 A Non-Noble Front Metallization Process Using Mo/Sn Screen Printed Pastes: *A. Garcia III,** Spectrolab, Inc., Sylmar, CA 91342, and *B.D. Gallagher*, Jet Propulsion Laboratory/Cal Tech, Pasadena, CA 91109

This paper describes a front metallization process using an inexpensive Mo/Sn screen printed paste. The paste is first fired in air to burn off the organic vehicle, then fired in a reducing atomsphere to create ohmic contact between the silicon and Mo/Sn powder. A conductive AR coating (ITO) is used to reduce the inherent series resistance of the system. Cells have been produced with efficiency identical to that of silver paste controls.

228 Zinc Oxide Synergistic Systems for the Weathering Stabilization of Polyolefins: *B. Baum** and *D.S. Carr*, Springborn Laboratories, Inc., Enfield, CT 06082

Zinc oxide is recognized as an unusually effective u.v. (opacifying) stabilizer for polyolefins, including low and high density polyethylene, polypropylene, and ethylene copolymers. Zinc oxide stabilization is superior to organic u.v. absorbers in efficiency and economics. Synergistic organic additives used jointly with zinc oxide increase outdoor life several fold compared to the organic absorbers. Such synergists include organic phosphites, (Polygard), zinc dialkyldithiocarbomates (Methyl and Ethyl Zimate), and nickel-based u.v. stabilizers (Cyasorb 1084 and Ferro AM 101). One such system stabilizes the ethylene/vinyl acetate copolymer used as the encapsulant, between the silicon and the substrate in the flat-plate photovoltaic module.

229 Transparent Conducting Oxide Films for Solar Cells: *K.L. Chopra*, Indian Institute of Technology, New Delhi-110016, India

The technology of preparing transparent conducting oxide films for solar cells, and the methods of controlling transparency and conductivity of these films are discussed. Effects of these parameters on the performance of solar cells are reviewed. Properties of typical transparent conducting oxide films, and techniques of modifying them for particular solar cell configurations are presented.

230 Cadmium Telluride Solar Cells: *R.H. Bube*, Department of Materials Science and Engineering, Stanford University, Stanford, CA 94305

The advantages of cadmium telluride for the fabrication of low cost solar cells are reviewed, and techniques for forming cadmium telluride-based solar cells are described. The current status of research on cadmium telluride-based cells are surveyed and the future for this technology is assessed.

231 High Efficiency Tandem Cells: *J.C.C. Fan*, Lincoln Laboratory, Massachusetts Institute of Technology, Lexington, MA 02173

Analysis indicates that a substantial increase in solar cell conversion efficiencies can be achieved by using two-cell, multiband-gap tandem structures instead of single-junction cells. Practical AM1 efficiencies of about 30% at one sun and over 30% at multiple suns are to be expected. For inexpensive two-cell tandem modules, Si is preferred for the bottom cell, and the top-cell material should have a bandgap of 1.75-1.80 eV. Significant advances have been obtained achieving this tandem structure. (This work was sponsored by the Department of the Air Force.)

232 Thin Film Compound Semiconductor Photovoltaic Devices: *T.L. Chu*, Southern Methodist University, Dallas, TX 75275

Thin films of direct gap semiconductors on suitable substrates are promising photovoltaic materials. During the past few years, considerable efforts have been directed to the deposition and characterization of several thin film systems and the use of these films for low cost photovoltaic devices. The materials problems associated with the thin film devices, including substrate selection, deposition process, surface effects, grain boundary effects, etc., are discussed. The present status of several promising devices are reviewed. (This work was supported by the Solar Energy Research Institute and Electric Power Research Institute.)

233 Thin Film Gallium Arsenide Solar Cells: *S.S. Chu,** *T.L. Chu, F.S. Zhang, W.J. Chen*, and *Q.H. Wang*, Southern Methodist University, Dallas, TX 75275

Thin films of gallium arsenide deposited on foreign substrates by the halide process have been used for the fabrication of $p^+/n/n^+$/substrate homojunction solar cells. To improve the electrical characteristics of the thin film devices, various grain boundary passivation techniques have been investigated. Thin film homojunction cells of 1 cm^2 area with an AM1 efficiency of about 9% have been prepared, and their characteristics are discussed. (This work was prepared for the Department of Energy under Contract No. EG-77-C-01-4042 and SERI Subcontract XE-2-02068-1.)

234 A Simplified Contacting Scheme for GaAs Solar Cells Using Silver: *S.J. Hogan** and *K. Firor*, Solar Energy Research Institute, Golden, CO 80401

The conventional contact process for GaAs/GaAlAs photovoltaic devices uses gold alloys to form ohmic contacts. We have studied the properties of evaporated silver contacts into epitaxial GaAs, and found that with adjusting certain process parameters, the contact properties become ohmic on both n-and p-type materials. Various parameters, including contact resistance, series resistivity, and cell I-V parameters are compared for both the gold alloy systems and silver contacts and found to be equivalent. Auger analysis of the GaAs/metal contacts interface was also examined.

235 Atomic Diffusion in Copper Indium Diselenide: *S. Wagner*, Dept. of Electrical Engineering and Computer Science, Princeton University, Princeton, NJ 08544

Atomic diffusion in $CuInSe_2$ plays an important role during the preparation of $CuInSe_2$ as film or bulk, and possibly during

$CuInSe_2$/(Zn,Cd)S heterodiode fabrication as well as solar cell operation. Some diffusion data have been derived from the motion of pn junctions associated with conductivity type conversion, and from motional narrowing in nuclear magnetic resonance. In current thin film device work the movement of the $p\pi$ boundary in $CuInSe_2$ is being studied. This paper addresses the elementary point defects in $CuInSe_2$, their charge state, and their equilibria. An estimate is made for the diffusion coefficient of copper under isoconcentration conditions, and in an activity gradient.

236 Preparation of $CuInSe_2$ Films by Reactive Co-Sputtering: *J.A. Thornton** and *D.G. Cornog*, Telic Company, Santa Monica, CA 90404, and *R.B. Hall* and *J.D. Meakin*, Institute of Energy Conversion, University of Delaware, Newark, DE 19711

$CuInSe_2$ coatings have been deposited onto glass and alumina substrates by co-sputtering from Cu and In planar magnetron sputtering sources in an $Ar\&H_2Se$ working gas. The coating structure and composition were controlled by the substrate temperature and the relative sputtering fluxes from the two sources. Single phase chalcopyrite coatings with a high degree of 112 preferred orientation were obtained at substrate temperatures in the 350°-450°C range when the coating flux arriving at the substrate contained a considerable excess of In. The resistivities of the near-stoichiometric coatings were of the order of 10^3 Ω-cm.

237 Chemical and Optical Characterization of $CuInSe_2$ Thin Films for Solar Cells: *C.A. Megerle,** *R.K. Gupta, G.A. Pollock, S.A. Vasquez, W.A. Chesarek, M.B. Ammons,* and *V.K. Kapur*, ARCO Solar Inc., Woodland Hills, CA 91365

A variety of complementary methods were used to characterize copper indium diselenide thin films. Results obtained by atomic absorption spectroscopy, inductively coupled plasma emission spectrometry, x-ray diffraction, energy dispersive x-ray analysis, Auger electron spectroscopy, x-ray photoelectron spectroscopy, secondary ion mass spectrometry, ellipsometry, u.v./visible/near infrared spectrophotometry, infrared spectroscopy, scanning electron microscopy, and optical microscopy is discussed. The impact of these studies upon the development of $CuInSe_2$/CdS photovoltaic devices is also addressed.

238 Thin Film Cadmium Telluride Solar Cells: *T.L. Chu,** *S.S. Chu, Y.T. Yang*, and *X.J. Yi*, Southern Methodist University, Dallas, TX 75275, and *J.M. Yu*, Poly Solar Incorporated, Garland, TX 75041

Cadmium telluride films have been deposited on foreign substrates by the direct combination of the vapors of the elements containing appropriate dopants. Their structural and electrical properties were evaluated. Heterojunction solar cells of 1 cm^2 area with the configuration n-ITO/p-CdTe/substrate prepared by ion-beam sputtering have an AM1 efficiency of about 7%. The problems associated with this type of solar cells and possible techniques to overcome these problems are discussed. (This work was supported by the Solar Energy Research Institute.)

239 Zinc Sulfoselenide Thin Films for Photovoltaic Applications: *W.B. Leigh, K.A. Christianson*, and *B.W. Wessels*,* Dept. of Materials Science and Engineering, and Materials Research Center, Northwestern University, Evanston, IL 60201

Zinc sulfoselenide has been heteroepitaxially deposited by hydrogen vapor transport. The films grown on GaAs are single crystalline and have excellent surface morphologies. Resistivities of the as-grown material ranged from 0.1 to greater than 10^3 Ω-cm, depending upon zinc partial pressure of the growth ambient and sulfur concentration in the films. For a film composition of S = 0.07, which is nearly lattice constant matched to GaAs, a carrier concentration of 3×10^{16} cm^{-3} and electron mobility of 150 cm^2/V-sec were observed. ZnSe/GaAs heterojunctions prepared by this technique has a uniform spectral response for energies between 1.6 and 2.6 eV, and quantum efficiencies ranging from 4-7%.

240 Dust-Equivalent Series-Resistance of a Photovoltaic Concentrator: *A.K.M. Zakzouk*, College of Engineering, King Saud University, Riyadh, Saudi Arabia

The effect of dust on the electrical performance of a photovoltaic concentrator has been studied. The change of the performance parameters as a result of dust accumulation was related to the amount of dust accumulated per unit area of the concentrator surface (g/m^2) rather than the exposure time. It has been shown that the major reductions in the electrical performance parameters were observed as the dust starts to deposit onto the concentrator surface. It has been also shown that the dust accumulation on the concentrator surface is equivalent to an extra series resistance. The dust equivalent series resistance is carefully studied. It has been shown that both the short-circuit current and the cell temperature have reduced steeply with dust accumulation until about 2 g/m^2. The efficiency has reduced to about 67% and 57% of its maximum value for an incident direct normal power of 445 W/m^2 and 370 W/m^2, respectively, for dust accumulation of about 2 g/m^2 with nearly negligible reduction for further accumulation.

DIELECTRICS AND INSULATION/HIGH TEMPERATURE MATERIALS

High Temperature Adhesives

241 High Temperature Adhesives Study: *R.J. Kuhbander** and *J.R. Rhodehamel*, University of Dayton Research Institute, Dayton, OH 45469

With the development of new air-to-air missile technology, which may utilize graphite/polyimide composites as body and/or control surfaces, it was discovered there is a lack of data available on adhesive systems suitable for use in the 1000°F plus temperature range. A program was initiated to evaluate several adhesives for tensile shear at temperatures up to 1000°F. Shear properties were developed on titanium, and to a lesser degree, stainless steel adherends. The shear properties were also evaluated after exposure to high humidity. Special attention was given the cure and postcure cycles so each would be suitable for bonding to composite structures.

242 High Temperature Adhesives Based on Thermid-600-Acetylene Terminated Polyimide: *T.J. Reinhart,** Air Force Wright Aeronautical Laboratories, Systems Support Division, WPAFB OH 45433 and *R.J. Kuhbander*, University of Dayton Research Institute, Non-Metallic Material Laboratory, Dayton, OH 45469

High temperature resistant structural adhesives have been formulated from Thermid 600 acetylene terminated polyimide resin. This resin, developed by the Hughes Corporation under Air Force sponsorship, is now available from the Gulf Oil Chemical Company and the Hughes Corporation in several forms. Thermid 600 resin was formulated into structural adhesives and evaluated in bonded joints involving titanium, stainless steel, and graphite polyimide composite adherents. Surface preparations, cure and post cure conditions as well as adhesive formulations and adhesive carrier material were studied. Long-term aging at elevated temperatures and humidity effects on the strength of the bonds and on the bonded joint failure modes were determined. Adhesive formulations, adhesive tape preparation, bonded joint processing studies, and mechanical properties of bonded joints are covered in this paper.

243 Polyquinoxaline (PQ) Adhesives—An Overview of Materials and Applications: *M.G. Maximovich*, Lockheed Missiles and Space Co., Sunnyvale, CA 94086

An overview of the polymers, their synthesis, formulation, processing, and performance is given. The preparation from *bis* (*O*—diamines) and aromatic diglyoxals is discussed. Adhesive formulation, fillers, antioxidants, scrim, and carriers are evaluated and processing schemes are reviewed. Applications from early SST adhesives to current applications as ultrahigh temperature adhesives for modern aerospace programs are discussed. These materials have shown excellent adhesive performance to temperatures as high as 650°C (1200°F), and have the additional virtues of high peel strength, toughness, and environmental existence.

244 Phthalonitrile Resins for High Temperature Adhesives: *J.R. Griffith*, Naval Research Laboratory, Washington, DC 20375

Two series of phthalonitrile resins have been synthesized which are generally classed as the aliphatic and aromatic series. The former series is stable in air for at least 1000 hr at temperatures up to 240°C and the latter series is similarly stable to 280°C. These resins have the virtue of being solventless, volatile-free syrups before cure which resemble epoxy resins in a higher temperature regime.

245 High Temperature Space Film Adhesives: *A.K. St. Clair** and *T.L. St. Clair*, NASA Langley Research Center, Hampton, VA 23665

For the past five years, research has been conducted in the Materials Division at NASA Langley Research Center toward the development of high temperature adhesives for bonding polyimide film for 300°C aerospace applications. The utilization of several linear aromatic polyimide resins as adhesives for bonding polyimide film, metal foils, and metallized film are reviewed. The development of a fully imidized thermoplastic polyimide, LARC-TPI, is discussed with regard to its use as a high temperature adhesive for laminating large areas of polyimide film.

246 Inorganic Ceramic Cements, Their Properties, and Applications in Industry for High Temperature Adhesion: *J.A. Crawford*, Sauereisen Cements Co., Pittsburgh, PA 15238

By delineating their bonding mechanisms and such properties as absorption, shrinkage, and strength, these specialty ceramic cements can be evaluated for various applications. They are useful at temperatures approaching those of refractories and yet offer the corrosion protection of organics. They give the engineer a product that requires low energy to finish, yet provide versatility in forming, placement, and application. In addition to temperature resistance and corrosion resistance, these ceramic cements offer abrasion resistance, adhesion, and electrical insulating and electrical conducting properties.

247 An XPS and TEM Study of Adhesion Between Polyimide and Cr Metallurgy: *N.J. Chou,** *D.W. Dong*, and *J. Kim*, IBM T. J. Watson Research Center, Yorktown Heights, NY 10598

In the rapidly developing VLSI packaging technology, the adhesion between polyimide (PI) and wiring metallurgy is a problem of both theoretical and practical interest. We have used transmission electron microscopy (TEM) and *in situ* ESCA (XPS) measurement to characterize the interface between PI and Cr. TEM examination reveals that the interface is smooth with no interpenetration on a microscopic scale. Monitoring of binding energy change of various elements during successive monolayer deposition of Cr on a PI film in an ultrahigh vacuum system indicates that Cr combines with oxygen on the imide side chains. It is concluded that chemical bonding rather than mechanical interlocking at the interface is the major factor influencing the adhesion between PI and Cr.

248 Anodized Titanium Immersed in Hot Water: Oxide Stability and Metal Corrosion: *M. Natan** and *J. D. Venables*, Martin Marietta Laboratories, Baltimore, MD 21227-3898

Changes occurring on the surface of chromic acid-anodized Ti-6Al-4V alloy immersed in hot water were investigated with Auger electron spectroscopy (AES), SEM, and TEM. It is shown that above a threshold temperature (*ca.* 70°C), the anodic film undergoes a change from an amorphous state to anatase, a crystalline TiO_2 polymorph. Simultaneously, corrosion of the Ti substrate increases the total mass of the oxide on the surface. Crystallization does not occur in the absence of humidity. Possible oxide transformation mechanisms are discussed.

249 Characterization of Anodic Films on Titanium Using AES and STEM: *M. Natan** and *J. S. Ahearn*, Martin Marietta Laboratories, Baltimore, MD 21227-3898

Pure titantium was anodized in a chromic-acid bath at constant voltages in the range 5-40V. Characterization included investigation of the stoichiometry, morphology, and crystal structure of the oxide films. The use of Auger sputter depth profiling to investigate the mechanism of film formation is demonstrated.

250 High Temperature Stability of a Polyimide Film: *R. Ginsburg** and *J. R. Sosko*, IBM Corp., General Technology Div., Endicott, NY 13760

Polyimide (PMDA-ODA) films were analyzed by mass spectroscopy to determine their high temperature (400°C) stability. The effluents detected were predominantly the small molecules CO_2, H_2O, and CO with CO_2 in greatest abundance. A relative comparison of the evolved products and the time required for their evolution was determined. The possibility of the decomposition of an isoimide as the source of CO_2 evolution is discussed. The presence of moisture and its participation in a mechanism for hydrolysis and subsequent degradation of polyimide is also considered.

ELECTRONICS

Computer Controlled IC Processing and Monitoring

251 IBM's "QTAT" Experience: A Foundation for VLSI Manufacturing Control System Development in the 80's (FCMS): *T. Francis,** *D. Griffin*, and *P. Bhalla*, IBM East Fishkill, Hopewell Junction, NY 12533

During the 1970's, semiconductor device manufacturing at IBM's East Fishkill facility underwent fundamental change. Small-scale integration devices manufactured for inventory in large production runs was a typical format in 1970. By 1979, however, most semiconductor manufacturing was of VLSI product, in made-to-order quantities from an open part number set. Using the case study approach, this paper reviews the fundamental changes which occurred in the site's manufacturing control methodology. Operating experience with the automated QTAT facility is shown to be instrumental in establishing technical direction for the development of FCMS—Fishkill's VLSI manufacturing control system for the 80's.

252 Economic Justification for FCMS (Factory Control and Monitoring System) at IBM E. Fishkill: Yield Management: *D. Griffin,** *P. Bhalla*, and *T. Francis*, IBM East Fishkill, Hopewell Junction, NY 12533

Establishment of a firm technical direction for FCMS development led to the requirement that the project be justified economically. This paper describes in some detail the methods and mathematics of justification. It is shown that the existence of the ongoing yield management effort at IBM East Fishkill was instrumental to developing the required economic perspective Process yield improvement expected under FCMS control was established for both present and future VLSI products. It is demonstrated that FCMS leverage on future VLSI products is greater than that expected on present products. Explicit recognition is given to key "intangible" FCMS benefits as well.

253 Successful Implementation of "FCMS" at IBM E. Fishkill: A Basis for Future VLSI Manufacturing Strength: *P. Bhalla,** *T. Francis*, and *D. Griffin*, IBM East Fishkill, Hopewell Junction, NY 12533

The decision to proceed with the FCMS (Factory Control and Monitoring System) project resulted in the establishment of 7 programming teams: *(i)* Product Logistics, *(ii)* Data Base Management, *(iii)* Rework Control, *(iv)* Reports and Analysis, *(v)* N/C Data Supply, *(vi)* Equipment Utilization, *(vii)* Line Support Software Diagnostics. This paper defines the objectives of each team. Special attention is given to the architectural master plan which supports the development effort. The importance of tool control software and systems is discussed, and details of the tool control hardware are described. Finally, the performance of the first FCMS installation (hot process) is reviewed, comparing early expectations to benefits actually realized.

254 Computer Aided IC Manufacturing at Hewlett-Packard Laboratories: *M. Parikh*, Hewlett-Packard Co., Palo Alto, CA 94304

This talk will outline recent developments and anticipated challenges in computer aided manufacturing of IC's at HP's Corporate R and D Laboratories. Several computer aided control and information systems have been developed to meet the R and D requirements of quick turnaround, flexibility, and engineering feedback; these are described. A new generation of R and D "manufacturing" must have an integrated computer aided manufacturing system for particle-free automated wafer handling, scheduling, and line loading, as well as operator-independent processing and judicious feedforward control. An architecture for such a system is presented.

255 IC Fabrication Information Control via an Electronic Message System: *D. K. Brotz*, Xerox Palo Alto Research Center, Palo Alto, CA 94304

This paper describes an information control system for integrated circuit fabrication in use at the Xerox Palo Alto Research Centers. This system, named Cholla, uses electronic message system components Laurel and Grapevine to propagate IC fabrication information among independent workstations, Integrated circuit laboratory technicians and computer controlled IC processing machines use and enhance this information as they perform their fabrication tasks. Cholla is capable of directly controlling IC processing equipment, while also allowing complete manual control.

256 Digital Automation: The Slave of the Electrochemist: *P. Rony, K. Mercure, I. Malkin, and V. Guruswamy*, Dept. of Chemical Engineering, Virginia Polytechnic Institute and State University, Blacksburg, VA 24061

Advances in electrochemistry have been associated to the application of signals to an electrode in a cell and monitoring the response to the signal. Today's integrated circuit allows the electrochemist a greater degree of versatility with respect to signal monitoring and data acquisition. A simple system is presented based on a Z-89 computer controlling an interfaced single board computer (MMD-1). The MMD-1 acts as an intermediate: providing input signals to the electrochemical system, converting the output of the electrochemical system to digital form, and temporarily storing this data. The monitoring of fast transients (10^{-8} sec) is discussed.

257 The Statistical Characterization of CMOS Inverters Using Noise Margins: *M. G. Buehler** and *T. W. Griswold*, Jet Propulsion Laboratory, California Institute of Technology, Pasadena, CA 91109

CMOS-bulk inverters have been characterized based on statistical variations in the inverter gain and threshold voltage. These variations were combined to derive the inverter noise margin, which was analyzed statistically. In this effort test chips were developed, fabricated at silicon foundries, and evaluated using parametric test equipment. Special measurement and analysis procedures were used to identify invalid data and to exclude outliers from the nominal data set. A procedure was developed for estimating the number of inverters per circuit that can be fabricated with a probability of 0.5 that all inverters are within a specified noise-margin window. Results from the best wafers indicate that it is possible with current technology to obtain circuits with more than 10^6 inverters per circuit that lie within a noise-margin window as small as 1.0V.

258 Use of a Defect Monitor Test Structure for Optimizing Process Yield in VLSIC Manufacturing: *R. Stanley,** Signetics, Sunnyvale, CA 94086, *T. Hasan*, Philips Research Laboratory, Sunnyvale, Sunnyvale, CA 94086, *V. Akylas*, Signetics, Sunnyvale, CA 94086, and *E. Lee*, Philips Research Laboratory, Sunnyvale, Sunnyvale, CA 94086

A single layer device for monitoring defects in VLSI processing is described, and methods of analysis are discussed. The monitor consists of a comb of conducting material forming serpentines of spaces whose lengths form a geometrical progression. It can be tested for short inducing defects immediately after definition of the conductor, which can be metal, polysilicon, or a diffused layer. An application to the selection of the optimal polysilicon etching process is demonstrated.

259 Systematic Control of Epitaxial Deposition Processes with a Microcomputer System: *T. L. Carlson, J. E. Chambers*, and *M. E. McPherson,** Tektronix, Inc., Beaverton, OR 97077

Although silicon epitaxy is widely used throughout the semiconductor industry, it is difficult to select epitaxial deposition parameters correctly when a buried collector structure is present. Adjustments to machine settings must be made to compensate for the effects of autodoping, which are dependent on reactor characteristics, buried collector area, and doping concentration. A simple microcomputer system described here can correctly determine compensated machine settings when target thickness, target resistivity, and buried collector area are varied.

260 Monochromatic IR Reflectance Method for Thickness Measurement of Thin (1.0 μm) Epitaxial Silicon Layers: *S. P. Weeks** and *B. Senitzky* (Present address: Polytechnical Institute of New York, Farmingdale, NY 11735), Bell Laboratories, Allentown, PA 18103

A monochromatic IR reflectance method has been developed for accurate measurement of the thickness of submicron silicon epitaxial layers. The technique uses a computer-generated calibration curve of thickness *vs.* intensity based on matching calculated IR reflectance spectra to the measured spectrum of a representative sample. Subsequent measurements are performed at a fixed wavelength. The technique is fast (~2 sec/measurement), accurate (± 0.02 μm), and precise (± 0.01 μm), and is independent of variations in the carrier concentration of the substrate or buried layer.

261 Measurement and Evaluation of Registration Errors of Step-and-Repeat Photolithographic Systems: *H. S. David,* J. A. Henson,* and *J. E. Heideman,* Tektronix, Inc., Beaverton, OR 97077

Registration errors produced by step-and-repeat exposure systems can be measured to an accuracy of 1% and an repeatability of 0.002 microns using a Nichrome Stickman pattern. At each test site, an error vector can be calculated from differential resistances which are proportional to the misregistration at that site. The components of registration error, including wafer alignment and rotation, misstepping, mask rotation, and machine-to-machine distortion, can be resolved using graphical analysis. The procedure that has been developed is suitable for regular monitoring of photolithographic processes.

262 Computerized Process Control via Shewhart Control Charting Techniques: *J. J. Delgado** and *W. J. Daughton,* NCR Microelectronics, Colorado Springs, CO 80907

The Shewhart statistical control chart techniques have been translated in Fortran software code for real-time analysis and control of common semiconductor processing steps. Seven tests for process change detection are incorporated: one sigma, two sigma, three sigma, total number of runs up or down, points on one side of mean, length of longest run, and total number of runs above and below the mean. The program is capable of analyzing both variable and attribute data. The development of this program is described, and typical examples of application of this program to process control are given.

263 VLSI Yield Management in the '80's: *T. Collopy, M. Cowan, W. Freitag, M. Lowe, D. Piscitelli,* and *E. Squarzini,* IBM East Fishkill Facility, Hopewell Junction, NY 12533

Yield management is a manufacturing control system which sets targets, gives real time visibility to losses and defect levels, and resolves deltas between actuals and targets. A yield model is used to generate final test targets, create in-line targets, and help explain deviations from the plan. Test sites are used as in-line monitors, and product yield can be predicted with the model knowing the test site yield. At the IBM East Fishkill semiconductor facility, a yield management system is in place which monitors key yield detractors, sets targets based on both past experience and future improvements, and forecasts final test yield of products which are still in process. A report card system is used to monitor the "health" of the manufacturing line, help interpret the yields, and prioritize the problem areas. This system allows real-time feedback of process losses *vs.* targets, and also allows for the timely implementation of appropriate corrective actions.

264 Process Engineering Tools in a Distributed Software Environment: *V. H. Brecher* and *J. K. Siudut,** IBM Corp., E. Fishkill Facility, Hopewell Junction, NY 12533

Rapid increases in computer automated tooling have created a need for a high level software interface to the engineer responsible for Process Monitoring and Control. At IBM East Fishkill, this interface is part of the site distributed architecture for manufacturing control. The software implementation of the functional distribution, engineering/operator interface, and micro-controller communications are discussed. Examples of installed manufacturing applications, including both the benefits and implementation problems, are described.

265 Host Computer Controls Process Equipment: *U. Kaempf,* Hewlett-Packard Laboratories, Palo Alto, CA 94304

Today's IC process equipment is commonly controlled by local computers and programs. The next step toward centralized fab management and control is in interfacing such stand-alone equipment to a central, factory level host computer. As an example, this discussion presents the hardware and software configuration of a fully automated plasma etcher. Process recipes are entered and stored at the central facility and down-loaded at the request of the operator. Performance monitoring of the equipment for recording in the lot history file and the handling of alarm conditions are also discussed.

266 Computer Aided Manufacturing (CAM) for Semiconductor Processing and Monitoring: *D. L. Cole** and *I. Smethurst,* Tektronix Inc., Beaverton, OR 97077

The role of computer aided manufacturing (CAM) systems in upgrading the operation of process oriented manufacturing is discussed. The concept of product flows is applied to the semiconductor business and forms a frame work to support manufacturing, materials management, and engineering. CAM consists of tracking, scheduling, and planning systems. Each module stands alone and is driven from a central bill of material. Electrical data are collected as part of the tracking system to aid in process and design improvements.

267 Computer Model of Laser Target Link Explosion in Redundant Memories: *J. D. Chlipala,** Bell Laboratories, Allentown, PA 18103 and *L. M. Scarfone,* Dept. of Physics, University of Vermont, Burlington, VT 05405

A computer-based model of the laser-induced temperature evolution and explosion of targets typically encountered in semiconductor memory redundancy schemes has been developed. This model has been used to investigate two controversies over choice of *(i)* short *vs.* long laser pulse and *(ii)* infrared *vs.* green laser wavelength. The role such a model plays in the development of this yield improvement technique is discussed. The effects due to horizontal and vertical structures, silicon doping levels, and laser-materials interactions are considered.

268 APL Application for Plating Process Control of IC Substrates: *S. A. McGarry,* IBM East Fishkill Facility, Hopewell Junction, NY 12533

The design and implementation of a software system to control rework on Multilayer Ceramic (MLC) integrated circuit (IC) substrates during metal plating operations within manufacturing is described. A programming language (APL) was chosen because of its versatility, responsiveness, and availability at East Fishkill. This APL system has been successfully tracking product for all levels of engineering and manufacturing for over two years. It has helped improve yields, control work in process (WIP), and enforce the logistics needed to control the process flow of the product during manufacturing.

ELECTRONICS

Defects in Silicon

269 Trends in Defect and Impurity Control for Fine Line Processing: *G. A. Rozgonyi,* North Carolina State University, Raleigh, N.C. 27650, and Microelectronics Center of North Carolina, Research Triangle Park, North Carolina 27709

It is generally recognized that manufacturing processes which permit adequate control of electronic charge in VLSI and VHSIC devices demand extraordinary control over the introduction and motion of dopants, the elimination of impurities, and the nucleation of extended defects. As the industry approaches widespread introduction of devices with design rules of 1 μm or less, fine line processing requirements are leading to reduced temperature and shorter time thermal treatments, as well as novel metallization, doping, and oxidation schemes. Of particular importance in understanding these processes, and the principle thrusts of this paper, are *(i)* the chemical purity and structural integrity of silicon interfaces during annealing, siliciding, oxidation, etc., and *(ii)* the role of point defects in influencing dopant diffusion, impurity precipitation, and gettering phenomena.

270 Silicon Defects and Their Effect on Integrated Circuits: *J. H. Matlock,* UTC/Mostek, Carrollton, TX 75006

It is becoming increasingly well recognized that for state-of-the-art integrated circuits one must tailor the exact specification of the polished silicon wafer to the particular device process to avoid detrimental effects of silicon defects and optimize overall device performance. The impact on defect levels and device behavior of controlled oxygen, oxygen precipitation, carbon, surface chemistry, and metallic impurities is discussed. Both intrinsic and extrinsic gettering methods are covered. Sensitivities are shown to the particular thermal cycles involved, as well as process cleaning cycles, chip geometry sizes, and other fabrication variables.

271 Oxygen Out-Diffusion Model for Denuded Zone Formation in Czochralski-Grown Silicon with High Interstitial Oxygen Content: *J. Andrews,* Bell Laboratories, Murray Hill, NJ 07974

Recently published data on the solubility and diffusivity of interstitial oxygen in Czochralski-grown silicon has been used to develop a simple out-diffusion model for denuded zone formation during thermal oxidation. Comparison with experimental observations on samples with high $[O_i]_0$, exposed to dry oxidation at 1100°C for various times up to 8 hr, reveals that SiO_2 precipitation occurs when the supersaturation ratio exceeds 4. The model implies an optimum denuding temperature near 1100°C for an oxidation time of 4 hr.

272 Gettering of P+ (100) Si Substrates for Epitaxial Growth: *W. Dyson,* L. Hellwig, J. Moody,* and *J. A. Rossi,* Monsanto Co., St. Peters, MO 63376

To produce substrates suitable for VLSI device fabrication, gettering techniques are often used to minimize defect formation. In this work, the precipitation of oxygen in P+ (100) substrates has been investigated for different oxygen concentrations and doping levels. We find that by proper thermal treatments, it is possible to produce substrates for epitaxy with the desired characteristics of a denuded zone and precipitated interior. In addition, effects of various back-side gettering techniques on denuded zone formation and precipitate density in these wafers have been investigated for the same oxygen concentrations and doping levels; we find the back-side treatment can have a major effect on both precipitate density and denuded zone depth. We also discuss the efficiency of the combined intrinsic and extrinsic gettering techniques, which has been evaluated by measuring the resultant epitaxial defect density.

273 Three-Step Anneals and Oxygen Precipitation in High Carbon CZ Silicon: *C. Y. Kung,* L. Forbes,* and *J. D. Peng,* Fairchild Semiconductor, Silicon Materials Div., Healdsburg, CA 95448

Two-step (low-high) and three-step (high-low-high) annealing experiments have been conducted on high carbon CZ silicon crystals to study the role of carbon in oxygen precipitation. Though a consistent carbon reduction has been detected with the two-step annealing, after three-step annealing no correlation between the carbon reduction and oxygen precipitation can be established. Apparently, the first high temperature anneal has dissolved the grown-in defects which are responsible for the oxygen precipitation at low

temperature. Microdefect features as delineated by Wright etch on cross-sectional samples are shown, in one case a two-step anneal results in 100% stacking faults, whereas a similar three-step anneal results in dislocation etch pits. An abnormal oxygen reduction behavior observed for both annealing sequences is discussed.

274 The Homogenization of Microdefects in the Bulk of Silicon Wafers by a 3-Step Thermal Heat-Treatment: *J. O. Borland*, National Semiconductor, Santa Clara, CA 95051

The high temperature heat-treatment in a 3-step thermal anneal cycle was observed to homogenize the microdefect generation mechanism in silicon wafers and reduce previous low temperature thermal history effects. Minority carrier lifetime measured by the microwave τ technique showed radial τ variations as low as 0.05 μsec reflecting uniform bulk crystallinity. By tayloring the thermal heat-treatments, control of the intrinsic material properties and microdefect generation in silicon wafers have been achieved.

275 Origins of Oxidation-Induced Stacking Faults in N-Type (100)-Oriented Silicon Wafers: *D. Cheng* and *S. Hahn*,* Siltec Corp., Mountain View, CA 94043

The origins of oxidation-induced stacking faults (OISF) were investigated in N-type (100) wafers grown by three phase a-c, d-c, and magnetic CZ crystal pullers. The OISF's found around the center of the wafer appear to be crystal-growth related. High OISF's near the edge of the wafer (R/8) appear to be generated during wafer processing. To reduce OISF density to a level below 300 cm^{-2}, both crystal growing and wafer processing techniques should be addressed.

276 Generation Lifetime Improvement Through Intrinsic Gettering in n-Type <100> Si Wafers: *E. M. Murray*,* Hewlett-Packard Laboratories, Palo Alto, CA 94304, *M. P. Scott*, Hewlett-Packard Laboratories, Palo Alto, CA 94304, and *S. Hahn*, Siltec Corp., Mountain View, CA 94043

Intrinsic gettering has been shown to promote greater generation lifetime improvement than back-side damage gettering in n-type <100> wafers. Generation lifetime maps of the wafers showed a significant improvement with a two-stage heat-treatment involving an 1100°C anneal followed by a 700°C anneal in nitrogen. Similar wafers with laser and mechanical back-side damage treatments showed no noticeable lifetime improvement. X-ray topography was used to correlate the generation lifetime with internal oxygen precipitates and oxidation-induced stacking faults.

277 Oxygen Precipitation, Denuded Zones, and Intrinsic Gettering Effects on Generation Lifetimes for (100) CZ Silicon: *L. Forbes*,* *C. Y. Kung*, and *J. D. Peng*, Fairchild Semiconductor, Silicon Materials Div., Healdsburg, CA 95448

Oxygen precipitation in (100) CZ silicon for MOS structures has been investigated and characterized following single step 930°-1050°C heat-treatments. A strong correlation has been found to starting interstitial oxygen concentration. It is demonstrated that oxygen precipitation and intrinsic gettering is in itself not sufficient to insure a long generation lifetime and that in the worst case excessive precipitation can result in a degradation of generation lifetime. A model for factors controlling the generation lifetime is presented and influence on MOS devices discussed.

278 Activation of the Intrinsic Gettering Mechanism by the Precipitation and Growth of Oxygen Related Precipitates in CZ-Grown Silicon Wafers: *J. O. Borland*, National Semiconductor, Santa Clara, CA 95051

The activation of the intrinsic gettering mechanism in a 3-step preprocessing thermal heat-treatment was monitored by minority carrier lifetime measurements on MOS fabricated capacitors. Changes in the interstitial oxygen concentration and microdefect generation in the bulk of the wafers were also used to monitor the degree of oxygen precipitation. For CZ-grown material, the third step of the heat-treatment cycle was responsible for inducing oxygen precipitation and growth and it was this step which activates the intrinsic gettering mechanism. A lifetime as long as 11 μsec was measured, which was an improvement by over three orders of magnitude.

279 Dark Current Dependence on Denuded Zone Depth for Intrinsic Gettering of Silicon: *D. N. Nichols*, Eastman Kodak Co., Research Laboratories, Rochester, NY 14650

The transient response of pulsed MOS capacitors is used to examine the dark current dependence on denuded zone depth for intrinsically gettered silicon wafers. A monotonic decrease in dark current for increasing denuded zone depth is found for depths up to 80 μm. The experimental results are compared with a one-dimensional model for a wafer with a large minority carrier diffusion length in the denuded zone and a short diffusion length in the defect zone.

280 Point Defect Complexing in Silicon: *E. Sirtl*, Heliotronic GmbH., Burghausen, Germany

A short survey of our fundamental knowledge on intrinsic and extrinsic point defects in silicon is used as an introduction to the deeper understanding of defect kinetics in the silicon crystal. Under these aspects, the highlights of the Munich Satellite Symposium to ESSDERC on "Aggregation Phenomena of Point Defects in Silicon" is discussed.

281 A Determination of Vacancy and Self-interstitial Contributions to Dopant and Self-Diffusivities in Silicon: *T. Y. Tan*,* IBM General Technology Div., Hopewell Junction, NY 12533, *F. Morehead*, IBM T. J. Watson Research Center, Yorktown Heights, NY 10598, and *U. Gosele*, Max Planck Institut fur Metallforsch, Stuttgart, Germany

Recent experimental and theoretical progress allowed a determination of the contributions of vacancies and self-interstitials to Si self-diffusion and to dopant diffusions in Si. The estimates arrived at are based on analysis of Au diffusion in Si, and on dopant diffusion in Si under oxidation. It is shown that vacancies contribute more to the Si self-diffusivity below about 1000°C while less above this temperature. Complicating factors involved in this determination are also discussed.

282 Diffusion of Impurities in Silicon and Defect Reactions: *G. M. Bisio*,* *S. De Pasquale*, and *P. G. Graglia*, Istituto di elettrotecnica, Università di Genova, 16145 Genova, Italy

The diffusion of gold in silicon is analyzed considering that the interchange between substitutional and interstitial gold atoms involves both vacancies and silicon self-interstitials. This model leads to a set of four diffusion equations coupled through the generation-recombination terms. Local equilibrium among the four defect species is assumed, thus reducing the problem to a couple of nonlinear diffusion equations, solved numerically under different boundary conditions. The model points out that the weight of the two competing mechanisms varies during diffusion depending on the relative concentration of vacancies and self-interstitials. Application of the model to the enhanced diffusion in the oxidation of silicon is also considered.

283 Bore Diffusion in Heavily n-Doped Silicon: *D. Tsoukalas* and *P. Chenevier*,* Laboratoire de Physique des Composants à Semiconducteurs, ERA CNRS No. 659, ENSERG, 23, 38031 Grenoble Cedex, France

The commonly used expressions for the bore diffusivity are unsatisfactory in the case of heavily n-doped silicon. An expression of diffusivity based on thermodynamic considerations is set up, taking account not only of the various charges of the vacancies but also of the correlation factors. We substitute in this expression the theoretical and experimental values of various energies. A very good agreement with the entire set of existing experimental results is obtained. It appears that diffusion is mainly controlled by the positively ionized vacancies, and at the same time it is confirmed that E_v^+ is 0.35 eV above the valence band.

284 Kinetics of Silicon Interstitial Defects from Oxidation Stacking Fault Observations: *K. Taniguchi** and *D. A. Antoniadis*, Massachusetts Institute of Technology, Cambridge, MA 02139

The growth of oxidation-induced stacking faults (OSF) in silicon are studied by using back surface oxidation of wafers. An analysis of the OSF growth data under the assumption of diffusion-controlled growth shows that the diffusion coefficient of silicon self-interstitials is of the order of 10^{-9} to 10^{-8} cm^2/sec in the range of 1100°-1200°C. Equilibrium concentration and surface reaction velocity of self-interstitials at the Si/SiO_2 interface are also obtained through simulation of the OSF growth. Previously observed depth dependence of oxidation-enhanced diffusion (OED) and the discrepancy between oxidation-induced excess interstitial concentrations derived from OSF growth and OED are explained by the low diffusivity of self-interstitials.

285 Effect of Phosphorus Diffusion on Oxidation-Induced Stacking Faults: *S. Matsumoto*,* Dept. of Electrical Engineering, Keio University, Yokohama, Japan, and *T. Niimi*, Tokai University, Hiratsuka, Japan

Correlation between the enhancement of phosphorus diffusion and the shrinkage of oxidation-induced stacking faults (OSF) has been investigated. Density and length-controlled OSF was introduced by a two step method. In order to avoid the stress and redox reaction effects of doped oxide source, phosphorus was introduced in the bulk by a two step annealing. Depth profiles of density and length of OSF were obtained. OSF disappears in the phosphorus-diffused layer.

286 Annealing of Interstitial Loops in As-Implanted Si: *N. R. Wu*,* *P. Ling*, *D. K. Sadana*, and *J. Washburn*, Lawrence Berkeley Laboratory, Materials and Molecular Research Div., Berkeley, CA 94720

Interstitials loops have been found to form after annealing of As-implanted (100) Si with screen oxide thicknesses in the range 30-775Å. The effect of annealing ambient (N_2, O_2 or $N_2 + O_2$) on the coarsening and shrinkage of the loops has been studied. The role of surface-oxide growth and implanted As on the annealing behavior of the loops is discussed.

287 Carbon Gettering in Silicon: *W. E. Bailey*, Texas Instruments Inc., Lubbock, TX 79408, and *R. A. Bowling* and *K. E. Bean*, Texas Instruments Inc., Dallas, TX 75265

The control of carbon and oxygen is of great importance in today's silicon materials and device processing, and will become a critical parameter in the immediate future for VLSI device processing. Considerable technology and some understanding are available today in the control of oxygen in silicon material through processing; however, there is little technology and even less understanding of carbon control. We have determined that carbon can be

gettered to damage sites such as dislocations and/or stacking faults, thus creating a carbon denuded zone in epitaxial silicon.

288 Oxygen Aggregation and Diffusivity in Silicon: *M. Stavola*, Bell Laboratories, Murray Hill, NJ 07974

The understanding of oxygen precipitation has become of great interest in silicon processing. Several experiments that provide greater understanding of oxygen aggregation at low temperatures ($T \leq 900°C$) have been reported recently. These include observation of a fast diffusion process at $T \sim 400°C$, characterization of rod-like oxygen precipitates that form at $T \sim 650°C$, and several studies of thermal donor formation. These are reviewed and a framework for understanding low temperature oxygen aggregation phenomena is presented.

289 Oxygen in Silicon: *W. C. O'Mara*, Rose Associates, Los Altos, CA 94022

The infrared absorption spectrum of oxygen in silicon consists of peaks at 9 and 19 μm at room temperature. An analysis of these peaks and those which appear at low temperatures indicates that each peak is due to oxygen in a different lattice site. The absorption at 19 μm is not due to a normal mode vibration of "interstitial" oxygen, but is related to carbon and boron peaks. The site symmetry for this second oxygen species must be the same as for carbon and boron.

290 Photoluminescence Study of Oxygen Related Donors in Silicon: *R. W. Shaw** and *R. A. Craven*, Monsanto Co., St. Louis, MO 63167

Photoluminescence measurements at 4.2 K of donor bound excitons are coupled with measurements of resistivity by four point probe and interstitial oxygen measurements by FTIR to analyze ≃450C donor states, and the more recently discovered ≥650C donor states in boron doped silicon. Photoluminescence peaks which are detectable near 1.14 μm after annealing at these different temperatures are broad, but distinct. The evolution of these signals is traced through a matrix of thermal processing. New thermal donors are strongly correlated with oxygen precipitation, although there is some evidence for boron complexing during the donor formation. Practical issues of avoidance and elimination of these donors are addressed.

291 Local Phonon Mode Calculations for Point Defects in Si: *R. J. Hauenstein,** *R. M. Feenstra*, and *T. C. McGill*, Dept. of Applied Physics, California Institute of Technology, Pasadena, CA 91125

Localized and resonant phonon modes have been calculated using the Green's function technique for substitutional and interstitial defects in Si. Energies and symmetries are presented as a function of the defect-bulk interaction for Fe and Cu defect modes. In both cases, the calculations predict a defect-mass-dependent, low energy T_2 mode. The relation to photoluminescence data is discussed. (Supported in part by Office of Naval Research under Contract No. N00014-81-C-0285.)

292 Isotope Shifts of the P,Q,R Lines in Indium-Doped Si: *T. E. Schlesinger** and *T. C. McGill*, Dept. of Applied Physics, California Institute of Technology, Pasadena, CA 91125

We have measured the isotopic shifts of lines identified as local vibrational modes of Fe in Si. Two sets of lines were studied, the P,Q,R luminescence lines in Si:In ascribed to (Fe, In) pairs, and lines at about 1.7 μm attributed to an isolated Fe complex. Both sets of lines have what appears to be a 9 meV phonon replica. No shift is observed in any of these phonon modes to less than 0.03 meV while theory predicts shifts of at least 0.15 meV. (Supported in part by Office of Naval Research Contract No. N00014-81-C-0285.)

293 Bulk Properties Improvement of CZ Silicon from Large Melts by Thermal Convective Flow Control: *G. Fiegl*, Siltec Corporation, Instrument Div., Menlo Park, CA 94025

The continued pressure for decreasing crystal production cost has led to a steady increase of melt size and crystal diameter. The problem of thermal convective flow in large melts is more severe and has a detrimental effect on the resulting material characteristics. In addition, an increased amount of oxygen from the melt contributes to further degradation of silicon bulk properties. Temperature oscillations caused by convective instability in the melt can be sufficiently controlled by placing the silicon melt into a homogeneous magnetic field. Implications of this effect on large production systems are discussed and the resulting material characteristics examined.

294 Defect Control for Silicon Epitaxial Processes Using Silane, Dichlorosilane, and Silicon Tetrachloride: *H.-R. Chang*, General Electric Corporate Research & Development, Schenectady, NY 12301

Better epitaxial films with low defect density are the key in the fabrication of high voltage devices and integrated circuits. This paper presents the results of a study of the defects in silicon epitaxial films grown by using silane, dichlorosilane, and silicon tetrachloride. The effects of pre-epitaxy growth conditions, growth temperature, and flow rates of source gases on the quality of silicon epitaxy have been examined. This study includes the (111), (110), and (100) orientations. It was found that in the SiH_4 system, an HCl etch is essential to obtain a good epitaxial layer with low defect density, but this is not the case for SiH_2Cl_2 and $SiCl_4$. For SiH_2Cl_2 and $SiCl_4$, preheating the substrates at higher temperatures than the deposition temperature before epitaxy growth gives very few defects. Using SiH_4 as the source gas, the defect density is higher than those observed in SiH_2Cl_2 and $SiCl_4$ systems. Epitaxial layers grown by using SiH_2Cl_2 contain fewer defects than $SiCl_4$. Decreasing flow rate increases perfection, but the effect of temperature is complex.

295 Defect Reduction by Dichlorosilane Epitaxial Growth: *S. B. Kulkarni*, IBM East Fishkill Facility, Hopewell Junction, NY 12533

Application of low pressure and temperature epitaxial growth process to advanced bipolar transistors is found beneficial to their performance and yield. The effect of growth parameters, such as temperature and chemical source, on the transistor chain yields is evaluated. The defect densities are reduced by using dichlorosilane as a source, as compared to silicon tetrachloride under otherwise identical growth conditions. Low level junction leakages are found to improve also. Results are analyzed using the model involving surface growth mechanisms.

296 Precise and Rapid Measurement of Oxygen and Carbon Concentrations in Silicon: *K. Krishnan*, Digilab, Div. of Bio-Rad Laboratories, Cambridge, MA 02139

It is important to know the accurate concentrations of interstitial oxygen and substitutional carbon in silicon. Normally, spectra taken of high refractive index materials suffer from multiple reflections inside the sample, and any precise routine should be able to correct for this effect regardless of the condition of the wafer, whether it be double-side polished or back-side damaged to a different degree. A technique for performing this measurement and results for double-and single-side polished silicon wafers of varying thicknesses is presented. Also, a novel technique for more precise determination of substitutional carbon is described.

297 Characterization of Back-Surface Damaged Wafers by Fourier Transform Infrared Spectroscopy: *A. Baghdadi*, Semiconductor Materials and Processes Div., National Bureau of Standards, Washington, DC 20234

In order to account properly for multiple passes of the infrared beam in back-surface damaged wafers in infrared spectrometers, the effective reflectivity of the back surface must be measured. Two methods for accomplishing this are evaluated in a comparative study. The first method is based upon an analysis of the spectrum and the second method is based upon an analysis of the interferogram.

298 Reproducibility of Oxygen and Carbon Determinations in Silicon from IR Absorbance Measurements: *W. M. Bullis.** Fairchild Advanced Research and Development Laboratory, Palo Alto, CA 94304, and *W. C. O'Mara*, Rose Associates, Los Altos, CA 94022

Today's requirements for defect control in silicon wafers have led to a desire for tighter tolerances in determination of oxygen and carbon concentrations. Numerous factors affect the reproducibility and accuracy of the most convenient and widely used method for such determinations, infrared absorption. Many measurement problems arise from, or are exacerbated by, the fact that silicon has a high index of refraction. These problems are assessed for their relative importance to measurement reproducibility. Suggestions are made for procedures to establish instrument performance and for areas where improved techniques are needed if the desired reproducibility is to be achieved.

299 The Effect of Striations on Compositional Analysis: *R. A. Forman,** *M. I. Bell*, *S. Mayo*, and *A. H. Kahn*, National Bureau of Standards, Washington, DC 20234

Semiconductor crystals typically contain compositional striations produced by periodic fluctuations during growth. Striations may lead to systematic errors in compositional analysis by optical or surface techniques. A model appropriate to such measurements is presented, and estimates of probable errors are given; the errors in optical measurement of oxygen and carbon content in silicon are often significant. The implications of these results for studies of intrinsic gettering are discussed.

300 Conversion Coefficient for IR Measurement of Oxygen in Si: *T. Iizuka*, JEIDA, Kikaishinkokaikan, Shibakoen, 3-5-8, Minatoku, Tokyo, Japan

Seventy CZ dislocation free Si wafers with the thickness of 2.0, 1.0, and 0.5 mm containing wide range of oxygen contents were prepared by 5 organizations, Musashino Electrocommunication Laboratory, and 4 Si venders. IR absorption coefficient of the 1 mm thickness wafers were repeatedly analyzed by charged particle activation with ^{16}O (^3He p) ^{18}F reaction. The result is: Oxygen atoms/cm^3 = $(3.03 \pm 0.02) \times 10^{17}\alpha$.

301 Improved Analysis Procedures for Deep-Level Measurements by Transient Capacitance: *W. E. Phillips,** *W. R. Thurber*, and *J. R. Lowney*, National Bureau of Standards, Semiconductor Materials and Processes Div., Washington, DC 20234

The procedures reported here provide a way to analyze data from nonexponential transient capacitance measurements made under conditions such that *(i)* the traps are charged in only a part of the depletion layer or *(ii)* the trap density is not small compared with the net shallow dopant density. This analysis requires C^{-2} *vs.* V data to be linear over the voltage range used, which may be a small range at low temperatures because of the compensation effect of traps. Computer simulations of C^{-2} *vs.* V plots are given for various ratios of trap and dopant densities at several temperatures and show

ranges which are sufficiently linear, but which have a trap-density-dependent slope. These effects are illustrated by experimental C^{-2} *vs.* V, isothermal transient capacitance (ITCAP), and DLTS measurements for a wide range of densities of platinum in p^+n and n^+p silicon diodes.

302 The Characterization of Heteroepitaxial Silicon by the Surface Photovoltage Technique: Improved Properties Resulting from Implant-Damage and Solid-State Regrowth: *J. Lagowski,** Massachusetts Institute of Technology, Cambridge, MA 02139, and *L. Jastrzebski, M. T. Duffy,* and *G. W. Cullen,* RCA Laboratories, Princeton, NJ 08540

Electronic properties of ion-implanted and recrystallized silicon-on-sapphire film were studied by surface photovoltage as a function of implantation dose (varied from 10^{13} to 10^{16} cm^{-2}). It has been found that all essential characteristics of SOS films undergo a pronounced improvement as a result of high dose ($4\text{-}8 \times 10^{15}$ cm^{-2}) implantation with Si^{++} ions followed by a brief annealing (4 hr at 600°C). The most essential improvement has been found with respect to reduction (about two orders of magnitude) in deep level concentration situated at the middle of the energy gap and a significant increase in the minority carrier lifetime.

303 The Effects of Pressure, Temperature, and Time on the Annealing of Ionizing Radiation Induced Insulator Damage in N-Channel IGFET's: *A. Reisman,** Microelectronics Center of North Carolina, Research Triangle Park, NC 27709 and *C. J. Merz,* IBM T.J. Watson Research Center, Yorktown Heights, NY 10598

The annealing of MOSFET gate insulator process induced ionizing radiation damage in hydrogen containing ambient atmospheres has been studied as a function of pressure, temperature, and time. The pressure range examined was 1-50 atm. The temperature range was 300°-450°C, and times ranged from several minutes to 14 hr. The initial and residual damage was assessed using hot electron injection, coupled with I-V measurements. It was found that 50 atmosphere treatments in 10% H_2-90% Ar mixtures at 400°C for 30 min reduce charged and neutral damage centers to acceptable design values.

304 Silicon Microdefects and Contamination Control in MOS Device Processing: *J. R. Carruthers,* Hewlett-Packard Laboratories, Palo Alto, CA 94304

Metallic contaminants, introduced inadvertently during MOS device processing, contribute to charge leakage as either dissolved constituents with deep levels close to the center of the gap or as metallic clusters or microprecipitates in the device space charge regions. The gettering of these contaminants by microdefects is a poorly understood phenomenon, because the diffusion and precipitation behavior of various fast-diffusing metallic contaminants varies widely. In addition, the gettering effectiveness of various types of dislocation structures seems to show large differences. Based on currently available information, strategies for measuring and managing contamination gettering are reviewed.

305 Iron Contamination in Silicon Processing: *K. G. Barraclough,* R.S.R.E.(M), Great Malvern, Worcs., England, and *P. J. Ward,* Plessey Research (Caswell) Ltd., Allen Clark Research Centre, Caswell, Towcester, Northants, England NN12 8BT

Iron contamination has been identified as a yield hazard in bipolar processing (1). Atomic absorption analysis has demonstrated sources of contamination, both in starting material and during processing. Studies of polycrystal, crystals, and melt residues have confirmed negligible solid-liquid segregation. The longitudinal and radial iron distributions in crystals indicate vapor phase transport from stainless steel furnace components. Contamination by sputtering within ion implanters has been quantified as a function of machine type, implant species, and cassette design.

1. P. J. Ward, *This Journal,* **129,** 2573 (1982).

306 Prismatic Punching of Dislocations from $NiSi_2$ Precipitates in Epitaxial Si: *P. D. Augustus,* Plessey Research (Caswell) Ltd., Allen Clark Research Centre, Caswell, Towcester, Northants, England NN12 8EQ

Transmission electron microscopy has been used to show that Ni from the substrate will precipitate at the surface of an epitaxial layer. Octohedral $NiSi_2$ precipitates, bounded by {111} faces and <110> edges occur. They fit coherently into the Si lattice, except that they are twinned with respect to the Si. The small misfit between the two lattices is responsible for the generation of rhombohedral shaped prismatic dislocation loops which glide along <110> directions.

307 Saucer Pit Defects in Silicon: *C. W. Pearce** and *V. C. Kannon,* Western Electric, Allentown, PA 18103

Small precipitates of various species are responsible for the saucer-pit etch features characteristic of oxidized wafers when preferentially etched. These defects have received little attention compared to defects such as oxidation-induced stacking faults, etc. This paper discusses the kinetics of formation of these defects in an oxidizing ambient and present TEM observations as to their size and composition. Additional data are presented on the influence these defects have on MOSFET and bipolar transistors. Part of the presentation reviews prior studies on saucer pit defects.

308 Survey of Microdefects on the Surface of Oxidized Silicon Wafers: *G. Keefe-Fraundorf* and *R. A. Craven,* Monsanto Co., St. Louis, MO 63167

Transmission electron microscopy was used to catalog surface microdefects responsible for S-pits in polished silicon wafers receiving an 1100°C steam oxidation. On P-type <111> wafers, small (≤ 0.1 μm) defects were observed. Most of these defects are irregularly shaped, but approximately one of these defects per thousand was a small stacking fault. Defects on slices intentionally contaminated with Ni, Cr, and Fe were compared with normally processed wafers. Based on the relative abundance of the small stacking faults, we propose that the stacking faults, not the irregular inclusions, turn into etchable stacking faults visible after multiple oxidation. N-type <111> wafers were also examined and contained, in addition to these irregular inclusions, colonies of small precipitate defects bounded by irregular dislocation loops.

309 Thickness Dependences of Dielectric Breakdown Failure of Thermal SiO_2 Films: *K. Taniguchi,** *K. Yamabe,* and *Y. Matsushita,* Toshiba Corp., R and D Center, IC Laboratory, Kawasaki-city, Kanagawa, 210, Japan

Thickness dependences of dielectric breakdown (DB) failure fractions of SiO_2 thermally grown at 1000°C in dry O_2 are studied. Oxide DB fractions below 8 MV/cm of Si wafers, with surface contaminations, decrease monotonically with oxide thickness as described in many papers. With controlled clean surface, however, thickness dependences of DB have minimum values around 150Å and maximum values around 400Å. It is considered that surface contamination prior to gate oxidations and microdefects in Si substrates are two main origins of DB failures, and, especially, oxide defects due to the latter are closely related to time dependent dielectric breakdown.

310 The Microstructure of Polysilicon Backsurface Gettering: *W. T. Stacy, K. N. Ritz, J. G. de Groot, M. C. Arst,* and *M. H. Norcott,* Philips Research Laboratories Sunnyvale, Signetics Corp., Sunnyvale, CA 94086

We have used TEM and x-ray diffraction to characterize the lattice disorder produced by a polysilicon layer on a wafer backsurface. Three general features have been observed: *(i)* Localized regions of stress are generated at the wafer backsurface; recent results show that backsurface roughness is part of the stress generation mechanism. *(ii)* Heat-treatments induce recrystallization in which grains which are coherent with the substrate grow at the expense of others. *(iii)* Dislocations and stacking faults develop in the wafer backsurface during processing and remain even when the polysilicon has been removed.

311 Gettering of Gold in Silicon Wafers Using Various Back-Side Gettering Techniques: *D. E. Hill,* Monsanto Co., St. Louis, MO 63167

Neutron activation analyses have been carried out on externally gettered silicon wafers which have been purposely gold doped by diffusion. Measurements of gold content before and after removal of the gettering layer are used to determine the degree of gettering. After an 1150°C heat-treatment, phosphorus diffused and polysilicon gettered layers have gold concentrations more than 10 times higher than that observed in the rest of the wafer. No similar increase in gold concentration on the gettered wafer back was detectable for mechanically back-side damaged or laser back-side damaged wafers.

312 Internal Gettering in Bipolar Process. I. Effect on Circuit Performance: *L. Jastrzebski** and *R. Soydan,* RCA Laboratories, Princeton, NJ 08540, and *B. Goldsmith,* RCA Solid State Division, Findlay, OH 45840

The effect of internal gettering on circuit performance has been studied for I^2L and linear logic bipolar circuits. The gettering has been introduced by controlled precipitation of oxygen in silicon wafers during processing, and its effect has been measured as reduction of circuit leakage current which has been reflected in yield improvement. The efficiency of internal gettering has been found to be a strong function of: the amount of precipitated oxygen and the morphology of precipitates, the type of precipitates and their geometrical distribution. It has also been found that the same factors affect mechanical strength (warpage) of silicon wafers.

313 Internal Gettering in Bipolar Process. II. Oxygen Precipitation Kinetics: *R. Soydan* and *L. Jastrzebski,** RCA Laboratories, Princeton, NJ 08540, and *B. Goldsmith,* RCA Solid State Division, Findlay, OH 45840

The efficiency of internal gettering is controlled by the amount of precipitated oxygen and the type of oxygen precipitates. Therefore, the oxygen precipitation kinetics during bipolar processing used to make I^2L and linear logic circuits has been investigated. Virgin wafers with various concentrations of oxygen in interstitial and noninterstitial sites, carbon concentrations, rates of oxygen precipitation, preheat-treatments, and commercial sources have been studied. It has been found that the oxygen precipitation kinetics is not only controlled by the concentration of interstitial oxygen in as-grown wafers, but also by additional factors which are discussed. For instance, similar amounts of precipitated oxygen have been observed in wafers in which the initial interstitial oxygen concentration differs by about 10 ppm. Carbon, within the limits commonly present, appears to play a minor role in the oxygen precipitation kinetics.

314 Sources of Emitter-Collector Shorts in Bipolar Transistors: *M. E. Lunnon,** *D. A. Allison,* and *W. T. Stacy,* Philips Research Laboratories Sunnyvale, Signetics Corp., Sunnyvale, CA 94086

Results are shown of emitter-collector shorts in a transistor array fabricated by a triple diffusion process. Anodic mapping combined with transmission electron microscopy reveals two distinct defect structures. Defective emitter regions contain dislocation arrays resembling phosphorus induced misfit dislocations. These are often connected by dislocations or stacking faults to dislocation loop-precipitate, defect colonies in the base regions. A model for the formation of these structures presented based on the presence of copper contamination.

315 Defect Induced Leakage from Bipolar Transistor Isolation Processing: *D. C. Ahlgren,* A. C. Domenicucci, M. R. Poponiak,* and *S. R. Mader,* IBM, General Technology Division, Hopewell, Junction, NY 12533

The impact of several bipolar transistor isolation process steps has been studied by measurement of transistor chain yields. Defect densities measured in these chains show a 40% reduction in defects by omitting p+ subisolation, and a reduction by a factor of five, if both p+ subisolation and ROI are eliminated. Individual piped transistors causing these chain fails are isolated, and physical analysis is done to characterize defect morphology.

316 Defect Formation for Ion Implantation: *S. Prussin,* D. I. Margolese,* and *R. N. Tauber,* TRW Electronics Systems Group, Redondo Beach, CA 90278

A series of silicon wafers was implanted with increasing As fluences under conditions of good and poor thermal sinking at constant beam currents. For implantation under ineffective thermal sinking conditions the amorphous/crystalline interface first moves in from the surface and then as the wafer temperature rises retreats back to the surface exposing the regrown crystalline layer to implantation damage. This dynamic annealing also contributes to defect generation by causing submerged amorphous layers to form at higher implant energies.

317 Understanding and Control of Residual Defects Generated by Implanted High Dose As^+ Bipolar Subcollectors: *D. Hagmann,* IBM Deutschland GmbH, 7030 Boeblingen, Germany

Minor variations of dose, target temperature, surface treatment, and high temperature anneals (drive in and reox) of bipolar high dose implanted As^+ subcollectors may introduce residual defects with detrimental impact on device yield. These dependencies are given and discussed. Defect densities are presented for various process combinations measured on test wafers after subcollector reoxidation and evaluated from yields of transistor chains.

318 Electrical Properties of Silicon Implanted with 11 MeV Arsenic: *P. F. Byrne,* N. W. Cheung,* and *D. K. Sadana,* Dept. of Electrical Engineering and Computer Sciences, University of California, Berkeley, CA 94720

Implantations of arsenic at 11 MeV have been performed into silicon (100) substrates. The buried arsenic layer centered at 4.4 microns has been used to fabricate p-n diodes. Reverse bias currents for the upper junction and the lower junction have been measured and correlated with cross-sectional electron micrographs of the residual damage. Large area diodes (100 μm^2) show breakdown voltages of 15V. From the breakdown characteristics estimations of the generation rate in the junctions have been obtained.

319 Localized Lifetime Control by Argon Ion Implantation into Silicon: *A. Mogro-Campero** and *R. P. Love,* General Electric Research & Development Center, Schenectady, NY 12301

The effect of argon ion implantation at 200 keV on carrier generation lifetime (τ_g) in silicon has been studied as a function of dose and annealing temperature. The lifetime was measured by the capacitance transient technique in MOS structures formed after implantation on n-type Si. Values of τ_g can be controlled over 4 orders of magnitude by argon doses up to 10^{14} cm^{-2}. Approximately 2 orders of magnitude of lifetime control remains after anneals at 1100° and 1200°C. These temperatures are within those used for epitaxial growth by CVD, so that localized lifetime control regions can be incorporated into fast switching devices.

ELECTRONICS

III-V Opto-Electronics Epitaxy and Device Related Processes

320 Challenges in III-V Semiconductor Compounds: *H.C. Gatos,* Massachusetts Institute of Technology, Cambridge, MA 02139

The immense potential of III-V compounds and their alloys for new quantum jumps in electronic and optoelectronic applications has already been assessed on sound principles and, in some instances, demonstrated. The realization of this potential, however, is confronted with a spectrum of challenges emanating from the unavailability of materials and materials structures with the necessary crystalline and chemical constitution. Representative challenges in the growth of bulk crystals, of layer structures and interfaces, and in the control of defect formation and defect interactions are discussed.

321 III-V Optoelectronic Devices: *H. Kressel,* RCA Laboratories, Princeton, NJ 08540

This paper reviews recent developments in the optoelectronic devices which are currently receiving the most attention. These include laser diodes and LED's in the spectral region from the red into the infrared, using various alloys, and light detectors for the same spectral region. Several epitaxial technologies are used. The areas discussed include current approaches aimed at improved laser mode control, and higher power emission levels and reliability. Increasing activity is also evident in the integration of optical components on the chip as a means of obtaining more effective device performance.

322 Liquid Encapsulated Czochralski (LEC) Growth of III-V Crystals: *W.A. Bonner,* Bell Laboratories, Murray Hill, NJ 07974

The technique of liquid encapsulation to suppress the volatility of dissociable melts has provided the basis for much of the present day compound semiconductor technology. This concept has proven especially important for both the synthesis and bulk single crystal growth of large, high quality III-V materials for substrates particularly those having dissociation pressures at the melting point in excess of one atmosphere, *e.g.*, GaP, InP, GaAs. In this paper the general technique and encapsulants are reviewed. The application, with emphasis on liquid encapsulated Czochralski (LEC) growth, is discussed, and encapsulated and nonencapsulated growth techniques are compared.

323 Reduction of Dislocation Densities of LEC-Grown InP Crystals by Aid of Thermal Analysis: *G. Müller,* E. Tomzig,* and *J. Völkl,* Universität Erlangen-Nürnberg, Kristallabor, Institut für Werkstoffwissenschaften, D 8520 Erlangen, Germany

The dislocation densities of LEC grown undoped InP crystals are decreased by a reduction of the temperature gradients in the growing crystal. This improvement was reached by a rigorous thermal analysis of the high temperature region of the growing crystal and an appropriate adjustment of the heating conditions. The occurrence of twin formation was also decreased by this measure which is in accordance with the results of the qualitative thermoelastic analysis.

324 Horizontal Bridgman Growth of Optoelectronics Grade GaAs: *S. Akai,* K. Fujita, S. Nishine, N. Kito, Y. Sato, S. Yoshitake,* and *M. Sekinobu,* Sumitomo Electric Industries, Ltd., 1-1-1, Koyakita, Itami-Shi Hyogo-Pref, 664, Japan

State-of-the-art HB technique for growing optoelectronics grade GaAs including semiconducting and semi-insulating substrates is reviewed. Laser grade low EPD substrate with a diameter up to 2 in., and solar cell and IC grade substrates with a diameter up to 3 in. are discussed in terms of residual impurities, EPD's, and semi-insulating properties which depend on thermal growth condition and doping condition.

325 The Effects of Melt Stoichiometry and Impurities on the Formation of Dislocations in Bulk GaAs: *J.M. Parsey, Jr.,* Bell Laboratories, Murray Hill, NJ 07974, and *J. Lagowski* and *H.C. Gatos,* Dept. of Materials Science and Engineering, Massachusetts Institute of Technology, Cambridge, MA 02139

Dislocation-free GaAs was grown in a horizontal Bridgman apparatus by precise control of the melt stoichiometry through the arsenic partial pressure. Deviation from this optimum arsenic pressure in either direction led to high dislocation densities. It was also found that the presence of Si-impurities in the melt has profound effects on the dislocation density and attenuates the effects of the arsenic pressure. A model for this behavior is presented, and the implications to the growth of GaAs crystals are discussed.

326 Growth and Characterization of GaAs Single Crystal by Magnetic Field LEC Technique: *K. Terashima** and *T. Fukuda,* Optoelectronics Joint Research Laboratory, 1333 Kamikodanaka, Nakaharaku, Kawasaki 211, Japan

<100> GaAs single crystals, 2 in. in diameter and striation-free, were successfully grown by magnetic field LEC technique. Temperature fluctuation of GaAs melt was suppressed from 15°C to less than 0.1°C by the magnetic field of more than 1250 oersted. Electrical resistivity was revealed to be drastically changed between conductive and semi-insulating states depending on the field strength. Impurity and deep level concentration of the crystal obtained with and without magnetic field were measured and discussed.

327 Theoretical Aspects of III-V Heterostructure Formation by LPE: *R. Ghez,* IBM T.J. Watson Research Center, Yorktown Heights, NY 10598

Heterostructure formation by multicomponent LPE is just a special case of epitaxial thin film processing. However, the methods required to analyze this process are closer to those in use for metallurgical junctions than to those generally applied to crystal growth. A general purpose computer program has been written for the eighteen most commonly used III-V ternary systems. It accepts arbitrary initial data that correspond to a wide range of experimental conditions. Results of these simulations are presented.

328 Unstable Region Behavior in Type $A_{1-r}B_rC_{1-y}D_y$ III-V Quaternary Solid Solutions with Short-Range Clustering: *K. Onabe,* Nippon Electric Co., Ltd., Opto-Electronics Research Laboratories, 4-1-1 Miyazaki, Miyamae-ku, Kawasaki 213, Japan

Unstable region behavior in type $A_{1-r}B_rC_{1-y}D_y$ III-V quaternary solid solutions is predicted, on the basis of a newly developed thermodynamic formalism, which takes the short-range clustering effect(1) (preferential pairing of atoms) into account. Compared with those calculated by the strictly regular solution approximation(2), a narrowing of the unstable region extent and corresponding lowering of critical temperature for immiscibility are noticeable. These

facts are numerically illustrated for $In_{1-x}Ga_xP_{1-y}As_y$ and others. Such an unstable region will still seriously limit the growth of the solid solution by near-equilibrium growth methods like liquid phase epitaxy.

1. K. Onabe, *J. Phys. Chem. Solids*, **43** (1982).
2. K. Onabe, *Jpn. J. Appl. Phys.*, **21**, L323 (1982).

329 An Experimental Investigation of the GaAs-InAs-GaP-InP Pseudo-Quaternary Phase Diagram: *A. J. Spring Thorpe*, Bell-Northern Research, Ottawa, Ont., Canada K1Y 4H7

The technique of sealed tube, iodine assisted, powder annealing and vapor transport has been used to invesgitage a range of alloy compositions within the GaAs-InAs-GaP-InP pseudo-quaternary phase-field at 780°C. Although some powder mixtures transported to form homogeneous single-phase compositions the majority formed two distinct phases. These results are interpreted as supporting evidence for an immiscibility domain within the phase-field, the dimensions of which are reasonably consistent with the theoretical phase diagram derived by De-Cremoux *et al.* (1)

1. B. De-Cremoux, P. Hirtz, and J. Ricciardi, *Inst. Phys. Conf. Series* **56**, 115 (1981).

330 Experimental Studies on LPE of 3-5 Compound Semiconductors: *E. Bauser*, Max-Planck-Institut für Festkörper Forschung, D-7000 Stuttgart 80, Germany

The surface micromorphology of GaAs layers grown by liquid phase epitaxy (LPE) was studied. Surface steps of monoatomic height were made visible by decoration and could therefore be included into the consideration. All step configurations observed lead to the conclusion that the macroscopic growth of the layer which occurs perpendicular to the solid/liquid interface, is achieved by a lateral microscopic growth (LMG) process. Different mechanisms of the LMG may develop, and they depend on the particular growth conditions, such as substrate orientation, dopant concentration, etc. Facet growth, near-facet growth or terrace growth are examples of frequently occurring LMG mechanisms in LPE. Simple models for these growth mechanisms are presented. The influence of LMG mechanisms on material properties, such as homogeneity of dopant distribution, surface planarity or morphological stability of the growth-interface, is illustrated. The investigation of LMG mechanisms seems to be important for further improvements in material properties.

331 Zone-Melting Recrystallization of InSb with Planar Patterning: *C.J. Keavney,* H.A. Atwater*, and *H.I. Smith*, Research Laboratory of Electronics, Massachusetts Institute of Technology, Cambridge, MA 02139

Zone-melting recrystallization of Si on SiO_2 has produced films consisting of elongated grains ~1 mm wide, with electron mobilities close to bulk value. Films of a single orientation can be produced by zone melting through planar constrictions (1). Large-grain polycrystalline films of InSb have been produced on insulating substrates by zone-melting recrystallization, following methods developed by Clawson and others (2). We report on efforts to combine zone-melting recrystallization of InSb and InP with planar patterning to yield single-crystal films on insulating substrates.

1. H.A. Atwater *et al.*, *Appl. Phys. Lett.*, **41**, 747 (1982).
2. A.R. Clawson, *Thin Solid Films*, **12**, 291 (1972).

332 Liquid Phase Epitaxy Growth of InGaAsP Double Heterostructure Laser Material: *P. Besomi,* R.B. Wilson, J. Degani*, and *R.J. Nelson*, Bell Laboratories, Murray Hill, NJ 07974

The protection technique using an excess phosphorus partial pressure provided by an Sn-In-P solution contained inside a quartz chamber is shown to virtually eliminate thermal degradation of InP substrates prior to growth of InGaAsP DH lasers. Nomarski contrast photomicrographs, as well as photoluminescence intensity and x-ray diffractometric measurements, indicate that Sn-doped InP substrates protected by this method suffer a negligible deterioration, while S-doped substrates do not exhibit any measurable thermal degradation, a substantial improvement over the cover wafer method. Finally, InGaAsP double heterostructures were grown by the near equilibrium LPE method on substrates protected in a quartz chamber. X-ray measurements showed that the active layer mismatch to the InP cladding layers was reproducibly in the 10^{-5}-10^{-6} range. Broad area laser thresholds were also measured, and it was found that low threshold double heterostructures could readily be obtained without prior meltback.

333 InGaAs Photodetector for the 1.8-2.0 Micron Region: *C.B. Morrison,* S.M. Bedair*, and *K.J. Bachmann*, Dept. of Electrical Engineering, North Carolina State University, Raleigh, NC 27650

InGaAs photodetectors for the 1.8-2.0 micron region have been fabricated by LPE growth of InGaAs layers on intermediate layers of InAsP on an InP substrate. Zn diffusion is used to create the p-type material. The effect of lattice mismatch on minority carrier lifetime is analyzed on the basis of minority carrier diffusion length data obtained by fitting a computer model to the experimentally observed quantum efficiency.

334 The Current State of III-V Molecular Beam Epitaxy for Optoelectronics: *M.B. Panish*, Bell Laboratories, Murray Hill, NJ 07974

The capabilities of molecular beam epitaxy for $GaAs/Al_xGa_{1-x}As$ structures are illustrated by a discussion of recent device structures, including double barrier, multiquantum well and graded index lasers, and by modulated barrier, modulation doped FET, and superlattice APD detectors. For optoelectronic devices in the currently important 1.3-1.7 μm wavelength range, MBE is in an early development stage, but injection lasers at 1.3, 1.55, and 1.65 μm have been demonstrated with several combinations of materials and structures.

335 Effect of Group V/III Flux Ratio on Optical and Electrical Properties of Si-Doped $Al_xGa_{1-x}As$ Grown by Molecular Beam Epitaxy: *Y. Nomura,* M. Mannoh, M. Mihara, S. Naritsuka, K. Yamanaka, T. Yuasa*, and *M. Ishii* Optoelectronics Joint Research Laboratory, 1333 Kamikodanaka, Nakahara, Kawasaki, 211 Japan

The influence of growth temperature and group V/III flux ratio on optical and electrical properties of Si-doped $Al_xGa_{1-x}As$ layers grown by molecular beam epitaxy has been studied. It is found that the near bandedge emission of helium temperature photoluminescence spectra sensitively depends on the V/III ratio. The dependence of electron mobility on the V/III flux ratio is also discussed.

336 TEM Studies of Defects in MBE-GaAs: *C.B. Carter*, Dept. of Materials Science and Engineering, Cornell University, Ithaca, NY 14853

The incorporation of n-type dopants such as Si, Ge, and Sn in GaAs is limited in MBE-grown material by the formation of defect clusters or segregation of the dopant to the surface. In this paper, the results of diffraction contrast and high-resolution TEM techniques are combined with electron diffraction and energy dispersive spectroscopic (EDS) observations to illustrate both the defect clusters and the new phases formed in heavily-doped materials grown by MBE.

337 Growth of Single-Crystalline Epitaxial Group-II Fluoride Films on InP(001) by Molecular Beam Epitaxy: *C.W. Tu,* T.T. Sheng, M.H. Read, A.R. Schlier, J.G. Johnson, W.D. Johnston, Jr.*, and *W.A. Bonner*, Bell Laboratories, Murray Hill, NJ 07974

Twin-free, single-crystalline, lattice-mismatched as well as lattice-matched, epitaxial dielectric films of group-II cubic fluorides (SrF_2, CaF_2, and $Ba_xSr_{2-x}F_2$) have been grown on InP(001) substrates by molecular beam epitaxy. The epitaxial growth and characterization by reflection high-energy electron diffraction, transmission electron microscopy, and other techniques are discussed. Such films have potential applications in passivation, in metal-insulator-semiconductor structures, as well as in epitaxial semiconductor-insulator-semiconductor structures and superlattices for integrated optoelectronics.

338 The Growth of III-V Compound Semiconductors by Metalorganic Chemical Vapor Deposition: *R.D. Dupuis*, Bell Laboratories, Murray Hill, NJ 07974

Metalorganic chemical vapor deposition (MO-CVD) has been used to grow epitaxial thin films of III-V compound semiconductors on both semiconducting and insulating substrates. Typically, the MO-CVD process employs mixtures of column III metal alkyls and column V hydrides that are pyrolized in hydrogen to produce the corresponding III-V semiconductor thin film. Recently, the MO-CVD growth of III-V compounds employing column III and column V alkyl sources has also been studied. This paper describes recent results on the MO-CVD growth of compound semiconductor materials and devices.

339 OMVPE Growth of GaP,InP, and GaInP: *C.C. Hsu* and *G.B. Stringfellow*, Dept. of Materials Science and Engineering, College of Engineering, University of Utah, Salt Lake City, UT 84112

Atmospheric pressure organometallic vapor phase epitaxial (OMVPE) growth of In and P containing alloys has been successfully accomplished using TMIn, TMGa, and PH_3. The effects of substrate temperature and V/III ratio on growth rate, composition, morphology, and photoluminescence have been systematically studied. The incorporation efficiency for In is found to be higher than for any previous reports. The addition of TEP to retard polymer formation is found to have little effect.

340 Preparation of Device Quality GaAs Using Plasma Enhanced MO-CVD Technique: *K.P. Pande,** Bendix Advanced Technology Center, Columbia, MD 21045, and *A. Seabaugh*, National Bureau of Standards, Washington, DC 20234

Low temperature (≤450°C) deposition of single crystal GaAs using a new plasma enhanced MO-CVD technique is described. In this technique, plasma is created by d-c potential, and the substrate is not directly exposed to the plasma. Deposition of GaAs was achieved at extremely low plasma power (<5W) using trimethylgallium (TMGa) and arsene (or trimethylarsenic) reactants. The epitaxial films show excellent surface morphology and thickness uniformity over a large area substrate. A linear dependence of growth rate upon TMGa concentration was observed with a typical growth rate of 0.1 μm/min for a TMGa flow rate of 15 cm^3/min. Undoped films were found to be n-type with a carrier mobility in the range of 5200 $cm^2V^{-1}sec^{-1}$. DLTS measurements show no electrically active El_2 trap level except a trap level at 0.43 eV. Measurements on Schottky barrier devices fabricated on n/n^+ layer show uniform impurity doping profile and 55V reverse breakdown voltage. Some data on photoresponse of these devices are also presented.

341 GaAs Millimeter Wave Mixer Diodes Grown by MOCVD: *R.W. Glew** and *M.J. Sisson*, GEC Research Laboratories, Hirst Research Centre, Wembley, England HA9 7PP

A study of the epitaxial growth of n/n$^+$ GaAs structures has been made by the metal organic chemical vapor deposition method. Layers have been successfully deposited both at atmospheric and reduced pressure. Problems associated with the growth are shown, and how significant improvements have been made. Good quality structures with 0.2 μm active layers doped to 10^{17} cm^{-3} have been fabricated into mixer diodes. At 94 GHz conversion, losses of 6 dB have been attained.

342 Emission Spectra of Doped ZnSe Grown Epitaxially on GaAs by Organometallic Chemical Vapor Deposition: *T.N. Chin*, U.S. Army ARRADCOM, Dover, NJ 07801

Since organometallic chemical vapor deposition (OM-CVD) can be performed (1) at relatively low temperatures, ZnSe epitaxially grown on (100) GaAs would be expected to have a low density of native defects. In this paper, cathodoluminescence spectra taken from ZnSe:Al and ZnSe:N are presented. The results indicate that the radiative recombinations are greatly affected by the presence of the dopants, Al, N, etc. These preliminary results are discussed and compared with those (2) determined from the undoped monocrystalline ZnSe layers.

1. W. Stutius, *J. Cryst. Growth* **59**, 1 (1982).
2. T.N. Chin, *J. Vac. Sci. Technol.*, To be published.

343 X-Ray Diffraction and Doping Studies of Strained-Layer Superlattices Grown by Metal Organic Chemical Vapor Deposition: *R.M. Beifeld,* G.C. Osbourn, P.L. Gourley*, and *I.J. Fritz* Sandia National Laboratories, Albuquerque, NM 87185

Metal organic chemical vapor deposition has been used to prepare strained-layer superlattices in the GaAs + GaP system. Both the composition and the layer thickness can be determined by x-ray diffraction. For very thick layers a direct measure of the strain in the layers can be obtained by x-ray diffraction. H_2Se and $(C_2H_5)_2$ Zn have been used to prepare n- and p-type superlattices, respectively. Carrier concentrations in the range of 5×10^{16} to 5×10^{18} cm^{-7} have been achieved for n-type superlattices and 1×10^{17} to 1×10^{18} for p-type superlattices. The growth and characterization of these materials are discussed. (This work was performed at Sandia National Laboratories supported by the U.S. Department of Energy under contract No. DE-AC04-76DP00789.)

344 Epitaxial Growth of InGaAs by the VPE-Hydride Technique Using a Ga-In Alloy as Source: *T.E. Erstfeld** and *K.P. Quinlan*, Rome Air Development Center, Solid State Sciences Div., Hanscom AFB, MA 01731

A study was carried out to determine the feasibility of growing epitaxial films of the ternary InGaAs into InP substrates using a Ga-In alloy as the source in the vapor phase epitaxial-hydride technique. The growth rates, morphologies, and compositions of InGaAs were studied as functions of hydrogen chloride flow rate, temperature (source, mixing, and deposition), and alloy composition. The parameters are discussed in the light of optimizing the morphology and growth rate of $In_{0.53}$ $Ga_{0.47}As$.

345 Growth and Characterization of High Purity VPE InP Prepared by the Hydride Process: *S.Y. Sun, C.A. Adams*, and *B.W. Wessels,** Dept. of Materials Science and Engineering, and Materials Research Center, Northwestern University, Evanston, IL 60201

High quality epitaxial InP films have been chemically vapor deposited using the hydride-chloride technique. Quality of the as-grown films was determined using photoluminescence, Van der Pauw and deep level transient spectroscopy measurements. The undoped as-grown films were n-type and had net carrier concentrations of the order of $1 - 20 \times 10^{15}$ cm^{-3}. Photoluminescence measurements at 77 K indicated the presence of a band at 1.18 eV in addition to transitions involving shallow donors and acceptors. DLTS on diffused junctions detected a single dominant level at $E_c - 0.26$ eV, present in concentrations on the order of 1×10^{14} cm^{-3}.

346 Morphological Study of Thermal Decomposition of InP Surfaces: *S.N.G. Chu,* C.M. Jodlauk*, and W.D. Johnston, Jr., Bell Laboratories, Murray Hill, NJ 07974

The morphological evolutions of the (100), (111), and (110) InP surfaces decomposed at typical VPE and LPE growth temperatures in hydrogen are examined in detail by SEM. The development of the decomposition pits on InP surfaces begins with the nucleation of indium droplets. The subsequent etching of the InP surface in contact with the indium droplet initiates the decomposition pits. The nucleation and the evolution of the decomposition pits are recorded on video tape. Detailed growth mechanisms and geometries of the pits are described. The effects of misorientation and hydrogen flow rate on the decomposition morphology are discussed.

347 Vapor Phase Deposition of Single Crystal GaAs Using the AsH_3-Ga-HCl Process: *A.R. Sears,** *P. Menditto*, and *P.M. Campbell*, General Electric Co., Corporate Research and Development, Schenectady, NY 12301

Single crystal gallium arsenide has been grown on both doped and undoped substrate wafers using a Crystal Specialties Model 410A reactor and the AsH_3-Ga-HCl process. Room temperature mobilities of 7700 cm^2/Vsec and 77 K mobilities of 95,000 cm^2/Vsec have been obtained. Controlled doping between 5×10^{14} and 7×10^{17} has been achieved using hydrogen sulfide. Wafer passivation and deposition conditions have been optimized to insure surface morphology adequate for device fabrication. Deposited layers have been characterized by Hall measurements and C-V profiling using a Polaron Profile Plotter.

348 Toward Understanding of Schottky Barriers and Related Phenomena: 3-5's: *W.E. Spicer,** *S. Eglash, D. Mo, P. Mahowald, S. Pan, W. Petro*, and *I. Lindau*, Stanford Electronics Laboratory, Stanford University, Stanford, CA 94305

How can there be so little fundamental understanding of Schottky barrier (SB) formation after one hundred years? Macroscopic models (work-function, electro-negative differences, etc.) have been popular despite their failures or inadequacies. Only "atomic level" experiments can give necessary insights. Models must be established for restricted semiconductor-metal systems. Thus, the "Unified Defect Model" was developed for 3-5's. Defects within the 3-5 lattice produced by surface deposition of foreign atoms pin the Fermi level forming the Schottky barrier. Extensions to 3-5 alloys and "engineered" Schottky barriers are discussed. (Supported by DARPA and ONR.)

349 An *In Situ* X-Ray Study of Metal-Semiconductor Interactions in the InGaAsP/InP System: *J.M. Vandenberg** and *H. Temkin*, Bell Laboratories, Murray Hill, NJ 07974

Metal-semiconductor interactions play an important role in the formation of ohmic contacts to III-V alloys. The alloy formation in the interface has been studied as a function of annealing temperature using *in situ* x-ray diffraction. A well-defined sequence of Au-In compounds has been identified, and their formation explained, in terms of thermodynamics of solid-state reactions. The effectiveness of barrier metals such as Ti, Ni, and Pt has also been evaluated using the same x-ray technique. The results of the *in situ* x-ray diffraction annealing studies are compared with those obtained for x-ray analysis of similar metal/III-V systems after postdeposition alloying.

350 Plasma Etching of III-V Compounds: *D.L. Flamm*, Bell Laboratories, Murray Hill, NJ 07974

Fundamentals and recent research results related to the plasma etching of III-V compound semiconductors are reviewed. Directional etching can be obtained by ion-assisted gasification of these substrates at low pressure or low frequency conditions that favor energetic ion bombardment, or by crystallographic chemical etching when the rate of ion-assisted attach is small. Isotropic chemical etching can also be observed. Mechanisms are related to design considerations in the choice of gases, discharge parameters, and substrate temperature.

351 Dielectric III-V Semiconductor Interactions: *H.H. Wieder*, Dept. of Electrical Engineering and Computer Sciences, University of California, San Diego, C-014, La Jolla, CA 92093

Electrical and galvanomagnetic measurements made on metal-insulator-semiconductor capacitors and field effect transistors show that the nature of the interfaces between binary, ternary, and quaternary III-V compounds and their native surface oxides determine, to a large extent, the equilibrium surface Fermi level, the dynamic displacement of their surface potentials, the density and the position within the fundamental bandgap of interface states. These parameters which agree quantitatively with the pinned surface Fermi level of fully oxidized free surfaces of the respective compounds and with the barrier height of their metal-semiconductor interfaces provide support for the surface defect model of Fermi level pinning.

352 Surface Structural Damage Produced in InP (100) by RF Plasma or Sputter Deposition: *W.C. Dautremont-Smith** and *L.C. Feldman*, Bell Laboratories, Murray Hill, NJ 07974

Rutherford backscattering detected at grazing angle under channeling conditions has been employed to observe and quantify surface structural damage to InP(100) produced by dielectric deposition methods involving direct 13.56 MHz rf-plasma exposure. Sputter deposition at any plasma power produced surface damage, to a maximum depth of ~30Å at power densities within the range 0.25-2.2 Wcm^{-2}. In contrast damage due to plasma deposition was not observable at any plasma power density up to 0.32 Wcm^{-2} for InP substrates at either 250° or 31°C. This power level produced the high SiO_2 deposition rate of 1500Å min^{-1}. Thus plasma deposition is particularly applicable to InP, whereas diode sputter deposition should be avoided for any application in which structural damage may be detrimental.

ELECTRONICS/DIELECTRICS AND INSULATION

Joint General Session

353 Characterization of II-VI Compounds by Electrochemical Photocapacitance Spectroscopy: *R. Haak** and *D. Tench*, Rockwell International Science Center, Thousand Oaks, CA 91360

Application of electrochemical photocapacitance spectroscopy (EPS) to the characterization of deep traps in II-VI semiconductors, particularly CdSe, is discussed. Emphasis is on interface states associated with oxygen adsorption. Results are presented for various materials (including thin films), surface pretreatments, and both aqueous and nonaqueous solvents, and compared to those reported for solid-state methods.

354 Characterization of GaAs by Electrochemical Photocapacitance Spectroscopy: *R. Haak* and *D. Tench,** Rockwell International Science Center, Thousand Oaks, CA 91360

Electrochemical photocapacitance spectroscopy (EPS) has been shown to be an extremely sensitive means for characterization of bulk and interface states in semiconductor materials. Excellent correlations between the energies and densities of states determined by EPS and those measured by solid-state techniques have been obtained. In the present paper, results for both n- and p-GaAs are discussed. EPS and DLTS results for the same material are also compared.

355 Anomalous Transient Response in Optically Excited GaAs MESFET's: *T. K. Plant** and *S. J. T. Owen*, Dept. of Electrical and Computer Engineering, Oregon State University, Corvallis, OR 97331

We report the anomalous behavior of the transient response of the S-D current of a 100 × 100 (μm^2) gate GaAs FAT-FET under illumination by a 670 nm LED. At room temperature and above, the turn-on and turn-off transients were nearly identical. At −180°C the turn-on transient was reduced by 10× but no change in the turn-off transient was observed. DLTS measurements done with pulsed optical excitation ($h\nu > E_g$) revealed 2 main e^- traps at 0.46 and 0.09 eV from the CB and traps with less transient response: 2 more e^- traps and one hole trap. Currently, more measurements are being made to identify the energy levels of the additional traps. These traps are responsible for the poor low-frequency characteristics of GaAs FET's and have backgating effects also. Similar measurements under a backgate substrate bias show the presence of the same traps but in considerably different proportions. This is evidenced by the different shaped transient responses with changing substrate bias. The exact traps responsible for this behavior are not yet known.

356 Long Wavelength Characterization of GeAs and SiAs: Two New Semiconductors: *D. G. Mead*, Nicolet Instrument Corp., Madison, WI 53711

The first room temperature long wavelength reflection spectra in the 50-400 wavenumber region of the infrared have been recorded for IV-VI monoclinic semiconductors, germanium arsenide and silicon arsenide. Analysis predicts fifteen group theoretical long wavelength optical zone phonon frequencies. A comparison is made for both GeAs and SiAs with their isomorph GaTe and a simple scaling relationship is shown to exist between their corresponding layer-plane phonon frequencies.

357 MOS Capacitors on CdTe: *R. T. Talasek** and *A. J. Syllaios*, Texas Instruments Inc., Dallas, TX 75266

Native anodic oxides have been successfully grown on high-resistivity CdTe substrates. These oxides have been used to fabricate MOS capacitors, which have been characterized by capacitance-voltage measurements, and the results are reported. The effects of a high resistivity semiconductor have been illustrated, and an equivalent circuit which incorporates this characteristic has been proposed.

358 LPE Growth of $Hg_{0.8}Cd_{0.2}Te$ on Horizontal Rotating Substrates: *W. L. Ahlgren*, Santa Barbara Research Center, Goleta, CA 93117

Epitaxial layers of $Hg_{0.8}Cd_{0.2}Te$ have been grown on horizontally disposed CdTe substrates mounted on a holder that allows rotation of the substrate during growth. A vertical "infinite melt" LPE system was used, in which the substrate rotated at 350-650 rpm, and dipped into a tellurium-rich melt as the melt was cooled through the liquidus temperature (~460°C). Layers from 4.7 to 30 μm thick were grown in 30 min. The surface morphology of the layers showed varying amounts of melt retention. A good layer was 11 μm thick, had a cutoff wavelength of 7.4 μm at 300 K (12.4 μm at 80 K), and was p-type as grown with a carrier concentration of 1.8×10^{17} cm^{-3} and mobility of 280 cm^{-2} V^{-1} sec^{-1}. Radial uniformity of thickness and composition was excellent. This can be attributed to two factors: (i) the radial temperature uniformity is good in the vertical infinite melt LPE system, and (ii) the horizontal rotating disk configuration leads to a diffusion boundary layer of uniform thickness. From the measured growth rate, it was estimated that $D_{cd} \approx 1.1 \times 10^{-5}$ cm^2 sec^{-1} in the melt.

359 Electronic Conductivity of Li_2MnO_3 Doped with Aluminum, Magnesium, or Zinc: *G. H. Kucera,* J. W. Sim,* and *J. L. Smith*, Argonne National Laboratory, Chemical Technology Div., Argonne, IL 60439

The electronic conductivity of porous polycrystalline Li_2MnO_3 doped separately with aluminum, magnesium, or zinc was measured in air in the temperature range of 525-975 K using the four-probe van der Pauw technique. Samples of doped Li_2MnO_3 were synthesized as powders, pressed into pellets (about 2.8 cm diam), and sintered into porous (>40%) bodies. The methods of synthesizing doped Li_2MnO_3, and the effect of dopant concentration and sintering temperature on the measured electronic conductivity are discussed. The chemical stability of the aluminum and magnesium doped Li_2MnO_3 in lithium-potassium carbonate eutectic was also examined for possible fuel cell applications.

360 Deep Levels in Device-Quality Ion-Implanted GaAs: *J. K. Rhee, S. J. Prasad,* P. K. Bhattacharya*, and *M. V. Rao*, Dept. of Electrical Engineering, Oregon State University, Corvallis, OR 97330, and *B. Venkatraman* and *R. Y. Koyama*, Tektronix Inc., Beaverton, OR 97077

Deep levels have been detected and characterized in semi-insulating GaAs, in active FET layers obtained by Si-implantation of the substrates, and Si-implanted VPE buffer layers. Cr as a hole trap and the EL2 (0.83 eV) electron trap are the dominant centers in the semi-insulating and VPE layers, respectively. Measurements on the implanted layers on both kinds of host material and direct measurements on fabricated FET's show two dominant traps: an electron trap with $\Delta E_T = 0.52 \pm 0.01$ eV around room temperature, and a hole trap with $\Delta E_T = 0.15$ eV. Annealing and trap-diffusion measurements are being conducted to study the physicochemical origin of these levels. PL spectra on the implanted material show evidence of the incorporation of some Si as acceptors and Cu-related impurities.

361 On the Redistribution of Implanted Be in Semi-Insulating InP after Annealing: *B. Molnar** and *G. Kelner*, Naval Research Laboratory, Washington, DC 20375, and *G. H. Morrison* and *G. Ramseyer*, Cornell University, Ithaca, NY 14853

The purpose of this paper is to present the salient features of both the atomic and the electronic profiles of implanted p-type Be dopants in S.I InP substrates and to provide insight into the mechanism which leads to these features. The in-depth atomic distribution of Be was determined by using SIMS and the majority carrier profile of the Be acceptors was derived from C-V measurements in combination with an etch and repeat procedure. The as-implanted Be profiles are Gaussian LSS profiles. The redistribution of a 10^{18}-5 × 10^{18}/cm^3 Be implant during thermal annealing (650°-750°C; 10-15 min) can be characterized by a high concentration region, which agrees reasonably well with the as implanted profile, and a tail section, which has a steep leading edge and a plateau of about 10^{17}/cm^3. The carrier profiles differ from the Be atomic profiles. Detailed studies of the effects of the substrate, the implantation level, and annealing parameters are presented.

362 Chlorine Levels in MOS Gate Oxides: *W. A. Bösenberg*, RCA Corp., Somerville, NJ 08876, and *C. W. Magee*, RCA David Sarnoff Research Center, Princeton, NJ 08540

The quantitative SIMS analysis for chlorine ions has been extended to a detection limit of 1×10^{11} cm^{-2}. This is the order of magnitude of sodium contamination that causes a threshold voltage shift of a few tenths of one volt. Insignificant chlorine has been found in 1000Å oxides grown with an azeotropic mixture of water and hydrochloric acid. The same is true for steam-grown oxides with the addition of gaseous HCl. Dry oxides grown with the addition of HCl gas or (1,1,1) trichloroethane show a chlorine level that increases with oxidation temperature. The problem of slow growth of dry oxides can be avoided by following steam oxides with a dry oxidation step incorporating chlorine. Chlorine levels from 1×10^{12} cm^{-2} at 750°C to 6×10^{15} cm^{-2} at 1150°C have been measured with an activation energy of 2.3 eV. This is within the range needed for sodium passivation of the gate oxides.

363 Annealing of Fixed Changes in Poly-Si Gate MOS: *J. P. McVittie,* G. Chang, D.-B. Kao*, and *G. L. Patton*, Integrated Circuit Laboratory, Stanford University, Stanford, CA 94305

The control of the fixed charge, Q_f, is critical to the operation of MOS devices. Traditionally, it has been thought necessary to lower Q_f by a high temperature anneal in an inert ambient before depositing the gate material. We show that for poly-Si, this anneal can be fully accomplished after the gate deposition, and it was found to be independent of the ambient. In other words, Q_f fully anneals during normal post poly-Si deposition processing. This can be attributed to the fact that poly-Si is impervious to O_2 and H_2O.

364 Hydrogen Gettering Effect of Mo_2N/Mo MOS Process: *M. J. Kim* and *D. M. Brown*, General Electric Co., Corporate Research and Development Center, Schenectady, NY 12345

Hydrogen plays a key role to maintain the integrity of molybdenum film during high temperature processing. Hydrogen not only prevents Mo oxidation but also reduces Mo oxide through oxygen gettering reaction at a high temperature. γ-phase molybdenum nitride formed by direct reaction with ammonia can be converted to pure molybdenum after utilizing its beneficial properties for MOS circuit fabrication. The recovery process is affected by hydrogen and the presence of an overglass layer. Effective recovery processes for producing high conductivity Mo from Mo_2N nitride and sputtered Mo film contaminated with oxygen were developed.

365 1.2 μm Process Design for CMOS VLSI's: *J.-I. Matsunaga, N. Matsukawa, K. Hashimoto, M. Nakase, H. Nozawa*, and *S. Kohyama*, Toshiba Corp., Semiconductor Device Engineering Laboratory, 72, Horikawa-cho, Kawasaki, 210, Japan

The next generation CMOS process technology, which follows current 2 μm CMOS process, has been developed for higher packing density and device performance. In this paper, 1.2 μm CMOS process design is presented, which can be applied for CMOS VLSI's such as 256 Kb static RAM's. C-SEPOX isolation technology without bird's beak formation is one of the key technologies which provide higher packing density. Signal propagation delay in polysilicon word lines is minimized by implementing double level metallization. 1.2 μm MOS FET structures are optimized, based upon process and device simulation, considering parameter controllability. In addition, device characteristics and physics relating to such as reliability, with the small geometry CMOS device structures, are also discussed.

370 Process for Borderless Source and Drain Contacts: *R. C. Dockerty,* G. T. Elie,* and *C. C. Hu,* IBM, East Fishkill Facility, Hopewell Junction, NY 12533

Pd_2Si-Al-Cu-Si metallurgy forms an ohmic contact to n^+ and p^- silicon. Source-drain to substrate shorts can result in an n-channel semi ROX FET if the diffusion contact overlaps the ROX region. Contacts borderless to the ROX are formed by etching the contacts and then doing a $POCl_3$ diffusion or phosphorus implant. SEM cross sections are shown. Junction breakdown, leakage and capacitance are discussed. Contact reliability under accelerated stressing is described. The borderless contact offers significant leverage in VLSI FET memory and logic.

371 Characterization of the Self-Aligned $TiSi_2$ Process: *C. K. Lau,* Texas Instruments, Inc., Dallas, TX 75265

Recently, self-aligned silicide technology for increasing conductivity of various levels of interconnects in MOS devices has attracted increasing attention (1). The self-aligned $TiSi_2$ process has been reported (2, 3). Characterization results of the self-aligned $TiSi_2$ process are presented. These include the effect of wafer preparation, titanium deposition, reaction temperature, and ambient on Ti-Si, Ti-SiO_2 reactions, as well as the silicide formed. A reproducible process has been established based on the results obtained from this investigation.

1. C. M. Osburn, M. Y. Tsai, S. Roberts, C. J. Lucchese, and C. Y. Ting, in "VLSI Science and Technology/1982, C. Dell'Oca and W. M. Bullis, Editors, pp. 213-231, The Electrochemical Society Softbound Proceedings Series, Pennington, NJ (1982).
2. C. Y. Ting, S. S. Iyer, C. M. Osburn, G. J. Hu, and A. M. Schweighart, *ibid.,* pp. 224-231.
3. C. K. Lau *et al.,* International Electron Dev. Meeting, Digest of Tech. Papers, Dec. 1982.

372 Phosphosilicate Glass Flow Analysis and Experiments: *J. B. Price* and E. Reed,* Motorola, Advanced Products R&D Laboratories, Mesa, AZ 85202

Phosphosilicate glass (PSG) flow is used to planarize sharp steps on IC surfaces. Although the PSG is placed into circuits as an electrical insulator, its secondary functions of planarization and gettering receive more attention. The planarizing ability of PSG is a function of the phosphorus content of the glass, x_p; the temperature of the flow furnace, T; the duration of the flow anneal, t; the PSG thickness, t_{ox}; the step height, t_s; and the flow furnace gas composition, P_{PH3}, P_{H2O}, and P_{O2}. In our work we varied x_p, T, and t and measured planarization.

373 Evidence of Surface State Induced Instability in NMOS IGFET's and a Process for Its Suppression: *P. K. Chaudhari,* IBM Corp., Poughkeepsie, NY 12602

Under positive stress aging at elevated temperatures, a positive threshold shift is experienced in N-channel insulating gate field effect transistor (IGFET) fabricated using DPS process. The shift is found to be neither related to hot electron effect nor to the mobile ion drift. Consistent with the experimental results, a model is presented which explains this observed shift. Possible sources of origin are also discussed. Based on the proposed process fix, the effectiveness on the problem mechanism is demonstrated with the experimental data.

374 Lateral Epitaxial Growth of Si over SiO_2 Using Strip Electron Beam: *Y. Hayafuji,* T. Yanada, S. Usui, S. Kawado, A. Shibata, N. Watanabe,* and *M. Kikuchi,* Sony Corp. Research Center, 174 Fujitsuka-cho, Hodogaya-ku, Yokohama 240, Japan, and *K. E. Williams,* Energy Sciences Inc., Woburn, MA 01810

Recrystallization of poly-Si films on a patterned SiO_2/Si structure has been investigated to obtain large-area single crystal Si films on SiO_2 by using a strip electron beam. The high intensity strip electron beam was used with a dimension about 60 μm wide and 3 cm long. Single crystal or single crystal-like Si films with subboundaries were obtained entirely over SiO_2 patterns 30-100 μm wide and 2 cm long by lateral seeding epitaxial growth method.

375 Low Voltage Programmable MNOS Process for VLSI Technology: *A. El Dessouky,* Valvo-Phillips, MOS-IC Div., 2000 Hamburg 54, Germany

A comparison between n-channel Si-gate MNOS and FLOTOX nonvolatile memory cell types demonstrates advantages and compatibility of the MNOS technology for VLSI fabrication of large EEPROM's. Program/erase voltages are reduced to 12V or less by scaling memory nitride thickness down to 20 nm without affecting memory retention or endurance. Investigated influence of the fabrication parameters: SiH_2Cl_2:NH_3 deposition ratio, nitride thickness, and nitride oxidation on memory characteristics are presented as well as chip fabrication process.

376 A Photoprocess and Test Results for a Two-Layer Metallization System for High Density Bipolar IC's: *B. D. Ulrich** and *D. L. Fehrs,* Tektronix, Inc., Beaverton, OR 97077

A two layer system, consisting of two levels of plate-up gold metallization separated by a plasma oxide interlevel dielectric, has been developed in support of high density bipolar IC's. All metal and via patterning is anisotropic. The photoprocess to support the two layer system is described as is electrically probed test structures used to characterize the process. Test results are presented for the first generation process—4 μm interlevel vias.

377 Low Noise Bipolar Process Using Ion Implantation: *T. Ajima, J. Ohshima, Y. Koshino,* and *T. Yonezawa,* Toshiba Corp., 1 Komukai Toshiba-cho, Saiwai-ku, Kawasaki 210, Japan

This paper presents a low noise bipolar technology. Features of the technology include lightly implanted base, defect sink formation by silicon implantation, and plasma CVD silicon nitride for passivation. Low dose boron implantation into silicon prevents the generation of secondary segregation. Silicon implantation into the isolation region or from the back surface forms a defect sink. Plasma CVD silicon nitride controls the current gain fall-off at low emitter current because of the reduced surface recombination velocity. Noise characteristics and reliability are compared with conventional devices.

378 Base-Etched Transistor: *G. R. Srinivasan,* J. S. Lechaton,* and *S. P. Gaur,* IBM General Technology Div., Hopewell Junction, NY 12533

This paper describes a new technique that permits the fabrication of very narrow base width bipolar transistors selectively on an integrated circuit chip. The technique consists of etching the active base of the transistor using precision reactive ion etching, which uses an *in situ* polysilicon thickness monitor with a laser interferometer. The bipolar device characteristics obtained as a function of the amount of etching are described and the results are discussed in terms of an analytical model.

379 Aluminum Spike Problem in Bipolar IC and the Impact of Various Processing Technologies: *A. Sharif,* IBM East Fishkill Facility, Hopewell Junction, NY 12533

The aluminum spike problem causing junction shorts or leakages is a major yield concern in bipolar IC. This paper discusses how the fabrication technologies such as the dry or wet etch techniques affect the spikes. Experiments are presented with variations of aluminum copper metallurgies, dielectric thicknesses, and sintering cycles. The experiments indicate that the metal spike problem can be greatly minimized by a reduction of the oxide undercutting in contacts. This may be accomplished by dry etching and reducing oxide thickness.

380 Annealing of Si Surfaces after Epitaxial Growth: *C. H. Orner,* IBM General Technology Div., Hopewell Junction, NY 12533

The effect of annealing Si surfaces after N-epitaxial growth was studied as a means of reducing junction leakage. Various anneal processes were investigated in an H_2 ambient in the range of 800°-950°C for up to 40 min. Anodic etch analysis shows that the density of electrically active defects increases at the Si surface with anneal time, but is significantly reduced with time on the Si surface after a subsequent oxidation. The results of a number of experiments suggest that the anneal provides the necessary mobility for contaminants associated with leakage to condense on the Si surface (or near surface) nucleation sites. Depletion and possible out diffusion of contaminants render the bulk regions more suitable for bipolar device structures, from the junction leakage point of view. Data further indicate that the anneal is optimized at 900°-925°C and ~30 min. Implementation of this process is shown to consistently improve yield by providing a desensitization to variations in leakage causing contaminants.

381 The Influence of Oxygen Internal Gettering on the Quality of Epitaxial Layers: *K. H. Yang* and *C. Orner,* IBM General Technology Div., Hopewell Junction, NY 12533

The MOS lifetime of epitaxial layers was measured to determine the influence of oxygen internal gettering in silicon substrates. Oxygen precipitation in CZ substrates induced by a process simulation causes a substantial improvement in the lifetime of epitaxial layers. Without the simulation, oxygen remains in solution after epitaxial growth. The lifetime of the epitaxial layers is relatively low and increases with the concentration of interstitial oxygen. The epitaxial layers grown on FZ substrates have an extremely low lifetime, due to lack of oxygen internal gettering.

382 The Effects of High Temperature Preannealing on the Formation of Oxygen Thermal Donors in Czochralski Silicon: *B.-Y. Mao, J. Lagowski,* and *H. C. Gatos,* Massachusetts Institute of Technology, Cambridge, MA 02139

The formation of a thermal donor at 450°C and a "new donor" at 600°-800°C in as-grown and in preannealed (at 1200°C) Czochralski silicon containing different acceptor dopants and different concentration of oxygen and carbon was investigated. The energy levels of thermal donors were determined after different heat-treatment processes. It was found that preannealing decreases significantly the maximum concentration of thermal donors and changes their energy configuration. An explanation of these findings is presented.

383 Laser Crystallization of Silicon Films on $LiNbO_3$: *G. Goetz,* M. Rivier,* and *A. Cserhati,* Bendix Advanced Technology Center, Columbia, MD 21045

Scanned CW lasers present a unique way of locally heating optically absorbing films on transparent thermally sensitive substrate to produce large grain materials. Crystallized silicon films on $LiNbO_3$ substrates can combine the electronic properties of the semiconductor with the piezoelectric or optoelectronic properties of the substrate. We present data on grain size and orientation of silicon crystallites obtained on $LiNbO_3$ with techniques that minimize optical or mechanical damage to the substrate.

384 Two-Dimensional Oxidation Mechanisms in Local Oxidation Process: *J. C.-H. Hui* and *W. G. Oldham*, Department of Electrical Engineering and Computer Sciences, the Electronics Research Laboratory, University of California, Berkeley, CA 94720

Various two dimensional oxidation mechanisms involved in the local oxidation (LOCOS) process are explored. The effects of the viscous flow of oxide, the two dimensional diffusion of oxidants, the rigidity of nitride film, and the stress affected oxidation rate are discussed. Experiments done at different oxidation conditions with various thin film structures are used to explore and characterize the effect of these mechanisms on the lateral oxidation profile and defect generation.

385 Control of Staining in a High Temperature Diborane Diffusion Process by Hydrogen Injection: *D. L. Meier** and *P. Rai-Choudhury*, Westinghouse R and D Center, Pittsburgh, PA 15235

High temperature diffusions of boron into silicon are known to be afflicted with an insulating stain which is insoluble in HF. In this work, hydrogen was injected along with oxygen in a diborane diffusion in order to limit B_2O_3, the active dopant species, and therefore to control straining. Diffusions carried out at 1150°C and 1050°C gave sheet resistances of 3 Ω/□ and 12 Ω/□, respectively, without stain. Diffusions using the same gas flows, but without hydrogen, resulted in severe staining.

386 Solid Phase Epitaxy of Amorphous Silicon Deposited over SiO_2 Windows: *Y. Y. Wang** and *N. W. Cheung*, Dept. of Electrical Engineering and Computer Sciences, University of California, Berkeley, CA 94720, *D. K. Sadana*, Lawrence Berkeley Laboratory, University of California, Berkeley, CA 94720, and *M. Strattman*, Charles Evans and Associates, San Mateo, CA 94402

Solid phase epitaxy of amorphous Si deposited by LPCVD over SiO_2 windows on (100) Si were obtained by transient annealing using an incoherent halogen lamp. Temperature range from 750°-1200°C were used with typical time durations of seconds. Crystallinity of the annealed films and the recrystallization kinetics were characterized by cross-sectional transmission electron microscopy, Rutherford backscattering spectrometry, and electron channeling. Profiles of the oxide window are vital to the regrowth process and oxides prepared by local oxidation have given best results so far.

387 Diffusion of Implanted Phosphorus in Polysilicon: *D. L. Losee,* J. P. Lavine, S. T. Lee, C. M. Jarman*, and *E. A. Trabka*, Eastman Kodak Co., Research Laboratories, Rochester, NY 14650

Diffusion of ion-implanted phosphorus in polysilicon layers has been studied by SIMS and Auger analysis. The diffusion rate is strongly dependent on concentration and significantly higher than rates measured in single-crystal silicon. The activation energy, however, is close to the single-crystal value. For higher temperatures (≥850°C) or longer diffusion times, we observe a pile-up of phosphorus at the substrate oxide-polysilicon interface. Measured profiles are compared with model simulations.

388 Diffusion of Pd and Si Through Pd_2Si: *E. C. Zingu,** Dept. of Materials Science and Engineering, Cornell University, Ithaca, NY 14853, *R. Pretorius*, Southern Universities Nuclear Institute, Faure 7131, South Africa, *C. Comrie*, University of Cape Town, Cape Town, South Africa, and *J. W. Mayer*, Dept. of Materials Science and Engineering, Cornell University, Ithaca, NY 14853

Two sets of experiments were performed to investigate the mobility of Pd and Si in Pd_2Si: Lateral diffusion couples of Pd on Si layers and Si on Pd layers were used with the electron microprobe to study the mobility of Pd and Si in Pd_2Si during its formation. Secondly, multilayered thin film structures such as Si/Pd_2Si/Cr and Pd/Pd_2Si/Cr were used with Rutherford backscattering to monitor the diffusion of Si and Pd through Pd_2Si. We found that Pd diffuses faster than Si.

389 A Comparative Study of Molybdenum Silicide Formation: *F. Arnaud d'Avitaya, G. Bomchil*, and *C. Arena*, CNET-CNS, 38240 Meylan, France

We have performed a comparative study, using Auger electron spectroscopy, RBS, and x-ray diffraction techniques, of molybdenum silicide formation in samples obtained by: (*i*) molybdenum evaporation and annealing in UHV conditions, (*ii*) molybdenum evaporation and annealing in standard technological conditions, with and without an encapsulating layer. We have found that basic mechanism of molybdenum silicide formation is equivalent in both cases. The well-known nodular structure, at high temperature, is always present. In the technological samples, oxygen segregation to the silicide-encapsulant interface occurs.

390 Oxygen Control and Intrinsic Gettering in CZ Silicon: *R. B. Swaroop** and *T. Fish*, Siltec Corp., Mountain View, CA 94043

Czochralski grown silicon wafers with varying interstitial oxygen content have been investigated for intrinsic gettering. Denuded zone width (DZW) from 10 to 50 microns have been reproduced using high-low-high thermal cycles. The effects of time, temperature, and environment on DZW and nucleation have been studied. At low interstitial oxygen contents (~30 ppma),[1] gettering can be enhanced using extrinsic damage on the back side of the wafer.

[1](ASTM: F121-79.)

391 Short Time Annealing of Coevaporated Tungsten Silicide Films: *T. O. Sedgwick,* F. M. d'Heurle*, and *S. A. Cohen*, IBM T. J. Watson Research Center, Yorktown Heights, NY 10598

Short time annealing of WSi_2 films can significantly reduce the time-temperature processing cycle in device fabrication while achieving high conductivity. Samples of 1300Å thick coevaporated WSi_2 deposited on single crystal silicon were annealed in a graphite strip heater in argon for 3-300 sec, and at temperatures of 1000°-1200°C. The silicide achieves low resistivity in lines as short as 3 sec and at 1200°C. The apparent low resistivity of 3.1 Ω/sq was reached in 3 sec.

392 Low Temperature Diffusion of Arsenic in Polycrystalline Silicon Films: *M. Arienzo,* Y. Komen* (Permanent address: Dept. of Materials Engineering, The Technion, Haifa 32000, Israel), and *A. E. Michel*, IBM T. J. Watson Research Center, Yorktown Heights, NY 10598 and *R. H. Kastl*, IBM East Fishkill Facility, Hopewell Junction, NY 12533

Layered structures consisting of doped and undoped polysilicon films were deposited on (001) p-type silicon substrates. The films were formed at atmospheric pressure by the thermal decomposition of silane at 650°C. These structures provide a vehicle for the study of the low temperature diffusion in polycrystalline silicon which occurs predominantly along grain boundaries. Secondary ion mass spectrometry is used to monitor the arsenic redistribution and transmission electron microscopy to examine the microstructure of the layers.

393 Accelerated Testing for Silicon Dioxide Breakdown: *W. Weick*, Bell Laboratories, Murray Hill, NJ 07974

Field-induced breakdown of silicon dioxide films between 150 and 650Å in thickness was studied with elevated constant stress and step-stress tests. Exposure to elevated fields caused changes in the oxide even where breakdown was not observed. Field accelerates breakdown, and an exponential distribution is given. The time-breakdown distribution had a high standard deviation. A Duane plot, showing cumulative failure rate *vs.* time smooths the data and the slope provides the instantaneous failure rate.

394 Charge Tunneling and Trapping and Trap Generation in Thin SiO_2: *C. Chang,* M.-S. Liang, C. Hu*, and *R. W. Brodersen*, Dept., of Electrical Engineering and Computer Sciences, University of California, Berkeley, CA 94720

Thermal SiO_2, 40-50Å, with poly-Si electrodes has been studied. Our theoretical model accurately predicts the tunneling I-V characteristics, which exhibit polarity dependence and a dramatic break at about 4V. Tunneling stress generates electron traps, acceptor-type interface traps (states), and causes hole trapping at the anode interface. These different charges have been separated for the first time and correlated to inversion mobility degradation and other MOSFET instabilities and are apparently responsible for intrinsic oxide wearout and EEPROM fatigue.

395 Generalized Technique for Measuring Specific Contact Resistance: *D. L. Meier** and *P. Rai-Choudhury*, Westinghouse R and D Center, Pittsburgh, PA 15235

A test pattern for measuring the resistance associated with the semiconductor/contact interface for source and drain contacts in VLSI devices has been developed and analyzed. This technique is particularly suitable for the measurement of silicide contacts where some underlying silicon is consumed in the formation of the silicide and where the resistance of the thin contact layer is not negligible. Measurements have been made on several contact systems, including $TiSi_2$ and Pd_2Si on diffused silicon.

396 A Novel Method for Measuring Low-Dose Implants: *M. J. Markert,* D. S. Perloff*, and *E. Lee*, Signetics Corp., Sunnyvale, CA 94086

A novel method which is fast, accurate, and inexpensive, extends the usefulness of sheet resistance measurements to implant doses well below 10^{11} ions/cm^2. The method uses materials and equipment readily available in most wafer fabrication areas. Using a four-point probe and a calculator, one may obtain dose values within minutes of removing the ordinary silicon test wafer from the implanter. Using automated wafer probing equipment, the data produced are suitable for uniformity mapping.

397 Scanning Auger Microscopy for Surface Potential Profiling of HV Devices: *D. M. Taylor, D. W. Tong,** and *W. R. Van Dell*, General Electric Corporate Research and Development, Schenectady, NY 12301

Scanning Auger microscopy is used to nondestructively measure the steady-state surface potential distribution of thin-film passivated semiconductor devices at biases over 1000V. The Auger electron energy peaks associated with surface atoms are identified and their shift from the zero bias point is directly related to the local surface potential. Two-dimensional profiling is possible with a spatial resolution of a few micrometers and a voltage resolution of better than 10V. Measurements are made on a power transistor and compared to computer-predicted profiles.

398 Structural Analysis of Silicon Implanted Polymethyl Methacrylate Films on Glass: *C. E. Bleil** and *B. A. MacIver*, General Motors Research Laboratories, Electronics Dept., Warren, MI 48090-9055

Recent developments in our laboratory have led to the formation of silicon-implanted polymethyl methacrylate films on glass for photo masking. They are opaque, chemically inert, hard, and more adherent than chromium. Differential etching in an oxygen plasma reveals a slowly etching phase in relief. Reflection electron

diffraction shows amorphous carbon to predominate near the surface, polycrystalline graphite and hexagonal diamond structures in the bulk, and silicon carbide near the film-glass interface.

399 A Rapid Method of Sampling Polycrystalline Silicon for Determination of Phosphorus, Boron, Arsenic, and Aluminum by Photoluminescence Analysis: *W. F. Tucker,* L. C. Winterton, P. L. Clem, Jr.,* and *B. D. Stone,* Monsanto Co., Electronics Div., St. Peters, MO 63376

With the introduction of photoluminescence analysis of single crystal silicon, old lengthy indirect methods seem less attractive. A method for sampling large diameter Siemens process polysilicon, followed by pedestal crystal growth to obtain a monocrystalline sample suitable for photoluminescence analysis, has been developed. This procedure provides a rapid straightforward means for the direct determination of boron, phosphorus, aluminum, and arsenic in polycrystalline silicon. Details of the sampling and pedestal-pulling techniques are presented along with a statistical description of the precision and accuracy of the method.

400 A Comparison of Donor and Acceptor Levels in Silicon as Determined by Infrared and Photoluminescence Analyses: *H. Mollenkopf,* Hemlock Semiconductor, Hemlock, MI 48626, and *L. Shive,** Monsanto Co., St. Peters, MO 63376

Infrared analysis and photoluminescence analysis have been used to determine donor and acceptor levels in a set of electronic grade silicon samples. The goal of this work was to compare the data from the infrared method, which looks through the bulk, and the PL method, which goes only *ca.* 50-100 μm into the bulk, and establish a correlation between them. We describe the results from this study.

401 Relation Between Two-Probe and Four-Probe Resistances on Nonuniform Structures: *H. L. Berkowitz,* U. S. Army Electronics Technology and Devices Lab, ERADCOM, Fort Monmouth, NJ 07703, and *J. Albers,** Semiconductor Devices and Circuits Div., National Bureau of Standards, Washington, DC 20234

A general relation between the two-probe spreading resistance and the four-probe resistance on nonuniform structures is derived. Numerical techniques are presented and discussed for the evaluation of the equations for nonuniform structures. The relation between the four-probe resistance and the incremental sheet resistance is shown to arise in the limit as the probe spacing becomes large compared to the distance to an insulating boundary. Also presented is a method for the self-consistent calibration of spreading resistance profiles.

402 Terminator Open-Short Reliability Testing: *S. Carbone,* J. Granda,* and *A. Sarkhel,* IBM Corp., Poughkeepsie, NY 12602

Multilayered ceramic modules are electrically tested in fluorocarbon cooling fluid for circuit continuity, using 0.18 mm tungsten probes. Invariably higher resistance readings (16-10$^{10}\Omega$) occurred as the probes were moved from one test site to another. An investigation of module surface contaminants, internal metallic structure, contaminants and surface analysis of probes, and the electrical tester spring actuation system unveiled the problem. An oxide film formed on the probes and was detected by a unique electrical sensing system. Confirmation was by Auger analysis. A reliability improvement of 1000X was achieved when a specialized palladium alloy was substituted for tungsten.

403 Infrared Studies of Silicon: *D. G. Mead,* Nicolet Instrument Corp., Madison, WI 53711

The use of infrared absorption measurements to characterize silicon is reviewed. Examples include (*i*) the radial profiling of substitutional carbon and interstitial oxygen, including precipitates, (*ii*) the detection of dopants as antimony, arsenic, boron and phosphorus, and (*iii*) the depth of the denuded zone region. The problems associated with such methods are highlighted, including photometric accuracy, and the needs for standardization are discussed.

404 On the Resistance Switching in Polycrystalline-Silicon Resistors: *C. Y. Lu,** Institute of Electronics, National Chiao-Tung University, Hsin-Chu, China, *N. C. C. Lu,* IBM T. J. Watson Research Center, Yorktown Heights, NY 10598, and *C. C. Shih, M. K. Lee,* and *C. S. Wang,* Institute of Electronics, National Chiao-Tung University, Hsin-Chu, China

Irreversible resistance reduction in highly resistive polysilicon resistors has been utilized in MOS PROM's. Low resistive polysilicon fuses have been employed in redundancy design. This paper reports the resistance switching in both the boron- and arsenic-doped LPCVD polysilicon resistors in various lengths, with doping levels ranging from 1×10^{16} to 1×10^{19} cm^{-3} and film thickness ranging from 0.1 to 1.0 microns. After being applied by a voltage, resistors can be either blown open or converted to a more conductive state by a factor of 10^7. The voltage and current at transition and the resistance after transition strongly depend on the doping level and species, film thickness, resistor length, and applied power level. A physical model is proposed to interpret the effects of these parameters on the switching.

405 Threshold Shift from As-Implantation of SiO_2: *R. Kazerounian** and *W. G. Oldham,* Dept. of Electrical Engineering and Computer Sciences, and the Electronics Research Laboratory, University of California, Berkeley, CA 94720

Anomalous negative threshold shifts are observed following annealing of thin oxides implanted with arsenic. Thermally grown oxide (650Å) is implanted with A_s^{+75} at 25 keV ($R_p \cong 150$Å, $\Delta R_p \cong 50$Å) with a dose of 10^{13}/cm^2. After annealing at ($T \leq 1000°C$, $t \leq 20$ min), a negative threshold shift of up to -5V is observed for n$^+$ polysilicon gate structures. Other experiments suggest penetration of the oxide by arsenic, despite the predictions of LSS scattering and As diffusion. (Research sponsored by the Defense Advanced Research Projects Agency under Contract number N00039-81-K-0251.)

406 Very Shallow Ion-Implanted Boron Junction: *T. M. Liu** and *W. G. Oldham,* Electronic Research Laboratory, Dept. of Electrical Engineering and Computer Sciences, University of California at Berkeley, Berkeley, CA 94720

Unintentional ion channeling in low energy boron ion implantation into silicon results in much deeper junctions than predicted by LSS theory, even for wafers tilted 8° from the normal. This partial channeling effect is examined by a calculation of the angular spreading for boron ion in silicon. Experiments show that the deep penetration tail is present even for BF_2^+ implant but may be suppressed by a silicon preimplant to drive the silicon surface amorphous. By this means, very shallow high concentration p$^+$n junction may be achieved. (Research sponsored by the Defense Advanced Research Projects Agency under Contract number N00039-81-K-0251.)

407 A Process-Parameter Model for the Lateral Junction Contour of Double-Diffused Gaussian Profiles: *J. P. Zigadlo,** Eastman Kodak Company, KAD-IC Fabrication, Rochester, NY 14650, and *G. M. Oleszek* and *K. L. Kasley,* Dept. of Electrical Engineering, Microelectronics Laboratory, University of Colorado, Colorado Springs, CO 80907-7150

In high-density, large-scale integrated circuits, device and circuit performance are to a large degree determined by the lateral distributions of the dopant impurities. As demand for circuit density continues to increase, it becomes increasingly necessary to accurately know the final geometry of fabricated structures which include the lateral outdiffusion of dopants. Design rules which include a large margin of error for lateral junction depth are not acceptable. The purpose of this work was to develop an analytical process-parameter model for the lateral junction contour of a Gaussian type diffusion into a nonuniform (Gaussian) background concentration. It was determined that the ratio of maximum lateral junction depth to maximum vertical junction can be written as the product of two factors: the first factor accounts for the two-dimensional nature of the diffusion process; the second results from the nonuniform nature of the background concentration. A simplified closed form expression was obtained for the lateral junction contour which is applicable for process and device modeling.

408 Avalanche Breakdown Voltages in Semiconductor Junctions: *K. Shenai,* Advanced Microwave Techniques Dept., COMSAT Laboratories, Clarksburg, MD 20871

Avalanche breakdown voltage and peak electric field at breakdown are computed as functions of junction depth and background doping concentration for Ge, Si, and GaAs semiconductor parallel-plane junctions. Two types of junctions are considered with Gaussian and erfc impurity profiles. The results are based on a closed form solution of the static Poisson's equation in the depletion layer. The orientation dependence of avalanche breakdown in GaAs is shown to be significantly different between abrupt junctions with uniform carrier concentration and the junctions with nonuniform doping distributions.

409 Collector-Emitter Leakage Caused by Highly As-Doped Emitter and Recessed Oxide Isolation: *M. Taguchi, G. Sasaki, A. Menjo,* and *K. Kanzaki,* Toshiba Semiconductor Div., and Toshiba Semiconductor Device Engineering Laboratory, 1, Komukai, Toshibacho, Saiwai-ku, Kawasaki, Kanagawa 210, Japan

One of the main yield limiting mechanisms in the fabrication of bipolar integrated circuits is collector-emitter (C-E) leakage. The marked increase of C-E leakage was found in the bipolar transistors with highly arsenic-doped emitter and deeply recessed oxide isolation structure. The leakage is caused by arsenic pipe diffusion along dislocation, and the dislocation generation is explained by the combined stress effect of high arsenic doping in Si and recessed oxide structure. The details of experimental results and process optimization to reduce the leakage are discussed.

410 Empirical Relationships Between Carrier Mobility and Carrier Concentration in Arsenic-, Phosphorus-, and Boron-Doped Silicon: *G. Masetti,* Department of Electronics, University of Ancona, Ancona, Italy, and *M. Severi* and *S. Solmi,** CNR-Istituto LAMEL, 40126, Bologna, Italy

New mobility data for arsenic-, phorphorus-, and boron-doped silicon in the carrier concentration range 10^{19}-5×10^{21} cm^{-3} are presented. The highest concentrations were achieved by laser annealing of ion implanted samples. The data definitely show that the electron mobility in As-doped silicon is significantly lower than in P-doped silicon, for carrier concentrations higher than 10^{19} cm^{-3}. Furthermore, for all the three dopants, mobility depends only on carrier concentration and continuously decreases as carrier concentration increases. Empirical relationships able to model the carrier mobility against carrier concentration in the whole experimental range examined up to date for As, P and B are derived. These new expressions, once implemented in the SUPREM II program, lead to reduced errors in the simulation of the sheet resistance.

411 Effect of Surface Beveling on Carrier Profiles: *J. Albers** and *C. L. Wilson*, Semiconductor Devices and Circuits Div., National Bureau of Standards, Washington, DC 20234, and *J. L. Blue*, Scientific Computing Div., National Bureau of Standards, Washington, DC 20234

The two-dimensional potential distribution is calculated for a beveled structure by means of finite-element techniques. The calculations are presented for several forms of the dopant distribution as well as a number of choices of the surface recombination velocity. The effects of both of these variables on the location of the electrical junction are presented with particular attention to the implications to electrical profile measurements. The principal result of this calculation is that the total depletion width goes to zero where the junction intersects the beveled surface.

412 Effects of Autodoped Aluminum on MOSFET Characteristics in SOS Double Solid-Phase Epitaxy: *S. Taguchi** and *M. Nakahara*, Semiconductor Device Engineering Laboratory, Toshiba Corp. 72, Horikawa-cho, Saiwai-ku, Kawasaki, 210 Japan, *T. Yoshii*, Integrated Circuits Laboratory, R and D Center, Toshiba Corp. 72, Horikawa-cho, Saiwai-ku, Kawasaki, 210 Japan, and *K. Maeguchi* and *H. Tango*, Semiconductor Device Engineering Laboratory, Toshiba Corp. 72, Horikawa-cho, Saiwai-ku, Kawasaki, 210, Japan

Double solid phase epitaxial technique (DSPE) is a key technology for the submicron CMOS/SOS VLSI's. Aluminum impurities were proved to be introduced into the silicon film from the irradiated sapphire surface during DSPE process by SIMS analysis. The behavior of threshold voltages, effective mobilities, and drain leakage currents in n- and p-channel MOSFET's on both 0.3 μm thick as-grown and DSPE films was investigated. As a result, these device parameters were found to be affected by the electrically active aluminum. In order to minimize the aluminum autodoping, silicon ion implantation and subsequent thermal annealing conditions were studied from the viewpoint of optimization of the DSPE process.

413 Control of Polycrystalline-Silicon Resistor by Implantation of N_2^+: *H. Hayashi,** *H. Yamoto*, and *T. Ohshima*, Sony Corp., Semiconductor Group, 4-14-1 Asahi, Atsugi 243, Japan

A new method for the control of polycrystalline-silicon resistor has been developed by use of N_2^+ implantation. Polycrystalline-silicon films were deposited on top of a layer of thermal SiO_2 grown on a silicon wafer. After nitrogen atoms were implanted into the polycrystalline-silicon film, the film was annealed in N_2 ambient. The dose of N_2^+ and annealing temperature were varied from 10^{14} to 10^{17} cm^{-2} and from 800° to 1000°C, respectively. The resistivity of polycrystalline-silicon films has been controlled in the range of 10^8-10^{11} Ω/sq which is in a suitable range for the resistor of MOS s-RAM.

414 The Effect of Deposition Temperature and Rate upon the Structure of LPCVD Silicon: *J. T. McGinn** and *J. Shaw*, RCA Laboratories, Princeton, NJ 08540, *H. F. Kuppert*, University of Dortmund, Dortmund, Germany, and *L. Krausbauer* and *A. E. Widmer*, Laboratories RCA, Ltd., Zurich, Switzerland

Undoped and *in situ* doped LPCVD silicon films deposited between 560° and 640°C using SiH_4 flow rates between 30 and 200 cm^3 min^{-1} have been characterized using cross-sectional and planar TEM, as well as x-ray techniques. The microstructure of these films is shown to be strongly dependent upon the deposition conditions. Two distinct mechanisms for silicon adatom incorporation into these films are shown to be operative in this temperature range. The effects of temperature upon the structure of the as-deposited film are compared to that of increased growth rate, resulting from increased SiH_4 flow rate.

415 High Quality Polysilicon by Amorphous LPCVD Growth: *G. Harbeke, E. F. Steigmeier*, and *A. E. Widmer**, Laboratories RCA Ltd., Zurich, Switzerland

Undoped and *in situ* phosphorus doped LPCVD polysilicon films grown at temperatures from 560° to 650°C have been studied by Raman and elastic light scattering, optical absorption and reflection, and other techniques to gain information on structure, crystallinity, strain, surface roughness, and electrical conductivity. We show that films of highest quality in terms of structural perfection and surface roughness are obtained by deposition in the amorphous phase and subsequent thermal crystallization.

416 LPCVD Deposition of P-Doped Polysilicon: *D. L. Flowers*, Motorola, Inc. SPS, Process Technology Laboratory, SRDL, Phoenix, AZ 85008

An *in situ*, phosphorus-doped, low pressure, polysilicon deposition process has been studied yielding specular films with an electrically active phosphorus concentration as high as 6.6×10^{19} cm^{-3}. Deposition rates are >1000Å per hour and thickness uniformity across 100-75 mm wafer loads is as low as 5.2% 2σ. The thickness spread across the load is <200Å.

417 Continuous CVD: A New Type of Silicon Epitaxial Reactor: *D. Bellavance** and *R. N. Anderson*, Texas Instruments Inc., Dallas, TX 75265

A new type of silicon epitaxial reactor has been designed and constructed in which the silicon wafers are processed through the reactor in a continuous, rather than a batch, mode. The reactor consists of a series of chambers which are effectively isolated from one another. Each chamber contains one step in the epi process. The silicon wafer is moved sequentially through the chambers for the complete epitaxial process. This new design makes it possible to establish and maintain deposition conditions at equilibrium for abrupt interfaces, multiple layer depositions, and reproducible epi thicknesses and carrier concentrations while maintaining the uniformity of single slice processing.

418 Low Pressure CVD of a Stibinosilicate Glass: *F. Pintchovski, P. J. Tobin*, and *J. B. Price*, Motorola, Inc., Integrated Circuits Div., Mesa, AZ 85202

This paper describes the low pressure CVD (LPCVD) of an antimony-doped glass (stibinosilicate glass) to be used as a diffusion source. The glass was deposited at 360°C and 0.6 Torr from silane, oxygen, and trimethyl antimony (a high vapor pressure liquid). Films were deposited with a thickness ranging from 200 to 1500 Å and an antimony concentration from 3 to 20 w/o antimony. It was observed that incorporation of antimony significantly decreased the deposition rate of the glass. Deposition parameters and film properties are discussed.

419 Metal-Organic Low Pressure Chemical Vapor Deposition of Al: *M. L. Green,** *R. A. Levy, R. G. Nuzzo*, and *E. Coleman*, Bell Laboratories, Murray Hill, NJ 07974

We have produced Al films by low pressure chemical vapor deposition, via the pyrolysis of tri-isobutylaluminum, and have characterized them extensively. The films, which are composed of grains ~1-3 μm in size, can have either a (100) or (111) texture, depending upon growth conditions. Film resistivity is 3.0-3.5 $\times$ 10^{-6} Ω-cm. The films have surface roughness on the order of 1500Å, which renders them milky-white in appearance. The effects of growth parameters on film properties are discussed.

420 Selective Low Pressure Chemical Vapor Deposition of Tungsten: *E. K. Broadbent,** Signetics Corp., Philips Research Laboratories, Sunnyvale, Sunnyvale, CA 94086, and *C. L. Ramiller*, Applied Materials Applications Laboratory, Santa Clara, CA 95051

Potential integrated circuit applications for tungsten thin-films prompted a fundamental study of the reaction mechanisms involved in low pressure chemical vapor deposition of this material. The LPCVD process allows for selective deposition on certain substrate materials. This paper discusses the reactions of WF_6 with H_2 and Si for a temperature range of 200°-500°C in a low pressure regime (0.1-5 Torr). The deposition kinetics and physical structure of tungsten films on various substrates are presented.

421 Limitations of SIPOS-Insulator Passivation: *R. D. Plummer*, Bell Laboratories, Reading, PA 19603

The ability of SIPOS, insulator passivation schemes, to protect the silicon surface from outside disturbances is frequently limited by insulators rather than the SIPOS. For passivation, the silicon surface must be capable of injecting into the SIPOS film with only minor disturbances of the silicon surface. When surface generation is unable to supply sufficient current to compensate for insulator leakage, the passivation protection ends.

422 Electrical Properties of SIPOS-Si_3N_4 Bilayers: *D. W. Tong,** *D. M. Taylor*, and *S. J. Rzad*, General Electric Co., Corporate Research and Development Center, Schenectady, NY 12301

Measurements of the d-c and a-c behavior (including C-V measurements) of semi-insulating polycrystalline silicon (SIPOS)-Si_3N_4 bilayers have been carried out. Based on these measurements, as well as those carried out on single SIPOS and nitride layers, it is shown that the bilayers can be modeled as lossy dielectrics, having associated capacitances and conductances that are both frequency and voltage dependent. The results imply that interface effects are not important in the bilayer conduction.

423 Structural and Electrical Properties of Photo-CVD Silicon Nitride Film: *Y. Numasawa,** *K. Yamazaki, K. Hamano*, and *K. Kobayashi*, Nippon Electric Co., Ltd., Process Development Dept., VLSI Development Div., 1120, Shimokuzawa, Sagamihara, Kanagawa 229, Japan

Silicon nitride films formed by mercury-sensitized photochemical reaction of SiH_4 and NH_3 were studied on their Si-H and N-H bond densities and their MIS diode characteristics in particular with respect to their deposition temperature/annealing temperature dependence. Infrared analysis showed that the films contain Si-H and N-H bonds of ~10^{21} cm^{-3}, respectively. Si-H bond density decreases with deposition temperature increase, while N-H bonds exhibit no marked dependence. Measurement results on the MIS diode characteristics are also presented.

424 Dielectric Relaxation and Charging and l/f Flicker Voltage Noise in Silicon Nitride Thin Insulating Films: *E. Siegel*, San Francisco, CA 94118

The time-independent, static limit of synergetics is used to evaluate the contribution of defect induced disorder to dielectric relaxation, loss and charging, and to l/f flicker voltage noise in silicon nitride thin film insulators. Utilizing the universal dielectric response/relaxation theory and experimental correlation technique of Jonscher (1) combined with the universal l/f flicker noise theory of Ngai (2) via infrared divergence combined with the universal collective-mode-softening driven by defect disorder of Siegel (3) these functional properties of silicon nitride thin insulating films are reversibly connected in an experimental model to the measurement of defect density induced disorder via external radiation

(x-ray, electron, neutron) scattering static structure factor diffraction pattern S(k).

1. A. Jonscher, *Physics of Dielectric Solids*, I.O.P. **58**, 22 (1980).
2. K. L. Ngai, *Commun. Sol. State Phys.*, **4**, 127 (1979); **9**, 5, 141 (1980).
3. E. Siegel, *J. Non-Cryst. Solids*, **40**, 453 (1980).

425 Characterization of Dielectric $BaTiO_3$ Thin Films Using Electrolyte Contacts: *T. L. Rose,* E. M. Kelliher, A. N. Scoville, S. E. Stone,* and *S. B. Brummer,* EIC Laboratories, Inc., Newton, MA 02158

Thin films of $BaTiO_3$ are being evaluated for use as capacitor electrodes for *in vivo* neural stimulation because of the high dielectric constant of $BaTiO_3$. The films were deposited on Pt and Ti substrates by rf sputtering. The a-c bridge capacitance and d-c leakage current of the films were measured using dilute phosphate buffered saline electrolyte as the top contact. The effect of substrate temperature during deposition, post-deposition heat-treatment, and film thickness on the morphology and measured electrical properties of the films was determined. (This work was supported by the National Institute of Neurological and Communicative Disorders and Stroke, National Institutes of Health, under Contract No. N01-NS-1-2356.)

426 Electrochromism in the Anodic Oxides of Molybdenum and Tungsten: *J. L. Ord,* Dept. of Physics, University of Waterloo, Waterloo, Ont., Canada N2L 3G1

Ellipsometric studies of electrochromism in the anodic oxides of molybdenum and tungsten show that film conversion takes place by different processes in the two systems. In molybdenum oxide, an interface separating bleached and colored layer sweeps across the film, whereas in tungsten oxide coloring and bleaching take place more or less uniformly throughout the oxide film. The results of a recent ellipsometric study of the two systems show that their behavior is more complex than was originally thought.

427 Silane Oxidation Studies: Analysis of LTCVD SiO_2 Film Deposition Data: *C. Cobianu* and *C. Pavelescu,* R and D Center for Semiconductors (CCSITS), R-72996, Bucharest, Romania

Recently, the bimolecular surface reactions theory has been used to explain the kinetics of LTCVD SiO_2 film deposition (1). The purpose of this paper is to determine the rate constant of reaction (k_r) and the equilibrium constants of oxygen (K_{O_2}) and silane (K_{SiH_4}) adsorption on the surface based on the fit of the experimental dependence of deposition rate on CVD conditions to theory. The results obtained are discussed in terms of: (i) an exponential temperature dependence of k_r with an activation energy close to that reported earlier and (ii) a temperature dependence of K_{O_2} and K_{SiH_4} which involves a transition in the adsorption process of reactant species from physical adsorption to chemisorption with temperatures increasing over 200°C.

1. C. Cobianu and C. Pavelescu, Paper 208 presented at The Electrochemical Society Meeting, Montreal, Canada, May 9-14, 1982.

428 Step Coverage Simulation and Measurement in a D-C Planar Magnetron Sputtering System: *I. A. Blech* and *H. A. Vander Plas,** Xerox Corp., Palo Alto Research Center, Palo Alto, CA 94304

Thin metallic films such as aluminum are used as electrical conductors in integrated circuits. In order to insure device reliability, it is essential that these films adequately cover all the surface features or steps on the circuit. Increasing the density of circuit elements in an integrated circuit requires that the surface features be more vertical and that the width of these features decrease. Both of these trends increase the problems associated with step coverage. In this paper, the step coverage of d-c planar magnetron sputtering system with a revolving substrate is analyzed by both computer simulation and measurement of the step coverage. The model assumes line of sight deposition, no reemission, and the cosine growth law. Good quantitative agreement has been obtained between the model and the experiments. The modeled system does not show the deep cracks typical of the planetary system. This is explained by comparing the vapor distribution functions of the planetary and the sputtering systems.

429 Reactively Sputtered Ti_xC Thin Films—Preparation and Properties: *M. Eizenberg** and *S. P. Murarka,* Bell Laboratories, Murray Hill, NJ 07974

The low resistivity and refractory nature of titanium carbide makes it potentially useful as a diffusion barrier in thin film metallization schemes. In the present investigation, deposition and properties of thin Ti-C films have been investigated. The films were prepared by reactive rf sputtering in methane-argon mixtures on a variety of substrates. The effects of methane to argon ratio, total sputtering pressure, and power on the film deposition rate, composition, and properties were determined. The results are presented and discussed.

430 Dry Etching with U.V. Light Irradiation: *H. Okano, Y. Horiike,* and *M. Sekine,* Toshiba Corp., Research and Development Center, IC Laboratory, Kanagawa 230, Japan

A dry etching approach which does not require charged particles has been investigated using u.v. light excitation method. The undoped poly-Si under the irradiation by focused Hg-Xe lamp is anisotropically etched in Cl_2 atmosphere (10 Torr). The result demonstrates that the present etching proceeds by a photo irradiation assisted reaction, which is analogous to the ion assisted chemical etching in RIE process. Accordingly, the poly-Si was successfully etched without resist by transferring the IC mask pattern exposed to Hg-Xe lamp.

431 Preferential Etching of Multilayered Chromium and Copper Based on the Electrochemical Technology: *M. Morijiri,* M. Fuyama,* and *M. Hanazono,* Hitachi Ltd., Hitachi Research Laboratory, Kujimachi 4026, Hitachi-city, Ibaraki pref. 319-12, Japan

In microcircuit fabrication technology Cr-Cu-Cr triplex metal films are used as conductors of interconnections. Fine patterns of Cr-Cu-Cr films are chemically etched. It is necessary to select a solution for etching only Cr coexistent with Cu, and another solution for etching only Cu coexistent with Cr. In this study the electrochemical properties of Cr and Cu in various solutions were studied. Results show that the solution containing potassium ferricyanide is suitable for etching Cr film and the solution containing ammonium persulfate is suitable for etching Cu film.

432 The Influence of Substrate Temperature and Annealing on AlN Films Deposited by Reactive RF Magnetron Sputtering: *A. Fathimulla** and *A. A. Lakhani,* Bendix Advanced Technology Center, Columbia, MD 21045

Reactive magnetron sputtering was used to deposit films of aluminum nitride on n-silicon. The influence of the substrate temperature (25°-300°C) on the electrical properties of the AlN films was investigated. Films deposited at low temperatures generally exhibited lower bulk resistivities compared with those deposited at temperatures above 200°C. Annealing of the films between 300° and 500°C for 1-60 min yields device quality films with bulk resistivity > 10^{15} Ω-cm, V_{FB} of 0.85V and an interface state density, n_{ss} of 2×10^{11} cm^{-2} at midgap. The chemical composition of the film by AES analysis is also presented.

433 Paper withdrawn.

434 Electromigration Capacity and Microstructure of Layered Al/Ta Film Conductor: *K. Hinode,* S. Iwata,* and *M. Ogirima,* Hitachi Ltd., Central Research Laboratory, Kokubunji, Tokyo 185, Japan

By heat-treating above 400° C, Al/Ta layered conductors showed better electromigration capacity than usual Al · Cu alloy conductors. The lifetime of the layered conductor was found to be strongly affected by the film deposition condition. Film microstructures (mainly grain sizes and grain boundary structures) were investigated by TEM and compared with the electromigration lifetimes. It was shown that Ta diffusion and Al_3Ta phase formation were enhanced by improving the deposition condition, and consequently the conductor lifetime increased.

435 A Two-Layer Gold Metallization Process: *D. Summers,* Tektronix, Inc., Beaverton, OR 97077

A two-layer gold metallization process has been developed as part of a bipolar VLSI program. The gold interconnect lines for both first and second levels are formed by electrochemical plating within the openings of a patterned photoresist layer. Nominal metal pitch is 4 μm. The interlayer dielectric is a plasma-deposited silicon dioxide. Vias are plasma etched anisotropically to a minimum geometry of 2.5 × 2.5 μm. An overall description of the process and structure is presented and includes comments on some of the unique features and problems characteristic of this process.

436 Thin-Film Interactions of Al and Al (Cu) on W and Ti: *I. Krafcsik, C. J. Palmstrom,* J. Gyulai, E. Colgan, E. Zingu,* and *J. W. Mayer,* Materials Science and Engineering, Cornell University, Ithaca, NY 14853

Rutherford backscattering and glancing-angle x-ray diffraction have been used to study the influence of Cu in Al-refractory metal interactions. In the temperature range between 400°-500°C, the presence of Cu in Al retarded the penetration of W in Al. In the Al-Ti system, the compound $TiAl_3$ was formed. With Cu-free Al the activation energy was 1.9 ± 0.1 eV. The presence of Cu retarded the reaction and caused an increase in activation energy.

437 Aluminum Intrusions or "Rat Bites": *P. S. Gwozdz** and *H. M. Bath,* Advanced Micro Devices, Sunnyvale, CA 94086

Intrusions in aluminum patterns are found to be dependent upon the metal deposition method, the heat-treatment of the deposited film, and the type of photoresist used. The density of very narrow regions (necks) in the pattern is calculated from the density of intrusions; the calculated neck density is confirmed by inspection. The statistics of early electromigration failure due to necks demonstrate that even a low density of intrusions can be a problem. We conclude that intrusion free processing is necessary and possible.

HIGH TEMPERATURE MATERIALS

High Temperature Materials Chemistry

438 Molecular Species in the As-O System: *R. D. Brittain, K. H. Lau,** and *D. L. Hildenbrand,* SRI International, Menlo Park, CA 94025

A surprisingly large number of stable molecular species including As_4O_6, As_4O_5, As_4O_3, As_2O_3, AsO_2, AsO, and perhaps As_2O_4 were identified by high temperature mass spectrometry in the vapors over various arsenic oxide condensed phases under saturated and unsaturated conditions in the range 370-1700 K. Vapor species were characterized largely from extensive appearance potential (AP)

measurements. Explanations of the temperature dependence of the threshold AP on As_3O_4 species and effects of temperature on the mass spectra of complex As-O species are discussed.

439 Transpiration Mass Spectrometry of Potassium Salt Systems: *J. W. Hastie,* K. F. Zmbov,* and *D. W. Bonnell,* National Bureau of Standards, Washington, DC 20234

The novel technique of transpiration mass spectrometry is described and new vapor pressure data are given for liquid KCl, KOH, and related systems. Unusual phenomena relating to the formation of cold molecular beams, such as temperature dependent electron impact ionization and molecular clustering, is also discussed. No major differences between the present results and the JANAF-evaluated data were found for the KCl system, but major differences occur with the KOH system.

440 Nucleation and Condensation of Fe, Si, Fe/Si, FeO_x, and SiO_x Vapors: *J. R. Stephens,** Los Alamos National Laboratory, Los Alamos, NM 87545, and *S. H. Bauer,* Dept. of Chemistry, Cornell University, Ithaca, NY 14853

Avalanche condensation temperatures and pressures, and cluster fluxes for homogeneously nucleated Fe, Si, Fe/Si, FeO_x, and SiO_x vapors are reported, and the results compared to a kinetic nucleation theory based on partition functions. Mixtures of $Fe(CO)_5$ and/or SiH_4 in Ar, N_2O/Ar, or H_2/N_2O/Ar were pyrolyzed behind reflected shocks. The cluster flux and condensation point were determined by particle scattering and turbidity in the subsequent expansion fan. Supersaturation ranged from 10 for Fe to several orders of magnitude for SiO_x, in substantial disagreement with the conventional classical and Lothe-Pound nucleation theories.

441 Preparation of Ductile Nickel Aluminides for High Temperature Uses: *C. T. Liu,* C. C. Koch,* and *C. L. White,* Metals and Ceramics Div., Oak Ridge National Laboratory, Oak Ridge, TN 37830

The nickel aluminide, Ni_3Al, is strong and stable at elevated temperatures; however, low ductility and brittle fracture restrict its use for structural applications. Microalloying has been employed to overcome the embrittlement associated with grain-boundary separation. Among the dopants added, boron has been found to be most effective in improving fabricability and ductility of polycrystalline Ni_3Al. Tensile elongation of >50% has been achieved at room temperature by control of boron concentration and thermomechanical treatment. The boron-doped Ni_3Al shows excellent strength and oxidation resistance at high temperatures. (This research was sponsored by the Division of Materials Sciences, U.S. Department of Energy under contract W-7405-eng-26 with the Union Carbide Corporation.)

442 Synthesis of Refractory Oxide Materials by Skull Melting: *C. C. Herrick* and *R. G. Behrens,** Los Alamos National Laboratory, Los Alamos, NM 87544

The technique of skull melting is a cold-crucible technique for melting large quantities of refractory materials. The technique was successfully developed by Aleksandrov and co-workers at the P. M. Lebedev Physical Institute in Moscow, and has been adapted and used at the Los Alamos National Laboratory to synthesize large (kilogram) quantities of high purity oxides. The present paper describes some of the oxide materials synthesized by this technique and discusses in detail the apparatus, technique, and results obtained for preparing large, high purity single crystals of UO_2 and ThO_2 from the melt. Experiments in which the equilibrium distribution of Y_2O_3 between solid and liquid UO_2 was investigated are also briefly discussed.

443 The Kinetics of the Gas/Solid/Liquid Reaction: *W. H. Siekhaus, M. Balooch,** and *D. R. Olander,* University of California, Berkeley, CA 94720

The reaction of molecular chlorine with liquid and solid In, Pb, Sn were studied by modulated molecular beam-mass spectrometric methods. InCl, $PbCl_2$ $SnCl_2$ were the only detectable volatile reaction products: Their production rates increased abruptly at the melting points being more pronounced for In. The surface coverage of chlorine was determined as a function of chlorine beam and surface temperature in a separate study. Reaction models based on dissociative absorption of chlorine beam developed from the experimental results.

444 Thermodynamic Properties of Alkali Metal Zirconates: *R. Kohli,* Battelle Columbus Laboratories, Columbus, OH 43201

A general parameterization scheme for estimating the standard enthalpy of formation, ΔH_f°, of alkali metal zirconates is outlined. This is based on an estimation equation which takes into account the anion and cation contributions to the enthalpy of formation of the compound. The agreement between the estimated and available experimental values of ΔH_f° is very good. Estimated values for the entropies of formation of these zirconates are also listed.

445 Ternary Phase Equilibria Considerations in Solubility and Diffusivity Studies of Cr in GaAs: *M. D. Deal** and *D. A. Stevenson,* Dept. of Materials Science and Engineering, Stanford University, Stanford, CA 94305

The analysis of the diffusion and solubility of Cr in GaAs is complicated by the ternary phase equilibria in the Ga-As-Cr system. The present report describes experimental results of phase equilibria in this system, with particular reference to the pseudo binary tie lines and ternary tie triangle regions. The significance of these results on Cr sources for diffusion and solubility is discussed and experimental data for diffusion coefficients and solubilities are presented for well-defined Cr sources. Finally, the significance of these results for the processing of GaAs devices is discussed.

446 The Control and *In Situ* Monitoring of Oxygen in Liquid Phase Gallium Arsenide Growth: *S. C. Chang** and *D. A. Stevenson,* Dept. of Materials Science and Engineering, Stanford University, Stanford, CA 84305

An electrochemical method is described that measures and controls the oxygen activity in liquid gallium in a vertical liquid phase epitaxial (LPE) growth system for GaAs. In this method, a yttria-stabilized zirconia tube serves both as Ga solvent container and as electrolyte in an oxygen concentration cell. The rate and extent of deoxygenation of the gallium solvent are reported for several deoxygenation procedures, including electrochemical deoxygenation. The properties of GaAs LPE layers grown at different measured oxygen levels are correlated with the oxygen activity in the gallium solvent.

447 High Temperature Chemistry and Physics of Optical Fiber Fabrication: *K. L. Walker** and *D. L. Wood,* Bell Laboratories, Murray Hill, NJ 07974

The chemistry and physics of the modified chemical vapor deposition (MCVD) process for fabrication optical fibers is reviewed. Submicron oxide particles are formed by the high temperature gas phase oxidation of $SiCl_4$, $POCl_3$, and $GeCl_4$. The $GeCl_4$ is only partially oxidized. A fraction of the particles are then thermophoretically deposited and consolidated to a pore-free glass. We discuss in detail the dependence of the germanium incorporation on thermodynamic equilibria, particle growth, and transport phenomena.

448 Spray Pyrolysis of Electronic Materials: *J. B. Mooney* and *R. H. Lamoreaux,* SRI International, Menlo Park, CA 94025

Spray pyrolysis is a method of film deposition by spraying a solution of the reactants on a heated substrate. The process has long been used commercially for the deposition of transparent tin oxide conductors on glass. The technique is reviewed, and some recent work on CdS photoconductors for office copying and n-CdS/p-$CuInSe_2$ solar cells is reported. The use of a free-energy minimization computer program to guide the deposition experiments is discussed.

449 Relationships Exhibited among Electrochemical, Thermodynamic, and Oxygen Potential Quantities in Lithium-Transition Metal-Oxygen Molten Salt Batteries: *N. A. Godshall,** Altus Corp., San Jose, CA 95112, and *I. D. Raistrick* and *R. A. Huggins,* Dept. of Materials Science and Engineering, Stanford University, Stanford, CA 94305

The interdependence of thermodynamics, phase equilibria, and electrochemical measurements can be used as a powerful tool in the development of high specific energy cells. These principles were used in the analysis of ternary lithium-transition metal-oxides (M=Mn, Fe, Co) as cathode materials for use in molten salt batteries. The equilibrium potential *vs.* Li was found to be a logarithmic function of the calculated oxygen partial pressure for any tie triangle in which Li_2O is present, or for any tie triangle not containing Li_2O, so long as the ternary oxide phases of which the tie triangle is composed are only marginally stable, with respect to Li_2O and their neighboring binary oxides. Deviations from this relation are also discussed.

450 Thermodynamic Studies of the Li-Al-Sb System: *C. M. Luedecke,* J. P. Doench,* and *R. A. Huggins,* Dept. of Materials Science and Engineering, Stanford University, Stanford, CA 94305

A thermodynamic study of the Li-Al-Sb system has been made using the galvanic cell Al, "LiAl"/LiCl-KCl (eut.)/Li-Al-Sb. The compositions of several alloys have been varied by adding and deleting lithium with the aid of the coulometric titration technique. Measurements were carried out at temperatures above 360°C. The results have been used to determine the thermodynamic data of the Li-Al-Sb ternary system, and a phase diagram has been proposed.

451 Ternary Alloys as Negative Electrodes in Lithium Systems: *J. P. Doench** and *R. A. Huggins,* Dept. of Materials Science and Engineering, Stanford University, Stanford, CA 94305

Ternary systems have been investigated for use as negative electrodes in intermediate and high temperature molten salt lithium cells. The influence of the addition of large quantities (>10 a/o) of a third component to negative electrode alloys currently under consideration for use in secondary lithium cells has been studied. The equilibrium coulometric titration technique has been used to determine the relevant portions of the ternary phase diagrams and thermodynamic quantities. The relationships between thermodynamics, phase diagrams, and negative electrode characteristics in ternary systems are discussed.

452 Electrical Conductivity of Sulfur-Doped Stabilized Zirconia and Diffusion of Sulfur in Stabilized Zirconia: *G. M. Mehrotra, A. Nakamura,* and *J. B. Wagner, Jr.,* Center for Solid State Science, Arizona State University, Tempe, AZ 85287

Diffusion of sulfur-35 in stabilized zirconia has been measured in the temperature range of 850°-1200°C using the Gruzin method. The penetration profiles show a sharp drop in the concentration of sulfur in the near surface region (up to a depth of ~10 microns) fol-

lowed by a relatively shallow drop in concentration with depth up to about 100-150 microns. A multimode diffusion possibility is suggested. Sulfur diffuses more slowly than oxygen. Alternating-current conductivity measurements at 1kHz have also been made on undoped and sulfur-doped samples between 600°-1250°C. Sulfur doping decreases the electrical conductivity. (This research was sponsored by the Army Research Office Contract DAAG-29-81-K-0109.)

453 Catalytic Effects in the Decomposition Behavior of Metal Sulfates: *R. D. Brittain** and *D. L. Hildenbrand*, SRI International, Menlo Park, CA 94025

The thermal decomposition behavior of the sulfates of magnesium, zinc, and copper has been studied by mass-loss torsion-effusion and by high temperature mass spectrometry. While SO_2 and O_2 are the thermodynamically favored gaseous decomposition products in all cases studied, SO_3 is observed experimentally in the initial stages of vaporization. In the presence of certain noble metal or metal oxide additives, however, the gas composition approaches the equilibrium condition. A model which explains the observed behavior is discussed.

454 Metastable Equilibrium in a Calcite Powder Bed: *M. G. Kim, A. W. Searcy,** and *D. Beruto*, Lawrence Berkeley Laboratory, Materials and Molecular Research Division, Berkeley, CA 94720

Small samples of >1 mm cross section calcite crystals decompose irreversibly when heated in an open crucible in vacuum, but <10 μm cross section calcite particles are shown to develop an apparent equilibrium CO_2 pressure about 10^{-3} times the equilibrium pressure for normal CaO formation. No metastable solid product has been observed in x-ray diffraction and transmission electron microscope studies by others. A possible explanation and experiments to test it are suggested.

455 The Determination of Carbon Thermochemical Properties by Laser Vaporization: *R. L. Baker,** Aerospace Corp., El Segundo, CA 90274, *M. A. Covington*, NASA Ames Research Center, Moffett Field, CA 94035, and *G. M. Rosenblatt*, Los Alamos National Laboratory, Chemistry Div., Los Alamos, NM 87545

A laser vaporization method has been utilized to determine carbon vapor pressure, vaporization coefficients, and melt temperature. The method employs a nonlinear Knudsen layer model to relate properties of interest to other measured macroscopic properties. The data analysis indicates that the JANAF thermochemical data predict a total vapor pressure too low by a factor of 2.5 at 4000 K. Approximate carbon species vaporization coefficients have been obtained, including for the first time their temperature dependence from 3300 to 4500 K. The melt temperature of carbon has been concluded to be greater than 4500 K.

456 Laser Pulse Vaporization of Uranium Dioxide: *C.-h. Tsai*, Department of Nuclear Engineering, University of California, Berkeley, CA 94720, and *D. R. Olander*, Materials and Molecular Research Division, Lawrence Berkeley Laboratory, Berkeley, CA 94720

Rapid heating of a small spot on a UO_2 specimen by a laser pulse generates a surface temperature excursion whose maxima range from 3700 to 4300 K. The temperature transient melts and vaporizes the surface and the vapor expands into the vacuum. A mass spectrometer identifies the species in the vaporizing flow and measures the rates of evaporation, from which the partial vapor pressure of each species and the composition in the vapor jet are deduced. The results are in agreement with thermochemical models based on extrapolation of low-temperature data.

457 Evaporation in the Presence of an Electrical Field: *Z. A. Munir*, Div. of Materials Science and Engineering, College of Engineering, University of California, Davis, CA 95616

Alkali halide crystals were evaporated in the presence of a parallel electric field. The imposition of a field resulted in changes in the evaporation rates and in the surface step morphology. Evaporation rates increased in the presence of a field with the degree of increase depending on temperature and the field gradient. Evaporation enhancement was only observable above a temperature-dependent threshold field gradient.

458 The Relationship Between the Vaporization of Atoms and Electrons: *E. Storms*, Los Alamos National Laboratory, Los Alamos, NM 87545

The energy required to remove an atom from a solid (enthalpy of vaporization) and the energy required to remove an electron (work function) are both sensitive to the energy of the electrons at the Fermi level of the compound. The Fermi energy can be changed in compounds that have a range of composition, and the amount of this change is influenced by the energy spectrum of electrons in the solid (density-of-states). The relationship between these properties is shown using the behavior of various hexaboride and carbide compounds.

459 Acoustic Emission Studies of High Temperature Oxidation: *R. A. Perkins*, Lockheed Palo Alto Research Laboratories, Palo Alto, CA 94304, and *G. H. Meier*, University of Pittsburgh, Pittsburgh, PA 15261

The oxidation of metals and alloys involves stress generation both during isothermal exposure (growth stresses) and on cooling following exposure (thermal stresses). The stresses can result in scale cracking, detachment of the scale from the substrate, and plastic deformation of the scale or substrate. The elastic energy released during these processes can be detected and analyzed to obtain information regarding the processes. Acoustic emission studies of the isothermal and cyclic oxidation of Cb and a number of Ni- and Co-base alloys are described and the results interpreted in terms of the physical processes giving rise to the emission.

460 The Use of Laser Raman Spectroscopy to Study the Hot Corrosion of Ni-Cr Alloys: *J. J. Truhan** and *R. E. Benner*, Lawrence Livermore National Laboratory, Livermore, CA 94550

Laser Raman spectroscopy was used to study the corrosion of a variety of Ni-Cr alloys by sodium sulfate at 1000°C. The analysis after exposure showed that the type of oxide formation was dependent on alloy composition. Raman results were correlated with energy dispersive x-ray analysis on scale cross sections.

461 *In Situ* Oxidation of Iron at High Temperature: *T. L. Jungling** and *R. A. Rapp*, Dept. of Metallurgical Engineering, The Ohio State University, Columbus, OH 43210

The *in situ* oxidation of iron was studied in the hot-stage environmental scanning electron microscope. At high temperature (1000°C) and low oxygen pressure (3×10^{-4} atm) a rugged, large grained wustite scale is formed. At 1250°C a similar wustite morphology exhibits pyramidal pits associated with dislocations which provide surface ledges for scale growth. A video tape of macroledge motion from dislocation pits and a proposed mechanism is presented.

462 The Effect of Hafnium on High Temperature Oxidation Resistance: *J. G. Smeggil*, United Technologies Research Center, East Hartford, CT 06108

Advanced superalloys are intended to provide enhanced mechanical properties at elevated temperatures. To achieve these improvements and still maintain adequate surface stability, reactive metal additions of elements such as hafnium and yttrium are introduced at low levels to enhance protective scale adherence. The effects of hafnium additions on the high temperature cyclic oxidation performance of the nickel base alloy MAR M-200 are presented.

463 Oxidation of Nickel Sulfides in Oxygen: *G. M. Mehrotra, V. B. Tare*, and *J. B. Wagner, Jr.*, Center for Solid State Science, Arizona State University, Tempe, AZ 85287

The kinetics of oxidation of NiS and Ni_3S_2 were studied at 700°C, in one atmosphere of oxygen. The first step during the oxidation of NiS was found to be the formation of Ni_3S_2 as an intermediate product which subsequently oxidized to NiO. Ni_3S_2 exhibits large deviations from stoichiometry with the composition varying from 38 to 42 a/o sulfur. The oxidation of Ni_3S_2 was strongly dependent on composition. Compositions with 38 to 40 a/o S increased in weight initially during oxidation. The increase was subsequently followed by a slow decrease in weight. For compositions with 41 and 42 a/o sulfur however, a continuous decrease in weight from the start of oxidation was observed. Oxidation products of all the compositions were identified by x-ray diffraction as NiO. The possible mechanisms of oxidation and importance to kinetics of mixed oxidant corrosion are discussed. (This research was supported by the Army Research Office under contract DAAG29-81-K-0109, and by a grant from the Center for Solid State Science.)

464 Reaction of Nickel with SO_2 at Elevated Temperatures: *W. L. Worrell*, Max-Planck-Institut fur Festkorperforschung, 7000 Stuttgart 80, Germany, and *N. Jacobson,** Dept. of Materials Science, University of Pennsylvania, Philadelphia, PA 19104

The reaction of nickel in SO_2 atmospheres is very complex leading to the formation of a nonequilibrated product scale and a maximum in the temperature variation of the reaction rate. Two different reaction mechanisms have been proposed. The first mechanism is the direct reaction of nickel with SO_2, while the second involves the formation of $NiSO_4$ as an intermediate reaction product. In this paper, the available experimental evidence is summarized and used to critically evaluate the two proposed mechanisms.

465 Effect of the Amount of Na_2SO_4 on the High Temperature Corrosion of U700: *A. K. Misra** and *F. J. Kohl*, NASA Lewis Research Center, Cleveland, OH 44135

The corrosion of U700 coated with different doses of Na_2SO_4 was studied in an isothermal thermogravimetric test in the temperature range 890°-950°C. The induction period is observed to increase with an increase in the amount of Na_2SO_4 applied. The end of the induction period is marked by the conversion of all of the Na_2SO_4 to Na_2MoO_4 (1). The final weight gain after long exposure is dependent on the total amount of Na_2MoO_4 formed. Corrosion experiments with different doses of Na_2MoO_4 confirm this. A mechanism is described to explain the accelerated corrosion in the presence of Na_2MoO_4 (1).

466 Kinetics of Corrosion of CoCrAlY by SO_3-Na_2SO_4: *C. M. Kramer** and *R. L. Jones*, Chemistry Div., Naval Research Laboratory, Washington, DC 20375

The corrosion rates of a CoCrAlY alloy (22Cr, 11Al, 0.5Y, bal Co by w/o) used for Navy gas turbine blade coatings were measured at 700°C as a function of SO_3 partial pressure, and Na_2SO_4 loading. The amount of Na_2SO_4 on the metal was varied from 1-20 mg/cm² and the pressure of SO_3 from 1×10^{-4} to 1.5×10^{-3} atm, with the SO_3 being introduced as a mixture of SO_2-SO_3 in air. The corrosion rates de-

pended not only on P_{SO_3} and the amount of salt, but on the preannealing of the alloy. The rates of corrosion decreased with time and were fitted to a polynomial expression (weight gain = $a + b \cdot t + c \cdot t^2 + \ldots$). The dependencies of the rate constants (a, b, c) on the salt loading and SO_3 partial pressure were determined and evaluated.

467 Reactions of NaCl with Gaseous SO_3, SO_2, and O_2: *W. L. Fielder,* C. A. Stearns,* and *F. J. Kohl,* NASA Lewis Research Center, Cleveland, OH 44135

Hot corrosion of gas turbine engine components involves deposits of Na_2SO_4 which are produced by reactions beween NaCl and oxides of sulfur. For the present investigation, NaCl single crystals were exposed at 100°-850°C to gaseous mixtures of SO_3, SO_2, and O_2. The products formed during this exposure depend primarily on the temperatures. The four product films were: NaCl · SO_3, $Na_2S_2O_7$, Na_2SO_4, and NaCl · Na_2SO_4. The kinetics of the reactions were measured.

468 Formation of Surface Layers during Oxidation of an Fe-Mn-Si Alloy: *J. M. Oh* and *M. J. McNallan,** Department of Civil Engineering, Mechanics and Metallurgy, University of Illinois at Chicago, Chicago, IL 60680, and *W. King,* Argonne National Laboratory, Materials Science Div., Argonne, IL 60439

Austenitic stainless steel substitute materials in the Fe-Mn-Ni-Si system undergo a surface phase transformation due to selective oxidation of manganese during exposure to oxygen at temperatures above 600°C. The kinetics of the growth of the transformed region are consistent with rate control by diffusion of manganese through the transformed region, but the mechanism for selective oxidation of manganese has not been established. Scanning and transmission electron microscopy techniques have been applied to determine the structure and compositions of the layers of oxide and metal produced by oxidation.

469 Oxidation of Cobalt-Chromium Alloys in Chlorine Contaminates Environments: *S. H. Kim* and *M. J. McNallan,* Department of Civil Engineering, Mechanics and Metallurgy, University of Illinois at Chicago, Chicago, IL 60680, and *W. W. Liang,* Gas Research Institute, Chicago, IL 60631

The effect of chromium on the rate of oxidation of cobalt-chromium alloys is well established, and chromium drastically reduces the rate of oxidation in high enough concentrations. Chlorine produces a drastic increase in the rate of oxidation of pure cobalt. The effect of chromium content on the kinetics of attack of cobalt-chromium alloys in a 1% Cl_2 – 50% O_2 – 49% Ar atmosphere at 1000K has been investigated using a thermogravimetric technique, and the corrosion products have been examined by optical and scanning electron microscopy.

470 A Model for the Growth of a Two-Phase Corrosion Scale: *S. B. Sutton,* J. J. Truhan,* and *D. W. Short,* Lawrence Livermore National Laboratory, Livermore, CA 94550

The growth of a two-phase corrosion scale is modeled by determining equilibrium concentrations after diffusion over short-time intervals. One phase is assumed to be continuous with a relatively impermeable, discontinuous second phase adding a "tortuosity" factor to the diffusivities. Predicted scale growth rates are compared with experimental results.

471 Analysis of Localized Heat Processes in Metal Oxidation: *D. Cubicciotti,* Electric Power Research Institute, Palo Alto, CA 94303

The overall chemical reaction occurring during a metal oxidation is separated into sets of localized reactions occurring at the two interfaces, namely, metal-oxide and oxide-gas. Evaluation of the enthalpy changes at the interfaces indicates they can individually be much larger in magnitude than the overall enthalpy change (although their sum must equal the total change). It is concluded that those local effects could give rise to unexpected heat transfers especially during rapid oxidation.

472 Use of the NASA CEC Code for the Prediction of Combustion Gas Deposit Compositions: *F. J. Kohl,* B. J. McBride,* and *F. J. Zeleznik,* NASA Lewis Research Center, Cleveland, OH 44135

The metal or mineral content of coal, coal-derived, or "dirty" fuels can lead to the formation of deposits during the combustion process. It is desirable to predict the compositions, amounts, and locations of such deposits to assess the magnitude of potential problems such as fouling, corrosion, or harmful particulate emissions. The use of the NASA Lewis Research Center Computer Program for Calculation of Complex Chemical Equilibrium Compositions (CEC) for the prediction of deposit compositions is described, along with the companion Program for Calculation of Thermodynamic Data (PAC) and the data base (THDATA). Examples are given for coal and coal-derived fuel combustion.

473 High Temperature Chemistry of Coal Ashing: *R. W. Carling,* R. W. Mar,* and *R. M. Allen,* Sandia National Laboratories, Livermore, CA 94550

The mineral matter in coal causes most of the problems (such as pollution, fouling, corrosion, etc.) associated with combustion of coal. High temperature ashing (HTA) is frequently used to characterize this mineral matter. However, these results are not a true representation of the original mineral matter. As a consequence misinterpretation of the role mineral matter plays may result. The work reported here concentrates on clarifying the chemistry of coal during HTA, the limitations of an HTA analysis, and how the HTA analysis may relate to the original inorganic species in the coal. (This work supported by U.S. Department of Energy, DOE, under Contract Number DE-AC04-76DP00789.)

474 Behavior of Mineral Matter during Coal Combustion: *R. J. Lauf* and *L. A. Harris,* Oak Ridge National Laboratory, Oak Ridge, TN 37830

Standard materials science techniques, particularly optical and electron microscopy, were used to elucidate the phases present in fly ash and bottom ash. The ash characteristics are related to the mineralogy of the feed coal to determine the behavior of mineral particles during combustion. Coal mineralogy is shown to play an important role in the redistribution of trace elements. These experiments suggest that volatilization plays only a limited part in trace element transport. (This work was supported by the Office of Basic Energy Sciences, U.S. Department of Energy under contract W-7405-eng-26 with Union Carbide Corporation.)

475 Equilibrium Relations with a Bearing on Refractory Corrosion in Slagging Coal Gasifiers: *A. Muan,* College of Earth and Mineral Sciences, The Pennsylvania State University, University Park, PA 16802

Phases containing chromium oxide have shown exceptional resistance to corrosion in slagging coal gasifiers. High-temperature equilibrium data on systems involving chromium oxide as a component at various oxygen partial pressures are discussed. Particular emphasis is given to the presence of Cr^{2+} in silicate melts under strongly reducing conditions. It is shown that the latter may cause large decreases in liquidus and solidus temperatures compared to those prevailing under more oxidizing conditions. Activity-composition data are reported for a number of chromium oxide-containing phases.

476 Experimental and Modeling Studies of Coal Slag Vaporization and Phase Equilibria: *J. W. Hastie,* E. R. Plante, D. W. Bonnell,* and *W. S. Horton,* National Bureau of Standards, Washington, DC 20234

A new modeling approach is described for thermodynamic predictions of multicomponent, multiphase high temperature silicate systems including coal slags. The model, which attributes negative deviations from ideal solution behavior to the formation of complex liquids and solids, is demonstrated for quarternary systems containing K_2O, Al_2O_3, CaO, and SiO_2. Good agreement between the model predictions and experimental vapor pressure data is found. Predictions concerning melting and phase composition are also given.

477 Oxidation-Sulfidation Corrosion in Fluidized Bed Combustor Environments: *J. Stringer, K. J. Mark, J. S. Lin,* and *D. A. Stevenson,** Dept. of Materials Science and Engineering, Stanford University, Stanford, CA 94305

A serious type of oxidation-sulfidation is often observed in fluidized bed coal combustor (FBC) environments. A laboratory scale apparatus was developed to create corrosion scales and penetration on metal alloys characteristic of those found on heat exchanger tubes operated in FBC systems. The use of this system for studying the mechanism of corrosion and for evaluating specific alloys is discussed. Particular attention is focused on the gas composition ranges that promote the sulfidation-oxidation, in contrast to simple oxidation.

478 High Temperature Erosion and Erosion/Corrosion in Coal Combustion Systems: *J. Stringer,* Electric Power Research Institute, Palo Alto, CA 94303

In pulverized coal combustion, a certain fraction of the incombustible material is entrained in the combustion gas as fly ash. This is capable of eroding some of the solid surfaces in the gas path, including the lower temperature heat exchangers and the induced draft fan. In addition, by becoming entrained in the soot-blower blast, it can erode the high temperature heat exchanger surfaces. In fluidized bed combustors the form of the entrained solids is somewhat different, and the loading may be higher. In addition, erosion can occur within the bed. The presence of alkali metal salts and oxides of sulfur in the combustion products can lead to corrosion, and there is a possibility that there are interactions between erosion and corrosion. The mechanisms of these various processes are discussed.

479 Materials Performance in Laboratory and Pilot Plant Coal Gasification Environments: *V. L. Hill,* Gas Research Institute, Chicago, IL 60631, and *B. A. Humphreys,* IIT Research Institute, Chicago, IL 60616

A research program has been in operation for several years to determine materials capable of providing acceptable service life when exposed to the hostile environment present in coal gasifiers. The reported work compares the corrosion rates determined for selected alloys exposed in pilot plants with laboratory data obtained for these alloys tested at high temperatures and pressures in a simulated coal gasification atmosphere. Results of the tests are intended to establish the limiting conditions under which materials can be utilized in gasifier internals and heat recovery components.

480 High Temperature Materials for Gas-Fired Industrial Applications: *C. J. Dobos** and *W. W. Liang,* Gas Research Institute, Chicago, IL 60631

Effective utilization of high-grade waste heat from high temperature industrial furnace flue gases increase the efficiency of these gas-fired process systems. The waste heat recovery systems presently in use generally suffer from poor corrosion resistance, thermal/mechanical failure, leakage, high maintenance requirements, and the inability to generate preheat temperatures sufficient for significant fuel savings. The needs for reliable, cost-effective high temperature materials are discussed. Current research programs to improve high-temperature thermal and mechanical properties and the development of cost-effective manufacturing techniques for ceramic components are presented.

481 The Corrosion Behavior of Some Candidate Heat-Exchanger Alloys in the AFBC Environment: *M. A. Rocazella** and *I. G. Wright*, Battelle Columbus Laboratories, Columbus, OH 43201

Corrosion and combustion diagnostic data were gathered in Battelle's coal-fired atmospheric fluidized-bed combustor (AFBC). Corrosion probes, constructed from candidate heat-exchanger alloys, were exposed to the fluidized-bed environment during 50%, 20%, and 0% excess air combustion conditions. An *in situ* oxygen probe was used to monitor the oxygen partial pressure at the exposure locations. Two different mechanisms of material degradation were identified, *i.e.*, both corrosion and erosion. The relative contributions and interactions of the different forms of degradation, and the implications for tube life are discussed.

482 Studies of Pulverized Coal Combustion Using Fourier Transform Infrared Spectrometry: *L. R. Thorne** and *D. K. Ottesen*, Sandia National Laboratories, Livermore, CA 94550

Fourier transform infrared spectrometry (FT-IR) is being used to measure the temperature and chemical composition of the gases near combusting coal particles. Absorption spectra in the 700-4000 cm^{-1} region is obtained by directing a 1.5 mm infrared beam through a laminar flow reactor into which pulverized coal is injected. The concentrations of CO, CO_2, H_2O, and light hydrocarbons are determined by comparing the observed spectra to those computed from published reference data; temperatures are determined from intensities of individual vibration-rotation transitions. Since the extent of reaction, chemical composition, and temperature are determined in these experiments, they provide a basis for further understanding of the chemical kinetics of pulverized coal combustion. (This work was supported by U.S. Department of Energy, DOE, under Contract Number DE-AC04-76DP00789.)

483 Temperature Measurements of Single Pulverized-Fuel Particles by Two-Color Pyrometry: *R. E. Mitchell, S. Niksa*, and *W. J. McLean*, Sandia National Laboratories, Combustion Research Div., Livermore, CA 94550

A two-color pyrometry system for measuring the temperatures of burning pulverized-fuel particles is described. We assume that the fuel particles behave as graybody emitters, and in this paper this assumption is assessed. In this paper, the optical-electronic configuration used to collect emission from discrete particles at two wavelengths simultaneously, as they flow through a sampling area, is described. The system operating procedures are outlined, and the calibration technique using a light source of known temperature and spectral emissivity is presented. Temperatures of coke and char particles burning in various combustion environments are analyzed. Results indicate that accurate temperature measurements can provide a sensitive method for the determination of pulverized-fuel burning rates.

484 High Temperature Corrosion of Candidate Ceramic Heat Exchanger Materials by Coal Combustion Products: *B. A. Nagaraj*,* GEC Mechanical Engineering Laboratory, Leicester LE8 3LH, England, and *J. R. A. Lowder*, Ruston Gas Turbines, Hague International. Portland, ME 04106

One way of developing a coal-burning gas turbine would be to use a high temperature heat exchanger, to isolate the turbine from the potentially damaging species in the coal-combustion gases. The principle of the indirectly fired gas turbine topping cycle is described in this paper, and the behavior of silicon carbide-based ceramics (candidate materials for the heat exchanger) in coal combustion products is examined, over a temperature range of 950°-1100°C. The overall corrosion rate of the ceramics was very low but the external silica layer, which is normally protective under oxidizing conditions, was found to be attacked by alkaline compounds present in coal ash. Corrosion pits were observed on exposure of ceramics to incompletely burnt ash; local regions of low oxygen partial pressure led to the depletion of silicon by the formation of volatile silicon monoxide and low melting silicon-iron eutectics. A mechanism for the corrosion of silicon carbide by coal ash is discussed.

HIGH TEMPERATURE MATERIALS/PHYSICAL ELECTROCHEMISTRY/ BATTERY/ENERGY TECHNOLOGY

New Solid Electrolytes for Energy Conversion

485 What Factors May Increase Superionic Conductivity?: *C. Delmas, A. Levasseur, M. Maazaz, J.M. Reau*, and *P. Hagenmuller*,* Laboratoire de Chimie du Solide du Centre National de la Recherche Scientifique, Université de Bordeaux I, 33405 Talence Cedex, France

Some recent concepts are developed showing that fast ionic conductivity is strongly dependent on factors such as chemical bonding, number of lattice defects, structural disordering or clustering, influence of cations with a lone pair, band structure of the structural matrix, presence of impurities. Significant examples are chosen illustrating the influence of such criteria on the ionic conductivity of the selected materials.

486 Na-Diffusion Paths and Na Potentials in NASICON: *H. Kohler* and *H. Schulz*,* Max-Planck-Institut für Festkörperforschung, D-7000 Stuttgart 80, Germany

Structure investigations of NASICON ($Na_{1-x}Zr_2Si_xP_{3-x}O_{12}$) single crystals were carried out with x-ray diffraction in the temperature range room temperature up to 510°C. Investigated were both phases, the low conducting rhombohedral phase, and for the first time, the high conducting monoclinic phase. A Zr^{4+}-underoccupation was found in both crystals. The monoclinic phase showed underoccupation of both Na sites. Our investigations give clear evidence, that both Na positions are involved in the fast diffusion process of the Na ions. The height of the potential barrier derived from diffraction measurements (0.22 eV) is in excellent agreement with the activation energy from conductivity measurements.

487 Preparation of New Divalent Ion Conducting Beta" Aluminas: *S. M. Griep*,* *D.L. Yang*, and *B. Dunn*, Dept. of Materials Science, University of California, Los Angeles, CA 90024, and *B. Ghosal* and *G. C. Farrington*, Dept. of Materials Science and Engineering, University of Pennsylvania, Philadelphia PA 19104

We have prepared several new divalent beta" alumina compositions which exhibit high conductivity for divalent cations. Ions of Zn^{2+}, Hg^{2+}, Sn^{2+}, Eu^{2+}, and Mn^{2+} rapidly replace the total sodium or silver content of beta" alumina at temperatures of 450°-700°C. Results indicate that the exchange characteristics are strongly influenced by the composition of both the starting crystal and the molten salt bath. Thermodynamic calculations are quite useful in explaining the exchange behavior of various beta" alumina systems.

488 Transport and Structural Properties of New Divalent Beta" Aluminas: *G. C. Farrington*,* *L. Cratty*, and *B. Ghosal*, Dept. of Materials Science and Engineering, University of Pennsylvania, Philadelphia, PA 19104, *D.L. Yang* and *B. Dunn*, Dept. of Materials Science, University of California, Los Angeles, CA 90024, and *J. O. Thomas*, Institute of Chemistry, Uppsala University, Uppsala, Sweden

Transport measurements indicate that single crystal Zn^{2+}, Hg^{2+}, Sn^{2+}, Eu^{2+}, and Mn^{2+}, beta" aluminas exhibit rapid divalent ion motion. Conductivities at 300°C are typically 10^{-3} $(\Omega\text{-cm})^{-1}$, although Sn^{2+}, beta" alumina appears to be considerably more conductive. Diffusion coefficients derived from ion exchange experiments are consistent with those obtained from conductivity measurements. Recent structural studies show that the site distributions for the divalent cations within the conduction plane are dependent upon the specific divalent beta" alumina composition.

489 Ionic Transport in Ternary Di-Anionic Lithium Compounds: *W. Weppner*, Max-Planck-Institut für Festkörperforschung, D-7000 Stuttgart-80, Germany

Ternary lithium compounds which are formed by reaction or solid solution from binary lithium salts and only contain lithium cations form a large group of solid lithium ion conductors. These compounds are in most cases thermodynamically stable with elemental lithium and are therefore of practical interest. Important materials parameters, such as structure, lattice constants, defect concentrations, and thermodynamic properties, vary over wide ranges and may be related to the transport process of lithium ions. Results are presented for ternary compounds using LiF as one of the binary compounds. The systems LiF-LiH, -LiOH, $-Li_2O$, and Li_3N were investigated with regard to conductivities, structural properties, and phase equilibria.

490 Concentration Dependence of Ion Transport in Polymer Electrolytes: *D.F. Shriver*,* *R. Dupon*, and *M. Stainer*, Dept. of Chemistry, Northwestern University, Evanston, IL 60201

Poly(ethylene succinate), PESc, forms complexes with sodium and lithium salts. The identities of the phases and conductivities were investigated between a polymer:salt ratio of 1:1 to 8:1. A maximum in conductivity is observed at 3:1, which is attributed to the high thermal motion of the amorphous complex of this composition. At higher salt concentration, the conductivity decreases owing to constrained polymer motion. At higher polymer concentrations, the low conductivity is attributed to the influence of a crystalline polymer phase.

491 Fast Ion Conductors: Lithium Ionomers and Salts—Polymer Based Materials: *J.R. Wasson*,* Kings Mountain Specialties, Inc., Kings Mountain, NC 28086, and *D. E. Bolster* and *W. E. Hatfield*, Dept. of Chemistry, University of North Carolina, Chapel Hill, NC 27514

Poly(ethylene oxide) and poly(propylene oxide) alkali salt complexes have substantial solid-state conductivities. These complexes have potential advantages in solid-state batteries since electrode changes can be accommodated by the polymeric species. In an extension of this work a search for other lithium fast ion conductors has been initiated in which the solid-state conductivity of similar neutral complexes and salts of monomeric and polymeric carboxylic and sulfonic acids are being evaluated. Progress with this work is reported. (This work was supported in part by the Office of Naval Research.)

492 Limiting Current Effect in Poly(Ethylene Oxide) Based Solid Electrolytes: *J. R. Owen, P.C. Spurdens, J. E. Shemilt,* and *B. C. H. Steele,* Wolfson Unit for Solid State Ionics, Dept. of Metallurgy and Materials Science, Imperial College, London, England SW7 2BP.

Poly(ethylene oxide) can be doped with various lithium salts to give materials with suitable mechanical and electrical properties, for use as electrolytes in solid-state lithium batteries. In contrast with the majority of lithium solid electrolytes, these materials have a significant anion transference number, and consequently, are subject to variations in dopant concentration. The passage of direct current through the electrolyte then causes salt depletion and accumulation at the cathode and anode, respectively, which in turn gives increased resistive losses. The theory of this effect is discussed and supported by experimental data on transference number values, as well as direct observation of limiting current in cells.

493 Electrical Breakdown in Polyethylene Oxide-Based Lithium Ion Conducting Polymers: *C. A. C. Sequeira,* Laboratorio de Electroquimica, Instituto Superior Technico, University of Lisbon, Lisbon, Portugal and *A. Hooper,* Materials Development Division, A.E.R.E, Harwell, Didcot, Oxon, England OX11 0RA

One failure mode of the solid-state cell, lithium/(polyethylene oxide) $LiCF_3SO_3/V_6O_{13}$ has been identified as a localized degradation of the polymer electrolyte. To characterize fully this phenomenon and to establish precisely under which conditions it occurs, a range of polymer compositions has been studied using symmetrical cells with either lithium or platinum electrodes. Breakdown of the polymer is initiated above a threshold charge level which is a function of temperature, electrolyte composition and thickness, and the mechanical loading of the cell.

494 Polymeric Electrolytes: Application to the Thermodynamics of the Lithium-Aluminum Electrode: *M. Armand** (Present address: Lawrence Berkeley Laboratory 62-203, Berkeley, CA 94720), and *B. Kapfer,* Laboratoire d'Energetique Electrochimique LA 265, ENSEEG B.P. 44 Domaine Universitaire, 38401 Saint Martin D'Heres, France, and *A. Belanger* and *M. Robitaille,* Institut de Recherches d'Hydro-Quebec (IREQ), Varennes, Quebec, J0L 2P0 Canada

Poly(ethylene oxide) solutions of lithium salts are solid electrolytes with a large stability window. Compact lithium-aluminum alloys have been prepared by direct electrochemical injection of the alkali metal into an aluminum foil. The titration curve and a diffusion coefficient $D = 10^{-10}$ cm²/sec at 65°C agree with the extrapolation of high temperature determinations. However, the D value is 100-fold lower than those obtained previously with nonaqueous liquids when the real surface is increased by particulation and wicking.

495 Electrochemical Investigations of Cointercalated TiS_2 Using a Polymeric Electrolyte: *W. B. Johnson* (Present address: Dept. of Metallurgical Engineering, Ohio State University, Columbus, OH 43210) and *W. L. Worrell,* Dept. of Material Science and Engineering, University of Pennsylvania, Philadelphia, PA 19104.

The open-circuit voltage *vs.* lithium has been measured in cell [A] as a function of lithium concentration between 30° and 80°C

$$Li/(LiC_2O_2F_3)\text{Polyethylene oxide}_{5.9}/Li_yNa_xTiS_2 \qquad [A]$$

for $y = 0.0$, 0.04, 0.16, 0.34, and 0.50. The results for $y = 0.0$ indicate that the cell arrangement, which employed a solid polymer electrolyte, was suitable for measuring open-circuit voltages *vs.* lithium. The variation of the emf as a function of lithium composition, x, was the same in $Li_xNa_yTiS_2$ for $x + y < 1.0$ as that in Li_xTiS_2 when $x < 1.0$. The open-circuit voltage *vs.* lithium decreased to approximately 1.0V when $x + y > 1.2$ and was nearly constant up to $x + y \approx 2.0$. The solid polyethylene oxide electrolyte is thus satisfactory for measuring open-circuit potentials from ~ 1.0 to ~ 3.0V *vs.* lithium.

496 Electrochemical Studies of the Conductivity in Oxide-Doped CaF_2: *T. L. Wen* and *W. Weppner,** Max-Planck-Institut für Festkörperforschung, D-7000 Stuttgart-80, Germany

CaF_2 is known to show the same emf as an oxygen ion electrolyte when used in oxygen concentration cells. Two different explanations are discussed: *(i)* CaF_2 is a co-ionic conductor which also allows the transport of oxygen ions; *(ii)* The presence of small amounts of CaO provides secondary equilibria between the electrodes and the electrolyte. CaF_2 was doped by various oxides in order to promote potential transport of oxygen ions. Among these dopants, CeO_2 has shown the largest enhancement in the ionic conductivity. The results of electrochemical transference and potential measurements are reported which provide information on the type of mobile and potential determining species in CaF_2 in oxygen concentration cells.

497 Electrochemical Investigation of Electrode Processes on $PbSnF_4$ Electrolyte: *E. Siebert** and *J. Fouletier,* Laboratoire d'Energétique Electrochimique (LA 265), ENSEEG, 38402 Saint Martin d'Heres Cedex, France

In recent years there has been widespread interest in the conduction mechanisms of halides which are candidates for use in solid-state batteries, gas sensors, and ion-selective electrodes. The studies of electrode processes have been restricted to symmetric and asymmetric cells involving β-PbF_2 or LaF_3 electrolytes. An investigation of the electrode processes on $PbSnF_4$ electrolyte is reported. This material is, at present, one of the anionic conductors exhibiting the highest conductivity at room temperature. A three-electrode all-solid cell was designed to study the electrode reaction at the interface $M/MF_2/PbSnF_4$ (M : Pb, Sn). The experimental techniques employed were cyclic voltammetry, impedance spectroscopy, and electronic trap levels determinations.

498 Ceramic-Metal Solid Electolytes: *R. J. Lauf* and *J. B. Bates,* Oak Ridge National Laboratory, Oak Ridge, TN 37830

Technology developed at ORNL to produce shock-resistant mechanically tough α-Al_2O_3-based cermets has been extended to include solid electrolytes based on sodium β-Al_2O_3. Compositions examined, β-Al_2O_3-Pt and β-Al_2O_3-Cr, were found to have conductivities comparable to pure β-Al_2O_3 fabricated in the same way. No special problems with the submicron-size metal inclusions were observed in preliminary tests. This concept is generic and could conceivably be applied to ceramic electrolytes in other chemical systems. (This work was supported by the Office of Conservation and Renewable Energy, U.S. Department of Energy under contract W-7405-eng-26 with Union Carbide Corporation.)

499 Adaptation of a Network Analyzer for Four-Point A-C Electrical Measurements of Ionic Conductors: *J. B. Bates,** *N. J. Dudney,* and *S.M. Casey,* Oak Ridge National Laboratory, Solid-State Div., Oak Ridge, TN 37830

Determining the impedance of ionic conductors from two-point a-c measurements is complicated by the fact that the measured amplitude and phase is the result of a sum of contributions from the sample and electrodes, as well as from the sample holder and measuring circuitry. As a consequence, the sample resistance obtained by a least squares fit of the amplitude and phase or $Z(\omega)$ to an equivalent circuit is often subject to large errors. We found that by using two-high impedance differential amplifiers, a four-point measurement of the resistance of materials such as β''-aluminum and zirconia can be made directly and accurately with the network analyzer, without requiring complex circuit analysis. The limitations of this technique have been explored using computer simulation of the total electrical network including the measuring circuitry. (Research sponsored by the Division of Materials Sciences, U. S. Department of Energy under contract W-7405-eng-26 with Union Carbide Corporation.)

500 D-C Polarization Measurements on Lithium Silicate-Based Solid Electrolytes: *R. F. Aspandiar,** *I. D. Raistrick,* and *R. A. Huggins,* Dept. of Materials Science and Engineering, Stanford University, Stanford, CA 94305

Wagner asymmetric d-c polarization measurements were carried out on solid electrolytes in the Li_3PO_4-Li_4SiO_4 system, with the aim of determining the stability limits and evaluating the minority electronic conduction parameters. Results indicate that electron conduction predominates over hole conduction within these electrolytes. The range of stability to oxidation extends to quite high potentials. The Li-Si-O phase diagram was also determined from known thermodynamic data, and the experimentally determined stability range of undoped Li_4SiO_4 was compared to that expected from this phase diagram.

501 Re-Examination of Beta-Alumina Doped with Chromium Using Photo-Acoustic Spectroscopy: *J. H. Kennedy** and *A. M. Schuler,* Dept. of Chemistry, University of California, Santa Barbara, CA 93106

A previous publication presented evidence that strongly supported the hypothesis that chromium-doped β-alumina was oxidized to Cr (IV) during air-sintering. This evidence included chemical reactions observed, magnetic susceptibility, and conductivity, but, in particular, the strongest supporting evidence came from absorption spectroscopy. However, the technique used, powder dispersed in a KBr pellet, was not conducive to high quality spectra. For this reason, a much more powerful technique for solid samples, photo-acoustic spectroscopy, has been applied to chromium-doped β-alumina. Additional absorption peaks have been observed that now clearly show that chromium remains as Cr (III) in β-alumina. The other previous evidence has been reexamined, and it too can be interpreted as resulting from the presence of chromium (III).

502 Use of Ca-β''Alumina as a Solid-State Electrolyte: *E. E. Hellstrom,* Sandia National Laboratories, Albuquerque, NM 87185

Polycrystalline, divalent cation β''-aluminas have been prepared by ion exchange as dense, crack-free disks. Ca-β''-alumina is being used as a solid-state electrolyte to electrochemically investigate the thermodynamic properties and phase relations in the Ca-Cr-O system. The experimental cell is Al_4Ca, $Al_2Ca|Ca$-β''-alumina$|3\phi$ Ca-Cr-O in which $Al_4Ca + Al_2Ca$ fix a reference Ca activity, and 3ϕ Ca-Cr-O is a mixture of 3 phases in the Ca-Cr-O system, which coexist in equilibrium.

503 Fast Proton Conductivity in $H_3OTi_2NbO_7 \cdot H_2O$: *C. Schüler,* BBC Brown, Boveri & Co. Research Center, Baden, Switzerland

$CsTi_26NbO_7$ has a layer structure built from sheets of facesharing TiO_6 and NbO_6 octahedra with Cs-ions between them. By ion-exchange in strong mineral acids, $H_3OTi_2Nb_7 \cdot H_2O$ is obtained (1). The hydrated protons proved to be highly mobile. We have studied the ionic conductivity of pellets fabricated by compressing $H_3OTi_2NbO_7 \cdot H_2O$ powder. From measurements between d.c. and 500 kHz over a temperature range from 20° to 90°C, $\sigma(90°) = 2 \cdot 20^{-3}$ $(\Omega cm)^{-1}$, and an activation energy of $\Delta E = 0.23$ eV was found.

No significant changes were observed in runs extending over several weeks.

1. H. Rebbah *et al.*, *Mater. Res. Bull.*, **16**, 149 (1981).

ENERGY TECHNOLOGY

Novel Photoelectrochemical Synthetic Routes

504 Photoelectrochemical Synthetic Processes: *M.S. Wrighton*, Dept. of Chemistry, Massachusetts Institute of Technology, Cambridge, MA 02139

Unique surface chemistry of semiconductors coupled with the ability to use light as the energy source may make semiconductors the electrode materials of choice in electrochemical synthesis. Criteria for useful systems are given and results for semiconductor photoelectrodes in Cl_2, H_2O_2, and $S_2O_4^{2-}$ synthesis are summarized.

505 Chemical Control of Work Functions of Platinum Group Metal Catalysts. I. 16% Efficient Solar to Hydrogen Conversion: *A. Heller** and *E. Aharon-Shalom*, Bell Laboratories, Murray Hill, NJ 07974

Dissolution of hydrogen in platinum group metals such as Pt, Rh, Ru, and Re lowers the work function of the metals. Consequently, hydrogen dissolution increases the barrier height of junctions with p-type semiconductors and thereby the solar to chemical conversion efficiency. The p-InP (hydrogen-saturated rhodium) photocathode reaches an efficiency of 16.2% based on the energy conserved in the photoelectrolysis of 1M $HClO_4$ at 87 mW/cm² sunlight. Its conversion efficiency, based on the electric power that can be generated from photoelectrochemically formed hydrogen in an ideal fuel cell, is 13.3%.

506 Chemical Control of Work Functions of Platinum Group Metal Catalysts. II. The Reason for Hydrogen Evolution in Illuminated Pt Group Metal Activated Suspensions of n-Type Semiconductors: *A. Heller*, Bell Laboratories, Murray Hill, NJ 07974

Photoelectrochemical splitting of water by catalyst activated suspensions of n-TiO_2, n-$SrTiO_3$, and n-CdS has been reported. To catalyze hydrogen evolution, a Pt group metal is incorporated in the surface of the particles. The pure metals (Pt, Rh, etc.) can, however, not act as catalysts, because their work functions are high and the Schottky junctions formed prevent electrons from reaching the catalyst. Hydrogen dissolution in the metals lowers the work functions, converting the Schottky junctions to ohmic contacts, thus making electron transport to and reduction reactions on the metal possible.

507 The Role of Catalysts in Light-Induced Electrochemical Reactions at Semiconductors: *D. Meissner* and *B. Kastening*, Institut f. Physikalische Chemie d.Universität, Hamburg 13, Laufgraben 24, Germany, and *R. Memming*, Philips Forschungslaboratorium, Vogt-Kölln-Str.30' 2 Hamburg 54, Germany

During the last couple of years it has been reported that the stability of semiconductor electrodes or particles can be improved by depositing catalysts. We have investigated various light-induced redox reactions and also the formation of H_2 and O_2 at solid semiconductor electrodes and at small particles, the surfaces of which were loaded with a catalyst. We especially studied monograin membranes consisting of small CdS-particles embedded in a polymer film. The role of catalysts is discussed in detail.

508 Hot Carrier Photoelectrochemistry: *A.J. Nozik,** *G. Cooper*, *J.A. Turner*, and *B.A. Parkinson*, Solar Energy Research Institute, Golden, CO 80401

Hot carrier effects have been found in InP and GaP photoelectrodes. Novel photoelectrochemical reactions are possible with hot carriers, and initial results are discussed.

509 Organic Oxidative Cleavage on Irradiated Semiconductor Powders: *M.A. Fox,** *M.-J. Chen*, and *C.-C. Chen*, Dept. of Chemistry, University of Texas at Austin, Austin, TX 78712

Although many inorganic single electron oxidations can be induced by bandgap irradiation of semiconductor powders, relatively few parallel organic functional group transformations have been reported. Chemically efficient oxidative cleavage of olefins, arenes, amines, and 1,2-dicarboxylic acids have been observed upon irradiating metallized TiO_2 powders as suspensions in nonaqueous solvents. Choice of reaction paths can be controlled, at least partially, by judicious selection of initial reactant concentrations. Mechanistic details of these oxidations are presented.

510 Photoelectrochemical Reactions of Lactic Acid on n-Type Semiconductor Powders: *M.A. Ratcliff* and *H.L. Chum*, Solar Energy Research Institute, Golden, CO 80401.

The photo-Kolbe reaction of aqueous lactic acid at various n-type semiconductor powders has been investigated. Illumination of aqueous slurries containing the lactic acid and the n-type semiconductor powder (TiO_2, Fe_2O_3, or WO_3) generate electron/hole pairs which overall decarboxylate the acid and further oxidize the intermediate radical to a carbonyl. The volatile acetaldehyde is rejected from the solution and trapped as the 2,4-dinitrophenyl hydrazone derivative. Reactions at different pH's, doped, undoped, metallized, and unmetallized powders, are discussed.

511 Photo-Oxidation of Organic Compounds at Doped α-Fe_2O_3 Electrodes: *J.H. Kennedy** and *D. Dünnwald*, Dept. of Chemistry, University of California, Santa Barbara, CA 93106

Photo-oxidation of organic compounds at doped α-Fe_2O_3 electrodes was investigated in aqueous and nonaqueous solutions. Oxalic and formic acids in 0.5M H_2SO_4 showed distinctly different reactivities. Photo-oxidation of alcohols, *e.g.*, methanol and 2-propanol was investigated in propylene carbonate, and compared to their oxidation in water. The oxidation products (formaldehyde, acetone, and oxygen) were analyzed quantitatively, and accounted for 100% of the current. Competition between methanol and 2-propanol, and between these alcohols and water were also studied.

512 Oxidation Processes on CdSe and Se Electrodes: *W.M. Sears* and *S.R. Morrison*,* Energy Research Institute, Faculty of Science, Simon Fraser University, Burnaby, B.C., Canada. V5A 1S6

Measurements of the oxidation of various alcohols, acids, and aldehydes on CdSe and Se-coated CdSe have been made. The pH dependence was emphasized. The current doubling technique was used to monitor the relative capture cross section for the reactants. It is tentatively concluded that the photoproduced holes in the CdSe are transferred to an Se surface state or to the valence band of the Se. The possible mechanism of the reaction and the reasons for the selectivity in the reaction are discussed.

513 A New Look at the Photo-Kolbe Reaction: Where Do We Go From Here?: *R.E. Schwerzel*, Battelle Columbus Laboratories, Columbus, OH 43201

The photo-Kolbe reaction, the photoelectrochemical conversion of simple carboxylic acids to hydrocarbons, has been shown in recent years to be an intriguing and complex process. A variety of water-soluble products are formed in addition to the expected gaseous products, and both alcohols and aldehydes have been observed. In virtually no case reported to date has a complete material balance been obtained, so still other products remain undetected. Moreover, the product ratios observed depend heavily on reaction conditions: solute composition, pH, semiconductor material, the presence or absence of catalytic metal surfaces, and the use of discrete electrodes or illuminated particles all play important roles. This paper considers the status of the photo-Kolbe reaction today, and speculates on its prospects for the future.

514 Photo-Kolbe Studies of Aromatic Acids Using Platinized Magnéli Phases of TiO_x: *J.S. Cantrell*, Dept. of Chemistry, Miami University, Oxford, OH 45056

Magnéli phases of the type Ti_nO_{2n-1} ranging from n = 4-9 have been prepared using a furnace, Vycor tubing, and Ti powder mixed with TiO_2 (anatase) heated to 900°-950°C in an inert atmosphere for approx. 3 days. Pt was photochemically grown into these powders using H_2PtCl_6 and formic acid (pH ~ 3.5, Na_2CO_3) to form photodiodes. An effort was made to produce pure Magnéli phases which were used in a Hanovia photo-chemical reactor to study the reactions of a number of different aromatic acids. The progress of the reaction was followed by CO_2 evolution, measured as $BaCO_3$. HPLC and GC-Mass Spectra were used to analyze the products. Powder x-ray diffraction and scanning electron microscopy were used to evaluate the photodiode catalysts before and after use in photo-Kolbe reactions. Results of these studies are given.

515 Photoelectrochemical Reduction of CO_2 and Cleavage of H_2S: Catalytic Effects in Semiconductor Powder Suspensions and on Electrodes: *A. Mackor,** *A.H.A. Tinnenmans*, and *D.H.M.W. Thewissen*, Institute of Applied Chemistry TNO, Utrecht, The Netherlands

The photoreduction of CO_2 over aqueous suspensions of titanate powders leads to formic acid (main product), formaldehyde, methanol, ethanal, and ethanol in a total optical to chemical yield of 0.03%. The fate of the intermediates formic acid and formaldehyde has been determined. Oxidation to ultimately yield CO_2 is the predominant process. The electrolytic reduction of CO_2 does not indicate a preference of CO_2 over H_2O reduction. An improved H_2S cleavage by addition of sulfite ions to give H_2 and thiosulfate ions over CdS powders is reported.

516 Photocatalyzed Light-Driven Reduction of CO_2 and N_2 on Semiconductor Surfaces: *N.N. Lichtin** and *K.M. Vijayakumar*, Dept. of Chemistry, Boston University, Boston, MA 02215

CO_2 and N_2, separately or in admixture with O_2, have been reduced under illumination with light of $\lambda > 400$ nm on surfaces of finely divided semiconductors held in suspension in water or used as dry, coated films in the presence of water vapor. Yields of CH_2O, CH_3OH, and NH_3 do not bear any simple relationship to bandgaps or flatband potentials of many semiconductors, but this conclusion is complicated by reverse reactions. Activation energies for formation of several products under a variety of conditions fall in the range 2-12 kcal/mol. Engineering efficiences for conversion at 30° of incident light into stored energy greater than 0.1% for reduction of CO_2 and greater than 0.001% for reduction of N_2 have been observed.

517 Reduction of CO_2 at n-Type Semiconductor Electrodes: *K.W. Frese, Jr.*,* and *D. Canfield*, SRI International, Menlo Park, CA 94025

Current-voltage curves for the reduction of CO_2 (aq) have been determined for various n-type single crystal electrodes. A preliminary discussion of the kinetics of CO_2/HCOOH system is given. The Marcus-Gerischer model and published results on the energy surfaces of CO_2/CO_2^- are used to estimate rates for a weakly interacting system. The results, when compared with experiments, suggest that electrocatalytic effects are very important. Results of electrolysis

experiments are also presented. The reduction of CO_2 to CH_3OH occurs with ~100% Faradaic efficiency on n-GaAs electrodes under certain conditions.

518 Photo-Assisted Hydrogen Evolution at Platinized p-Type InP Electrodes—Effects of Methods of Platinization on the Electrode Properties: *H. Tamura, H. Yoneyama,* and *M. Azuma,* Dept. of Applied Chemistry, Faculty of Engineering, Osaka University, Yamada-oka 2-1, Suita, Osaka, 565, Japan

Cathodic current-potential curves of platinized p-type InP electrodes, obtained in 0.5M H_2SO_4 under illumination, are markedly influenced by the method of platinization. Platinized electrodes prepared by electrodeposition under illumination are the most active for hydrogen evolution, those prepared by electrodeposition in the dark are the least active, and those prepared by evaporation are intermediate. Results obtained for photoassisted reduction of other several oxidizing agents which occurs in competition with hydrogen evolution are also presented, and discussion is made on principal causes responsible for bringing about such differences observed.

519 Water Cleavage Reaction via Polypyrrole and Ruthenium Oxide Modified CdS Photochemical Diodes: *A.J. Frank** and *K. Honda,* Solar Energy Research Institute, Golden, CO 80401

Polypyrrole and ruthenium oxide modified CdS photochemical diodes in the visible light-induced water cleavage reaction have been investigated. The experimental results of the studies are discussed.

520 Silicon Electrodes Modified with Polymer Bound Metal Phosphine Complexes: *D.L. DuBois,* Solar Energy Research Institute, Golden, CO 80401

A series of polymers containing pendant monodentate, bidentate, and tridentate phosphine ligands have been synthesized. These polymers react with transition metals to form polymer-bound metal phosphine complexes. These polymers can be used for modifying various electrodes. Silicon electrodes have been modified with a variety of metal phosphine complexes ranging from molybdenum to nickel.

521 Organometallic Coatings for CdS: *M. Cocivera,* J.H. Reeves,* and *P. Szczecinski,* The Guelph-Waterloo Centre for Graduate Work in Chemistry, University of Guelph, Guelph, Ont., Canada, N1G 2W1

Insoluble metal organosulfur compounds can be deposited electrochemically at the anode or cathode (on metals and semiconductors). The identity and purity of the compounds are determined by a variety of spectroscopic techniques. The conductivity, which is low for a number of coatings, can be increased substantially by electrochemical procedures. Capacitance, onset potential, and power efficiency data for coated *vs.* uncoated single crystal and polycrystalline CdS are discussed.

522 Effects of Adsorbents on Photoelectrochemical Properties of MoS_2: *S.M. Ahmed,* Canada Centre for Minerals and Energy Technology, (MSL), Ottawa, Ont., Canada K1A 0G1

Electroreduction of Mo(V1) to lower oxidation states and their adsorption on MoS_2 occurs predominantly on $\perp$-c surface, in the -0.35 to -0.90V(SCE) range, at pH 1.5. The corresponding PEC effects and charge transfer processes using RDE were studied, and the surface composition was analyzed by ESCA. Results indicate that Mo(V1) → Mo(V) introduces acceptor like adsorbed states near the conduction bandedge, resulting in an inversion layer on n-MoS_2. The same states on p-MoS_2 can capture minority carriers (electrons) from conduction band, resulting in a large increase of photocurrents. Xanthate and pyrogallate are adsorbed on ∥-c surfaces of MoS_2 and greatly increased photocurrents at low band bending by neutralizing these surface states, which would otherwise reduce photocurrents substantially.

523 A Photoelectrochemical Comparison of Chloro-Gallium Phthalocyanine to Other Phthalocyanine Derivatives: *C.A. Linkous,** Brookhaven National Laboratory, Dept. of Energy and Environment, Upton, NY 11973, and *N.R. Armstrong,* Dept. of Chemistry, University of Arizona, Tucson, AZ 85721

It has been shown that chloro-gallium phthalocyanine (GaPc-Cl) thin-film electrodes become reversible toward hydroquinone when exposed to visible wavelength light. In order to determine why the chloro-gallium derivative exhibits this behavior, a number of phthalocyanine derivatives, including the chloro-aluminum and the fluoro and iodo-gallium derivatives, were examined. Only GaPc-I showed the same voltammetric behavior as GaPc-Cl. Furthermore, electron micrographs of these two derivatives showed the most crystalline order, implying that a photoconductive effect is responsible for the observed contrast between light and dark voltammetry. (This work was performed under the auspices of the U.S. Department of Energy under Contract No. DE-AC02-76CH00016 and the National Science Foundation under Grant No. CHE 80-17571.)

524 Efficient n-Type Gallium Arsenide Phosphide Anodes in Aqueous Electrolytes: *C.M. Gronet* and *N.S. Lewis,** Dept. of Chemistry, Stanford University, Stanford, CA 94305

A major barrier to unassisted photoelectrosynthesis of fuels from sunlight is the inability to obtain the necessary voltages from semiconductor/liquid junctions. We have investigated trends in photovoltage of a series of semiconductor solid solutions, n-$GaAs_{1-y}P_y$. Variations in interface parameters with changes in bulk semiconductor composition should allow manipulation of the voltage at the semiconductor/liquid junction. We find that increases in bandgap produce large values of the open-circuit voltage and maximum power voltage under 88 mW/cm² tungsten-halogen irradiation. For n-$GaAs_{0.72}P_{0.28}$, we find open-circuit voltages of 0.99V, and operating voltages of 0.8V. Solar conversion efficiencies are in excess of 10% in this system, with efficiencies for conversion of monochromatic 632.8 nm visible light of over 30% at photocurrent densities of over 5 mA/cm². Applications of these high voltage devices to photoelectrosynthetic applications are discussed in depth.

ENERGY TECHNOLOGY

General Session

525 Electric Birefringence and Ellipsometric Spectroscopy of the Semiconductor/Electrolyte Interface: *P.G.P. Ang** and *A.F. Sammells,* Eltron Research Inc., Naperville, IL 60540

The semiconductor/liquid electrolyte interface is being investigated *in situ* using electro-optical techniques. These techniques provide information on the solid-state physics of the semiconductor surface and on the influence of surface states on photoelectrochemical performance. Major emphasis is on transient electric-birefringence and ellipsometric spectroscopy for studying this interface. The electric-field-induced changes in optical retardation (the Kerr effect) is used as a natural probe of the electric field at the semiconductor/liquid electrolyte interface. The voltage-dependence, wavelength-dependence, and relaxation behavior of the electric-birefringence signal are used to delineate the nature of the semiconductor/liquid interface. (This work was supported by the Gas Research Institute.)

526 Photoeffects at Semiconductor/Solid-Electrolyte Junctions: *A.F. Sammells* and *P.G.P. Ang,* Eltron Research Inc., Naperville, IL 60540

Photoelectrode/solid-electrolyte junctions can be considered as the solid-state analog of the liquid-electrolyte junction, which is widely studied in photoelectrochemical cells. Solid electrolyte cells evaluated have included n-CdSe/$\beta''Al_2O_3$/Ag, n-$MoS_2/\beta''Al_2O_3$/Ag, and n-CdSe/$RbAg_4I_5$/Ag. Electronic contact to the photoelectrodes was made using conducting glass. Halide or chalcogenide redox species were introduced onto part of the semiconductor/solid-electrolyte interface. Upon illumination, photopotentials in the 100 mV range were observed using ELH illumination. Photocurrent densities through the 3 mm thick β'' Al_2O_3 pellet were in the 5 μA/cm² range. The features of such solid-state junctions and their comparison to semiconductor/liquid-electrolyte interface are discussed. (This work was funded by the Office of Naval Research).

527 Stabilization of Semiconductor Photoanodes by Selective Electrodepositions: *L. Fornarini* and *B. Scrosati,** Instituto di Chimica Fisica, University of Rome, Rome, Italy

The processes of selective electrodeposition in the dark on defective layered semiconductor electrodes have been examined under various experimental conditions. The results indicate that these processes may be used to stabilize the layered semiconductors in view of their utilization in photo-electrochemical solar cells.

528 Photoelectrolysis at Ordered Polycrystalline GaPc-Cl Thin-Film Surfaces: *P. Rieke,* C. Linkous,* and *N.R. Armstrong,* Dept. of Chemistry, University of Arizona, Tucson, AZ 85721

Chloro-gallium phthalocyanine films sublimed onto gold electrodes showed variable photoelectrochemical behavior dependent on the deposition rate. Enhanced kinetic activity towards the hyroquinone/benzoquinone reaction, compared to the gold substrate, was observed on all films. A photoassisted shift of the apparent reduction potential to more negative values was observed on films grown with a slow deposition rate. Scanning electron microscope studies related the reduction potential shift to larger crystallite size.

529 Investigation of Liquid Dopants for High Efficiency Solar Cell Production Using Silicon Dendritic Web Material: *K.S. Tarneja** and *R.B. Campbell,* Westinghouse Electric Corp., Pittsburgh, PA, 15235, and *P. Alexander,* Jet Propulsion Laboratory, Pasadena, CA 91109

This paper discusses the use of liquid dopants including liquid SiO_2 as a diffusion mask for the fabrication of high efficiency (13-15%) solar cells using silicon dendritic web 2.5 cm wide × 33 cm long × 6-7 mils thick strips. Data on time-temperature relationship on sheet resistance, junction depth, and quality of junctions obtained are presented. A step-by-step comparison of the conventional baseline process as compared to the liquid dopant technique is made, and both advantages and disadvantages of this technique are discussed in detail. Electrical characteristics are presented and compared with the baseline efficiencies. Various application techniques for applying the liquid dopants to the substrates including a meniscus coating machine are presented. (This work was supported in part by the U.S. Department of Energy under JPL Contract No. 955909.)

530 Photoelectrochemical Activity of Solid Solutions of Lanthanum and Chromium Salts in Lanthanum Titanates: *V. Guruswamy* and *S. Alexander,* Dept. of Chemical Engineering, Virginia Polytechnic Institute and State University, Blacksburg, VA 24061

Chromium complex salts of the pyrachlore and perovskite structure have optimum d-band splitting in relation to absorbtion in the visible spectrum. Their low conductivity can be compensated by making solid solutions of each of these salts separately in similar structured lanthanum and titanium salts. This allows for extended activity in the visible range. The photoelectrochemical activity is presented along with electron microscope pictures of the surface structure.

531 Electrodeposition of CdS from Diethylene Glycol Solutions: *A.S. Baranski,* M. Bennett,* and *W.R. Fawcett,* Guelph-Waterloo Centre for Graduate Work in Chemistry (Guelph Campus), Dept. of Chemistry, University of Guelph, Guelph, Ont. Canada N1G 2W1

A method for electrodepositing a semiconducting film of CdS from diethylene glycol solutions containing elemental sulfur and cadmium salts is described. The properties of the films which are smooth, coherent, and polycrystalline are discussed. The structure and electrical properties are shown to depend on growing conditions. Carrier concentration can be varied from 10^{17} and 2×10^{18} cm^{-3}, and electron mobility from 5 to 16 cm $V^{-1}sec^{-1}$. Results of a study of the mechanism are discussed in detail.

532 Grain Boundary Passivation in Polycrystalline Silicon: *D.S. Ginley** and *D.M. Haaland,* Sandia National Laboratories, Albuquerque, NM 87185

Polycrystalline silicon solar cell improvement through grain boundary passivation with atomic hydrogen plasmas is discussed. Results with a large scale d-c plasma apparatus are covered as are our continuing efforts to employ Fourier transform infrared spectroscopy to directly monitor the incorporated hydrogen. Results are presented using a new infrared cell capable of *in-situ* treatment and thermal annealing. The potential applications of the plasma treatment technique to other devices is discussed. [This work, was performed at Sandia National Laboratories supported by the U.S. Department of Energy (DOE) under contract number DE-AC04-76DP00789.]

533 Iodidric Acid Photodecomposition on Layered-Type Transition Metal Dichalcogenides: *L. Peraldo Bicelli** and *G. Razzini,* Dept. of Applied Physical Chemistry of the Milan Polytechnic, Research Centre on Electrode Processes of the C.N.R., 20133 Milan, Italy

The photocatalytic decomposition of iodidric acid on platinized n-WSe_2 single crystals has been studied. A special *in situ* technique has been followed, illuminating only a small region of the sample surface and simultaneously observing it under an optical microscope. The experimental results are discussed taking into account the conclusions reached in previous research on the photoelectrochemical behavior of layered-type transition metal dichalcogenides in iodine-iodide containing solutions.

534 Interaction Plasma-Silicon Surface at Low and High Temperature—Application to the Modification of the Surface Properties of the Material: *D. Morvan, M.P. Bergougnan,* and *J. Amouroux,** Ecole Nationale Superieure de Chimie de Paris, Equipe des reacteurs chimiques en phase plasma, 75005 Paris, France, and *A. Salesse,* Université de Paris 7, Laboratoire de physico-chimie instrumentale, 75005 Paris, France

The interaction of the plasma-silicon surface is studied in connection with photovoltaic and electronic applications. At low pressure plasma (1-10 Torr) the objectives are the passivation and the nitriding of the target controlled by the temperature of the solid, the composition of the gas, and the energy of the plasma in the boundary layer, *i.e.* the vibrational, rotational, and electronic temperatures of the excited species. The evolution of the chemical composition of the surface is measured by ESCA, resistivity, and photovoltaic properties. At high pressure plasma (1 atm), by using an argon plasma with 0.01% of O_2, we have studied the elimination of boron controlled by ESCA and mass balance techniques. In conclusion the interaction of the plasma-silicon surface seems to be very efficient with a short treatement in these different cases where chemical composition and energy density are the key parameters.

535 Electroreduction of Oxygen by Cobalt Tetraazaannalene in Acid Media: *H. P. Dhar,* M. Yamana, R. Darby,* and *R. E. White,* Dept. of Chemical Engineering, Texas A&M University, College Station, TX 77843

Stability and catalytic activity of a macrocyclic chelate as an oxygen reduction cathode in acid media could be increased through electrodeposition and through chemical attachment of the chelate to a chemically modified carbon surface. Electrodeposition of cobalt tetraazaannulene dibromide on graphite electrodes showed that the electrosorbed catalyst which may have undergone polymerization on the electrode, enhances both stability and activity in 4*N* H_2SO_4. The same chelate complex could also be attached to a chemically modified carbon surface, which also yielded similar results.

536 Transport Properties of Phosphoric Acid Fuel Cell Electrolytes: *H.H. Chang, K-L. Hsueh,* and *D-T. Chin,* Dept. of Chemical Engineering, Clarkson College of Technology, Potsdam, NY 13676, and *S. Srinivasan,* Electronics Div., Los Alamos National Laboratory, Los Alamos, NM 87545

The transport properties of the phosphoric acid fuel cell electrolyte have not been well understood. This is especially true at the high concentrations and high temperatures normally encountered in the fuel cell operations. In this work, the viscosity and conductivity of the electrolyte and the solubility and diffusivity of dissolved oxygen have been measured over a range of H_3PO_4 concentrations from 5 to 100 w/o and a temperature range of 25°-200°C. The change in the transport mechanisms and the semi-empirical correlations of these properties is discussed.

537 Electro-Oxidation of CO from Coal in Alkaline Media: *E. Findl,* Brookhaven National Laboratory, Upton, NY 11973

The major difficulty with electro-oxidation of $CO \rightarrow HCOO^-$ in alkaline media is the formation of CO_3^{-2} and HCO_3^-. These reaction products lead to pH reduction and salt deposition. A number of approaches to circumventing the problem of electrolyte variability were investigated. A practical solution to the problem resulted from the coupling of a fuel cell using a mixed CO_3^{-2}/HCO_3^- electrolyte and a CO_2 desorption column in a closed loop flow system.

538 Thermodynamics of Metallic Fission Products in Reactor Fuel Rods: *R. Kohli,* Battelle Columbus Laboratories, Columbus, OH 43201

The behavior of the metallic fission products, Mo, Ru, Rh, Pd, and Tc, is considered in detail for high and low burnup fuel rods. Regular solution theory is used with recent experimental data to estimate the activities of the individual elements in a multicomponent system of these elements, such as the metallic precipitates in fuel rods. With the help of this information quantitative decisions are made about the distribution of these fission products in fuel rods. The predictions of the model are used to successfully explain the experimental observations from postirradiation examination of LWR fuel rods.

539 $CuFeS_2$, a New Cathode Material for Lithium Secondary Cells: *R.S. McMillan** and *R.R. Haering,* Dept. of Physics, University of British Columbia, Vancouver, B.C. Canada V6T 1W5

The electrochemical cell $Li/LiClO_4$ (1.0M) in P.C./$CuFeS_2$ was found to function reversibly at ambient temperatures for over twenty cycles. At constant intermediate discharge rates (C/20) the cell was characterized by a cell voltage of *ca.* 1.5V over 80% of discharge, a coulombic efficiency of near 100% and an energy efficiency of *ca.* 80%. Typically the extent of discharge varied from $n Li/nCuFeS_2 \cong 4$ on the first discharge to *ca.* ½ on the twentieth with an accumulated discharge capacity of $n Li/nCuFeS_2 \cong 35$ after the twentieth discharge. The discharge/charge reactions of the chalcopyrite cathodes were investigated using standard electrochemical techniques and *in situ* x-ray diffraction

540 Cycling Characteristics of the Lithium-Aluminum Electrode in Nonaqueous Solutions at Ambient Temperatures: *A.S. Baranski,* W.R. Fawcett,* and *T. Krogulec,* Guelph-Waterloo Centre for Graduate Work in Chemistry (Guelph Campus), Dept. of Chemistry, University of Guelph, Guelph, Ont. Canada N1G 2W1

The formation of LiAl intermetallic compounds on pure aluminum and aluminum alloy electrodes was studied in various organic solvents using galvanostatic, potentiostatic, and a-c impedance techniques. The role of the α-LiAl phase as an intermediate in the formation of β-LiAl was determined. The results are used to discuss the factors effecting the cycling efficiency of the LiAl anode. The advantages and disadvantages of this material as an anode in ambient temperature rechargeable batteries are discussed in comparison with those of pure lithium.

541 Complex Impedance Methods for Study of the MoS_2/Electrolyte Interface: *L.G. Thompson* and *L.B. Anderson,** Dept. of Chemistry, The Ohio State University, Columbus, OH 43210

We describe an a-c impedance study of the interface between MoS_2 crystals and an aqueous solution containing 0.1*M* KBr. Several equivalent circuit models are fitted by gradient search and simplex techniques to data taken at frequencies from 10 kHz to 0.1 Hz. Impedance changes caused by degradation of the MoS_2 surface during photoelectrolysis are studied, and physical changes in the surface as observed with Auger spectroscopy and electron microscopy are discussed.

542 Diffusion in Salt-Gradient Solar Ponds: *C.C. Herrmann,* Water Thermal and Chemical Technology Center, University of California, Berkeley, Richmond, CA 94804

Solar ponds are of interest as inexpensive energy collectors: a sufficient salt gradient can inhibit convection, permitting capture and storage of heat at depths of one to several meters. Computer calculation of the density profile is useful for predicting stability and maintenance requirements. The calculation is based on the diffusion coefficient as function of temperature and concentration, the Soret coefficient, and light absorption *vs.* depth. Results are reported for sodium sulfate diffusion, as a model for ponds based on reject brines from agricultural wastewater desalination.

ENERGY TECHNOLOGY/BATTERY/DIELECTRICS AND INSULATION

Conducting Organic Polymers in Energy Conversion and Storage

543 Synthesis and Chemical Doping of New Tractable Electrically Conducting Polymers: *Y.S. Papir,* V.P. Kurkov,* and *S.P. Current,* Chevron Research Co., Richmond, CA 94802

The synthesis, sample preparation, doping procedures, and conductivity of new tractable electrically conducting polymers are described and discussed. Specifically, the effect of chemical structure, copolymerization, dopants, and doping conditions on the electrical conductivity of these novel processible new polymers is presented.

544 Electrochemistry and Conductivity of New Tractable Electrically Conducting Polymers: *A. H. Schroeder,* Y. S. Papir,* and *V. P. Kurkov,* Chevron Research Co., Richmond, CA 94802

The electrochemical characteristics of a series of new tractable electrically conducting polymers are reported. Data have been obtained from thin coatings on electrode surfaces and from electrochemical doping of thicker, free-standing films. Redox potentials, cyclic voltammetric behavior, charge/discharge reversibility, maximum doping levels, and dependence of conductivity on doping level are discussed.

545 Conducting Polymers Derived from Pyrroles: *G. B. Street,* IBM Research Laboratory, San Jose, CA 95193

Conducting polymers derived from pyrroles are attractive because they possess, to an encouraging degree, the mechanical properties and stability which will be required for widespread commercial application of this class of materials. Furthermore, these polymers are much more readily functionalized than other conducting polymers, such as $(SN)_x$ or $(CH)_x$, an important property if the polymer properties are to be controlled. In this paper the results of extensive characterization of several pyrrole based conducting polymers is discussed. These data have given much insight into the criteria essential for conductivity in these systems, and have significantly advanced our understanding of the physics and chemistry of these polymers.

546 Electroactive Properties of Polyaromatic Polymer Films: *R. J. Waltman,* J. Bargon, S. Mohmand,* and *A. F. Diaz,* IBM Research Laboratory, San Jose, CA 95193

Polymers derived from electrochemical oxidation of pyrroles, thiophenes, and azulene give rise to highly conducting polymers of 10^{-3}-10^{2} Ω^{-1} cm^{-1}. These films are electroactive and can be cycled between the conducting and insulating state with coulombic reversibility. These materials are active in different solvents and over a wide range of temperatures. Complementary chemical studies with polyazulene also suggest that these and other related monomers electropolymerize via a general process.

547 Electrochemistry of Thin Film Heteroaromatic Ladder Polymers: *L. Polyak, D. Rolison,* and *R. J. Nowak,** Naval Research Laboratory, Washington, DC 20375

Thin films of aromatic heterocyclic ladder polymers, *e.g.*, poly[(7-oxo- 7 ,10 *H* -benz[*de*]imidazo[4',5':5,6]benzimidazo[2,]-*a* [isoquinoline-3,4:10,11-tetrayl)-10-carbonyl], commonly referred to as BBL, have been cast as thin films on electrode substrates. Coverages were obtained in the 10^{-8}-10^{-7} mol/cm^2 range based on the monomeric molecular weight (334 g/mol). Unlike many other conducting polymers and polymer-coated electrodes, the electrochemistry of the BBL polymer was found to be remarkably stable and reproducible in aqueous media. The films were particularly stable in 4M sulfuric acid solution. A reversible reduction was observed at a formal potential of +0.075 V *vs.* SCE with a peak separation of 14 mV. The electrochemistry of the film was unaffected by storage in moist air.

548 *In Situ* Mossbauer Spectroscopy of Iron Complexes Incorporated into a Conducting Polymer Matrix: *M. Daroux,* H. Gerdes, D. Scherson, J. Eldridge, M. Kordesch,* and *R. Hoffman,* Case Center for Electrochemical Sciences, Case Western Reserve University, Cleveland, OH 44106

Mossbauer effect spectroscopy has been used to examine counterion species involving iron incorporated into electronically conducting polymers to balance the charge when the polymer backbone is oxidized or reduced. The anionic complex ion hexacyanide and other iron complexes were incorporated into polypyrrole during the electropolymerization process. The results indicate that strong signals can be obtained from the polymer films without ^{57}Fe enrichment. The information that can be obtained with this technique in conjunction with electrochemical measurements is discussed.

549 Properties of Polyphenylene Films Deposited Electrochemically in HF-Benzene System: *I. Rubinstein,* General Electric Co., Corporate Research and Development, Schenectady, NY 12301

Polyphenylene films were deposited on electrodes by anodically oxidizing benzene in liquid hydrogen fluoride. The polymer is electroactive in liquid HF with remarkably low oxidation potential, and can also undergo repetitive charging-discharging in dry organic solvents. The polymer film is highly suitable for electrode surface modification, by means of simple chemical reactions performed on coated electrodes. Free-standing polyphenylene films similarly produced become conductive upon vapor-phase AsF_5 doping, and are relatively stable in air.

550 Characteristics of Electrochemically Reduced Polyacetylene: *R. B. Kaner* and *A. G. MacDiarmid,* Dept. of Chemistry, University of Pennsylvania, Philadelphia, PA 19104

The electrochemical reduction of polyacetylene $(CH)_x$, using several different dopant species is explored. The properties of the electrochemically reduced $(CH)_x$ using tetrabutylammonium ions, including constant current discharge characteristics, coulombic efficiency, stability, and its ability to be recharged, are compared to the properties of $(CH)_x$ reduced by lithium ions. The possibility of reversible electrochemistry using tetrabutylammonium ions with $(CH)_x$ and lithium electrodes without dendrite formation is discussed.

551 Electrochemical Characteristics of Chemically Doped Polyacetylene: *W. H. Smyrl,* S. R. Kurtz, C. D. Jaeger, J. M. Zeigler,* and *D. S. Ginley,* Sandia National Laboratories, Albuquerque, NM 87185

Chemical doping of polyacetylene yields material that may be used as an electrode in electrochemical applications. The thermodynamics of doping I_2 and Li-biphenyl from dimethoxyethane solutions have been investigated. The chemical potential of the intercalant has been measured with concentration cells, both in the semiconductor and metallic regimes. The doped material behaves as a microporous conductor with the void space filled at least partially with the solution contacting it. Other experiments are reported on doped materials that may be useful as battery and fuel cell electrodes. (This work was supported by the U.S. Department of Energy (DOE), under Contract Number DE-AC04-76-DP00789.)

552 The Kinetics and Properties of Doped Polyacetylene in Nonaqueous Electrolytic Solutions: *W. H. Smyrl,* S. R. Kurtz,* and *D. S. Ginley,* Sandia National Laboratories, Albuquerque, NM 87185

Digital impedance for faradaic analysis (DIFA) measurements have been made on polyacetylene doped with Li, in Li Br-propylene carbonate solutions. Results have been obtained during the doping process and on the material after different doping levels have been achieved. The latter are emphasized here. The results show the interfacial impedance to be composed of a contribution from charge transfer kinetics at high frequencies and diffusion at lower frequencies. The charge transfer rate increases in general as the dopant level increases in the polyacetylene, both in the semiconductor and in the metallic regimes. Measurements have been made over the range of 10^{-2} Hz to 500 Hz. (This work was supported by the U.S. Department of Energy (DOE), under Contract Number DE-AC04-76-DP00789.)

553 Anodic Deterioration of Polyacetylene Film in Nonaqueous Electrolyte: *K. Abe,* F. Goto, T. Yoshida,* and *H. Morimoto,* Toyota Central Research and Development Laboratories, Inc., 41-1, Aza Yokomichi, Oaza Nagakute, Nagakute-cho, Aichi-gun, Aichi-ken, 480-11, Japan

The anodic potential of polyacetylene in $LiClO_4$/propylene carbonate electrolyte shows three plateaus mainly corresponding to the following reactions: *(i)* a reversible doping reaction of ClO_4^- as elucidated by higher discharge/charge coulombic efficiency; *(ii)* irreversible anodic reaction, in which polyacetylene gradually loses its crystallinity, the fibrils swell, and more C-Cl bonds are involved; *(iii)* electrochemical decomposition of the solvent, accompanied by a sharp potential rise at a charging amount of about 1.1 A-hr/g of polyacetylene.

554 Kinetics of Electrochemical Doping and Undoping of Polyacetylene: *F. G. Will,* General Electric Corporate Research and Development, Schenectady, NY 12301

The kinetics of anodic doping (charging) and cathodic undoping (discharging) of polyacetylene electrodes is studied in organic solutions of $LiBF_4$. Both as-prepared polyacetylene films and pressed powder electrodes are employed. The galvanostatic pulse technique is used to obtain potential-time transients and polarization curves at various constant times after pulse initiation. Polyacetylene is found to have rather slow kinetics, with the transport of the dopant ion, BF_4^- into and out of the polymer structure controlling the rate.

555 The Thermal and Oxidative Stability of Polyacetylene: *F. G. Will,* General Electric Corporate Research and Development, Schenectady, NY 12301

This review addresses the stability of both doped and undoped polyacetylene when heated *in vacuo* or exposed to air. The effects of thermal and oxidative conditions on the structure and properties of polyacetylene are discussed. Particular emphasis is placed on changes in molecular structure and conductivity resulting from oxidation in air at various temperatures. The present state of knowledge of the kinetics and mechanisms of oxidation is summarized.

556 Solid Polymer Electrolyte Photovoltaic Cells: *T. A. Skotheim,* M. V. Rosenthal,* and *S. W. Feldberg,* Brookhaven National Laboratory, Dept. of Energy and Environment, Upton, NY 11973

We have studied photoelectrochemical cells based on interfaces between n-type semiconductors coated with electrochemically polymerized heterocycles (polypyrrole, polythiophene) and solid polymer electrolytes. The solid polymer electrolytes consist of solvent free polyether macrocycles with solvating capabilities for ionic species. We report recent attempts to produce polymer composites of chemically modified polypyrrole films and complexed poly(ethylene oxide), in order to increase the interfacial contact area between the two polymer phases, thus improving the charge transfer characteristics.

557 The Electrochemistry of Polyacetylene: Application in High Power Density Rechargeable Batteries: *A. G. MacDiarmid,* M. Aldissi, R. B. Kaner, M. Maxfield,* and *R. J. Mammone,* Dept. of Chemistry, University of Pennsylvania, Philadelphia, PA 19104.

The energy density, power density, and other characteristic properties of four different types of rechargeable batteries using $(CH)_x$ electrodes are described. The batteries are illustrated below by equations representing their discharge reactions: *Type I: $(CH)_x$ cathode; Li anode*

(i) $[CH^{+y}(ClO_4)^{-1}]_x + xyLi \rightarrow (CH)_x + xyLiClO_4$
(ii) $(CH)_x + xyLi \rightarrow [Li_y^{+1}CH^{-y}]_x$
Type II: (CH)$_x$ cathode; (CH)$_x$ anode
(iii) $(CH)_x + [Li_y^{+1}CH^{-y}]_x \rightarrow 2[Li^-_{y/2}{}^+CH^{-y/2}]_x$
(iv) $[CH^{+y}(ClO_4)_y^{-1}]_x + [Li_y^{+1}CH^{-y}]_x \rightarrow 2(CH)_x + xyLiClO_4$

558 Electrochemical Cells Based on the Reduction of Polyacetylene, Poly(p-Phenylene), and Polythiazyl: *L. W. Shacklette,* R. H. Baughman,* and *J. M. Sowa,* Allied Corp., Polymer Laboratory, Morristown, NJ 07960

Batteries have been constructed with alkali-metal anodes and with polyacetylene, $(CH)_n$, polyphenylene, $(C_6H_4)_n$, or polythiazyl, $(SN)_n$, cathodes. Polythiazyl is a highly conducting polymer in its pristine state; polyacetylene and poly(p-phenylene) become highly conducting upon reduction. The variation of structure and reduction potential of the polymers is discussed as a function of capacity (doping level). The doping process for polyacetylene and polyphenylene is shown to be completely reversible. The electrochemical reduction of polythiazyl, on the other hand, appears irreversible, but occurs at a high voltage (2.7V *vs.* Li/Li$^+$) with a capacity of ⅓ to ¼ electron per SN unit.

559 An Approach to the Evaluation of Conductive Polymers for Batteries: *B. L. McKinney** and *R. G. Burrow,* Johnson Controls, Inc., Corporate Applied Research Group, Milwaukee, WI 53209

Conductive polymers, such as polyacetylene and p-polyphenylene, have received much interest recently as potential battery electrode materials. A general approach has been developed at Johnson Controls to evaluate new conductive polymers as active materials for batteries. The approach is based on four basic criteria which define battery performance: rate capability, energy density, energy efficiency, and stability. The experimental techniques required to establish these criteria are cyclic voltammetry, cycle tests, and stand-loss tests. To illustrate the application of this approach, data are presented for conductive polyacetylene.

INDUSTRIAL ELECTROLYTIC

Science and Engineering of Membranes and Separators

560 A Simple Model of a Diaphragm-Type Chlorine Cell: *R. E. White,* J. S. Beckerdite,* and *J. Van Zee,* Dept. of Chemical Engineering, Texas A&M University, College Station, TX 77843

A simple model of a diaphragm-type chlorine cell is presented and discussed. The model consists of an earlier model with a simple, but important, extension. The extension is the inclusion in the model of a measurable property of the diaphragm, referred to as the MacMullin number (N_{Mac}) or resistivity ratio of the electrolyte filled diaphragm relative to the electrolyte. It is shown theoretically that the product of N_{Mac} and the diaphragm thickness (the "effective" diaphragm thickness, $N_{Mac}t$) is actually the important diaphragm characterizing parameter and not N_{Mac} or the diaphragm thickness separately.

561 A Simple Model of a Diaphragm-Type Chlorine/Caustic Cell with Acidified Brine Feed: *J. Van Zee** and *R. E. White,* Dept. of Chemical Engineering, Texas A&M University, College Station, TX 77843

A simple model of a diaphragm-type chlorine/caustic cell which includes the effect of an acidic anolyte and the relationship between differential head and velocity is presented and discussed. The location of the acidic-base reaction plane which determines cell performance is shown theoretically to deviate from the anolyte-diaphragm interface as a function of three measurable properties of the diaphragm; these properties are the MacMullin number or resistivity ratio of the electrolyte filled diaphragm relative to the electrolyte, the diaphragm permeability, and the diaphragm thickness.

562 Transport in a Chloroalkali Diaphragm: *R. R. Chandran* and *D-T. Chin,* Dept. of Chemical Engineering, Clarkson College of Technology, Potsdam, NY 13676, and *K. Viswanathan,* Hooker Chemical Co., Hooker Development Center, Niagara Falls, NY 14302

An experimental and theoretical work is being carried out to elucidate the mechanism of ionic transport within a chloroalkali diaphragm. The concentration distribution of hydroxyl ion, the effective diffusivity, the ohmic resistance, and various overpotential losses are measured with a laboratory cell. The optimal structure and operating conditions of the diaphragm are subsequently determined with a numerical computation.

563 Transport Through Charged Porous Membranes: *G. B. Westermann-Clark,* Dept. of Chemical Engineering, University of Florida, Gainesville, FL 32611

The ionic concentration profiles in the electrolyte solutions inside the pores of a charged membrane can have a tremendous influence on electrolyte, charge, and fluid transport through the membrane. Classical Gouy-Chapman theory often predicts unrealistically high concentration profiles in the diffuse layer. GC theory is compared here with statistical mechanical (MSA) calculations for the diffuse layer, and the implications of the MSA and GC approaches on transport in charged porous media are discussed.

564 Influence of Cell Parameters on the Current Efficiency of a High Performance Chlor-Alkali Membrane: *H. L. Yeager* and *J. D. Malinsky,* Dept. of Chemical, University of Calgary, Calgary, Alta. Canada T2N 1N4

Sodium ion is the major current-carrying species in chlor-alkali cell membranes, and the optimization of its transport over that of hydroxide ion is essential for efficient operation of a membrane cell. Previously we have reported the development of a computer-controlled apparatus which is designed to automatically measure the membrane transport number of sodium ion, under conditions similar to an operating cell, as a function of several cell parameters. These include temperature, current density, brine concentration, and caustic concentration. Three-dimensional computer-generated displays of these results allow the variation of sodium ion transport number to be seen as a function of two of these variables. These "performance surfaces" have also been animated, so that the effects of all cell parameters on the perselectivity of the membrane can be seen. This animated approach is demonstrated using the results of measurements on newly developed high performance membrane produced by the du Pont Company. Discussion of the possible physical significance of the combined effects of these parameters on membrane performance is provided.

565 Solubility Characteristics of Perfluorinated Polymers with Sulfonyl Fluoride Functionality: *G. H. McCain* and *M. J. Covitch,** Diamond Shamrock Corp., T. R. Evans Research Center, Painesville, OH 44077

Perfluorosulfonate ionomers of relatively low ion exchange capacity (≤0.91 meq/g) have generally been considered to be insoluble although similar materials of higher ionic content have been reported to dissolve in simple alcohols. This paper presents evidence for the high-temperature dissolution of perfluorinated polymers with sulfonyl fluoride functionality (0.83-0.91 meq/g) in high-boiling perhalogenated liquids. Various properties of these solutions, such as viscosity and gelation characteristics, are discussed in relation to Yeo's description of the dual cohesive energy density behavior of perfluorosulfonate ionomers. Finally, it is shown that membranes may be prepared from these solutions by solvent casting or common coating techniques.

566 Fluorescence Probe Studies of Solutions of Poly(Perfluorosulfonates): *N. E. Prieto* and *C. R. Martin,** Dept. of Chemistry, Texas A & M University, College Station, Texas 77843

Perfluorosulfonate ionomer membranes are currently the focus of a massive international research effort. These studies hope to provide information about the supermolecular-structures, the chemical properties of the cluster phases, and the transport characteristics of these unique membrane materials. This laboratory has recently described a procedure for dissolving perfluorosulfonate ionomer membranes. This has provided a means of studying the chemical properties of the free poly(perfluorosulfonate) molecules. We are using fluorescence probe techniques to study these molecules (in dilute aqueous solution); results of these studies are reported. Key points discussed are the nature of the interactions of these polyions with their counterions, and the consequences of these interactions to rates of counterion diffusion in ionomer membranes.

567 Electrochemical Generation and Characterization of Electrode Coatings Containing Molecular Sieve Particulates: *C. Murray, R. J. Nowak,* and *D. R. Rolison,** Naval Research Laboratory, Washington, DC 20375

Thick, heterogeneous coatings form on Pt and glassy carbon electrodes after performing rotated voltammetry in an aprotic solution containing molecular sieve fines and a reducible species. Voltammograms for species such as 1,4-dinitrobenzene, *tris*-2,2′-bipyridylruthenium(II), and TCNQ are classically shaped in the absence of sieve fines. Upon adding the ground zeolite and cycling into the reduction wave, the cathodic current decays and the wave shape degrades until the voltammogram resembles an irreversible cyclic voltammogram. After such treatment, the electrode has a thick, nonuniform, colored coating which persists with soaking in clean solvent. A common feature of such coatings is a reversibly oxygen reduction wave in blank, deaerated acetonitrile electrolyte, even for electrodes stored under vacuum, presumably due to the sequestering of oxygen by the molecular sieve coating upon exposure to the atmosphere.

568 Structure Characterization of Sulfonated Polysulfone Membranes: *W. Koh** and *H. Silverman,* Duracell Inc., Burlington, MA 01803, and *K. Kem,* Occidental Research Corp., Irvine, CA 92707

A series of sulfonated polysulfones have been prepared, characterized, and fabricated into cation-exchange membranes for applications in electrochemical separation processes. Macrostructure analysis using thermal, mechanical, and spectroscopic techniques is described. The membranes exhibit little evidence of the presence of large ionic clusters. Rather, a large shift in Tg and a strong affinity for water are observed. Evidence supporting a structure consisting largely of ionic multiplets is offered.

569 Supported Liquid Membrane Battery Separators: *J. P. Pemsler** and *M. D. Dempsey,* Castle Technology Corp., Woburn, MA 01801

Supported liquid membranes have been investigated as battery separators. Membranes are prepared by infiltrating microporous membrane supports with liquid ion exchange reagents, which then exhibit selective ion transport behavior. Separator resistances as low as 1 Ω cm^2 have been measured. These battery separators are believed to be applicable to a number of alkaline systems. Ni-Zn cells have been prepared using supported liquid membranes in an effort

to prevent zinc dendrite shorting and shape change. Results of cycling tests are reported. (This work was supported by the U.S. Dept. of Energy, Lawrence Berkeley Laboratory under Contract No. 4512210.)

570 Equilibrium Parameters for a Sodium-Hydroxide-Water System in a Nafion Membrane: *S. D. Bhakta* and *D. N. Bennion*, Dept. of Chemical Engineering, Brigham Young University, Provo, UT 84602

Equilibrium solubility parameters were determined using a Nafion membrane over a wide range of concentrations of NaOH and temperature. These parameters were determined by a combination of soaking, blotting, and analysis techniques. The wet membrane density, fixed ion concentration, and the membrane anion and cation concentration increased with the external NaOH concentration (C_e) whereas the water concentration decreased with C_e at a particular temperature. Mathematical description and physical interpretations of ion and water transport anion membranes are discussed.

571 Electrical Impedance of Electrodialysis Membranes: *C. C. Herrmann*, Water Thermal and Chemical Technology Center, University of California, Berkeley, Richmond Field Station, Richmond, CA 94804

Electrical impedance of anion-exchange and cation-exchange membranes is a useful measurement in evaluating performance and polarization. Results are reported for several membranes under normal desalting current densities, and at high densities which cause acid-base formation, with and without presence of a fouling layer. Alternating-current and Laplace-transformed pulse methods were used. Impedance maxima were found at limiting currents. Fouling increases low-frequency (diffusion) impedance more than high-frequency (resistive) impedance.

572 Pore Size Engineering of Separators for Nickel-Hydrogen Batteries: *K. M. Abbey,* D. L. Britton*, and *O. Gonzalez-Sanabria*, NASA Lewis Research Center, Cleveland, OH 44135

The design of separators for nickel-hydrogen batteries involves optimizing the electrolyte management processes through appropriate control of the capillary pressure characteristics. The effects on electrolyte management of altering pore size distribution, wettability, and thickness have been studied for a number of microporous separators composed of inorganic fibers and particles. Asymmetric separators have been fabricated and some polymeric membrane materials studied. Separators, which exhibit tolerances to large changes in electrolyte content, have been selected for further testing in boiler plate cells.

573 *In Situ* Production of Ozone in Water Using an SPE Electrolyzer: *S. Stucki** and *G. Theis*, BBC Brown, Boveri & Co., Ltd., Research Center, Baden, Switzerland

A new application of electrochemical cells using chemically stable ion exchange membranes as electrolyte (SPE-cells) is described. SPE water electrolyzers with an appropriate anode structure can be used to produce ozone. The main advantage that these have over classical electrochemical cells is that they do not require a liquid electrolyte. Hence, they have great potential for the treatment of water *in situ*. Laboratory cells running on demineralized or softened tap water at room temperature have shown current efficiences in the order of 10%. The factors influencing the efficiency of the cell, engineering aspects, and potential applications are discussed.

574 Metal-Net-Backed Porous Oxide Ceramic Diaphragms; A Solution for the Separator Problem of Caustic High Temperature (160°) Water Electrolysis: *H. Wendt* and *H. Hofmann*, Institut für Chemische Technologie, TH Darmstadt, D-6100 Darmstadt, Germany

The aim to improve water electrolysis technique remarkably in order to make large scale hydrogen-production from nuclear energy economically attractive can only be achieved by simultaneously increasing current density and decreasing the cell voltage. The approach to increase the process temperature sizably beyond 90°C seems to be one of the most promising steps in this direction. This step demands a new type of separator instead of asbestos cloth which is neither stable against caustic potash above 100°C nor can be fabricated thin enough to reduce the instrinsic cell resistance. The authors report on the properties and production costs of a composite separator made of a supporting metal net and a porous oxide ceramic cover that possesses very low resistance (0.2 Ω cm^2 at 30°C in 50 w/o KOH) and that allows constructing a distance-free sandwich-pack of the electrodes and the diaphragm.

INDUSTRIAL ELECTROLYTIC/CORROSION/ELECTRODEPOSITION

Anode and Cathode Materials

575 State of Oxidized Noble Metal Anodes: *B. E. Conway*, Dept. of Chemistry, University of Ottawa, Ottawa, Ont., Canada K1N 9B4

Despite high costs of noble metal anode materials, or of their oxides, their use in some electrolytic processes is advantageous with respect to favorable or desired electrocatalysis and/or corrosion resistance. In most anodic processes in aqueous solution, such anode materials bear an oxide film which is electrolytically generated in the anodic process itself or which is generated thermally, e.g. IrO_2 or RuO_2. A review of the electrochemical behavior of oxide films on Pt, Ir, Ru, and Au is given in a comparative way with regard to (a) characteristics of the oxide formation processes; (b) morphologies of thick-film oxides, and (c) electrocatalysis of several processes at such oxide films.

576 Fundamentals of the Behavior of Insoluble Oxide Anodes: *S. Trasatti*, Laboratory of Electrochemistry of the University, 20133 Milan, Italy

The main physicochemical and electrochemical features of conducting oxides are described. Emphasis is placed on the effect of the heat-treatment temperature on such properties as conductivity, surface area, surface acid-base equilibrium, proton exchange and penetration, and kinetic parameters. The role of the morphology of the active layer is illustrated in connection with the nature of the electrochemical process. The relation between nature of the oxide and electrocatalytic behavior is discussed.

577 Activated Carbon as a Fluidized-Bed Anode: *H. H. Law** and *V. Tierney*, Bell Laboratories, Murray Hill, NJ 07974

An inert fluidized-bed anode would have many potential applications involving both homogeneous and heterogeneous reactions. The present investigation is on the use of activated carbon as a fluidized-bed anode for etching of copper printed circuit boards. In a 0.5*N* H_2SO_4 solution, activated carbon was found to absorb a charge of 36 C/g before oxygen evolution. The dissolution was shown to be limited by the charge transfer by the activated carbon particles to the copper surface and not by the reaction kinetics. This indicates that the method of circulating the carbon particle slurry would determine the etching rate.

578 Glassy Carbon Anodes and Air-Depolarized Cathodes for the Generation of Ozone: *P. C. Foller,** Chevron Research Co., Richmond, CA 94802, *M. L. Goodwin*, Oxidation Technologies, Inc., Cupertino, CA 95014, and *C. W. Tobias*, University of California, Berkeley, CA 94720

The use of glassy carbon anodes for the evolution of ozone in fluoro-anion electrolytes is described. Corrosion is severe under conditions of low acid concentration and high temperature. However, at temperatures of less than 30°C and at high acid concentrations, corrosion diminishes anomalously to quite low levels. Trends of ozone current efficiency with anode heat-treatment temperature, current density, and acid concentration are described. The ambient temperature performance of air-cathodes is presented. Operating data from a single cylindrical geometry cell are discussed with respect to the requirements of relevant applications.

579 Activated Lead Anode for Metal Electrowinning: *H. B. Beer*, Scientific Research Society, N.V., Heikantvenstraat 41, 2190 Essen, Belgium

An anode for metal electrowinning cells has a catalyst arranged on a lead base and operates at a reduced oxygen potential while the lead base serves as an inert conductive support. Significant energy savings and high product purity were achieved in an industrial copper electrowinning plant without modifying the existing cell structure. The anode cost is economically justified by improved cell performance with respect to conventional lead alloy anodes.

580 Anode Materials for Electroplating: *D. R. Turner*, Bell Laboratories, Murray Hill, NJ 07974

The anode of an electroplating cell is often given little attention when developing or utilizing a plating process. Often overlooked is the fact that anode reactions can degrade the process so that poor deposits result at the cathode. The anode material can be an important factor. Soluble anodes generally are preferred, but there are situations where insoluble anodes are better. The advantages, disadvantages, and optimum conditions for both anode types are discussed.

581 A Review of the Anodic Behavior of Nickel in Electroplating Solutions: *G. A. DiBari*, The International Nickel Co., Inc., Inco-Sterling Forest, Suffern, NY 10901

The anodic behavior of conventional electrolytic nickel is affected by the tendency for the metal to passivate in electroplating solutions. As a result, its behavior is less than ideal. The tendency to passivate is observable in nickel sulfate solutions, with and without chlorides, and can be precisely measured by means of potentiostatic anodic polarization curves. This paper reviews the anodic behavior of nickel and summarizes the efforts made to improve its behavior in electroplating applications. Also discussed is the mechanism of anodic dissolution and the problem of deriving an expression that describes the electrochemical behavior of nickel in the active, passive, and transpassive regions of the anodic polarization curve.

582 Formation of Salt Films during Anodic Metal Dissolution in the Presence of Fluid Flow: *R. Alkire* and *A. Cangellari*, Dept. of Chemical Engineering and Materials Research Laboratory, University of Illinois, Urbana, IL 61801

Anodic dissolution of a metal in the presence of flowing electrolytic solution was studied. A mathematical model was developed that included the potential field distribution near the dissolving electrode and convective diffusion effects under both laminar and turbulent flow. Critical conditions were identified for saturation, by dissolved metal salt, of the solution adjacent to the anodic surface. Theoretical results were compared with measurements, obtained in a channel flow system, of the critical flow velocities above which pure iron would not repassivate in 0.5M H_2SO_4.

583 The Morphology of Copper Deposits Powder Deposition: *A. Kindler,** Celanese Research Co., Summit, NJ 07901, and *C. W. Tobias*, Dept. of Chemical Engineering, University of California, Berkeley, CA 94720

Copper powder morphology was investigated with an SEM after electrodeposition from an aqueous $CuSO_4$-H_2SO_4 solution in a flow channel with plane parallel electrodes. Because of the uniform current distribution and well-defined mass transfer conditions, it was possible to demonstrate that nodular powder deposits are due to a transformation from a dendritic structure to a coherent one as a powder particle penetrates the cathode diffusion layer during growth under galvanostatic conditions. Coherent growth arises because boundary layer penetration ends the mass transfer control required for dendritic growth.

584 High Performance Electrode Materials for the Hydrogen Evolution Reaction from Alkaline Media: *B. V. Tilak*, Occidental Chemical Corp., Hooker Research Center, Grand Island, NY 14072

One of the main component electrochemical reactions in alkaline water electrolyzers, chlor-alkali and chlorate cells is the hydrogen evolution reaction. Development of high performance materials for this reaction is receiving ever increasing attention in an effort to lower the energy consumption involved in these processes. Kinetic data for the hydrogen evolution reaction from alkaline media on various materials are presented with focus on the mechanistic behavior and electrocatalytic effects arising from the incorporation of metals and nonmetals into nickel lattice, and criteria required of electrode materials for efficient performance under industrial operating conditions are highlighted.

585 Hydrogen Evolution Cathodes for Alkaline Electrolytes: *D. E. Hall** and *V. R. Shepard, Jr.*, Inco Alloy Products Co. Research Center, Sterling Forest, Suffern, NY 10901

Three forms of cathodes were made with high efficiency hydrogen evolution catalysts. Plastic-bonded cathodes contained very high catalyst loadings and gave over-potentials of 30-60 mV at a current density of 200 mA/cm^2. Pressed pellet cathodes with a nickel binder contained lower catalyst fractions and were slightly less efficient but mechanically stronger. The catalysts were also incorporated into thin porous coatings which were applied to several types of cathode substrates. A critical minimum catalyst content was necessary for low overpotentials. The effects of cathode preparation and structure on efficiency are discussed.

586 Thermal Oxidation Effects on Nickel and Steel Cathodes: *D. E. Hall*, Inco Alloy Products Co., Research Center, Sterling Forest, Suffern, NY 10901

Thermal oxidation significantly decreases the hydrogen evolution overpotentials of nickel and steel cathodes in alkaline electrolytes. Optimum oxidation conditions have been defined for both nickel and steel cathodes. When cathodes with porous nickel coatings on steel substrates were oxidized, the effects of both coating and substrate oxidation were evident. Reduction of the cathodes under hydrogen gas reduces or eliminates the efficiency gains produced by thermal oxidation.

587 The High Rate Aqueous Anodic Oxidation of Carbonaceous Crude Fuels: *R. L. Clarke, P. C. Foller*, and *R. J. Vaughan*, Chevron Research Co., Richmond, CA 94802

Various types of carbonaceous crude fuels may be anodically oxidized to nearly complete consumption utilizing Fe^{2+}/Fe^{3+} catalysis. Reaction rates of possible commercial significance may be achieved and sustained with proper fuel and electrolyte management. Limitations imposed by reaction kinetics and mass transport are analyzed. The requirements of the application of the technology as an anodic depolarizer for hydrogen evolution are discussed.

588 An Electrochemical Investigation on Operational Parameters for Laminated Fuel Cell Cathodes: *P. W. T. Lu*, Westinghouse Electric Co., Advanced Energy Systems Div., Pittsburgh, PA 15236

In subscale phosphoric acid fuel cells, effects of operational parameters on performance characteristics of laminated air electrodes have been studied at ambient pressure and at 191°C. The flow rate of oxidant gases plays a significant role in determining acid concentration, ionic conduction, and voltage losses in both gas and liquid phases. It has been found that the internal resistance and electrolyte concentration increase distinctly with rising flow rate, but decrease with the operating current density. However, preheating the inlet air results in no improvement in the cathode performance. The measured Tafel slopes (~100 mV/decade) and limiting current densities for O_2 reduction at a constant flow rate (in stoich) are approximately independent of oxygen content in the inlet gases.

589 A Voltametric Study of the Reduction of Chromic Acid on Bright Platinum: *J. P. Hoare*, General Motors Research Laboratories, Electrochemistry Dept., Warren, MI 48090-9055

The reduction of chromic acid catalyzed and uncatalyzed with H_2SO_4 was studied on Pt microelectrodes by steady-state (galvanostatic and potentiostatic voltammetry) and nonsteady-state (cyclic voltammetry) polarization techniques. The rest potential of Pt in chromic acid is a mixed potential. Although the reduction of hexavalent Cr to trivalent occurs readily at Pt cathodes, the reverse process does not take place at Pt anodes due to the high overvoltage for $[Cr(H_2O)_6]^{+3}$ ion oxidation. It is for this reason that PbO_2 anodes are used in commercial Cr plating practice since the overvoltage for O_2 evolution is much higher on PbO_2 than on Pt, thus allowing the current to be used in the oxidation of $[Cr(H_2O)_6]^{+3}$ ion instead of O_2 evolution. Metallic Cr is deposited in catalyzed chromic acid at the expense of the reduction of Cr VI to Cr III and H_2 evolution.

590 A Protective Conducting Silica Film on n-Silicon: *A. Q. Contractor* and *J. O'M. Bockris*, Dept. of Chemistry, Texas A&M University, College Station, TX 77843

A new approach to the stabilization of n-Si photoanodes is described. Unlike the conventional approach of coating the electrode surface with a thin film of a conducting material, we have attempted to make conducting the incipient film of SiO_2 which normally tends to grow under anodic fields on the silicon surface. This results in a stable photoanode capable of sustained oxygen evolution. Improvement in the performance of the anode can result from the application of small amounts of a catalyst on the surface as shown by preliminary results with $LaNiO_3$ catalyst.

591 Preparation of Transition Metal Phosphides with Varying Phosphide Contents: *M. Robbins,** *J. T. Plewes, P. K. Gallagher, V. G. Lambrecht*, and *J. J. Auborn*, Bell Laboratories, Murray Hill, NJ 07974

Transition metal phosphides with varying phosphide contents (20-35 a/o) have been prepared by vapor phase and electrochemical deposition. Films prepared by vapor phase reaction of phosphorous with transition metals yield films with the composition M_2P. The composition of electrochemically deposited films could be varied over broad limits by alteration of solution chemistry. The influence of plating bath chemistry, plating rate, and anode material, on the composition of the films are discussed.

592 Characterization of Transition Metal Phosphide Films with Varying Phosphide Contents: *J. T. Plewes,** *M. Robbins*, and *R. C. Stoffers*, Bell Laboratories, Murray Hill, NJ 07974

Transition metal phosphides with varying phosphide contents (20-35 a/o) have been evaluated with respect to their chemical, physical, and electrical properties. It was observed that all electrochemically deposited phosphide films were amorphous and exhibited metallic conductivity. Large differences were observed in chemical and thermal stability as a function of phosphorous content in the region of 20-35 a/o. Properties such as wear resistance, adhesion, thermal stability, thermal expansion coefficient, and solderability are discussed.

LUMINESCENCE AND DISPLAY MATERIALS

Display Technology

593 Electrochemical Displays: *G. Beni*, Bell Laboratories, Holmdel, NJ 07733

Various electrochemical effects have been studied for application to display devices. We review these effects with emphasis on their current potential for applications. Detailed discussion of electrochromic, electrophoretic, and electrowetting displays is presented.

594 Photoelectrochromism of Prussian Blue Films: *A. Viehbeck** and *D. W. DeBerry*, SumX Corp., Austin, TX 78761

The photo-electrochromic characteristics of thin Prussian blue (PB) films on single crystal and anodic n-type TiO_2 electrodes have been investigated. The PB layers were cathodically deposited from a ferric-ferricyanide solution. Image formation occurs when the reduced form of PB (clear) is photo-oxidized (blue) under irradiation with light absorbable by the semiconductor. The photocharge storage efficiency is above 95% up to the total film charge under anodic bias. Erasing is accomplished by cathodically polarizing the electrode.

595 Improved Electrochromic Properties of Flash Evaporated High Density Tungsten Oxide Layers: *P. Schlotter** and *L. Pickelmann*, Fraunhofer-Institut für Angewandte Festkörperphysik, D-7800 Freiburg, Germany

Electrochromic tungsten oxide layers prepared by flash evaporation of WO_3 on preheated substrates show, in spite of their 20% higher density (6.2 cm^{-3}), a shorter electrochromic response time (100-200 msec) than those layers prepared by standard evaporation technique. The influence of the preparation technique on the microstructure, the stability, and the electrochromic response time as well as the influence on the reproducibility of these parameters are discussed. Suggestions for the optimization of tungsten oxide layers for ECD applications are given.

596 Spectroelectrochemical Properties of Polyheterocycles—Application to Electrochromic Display Devices: *M. Gazard,** *J. C. Dubois*, and *M. Champagne*, Thomson-CSF Laboratoire Central de Recherches, 91401 Orsay, France, and *F. Garnier* and *G. Tourillon*, Laboratoire de Photochimie Solaire, CNRS, 9420 Thiais, France

Heterocycles such as pyrrole or thiophen are electrochemically polymerized on metallic electrodes where they form very adherent thin films. The films are characterized by cyclic voltametry and chronoamperometry. The polymer-modified electrodes change color reversibly, their visible absorption spectra depending on the nature of the polymer, for example, thiophen polymers are blue in the oxidized form and red in the reduced form. The switching speed between the two forms varies with the nature of the electrolyte and may be as low as 200 msec.

597 Rapid Anisotropic Diffusion of Lithium in Electrochromic $Li_yK_xWO_3$: *S.-K. Joo,* I. D. Raistrick,* and *R. A. Huggins,* Dept. of Materials Science and Engineering, Stanford University, Stanford, CA 94305

It has been shown that lithium diffuses rapidly into $K_{0.3}WO_{3.15}$, and that this material is an interesting candidate for use in lithium-based electrochromic systems. The chemical diffusion coefficient of lithium in preferentially oriented thin films is about 10^{-9} cm²/sec at room temperature. This is 3 orders of magnitude lower than that found for single crystals of $K_{0.3}WO_3$ over the same range of lithium concentration. The explanation for this large difference in chemical diffusion coefficients between single crystals and preferentially oriented thin films has been studied with respect to the different possible lithium diffusion paths in this anisotropic structure.

598 Optimization of Electrochromics for Complex Displays: *D. J. Barclay,* C. L. Bird, A. C. Lowe,* and *D. H. Martin,* IBM UK Labs, Ltd., Hursley Park, Winchester, England

The performance requirements of the electrochromic display effect is significantly more demanding for text displays than for segment displays. This paper describes the path taken to develop a viologen-based electrochromic system to a level whereby millisecond response times may be realized. The implementation of this system in a 72,000 picture element display is described.

599 Liquid Crystal Technology—A Review: *G. J. Sprokel,* IBM Research Div., San Jose, CA 95193

Electro-optic effects in Nematic and Smectic A liquid crystals are reviewed. The role of the interface between the glass surface and the LC film is examined in detail. Problems remaining in matrix addressing TN cells are discussed and the state of the art of dichroic cells is reviewed. Storage cells employing Sm A material solved the addressing problem, but introduced a new set of problems related to erasure. New work established the conditions for successful storage.

600 Electrical Control of the Hysteresis Behavior in A-C Thin-Film Electroluminescent Devices: *K.-W. C. Yang,* Tektronix, Inc., Display Research, Beaverton, OR 97077, and *S. J. T. Owen,* Dept. of Electrical and Computer Engineering, Oregon State University, Corvallis, OR 97330

The negative resistance model describing the hysteresis characteristics of the ZnS:Mn a-c thin-film electroluminescent devices has been discussed previously (1). This model suggests that electrical control of the device hysteresis is feasible by appropriately tailoring the excitation waveform. Experiments have been carried out on the effects of changes in the excitation wave form on the resultant hysteresis width. For devices with a concentration of 2 m/o Mn, control of the hysteresis width between 2 and 28V has been achieved. The paper discusses the significance of the experiments in advancing the theory of device operation.

1. International Display Research Conference, Cherry Hill, NJ, October 1982, p. 42.

LUMINESCENCE AND DISPLAY MATERIALS

General Session

601 X-Ray Screen Performance Profile: Effect of Mechanical Energy during Phosphor Dispersion: *P. De Maayer,* W. Van Landeghem,* and *A. Neyens,* AGFA-Gevaert NV, R&D X-Ray Div., Mortsel, Belgium B2510

Brightness and resolution of intensifying screens made from various x-ray phosphors have been studied as a function of ball-milling time during predispersion. In the case of the rare earth oxysulfides ($Gd_2O_2S:Tb^{3+}$ and $Y_2O_2S:Tb^{3+}$) sharp changes in both parameters are correlated to the appearance of characteristic absorption bands in the visible along with an overall increase in diffuse spectral reflection density. The more continuous variation for $BaFCl:Eu^{2+}$ as a function of milling time may be accounted for by gradual particle size reduction, size distribution changes, and possible alterations in surface scattering characteristics of individual phosphor particles.

602 Factors Influencing the Stability of Rare Earth Oxyhalides: *J. G. Rabatin,* General Electric Co., Quartz and Chemicals Dept., Cleveland, OH 44110

Lanthanum oxybromide phosphors are used extensively in medical x-ray intensifying screens to reduce x-ray exposure and improve image quality. As screen resistance to discoloration and moisture degradation was being improved, factors influencing the stability of rare earth oxyhalides were studied. TGA, DTA, and chemical studies show progressive changes in decomposition due to the "lanthanide contraction." LaOCl decomposes in air, moist N_2, and CO_2 at over 1100°C as compared to LuOBr which decomposes at about 600°C. At room temperature, rare earth oxyhalides show similar decomposition trends while reacting very slowly with water vapor forming incipient surface of LnO(OH) which subsequently hydrolyzes to $Ln(OH)_3$ and LnX_3. Surface treatment with water soluble Sb^{3+} compounds greatly impedes this process by factors of over 20. These antimony compounds also inhibit the oxidation of resorcinol type compounds used in x-ray films which tend to migrate into the screen and form yellow quinone type compounds. Other aspects of screen stability are also described.

603 Luminescence of ZnS:Tm, Ag Phosphors: *T. E. Peters,* J. R. McColl,* and *R. G. Pappalardo,* GTE Laboratories, Waltham, MA 02254

The luminescence of ZnS:Tm has been the subject of a number of earlier studies. Two types of emission spectrum have been observed, depending upon whether radiative recombination occurs at a Tm^{+3} center or at a center comprised of a coactivator, an impurity, or lattice defect. In the former case, the spectrum is dominated by the three emitting Tm manifolds located at ≈478, 645, and 775-800 nm, while in the latter the Tm emission appears as weaker lines superimposed on a stronger broad band emission. In both types of spectrum, the major part of the radiation emitted by the thulium ion is found to be concentrated in the blue manifold at ≈478 nm. Recently, we have observed still another type of emission from ZnS:Tm, Ag phosphors. Instead of the broad blue Ag band with superimposed Tm emission that was expected, we obtained only the simpler rare earth line spectrum. In this instance, however, the majority of the emitted radiation was from the near infrared Tm manifold rather than the one located in the blue. This paper reviews some of the earlier work on ZnS:Tm and attempts to explain the observed emission properties.

604 The Saturation of Luminance in A-C Electroluminescent Thin Films: *P. Thioulouse,* Centre National d'Etudes des Télécommunications, 92220 Bagneux, France

In EL ZnS:Mn devices, luminance saturation is responsible for the drastic decrease of luminous efficiency when brightness reaches high levels and also limits the maximum attainable luminance. For our ACTFEL devices, the blue "self-activated" luminescence intensity, which is proportional to the useful dissipated power, was used for finer measurements of Mn EL efficiency. The influence of saturation on EL efficiency was studied as a function of conduction current for various Mn concentrations. Contribution of the different Mn species to saturation was evaluated from decay measurements.

605 A Special Mechanism of Depreciation in Reduced Wattage Fluorescent Lamps: *F. M. Ryan** and *S. Sinharoy,* Westinghouse R&D Center, Pittsburgh, PA 15235

The introduction of reduced wattage fluorescent lamps created new phosphor maintenance problems. In this lamp type, a transparent conductive SnO_2 coating is placed inside the lamp to aid starting. The presence of the SnO_2 coating can lead to a rapid graying of the phosphor and a resultant loss of efficacy. Through the use of various analytical and diagnostic techniques we have determined the mechanism responsible for the depreciation. Electrons in the vicinity of the cathode can penetrate the phosphor layer which acts as an imperfect dielectric. These electrons reach the conductive SnO_2 layer underneath, causing it to follow the cathode potential rather than the positive column potential. A strong radial electric field gradient is thereby created which can greatly enhance Na^+ diffusion from the glass to the phosphor surface where dark Na-Hg complexes form. This field can also create enhanced ion impact damage of the phosphor. A complete physical description of this model and of special diagnostic techniques developed is presented.

606 Sensitization of Eu^{3+} Emission by Mn^{2+} in Fluoroapatites: *R. G. Pappalardo, T. E. Peters,* and *R. B. Hunt, Jr.,* GTE Laboratories, Waltham, MA 02254

Calcium fluoroapatites and Sr fluoroapatites activated with Eu^{3+} and a suitable sensitizer (Sb^{3+} or Bi^{3+}) exhibit Eu^{3+} emission under excitation at 254 nm. The intensity of such an emission was found to be consistently higher, by at least a factor of two, in triply-activated materials containing Mn^{2+}. Conversely the Mn^{2+} emission intensity in these triply-activated materials was consistently lower. These observations suggest a transfer of excitation energy from Mn^{2+} centers to excited levels of Eu^{3+}. This model appears to be supported by the following additional evidence. Excitation spectra in the blue spectral region, for Eu^{3+} emission at 699 nm, show contributions from both Eu^{3+} and Mn^{2+} absorptions. The emission decay of Mn^{2+} in the triply-activated materials is definitely shorter, and that of Eu^{3+} conversely longer. Dye-laser spectroscopy is being used to determine the kinetics of the energy-transfer process.

607 New (Eu-Activated) Barium and Strontium Aluminates with Very Efficient Eu^{2+} Luminescence: *J. T. C. van Kemenade** and *G. P. F. Hoeks,* N.V. Philips' Gloeilampen Fabrieken, Lighting Div. EDW-6, Eindhoven, The Netherlands

A thorough investigation of the binary systems $BaO-Al_2O_3$ and $SrO-Al_2O_3$ has led to the discovery of two new compounds. These compounds, with composition $BaAl_4O_{13}$ and $Sr_4Al_{14}O_{25}$, can be synthesized in a pure form by the use of specific fluxes combined with the proper firing conditions. Both new compounds are very good host lattices for efficient Eu^{2+} luminescence, showing quantum efficiencies of over 80% upon excitation by 254 nm radiation. In the $BaAl_4O_{13}$ lattice of which the structure has not yet been resolved, the Eu^{2+} emission maximum is located at 477 nm. In the orthorhombic $Sr_4Al_{14}O_{25}$ lattice (space group *Pbcm*), the Eu^{2+} emission maximum is located at 491 nm. Both phosphors show a high output and good maintenance behavior in low pressure Hg discharge lamps. We describe the preparation method for these new phosphors and discuss the characteristic features of their luminescence. In addition we indicate some possible applications in fluorescent lamps.

608 Rare Earth Activated Niobates: *W. A. McAllister,* Westinghouse Electric Corp., Lamp Business Unit, Bloomfield, N.J. 07003

The luminescence of calcium and cadmium niobates and their solid solutions have been studied, cadmium-rich members having superior (470 nm peak) emission intensities comparable to Blue

Halo, under 254 nm excitation. Incorporation of rare earths, with sodium charge compensation, resulted in phosphors with differing combinations of rare earth and host emission intensities. In the best materials, containing dysprosium or europium, the host emission is almost completely suppressed, the result with dysprosium being greater yellow emission intensity than that of cool white phosphor.

609 Luminescence of (Sr, Ce)-Hexa-Aluminates: *M. N. Alexander,* A. G. Sigai,* and *C. W. Struck,* GTE Laboratories, Inc., Waltham, MA 02254

$Sr_{1-x}Ce_xAl_{12-1/3x}O_{19}$ phosphors exhibit broad blue emissions which, like those of Ce aluminates (1), consist of subbands. Direct excitations into blue subbands have been found to occur at approximately 318, 340, and 370 nm. U.V. emission, also present, increases in relative intensity as x decreases; at $x = 0.1$, only u.v. is significant. Three u.v. doublets, at approximately (300, 320), (325, 345), and (330, 350) nm, have been observed.

1. M. N. Alexander, A. G. Sigai, and C. W. Struck, Abstract 507, p. 828, The Electrochemical Society Extended Abstracts, Montreal, Canada, May 9-14, 1982.

LUMINESCENCE AND DISPLAY MATERIALS

Phosphor Synthesis and Characterization

610 Optical and Electronic Properties of ZnSe Luminescent Thin Films: *W. B. Leigh* and *B. W. Wessels,** Dept. of Materials Science and Engineering, and Materials Research Center, Northwestern University, Evanston, IL 60201

Single crystalline ZnSe thin films have been heteroepitaxially deposited on GaAs using hydrogen vapor transport. Relatively low deposition temperatures of 700°-770°C were used in order to obtain high purity material. The resistivity, defect structure, and luminescent properties of the thin films were influenced by the zinc partial pressure used during film growth. Photoluminescence measurements on the as-grown films at 77 K indicated two narrow blue bands at 4430 and 4540Å, and a deeper band at 5260Å.

611 Effects of Barium Fluoride on the Synthesis of $Y_3Al_5O_{12}$:Tb Phosphor: *K. Ohno** and *T. Abe,* Sony Corp. Research Center, Yokohama, Japan

The luminescence efficiency of YAG:Tb phosphor was found to be much improved on firing with flux of barium fluoride. Raw yttrium and aluminum oxide powder were converted to single phase YAG by using this flux. To get single phase YAG is an essential factor determining the luminescence efficiency. This phosphor, when applied to the projection CRT, shows a good stability in the temperature and current dependences of the brightness as well as in burning.

612 An X-Ray Microanalysis Investigation of the Microhomogeneity of Garnet CRT Phosphors: *S. E. Bulpett* and *B. J. Green,** Thorn EMI Central Research Laboratories, Hayes, Middlesex UB3 1HH, England

Phosphors with a garnet structure are finding applications in high performance avionic crts. The production of these phosphors in small lots with closely controlled parameters and uniform performance has set high standards of process capability and control. As part of the development of a manufacturing process, an investigation was undertaken using x-ray microanalysis of the microhomogeneity of $(Y_{1-x}Tb_x)_3Al_{5-y}Ga_yO_{12}$ compositions prepared by different routes. The technique used and the theoretical background of the method are outlined.

613 Synthesis of Eu^{2+}-Activated $MgO \cdot CaO \cdot 2SiO_2$ and Terbium- and Cerium-Activated $ZnAl_2O_4$: *Y. Kotera,* A. Ueno, K. Yamazaki,* and *M. Kage,* School of Materials Science, Toyohashi University of Technology, Toyohashi, 440, Japan

Two kinds of new phosphor were prepared, and their optical properties were measured. Both phosphors were prepared in the reducing atmosphere. One is Eu^{2+}-activated $MgO \cdot CaO \cdot SiO_2$ and its emission peak is observed at 4500Å. It has excellent current characteristics when used as a blue component of color television. Another is terbium- and cerium-activated $ZnAl_2O_4$, whose emission under ultraviolet excitation has several peaks due to terbium.

614 Study on the Stability of Terbium Activated Lanthanum Oxybromide: *M.-Z. Su** and *Y. J. Wang,* Dept. of Chemistry, Peking University, Beijing, China

In order to explain the reason why the phosphor LaOBr:Tb gradually loses its luminescence ability in atmospheric conditions, the action of water vapor on the matrix compound LaOBr has been investigated. With the aid of several experimental methods, the reaction mechanism has been identified as follows: $LaOBr + H_2O \xrightarrow{\leq 160°} LaOBr\,H_2O \xrightarrow{160°} La(OH)_2Br \xrightarrow{360°} LaOBr$. The two intermediate products (activated by Tb) are nonluminescent. Moreover, several factors in the preparation process have been proven to have influence on the chemical and luminescent stability of LaOBr:Tb.

ORGANIC AND BIOLOGICAL ELECTROCHEMISTRY

Mechanism and Modeling of Electrochemical Membrane Processes

615 Biocatalytic Processes at Potentiometric Membrane Electrodes: *G. A. Rechnitz,* Dept. of Chemistry, University of Delaware, Newark, DE 19711

Recent progress in the empirical development of biocatalytic potentiometric membrane electrodes has far outpaced our mechanistic understanding of the operation of such probes. This situation is particularly acute in the case of electrodes where the biocatalytic phase is not simply a single enzyme but, rather, consists of intact micro-organisms or portions of plant or animal tissue. This paper addresses contemporary efforts at rationalizing possible mechanistic models and likely approaches for the experimental testing of such models.

616 Electron Transfer across Biological Membranes: An Electrodic Model of Membrane-Solution Interface: *J. O'M. Bockris** and *M. A. Habib,* Dept. of Chemistry, Texas A&M University, College Station, TX 77843

Electron transfer across biological membranes is believed to play an important role in many biological phenomena. Several redox reactions at the membrane-solution interfaces are studied and the results of Tafel slopes and transfer coefficients are found to be consistent with an electrodic model proposed. The open-circuit potential difference across the membranes is explained in terms of the difference in redox potentials of the redox couples present on each side of the membrane.

617 Noise in Ion Selective Field Effect Transistors under Nonequilibrium Conditions: *J. M. Reijn,* J. Janata,* and *J. J. Brophy,* Dept. of Bioengineering, University of Utah, Salt Lake City, UT 84112

Spectra of noise in the drain current of ion selective field effect transistors (ISFET's) can be measured for both equilibrium and nonequilibrium conditions. From these spectra physical-chemical parameters related to the interface of the solution and the FET structure may be derived. Also modeling of the ISFET can be performed with the aid of the spectra. A detailed description of the instrumentation is provided.

618 Proton Transfer in Artificial Membranes: *J. H. Fendler,* Dept. of Chemistry, Clarkson College of Technology, Potsdam, NY 13676

Proton transfer rates have been determined in aqueous micelles, bilayer surfactant, and polymerized surfactant vesicles using indicators as proton donors and/or acceptors. Steady-state absorption and emission spectroscopy have been utilized for monitoring transbilayer proton transfer occurring on slow (minutes) timescales. A laser pulse pH-jump technique allowed direct observations of ultrafast (microsecond) proton transfers. Effects of surface and transbilayer potentials, phase changes, and ionophores are discussed.

619 Induced Irreversibility of Ion Transfers across Liquid/Liquid Interfaces: *R. P. Buck,* J. D. Reid, O. R. Melroy,* and *W. E. Bronner,* Dept. of Chemistry, The University of North Carolina, Chapel Hill, NC 27514

Approximation of the equilibrium interfacial p.d. at water/nitrobenzene interfaces for partitioned salts follows from Popovych's method. Subsequent correlations of interfacial tensions using data from max. bubble pressure method and reversible Lippmann analysis show that virtually all p.d. occurs in the diffuse layers, *e.g.*, there may be no compact layer. However, chronopotentiometric data for ion transfers to and from the organic phase show typical irreversibility by curve-shape analysis. Surprisingly, apparent α values are current-dependent. Systematic variation of experimental parameters shows the irreversibility is induced by precipitation of hydrophobic anions (typically tetraphenylborate), as tetraalkylammonium salts at the aq. side of the interface. A small, but significant fraction of the current is carried by the anion, although the major fraction of the current is carried by tetraalkylammonium ions entering (or hydrophilic anions leaving) the organic phase. The current-dependent interfacial blockage with generation of time-dependent IR drop, explains the observed responses. Loss of water by hydrated ions entering the organic phase cannot explain the observations. At low current densities, and for very dilute solutions, analytical log plots of the chronopotentiograms show that the processes appear reversible.

620 Transport Properties of Phospholipid Monolayer Membrane Models: *L. Berlouis, J. Chatham, H. H. J. Girault,* and *D. J. Schiffrin,** Wolfson Centre for Electrochemical Science, Dept. of Chemistry, The University, Southampton, S09 5NH, Hants., England

Ion transfer across a 1-2 dichloroethane-aqueous LiCl interface has been investigated using impedance and interfacial tension techniques. A monolayer of phospholipid adsorbed at this interface has been used for modeling ion transport across biological membranes. Interfacial tension measurements using a recently developed image processing technique of axisymmetric drop has been applied to the study of the interfacial structure, and the mechanisms of ion transfer through lipid layers are discussed.

621 The Role of Surface Charge in Membrane Permeability Changes: *M. Blank,* Dept. of Physiology, College of Physicians and Surgeons, Columbia University, New York, NY 10032

Small shifts of surface charge across excitable membranes, *i.e.*, the gating currents, precede the ion permeability changes of the action potential. If we assume that an increase in ion permeability is due to the opening of a molecular pore, we can model this process like subunit dissociation in oligomeric proteins. (The dissociation of hemoglobin tetramers into dimers is sensitive to changes in charge and occurs when the surface charge is approximately the same as on

the inner face of the squid axon membrane.) The relation between the hemoglobin dissociation constant and charge, together with the estimated number of pores in the axon membrane, lead to a relation between the fraction of pores open and the surface charge density. This latter relation can be incorporated into the surface compartment model (SCM), so that the gating currents give rise to voltage (polarization) dependent changes in ion permeability.

622 Ion Gates. Electroactive Membranes with Embedded Electrodes: *P. Burgmayer* and *R. W. Murray,** Dept. of Chemistry, Kenan and Venable Laboratories, University of North Carolina, Chapel Hill, NC 27514

The ionic permeability of a polypyrrole membrane is higher for the oxidized (poly-cationic) form of this electroactive polymer than it is for the reduced (neutral) form. By embedding a porous gold electrode in the membrane, thereby controlling the membrane oxidation state, one can turn "on and off" (ion gate) the flow of ions between two electrolyte solutions separated by the membrane.

623 Enhanced Charge Transport by Electron Exchange Between Redox Reagents Incorporated in Polymer Films: *F. C. Anson* and *D. A. Buttry,** Div. of Chemistry and Chemical Engineering, California Institute of Technology, Pasadena, CA 91125

The enhancement of electron exchange of the diffusion-like propagation of redox reagents within polymer films is discussed. The consequences of such an enhancement along with the conditions necessary for its presence are presented. Procedures for extracting information about the kinetics of the electron exchange process from the experimental data are described.

624 Charge Transfer Reactions Involving Physically Constrained Molecules: *B. S. Pons* and *J. F. McAleer,** Dept. of Chemistry, University of Alberta, Chemistry Centre, Edmonton, Alta., Canada T6G 2E1

Polymer films containing trapped redox centers have been prepared in order to study: *(i)* the effects of such centers on the charge transfer characteristics of the film, *(ii)* reactions which would not be observable if the electrogenerated species were not constrained. The polymerization of biphenyl is shown to be analogous to pyrrole with the advantages of easily modified conductivity and extensive "trapping" ability at considerably lower cost. F.T.I.R. was used extensively in film characterization.

625 Characterization of Electrodes Coated with Polymer Networks Cross-Linked by Gamma-Irradiation: *E. S. DeCastro, D. A. Smith, D. Villarroel, J. E. Mark,* and *W. R. Heineman,** Dept. of Chemistry, University of Cincinnati, Cincinnati, OH 45221

Cross-linking by gamma-irradiation is a convenient means of immobilizing thin films of ionic, water-soluble polymers on electrode surfaces for subsequent use in aqueous solutions. Redox mediators can be covalently attached to the polymer network by the irradiation procedure. The electrochemical properties of electrodes prepared by coating poly(diallyldimethylammonium chloride) (DDAC) and poly(vinylbenzyltrimethylammonium chloride) (VTAC) on graphite or platinum, and irradiated with 0.1-25 Mrad doses have been evaluated. The efficiency of permanent incorporation of 2,6-dichlorophenolindophenol (DCIP) and hydroquinone (HQ) into ionic polymer films by cross-linking has been evaluated by electrochemical and spectroelectrochemical methods. The applicability of these electrodes to catalysis has been demonstrated by reduction/oxidation of cytochrome c at a Pt-DDAC-DCIP electrode, and by oxidation of NADH at a graphite -VTAC-HQ electrode.

626 Electron Transfer Reactions across the Polymer/Polymer Interface of Bilayer Electrodes: *C. R. Leidner** and *R. W. Murray,* Dept. of Chemistry, Kenan and Venable Laboratories, University of North Carolina, Chapel Hill, NC 27514

Pt electrodes coated sequentially with two different spatially-segregated polymers [for example poly-(Fe[vbpy]$_3^{2+}$) *(I)* and poly-(Ru[vbpy]$_3^{2+}$) *(II)*] exhibit charge trapping phenomena due to the redox conductivity properties of the polymer films. The kinetics of charge trapping appear, under some circumstances, to be limited by the rate of electron transfer across the polymer/polymer interface. To try to understand this phenomenon better, we have devised cyclic voltammetric and rotated disk voltammetric methods to measure the interfacial electron transfer rates for Pt/*(I)*/*(II)* and Pt/*(II)*/*(I)*.

627 Electrocatalysis at Modified Polysulfurnitride and Other Conducting Polymers: *H. B. Mark, Jr.,** *J. F. Rubinson, L. Laguren, K. Shenoy, D. Cunningham,* and *H. Zimmer,* Dept. of Chemistry, University of Cincinnati, Cincinnati, OH 45221

Molybdenum ions and complexes immobilized on polysulfurnitride membrane electrodes have been found to reduce acetylene to ethylene/ethane in basic media. The nature of the active site and the mechanism of the reaction are discussed. The results of attempts to reduce dinitrogen to ammonium is also presented. The syntheses, conductivity, and electrode properties of metal containing substituted polyacetylenes, $(CR)_x$, are described. These systems may be possible models for the study of metal binding to biological membranes.

628 Photoelectrochemical Behavior of TiO_2 Pigmented Membranes: *J. Li* and *L. M. Peter,** Dept. of Chemistry, The University, Southampton, England S09 5NH

Titanium dioxide pigments have been incorporated into thin nitrocellulose membranes on a glassy carbon/gold rotating ring-disk electrode. The membrane electrode is photosensitive, and illumination in air saturated electrolyte solutions produces hydrogen peroxide which is detected either at the carbon disk or at the gold ring. The resulting photocurrents can be used to characterize the spectral response and the photoactivity of TiO_2 pigments, factors which play an important role in the photodegradation of TiO_2 based paints. Pulsed illumination of the pigment/membrane system has been used to characterize the diffusion of H_2O_2 in the membrane, allowing criteria for the design of a sensitive detection system to be established.

629 Theory of the Gated and Channeled Transfer of Ions Across Lipid Membranes: *S. Chang, C. Korzeniewski,* and *P. P. Schmidt,** Dept. of Chemistry, Oakland University, Rochester, MI 48063

The cationic conduction channel across a lipid membrane is modeled with helical strands of alamethicin-type molecules. Ring-like aggregates of phosphate and bound counterion impede cationic migration. By virtue of a surface breathing mode, the ring-like structures can expand. The barrier to ionic migration then disappears. This fact is demonstrated with the use of model potentials. Also presented are the expressions for tunneling and migrational rate constants.

630 Dynamic Impedance Models for *In Situ* Determinations of Ion Binding and Transport Kinetics: Application to Living Cell Membranes: *A. A. Pilla,* Bioelectrochemistry Laboratory, Dept. of Orthopedic Surgery, Mount Sinai School of Medicine, New York, NY 10029

This study presents an approach, using Laplace plane analysis, which allows any mechanistic combination of ion binding and transport to be described via an impedance function. These functions are represented by topologically restricted electrical equivalent circuits for ease in parameter determination. These models have been tested on isolated living cell membranes using equipment having 10 nsec time resolution. To date, dielectric membrane capacitance, specific adsorption, and ion transport pathways have been isolated and related to extracellular ion composition and cell functional state.

631 Proton Transport in Beta″ Alumina: *K. Frase* and *G. C. Farrington,** Dept. of Materials Science, University of Pennsylvania, Philadelphia, PA 19104, and *J. Thomas,* Institute of Chemistry, University of Uppsala, Uppsala, Sweden

Hydronium beta″ alumina is a high conductivity solid electrolyte for protons. This paper discusses the mechanism of proton diffusion in this compound on the basis of new stability, conductivity, and structure analyses.

632 Adsorbed Proteins in Simulating Membrane Processes: *J. Haladjian** and *P. Bianco,* Laboratoire de Chimie et Electrochimie des Complexes, Universite de Provence, Marseille, Cedex 3, France

The elementary system (electrode/adsorbed protein/solution) constitutes a suitable pattern to simulating the link of an electron carriers chain. This approach is used for several mono- and polyhemic c-type cytochromes. The role played by the adsorbed proteins layer in the mechanism of electron transfer is discussed. The effect of some adsorbable substances on the nature of the adsorbed layer is studied.

633 An Electrochemical Investigation of the Reaction of Cytochrome c with Mitochondria and Models Thereof: *F. A. Armstrong,** *H. A. O. Hill,* and *N. J. Walton,* Inorganic Chemistry Laboratory, Oxford, England OX1 3QR

The advent of electrodes that allow rapid, direct electron transfer to redox proteins has extended the range of application of electrochemical methods to the study of biological systems. We have investigated the electrochemistry of horse heart cytochrome c at a number of modified electrodes and have recently investigated its reactions with enzymes that are components of respiratory chains. The natural extension of this work is to study the reactions of cytochrome c with mitochondria, or fractions thereof. *Paracoccus denitrificans* has been proposed as a model of the precursor of the mitochondrion. Its reactions with horse heart cytochrome c are described.

634 Electron Transfer Properties of Immobilized Cytochrome c: *M. A. Schafer* and *G. S. Wilson,** Dept. of Chemistry, University of Arizona, Tucson, AZ 85721

The electron transfer properties of immobilized biocatalysts are of interest not only as models for biological systems, but also as electrocatalytic mediators. There are many examples of biological activity modification resulting from covalent attachment of protein to surfaces, so it is necessary to establish that desirable properties can be preserved. The properties of immobilized cytochrome c, and its respective reactions with cytochrome reductase and oxidase is discussed in this context.

635 Photosynthetic Oxidation of Water to Dioxygen in Chloroplast Membranes: *K. Sauer** and *J. L. Casey,* Dept. of Chemistry and Chemical Biodynamics Div., Lawrence Berkeley Laboratory, University of California, Berkeley, CA 94720

The absorption of visible light by chlorophyll in chloroplast membranes results in the transfer of four electrons from two water molecules to form O_2. The four-electron transfers occur one-at-a-time, and oxidizing equivalents at high reduction potential are stored in the membrane for the order of a minute. Manganese is in-

volved in the water-oxidation complex. Five intermediate states have been identified kinetically, and one of these has been detected by EPR. We have used the temperature dependence of these reactions to explore the energies of photosynthetic water oxidation.

636 Direct Observation by Laser Flash Photolysis of Light-Induced Electron Transfer Within and Across Chlorophyll-Containing Lipid Bilayer Vesicle Membranes: *G. Tollin,* W. E. Ford,* and *Y. Fang,* Dept. of Biochemistry, University of Arizona, Tucson, AZ 85721

The radical products of electron transfer between chlorophyll (C) triplet and acceptors (A) such as quinones or methyl viologen (C^+ and Av) can either recombine or, in the presence of an electron donor, C^+ can be reduced. The latter process will proceed when acceptor and donor are asymmetrically localized, resulting in vectorial electron transport across the vesicle via intrabilayer electron transfer. Reactions at the outer or inner bilayer-water interfaces display marked asymmetry and are sensitive to the charge state of the bilayer surface.

637 Similarities in the Redox Behavior of Two Flavoprotein Oxidase Enzymes: *M. Stankovich,* Dept. of Chemistry, University of Minnesota, Minneapolis, MN 55455

The redox properties of the flavoprotein L-amino acid oxidase have been measured at pH 7.0 at 4°C using spectroelectrochemical methodology. During the course of reductive titrations, the enzyme stabilizes 95% of the one electron reduced form. Therefore the enzyme appears to transfer electrons in single electron steps. When redox potential measurements of the 2 electron transfers were made, the $E°$ values of the two electrons were separated by 150 mV. This behavior is very similar to that observed for lactate oxidase, another well-characterized flavoprotein oxidase enzyme.

ORGANIC AND BIOLOGICAL ELECTROCHEMISTRY

Structure and Reactivity in Organic Chemistry and Electrochemistry

638 Ring Forming Reactions Using Electrochemical and Nonelectrochemical Methods. II. Electrochemical Conversion of Secondary Nitroalkanes to Ketones: *R. D. Little,* M. M. Baizer, S. T. Nugent, W. T. Monte,* and *L. Moens,* Dept. of Chemistry, University of California, Santa Barbara, CA 93106

A comparison between the *MIRC* (Michael initiated ring closure) and the analogous *ERC* (electroreductive cyclization) reaction is made, particular attention is focused upon the fact that with the same substrate, either α or β closure can be achieved by using either *MIRC* or *ERC* techniques, respectively. Several of the many nonelectrochemical means of converting nitroalkanes to ketones are compared with our recently discovered electrochemical analogue involving the use of electrogenerated superoxide in the presence of molecular oxygen.

639 Cathodic Processes in Solutions Containing CO_2 and Aromatic Hydrocarbons: *L. A. Avaca, E. R. González,* and E. A. Ticianelli,* Instituto de Física e Química de São Carlos, 13.560 São Carlos, SP, Brazil

The cathodic processes occurring on Hg in 0.1M TEAB/DMF solutions containing CO_2 and a series of ten polynuclear aromatic hydrocarbons were studied by cyclic voltammetry and double potential step chronoamperometry. When the aromatic reduces clearly before or after CO_2, the results indicate that the initial electron transfer is followed by a coupling reaction, while for those reducing close to CO_2, the interpretation is not straightforward. In those cases when the aromatic reduces reversibly before CO_2, it was possible to obtain the rate constant for the coupling reaction as well as to establish that this reaction is followed by an homogeneous electron transfer between the aromatic radical anion and the coupling product. (This work was supported by CNPq, Brazil.)

640 A Tetraalkylammonium Amalgam: *E. Kariv-Miller** and *C. Nanjundiah,* Dept. of Chemistry, University of Minnesota, Minneapolis, MN 55455

Tetraalkylammonium amalgams, in principle, should be powerful reducing agents. But, although mentioned in literature, they are virtually unknown. The electrochemical reduction of dimethylpyrrolidinium iodide (DMP) on mercury was investigated, and it was shown that it reacts by a reversible one electron process. The product is an insoluble amalgam which consequently reacts with the solvent regenerating the DMP cation. The catalytic nature of the sequence and the possible use in synthesis are being explored.

641 Mechanism of the Decomposition of Benzoate Ester Radical-Anions: *J. H. Wagenknecht,* R. D. Goodin, P. J. Kinlen,* and *F. E. Woodard,* Monsanto Co., St. Louis, MO 63167

The electrochemical reduction of simple benzoate esters to the radical anions has been known for many years. However, the mechanism of decomposition of the radical-anions has not been reported. This paper shows that the radical anions cleave to give benzoate anion and the alkyl radical based on the kinetics of first-order decomposition of various esters and the products of the reactions.

642 Relationship Between Electrochemical and Chemical Oxidation of Organic Sulfur Compounds: *W. K. Musker,* Dept. of Chemistry, University of California, Davis, CA 95616

The influence of neighboring groups on the reactivity of organic molecules is extended to include redox reactions. Detailed studies of the oxidation of a number of appropriately substituted thioethers with various oxidizing agents [nitrosyl tetrafluoroborate, iodine, sodium periodate, copper(II) salts, etc.] have recently been carried out and can be compared with electrochemical data. For certain thioethers, the chemical oxidation rate can be accelerated by $\sim 10^6$ and the oxidation potential can be lowered by almost a volt. Similar effects are observed with other organic molecules containing divalent sulfur.

643 Cation Radical Reactions: *H. J. Shine,* Dept. of Chemistry, Texas Technological University, Lubbock, TX 79409

Comparisons of a number of homogeneous aromatic and heteroaromatic cation radical reactions with nucleophiles are made with their anodic counterparts or analogous organic reactions. Thus, reactions with fluoride, cyanide, nitrite, and nitrate ions are compared with anodic fluorination, cyanation, and nitration. The role of cation radicals in certain electrophilic aromatic substitutions (e.g., nitration) and rearrangements (e.g., nitramine) is discussed and also compared with homogeneous reactions of cation radicals with nucleophiles. Other electron exchange reactions are discussed.

644 Electron-Transfer from Photo-Excited Ion Radicals: *H. Lund** and *J. Eriksen,* Dept. of Organic Chemistry, University of Aarhus, DK-8000 Aarhus C, Denmark

Anion radicals in their photochemically excited state are better electron donors than the parent anion radicals. The rate of electron transfer from photochemically excited anion and cation radicals has been measured using the fluorescence quenching method, and the results discussed in terms of Marcus' theory. The use of photochemically excited anion radicals in preparative electrolysis makes it possible to generate a strongly reducing agent in a generally much less reducing environment, which may influence a competition between different reaction pathways.

645 The Application of Electrocatalysis to Difficult Organic Conversions: *P. J. Peerce-Landers,* Occidental Research Corp., Irvine, CA 92714

Electrocatalysis can increase the attractiveness of electrochemical routes for the production of organic chemicals. This is especially true when the classical approach involves the use of forcing conditions, stoichiometric quantities of environmentally objectionable reagents, multiple steps and/or is relatively nonselective. Recent literature examples illustrating how electrocatalysis can overcome these disadvantages are described. Moreover, the lifetimes of homogeneous catalysts susceptible to redox deactivation can be electrolytically prolonged *in situ* with little power consumption. Examples of the successful use of this strategy are discussed.

646 Chemical Events in Kinetically Heterogeneous Systems Involving Reactants All Dissolved in the Same Solvent: *J. F. Bunnett,* University of California, Santa Cruz, CA 95064

Alkali metals dissolved in ammonia react with many organic halogen compounds to form radicals which may *(i)* be terminated by reaction with further electrons or *(ii)* undergo other reactions (intramolecular additions or attachment to nucleophiles in $S_{RN}1$ chain processes). These rapid reactions occur during mixing. The extent to which reactions *(ii)* occur during the short interval between the times of arrival of the initiating and terminating electrons varies with the identity of the halogen and other factors.

647 Electron-Transfer Mechanisms in Organic Chemistry: *C. L. Perrin,* Dept. of Chemistry, University of California, San Diego, La Jolla CA 92093

Structure-reactivity correlations involving both kinetic and electrochemical parameters can be used to judge the possibility of an electron transfer mechanism. The cases where the electron transfer is endergonic must be distinguished from those rare cases where the electron transfer is exergonic or thermoneutral. Special attention is devoted to the particular example of nitration of reactive aromatics. The fates of the radical ion, under conditions of homogeneous kinetics and of electrochemical generation, are compared.

648 Linear Free Energy Relationships in Organic Electrochemistry: *P. Zuman,* Dept. of Chemistry, Clarkson College of Technology, Potsdam, NY 13676

Successful applications of Hammett and Taft type equations for treatment of half-wave potentials or equivalent data for both reversible and irreversible systems as well as for heterogeneous rate constants of irreversible systems indicate that reactivity of organic compounds depends on structure similarly for both chemical and electrochemical reactions. Thus, for electrochemical reactions, the electron density distribution rather than adsorbability plays primary role. Electrochemistry is particularly suited for investigation of the effect of the structure of the reactive center on the susceptibility to substituent effects (σ-values). Correlation between electrochemical data and C^{13} NMR chemical shifts is discussed.

649 Electrochemistry of Adsorbed Aromatic Intermediates: *A. T. Hubbard, M. P. Soriaga, J. L. Stickney,* and *J. H. White,* Dept. of Chemistry, University of California, Santa Barbara, CA 93106

Accurate packing density measurements as a function of concentration for twenty-nine aromatic compounds adsorbed on smooth platinum thin-layer electrodes from aqueous solutions have revealed a series of sharp orientational transitions [*J. Amer. Chem. Soc.*, **104**, 2735 (1982); *ibid.*, 2742; *ibid.*, 3927]. Anion adsorption also triggers these transitions, as does adsorption of typical nonaqueous solvents. Comparison at packing densities with molecular models

permits assignment of these orientational transitions. Coulometric measurements of the electrolytic charge to oxidize these oriented adsorbed molecules are reported, which indicate that each adsorbed orientation displays unique electrochemical reactivity. Details of reactivity as a function of orientation are presented. Studies of the temperature-dependence of orientation are also reported. Raising the temperature partially converts a flat-oriented layer to edge-bonded states, and excites librational modes of the edge-bonded states. Reactivity of the attached species changes accordingly. Implications of these observations for electro-organic chemistry and for nonelectrochemical applications of these same compounds and surfaces are dicussed.

650 Electropolymerization Reactions of Aromatic Compounds: *A. F. Diaz*, IBM Research Laboratory, San Jose, CA 95193

Thick polymeric films can be readily prepared by the electrooxidation of some derivatives of aniline, pyrrole, and thiophene. The reaction is ECE type, has electrochemical stoichiometry, and proceeds via a highly reactive π-radical cation. The reaction has chemical specificity where the main product is the α,α'-condensed linear polymer and, as expected for cation reactions, it is influenced by steric effects and the nucleophilicity of the solution. The corresponding chemical route to these polymers is less straight forward and leads to materials which have different properties. The characteristics of these reactions and their products are described.

651 Oxidative Electropolymerization of Aromatic Molecules: *J. Bargon,* S. Mohmand*, and *R. T. Waltman*, IBM Research Laboratory, San Jose, CA 95193

Electrochemical oxidation of many benzenoid, nonbenzenoid, and heterocyclic aromatic monomers yields electrically conducting polymers. The reaction mechanism involves combination of intermediate radical cations, followed by deprotonation via a base. The oligomers so obtained oxidize more readily than the corresponding monomer and react further with oxidized monomer. This electrochemically induced process differs from typical homogeneous polymerization mechanisms, which all feed on neutral monomer. In the vicinity of electrodes (and possibly enzymes) only oxidized monomer is available.

652 Neighboring Group Participation in Electron Transfer from Dialkyl Thioethers: *R. S. Glass,* B. R. Coleman, W. N. Setzer*, and *G. S. Wilson*, Dept. of Chemistry, University of Arizona, Tucson, AZ 85721

Neighboring group participation at carbon, that is interaction of a substituent with a carbon reaction center resulting in partial or complete bonding, has been well studied. Extension of this concept to redox reactions of thioether sulfur centers is of considerable current interest. Insight into this phenomenon is provided by electrochemical and spectroscopic studies on the influence of molecular architecture on electron transfer from dialkyl sulfides appended with neighboring groups.

653 Electrochemical Reduction of Dinitrotoluene Isomers: *M. H. Miles** and *D. A. Fine*, Chemistry Div., Research Dept., Naval Weapons Center, China Lake, CA 93555

All six isomers of dinitrotoluene (DNT) were investigated using silver electrodes. Experimental potentials for the reductions decreased in the order 2,5-DNT>3,4-DNT>2,3-DNT>3,5-DNT>2,6-DNT~2,4-DNT. These results suggest that *ortho* or *para* $-NO_2$ and meta $-CH_3$ groups favor the reduction of the other $-NO_2$ group while a *meta* $-NO_2$ or *ortho* $-CH_3$ group hinders the reduction. Cyclic voltammetric studies at 100 mV/sec in 0.5M NaCl-0.1M Na_2CO_3-0.1M $NaHCO_3$ solutions showed three reduction peaks for 3,4-DNT, two reduction peaks for 2,5-DNT and 2,3-DNT, and only a single reduction peak for the other three isomers. Preliminary kinetic studies suggest that the rate-determining step may involve the simultaneous transfer of $3e^-$, $2e^-$, or $1e^-$ depending on the isomer. An exhaustive electrolysis study of 2,5-DNT gave two waves with $2e^-$/molecule for the first step and $6e^-$/molecule for the second step. A dramatic color change from colorless to bright orange-red occurs during the first reduction wave which then fades to nearly colorless during the second wave.

654 The Probable Condensed-Phase Preparation of the p-Nitrophenyl Nitrene Anion Radical: *D. E. Herbranson, R. N. McDonald*, and *M. D. Hawley,** Dept. of Chemistry, Kansas State University, Manhattan, KS 66506

The electrochemical reduction of p-nitrophenyl azide in DMF-0.1M (n-Bu)$_4$NClO$_4$ affords an anion radical ($t_{1/2}$ < 1 msec at −51°C) which rapidly reacts to give p-$O_2NC_6H_4NH^-$, p-$O_2NC_6H_4NC(O)NMe_2^-$, and p,p'-$O_2NC_6H_4N{=}NC_6H_4NO_2$ as the principal electroactive products. When electroinactive $(CH_3C{=}O)_2$ is added to the electrolysis mixture, p-$O_2NC_6H_4NC(O)CH_3^-$ is formed by a reaction channel involving addition of an intermediate anion radical to $(CH_3C{=}O)_2$, followed by β-fragmentation of the adduct anion radical. The anion radical which is trapped by $(CH_3C{=}O)_2$ is believed to be the nitrene anion radical, p-$O_2NC_6H_4N^-$.

655 Reaction Pathways of Aryl Ether Radical Anions: *D. E. Bartak,* M. D. Koppang, T. A. Thornton*, and *N. F. Woolsey*, Dept. of Chemistry, University of North Dakota, Grand Forks, ND 58202

The reductive cleavage of the carbon-oxygen bond in a series of aryl alkyl and diaryl ethers was studied by both chemical and electrochemical techniques. Cyclic voltammetric, double and single potential step chronoamperometric, and controlled potential coulometric techniques in conjunction with alkali metal/hexamethylphosphoramide (HMPA) homogeneous chemical systems were utilized. A series of alkyl aryl ethers was shown to reductively cleave beta to the aryl moiety. In contrast, a series of phenoxy-substituted aryl ethers cleaved alpha to the larger aryl moiety. The reaction pathways for the ether radical anions were dependent on structural features of the ether. Both unimolecular and bimolecular reaction pathways of the ether radical anions are shown to be important. Kinetic evidence for the above reactions is presented. Mechanisms for the carbon-oxygen bond cleavage is postulated.

656 Photochemical and Electrochemical Generation and Reactions of Olefin Radical Cation-Superoxide Ion Pairs: *C. S. Foote,* K. J. Lee*, and *P. M. Allen*, Dept. of Chemistry, University of California-Los Angeles, Los Angeles, CA 90024

Photosensitized electron transfer reactions produce radical anion-radical cation pairs in solution. Interaction of the radical anion with oxygen leads to superoxide ion, which can react with the radical cation either to give products or back electron transfer. Electrochemical generation of the superoxide/radical cation pair can also be carried out with similar results, although this reaction is complicated by radical cation-neutral reactions.

657 Electro-organic Reaction with A-C Electrolysis: *C. Y. Cheng* and *D-T. Chin*, Dept. of Chemical Engineering, Clarkson College of Technology, Potsdam, NY 13676

Recently alternating current (a-c) has been shown to be capable of improving the kinetics of slow electrochemical reactions. In this work sinusoidal alternating voltage was superimposed onto a lead rotating disk electrode, and a potentiostatic method was used to determine the apparent exchange current density and Tafel slopes of several electro-organic reactions, such as the oxidation of phenol to hydroquinone and the reduction of benzoic acid to benzyl alcohol. The improvement by a.c. on the reaction rate and current efficiency is discussed.

658 The Chemical and Electrochemical Oxidation of Indoles and Isoquinolines: *M. Sainsbury*, School of Chemistry, University of Bath, Claverton Down, Bath, England BA2 7AY

Correct transition state geometries play an important role in determining the course of aryl aryl coupling reactions. Relatively small changes in stereochemistry may lead to intermolecular rather than to intramolecular bond formation. In chemical oxidations of the same substrates different structures often form, possibly reflecting the involvement of organometallic intermediates en route to the final products. These remarks are exemplified by reference to our results from the chemical and electrochemical oxidations of isoquinoline and indole derivatives.

ORGANIC AND BIOLOGICAL ELECTROCHEMISTRY

Ions and the Electrochemical Control of Cell Functions

659 Molecular Considerations Relevant to the Mechanism of Active Transport: *J. Kyte*, Dept. of Chemistry, University of California, San Diego, La Jolla, CA 92093

A small group of closely related proteins is responsible for all active transport in animal cells, and inorganic cations are the only substances transported by these enzymes. They share a common kinetic mechanism in which two fundamental conformations participate, each receiving and dispatching substrates from its unique side of the membrane. During transport the cations must pass through their enzyme to cross the membrane. A monomer of the catalytic subunit from these enzymes comprises the functional unit of active transport.

660 Monoclonal Antibodies, Ion Flux Regulation, and the Control of Hepatocyte Proliferation: *H. L. Leffert,* K. S. Koch, D. Schenk, P. Shapiro, H. Skelly*, and *M. Schumaker*, Dept. of Medicine, M-013-H, Div. of Pharmacology, School of Medicine, University of California, San Diego, La Jolla, CA 92093

Polypeptides that stimulate rat hepatocyte proliferation (EGF, glucagon, and insulin) activate amiloride and ouabain-sensitive influxes of sodium and rubidium ions, respectively. To evaluate causal relationships between these membrane cation fluxes and mitogenesis, suggested from but not established by findings that both drugs reversibly block growth initiation, a panel of monoclonal antibodies to preparations of rat (Na^+-K^+)ATPase has been generated from mouse hybridomas. The immunochemical and biological properties of these antibodies are described.

661 Is "Turned-On" ($Na^+ + K^+$)-ATPase of Mouse Embryonic Fibroblasts Secondary to Activation of a Protein Kinase?: *C.E. Wenner** and *K.J. Leister*, Roswell Park Memorial Institute, Buffalo, NY 14263

The basis for the stimulation of ouabain sensitive $^{86}Rb^+$ uptake by TPA in post confluent C3H 10T½ fibroblasts or for that of stimulation of basal activity of MCA C3H 10T½ fibroblasts is not yet established. ($Na^+ + K^+$)-ATPase activity of the transformed cells is elevated in 0.5% FCS serum and exhibits marginal stimulation with 10% serum as compared to post-confluent normal fibroblasts. The role of Na/H^+ antiport and Ca^{2+}-calmodulin dependent reactions and/or associated protein kinase-reactions in the stimulated responses is discussed.

662 Induced Pulsating Currents Affect Membrane Bound Enzyme Kinetics: Application to Na-K ATPase Using a New Flow System: *K. Gary, A.A. Pilla,* and C. Mayaud,* Bioelectrochemistry Laboratory, Dept. of Orthopedic Surgery, Mount Sinai School of Medicine, New York, NY 10029

We have previously reported that low level electromagnetically induced currents, designed to affect cell surface electrochemistry, can modulate ouabain-sensitive Na efflux from human erythrocytes. This study further quantitates the relationship between waveform parameters and Na efflux rate. A newly developed flow system, utilized in conjunction with Na and K ion specific electrodes and ATP determinations, has allowed a more precise evaluation of the effect of pulse duration amplitude and repetition rate for specific exposure times. Frequency domain spectral analysis is used to correlate this with observed ion adsorption kinetics from transient impedance studies, and with known enzyme turnover times.

663 Intracellular pH and Control of Cellular Proliferation: *R.J. Gillies,* Dept. of Biochemistry, Colorado State University, Fort Collins, CO 80523

Within the past decade or so, it has become feasible to accurately determine the cytoplasmic pH (pH^{in}) of living cells. Using a variety of techniques, we have seen that pH^{in} is highly regulated in cells as diverse as *E. coli* and mammalian cells. In addition, changes in the pH^{in} can be correlated with cellular functions related to proliferation, such as DNA synthesis and energy metabolism. In a few instances, manipulation of pH^{in} has been shown to have dramatic effects on cell growth. Despite these considerable efforts, it remains unclear what role pH^{in} plays in the regulation of cellular proliferation.

664 Microenvironmental Changes Associated with Electrical Stimulation of Osteogenesis by Direct Current: *T.J. Baranowski, Jr.,* J. Black,* and *C.T. Brighton,* McKay Laboratory of Orthopaedic Surgery Research, Dept. of Orthopaedic Research, University of Pennsylvania, Philadelphia, PA 19104

It has been suggested that osteogenesis elicited by a direct current is a cellular response to a decrease in oxygen tension and an increase in pH as a result of reduction processes at the cathode. This investigation was performed to determine *in vivo* if microenvironmental changes in the pO_2 and pH near a stainless-steel cathode could be correlated with the degree of biological response stimulated electrically in the medullary canal of a rabbit tibia. Osteogenesis stimulated by an optimal direct current of 20 μA is associated with large reduction of pO_2 and a slight elevation of pH. At a lower current of 1 μA, there is no significant osteogenesis and no change in either pO_2 or pH. At a higher current of 50 μA, there is a failure to achieve a large reduction of pO_2 though a considerable alkaline shift of pH does occur. This is associated with less new bone growth than that found at an optimal current and cellular necrosis as well as void spaces within the canal secondary to electrolysis at the cathode.

665 Why Use Ions to Regulate Cells?: *R.A. Steinhardt,* Dept. of Zoology, University of California, Berkeley, CA 94720

Using fertilization and other important cell transitions as examples, this paper examines how ionic activities can serve to coordinate several diverse metabolic pathways. Additionally, it discusses whether intracellular pH is a general regulator or whether it is reserved for special situations such as the transition from dormancy to cell growth.

666 The Role of Electrogenic Sodium Transport in Early Embryonic Development: *C.D. Stern,* Dept. of Anatomy and Embryology, University College London, London, England, WC1E 6BT

The transporting properties of the ectoderm of early chick embryos were investigated by several techniques. It was found that this tissue generates a potential across itself amounting to about 20 mV, resulting mostly from unidirectional sodium transport. The resulting electrochemical gradients also drive water across the epithelium. Applying voltages of similar magnitude but of opposite polarity, very quickly and stably reverses the morphological and functional polarity of the tissue. These gradients probably control many of the steps involved in the formation of the primary embryonic body axis.

667 How a Transient Rise in Calcium Causes Activation of the Egg at Fertilization: *D. Epel* and *M. Poenie,* Dept. of Biological Sciences, Hopkins Marine Station of Stanford University, Pacific Grove, CA 93950

Recent studies on eggs from a variety of organisms demonstrates that shortly after fertilization the free calcium level transiently increases for several minutes. This rise in calcium is somehow a causal trigger for activation since increasing calcium levels will artificially activate eggs and preventing the increase, as with chelators, will prevent egg activation. This paper centers on the mechanism of calcium release at fertilization and the targets with which calcium interacts with during this brief period.

668 Injury, Electrical Fields, and Regeneration: *R.B. Borgens,* Dept. of Anatomy, School of Veterinary Medicine, Purdue University, West Lafayette, IN 47907

Steady electric (ionic) currents and their associated fields are now understood to play a role in the early development of a variety of plants and animals. Such endogenous fields are also produced when a cell or tissue is injured, and are probably an early controlling factor in the ultimate response to injury. The evidence supporting this view comes from studies into the electrical controls of amphibian regeneration, and the electrical control of CNS nerve regeneration in lamprey. [Borgens, *Int. Rev. Cytol.* **76**:245 (1982)].

669 The Transducer System Activated by Nerve Growth Factor (NGF): *K.H. Pfenninger,* Dept. of Anatomy and Cell Biology, College of Physicians and Surgeons, Columbia University, New York, NY 10032

Hirata and Axelrod (1980) have described a complex membrane transducer system which is initiated by receptor-mediated phospholipid transmethylation. This leads to Ca^{2+} influx, and the Ca^{2+}-calmodulin complex then activates phospholipase A_2 (PLA_2), probably via two protein phosphorylation steps (Hirata, 1981). PLA_2 cleaves phosphatidylcholine into lysophosphatidylcholine, the putative fusogen for exocytosis, and arachidonic acid, a precursor of prostaglandins, and other second messengers. NGF has been demonstrated to trigger rapid and transient phospholipid methylation, as well as arachidonic acid release in the nerve growth cone region. Furthermore, growth cones are rich in calmodulin, and the importance of Ca^{2+} influx has been suggested by the work of Gundersen and Barrett (1980). Thus, NDG activates a transducer system that is believed to control vectorial growth, and that includes Ca^{2+} influx as an intermediary step. This may explain the influence ions and electric fields have on vectorial growth of neurons.

670 Inorganic Ion Requirements for Proliferation of Normal Cells in Defined Media: *R.G. Ham,* Dept. of Molecular, Cellular and Developmental Biology, University of Colorado, Boulder, CO 80309

After a brief summary of defined medium culture systems and of qualitative requirements for inorganic ions, attention is focused on quantitative requirements. The amount of calcium ion that supports optimal proliferation is of particular interest. Variables that affect the calcium requirement include the type of cell, whether it is normal or transformed, the kinds and amounts of growth factors and/or undefined supplements that are in the medium, and the cellular population density. Cells that are stimulated by high levels of magnesium are also discussed.

671 Comparative Effects of Pulse Electromagnetic Fields and Growth Factors upon Culture Chondrocytes: *M.T. Corvol,* Unite de Recherche sur les Maladies du Metabolisme chez l'enfant, INSERM U30, Hopital Necker-Enfants malades, Paris, France, and *J.D. Monet, N. Dautigny,* and *J. Assailly,* Centre de Technologie Biomedicale, INSERM SC24, Hopital Necker-Enfants malades, Paris, France

Effects of PEMF's and growth factors such as fibroblast growth factor and eye derived growth factor were studied comparatively upon DNA synthesis and cell multiplication of chondrocytes grown in culture. Since the growth promoting effect of growth factors is time and dose dependent with maximum effect around 100 ± 10% over controls, PEMF's induce only an "all or nothing" response, which never exceed 20 ± 5% over control values. Furthermore, the stimulating effct of PEMF's is only observed on dividing cells. These observations suggest that PEMF's act on this model through different pathways than those initiated by growth factors.

672 Calcium Activities Inside Small Intact Cells Such as Lymphocytes: *R.Y. Tsien,* T. Pozzan,* and *T.J. Rink,* Dept. of Physiology-Anatomy, University of California, Berkeley, CA 94720

Understanding how calcium controls the functions of cells of medical importance requires measuring calcium ion activities as low as 10^{-8}M, in the presence of 10^{-3}M magnesium, inside cells with volumes of 10^{-4}-10^{-12} liters. Recent technical progress has made such measurements routine and shows that increases in calcium activity and in plasma membrane potential are among the first events in lymphocytes upon stimulation by mitogens.

673 Human Lymphocytes Membrane Receptors, Lectins, and Electric Fields: Modeling and Experimental Results: *M. Grattarola* and A. Chiabrera,* Institute of Electrical Engineering, University of Genoa, Genoa, Italy, *G. Bonanno,* Institute of Pharmacology, University of Genoa, Genoa, Italy, and *A. Raveane,* Institute of Electrical Engineering, University of Genoa, Genoa, Italy

Weak electric fields have been shown to influence several properties of many biological systems. Following our previous findings about the inhibitory effect exerted on lectin-stimulated human lymphocytes by the same electromagnetic signal already clinically utilized for bone healing, we describe a model of possible mechanisms underlying this effect at microscopic level. These mechanisms involve the influence of an external electric field on the kinetic of formation of membrane receptor couples and of the binding between lectins and receptors. The predictions of the model about the dependence of the inhibitory effect on the frequency content of the electromagnetic field are discussed and preliminary results with sinusoidal signals are described.

674 Calcium, Cyclic AMP, and Protein Kinases Combine to Trigger Chromosome Replication in Regenerating Liver: *J.F. Whitfield, R.H. Rixon,* and M. Sikorska,* Cell Physiology Group, Biological Sciences Div., National Research Council of Canada, Montreal Road Laboratories, Ottawa, Ont., Canada K1A OR6

Partial hepatectomy triggers a complex series of events which commits the remaining liver cells to a round of chromosome replication and cell division. The events require the actions of Ca^{2+}, Ca^{2+}-calmodulin complexes and cyclic AMP and include transient rises

in a cytoplasmic cyclic AMP-dependent protein kinase, a nuclear Ca^{2+}-calmodulin-stimulable nuclear protein kinase, and a Ca^{2+}-activated protein kinase in the plasma membrane. Removing the thyroid-parathyroid complex (which removes the source of calcitonin and parathyroid hormone, lowers the blood calcium level, and inhibits synthesis of the active form of vitamin D, 1,25-dihydroxyvitamin D_3) does not stop liver cells from being stimulated by partial hepatectomy, but does stop the transient increases in the protein kinases and the later initiation of chromosome replication. Restoration of cell replication requires the injection of a "cocktail" of calcitonin, 1,25-dihydroxyvitamin D_3, and parathyroid hormone, which raises the blood calcium level and restores the prereplicative surges of the protein kinases.

675 The Extracellular Calcium Ion Is Required for G1/S Transition of Non-Neoplastic Cells but Not Their Neoplastic Counterparts: *A.L. Boynton, L.P. Kleine,* and *J.F. Whitfield,* Animal and Cell Physiology Section, Biological Sciences Div., National Research Council of Canada, Ottawa, Ont., Canada K1A OR6.

The extracellular calcium ion is required by most if not all non-neoplastic cells both *in vivo* and *in vitro* for G1/S transition. Thus, hepatocytes or parotid gland acinar cells *in vivo* or T51B rat liver cells, BALB/3T3, C3H10T½ mouse cells, or primary cultures of bovine pancreatic acinar cells cannot synthesize DNA or divide in a calcium deficient environment. This calcium-induced G1/S transition is mediated by calmodulin, cyclic AMP, and cyclic AMP-dependent protein kinases. Neoplastic cells of both mesenchymal and epithelial origin require fifty to one hundredfold less extracellular calcium for G1/S transition and cell division. Tumor promoting agents such as TPA, saccharin, phenobarbital, etc. cause non-neoplastic cells to behave as neoplastic cells and replicate their chromosomes and divide in calcium-deficient medium. This action of tumor promoters is mediated by calmodulin, cyclic AMP, and cyclic AMP-dependent protein kinases. (This work was supported in part by a research grant awarded by the NCI(USA) No. CA 28340.)

676 Calplasin: A Growth-Sensitive Nucleolar Calmodulin Acceptor Protein: *J.R. Dedman** and *M.A. Kaetzel,* Division of Endocrinology, University of Texas Medical School at Houston, Houston, TX 77025

Calcium, mediated via specific cellular acceptor proteins, is an important regulator of proliferation. Calmodulin acceptor proteins (CAP's) have been isolated from exponentially growing 3T3 cells and antibodies produced. Two CAP's were localized in nucleus, one in the nucleoli. The latter is present as globular clusters only under growth condition. Immunofluorescent staining is lost following serum and calcium depletion and actinomycin D treatment. We are now pursuing the role of calcium in nuclear events coupling the calcium signal with proliferation.

677 The Effect of PEMF on Cellular Control Mechanisms: *D.B. Jones,* Wissenshaftliches labor, Orthopädische klinik, Wilhelms Universität, 4400 Münster, Germany

Modulation of hormone receptor coupling and second messenger activation was studied in a number of cell and organ culture systems. The action of PEMF on cAMP and calcium ion activation of protein kinases was studied and the consequential activation of various protein substrates was measured. It was found that PEMF can mimic the action of certain hormones and also synergistically increase their effect. Although this effect could occur in the absence of the hormone, it could only occur when the cell was physiologically able to respond to hormonal activation.

678 The Effect of Selected Electromagnetic Fields on Protein Biosynthesis: *R. Goodman,** Dept. of Pathology, Columbia University, College of Physicians and Surgeons, New York, NY 10032, *J. Ryaby,* Mt. Sinai College of Medicine, New York, NY 10029, and *E. Zegarelli-Schmidt, C.A.L. Bassett,* and *A.S. Henderson,* Dept. of Human Genetics and Development and Orthopedic Surgery, Columbia University, College of Physicians and Surgeons, New York, NY 10032

Single pulse and pulse burst were used to determine the effect of electromagnetic fields on protein biosynthesis in isolated salivary gland cells of *Sciara coprophila.* Protein biosynthesis was followed by monitoring the incorporation of either ^{3}H leucine or ^{35}S methionine into protein over periods of time in the electromagnetic fields up to 60 min. The protein content and change in patterns of biosynthesis were followed using SDS-polyacrylamide gel electrophoresis and subsequent autoradiography of the stained gels. A general increase in protein biosynthesis, as well as distinct differences in the biosynthetic pattern, was noted at time intervals which correlate with bursts of RNA transcriptional activity (Goodman *et al., Science,* In press). Both quantitative and qualitative differences in translational patterns are found when the effects of the single pulse and the pulse burst are compared. The results suggest that the two signals evoke distinctly different cellular responses.

679 A Novel Approach to Augmenting Anticancer Chemoimmunotherapy with Pulsatile Electromagnetically Induced Currents (PEMIC): *L. Norton, S. Geller,* and *L. Tansman,* Dept. of Neoplastic Diseases, Mount Sinai School of Medicine, New York, NY 10029, and *A.A. Pilla,* Bioelectrochemistry Laboratory, Dept. of Orthopedic Surgery, Mount Sinai School of Medicine, New York, NY 10029

Investigations of the anticancer effect of PEMIC have confirmed an association between induced current amplitude within the tumor geometry and efficacy. Hybrid mice bearing transplanted tumor nodules have been examined multifactorially to define the interactions of cytotoxins, immune modulation, and PEMIC. In B16 melanoma, Ridgeway osteogenic sarcoma, and spontaneous C3H mammary adenocarcinoma, the tumor-regression and survival-prolongation synergy of PEMIC plus chemotherapy is associated with either a central necrosis of individual nodules or marked cellular volume expansion. Impedance measurements in BDF, mice show that the B16 melanoma mass is electrically insulated from surrounding normal tissue. Hence, the morphological results are most consistent with a biologically active, geometrically determined amplitude window.

680 Effect of Repetition Rate and Duty Cycle on Pulsed Magnetic Field Modulation of LSA Tumors in Mice: *S.D. Smith** and *J.M. Feola,* Dept. of Anatomy and Radiation Medicine, University of Kentucky College of Medicine, Lexington, KY 40536-0084

Adult C-57 NAPD/Feola mice were injected with 10^6 cells of LSA, a converted lymphoid ascites tumor. Five days after injection, the mice were treated as 4 groups; Control—no further treatment; PMF-pulsed magnetic fields (EBI-BIO-OSTEOGEN at 1, 2, 5, 10, 15, and 25 Hz for a 50%, 12/12 hr on/off duty cycle); BCNU—5 mg/kg of 1,2-bis-dichloronitrosourea; and COMB – PMF + BCNU. More mice were similarly inoculated and treated, except that the PMF and COMB mice all received PMF at 15 Hz, but for 50% duty cycles of 1/1, 2/2, 4/4, 6/6, and 12/12 hr, plus a set at 24/0 hr. Results indicate that the fields restrain the tumor only at 1, 5, 15, and 25 Hz, and only at duty cycles of 1/1, 6/6, and 12/12 hr. The effects were seen in the spleen, liver, ascites accumulation, and lymph nodes. Repetition rate and duty cycle were not critical factors in extension of survival.

681 Ion-induced Modifications in the Conformation of Chromatin in Intact Cell Nuclei Measured by Means of Flow Microfluorimetry: *A. Chiabrera, M. Grattarola,* M. Parodi,* and *R. Finollo,* Electrical Engineering Institute, University of Genoa, Genoa, Italy, and *P. Carlo,* Institute of Pharmacology, University of Genoa, Genoa, Italy 16145

Small variations in the balance of cations (mainly Mg^{++}) are known to induce large modifications in the conformational properties of DNA and chromatin in solution, suggesting a possible role played by these cations in affecting chromatin conformation also in living cells. We present here a technique which allows the measurements of subtle modifications in the packing of nuclear chromatin in intact nuclei, as a consequence of modifications in the concentration of Mg^{++} in the medium, under conditions mimicking a physiological environment. Nuclei of rat hepatocytes suspended in an isotonic medium (mainly KCL) are exposed to concentrations of Mg^{++} in the range 0.30 mM. Subsequently, they are stained with the DNA-intercalating dye, Acridine Orange. The differences in the packing properties of nuclear chromatin induced by the variations in Mg^{++} concentrations result in variations in the amount of the fluorescence emitted by each nucleus, which is easily detected by our FACS III cell sorter. The results are briefly discussed in the light of the polyelectrolytes theory.

682 Electrochemical Control of Membrane Permeability: *A.J. Grodzinsky,* Dept. of Electrical Engineering and Computer Science, Massachusetts Institute of Technology, Cambridge, MA 02139

An electric field applied across a membrane can act as a switch to change the transport properties of the membrane. Experiments have demonstrated that transport of neutral solutes can be altered by changing the membrane's charge density (via pH) or by changing intramembrane ionic strength using an applied electric field. Deformable (model) membranes have been used, *e.g.,* collagen and PMAA. The method involves the control of intermolecular repulsion forces that govern the equivalent pore size of the membrane.

683 Dielectrophoretic Cell Sorting: *H.A. Pohl* and *K. Pollock,** Dept. of Physics, Oklahoma State University, Stillwater, OK 74078

Living cells can be sorted with the use of dielectrophoresis (DEP). The method depends upon the natural differences in the effective dielectric properties. Since the DEP of cells or their parts is highly frequency sensitive, a selected frequency (based upon the known DEP spectra) sorts the cell mix as it passes through a specially designed electrode set. Results for a number of cell mixtures are presented, together with studies of the mechanisms of the phenomena concerned.

H.A. Pohl, "Dielectrophoresis," Cambridge University Press (1978).

684 Electromagnetic Modulation of Biological Processes: Evidence for a Role of the Plasma Membrane in Signal Coupling: *G. Colacicco** and *A.A. Pilla,* Bioelectrochemistry Laboratory, Dept. of Orthopedics, Mount Sinai School of Medicine, New York, NY 10029

Calcium uptake by biological and artificial systems as well as DNA synthesis by cultured cells were used as models in the study of coupling of very low frequency electromagnetic fields with biological processes. The field did not affect Ca-uptake by either artificial ion sorbing systems, isolated mitochondria and microsomes, or embryonal chick tibia rudiments that had been killed by glutaraldehyde fixation. The field, however, stimulated *(i)* Ca-uptake by living systems in the presence of bicarbonate in a possible coupling of the field with a bicarbonate-dependent Ca^{++}-ATPase, and *(ii)* ATPase-controlled DNA synthesis which had been depressed by

exogenous ATP. All available data suggest that plasma membrane ATPases are the link between field and biological systems.

685 Cellular Spin Resonance of Cells and Small Particles in Rotating Electric Fields: *H.A. Pohl* and *M. Mischel* (Present address: Fachbereich Biologie, Institut fur Biophysik, Freie Universitat, Berlin, Germany), Dept. of Physics, Oklahoma State University, Stillwater, OK 74078

Cells and certain electrically polarizable objects suspended in aqueous media can be observed to spin when in a rotating electric field. In a frequency range of 500-80,000 Hz, living cells exhibit two or three response peaks, and dead cells only one. Whereas living cells spin in the co-field rotational direction, dead cells spin oppositely. Yeast exhibits two well-separated peaks, mammalian mouse myeloma cells exhibit three. The nature of these cellular spin resonances is under active study.

686 Electromagnetic Signal Analysis Applied to Controlling Cell Functions Electrically: *B. R. McLeod*, Dept. of Electrical Engineering and Computer Science, Montana State University, Bozeman, MT 59717

In the past two years, many workers have concluded that electrical control of biological cell functions occurs at the cell membrane. Our work has been directed at solving for the electromagnetic field quantities such as current density that the cell is exposed to in an *in vitro* situation. This paper presents the results of our current research on solving the boundary value problem at the cell membrane as well as a discussion of a technique for comparing various biologically active electromagnetic signals.

687 Electromagnetic Response of Cells and Tissues *vs.* Macroscopic Measurements: *B. Tuerlinckx,* M. Dierickx*, and *L. Rybowski*, Electricite Generale, Faculte des Science Appliques, Université Libre de Bruxelles, B-1050 Brussels, Belgium, and *M. Hinsenkamp* and *F. Burny*, Chirurgie Osseuse, Hôpital Erasme, Université Libre de Bruxelles, Brussels, Belgium

Most of the time, macroscopic voltage and current measurements are used for estimating the dielectric properties of biological tissues or for identifying models of cellular electromagnetic response. However, the relationship between cellular and large-scale properties depends on several parameters contributing to the so-called beta-dispersion, which have often been overlooked. We are presenting experimental and simulation results to assess the relative importance of four among those variables: electrode geometry, medium anisotropy, statistical dispersion of microscopic properties, and capacitor response.

688 Electrochemical Study of Chlorpromazine (CPZ) Effect on Platelet Membrane Potential (PMP) and the Ca^{2+} Level: *H. Vainer*, Institut de Recherches sur les Maladies du Sang, Hôpital Saint Louis, Paris Cedex 10, France, and *A. Caprani,** Hôpital Broussais, Paris Cedex 14, France

Evidence so far accumulated has indicated that Ca^{2+} and Ca-binding proteins, such as calmodulin, modulate platelet function in haemostasis and thrombosis. To investigate possible interactions between cell surface components and these agents, the effect on the PMP and Ca^{2+} level of CPZ, a specific antagonist of intracellular Ca^{2+}, alone or in combination with added Ca^{2+} and calmodulin, were studied. An electrochemical method, and the Ca^{2+} electrode, respectively, were used. At 50 μM, CPZ, platelet membrane is depolarized, whereas platelet aggregation is inhibited.

689 A Potential Step Change Cause of Blood Clot Breakaway: *V. Guruswamy* and *G. Helm*, Dept. of Chemical Engineering, Virginia Polytechnic Institute and State University, Blacksburg, VA 24061

Blood clots form on the anodes of a thin film flow type cell. The initial formation of the clot was fast and slowed down with time. No breakaway of the clot was observed as long as an anodic potential was maintained. However, when the electrode potential underwent a negative potential step change, breakaway of the blood clot at its outer peripheries was observed. These *in vitro* experiments may give insight to the *in vivo* situation.

690 The Physiological Relevance of Laplace Plane Membrane Impedance Determinations: *A.A. Pilla,* G. Cerf*, and *C. Mayaud*, Bioelectrochemistry Laboratory, Dept. of Orthopedic Surgery, Mount Sinai School of Medicine, New York, NY 10029

The transient impedance technique has been further developed to enable better isolation of cell membrane relaxation phenomena. This study presents several new models which take into account the kinetics of specific adsorption and ion transport. New digital instrumentation achieves 10 nsec time resolution allowing the isolation of (particularly) dielectric membrane capacitance and ion binding steps. Optimization techniques are utilized for parameter evaluation *vs.* most relevant model. The effect of extracellular ion concentration and state of differentiation on the isolatable kinetic parameters is examined in detail.

691 An *In Vivo* A-C Impedance Measurement of the Cutaneous Effect of a Harsh Substance on the Dielectric Spectra of Human Skin: *L.S. Lu,** S.C. Johnson & Son, Inc., Corporate Research, Racine, WI 53403, *J.M.C. Roberts* and *W.I. Archer*, S.C. Johnson & Son, Inc., International Consumer Products Research, Milton Park, England, and *E.J. Lajiness*, S.C. Johnson & Son, Inc., Corporate Research, Racine, WI 53403

An *in vivo* a-c impedance data of human skin measured with frequency in the range from 0.5 to 10 kHz exhibits a depressed semicircle in a comlex plane. An application of 2% sodium lauryl sulfate (SLS) solution on human forearm shows a systematic displacement of impedance loci curve several Hertz towards high frequency domain. This suggests the activity of Debye dielectric relaxation at epidermis layer. A complex dielectric permittivity is expressed theoretically as a function of measured impedance data. The dielectric spectra of aggravated skin from which relaxation behavior and viscoelastic property derived provides a semiquantitative evaluation of the cutaneous effect of 2% SLS solution on human skin. Moreover, Cole-Cole type plot of impedance data indicates the SLS solution penetration into skin is controlled by a diffusion process and the value of diffusion coefficient increases with prolonging skin aggravation in accordance with Lorenz's theory of adsorption kinetics. Defatting, protein denaturation, hygroscopic molecule dissolution and membrane injury, etc., caused by SLS solution are related to variation in electrical and dielectrical property of skin.

ORGANIC AND BIOLOGICAL ELECTROCHEMISTRY

General Session

692 Detection and Measurement of Kolbe Electrolysis Products Using Permeable Membrane Mass Spectrometry: *T. J. Brockman* and *L. B. Anderson,** Dept. of Chemistry, The Ohio State University, Columbus, OH 43210

Decarboxylation of carboxylate anions may be accomplished in a variety of solvents at a gold electrode. The mechanism of this reaction is complex, but several of the probable products may be detected and measured by mass spectrometry, using a silicone rubber membrane to separate the volatile products from the electrolyte solution. We describe measurement of CO_2 and ethane evolution at a gold electrode in DMSO and aqueous solutions.

693 The Electrochemical Carbon-Carbon Bonding of CO_2: *V. Guruswamy* and *L. Pillis*, Dept. of Chemical Engineering, Virginia Polytechnic Institute and State University, Blacksburg, VA 24061

Carbon dioxide was electrolyzed in an aprotic solvent, dimethyl-formamide, (DMF) containing small amounts of H_2O. The electroreduction involves a coupling mechanism which enables the synthesis of carbon-carbon bonded compounds. Formic, oxalic, malonic, and succinic acids have been identified by GC-MS as electrosynthesis products. The relative product concentration appears to be dependent upon H_2O concentration in the solvent, the applied electrode potential, and the duration of electrolysis.

PHYSICAL ELECTROCHEMISTRY

The Chemistry and Physics of Electrocatalysis

694 Molecular Ingredients of Heterogeneous Catalysis: *G. A. Somorjai*, Materials and Molecular Research Div., Lawrence Berkeley Laboratory and Dept. of Chemistry, University of California, Berkeley, CA 94720

The purpose of this paper is to present a review and status report of the rapidly developing surface science of heterogeneous catalysis. For this purpose the paper is divided into several sections. The brief introduction to the methodology and recent results of the surface science of heterogeneous catalysis is followed by a review of the concepts of heterogeneous catalysis. Then, we describe the experimental results that identified the three molecular ingredients of catalysis: the *(i)* structure, *(ii)* carbonaceous deposit, and *(iii)* oxidation state of surface atoms. Each section is closed with a summary and a list of problems that, in my view, require theoretical and experimental scrutiny. Finally we describe attempts to build new catalyst systems and the theoretical and experimental problems that appeared in the course of this research.

695 Lattice Models, Interactions, and Solvent Effects in Electrochemical Monolayer Formation: *B. E. Conway,* S. Marshall*, and *K. Tellefsen*, Dept. of Chemistry, University of Ottawa, Ottawa, Ont., Canada K1N 9B4

The development of lattice arrays in electrochemical underpotential deposition processes is examined from the point of view of *(i)* the entropy of the upd process; *(ii)* the role of adsorbed solvent and its displacement from the substrate metal interface during a upd process, *e.g.*, of metal ad-atoms, and *(iii)* the possible participation of 2-d order-disorder transitions with changing temperature or coverage. A combination of lateral interaction effects in an ad-atom array of partially charged species with site-localized, directed chemisorption bonds can lead under certain conditions to the multiple state adsorption commonly found with metal ad-atom monolayers on well-characterized single-crystal substrate surfaces. New experimental results on upd of metal ad-atoms from nonaqueous solvents over a wide range of temperature are reported.

696 The Bornian Hiatus in Electrode Kinetics: *S. U. M. Khan* and *J. O'M. Bockris,** Dept. of Chemistry, Texas A&M University, College Station, TX 77843

The Bornian continuum contribution to activation of ions in solution and at electrodes has been critically analyzed. It was found that virtually no system is in conformity with the continuum electrostatic fluctuation theory. The electrode kinetic theory originated by Gurney on the basis of molecular vibrational and collisonal

model and later developed by Butler, Gerischer, Christov, Bockris, *et al.* is found in conformity with experiment. Predominance of vibrational stretching contribution has been presented in terms of a phonon-vibron coupling model of activation. Time dependent perturbation theory is used for the prediction of electrocatalytic effect. Absorption energy on an electrocatalyst has been analyzed in terms of Anderson-Hamiltonian formalism.

697 Structure of Metal and Semiconductor Surfaces and Chemisorption on These Surfaces: *W. A. Goddard III*, Arthur Amos Noyes Laboratory of Chemical Physics, California Institute of Technology, Pasadena, CA 91125

This paper examines current understanding of the geometry and electronic structure of metal, semiconductor, and metal oxide surfaces with an emphasis on predicting and understanding the differences for various surfaces. This understanding is used in examining the chemisorption of various O-, N-, and C-containing molecules and radicals on these surfaces. The paper emphasizes recent results from theoretical studies at the solid gas interface; however, an attempt is made to use these ideas to elucidate the more complex situation at the electrode-electrolyte interface.

698 Surface Chemistry of Copper: Reactions of Small Molecules with and on Cu(110): *R. J. Madix*, Dept. of Chemical Engineering, Stanford University, Stanford, CA 94305

The reactions of copper with small molecules are important for the understanding of electroless plating operations. In the course of our work on copper, we have studied the reactions of carboxylic acids, alcohols, unsaturated hydrocarbons, cyanogen, and acetronitrile with copper single crystals. Reactions occurring following adsorption of the gas and heating of the adsorbate-surface complex were followed using a variety of spectroscopic techniques in ultrahigh vacuum. The results of these studies are discussed.

699 Electrocatalysis at Single Crystal Electrodes. The Role of Surface Defects and Adatoms: *J. D. E. McIntyre** and *W. F. Peck, Jr.*, Bell Laboratories, Murray Hill, NJ 07974

The influence of the surface structure of the clean (110), (100) and (111) faces of single-crystal gold rotating disk electrodes on the catalysis of the electrochemical reduction of O_2 is reported. In aqueous 0.5M H_2SO_4 at 25°C, the electrocatalytic activities of Au(110) and Au(100) are related to their pzc values. The Au(111) surface, however, is catalytically inactive and reduction occurs primarily at surface defects ($\sim 2 \times 10^9$ cm^{-2}). In aqueous 1.0M KOH, the low index faces of gold exhibit remarkable differences in activity for reduction of O_2 and HO_2^-. The Au(100) face is highly active for HO_2^- decomposition, whereas Au(111) is inactive. Strong electrocatalytic effects are induced by monoatomic steps on the clean Au(S)-5(111)× (100) surface and by adsorbed heavy metal atoms (Tl, Pb, Bi) on the low index faces. These studies offer a new atomic scale approach to revealing the roles of surface geometric and electronic structure in electrocatalysis.

700 Electrodeposition at Well-Defined Electrode Surfaces: *A. T. Hubbard,* J. L. Stickney, S. D. Rosasco,* and *M. P. Soriaga*, Dept. of Chemistry, University of California, Santa Barbara, CA 93106

Studies by LEED and Auger spectroscopy of Ag electrodeposited from aqueous solutions on well-characterized Pt single crystal surfaces are reported. Prior to electrodeposition the Pt surface was treated with I_2 vapor to form highly stable superlattices, which protected the Pt surface from attack by the electrolyte and residual gases. Electrodeposition occurred in three narrow voltammetric underpotential deposition peaks and one diffusion-controlled bulk deposition peak. LEED photographs obtained at various points along the voltammetric scans revealed that ordered layers were formed at all silver coverages from the onset of deposition to the highest coverages studied, about twenty atomic layers. Those were identified as superlattice structures and coincidence lattices of high symmetry. The structures were formed nearly reversibly, at all stages, in numerous cycles of deposition and dissolution. Quantitative Auger spectroscopy revealed that the layer of iodine atoms was located on top of the Ag surface and remained attached to the surface throughout the deposition and dissolution process. Auger spectroscopy also confirmed that the silver coverages were determined by integration of the voltammetric current. Each voltammetric peak produced a change in the LEED pattern. Structural models consistent with these results are presented. Related studies of chemisorption and metal deposition in vacuum are discussed.

701 Crystal Face Specificity of Double Layer Structure and Electrocatalysis: *S. Trasatti*, Laboratory of Electrochemistry of the University, 20133 Milan, Italy

The structure of the double layer at different crystal faces of metals is described in terms of preferential orientation of solvent molecules. Effects on the kinetics of redox reactions involving specific interactions between intermediates and electrode surface are highlighted. Adsorption on single crystal faces of metals in electrochemical systems is compared with data from the gas phase. The approach to electrocatalysis in terms of collective properties of metals is discussed on the basis of experimental data for single crystal faces.

702 Strong and Weak Overlap Reactions; Similarities and Differences: *R. A. Marcus*, Div. of Chemistry and Chemical Engineering, California Institute of Technology, Pasadena, CA 91125

Strong overlap reactions are of many types, including atom transfers, electron transfer in which the two reactants share a common atom or group, and proton transfers. The potential energy surface for treating atom transfer or other strong overlap reactions differs substantially from that for treating weak overlap transfers, requiring a difference in the theoretical analysis. These aspects are discussed, along with adaption of small-molecule electron-transfer theory to larger biological systems.

703 Electron Transfer Through Intermediate States in Solid: Electrolyte and Solid:Solid Systems: *A. M. Kuznetsov*, Institute of Electrochemistry of the Academy of Sciences of the USSR, Leninskij Prospect 31, Moscow V-71, USSR, and *J. Ulstrup,** Chemistry Dept., The Technical University of Denmark, 2800 Lyngby, Denmark

We have considered electron transfer between two localized electronic states, or between metal and a localized state, where the localization originates from coupling to local nuclear modes or the surrounding medium. The electron transfer furthermore proceeds through a third "impurity" state, for example, in isolating films covering a metal electrode, which can be either delocalized, weakly, or strongly localized by coupling to the phonon system. We have derived rate expressions which cover weak and strong coupling, low and high energies of the intermediate state, and incorporates explicitly the modulation of the electronic wave functions by the nuclear system.

704 The Effect of Adsorbed Molecules on the Kinetics of Heterogeneous Electron Transfer: *W. R. Fawcett*, Guelph-Waterloo Centre for Graduate Work in Chemistry, Dept. of Chemistry, University of Guelph, Guelph, Ont., Canada N1G 2W1

The theoretical treatment of the effects of adsorbed organic species on the kinetics of heterogeneous electron transfer developed in the last few years is reviewed. Methods of estimating the local field and potential at the reaction site are discussed with emphasis on the molecular approach. The analysis of kinetic data obtained in the presence of organic adsorption is discussed within the context of these theories.

705 Redox Pathways. Applications in Catalysis: *T. J. Meyer*, Dept. of Chemistry, The University of North Carolina, Chapel Hill, NC 27514

Recent work based on polypyridyl complexes of ruthenium and osmium has led to the identification of a series of well-defined redox pathways including: hydride transfer, electron transfer, hydrogen atom transfer, and oxidative coupling. These reactions have found application in electrocatalysis in the oxidation of water to oxygen, the oxidation of chloride ion to chlorine, the oxidation of organics such as alcohols and aromatic hydrocarbons, the reduction of nitrate to nitrite, and the catalytic reduction of nitrite ion to ammonia.

706 Mechanistic Aspects of Oxygen Electrochemistry: *E. Yeager,* D. Scherson,* and B. Simic-Glavaski*, Case Center for Electrochemical Sciences and Dept. of Chemistry, Case Western Reserve University, Cleveland, OH 44106

Various pathways for the electroreduction of O_2 and the corresponding electrocatalyst requirements are discussed. For the four-electron overall reduction of O_2 with solution phase peroxide as an intermediate, these requirements include *(i)* strong interaction of oxygen species with the catalyst in a manner that promotes O—O bond cleavage and *(ii)* the proper redox potentials for the catalyst and its oxygen species adducts. Recent fundamental developments are reviewed with emphasis on the transition metal macrocyclic catalysts.

707 Potential Step Methods for the Study of the Electrocatalytic Reactions of Organic Molecules: *D. Pletcher*, Dept. of Chemistry, The University, Southampton, England SO9 5NH

The application of potential step methods to the development of a detailed picture at a molecular level of the processes occurring during electrocatalysis is discussed. Such studies lead to new information about the catalysis in acidic perchlorate media of formic acid oxidation at Pt surfaces partially covered by Bi, Cd, Cu, Pb, and Tl adatoms. The method also allows the study of electrocatalytic hydrogenation at growing metal centers on inert substrates.

708 Ad-Atom Coverage Studies during the Catalysis and Inhibition of Formic Acid Electro-Oxidation by Underpotential Deposition: *M. Shabrang* and *S. Bruckenstein,** Dept. of Chemistry, State University of New York at Buffalo, Buffalo, NY 14214

The catalysis and inhibition of formic acid electro-oxidation as a result of metal submonolayer formation on polycrystalline platinum was studied. One can approach limiting current behavior for the oxidation of formic acid and the optimum ad-atom coverage for Pb and Bi was 25-35% of the platinum electrode real area. These experiments are correlated with the literature dealing with polycrystalline and single crystal studies of hydrogen adsorption and formic acid oxidation to explain differences for the electrocatalytic behavior of various underpotentially deposited (UPD) species. Submonolayers of Ag and Cu do not deposit significantly on Pt(100), which is responsible for most of the electro-oxidation of formic acid and therefore cannot prevent poisoning of the formic acid oxidation process via a third body mechanism. Bi, Pb, and other UPD species with radii larger than platinum do deposit significantly on Pt(100) at low UPD coverages, and can therefore slow the poisoning of the formic acid process on this plane.

709 Investigations of Adsorbed Species in Electrocatalytic Oxidations Using *In Situ* Infrared Spectroscopy: *A. Bewick*, Dept. of Chemistry, University of Southampton, Southampton, England SO9 5NH

The identification of adsorbed species, formed during the electrocatalytic oxidation of small organic molecules, from the vibrational spectra obtained by electrochemically modulated infrared spectroscopy is described. The spectroscopic results for a range of substrates and electrode materials is correlated with the known electrochemical behavior. The discussion on the influence of the nature of the electrode material includes data from single crystal electrodes. Particular attention is given to the identification of reaction intermediates as well as strongly adsorbed poisons; the species observed on strongly catalytic and on noncatalytic surfaces is contrasted.

710 New Approaches to Improving the Sensitivity and Generality of SERS: *R. P. Van Duyne*, Dept. of Chemistry, Northwestern University, Evanston, IL 60201

Although surface enhanced Raman spectroscopy has been shown to be an extremely sensitive and selective method for studying the molecular structure of interfaces, it still does not have enough sensitivity to observe high quality spectra at the 0.01 monolayer level even under the most favorable circumstances. Furthermore, its applicability is restricted at the present time to the coinage metal substrates Ag, Cu, and Au, and it is generally believed that the relative enhancement factors for these substrates are Ag = 1, Cu = 0.1, and Au = 0.01. If surface enhancement exists on other metallic substrates, all indications are that the magnitude of this enhancement is <1000. Consequently, a great deal of our research effort in the last two years has gone into trying to improve both the sensitivity of SERS and its applicability. This paper outlines some of our studies in this area concentrating on: *i*) controlling the surface microstructure (viz., roughness) to produce SERS sensitivities on Cu and Au that are comparable to those on Ag, *ii*) demonstrating that SERS enhancement factors can be increased by another factor of 10 or possibly 100 on Ag by making measurements under transient conditions rather than the usual steady-state conditions, and *iii*) inducing SERS behavior on substrates that normally do not support an enhancement; the case of GaAs is discussed.

711 Influence of Crystallographic Orientation on the Electrochemical Properties of Some sp Metals: *A. Hamelin*, Laboratoire d'Electrochimie Interfaciale du C.N.R.S., 92190 Meudon-Bellevue, France

Some of the ideas of crystallography are necessary for the understanding of the results obtained in electrochemistry. For some face-centered cubic (fcc) metals, these ideas are related to results obtained with atomically "flat" and "stepped" faces through the projected unit stereographic triangle. It is shown that for the fcc metals the crystallographic orientations (111), (110), (100), (210), and (311) have extrema in electrochemical characteristics such as the potential of zero charge and anion adsorption capacity peaks. Other electrochemical properties are independent of orientation.

712 Electrocatalysis by Ad-Atoms: *S. Motoo*, Laboratory of Electrocatalysts for Fuel Cells, Faculty of Engineering, Yamanashi University, Takeda-4, Kofu, Japan

This paper starts with a short summary of electrocatalysis by ad-atoms in general followed by the description of some concepts S_M, S_{hole}, S_R. And then some knowledge of oxygen adsorbing ad-atoms is given. On this basis, some examples of electrocatalyst design and explanation of the effect of ad-atoms are mentioned. The reactions in this paper are the hydrogen evolution reaction, the oxidation of CO, formic acid, formaldehyde, methanol, ethanol, and ethylene glycol, and the hydrogenation of ethylene.

713 Clusters and Surfaces in Catalysis: *E. L. Muettepties*, Dept. of Chemistry, University of California, Berkeley, CA 94720

Although metal *d*-levels in molecular metal clusters lie at lower energy than those for surface atoms of metals, there are striking similarities between the clusters and metal surfaces. For both, the metal-atoms are typically close-packed and metal-metal distances are similar. In the bonding of molecules or radicals to clusters and to surfaces, the stereochemistry, the metal to ligand distances and the metal-ligand bond energies are similar. Nevertheless, there are important differences between these regimes as discussed with respect to catalysis.

714 Determination of the Structure of Dispersed Metal Catalysts by the EXAFS Technique: *F. W. Lytle** and *R. B. Greegor*, The Boeing Co., Seattle, WA 98124, *E. C. Marques* and *D. R. Sandstrom*, Washington State University, Pullman, WA 99164, and *G. H. Via* and *J. H. Sinfelt*, Exxon Research and Engineering Co., Linden, NJ 07036

We used the element specific advantage of x-ray absorption spectroscopy and the EXAFS technique to determine the atomic arrangement in the neighborhood of supported metal clusters. These structural parameters were used to infer size and shape of the cluster, distribution of atomic species in bimetallic clusters, and interaction with the support. The presence of chemisorbed ligands was also detected and characterized. The penetrating quality of x-rays permitted *in situ* preparation and examination of the desired sample conditions under realistic catalytic conditions. (This research was supported in part by NSF.)

715 Microstructure of Highly Dispersed Pt Catalysts and the Relation to Activity for Oxygen Reduction: *P. N. Ross, Jr.*, Lawrence Berkeley Laboratory, Materials and Molecular Research Division, Berkeley, CA 94720

In recent years there have been a number of studies published on the structure sensitivity of oxygen reduction on Pt catalysts in acid electrolyte. In most of these studies the activity of Pt foils or disks was compared to supported Pt at fixed acid concentration and temperature. The results in these studies are somewhat contradictory, but indicate that there appears to be a critical dimension below which Pt activity drops dramatically. The physical basis for understanding critical dimension is presented here. Although highly dispersed Pt takes on nonideal microstructure, the nonideal structure is not the primary cause of activity decline. Rather, the critical parameter is the degree of dispersion or percent exposed, regardless of shape/size. Above 40% exposed, strong interaction with oxygen leads to passivation. The too strong interaction is related to a change in the electronic properties at the critical level of dispersion.

716 Adventures in Electrocatalysis: Acceleration of Electrode Reactions by Adsorbed Ions, Molecules, or Polymers, *F. C. Anson*, Div. of Chemistry and Chemical Engineering, California Institute of Technology, Pasadena, CA 91125

The careful and precise measurement of ionic and molecular adsorption at electrodes, as exemplified in the work of David Grahame, has provided much of the data needed to inspect the potency of the adsorbed species as catalysts for electrode processes. Such catalysis ranges from reactions as simple as the one-electron oxidation of Cr(II) to Cr(III), to more complex reactions in which several electrons are transferred and chemical bonds are broken and made as in the reduction of O_2 to H_2O. Some of the approaches that we have utilized to examine the catalysis of electrode reactions are reviewed and examples presented in which metalloporphyrins or polymers adsorbed on electrode surfaces are exploited as efficient electrocatalysts.

717 The Kinetics of Electron Transfer Reactions in and at Films of Electroactive Polymers: *C. R. Leidner, R. H. Schmehl, P. Pickup*, and *R. W. Murray**, Dept. of Chemistry, Kenan and Venable Laboratories, University of North Carolina, Chapel Hill, NC 27514

Films of polymers and copolymers of transition metal complexes can be prepared on electrodes by reduction of vinyl substituted monomers like $[Os(bpy)_2(vpy)_2]^{2+}$ and $[Ru(bpy)_2(4\text{-}pyNHCOCH{=}CHPh)_2]^{2+}$. Using several methods, we have studied the transport of electrons through the mixed valent oxidation state of the films, and the electrocatalytic oxidation and reduction of other electroactive substances contacting the film from the solution side. The interrelationship of the rate of these processes in electrocatalytic electrode design is also discussed.

718 Luminescence as a Means for Probing Model Electrocatalytic Systems *In Situ: L. R. Faulkner** and *J. S. Pflug*, Dept. of Chemistry, University of Illinois, Urbana, IL 61801, and *W. R. Seitz*, Dept. of Chemistry, University of New Hampshire, Durham, NH 03824

Deposits on electrode surfaces have been studied extensively by some new methods based on the natural fluorescence of the species in the deposit. Most work has involved zinc tetraphenylporphyrin deposited onto indium oxide, gold, graphite, or silicon, but some work has been done on luminescent centers in polymeric modifying layers. The extent of fluorescence quenching induced by electrode reactions and the angular dependence of luminescence polarization provide structural information about the modifying layer.

719 Influence of Specific Reactant-Surface Interactions upon Electrochemical Reactivity: *M. J. Weaver*, Dept. of Chemistry, Purdue University, West Lafayette, IN 47907

A central topic in electrochemical kinetics concerns understanding the manner and extent to which specific interactions, especially chemical binding, between the reactant and the electrode surface can influence the energetics of heterogeneous electron transfer. A general treatment of this problem is outlined, involving the evaluation or estimation of unimolecular rate constants (sec^{-1}) as a function of reaction environment and transition-state geometry. Some applications are outlined, including the mediation of transition-metal electron transfers by organic bridging ligands.

720 Catalysis of Redox Processes at Illuminated Semiconductor Electrodes: *M. S. Wrighton*, Dept. of Chemistry, Massachusetts Institute of Technology, Cambridge, MA 02139

A variety of redox processes of importance can be catalyzed at illuminated semiconductor electrodes by rational modification of the surface. Reactions include O_2 reduction to H_2O_2, oxidation and reduction of H_2O, oxidation of Cl^- and redox processes of biological reagents. The principles of electrocatalysis on semiconductor surfaces are given along with results to illustrate the concepts.

721 Photocatalysis with Colloidal Semiconductor Particles: *M. Grätzel*, Institut de Chimie Physique, Ecole Polytechnique Fédérale, 1015 Lausanne, Switzerland

This paper gives an overview on photocatalytic studies involving colloidal semiconductor dispersions. Preparation and optical properties (absorption luminescence) of ultrafine (50-500Å sized) particles of semiconducting materials such as TiO_2, WO_3, Fe_2O_3, CdS, and CdSe are described. Transient luminescence, ab-

sorption and conductance technique as well as time-resolved Raman spectroscopy are employed to probe interfacial electron and hole transfer to species dissolved in solution or catalysts deposited on the particles. Applications of these systems include multielectron storage, H_2S and water cleavage by visible light.

722 Design of Efficient Semiconductor/Liquid Junction Solar Cells in Nonaqueous Solvents: *C. M. Gronet* and *N. S. Lewis*,* Dept. of Chemistry, Stanford University, Stanford, CA 94305

Nonaqueous electrolytes present advantages for photoelectrochemical cells such as a wide range of solution redox couples and stable electrode materials. However, very few efficient nonaqueous electrolyte systems have been reported to date. We describe here results which show that proper electrode control can lead to formulation of efficient semiconductor/liquid junctions in nonaqueous solvents. We have concentrated upon the electrochemistry of two systems in nonaqueous solvents, n-$GaAs_{1-x}P_x$ and n-Si. Each of these systems is discussed in detail, and demonstrated to produce cells with over 10% solar-to electrical conversion efficiency under stable conditions.

723 Chemically Induced Interface States on Semiconductor Electrodes: *M. A. Butler** and *D. S. Ginley*, Sandia National Laboratories, Albuquerque, NM 87185

Sub-bandgap photocurrent spectroscopy has been used to observe interface states on GaP surfaces induced by treatment with various metal ions. In particular, Ru treatment induces a discrete level near the center of the gap which improves the ability of the electrode to evolve hydrogen. This result is contrary to present expectations which correlate improved electrochemical efficiency with a reduction in interface states. A new model based on kinetic considerations is proposed to explain this behavior. (This work was performed at Sandia National Laboratories supported by the U.S. Department of Energy (DOE) under contract No. DE-AC04-76DP00789.

724 Structure-Property Behavior of Perovskite Oxide Electrocatalysts: *E. J. Calvo,* J. Drennan, J. A. Kilner, W. J. Albery*, and *B. C. H. Steele*, Imperial College of Science & Technology, South Kensington, London, England SW7 2BP

A comprehensive study of the La-Ni-O perovskite related family of oxides has been carried out. These studies have included high resolution electron microscopy to ascertain the crystallography and morphology of the electrocatalytic particles, and preparation of dense and porous electrodes for electrochemical studies. Novel rotating ring disk techniques have been developed to study both suprafacial and intrafacial oxygen reactions on these materials, and the mobility of oxygen ions in the bulk oxide material has been investigated by SIMS ^{18}O diffusion profiles. Particular attention is given to discussions of any relationship between the bulk properties and the associated electrocatalytic behavior.

725 Effect of Crystallographic Orientation of Single Crystal RuO_2 Electrodes on the Reversibility of the Electrochemical Hydrogen Adsorption Reactions: *T. Hepel** and *F. H. Pollak*, Dept. of Physics, Brooklyn College of CUNY, Brooklyn, NY 11210, and *W. E. O'Grady*, Brookhaven National Laboratory, Dept. of Energy and Environment, Upton, NY 11973

Electrochemical reactions of hydrogen adsorption have been studied on five different "as-grown" surfaces [*e.g.*, (001), (110), (100), (101), and (111)] of single crystals of RuO_2. For the (001) and (110) faces, two distinct peaks corresponding to hydrogen absorption are seen. Both reactions are quite reversible with two anodic peaks of hydrogen desorption appearing at the same potentials as the corresponding hydrogen adsorption. For the (100), (101), and (111) faces only one pair of reduction-oxidation peaks is seen. On the latter two surfaces this peak is below the H^+/H_2 equilibrium potential while for the (100) surface the peak lies above this potential. The various observations are correlated with the features of the "ideal" atomic composition of these various surfaces. (This work was supported by the United States Department of Energy under Contract DE-AC02-80ER10654).

726 Photocatalysis by Ruthenium Dioxide on p-Type Semiconductors: *W. Gissler* and *A. J. McEvoy*, Joint Research Centre, Physics Div., Commission of the European Communities, 21020 Ispra (Varese), Italy

RuO_2 is known to catalyze the oxygen evolution in an electrochemical cell. It has therefore been also assumed to have a photocatalytic effect on the photogenerated oxygen evolution in heterogeneous systems of n-type semiconductor particles, in aqueous electrolytes. Investigations on extended n-type semiconductor electrodes, however, provided no unequivocal evidence for this hypothesis. We have found, on the contrary, that RuO_2 significantly catalyzes the cathodic photocurrent observed at p-type semiconductor electrodes in an electrochemical cell. Experimental results obtained on p-GaAs and p-Se are presented and discussed.

727 Cobalt-Containing Mixed Oxides as Electrocatalysts for Anodic Oxygen Evolution. Preparation, Electrode Kinetics, and Their Use in Alkaline Water Electrolysis: *H. Wendt** and *V. Plzak*, Institut für Chemische Technologie, Darmstadt, D-6100 Darmstadt, Germany

Cobalt containing perovskites like $La_{0.5}Sr_{0.5}CoO_3$ or $Ni_{0.2}Co_{0.8}LaO_3$ and spinels like $NiCo_2O_4$ and Co_3O_4 were prepared en masse by thermal decomposition of metal nitrates ($NiCo_2O_4$ and Co_3O_4) at temperatures below 500°C and by cosintering of the respective oxides (perovskites). Preparation of catalytic covers could only be performed by nitrate decomposition and yields only for $NiCo_2O_4$ and Co_3O_4 in the desired compound whereas intended formation of perovskites yields always in a mixture of a number of different phases. Among these Co_3O_4 is the most powerful electrocatalyst (nearly comparable to RuO_2). Electrode kinetic data for O_2-evolution from caustic potash solutions in temperature range 60°-130°C are determined for different oxidic electrocatalyst. The authors achieved a method for *in situ* preparation of Co-oxide-electrocatalyst on nickel substrate.

728 *In Situ* X-ray Absorption Spectra of Supported Platinum Electrodes: *W. E. O'Grady** and *S. M. Heald*, Brookhaven National Laboratory, Dept. of Energy and Environment, Building 801, Upton, NY 11973, *D. E. Sayers*, North Carolina State University, Raleigh, NC 27607, and *J. I. Budnick*, University of Connecticut, Storrs, CT 06268

In situ determination of atomic level information on well-defined electrode surfaces is difficult at best, but on electrodes with supported catalyst structures it is essentially nonexistent. The technique of x-ray absorption spectroscopy can be applied to both well-defined electrode surfaces and to supported catalyst electrode surfaces. In this study, we have made use of both x-ray absorption near edge structure (XANES) and extended x-ray absorption fine structure (EXAFS) to obtain structural data on Pt supported on carbon under fuel cell operating conditions. XANES is directly related to the electronic structure, while EXAFS is related to the geometric structure of the catalyst particles. We have observed that the structure of the particles is perturbed by both the electrolyte and the electrode voltage. (This work was performed under the auspices of the U.S. Department of Energy under Contract No. AC-02-76CH00016.)

729 Importance of Interatomic Spacing in Catalytic Reduction of Oxygen in Phosphoric Acid: *V. Jalan** and *E. J. Taylor*, Giner, Inc., Waltham, MA 02154

Recent research at this laboratory has been concerned with the improvement of the phosphoric acid fuel cell electrode via an understanding of the fundamental factors affecting electrocatalytic activity. Both enhanced specific activity and improved stability have been demonstrated by platinum alloys and a "platinum carbide." These catalysts were characterized by x-ray diffraction and a correlation between catalytic activity and the crystallographic nearest neighbor distance has been observed. This correlation is discussed in light of recent theoretical developments in the understanding of the oxygen reduction reaction in hot concentrated phosphoric acid.

730 Electrokinetics of Oxygen Reduction on Platinum in Trifluoromethanesulfonic Acid: *K-L. Hsueh, H. H. Chang*, and *D-T. Chin*, Dept. of Chemical Engineering, Clarkson College of Technology, Potsdam, NY 13676, and *S. Srinivasan**, Electronics Div., Los Alamos National Laboratory, Los Alamos, NM 87545

Trifluoromethane sulfonic acid (TFMSA) has been considered as an alternate electrolyte in phosphoric acid fuel cells. A rotating ring-disk electrode technique and a cyclic voltametry have been used to study oxygen reduction reaction on Pt in TFMSA (0.06-6.0 M) and in a mixed TFMSA/phosphoric acid electrolyte. The apparent reaction order, the intermediate reaction rate constants, and the formation of hydrogen peroxide as the intermediate product are discussed in this paper.

731 A New Look at the Kinetics and Mechanisms of Oxygen Evolution at Pt in Alkaline Solutions: *V. I. Birss**, Dept. of Chemistry, University of Calgary, Calgary, Alta., Canada T2N-1N4, and *A. Damjanovic*, Allied Corporation, Morristown, NJ 07960

Oxygen evolution reaction at Pt electrodes in alkaline solutions of different pH's and at room temperature is reexamined. Following anodic polarization of a prereduced electrode with a constant, high current, V-i measurements reveal two Tafel regions with slopes of 120 mV and 60 mV at higher and lower currents, respectively. The region with the slope of 120 mV is sensitive to time and current density of the anodic pretreatment. In contrast, the region with the slope of 60 mV is only insignificantly affected by these variables. The former Tafel region is unusually sensitive to pH with V decreasing 170 mV as pH increases one unit. The latter region, also, is strongly affected by pH. In this region V decreases 120 mV as pH increases one unit. These pH dependences cannot be accounted for in terms of simple, classical electrode kinetics. The unusual pH dependences are related to the mechanism of O_2 evolution at insulating, thin anodic oxide films at Pt electrodes with complex interfacial structure.

732 On the Kinetics of Fast Redox Reaction Results Obtained with the Ring Electrode in Turbulent Pipe Flow: *T. Iwasita**, *W. Schmickler*, and *J. W. Schultze*, Institut für Physikalische Chemie, Universität Düsseldorf, Düsseldorf, Germany

A theoretical analysis of the ring electrode in turbulent pipe flow (1) is given. Our experimental setup was tested by measuring the exchange current density of the $Fe(CN_6)^{3-/4-}$-couple; we obtained values much higher than those reported in the literature. The method is used to determine the kinetic parameters of a fast outer-sphere redox reaction on a series of metal electrodes. The results are discussed with reference to current theories concerning the influence of the metal on reaction rates.

1. Ch. Bernstein and W. Vielstich, in "Electrode Processes 1979," S. Bruckenstein, B. Miller, J. D. E. McIntyre, and E. Yeager, Editors,

p. 350, The Electrochemical Society Softbound Proceedings Series, Princeton, N.J. (1980).

733 Electrocatalytic Properties of Phthalocyanines: *J. Zagal,* P. Herrera, K. Brinck,* and *S. Ureta-Zañartu,* Dept. de Química, Facultad de Ciencia, Universidad de Santiago de Chile, Santiago 2, Chile

The electrocatalytic properties of phthalocyanines for O_2 electroreduction are well known. However, there is evidence that these materials are potent catalysts for a great variety of electrochemical reactions involving both the oxidation and the reduction of species. In this work, we compare the catalytic activity of different metal phthalocyanines in the electro-oxidation of hydrazine, electro-oxidation and electroreduction of hydroxylamine, electro-oxidation of cysteine, and electroreduction of cystine. We have found that for all these reactions the transition metal in the phthalocyanine plays the key role in determining the catalytic activity and the reaction mechanism. The iron derivatives are the most active materials and show the smaller Tafel slopes. The trends are as follows: Fe > Mn Co > Ni Cu. These trends correlate well with those found for O_2 reduction, and with those found in chemical reactions like oxidation of organic substances by air promoted by phthalocyanines. The role of chemical structure, electronic and redox properties of the metal chelates in the electrocatalysis is discussed.

734 Electrocatalysis Studies on the Cathodic Reduction of Thionyl Chloride: *M. Madou,* K. Kinoshita,* and *M. C. H. McKubre,* SRI International, Menlo Park, CA 94025, and *S. Szpak,* Naval Ocean Systems Center, San Diego, CA 92117

The electrocatalytic activity of carbon and copper electrodes and additives such as Fe-, Co-, and Cu-phthalocyanines on the cathodic reduction of $SOCl_2$ were investigated by cyclic voltammetry and a-c impedance techniques. Results obtained by cyclic voltammetry indicate that cathodic reduction of $SOCl_2$ is enhanced by Fe- and Co- phthalocyanines but remains relatively unaffected by the presence of Cu-phthalocyanine. The effect of electrocatalysts on the cathodic reduction of $SOCl_2$ and possible mechanisms for enhanced activity are discussed.

735 $SOCl_2$ Reduction on Rotating Disk and Stationary Electrodes: *N. Doddapaneni,* Honeywell Power Sources Center, Horsham, PA 19044

The $SOCl_2$ reduction has been carried on rotating disk and stationary electrodes in $LiAlCl_4 \cdot SOCl_2$ electrolytes. The reduction process on both carbon and graphite electrodes with and without cobalt or iron phthalocyanine catalysts is first order and diffusion controlled. On catalyzed electrodes, however, the overall reduction mechanism seems to be modified. (This work was supported by the U.S. Army Electronics Research and Development Command under Contract No. DAAK20-81-C-0381.)

736 Electrochemical Reactions of Ethylene on Pt and Au in Sulfuric Acid: *G. Semrau* and *J. Heitbaum,** Institute of Physical Chemistry, University of Bonn, D-5300 Bonn 1, Germany

The electrochemical reactions of ethylene on Pt and Au in sulfuric acid were studied together with its adsorption. From cyclic voltammograms, quasistationary i/φ-curves and adsorption isotherms, kinetic parameters such as apparent transfer coefficients, reaction orders, and surface coverages were obtained, which were interpreted by means of plausible reaction mechanisms. Furthermore, mass spectroscopic cyclic voltammetry showed ethylene to be reduced to ethane on Pt and oxidized to CO_2. On Au, the main oxidation product is acetaldehyde with some CO_2 as by-product.

737 A Study of the Kinetics and Mechanisms of Anodic Oxidation of Carbonaceous Fuels: *J. Tweedie* and *P. Bindra,** IBM T. J. Watson Research Center, Yorktown Heights, NY 10598

The Wagner-Traud theory of mixed potentials has been applied to determine the kinetics and mechanisms of the anodic oxidation of carbonaceous fuels such as methanol, formaldehyde, and formic acid on noble metal substrates. The measurements were performed in acid, neutral, and alkaline media using cyclic voltammetry and the rotating disk electrode techniques. The effect of adsorbed metal ad-atoms on the oxidation reactions has also been investigated.

PHYSICAL ELECTROCHEMISTRY

Fourth International Symposium on Molten Salts

738 Vibrational Spectra of Chloroaluminates: *E. Rytter,* Institutt for uorganisk kjemi, Universitetet i Trondheim, N-7034 Trondheim-NTH, Norway

The joint information from Raman and infrared spectroscopy gives a firm basis for a structural study of entities in molten chloroaluminates. Investigations in the infrared range previously have been difficult due to the lack of suitable window materials. The problem has been solved by the use of a diamond windowed cell. Results will be presented for pure Al_2Cl_6, and mixtures with NH_3, and several Group IA-, Group IIA-, and transition metal chlorides. Topics discussed include reactions, species formation, the structure of $Al_2Cl_7^-$, and anion-cation interactions.

739 Molecular Dynamics Calculations of MAX_4 Melts: *M.-L. Saboungi, M. Blander,* and *A. Rahman,* Argonne National Laboratory, Argonne, IL 60439

Molecular dynamics calculations of molten ionic MX_4 for four different radius ratios of the A^{+3} and X^- ions emulated structures expected *e.g.*, for $NaAlCl_4$ and $LiYF_4$ melts. For the small ratios studied, A^{+3} ions were largely tetrahedrally coordinated ($Z \sim 4$) with very few tetrahedra having shared corners (*i.e.*, $A_2X_7^-$ ions). For the large ratios studied, the A^{+3} ions were largely octahedrally coordinated ($Z \leq 6$) with many bridging X^- ions, and long range ordering of A^{+3} ions to distances of at least 9 Å.

740 The Coupling Between Transport of Electric Charge and Chemical Reaction: *T. Førland,* Laboratory of Physical Chemistry, The Norwegian Institute of Technology, N-7034 Trondheim-NTH, Norway, *A. A. Makange,** Dept. of Chemical Engineering, University of Dar es Salaam, Dar es Salaam, Tanzania, and *S. K. Ratkji,* Laboratory of Physical Chemistry, The Norwegian Institute of Technology, N-7034 Trondheim-NTH, Norway

The coupling between transport of electric charge and chemical reaction has been described by irreversible thermodynamics. The method uses the minimum number of components as required by the phase rule, and transport coefficients of neutral salts. The method is applied to cells involving the acid-base reaction

$$HCl + KOH = H_2O + KCl \quad [1]$$

or the reciprocal salt reaction

$$LiBr + KCl = LiCl + KBr \quad [2]$$

It is shown how local contributions to emf and local energy losses can be calculated, and that the scalar Gibbs energy change of reactions [1] and [2] is not needed to describe processes in the cell.

741 Characteristic Diffusion Phenomena of Fluorine in Molten LiF-BeF_2 and NaF-BeF_2 Systems: *H. Ohno* and *K. Furukawa,* Japan Atomic Energy Research Institute, Molten Materials Laboratory, Tokai-mura, Ibaraki-ken 319-11, Japan

Self-diffusion coefficients of fluorine and cations in molten LiF-BeF_2 and NaF-BeF_2 systems are summarized by the capillary reservoir technique. The characteristic diffusion phenomena of fluorine in these molten fluoroberyllates are very similar to those of oxygen in molten $CaO\text{-}SiO_2$ and $CaO\text{-}SiO_2\text{-}Al_2O_3$ slag. The dynamic behavior of Li and F in molten Li_2BeF_4 and $LiBeF_3$ were also analyzed by NMR technique. The results are presented in comparison with those by self-diffusion.

742 Thermodynamic Properties of $AlCl_3$-Containing Melts: *H. A. Øye,* Institute of Inorganic Chemistry, Norwegian Institute of Technology, University of Trondheim, 7034 Trondheim-NTH, Norway, and *W. E. Wahnsiedler,* Alcoa Laboratories, Process Chemistry and Physics Div., Alcoa Center, PA 15069

The chloroaluminate melts exemplified by the system NaCl-$AlCl_3$ constitute a unique class of melts. Their properties vary from the high-melting ionic NaCl to the low-melting covalent $AlCl_3$. At intermediate compositions a variety of complexes is formed. A review of the thermodynamic properties of this class of melts is given and a unified model based on mass action law principles is discussed.

743 An Interpretive Review of Some Unusual Properties of $SbCl_3$-$AlCl_3$ and $SbBr_3$-$AlBr_3$ Melts: *G. P. Smith** and *M. Sørlie,* Chemistry Div., Oak Ridge National Laboratory, Oak Ridge, TN 37830, and *G. Mamantov,* Dept. of Chemistry, University of Tennessee, Knoxville, TN 37996-1600

Some of the properties of $SbCl_3$-$AlCl_3$ and $SbBr_3$-$AlBr_3$ melts differ in pronounced ways from those of their component halides, and to an extent that is quite unusual. Striking examples are provided by electrical conductivity (virtually nil for components, quite high for mixtures), and by the solubility of Sb^0 (very small in $SbCl_3$, quite high in $SbCl_3$-$AlCl_3$). Temperature dependences of both properties are also unusual. This paper reviews these topics from a structural viewpoint. (This research was sponsored by the Division of Chemical Sciences, Office of Basic Energy Sciences, U.S. Department of Energy under contract W-7405-eng-26 with the Union Carbide Corporation.)

744 Thermodynamics of Evaporation of Melts of $LiAlCl_4$, $NaAlCl_4$, and $KAlCl_4$: *U. Gesenhues* and *H. Wendt,** Institut für Chemische Technologie, TH Darmstadt, D-6100 Darmstadt, Germany

Vapor pressure and liquid vapor-equilibria have been investigated for alkali-chloride saturated Li, Na, and $KAlCl_4$ in the temperature range 200°-700°C (which is relevant for Al-electrowinning from chloride melts) by vapor transfer, Knudsen effusion deposition, and Knudsen effusion mass spectrometry. Mass-spectrometric investigations of the alkalichloride-aluminum-chloride vapors reveal that contrary to conventional assumptions, appreciable amounts of evaporated $AlKAlCl_4$ molecules exist in dimeric form. Dimerization tendency increases from potassium over sodium to lithium and $AlCl_3$ activity, and hence volatility increases likewise in the same sense.

745 The Use of Lithium Aluminum Chloride Molten Salt as an Electrolyte in Lithium Cells: *I. D. Raistrick** and *R. A. Huggins,* Dept. of Materials Science and Engineering, Stanford University, Stanford, CA 94305

$LiAlCl_4$, either as a solid or as a molten salt, is unstable to reduction by lithium at high activities. The melt, however, forms a stable reversible interface with aluminum metal, which can therefore be used as a negative electrode in cells of the type

$$- Al(s) \mid LiAlCl_4(l) \mid Li_xA +$$

where A represents a suitable positive electrode reactant for lithium. The thermodynamic aspects of this cell are discussed and possible positive electrode materials identified.

746 The Fischer-Tropsch Reaction in Chloroaluminate Melts: *G. Mamantov** and *S. E. Walters*, Dept. of Chemistry, University of Tennessee, Knoxville, TN 37996-1600

The Fischer-Tropsch reaction, *i.e.*, the reduction of carbon monoxide by hydrogen, can be performed in chloroaluminate melts using metallic dispersions or metal carbonyls as catalysts. Alkanes are the principal products of these reactions, with their distribution depending on the nature of the catalyst, temperature, pressure, and reaction time. Promoters such as aluminum metal also affect the distribution and overall yield or alkanes. Some aspects of this work are presented. (This research was supported by the National Science Foundation.)

747 The Role of Coupled-Transport Reactions in the Preparation of Metal Halides and Chalcides Using Molten Aluminum Halide Solvents: *W. B. Jensen* and *E. M. Larsen*, Dept. of Chemistry, University of Wisconsin-Madison, Madison, WI 53706

The successful synthesis of metal halides and chalcides using the "tilted tube" technique and molten Al_2X_6 solvents is postulated to be the result of a "coupled transport" reaction in which the favorable physical transport of the volatile Al_2X_6 solvent, via the vapor phase, is used to drive an unfavorable chemical transport of the reaction product, via the liquid phase. This postulate is supported by approximate thermodynamic calculations.

748 Molten Gallium Halides as Media for Reactions of Polycyclic Aromatic Hydrocarbons (PAH's): *A. S. Dworkin,** *A. C. Buchanan III*, and *G. P. Smith*, Chemistry Div., Oak Ridge National Laboratory, Oak Ridge, TN 37830

Molten gallium trihalides are both strong Lewis acids and good oxidizing agents, functions which may be tuned by additions of Ga metal. Catalytic hydrogen transfer reactions of PAH's in molten gallium chlorides and bromides are reported and compared with those in molten $SbCl_3$, an exceedingly weak Lewis acid and relatively poor oxidizing agent, and in molten solutions of $SbCl_3$ in which the Lewis acidity and oxidizing functions have been enhanced by additions of $AlCl_3$. (This research was sponsored by the Division of Chemical Sciences, Office of Basic Energy Sciences, U.S. Department of Energy under contract W-7405-eng-26 with the Union Carbide Corporation.)

749 Phase Diagram of LiCl-NaCl-$AlCl_3$ Ternary System: *Y. Sato** and *T. Ejima*, Dept. of Metallurgy, Faculty of Engineering, Tohoku University, Sendai 980, Japan

Phase diagram was determined for the LiCl-NaCl-$AlCl_3$ ternary system containing 0-5 m/o $AlCl_3$ over the whole composition range of LiCl and NaCl. Liquidus temperatures were measured by means of the direct visual observation method and DTA method. Ternary eutectic composition was considered to be close to eutectic composition of $LiAlCl_4$-$NaAlCl_4$ quasi-binary system. Thermodynamic property of the ternary system, which was considered as a reciprocal system of (Li^+, Na^+ || Cl^-, $AlCl_4^-$) in the composition range of the present study, is discussed.

750 Transition Metal Chloro Complex Formation in Room Temperature Chloroaluminate Melts: *T. M. Laher, T. B. Scheffler*, and *C. L. Hussey**, Dept. of Chemistry, University of Mississippi, University, MS 38677

Mixtures of aluminum chloride ($AlCl_3$) and either *N*-(*n*-butyl)pyridinium chloride (BPC) or 1-methyl-2-ethylimidazolium chloride (MEIC) are liquid at room temperature. Variation of the ratio of $AlCl_3$ to BPC or MEIC in these salts can be used to effect considerable changes in melt chloride ion activity at low liquidus temperatures. The coordination of copper (I), copper (II), iron (II), iron (III), lead (II), molybdenum (IV), molybdenum (III), nickel (II), and silver (I) was studied in basic (chloride ion-rich) melts as a function of the melt chloride ion activity. The stability of each chloro complex ion formed in basic melt was estimated relative to the respective 2:1 molar ratio $AlCl_3$-BPC or $AlCl_3$-MEIC melt.

751 Prospect for Alkyl Pyridinium Chloride Aluminum Chloride Melts: *C. D. Desjardins**, and *T. Cadger*, N. B. Research and Productivity Council, Fredericton, N.B. Canada E3B 5H1, *E. J. Casey*, Defense Research Establishment, Ottawa, Ont. Canada, and *R. S. Salter*, N.B. Research and Productivity Council, Fredericton, N.B. Canada E3B 5H1

The recent preparation of molten salts which are liquids at room temperature and below has awakened interest in their physicochemical properties and their technological uses. A cooperative effort, both fundamental and applied, has been directed to determine their possible utilization as electrolytes in electrochemical cells whether for batteries, electrometallurgy, or surface preparation. Specifically, various n-butyl pyridinium chloride-aluminum chloride melts have been synthesized and examined for their stability to oxidation/reduction and their reactions with electrode materials such as Li, Ca, Ti, Al, and MoO_3. Stringent attention to purity is essential.

752 Reduction of Aromatic Ketones in an Aluminum Chloride: Dialkylimidazolium Chloride Molten Salt System: *R. Herzog* and *G. T. Cheek**, Dept. of Chemistry, U.S. Naval Academy, Annapolis, Maryland 21402

The reductions of several aromatic ketones at vitreous carbon in acidic and basic aluminum chloride:methylbutylimidazolium chloride ionic liquids are studied. Reduction processes observed for benzil (−1.00V, −1.28V *vs.* Al/2:1 melt reference), benzoin (−1.40V), and benzophenone (−1.60V) in the basic melt (0.8 : 1.0 for the above ratio) are found to be irreversible. Preparative electrolyses, involving hydrolysis of the reduction mixture, show that reduction involves two electrons per carbonyl group. In the acidic melt, the reduction potential for benzil (+0.6V) indicates complexation of benzil by aluminum chloride.

753 Organic Reactions in Low Melting Chloroaluminate Molten Salts: *J. A. Levisky, J. L. Pflug*, and *J. S. Wilkes**, The Frank J. Seiler Research Laboratory, United States Air Force Academy, Colorado Springs, CO 80840

Mixtures of 1, 3-dialkylimidazolium chlorides and aluminum chloride are liquid considerably below room temperature, and they promote certain organic reactions. Acidic mixtures of 1-methyl-3-ethylimidazolium chloride and $AlCl_3$ act both as a solvent and a catalyst for alkylation and acylation of aromatic compounds. The rate of reaction may be readily controlled by changing the Lewis acidity of the melt and the temperature. The melts that were used permit reactions at sub-zero temperatures. Spectroscopic experiments showed the identity of the catalytic species in the melt and the reactive intermediate.

754 A Survey of the Electrochemistry and Spectroelectrochemistry of Some Arenes in $SbCl_3$-Rich Room Temperature Melts: *D. M. Chapman,** *M. Sørlie*, and *G. P. Smith*, Chemistry Div., Oak Ridge National Laboratory, Oak Ridge, TN 37830, and *C. Petrovic* and *G. Mamantov*, Dept. of Chemistry, University of Tennessee, Knoxville, TN 37996-1600

We report the investigation of the electrochemical and spectroelectrochemical behavior of some polycyclic aromatic hydrocarbons in basic and acidic $SbCl_3$-rich room temperature melts. The spectroelectrochemical experiments of some electrogenerated radical cations were studied using an OMA-2 multichannel spectrometer. The more easily oxidizable arenes undergo homogeneous electron transfer in an acidic melt. We also report conductivity and viscosity measurements performed on the melts. (This research was sponsored by the Division of Chemical Sciences, Office of Basic Energy & Sciences, U.S. Department of Energy under contract W-7405-eng-26 with the Union Carbide Corporation.)

755 Use of $AlCl_3$-Containing Molten Salts for Carbonization as Solvent and Catalyst: *E. Ota,** College of Technology, Gunma University, Kiryu, Gunma 376, Japan, and *S. Otani*, Faculty of Technology, Gunma University, Kiryu, Gunma 376, Japan

Liquid-phase carbonization was studied successfully using two kinds of molten salts containing $AlCl_3$ as the main ingredient. Many organic substances were carbonized in these melts at temperatures below 300°C, yielding graphitizable carbon in many cases. The melts act there as the solvent and the catalyst, and are thought to be a superacid. The character of the reaction is interpreted in terms of ionic mechanism in connection with the nature of the melts.

756 Influence of Redox and Lewis Acid Functions of $SbCl_3$-Rich Molten Salt Catalysts on the Reactions of Coal Model Compounds: *A. Buchanan III,** *A. S. Dworkin*, and *G. P. Smith*, Chemistry Div., Oak Ridge National Laboratory, Oak Ridge, TN 37830

Both the redox and Lewis acid functions of $SbCl_3$-based melts can play key roles in catalyzing reactions of coal model compounds. These two catalytic functions are demonstrated by two recently discovered reaction types. These reactions are the selective transfer hydrogenation of polycyclic arenes by tetralin that involves the formation of arene radical cation intermediates, and the transaralkylation reaction for the α,ω-diphenylalkanes, $C_6H_5(CH_2)_nC_6H_5$ [n = 1-4], that involves the selective cleavage of the sp^2-sp^3 bond via the formation of benzylic carbenium ion reactive intermediate. (This Research was sponsored by the Division of Chemical Sciences, Office of Basic Energy Sciences, U.S. Department of Energy under contract W-7405-eng-26 with the Union Carbide Corporation.)

757 Reactivity of Anthracene in a Novel Antimony Trichloride-Rich Room-Temperature Melt: *S. P. Zingg,** *A. S. Dworkin, M. Sørlie, D. M. Chapman, A. C. Buchanan III*, and *G. P. Smith*, Chemistry Div., Oak Ridge National Laboratory, Oak Ridge, TN 37830

A new ternary solvent system consisting of antimony chloride, aluminum chloride, and butylpyridinium chloride has been developed which is liquid at room temperature. The reactivity of anthracene in this solvent system was investigated by product analysis and spectroscopic techniques. A comparison is made between the reactivity of anthracene in the ternary system and in a binary system consisting of antimony chloride and varying amounts of aluminum chloride. (This research was sponsored by the Division of Chemical Sciences, Office of Basic Energy Sciences, U.S. Department of Energy under contract W-7405-eng-26 with the Union Carbide Corporation.)

758 Interaction Between Aromatics and Molten or Supported Zinc Chloride: *M. Morita, K. Hirosawa*, and *T. Sato*, Government Industrial Development Laboratory, Sapporo-shi, Hokkaido, Japan, and *K. Ouchi*, Dept. of Applied Chemistry, Faculty of Engineering, Hokkaido University, Sapporo-shi, 061-01 Japan

The interaction between aromatics and molten or supported zinc chloride, and the hydrogenation over the catalyst were investigated by measurements of electronic spectra. The results showed the formation of electron donor-acceptor complexes and cation radicals by reaction of aromatics with zinc chloride, and the production of monopositive ions during introduction of hydrogen gas over the complexes.

759 Kinetics of Organic Substitution Reactions in Molten Acetate and Thiocyanate Salts: *T. I. Crowell,* E. H. Braue, Jr.,* and *P. S. Hillery,* Dept. of Chemistry, University of Virginia, Charlottesville, VA 22901

Two molten-salt eutectics with nucleophilic anions were used as solvents for kinetics of organic reactions at 140°-250°C: K^+, Na^+/SCN^- (A) and K^+, Li^+, Na^+/OAc^- (B). Hydroxylic substrates were soluble in these melts and nucleophilic displacements on esters were studied extensively in A and B

$$HOC_6H_4COOR + OAc^- \xrightarrow{B} HOC_6H_4COO^- + ROAc$$
(RSCN and RNCS in melt A)

The dependence of rate on R, and inversion of chiral R indicate an SN2 mechanism. Acetic acid, strongly solvated in the basic melt B, functions in the cleavage of the product to CO_2 and phenol. Brief studies were made of indicator equilibria, HOAc partial pressure, and other interactions. The rate of isomerization of anilinium thiocyanate to phenylthiourea was determined over the complete range of ionic strength, dilute solution to anhydrous melt A.

760 Reactions of Ethane, Chloroethane, and Chloroethene with Chlorine in Molten Salts: *M. Sørlie,* Institute of Inorganic Chemistry, Norwegian Institute of Technology, University of Trondheim, 7034 Trondheim-NTH, Norway, *P. G. Wahlbeck,* Dept. of Chemistry, Wichita State University, Wichita, KS 67208, and *H. A. Øye,* Institute of Inorganic Chemistry, Norwegian Institute of Technology, University of Trondheim, 7034 Trondheim-NTH, Norway

Reactions of ethane, chloroethane, and chloroethane with gaseous chlorine have been studied in molten LiCl-KCl eutectic, 40% $CuCl_2$-KCl, and 60% $CuCl_2$-KCl baths as a function of temperature and organic/chlorine feed gas composition. Product gases were analyzed by gas chromatography. Mainly C_2 products were observed. Products included chlorinated ethanes, ethene, chlorinated ethenes, and ethyne. The catalytic functioning of the molten salt was analyzed by comparison of product compositions with equilibrium calculated results among C_2 molecules. Baths containing Cu showed higher catalytic activity than the LiCl-KCl eutectic.

761 Molten Salt Batteries: *E. J. Cairns,* Energy and Environment Div., Lawrence Berkeley Laboratory, University of California, Berkeley, CA 94720

Molten salts are used in a number of high-specific-energy cells and batteries. They serve as electrolytes and, in some cases, as reactants. The recent research and performance results on molten salt cells and batteries are summarized and assessed, with emphasis on the most promising systems.

762 A Review of the Chemistry of Rechargeable Molten Salt Cells: *G. Mamantov,* Dept. of Chemistry, University of Tennessee, Knoxville, TN 37996-1600

The chemical and electrochemical aspects of rechargeable molten salt cells that are of current interest are reviewed. The emphasis is placed on the processes taking place in the positive electrode compartment.

763 Alkali Nitrite Molten Salt for Use in Intermediate Temperature Lithium Cells: *J. Poris,* I. D. Raistrick,* and *R. A. Huggins,* Dept. of Materials Science and Engineering, Stanford University, Stanford, CA 94305

The properties of a new intermediate temperature molten salt electrolyte $LiNO_3$-KNO_3 (40-60 m/o) are discussed. The behavior of elemental solid lithium in this electrolyte is analogous to the behavior of lithium in organic solvent-based electrolytes, as well as in the similar intermediate temperature nitrate electrolyte. The thermodynamic reduction and oxidation stability limit reactions have been shown to be at lower potentials (*vs.* Li^+/Li) compared with their counterparts in the nitrate electrolyte. Possible applications of this electrolyte in lithium cells are also examined.

764 Molten Onium Polyiodide Salt—Iodine Cathode Materials in Lithium Cells: *T. G. Hayes, B. B. Owens, J. B. Phipps, P. M. Skarstad,* and D. F. Untereker,* Medtronic Inc./Energy Technology, Brooklyn Center, MN 55430

Ammonium polyhalides have been employed as cathode materials in a number of cell systems. Many ammonium salts undergo eutectic melting with iodine below room temperature. Such liquids are conductive and can be mixed with crystalline iodine to make iodine cathode materials. Some Li/I_2 cell systems employing substituted heterocyclic aromatic ammonium polyiodide-iodine cathode materials have already been described by others. We have investigated the properties and cell performance of a number of aliphatic and phenyl-substituted ammonium and phosphonium iodide-iodine materials in lithium cells with *in situ* formed electrolytes. We find such materials to be highly efficient cathodes when discharged at low rates (>90%). Practical cells employing these cathodes are projected to be capable of delivering 1.0 W-hr/cm³ at optimum discharge rates.

765 Thermal Behavior of the Potassium-Sulfur Electrolyte in Advanced Battery Concepts: *G. J. Janz** and *D. J. Rogers,* Dept. of Chemistry, Rensselaer Polytechnic Institute, Troy, NY 12181

Characterization of the thermal behavior of salt systems as candidate materials in high temperature batteries requires measurements of heat capacities, heats of transition, heats of fusion, and the detection of exothermic chemical events. Results are reported for sulfur and for a series of polysulfide compositions of increasing sulfur content (from ~ 45 to ~ 82 w/o sulfur). The melting-crystallization behavior of the polysulfide compositions on repeated thermal cycling has been investigated as part of this work, and is described in this communication.

766 Ceramic Oxides as Container/Current Collector Materials for the Sulfur Electrode: *R. P. Tischer, H. Wroblowa, G. M. Crosbie,* and *G. J. Tennenhouse,* Ford Motor Co., Dearborn, MI 48121

The polysulfide/sulfur (PS) melt of the Na/S cell, operating at 300°-350°C, is extremely corrosive. In the search for a material suitable for container/current collector of the sulfur electrode, several conducting ceramic oxides were synthesized and corrosion tested in the entire potential range to which the current collector can be exposed (even locally) in practical Na/S cells. Results of electrochemical and surface (SEM, EDAX, Auger) studies are reported and the observed changes in the conductivity of the oxides, during prolonged cycling in the PS melt, are interpreted.

767 Solubility of Li_2S in LiF-LiCl-LiBr Electrolyte: Measurements and Calculations: *Z. Tomczuk, D. R. Vissers,* and *M. L. Saboungi,* Argonne National Laboratory, Chemical Technology Div., Argonne, IL 60439

The solubility of Li_2S in LiF-LiCl-LiBr (22 m/o-31 m/o-47 m/o) electrolyte was determined using the electrochemical cell: Ni/(α + β)Li-Al/LiF-LiCl-LiBr/Ni_3S_2/Ni. The measured values were 6840 and 8700 ppm at 739 and 773 K, respectively. The experimental results agree with independent calculations based on thermodynamic considerations. The calculated values (6350 and 8175 ppm, respectively) were obtained using previous solubility measurements of Li_2S in the LiCl-KCl eutectic. The observed increase of Li_2S solubility as the solvent is changed from LiCl-KCl to LiF-LiCl-LiBr, and then to LiF-LiCl is explained in terms of known molten salt solution theories.

768 Electrolytic LiCl Precipitation from LiCl-KCl Melt in Porous Anodes: *C. E. Vallet, D. E. Heatherly,* and *J. Braunstein,* Oak Ridge National Laboratory, Chemistry Div., Oak Ridge, TN 37830, and *L. Heatherly,* Oak Ridge National Laboratory, Metals and Ceramics Div., Oak Ridge, TN 37830

Composition gradients such as those predicted to occur during discharge of porous Li-Al negative electrodes of Li/S batteries with LiCl-KCl eutectic electrolyte were generated and measured in the LiCl-KCl anolyte of an electrolysis cell with Li-Al electrodes. LiCl precipitation during electrolysis was observed by two-dimensional scanning of electrolyte composition in the front part of quenched porous Li-Al anode sections using SEM/EDX. The distribution of sites of increased or decreased LiCl concentration, LiCl saturation and precipitation was mapped. Cathodic regions were observed near the cell walls. Preliminary results of analysis by Auger spectroscopy confirm LiCl precipitation in the porous anode. (This work was sponsored by the Division of Energy Storage Systems, U.S. Department of Energy under contract W-7405-eng-26 with the Union Carbide Corporation through Memorandum Request LBL 4506210 from Lawrence Berkeley Laboratory.)

769 Spectroscopic Studies of Solutions of Transition Metal Ions in Molten Alkali Metal Carboxylates: *V. A. Maroni** and *M. L. Maciejewski,* Chemical Technology Div., Argonne National Laboratory, Argonne, IL 60439

This paper describes results of ^{13}C NMR studies of molten alkali metal formate and acetate eutectics and of absorption and NMR spectral studies of transition metal ions in these same eutectics. Information on transport properties and coordination chemistry in the low-melting carboxylates, derived from the spectroscopic studies, is presented. The paper highlights (*i*) the viscous/glass-like character of the carboxylate eutectics near their melting points, (*ii*) the correlation of transition metal coordination behavior with predictions of electrostatic crystal field theory, and (*iii*) the many similarities between transition metal complexation in the molten carboxylates and in aqueous solution.

770 Spectroelectrochemistry of Molten Salts with an OMA-2 Optical Multichannel Analyzer: *G. P. Smith,* M. Sørlie,* and *S. P. Zingg,* Chemistry Div., Oak Ridge National Laboratory, Oak Ridge, TN 37830

We describe a fast, high-performance, optical absorption spectrometer interfaced to a molten salt spectroelectrochemical cell with an optically transparent electrode. The spectrometer is based on an EG&G Princeton Applied Research OMA-2 optical multichannel analyzer. The optical parameters can be varied over wide ranges to meet different experimental needs. Examples are given of its application to studies of reactive intermediates in melts. (This research was sponsored by the Division of Chemical Sciences, Office of Basic Energy Sciences, U.S. Department of Energy under contract W-7405-eng-26 with the Union Carbide Corporation.)

771 On the Thermodynamic Characteristics of Water in Hydrated Melts of Magnesium Chloride: *H.-H. Emons** and *W. Voigt*, Sektion Chemie, Bergakademie Freiberg, DDR-9200 Freiberg, Germany

An apparatus for vapor pressure measurements by a static method had been developed, which allows examination of very corrosive systems up to temperatures of 523 K. The binary system $MgCl_2$-H_2O with water contents between 4-8 mols per mol $MgCl_2$ was investigated. The activities and enthalpies of vaporization of water are presented and interpreted in connection with the transition "concentrated electrolyte solution—molten hydrate—molten salt." For treating the data quantitatively the applicability of the BET equation is tested and discussed.

772 Electroactivity of Water in Nitrate Melts: New Results and Remarks on Recent Literature Findings: *P. G. Zambonin,** *E. Desimoni*, *F. Palmisano*, and *L. Sabbatini*, Laboratorio di Chimica Analitica, Dipartimento di Chimica, Università, 70126 Bari, Italy

Despite extensive investigations the actual water electroreduction mechanism in nitrate melts is still widely debated. The subject is of topical interest since fused nitrates are finding even more widespread applications in industrial heat-treatments, thermal energy storage, and thermal batteries. A critical analysis of literature findings, complemented by information on work in progress in our laboratory seems to suggest a model consistent with experimental results obtained by several authors in the last twenty years.

773 The Behavior of Water in Molten Salts: *S. H. White* and *U. M. Twardoch*,* EIC Laboratories, Inc., Newton, MA 02158

The chemical and electrochemical properties of water in molten salts are important because water is often present as an undesirable impurity which can be difficult to remove and which wastefully consumes materials (corrosion), or it is deliberately added as a reactant in processes which generate new materials and/or energy. The solubility and electrochemical reactivity of water in several melts of differing anion composition are compared. The influence of solvent cation and temperature is discussed.

774 Vapor Pressures of Hydrate Melts Containing Lithium Nitrate and Alkali Nitrites: *T. B. Tripp*, Div. of Mathematics and Science, University of Maine at Presque Isle, Presque Isle, ME 04769

Measurements of the physical properties of hydrate melts have been made on only a very limited number of systems, mainly because few systems exist in the liquid state at temperatures below 200°. Such data are needed to test generalized models of electrolyte-water solutions. This paper reports the results of a vapor pressure study on hydrate melts containing a mixture of lithium nitrate and alkali nitrites over the concentration range 0.05-1.7 mol H_2O/mol cation at five temperatures between 110° and 150°. The system is attractive because it exists in the liquid state over the whole range of composition from molten salt to pure water at temperatures above 120°C and is suitable for extending the vapor pressure measurements into the transition region where the electrolyte and water mol fractions are approximately equal. The vapor pressure obeys Henry's law over the range 0-1 mol H_2O/mol cation; the same behavior is observed for hydrate melts containing $LiNO_3$-KNO_3. The results are discussed in terms of models proposed for hydrate melts.

775 Vapor Pressures and Thermodynamics of Molten Halide Mixtures: *H.-H. Emons** and *W. Horlbeck*, Sektion Chemie, Bergakademie Freiberg, DDR-9200 Freiberg, Germany

Vapor pressure measurements by the Knudsen effusion method in combination with high-temperature mass spectrometry were used to obtain thermodynamic activity data of molten mixtures alkaline earth halide-alkali halide. The gas phase over these mixtures contains, except molecules of the pure halides, also heterocomplexes. Using the experimental results of vapor pressure measurements, thermodynamic parameters were calculated. The dependence of G^E from the kind of cations or anions supports our assumption about the structure of molten salt mixtures, derived by other physicochemical properties.

776 Performance of Al-Deposition from Chloride Melts: *H. Wendt** and *K. Reuhl*, Institut für Chemische Technologie, TH Darmstadt, D-6100 Darmstadt, Germany

Cathodic deposition of aluminum from alkalichloride-aluminum-chloride mixed melts had been investigated over a variation in process parameters (melt composition, temperature, current density, electrode arrangement, and nature of cathode materials). Usual measurements of electrode potentials, cell voltages, and current yields were supplemented by visual inspection of the process in order to obtain additional information on the redispersion of deposited metal and its reoxidation by homogenously dissolved chlorine, which is the most important reason for low current efficiencies. As consequence of these investigations a process-scheme which is different from ALCOA's and a different cell geometry is being proposed as basis of a future R and D program in this field.

777 Electrochemical Intercalation of Lithium into Transition Metal Compounds in Low-Temperature Chloroaluminate Melts: *J. Devynck*, *R. Messina*, *J. Pingaron*, and *B. Tremillon*,* Université Pierre et Marie Curie, Ecole Nationale Supérieure de Chimie de Paris, Paris Cedex 05, France

We have in progress an investigation on electrochemical intercalation of lithium into several transition metal compounds (TiS_2, V_2O_5, V_2O_3, V_2O_4 . . .), in low-temperature chloroaluminate melts: $AlCl_3$-butylpyridinium chloride-LiCl at 60°C, $AlCl_3$-LiCl at 175°C. The reversibility of the different intercalation and deintercalation steps has been examined in the case of vanadium oxides. Cycling tests showed good stability and capacity in these molten salt media.

778 Oxygen Evolution at Platinum and Ceramic Oxide Anodes in Cryolite-Alumina Melts: *P. G. Russell*, Great Lakes Research Corp., Elizabethton, TN 37643

Polarization curves for Pt and a number of sintered high density ceramic oxide anodes were obtained in cryolite-alumina melts at 970°C. Platinum has low overpotential for O_2 evolution and shows high resistance to anodic corrosion. Many Fe_2O_3-based compositions exhibit large corrosion currents below the decomposition potential for alumina. The effects of melt composition and stirring on the IR corrected polarization curves are discussed.

779 The Electrochemical Behavior of Sulfide Ions in Molten Cryolite: *N. Q. Minh** and *N.-P. Yao*, Argonne National Laboratory, Chemical Technology Div., Argonne, IL 60439

The electrochemical behavior of sulfide ions has been studied in molten cryolite by linear sweep voltammetry using graphite electrodes at 1323 K. The oxidation of sulfide ions is found to proceed via a quasireversible mechanism, *i.e.*, one in which the current is controlled by both diffusion and charge transfer kinetics

$$S^{2-} \underset{}{\overset{k_s,\beta}{\rightleftarrows}} S + 2\bar{e}$$

The transfer coefficient β and the standard rate constant k_s are estimated to be 0.5 and 0.0042 cm/sec, respectively. The apparent diffusion coefficient for sulfide ions in cryolite at 1323 K is about 3.93×10^{-5} cm²/sec.

780 Corrosion of Metals and Alloys by Molten Salts Containing Aluminum Ions: *T. R. Griffiths*,* *K. King*, and *S. H. Marchant*, Dept. of Inorganic and Structural Chemistry, The University, Leeds, England LS2 9JT

Corrosion on superheater tubes in coal fired generating plant arises from molten salt attack. This sulfate deposit generally contains a significant proportion of aluminum, but previous studies have not investigated its role. The sulfate mixture having mol cation % Na, 42.5; K, 42.5; Al, 15 is molten at superheater operating temperatures. Electronic absorption spectroscopy studies of the corrosion products in this melt, and conventional metallurgical posttest examinations, has helped elucidate the contribution of aluminum ions to hot corrosion.

781 Corrosion Studies of Iron, Nickel, and Incoloy 800 in Sodium-Potassium Nitrate Melts at 250°-550°C: *H. Fernandez*, *M. Carter*, and *R. A. Osteryoung*,* Dept. of Chemistry and Div. of Restorative Dentistry, State University of New York at Buffalo, Buffalo, NY 14214

The corrosion behavior of iron, nickel, and Incoloy 800 alloy (I800) electrodes in molten (Na, K) NO_3 has been investigated over a temperature range of 250°-550°C. Anodic polarization curves as well as open-circuit potential measurements for Fe, Ni, and I800 show evidence of spontaneous passivation when these metals are in contact with the melt at any temperature studied. Pitting corrosion has been found in I800 at potentials more anodic than the steady-state potential, this phenomenon being more important at the lowest temperature investigated (250°C), than at the highest (550°C). Results of metallographic examination of the samples are discussed.

782 Oxide Ion Chemistry and Corrosion in Molten Alkali Nitrates and Nitrites: *N. Ramasubramanian*, Atomic Energy of Canada Ltd., Chalk River Nuclear Laboratories, Chalk River, Ont., Canada K0J 1J0

It has generally been assumed that corrosion in molten alkali nitrates proceeds by the participation of oxide ions (O^{2-}) directly from the melt. Such an assumption is erroneous because oxide ions are completely converted to peroxide and superoxide ions in dry melts and to hydroxyl ions in melts exposed to water vapor. Oxide ions, however, could be stabilized by the addition of nitrite. To check whether corrosion in such melts depended on the concentration of oxide ions experiments were carried out on zirconium and Zircaloy-2 in melts containing alkali metal nitrates, nitrite, and hydroxide under different conditions. The oxide ion concentration in the melts is estimated to vary from 10^{-12} to $\leq 10^{-20}$ m (mol kg^{-1}); too small to account for the observed kinetics and polarization data. The source of oxide ions has to be the reaction of nitrate, nitrite, and hydroxyl ions with the anion vacancies emerging on the surface.

783 Solubility of the NiO Fuel Cell Cathode in Li_2CO_3-K_2CO_3 Melts as Determined by Cyclic Voltametry: *T. D. Kaun*, Argonne National Laboratory, Chemical Technology Div., Argonne, IL 60439

At Argonne National Laboratory, development of molten carbonate fuel cells is concerned with the stability of its NiO (lithiated) cathode. Cyclic voltametry has been applied to examine Ni^{2+} concentration in Li_2CO_3-K_2CO_3 melts with NiO present. A test cell with three gold electrodes, one being the reference with 1/3 O_2-2/3 CO_2 gas purge, employed voltage limits of +0.2-−1.2 V. Data and physical samples were collected at temperatures between 823 and 1023 K, and Li_2CO_3-K_2CO_3 melt compositions ranging from 35 to 62 m/o K_2CO_3. Solubility of NiO as a function of increasing temperature (823-1023 K) differed for the respective carbonate melt compositions, increasing in a range from 10 to 30 wt ppm for 38 m/o K_2CO_3,

while decreasing in a range from 15 to 5 wt ppm for 62 m/o K_2CO_3. Humidified cathode gas gave a general increase in NiO solubility.

784 Solubility of Iron Disulfide in LiCl-KCl Eutectic Melts: *R. A. Sharma** and *R. N. Seefurth*, General Motors Research Laboratories, Warren, MI 48090-9055

Solubilities of FeS_2 in LiCl-KCl eutectic melts between 720 and 900 K are represented by the equation

$$\log (\text{mol fraction}, X_{FeS_2}) = -\frac{5157.33}{T} + 0.666$$

They were measured by a new optical technique. This was necessitated by an excessive scatter in the solubility data determined analytically after establishing equilibria between the melts and FeS_2 by diffusion and counter diffusion. The solubilities of FeS in these melts are expected to be the same as those of FeS_2.

785 Metal Displacement Reactions: *W. H. Smyrl*, Sandia National Laboratories, Albuquerque, NM 87185

The modeling of metal displacement reactions in molten salt systems has been shown recently (1, 2) to have important applications in the modeling of behavior of a Ca-CrO_4 thermal battery. The treatment of multiple diffusion zones in multiple phase systems by use of the Stefan-Maxwell relationships (3) is briefly reviewed. Application of the modeling techniques is focused on three general areas for this paper: (*i*) the emf of galvanic cells in which metal displacement reactions occur, (*ii*) the superposition of side reactions on the metal displacement reaction, and (*iii*) metal displacement reactions with one component of a multicomponent alloy. Comparison with classical treatments of simple systems is made where possible.

1. W. H. Smyrl *et al.*, Paper 253 presented at The Electrochemical Society Meeting, Montreal, Que., Canada, May 9-14, 1982.
2. W. H. Smyrl, Unpublished results.
3. R. Pollard and J. Newman, *This Journal*, **127**, 744 (1980).

786 Measurements of the Partial Electronic Conductivity in Lithium Chloride-Potassium Chloride Molten Salts: *G. J. Reynolds** and *R. A. Huggins*, Dept. of Materials Science and Engineering, Stanford University, Stanford, CA 94305

The partial electronic conductivity of the lithium chloride-potassium chloride molten salt electrolyte has been determined by d-c polarization experiments using the Wagner asymmetric cell technique. Measurements were made on the eutectic composition (41 m/o KCl-59 m/o LiCl) over a range of temperature and lithium activity.

787 Cell Design Principles for the Measurement of Kinetics of Fast Electrode Reactions: *Z. Nagy** and *J. L. Settle*, Argonne National Laboratory, Chemical Technology Div., Argonne, IL 60439

The rates of electrode processes in high temperature molten salts are often very fast and special precautions are needed in their measurements. The measurement methods are invariably some sort of relaxation technique where a fast perturbation of the current (or the potential) is applied and the resulting potential (or current) relaxation is recorded. The measuring cells used in these experiments have to be carefully designed so that the distortion of the fast electrical signals and the introduction of spurious signals are avoided. The two requirements of a good design can be simply stated as: (*i*) the assurance of uniform current distribution on the working electrode surface and (*ii*) small impedance. The latter requirement includes small stray capacitances and small inductance, to avoid detrimental phase shifts and inductive spikes in the signals, and small ohmic resistance of the solution between the reference and the working electrodes. Three cell designs, aimed at fulfilling these requirements, are described.

788 The Electrocrystallization of Chromium from Molten LiCl-KCl at 450°C: *D. Inman,** *T. Vargas*, *S. Duan*, and *P. Dudley*, Dept. of Metallurgy and Materials Science, Imperial College, London, England SW7 2BP

The ion Cr^{2+} is stable in molten LiCl-KCl at 450°C and chromium metal can be deposited from it by a two-electron charge transfer process. Electrocrystallization has been studied both by electrochemical, *e.g.*, chronoamperometry and structural, *e.g.*, scanning electronmicroscopy techniques, in the latter case both at the initial nucleation stage and after the growth of the electrodeposit. On this basis, high quality deposits have been obtained by the use of a double-pulse potentiostatic procedure.

789 The Electrochemical Deposition of Refractory Metals from Chloride Melts: *S. H. White** and *U. M. Twardoch*, EIC Laboratories, Inc., Newton, MA 02158

For certain applications, the deposition of the refractory metals and their alloys from low melting molten salts (less than 500°C) is a desirable goal. The factors involved in the production of coherent, thick deposits of metal require the consideration of both solution properties and the electrocrystallization mechanism. The results to be presented address these two aspects for the cases of molybdenum and chromium deposition from low melting molten chloride baths.

790 The Electrochemistry of Tungsten (V), (IV), and (III) in Molten LiCl-KCl Eutectic: *D. Zuckerbrod*,* Westinghouse Electric Corp., Research and Development Center, Pittsburgh, PA 15235, and *R. A. Bailey*, Dept. of Chemistry, Rensselaer Polytechnic Institute, Troy, NY 12181

The electrochemistry of tungsten (V), (IV), and (III) in molten LiCl-KCl eutectic was studied using cyclic voltammetry. Reduction of W(V) or W(IV) produced W(II), which disproportionated to W(IV) and metal. The latter was deposited in powdery form on the anode from W(V), but with excess W(IV) present (as K_2WCl_6), a tungsten mirror formed over all cell surfaces. Tungsten (III), added as $K_3W_2Cl_9$, yielded an insulating coat on a platinum electrode, but deposited tungsten powder on a tungsten electrode.

791 Study of the Electrowinning of Lanthanum-Nickel Alloys in LiCl + KCl Eutectic Melt: *B. Tremillon,** *G. Picard*, and *Y. Mottot*, Laboratoire d'Electrochimie Analytique at Appliquée, associé au CNRS (LA 216), Paris Cedex 05, France

The electrolytic behavior of lanthanum (III) ions dissolved in molten chlorides was investigated by means of potentiometric and voltammetric techniques between 400° and 530°C. The reactions of formation and stability of La(III)-O(−II) compounds were studied in the LiCl + KCl eutectic melt by means of a yttria stabilized zirconia electrode. Thanks to these results, the experimental conditions for the elaboration of La containing alloys in the melt were determined. In particular, the thermodynamic parameters relative to the formation of the La-Ni alloys were obtained by emf measurements.

792 Further Developments in Molten Salt Anodizing: *D. G. Lovering** (Present address: Louisiana State University, Baton Rouge, LA 70803-1804), R.M.C.S., Shrivenham, Swindon, England, and *K. P. D. Clark*, R.C.M.C., Kingston, Ont., Canada

Ostensibly, molten salts offer a convenient nonaqueous medium in which metals might be anodized to produce unhydrated oxide films. While earlier work indicates that films formed in melts are indeed different from those formed in aqueous solutions, caution in assessing their various claimed properties is required since insufficient attention has been paid to the presence and role of dissolved water. Results from our laboratory for anodized specimens of Al, Ti, W, Nb, and Mo in a range of nitrate melts containing various amounts of water, demonstrate that the temperature, anodizing method, and water content significantly influence the nature of the films produced.

793 Electrodeposition of Tungsten Carbide Coatings from Molten Salts: *K. H. Stern* and *S. G. Gadomski*, Chemistry Div., Naval Research Laboratory, Washington, DC 20375

Dense, adherent coatings of tungsten carbide have been electrodeposited on nickel substrates from the ternary (Li, Na, K)F eutectic at 750°-800°C. The source of tungsten was Na_2WO_4; the source of carbon was K_2CO_3. The concentration of both solutes was less than 10 w/o. By applying a voltage between a tungsten anode and the nickel cathode, the anions are reduced to the elements and react on the cathode to form the carbide. Current efficiencies of up to 50% have been achieved for the deposition of W_2C.

794 Anode Depolarization by Coal in the Electrolysis of Calcium Nitrate Tetrahydrate Melts: *K. E. Johnson** and *F. W. Yerhoff*, Dept. of Chemistry, University of Regina, Regina, Sask., Canada S4S 0A2

The decomposition potential of calcium nitrate tetrahydrate melt is lowered 0.65-0.75V by a slurry of lignite or char. The anode reaction (oxidation of water in the solvent) appears to give carbon oxidation products. The solvent cathode reaction is complex: a clean platinum cathode appears to reduce water at the lowest potential, but as a film forms on the cathode nitrate reduction becomes dominant; additional film formation results in secondary production of peroxide. Chemical solvent-coal reactions also occur.

795 Equilibrium Measurements for the Absorption of H_2S, COS, and HCl by Alkali Metal Carbonates: *S. E. Lyke,** *R. T. Hallen*, and *L. J. Sealock*, Battelle Northwest, Richland, WA 99352

Battelle Northwest has developed through the bench scale a process to remove H_2S and COS from hot fuel gas with a solution of Li, K, Na, and Ca carbonates supported on a solid substrate. In order to extend this process to operate in integrated coal gasification/molten carbonate fuel cell power plants, equilibrium data are needed for various cation compositions in the presence of high CO_2 and H_2O backpressures.

796 Effect of Oxoacidity on the Thermochemical Stability of Molten Sodium Nitrate-Nitrite Mixtures: *G. Picard,** *T. Flament*, and *B. Tremillon*, Laboratoire d'Electrochimie Analytique at Appliquée, associé au CNRS (LA 216), Paris Cedex 05, France

Molten sodium nitrite and sodium nitrate mixtures have various industrial applications. Among them, their use as heat transfer fluids requires a good knowledge of their thermochemical stability as a function of the temperature. A thermodynamical study by means of a yttria stabilized zirconia electrode has been realized and has shown that experimental conditions necessary to a good thermochemical stability of these mixtures can be deduced from potential-pO^{2-} diagrams.

797 Electrode Reactions Involving Lead or Cadmium Ions in Molten Nitrates: *M. H. Miles,** *G. E. McManis*, and *A. N. Fletcher*, Chemistry Div., Research Dept., Naval Weapons Center, China Lake, CA 93555

Cyclic voltammetric studies show that the addition of either Pb^{++} or Cd^{++} ions to molten nitrates produces a new cathodic wave, yet no reversible anodic wave is observed. Previous workers have

always attributed this observation to the reduction of the metal ion to the free metal followed by rapid reaction of the deposited metal with the molten nitrate. Our studies suggest that reduction to the free metal never occurs in molten nitrates for lead and cadmium ions; instead the nitrate ion in $Pb(NO_3)^+$ or $Cd(NO_3)^+$ complexes is the actual substance reduced, *i.e.*, $Cd(NO_3)^+ + 2e^- \rightarrow CdO\downarrow + NO_2^-$. Electrons, not the metal ions, transfer charge across the double layer. This reaction is shifted to more positive potentials than the normal NO_3^- reduction wave due to the strong electric field of the metal ion in the complex.

798 Electrolysis Reactions in Inorganic Acetate Melts: *E. Rhodes*, Dept. of Chemical Engineering, University College of Swansea, Singleton Park, Swansea, England SA2-8PP

Analysis of the electrolysis products of various molten inorganic acetates in the temperature range 230°-330°C shows that the only gaseous cathode product is methane. Carbon dioxide is the major anode product. Cyclic linear potential sweeps over the range 0.5-0.8V cathodic using a platinum reference electrode indicated that the system was only quasi-reversible. When hydrogen gas was fed to the working electrode, the redox reaction for hydrogen was observed.

799 Chlorinating Gaseous Mixtures in Molten Chlorides: *G. Picard,* F. Seon*, and *B. Tremillon*, Laboratoire d'Electrochimie Analytique at Appliquée, associé au CNRS (LA 216), Paris Cedex 05, France

Ores constituted by mixtures of oxides are among the principal mineral sources of metals. These ores can be treated in molten salts in order to be transformed into compounds allowing the corresponding metals to be obtained in an easy way. In particular, it is possible to use gaseous mixtures for the chlorination of oxides in suspension in molten chlorides. The use of gaseous mixtures like $HCl + H_2O$, $HCl + H_2 + H_2O$, $HCl + CO + H_2$, $Cl_2 + O_2$, $Cl_2 + CO$ or $COCl_2$ (and also $Cl_2 + C(s)$) for chlorination of oxides is explained in terms of oxidoreduction and oxoacidity. As an example molten LiCl + KCl eutectic at various temperatures is considered and selective chlorinations of oxides are given.

800 Standard Reference Electrode for Molten Salts: *J. A. Plambeck*, Dept. of Chemistry, University of Alberta, Edmonton, Alta., Canada

It is proposed that a standard reference electrode for fused salt measurements be based upon the Ag(I)/Ag couple at the temperature of measurement. The conditions of the Ag(I) species are those prevailing in dilute concentration in the pure solvent molten salt or molten salt mixture. The electrode potential is measured within the range of concentrations where potential is linearly dependent upon logarithm of concentration. It is extrapolated to unit concentration on the desired concentration scale (mol/total mol, mol/kg solvent, or mol/dm³) using the value of $RT/\mathbf{F}$ appropriate for the temperature of measurement.

PHYSICAL ELECTROCHEMISTRY

General Session

801 O_2 Reduction Kinetic in Deuterated Phosphoric Acid: *M. M. Ghoneim,** Dept. of Chemistry, Tanta University, Tanta, Egypt, and *S. Clouser* and *E. Yeager*, Case Western Reserve University, Case Center for Electrochemical Sciences, Cleveland, OH 44106

The O_2 reduction on Pt disks in 86% D_3PO_4 has been carried out in a manner parallel to that in 85% H_3PO_4 at 25°-30°C. The purpose is to gain insight into the mechanistic aspects of O_2 reduction and the role of protons in the rate-controlling step. Oxygen reduction in 86% D_3PO_4 involves a small inverse kinetic isotope effect. This provides evidence that the rate-controlling step in O_2 reduction in concentrated phosphoric acid does not involve protons.

802 Thermal Desorption and Auger Electron Spectroscopic Studies of Anodic Oxygen on Pt(100): *F. T. Wagner** and *P. N. Ross, Jr.*, Lawrence Berkeley Laboratory, Berkeley, CA 94720

Anodic layers formed at 1.0-2.3V RHE on Pt(100) in 0.1M HF were studied in a coupled electrochemical-UHV surface analytical apparatus. Auger, thermal desorption, and coulometry gave good agreement as to the amount of oxygen bound on the surface. O_2 thermal desorption from anodic films yielded unusually sharp peaks at temperatures which increased at higher coverages, suggesting an autocatalytic decomposition. Similar peak shapes were seen for gas-phase oxygen adsorbed on Pt(100). The electrode assemblies gave broad H_2O desorption peaks at 400 K, about 200 K below the O_2 desorption. Submonolayer quantities of water desorbed from electrodes which were contracted with electrolyte below 1V RHE; at higher potentials larger but poorly reproducible amounts of water desorbed. Further work quantifying the water associated with surface-oxides, with residues from the emersed electrolyte layer, and with other sources is underway. Once all factors are understood, thermal desorption may provide a new tool for the study of surface hydration.

803 The Effect of $H_2PO_4^-$ Anion on the Kinetics of Oxygen Reduction on Pt: *P. E. Andricacos** and *P. N. Ross, Jr.*, Lawrence Berkeley Laboratory, Materials and Molecular Research Div., Berkeley, CA 94720

Recent studies of anion adsorption on Pt have shown that TFMSA is a nonadsorbing electrolyte. Previous comparisons of the kinetics of oxygen reduction on Pt in TFMSA to the kinetics in H_3PO_4 show qualitatively that better kinetics were obtained in TFMSA electrolyte, but these studies were not done in a manner in which the effect of specific adsorption by $H_2PO_4^-$ anion was apparent. The effect is shown directly in this study by adding small aliquots of H_3PO_4 to 0.1M TFMSA while determining the oxygen reduction kinetics with a Pt rotating disk electrode. The range of $H_2PO_4^-$ concentrations varied from 2.9×10^{-5} to 7.3×10^{-2} M. Based on $H_2PO_4^-$ coverage data reported in the literature, the dramatic decrease in rate observed was greater than expected from just a site blocking effect. A small (<1 kcal/mol) increase in activation energy occurs in addition to the steric effect. The kinetic effect due to surface poisoning by specifically adsorbed $H_2PO_4^-$ anion at saturation coverage is about a factor of 15 relative to the rate in a nonadsorbing electrolyte.

804 Electrocatalysis for Oxygen Reduction by Adsorbed Dicobalt Cofacial Porphyrins: *H. Y. Liu, M. J. Weaver,* C-B. Wang*, and *C. K. Chang*, Dept. of Chemistry, Michigan State University, East Lansing, MI 48824

Rate parameters have been determined for oxygen reduction at graphite electrodes coated with several dicobalt cofacial porphyrins and related monomers to investigate how the electrocatalyses of the four- and two-electron pathways depend on the catalyst structure. In harmony with the results of Collman and Anson, unusually facile four-electron kinetics were obtained with a dicobalt diporphyrin having a four-atom linkage. The kinetics data combined with epr spectra for corresponding μ-superoxo complexes suggest that the four-electron route involves a *cis*-configuration of the bound oxygen intermediate.

805 Spatio-Temporal Organization of the Adsorbates Involved in the Reduction of Dissolved Oxygen at the Titanium/Acidic Media Interface: *J. P. Frayret*, LEEC-ENSM, 44072 Nantes, France, *M. Keddam*, and *P. Morel*, GR 4 du CNRS, 75230 Paris Cedex 05, France, and *A. Caprani,** ER 248 du CNRS, Hôpital Broussais, 75674 Paris Cedex 14, France

Analyzing the discrepancies with respect to the laws of diffusion at a uniformly accessible RDE reveals that the adsorbates involved in the consumption of oxygen are gathered into islets. This particular topography, which can be interpreted by spatio-temporal interactions between various adsorbates, depends on the electrolyte composition (HCl, H_2SO_4, $HCl + H_2SO_4$) and the substrate nature (morphology and composition Ti/TiH_2). Moreover, it is shown that the composition of the electrolyte influences the nature of the substrate and the HER.

806 Low Energy Electron Diffraction (LEED) Characterization of Metal Electrode Surfaces: *F. T. Wagner* and *P. N. Ross, Jr.,** Lawrence Berkeley Laboratory, Berkeley, CA 94720

The atomic-scale structural effects of potentiodynamic cycling of Pt single-crystal surfaces were investigated through the clean transfer of samples between a 3-electrode cell and a UHV surface analysis system, where LEED analysis of the surface structure was conducted. Achievement of the appropriate emersed state of the electrode for such *ex situ* analysis is shown to be of paramount importance. Pt(100) electrodes in HF electrolyte cycled into the oxygen electrosorption region (0.8-1.5V RHE) maintained long range order, but exhibited LEED spot broadening characteristic of randomly oriented steps of predominantly monatomic height. No such steps were observed on electrodes cycled within the double layer charging region. It was concluded that a few cycles to 1.5V in HF electrolyte is sufficient to remove characteristic impurities from low index surfaces and preserve short-range order (20Å domains), but the defect concentration is increased to *ca.* 1×10^{-14} sites cm^{-2}.

807 Conductivity Studies in Mixed Solvents: *M. Salomon** and *E. Plitcher*, U.S. Army Electronics Technology and Devices Laboratory, ERADCOM, Fort Monmouth, NJ 07703

The molar conductivities, Λ, for $LiClO_4$, $LiAsF_6$, $Bu_4N \cdot BPh_4$, and $Bu_4N \cdot ClO_4$ have been determined in propylene carbonate-dimethoxymethane (PC-DMM) mixtures over the concentration range of 2×10^{-4}-2×10^{-2} mol dm^{-3}. The electrolytic conductivities of $LiAsF_6$ have also been determined for concentrations of 2×10^{-4} – 1.0 mol dm^{-3}. A maximum in the electrolytic conductivities occurs at around 40 mass % PC, and the magnitude is almost twice that for either of the pure components. This "synergistic" effect is due to a combination of solvent viscosity effects, ion-ion and ion-solvent interactions. Ion asssociation constants have been determined in the pure and mixed solvents, and molar conductivities at infinite dilution have been calculated using the assumption $\lambda^\infty(Bu_4N^+) = \lambda^\infty(BPh_4^-)$.

808 Electrochemical Behavior of Lithium Closoborane Electrolytes: *H. H. Law, J. J. Auborn*, and *K. T. Ciemiecki*, Bell Laboratories, Murray Hill, NJ 07974

Lithium closoborane salts ($Li_2B_{10}Cl_{10}$ and $Li_2B_{12}Cl_{12}$) are expected to exhibit a high degree of stability, qualifying them for consideration as electrolytes for rechargeable lithium batteries. Solutions of these salts in ether-type solvent mixtures were prepared and studied by cyclic voltammetry. The presence of a passivating layer on the lithium electrode surface was observed. The reduction of cycling efficiency by such passivation reaction suggests that closoborane electrolytes are inappropriate for use in secondary lithium cells. Investigation of the anodic stripping behavior of fresh lithium deposited on a nickel substrate revealed no anodic current, but indicated reaction between the solution and the freshly deposited lithium.

809 Raman Spectroscopic Studies of the Chemistry of SO_2 in the Solvents Pyridine and α-Picoline: *W. A. Adams*, Defence Research Establishment Ottawa, Dept. of National Defence, Ottawa, Ont., Canada K1A 0Z4, and *L. A. Dierker*, University of Waterloo, Waterloo, Ont., Canada

Raman spectra of solutions of SO_2 (0-100%) in pyridine and α-picoline have been obtained as a function of temperature. A quantitative study of the bands of SO_2 and the solvent using component band analysis techniques indicates that SO_2 forms a range of complexes of the form SO_2: solvent including 1:1, 1:2, and 2:1 types. The shape and intensity of the ν_s (SO_2) band in these binary mixtures shows evidence of strong charge-transfer complex formation between SO_2 and these nitrogen base solvents.

810 Voltammetric Reduction of Sulfur Oxychloride Solvents in the Presence of Calcium Tetrachloroaluminate: *W. K. Behl*, Power Sources Div., Electronics Technology and Devices Laboratory (ERADCOM), Fort Monmouth, NJ 07703

Results of cyclic voltammetric studies at glassy carbon electrodes in sulfur oxychloride solutions containing lithium tetrachloroaluminate and/or calcium tetrachloroaluminate are presented. Experiments with sulfuryl chloride solutions indicate that the presence of even small concentrations of calcium tetrachloroaluminate in $LiAlCl_4$-SO_2Cl_2 solutions cause a large decrease in sulfuryl chloride reduction peak heights. Experiments with thionyl chloride solutions are now in progress and their results are also summarized.

811 Factors Influencing Lithium Rechargeability in Aprotic Solvent Based Electrolytes: *R. S. Salter,* C. D. Desjardins*, and *T. Cadger*, N. B. Research and Productivity Council, Fredericton, N.B. Canada E3B 5H1

Investigations have been conducted at the New Brunswick Research and Productivity Council over the past 3 years on identifying factors important to the rechargeability of the lithium electrode. The primary electrolyte used for this study was 1M $LiAsF_6$-2MeTHF. The influence of various distillation and purification procedures for solvent, solute, and electrolyte were examined using analytical, electrochemical, and half-cell cycling techniques. These procedures include the use of drying agents and pre-electrolysis, the purity and concentration of solute, cycling conditions, and the effect of electrolyte aging. Evidence for degradation of electrolyte cycling performance on aging is presented.

812 Study of Metal Solvent Interaction by XPS for the Case of Molybdene Naphtalocyanine in the Presence of $SOCl_2$: Application to the Reduction of $SOCl_2$ in Batteries: *J. Riga* and *J. J. Verbist*, Faculté Universitaire Notre Dame de la Paix, B 5000 Namur, Belgium, and *M. Savy, G. Magner*, and *G. Scarbeck*, L.E.I. du CNRS, 92190 Meudon-Bellevue, France

NPc Mo is a highly stable catalyst for the evolution of oxygen. Because of its stability, it is to be expected that $SOCl_2$ can be chemisorbed without damaging the molecular structure of NPc Mo. The first results from a study with XPS show an increasing rate of oxidation of molybdenum (from IV and VI) with NPc Mo as compared to NPcFe. The molecule is bound to the carbon black support by the ligand and not by the central ion. In the presence of $SOCl_2$, the molybdenum is mainly at the valance VI, and oxygen is mainly replaced by chlorine on the sites.

813 Complex Impedance Measurements of $SOCl_2$ Reduction: *N. Doddapaneni,** Honeywell Power Sources Center, Horsham, PA 19044, and *F. M. Delnick*, Sandia National Laboratories, Exploratory Battery Div., Albuquerque, NM 87115

Impedance measurements of cathode reactions are made in 1.5M $LiAlCl_4/SOCl_2$ electrolyte. An extremely slow electron transfer process of $SOCl_2$ reduction occurs on both carbon and graphite electrodes. However, when carbon or graphite surfaces are preadsorbed with the iron phthalocyanine catalyst, a tenfold improvement in the $SOCl_2$ reduction rate is observed. (The work was supported by the U.S. Army Electronics Research and Development Command under Contract No. DAAK20-81-C-0381.)

814 Cathode Studies of a High Rate Li/$SOCl_2$ Cell: *N. Doddapaneni,** Honeywell Power Sources Center, Horsham, PA 19038, and *S. Szpak*, Naval Ocean Systems Center, San Diego, CA 92152

The rate capability and the specific cathode capacity of porous carbon cathodes in Li/$SOCl_2$ systems increase dramatically when cathodes are doped with small amounts of metal-phthalocyanine catalysts. The improvements with electrocatalysts, such as iron phthalocyanine, are found to be superior to the cathodes doped with copper. The reaction zone thickness decreases with increased discharge current rates. SEM and EDS studies of discharged cathodes show the structure and growth of LiCl crystals in the cathode depend on the cathode dopant.

815 On the Limitations of Stationary Methods for the Study of Fast Electrode Reactions: *W. Vielstich*, Institut für Physikalische Chemie der Universität Bonn, D-5300 Bonn, Germany 0228

During the last decade, the investigation of fast electrochemical reactions has improved with the development of suitable methods. The possibilities of unstationary and stationary techniques often has been overestimated. It is shown by the results of a computer analysis, as well as by experimental data that rotating disk and ring electrodes only can be used for charge transfer reactions with a rate constant $k < 0.1$ cm/sec. The application of a ring electrode in turbulent pipe flow allows measurements of k's up to 1.5 cm/sec with an error of less than 15%.

816 Information Sources for Electrochemistry: *C. W. Moulton** and *H. D. Hannan*, Chemical Abstracts Service, Columbus, OH 43210

With the proliferation of the primary literature, journals, conference and symposium proceedings, reports, and patents, it becomes progressively more difficult to stay abreast of technical advances. The electrochemist must rely to an ever greater degree on the secondary information sources not only the traditional types, but also such advanced means as computerized information retrieval. The various modes of access to electrochemical information are discussed.

817 Proton and Water Transport Through SPE Membranes: *N. E. Vanderborg** and *T. Springer*, Electronics Div., Los Alamos National Laboratory, Los Alamos, NM 87545

Nafion or other ion exchanging polymer films are active components in contemporary SPE fuel cells. Ion transport through these films is a complex function of molecular geometry that is altered by moisture content. Engineering analyses have shown that water drag is a key concern in cell operation. A series of experiments using Nafion and other membrane materials is described. Proton transport measured at SPE operating temperatures is monitored by concentration measurements. New techniques, using mass spectral measurements of hydrogen oxide/deuterium oxide ratios, give rapid assessment of the H^+/H_2O ratio during transport. These results are described with an ion-clustering model.

818 Electrochemical and Radiotracer Study of Iron Electrode in CO_2 Saturated Neutral Electrolytes: *A. Wieckowski** and *E. Ghali*, Faculté des Sciences et de Génie, Dépt. de Mines et Métallurgie, Université Laval, Québec, Qué., Canada G1K 7P4, and *M. Szklarczyk* and *J. Sobkowski*, Dept. of Chemistry Radiochemistry, Warsaw, Poland 02-089

Cyclic voltammetry of stable Fe and RDE-Fe electrodes was made in 0.25M NaCl electrolyte saturated with CO_2. The mechanism of reduction of carbonic acid under voltammetric conditions was established by taking into account the dissolution of $Fe(OH)_2$ from the electrode by H_2CO_3 and the increased reduction capability of "bare" Fe surface toward H_2CO_3 molecules ($E_rC'_i$ catalytic reaction). Adsorption of carbonic acid was detected by radiotracer method only when iron oxidation products were present on the surface. The role of the adsorption process in the accelerated dissolution of iron under mixed potential conditions is discussed.

819 Electrochemical Reduction of Ag_2CrO_4 in $LiClO_4$-PC Electrolyte: *J.-Q. Wang** (Present address: Dept. of Materials Science, Stanford University, Stanford, CA 94305) and *Y.-H. Sun*, Tianjin Institute of Power Sources, Tianjin 300381, China

Films of Ag_2CrO_4, Ag_2MoO_4, and Ag_2WO_4 were deposited from dispersions on Pt substrates. Voltammograms of the reaction of these materials with lithium in $LiClO_4$-PC have been measured and compared. Cathodic voltammograms of Ag_2CrO_4 films in the $LiClO_4$-PC electrolyte, as well as chemical analytical data of the discharge products in such Li-Ag_2CrO_4 cells, provide information about the reduction reactions in the positive electrode.

820 Effects of Chloride Ion Adsorption on Oxide Film Formation at Pt Electrodes as a Function of pH: *C. Vielma, B. Scharifker*, and *J. Mozota,** Dpto. de Química, Universidad Simón Bolivar, Sartenejas, Baruta, Apdo. 80659, Caracas, Venezuela

As the pH of the electrolyte increases, the potential of the oxide formation reaction is displaced towards more negative potentials (*i.e.*, 59 mV pH^{-1}), while the potential of zero charge of Pt remains fairly constant. Thus, the net effect is that at higher pH's, the electrode bears a negative charge making it more difficult for chloride, as well as for the electrolyte anions, to adsorb on the surface. This produces two effects: the onset of oxidation is displaced towards less positive potentials (*vs.* RHE in the same solution) on account of diminished anion adsorption, and the Cl^- concentration needed to start blocking the oxide deposition is increased for the same reason. Both effects, together with changes in the oxide reduction behavior, are reported and quantitatively analyzed.

821 Behavior of Superacid Electrolytes in Fuel Cells: *R. Atanasoski** (Present address: Institute of Electrochemistry, POB 815, 11001 Beograd, Yugoslavia), *W. O'Grady*, and *H. Olender*, Brookhaven National Laboratory, Upton, NY 11973

The behavior of several superacids including TFMSA as electrolytes for hydrogen-oxygen fuel cell has been explored. The acids were obtained by conversion of their correspondent salts. Basic physicochemical and electrochemical properties of the acids have been determined. The cell performance as well as the individual reactions have been examined. The open-circuit potential and the polarization characteristics have been measured as a function of the acid concentration and temperature. The effect of the temperature change has been found to be extremely pronounced.

822 Effect of Rhodamine-B on Pb Electrodeposition on Ag and Cu: *J. C. Farmer** and *R. H. Muller*, Lawrence Berkeley Laboratory, Materials and Molecular Research Div., Berkeley, CA 94720

Rhodamine-B chloride (6 μM) has been used as a model substance of plating additives in a study of the electrodeposition of Pb

from 1M $NaClO_4$, 0.5 and 5 mM Pb^{++} (pH 3) on Ag and Cu. Ellipsometer measurements during cyclic voltammetry have shown that the dye prevents complete formation of the Pb underpotential deposit, and shifts the bulk deposition peak to more cathodic potentials during the first potential cycle, resulting in a more compact bulk deposit than obtained in the absence of the dye. Dye effects disappear after subsequent cycling, but reappear after relaxation periods at open circuit.

823 Nucleation of Pb Electrodeposits on Ag and Cu: *J. C. Farmer** and *R. H. Muller*, Lawrence Berkeley Laboratory, Materials and Molecular Research Div., Berkeley, CA 94720

Initial stages in the deposition of Pb from 1M $NaClO_4$, 0.5 and 5 mM Pb^{++}, pH 3, have been investigated by ellipsometry and light scattering during cyclic voltammetry. Optical constants, thickness, valence, and free energy of adsorption of the underpotential deposit have been determined. An optical model fitting experimental data for fractional coverage is presented, which implies island-like growth. The bulk deposit (less than 20Å thick) immediately following formation of the underpotential monolayer is of a particulate, porous nature.

824 Electrocrystallization of Zinc from Concentrated Zinc Solid Electrolytes: *J. McBreen** and *E. Gannon*, Brookhaven National Laboratory, Dept. of Energy and Environment, Upton, NY 11973

The electrocrystallization of zinc on glassy carbon from concentrated $ZnCl_2$ and $ZnBr_2$ electrolytes was studied using cyclic voltammetry, the potential step method, and scanning electron microscopy. In pure electrolytes the current transient from the potential step measurements can be interpreted in terms of instantaneous nucleation of three dimensional centers and growth under kinetic control. The kinetics are faster in $ZnBr_2$ than in $ZnCl_2$ electrolytes. Fluorinated surfactants and additions of Pb^{++} and Br^{+++} ions slow the reaction kinetics. (This work was performed under the auspices of the U.S. Department of Energy under Contract No. DE-AC02-76CH00016.)

825 Study of Model Zinc Electrode Pores in Alkaline Electrolyte: *J. H. Flatt*,* *F. R. McLarnon*, and *E. J. Cairns*, Lawrence Berkeley Laboratory, Energy and Environment Div., Berkeley, CA 94720

An electrochemical cell has been developed to study the behavior of a model zinc electrode pore in alkaline electrolyte. The cell design permits *in situ* microscopic observation of the electrode surface, and multiple zinc reference microelectrodes provide simultaneous measurements of local electrochemical potentials. Zinc electrode discharge phenomena have been studied at current densities typical of zinc/nickel oxide batteries for various pore diameters, electrode thicknesses, and electrode area/electrolyte volume ratios.

826 XPS and Electrochemical Characterization of Copper Electrodes in Aqueous Base: *W. Kautek* and *J. G. Gordon II*,* IBM Research Laboratory, San Jose, CA 95193

X-ray photoelectron spectroscopy and potentiodynamic experiments in 0.1M Na_2SO_4, 0.01M NaOH show that copper oxide grows in three stages. The first layer is Cu_2O, generated at −0.4V (*vs.*SCE) and is followed by the formation of $Cu(OH)_2$ at about +0.2V. A third, unidentified, species is generated at *ca.* +0.2V. The Cu_2O layer attains a thickness of about 20Å, and remains constant after $Cu(OH)_2$ formation begins. The XPS spectra are consistent with the formation of Cu_2O at potentials negative of −0.2V and $Cu(OH)_2$ at more positive potentials. We find no evidence for CuO.

827 Double-Layer Structure of Polycrystalline Electrodes: *D. Larkin*, Dept. of Chemistry, Towson State University, Towson, MD 21204

An understanding of electrocatalysis implies a knowledge of the detailed structure of the electrode/electrolyte interface. For polycrystalline metal electrodes, information on the double-layer structure is limited. Recent work using polycrystalline silver and lead electrodes is presented. The double-layer structure at a polycrystalline silver electrode is discussed in terms of the Gouy-Chapman-Stern model and the recent models proposed by Damaskin. The effect of electrode surface modification on the extent of simple anion adsorption and double-layer structure is also presented and discussed.

828 Heats of Dilution of Aqueous Zinc Bromide: *H. F. Gibbard*, Gould Research Center, Rolling Meadows, IL 60008

Heats of dilution of aqueous zinc bromide were measured in a titration calorimeter at 25°C, for molalities of 0.1-3.0 mol/kg. Partial molal enthalpies of the solute derived from these measurements were in good agreement with those calculated from the temperature dependence of the activity coefficient. The thermal properties exhibit abrupt changes in slope, when plotted against molality, in the vicinity of 0.5 mol/kg. This is attributed to the formation of Zn^{2+}/Br^- complex species. This work was carried out as part of an investigation of the physical chemistry of the zinc-bromine battery.

829 Bromine Complexing Agents for Energy Storage Applications: *H. F. Gibbard*, Gould Research Center, Rolling Meadows, IL 60008

Complexing agents for bromine were discovered that are soluble in aqueous solutions but form in the presence of bromine a water-immiscible, bromine-rich phase. These inexpensive quaternary ammonium compounds are stable for years in the environment of a Br^-/Br_2 electrode. Measurements are presented of the density, viscosity, aqueous phase/organic phase partition equilibrium, and electrical conductivity of several bromine complexes. Molecular factors which favor the formation of liquid, as opposed to solid or semi-solid bromine complexes, are described, and properties of the compounds relevant to their use in aqueous electrochemical energy storage devices are discussed.

830 Electrochemical Measurements on Metal Oxide Electrodes: *K. Kinoshita** and *M. Madou*, SRI International, Menlo Park, CA 94025

Electrochemical studies were conducted on metal oxide electrodes with the aim of developing pH monitors for high temperature/high pressure aqueous systems. The relationship between pH and the open-circuit potential (OCP) and flatband potential (V_{fb}) of oxides of Pt, Ir, Zr, and Ti were investigated. A linear relationship between pH and either OCP or V_{fb} was obtained, depending on the electronic conductivity of the metal oxide electrode.

831 Impedance Measurements on Single Crystal Nb-Doped TiO_2: *M. Madou*,* *K. Kinoshita*, and *M. C. H. McKubre*, SRI International, Menlo Park, CA 94025

Mott-Schottky plots were measured on single crystal Nb-doped TiO_2 in KCl electrolytes of concentration between 1 and 10^{-4}M. The flatband potential for Nb-doped TiO_2 was negative of that for hydrogen reduced TiO_2. This result is explained by a change in the point of zero charge to more acidic pH values when the TiO_2 electrode surface becomes enriched with Nb_2O_5. The effect of pH on the degree of frequency dispersion for the Mott-Schottky plots is discussed.

832 Calorimetric Investigations on the AgI-AgBr System: *A. Khandkar, V. B. Tare, A. Navrotsky*, and *J. B. Wagner, Jr.*, Center for Solid State Science, Arizona State University, Tempe, AZ 85287

The enthalpy, H_T-H_{298}, from 298 K to 518 K of melted and unmelted mixtures of AgI and AgBr of various compositions within the two-phase region of the phase diagram has been obtained using a Calvet type twin microcalorimeter as a transposed-temperature drop calorimeter. Enthalpies of solution in $AgNO_3$ at 518 K of different AgI-AgBr compositions have also been measured. The effect of AgBr on the temperature and enthalpy of transformation of β-AgI to αAgI has been investigated using a Perkin Elmer differential scanning calorimeter. Striking similarity between the anomalous electrical conductivity in the two phase region (1) and the variation in (H_T-H_{298}) has been pointed out. The results are discussed with particular reference to the transport properties of these compositions. (This research was supported by DOE contract DE-AC02-82ER12091, and by a grant from the Center of Solid State Science.)

1. K. Shahi and J. B. Wagner, Jr., *Appl. Phys. Lett.* **37** 757 (1980).

833 Electrical Conduction in the Two-Phase AgCl-Al_2O_3 System: *A. Khandkar* and *J. B. Wagner, Jr.*, Center for Solid State Science, Arizona State University, Tempe, AZ 85287

Electrical conductivity of the two-phase AgCl-Al_2O_3 system has been investigated. The conductivity increases by a factor of 4 at 15 m/o Al_2O_3 for fused composites, and a factor of 29 at 10 m/o Al_2O_3 for precipitated composites. Particle sizes of the matrix and dispersoid play a role in conductivity enhancement. Composite morphology studied by SEM has been correlated to conductivity enhancement. The results indicate that conductivity is dependent on interfacial area. Both increased defect concentrations and increased mobilities at the interface are suggested to play significant roles in the enhancement. An empirical relationship is proposed to explain the observed behavior. [This research was supported by a grant from NASA (Nas 8-32937), and the Center for Solid State Science, ASU.]

834 Enhanced Modes of Electroanalysis for Hydrodynamically Modulated Rotating Disk Electrodes: *B. Miller** and *J. M. Rosamilia*, Bell Laboratories, Murray Hill, NJ 07974

The hydrodynamically modulated rotating disk electrode (HMRDE) with superimposed sinusoidal speed programming has many applications to the study of electrode kinetics, photoelectrochemistry, and electroanalysis. Instrumental and data analysis improvements allowing fuller exploitation of modulation amplitude increase of sensitivity, automatic amplitude scanning, and a new derivative mode have particularly extended the electroanalytical capabilities. A number of illustrative experimental examples with platinum, gold, and mercury-filmed rotating disk electrodes are given.

835 Inelastic Neutron Scattering of Lead Dioxides: *R. Varma*,* Argonne National Laboratory, Argonne, IL 60439, *J. Eckert, J. A. Goldstone*, and *A. D. Taylor*, Los Alamos National Laboratory, Los Alamos, NM 87545, and *J. Jorgensen*, Argonne National Laboratory, Argonne, IL 60439

Vibrational spectra of chemically prepared and heated sample of β-PbO_2, as well as those obtained from lead-acid plates cycled in H_2SO_4 and plates "formed" exclusively in H_2O + H_2SO_4 and D_2O + D_2SO_4 environments, obtained by inelastic neutron scattering measurements at LANL, have been qualitatively analyzed. The chemical sample gave strong vibrational bands at 560, 490, 1050, and 785 cm^{-1}, the first two perhaps assignable to symmetric and asymmet-

ric stretches, and the third to a combination thereof. The 785 cm^{-1} band may possibly arise from the Pb—O group deformation, and as expected was found to be sensitive to lattice-protons as observed in a slight downward frequency shift and line broadening from loose complexation with protons. It appears that free (from bands near 1700 cm^{-1}) as well as bound (from weak modes in 600-300 cm^{-1} region) water molecules may also be associated with the dioxide battery materials.

836 The Preparation and Behavior of Activated Tantalum Anodes: *Ch. Comninellis** and *E. Plattner*, Institut de Génie chimique, Ecole Polytechnique Fédérale de Lausanne, CH 1015 Lausanne, Switzerland

During the last years there have been many studies of the electrochemical properties of titanium anodes coated with a conductive layer (Pt, RuO_2-TiO_2, PbO_2). The region of application of these anodes depends on the stability of coating and of titanium base metal which, if corroded, can contribute to loss of adhesion by undermining. In general terms the higher the acidity of the medium the greater the residual dissolution of titanium and the more likely any coating is to become undermined. The activated tantalum (A.T) anodes have been prepared by deposition of PtO_x and Ta_2O_5 on tantalum (which is very stable in acidic medium). The behavior of the (A.T) anodes depends on the PtO_x content in the film, above 50 m/o PtO_x the film shows metallic conduction and below 50 m/o PtO_x dielectric conduction. The electrode has been used in the electrochemical oxidation of $MnSO_4$ to $Mn_2(SO_4)_3$.

837 Heterogeneous Electrocatalysis of the Acidic Coal Slurries: *S. B. Lalvani** and *R. W. Coughlin*, Dept. of Thermal and Environmental Engineering, Southern Illinois University at Carbondale, Carbondale, IL 62901

Expressions for limiting currents are obtained to describe the heterogeneous electrocatalysis of a suspended solid particle in a stirred liquid. The electrochemical reaction involves oxidation of a dissolved cation (electrocatalyst) in the electrolyte. The solid particle is then oxidized by this cation via an irreversible pseudo first order chemical reaction. This model is applied to bulk electrolysis of the acidic coal slurries in presence of Fe(II), and the observed limiting currents permit evaluation of the chemical rate constant of coal oxidation.

838 On the Mechanism of Laser-Enhanced Copper Deposition: *U. Stimming,* G. Arbach*, and *P. Bindra*, IBM T. J. Watson Research Center, Yorktown Heights, NY 10598

Laser illumination enhances the rate of copper deposition on copper in the kinetically as well as in the mass transfer controlled part of the current. In order to investigate the mechanism the following measurements were carried out in $10^{-2}M$ $CuSO_4$/1M H_2SO_4 using the rotating disk electrode: current potential curves under laser illumination as a function of wavelength and laser power; measurement of the rest potential under laser illumination; temperature dependence of the kinetic and the diffusion limited current. The results are discussed to distinguish in particular between thermal and excitation effects of the laser illumination on the deposition reaction.

839 The Effect of Neutral Surface Active Additives on the Kinetics of the Cu(II)/Cu Electrode: *D. Light, D. Rath*, and *P. Bindra,** IBM T. J. Watson Research Center, Yorktown Heights, NY 10598

The rotating disk electrode method and the galvanostatic pulse method have been used to study the inhibitory effect of neutral organic additives on the kinetics of Cu(II) discharge on mercury, copper amalgam, and copper metal. The adsorption characteristics of the organic additives and the double layer parameters for quantitative interpretation of the rate constants were determined by differential capacitance measurements. The results are explained in terms of the modern theories of charge transfer.

840 The Direct Measurement of Anionic Adsorption at Pt Electrodes by a High-Sensitivity Computer-Operated Automatic Ellipsometer: *S. Gottesfeld* (Permanent address: Dept. of Chemistry, University of Tel-Aviv, Tel-Aviv, Israel), *P. J. Hyde, C. J. Maggiore*, and *S. Srinivasan*, Los Alamos National Laboratory, Los Alamos, NM 87545

The effects of anionic adsorption on electrocatalystic processes at Pt electrodes is of major interest. The small ellipsometric effects monitored for anionic adsorption resulted in the past in limited information of approximate nature. We describe the development of an automatic photoelastic-modulated ellipsometer, operated by a minicomputer which allows effective signal averaging. Direct highly reproducible and reliable measurements of Δ and Ψ transients, with a sensitivity of 10^{-4} deg and total amplitudes of $< 10^{-2}$ deg were performed. Monitoring of time resolved anionic coverage variations within the Pt-H region, of charge-transfer during adsorption and of optical effects due to H_2O and OH adsorption are demonstrated.

841 Combined Ellipsometric and A-C Impedance Measurements of Porous Ruthenium Oxide Films: *J. Rishpon, I. Reshef*, and *S. Gottesfeld*, Dept. of Chemistry, University of Tel Aviv, Tel Aviv, Israel

The nature of transition metal oxide-electrolyte interfaces is of interest in the field of electrocatalysis and electrochromism. We describe a detailed study of surface reactions and transport processes in porous ruthenium oxide films. Optical *in situ* measurements were employed to evaluate film thickness and water content, while a-c impedance measurements in solutions of different *p*H levels and anionic composition yielded results on the rate-limiting steps in oxide-electrolyte interfacial processes. A single microprocessor was employed for both automatic (rotating-analyzer) ellipsometry and or automatic network analysis in a wide frequency range. The instrumental setup is described.

842 Electrode Kinetics in Nonaqueous Solvents: *J. Jorne*, Dept. of Chemical Engineering, University of Rochester, Rochester, NY 14627, and *P. G. Pai*, Dept. of Chemical Engineering, Wayne State University, Detroit, MI 48202

A comparative study of the electrode kinetics of Na^+ reduction was conducted in four aprotic solvents: propylene carbonate (PC), dimethylformamide (DMF), dimethylsulfoxide (DMSO), and acetonitrile (AN), using dropping mercury electrode and the Faradaic impedance method. The true kinetic rate constants measured for 1M $NaClO_4$ in PC, DMF, DMSO, and AN are 0.38, 0.21, 0.05, and 0.35 cm sec^{-1}, respectively. A standard potential for Na^+/Na is established in four solvents, and the surface potentials of all four solvents are calculated to be positive. Comparison of kinetic rate constants and free energies of Na^+ solvation indicates that the trend of standard rate constants follows the trend of free energies of Na^+ ion solvation, in aprotic nonaqueous solvents: PC $\cong$ AN $<$ DMF $<$ DMSO.

843 The Reduction of Ni(II) on Hg in Uncomplexating Acetonitrile Solutions: *L. A. Avaca, E. R. Gonzalez,** and *G. Tremiliosi-Filho*, Instituto de Física e Química de São Carlos, 13.560 São Carlos, SP, Brazil

The reduction of uncomplexed Ni(II) in acetonitrile solutions appears as a straightforward process in the presence of sodium perchlorate as the supporting electrolyte. Thus, a single irreversible wave with diffusion control limiting current is observed. However, by changing the electrolyte to tetraalkylammonium salts the $E_{1/2}$ is shifted considerably in the cathodic direction. The phenomenon was interpreted as a double layer effect that influences the characteristics of the electron transfer process. The effect of trace quantities of bromide ions on the reduction process was also investigated. The results were interpreted in terms of a surface complexation between Ni(II) and absorbed bromide ions. (This work was supported by CNPq, Brazil.)

844 The Electrochemical Behavior of Macrocyclic Complexes of Ni(II) in Acetonitrile Solutions: *L. A. Avaca, E. R. González,** and *G. Tremiliosi-Filho*, Instituto de Física e Química de São Carlos, 13.560 São Carlos, SP, Brazil

The behavior of four tetradentate macrocyclic amine complexes of Ni(II) was studied by cyclic voltammetry in 0.1M TBAP/acetonitrile solutions on Hg, Pt, and vitreous carbon electrodes. The ligands consisted of two dienic and two tetraenic isomers (*cis* and *trans*). In all cases the reduction showed an initial le reversible wave followed by an irreversible process in which Ni is deposited. The tetraenic complexes are reduced at lower potentials, while no differences are observed for the *cis-trans* isomers. The anodic oxidation of the compounds was examined on vitreous carbon and showed a single le quasi-reversible wave. Rate constants were estimated by cyclic voltammetric analysis. (This work was supported by CNPq, Brazil.)

845 Scanning and Transmission Microscopy Studies of Hyper-Extended Oxide Films at Ir and Ru: *V. Birss, R. Myers, H. Angerstein-Kozlowska*, and *B. E. Conway,** Dept. of Chemistry, University of Ottawa, Ottawa, Ont., Canada K1N 9B4

The state of oxide films formed anodically on noble metals is of interest in electrocatalysis of anodic Cl_2 and O_2 evolution. At oxidized Ir, anodic Cl_2 evolution currents, at a given potential, progressively increase with increasing film thickness while at Ru this effect is much smaller. Elucidation of this behavior is made by comparing the morphologies of thermally and electrochemically formed oxide films on these metals by means of electron microscopy up to high levels of magnification. At Ir, a hyperextended oxide film seems to be formed which accounts for the apparent increase of electrocatalytic effectiveness of oxidized Ir electrodes for Cl_2 evolution with oxide film thickness.

846 The Potential of Zero Charge of Oriented Single Crystal RuO_2 in Aqueous Electrolytes: *M. Tomkiewicz,* Y. S. Huang*, and *F. H. Pollak*, Dept. of Physics, Brooklyn College of the City of New York, Brooklyn, NY 11210

The impedance of 5 virgin faces of single crystal RuO_2 was measured over the frequency range of 1-10^6 Hz, in three electrolytes—10^{-3}M and 1M Na_2SO_4, and 10^{-3}M KF. The fastest relaxing capacitive element was identified, and its values measured as a function of the electrode potential. A major contribution to this capacitance is due to the double layer capacitance. The potential of zero charge in 10^{-3}M Na_2SO_4 was measured for the five crystalline faces. The variations of the potential of zero charge with the crystalline faces are small. "Average" value is ($-$ 0.09 $\pm$ 0.1) V *vs.* SCE. The potential of zero charge correlates well with the reported work functions of RuO_2 and Ru metal.

847 Fuel Cell Performance under Extreme Operating Conditions: *L. S. Joyce,* A. A. Adams, A. J. Coleman,* and *J. A. Joebstl,* US Army Mobility Equipment R and D Command, Electrochemical Div. (DRDME-EC), Fort Belvoir, VA 22060

Subscale phosphoric acid fuel cells using commercial and experimental C-supported Pt electrodes are subjected to operating conditions which simulate fuel cell use for small mobile power unit applications. Tests include duty cycling in temperatures to −55°C employing a variety of shutdown and startup modes. Diagnostic measurements are routinely performed to evaluate fuel cell and individual component performance over the lifetime of the cell. Experiments since our last report examine in more detail the critical role of electrolyte concentration and volume during periods of shutdown. Characterization of catalyst surfaces on new and used electrodes provides information on alterations in electrode structure over the course of testing.

848 Composite Electrocatalysts for Carbon Monoxide Resistant Fuel Cell Anodes: *A. J. Coleman, A. A. Adams, J. A. Joebstl,* and *L. S. Joyce,* US Army Mobility Equipment R and D Command, Electrochemical Div. (DRDME-EC), Fort Belvoir, VA 22060

In fuel cells utilizing methanol reformate as a fuel, carbon monoxide resistant electrocatalysts are preferred for the anode to facilitate low temperature startup. Two systems, an alloy (Pt-50% Ru) and platinum on an active support (WC), were evaluated for this role in both half-cell and subscale single cell experiments. The anode polarizations associated with hydrogen-carbon monoxide mixtures, at temperatures below 120°C, indicated that both systems have promise as anode electrocatalysts. The observed improved performance of the platinum-ruthenium alloy over platinum is attributed to reduced carbon monoxide adsorption on the alloy. The low temperature activity of platinum dispersed on tungsten carbide is due to the nonadsorption of carbon monoxide on the support. This allows the WC to function as the electrocatalyst at low temperatures, and the platinum to become active as the temperature is increased.

849 Electrosorption Characteristics of Thin Layers of Gold Deposited on Palladium Substrate: *M. E. Gamboa* and *J. Genescá,** Dpto. Fisicoquimica, D.E.Pg. Fac. Química, UNAM, Ciudad Universitaria, 04510 Mexico D.F.

The oxygen electrosorption properties of Pd-Au alloys were found to change on continuous potential cycling, owing to the preferential dissolution of Pd from the surface. There is evidence that Au can be concentrated at the surface. In consequence, the surface zone involved in chemisorption and catalysis reactions consists of a few atomic layers richer in Au than the bulk. In this work the electrosorption characteristics of thin layers of vacuum deposited gold on palladium has been studied by linear sweep voltammetry, SEM-EDAX, and AES in order to compare with Pd-Au alloy. A comparison of catalytic activities for oxygen evolution in the Pd-Au system studied, Pd-Au alloy, and the pure metals in 1M H_2SO_4 at 25°C, has demonstrated that the rate of oxygen is faster than that of pure metals and Pd-Au alloy.

850 Lateral Interactions of Adsorbed Species on Single Crystal Metal-Oxide Electrodes: *T. Hepel,* Dept. of Physics, Brooklyn College of the City University of New York, Brooklyn, NY 11210

Theory of lateral interactions between electroactive species adsorbed on two energetically different sites S^1 and S^2 on the electrode surface has been developed for the case of single crystal oxide electrodes with semi-metallic conductivity type. Strong influence of interactions between adsorbates A^1 and A^2 has been found. The effect of different parameters on simulated LSV characteristics is presented and discussed in detail. The dependences of the peak currents and peak potentials upon the interaction parameters g_{11}, g_{12}, and g_{22}, as well as the concentrations C_1 and C_2 of electroactive species in solution and the energy of perpendicular bonding of chemisorbed species, correspond to the significant changes in the respective adsorption isotherms for A^1 and A^2. All calculations have been performed for a reversible, "independent" adsorption of A^1 and A^2 without effect of slow redistribution of adsorbates between different active sites S^1 and S^2. (This work was supported by the United States Dept. of Energy under Contract DE-AC02-80ER10654.)

851 Kinetic Aspects of the New Adsorption Isotherm and the Approach to Dynamic Adsorption Equilibrium: *R. Heyrovská,* Na Slåhlavce 6, 160 00 Praha 6, Czechoslovakia

Adsorption is a process in which a certain fraction of the substrate-adsorbate encounters results in specific interaction (coordination) for a period longer than the 10^{-13} sec (approx) for elastic collisions. At any time t less than t_e more adsorptive contacts are made than broken until equilibrium is reached at time t_e when equal numbers are made and broken. The adsorption isotherm is derived from the kinetic aspects of the dynamic adsorption equilibrium established at constant area substrate and at dropping mercury surfaces.

852 Determination of the Substrate and Adsorbate Characteristics from the Hg/aq. Solution Interfacial Tensions; Applicability of the New Isotherm for $0 < \Theta < 1$: *R. Heyrovská,* Na Slåhlavce 6, 160 00 Praha 6, Czechoslovakia

A simple method of obtaining Θ, the surface coverage, from the interfacial tension *vs.* $m\phi$ plots without calculation of the "surface excess" has been outlined, where m is the molality and ϕ is the molal osmotic coefficient. From the $\Theta/m\phi$ *vs.* $1\text{-}\Theta$ and the adsorption coefficient *vs.* Θ dependences, the determination of the adsorbate concentration for monolayer coverage as well as of the other adsorption parameters in the new adsorption isotherm has been demonstrated.

INDEX TO AUTHORS

Abstract No.

Abbey, K. M. 572
Abe, H. 150, 200
Abe, K. 18, 553
Abe, T. 611
Adams, A. A. 847, 848
Adams, C. A. 345
Adams, W. A. 809
Aerora, A. 75
Aharon-Shalom, E. 505
Ahearn, J. S. 249
Ahlgren, W. L. 358
Ahmed, S. M. 522
Ajima, T. 377
Akai, S. 324
Akylas, V. 258
Alam, M. K. 212
Albers, J. 401
Albery, W. J. 724
Aldissi, M. 557
Alexander, M. N. 609
Alexander, P. 219, 529
Alexander, S. 530
Alkire, R. 59, 582
Allen, P. M. 656
Allen, R. M. 473
Allison, D. A. 314
Amick, J. A. 208, 210
Amouroux, J. 135, 534
Anderson, L. B. 541, 692
Anderson, R. N. 417
Andrews, J. 271
Andricacos, P. E. 803
Ang, P. G. P. 525, 526
Angerstein-Kozlowski, H. 845
Anson, F. C. 623, 716
Antoniadis, D. A. 284
Arbach, G. 838
Archer, W. I. 691
Arena, C. 389
Arienzo, M. 392
Armand, M. 494
Armstrong, F. A. 633
Armstrong, N. R. 528
Armstrong, N. R. 523
Arnaud, F. 389
Arst, M. C. 310
Ashok, S. 175
Aspandiar, R. F. 500
Assailly, J. 671
Assur, I. 105
Atanasoski, R. 821
Atwater, H. A. 331
Auborn, J. J. 591, 808
Aucoin, R. L. 124
Avaca, L. A. 639, 843, 844
Avitaya, D. 389
Azuma, M. 518

Bacarella, A. L. 62
Bachmann, K. J. 333
Badcock, C. C. 15
Baerg, W. 138
Baghdadi, A. 297
Bailey, R. A. 790
Bailey, W. E. 287
Baizer, M. M. 638
Baker, R. L. 455
Baliga, B. J. 110
Balooch, M. 443
Bandy, R. 78
Baranowski, Jr., T. J. 664
Baranski, A. S. 540
Barclay, D. J. 598
Bargon, J. 651, 546
Barna, G. G. 23
Barnes, J. A. 2
Barraclough, K. G. 305
Bartak, D. E. 655
Basseches, H. 92
Bassett, C. A. L. 678
Bates, J. B. 498, 499
Bath, H. M. 437
Battles, J. E. 85
Bauer, S. H. 440
Baughman, R. H. 558
Baum, B. 228
Bauser, E. 330
Bean, K. E. 287
Beckerdite, J. S. 560
Bedair, S. M. 333
Beer, H. B. 579
Behl, W. K. 810
Behrens, R. G. 442
Beinvogl, W. 197
Belanger, A. 494
Belka, A. 178
Bell, M. I. 299
Bellows, R. 25, 482
Beni, G. 593
Benner, R. E. 460
Bennett, M. 531
Bennett, R. S. 174
Bennion, D. N. 570
Berchielli, A. S. 38
Bergougnan, M. P. 135, 534

Abstract No.

Berk, L. 77
Berkenblit, M. 139
Berkowitz, H. L. 401
Berlouis, L. 620
Bernacki, S. E. 167
Berry, W. 105
Besomi, P. 332
Bewick, A. 709
Bhakta, S. D. 570
Bhalla, P. 251, 252, 253
Bhattacharya, P. K. 360
Bianco, P. 632
Bibyk, S. B. 120
Biefeld, R. M. 343
Binder, M. 51
Bindra, P. 737, 838, 839
Bingle, W. D. 185
Bird, C. L. 598
Birss, V. I. 731, 845
Bis, R. F. 2
Bisaro, R. 226
Bisio, G. M. 282
Black, J. 664
Blander, M. 739
Blank, M. 621
Blech, I. A. 428
Bleil, C. E. 398
Blue, J. L. 411
Blumenstock, K. 123
Bockris, J. O'M. 58, 696
Bolster, D. E. 491
Bomchil, G. 389
Bonanno, G. 673
Bondur, J. 319
Bonino, F. 12
Bonnell, D. W. 476
Bonnell, D. W. 439
Bonner, W. A. 322, 337
Boothroyd, A. R. 96
Borgens, R. B. 668
Borland, J. O. 274
Bourelier, F. 71
Bowden, W. 11
Bowling, R. A. 91, 287
Boyer, P. K. 111
Boynton, A. L. 675
Brady, M. E. 221
Braue, Jr., E. H. 759
Braunstein, J. 768
Brighton, C. T. 664
Brinck, K. 733
Brittain, R. D. 438, 453
Britton, D. L. 572
Bro, P. 1
Brockman, T. J. 692
Brodersen, R. W. 394
Bronner, W. E. 619
Brophy, J. J. 617
Brotz, D. K. 255
Brown, D. M. 364
Brown, G. M. 60
Bruckenstein, S. 708
Brummer, S. B. 425
Bube, R. H. 230
Buchanan III, A. C. 748, 756, 757
Buck, R. P. 619
Budniek, J. I. 728
Buehler, M. G. 257
Bui, N. 84
Bullis, W. M. 298
Bulpett, S. E. 612
Bump, D. 31, 33
Bunnett, J. F. 29, 30, 646
Burger, D. R. 224
Burgmayer, P. 622
Burke, R. L. 179
Burny, F. 687
Burrow, R. G. 559
Burton, S. 105
Bush, D. M. 17
Butler, M. A. 723
Butler, P. C. 24
Buttry, D. A. 623
Byrne, P. F. 318

Cabral, S. M. 153, 172
Cadger, T. 751, 811
Cahan, B. D. 76
Cairns, E. J. 761, 825
Calder, I. D. 96
Calligarich, C. 218
Calvo, E. J. 724
Campbell, P. M. 110, 347
Campbell, R. B. 529
Canfield, D. 517
Cangellari, A. 582
Cantos, B. D. 146
Cantrell, J. S. 514
Caprani, A. 688
Carbone, S. 402
Carle, P. 681
Carling, R. W. 473
Carlson, T. L. 259
Carr, D. S. 228
Carruthers, J. R. 304

Abstract No.

Carter, C. B. 336
Carter, M. 781
Casey, E. J. 751
Casey, J. L. 635
Casey, S. M. 499
Cerf, G. 690
Chambers, J. E. 259
Champagne, M. 596
Chandran, R. R. 562
Chang, C. K. 804
Chang, G. 363
Chang, H. H. 536, 730
Chang, H. R. 294
Chang, P. C. 164
Chang, S. 629
Chang, S. C. 446
Chapman, D. M. 754, 757
Chappell, T. I. 174
Chatham, J. 620
Chaudhari, P. K. 373
Cheek, G. T. 752
Chemilli, C. 218
Chen, C.-C. 509
Chen, D. M. 99, 143
Chen, M. M. 187
Chen, W. J. 233
Chenevier, P. 283
Cheng, C. Y. 657
Cheng, D. 275
Cheung, K. Y. 3
Cheung, N. W. 318, 386
Chiabrera, A. 673, 681
Chin, D-T. 70, 536, 562, 657, 730
Chin, T. N. 342
Chiu, K. C. R. 193, 195
Chiu, T. Y. 129
Chlem, Jr., P. L. 399
Chlipala, J. D. 267
Chopra, K. L. 229
Chou, N. J. 247
Chow, L. 11
Chow, T. P. 86, 175, 202
Christianson, K. A. 239
Chu, S. N. G. 346
Chu, S. S. 233, 238
Chu, T. L. 232, 233, 238
Chum, H. L. 510
Ciemiecki, K. T. 808
Cipris, D. 35
Claassen, W. A. P. 134
Clark, K. P. D. 792
Clarke, R. L. 587
Class, W. 158
Clouser, S. 801
Cobianu, C. 427
Cocivera, M. 521
Cohen, S. A. 391
Cole, D. L. 266
Coleman, A. J. 847, 848
Coleman, B. R. 652
Coleman, E. 419
Colgan, E. 436
Collins, G. J. 111
Collopy, T. 263
Comninellis, Ch. 836
Comrie, C. 388
Contractor, A. Q. 590
Conway, B. E. 575, 695, 845
Cooper, G. 508
Coopmans, F. 147
Corbett, R. E. 14
Corboy, J. F. 93
Cornog, D. G. 236
Corvol, M. T. 671
Coughlin, R. W. 837
Covington, M. A. 455
Covitch, M. J. 565
Cowan, M. 263
Crabbe, E. 163
Crafts, C. C. 26
Cratty, L. 488
Craven, R. A. 290, 308
Crawford, J. A. 246
Crosbie, G. M. 766
Crowell, T. I. 759
Cserhati, A. 383
Cubicciotti, D. 471
Culik, J. S. 219
Cullen, G. W. 302
Cunningham, D. 627
Current, S. P. 543

D'Altroy, F. A. 92
D'Angelo, J. C. 7
d'Heurle, F. M. 391
Dabos, F. 84
Dale, J. M. 62
Dalle Ave, J. 154
Dallek, S. 20
Damjanovic, A. 731
Darby, R. 767
Daroux, M. 548
Daughton, W. J. 262
Dautigny, N. 671
Dautremont-Smith, W. C. 352

Abstract No.

Davari, B. 100
David, H. S. 261
Day, A. 165
de Groot, J. G. 310
De Pasquale, S. 282
Deal, D. B. 146
Deal, M. D. 445
DeBerry, D. W. 594
DeBold, F. C. 2
DeCastro, E. S. 625
Declerck, G. 147
Dedman, J. R. 676
Degani, J. 332
DeHaan, A. 31
DeHaan, A. 33
Delgado, J. J. 262
Delmas, C. 485
Delnick, F. M. 813
Dempsey, M. D. 569
Demuth, D. 11
Desimoni, E. 772
Desjardins, C. D. 751, 811
Dessouky, A. El 375
Dhar, H. P. 535
Diaz, A. F. 546, 650
DiBari, G. A. 581
Dieleman, J. 191
Dierickx, M. 687
Dierker, L. A. 809
Dietl, J. 207
Dismukes, J. P. 208, 209, 210
Dobkin, D. M. 146
Dobos, C. J. 480
Dockerty, R. C. 370
Doddapaneni, N. 813, 814
Dodson, W. H. 117
Doench, J. P. 750
Domenicucci, A. C. 315
Dong, D. W. 247
Downey, D. F. 194
Drennan, J. 724
Duan, S. 788
Dubin, R. R. 82
DuBois, D. L. 520
Dubois, J. C. 596
Dudley, P. 788
Dudney, N. J. 499
Duffy, M. T. 165
Dumas, K. A. 217
Dunn, B. 487, 488
Dunnwald, D. 511
Dupon, R. 490
Dupuis, R. D. 338
Dutta, S. 94
Dworkin, A. S. 748, 756, 757
Dybwad, G. L. 199
Dyson, W. 272

Eckert, J. 835
Economou, N. P. 153
Eglash, S. 348
Ehrenreich, H. 205
Einstein, H. 25, 482
Eisenberg, M. 44, 429
Ejima, T. 749
El Safty, M. 84
Eldridge, J. 55, 548
Elie, G. T. 370
Elsayed, K. R. 132
Emmi, F. 185
Emons, H. H. 775, 776
Engel, P. 138
Engelbrecht, J. A. A. 217
Epel, D. 667
Ephrath, L. 174
Epstein, J. 9
Eriksen, J. 644
Ernst, D. W. 43
Erstfeld, T. E. 344
Evans, D. R. 148

Fan, J. C. C. 231
Fang, Y. 636
Farmer, J. C. 822, 823
Farrington, G. C. 487, 488, 633
Fathimulla, A. 432
Faulkner, L. R. 718
Fawcett, W. R. 531, 704
Fedoroff, M. 71
Fedors, R. F. 13
Feenstra, R. M. 291
Fehrs, D. L. 376
Feldberg, S. W. 556
Feldman, L. C. 352
Fendler, J. H. 618
Feola, J. M. 680
Fernandez, H. 781
Ferrando, W. A. 39
Fiegl, G. 293
Fielder, W. L. 467
Findl, E. 537
Fine, D. A. 653
Finollo, R. 681
Firor, K. 234
Fish, T. 390
Fitzgerald, D. J. 221
Flagan, R. C. 212
Flament, T. 796
Flamm, D. L. 350
Flatt, J. H. 825

Abstract No.

Fletcher, A. N. 797
Foller, P. C. 578, 587
Forbes, L. 273, 277
Ford, W. E. 636
Forland, T. 740
Forman, R. A. 299
Fornarini, L. 527
Fougere, P. G. 14
Fouletier, J. 497
Fouts, S. 168
Fox, M. A. 509
Francis, R. W. 208, 209, 215, 216
Francis, T. 251, 252, 253
Frank, A. J. 529
Frank, S. N. 23
Frase, K. 631
Frayret, J. P. 805
Freeston, N. 19
Freitag, W. 263
Fritz, I. J. 343
Fujimoto, F. 222
Fujita, K. 324
Fujita, S. 122
Fukuda, T. 326
Fung, C. D. 112, 132
Furukawa, K. 741
Furumura, Y. 130, 131
Fuyama, M. 431

Gadomski, S. G. 793
Gallagher, B. 223
Gallagher, B. D. 227
Gallagher, P. K. 591
Gamboa, M. E. 849
Gannon, E. 824
Garcia III, A. 227
Gargini, P. A. 138
Gary, K. 662
Gasnarini, M. 218
Gatos, H. C 325, 382
Gaur, S. P. 378
Gay, C. F. 206
Gay, E. C. 47
Gazard, M. 596
Geller, S. 679
Genesca, J. 849
Gerdes, H. 548
Gesenhues, U. 744
Ghali, E. 64, 818
Ghez, R. 327
Ghoneim, M. 801
Ghosal, B. 487, 488
Ghosh, A. K. 216
Gibbard, H. F. 828, 829
Gicquel, A. 135
Gill, M. 178
Gillies, R. J. 663
Gilman, S. 51
Ginley, D. S. 551, 532, 552, 723
Ginsburg, R. 250
Girault, H. H. J. 620
Giridhar, R. V. 125
Gissler, W. 726
Glass, R. S. 57, 61, 652
Glew, R. W. 341
Goddard III, W. A. 697
Godshall, N. A. 49, 449
Goetz, G. 383
Goldberg, R. 632
Goldberg, G. M. 170
Goldsmith, B. 312, 313
Goldstone, J. A. 835
Gonzales, E. M. 48
Gonzalez, E. R. 639, 843, 844
Gonzalez-Sanabria, O. 572
Goodin, R. D. 641
Goodman, R. 678
Goodwin, M. L. 578
Gordon II, J. G. 826
Gosele, U. 281
Goto, F. 553
Gottesfeld, S. 840, 841
Gourley, P. L. 343
Graglia, P. G. 282
Granda, J. 402
Granteer, D. 88
Grattarola, M. 673, 681
Greegor, R. B. 714
Green, B. J. 612
Griep, S. M. 487
Griffin, D. 251, 252, 253
Griffith, J. R. 244
Griffiths, T. R. 780
Grimes, P. 25, 42
Grinolds, H. R. 127
Griswold, T. W. 257
Grodzinsky, A. J. 682
Gronet, C. M. 524, 722
Gross, S. 4
Gruss, L. 83
Guegan, G. 115
Gunkel, C. 137
Gupta, R. K. 235
Guruswamy, V. 256, 530, 689, 693
Gyulai, J. 436

Haak, R. 353, 354
Haaland, D. M. 532
Haberman, J. I. 216
Habib, M. A. 616

Abstract No.

Habraken, F. H. P. M. 13
Haering, R. R. 53
Hagans, P. L. 7
Hagenmuller, P. 48
Hagmann, D. 31
Hahn, S. 275, 27
Haladjian, J. 63
Hall, D. E. 585, 58
Hall, J. C. .....
Hall, N. H. .....
Hall, R. B. 23
Hallen, R. T. 79
Hamakawa, Y. 20
Hamelin, A. 71
Hammano, K. 42
Hanazono, M. 43
Hannan, H. D. 81
Harazono, M. 13
Harbeke, G. 41
Harris, L. A. 47
Hart, R. G. 6
Hart, D. L. 3
Hartsough, N. 16
Hasan, T. 25
Hasegawa, H. 9
Hashimoto, K. 36
Hastie, J. W. 439, 47
Hatanaka, M. 15
Hatfield, W. E. 49
Hauenstein, R. J. 29
Hawley, M. D. 65
Hayafuji, Y. 37
Hayes, T. G. 76
Heald, S. M. 72
Heatherly, D. E. 76
Heatherly, L. 76
Heideman, J. E. 26
Heimann, P. A. 16
Heineman, W. R. 62
Heitbaum, J. 73
Heller, A. 506, 50
Hellstrom, E. E. 50
Hellwig, L. 27
Helm, G. 68
Henderson, A. S. 67
Henson, J. A. 26
Hepel, M. 2
Hepel, T. 725, 85
Herbranson, D. E. 65
Herndon, T. O. 17
Herrera, P. 73
Herrick, C. C. 442, 542, 57
Herzog, R. 75
Heslop, C. J. 17
Heyns, G. L. 114, 11
Heyrovska, R. 851, 85
Hezel, R. 12
Hildenbrand, D. L. 453, 43
Hill, D. E. 31
Hill, H. A. O. 63
Hill, V. L. 47
Hillery, P. S. 75
Hine, R. E. 17
Hinode, K. 43
Hinoul, M. 13
Hinsenkamp, M. 68
Hinson, D. 15
Hiratsuka, Y. 13
Hirosawa, K. 75
Hoare, J. P. 58
Hoeks, G. P. F. 60
Hoff, G. F. .....
Hofmann, H. 57
Hoffman, R. 54
Hoffman, R. W. 5
Hogan, S. J. 23
Hollandsworth, R. P. 4
Hollins, J. 19
Hollowell, K. 78
Holmes, C. F. 2
Holmes, R. H. 1
Honda, K. 51
Hong, Y. K. 56, 57, 61, 7
Hooper, A. 49
Horiike, Y. 43
Horlbeck, W. 77
Horton, W. S. 47
Horwath, R. S. 18
Horwitz, C. M. 17
Hsu, C. C. 33
Hsueh, K-L. 536, 73
Hu, C. 39
Hu, C. C. 37
Huang, Y. S. 84
Hubbard, A. T. 649, 70
Huggine, R. A. 449,500,550,551,597,745,763, 78
Hughes, R. C. 11
Hui, J. C.-H. 38
Hulett, Jr., L. D. 6
Humphreys, B. A. 47
Hunt, L. P. 208, 209, 210, 214, 21
Hunt, Jr., R. B. 60
Hussey, C. L. 75
Hwang, W. C. 1
Hyde, P. J. 84
Hyland, S. 21

Iizuka, T. 30
Ikeda, H. 3
Inman, D. 78

Abstract No.

Inoue, S. 130, 131
Ishii, M. 335
Itakura, H. 150, 200
Iwasita, I. 732
Iwata, S. 434
Iwata, Y. 222

Jacobson, N. 464
Jaeger, C. D. 7, 551
Jalan, V. 729
Jallerat, N. 71
Janata, J. 617
Janz, G. J. 765
Jarman, C. M. 387
Jastrzebski, L. 93, 302, 312, 313
Jensen, J. D. 2
Jensen, W. B. 747
Jodlauk, C. M. 346
Joebstl, J. A. 847, 848
Johns, R. 88
Johnson, J. G. 337
Johnson, K. E. 794
Johnson, W. B. 495
Johnston, Jr. W. D. 337, 346
Jones, D. B. 677
Jones, R. L. 466
Jones, R. V. 117
Joo, S.-K. 597
Jorgensen, J. 835
Joyce, L. S. 848
Jungling, T. L. 461

Kaempf, U. 265
Kaetzel, M. A. 676
Kage, M. 613
Kahn, A. H. 299
Kane, P. 9
Kaner, R. B. 550, 557
Kannon, V. C. 307
Kantner, E. 25, 482
Kanzaki, K. 409
Kao, D.-B. 363
Kapfer, B. 494
Kapoor, V. J. 108, 109, 120, 206, 235
Karagounis, V. A. 145
Kariv-Miller, E. 640
Kasley, K. 88
Kasley, K. L. 407
Kastening, B. 507
Kastl, R. H. 392
Kato, T. 222
Katz, W. 86
Katzir, A. 161
Kaun, T. D. 45, 783
Kautek, W. 826
Kawado, S. 374
Kawamoto, Y. 171
Kazerounian, R. 405
Keavney, C. J. 331
Keddam, M. 805
Keefe-Fraundorf, G. 308
Kelliher, E. M. 425
Kelner, G. 361
Kem, K. 568
Kendig, M. 74, 75
Kennedy, J. H. 501, 511
Khan, S. U. M. 696
Khandkar, A. 832
Kikuchi, M. 374
Kim, M. J. 364
Kim, S. H. 469
Kim, J. 247
Kim, Y. J. 79
Kindler, A. 583
King, K. 780
King, W. 468
Kinlen, P. J. 641
Kinoshita, K. 53, 734, 830, 831
Kirk, C. T. 124
Kito, N. 324
Kleine, L. P. 675
Kline, F. M. 10
Klinedinst, K. A. 52
Kliner, J. A. 724
Ko, W. H. 22, 112
Kobayashi, K. 423
Koch, C. C. 441
Koch, K. S. 660
Koh, W. 568
Kohl, F. J. 465, 476, 472
Kohler, H. 486
Kohli, R. 444, 538
Kolodner, P. 161
Kolodzey, S. 83
Komaki, K. 222
Komen, Y. 392
Kopanski, J. J. 132
Koppang, M. D. 655
Kordesch, M. 548
Kordesch, M. E. 55
Korzeniewski, C. 629
Koshino, Y. 377
Kosicki, B. B. 167
Kotera, Y. 613
Kowalchik, L. A. 2
Koyama, R. Y. 360
Krafcsik, I. 436
Krausbauer, L. 414
Krawiec, T. 319
Kressel, H. 321

Abstract No.

Krishnan, K. 296
Krogulec, T. 531
Kucera, G. H. 359
Kuhbander, R. J. 241, 242
Kulkarni, S. B. 295
Kung, C. Y. 273, 277
Kuppert, H. F. 414
Kurkov, V. P. 543, 544
Kurtz, S. R. 551, 552
Kuznetsov, A. M. 703
Kwan, S. H. 127
Kyte, J. 659

Laber, T. M. 750
Laes, E. 147
Lagowski, J. ..... 302, 325. 382.
Laguren, L. 627
Lajiness, E. J. 691
Lakhani, A. A. 432
Lalvani, S. B. 837
Lambrecht, V. G. 591
Lamoreaux, R. H. 448
Landeghem, W. Van 601
Landoch, W. J. 179
Langlais, R. 780
Laporte, Ph. 166
Larkin, D. 827
Larrabee, G. B. 91
Larrick, B. F. 20
Larsen, K. 208, 210
Larsen, E. M. 747
Lassagne, P. 166
Lau, C. K. 371
Lau, K. H. 438
Lauf, R. J. 474
Lavine, J. M. 170
Lavine, J. P. 387
Law, H. H. 577, 808
Lazzari, M. 12
Leahy, M. F. ..... y 152
Lechaton, J. S. 378
Lee, E. 258, 396
Lee, H. P. 66, 67
Lee, K. J. 656
Lee, M. K. 404
Lee, S. T. 387
Lee, W. W. 39
Lee, Y. H. 187
Leffert, H. L. 660
Leidner, C. R. 626, 717
Leigh, W. B. 239, 610
Leister, K. J. 661
Leung, D. 217
Levasseur, A. 485
Levisky, J. A. 753
Levy, D. J. 48
Levy, S. C. 5, 26
Levy, R. A. 419
Lewis, N. S. 524, 722
Li, J. 628
Liang, M. S. 394
Liang, W. W. 469, 480
Liao, J. L. 132
Lichtin, N. N. 516
Light, R. W. 169
Lin, I. 158
Lin, J. S. 477
Lindau, I. 348
Lindsay, W. S. 3
Ling, P. 286
Linkous, C. 528
Linkous, C. A. 523
Lis, S. A. 170
Lischner, D. J. 92
Littauer, E. L. 48
Little, R. D. 638
Liu, C. C. 145
Liu, C. T. 441
Liu, D. C. 109
Liu, H. Y. 804
Liu, T. M. 406
Loos, H. 114
Losee, D. L. 387
Love, R. P. 319
Lovering, D. G. 792
Lovgren, J. 14
Lowder, J. R. A. 484
Lowe, A. C. 598
Lowe, M. 263
Lowney, J. R. 301
Lu, C. Y. 404
Lu, L. S. 691
Lu, N. C. C. 404
Lu, W. J. 86
Luedecke, C. M. 450
Lund, H. 644
Lunnon, M. E. 314
Lyke, S. E. 795
Lytle, F. W. 714

Ma, W. 162
Maayer, P. De. 601
Maazaz, M. 485
MacDiarmid, A. G. 550, 557
Macdonald, D. D. 72
Maciejewski, M. L. 769
MacIver, B. A. 398
Mackor, A. 515
Mader, S. R. 315
Madix, R. J. 698

Abstract No.

Madou, M. 130, 131, 734, 830, 831
Madou, M. J. 53
Maeguchi, K. 412
Maes, H. E. 104, 106, 114, 118, 133
Magarino, J. 226
Magee, C. W. 362
Maggiore, C. J. 840
Magner, G. 812
Mahowald, P. 348
Majeed, A. 658
Makange, A. A. 740
Malachesky, P. 25, 482
Malinsky, J. D. 564
Malkin, I. 256
Mamantov, G. 743, 746, 754, 762
Mammone, R. J. 557
Mannoh, M. 335
Mansfeld, F. 74, 75
Mantei, T. D. 156
Mao, B.-Y. 382
Mar, R. W. 473
Marchant, S. H. 780
Marcus, R. A. 702
Margolese, D. I. 316
Marincic, N. 9
Mark, Jr., H. B. 627
Mark, J. E. 625
Mark, K. J. 477
Markert, M. J. 396
Maroni, V. A. 769
Marques, E. C. 714
Marshall, S. 695
Martin, C. R. 566
Martin, D. H. 598
Martino, F. J. 47
Mashiko, Y. 87
Masters, J. I. 170
Matlock, J. H. 270
Matsukawa, N. 365
Matsumoto, S. 285
Matsunaga, J. I. 365
Matsushita, Y. 309
Mattox, R. J. 159
Maxfield, M. 557
Maximovich, M. G. 243
May, P. 118
Mayaud, C. 662, 690
Mayer, J. W. 388, 436
Mayo, S. 299
McAleer, J. F. 624
McAllister, W. A. 608
McBreen, J. 824
McBride, B. J. 472
McCain, G. H. 565
McColl, J. R. 603
McDermott, P. P. 16
McDonald, R. N. 654
McEvoy, A. J. 726
McGarry, S. A. 268
McGill, T. C. 291, 292
McGinn, J. T. 93
McIntyre, J. D. E. 699
McKinney, B. L. 559
McKubre, M. C. H. 53, 734, 831
McLarnon, F. R. 632, 825
McLean, W. J. 483
McLeod, B. R. 686
McManis, G. E. 797
McMillan, R. S. 539
McMullin, P. G. 94
McNallan, M. J. 468, 469
McPherso, M. E. 259
McVittie, J. P. 363
Mead, D. G. 365, 403
Meakin, J. D. 236
Megerle, C. A. 237
Mehrotra, G. M. 452, 463
Meier, G. H. 459
Meier, D. L. 385, 395
Meissner, D. 507
Melroy, O. R. 619
Memming, R. 507
Menditto, P. 347
Menjo, A. 409
Mercure, K. 256
Merz, C. J. 303
Messina, R. 777
Metz, W. 111
Meyer, T. J. 705
Michel, A. E. 392
Mihara, M. 335
Miles, M. H. 653, 797
Miller, D. W. 17, 24
Miller, B. 834
Minhn, N. Q. 779
Mischel, M. 685
Misra, A. K. 465
Mitchell, R. E. 483
Mo, D. 348
Moens, L. 638
Mohmand, S. 651
Mohmand, S. 546
Mollenkopf, H. 400
Molnar, B. 361
Monet, J. D. 671
Monte, W. T. 638
Moody, J. 272
Mooney, J. B. 448
Morehead, F. 281
Morel, P. 805

Abstract No.

Morgro-Campero, A. 319
Morijiri, M. 431
Morimoto, H. 18, 553
Morita, H. 222
Morita, M. 758
Morrison, C. B. 333
Morrison, G. H. 361
Morrison, S. R. 512
Moslehi, M. 126
Motoo, S. 712
Mottot, Y. 791
Moulton, C. W. 816
Mountain, R. W. 172
Moustakas, T. D. 225
Mozota, J. 820
Muan, A. 475
Muettepties, E. L. 713
Muller, G. 323
Munir, Z. A. 457
Murarka, S. P. 429
Murphy, O. J. 58
Murray, C. 567
Murray, E. M. 276
Murray, R. W. 622, 626, 717
Myers, R. 845

Naem, A. A. 96
Nagaraj, B. A. 484
Naguib, H. M. 96
Nagy, T. E. 112
Nagy, Z. 787
Naiman, M. L. 124
Nakahara, M. 412
Nakamura, A. 452
Nakano, M. 97
Nakase, M. 365
Nanjundiah, C. 640
Naritsuka, S. 335
Natan, M. 248, 249
Navrotsky, A. 832
Nazri, Gh. 54, 76
Nelson, P. A. 47
Nelson, R. J. 332
Nelson, C. 29, 30
Neureuther, A. R. 192
Newby, K. 482
Newby, K. R. 25
Newman, M. R. 145
Newman, R. C. 65
Neyens, A. 601
Nguyen, V. S. 136
Nichols, D. N. 279
Niimi, T. 285
Niksa, S. 483
Nishine, S. 324
Nobe, K. 66, 67
Nolton, A. 31
Nomura, Y. 335
Norcott, M. H. 310
Norton, L. 679
Nowak, R. J. 547, 567
Nozawa, H. 365
Nozik, A. J. 508
Nugent, S. T. 638
Numasawa, Y. 423
Nuzzo, R. G. 419

O'Grady, W. 821
O'Grady, W. E. 725, 728
O'M. Bockris, J. 590, 616
O'Mara, W. C. 289, 298
Oehrlein, G. S. 98
Ogawa, T. 97
Ogirima, M. 434
Oh, J. M. 468
Ohno, H. 741
Ohno, K. 611
Ohshima, J. 377
Ohshima, T. 413
Ohya, Y. 18
Okano, H. 430
Olander, D. R. 443, 456
Oldham, W. G. 127, 129, 384, 405, 406
Olender, H. 821
Oleszek, G. 88
Oleszek, G. M. 407
Olson, J. M. 211
Onabe, K. 328
Onoe, A. 222
Ootuka, A. 222
Ord, J. L. 426
Oriani, R. A. 56, 79
Orner, C. 381
Osbourn, G. C. 343
Osteryoung, R. A. 781
Ota, E. 755
Otani, S. 755
Ottesen, D. K. 482
Ouchi, K. 758
Owen, J. R. 492
Owen, S. J. T. 355, 600
Owens, B, B. 764
Oye, H. A. 742, 760

Pachter, R. J. 183
Padula, A. 12
Pai, P. G. 842
Palanisamy, T. 35
Palmisano, F. 772
Palmstrom, C. J. 436

Abstract No.

Pan, A. I-T. 151
Pan, P. 105
Pan, S. 348
Pande, K. P. 340
Pang, S. W. 172
Panitz, J. K. G. 220
Papir, Y. S. 543, 544
Pappalardo, R. G. 603
Parikh, M. 254
Park, K. O. 155, 196
Parker, J. 223
Parker, A. A. 183
Parkhurst, W. A. 20
Parkinson, B. A. 508
Parodi, M. 681
Parsey, Jr., J. M. 325
Patton, G. L. 363
Pauwels, H. 114
Pavelescu, C. 427
Pearce, C. W. 307
Pearlstein, A. J. 66
Peccoud, L. 166
Peek, H. L. 90
Peck, Jr., W. F. 699
Peerce-Landers, P. J. 645
Peercy, P. S. 101
Peeters, G. 147
Pemsler, J. P. 569
Peng, J. D. 273, 277
Peraldo Bicelli, L. 533
Perkins, R. A. 459
Perloff, D. S. 396
Perrin, C. L. 647
Perusich, S. 59
Peter, L. M. 19
Peters, D. T. 37
Peters, T. E. 603, 606
Petro, W. 348
Petrovic, C. 754
Pfenninger, K. H. 669
Pflug, J. L. 753
Pflug, J. S. 718
Phillips, W. E. 301
Phipps, J. B. 764
Picard, G. 791, 796, 799
Pickelmann, L. 595
Pickup, P. 717
Picraux, S. T. 63
Pilla, A. A. 662, 630, 679, 684, 690
Pillis, L. 693
Pingaron, J. 777
Piscitelli, D. 263
Pizzini, S. 218
Plambeck, J. A. 800
Plant, T. K. 355
Plante, E. R. 476
Plattner, E. 836
Plewes, J. T. 591, 592
Plichter, E. 807
Plzak, V. 727
Pohl, H. A. 683, 685
Pollak, F. H. 725, 846
Pollock, K. 683
Polyak, L. 547
Pons, B. S. 624
Poponiak, M. R. 315
Pou, T. E. 58
Pound, D. G. 72
Powell, R. A. 194
Pozzan, T. 672
Prasad, S. J. 360
Pretorius, R. 388
Price, J. B. 372, 418
Prieto, N. E. 566
Prieve, D. C. 81
Proust, N. 226
Prussin, S. 316

Quang, K. V. 71
Quinlan, K. P. 344

Rabatin, J. G. 602
Rahman, A. 739
Rai-Choudhury, P. 385, 395
Raistrick, I. D. 449, 500, 745, 597, 763
Ramasubramanian, N. 782
Ramiller, C. 141
Ramiller, C. L. 420
Ramseyer, G. 361
Ransom, C. M. 174
Rao, M. V. 360
Rapeaux, M. 177
Rapp, R. A. 461
Ratcliff, M. A. 510
Rath, D. 839
Rathman, D. D. 153, 172
Ratkji, S. K. 740
Rava, P. 218
Raveane, A. 673
Ravi, K. V. 213
Ravishankar, P. S. 208, 215
Ray, A. K. 89
Ray Chiu, K. C. 149
Razzini, G. 533
Read, M. H. 337
Reau, J.M. 485
Rechnitz, G. A. 615
Redey, L. 46, 47
Reed, E. 372
Reeves, J. H. 521

Abstract No.

Reif, R. 14
Reijn, J. M. 61
Reinberg, A. R. 15
Reinhart, T. J. 24
Reisman, A. 98, 30, 13
Remmerie, J. 104, 13
Reshef, I. 84
Reuhl, K. 77
Reynolds, G. J. 78
Reynolds, J. L. 19
Rhee, J. K. 36
Rhodes, E. 79
Rhodes, R. J. 18
Ried, J. D. 61
Rieke, P. 52
Riga, J. 81
Riggs, J. B. 41
Rink, T. J. 67
Rishpon, J. 84
Ritchie, W. H. 11
Ritz, K. N. 31
Rivier, M. 38
Rixon, R. H. 67
Robb, F. 17
Robbins, M. 591, 59
Roberts, J. M. C. 69
Robinson, McD. 9
Robitaille, M. 49
Rocazella, M. A. 48
Rock, F. C. 155, 19
Rogers, D. J. 76
Rolison, D. 54
Rolison, D. R. 56
Romankiw, L. T. 14
Rony, P. 25
Rosamilia, J. M. 83
Rosasco, S. D. 70
Rose, K. 12
Rose, T. L. 42
Rosenblatt, G. M. 45
Rosenthal, M. V. 55
Ross, Jr., P. N. 715, 802, 80
Ross, Jr., P. N. 80
Ross, Jr., P. N. 71
Ross, R. R. 18
Rossi, J. A. 27
Rozgonyi, G. A. 26
Rubinson, J. F. 62
Rubinstein, I. 54
Russell, P. G. 77
Rust, R. D. 182, 18
Ryaby, J. 67
Ryan, F. M. 60
Rybowski, L. 68
Rytter, E. 73
Rzad, S. J. 42

Sabbatini, L. 772
Sabin, E. 141
Saboungi, M. L. 739, 767
Sachdev, S. 138
Sadan, D. K. 286, 318, 386
Safford, M. M. 27
Sainsbury, M. 658
Salesse, A. 534
Salomon, M. 807
Salter, R. S. 751, 811
Sammells, A. F. 525, 526
Sanders, F. H. M. 191
Sandstrom, D. R. 714
Saraswat, K. C. 126
Sardi, L. 218
Sarkhel, A. 402
Sasaki, A. 122
Saski, G. 409
Sato, A. 222
Sato, T. 758
Sato, Y. 324
Sauer, K. 635
Savy, M. 812
Sayers, D. E. 728
Scarbeck, G. 812
Scarfone, L. M. 267
Schafer, M. A. 634
Schalch, D. 137
Scharifker, B. 820
Scharmann, A. 137
Scheffler, T. B. 750
Schei, A. 208, 210
Schenk, D. 660
Scherson, D. 55, 548, 620, 706
Schiffrin, D. J. 620
Schlier, A. R. 337
Schlotter, P. 595
Schmehl, R. H. 717
Schmickler, W. 732
Schmidt, P. P. 629
Schneider, M. 208
Schols, G. 106
Schorner, R. 123
Schroeder, A. H. 544
Schuermeyer, F. L. 107
Schuler, A. M. 501
Schuler, C. 503
Schultze, J. W. 732
Schulz, H. 486
Schumaker, M. 660
Schutz, R. J. 160
Schwarzl, S. 197
Schwerzel, R. E. 513

	Abstract No.
Schwuttke, G. H.	217
Scott, M. P.	276
Scoville, A. N.	425
Scrosati, B.	12, 527
Seabaugh, A.	340
Seager, C. H.	220
Sealey, J. D.	17
Sealock, L. J.	795
Searcy, A. W.	499
Sears, A. R.	347
Sears, W. M.	512
Sedgwick, T. O.	391
Seefurth, R. N.	784
Sehil, R.	71
Seitz, W. R.	718
Sekine, M.	430
Sekinobu, M.	324
Semrau, G.	736
Senitzky, B.	260
Senturia, S. D.	124
Seon, F.	799
Sequeira, C. A. C.	493
Settle, J. L.	787
Setzer, W. N.	652
Severi, M.	410
Shabrang, M.	708
Shackiette, L. W.	558
Shanfield, S. R.	144
Shapiro, P.	60
Sharif, A.	379
Sharma, R. A.	784
Sharp, D. J.	220
Shaw, J.	414
Shaw, R. W.	290
Shemilt, J. E.	492
Sheng, T. T.	337
Shenoy, K.	627
Shepard, Jr., V. R.	585
Shia, G. A.	36, 37
Shibano, T.	150, 200
Shibata, A.	374
Shih, C. C.	404
Shine, H. J.	643
Shive, L.	400
Short, D. W.	470
Shriver, D. F.	490
Shuman, R. F.	180
Sides, P. J.	81
Siebert, E.	497
Siegel, E.	140
Siegel, G.	424
Siekhaus, W. H.	443
Sigai, A. G.	609
Sikorska, M.	674
Silverman, H.	568
Silversmith, D. J.	172
Sim, J. W.	359
Simic-Glavaski, B.	706
Sinfelt, J. H.	714
Sinharoy, S.	605
Sirkin, E. R.	163
Sirtl, E.	280
Sisson, M. J.	341
Skarstad, P. M.	764
Skelly, H.	660
Smaga, J. A.	85
Smeggil, J. G.	462
Smethurst, I.	266
Smith, C. P.	743
Smith, D. A.	625
Smith, G. P.	748, 754, 756, 757, 770
Smith, H. I.	331
Smith, J. L.	359
Smith, S. D.	680
Smyrl, W. H.	551, 552, 785
Snow, W. R.	149
Sobkowski, J.	818
Soller, B. R.	180
Solmi, S.	410
Solomon, S.	8
Soltis, R. A.	165
Somorjai, G. A.	694
Sorensen, N. R.	63
Soriaga, M. P.	649, 700
Sorlie, M.	743, 754, 757, 760, 770
Sowa, J. M.	558
Soydan, R.	312, 313
Spencer, J. E.	198
Springer, T.	817
SpringThorpe, A. J.	329
Sprokel, G. J.	599
Spurdens, P. C.	492
Squarzini, E.	263
Srinivasan, G. R.	378
Srinivasan, S.	536, 730, 840
St. Clair, A. K.	245
St. Clair, T. L.	245
Stacy, W. T.	310, 314
Stainer, M.	490
Stankovich, M.	637
Stanley, R.	258
Stavola, M.	288
Stearns, C. A.	467
Steckl, A. J.	86, 202
Steele, B. C. H.	492, 724
Stefano, S. Di	13
Steigmeier, E. F.	415
Stein, H. H.	121
Stein, H. J.	101
Steinberg, G. N.	157
Steinhardt, R. A.	665
Stephens, J. R.	440
Stern, C. D.	666
Stern, K. H.	793
Stevenson, D. A.	445, 446, 477
Stickney, J. L.	649, 700
Stimming, U.	838
Stinebring, R. C.	27
Stoffers, R. C.	592
Stone, B. D.	399
Stone, S. E.	425
Storms, E.	458
Strattman, M.	386
Street, G. B.	545
Stringer, J.	477
Stringfellow, G. B.	339
Struck, C. W.	609
Studut, J. K.	264
Su, M. Z.	614
Sugerman, A.	174
Summers, D.	181, 435
Sun, S. Y.	345
Sun, Y.-H.	819
Surprenant, J. K.	49
Susko, J. P	250
Sutton, S. B.	470
Sutula, R. A.	39
Swaroop, R. B.	390
Syllaios, A. J.	357
Sylvain, R.	328
Szczecinski, P.	521
Szklarczyk, M.	818
Szpak, S.	50, 734, 814
Szwarc, R.	10
Tabib-Azar, M.	100
Takagi, M.	130, 131
Takei, H.	201
Talasek, R. T.	357
Tamminga, Y.	134
Tamura, H.	518
Tan, T. Y.	281
Tango, H.	412
Tanguay, D. J.	152
Taniguchi, K.	284, 309
Tansman, L.	679
Tare, V. B.	463, 832
Tataria, H.	31, 33
Tauber, R. N.	316
Tay, S. P.	96
Taylor, A. D.	835
Taylor, D. M.	397, 422
Taylor, E. J.	36, 37, 729
Tellefsen, K.	695
Temkin, H.	349
Tench, D.	353, 354
Tennenhouse, G. J.	766
Terashima, K.	326
Terry, F. L.	124
Theis, G.	573
Thewissen, D. H. M. W.	515
Thioulouse, P.	604
Thomas, J.	631
Thomas, J. O.	488
Thompson, L. G.	541
Thorne, L. R.	482
Thornton, J. A.	236
Thornton, T. A.	655
Thurber, W. R.	301
Ticianelli, E. A.	639
Tiedje, T.	216
Tierney, V.	577
Tilak, B. V.	584
Tinnemans, A. H. A.	515
Tischer, R. P.	766
Tobias, C. W.	578, 583
Tobin, P. J.	418
Tollin, G.	636
Tomczuk, Z.	767
Tomkiewicz, M.	21, 846
Tomzig, E.	323
Tong, D. W.	397
Tong, H. S.	468
Topich, J. A.	102
Townsend, H. E.	69
Trabka, E. A.	387
Trasatti, S.	576, 701
Tremiliosi-Filho, G.	843, 844
Tremillon, B.	777, 796, 799
Tripp, T. B.	774
Truhan, J. J.	460, 470
Tsai, C.-H.	456
Tsao, K. P.	780
Tsien, R. Y.	672
Tsoukalas, D.	283
Tsukada, T.	201
Tu, C. W.	337
Tuck, C. D. S.	80
Tucker, W. F.	399
Tuerlinckx, B.	687
Turban, C.	177
Turner, D. R.	580
Turner, J. A.	508
Twardoch, U. M.	773, 789
Tweedie, J.	737
Ueno, A.	613
Ukai, K.	201
Ulrich, B. D.	376
Ulstrup, J.	703
Untereker, D. F.	764
Ureta-Zanartu, S.	733
Usui, S.	374
Vail, P. J.	116
Vainer, H.	688
Valco, G. J.	108
Valkenburg, W. G. J. N.	134
Vallet, C. E.	768
Van Calster, A.	114
Van Dell, W. R.	397
van den Hoek, W. G. M.	173, 190
Van Duyne, R. P.	710
van Kemenade, J. T. C.	607
Van Overstraeten, R. J.	204
Van Zee, J.	560, 561
Vanden Berghe, R.	133
Vandenberg, J. M.	349
Vander Plas, H. A.	428
Vanderborgh, N. E.	817
Vargas, T.	788
Varma, R.	835
Vasile, M. J.	186
Vaughan, R. J.	587
Venables, J. D.	248
Venkatasetty, H. V.	50
Venkatraman, B.	360
Verardo, A. E.	17
Verbist, J. J.	812
Verdonck, P.	147
Via, G. H.	714
Viaeminck, R.	133
Viehbeck, A.	594
Vielma, C.	820
Vielstich, W.	815
Vijayakumar, K. M.	516
Villarroel, D.	625
Vissers, D. R.	46, 767
Viswanathan, K.	562
Vogel, D.	168
Voigt, W.	771
Volkl, J.	323
Wada, K.	97
Wade, Jr., W. L.	51
Wagenknecht, J. H.	641
Wagner, F. T.	802, 806
Wagner, S.	235
Wagner, Jr., J. B.	832, 463, 832, 833
Wahlbeck, P. G.	760
Walker, K. L.	447
Walters, S. E.	746
Waltman, R. J.	546
Waltman, R. T.	651
Walton, N. J.	633
Wang, C-B.	804
Wang, C. S.	404
Wang, J. Q.	819
Wang, Q. H.	233
Wang, Y. J.	614
Wang, Y. Y.	386
Wani, E.	201
Wantanabe, M.	139
Warburton, D. L.	2
Ward, P. J.	305
Washburn, J.	286
Washide, H.	222
Wasson, J. R.	491
Watanabe, N.	374
Weaver, M. J.	719, 804
Weedon, L. D.	23
Weeks, S. P.	260
Weick, W.	393
Wen, T. L.	496
Wendt, H.	574, 727, 744, 776
Wendt, J. L.	70
Wenner, C. E.	661
Weppner, W.	489, 496
Wessels, B. W.	239, 345, 610
Westermann-Clark, G. B.	563
Wheater, R. H.	185
White, C. L.	441
White, J. H.	649
White, R. E.	560, 560, 767
White, R. F.	185
White, S. H.	773, 789
Whitfield, J. F.	674, 675
Wicker, T.	156
Widmer, A. E.	414
Wieckowski, A.	64, 818
Wieder, H. H.	351
Wilkes, J. S.	753
Will, F. G.	554, 555
Williams, K. W.	374
Wilson, G. S.	634, 652
Wilson, R. B.	332
Winterton, L. C.	399
Wohlgemuth, J. H.	219
Wong, S. S.	127
Wood, D. L.	447
Woodard, F. E.	641
Woolsey, N. F.	655
Worrell, W. L.	464, 495
Wright, I. G.	481
Wright, S. J.	178
Wrighton, M. S.	504, 720
Wroblowa, H.	766
Wu, N. R.	286
Wu, X.	56
Wurzbach, J. A.	103

	Abstract No.
Wyatt, P. W.	124
Yamahe, K.	309
Yamana, M.	766
Yamazaki, K.	423, 613
Yamoto, H.	413
Yanada, T.	374
Yang, C. Y.	113
Yang, D. L.	488
Yang, K. H.	381
Yang, K. W. C.	600
Yang, Y. T.	238
Yao, N. P.	779
Yeager, E.	54, 706, 801
Yeager, H. L.	564
Yerhoff, F. W.	794
Yi, X. J.	238
Yoneda, M.	150, 200
Yoneyama, H.	518
Yonezawa, T.	377
Yoshida, T.	18, 553
Yoshii, T.	412
Yoshitake, S.	324
Yu, J. M.	238
Yuasa, T.	335
Zagal, J.	733
Zakzouk, A. K. M.	240
Zambonin, P. G.	772
Zarowin, C. B.	154, 157, 188, 189
Zegarelli-Schmidt, E.	67
Zeigler, J. M.	55
Zeleznik, F. J.	47
Zellama, K.	22
Zemanian, T.	7
Zhang, F. S.	23
Zigadlo, J. P.	40
Zimmer, H.	62
Zimmerman, A. H.	4
Zingg, S. P.	757, 77
Zingu, E. C.	388, 43
Zmbov, K. F.	43
Zolla, A.	4
Zuckerbrod, F.	77, 79
Zuman, P.	64

HIGHLIGHTS OF THE SAN FRANCISCO MEETING

Nick Holonyak, Jr. to Receive the Solid State Science and Technology Award

Nick Holonyak, Jr., Professor of Electrical Engineering at the University of Illinois, has been selected as the sixth recipient of the Electrochemical Society Award in Solid State Science and Technology. The award will be presented at the Awards and Recognition session on Tuesday, May 10, at 4:30 PM in the Grand Ballroom of the St. Francis Hotel at the 163rd Meeting of the Society in San Francisco, California. Dr. Holonyak's address, entitled "From Silicon to III-V Compounds," will immediately follow the presentation.

The Solid State Science and Technology Award, which consists of a silver medal (and a bronze replica thereof) and a $1500 prize, was established by the Board of Directors of The Electrochemical Society to be bestowed every two years for "outstanding contributions to the field of Solid State Science and Technology."

Dr. Holonyak was born in Zeigler, Illinois in 1928. He attended the University of Illinois and received a B.S. (1950), M.S. (1951), and Ph.D. (1954) in electrical engineering. A Texas Instruments Fellow in Semiconductor Physics (1953-1954) at the University of Illinois, he did his graduate work under the direction of Dr. John Bardeen.

Dr. Holonyak was employed as a member of Technical Staff at Bell Laboratories (1954-1955) and helped demonstrate feasibility of the first diffused-impurity silicon devices, including transistors, p-n-p-n switches, and SCR's. He served with the U.S. Army Signal Corps (1955-1957) at Fort Monmouth, New Jersey, and at Isogo-ku, Yokohama, Japan. In 1957 he joined the Advanced Semiconductor Laboratory of the General Electric Company, Syracuse, New York, and was successively employed (1957-1963) as a physicist, unit manager, and manager of the Advanced Semiconductor Laboratory. Here he made contributions in the areas of power and signal p-n-p-n devices (including the first shorted-emitter and symmetrical switches, such as the TRIAC and the household wall dimmer), tunnel diodes, phonon-assisted tunneling, halide transport and epitaxial growth of intermetallic compounds and compound mixtures (1960-1963), double injection and deep-impurity-level effects, junction luminescence (GaAsP LED's), and ternary semiconductor lasers, including the first semiconductor laser (GaAsP, 1962) to operate in the visible spectrum. His work from 1960 to 1962 on GaAsP and first construction (1960) of a p-n junction in this crystal system led to the commercial introduction of GaAsP LED's.

Since 1963 Dr. Holonyak has been a Professor at the University of Illinois in the Department of Electrical Engineering and Materials Research Laboratory, and is a member of the University of Illinois Center of Advanced Study. He and his over 30 doctoral students have worked primarily on III-V semiconductors, including stimulated emission on nitrogen trap transitions in the alloys $GaAs_{1-x}P_x$ and $In_{1-x}Ga_xP$, and heterojunctions in the quaternaries $Al_xGa_{1-x}As_{1-y}P_y$ and $In_{1-x}Ga_xP_{1-z}As_z$. His recent research has been concerned with quantum-well light emitters and lasers.

Dr. Holonyak is coauthor of the book "Semiconductor Controlled Rectifiers" (Prentice-Hall, Inc., 1964), editor of the Prentice-Hall series "Solid State Physical Electronics," has served on the Editorial Board of the Proceedings of the IEEE (1966-1974), Applied Physics Letters (1978-1980), and is a member of the Board of Editorial Associates of Semiconductors and Insulators. He received a General Electric Cordiner Award (1962), and for his contributions to the field of visible light-emitting diodes and diode lasers, he is the recipient of the IEEE Morris N. Liebmann Award (1973), and 1975 John Scott Medal (City of Philadelphia), the 1976 GaAs Symposium Award, and the IEEE Jack A. Morton Award (1981). He is a member of the National Academy of Engineering, Fellow of the IEEE, Fellow of the APS, and has served on various IEEE, APS, and NAS committees. He has twice been invited by the Academy of Sciences of the U.S.S.R. (1967 and 1974) to visit laboratories in the Soviet Union.

C. Lester Hogan to Give The Electrochemical Society Lecture

C. Lester Hogan has been selected to deliver the ECS Lecture at the Plenary Session of the 163rd Society Meeting in San Francisco, California. His lecture, entitled "VLSI Processes—and the Future" is to be presented at 9:00 A.M. on Monday, May 9, in the Grand Ballroom of the St. Francis Hotel.

Dr. Hogan graduated from Montana State University in 1942 with a B.S. in chemical engineering. Serving as a U.S. Naval officer during World War II, he then earned his M.S. and Ph.D. degrees in physics, emphasis on solid-state and electromagnetic theory, at Lehigh University.

Dr. Hogan first came to world attention in scientific circles after joining Bell Laboratories where he performed experiments which demonstrated nonreciprocity at microwave frequencies and carried out a theoretical analysis substantiating the experiments. This work, published in 1952, has become a classic reference. It was this work that led Dr. Hogan to the invention of the microwave gyrator, microwave isolator, and microwave circulator, which were the world's first passive nonreciprocal circuit elements. These devices, in one form or another, are now used in nearly every microwave system in the world today.

Subsequently, Dr. Hogan joined the Harvard University faculty and was awarded the Gordon McKay Professorship of Applied Physics. He also led the widely acclaimed 1956 Harvard symposium on Microwave Properties and Applications of Ferrites, and he organized and edited the October 1956 special issue of the Proceedings of I.R.E. on Ferrites. From 1958 to 1968, he served as General Manager of the Motorola Semiconductor Products Di-

Continued on next page

vision, and during that period, became Executive Vice-President of the parent company.

Dr. Hogan joined Fairchild Camera and Instrument Corporation in 1968 as President, Chief Executive Officer, and a Director. He directed his company in the development of the Isoplanar process in both bipolar and CMOS circuits; the first commercially available CCD imaging device; subnanosecond ECL, the Sentry LSI testing system, and other important products and processes. He was elected Vice-Chairman of the Board of Directors in 1974, and is presently Consultant to the President.

Dr. Hogan has held key posts in major professional scientific organizations. He served on the Advisory Council of the Electrical Engineering Department of Princeton University from 1957 to 1968. Listed in "Who's Who in America" and "American Men of Science," Dr. Hogan holds honorary degrees from Harvard, Lehigh, Montana State, and Worcester Polytechnic Institute. In addition, he served on the Board of Trustees of Lehigh University and the Board of Regents of the University of Santa Clara. He serves on the Advisory Board for the College of Engineering of the University of California at Berkeley, the Visiting Committee for the Department of Electrical Engineering and Computer Sciences at Massachusetts Institute of Technology, and the Advisory Council of the School of Engineering at Stanford University. Dr. Hogan is also a member of the Board of Directors of First Interstate Bank, Rolm Corporation, Tab Products Company, Timeplex, Incorporated, Semiconductor Specialists, Incorporated, and the Osborne Computer Company.

In 1969, Dr. Hogan received the Golden Plate Award from the American Academy of Achievement. In May, 1976, he was awarded the Frederik Philips Gold Medal by the Institute of Electrical and Electronics Engineers (IEEE) in recognition of his achievements at Motorola and Fairchild. He is also a Fellow of the organization. Dr. Hogan was elected to membership in the National Academy of Engineering in 1977. Election to the Academy honors those who have made important contributions to engineering theory and practice. The Academy shares responsibility with the National Academy of Science for serving the United States Government by examining issues involving science and technology. He was elected an Honorary Fellow of the Institution of Electrical Engineers (IEE) (London) in 1978 for his contributions to the development of electronic technology and leadership in the semiconductor industry. He is the only living American to receive this honor from the United Kingdom's professional organization. The American Association for the Advancement of Science elected Dr. Hogan a Fellow in 1978 for his pioneering contributions in microwave electronics and his leadership in industrial research and engineering. In 1979, Dr. Hogan received the Medal of Achievement from the American Electronics Association, again in recognition for his contributions at Motorola and Fairchild, and in 1981 he received the Berkeley Citation from the University of California at Berkeley. He has also received many community service awards.

DIVISION NEWS

Electronics Division

Report of the Nominating Committee

The Nominating Committee of the Electronics Division has selected candidates for the 1983-1985 elective offices for the Division. As a result, the Committee nominates the following candidates to hold office beginning May 14, 1983 to the end of the 1985 Spring Meeting:

Chairman—Edward H. Nicollian
Vice-Chairman, Semiconductors—Patricia Castro
Vice-Chairman, New Electronic Technologies—Prosenjit Rai-Choudhury
Secretary—W. Murray Bullis
Treasurer—Mort Jones
Past Chairman—Ronald E. Enstrom
Members-at-Large—K. E. Bean, G. M. Blom, I. F. Chang, G. W. Cullen, B. E. Deal, C. J. Dell'Oca, D. A. Doane, M. Duffy, J. M. Eldridge, L. Ephrath, J. C. C. Fan, D. B. Fraser, H. J. Geipel, Jr., J. Hwang, H. R. Huff, V. G. Keramidas, C. Kirkpatrick, R. P. Kramer, M. A. Littlejohn, S. Mahajan, W. A. McAllister, D. V. McCaughan, C. M. Osburn, E. M. Pell, K. A. Pickar, W. A. Pliskin, R. G. Poulsen, M. J. Rand, A. Reisman, G. A. Rozgonyi, G. C. Schwartz, F. N. Schwettmann, D. W. Shaw, E. Sirtl, G. R. Srinivasan, B. G. Streetman, F. J. Strieter, A. M. Voshchenkov, and P. N. Yocum.

These nominees, together with any others submitted in accordance with the bylaws of the Division, will be voted upon by the membership of the Electronics Division at its luncheon business meeting to be held at 12:15 p.m. Monday, May 9, in the Italian Room, Mezzanine, at The Westin St. Francis Hotel, at the Society's Meeting in San Francisco.

Nominations for the Electronics Division Award

Nominations for the 1984 Electronics Division Award of The Electrochemical Society are now being solicited. The Electronics Division Award is presented annually in order to give recognition to active members of the Society who have made outstanding scientific contributions and enhanced the scientific stature of the Society by presentations of this work in papers in the **Journal** and at Society meetings.

To be considered, a nominee must be a member of the Society and have been an author or coauthor in the publication of more than one paper in the **Journal** and/or presentation of more than one full paper or more than two recent news papers at a Society meeting within the previous five years.

Besides the aforementioned requirements, nominations should contain other supporting data such as a list of publications, patents, activities, and a brief summary outlining the accomplishments on which the award will be based. Nominations should be submitted to the Chairman of the Committee: P. N. Yocom, RCA Laboratories, David Sarnoff Research Center, Princeton, NJ 08540 on or before May 1, 1983.

High Temperature Materials Division

Report of the Nominating Committee

The following nominations for officers in the High Temperature Materials Division executive committee, 1983-1985, have been made by the Nominating Committee (W. W. Smeltzer, Chairman, J. B. Berkowitz, and J. M. Blocher, Jr.). All nominees have been notified of their nomination; all have accepted and have indicated their willingness to serve in their respective offices:

Chairman—Lee P. Hunt
Senior Vice-Chairman—Wayne Worrell
Junior Vice-Chairman—Frederick S. Pattit
Secretary-Treasurer—Vishu D. Dosaj
Past Charman—William A. Adams
Members-at-Large—K. E. Johnson, W. W. Liang, P. J. Meschter, Z. A. Munir, L. Rothman, A. Sanjuro, D. A. Shores, and J. B. Wagner, Jr.

Nominations may also be made from the floor at the annual general meeting in accordance with the Divisional bylaws.

The election of officers will be held at the Division's luncheon and business meeting to be held at 12:15 p.m. on Monday, May 9, in the City Club, 12th Floor, at The Westin St. Francis Hotel, at the Society's Meeting in San Francisco.

Physical Electrochemistry Division

At the luncheon and business meeting of the Physical Electrochemistry Division, on Monday, May 9 in the Monterey Room of the Sir Francis Drake Hotel, San Francisco, California, the Members will vote on proposed amendments of the Division bylaws.

The proposed amendments are as follows:

Article II, Section 1, add "and to advance the purpose of the Society."

Section 2, change the wording from "and break off" to "to form."

Article IV, Section 2, add the sentence "These officers shall perform the duties prescribed by the Constitution and Bylaws of the Society, by these bylaws, and by parliamentary authority adopted by the Division."

Add Section 5, "The elected Vice-Chairman shall be considered eligible and designated by the Chairman or, in the absence of such designation, by vote of the Executive Committee, to serve as the alternate for the Chairman in attending meetings of the Board of Directors of the Society from which the Chairman is absent and in exercising at such meetings the rights, powers, and privileges of the absent Chairman. Written notice of this designation shall be provided to the Secretary of the Society prior to the meeting of the Board."

Article V, Section 1, add "of the Division."

Section 2, add the sentence "The nominations shall be approved by the Executive Committee.

Section 3, insert in the first sentence "and the Chairman shall notify the Secretary of the Division of the nominees at least . . . "

Section 3, insert in the second sentence "nomination of candidates for positions of . . ."

Continued on next page

Section 5, change the word "Division" to "Society."

Article VI, Section 1, (b) delete the sentence "If he is unable to be present he may appoint a Divisional representative who serves without vote."

Section 3, (c) add the phrase "in excess of $100" to the third sentence.

Article VII, Section 4, change the wording from "be responsible for the Technical Sessions and shall choose subjects for the symposia" to "have general supervision of the affairs of the Division between its business meetings, shall be responsible for the planning, organization, and execution of the technical programs and publications sponsored by the Division, shall make recommendations to the Division and, through the Chairman of the Division, to the Board of Directors of the Society, and shall perform such other duties as are specified in these bylaws. The Executive Committee shall be subject to the orders of the Division, and none of its acts shall conflict with action taken by the Division or by the Society."

These amendments are being proposed to bring the Division bylaws into agreement with the suggested model Division bylaws prepared by the Ways and Means Committee and approved by the Board of Directors.

There are two significant changes. One is the addition of Section 5 to Article IV which provides the mechanism for the Vice-Chairman to serve as an alternate for the Chairman at meetings of the Board of Directors. The other is the broader definition of the responsibilities of the Executive Committee found in Section 4 of Article VII.

Minor changes in punctuation and elimination or change of a word or phrase are incorporated into these amendments.

A complete copy of the draft of proposed changes is available from the chairman of the Division, Elton J. Cairns, or Society Headquarters office. Copies will be available at the Divisional luncheon and business meeting, at 12:15 p.m., on Monday, May 9, in the Monterey Room, 2nd Floor, of the Sir Francis Drake Hotel, at the Society's Meeting in San Francisco.

Report of the Nominating Committee

The Nominating Committee of the Physical Electrochemistry Division has proposed the following slate, of officers for election at the Division Business Meeting in San Francisco in May. the nominees have been contacted and indicated their willingness to serve, if elected.

Chairman
Robert A. Osteryoung

Vice-Chairman
Larry R. Faulkner

Secretary-Treasurer
Jose Giner

Members-at-Large (2)
Fred C. Anson
Gleb Mamantov
Barry Miller
M. Stanley Whittingham

The election of officers will be held at the Division's luncheon and business meeting to be held at 12:15 p.m. on Wednesday, May 11, in the Monterey Room, in the Sir Francis Drake Hotel, at the Society's Meeting in San Francisco.

GROUP NEWS

Energy Technology Group

Report of the Nominating Committee

The Nominating Committee (S. Srinivasan, Chairman, S. Wagner, and J. McBreen) of the Energy Technology Group has proposed the following slate of officers:

Chairman—A. J. Nozik, Solar Energy Research Institute

Vice-Chairman—A. J. Appleby, Electric Power Research Institute

Secretary—V. K. Kapur, ARCO Solar, Incorporated

Treasurer—H. Maru, Energy Research Corporation

In accordance with the bylaws of the Group, additional nominations for office may be made by a petition signed by five members of the Group. Such petitions must be in the hands of the chairman of the nominating committee at least ten days before the election, together with the assurance of the nominees willingness to serve, if elected.

The election of officers will be held at the Division's luncheon and business meeting to be held at 12:15 p.m. on Wednesday, May 11, in The City Club, 12th Floor in The Westin St. Francis Hotel, at the Society's Meeting in San Francisco.

SECTION NEWS

Southern Wisconsin Section

The December 2, 1982 meeting of the Southern Wisconsin Section was held at the Tyrolean Towne House Restaurant. Twenty people attended the technical session which featured Professor Arthur B. Ellis of the University of Wisconsin-Madison. Professor Ellis spoke an luminescent photoelectrochemical cells (PEC's). The PEC's are semiconductors which convert optical (solar) energy directly into electricity and/or chemical fuels. Many of these materials luminesce in this process and provide a means for investigating recombination processes which defeat energy conversion. The emissive properties of several cadmium selenide PEC's were demonstrated.

Metropolitan New York Section

President's Night for the Metropolitan New York Local Section featured Dr. Frederick Strieter, President of the Society, and Director of Materials Development and Fabrication of the Optoelectronics Division of Honeywell, Incorporated, for the January 12th dinner meeting at the Sheraton Inn—Newark Airport. Some forty members and guests heard Dr. Strieter give a brief review of the Society's recent progress and current status before presenting the subject for the evening, "Trends in Solid State Technology." Current new technologies, such as E-beam, laser annealing, and plasma processing were examined for their impact on the future growth of electronics. Advances in integrated circuits, bubble memory, solid-state displays, and fiber optics were reviewed. The doubling in output each year for many years for semiconductor devices was noted. Audience participation followed the talk.

MATERIALS SCIENCE FACULTY

MIT's Department of Materials Science & Engineering has several professorships at varying levels available for the current academic year as well as 1983-84. The positions involve teaching and research in the following:

- **ELECTRONIC MATERIALS:** Focuses on semiconductors. Background in processing electronic properties relationships, thin films, and interfaces preferred. **Assistant/Associate/Full Professorships.**
- **ELECTRONIC MATERIALS:** Focuses on superconducting materials. Background in processing electrical materials properties, and thin films preferred. **Assistant/Associate Professorships.**
- **POLYMERS: Full professorships** being offered jointly with Department of Chemical Engineering.
- **CERAMIC PROCESSING:** Background in colloid-surface chemistry preferred. **Assistant/Associate Professorships.**

Requires doctorate in relevant field, while industrial experience is preferred. Salaries are competitive and benefits excellent.

Submit resume, including citizenship and/or visa status, publications list and references to: Prof. Merton C. Flemings, Department Head of Materials Science & Engineering, Massachusetts Institute of Technology, 8-307, 77 Massachusetts Avenue, Cambridge, MA 02139. MIT is an equal opportunity/affirmative action employer.

MIT

NEWS ITEM

The J. C. Schumacher Company, a long time sustaining member of the Society, has announced the following Vice-Presidential promotions:

Richard E. Howard has joined the Company as Vice-President of Operations. Mr. Howard's educational background includes a B.S.E. in electronics from Arizona State University and an M.S.M.E. in manufacturing from the University of Massachusetts. He was a part-time faculty member of Northeastern University's Graduate School and is a textbook author.

Dr. Michel Jeunehomme, Technology Director for the Schumacher Company, is promoted to Vice-President of Technology. Dr. Jeunehomme's extensive educational credentials include a B.S. in physics, and an M.S. and Ph.D. in physical chemistry from the Free University of Brussels, Belgium. He also holds an M.B.A. in finance from Long Island University, and is a Senior Member of the Instruments Society of America.

Gerald G. Lyman, Director of Marketing for Schumacher, has been named Vice-President of Planning and Development. Mr. Lyman brings to this position an outstanding background in marketing and finance. He received a B.S.E. with honors from Princeton University and an M.B.A. in finance and marketing from Harvard Business School.

San Francisco, California, Meeting Program 49C-141C

Nick Holonyak, Jr. to Receive the Solid State Science and Technology Award 142C

C. Lester Hogan to Give The Electrochemical Society Lecture 142C-143C

Division News 143C-144C

Group News 144C

Section News 144C

News Items 145C

New Members 145C-146C

Obituaries 146C

Call for Recent News Papers—San Francisco, California Meeting 146C

Notice to Members 147C

The Electrochemical Society Short Course: Plasma Chemistry for IC Fabrication 148C

Call for Papers—First International Symposium on Very Large Scale Integration Science and Technology 149C

Call for Papers—Washington, DC Meeting .....

NEW MEMBERS

It is a pleasure to announce the following new members of The Electrochemical Society as recommended by the Admissions Committee and approved by the Board of Directors in January 1983.

Active Members

Anderson, J. H., Hopewell Junction, NY
Bowden, E. F., Minneapolis, MN
Chiang, D. T. T., Menlo Park, CA
Ciemiecki, K. T., Murray Hill, NJ
Douglas, M. A., Dallas, TX
Evans, D. H., Madison, WI
Fey, E. O., Vestal, NY
Fox, M. A., Austin, TX
Groover, R., Richardson, TX
Han, Y.-P., Dallas, TX
Hunter, W. L., Scottsdale, AZ
Kobayashi, F., Secaucus, NJ
Konno, H., Sapporo, Japan
Larkin, J. B., The Colony, TX
Morijiri, M., Ibaraki-ken, Japan
Newby, K. R., Linden, NJ
Nikles, D. E., Summit, NJ
Orsino, J. A., San Clemente, CA
Parker, D. A., Windsor Locks, CT
Porumbescu, S., Santa Clara, CA
Raub, C. J., Schwabisch Gmund, Germany
Robbins, D. J., Worcs, England
Schei, A., Vagsbygd, Norway
Schroeder, A. H., Richmond, CA
Shimura, F., St. Louis, MO
Sivo, L. L., Saratoga, CA
Stocker, H. J., Murray Hill, NJ
Tomantschger, K., Huntsville, AL
Tseng, E. S., Inglewood, CA
Uchida, Y., Kanagawa, Japan
Waggoner, J. R., Gainsville, FL
Walsh, F., Newton, MA
Wauk, M. T., Santa Clara, CA
Weaver, J. C., Colorado Springs, CO
Wickershama, T. W., Milwaukee, WI

Continued on next page

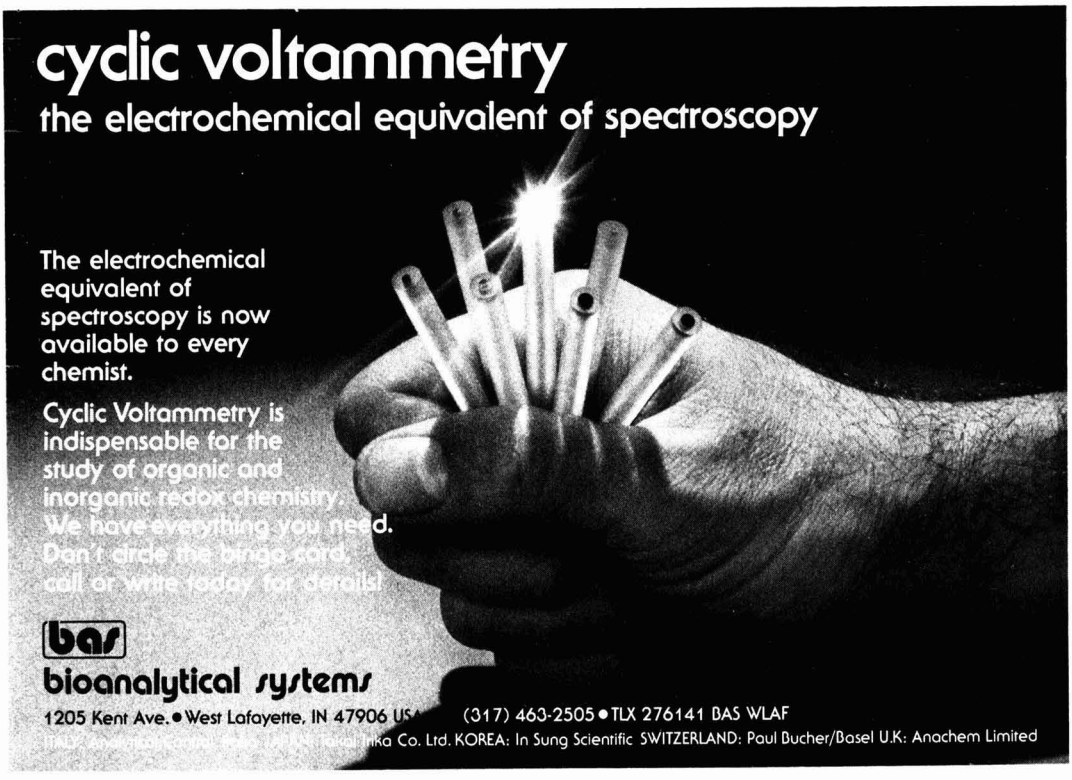

Student Members

Crawley, C. D. Newark, DE
D'Agostino, A. T., Logan, UT
Fierro, C. A., Cleveland, OH
Kannangara, D., Ottawa, Ont., Canada
Loh, W. M., Stanford, CA
Lott, S. E., Urbana, IL
Schlesinger, T. E., Pasadena, CA
Tyagi, S. K., Norman, OK
Wu, J., West Lafayette, IN

Reinstatements

Lee, K. S., Milpitas, CA
Nonnenmacher, H., Palo Alto, CA
Staniewicz, R. J., Cockeysville, MD

Member Representatives

Hashimoto, N., Hitachi, Ltd.

OBITUARIES

Jay Wesley Thornhill, an electrical engineer and the manager of the Technical Assessment Task for the Photovoltaic Technology Development and Application Lead Center at the Jet Propulsion Laboratory, died in Van Nuys, California, November 29, 1982.

Mr. Thornhill was born in Syracuse, New York, in 1920, and received his bachelors degree from Pennsylvania State University, as well as his masters degree from Purdue University. He moved to Phoenix, Arizona in 1967, and worked for Motorola and later Spectrolab before going to work for the Jet Propulsion Laboratory in Pasadena, in 1977. Mr. Thornhill worked in Pasadena for the past five years.

Mr. Thornhill was an Active Member of the Society, and a member of the Institute of Electrical and Electronic Engineers. He was an Army veteran of World War II, having served as a lieutenant in the Signal Corp.

Dan Trivich, a Wayne State University chemistry professor and an international authority on solar energy, died December 18, 1982, in Detroit, Michigan.

A Wayne State faculty member since 1948, Dr. Trivich was a pioneer in graduate education at Wayne, and devoted over 30 years to electrochemical and solar research, supported in part by the National Science Foundation and the U.S. Department of Energy.

Dr. Trivich obtained his B.A. and Ph.D. degrees in 1938 and 1942, respectively, from Ohio State University. His main fields of research focused on solid state electrochemistry, preparation and properties of single crystal cuprous oxide, photovoltaic cells, and solar energy conversion. He received several Fulbright and Fulbright-Hays lectureships for study abroad. In 1980, he was given the Faculty Research Award of the Wayne State University Chapter of Sigma Xi. He was an Active Member of the Society since 1950, and served as first Vice-Chairman of the Detroit Local Section in 1952-1954 and Chairman of the Electrodeposition Division in 1965.

THE ELECTROCHEMICAL ENGINEERING of BATTERIES SHORT COURSE

Berkeley, CA, June 20-24, 1983,
Marriott Hotel

Instructors:
Douglas N. Bennion, Brigham Young Univ.
Elton Cairns, Lawrence Berkeley Lab and UCB
Karl Kordesch, Tech. Univ. of Graz
John Newman, Univ. Calif., Berkeley
William H. Tiedemann, Johnson Controls, Milwaukee, Wisc.
Charles W. Tobias, Univ. Calif., Berkeley

For information/registration please contact Douglas N. Bennion, 1742 No. Driftwood Dr., Provo, Utah 84604. Advance registration required.

CALL FOR RECENT NEWS PAPERS AND EXTENDED RECENT NEWS PAPERS

San Francisco, California Meeting May 8-13, 1983

TRIPLICATE copies of a 75-word abstract of a Recent News Paper, for a 10-minute presentation, must be received by the Symposium Chairman not later than March 24, 1983.
TRIPLICATE copies of a 75-word abstract and, ALSO a 200-300 word abstract of an Extended Recent News Paper, for a 20-minute presentation, must be RECEIVED by the Symposium Chairman not later than March 14, 1983.

ELECTRONICS DIVISION AND DIELECTRICS AND INSULATION DIVISION

Recent News Papers and Extended Recent News Papers are invited for the sessions sponsored by the Electronics and Dielectrics and Insulation Divisions for the 1983 Spring Meeting in San Francisco, California. The time allotted for the 75-word Recent News Paper will be 10 minutes, including 2 minutes for discussion. The time allotted for the Extended Recent News Paper will be 20 minutes, including the question/answer period.

The Extended Recent News Paper requires, in addition to the 75-word abstract, a 200-300 word abstract in triplicate and should be received significantly earlier than the normal deadline date because these papers will be reviewed for technical content, appropriateness of the paper, time limitations, duplication of material, etc. Topics for Recent News Papers and Extended Recent News Papers include:

1. Dielectric Isolation
2. Silicon Nitride Insulating Films
3. Fourth Symposium on Plasma Processing
4. Computer Controlled IC Processing and Monitoring
5. Defects in Semiconductors
6. III-V Opto-Electronics Epitaxy and Device Related Processes
7. Materials and New Processing Technologies for Photovoltaics

Copies of all abstracts, as outlined above, should be sent to the Recent News Papers Symposium Chairman: W. A. Pliskin, IBM Corporation, Department 025, Zip 48A, Route 52, Hopewell Junction, New York 12533. Please note the deadlines are for receiving the papers and not for mailing them.

ADVERTISERS' INDEX

Aeronautical Systems Div. 147C

Bioanalytical Systems, Inc. 145C

Catalyst Research Corp. 147C

The Electrochemical Engineering of Batteries Short Course 146C

Electrosynthesis Co. 150C

The I.C. Sample Office 152C

Massachusetts Institute of Technology.. 144C

Material Concepts Inc. 147C

Princeton Applied Research Corp. 151C

USS Agri-Chemicals 147C

BATTERY CHEMIST (ELECTROCHEMIST)

Battery Chemist (Electrochemist), Aero Propulsion Laboratory, Wright-Patterson Air Force Base, Ohio. The Aero Propulsion Laboratory is seeking candidates for a research electrochemist to be responsible for in-house fundamental investigations on nonaqueous electrolyte batteries. The electrochemical systems to be studied are energetic couples, such as lithium/thionyl chloride or other primary and rechargeable generic types. The specific areas to be emphasized will depend on candidate's qualifications and those of mutual interest. Qualifications are an advanced degree (Ph.D) with 3 years pertinent experience. United States citizenship is required. This is an expert level research position at the GS-13 level, starting salary $34,930 with excellent fringe benefit package. Publication of results and travel to technical meetings encouraged.

Application packages may be requested from the Civilian Personnel Office at ASD/DPCEA (Mr. Gerald W. White), Wright-Patterson AFB OH 45433, or by calling Mr. White at (513) 255-4336/7. Selection for this position will be based upon merit without regard to race, color, religion, sex, national origin, age, marital status, physical handicap, political affiliation, or other nonmerit factors. Closing date for application is 30 April 1983. Applications received after closing date will be returned without action.

Electrochemists

Catalyst Research, one of the world's leading producers of advanced battery systems and electrochemically-based gas sensing devices, is expanding its research organization. Openings currently exist for scientists and engineers with advanced degrees and all levels of experience in electrochemistry.

Responsibilities will include research and development on small moderate-rate cells with emphasis on primary lithium battery systems such as lithium-thionyl chloride or similar lithium inorganic electrolyte systems. A working knowledge of electrochemically-based gas sensing devices, fuel cells, and electronics is desirable.

Catalyst Research offers competitive salaries, excellent benefits, and a liberal relocation policy.

For confidential consideration, please send your resume to:

Manager, Human Resources
Catalyst Research Corporation
1421-B Clarkview Road
Baltimore, MD 21209

CATALYST RESEARCH CORPORATION

An Equal Opportunity Employer/M-F/H

LiAsF$_6$

(Lithium Hexafluoroarsenate)

USS **Lectro-Salt™**

The superior electrolyte salt for nonaqueous lithium cells. Available in commercial quantities.

Pure $LiAsF_6$ is not toxic by dermal absorption, and is only slightly toxic when ingested. Ames test results indicate $LiAsF_6$ is not a carcinogen.

ELECTROCHEMICAL GRADE

1. Less than 100 ppm H_2O
2. Completely soluble in organic solvents
3. Acid equivalent near zero

For technical bulletins, and price information, call or write:

USS **Agri-Chemicals**
Division of United States Steel

Atlanta Technical Center
685 DeKalb Industrial Way
Decatur, GA 30033
Phone 404 292-2525

Notice to Members

April 1 is Cut-Off Date

Your attention is called to Article III, Section 8 of the Society Constitution which states: "Any member delinquent in dues after April 1 of each year shall no longer receive the Society's publications, and will not be allowed to vote in any Society election until such dues are paid. All members in arrears for one year after the first of April shall lose their membership status and can be reinstated only by action of the Board of Directors." Members who have not sent in 1983 payments were mailed a second notice in February and are urged to make payment promptly in order to avoid delay in receipt of the JOURNAL.

Electrochemist

High Tech company desires electrochemist for specialty electroplating and related coating studies. Should be experienced in a variety of techniques and capable of innovation. Production and R&D experience desirable. Excellent benefit package includes profit sharing, tuition assistance, medical and life insurance.

Submit resume in complete confidence with salary requirements to
Material Concepts, Inc.
666 N. Hague Avenue
Columbus, OH 43204
Attention: M. Pastor

EEO M/F

THE ELECTROCHEMICAL SOCIETY
SHORT COURSE
PLASMA CHEMISTRY FOR IC FABRICATION
SAN FRANCISCO, CALIFORNIA

Sunday, May 8, 1983, St. Francis Hotel

Limited attendance—Advance registration required

The Electrochemical Society will sponsor a short course in conjunction with the 163rd Meeting of the Society in San Francisco at the St. Francis Hotel on Sunday, May 8, 1983. The course will consist of four lectures, two from 9:00 AM to 12:00 noon, and two from 1:30 to 4:30 PM. Copies of the slides, along with an outline and bibliography will be distributed to each registrant at the time of the course. The registration fee is $150 for members and $200 for nonmembers. The fee covers the course, luncheon, and text material; it is not applicable to any other activities of the Society's 163rd Meeting. The attached registration form and a check for the correct registration fee must be received not later than April 15, 1983, at The Electrochemical Society, Inc., 10 South Main St., Pennington, N.J. 08534-2896.

FUNDAMENTALS AND APPLICATIONS OF PLASMA CHEMISTRY FOR IC FABRICATION

Alexis T. Bell and Dennis W. Hess

Department of Chemical Engineering, University of California, Berkeley, California

This course will emphasize the physics and chemistry of rf glow discharges as they pertain to the fabrication of integrated circuits. The course is intended to serve as an introduction to plasma processing for those involved in the production of semiconductor devices. Course attendees should have the background normally contained in a standard undergraduate program with a major in physics, chemistry, or electrical engineering.

This first half of the course will cover basic principles of plasma physics and chemistry and will discuss some of the techniques available for plasma diagnostics. The fundamental physical characteristics of low pressure, nonequilibrium plasmas will be defined and their relationship to the kinetics of forming chemically active species will be demonstrated. The relationship of the free atoms, radicals, and ions produced in a plasma to the progress of overall chemical reactions (e.g., film deposition, etching, etc.) will be shown and a brief introduction to the modeling of plasma-chemical processes will be presented. The physical and chemical characterization of plasmas by means of electrical probes, mass spectrometry, and optical spectroscopy will be surveyed for the purpose of identifying the type of information obtainable from each technique.

The second half of the course will be devoted to a discussion of the applications of high frequency discharges to thin film etching and deposition processes used in integrated circuit fabrication. Examples will be chosen from the areas of photoresist stripping; semiconductor, insulator, and metal film etching; and silicon-based materials deposition. Recent results will be presented and discussed in terms of plasma physics and chemistry. Chemical and physical models which generate insight into the "tailoring" of etch rates and profiles, and deposited film properties will be indicated. Degradation of device properties due to plasma exposure will be considered.

SHORT COURSE REGISTRATION FORM

PLASMA CHEMISTRY FOR IC FABRICATION

Payment Enclosed:

☐ ECS Member—$150.00 ☐ Nonmember—$200.00

Name _____

Address _____

City, State, Zip _____

Business Affiliation _____

Please return this form by April 15, 1983, with your payment to:
The Electrochemical Society, Inc., 10 South Main St., Pennington, N.J. 08534-2896.

CALL FOR PAPERS

SECOND INTERNATIONAL SYMPOSIUM ON VERY LARGE SCALE INTEGRATION SCIENCE AND TECHNOLOGY: MATERIALS FOR HIGH SPEED/HIGH DENSITY APPLICATIONS

MAY 6-11, 1984—CINCINNATI, OHIO

The Second International Symposium on Very Large Scale Integration Science and Technology will focus on Materials specifically for High Speed/High Density Applications. The symposium, cosponsored by the Electronics and the Dielectrics and Insulation Divisions, will be held as a part of the 165th Meeting of The Electrochemical Society in Cincinnati, Ohio, May 6-11, 1984.

The symposium will be specifically on materials, elemental and compound for high speed/high density applications and will cover all aspects of materials development such as: 1. Synthesis. 2. Bulk Crystal Growth. 3. Epitaxy. 4 Dopant and Impurity Control. 5. Formation and Properties of Dielectric and Insulation Materials. 6. Metallization and Contacts. 7. Defects and Control. 8. Materials Characterization.

Emphasis will be placed on Novel and/or New Electronic Materials. A symposium proceedings volume will be published, available at the symposium.

Authors must submit five copies of a 500 word, or longer, abstract specifically stating the contribution that the paper makes to the field. These abstracts will be used solely to select papers for presentation at the symposium. In-depth review papers which give wide coverage of a field are also sought, and those eminent in the fields of materials related device and VLSI technologies are invited to submit abstracts. The abstracts should be submitted by July 15, 1983, to either of the Co-Chairmen, Ken Bean, Texas Instruments Incorporated, P.O. Box 225936, MS 147, Dallas, TX 75265 and George Rozgonyi, Microelectronics Center of North Carolina, P.O. Box 12889, Research Triangle Park, North Carolina 27709. Authors submitting abstracts will be notified if their papers have been accepted for presentation and will be given specific instructions for subsequent manuscript preparation for the proceedings. Authors of accepted papers will also be required to submit a 75-word abstract (deadline—December 1, 1983) and a 500-1000 word extended abstract (deadline—January 1, 1984) to The Electrochemical Society, Inc., 10 South Main Street, Pennington, New Jersey 08534-2896.

THE ELECTROSYNTHESIS COMPANY, INC.

ELECTROCHEMICAL EQUIPMENT, INSTRUMENTATION & ACCESSORIES

ESC MODEL 800 IR MEASUREMENT SYSTEM

APPLICATIONS

- ELECTROLYSIS, BATTERY AND FUEL CELL RESEARCH
- ELECTROLYTE MONITORING FOR PROCESS CONTROL
- IR MONITORING FOR LONG TERM DATA COLLECTION

— FEATURES —

- Direct digital readout of IR values to 1.999 volts
- No special cell or reference electrode required
- Short current interruption time
- Continuous IR sampling
- Floating analog output for data acquisition

— DESCRIPTION —

An accurate measurement of IR values is obtained using a sampling differential voltmeter integrated with a fast FET current switch. The model 800 can be used to measure IR between any two electrodes, or half cell IR values may be determined with the use of most standard reference electrodes. It permits continuous monitoring of IR conditions and provides a floating analog output for connection to data collection systems or other recording devices. A direct reading of the IR value is obtained without the use of an oscilloscope or the problems associated with the interpretation of data taken from a waveform.

— SPECIFICATIONS —

Maximum input voltage, sampling voltmeter	10 Volts
Maximum measurable IR value	1.999 Volts
Resolution	± 1 mV
Accuracy	± 2 mV
Sample rate	10/Second
Interrupt time	20 microseconds
Interrupt voltage, max	20 Volts
Interrupt current, max	2 to 10 Amperes
Analog output option	0 to 2 Volts Floating to ± 200 V.
Minimum recommended electrode capacitance	50 microfarads

THE ELECTROSYNTHESIS CO., INC.

P.O. Box 16, E. Amherst, N.Y. 14051 • 716-684-0513

Research Caliber Cyclic Voltammetry at a modest price

Our *new* Model 362 Scanning Potentiostat for
• Basic Research • Battery Testing • Corrosion Measurements

The Model 362 combines a ±1 A/±30 V potentiostat/galvanostat with a versatile waveform generator that permits scan rates from 0.1 mV/sec to 5 V/sec. It also allows controlled current scans between preset potential limits for convenient battery testing.

Our Applications Staff would be pleased to discuss the Model 362's capabilities for your electrochemical work. We invite you to write or call for more information.

EG&G PRINCETON APPLIED RESEARCH

P.O. BOX 2565 • PRINCETON, NJ 08540, U.S.A. • 609/452-2111 • TELEX: 843409

Visit us at NACE Booths 308A and 308B

Advertisement

1 New Materials & New Processes, Vol. 2 (1983), 560 pages Special Issue On Batteries & Metal Finishing Technologies

Edited by Nagayama, Yeager, Osa, Okinaka, Kozawa, etc. Publisher: JEC Press, $55. (Shipping $18 for air, $6 for surface). Total of 95 articles.

View from the Top by B. Owens, R. J. Brodd, R. Surd, K. Suematsu, K. Fuchida, F. Hine

Batteries Chemical MnO_2 by Picquet and Welsh, Lithium Batteries in Japan by Ikeda, New Solid Electrolytes by Kudo et al, Stable Divalent Silver Oxide for Primary Cells by Y. Ohya et al, Li-Copper Vanadate Cells by Yamaji et al, Seiko's Ultra-Thin Batteries, Air Cell Using Cobalt phthalocyanine Catalyst, Long Life Power Sources for Implantable Insulin Delivery, High Compression Lead-Acid Batteries for EV. Recent Progress in Automotive Batteries in Japan. Cupric Oxalate Sea Water Battery, etc.

Metal Finishing The latest techniques in Plating on Ceramics and Glass for Electronics Parts, A High Speed Aluminum Anodizing Process, New Techniques for Measuring Electroless Plating Rate, Water Conservation and Recycling Systems, Use of Dialysis Technique in Metal Finishing, MultiCoating Techniques for Continuous Casting Molds, Pollution-Free High Speed Plating System, New Developments in Plating on Plastics, Super-Hard Chromium Deposit, Acid Zinc Chloride Bath, Automatic Control System for High Speed Electroless Copper Plating, Cu-Ni Alloy Plating, etc.

Energy Related Articles (20 articles) Si Photovoltaic Cells, Na-S Batteries, Phosphoric Acid Fuel Cells, Lead-Acid Batteries for Railroad Use, Molten Salt Batteries, Hybrid Battery Systems, Hydrazine-Air Batteries Molten Carbonate Fuel Cells, Batteries in Load Leveling, etc.

New Materials & New Processes Non-electric Aluminum Production, Silicon Carbide Fibers, Polycarbon-Monofluoride Chlor-Alkali Cells with Ion-Exchange Membrane, Development of Ferrite and New Metal Anode, Reliable and Low Cost Printed Boards, Metal Hydrides for Energy Conversion, New Lithium Ion Conductor Li_3PO_4, Electrochemical Oxygen Remover, Recent Advances in HID Lamp, etc.

Electronics, Medical, etc. Recent Progress in Solid State Electronics, Electret Transducers for Audio Frequencies, Transition Metal Carbides, Sympathetic Nervous Control of the Heart, etc.

2 "Progress in Batteries & Solar Cells" Vol. 4 (1982), 400 Pages

Edited by A. Kozawa, K. V. Kordesch, H. Tamura, E. Voss, H. Joseph, H. Shimotake, etc. About 400 pages. Published by JEC Press Inc. $55. (Shipping $18 for air, $6 for surface) Contents: about 100 articles under "View From The Top," "Miniature Cells, Li-cells, Silver Cells, etc.," "MnO_2 and MnO_2 Cells," "Lead-acid Batteries," "Electric Vehicles, Fuel Cells, Military or Energy-Related Batteries," "Ni-Cd, Ni-H_2, and Other Rechargeable Batteries," "Solar Cells, Photoelectrochemical Cells," "Patents and News."

3 Battery Active MnO_2 Samples and New Carbon Samples for Batteries

I.C. No. 1 Electrolytic MnO_2 made by Ti anode
I.C. No. 2 Electrolytic MnO_2 made by Pb anode
I.C. No. 3 Electrolytic MnO_2 made by C anode
I.C. No. 4 Electrolytic MnO_2
I.C. No. 5 Chemically prepared MnO_2
I.C. No. 6 Beta MnO_2
I.C. No. 7 Natural MnO_2 ore
I.C. No. 9 Electrolytic MnO_2 (coarse grade)
I.C. No. 10 Electrolytic MnO_2
I.C. No. 12 Chemical MnO_2
I.C. No. 13 Natural MnO_2 ore (Comilog)
I.C. Carbon No. 1 (graphite)
I.C. Carbon No. 2 (acetylene black)

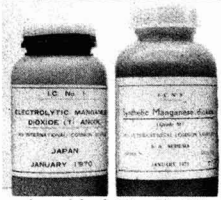

Price: MnO_2 $18 per bottle (1 Kg, except No. 6, 500g). **Carbon** $18 per bottle, **graphite** (No. 1) 400g per bottle, acetylene black (No. 2), 450g. **Shipping charge:** about $4 for surface and about $18 for air.

4 Manganese Dioxide Symposium, Vol. 2 (Tokyo) 1980, 700 pages

Compiled and Edited by B. Schumm, Jr., H. M. Joseph and A. Kozawa (The I.C. Sample Office). $48 (Shipping: $6.00 surface and $18 for air). This book is a collection of full papers presented at the 2nd MnO_2 Symposium in Tokyo with the discussions in the meeting.

5 Other Books on Carbon, Battery and Electrochemistry in English

1. **Surface Electrochemistry by T. Takamura and A. Kozawa,** $50, 250 pages (Hard cover book)
2. **Rechargeable Batteries in Japan by Y. Miake and A. Kozawa,** $45, 528 pages (Hard cover book)
3. **Manganese Dioxide Symposium Vol. 1 by A. Kozawa and R. J. Brodd,** $48, 535 pages
4. **Progress in Batteries & Solar Cells, Vol. 2, 3,** $48, 300-400 pages
5. **Electrochemistry of MnO_2 and MnO_2 Batteries,** $35, 400 pages
6. **An Electric Car and Lead-Acid Batteries,** $25, 154 pages
7. **Recent Carbon Technology by Ishikawa and Nagaoki, $55,** about 400 pages
8. **Applications of Solid Electrolyte by T. Takahashi and A. Kozawa,** $48, 210 pages.

6 MnO_2 Brussels Meeting, Sept. 15 and 16, 1983, write to the I.C. Sample Office below

How To Order

Please send your order for (1), (2) and (5) above to JEC Press, P.O. Box 35241, Cleveland, Ohio 44135 USA. Please send orders for (3), (4) and (6) above to the I.C. Sample Office, Box 45035, Cleveland, Ohio 44145 USA (Tel: 216-835-7695)

APPLICATION FOR ADMISSION
TO
The Electrochemical Society, Inc.

Return completed application to:

Secretary
The Electrochemical Society, Inc.
10 South Main Street, Pennington, New Jersey 08534-2896
609-737-1902

For office use only

Date Rec'd. _____ $ _____

Notice of Ackn. _____

Checked: _____

Approved: _____

To the Board of Directors of The Electrochemical Society, Inc:

Please print complete name and address as it should appear on mailings.

Name: _____

Address: _____

_____

_____

_____

_____

Business Telephone: (include area code) _____

I hereby make application for admission to The Electrochemical Society, Inc., as a _____ member, and enclose the amount of $ _____ covering the first year's dues. (Please see reverse side for proper class of membership and dues applying thereto, noting the options with regard to the date of election and active life membership and the credit available for nonmember meeting registration.)

1. Date of Birth: _____ (month) _____ (day) _____ (year)

2. Please check LOCAL SECTION with which you wish to affiliate:

— Boston (05)
— Chicago (10)
— Cleveland (15)
— Columbus (20)
— Detroit (25)
— European (27)
— Indianapolis (30)
— Metropolitan N.Y. (35)
— Midland (Mich.) (40)
— Natl. Capital Area (45)
— North Texas (55)
— Ontario-Quebec (60)
— Oregon (62)
— Pacific Northwest (65)
— Philadelphia (70)
— Pittsburgh (75)
— Rocky Mountain (80)
— San Francisco (85)
— So. Calif.-Nevada (90)
— Southern Wisconsin (92)
— Twin Cities (96)
— None (99)

3. Please indicate your DIVISIONAL and GROUP interests, noting your primary interest(s) with the number 1 and secondary interest(s) with the number 2.

— Battery (AO)
— Corrosion (BO)
— Dielectrics and Insulation (CO)
— Electrodeposition (DO)
— Electronics (EO)
☐ New Electronic Technologies (E1)
☐ Semiconductors (E3)
— Energy Technology (GO)
— High Temperature Materials (HO)
— Industrial Electrolytic (IO)
— Luminescence and Display Materials (KO)
— Organic and Biological Electrochemistry (FO)
— Physical Electrochemistry (JO)

4. Education:

Institution	Dates Attended	Major Subject	Degree Earned

5. Work Experience:

Name of Employer (current, followed by previous)	Dates	Position

6. The Society's Constitution provides that two Active Members of the Society (who can substantiate the above record) must recommend you for admission to membership. It will facilitate the handling of your application if you are able to have your references sign this application form; if this is not convenient, please list their names and addresses. On a student application, only a single faculty member recommendation with signature (including title and and institution) is required.

Name (please print)	Signature	Address
Name (please print)	**Signature**	**Address**

The undersigned certifies that the above statements are correct and agrees, if elected to the Society, to be governed by its Constitution and Bylaws and to promote the objects of the Society as stated in its Constitution.

Date _____ 19 —

_____
(Signature)

Rev. 9/82

EXTRACTS FROM THE CONSTITUTION AND BYLAWS

CONSTITUTION—Article II

Membership

Section 1. The individual membership shall consist of Active, Honorary and Emeritus Members. The Board of Directors may from time to time authorize other classifications of membership as defined in the Bylaws of the Society.

(Active Member—Annual Dues $50.00)

Active Member

Section 2. An Active Member shall be interested in electrochemistry or allied subjects and possess a Bachelor's degree, or its equivalent, in engineering or natural science. In lieu of a Bachelor's degree, or its equivalent, any combination of years of undergraduate study and years of relevant work experience in electrochemistry or allied subjects adding to at least seven years shall be required. Election to Active Membership shall require the recommendation of two Active Members in good standing.

BYLAWS—Article II

Non-Voting Membership
(Student Member—Annual Dues $10.00)

Student Member

Section 1. Student Member. A Student Member shall be a full-time undergraduate or graduate student registered for a degree in natural science or engineering. The applicant for Student Membership shall be recommended by a member of the faculty of the school. Upon graduation with a Bachelor's degree or equivalent in natural science or engineering, the Student Member may apply for Active Membership. The application shall be approved by two Active Members of the Society in good standing. If the Student Member enters graduate school as a full-time student, the person may choose to apply for Active Membership or remain a Student Member.

BYLAWS—Article XXI

Dues and Fees

Dues

Section 1. The annual dues for Active Members shall be fifty dollars. The annual dues for Student Members shall be ten dollars. Each member shall receive the JOURNAL OF THE ELECTROCHEMICAL SOCIETY.

Date of Election

Section 2. When individuals are elected to membership, they must elect to initiate their membership as of January 1 or July 1 of the year of election; or, if elected during the last quarter, January 1 of the year following election. In the case of a July 1 election for starting membership, dues will be prorated.

Active Life Membership

Section 3. Any Active Member who shall pay in one lump sum the amount equivalent to two-thirds of the remaining dues to age sixty-five at the time of payment, but not less than an amount of 5 years of full dues, shall be exempt from payment of any further dues and shall be considered an Active Member during the remainder of his or her life.

BOARD OF DIRECTORS ACTION OF OCTOBER 9, 1960

Nonmember Meeting Registration Credit

If application for new membership is received within four months of the payment of nonmember registration at a Society Meeting by the applicant, the difference between the nonmember and member registration fees shall be credited toward the first year's dues.

CONSTITUTION—Article III

Admission and Dismissal of Members

Section 1. Application for individual membership shall be in writing on a form adopted by the Board of Directors.

Section 2. The Admissions Committee shall be a rotating committee consisting of three members. One member shall be appointed each year by the President with the approval of the Board of Directors for a term of three years to replace the outgoing member. This Committee shall receive from the Secretary all properly executed and properly recommended applications for admission which he has received from persons desirous of becoming members of the Society. It shall be the duty of this Committee, after examining the credentials of applicants, to make appropriate recommendation to the Board as to approval or rejection of the applications. Unanimous approval of an applicant by this Committee shall be required before the candidate's name may be submitted to the Board of Directors for election. The election to membership shall be by a mail vote of the Board of Directors. The candidate shall be considered elected two weeks after the date the proposed membership list is mailed to the Board if no negative votes have been received by the Secretary. If a candidate receives one negative vote, his application shall then be considered and voted upon at the next meeting of the Board of Directors. Two negative votes cast at this meeting shall exclude a candidate. The Board of Directors may refuse to elect a candidate who, in its opinion, is not qualified for membership. The names of those elected shall be announced to the Society. Duly elected candidates shall have all the rights and privileges of membership as soon as their entrance fee, if any, and dues for the current year have been paid.

Section 3. A member desiring to resign shall send a written resignation to the Office of the Society.

Section 4. Upon the written request of ten or more Active Members that, for cause stated therein, a member be dismissed, the Board of Directors shall consider the matter and, if there appears to be sufficient reason, shall advise the accused of the charges against him. He shall then have the right to present a written defense, and to appear in person before a meeting of the Board of Directors, of which meeting he shall receive notice at least twenty days in advance. Not less than two months after such meeting the Board of Directors shall finally consider the case and, if in the opinion of the majority of the Board of Directors a satisfactory defense has not been made and the accused member has not in the meantime tendered his resignation he shall be dismissed from the Society.

Section 7. The entrance fee, if any, annual dues and any other payments to be made by the members of the Society shall be paid in accordance with regulations set forth in the Bylaws.

Section 8. Any member delinquent in dues after April 1 shall not receive the Society's publications and will not be allowed to vote in any Society election until such dues are paid. All members in arrears for one year after April 1 shall lose their membership status and can be reinstated only by action of the Board of Directors.

Call for Papers
164th Meeting,
Washington, D.C., October 9-14, 1983

Divisions which have scheduled sessions are listed on the overleaf, along with the symposium topics.

1. Symposium Papers.

Authors desiring to contribute papers to a symposium listed on the overleaf should check first with the symposium chairman to ascertain appropriateness of the topic.

2. General Session Papers.

Each of the Society Divisions or Group which will meet in Washington, D.C., can plan a general session. If your paper does not fit readily into a planned symposium, you should specify "General Session."

3. To Submit a Meeting Paper.

Each author who submits a paper for presentation at a Society Meeting must do three things:

A—Submit one original 75-word abstract of the paper on the attached form or a facsimile thereof. **Deadline for receipt of 75-word abstract is May 1, 1983.**

B—Submit original and one copy of an Extended Abstract of the paper. **Deadline for receipt of Extended Abstract is June 1, 1983.** See (6) below for details.

C—Determine whether the meeting paper is to be submitted to the Society Journal for publication. See (7) below for details.

Send all material to The Electrochemical Society, Inc., 10 South Main Street, Pennington, NJ 08534-2896.

Unless the 75-word and required Extended Abstracts are received at Society Headquarters by stated deadlines, the papers will not be considered for inclusion in the program.

4. To Submit a Recent News Paper.

Recent News Papers and Extended Recent News Papers are invited for this meeting. Each author must submit one of the following items to the Session Chairman:

A—Triplicate copies of a 75-word abstract of a Recent News Paper, for a 10-minute presentation. Deadline for receipt is August 23, 1983.

B—Triplicate copies of a 75-word abstract and, also, a 200-300 word abstract of an Extended Recent News Paper, for a 20-minute presentation. Deadline for receipt is August 16, 1983.

Send all material to the appropriate Session Chairman listed, for Recent News Papers only.

5. Meeting Paper Acceptance.

Notification of acceptance for meeting presentation, along with scheduled time, will be mailed to authors with general instructions no earlier than two months before the meeting. Those authors who require more prompt notification are requested to submit with their abstracts a self-addressed postal card with full author-title listing on the reverse.

6. Extended Abstract Volume Publication.

All scheduled papers will be published in the EXTENDED ABSTRACTS volume of the meeting. The volume is published by photo-offset directly from typewritten copy submitted by the author. Please note that the EXTENDED ABSTRACTS will be in a new double column format. Please follow the NEW instructions listed below.

A—Abstracts are to be from 500 to 1000 words in length. The abstract should contain to whatever extent practical all significant data to be presented during oral delivery.

B—Abstracts are to be typed single spaced on the special double column typing forms which are sent to each author after the submission of a short abstract. The text of the abstract must not exceed two (2) columns in length. An additional two columns is permitted for figures if necessary. The maximum size of four columns has been established as formal operating policy to maintain reasonable publication costs, and papers exceeding this limit may be returned or rejected.

C—Title of paper is to be in capital letters centered. Author(s) name, affiliation, and address is typed immediately below in capital and lower case letters centered.

D—All tables and figures must be securely mounted on the special typing guides within the margins; rubber cement is recommended for this purpose. What is submitted will be reproduced photographically exactly as it is sent. However, it will be reduced so that graphs and tables will be half their original size. Keep the lettering large enough to be legible when later reduced to half size. Place references and figures after the text.

E—Mail original and one copy of the abstract to: The Electrochemical Society, Inc., 10 South Main St., Pennington, NJ 08534-2896.

7. Manuscript Publication in Society Journal.

All meeting papers upon presentation become the property of The Electrochemical Society, Inc. However, presentation incurs no obligation to publish. If publication in **Journal** is desired, papers should be submitted as promptly as possible in full manuscript form in order to be considered. If publication elsewhere after presentation is desired, written permission from Society Headquarters is required.

Washington, DC, Meeting Symposia Plans—Fall 1983
October 9-14, 1983

a.) For receipt no later than May 1, 1983, submit a 75-word abstract of the paper to be delivered on the attached overleaf.
b.) For receipt no later than June 1, 1983, submit two copies of an extended abstract, 500-1,000 words.
c.) Send all abstracts to The Electrochemical Society, Inc., 10 South Main Street, Pennington, NJ 08534-2896 with the exception of Recent News Papers. For Recent News Papers see preceding page.

BATTERY

Secondary Alkaline Batteries

This symposium will provide a forum for discussion of theoretical and applied research in secondary alkaline batteries. The symposium will focus on the development of components to extend cycle life, reduce costs and improve energy density. Among the alkaline systems of interest are nickel-hydrogen, nickel-zinc, nickel-iron, zinc-air, nickel-cadmium, iron-air, and silver-zinc.

Topics which are encouraged for this symposium are as follows: 1. fundamental studies and reaction mechanisms; 2. analytical techniques for characterization of components; 3. effects of electrode and electrolyte additives; 4. methods of component and cell testing and failure analyses; 5. modeling of electrodes and battery designs; 6. synergistic effects between components; 7. component selection and design related to application requirements; and 8. fabrication processes.

Suggestions and inquiries should be sent to the Symposium Co-Chairmen: R. L. Beauchamp or B. L. McKinney, Johnson Controls, Inc., P.O. Box 591, Milwaukee, WI 53201.

Flow Batteries

Flow batteries are presently being developed for load leveling and electric vehicle applications. The advantages of the flow batteries are the continuous supply and removal of reactants and products, good mass transport, external storage of active reactants, and flexibility of operation.

Papers are solicited on the general subject of flow batteries, their design, performance, and applications. Both reviews and original papers are being invited on flow batteries including zinc-chlorine, zinc-bromine, hydrogen-halogens, redox flow batteries, regenerative redox batteries, and other novel batteries.

The publication of a proceedings volume is being considered. Papers published in a proceedings volume may also be submitted to the **Journal.**

Suggestions and inquiries should be sent to the Symposium Chairman: J. Jorné, Dept. of Chemical Engineering, University of Rochester, Rochester, NY 14627.

Lithium Batteries

This symposium will aim at covering a wide spectrum of topics on the lithium battery technology, starting from exploratory and basic studies to the development, engineering, and the manufacturing of commercially available cells. The purpose is to bring together all of the technical issues that have an impact on the commercial success of the lithium batteries. The symposium will be limited to the ambient temperature batteries only and will include both the primary and the secondary batteries.

Papers are solicited on the following topics: 1. exploratory studies on new electrochemical couples and on new electrolytes; 2. basic studies on Li and alloy electrodes, on various positive electrodes and on electrolytes; 3. safety studies; 4. development of new cell sizes and shapes; 5. performance characteristics of lithium batteries in new applications; and 6. manufacturing technologies.

The publication of a proceedings volume is being considered. Papers published in a proceedings volume may also be submitted to the **Journal.**

Suggestions and inquiries should be sent to the Symposium Chairman: A. N. Dey, Duracell Inc., Laboratory for Physical Science, Third Ave., Burlington, MA 01803.

General Session

Papers concerning any aspect of batteries not included in the topic areas of the symposia are welcome.

Suggestions and inquiries should be sent to the Session Chairman: E. G. Gagnon, General Motors Corp., Research Laboratories, Electrochemistry Dept., Warren, MI 48090-9055.

BATTERY/ENERGY TECHNOLOGY

Advances in Battery Materials and Processes

Papers are solicited on the recent progress in battery science and engineering. It is intended that this symposium should summarize the state-of-the-art and underline the growing interest in all battery systems. It is hoped that we will have adequate representation from such diverse areas as aqueous and nonaqueous batteries as well as molten salt and solid electrolyte batteries. Emphasis should be placed on the novel aspects of materials, processes, and related problems.

Papers are solicited in such areas as: 1. electrocatalysis for battery systems; 2. battery electrodes and cell materials; 3. battery separators; 4. new electrolytes; 5. battery corrosion problems; 6. energy efficiency of battery systems; 7. modeling and optimization; and 8. novel battery testing methods.

The symposium will consist of invited papers in key areas and contributed papers. The publication of a proceedings volume is being considered. Papers published in a proceedings volume may also be submitted to the **Journal.**

Suggestions and inquiries should be sent to the Symposium Co-Chairmen: D-T. Chin, Dept. of Chemical Engineering, Clarkson College of Technology, Potsdam, NY 13676; J. McBreen, Brookhaven National Laboratory, DAS Building 801, Upton, NY 11973; A. C. C. Tseung, Dept. of Chemistry, The City University, London, England, EC1V OHB; or R. S. Yeo, Pinnacle Research Institute, 10432 N. Tantau Ave., Cupertino, CA 95014..

BATTERY/PHYSICAL ELECTROCHEMISTRY

Alkaline and SPE Fuel Cells, Electrolyzers and Regenerative Systems

Fuel cells and water electrolyzers have been used to generate primary power and electrolyze water respectively for many years. New system concepts incorporating fuel cells with an electrolyzer unit as part of a rechargeable energy storage system have recently appeared. Electrochemical compressors, carbon dioxide scrubbers, and hydrogen generators have also been made based on alkaline and/or SPE technologies. The electrocatalysts, the materials of construction, the electrolyte volume, and water management techniques of these technologies are quite different. This symposium will cover a wide spectrum of topics. Papers are being solicited that focus on the fundamental electrochemistry, the materials of construction and associated construction techniques, the contemporary hardware performance and life test results, and finally conceptual system configurations with their projected performance levels.

Suggestions and inquiries should be sent to the Symposium Co-Chairman: L. H. Thaller, NASA Lewis Research Center, MS 301-3, 21000 Brookpark Rd., Cleveland, OH 44135; or J. McBreen, DEE, 801, Brookhaven National Laboratory, Upton, NY 11973.

CORROSION

General Session

Papers on all aspects of low and high temperature corrosion and associated phenomena will be considered. Experimental techniques for the study of corrosion processes and corrosion products are also of interest.

Suggestions and inquiries should be sent to the Session Chairman: F. Mansfeld, Rockwell International Science Center, 1049 Camino Dos Rios, Thousand Oaks, CA 91360.

CORROSION/EUROPEAN FEDERATION OF CORROSION

Fundamental Aspects of Corrosion Protection by Surface Modification

This symposium will focus on the fundamental behavior and properties of metal surface which exhibit enhanced corrosion resistance due to surface modification. Subjects of interest include basic mechanisms of corrosion protection by surface modification, fundamental properties of physically or chemically modified surfaces, and recent progress and new approaches in surface modification.

Contributions are requested which consider all types of corrosion processes that respond to surface modification. Thus, subjects include, but are not limited to: aqueous corrosion, localized corrosion, mechanically assisted corrosion, high temperature oxidation and corrosion, and atmospheric corrosion.

Topics of interest include: 1. surface modification by directed energy beams, including ion implantation, ion mixing, laser-surface alloying and melting, and electron beam processing; 2. chemical modification of surfaces by permanently attached chemical species, such as covalently bonded organic molecules; 3. modification of surface oxide films; and 4. emerging new techniques or novel methods of surface modification.

The publication of a proceedings volume, which will be available at the symposium, is being planned. Camera-ready manuscripts are required by the Symposium Co-Chairmen by May 1, 1983. Detailed instructions on manuscript preparation for the proceedings volume are available from the Symposium Co-Chairmen. Papers published in a proceedings volume may also be submitted to the **Journal.**

Suggestions and inquiries should be sent to the Symposium Co-Chairmen: E. McCafferty, Naval Research Laboratory, Code 6314, Washington, DC 20375; C. R. Clayton, Dept. of Materials Science, State University of New York, Stony Brook, NY 11794; P. A. Parrish, Army Research Office, P.O. Box 12211, Research Triangle Park, NC 27709; or J. Oudar, Universite Pierre et Marie Curie, Laboratoire de Physico-chimie des Surfaces, Ecole Nationale Superieure de Chimie de Paris, 75231 Paris Cedex 05, France.

CORROSION/PHYSICAL ELECTROCHEMISTRY

Hydrodynamic Effects of Corrosion

Contributions are invited on the full range of hydrodynamic aspects of corrosion. These could be from fundamental to practical studies as indicated by the following examples: 1. effect of convective mass transfer on the rate of corrosion reactions; 2. engineering correlations for specific flow systems; 3. forced hydrodynamic modulations of localized corrosion reactions; 4. effect of natural convection on pitting, crevice corrosion, and stress corrosion cracking; 5. mass transfer and solubility effects on the formation and stability of passivating films; 6. new measurement techniques to study hydrodynamic effects on corrosion; and 7. periodic or cyclic corrosion reactions and the influence of hydrodynamics.

Suggestions and inquiries should be sent to the Symposium Co-Chairmen: W. H. Smyrl, Sandia National Laboratories, Albuquerque, NM 87185; or R. C. Alkire, Dept. of Chemical Engineering, University of Illinois, Urbana, IL 61801.

DIELECTRICS AND INSULATION/CORROSION/ELECTRONICS

Materials Problems in Device Packaging

Papers are requested concerning all aspects of materials problems in semiconductor device packaging. This includes problems leading to corrosive and environmental

degradation of device operation, and may include effects of processing, mass transport, radiation, electrochemical reactions, and mechanical stress. Reports on new techniques that inhibit or prevent environmental degradation, or that can nondestructively evaluate the onset of materials degradation are encouraged.

Publication of a proceedings volume is being considered. Papers published in a proceedings volume may also be submitted to the **Journal.**

Suggestions and inquiries should be sent to the Symposium Co-Chairmen: M. W. Kendig, Rockwell International Science Center, 1049 Camino Dos Rios, P.O. Box 1085, Thousand Oaks, CA 91360; or W. L. Hunter, Motorola, Inc., B-136, 5005 E. McDowell Rd., Phoenix, AZ 85008.

DIELECTRICS AND INSULATION/ ELECTRONICS

Patterning Science and Technology 1983

A symposium will be held to discuss various aspects of the microlithographic processes and materials used in the fabrication of silicon and compound semiconductor integrated circuits, printed circuit boards, information storage devices, and other novel applications. Of special interest are techniques to characterize and control these processes and materials.

Original work or substantial review papers are solicited for the following topics: 1. resists: organic and inorganic materials (for photon, x-ray, electron, and ion source exposure), chemistry, characterization, processing techniques (coating, exposure, development, baking, stripping); 2. printing: new techniques and equipment (or substantive extensions of older ones) for transferring patterns into resists (photon, x-ray, electron and ion beam); measurement and control of overlay accuracy and image distortion; mask technology (fabrication inspection, repair, and cleaning); 3. pattern transfer: selective material removal (plasma, ion-assisted, sputter and wet chemical etching) or selective material addition (lift-off, plating, vapor deposition); dimensional control in microlithography (multilevel resist systems, proximity corrections, optical and electrical measurement methods); 4. modeling: image formation in resists, pattern transfer, resist processing lithographic yield, limits of lithographic processes; and 5. device results: high resolution devices and structures that exemplify the application of advanced micro'ithographic techniques.

Suggestions and inquiries, as well as comments on the structure of this symposium, should be sent to the Symposium Co-Chairmen: N. Goldsmith, RCA Laboratories, Princeton, NJ 08540; A. M. Voschenkov, Bell Laboratories, Crawfords Corner Rd., Ho'mdel, NJ 07733; or A. McCullough, Perkin-Elmer Corp., M/S 283, Main Ave., Norwalk, CT 06852.

Thin Film Interfaces and Interactions

This symposium will cover a range of topics in manufacturing science and technology, characterization, and device applications of thin-film insulators and interfaces for semiconductor integrated circuits including: 1. thin gate insulators including oxides, thermal oxynitrides and deposited dielectrics with regard to interface traps, slow-trapping effects, hot-electron effects, dielectric breakdown, and time-dependent breakdown; 2. interlevel insulators including deposited and thermally grown dielectrics for polysilicon, silicide and multilevel metal structures; and 3. tunneling dielectrics for floating-gate EEPROM applications with regard to interface and bulk trap generation, effects of electrode texture, degradation mechanisms, and long-term reliability.

The publication of a proceedings volume is being considered. Papers published in a proceedings volume may also be submitted to the **Journal.**

Suggestions and inquiries should be sent to the Symposium Co-Chairmen: L. Faraone, RCA Laboratories, Princeton, NJ 08540; and E. Nicollian, Bell Laboratories, Murray Hill, NJ 07974.

ELECTRODEPOSITION

Nonaqueous Electrodeposition Processes

This symposium will be devoted to the application of both molten salts and organic solvents as electrodeposition solvent systems and will include both fundamental concepts and engineering applications.

Topics of interest for the molten salt sessions include, but are not limited to: mass transport and current distribution studies; preparation of elemental, alloy, and compound coatings; the influence of solvent and plating techniques on deposit properties and structures; and electrowinning.

The organic solvent sessions will include papers on: anodic, cathodic, and solution processes involved in the deposition of substances from nonaqueous systems and the influence of solvent and plating techniques on the deposit properties. Papers on the deposition of metals in the charging of nonaqueous batteries are also invited.

Suggestions and inquiries on the molten salt program should be sent to the Symposium Co-Chairman: D. Flinn, U.S. Bureau of Mines, 4900 La Salle Rd., Avondale, MD 20782. Suggestions and inquiries on the organic solvent program should be sent to the Symposium Co-Chairman: T. C. Franklin, Dept. of Chemistry, Baylor University, Waco, TX 76798.

General Session

Orlginal papers dealing with theoretical, experimental, and applied aspects of electrodeposition, and that do not fall within the field of other Electrodeposition symposia, are invited for this session. Experimental techniques for the study of the resulting deposits are also of interest.

Suggestions and inquiries should be sent to the Session Chairman: R. E. Acosta, IBM T. J. Watson Research Center, P.O. Box 218, Yorktown Heights, NY 10598.

ELECTRODEPOSITION/CORROSION

Electric Contacts, Connectors, and Interconnections

This symposium will include topics in the design, fabrication, characterization, and testing of electrical contacts, connectors, and device interconnections in electronic equipment for telecommunications, computer, automotive, military, aerospace, and consumer products. Suggested subjects include: 1. electrodeposition for static and separable electrical connectors: precious metals, base metals, precious metal substitutes, and alloys; 2. electrodeposited interconnections for microcircuits and microcircuit packaging: pattern plating, uniformity, bonding, reliability, and interdiffusion; 3. materials and processes for connectors: metallurgical properties, adhesion, wear, and fretting; 4. environmental effects on contact materials: corrosion and tarnishing, testing procedures, validity of testing environments, and reproducibility.

Both original papers and reviews on these and related topics are solicited.

Suggestions and inquiries should be sent to the Symposium Co-Chairmen: J. M. Deuber, Degussa Corp., Rt. 46 and Hollister Rd., Teterboro, NJ 07608; or W. O. Freitag, Sperry-Univac, E8-134, Box 500, Blue Bell, PA 19424.

ELECTRONICS

Business and Government Aspects of the Semiconductor Industry

The semiconductor industry has grown to a size that has attracted interest of financial institutions and government organizations, among others. That growth, and the impact of semiconductor technology on the electronic products that are made possible by semiconductor devices, is expected to continue. Issues related to international competition, balance of payments, national defense, employment, transfers of technology, and the like are discussed with increasing frequency in the press and other media. These issues have technological roots and wide effects, and can be expected to affect the semiconductor industry in the future in ways that are difficult to forecast. Papers are invited that deal with the above or similar topics. Preference will be given to authoritative, tutorial submissions that give some historical perspective, discuss the present state of affairs, and provide insight on what may be expected to occur, in a manner that will interest a largely technological audience.

Suggestions and inquiries should be sent to the Symposium Chairman: R. I. Scace, National Bureau of Standards, A305 Technology, Washington, DC 20234.

ELECTRONICS/DIELECTRICS AND INSULATION

High Pressure Oxidation for Semiconductor Devices

This symposium will focus on the application of high pressure processing, particularly oxidation, to the fabrication of semiconductor devices and integrated circuits. Emphasis will be placed on those applications where high pressure processing offers a specific advantage over conventional atmospheric processes. Papers are solicited on the following and related topics: 1. oxidation kinetics at high pressure for materials used in semiconductor devices; 2. dopant diffusion, redistribution, segregation, and enhanced diffusion during oxidation; 3. heavy doping effects in high pressure processing; 4. physical properties of high pressure grown oxides such as: refractive index, dielectric constant, density, and stoichiometry; 5. electrical properties of oxides grown at high pressure such as bulk and interfacial charge densities, dielectric strength, and polarization; 6. local oxidation using high pressure; 7. defect formation during high pressure/low temperature processing; 8. oxide-ambient interaction during high pressure processing.

Suggestions and inquiries should be sent to the Symposium Co-Chairmen: R. R. Razouk, Fairchild Advanced R&D, Palo Alto, CA 94304; or L. E. Katz, Bell Laboratories, Allentown, PA 18103.

Semiconductor Interconnects and Contacts

This symposium addresses scientific and technological issues pertinent to the formation and performance of thin-film interconnections and contacts in silicon and compound semiconductor devices. Papers are solicited on experimental and theoretical investigations concerning materials for, processes relevant to, and the characteristics of multilevel interconnections and metal-semiconductor contacts. The manufacturing aspects will be included as far as they elucidate basic features and technology achievements. The scope of the symposium includes: 1. interconnections and contact formation processes such as deposition techniques, pattern delineation; 2. characterization of thin-film materials (metals, insulators, silicides, nitrides, etc.) for interconnections and contacts; 3. present and future device application with particular emphasis on small geometry fine line definition and its limitations; 4. interface studies between metal to metal, metal to semiconductor, and metal to insulator, relevant to interconnections and contacts; 5. physical and chemical changes under thermal, electrical, and chemical stresses such as thermal annealing, electromigration, oxidation of silicides, and corrosion; 6. electrical performance such as ohmic contact to shallow junction, contact resistivity, Schottky barrier contact, line signal delay and dispersion; 7. device modeling of interconnections and contacts.

Suggestions and inquiries should be sent to the Symposium Co-Chairmen: C. Y. Ting, IBM T. J. Watson Research Center, P. O. Box 218, Yorktown Heights, NY 10598; or M.-A. Nicolet, California Institute of Technology, 116-81, Pasadena, CA 91125.

Joint General Session

Papers that deal with all aspects of materials of interest for electronic devices including their preparation, characterization, interactions, and device applications, and whose subject matter is not covered by the special symposia are invited to be submitted to this session. Also invited are papers on the basic chemistry and physics of materials processing, and computer modeling of the formation and of the characterization of materials and devices. Of particular interest are new materials and processes.

Suggestions and inquiries should be sent to the Session Co-Chairmen: P. L. Castro, Hewlett-Packard Laboratories, 3500 Deer Creek Rd., Palo Alto, CA 94304; P. Rai-Choudhury, Westinghouse R&D Center, Power Devices, Beulah Rd., Pittsburgh, PA 15235; or G. C. Schwartz, IBM Corp., Dept. 206, Bldg. 300-48A, Hopewell Junction, NY 12533.

Joint Recent News Papers Session

Recent News Papers and Extended Recent News Papers consisting of topics covered by the symposia and sessions being sponsored or cosponsored by the Electronics and Dielectrics and Insulation Divisions are invited for presentation.

Suggestions and inquiries should be sent to the Session Chairman: G. C. Schwartz, IBM Corp., Dept. 206, Bldg. 300-48A, Hopewell Junction, NY 12533. A special Call for Recent News Papers will appear in the June, July, and August 1983 issues of the **Journal**.

ELECTRONICS/PHYSICAL ELECTROCHEMISTRY

Electrochemistry in Semiconductor Technology

The purpose of this symposium is to provide an interdisciplinary forum which permits researchers in the diverse areas of solution electrochemistry and solid-state device electronics to discuss problems of mutual interest. Papers are sought addressing all applications of electrochemistry and photoelectrochemistry to semiconductor technology, including the following specific topics: 1. measurement of semiconductor electronic properties, 2. passivation of surfaces and interfaces, 3. doping, 4. etching, 5. contact pattern generation, 6. heterojunction and Schottky barrier formation, 7. thin-film semiconductor deposition, and 8. new application and devices based on the semiconductor/liquid junction (excluding solar cells).

Suggestions and inquiries should be sent to the Symposium Co-Chairmen: D. L. Nelson, Office of Naval Research, 800 North Quincy St., Arlington, VA 22217; or R. D. Rauh, EIC Laboratories, Inc., 111 Chapel St., Newton, MA 02158.

ENERGY TECHNOLOGY

General Session

Papers are solicited in areas of energy conversion and storage not covered by current symposia. Of particular interest are new developments in photoelectrochemistry, and novel methods for energy storage and transmission. Suggestions and inquiries should be sent to the Session Co-Chairmen: A. J. Appleby, EPRI, P.O. Box 10412, Palo Alto, CA 94303; or A. J. Nozik, SERI, 1617 Cole Blvd., Golden, CO 80401.

ENERGY TECHNOLOGY/BATTERY

Operational Experience with Emerging Energy Conversion and Storage Technologies

With the recent emphasis on the development of new energy technologies, several major programs on energy conversion and storage have been launched by the government, research institutes, and private industry in the United States and abroad. It is the object of this symposium to present the results and operational and economic feasibility of such projects. Both the testing of prototypes at the developer site under simulated conditions and actual field testing, either in progress or completed, are of interest.

Topics of interest include solar energy conversion, fuel cells, electrical energy storage, electric vehicles, and others employing electrochemical devices or processes. Proposed papers may cover the following aspects: engineering of a prototype or field unit, life and performance data, steady-state and transient response, practical experience in dealing with local conditions, regulations, environmental and safety considerations, maintenance requirements, equipment modification and data analysis.

Suggestions and inquiries should be sent to the Symposium Co-Chairmen: A. R. Landgrebe, Dept of Energy, MS IG-080, FORSTL, Washington, DC 20585; H. C. Maru, Energy Research Corp., 3 Great Pasture Rd., Danbury, CT 06810; or V. K. Kapur, ARCO Solar, Inc., 20554 Plummer St., Chatsworth, CA 91311.

ENERGY TECHNOLOGY/BATTERY/ INDUSTRIAL ELECTROLYTIC/ PHYSICAL ELECTROCHEMISTRY

Oxygen Electrodes for Energy Applications

This symposium will focus on oxygen electrodes for various energy conversion, storage, and conservation applications including fuel cells, metal-air batteries, and oxygen-consuming and generating electrodes for industrial electrolysis. Electrolytes of interest include molten salts and solid polymer electrolytes as well as aqueous solutions. Topics to be covered will include oxygen electrode kinetics, mechanisms, and pathways for the O_2 electrode reactions, factors controlling the performance of air cathodes, new and improved O_2 electrocatalysis, models for mass transport in air cathodes, failure modes, and structural innovations.

The symposium will include several invited lectures plus contributed papers. A proceedings volume is being considered. Papers published in a proceedings volume may also be submitted to the **Journal**.

Suggestions and inquiries should be sent to the Symposium Co-Chairmen: P. N. Ross, Jr., Lawrence Berkeley Laboratory, University of California, Bldg. 52, Rm. 309, Berkeley, CA 94720; or E. Yeager, Case Center for Electrochemical Sciences, Case Western Reserve University, Cleveland, OH 44106.

HIGH TEMPERATURE MATERIALS/ CORROSION

High Temperature Erosion and Corrosion

Fundamental and applied papers are solicited to promote a thorough interdisciplinary approach to the following topics of high temperature materials erosion and corrosion: 1. erosion by inert and reactive liquid and solid particulates at low and high flow velocities, 2. mechanisms of metal oxidation and degradation of materials in pure and mixed gaseous oxidants, 3. experimental methods and techniques for determining reaction processes and properties of reaction products, 4. corrosion and erosion of metallic and ceramic materials and the associated industrial problems, 5. development of high temperature corrosion and erosion resistant materials and coatings.

Suggestions and inquiries should be sent to the Symposium Co-Chairmen: F. S. Pettit, Dept. of Metallurgical and Materials Engineering, University of Pittsburgh, Pittsburgh, PA 15261; or W. W. Smeltzer, Institute for Materials Research, McMaster University, Hamilton, Ont., Canada L8S 4M1.

HIGH TEMPERATURE MATERIALS/ ELECTRODEPOSITION/INDUSTRIAL ELECTROLYTIC

Electrodeposition of Refractory Metals

Papers are solicited for this symposium which will address the electrochemical processing, physical aspects, and applications of electrodeposited refractory metals and metalloids. Beside the advances in electrochemical processes and systems for the recovery of well-known refractory metals, emphasis will be placed on the formation of refractory metal compounds, intermetallics, and composites, together with studies of kinetics, thermodynamics, domain characterization, and any subsequent purification.

Suggestions and inquiries should be sent to the Symposium Chairman: N. E. Richards, Reynolds Metals Co., P.O. Box 1200, Sheffield, AL 35660.

INDUSTRIAL ELECTROLYTIC

General Session

Original papers concerning any aspect of industrial electrolysis not included in other scheduled symposia are invited for this session. Of particular interest are new processes, developments, techniques, and applications in industrial electrochemistry.

Suggestions and inquiries should be sent to the Session Chairman: M. P. Grotheer, Kerr-McGee Corp., Oklahoma City, OK 73125.

LUMINESCENCE AND DISPLAY MATERIALS/ELECTRONICS

Materials and Fabrication Techniques for Display Devices

The main purposes of this symposium are as follows. First, the symposium will provide up-to-date reviews on current display technologies for scientists and professionals in the discipline of materials science and technology so that an interactive dialogue with the display community will be stimulated. Second, the symposium will focus on the understanding and characterization of material problems associated with current display devices. This means to complement the display device and system conferences such as SID (society for information display) symposia which usually do not cover in-depth presentations on display material problems. Third, this symposium encourages discussions on exploratory work on display such as new and novel materials, phenomena, and effects.

Invited papers will be arranged to lead off individual sessions. Contributed papers are solicited within the general purposes of this symposium. The suggested topics are: 1. CRT technology: improvements made on CRTs and color CRTs such as phosphor materials, cathode materials, screening techniques, high resolution shadow mask contrast enhancement materials, antireflection coatings, etc. 2. Liquid crystal displays: new liquid crystal materials and fabrication techniques, properties and modeling of liquid crystals and devices, and memory effects. 3. Vacuum fluorescent displays: screen and grid materials and fabrication improvements, device packaging and integration techniques. 4. Electroluminescent displays: electroluminescent materials for displays, II-VI electroluminescent devices, EL thin films and phosphors, materials preparation and characterization, device fabrication techniques, and insulating and passivating materials for electroluminescent devices. 5. Plasma displays: fabrication and packaging techniques, material problems of d-c and a-c gas discharge devices. 6. Electrochemical displays: electrophoretic, electrochromic, and electrochemiluminescent display materials and properties, fabrication techniques and degradation studies and improvements. 7. Phosphors: long persistent phosphors, color and white phosphor for information displays and color plasma panels, low voltage phosphors, penetration phosphors, phosphor synthesis and characterization.

The publication of a proceedings volume is being considered. Papers published in a proceedings volume may also be submitted to the **Journal**.

Suggestions and inquiries should be sent to the Symposium Chairman: I. F. Chang, IBM T. J. Watson Research Center, P.O. Box 218, Yorktown Heights, NY 10598.

PHYSICAL ELECTROCHEMISTRY

The Use of Computers in Experimental Electrochemistry

The real time application of computers and microprocessors for experimental control, data acquisition, and data analysis in real time in the laboratory and in industrial processes will be the subject of this symposium. A limited number of tutorial papers will be presented.

Papers are solicited in the following areas: 1. Interfacing of instruments with multipurpose capabilities, dedicated instruments and the interconnection to computer and experiment. This may include papers on the technique themselves or special problems that can arise in a digital vs. an analog environment. 2. Real time control of experiments including the synchronization of multiple instrument systems and the generation of control signals. 3. Microprocessor-based instruments dedicated to specific tasks. 4. Interactive computer-experimental setups in which the results of real time measurements can be used to control or optimize the experiment or process.

Theoretical papers dealing with the principles of on-line information gathering and retrieval are encouraged. However, papers dealing exclusively with off-line manipulation of data will not be accepted.

Suggestions and inquiries should be sent to the Symposium Co-Chairmen: B. D. Cahan, Dept. of Chemistry, Case Western Reserve University, Cleveland, OH 44106; or J. Osteryoung, SUNY at Buffalo, Buffalo, NY 14214.

General Session

Papers concerning any aspect of physical electrochemistry not included in the topic areas of the symposia are welcome.

Suggestions and inquiries should be sent to the Session Chairman: R. A. Osteryoung, Dept. of Chemistry, SUNY at Buffalo, 264 Acheson Hall, Buffalo, NY 14214.

NEW TECHNOLOGY SUBCOMMITTEE

Reindustrialization of the United States

It is the current wisdom that the United States is losing its competitive edge. Our markets for United States that produced consumer electronics, sewing machines, and wrist watches have long since shriveled, and we are currently watching the attrition of our markets for United States-produced steel, automobiles, and semiconductor memory. To recover may require a struggle approaching an industrial revolution, but before we can embark upon this, we need to better under-

stand how and why our position has become so eroded. Education, government policy, management, investment strategy, etc., have all been identified as the villains, and, indeed, some or all of these factors are undoubtedly very important. It is not clear whether our traditional industries can find new life-saving modes or whether we shall need to find new industrial areas better matched to unique strengths and resources that have yet to be defined.

This symposium will consider these problems and what the United States might do about them, especially in the business areas that rely upon the technologies of The Electrochemical Society. It will examine the strategies that have been used in other nations to guide the research, development manufacture, and marketing of many very successful products.

Suggestions and inquiries should be sen to the Symposium Chairman: E. Pell, Xerox Corporation, 800 Phillips Rd. (W-105), Webster, NY 14580.

---

a.) For receipt no later than May 1, 1983, submit a 75-word abstract of the paper to be delivered on the attached overleaf.
b.) For receipt no later than June 1, 1983, submit two copies of an extended abstract, 500-1,000 words.
c.) Send all abstracts to The Electrochemical Society, Inc., 10 South Main Street, Pennington, NJ 08534-2896 with the exception of Recent News Papers. For Recent News Papers see preceding pages.

Use overleaf in submitting your abstract for
The 1983 Fall Meeting
of
The Electrochemical Society, Inc.
to be held at the
Sheraton-Washington Hotel
Washington, D.C.
October 9-14, 1983

75-Word Abstract Form

(Deadline for receipt—May 1, 1983)

WASHINGTON, D.C., MEETING—OCTOBER 9-14, 1983

Submit to: The Electrochemical Society, Inc.
10 South Main Street, Pennington, NJ 08534-2896

Schedule for ..... of .....
Symposium **ECS Division**

Abstract No. .....
(do not write in this space)

(Title of paper) .....

.....

(Authors) (Underline name of author presenting paper) .....

.....

(Business Affiliation and Address) .....

.....

.....
(ZIP Code) (Tel. No.)

(Type abstract in this area—double spaced.)

Do you require any audiovisual equipment?
☐ **35 mm (2 x 2 in.) slide projector**
☐ **Vu-Graph**
☐ **other (specify)**
Is a full length paper on this work to be submitted for Society Journal publication?
☐ **Yes** ☐ **No**

Papers presented before a Society technical meeting become the property of the Society and may not be published elsewhere without written permission of the Society. Papers presented at Society technical meetings must be authored by a member or sponsored by an active member.

.....
Insert name of Society member author or sponsor

SUSTAINING MEMBERS (CONTINUED)

Fairchild Camera & Instrument Corp.
Research & Development Laboratory
Palo Alto, CA

FMC Corp.
Inorganic Chemicals Div.
Buffalo, NY

Ford Motor Co.
Dearborn, MI

The Gates Corporation
Denver, CO

General Motors Corp.
Delco-Remy Div., Anderson, IN
Research Laboratories Div.
Warren, MI

Gould Inc.
Gould Research Center
Rolling Meadows, IL

Grelcon, Inc.
Niagara Falls, NY

GTE Laboratories
Waltham, MA

GTE Sylvania Inc.
Chemical & Metallurgical Div.
Towanda, PA

The Harshaw Chemical Co.
Cleveland, OH

Heliotronic GmbH
Burghausen, Germany

Hewlett Packard Co.
Loveland, CO

Hewlett Packard Laboratories
Palo Alto, CA

Hill Cross Co., Inc.
West New York, NJ

Hitachi, Ltd.
Central Research Laboratory
Tokyo, Japan

Hoechst-Uhde Corp.
Englewood Cliffs, NJ

Honeywell, Inc.
Power Sources Center
Horsham, PA

Hughes Research Laboratories
Div. of Hughes Aircraft Co.
Malibu, CA

IMI Marston Limited
Wolverhampton, England

Imperial Clevite, Inc.
Technology Center
Cleveland, OH

INCO ElectroEnergy Corp.
Engineering & Development Center
Ray-O-Vac Corp.
Madison, WI

International Lead Zinc Research Organization, Inc.
New York, NY

International Minerals and Chemical Corp.
Electrochemical Div.
Orrington, ME

Johnson Controls, Inc.
Milwaukee, WI

Kaiser Aluminum & Chemical Corp.
Pleasanton, CA

KBI
a division of Cabot Corp.
Boyertown, PA

Arthur D. Little, Inc.
Cambridge, MA

Lockheed Missiles & Space Co., Inc.
Research Laboratory
Palo Alto, CA

Marathon Battery Co.
Waco, TX

Mead Advanced Systems Research and Development Laboratories
Dayton, OH

Medtronic Energy Technology
Minneapolis, MN

Mepco/Electra, Inc.
Columbia, SC

Microwave Associates, Inc.
Burlington, MA

Molycorp, Inc.
New York, NY

Monsanto Co.
St. Louis, MO

Motorola Inc.
Phoenix, AZ

M&T Chemicals Inc.
Detroit, MI

NIFE Jungner AB
Oskarshamn, Sweden

Noranda Research Centre
Pointe Claire, Que., Canada

Occidental Chemical Corporation
Research & Development
(2 memberships)
Grand Island, NY
Udylite/Sel-Rex
Warren, MI

Occidental Research Corp.
La Verne, CA

Olin Corp.
Metals Research Laboratories
New Haven, CT

Owens-Illinois Inc.
Toledo, OH

Perkin-Elmer Corp.
Norwalk, CT

Phelps Dodge Refining Corp.
Maspeth, NY

Philips Laboratories, Inc.
Briarcliff Manor, NY

PPG Industries, Inc.
Chemical Div.
Pittsburgh, PA

Prototech Co.
Newton Highlands, MA

Public Service Electric and Gas Co.
PSE&G Research Corp.
Newark, NJ

RCA Corp.
Color Picture Tube Div.
Lancaster, PA

Reynolds Metals Co.
Reduction Research Div.
Sheffield, AL

Rockwell International
El Segundo, CA

SAFT America, Inc.
Power Sources Division,
Valdosta, GA
Advanced Battery Systems Division,
Cockeysville, MD

Sandia National Laboratories
Albuquerque, NM

Sanyo Electric Co., Ltd.
Shioya Research Center
Kobe, Japan

J. C. Schumacher Co.
Oceanside, CA

Shipley Company, Inc.
Newton, MA

Siemens Aktiengesellschaft
Munich, Germany

Signetics Corp.
Sunnyvale, CA

Siltec Corp.
Menlo Park, CA

Sperry Research Center
Sudbury, MA

Sprague Electric Co.
North Adams, MA

Standard Telecommunication Laboratories Ltd.
Essex, England

Stauffer Chemical Co.
Dobbs Ferry, NY

St. Joe Minerals Corp.
Monaca, PA

Tektronix, Inc.
Beaverton, OR

Teletype Corp.
Skokie, IL

Texas Instruments Inc.
Attleboro, MA
Dallas, TX

Tokyo Shibaura Electric Co., Ltd.
Toshiba Research and
Development Center
Kawasaki, Japan

Toyota Central Research and Development Labs, Inc.
Nagoya, Japan

Union Carbide Corp.
Battery Products Div.,
Corporate Research Dept.
New York, NY

United States Steel Corp.
Research Laboratory
Monroeville, PA

Varian Associates
Palo Alto, CA

Wacker Chemitronic
Burghausen, Germany

Western Electric
Princeton, NJ

Xerox Corp.
Webster Research Center
Rochester, NY

Yardney Electric Corp.
Pawcatuck, CT

Yuasa Battery Co., Ltd.
Osaka, Japan

THE ELECTROCHEMICAL SOCIETY PATRON MEMBERS

Bell Laboratories
Murray Hill, NJ

Dow Chemical Co.
Inorganic Chemicals Dept.
Midland, MI

Exxon Research and Engineering Co.
Corporate Research
Advanced Energy Systems Laboratory,
Materials and Catalysis Sciences Laboratory
Linden, NJ
Technology Department
Chemical Engineering Technology Div.
Materials Technology Div.
Florham Park, NJ

General Electric Co.
Battery Business Dept., Gainesville, FL
Chemical Laboratory, Knolls Atomic Power Laboratory,
Schenectady, NY
Lamp Div., Cleveland, OH
Materials & Process Laboratory, Large Steam
Turbine-Generator Dept., Schenectady, NY
Research and Development Center,
Inorganic Materials Laboratory
Schenectady, NY

General Electric Co. (continued)
Signal Processing & Communication Laboratory,
Schenectady, NY
Semiconductor Products Dept.,
Syracuse, NY

International Business Machines Corp.
New York, NY

INCO Research and Development Center
Suffern, NY

Olin Corp.
Chemicals Div.
Charleston Technology Center
Charleston, TN

Philips Research Laboratories
Eindhoven, The Netherlands

Tadiran, Israel Electronics Industries, Ltd.
Tel Aviv, Israel

Westinghouse Electric Corp.
Electronic Tube Div., Elmira, NY
Lamp Div., Bloomfield, NJ
Semiconductor Div., Youngwood, PA
Research Laboratories, Pittsburgh, PA

THE ELECTROCHEMICAL SOCIETY SUSTAINING MEMBERS

The Aerospace Corp.
Los Angeles, CA

Airco Industrial Gases
Murray Hill, NJ

Allied Corporation
C&D Batteries,
Plymouth Meeting, PA
Prestolite Div., Toledo, OH
Syracuse Research Laboratories,
Solvay, NY

Aluminum Co. of America
New Kensington, PA

AMAX Inc.
Greenwich, CT

AMP Inc.
Harrisburg, PA

Analog Devices, Inc.
Norwood, MA

Applied Materials, Inc.
Santa Clara, CA

ASARCO, Inc.
South Plainfield, NJ

Battelle Memorial Institute
Columbus, OH

Battery Technology Co.
A Division of Duracell International
Tarrytown, NY (2 memberships)

Bell-Northern Research
Ottawa, Ont., Canada

Boeing Co.
Seattle, WA

The Borg-Warner Corp.
Roy C. Ingersoll Research Center
Des Plaines, IL

BP Research Centre
Middlesex, England

Brown, Boveri & Co., Ltd.
Research Center
Baden, Switzerland

C-I-L Inc.
Industrial Chemicals Div.
Montreal, Que., Canada

Cominco Ltd.
Trail, B.C., Canada

Corning Glass Works
Corning, NY

Crawford & Russell Inc.
Stamford, CT

Diamond Shamrock Corp.
Painesville, OH

Duro-Test Corp.
North Bergen, NJ

Eagle-Picher Industries, Inc.
Electronics Div.
Joplin, MO

Eastman Kodak Co.
Rochester, NY

EG&G Princeton Applied Research Corp.
Princeton, NJ

Electric Power Research Institute
Palo Alto, CA

Electrochemical Technology Corp.
Seattle, WA

ELTECH Systems Corp.
Chardon, OH

Energy Development Associates
A Gulf and Western Co.
Madison Heights, MI

Ever Ready Co. (Holdings) Ltd.
Whetstone, London, England

Exmet Corp.
Bridgeport, CT